IN-34

35673

NASA Contractor Report 198465
UM–MEAM–95–01

Report on Pool Boiling Experiment Flown on STS-47 (PBE-IA), STS-57 (PBE-IB), and STS-60 (PBE-IC)

Herman Merte, Jr., Ho Sung Lee, and Robert B. Keller
The University of Michigan
Ann Arbor, Michigan

March 1996

Prepared for
Lewis Research Center
Under Contract NAS3–25812

National Aeronautics and
Space Administration

Abstract

Experiments were conducted in the microgravity of space in which a pool of liquid (R-113), initially at a precisely defined pressure and temperature, is subjected to a step imposed heat flux from a semi-transparent thin-film heater forming part of one wall of the container such that boiling is initiated and maintained for a defined period of time at a constant pressure level. Transient measurements of the heater surface and fluid temperatures near the surface are made, noting in particular the conditions at the onset of boiling, along with motion photography of the boiling process in two simultaneous views, from beneath the heating surface and from the side. The conduct of the experiment and the data acquisitions are completely automated and self-contained. A total of nine tests were conducted at three levels of heat flux and three levels of subcooling under three essentially identical circumstances in three space experiments designated as PBE-IA, -IB, -IC on the STS-47, -57, -60, respectively. Minor differences in lengths of various components of the experiments were programmed in the three flights. Two of the flights (STS-47, -60) took place with the same physical hardware, while the other (STS-57) used an identically fabricated hardware.

The basic mechanisms of pool boiling are reviewed, with particular emphasis on the roles of buoyancy, and the experimental concepts and parameters used are given. The hardware and operating procedures followed are described in some detail.

The experimental results for each of the nine (9) Runs in each of the space flights, along with those from several post-flight ground tests, are given in sufficient detail that the derived parameters and conclusions can be independently obtained, if desired. Sample images are provided for each Run, following digitizing from the 16 mm film.

The absence of buoyancy permitted the onset of boiling at low heat flux levels, with what is deemed as homogeneous nucleation taking place. The influence of these low levels of heat flux and the pressure effect used to produce the bulk liquid subcooling are accounted for by a modification of classical homogeneous nucleation theory. The high levels of liquid superheat at nucleation produced extremely energetic bubble growth rates, which resulted in unusual interfacial behaviors. In certain circumstances vapor bubbles appear to be formed both within the residual liquid microlayer remaining on the surface as the primary boiling front passes by, and in advance of this front. It appears that long term steady nucleate boiling can take place on a flat heater surface in microgravity under special conditions in which a large vapor bubble somewhat removed from the heater surface is formed, which acts as a thermal sink to remove the nucleating bubbles from the heater surface. The steady nucleate boiling heat transfer is enhanced significantly compared to

that in earth gravity. Using quasi-steady data obtained from the measurements it was possible to construct two distinct composite approximate micro-gravity pool boiling curves for R-113, one for the higher level of subcooling and one for the lower level of subcooling. This is compared with a Reference Curve for pool boiling at $a/g = +1$. The microgravity pool boiling curves bear some resemblance to the Reference Curve, although the maximum heat flux is reduced considerably.

Table of Contents

	Page No.
Abstract	i
List of Figures	iv
List of Tables	vii
List of Appendices	viii
Nomenclature	ix
1. INTRODUCTION	1
1.1 General Background	1
1.2 Objectives of Study	3
1.3 Basic Mechanisms of Pool Boiling	5
1.3.1 Nucleate Boiling	5
1.3.2 Dryout (Film Boiling in Earth Gravity)	9
2. EXPERIMENTAL CONCEPTS AND PARAMETERS	10
2.1 Geometry and Configuration	11
2.2 Fluid	12
2.3 Controlled Variables	13
2.4 Measured Parameters	13
3. HARDWARE DESCRIPTION	19
3.1 Heater Surface	19
3.2 Test Vessel	22
3.3 Accelerometer System	22
3.4 Optical System	23
4. TEST MATRICES	34
5. EXPERIMENTAL RESULTS	39
5.1 Measured Parameters	39
5.1.1 Internal to Test Vessel	39
5.1.2 Accelerometer	46
5.2 Results	51
5.2.1 Canister Ambient	51
5.2.2 Text Matrix Results Organization	51
6. DISCUSSION	55
6.1 Conduction Effects	55
6.1.1 Conduction in Substrate	56
6.1.2 Conduction in Fluid	57
6.2 Natural Convection Effects	61
6.3 Nucleation	62
6.4 Bubble Dynamics	78
6.5 Heat Transfer to Fluid	84
7. CONCLUSIONS & RECOMMENDATIONS	130
References	132
Appendices	134

List of Figures

		Page No.
Figure 2.1.	R-113 Degassing Unit Schematic.	18
Figure 3.1.	Transparent gold film heater/resistance thermometer on quartz substrate.	24
Figure 3.2.	Schematic of Test Vessel with concepts to provide constant pressure and initially uniform fluid temperature.	25
Figure 3.3.	Locations of Sensors for Scientific Analysis.	26
Figure 3.4.	Locations of R-113 fluid thermistors in test vessel.	27
Figure 3.5.	Test vessel. Relative locations of internal components, lights and viewing windows.	28
Figure 3.6.	PBE Components in GAS canister. Side view.	29
Figure 3.7.	PBE Components in GAS canister. Front view.	30
Figure 3.8.	Typical correlation between coordinates of the PBE accelerometer and SAMS and STS units. Above applies to PBE-IA (STS-47).	31
Figure 3.9.	Correlation between PBE-IA accelerometer and Photographic view on STS-47. Primary heater is in use on left side.	32
Figure 3.10.	Scheme for LED timing lights in camera field of view.	33
Figure 5.1.	PBE-IA structure temperature in GAS canister.	50
Figure 6.1.	Comparison of 1 - D and 3 - D predicted temperatures with measurements. PBE-IA (STS-47). Run No. 3. $q_T'' = 1.8$ w/cm^2. $\Delta T_{sub} = 10.9°C$.	94
Figure 6.2.	Isometric plot of 3 - D temperature distribution in quartz substrate at 40 seconds. PBE-IA (STS-47). Run No. 3.	95
Figure 6.3.	Isometric plot of 3 - D temperature distribution in quartz substrate at 90 seconds. PBE-IA (STS-47). Run No. 3.	96
Figure 6.4.	Comparison of fluid heat transfer coefficients computed from measured mean heater surface temperatures using 1 - D finite difference and 3 - D finite element models.	97
Figure 6.5.	Measured heater surface temperature filtered by averaging three (3) successive measurement points sequentially.	98
Figure 6.6.	Measured heater surface temperature filtered by averaging five (5) consecutive measurement points sequentially.	99
Figure 6.7.	Comparison of the fluid heat transfer coefficients obtained by taking the input heat flux as constant or variable.	100

Page No.

Figure 6.8. Layout of gold film heater surfaces on quartz substrate. 101

Figure 6.9. Layout of heater surfaces from underside, with 3 - D finite element grid and nucleation sites superimposed. PBE-IA-IB-IC. (STS-47-57-60). 102

Figure 6.10. Heater surface temperature at Nodes of Figure 6.9 computed with 3 - D finite element model of PBE heater geometry. $q_T'' = 7.0$ w/cm^2. Run Nos. 1-3. 103

Figure 6.11. Heater surface temperature at Nodes of Figure 6.9 computed with 3 - D finite element model of PBE heater geometry. $q_T'' = 3.5$ w/cm^2. Run Nos. 4-6. 104

Figure 6.12. Heater surface temperature at Nodes of Figure 6.9 computed with 3 - D finite element model of PBE heater geometry. $q_T'' = 1.75$ w/cm^2. Run Nos. 7-9. 105

Figure 6.13. Local R-113 temperature distribution at nucleation at heater surface sites indicated on Figure 6.9. PBE-IA (STS-47). 106

Figure 6.14. Local R-113 temperature distribution at nucleation at heater surface sites indicated on Figure 6.9. PBE-IB (STS-57). 107

Figure 6.15. Local R-113 temperature distribution at nucleation at heater surface sites indicated on Figure 6.9. PBE-IC (STS-60). 108

Figure 6.16. Schematic for development of heterogeneous nucleation. 109

Figure 6.17. Values of maximum critical size nucleation cavities computed from measured heater surface superheats of the PBE in GAS. 110

Figure 6.18. Values of minimum critical size nucleation cavities computed from measured heater surface superheats of the PBE in GAS. 111

Figure 6.19. Values of maximum and minimum critical size nucleation cavities computed from measured heater surface superheats of PBE-IA (STS-47). 112

Figure 6.20. Values of minimum critical size nucleation cavities superimposed at physical locations of nucleation for PBE-IA and -IC (STS-47 and -60)... 113

Figure 6.21. Values of minimum critical size nucleations cavities superimposed at physical locations of nucleation for PBE-IB (STS-57). 114

Figure 6.22. Relationship between minimum critical size nucleation cavities computed from measured heater surface superheat and typical grit size used for polishing the heater surface, and liquid temperature distribution at nucleation. PBE-IA (STS-47). 115

Page No.

Figure 6.23. Relationship between minimum critical size nucleation cavities computed from measured heater surface superheat and typical grit size used for polishing the heater surface, and liquid temperature distribution at nucleation. PBE-IB (STS-57). 116

Figure 6.24. Relationship between minimum critical size nucleation cavities computed from measured heater surface superheat and typical grit size used for polishing the heater surface, and liquid temperature distribution at nucleation. PBE-IC (STS-60). 117

Figure 6.25. Gibbs Number for R-113. 118

Figure 6.26. Homogeneous nucleation model for R-113 with transient heating in microgravity. Nucleation measurements with PBE-IA-IC (STS-47-60). K^* evaluated for PBE-IA. Run No. 9. 119

Figure 6.27. Homogeneous nucleation model for R-113 with transient heating in microgravity. Nucleation measurements with PBE-IB (STS-57). K^* evaluated for PBE-IB. Run No. 5. 120

Figure 6.28. Semi-log plot. Homogeneous nucleation model for R-113 with transient heating in microgravity. Measurements with PBE-IA-IC (STS-47-60). K^* evaluated for PBE-IA. Run No. 9. 121

Figure 6.29. Semi-log plot. Homogeneous nucleation model for R-113 with transient heating in microgravity. Measurements with PBE-IB (STS-57). K^* evaluated for PBE-IB. Run No. 5. 122

Figure 6.30. Comparison of measured mean heater surface superheat and derived heat transfer coefficient between Space Flight and a/g = +1 Post Flight Test. PBE-IC (STS-60). Run No. 2. 123

Figure 6.31. Comparison of Post Flight nucleate pool boiling data with other R-113 data at a/g = +1 to demonstrate variability with different systems of gold films on quartz substrates. 124

Figure 6.32. Direct comparisons of nucleate pool boiling of R-113 between identical systems at a/g = +1 and approximate microgravity conditions... 125

Figure 6.33. Comparison of nucleate pool boiling data in microgravity with a Pool Boiling Reference Curve for R-113 at a/g = +1. 126

Figure 6.34. All heat transfer coefficient data obtained with PBE-IA-IB-IC (STS-47-57-60) under quasi-steady conditions, both at a/g = +1 and in microgravity. 127

Figure 6.35. Quasi-steady heat transfer coefficient data as a function of heat flux to fluid, for high subcooling level. 128

Figure 6.36. Approximate composite microgravity pool boiling curves for R-113 from steady and transient measurements on PBE-IA-IB-IC (STS-47-57-60). 129

List of Tables

		Page No.
I.	Specific Technical Requirements	16
II.	Coefficients for the Vapor-Pressure Curve for R-113.	17
III.	Heater Surface Calibration Coefficients for PBE-IA.	21
IV.	Test matrix for PBE-IA on STS-47. (Prototype Hardware)	36
V.	Test matrix for PBE-IB on STS-57. (Flight Hardware)	37
VI.	Test matrix for PBE-IC on STS-60. (Prototype Hardware)	38
VII.	PBE-IA. Parameters measured at ag = -1 and a/g = +1 in Pre flight and Post flight tests, and during STS-47 Space Flight.	40
VIII.	PBE-IB. Parameters measured at a/g = -1 in Pre-flight and Post-flight tests, and during STS-57 Space Flight.	42
IX.	PBE-IC. Parameters measured at a/g = -1 and a/g = +1 in Preflight and Post-flight tests, and during STS-60 Space Flight.	44
X.	Summary of relatively large acceleration excursions during PBE-IA in STS-47 Flight.	47
XI.	Summary of relatively large acceleration excursions during PBE-IB in STS-57 Flight.	48
XII.	Summary of relatively large acceleration excursions during PBE-IC in STS-60 Flight.	49
XIII.	Gibbs Number for R-113.	70
XIV.	Number of film frames obtained with hemispherical bubbles following nucleations. PBE-IA-IB-IC (STS-47-57-60).	79
XV.	Comparison of measured mean heat transfer coefficients between STS-47-57-60 Space Flights and a/g = +1 Post Flight Tests.	85
XVI.	Measurement summary of transient dry-out and rewetting on heater surface in microgravity. PBE-IA-IB-IC (STS-47-57-60).	93

List of Appendices

Page #

A. PBE-IA (STS-47). Experimental Results. A-1
B. PBE-IB (STS-57). Experimental Results. B-1
C. PBE-IC (STS-60). Experimental Results. C-1
D. Thin Film Heater/Resistance Thermomete: Assessment of Effect of Local Temperature Variations on Mean Temperature Measurement..... D-1
E. Procedure for Computation of Mean Microgravity Nucleate Boiling Heat Transfer Coefficient E-1

Nomenclature

a	Thermal diffusivity
b	$= (P_s - P_\ell)/Ps$
C	Defined in Eq. (6.12)
F_g	Bubble growth fraction - Eq. (6.36)
G	Gibbs No. - Eq. (6.15)
h	Planck constant
h_{fg}	Latent heat of vaporization
k	Boltzmann constant, Thermal conductivity
m	Mass/molecule
n	No. of molecules/liquid volume
P	Pressure
q''	Heat flux
r_c	Critical bubble radius
R	Bubble radius, Electrical resistance
T	Temperature
t	Time
v	Specific volume
W	Work of formation of vapor bubble
x	Distance from heater surface
λ_m	Latent heat/molecule
ρ	Density
σ	Surface tension
τ	Nucleation time

Subscripts

cr	Critical
i	Initial
ℓ	Liquid
s	Saturation
v	Vapor
w	Wall

1. INTRODUCTION

1.1 General Background

Nucleate boiling is an important mode of heat transfer in that relatively small temperature differences can provide large rates of heat transfer, which can result in significant economic and other benefits associated with the smaller heat transfer areas necessary to accomplish a given function.

A limitation in the development of more compact power sources using nuclear energy lies in the ability to remove the large heat generation rates possible from the reactor core in a manner that is consistent, reliable and predictable. Nucleate boiling would be a candidate for wide spread use in such an application were the fundamental mechanisms that govern the process sufficiently well understood. Additional important applications of nucleate boiling exist, such as steam generation in conventional power plants, distillation processes in petroleum and other chemical plants, and the boiling of refrigerants in cooling coils, in which the motion of the bulk liquid is generally imposed externally. This is termed forced convection boiling, and the liquid motion moves the vapor formed away from the heated surface so that the vapor may be utilized and/or further processed and the nucleate boiling process can continue.

Other applications exist in which externally forced flow is absent, where buoyancy provides the major mechanism for vapor removal from the vicinity of the heating surface, and is generally designated pool boiling. Even in circumstances where forced convection exists to some extent, the forces associated with flow acting on the vapor bubbles may be sufficiently small that buoyancy or body forces will continue to be responsible for the vapor removal process. It should then be possible to describe the behavior, in terms of the basic governing mechanisms, by the pool boiling process. Devices in which pool boiling occurs are two-phase closed thermosyphons, reboilers, and heat pipes, whether gravity assisted or not. Potentially significant applications exist in the cooling of microelectronic circuitry and the internal cooling of gas turbine blades. The latter would involve pool boiling under high gravity fields, and its successful application would permit higher operating temperatures with attendant higher efficiencies, and would also eliminate the need for the development of exotic ceramic materials with the difficulties of thermal stresses and reliability. Another important and as yet poorly understood area incorporated in the mechanism of pool boiling is the breakdown of film boiling into the transition boiling regime. This is of concern in the loss-of-coolant accident in nuclear power plants, and is encompassed in the reflooding and fuel element rewetting processes. A good

understanding of this rewetting process in microgravity or in the absence of buoyancy would improve its application with buoyancy.

The effective and enhanced applications of both nucleate pool and forced convection boiling requires a sound understanding of the mechanisms governing the processes. The vapor removal from the vicinity of the heater surface, as understood to this point, occurs primarily by buoyancy in the case of pool boiling and bulk liquid inertia in the case with forced convection. Although the variation of both gravity and forced flow are known to influence the overall heat transfer processes, other forces or potentials are acting as well, and the relative significances of these are as yet poorly understood.

Requirements for the proper functioning of equipment and personnel in the space environment of reduced gravity and vacuum, as will be necessary in space station modules and space power generation, introduce unique problems in temperature control, power generation, energy dissipation, the storage, transfer, control and conditioning of fluids (including cryogenic liquids), and liquid-vapor separation.

The temperature control in certain locations where internal heat generation takes place as a result of dissipation, as from friction or joulian heating in electronic equipment, or as a consequence of a nuclear or chemical heat source, may require that this energy be transported to other locations of the facility or stored locally for later transport and elimination. The use of the phase changes of vaporization and condensation to transport energy have the advantage of accommodating large variations in heat loads with relatively small temperature gradients and changes in temperature levels, along with the economical use of pumping power. Energy storage might be advantageous for intermittent processes or for processes where momentary surges could not be accommodated by a steady transfer of mass to a remote location, and also could take advantage of the latent heat associated with phase changes.

A distinction must be made between pool boiling and flow boiling when considering applications in the space environment of microgravity, since these two processes may arise in quite different specific technical applications. Pool boiling, for example, would be important for the short term cooling of high power electronic and other devices, and for the long term space storage of cryogens. Flow boiling, on the other hand, occurs in applications where liquid flow is imposed externally, such as in Rankine cycle vapor generation or in thermal energy management using pumped latent heat transport.

Certain effects which can be neglected at normal earth gravity, such as surface tension and vapor momentum, can become quite significant at microgravity conditions. Momentum imparted to the liquid by the vapor bubble during growth tends to draw the vapor bubble away from the surface, depending on the rate of growth, which in turn is

governed by the temperature distribution of the liquid. Thermocapillary forces, arising from the variation of the liquid-vapor surface tension with temperature, on the other hand, tend to move the vapor bubble toward the region of higher temperature. The bubble motion will be governed by which of these two effects prevail. In addition, thermocapillary forces acting at the liquid-vapor interface of vapor bubbles in contact with a heated surface could act to bring cooler liquid to the heater surface, delaying or inhibiting the onset of dryout, or promoting and enhancing the rewetting of the heater surface.

1.2 Objectives of Study

The research as originally proposed was intended to seek to improve the understanding of the fundamental mechanisms that constitute nucleate pool boiling. The vehicle for accomplishing this is an investigation, including experiments conducted in microgravity and coupled with appropriate analyses, of the heat transfer and vapor bubble dynamics associated with nucleation, bubble growth/collapse and subsequent motion, considering the interrelations between buoyancy, momentum and surface tension which will govern the motion of the vapor and surrounding liquid, as a function of the heating rate at the heat transfer surface and the temperature level and distribution in the bulk liquid.

As will become clear when the results obtained to date are examined below, a more accurate representation of the objectives would have been a proposal for a general study of pool boiling in microgravity. The circumstances under which nucleate boiling and what is generally termed, to this point, film boiling take place with pool boiling in microgravity is as yet unclear. Both of these processes were observed, sometimes simultaneously, in the work to be presented here.

An adequate understanding of the mechanisms in any process implies that its behavior can be predicted in terms of the governing parameters. The behavior here would include the conditions for the onset of boiling, the dynamics of the vapor bubbles, including both the number density of active nucleating sites and the frequency of formation, and the associated heat transfer. Although a considerable amount of research has been conducted on nucleate boiling over the years, and has been useful with respect to application to various technologies on earth, the ability to predict its behavior is as yet very limited, owing to the involvement and interactions of the many parameters. To this now should be added also the limitations in predicting the onset of dryout or rewetting, whether in earth gravity or microgravity.

For the basic study proposed and conducted, with results presented here, it was deemed essential to establish a well-defined "bench mark" which could withstand future interrogations. The availability of a long period of quiescence prior to the onset of each

test, as a result of the microgravity environment, means that the initial state at the onset of heating and at the onset of boiling (nucleation) will be well-defined. This is not possible in a gravity field. The availability of relatively long test periods permit the use of combinations of low heat flux and subcooling that require more time for the inception of boiling than is available in a drop tower, and also permit the observing of long-term vapor dynamic behavior following the transient bubble growth.

The components which constitute the nucleate boiling process-nucleation, growth, motion, collapse (if subcooled) of the vapor bubbles - are common to both pool and flow boiling. The study here focuses on the fundamental mechanisms of pool boiling only, under microgravity conditions. This eliminates the complications associated with having an external flow field superimposed on that generated by growing/collapsing vapor bubbles. In addition, this eliminates the possibility of having other effects masked by an external flow field similar to that produced by buoyancy.

In the experiments as conducted, a pool of liquid, initially at a precisely defined pressure and temperature, is subjected to a step imposed heat flux from a semi-transparent thin-film heater forming part of one wall of the container such that boiling is initiated and maintained for a defined period of time at a constant pressure level. Transient measurements of the heater surface and fluid temperatures near the surface are made, noting in particular the conditions at the onset of boiling, along with motion photography of the boiling process in two simultaneous views, from beneath the heating surface and from the side. The conduct of the experiment and the data acquisitions are completely automated and self-contained. Three space flights were successfully carried out, with each one consisting of a total of nine tests at three levels of heat flux and three levels of subcooling.

Following the successful development work conducted during the ground-based activity under NASA Grant NAG3-663, which included reduced gravity testing in the evacuated 5 second drop tower at the NASA Lewis Research Center, the results of which were reported in Ervin and Merte (1991), Ervin et al (1992), and Lee and Merte (1993), approval was given for a space experiment. An Engineering Model was developed by the NASA Lewis Research Center for testing the feasibility of incorporating the experimental concepts described in the Science Requirements Document by Merte (1989) into the space available in a Get-Away-Special (GAS). Following the successful demonstration of the operation of the Engineering Model, the construction of a Prototype Version was undertaken. This proved to operate so successfully with full testing in earth gravity that when an opportunity for an unexpected early GAS flight came to light a request was made to fly the Prototype Version. This was justified primarily as an opportunity to further test the heretofore untried engineering concepts in the facility, and to confirm the camera

timings which could not be determined in the drop tower testing. The successful acquisition of any experimental measurements was thus viewed to be a bonus. This experiment flew in the STS-47 on September 12, 1992, and was designated as PBE-IA. The basic results are presented in Merte et al (1994), and are included in the present report for the sake of completeness, together with additional material resulting from subsequent analyses.

The Flight Version of the experimental apparatus was designated as PBE-IB, and flew in the STS-57 on June 21, 1993. Subsequent to this, another opportunity for a space flight with the Prototype Version occurred, which was approved and designated as PBE-IC, and took place in the STS-60 on February 3, 1994.

The experimental parameters in these three flights are identical, with differences only in the length of the individual test runs and the timing of the on-off and speed of the camera, to optimize the use of the fixed film length. As will be demonstrated when the experimental results are examined, the fortuitous opportunity for conducting the seemingly same experiment three times contributes immensely to authenticating some of the conclusions reached to this point. By using the identical physical facility, as between the STS-47 (PBE-IA) and STS-60 (PBE-IC), the issue of repeatability could be addressed. By using a physical facility with the same design and fabrication techniques, as with PBE-IB on STS-57, the matter of reproducibility could be examined.

1.3 Basic Mechanisms of Pool Boiling

As stated above, consideration of any externally imposed flow field on the boiling process, termed as forced convection boiling, is explicitly excluded here in order to:

(a) Eliminate an additional complicating variable from an already complex process at the outset. Pool boiling is the limiting case of forced convection boiling as the imposed velocity is reduced to zero.

(b) Minimize the possibility that certain weak effects would be overshadowed by the kinetic energy associated with the imposed bulk liquid flow. The supposedly weak effects were considered to consist primarily of thermocapillary and molecular momentum forces.

1.3.1 Nucleate Boiling

Nucleate boiling may be characterized by the following:

(i) A liquid-vapor phase change occurs with the formation of discrete bubbles at individual sites.

(ii) The energy transfer rates are large with small temperature difference driving potentials.

(iii) The process is inherently transient, although quasi cyclic repetitions are possible with vapor removal mechanisms acting, such as buoyancy.

Before a nucleate pool boiling system can attain the steady periodic behavior normally observed in a gravity field, where buoyancy is the dominant vapor removal mechanism, the process must pass through a transient phase referred to as the nucleation, initiation or onset of nucleate boiling. Before understanding the cyclic nature of nucleate boiling, one must first understand the elements of the initial transient process.

To provide a perspective of the relationship between the study conducted here and the overall processes which constitute pool boiling, a qualitative physical description of the sequence of events which occur is presented, beginning with the transient heating of a liquid at a solid-liquid interface.

a. Conduction

With an initially static liquid the heat transfer process can be described by conduction alone until buoyancy, thermophorysis, thermocapillarity or other forces set the liquid in motion. The rate of temperature rise and the temperature distributions in this early interval depend on the nature of the heat source and the dynamic interactions with the system. The common idealizations taken as limits in analyses are step changes in either temperature or heat flux at the solid-liquid heater interface. The degree and extent to which the liquid becomes superheated above its saturation temperature in a given time depends on whether and by how much the bulk liquid is subcooled. This temperature distribution will be modified by the onset of natural convection or by other disturbances.

b. Onset of Natural convection

Natural convection is driven by buoyancy, and its onset is described in terms of an instability, in which enervating disturbances are always present. Reducing the buoyancy by reducing the body forces such as to microgravity delays the onset of the convection and reduces the resulting convection velocities. Both of these serve to increase the temperature levels in the liquid adjacent to the heating surface for a given heating time, regardless of whether the bulk liquid is initially saturated or subcooled. The liquid temperature levels and distributions adjacent to the heater surface are thus influenced by buoyancy, and in turn can influence the next two elements of nucleate boiling: the nucleation and bubble growth rates.

c. Nucleation

Vaporization can take place only at an existing liquid-vapor interface, which then constitutes the growth phase of nucleate boiling. If an interface does not exist it must be formed. The formation of a vapor nucleus is called nucleation, and is classified either homogeneous or heterogeneous, depending on the presence of other components or species in the vicinity of the nucleation. The circumstances under which nucleation takes place on a heated solid surface depends on:

(i) The Heater Surface Microgeometry. This can provide the crevices and intergranular defects which serve as pre-existing interfaces. The temperature levels required to activate these pre-existing nuclei have been modeled in terms of thermodynamic equilibrium at curved liquid-vapor interfaces. Assuming that the pre-existing interface has the form of a hemisphere of the size of the surface defect, the liquid superheat required for subsequent bubble growth can be related to cavity size. The smaller is the cavity, the larger is the heater surface superheat required for the onset of nucleate boiling, and the larger will be the bulk liquid temperatures at the onset of the next element of the boiling process.

(ii) The Solid-Fluid properties. This governs not only the temperature distributions in both the heater and fluids, related by their respective thermal properties, but also the surface energy relationships between the solid-liquid-vapor, often expressed in terms of a contact angle or wettability.

(iii) The Liquid Temperature Distribution. This includes the solid-liquid interface temperature, since this is one spatial limit of the liquid temperature. As discussed under "b" above, the onset of natural convection governs the subsequent temperature distributions, as does also the initial imposed heat flux. Once nucleation has occurred, the subsequent bubble growth rates will be governed by the bulk liquid temperature distribution at this time.

d. Vapor Bubble Growth/Collapse

Vapor bubble growth requires that the liquid at the liquid-vapor interface be superheated with respect to the saturation temperature corresponding to the interfacial liquid pressure. The rate of vapor formation, and hence bubble growth, depends on this superheat and on the liquid temperature gradient at the interface, and thus on the liquid temperature distribution at the onset of bubble growth. The interfacial liquid superheat governs the internal vapor bubble pressure, which acts to move the bulk liquid away from

the vicinity of the heater surface. In the dynamics of the growth process this pressure is balanced in a complex manner by the liquid inertia, liquid viscosity, buoyancy, and surface tensions. If the bulk liquid is subcooled, the pressure difference can reverse with the subsequent collapse of the vapor bubble. The various forces acting in the bubble growth/collapse can be summarized:

(i) Internal Bubble Pressure. This is governed by the liquid temperature distribution, which in turn is influence by buoyancy.

(ii) Liquid Momentum. This is sometimes referred to as bulk liquid inertia.

(iii) Buoyancy. The pressure differences associated with the liquid-vapor density differences in a body force field act in addition to those natural convection effects which influence the liquid temperature distribution.

(iv) Surface Tension. This includes both that occurring at the liquid-vapor interface and at the liquid-solid-vapor interline.

(v) Viscosity. This refers primarily to the liquid viscosity acting in the vicinity of the solid surface, but could include the viscous normal shear at the liquid-vapor interface away from the solid surface in circumstances where the radial growth rate is very large. Vapor viscosity could also be a factor during the very early periods when surface rates of vapor formation are large.

Since the liquid-vapor interface is deformable, the interfacial shape during growth will be governed by the net balance of the dynamic forces acting at each point on the interface, and the interface will not necessarily be spherical or hemispherical, as has been assumed in the absence of capabilities for dealing with flexible interfaces.

e. Departure

The subsequent motion of the vapor bubble depends on the net effect of the forces listed in "d" above, plus a phenomena associated with simultaneous evaporation and condensation across a vapor bubble, referred to as a molecular momentum effect. This is related to the molecular kinetic energy necessary for vapor molecules to escape or to be retained at a liquid-vapor interface. With thermodynamic equilibrium the net rate of evaporation and condensation is zero, but the normal nucleate boiling process is highly non-equilibrium. The net resulting molecular momentum forces are generally unobservable in the presence of the overwhelming body and other forces which usually exist. The bulk liquid momentum induced by the rapid bubble growth can act to assist in the removal of the bubble from the heater surface. In microgravity, of course, buoyancy effects are reduced significantly.

f. Motion Following Departure

If the circumstances of the forces acting on the vapor bubble are such that departure takes place, the subsequent motion depends on the following:

(i) Buoyancy

(ii) Initial velocity upon departure. This velocity induces momentum in the bulk liquid, which must be considered, and can tend to accelerate the vapor bubble if collapse takes place, or will decelerate the bubble if it grows.

(iii) Degree and distribution of liquid superheat and/or subcooling. The bulk liquid temperature distribution can act via the liquid-vapor surface tension or Marangoni-induced effects, via the bulk liquid momentum effects associated with growth or collapse, together with liquid viscosity, and via the molecular momentum effects. In microgravity conditions, only buoyancy will be changed, except for its more indirect influence on the bulk liquid temperature distribution.

1.3.2 Dryout (Film Boiling in Earth Gravity)

Nucleate boiling can take place only in circumstances where the liquid substantially wets the heater surface. This entails two implications. First, the liquid itself must be inherently wetting on the heater surface. As observed and discussed by Merte (1967), it is well known, for example, that mercury is generally non-wetting except for materials with which it forms amalgams. For the operation of power generation plants with mercury boilers it was necessary to add traces of Magnesium and Titanium to the mercury to promote wetting and nucleate boiling in the boiler tubes. The second implication is that the vapor generation rate and hence the heat flux level is not sufficiently high to reach the critical heat flux, sometimes referred to as the first boiling crisis, the nucleate boiling maximum heat flux, or the burnout heat flux. A specific heater surface temperature is generally related to this heat flux, and if the heater surface temperature exceeds this level a decrease in the heat transfer rate takes place, hence the term maximum heat flux. This decrease takes place because of a progressive increase in the dryout of the surface until the liquid is no longer in contact with the heater surface. This condition is then referred to as film boiling, since in the buoyancy of earth gravity the vapor takes on the form of a thin vapor film or boundary layer in contact with the heater, and departure of the vapor from the vicinity of the heater occurs in various ways depending on the heater surface configuration and orientation relative to gravity. The minimum heater surface temperature at which film boiling can be sustained at its corresponding heat flux is referred to as the minimum film boiling heat flux, the Leidenfrost point, or the second boiling crisis.

The so-called transition boiling region between the first and second boiling crises can be considered as a spatially averaged combination of nucleate boiling and film boiling, in which the fractional proportion of film boiling or dryout changes from 0 to 1 over this domain. This perspective neglects the contributions of dry areas under individual bubbles at the individual nucleation sites. In the present work, the use of the transparent heater surface permits the direct viewing and assessment of the relative proportions of the dry areas on the heater surface. The processes of the first and second boiling crises, including the transition boiling regime between, can be generically designated by a single term as dryout or wetting, depending on the direction in which this inherently transient or dynamic process is taking place. It appears that the circumstances of operation in the transition region taking place during pool boiling in microgravity are considerably less well-defined than in earth gravity, and could be the subject of further studies.

2. EXPERIMENTAL CONCEPTS AND PARAMETERS

The basic study conducted here is intended to assist in extending the understanding of the mechanisms of nucleate pool boiling. Because of the complexity associated with the conduct of research in a microgravity environment it is essential to establish a well defined "bench mark" which will not require repeating, insofar as is practicable in view of present understandings. The availability of a reasonably long period of quiescence prior to the onset of each test means that the initial state at the onset of heating and at the onset of boiling (nucleation) can be well-defined. The availability of relatively long test periods for each run, with a maximum value of 2 minutes selected as representing a compromise, permits the combinations of low heat flux and subcooling that require more than the 5 seconds previously available in a drop tower for the inception of boiling, and also permits the observing of long-term vapor dynamic behavior following the transient bubble growth. Although the experiment as conducted is quite specific and well defined, it is also exploratory in nature, and has the potential for relatively fast turn-around with follow-on experiments.

The elements of nucleate boiling for which research conducted under microgravity would advance the basic understanding are stated in brief here:

(i) Nucleation or onset of boiling. Indications are that both heater surface temperature and temperature distribution in the liquid are necessary to describe nucleation, in addition to the character of the heater surface itself.

(ii) The dynamic growth of a vapor bubble in the vicinity of the heater surface. This includes the shape as well as motion of the liquid-vapor interface as growth is taking place. These are influenced by the liquid temperature distribution at the initiation of growth.

(iii) The subsequent behavior of the vapor bubble. This includes the motion, whether departure takes place or not, and the associated heat transfer.

Each of the specific features of the experiment were selected so as to provide data which will be consistent with and maximize the objectives of improving the basic understanding embodied in these elements. These features are described individually below.

2.1 Geometry and Configuration

(a) Pool boiling. This eliminates the complications associated with having an external flow field superimposed on that generated by a growing/collapsing vapor bubble.

(b) Large flat heater surface. A flat surface avoids poorly defined local surface tension effects associated with curved interfaces, and with a transparent substrate can permit viewing from beneath the heater surface. A size as large as possible consistent with other constraints is desirable in order to minimize edge effects, and to permit a reasonable degree of axial symmetry of the vapor bubble as it grows to a quasi-steady condition. Additional considerations associated with large flat heater surfaces are:

(i) With heating from curved surfaces, different liquid flow patterns will occur during bubble growth depending on whether the liquid is on the convex or concave side.

(ii) With flat surfaces, which may also be approximations of curved surfaces, the orientation with respect to the body force vector will affect the flow behavior, down to some (as yet) unknown body force level.

(iii) The fluid motion with large surfaces will differ depending on whether the surface is heated uniformly or locally.

One further facet of vapor bubble nucleation and growth as influenced by surface tension and related to geometry can be mentioned here. The superheat that the liquid acquires in the boundary layer adjacent to the heater surface can be considerable, prior to nucleation. It is thus possible for the vapor formed initially to completely envelope the heater surface. With certain configurations such as small wires or cylinders it is possible that subsequent surface tension effects will maintain a stable "pseudo" film boiling process only because of the particular geometry used. It is expected that even if film boiling becomes suppressed to nucleate boiling on a small wire or cylinder, thermocapillary and surface tension effects and the resulting heat transfer will be quite different than with flat surfaces. Observations made by Weinzierl and Straub (1982) that pool nucleate boiling is uninfluenced by changes from earth gravity to microgravity are believed to be a result of the large surface tension effects associated with the fine wire used, so that buoyancy is indeed relatively unimportant.

(c) Transparent heater surface. This permits the observation of the detailed behavior of the boiling process from beneath the heating surface, including rewetting of the heater surface and possibly the microlayer behavior, without distortions due to intervening liquid-vapor interfaces. The transparent surface also permits viewing of the behavior of the liquid-vapor interfaces simultaneously from the side and from under the heater surface, providing details of behavior otherwise not observable.

(d) Thin-film heater. Using the technique of a thin gold film as a simultaneous heater and resistance thermometer provides a well-defined heat flux and temperature at a precise location, as well as a transparent heater surface.

2.2 Fluid

The fluid to be boiled must be non-conducting at present. The fluid is in direct contact with the electrical resistance heat source, and a conducting fluid such as water would quickly destroy the thin film surface. For energy conservation in the conduct of the experiment and convenience in comparing results with ground tests it is desirable that the fluid have a boiling point in the vicinity of earth ambient temperatures at near atmospheric pressures. It is further desirable that the fluid used initially have wetting characteristics with the heater surface such that the contact angle is relatively small, in order to evaluate

fluids expected to be early candidates for space use, such as cryogenic liquids. The fluorocarbon R-113 meets these requirements, and its properties are well established.

2.3 Controlled Variables:

(a) Pressure. This defines the liquid saturation temperature, and maintaining it constant keeps the temperature at the liquid-vapor interface constant at the saturation level during the transient process. The pressure level also defines the initial liquid subcooling.

(b) Initial uniform temperature in the bulk liquid. This permits the precise calculation of the temperature distribution in the liquid at the onset of boiling, in the absence of buoyancy.

(c) Step change in a uniform heat flux. This permits the ready computation of the temperature distribution in the liquid at the point of nucleation. A constant imposed heat flux provides a well-defined temperature gradient in the liquid at the heat transfer surface. Additionally, it is possible to construct all other desired functional behaviors in heat flux from combinations of step changes.

(d) Length of test. Each individual test should be as long as possible consistent with compromises arising between the internal volume of the test vessel, heater surface size and heat flux, so that a reasonably quasi-static condition can be attained when the early dynamic growth transients are completed. Additionally, certain liquid temperature distributions at the time of nucleation will only be possible with low levels of heat flux, which will require relatively long test periods to achieve nucleation. Independent control of the initial liquid subcooling and imposed heat flux permit the independent variation of the transient temperature distribution in the liquid.

2.4 Measured Parameters:

(a) Bulk liquid temperature distribution. This is necessary to be assured of the uniformity of the initial temperatures.

(b) Transient temperature of the thin film heater surface. During the non-boiling phase, this serves as an indication of the presence/absence of natural convection effects. During the boiling phase this provides a means for computing the net mean heat flux to the boiling fluid. It also provides a measure of the effectiveness of the boiling heat transfer process.

(c) Local system acceleration. This is necessary to assess the presence/absence of uncontrolled acceleration forces acting on the experimental vessel.

(d) Precision current/voltage drops across the thin film electrical heater. This permits computation of the heater resistance and hence mean heater surface temperature, as well as the heat flux.

(e) Photography. This enables the determination of the time interval between the onset of heating and boiling, along with the transient growth of the vapor bubble and its subsequent motion, as a function of the initial liquid temperature distribution, governed by the heat flux and initial liquid subcooling.

The specific technical requirements for the experiment, taken from the Science Requirements Document, are listed in Table I. These are identical for each of the three flights, and were attained in each of the experiments.

The vapor-pressure equation and coefficients used for the R-113 are given in Table II. The commercial R-113 was purified and degassed by distillation, filtering, and freezing under a vacuum on stainless steel fins cooled to liquid nitrogen temperatures. The apparatus used is shown schematically in Figure 2.1. The distillation was repeated, and followed by measurement of the vapor-pressure under equilibrium conditions. The R-113 was deemed to be adequately degassed when the measured vapor-pressure corresponded to that given by the equation in Appendix B to within $\pm$ 0.025 psia for temperatures measured to within a calibrated accuracy of $\pm$ 0.1°F in the laboratory.

The Resistance — Temperature relationship for the heater surface was determined by calibration over the anticipated temperature operating range prior to installation in the experiment test vessel. Prior experience had demonstrated that a linear relationship was entirely adequate. Although maximum laboratory absolute measurement uncertainties of $\pm$ 1°F ($\pm$ 0.6°C) in the mean heater surface temperatures were attained, these were increased to $\pm$ 3°F ($\pm$ 1.7°C) for the space experiments. However, instrumentation equipment

sensitivities were requested to detect changes in heater surface temperatures of ± 1°F (± 0.6°C), if not the absolute uncertainty. To reduce the uncertainties, a single point calibration was conducted prior to each test run of the test matrix, using the prevailing equilibrium system temperature as an anchor point of the linear calibration curve. A post-flight calibration was conducted of the prototype version following the STS-60 (PBE-IC), and included the calibration of the power supply measurements simultaneously. Although a total shift of 10.4°F (5.8°C) took place since the pre-flight calibration for the STS-47 (PBE-IA), the change in the R-T slope was negligibly small, and the shift was compensated by the procedure of a single-point calibration prior to each Run.

Table I.

Specific Technical Requirements

Parameter	Requirement
Test Fluid	Fluorocarbon R-113
Heating Surfaces	19.05 mm x 38.1 mm (3/4" x 1-1/2" Gold on Quartz ($7.25\ cm^2$) Nominal thickness corresponding to a resistance of 3.8 ± 0.2 ohms (Approximately 400 Angstroms), uniform to ± 5% desired.
Test Heat Flux	2 watts/cm^2 14.5 watts 4 watts/cm^2 29.0 watts 8 watts/cm^2 58.0 watts
Test Chamber	15.2 cm (6") Dia. x 10.2 cm (4") High
Temperature Uniformity	± 0.22°C (± 0.4°F)
Nominal Test Temperature	48.9°C (120°F)
Pressure Control	± 690 N/m^2 (± 0.1 psi)
Heater Power	Constant voltage ± 1%. Heater calibration current should not raise heater temperature more than 0.11°C (0.2°F).
Temperature Sensor	12 Sensor Locations 3 Vicinity of each Heater Surface 3 in Bulk Liquid 2 on the Rear of Heater Substrate 1 in surrounding area behind substrate.
Data Requirements	V, I, Time... (19 parameters).
Heater V & I	± 0.1% Meas. Accuracy, but with a sensitivity of ± 0.03% x a full scale.
Temperatures	± 0.06°C (± 0.1°F) Meas. Accuracy
Pressure	± 345 N/m^{2-} (± 0.05 psi) Meas. Accuracy.
Acceleration (3 Axis)	Levels less than 10^{-3}g desired.
Data Requirements	Time correlated to experimental elapsed time Sample Rate - 10 Hz Accuracy - ± 10^{-4} Range - 10^{-2} thru 10^{-4} g Frequency - D.C. thru 2.5 Hz
Photography	100 pps, 10 pps, 0.18 mm (0.007") Resolution
Clock	Nearest 0.01 Sec. Elapsed Time

Table II.

Coefficients for the Vapor-Pressure Curve for R-113

(From Mastroianni et al, 1978)

$$\ell n\, p = A + \frac{B}{T} + CT + DT^2 + (E)\left[\frac{(F - T)}{T}\right]\left[\ell n\,(F\text{-}T)\right]$$

where:

p	=	pressure = psia
T	=	Temperature in °R ≡ °F + 459.67
A	=	+ 23.428348
B	=	- 9095.6033
C	=	- 0.012548607
D	=	+ 5.3391227 x 10^{-6}
E	=	+ 0.14025795
F	=	+ 878.48416
ℓn x	=	Natural logarithm of argument x.

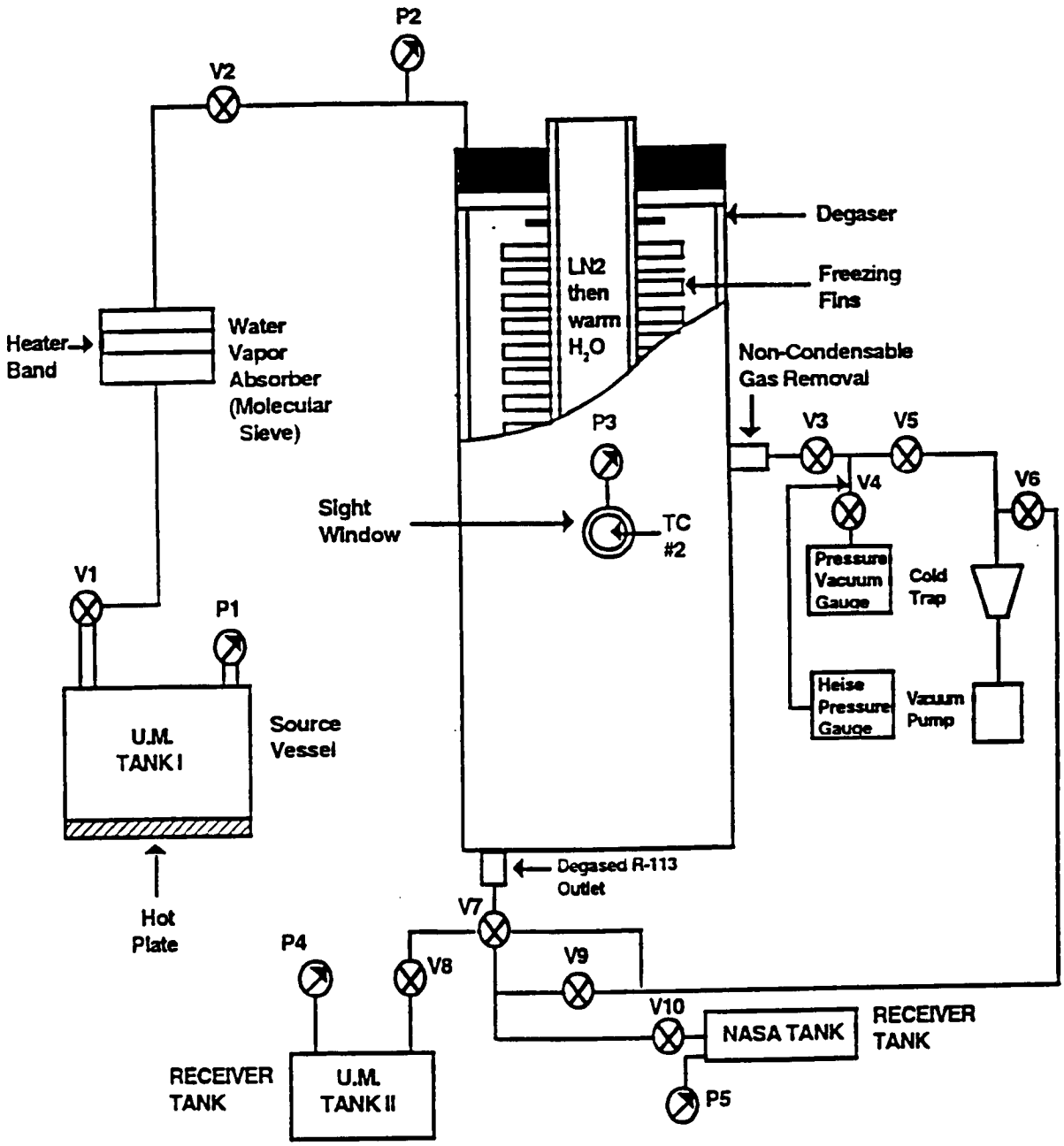

Figure 2.1. R-113 Degassing Unit Schematic.

3. HARDWARE DESCRIPTION

3.1 Heater Surface

A sketch of the transparent gold film heater is shown in Figure 3.1. Two separate heaters are mounted on each surface, identified as the primary and backup heaters, and configured so that should the primary heater fail the backup heater is automatically activated for the next test run of the matrix. A nominal film thickness of 400 Angstroms in the central heater section of size 0.75" × 1.50" (19.1 mm × 38.1 mm) corresponds to a nominal resistance of 3.8 ohms, and provides the desired transparency for viewing the boiling process from beneath. Power to the heater is provided by Silver-Zinc batteries, and the voltage is controlled, with the voltage drops across the potential taps and the calibrated shunt resistor (for the current measurement) stored in the data acquisition system. The instantaneous heat flux input and the mean heater surface temperature are computed from the voltage drop across the potential tap and the current.

The primary heater was used in both the PBE-IA and -IC (STS-47 and -60), while the backup heater was used from the onset in the PBE-IB (STS-57) because of the presence of a persistent premature nucleation site on the primary heater, observed during pre-flight testing.

Calibration of both the primary and backup heaters took place prior to installation in the test vessel over temperature ranges of 66°F to 152°F (18.9°C to 66.7°C). Only the heaters used in the flight experiments were calibrated following the completion of the experiment. The electrical resistance — temperature follows a linear relationship within ± 1°F (± 0.6°C), well within the precision tolerances specified.

A slope — intercept equation of the form:

$$\overline{T} = A + B \times \overline{R} \tag{3.1}$$

is used to compute the mean heater surface temperature $\overline{T}$ from the mean resistance $\overline{R}$ measured. The coefficient B is the slope, while A is the intercept at R = O. A single-point calibration is conducted just prior to each Run of the test matrix, using the bulk liquid temperature measured with a calibrated thermister in the immediate vicinity of the heater surface, 1 mm away. This is used to modify the coefficient A for each Run, using an appropriate value of B, which generally was found to change relatively little with a suitably aged heater surface. The surfaces were calibrated again over the temperature range following the experiments, and a new value of B obtained. The single-point calibration procedure significantly reduces the effects of any large changes in B taking place over a

period of time. The values of A and B for each of the experiments are given in Table III below. It is noted that a significant change took place in the coefficient B for the Backup Heater in the PBE-IB. This was a consequence of insufficient operation with this heater prior to the space experiment, and so the post-flight value of B was used for data reduction. It was determined that a difference of only 1.5°F (0.8°C) existed between the single point calibration and the post-flight calibration values.

Table III. Heater Surface Calibration Coefficients

		Primary	Backup
PBE-IA (STS-47)	A(°F)	-1306.46	-1375.72
Pre-Flight 2/13/92	B(°F/ohm)	402.065	404.876
PBE-IC (STS-60)	A(°F)	-1305.84	-
Post-Flight 9/20/94	B(°F/ohm)	403.882	-
PBE-IB (STS-57)	A(°F)	-	-1489.44
Pre-Flight	B(°F/ohm)	-	460.635
PBE-IB (STS-57)	A(°F)	-	1356.92
Post-Flight	B(°F/ohm)	-	427.32

3.2 Test Vessel

A schematic of the test vessel is shown in Figure 3.2, together with the hardware concepts necessary to provide a constant pressure and an initially uniform fluid temperature during each Run. Although the stirrer was intended to be activated only between the various runs of the matrix in order to promote the uniformity of temperature of the fluid, it was also activated toward the end of several runs so as to observe its influence on the vapor bubbles and, in some cases, on the heat transfer.

Figure 3.3 shows the locations of the various sensors used to determine the behavior of the boiling process. PRHV and PRHI are the primary heater voltage taps and current readings, while BRHV and BRHI are the respective values for the back up heater, when used. TM01—TM03 and TM07—TM09 are thermistors above the primary and back up heaters to measure the respective fluid temperatures, at locations 1 mm, 5 mm, and 10 mm above the center of each heater. The thermister beads have a maximum diameter of 0.6 mm, and are stated by the manufacturer as having a time constant of 23 msec when plunged into water. The respective locations of TM04—TM05—TM06 are given in Figure 3.4 as A, B and C, and are provided to check the uniformity of fluid temperatures prior to the beginning of each Run.

Thermistors TM12 and TM11 are cemented to the quartz substrate on the side opposite the gold film, at the center of the primary and back up heaters, respectively, while TM13 is in the canister air space very near the quartz substrate backside.

Figure 3.5 gives the relative locations of the internal components of the test vessel, including the viewing and lighting windows. The lighting is diffused internally for maximum clarity. The maximum internal dimensions of the R-113 chamber are also given, as 14.48 cm diameter by 11.5 cm long, which implies that the maximum diameter of a vapor bubble that can be accommodated without pressing on the heater surface is about 12 cm.

Figures 3.6 and 3.7 present the side and front views of the entire system components within the GAS canister, with the optical path followed to the 16 mm camera, which has a 400 ft. film capacity. This gives a total of approximately 18,000 frames, which must be budgeted among the various Runs.

3.3 Accelerometer System

A space Acceleration Measurement System (SAMS) type trixial accelerometer head is included in the payload, shown in Figure 3.7. This provides acceleration data in the direct vicinity of the test chamber. The use of an internal accelerometer also eliminates the need to correlate experiment data with a remote acceleration measurement system. Three Sunstrand

QA2000-030 accelerometers are used. The manufacturer resolution specification for this model is 1 micro-g, and the accuracy is given as ±100 micro-g, found by using the root sum of squares of the various stabilities (thermal, shock and time).

A typical correlation between the accelerometer outputs and the local and vehicle coordinates is given in Figures 3.8 and 3.9, for PBE-IA on the STS-47. The upper right view in Figure 3.9 is taken through the heater surface, viewed from left to right in the right side of Figure 3.5, while the upper left view is taken from the side, viewed from the bottom side of Figure 3.5.

3.4 Optical System

The views in the upper part of Figure 3.9 are obtained by combining the images, as illustrated in Figure 3.6. Also within the camera field of view, seen in Figure 3.9 are LED timing lights for synchronization with the Data Acquisition Unit. The binary code used for time is given in Figure 3.10.

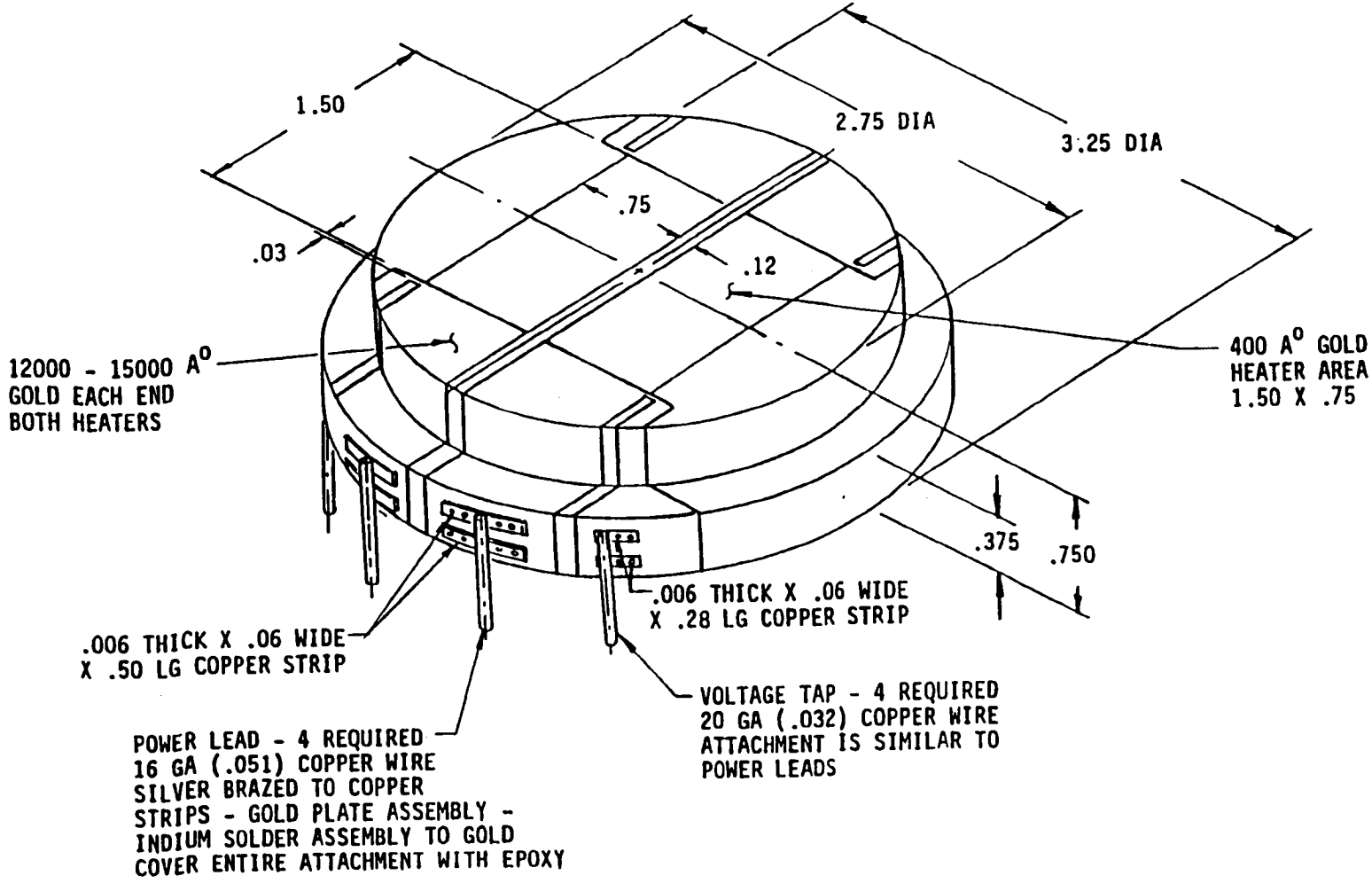

Figure 3.1. Transparent gold film heater/resistance thermometer on quartz substrate.

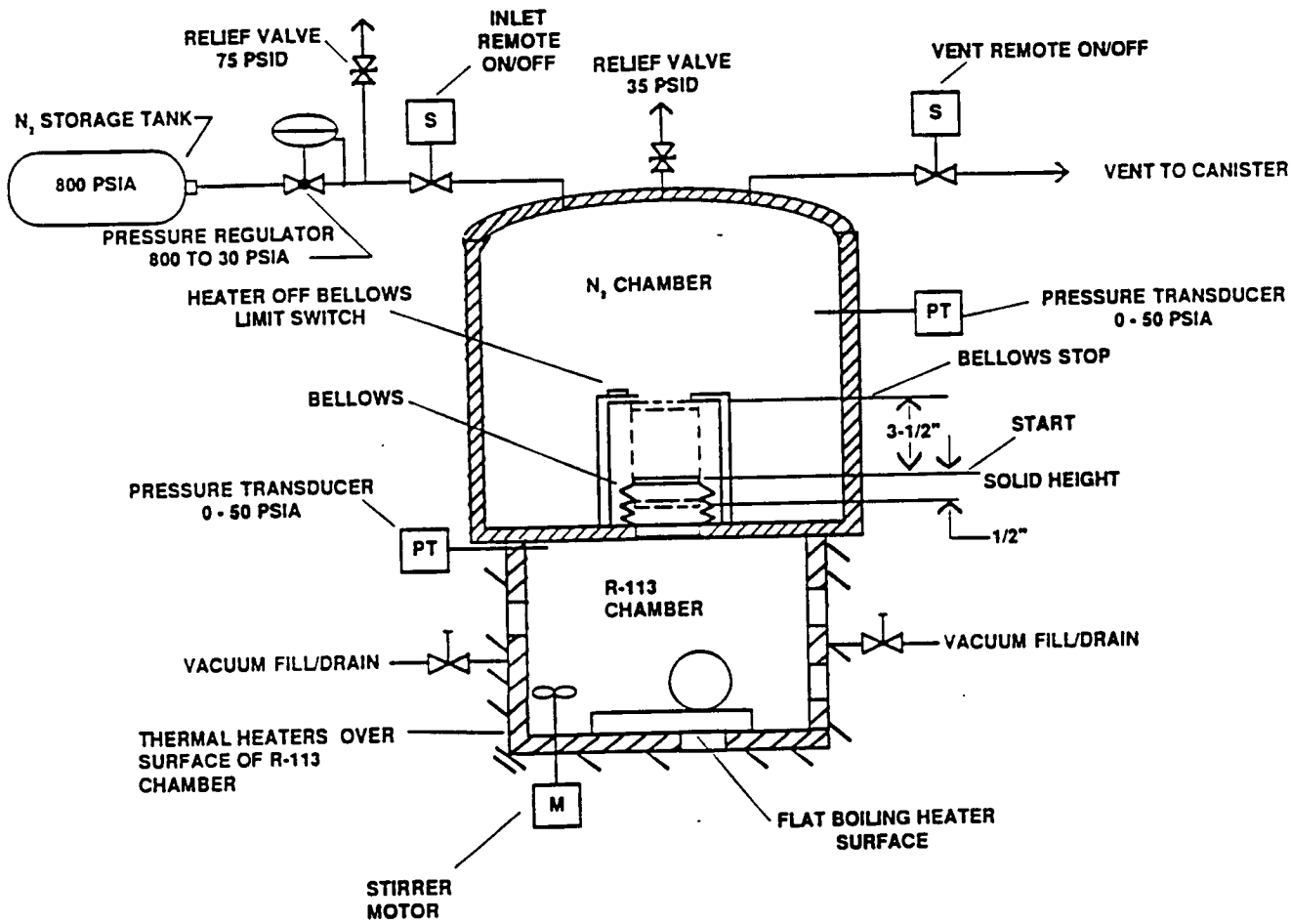

Figure 3.2. Schematic of Test Vessel with concepts to provide constant pressure and initially uniform fluid temperature.

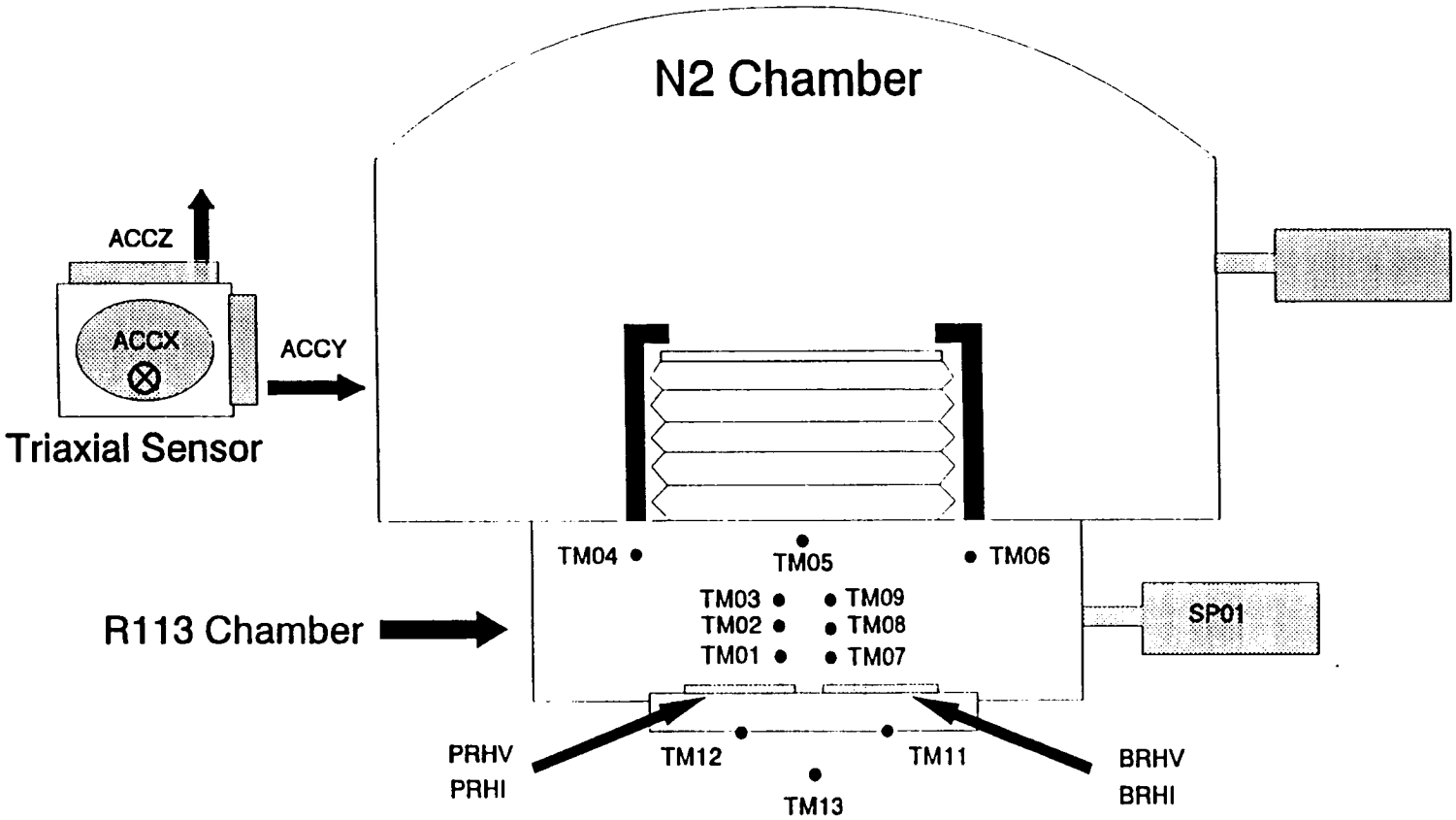

Figure 3.3. Location of Sensors for Scientific Analysis.

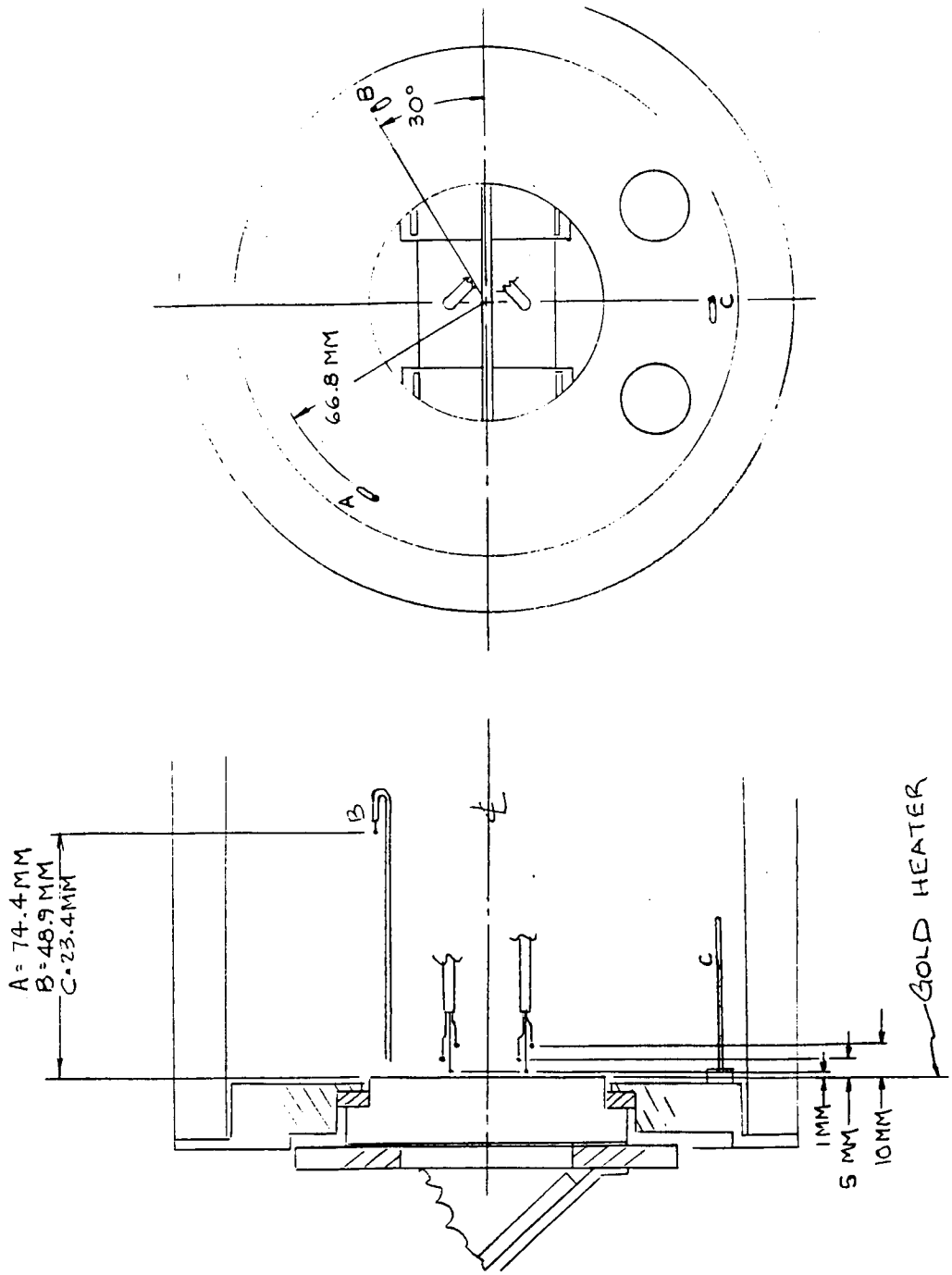

Figure 3.4. Locations of R-113 fluid thermistors in test vessel.

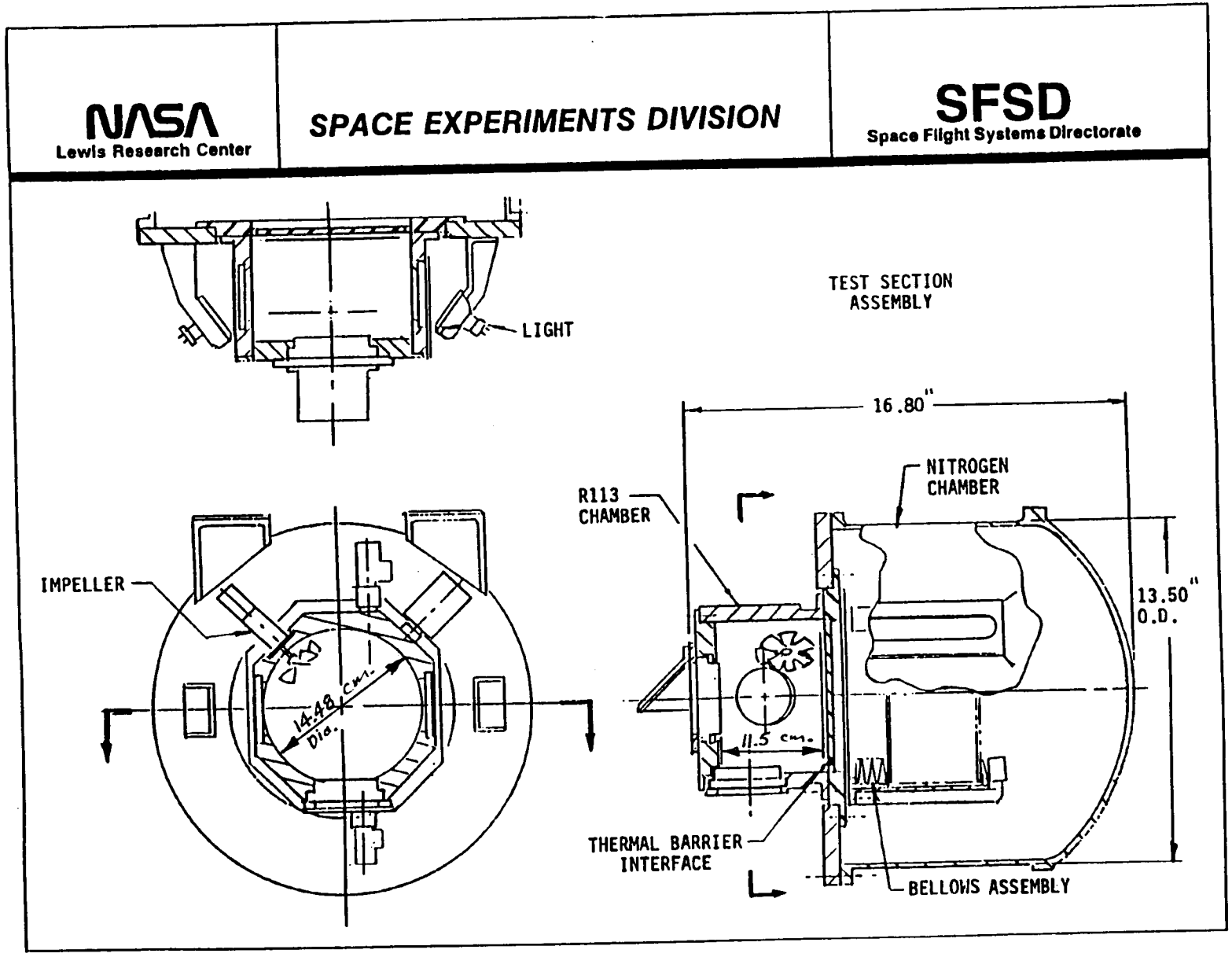

Figure 3.5. Test vessel. Relative locations of internal components, lights and viewing windows.

NASA
Lewis Research Center

SPACE EXPERIMENTS DIVISION

SFSD
Space Flight Systems Directorate

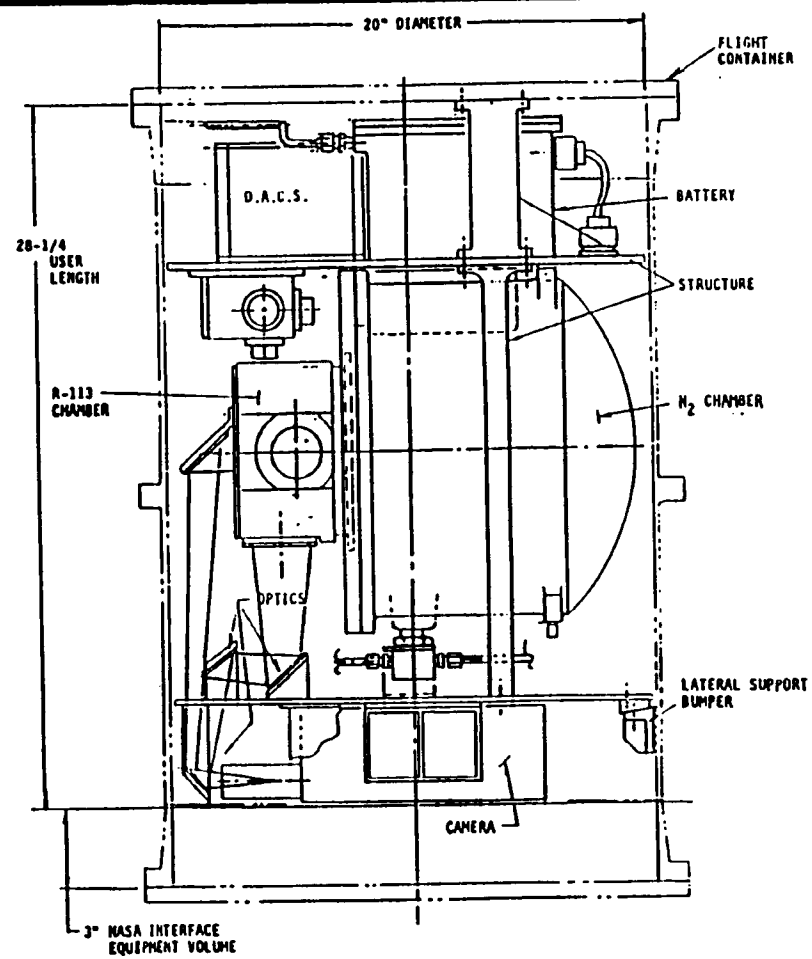

Figure 3.6. PBE components in GAS canister. Side view.

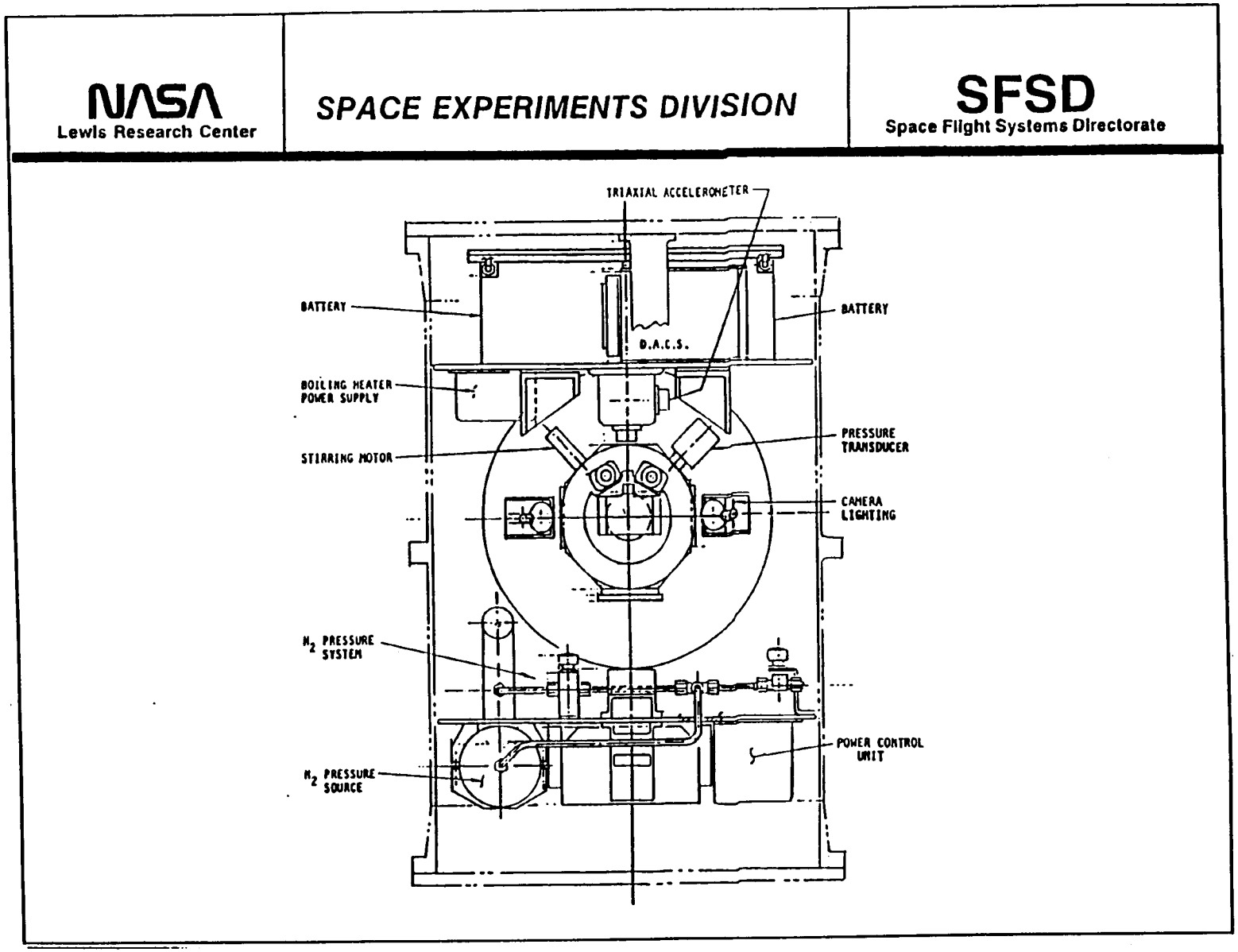

Figure 3.7. PBE components in GAS canister. Front view.

PBE/STS AXIS TRANSLATION

SED-PBE-DOC-028

PBE	STS	SAMS
+Y	+X	+Y
+Z	+Y	-X
+X	+Z	+Z

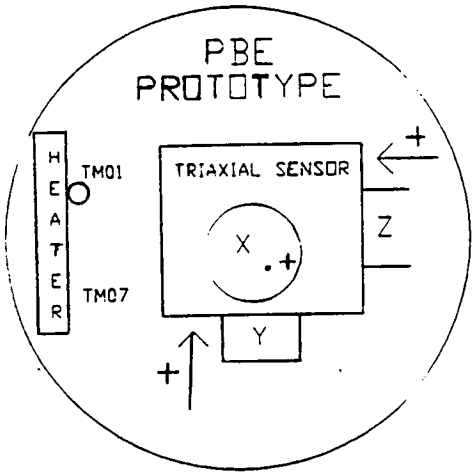

+Z signal indicates that acceleration is in direction indicated above.
e.g., - this decreases buoyancy moving vapor bubble away from heater, or would move the vapor bubble toward heater.

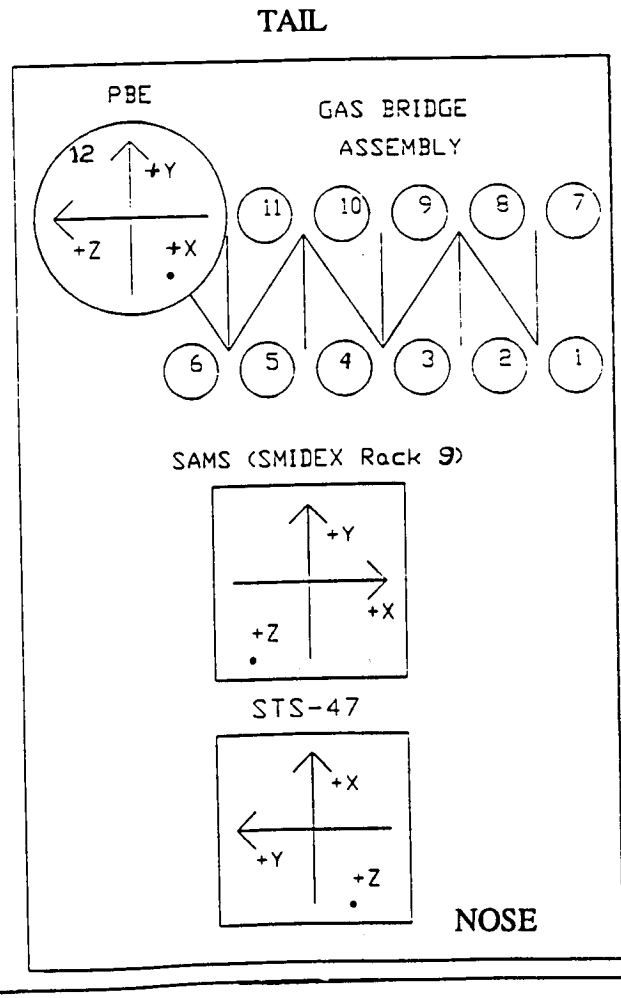

Figure 3.8. Typical correlation between coordinates of the PBE accelerometer and SAMS STS units. Above applies to PBE-IA (STS-47).

Acceleration coordinate for the space experiment

Example

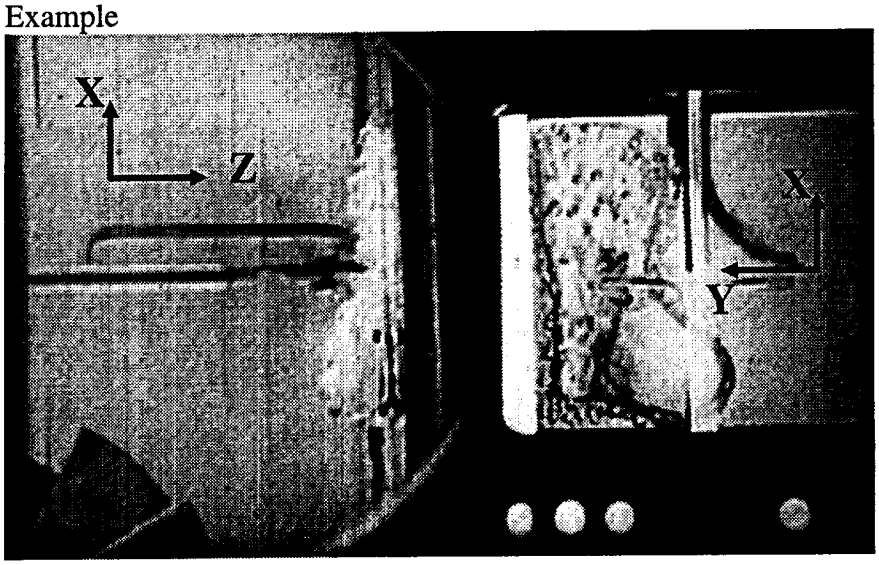

* The above figure shows both side view in left hand side and bottom view in right hand side.

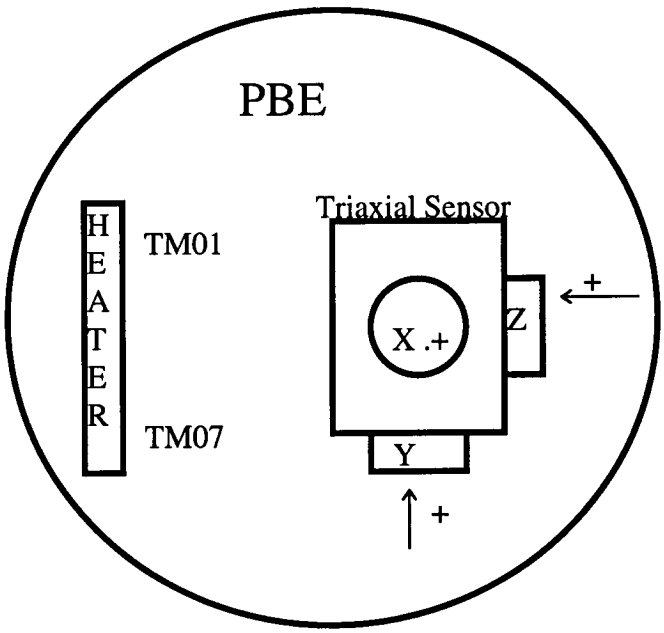

Figure 3.9. Correlation between PBE-1A accelerometer and photographic view on STS-47. Primary heater in use on left side.

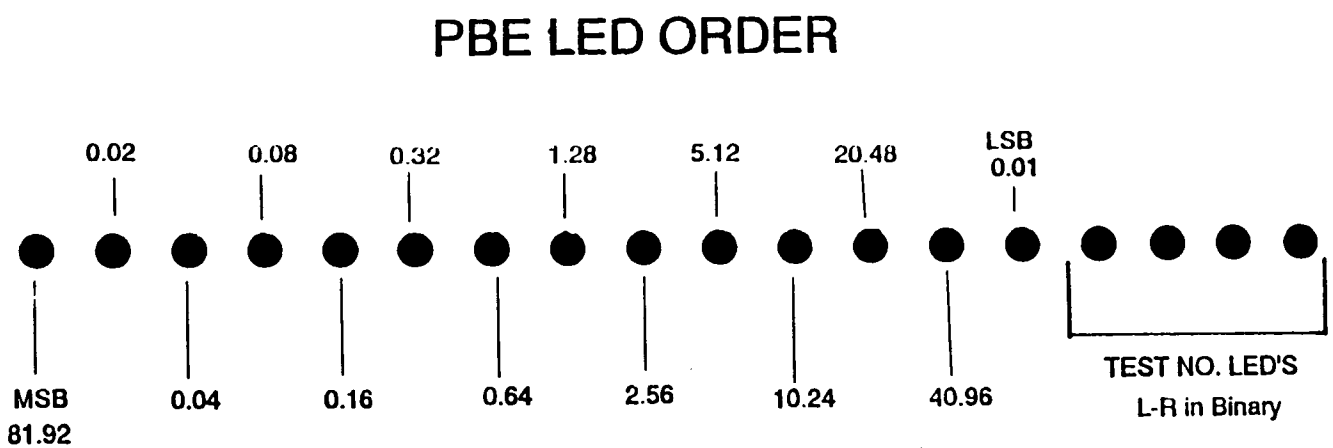

THE LED's COUNT IN BINARY FROM LEFT TO RIGHT, EXCEPT THAT THE LEAST AND MOST SIGNIFICANT BITS HAVE BEEN SWAPPED.

NUMBERS INDICATED WITH EACH LED ARE IN SECONDS. JUST ADD UP THE LIT LED'S TO GET THE TOTAL TIME.

Figure 3.10. Scheme for LED timing lights in camera field of view.

4. TEST MATRICES

The test matrices followed for the PBE-IA -IB -IC on the STS-47 -57 -60 are given as Tables IV - VI, respectively, below. The nominal levels of heat flux input (in w/cm^2) and the initial bulk liquid subcooling (in °F) are given for each Test Run, followed by the timing sequences used. The test is initiated with the heater power at 10 seconds. The camera is operated at the maximum speed of 100 pps in the time domain when nucleation is expected to occur in microgravity, based on the prior drop tower testing and extrapolations, and then followed by operation at 10 pps during the remainder of each Experiment Run. The total number of frames in a 400 ft. roll of 16 mm film is approximately 18,000, so careful consideration was given as to how these were divided amount the various Runs in order to maximize the opportunities for new knowledge.

The times for the maximum camera speed of 100 pps are identical in PBE-IA and -IB (STS-47 and 57), as noted in Tables IV and V. The early bubble growth following nucleation was not captured at 100 pps for Run No. 5 of PBE-IA, with nucleation occurring at $t^* = 26.15$ sec., while the 100 pps took place during the 15 - 25 sec. interval, nor was it captured in Run No. 9, with $t^* = 51.48$ sec, while the 100 pps. took place during the 30 - 50 sec. interval. The early bubble growth was missed in two Runs of PBE-IB (STS-57): In Run No. 2 $t^* = 25.71$ sec. (100 pps camera speed at 15 - 25 sec.) and in Run No. 6 $t^* = 58.36$ sec. (100 pps camera speed at 30 - 50 sec.). No nucleation took place in Run No. 9 of PBE-IB because of the inability to repressurize the vessel sufficiently, following Run No. 8, to condense the vapor formed. The timing of the fast camera speeds were readjusted for Run Nos. 5 and 9 of PBE-IC (STS-60), which used the same facility as for PBE-IA, in which the nucleation was not captured at the 100 pps for these Runs. The early bubble growths nevertheless were missed in three Runs of PBE-IC (STS-60): In Run No. 2 $t^* = 30.85$ sec. (100 pps camera speed at 15 - 25 sec.), in Run No. 3 $t^* = 50.17$ sec. (100 pps camera speed at 30 - 50 sec.), and in Run No. 5 $t^* = 19.60$ sec (100 pps camera speed at 20 - 30 sec). All of the nucleation misses took place in Run Nos. 2, 3, 5, 6 and 9, with one each in Runs 3, 6 and 9. These latter three operated at the lowest heat flux level used. However, the most variability in nucleation times took place with Run Nos. 2 and 5, with a total of four misses in the three space flights. These happen to operate at the intermediate level of heat flux used, and this variability is related to the variability of what is termed the homogeneous nucleation taking place in the vicinity of the heater surface. This phenomena will be described in detail later.

The stirrer was activated in a number of cases near the end of the Runs in order to determine the influences of the relatively weak random liquid motion on the vapor bubble

behavior in microgravity, initially attached to the heater surface. Qualitative effects on the heat transfer were also obtained. For Runs with subcooled liquids, the stirrer operation produced rapid condensation of the vapor bubbles, which otherwise persisted for long periods of time because of the low thermal conductivity of R-113.

The repressurization taking place with initially saturated liquid case in run No. 7 was planned in order to obtain data for vapor bubble collapse in microgravity. However, from results of PBE-IA and -IB (STS-47 and -57), it was observed that if too much vapor was initially present, the collapse process became chaotic; surface tension forces were not sufficient to provide a reasonably smooth single vapor bubble. In the last experiment, PBE-IC (STS-60), the heater-on time was reduced to 5 seconds followed by a settling period of 5 seconds, at which time the pressurization process was initiated, taking a total of 6 seconds to the new steady pressure level. This produced a reasonably well-defined collapsing vapor bubble, and the results will be given below.

Both pre flight and post flight ground tests were conducted conforming to the test matrix with the heater surface in the inverted position, at a/g = -1, in order to confirm that the system operated reproducibly following the space flight. A post flight ground test was also conducted at a/g = +1, when practical, in order to provide normal gravity boiling data, if such took place, with which to compare the microgravity boiling behavior. Results of both the pre-flight and post-flight ground tests at a/g = -1 for PBE-IA (STS)-47 are given in Merte et al (1994). Except for the nucleation data at a/g = -1, which are included in the present report, any other scientific data was deemed to be minimal and no other results for a/g = -1 are given herein. Post-flight experimental results at a/g = +1 were obtained only for PBE-IA and -IC (STS-47 and -60), the prototype version, and are included in the Appendix.

PBE Prototype System Test Matrix (STS-47)

RUN NO.	HEAT FLUX W/CM^2	SUBCOOLING (°F)	HEATER POWER ON/OFF (SEC)	10 FPS ON/OFF (SEC)	100 FPS ON/OFF (SEC)	STIRRER START (SEC)	REPRESS. START (SEC)	TOTAL TEST TIME (SEC)
1	8	20 ± 2	10--70	15--80	10--15	65-	-	80
2	4	20 ± 2	10--100	10--15, 25--130	15--25	-	-	130
3	2	20 ± 2	10--120	20--30, 50--130	30--50	110-	-	130
4	8	5 ± 1	10--55	15--65	10--15	50-	-	65
5	4	5 ± 1	10--100	10--15, 25--105	15--25	-	-	105
6	2	5 ± 1	10--105	20--30, 50--115	30--50	-	-	115
7	8	0.5 ± 0.4	10--40	15--55	10--15	-	45-	55
8	4	0.5 ± 0.4	10--70	10--15, 25--80	15--25	65-	-	80
9	2	0.5 ± 0.4	10--115	10--30, 50--125	30--50	105-	-	125

Table IV. Test matrix for PBE-IA on STS-47. (Prototype Hardware).

PBE Flight System Test Matrix (STS-57)

RUN NO.	HEAT FLUX W/CM^2	SUBCOOLING (°F)	HEATER POWER ON/OFF (SEC)	10 FPS ON/OFF (SEC)	100 FPS ON/OFF (SEC)	STIRRER START (SEC)	REPRESS. START (SEC)	TOTAL TEST TIME (SEC)
1	8	20 ± 2	10--70	15--80	10--15	55-	-	80
2	4	20 ± 2	10--110	10--15, 25--135	15--25	-	-	135
3	2	20 ± 2	10--120	20--30, 50--130	30--50	110-	-	130
4	8	5 ± 1	10--55	15--65	10--15	45-	-	65
5	4	5 ± 1	10--100	10--15, 25--105	15--25	90-	-	105
6	2	5 ± 1	10--85	20--30, 50--100	30--50	-	-	100
7	8	0.5 ± 0.4	10--35	15--65	10--15	-	45-	65
8	4	0.5 ± 0.4	10--70	10--15, 25--80	15--25	60-	-	80
9	2	0.5 ± 0.4	10--115	10--30, 50--125	30--50	95-	-	125

December1,1992
Version 1.0

Table V. Test matrix for PBE-IB on STS-57. (Flight Hardware).

PBE Prototype System Test Matrix (STS-60)

RUN NO.	HEAT FLUX W/CM^2	SUBCOOLING (°F)	HEATER POWER ON/OFF (SEC)	10 FPS ON/OFF (SEC)	100 FPS ON/OFF (SEC)	STIRRER START (SEC)	REPRESS. START (SEC)	TOTAL TEST TIME (SEC)
1	8	20 ± 2	10--15	13--55	10--13	-	-	55
2	4	20 ± 2	10--110	10--15, 25--130	15--25	-	-	135
3	2	20 ± 2	10--120	20--30, 50--130	30--50	110-	-	130
4	8	5 ± 1	10--55	13--60	10--13	45-	-	60
5	4	5 ± 1	10--100	10--20, 30--105	20--30	90-	-	105
6	2	5 ± 1	10--85	20--30, 50--100	30--50	-	-	100
7	8	0.5 ± 0.4	10--15	25--40	10--25	-	20-	40
8	4	0.5 ± 0.4	10--70	10--15, 25--80	15--25	60-	-	80
9	2	0.5 ± 0.4	10--115	10--40, 60--125	40--60	95-	-	125

June 30,1993

Version 3.0

Table VI. Test matrix for PBE-IC on STS-60. (Prototype Hardware).

5. EXPERIMENTAL RESULTS

5.1 Measured Parameters

5.1.1 Internal to Test Vessel

Table VII gives the parameters as measured for each of the Runs of PBE-IA during the pre- and post- flight tests at a/g = -1 and a/g = +1, and during the STS-47 Space Flight. These are identified in each Run No. by the date conducted and the orientation. Following this are the nominal and actual levels of input heat flux, followed by the nominal and actual initial bulk liquid subcooling. The initial bulk liquid temperature is virtually constant, and the subcooling is changed by varying the system pressure, which changes the saturation temperature, as indicated in the succeeding columns of Table VII. T_w^*, T_{sup}^* and t^* are the mean heater surface temperature, the mean heater surface superheat, and the time interval from the onset of heating that nucleation or the onset of boiling takes place, respectively. The last column gives the high speed camera on-off times relative to the heater power on.

Tables VIII and IX give the measured parameters for each of the Runs corresponding to PBE-IB (STS-57) and PBE-IC (STS-60), respectively. Details of the measurements are given in Appendices A, B, C for PBE-IA, -IB, -IC, on the STS-47, -57, -60, respectively, and Tables VII - IX are repeated therein for convenience.

Test Matrix for Pool boiling-STS-47

a/g -1 experiment based on date 4/28/92
a/g 0 experiment based on date 9/11/92 STS-47
a/g -1 experiment based on date 12/22/92
a/g+1 experiment based on data 11/4/92

Run#	Date of Experiment	Flight system	Gravit a/g	Heat Flux, W/cm^ Nom.	Heat Flux, W/cm^ Actual	Subcool,oF Nom.o	Subcool,oF Actual oF	Tbulk oC	Sys.Press kPa	Tsat oC	T*wall oC	T*sup oC	t* time sec	100pps On-Off	Remark
1	4/28/92	Prototype	-1	8.00	6.70	20	21.00	49.44	153.48	61.11	93	31.89	1.20	0 -- 5	
	9/11/92	Prototype	0	8.00	7.00	20	18.50	49.44	149.00	59.72	95	35.28	1.58	0 -- 5	
	12/22/92	Prototype	-1	8.00	6.22	20	19.94	49.42	152.99	60.50	77	16.50	0.54	0 -- 5	
	11/4/92	Prototype	1	8.00	7.02	20	20.02	48.31	147.89	59.43	93	33.57	2.10	0 -- 5	
2	4/28/92	Prototype	-1	4.00	3.65	20	19.80	49.00	151.55	60.00	81	21.00	2.68	5 --15	
	9/11/92	Prototype	0	4.00	3.60	20	21.50	49.17	154.44	61.11	110	48.89	12.38	5 --15	
	12/22/92	Prototype	-1	4.00	3.37	20	19.92	49.28	152.31	60.35	100	39.65	8.50	5 --15	
	11/4/92	Prototype	1	4.00	3.56	20.00	20.00	48.14	147.07	59.25	101	41.75	51.20	5 --15	
3	4/28/92	Prototype	-1	2.00	1.78	20	21.00	49.44	154.44	61.11	89	27.89	23.40	20 -- 40	
	9/11/92	Prototype	0	2.00	1.80	20	19.70	49.06	151.20	60.00	95	35.00	31.39	20 -- 40	
	12/22/92	Prototype	-1	2.00	1.80	20	20.28	49.56	154.30	60.83	102	41.17	90.00	20 -- 40	
	11/4/92	Prototype	1	2.00	1.81	20	19.95	48.49	148.51	59.57				20 -- 40	No Nucleation
4	4/28/92	Prototype	-1	8.00	6.50	5	5.30	49.00	116.87	51.94	91	39.06	1.10	0 -- 5	
	9/11/92	Prototype	0	8.00	7.00	5	4.80	49.00	115.83	51.67	91	39.33	1.34	0 -- 5	
	12/22/92	Prototype	-1	8.00	6.30	5	4.22	49.08	115.21	51.43	75	23.57	0.50	0 -- 5	
	11/4/92	Prototype	1	8.00	7.05	5	5.05	47.81	112.04	50.62	94	43.38	1.90	0 -- 5	
5	4/28/92	Prototype	-1	4.00	3.40	5	5.40	49.22	117.21	52.22	102	49.78	8.70	5 --15	
	9/11/92	Prototype	0	4.00	3.60	5	5.00	48.89	115.83	51.67	120	68.33	16.15	5 --15	
	12/22/92	Prototype	-1	4.00	3.38	5	4.93	49.04	116.52	51.78	109	57.22	12.70	5 --15	
	11/4/92	Prototype	1	4.00	3.54	5	4.98	47.92	112.32	50.69				5 --15	No Nucleation

Page 2 of 2

Table VII. PBE-IA. Parameters measured at a/g = -1 and a/g = +1 in pre-flight and post-flight tests, and during STS-47 Space Flight.

Run#	Date of Experiment	Flight system	Gravit a/g	Heat Flux, W/cm^ Nom.	Actual	Subcool,oF Nom.o	Actual oF	Tbulk oC	Sys.Press kPa	Tsat oC	T*wall oC	T*sup oC	t* time sec	100pps On-Off	
6	4/28/92	Prototype	-1	2.00	1.76	5	4.70	49.06	115.83	51.67	87	35.33	34.30	20 -- 40	
	9/11/92	Prototype	0	2.00	1.82	5	5.00	49.17	116.52	51.94	98	46.06	37.47	20 -- 40	
	12/22/92	Prototype	-1	2.00	1.77	5	4.95	49.25	117.35	52.00				20 -- 40	No Nucleation
	11/4/92	Prototype	1	2.00	1.81	5	5.01	48.04	112.87	50.82				20 -- 40	No Nucleation
7	4/28/92	Prototype	-1	8.00	6.70	0.50	1.20	48.78	106.87	49.44	93	43.56	1.18	0 -- 5	
	9/11/92	Prototype	0	8.00	7.00	0.50	1.00	48.89	106.87	49.44	94	44.56	1.36	0 -- 5	
	12/22/92	Prototype	-1	8.00	6.42	0.50	4.92	48.79	115.56	51.52	86	34.48	1.00	0 -- 5	
	11/4/92	Prototype	1	8.00	7.06	0.50	4.74	47.51	110.32	50.14	91	40.86	1.90	0 -- 5	
8	4/28/92	Prototype	-1	4.00	3.50	0.50	1.40	48.67	106.87	49.44	101	51.56	9.30	5 --15	
	9/11/92	Prototype	0	4.00	3.50	0.50	0.70	49.06	106.87	49.44	106	56.56	10.63	5 --15	
	12/22/92	Prototype	-1	4.00	3.42	0.50	0.45	49.09	107.63	49.34	111	61.66	14.50	5 --15	
	11/4/92	Prototype	1	4.00	3.55	0.50	0.56	47.42	101.90	47.73				5 --15	No Nucleation
9	4/28/92	Prototype	-1	2.00	1.80	0.50	1.00	48.72	106.18	49.28	99	49.72	65.90	20 -- 40	
	9/11/92	Prototype	0	2.00	1.80	0.50	0.40	49.22	106.87	49.44	100	50.56	41.48	20 -- 40	
	12/22/92	Prototype	-1	2.00	1.76	0.50	0.41	49.05	107.42	49.28	89	39.72	27.00	20 -- 40	
	11/4/92	Prototype	1	2.00	1.81	0.50	1.23	47.49	103.42	48.17				20 -- 40	No Nucleation

Table VII. Continued.

Test Matrix for Pool boiling - STS-57

a/g -1 experiment based on date 1/22/93
a/g 0 experiment based on date 6/ 2 /93
a/g -1 experiment based on date 9/30/93

Run#	Date of Experiment	Flight system	Gravit a/g	Heat Flux, W/cm^ Nom.	Heat Flux, W/cm^ Actual	Subcool,oF Nom.o	Subcool,oF Actual of	Tbulk oC	Sys.Press kPa	Tsat oC	T*wall oC	T*sup oC	t* time sec	100fps On-Off	Remark
1	1/22/93	Flight Syste	-1	8.00	7.023	20	19.87	49.46	152.95	60.5	86.60	26.10	0.74	0 -- 5	
	6/2/93	Flight Syste	0	8.00	7.804	20	19.83	46.96	141.66	57.98	87.81	29.83	0.79	0 -- 5	
	9/30/93	Flight Syste	-1	8.00	7.024	20	19.87	49.86	155.00	60.9	86.45	25.55	0.62	0 -- 5	
2	1/22/93	Flight Syste	-1	4.00	3.725	20	19.94	49.31	152.46	60.39	119.35	58.96	12.27	5 -- 15	
	6/2/93	Flight Syste	0	4.00	3.999	20	19.86	49.04	151.00	60.07	127.46	67.39	15.71	5 -- 15	
	9/30/93	Flight Syste	-1	4.00	3.727	20	19.92	49.32	152.47	60.39	126.14	65.75	17.11	5 -- 15	
3	1/22/93	Flight Syste	-1	2.00	1.982	20	19.92	49.62	153.85	60.69				20 -- 40	No Nucleation
	6/2/93	Flight Syste	0	2.00	2.027	20	19.85	48.66	149.26	59.69	96.69	37.00	23.63	20 -- 40	
	9/30/93	Flight Syste	-1	2.00	1.983	20	19.84	50.05	155.65	61.07				20 -- 40	No Nucleation
4	1/22/93	Flight Syste	-1	8.00	7.126	5	4.92	49.09	116.67	51.82	91.10	39.28	0.89	0 -- 5	
	6/2/93	Flight Syste	0	8.00	7.287	5	4.88	48.61	114.79	51.32	88.86	37.54	1.28	0 -- 5	
	9/30/93	Flight Syste	-1	8.00	7.119	5	4.91	48.66	115.05	51.39	82.09	30.70	0.55	0 -- 5	
5	1/22/93	Flight Syste	-1	4.00	3.742	5	4.89	49.18	116.97	51.90	112.56	60.66	10.00	5 -- 15	
	6/2/93	Flight Syste	0	4.00	3.978	5	4.84	49.00	116.17	51.69	123.44	71.75	13.51	5 -- 15	
	9/30/93	Flight Syste	-1	4.00	3.737	5	4.90	49.48	118.11	52.20	124.77	72.57	16.05	5 -- 15	
6	1/22/93	Flight Syste	-1	2.00	1.993	5	4.96	49.22	117.27	51.98				20 -- 40	No Nucleation
	6/2/93	Flight Syste	0	2.00	2.012	5	4.93	48.87	115.89	51.61	110.47	58.86	48.36	20 -- 40	
	9/30/93	Flight Syste	-1	2.00	1.995	5	4.88	49.01	116.30	51.72				20 -- 40	No Nucleation

Table VIII. PBE-IB. Parameters measured at a/g = -1 in pre-flight and post-flight tests, and during STS-57 Space Flight.

Run#	Date of Experiment	Flight system	Gravit a/g	Heat Flux, W/cm^ Nom.	Heat Flux, W/cm^ Actual	Subcool,oF Nom.o	Subcool,oF Actual of	Tbulk oC	Sys.Press kPa	Tsat oC	T*wall oC	T*sup oC	t* time sec	100pps On-Off	Remark
7	1/22/93	Flight Syste	-1	8.00	7.32	0.50	0.38	49.01	107.21	49.22	93.09	43.87	0.92	0 -- 5	
	6/2/93	Flight Syste	0	8.00	7.433	0.50	0.32	48.59	105.63	48.77	82.83	34.06	0.59	0 -- 5	
	9/30/93	Flight Syste	-1	8.00	7.312	0.50	0.43	49.11	107.65	49.35	83.07	33.72	0.55	0 -- 5	
8	1/22/93	Flight Syste	-1	4.00	3.788	0.50	0.37	48.94	106.97	49.15	97.96	48.81	6.56	5 -- 15	
	6/2/93	Flight Syste	0	4.00	3.953	0.50	0.50	48.73	106.45	49.01	119.04	70.03	13.77	5 -- 15	
	9/30/93	Flight Syste	-1	4.00	3.799	0.50	0.41	49.10	107.59	49.33	129.02	79.69	19.41	5 -- 15	
9	1/22/93	Flight Syste	-1	2.00	1.98	0.50	0.34	49.05	107.29	49.24	107.60	58.36	57.07	20 -- 40	
	6/2/93	Flight Syste	0	2.00	1.961	0.50	1.64	48.61	108.28	49.52				20 -- 40	No Data
	9/30/93	Flight Syste	-1	2.00	1.983	0.50	0.43	49.30	108.34	49.54	114.43	64.89	83.28	20 -- 40	

Table VIII. Continued

NASA test Matrix for Pool boiling - STS-60

a/g -1 experiment based on date 7/6/93
a/g 0 experiment based on date 2/3 /94
a/g -1 experiment based on date 5/3/94
a/g +1 experiment based on date 5/4/94

Run#	Date of Experiment	Flight system	Gravit a/g	Heat Flux, W/cm^ Nom.	Heat Flux, W/cm^ Actual	Subcool,oF Nom.o	Subcool,oF Actual o	Tbulk oC	Sys.Press kPa	Tsat oC	T*wall oC	T*sup oC	t* time sec	100fps On-Off	Remark
1	7/6/93	Prototype	-1	8.00	6.834	20	20.75	49.46	155.27	60.99	78.73	17.74	0.56	0 -- 3	
	2/3/94	Prototype	0	8.00	7.044	20	20.7	48.34	149.96	59.84	91.30	31.46	0.91	0 -- 3	
	5/3/94	Prototype	-1	8.00	6.866	20	20.75	49.62	156.01	61.15	83.26	22.11	0.67	0 -- 3	
	5/4/94	Prototype	1	8.00	7.03	20	20.81	48.02	148.78	59.58	96.90	37.32	2.26	0 -- 3	bubble appeared before film began; time is sudden growth
2	7/6/93	Prototype	-1	4.00	3.365	20	20.74	48.65	151.44	60.17	122.20	62.03	19.53	5 -- 15	
	2/3/94	Prototype	0	4.00	3.601	20	20.72	47.43	145.88	58.94	122.70	63.76	20.85	5 -- 15	
	5/3/94	Prototype	-1	4.00	3.372	20	20.75	48.38	150.29	59.91	102.39	42.48	7.99	5 -- 15	
	5/4/94	Prototype	1	4.00	3.584	20	20.77	48.35	150.18	59.89	97.30	37.41	35.08	5 -- 15	
3	7/6/93	Prototype	-1	2.00	1.763	20	20.7	50.09	158.08	61.59	101.13	39.54	59.11	20 -- 40	
	2/3/94	Prototype	0	2.00	1.804	20	20.81	48.85	152.55	60.41	99.70	39.29	40.17	20 -- 40	
	5/3/94	Prototype	-1	2.00	1.768	20	20.75	49.94	157.53	61.47	99.50	38.03	52.82	20 -- 40	
	5/4/94	Prototype	1	2.00	1.811	20	20.74	48.62	151.34	60.14				20 -- 40	No Nucleation
4	7/6/93	Prototype	-1	8.00	6.293	5	5.76	49.09	118.45	52.29	69.00	16.71	0.29	0 -- 3	
	2/3/94	Prototype	0	8.00	6.491	5	5.8	48.77	117.30	51.99	86.30	34.31	0.74	0 -- 3	
	5/3/94	Prototype	-1	8.00	6.327	5	5.81	48.86	117.69	52.09	82.34	30.25	0.65	0 -- 3	
	5/4/94	Prototype	1	8.00	7.06	5	5.78	47.93	114.14	51.14	90.90	39.76	0.76	0 -- 3	
5	7/6/93	Prototype	-1	4.00	3.366	5	5.76	49.24	119.02	52.44	115.35	62.91	13.56	10 -- 20	
	2/3/94	Prototype	0	4.00	3.476	5	5.72	48.88	117.58	52.06	103.80	51.74	9.6	10 -- 20	
	5/3/94	Prototype	-1	4.00	3.39	5	5.8	49.32	119.38	52.54	114.89	62.35	14.15	10 -- 20	
	5/4/94	Prototype	1	4.00	3.556	5	5.80	47.99	114.39	51.21				10 -- 20	No Nucleation

Page 2 of 2

Table IX. PBE-IC. Parameters measured at a/g = -1 and a/g = +1 in pre-flight and post-flight tests, and during STS-60 Space Flight.

Run#	Date of Experiment	Flight system	Gravit a/g	Heat Flux, W/cm^ Nom.	Actual	Subcool,oF Nom.o	Actual o	Tbulk oC	Sys.Press kPa	Tsat oC	T*wall oC	T*sup oC	t* time sec	100pps On-Off	Remark
6	7/6/93	Prototype	-1	2.00	1.775	5	5.8	49.09	118.52	52.31	102.02	49.71	54.04	20 -- 40	
	2/3/94	Prototype	0	2.00	1.805	5	5.78	49.28	119.22	52.49	98.50	46.01	37.94	20 -- 40	
	5/3/94	Prototype	-1	2.00	1.784	5	5.8	48.9	117.80	52.12	101.74	49.62	57.55	20 -- 40	
	5/4/94	Prototype	1	2.00	1.815	5	5.87	47.95	114.40	51.21				20 -- 40	No Nucleation
7	7/6/93	Prototype	-1	8.00	6.826	0.50	1.33	48.91	108.74	49.65	83.59	33.94	0.78	0 -- 15	
	2/3/94	Prototype	0	8.00	6.948	0.50	1.37	48.35	106.80	49.11	88.10	38.99	0.75	0 -- 15	
	5/3/94	Prototype	-1	8.00	6.858	0.50	1.35	48.8	108.38	49.55	78.86	29.31	0.6	0 -- 15	
	5/4/94	Prototype	1	8.00	7.083	0.50	2.7	47.49	106.40	48.99	84.80	35.81	0.73	0 -- 15	
8	7/6/93	Prototype	-1	4.00	3.412	0.50	1.4	48.87	108.74	49.65	104.17	54.52	9.31	5 -- 15	
	2/3/94	Prototype	0	4.00	3.513	0.50	1.28	48.34	106.62	49.05	98.30	49.25	8.03	5 -- 15	
	5/3/94	Prototype	-1	4.00	3.428	0.50	1.39	48.85	108.62	49.62	103.43	53.81	8.09	5 -- 15	
	5/4/94	Prototype	1	4.00	3.569	0.50	1.33	47.50	103.80	48.24				5 -- 15	No Nucleation
9	7/6/93	Prototype	-1	2.00	1.765	0.50	1.39	48.86	108.66	49.63	97.90	48.27	49.95	30 -- 50	
	2/3/94	Prototype	0	2.00	1.81	0.50	1.3	48.64	107.70	49.36	93.70	44.34	30.52	30 -- 50	
	5/3/94	Prototype	-1	2.00	1.765	0.50	1.4	48.89	108.80	49.67	97.90	48.23	44.13	30 -- 50	
	5/4/94	Prototype	1	2.00	1.81	0.50	1.37	47.70	104.57	48.46				30 -- 50	No Nucleation

Table IX. Continued.

5.1.2 Accelerometer

Tables X - XII list a summaries of the relatively larger acceleration excursions measured during each of the Runs in the PBE-IA, -IB, -IC of STS-47, -57, and -60, respectively. The accelerometer units here are given as micro-g's, and the heating for each Run begins at 10 seconds. The larger excursions are indicated in bold type, and no consistent observable effects were noted at these times in the boiling process either in the vapor bubble boiling behavior from the motion picture films, or in the heat transfer behavior as might be reflected in the heater surface temperature measurements. The interface motions during boiling are reasonably intense, and the relatively large surface tensions acting are believed to mask influences of these residual acceleration levels, having maximum values on the order of 0.5 milli-g's.

The accelerometer measurements from which the data in Table X were extracted are plotted as functions of time for each Run, and are given in Appendix C of Merte et al (1994). Any deviations from the background least reading of ± 1, as indicated by the term noise levels in Tables X - XII, were recorded.

The effect of the larger excursions could be detected only in special circumstances where a particular sensitivity to buoyancy exits. An example will be noted in PBE-IC (STS-60) Run No. 4 at about 30 seconds, where substantial dryout of the heater surface existed. A sustained acceleration of about 0.25 mg for 2 - 3 sec. in the X direction of Figure 3.9 produces a small dip in the measured mean heater surface temperature, which results in an increase in the computed mean heater surface heat transfer coefficient of about 25%, from h = 200 to h = 250 w/m^2K. Another example arises in PBE-IC (STS-60) Run No. 8, during the single phase transient heating process. At about 16 sec. a disturbance of about 0.3 mg perpendicular to the heating surface for approximately 2 seconds induces a slight amount of natural convection, which is reflected in both the mean surface temperature and in the computed heat transfer coefficient. These observations appear to be reasonably consistent with the tolerable residual accelerations defined in Figure 6 of Monti et al (1987), which gives acceleration levels as a function of frequency for a fluid physics experiment involving a temperature gradient.

RUN #	Time, sec	Plots	Max value			Uncertainty (Noise)	Comments
			x	y	z		
1		no	50	52	50	2.40E+01	
2		no	76	77	50	2.40E+01	
3		no	51	77	50	2.40E+01	
4		no	101	77	75	2.40E+01	
5	98.3	yes	**179**	52	**348**	2.40E+01	
5	98.4	yes	51	**103**	50	2.40E+01	
6	89.9	yes	51	52	**273**	2.40E+01	
6	90.1	yes	51	**258**	50	2.40E+01	
6	90.2	yes	**254**	52	50	2.40E+01	
7		no	76	77	75	2.40E+01	
8	4.9	yes	**306**	52	75	2.40E+01	
8	5	yes	51	**103**	75	2.40E+01	
9	48.1	yes	51	**103**	50	2.40E+01	
9	60.4	yes	**281**	52	75	2.40E+01	

Notes: (1) Accelerometer units are given as micro-g's.

(2) Heating in each run begins at t = 10 sec.

Table X. Summary of relatively larger acceleration excursions during PBE-IA in STS-47 Flight.

RUN #	Time, sec	Plots	Max Value			Uncertainty (Noise)	Comments
			x	y	z		
1		no	50	50	26	2.40E+01	
2		no	50	50	51	2.40E+01	
3		no	25	50	51	2.40E+01	
4		no	25	50	51	2.40E+01	
5		no	50	49	51	2.40E+01	
6		no	50	50	26	2.40E+01	
7		no	25	50	26	2.40E+01	
8	12.8	yes	**98**	25	25	2.40E+01	
8	69.5	yes	50	**100**	**178**	2.40E+01	
9		no	50	25	26	2.40E+01	

Notes: (1) Accelerometer units are given as micro-g's.

(2) Heating in each run begins at t = 10 sec.

Table XI. Summary of relatively large acceleration excursions during PBE-IB in STS-57 Flight.

RUN #	Time, sec	Plots	Max Value			Uncertainty (Noise)	Comments
			x	y	z	2.40E+01	
1	19.9	yes	26	52	**99**	2.40E+01	
2	30.8	yes	26	39	**99**	2.40E+01	
2	39.8	yes	26	**64**	50	2.40E+01	
2	102	yes	**179**	39	50	2.40E+01	
3	112.3	yes	54	**129**	149	2.40E+01	
3	113.6	yes	**255**	0	**199**	2.40E+01	
4	27.5	yes	**255**	77	0	2.40E+01	
4	28.9	yes	230	**129**	**224**	2.40E+01	
5	19.9	yes	0	13	**100**	2.40E+01	
5	79.7	yes	25	**90**	25	2.40E+01	
5	90.9	yes	**77**	13	0	2.40E+01	
6	39.7	yes	**382**	13	224	2.40E+01	
6	74.1	yes	179	193	**497**	2.40E+01	
6	74.6	yes	128	**219**	348	2.40E+01	
7		no	51	64	50	2.40E+01	
8	15.9	yes	153	**142**	**348**	2.40E+01	
8	17.3	yes	**179**	64	224	2.40E+01	
9	24	yes	0	**90**	25	2.40E+01	
9	76.6	yes	0	39	**75**	2.40E+01	
9	83.2	yes	**77**	39	0	2.40E+01	

Notes: (1) Accelerometer units are given as micro-g's.

(2) Heating in each run begins at t = 10 sec.

Table XII. Summary of relatively large acceleration excursions during PBE-IC in STS-60 Flight.

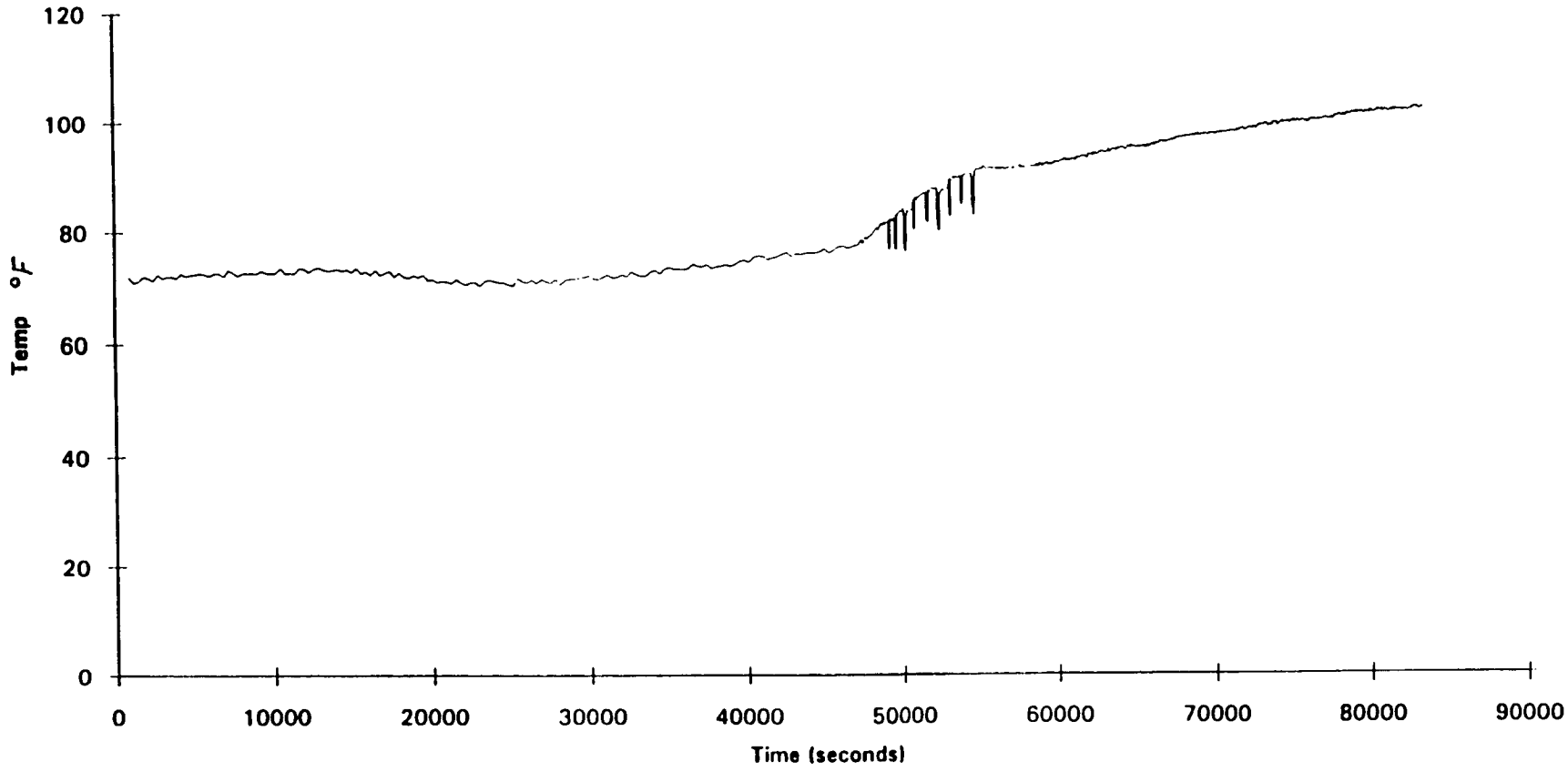

Figure 5.1. PBE-IA structure temperature in GAS canister.

5.2 Results

5.2.1 Canister Ambient

Figure 5.1 presents the output of a thermistor mounted on one of the structural members of the PBE-IA, following liftoff of the STS-47. The disturbances initiated by the onset of each of the nine (9) Runs in the test matrix is clearly discernible. The general increase in temperature during and following the tests is a consequence of heating the R-113 to its nominal 120°F (48.9°C) operating temperature level. Figure 5.1 is also representative of the behavior of PBE-IB and -IC.

5.2.2 Test Matrix Results Organization

The experimental data, including representative photographic views from the films, for each of the nine (9) Runs of PBE-IA, -IB, -IC conducted in the microgravity of space on the STS-47, -57, -60 are given, respectively, in Appendices A, B, and C. The organization of these three (3) Appendices are parallel with respect to the Figure Numbers, Titles and Subjects treated, so the contents of only Appendix A will be described in some detail here. Comments on the behavior and special differences observed in the experiments will be deferred to the following discussion section.

The test matrix, measured parameters and summary of relatively large acceleration excursions are repeated in Appendix A as Tables A-I, A-II and A-III, respectively, for convenience in reviewing the results.

Each of the Figures A-1 through A - 6 and A - 9 through A - 13 are subdivided as a - i, corresponding to Run Nos. 1 - 9, and follow the sequences of Tables A-I, A-II, A-III.

Figures A-1a — A-1i include the measured mean heater surface temperature and the heat transfer coefficient computed from a one-dimensional finite difference procedure in the quartz substrate, using the measured surface temperature as a boundary condition. Cubic splines are fitted through successive data points to provide interpolation between the measured points. The procedure is described by Merte (1992). During the conduction phase of heating the heat transfer coefficient is defined in terms of the difference between the heater surface temperature and the initial temperature. This permits a comparison with the well-known analytical solution of conduction in two semi-infinite solids with a step input in heat flux at the plane between the two solids. This is shown by the labeled dotted curves in Figures A-1a - A-1i. Once motion takes place in the fluid, comparison with the analytic conduction solution is no longer appropriate. However, it is included in all such plots in order to provide a reference. It becomes obvious that deviations from the one-

dimensional conduction behavior takes place because of the finite lateral heater dimensions. This issue will be addressed below. Once nucleation takes place the heat transfer coefficient is appropriately defined in terms of the difference between the measured heater surface temperature and the liquid saturation temperature.

Figures A-2a — A-2i show the temporal variation of the input heat flux to the thin gold film. The changes measured are a consequence of the increase in resistance of the gold film as it is heated, with the imposed voltage being controlled to remain essentially constant. This variation is relatively small, except when substantial heater surface dryout takes place, and it was not deemed worthwhile to control the power input to remain constant.

The measured system pressures are plotted in Figures A-3a — A-3i, along with the heat flux to the fluid as computed from the measured power input and the heat flux to the substrate, computed in turn from the measured heater surface temperature. This parameter makes it convenient to determine when steady-state conditions are reached, since the heat flux to the fluid becomes equal to the heat flux input to the film heater. This condition is almost attained in Run Nos. 2, 3, 6 and 9. In some cases pressure spikes are observed at the moment of nucleation, associated with the rapid formation of vapor before the pressure control system can respond. The relatively low sample rate of 10 Hz for pressure is responsible for the seemingly random sensing of these pressure spikes. Figure A-3g shows the increase in pressure planned while the camera was running with the intention of obtaining measurements of a single vapor bubble collapse. This was successful only with PBE-IC. The pressure increases near the ends of some Runs, as in Figures A-3h and A-3i, are due to the pressure control bellows reaching the stops at the maximum limit of volume.

Figures A-4a — A-4i give the fluid temperatures above the active primary heater, labeled TM01, TM02 and TM03, at distances of 1 mm, 5 mm and 10 mm above the heater surface, as indicated in Figures 3.3 and 3.4. The lower plot shows TM04, TM05 and TM06, the bulk liquid temperatures at the various distances indicated above the heater surfaces, around the perimeter as given in Figures 3.3 and 3.4. The measured mean heater surface temperature is included at the top in order to provide temporal reference marks for the various temperatures measured. The measured fluid temperatures provide an indication as to the uniformity of temperature of the beginning of each Test Run.

Figures A-5a — A-5i show the changes in liquid temperature above the secondary heater, labeled TM07, TM08 and TM09, at 1 mm, 5 mm, and 10 mm above its center, and thus gives an indication of the effects of lateral motions of the vapor bubble for the case where the primary heater is active. In the lower part of these Figures, TM11 measures the quartz surface temperature centered under the secondary heater, while TM12 measures the

quartz surface temperature under the center of the primary heater. TM13 measures the air space temperature slightly removed from the center of the underside of the quartz substrate. If necessary, this permits estimating the heat loss from the back side of the quartz substrate.

Twelve (12) selected representative frames from the 400 ft. 16 mm motion film are presented for each Run in Figures A-6a — A6i, along with the frame number, counted from frame 100 at the onset of heating, and with the time from the onset of heating, at 10 seconds. Filming took place at either 10 or 100 pps, as indicated in the matrix given in Table A-I. The images were obtained by projecting the film on a large screen, picking it up with a video camera, and using a frame grabber and digitizer for storage on laser discs. The times shown may differ slightly from the frame number because the camera speed may vary, as when changing framing speed. The LED's seen in the bottom of each image provide synchronization with the thermal data, following the time format given in Figure 3.10.

The nucleation delay time here is defined as the time interval between the onset of heating and the moment when the first vapor bubble appears. For a given input heat flux a distinct relationship exists, in the absence of buoyancy, between the nucleation delay time, the heater surface superheat, and the liquid temperature distribution at the onset of boiling. The latter quantities govern the character of the early bubble dynamics and the spread of the boiling across the heater surface. Such processes are described in detail in Ervin and Merte (1991), Ervin et al (1992), and Lee and Merte (1993), using the results of transient boiling tests in the 5.1 second drop tower at the NASA Lewis Research Center. Based on these tests an optimum correlation was developed, as shown in Figure A-7, in order to estimate the delay times expected in the flight experiment. All nucleation delay times measured with the PBE-IA, including the pre-and post-flight ground tests, are plotted in Figure A-7. The comparison with the flight data is quite good, while convection effects result in some scattering. The limitations on the lower levels of input heat flux become obvious in such a plot, where nucleation can not take place in a 5.1 second drop tower below a heat flux of about 5.5 w/cm^2.

Figure A-8 is a plot of the mean heater surface superheat at nucleation for the same tests plotted in Figure A-7. It is noted that a peak exists in the mean heater surface superheat on nucleation between the high and low levels of heat flux, even with different subcooling levels, and is particularly high in microgravity. In addition, for the most part, as the subcooling level increases the heater surface superheat on nucleation is smaller. These phenomena will be discussed below in terms of heterogeneous and homogeneous nucleation theories, with the influence of the liquid temperature gradients at the heater surface and bulk liquid subcooling incorporated in the latter.

In certain circumstances of the test matrix followed here, it was noted that after the initial nucleation and prior to the spreading of the boiling process across the heating surface, the vapor bubble appeared to be growing spherically or hemispherically. Measurements of size as a function of time were made for these bubbles, since such growths can be compared with predictions of spherically symmetric analytic models, such as developed by Lee and Merte (1993). The measurements and corresponding experimental parameters are given in Figures A-9a — A-9i, while discussion of the comparisons with the models will be deferred until the next section. The analytical plots are included for all Runs of the matrix, even though measurements were not possible in cases where the growth rates were extremely large. This was universally true for the intermediate nominal heat flux level, $q''_T = 4$ w/cm^2, and in isolated cases for the low heat flux level of $q''_T = 2$ w/cm^2. From Figure A-8 it can be noted that the intermediate heat flux level corresponds to the maximum heater superheat level at nucleation.

From the photographic data taken through the transparent heating surface from the underside, it is possible to discern quite distinctly those portions of the heater surface on which dryout has taken place. Examples are abundant in Figures A-6a — A-6i. It is observed that under some circumstances this is a time varying phenomena, and is related in some fashion to both the transient mean heater surface temperature and heat transfer coefficient. If measurements of the time varying fractional area of the heat transfer surface in contact with vapor, which will be termed the fractional dryout area, can be made with sufficient temporal detail, it is felt that the possibility exists for quantifying the contributions to the total heat transfer of the different modes of heat transfer taking place. Since only mean heater surface temperatures and heat transfer coefficients are measurable at present, only spatial mean parameters can be determined: local measurements in the future would permit determination of these parameters on a spatially local basis.

In order to provide an efficient means for quantifying the time varying fractional dry portion of the heater area from the 16 mm films, an optical processing system was set up in which the 16 mm film is projected on a screen with a motion picture projector; the motion is stopped at the desired frame; the time noted; the image picked up with a video camera, which can then be stored on a VCR and/or immediately digitized with a frame grabber for greater resolution; the digitized data is stored on an optical disc for later processing. The fractional dry area measurements were made from the digitized data for selected portions of each Run, which are indicated on the index, Table A-IV. The fractional dry area and corresponding mean heater surface temperatures are plotted in Figures A-10a--i — A-10i--i. A predictable conformity is to be noted in each Run between the fractional dry area and the mean heater surface temperature: As the fractional dry area increases for a

given heat flux input, so does the mean heater surface temperature. Sample images showing dryout and rewetting in each of the selected portions of each Run are included as Figures A-10a--iv — A-10i--iv. Discussion of the development of the microgravity boiling heat transfer coefficients, presented in the intermediate Figures will be deferred until the next section.

Figures A-11 — A-13 provide the same experimental results as described for Figures A-1 — A-3 above, except that the former were obtained at a/g = +1 during the post-flight testing of the hardware, following the identical automated matrix cycle as for the space flight. These results provide data by which direct comparisons can be made of behavior between earth gravity and microgravity under otherwise identical circumstances. For the present here it may be stated that nucleate boiling always took place at the highest heat flux level, never took place at the lowest heat flux level, and sometimes took place at the intermediate heat flux level. An additional benefit of the tests conducted at a/g = 1 is the reasonable agreement to be noted between the measured heat flux inputs in Figures A-12a — A-12i and the asymptotic steady state values computed from the measured mean heater surface temperatures, as plotted in Figures A-13a — A-13i. This reinforces both the measurements conducted and the computational procedures adopted.

6. DISCUSSION

6.1 Conduction Effects

In the absence of buoyancy and forced convection, heat transfer in fluids takes place by pure stationary conduction, as in solids. This was confirmed for relatively short periods (up to 5.1 seconds) in microgravity, in solids and in fluids before nucleation take place, by the measurements of Ervin and Merte (1991), also appearing in Ervin et al (1992). In this case the physical processes of conduction conformed closely to the analytical solution for two semi-infinite solids, initially at a uniform temperature, with a uniform step in a plane heat source at the interface.

An important consideration in the measurement of the mean heater surface temperature as determined from the measurement of the mean electrical resistance of the thin gold film, from Equation (3.1), is how accurately the mean resistance actually represents the mean temperature. This question is examined analytically in detail in Appendix D, with the conclusion that the maximum discrepancy between the true mean surface temperature and that computed from the mean surface electrical resistance is less than the absolute uncertainty in the heater surface temperature measurement, under the most adverse temperature distribution over the surface.

6.1.1 Conduction in Substrate

The analytic solution in the interface temperature between the two semi-infinite solids, which corresponds to the gold film heater surface temperature in the physical system, is plotted as the 1 - D Analytical Surface temperature for reference purposes for each of the Runs of the matrices of PBE-IA-IB-IC in Figures 1a - 1i of Appendices A, B, C.

The discrepancy between the analytical and the measured values increases for the lower level of heat fluxes, for which longer periods of conduction heat transfer in both the solid and fluid domains take place before nucleation occurs. This discrepancy is attributed to three-dimensional conduction effects during this period, primarily in the quartz substrate domain, which has a larger thermal diffusivity, $a = k/\rho c = 8.34 \times 10^{-7} m^2/s$, compared to a $= 5.24 \times 10^{-8} m^2/s$ for R-113. Comparisons of the short 5.1 second drop-tower ground based testing were excellent with the one-dimensional solutions. In this case the quartz substrate was less massive than that in the PBE, and the single heater surface on the substrate was located symmetrically. To confirm that three-dimensional effects were operating in the PBE a 3 - D finite element model was developed for the particular geometry of the PBE. The results are presented here for demonstration purposes.

Figure 6.1 shows the measured mean heater surface temperature for Run No. 3 of the PBE-IA on STS-47 from Figure A-1c. Also shown are the measured underside surface quartz temperatures under the center of each of the heaters from Figure A-5c, with the active heater side measurement being TM11, the larger increase of the two, as anticipated. Also indicated are the 1 - D analytical heater surface predictions from the semi-infinite solid solution, and the 3 - D predictions of both the heater surface and the quartz undersides using the finite element solution procedure with the heat flux input up to the nucleation point, followed by an imposed uniform surface temperature, which approximates quite well the measured value following nucleation. The 2 - D temperature distribution of the heater surface produced by the 3 - D finite element model is spacially averaged to give a single mean value, for purposes of comparison with the measurements. It is noted that this computation closely approximates the measured surface temperatures up to the nucleation point. The measured temperature rise occurring at 85 seconds was not incorporated into the 3 - D finite element model. Nevertheless, it is noted that the measured quartz underside temperatures follow the computed changes. The difference of 2°C between the measured and computed quartz underside temperatures is a consequence of taking the initial quartz temperature to be uniform at the initial bulk liquid temperature, in the computational process. An initial difference of 2°C across the quartz existed as a result of the heat transfer from the quartz to the surroundings, which were about 10°C cooler than the quartz surface.

This had little effect on net heat losses from the heater surface itself because of the low thermal conductivity of the quartz.

Figure 6.2 is an isometric plot of the 3 - D temperature distribution in the quartz substrate computed by the 3 - D finite element model, at the onset of nucleation at 40 seconds on Figure 6.1. This shows clearly the conduction taking place as departures from the 1 - D semi-infinite solid model. The potential influence that 3 - D conduction effects might have on the computation of the heat transfer coefficient to the fluid will be considered in the next section. The upper part of Figure 6.2 is a central section showing the 2 - D temperature distribution in the R-113 after 30 seconds of heating, and demonstrates that the extent of the penetration of the temperature disturbance is quite small.

Figure 6.3 presents an isometric plot of the 3 - D temperature distribution in the quartz substrate at 90 seconds in Figure 6.1, using a constant mean surface temperature of 75°C as measured, following nucleation at 40 seconds. This indicates that the temperature of the quartz underside surface has increased by approximately 3°C, in agreement with Figure 6.1. The 2 - D central section temperature distribution in the R-113 is also given at the top, but has no physical significance, since boiling has begun at 40 seconds.

6.1.2 Conduction in Fluid

Figure 6.4 shows the measured mean heater surface temperatures as fitted from the measurements of heater current and voltage at 10 Hz. Also repeated from Figure 6.1 are the 1 - D and 3 - D computed heater surface temperatures prior to nucleation, which include conduction heat transfer taking place in the fluid, valid as long as the fluid is motionless. The heat transfer coefficients to the fluid are computed from the measurements with the 1 - D finite difference procedure for the case where a polynomial fit is used between each of the measurement points for interpolation purposes, and results in the oscillations observed. The 3 - D finite element computation of the heat transfer coefficient during the conduction phase up to nucleation provides a reasonable fit to the heat transfer coefficients computed by the finite difference method when some visual filtering is applied. Once nucleation occurred the 3 - D finite element model in Figure 6.4 imposed a constant heater surface temperature, which approximates the measurements out to about 85 seconds when dry-out begins. The heat transfer coefficient computed from the 3 - D finite element model during the 40 seconds to 85 second interval follows the smoothed version of that computed from measurements with the 1 - D finite difference model. This is a consequence of the relatively low thermal diffusivity of the quartz, which means that the penetration depth of the disturbances taking place at the surface with these frequency levels are not influenced by three dimensional effects.

In order to determine the effect that filtering of the measured mean heater surface temperature would have on the heat transfer coefficient computed with the 1 - D finite difference model, two different degrees of filtering techniques were applied, presented in Figures 6.5 and 6.6 for the same Run No. 3 of PBE-IA (STS-47). Figure 6.5 presents the mean heater surface temperature and computed heat transfer coefficient taking three (3) successive heater surface temperatures at 100 ms intervals averaged to provide the temperature at the middle point on the time scale. This procedure was advanced for each 100 ms data point. The smoothing obtained is noted by comparison with Figure 6.4.

Figure 6.6 is similar to Figure 6.5, except the averaging process was conducted over five (5) successive measurements, advancing also in 100 ms steps. Excessive filtering is to be avoided, since it is possible that a real transient might be eliminated. The results presented in Figures 1a — 1i of Appendices A - C were obtained using the 3 point averaging technique, with a polynomial fit for interpolation between data points.

One further assessment of the procedures followed in the numerical computation of the heat transfer coefficient from the measured mean heater surface temperatures is necessary. In carrying these computations out it is assumed that the heat flux input to the heater surface is constant, at some interpreted mean value. That this is not the case can be noted by examining Figures A-2a — A-2i, for example.

A detailed examination of the effect of taking a constant heat flux was conducted for PBE-IA Run No. 3, using the 3 - D finite element model developed here. In one case a curve is fitted to the measured variation in the input heat flux, while in the other case the input heat flux is taken to be constant. The results are given in Figure 6.7, and it is noted that any discernible discrepancy occurs only in the immediate vicinity of the nucleation point, where the largest temperature change occurs, with the maximum variation in the input heat flux. At this point the peak computed heat transfer coefficient is reduced from 2100 to 1600 w/m^2K. Actual two dimensional variations over the heat transfer surface make such distinctions between the mean input heat fluxes difficult to justify, and a constant mean input heat flux is used here throughout.

The temperature distribution in the liquid at the nucleation sites at the moment of nucleation is necessary for assessing the vapor bubble nucleation process in microgravity, to be examined below. These are computed as 1 - D transient conduction processes in the liquid using as boundary conditions, however, the local heater surface temperatures and liquid heat flux computed using the 3 - D finite element model for the substrate. This procedure was necessary because the grid spacing of the finite element model was too coarse to provide the spacial temperature resolution necessary in the liquid. The results of the computations are presented here, although the application will be made in the analysis

of the nucleation process below. Figure 6.8 is a sketch of the gold film heater surfaces on the quartz substrate, for purposes of orientation here. The camera view as placed on the film is from the underside of the heater, given in the upper portion of Figure 6.9. Also superimposed are the grid for the 3 - D finite element model and the nucleation site locations as observed from the motion picture films. As described earlier PBE-IA (STS-47) and PBE-IC (STS-60) use identical hardware, so the nucleation sites for both are placed on the left side, the primary heater, while PBE-IB (STS-57) used the backup heater of a different system, and the nucleation sites are shown on the right side.

It was originally expected that nucleation and early bubble growth would always occur in that part of the heater having the highest temperature, in the central portion, and not near the edges of the heater where the temperature falls off sharply because of 3-Dimensional conduction in the substrate. The latter behavior was confirmed by early finite difference computations of the 3 - D substrate temperature distributions, and by the recent 3 - D finite-element transient computations presented above.

Results have indicated that under certain circumstances nucleation does not take place of the domains of highest surface temperature, but sometimes takes place at locations on the heater surface where the temperatures are lower - near the edges, depending on the heat flux level. This is illustrated in the upper part of Figure 6.9, in which the locations of the nucleation sites are indicated for each Run in the three PBE experiments flown to date. It is noted that the highest heat flux cases, Run Nos. 1, 4, 7 nucleated at the identical site near an edge on both the STS-47 and STS-60, identified as (a). For the same Run No. 1, 4, 7 on the STS-57, nucleation also occurred at a single site near an edge, identified as (h) in Figure 6.9. Where the nucleation sites in particular Run Nos. are identified as not determined, this corresponds to the cases where the vapor bubble growth was quite energetic, such that no vapor bubble was visible in one film frame but filled the entire heater surface in the next. It is assumed in these cases that nucleation occurred in the highest superheat domain - in the central part of the heater. This is consistent with Run Nos. 2 and 5 on STS-47 and -60, point (b) in Figure 6.9.

To illustrate the extent to which temperature differences exist across the heater surfaces, and in particular to determine how local values may differ from the mean heater surface temperature determined from the measurement of the overall electrical resistance, computations from the 3 - D finite element model are plotted in Figures 6.10 - 6.12 for the representative input heat flux levels of 7.0, 3.5, and 1.75 w/cm^2, respectively, used in the PBE. The upper solid curve is the uniform surface temperature computed from the 1 - D transient model, while the dashed curve is the mean heater surface temperature computed from the 3 - D transient finite element model. The nodes indicated on each of Figures 6.10

- 6.12 are located as shown on Figure 6.9. The same initial temperature of 49°C was used in all cases. The nodal temperatures were utilized for interpolation to determine the heater surface temperatures at the location and moment when nucleation took place, as well as the temperature distribution in the liquid at this time, in order that the circumstances under which both the nucleation and subsequent vapor bubble growth might be more accurately described.

Several observations can be made from Figures 6.10 - 6.12:

(1) The 1-D model computations provide the largest temperature rise, due to the absence of lateral conduction.

(2) Nodes 2 and 5 provide the highest local temperature, and are virtually identical for short periods of time, to 20 seconds, because these are interior points. With the lowest heat flux level at longer times, in Figure 6.12, the temperature of Node 2 becomes slightly higher than that of Node 5, for the same reason.

(3) Nodes 7 and 9 are virtually identical, with the lowest temperature rises, since these are at the farthest corner of the heater surface. Note 9 has a slightly higher temperature because it is closer to an adiabatic boundary.

(4) Nodes 1, 4, 8, 6, 3 are similar in behavior, since all have similar locations at the boundary of the thin-film heating surface. Node 8 becomes slightly lower in temperature at longer times, as in Figure 6.12, because of lateral conduction effects.

(5) The discrepancy between the mean and 1 - D surface temperatures increase with time, again because of lateral conduction in the substrate.

The local heater surface temperatures and heat flux were then used to compute the local temperature distributions in the liquid normal to the heater surface at the moment of nucleation, for each of the nine (9) Runs for each of the three PBE space flights to date. These are presented in Figures 6.13 - 6.15 for PBE-IA (STS-47), PBE-IB (STS-57), and PBE-IC (STS-60), respectively, as local liquid superheats. It is noted that the Runs with the highest heat flux, Nos. 1, 4 and 7, have the lowest total superheated liquid content at nucleation, which is related to the non-dynamic bubble growth rates. The medium heat

flux case, Run Nos. 2, 5 and 8, have the highest local surface temperature at nucleation, with some variability with subcooling between them.

It should be recalled that PBE-IA (STS-47) and PBE-IC (STS-60) use the identical hardware, so similarities in behavior should be expected. In particular, in Figures 6.13 and 6.15, the positions of Run Nos. 6 and 9 which are low subcooling and saturated, respectively, are high relative to Run No. 3, which has a high subcooling. This means that for the same heat flux that nucleation took place preferentially at a lower heater surface temperature, and from Figure 6.9, at a location where the superheats indeed were lower. This is confirmed in Figure 6.14, PBE-IB (STS-57) where the experimental apparatus was similar, but not identical. Run No. 9 is missing in Figure 6.14 because the nitrogen gas remaining at the end of the experiment was not sufficient to pressure the system, necessary to collapse the vapor remaining from Run No. 8. Nucleation therefore could not take place.

6.2 Natural Convection Effects

Natural convection is driven by buoyancy, and its onset may be described in terms of an instability in which disturbances are always present. Reducing the buoyancy by reducing the body forces delays the onset of the convection and reduces the resulting convection velocities. However, acting over a sufficiently long period of time it can be anticipated that any non-zero level of body force, no matter how small, will produce motion, depending on the stabilizing forces acting in the particular circumstance. Reference was previously made to PBE-IC (STS-60) Run No. 8, during the single phase transient heating process, in which a disturbance of about 0.3 mg perpendicular to the heating surface at about 16 seconds (Table XII) and lasting approximately 2 seconds induces a slight amount of natural convection. It can be noted in figure C-1h that this natural convection in turn affects the mean surface temperature and the heat transfer coefficient.

The results of the post-flight tests at $a/g = +1$, in which non-boiling natural convection took place, provided an opportunity to compare values of the natural convection heat transfer coefficients generated by the procedure followed for the microgravity boiling cases with values from well established natural convection correlations. For example, the correlation of Lloyd and Moran (1974) for a horizontal surface facing upward predicts a heat transfer coefficient of $h = 460$ w/m^{2}k for R-113 at earth gravity. This is to be compared with measurements over the range $h = 490 - 550$ w/m^{2}k from Figures 11b, 11c, 11e, 11f, 11h, 11i, in both Appendices A and C.

6.3 Nucleation

The mean heater surface superheat at nucleation, or the onset of boiling, are plotted for PBE-IA-IB-IC in Figures 8 of Appendices A, B, C, respectively, as a function of the input heat flux, which is directly proportional to the heat flux to the fluid in the microgravity non-boiling conduction heat transfer domain. It is noted that in all cases except for a/g = +1, where natural convection is dominant, that a distinct peak exists in the mean heater surface superheat at nucleation between the high and low levels of heat flux, and is particularly high in microgravity. In addition, for the most part the heater surface superheat on nucleation is smaller as the subcooling level increases, which would appear to counter intuition.

The possibilities for both heterogeneous and homogeneous nucleation were considered, and will be discussed below. The role of the liquid temperature gradient at the heater surface interface at nucleation, along with bulk liquid subcooling, were also examined. It was demonstrated by Ervin and Merte (1991) that nucleation of R-113 on a large gold film heater can occur at heater surface superheat levels on the order of 4°C if a sufficiently rapid heater surface temperature increase can be instituted. In this latter case, approximations to step changes in heater surface temperatures were being attempted. On the other hand, as reported by Iida et al (1993), high rates of heating of ethyl alcohol at atmospheric pressure by a small (0.1 mm × 0.25 mm) platinum film 20 Angstroms thick on quartz, to 10^7°C/s, produced nucleation at the theoretical homogeneous nucleation point of 129°C superheat. In this case the liquid subcooling was 53°C, and the formation of the vapor bubbles was described as "Caviarwise bubble generation".

The transient heating of a liquid from a flat heater surface with a constant imposed heat flux while in microgravity implies that the transient temperature distribution in the liquid can be determined with confidence by computation, including the two-and three-dimensional conduction effects arising in finite systems. This was demonstrated above. By measurement of the time at which nucleation takes place, as determined from the photographic images obtained and generally confirmed by the associated transient disturbances of the measured mean heater surface temperatures and the system pressure, the physical circumstances existing at nucleation are known. Of particular interest here, with the R-113 test fluid used, is the heater surface superheat at nucleation as a function of the parameters of system pressure, initial bulk liquid subcooling, and imposed heat flux level.

The heater surface superheats at nucleation corrected for 3-dimensional conduction effects, representing the local rather than mean values of Figures in Appendices A, B, C, are given in Figures 6.13, 6.14, 6.15, for PBE-IA, -IB, -IC, respectively. It is noted here

also that the heater surface temperature for Run Nos. 1, 4, 7, are the lowest in all cases, although having the highest heat flux level. The intermediate levels of heat flux, represented in these Figures by dashed lines, have the highest heater surface superheat levels, while the lowest heat flux levels, represented by the heavy solid lines, have somewhat lower heater surface superheat levels at nucleation.

Referring now back to Figure 6.9, which shows the locations of the nucleation sites, it is noted that in the three Run Nos. 1, 4, 7 (the high heat flux level case) of PBE-IA and -IC, which were conducted with the same hardware, the nucleations all occurred at precisely the same location on the heater surface, designated by the letter (a). For Run Nos. 1, 4, 7 of PBE-IB, the nucleations also took place at the same location, except different than the preceding PBE-IA and -IC, designated by the letter (h). It may be concluded that these nucleations at the highest nominal heat flux level of $q''_T = 8$ w/cm^2 consist of heterogeneous nucleation, since they are associated with specific locations on the solid heater surface. This implies the presence of reproducible artificial nucleation sites. In all other cases presented the nucleation sites are at different random locations, and are termed as a form of homogeneous nucleation, in the sense that these cannot be associated directly with a specific nucleation site. The development of the expression for the effective cavity size necessary to produce these heterogeneous nucleations will now be presented, to be followed by the development of a homogeneous nucleation theory in the presence of a temperature gradient.

Heterogeneous nucleation theory considers that vapor bubble growth begins from a cavity at the solid heater surface in which vapor is assumed to be pre-existing. Cavities or crevices are present at the surfaces of all solids, differing only in size, number, and distribution of sizes, which depend in turn on how the solid was originally formed and on the subsequent mechanical treatment to which the material was subjected, such as machining, grinding, polishing, etc. Such cavities are filled initially with a gas, such as air, which can later then be expected to be displaced by the vapor of the liquid with which it might be placed in contact.

In the present case the solid surface is quartz, which is given a final finish by polishing with a material of typical dimensions of 1.4 microns (μ). If a spherical shape is assumed for these particles, the surface cavities remaining after polishing can be expected to have effective radii of 0.7μ or less. A scanning electron microscope was used to obtain back scattered electron images of a typical gold-film coated quartz surface used for boiling R-113. It was necessary to fracture the surface to a size small enough to fit within the apparatus. Using resolutions down to about 0.1μ, what appeared to be scratches on the surface could be observed, having a maximum width of 2.5μ, down to 0.1μ. The

objective of the analysis here is to demonstrate that experimental measurements of the nucleation process taking place are consistent with predictions of heterogeneous nucleation to within an order of magnitude of the size of potential cavities. Heterogeneous nucleation, however, does not account for the observed effects of the heat flux and bulk liquid subcooling, and hence the examination for the possibility of homogeneous nucleation was dictated.

A schematic for the development of the expression for the critical size nucleation cavity is given in Figure 6.16. The cavity is assumed to be circular in opening, and filled with vapor protruding hemispherically into the bulk liquid, with radius R_c. This nucleus will become activated and begin growing when the liquid temperature at the top of the vapor hemisphere equals or exceeds that predicted from liquid-vapor thermodynamic equilibrium on a curved interface. Such a concept is quite well known, was first presented by Griffith and Wallis (1960), and later modified and utilized by Hsu (1962).

The condition for mechanical equilibrium of a spherical (or hemispherical) vapor bubble is given by:

$$P_v - P_\infty = \frac{2\sigma}{R_c} \tag{6.1}$$

The integrated form of the Clausius-Clapyron Equation gives the relationship between the vapor pressure and temperature at a flat interface:

$$\left(\frac{dP}{dT}\right)_{sat} = \frac{P_v - P_\infty}{T_v - T_{sat}} = \frac{h_{fg}\rho_v}{T_{sat}} \tag{6.2}$$

Combining Eq. (6.1) with Eq. (6.2) provides the liquid superheat required for mestastable equilibrium of a spherical vapor bubble, Eq. (6.3).

$$T_v - T_{sat} = \frac{T\sigma T_{sat}}{\rho_v h_{fg} R_c} \tag{6.3}$$

Eq. (6.3) can be expressed in terms of heater surface superheat as:

$$T_w - T_{sat} = \frac{2\sigma T_{sat}}{\rho_v h_{fg} R_c} + (T_w - T_v) \tag{6.4}$$

Eq. (6.3) is plotted in Figure 6.16. With an imposed heat flux to the liquid, as is the case in the PBE, the temperature distribution in the immediate vicinity of the heater surface can

be taken to be approximately linear, as given by Eq. (6.5) and also indicated in Figure 6.16, when dealing with bubble dimensions of the order of microns, encountered here:

$$q'' = k\frac{T_w - T_v}{R_c} \tag{6.5}$$

T_v in Eq. (6.4) can be eliminated with the use of Eq. (6.5), resulting in:

$$T_w - T_{sat} = \frac{2\sigma T_{sat}}{\rho_v h_{fg} R_c} + \frac{q'' R_c}{k} \tag{6.6}$$

As a practical matter, the difference between T_w and T_v is negligibly small. Eq. (6.6) can be placed in an implicit form for R_c as in Eq. (6.7), or solved explicitly for R_c as in Eq. (6.8). The last term in the denominator of Eq. (6.7) is identical to the last term of Eq. (6.8), by the use of Eq. (6.3).

$$R_c = \frac{2\sigma T_{sat}}{\rho_v h_{fg}(T_w - T_{sat})\left(1 - \frac{q'' R_c}{k(T_w - T_{sat})}\right)} \tag{6.7}$$

$$R_c = \frac{k(T_w - T_{sat})}{2q''}\left\{1 \pm \left[1 - \frac{8\sigma T_{sat} q''}{\rho_v h_{fg}(T_w - T_{sat})^2}\right]^{1/2}\right\} \tag{6.8}$$

The simultaneous solution of Eqs. (6.3) and (6.5), given by Eqs. (6.7) or (6.8), is illustrated as their intersection in the sketch of Figure 6.16. The last term within the brackets in Eq. (6.8) has a value on the order of 0.05 for the typical experimental conditions of PBE with R-113. Thus, the resulting value of R_{cmax} becomes so large that the linearity of liquid temperature implicit in Eq. (6.5) is no longer valid. Only R_{cmin} remains, given by Eq. (6.7) if the last term in the denominator is neglected. From the measurement of q'' in the PBE and T_w at the moment of nucleation, both R_{cmin} and R_{cmax} can be computed.

For reference purposes only, R_{cmax} is plotted in Figure 6.17 for each of the 9 Runs conducted as PBE-IA, -IB, -IC on the STS-47, -57, -60, respectively, and are functions of the combination of liquid heat flux and local heater surface superheat at nucleation. The values tabulated range from 0.3 mm to 6.8 mm for the diameters of the cavities assumed to exist, which are unrealistic in this case. The corresponding values of R_{cmin} are plotted in Figure 6.18. Except for the effects of pressure on the properties in Eq. (6.8), used to vary the initial bulk liquid subcooling, the smaller the radius in Figure 6.18 the higher was the local heater surface superheat at nucleation. The consistency between any sets of these

minimum values of the critical size then is a measure of the consistency of the local heater surface superheats at nucleation.

Both R_{cmin} and R_{cmax} as computed from Eq. (6.8) for the experimental conditions for PBE-IA (STS-47) are plotted in Figure 6.19, using a logarithmic scale for the radius of the critical size nucleus. Also shown for reference purposes is a radius of 0.7μ, the typical radius of particles used for polishing by the fabricator of the quartz substrate. It is quite noteworthy that this dimension is of the order of magnitude of the theoretical values obtained from the measurements of heater surface superheat at nucleation. That these latter values are smaller than the polishing grit size is an indication of the true smoothness of the quartz surface.

Figure 6.20 is a plot of the minimum critical size nucleation cavities from Figure 6.19 for PBE-IA (STS-47) and the corresponding data from the PBE-IC (STS-60), superimposed on the locations at which these nucleations took place. The entire heater surface is shown. These two sets of experiments have the identical hardware and heater surface, and the locations were given previously in Figure 6.9. For convenience of visualization the letters corresponding to the nucleation sites in this latter Figure are reproduced in Figure 6.20. It is noted that the nucleation cavity sizes are smallest at the center, where the superheats are largest with the intermediate heat flux level. This heat flux level also produced the most violent early bubble growth rates. Figure 6.21 is similar to Figure 6.20 except that it applies to PBE-IB (STS-57).

The value of R_{cmin} given by Eq. (6.8) is plotted as a function of the wall superheat $T_w - T_{sat}$ in Figure 6.22 for each of the three pressure levels used to produce the subcooling in PBE-IA (STS-47). The intersection of the local heater surface superheat at nucleation with the corresponding pressure level then provides the theoretical nucleation cavity size for each Run No., indicated by the numbers attached to the points. A band corresponding to the typical radius of the particles used for polishing is included with an arbitrary uncertainty as $R = 0.7\mu \pm 0.1\mu$. This point at 0°C wall superheat is connected with each Run No. in order to identify and relate more clearly the corresponding input heat flux levels. It is noted in particular that the three Run Nos. 1, 4, 7 at the high heat flux level are clustered at low nucleation wall superheat levels, while the remaining Runs are clustered at a high superheat level, except for Run No. 3 which appears to be an anomaly. The nucleation for Run Nos. 1, 4, 7 all occurred at precisely the same point on the heater surface, and also with PBE-IC (STS-60), as was shown on Figures 6.9 and 6.20. These nucleations are identified as heterogeneous nucleations, since they all took place at a unique location on the heater surface, whereas the other nucleations took place at various scattered

locations on the heater surface. Figures 6.23 and 6.24 are similar to Figure 6.22, except that these correspond to PBE-IB (STS-57) and PBE-IC (STS-60), respectively.

Also plotted on Figures 6.22 - 6.24 are the temperature distributions in the liquid for Run Nos. 1 and 9, corresponding to the highest and lowest levels of heat flux. Over the maximum range of R_c covered here, 1 micron, the liquid temperature changes are 0.12°C and 0.038°C, respectively. These changes cannot be detected on the temperature scales used here. Also noteworthy here is that the superheated boundary layers are considerably larger in size than the diameters of the critical size nuclei represented in Figure 6.22 - 6.24. This means that the possibility for homogeneous nucleation to take within these superheated boundary layers should be given serious consideration for explaining the seemingly random locations of the nucleation sites, under certain circumstances. This is reinforced by the observation that the nucleations taking place at the highest level of heat flux, corresponding to Run Nos. 1, 4, 7 in PBE-IA-IB-IC, all occurred at fixed physical locations, so as to be classified as heterogeneous nucleation. If heterogeneous nucleation explains the low level of heater surface superheat at nucleation at the high levels of heat flux in Figures 8 of Appendices A-C, then what remains is to describe or predict the increase of the heater surface superheat with increase in heat flux, as observed at the lower levels of heat flux of $q_T'' = 2$ w/cm^2 and 4 w/cm^2. This will now be examined.

In general terms, homogeneous nucleation refers to nucleation taking place in the absence of any other phases or foreign materials. As acknowledged by Skripov (1974), liquids can be superheated even in the presence of so-called artificial centers, provided that the liquid is heated at a sufficiently high rate such that the energy imparted to the liquid exceeds the latent heat of evaporation being absorbed at the active centers. A criteria is developed, with sample results for water, for the parameters necessary to obtain "impact" boiling, or homogeneous nucleation. These do not readily lend themselves to computation, requiring for calculation purposes assumptions of pending or available nucleation sites densities as $\tilde{\Omega} = 10^2$ cm^{-3} within the bulk liquid and $\tilde{\Omega}_A = 10^2$ cm^{-2} at the heating surface for homogeneous nucleation to take place. A construction similar to this will be developed below, except that no arbitrary values will be assumed — only that these quantities required for nucleation remain constant as other parameters, such as system pressure and heater surface flux, are varied.

The net conclusion of Skripov (1974) in the above is that high levels of heater power are required to produce the necessary conditions for impact boiling or homogeneous nucleation. On the other hand, the experiments conducted in the PBE-IA, -IB, -IC experiments demonstrate that just the opposite appears to happen in the absence of buoyancy, that homogeneous nucleation takes place as the heat flux is reduced.

The initial attempt made here will be to predict the behavior of homogeneous nucleation as the heat flux and system pressure are varied, since homogeneous nucleation has been observed at different levels of both of these parameters. Calculations based on the procedures established by Skripov (1974) were also carried out by Avedisian (1985) to predict homogeneous nucleation as produced by the pulse heating method, using as heater surface nucleation site densities of $n'' = 10^3 — 10^6\ cm^{-2}$. These resulted in calculations of volumetric nucleation rates of $J = 10^{15} — 10^{22}$ nuclei/cm^3-sec., producing homogeneous nucleation.

Homogeneous nucleation is viewed by Volmer (1939), among others, as the spontaneous formation and subsequent growth of a vapor bubble associated with random statistical energy fluctuations on a molecular scale within otherwise uniformly superheated liquids. Disturbances associated with the temperature gradients inherent in the pulse heating method, as utilized by Skripov (1974), also arise in the vicinity of rapidly growing vapor bubbles, and also was treated briefly by Skripov (1974). This phenomena may explain the behavior observed in the PBE during certain circumstances of boiling in which bubbles were observed to nucleate and grow in front of the main advancing liquid-vapor interface, and may also explain the phenomena of boiling spread in earth gravity described by Ervin et al (1992) as the rupture of a smoothly growing liquid-vapor interface.

When the thermodynamic state of the liquid is not near the critical state, so that $v_v >> v_\ell$ and the related condition of $P_v \cong P_s$ thus applies, thermodynamic equilibrium provides the critical size vapor bubble radius as:

$$r_c = 2\sigma/\left(P_s - P_\ell\right) \tag{6.9}$$

The integration of the Clausius-Clapyron equations relates the vapor pressure to the bulk liquid superheat:

$$P_s - P_\ell = \frac{r_v\, h_{fg}}{T_s}\,(T - T_s) \tag{6.10}$$

Substituting Eq. (6.10) into Eq. (6.9), the critical vapor bubble radius is now expressed in terms of the bulk liquid superheat:

$$r_c = 2\sigma\, T_s/\left[\rho_v\, h_{fg}\,\left(T - T_s\right)\right] \tag{6.11}$$

Classical homogeneous nucleation theory, treated abundantly elsewhere (e.g., - Volmer (1939), Skripov (1974)) and based on statistical treatment of thermal fluctuations, provides an expression for predicting the rate of formation of critical size nuclei per unit volume of the form:

$$J = C\, e^{-G} \tag{6.12}$$

It should be recognized that the formation of a critical size nucleus does not insure that a vapor bubble will subsequently grow from this nucleus, but rather that this J constitutes a proportionality or a probability that such growth will take place. Volmer (1939) defines the product of J and a time interval dt as the nucleus formation probability.

The exponent G in Eq. (6.12) is the Gibbs No., defined as:

$$G(T) = W_{cr}/kT \tag{6.13}$$

where W_{cr} is the work of formation of a critical size bubble nucleus, and kT represents the mean molecular fluctuation energy per degree of freedom. The work of formation in Eq. (6.13) is given by:

$$W_{cr} = 16\pi\, \sigma^3/3T \left(P_s - P_\ell\right)^2 \tag{6.14}$$

Substituting Eq. (6.14) into Eq. (6.13) and then using Eq. (6.10), the Gibbs No. is expressed in terms of the fluid properties, including the bulk liquid temperature, as:

$$G(T) = \frac{16\pi\, \sigma^3}{3\ k}\left(\frac{T_s}{\rho_v\, h_{fg}}\right)^2 \frac{1}{T\left(T - T_s\right)^2} \tag{6.15}$$

This property is tabulated in Table XIII for R-113, for the nominal pressures used in the PBE, over the range of liquid superheat 21°C - 151°C, and is plotted in Figure 6.25. It is noted that as the superheat rises the Gibbs No. decreases at a successively increasing rate. If the nucleation probability is given by a form of Eq. (6.12), the limiting superheat necessary for homogeneous nucleation becomes readily apparent. However, the coefficient C in Eq. (6.12) remains to be established quantitatively.

According to Volmer (1939), the coefficient C is proportional to the concentration of elementary vapor bubbles arising from thermal fluctuations, and gives it as:

Gibbs No. for R113			
Superheat (C)	**P=107 kPa**	**P=116 kPa**	**p=150 kPa**
21	9.62E+05	7.99E+05	4.36E+05
22	8.32E+05	6.91E+05	3.76E+05
23	7.21E+05	5.99E+05	3.27E+05
24	6.28E+05	5.22E+05	2.84E+05
25	5.49E+05	4.56E+05	2.49E+05
26	4.81E+05	4.00E+05	2.18E+05
27	4.23E+05	3.51E+05	1.91E+05
28	3.73E+05	3.10E+05	1.69E+05
29	3.29E+05	2.73E+05	1.49E+05
30	2.91E+05	2.42E+05	1.32E+05
31	2.58E+05	2.15E+05	1.17E+05
32	2.30E+05	1.91E+05	1.04E+05
33	2.05E+05	1.70E+05	92478
34	1.82E+05	1.52E+05	82460
35	1.63E+05	1.35E+05	73640
36	1.46E+05	1.21E+05	65859
37	1.31E+05	1.09E+05	58979
38	1.17E+05	97415	52884
39	1.05E+05	87501	47475
40	94748	78686	42666
41	85304	70835	38384
42	76880	63833	34565
43	69355	57577	31155
44	62624	51981	28105
45	56594	46969	25373
46	51186	42473	22925
47	46330	38437	20726
48	41965	34809	18751
49	38037	31544	16975
50	34499	28603	15375
51	31308	25951	13934
52	28428	23558	12634
53	25827	21397	11460
54	23476	19443	10400
55	21348	17675	9441.4
56	19422	16075	8574.3
57	17677	14626	7789.3
58	16094	13312	7078.3
59	14659	12120	6433.9
60	13355	11038	5849.5
61	12171	10055	5319.3
62	11096	9162.5	4838
63	10117	8350.9	4400.9
64	9227.6	7612.8	4003.8
65	8417.7	6941.2	3643
66	7680.2	6329.8	3314.9
67	7008.5	5773.1	3016.5
68	6396.4	5266	2745.1

Table XIII. Gibbs Number for R-113.

69	5838.5	4803.8	2498
70	5329.7	4382.5	2273.2
71	4865.6	3998.4	2068.5
72	4442.2	3648	1882.1
73	4055.8	3328.4	1712.3
74	3703	3036.8	1557.7
75	3380.9	2770.6	1416.8
76	3086.8	2527.6	1288.5
77	2818.1	2305.7	1171.6
78	2572.6	2103.1	1065
79	2348.3	1918.1	967.91
80	2143.4	1749.1	879.43
81	1956	1594.8	798.8
82	1784.8	1453.8	725.34
83	1628.4	1325	658.4
84	1485.3	1207.4	597.42
85	1354.6	1099.9	541.87
86	1235	1001.7	491.28
87	1125.8	912.08	445.21
88	1025.9	830.17	403.26
89	934.64	755.37	365.07
90	851.21	687.06	330.32
91	774.97	624.68	298.7
92	705.3	567.74	269.94
93	641.65	515.76	243.8
94	583.5	468.32	220.03
95	530.39	425.04	198.44
96	481.9	385.55	178.83
97	437.62	349.55	161.02
98	397.21	316.72	144.87
99	360.33	286.8	130.22
100	326.69	259.54	116.94
101	296.02	234.71	104.92
102	268.05	212.11	94.029
103	242.56	191.54	84.178
104	219.34	172.83	75.274
105	198.2	155.82	67.229
106	178.96	140.36	59.969
107	161.45	126.32	53.421
108	145.54	113.57	47.521
109	131.07	102.01	42.21
110	117.93	91.533	37.434
111	106.01	82.039	33.143
112	95.189	73.445	29.294
113	85.382	65.67	25.845
114	76.498	58.644	22.757
115	68.457	52.299	19.997
116	61.184	46.575	17.535
117	54.612	41.416	15.34
118	48.679	36.771	13.387

Table XIII. Continued.

119	43.327	32.593	11.653
120	38.504	28.839	10.116
121	34.163	25.472	8.7563
122	30.261	22.454	7.5558
123	26.756	19.754	6.4983
124	23.613	17.341	5.5691
125	20.797	15.188	4.7548
126	18.279	13.27	4.0431
127	16.03	11.565	3.4229
128	14.025	10.051	2.8843
129	12.24	8.711	2.4181
130	10.654	7.5261	2.0162
131	9.2479	6.4812	1.6711
132	8.0033	5.5618	1.376
133	6.9041	4.755	1.125
134	5.9358	4.049	0.91267
135	5.0848	3.433	0.73405
136	4.339	2.8972	0.58478
137	3.6871	2.4329	0.46096
138	3.1192	2.0319	0.35906
139	2.6261	1.6871	0.27597
140	2.1994	1.3918	0.20891
141	1.8316	1.1402	0.15543
142	1.516	0.927	0.11333
143	1.2464	0.7473	0.080727
144	1.0173	0.59685	0.055927
145	0.82362	0.47176	0.037476
146	0.66091	0.36858	0.024109
147	0.52514	0.28424	0.014738
148	0.4127	0.21598	0.0084359
149	0.32036	0.16136	0.0044229
150	0.24525	0.11823	0.00205
151	0.1848	0.084688	0.00078907

Table XIII. Continued.

$$C = n\left[\frac{6\ s}{(3 - b)\ \pi\ m}\right]^{1/2} e^{-\frac{\lambda m}{kT}} \tag{6.16}$$

The exponent is the ratio of the latent heat per molecule to the mean fluctuation energy per degree of freedom, which is typically quite small, so that the exponential term may be approximated by unity. In Eq. (6.16), b is defined as:

$$b = \left(P_s - P_\ell\right)/P_s = \frac{P_\ell\ h_{fg}}{T_s\ P_s}\ (T - T_s) \tag{6.17}$$

Fisher (1948) estimates the coefficient C in Eq. (6.12) from the theory of absolute reaction rates as:

$$C = \frac{n\ k\ T}{h}\ e^{-\Delta f_0^*/kT} \tag{6.18}$$

where Δf_0^* is the free energy of activation for the motion of an individual molecule of liquid past its neighbors into or away from the bubble surface, and may be considered equivalent to the latent heat per molecule, λ_m in Eq. (6.16).

Cole (1974) cites two additional expressions for C in Eq. (6.12): One due to Moore (Eq. (62) in Cole) reduces to Eq. (6.16) above, and the other due to Zeldovich - Kagan (Eq. (64) in Cole) reduces to Eq. (6.16) with b = 0.

The parts of C in Eqns. (6.16) and (6.18) excluding the exponentials, which are close to unity, were evaluated for R-113, at atmospheric pressure over the range of liquid superheats of 90°C - 150°C. It is obvious from the expressions themselves that these are weak functions of system pressure, and are also relatively weak functions of the liquid superheat. However, these two terms differ from one another by two orders of magnitude, being 4.90×10^{38} and 3.43×10^{40}, respectively, at a liquid superheat of 100°C. In computations of the classical isothermal homogeneous nucleation temperatures by Skripov (1974), it is demonstrated that a two order of magnitude difference in J corresponds to a difference in the nucleation temperature between 0.7°C and 5.0°C, depending on the value of b in Eq. (6.16), and represents a negligible difference in view of other uncertainties in the homogeneous nucleation theories. For R-113 at atmospheric pressure and 100°C superheat b has the value of 0.91, and a difference of 100 in J results in a difference of 5°C in the homogeneous nucleation temperature.

For present purposes it will be assumed that C in Eq. (6.12) is constant for a given fluid and that J varies only because of the Gibbs No. G.

As described earlier, the heater surface for the PBE consists of a flat polished quartz substrate coated with a gold film approximately 400 Angstroms thick, producing a flat heater surface 119 mm × 38 mm (0.75" × 1.50"). Except for a narrow band around the edge of the heater surface, the heat transfer process to the fluid is a transient one-dimensional conduction process. The edge effects will be neglected in the analytical development below, except it is recognized to result in a lower heat flux to the liquid within this narrow band. It was demonstrated in Figures 6.22-6.24 that the critical size nucleation cavity associated with the heterogeneous nucleation taking place is quite small relative to the corresponding temperature gradients at these levels of heat flux. Since the critical size nuclei with homogeneous nucleation are even smaller, it seems appropriate to consider the homogeneous nucleation taking place during the transient heating process to occur in a quasi-isothermal temperature field near the heater surface. A specific relationship should then exist between the rate of formation of the critical size nuclei per unit volume given by Eq. (6.12) and the rate of formation of these critical size nuclei per unit heater surface area in the presence of the transient temperature gradient normal to the heater.

In a manner similar to that given by Skripov (1974), the number formed within a time τ and within a distance x from the heater surface is given by:

$$n'' = \frac{n}{A} = \int_o^{\tau} \int_o^{x} J \, dx \, dt \tag{6.19}$$

where J is given by Eq. (6.12), and G(T) is given by Eq. (6.15), and T (x,t). Thus:

$$G(T) = G\,[T\,(x, t)] \tag{6.20}$$

Expanding T(x,t) in a Taylor Series about x = 0, t = τ, neglecting the higher order terms:

$$T(x,t) = T(o, \tau) + X\left(\frac{\partial T}{\partial x}\right)_{\substack{x = o \\ t = \tau}} + (t - \tau)\left(\frac{\partial T}{\partial t}\right)_{\substack{x = o \\ t = \tau}} \tag{6.21}$$

Expanding G(T) of Eq. (6.20) in a Taylor series about T(o, τ):

$$G[T(x, t)] = G\big[T(o, \tau)\big] + \big[T(x, t) - T(o, \tau)\big]\left(\frac{dG}{dT}\right)_{\substack{x = o \\ t = \tau}} \tag{6.22}$$

Substituting Eq. (6.21) into Eq. (6.22) gives:

$$G[T(x, t)] = G\left[T(o, \tau)\right] + \left(t - \tau\right) \left(\frac{\partial T}{\partial x}\right)_{\substack{x = o \\ t = \tau}} \left(\frac{dG}{dT}\right)_{\substack{x = o \\ t = \tau}} + X \left(\frac{\partial T}{\partial x}\right)_{\substack{x = o \\ t = \tau}} \left(\frac{dG}{dT}\right)_{\substack{x = o \\ t = \tau}} \tag{6.23}$$

Integrating Eq. (6.19) first with X:

$$\int_o^x J\, dx = \int_o^x C e^{-G[T(x, t)]}\, dx$$

$$= C \int_o^x \exp\left[-G(o, \tau) - (t - \tau)\, \dot{T}\, G_T - X\, T_x\, G_T\right] dx$$

$$= \frac{-C}{G_T\, T_x} e^{-G(o,t)} \times e^{-(t - \tau)\, \dot{T}\, G_T} \times \left(e^{-xT_x G_T} - 1\right) \tag{6.24}$$

For convenience here and below, the terms T_x, $\dot{T}$ and G_T represent the definitions given in Eq. (6.23). Now integrating Eq. (6.24) (and Eq. (6.19)) with t:

$$n'' = \frac{C}{G_T^2\, T_x\, \dot{T}} e^{-G(o, \tau)} \left(e^{-xT_x G_T} - 1\right)\left(1 - e^{\tau \dot{T} G_T}\right) \tag{6.25}$$

The derivatives in Eq. (6.25) are all to be evaluated at the moment of nucleation. The term G_T is evaluated from:

$$G_T \equiv \frac{dG}{dT} = -G(T) \times \frac{1}{T} \frac{(3T - T_s)}{(T - T_s)} \tag{6.26}$$

where G(T) is given by Eq. (6.15). It can be demonstrated that for reasonable values of x and τ the two exponentials in the brackets of Eq. (6.25) are negligible compared to unity, so Eq. (6.25) may be written as:

$$n'' = \frac{-C \times e^{-G(o, \tau)}}{G_T^2\, T_x\, \dot{T}} \tag{6.27}$$

From Eq. (6.12), the numerator of Eq. (6.27) represents J evaluated at the heater surface conditions at the moment of nucleation, or:

$$\frac{n''}{J} = -\frac{1}{G_T^2\, T_x\, \dot{T}} \tag{6.28}$$

It is assumed that for a given fluid the left side of Eq. (6.28) is constant at the moment of nucleation as any other conditions are varied, such as system pressure and/or heat flux, in the present case. If true, it thus should be possible to predict the influence of these variables on the temperature at which homogeneous nucleation takes place in the vicinity of a flat heat surface under slowly varying temperatures. It thus becomes unnecessary to assume any specific values of n" or J to compute the homogeneous nucleation temperature, as was necessary to determine the superheat limit, or maximum value arising with large heating rates, termed impulse heating by Skripov (1974).

Using the imposed power input to the thin film gold heater it is possible to write expressions for the spatial and temporal derivatives in Eq. (6.28) at the moment of nucleation in the absence of buoyant effects in microgravity, from the solution for transient conduction in semi-infinite solids:

$$T_x = \left(\frac{\partial T}{\partial x}\right)_{x=o} = -\frac{q''_\ell}{k_\ell} \tag{6.29}$$

$$\dot{T} = \left(\frac{\partial T}{\partial t}\right)_{x=o} = \frac{q''_\ell}{k_\ell}\left(\frac{a_\ell}{\pi}\right)^{1/2} \times \frac{1}{t^{1/2}} \tag{6.30}$$

The time in Eq. (6.30) can be expressed in terms of the heater surface temperature:

$$T(o,t) - T_i = \frac{2\, q''_\ell}{k_\ell}\left(\frac{a_\ell t}{\pi}\right)^{1/2} \tag{6.31}$$

From the solution for a plane heat source at the interface of two semi-infinite solids, the heat flux to the motionless liquid is a constant fraction of the input flux, written here as:

$$q''_\ell = C_1 \times q''_T \tag{6.32}$$

Substituting Eqs. (6.29) - (6.32) into Eq. (6.28) and rearranging with all constants on the left:

$$K^* \equiv \frac{J \times k_\ell^3}{2\, n''\, C_1^3} \left(\frac{\pi}{a_\ell}\right) = \frac{G_T^2 \times q_T''^3}{T_n - T_i} \tag{6.33}$$

T_n is the heater surface temperature at nucleation, while T_i is the initial uniform bulk liquid temperature. The denominator of Eq. (25) can be expressed in terms of the heater surface superheat at nucleation and the bulk liquid subcooling as:

$$(T_n - T_i) = (T_n - T_s) + T_s - T_i)$$

$$\equiv (T - T_s)^* + \Delta T_{sub} \tag{6.34}$$

Substituting Eq. (6.34) into Eq. (6.33) and rearranging:

$$(T - T_s)^* = q_T''^3 \times \frac{G_T^2}{K^*} - \Delta T_{sub} \tag{6.35}$$

Eq. (6.35) is plotted in Figures 6.26 - 6.29 for R-113 as heater surface superheat at nucleation versus the total heat flux into the gold film for the nominal system pressures used to provide the desired initial bulk liquid subcoolings. According to the analysis here, subcooling influences the nucleation phenomena only indirectly as to the time required to attain a given heater surface superheat. Figures 6.26 and 6.27 are linear plots of the heater surface superheat at nucleation versus input heat flux, while Figures 6.28 and 6.29 are semi-log plots, logarithmic on the heat flux axis in order to cover a wider range of input heat flux. Figures 6.26 and 6.28 include the measurements from the PBE-IA and -IC (on the STS-47 and -60), which utilized the identical hardware, the prototype version of the PBE system. In order to plot the data, K^* in Eq. (6.35) was evaluated for PBE-IA Run No. 9, the saturated liquid case. The superheats follow the effect of system pressure reasonably well at the low heat flux level of 1.8 w/cm^2, but produce a higher superheat for two of the runs at 3.6 w/cm^2. However, these all follow the influence of the heat flux well, with the heater surface superheat increasing with heat flux. The estimated superheat limits resulting from the classical homogeneous nucleation theory with uniform bulk liquid temperatures are also indicated in Figures 6.28 and 6.29 for R-113. The decrease in the superheat as heat flux is reduced, as predicted by Eq. (6.35), occurs because more time exists for the random thermal fluctuations, always present, to produce nucleation. Such

can be observed only in a microgravity environment, because convection effects in earth gravity prevail over these fluctuations.

Figures 6.27 and 6.29 include the measurements from the PBE-IB (STS-57), designated as the Flight version, which is of the same construction as the prototype whose data are in Figures 6.26 and 6.28. Insufficient gas remained to pressurize the system prior to the last Run, No. 9, of the matrix for PBE-IB (STS-57) so that this Run began with residual vapor from the prior run. Run No. 5 was thus used to determine K^* for Figures 6.27 and 6.29. Reasonable good qualitative agreement is also present here with respect to the influence of both subcooling and heat flux.

In all cases of the highest heat flux levels included in Figures 6.26 - 6.29, the striking behavior arising with the heterogeneous nucleation described earlier is obvious. Attempts have been made to account for heterogeneous nucleation behavior by considering the wetting action of the liquid on the heater surface, in terms of the contact angle. A recent example is that of Iida et al (1994). However, as indicated in Cole (1974), the influence of the contact angle is insufficient to explain the low values of superheat observed in practice: a contact angle of 90° reduces the superheat by only approximately 30%. For a completely wetting liquid the predicted superheat is the same as for homogeneous nucleation.

Using the empirical value of K^* in Eq. (6.33) from one Run in each physically distinct facility, it is possible to estimate orders of magnitude of J at nucleation. For example, using $K^* = 2.57 \times 10^6\ w^3/°k^3\ cm^6$ from Figure 6.26, together with the properties of R-113, the ratio $J/n'' = 1.22 \times 10^{10}\ (cm\text{-}s)^{-1}$ from Eq. (6.33). If the minimum value of $n'' = 1\ cm^{-2}$ is taken as necessary for nucleation, then the rate of formation of the critical size nuclei becomes $J = 1.22 \times 10^{10} \left(cm^3\text{-}s\right)^{-1}$. If the range of n" is instead taken as $10^3 < n'' < 10^6$, as used by Avedesian (1985), then from Eq. (6.33) $1.22 \times 10^{13} < J < 1.22 \times 10^{16}$, which covers the range 10^{15} - 10^{22} for many organic liquids and water, as stated by Avedesian (1985).

6.4 Bubble Dynamics

Following the initial nucleation of vapor bubbles and prior to the spreading of the boiling process across the heating surface, for certain conditions the vapor bubbles appeared to be spherical or hemispherical, appropriate for measurement and comparison with predictions of spherically symmetric models. The number of film frames so obtained are listed in Table XIV for each of the nine runs in the three space flights, and the radii plotted as functions of time in Figures 9a — 9i of Appendices A, B, C. It is noteworthy that consistent measurements were possible only for Run Nos. 1, 3, 4, 7. Run Nos. 1, 4,

7 are those having the highest imposed heat flux (nominally $q_T'' = 8$ w/cm^2), and Run 3 has the lowest heat flux (nominally $q_T'' = 2$ w/cm^2), but the high level of subcooling (nominally $\Delta T_{sub} = 12°C$). Reexamining Figures 6.22 — 6.24 it is further noted that these Runs also have the lowest levels of heater surface superheat at nucleation, and Run Nos. 1, 4, 7 were associated with heterogeneous nucleation. Except for one (1) frame each in Run Nos. 6, 8, 9 of PBE-IC (STS-60), the early vapor bubble growths of all other runs were so rapid or dynamic in microgravity that no measurements were possible. These constitute the cases with high heater surface nucleation superheats in Figures 6.22 — 6.24.

Table XIV. Number of film frames obtained with hemispherical bubbles following nucleation. PBE-IA-IB-IC (STS-47-57-60).

Run No.	Figure No.	-IA	PBE-IB	-IC
1	9a	8	4	30
2	9b	0	0	0
3	9c	24	2	1
4	9d	2	4	30
5	9e	0	0	0
6	9f	0	0	1
7	9g	3	5	27
8	9h	0	0	1
9	9i	0	-	1

Based on both observations and measurements conducted in earth gravity at a/g = + 1, a/g = - 1, and in the 5.1 second NASA-Lewis drop tower, once nucleation occurred the propagation of the boiling across the heater surface and the bubble growths could be classified into one of six categories, termed as follows:

A. Advancement of interface by irregular protuberances.
B. Growth of mushroom-like bubble with spreading along heater surface.
C. Orderly growth of bubble with a "smooth" interface.
D. Orderly growth followed by onset of interface instabilities.
E. Energetic growth of bubble with unstable interface.
F. Slow motion of bubbles toward region of higher temperature.

The circumstances under which these took place with R-113 are given in detail in Ervin and Merte (1991) and in Ervin et al (1992), and will be summarized here:

A took place only at a/g = +1 with $q_T'' \geq 7$ w/cm^2.

B occurred only at a/g = +1 with $2 \leq q_T'' < 7$ w/cm^2.

C took place at a/g = -1 with high levels of heat flux $q_T'' \geq 7$ w/cm^2.

D was observed with a/g = -1 with $q_T'' < 7$ w/cm^2 and a/g $\cong 10^{-5}$, also with $q_T'' < 7$ w/cm^2. However, the lowest heat flux level possible in the drop tower was $q_T'' \cong 6$ w/cm^2.

E was observed only with a/g $\cong 10^{-5}$ and gave rise to the explosive growth with protuberances appearing over the entire liquid-vapor interface. The lowest heat flux possible was $q_T'' \cong 6$ w/cm^2.

F occurred at a/g = -1 and a/g $\cong 10^{-5}$ with $q_T'' > 7$ w/cm^2. The motion is attributed to thermocapillary effects.

Although the initial bulk liquid subcooling was expected to play a part in these categories, its effect is not yet clear.

From examination of the photographs from the PBE-IA-IB-IC (STS-47-57-60), with samples given in Appendices A, B, C, all boiling propagations are in either categories D or E, depending on the combination of heat flux and subcooling. The difference between these two categories lies in whether the bubble growth and/or propagation takes place relatively slowly or dynamically (explosively).

The maximum camera speed of 100 pps in the PBE was not capable of following the dynamic cases of category E. It is estimated that a framing rate greater than 3000 pps would have been necessary. Another manifestation of the distinction between categories D and E lies in the absence or presence of measured pressure spikes in connection with nucleation. The rate of data acquisition for the system pressure was limited to 10 Hz (100 ms between readings), and the peak pressure can occur at any time between these measurements. Examples of such pressure spikes can be noted in Figure A-3b for Run No. 2, Figure A-3e for Run No. 5, in Figure A-3f for Run No. 6, and in Figure A-3i for Run No. 9. The pressure control system was not capable of responding to this nucleation spike, nor was it so intended.

From the films, Category D takes place with the highest heat flux and for all subcoolings, in Run Nos. 1, 4, 7, and in Run 3, with the lowest heat flux and the largest subcooling. All other Run Nos. 2, 5, 6, 8, 9 result in very energetic or explosive initial

vapor bubble growths, Category E, which include all runs at the medium heat flux $q_T'' \cong 4$ w/cm^2 for all subcoolings, and at the low heat flux $q_T'' \cong 2$ w/cm^2 for low or zero subcooling.

The spreading process of boiling across a flat heater surface and the 3 - Dimensional vapor bubble growths constitute a complex phenomena not yet amenable to analytic solution. However, the dynamic growth of 1 - Dimensional spherically symmetric bubbles have been successfully modeled from the thermodynamic critical size, in which all of the physical mechanisms acting, including surface tension, viscosity, liquid inertia, and conduction heat transfer in the liquid have been incorporated. The cases for both initial uniform and non-uniform superheat have been treated by Lee and Merte (1993).

The analytical results of the models are included in Figures 9a - 9i of Appendices A, B, C, as the vapor bubble radii for the maximum and minimum growth rates, corresponding to the initial uniform and non-uniform superheat cases of the spherical smooth surface bubble growth models of Lee and Merte (1993). Both the measurements and analyses apply to the absence of buoyancy in microgravity conditions. The two limits of the models become necessary because a spherical vapor bubble is growing in an initially one-dimensional Cartesian temperature field. Also included in Figures 9a - 9i are the bulk liquid superheat distributions at the moment of nucleation, which provide an indication of the initial superheated liquid boundary layer thickness relative to the early vapor bubble dimensions.

As described above, some of the early vapor bubble growths observed on the heater surface in the space experiments appear to be hemispherical in shape. As such, the growth in the direction perpendicular to the flat heat surface occurs in an initially non-uniform liquid temperature domain, while the growth in the direction parallel to the flat heater surface can be considered as taking place in an initially uniform liquid temperature field. The early growth of the actual bubble within a thermal boundary layer at the heater surface occurs as a combination of the evaporation from a source whose temperature varies over the bubble surface area.

The computation of the actual growth would entail, as a minimum, a complex and computationally intensive solution of the transient axial-symmetric coupled two-dimensional energy, momentum and mass equations, with unknown temperature, surface tension and shape at the liquid-vapor interface. In the current absence of resources sufficient to pursue this direction, it was deemed desirable to investigate the possibility for developing an approximate model, combining the initial uniform and non-uniform liquid superheat cases referred to above. The process of combining the cases is empirical at present, but is based on the mechanistic view of the phenomena taking place. The

quantification or correlation of this process in terms of the governing parameters will be addressed in the future.

At the time corresponding to the measurement of each vapor bubble radius, a growth fraction F_g is computed, defined as:

$$F_g = \frac{(R_m - R_{C\text{-}NUS})}{(R_{C\text{-}US} - R_{C\text{-}NUS})} \tag{6.36}$$

where

R_m = measured hemispherical bubble radius

$R_{C\text{-}NUS}$ = computed bubble radius from initial non-uniform superheat model

$R_{C\text{-}US}$ = computed bubble radius from initial uniform superheat model.

This growth fraction F_g can be viewed as a measure of the degree to which the hemispherical vapor bubble growth is influenced by a combination of growth in initially uniform superheat and non-uniform superheat domains: $F_g = 1$ applies to the case of growth entirely in a uniformly superheated liquid, while $F_g = 0$ applies to the growth of a spherical or hemispherical bubble symmetrically surrounded by a non-uniform temperature distribution corresponding to the local liquid temperature distribution perpendicular to the heater surface. For the growth in a direction parallel to the heater surface, the initially uniform liquid superheat case, the maximum heater surface temperature is used as computed from the two-dimensional temperature distribution over the heater surface. This is somewhat higher than the mean surface temperature determined from the measured mean heater surface electrical resistance, since computations indicate that the heater surface temperature drops rapidly in the vicinity of the heater edges. This procedure makes a difference in those cases where the initial nucleation takes place near the edges of the heater, as occurs in some cases.

For those cases in Table XIV where three (3) or more images of growing hemispherical bubbles were obtained, it was possible to demonstrate that taking F_g to be constant for a particular Run appeared to be a reasonable assumption for expressing the actual growth in terms of the combination of the initial uniform and non-uniform superheat models. The one exception to this is Run No. 1 of PBE-IB (STS-57) in Figure B9a.

All of the Figures 9a - 9i in Appendices A, B, C follow the same format and contain the following information:

(a) The measurements of bubble radius taken from beneath the heater surface as a function of time, including the uncertainties.

(b) The predictions of bubble radius for the initially uniform superheat model, with the specification of the superheat used, which corresponds to the maximum (at the center of the heater surface).

(c) The predictions of bubble radius for the initially non-uniform superheat model, with the specification of the local heater wall temperature at the moment of nucleation used for this computation, determined from the 3 - D conduction model for the substrate temperature distribution for that run.

(d) The prediction of the vapor bubble growth using the Growth Factor F_g indicated on each plot.

(e) The local bulk liquid superheat distribution normal to the heater surface, at the nucleation location and at the moment of nucleation. This distribution is used as the initial distribution surrounding the hemispherical bubble of critical size to compute the growth of the non-uniform superheat model. Also indicated on these plots are the saturation temperature (= 0 superheat) and the measured mean heater surface superheat at the moment of nucleation. From the saturation temperature it is possible to estimate the thickness of the superheated boundary layer relative to the growing vapor bubble radius.

Several ad-hoc comments can be made relative to Figures 9a - 9i at this time:

(1) Comparing Figures A9a and C9a, it is noted that the measurement time period in Figure A9a is much shorter than in Figure C9a. Figure A9a has a larger value of t*, which results in a larger heater surface superheat at nucleation, which then results in earlier spreading of the boiling process.

(2) For the most part with Runs at the high heat flux levels, the Growth Factor F_g lies in the range between 0.15 and 0.25, in Figures A9a, A9g, C9a, C9d, C9g-1.

(3) The behavior at the lower levels of heat flux is much more erratic, as a result of the higher heater surface superheats at nucleation, which increase the early bubble growth rates and provide fewer measurement opportunities.

One of the modifications made in the matrix of PBE-IC (STS-60) Run No. 7, was to reduce the heating time to 5 seconds, wait 5 seconds, then begin repressurization while the camera was running, in order to obtain data on the collapse rate of the vapor bubble. The liquid was initially at the saturation state, and the system required 6 seconds to achieve the final pressure, as shown in Figure C-3g. The data are plotted in Figure C9g-2, together with the prediction of the same model used for vapor bubble growth. The relatively large uncertainty of $\pm$ 1 mm in the measured bubble radius is a consequence of the residual non-spherical bubble shape resulting from the disturbance imposed by the pressurization, while the uncertainty in time of 4 seconds is an estimate related to the 6 seconds required for the pressurization to be completed. The time of t = 0 in Figure C9g-2 corresponds to t_o =

25.01 seconds in the experimental time. The model assumes that the pressurization occurs instantaneously at t = 0. It would, of course, be possible to reduce the uncertainty in time by incorporating a time-varying pressure into the model, but this was not deemed to be of sufficient importance at this time to warrant the additional expenditure of effort required. It is to be noted that reasonable agreement between the measurements and model predictions cover a remarkable time span of 12 seconds.

6.5 Heat Transfer to Fluid

As pointed out in connection with the bubble dynamics, the initial bubble growth in certain cases following nucleation was so rapid that the camera speed was not sufficient to capture the motion. Certain of these cases resulted in departures of the large vapor bubbles formed from the heat transfer surface due to the momentum imparted to the liquid, causing rewetting of the heater surface and sustaining the nucleate boiling process even in the absence of buoyancy. Upon examining the photographs and the associated heat transfer coefficients it was noted that such departures took place in Run No. 2 of PBE-IA-IB-IC and also in Run Nos. 5 and 8 of PBE-IB. These all are Runs corresponding to the medium level of heat flux, nominally $q''_T = 4$ w/cm^2, which also produce the largest heater surface superheat at nucleation, as noted in Figures 8 of Appendices A, B, C. Also common to each of these cases is the fact that following nucleation the mean heater surface superheat decreases and remains at low levels of on the order of 20°C, instead of subsequently increasing due to heater surface dryout. This extraordinary drop in surface temperature is related to the initial dynamic growth taking place, which in effect impels the large vapor bubble formed away from the heater surface.

An example of the above is seen in the photographs of Figure C-6b, which also clearly show the subsequent nucleate boiling taking place, from beneath the heater surface. The associated thermal behavior is given in Figure 6.30, in which the mean measured heater surface superheat and derived heat transfer coefficient for PBE-IC (STS-60), Run No. 2, from the Space Flight and the a/g = + 1 Post Flight Test are combined. This is obtained by combining Figures C-1b and C-11b. It is noted that for all conditions being otherwise identical, operation in a microgravity environment with these conditions results in an enhancement in the nucleate boiling heat transfer, manifested here by an increase in the mean heater transfer coefficient from h = 1250 w/m^{2}k at a/g = + 1 to h = 1600 w/m^{2}k at a/g $\cong 10^{-4}$, an increase of about 25%.

The mean heat transfer behavior for all nine (9) Runs of the test matrix are summarized in Table XV for all three Space Flight Experiments PBE-IA-IB-IC (STS-47-57-60) and for the two a/g = + 1 Post Flight Tests following PBE-IA-IC (STS-47-60).

Run No.	q″ W/cm²	ΔT_{sub} °C	PBE-IA h W/m².K a/g~ 0 STS-47 9/11/92	PBE-IA h W/m².K a/g= +1 Post Flight 11/4/92	PBE-IB h W/m².K a/g~ 0 STS-57 6/2/93	PBE-IC h W/m².K a/g~ 0 STS-60 2/3/94	PBE-IC h W/m².K a/g= +1 Post Flight 5/4/94
1	8	11	700 Dry out	2430 (26) Nucleate Boiling	700 → 1000 Dry out → Rewet	Not Applicable Short Experiments	1930 (27) Nucleate Boiling
2	4	11	1230 (26) Steady State + Oscillating	1350 (25) Nucleate Boiling	1680 (22) Steady State	1630 (19) Steady State	1250 (26) Nucleate Boiling
3	2	11	1100 (16)→ 600 Steady S. → Dryout	480 (20) [350] Non-Boiling Convection	960 (18) Steady State	950 (16) Steady State	500 (18) Non-Boiling Convection
4	8	2.7	200 Dry out	2280 (28) Nucleate Boiling	200 Dry out	220 Dry out	2300 (28) Nucleate Boiling
5	4	2.7	400 → 200 Increased Dry out	550 (49) [430] Non-Boiling Convection	1420 (26) → 250 Steady S. → Dry out	400 → 200 Increased Dry out	550 (49) Non-Boiling Convection
6	2	2.7	1100 (16) Steady State + Oscillating (rewet)	500 (26) [350] Non-Boiling Convection	1080 (20) Steady State	980 (17) Steady State	500 (26) Non-Boiling Convection
7	8	0	200 Dry out	2350 (27) Nucleate Boiling	200 Dry out	200 Dry out	1930 (29) Nucleate Boiling
8	4	0	300 → 200 Increased Dry out	600 (47)[400] Non-Boiling Convection	1340 (29) → 200 Steady S. → Dry out	400 → 250 Increased Dry out	570 (49) Non-Boiling Convection
9	2	0	1030 (19) → 200 Steady State + Dry out & Rewet	500 (29) [350] Non-Boiling Convection	No Data	970 (18) → 200 Steady State → Dry out	500 (29) Non-Boiling Convection

( ) Steady state mean heater surface superheat (°C)

[ ] "h" computed from natural convection correlation: $Nu = 0.15 \times Ra^{1/3}$

Table XV. Comparison of measured mean heat transfer coefficients between STS-47-57-60 Space Flights and a/g = +1 Post Flight Tests.

For each Run the derived mean heat transfer coefficient is given, followed in parentheses by a mean steady heater surface superheat (when appropriate), followed in brackets by a computed natural convection heat transfer coefficient (when appropriate for a/g = + 1), followed by brief comments on the general behavior observed. Post Flight Tests were conducted also at a/g = - 1 following each space flight in order to confirm the continuing functional operation of the hardware. Although heater surface superheats at nucleation are included for these cases in Tables VII - IX dryout occurred subsequently for all runs because of buoyancy effects.

It is noted in Table XV that nucleate boiling at a/g = + 1 takes place only for the highest levels of heat flux, in Run Nos. 1, 4, 7, and also in Run No. 2, for the medium heat flux level but with the highest level of subcooling. In this latter case it appears that subcooling is playing an anomalous role in pool boiling. The heat transfer coefficient for PBE-IA at a/g = + 1 is the largest at h = 2430 w/m^2k in Run No. 1, with the largest subcooling, while those for Run Nos. 4 and 7 are slightly lower but almost identical at h = 2300 w/m^2k. On the other hand, for PBE-IC at a/g = + 1, h = 1930 w/m^2k. For this case the heating was terminated after 5 seconds, so a steady boiling condition was not yet reached, as can be noted by comparing Figures A-11a and C-11a. The same was true for Run No. 7 of PBE-IC.

Decreases in the heater surface temperatures accompanied by increases in the heat transfer coefficients can be noted at particular times in both the space and post flight experiments. For example, for PBE-IA (STS-47), these take place at the following times:

in Figure A-1a for Run No. 1 at 65 seconds
in Figure A-1c for Run No. 3 at 110 seconds
in Figure A-1d for Run No. 4 at 50 seconds
in Figure A-1h for Run No. 8 at 65 seconds
in Figure A-1i for Run No. 9 at 105 seconds.

These are all a result of activating the stirrer motor before the tests were concluded, as can be confirmed from the test matrix given in Table A-I. Similar behaviors took place in PBE-IB (STS-57) and PBE-IC (STS-60) when the stirrer was activated.

To be contrasted with the above, it was observed at certain times during the space experiments, not associated with dryout immediately following nucleation, that distinct increases in surface temperature took place accompanied by decreases in the heat transfer coefficient. These are summarized below with the Figures in Appendices A, B, C which indicate this behavior, together with the times of the events:

Figure No.	Run No.	Appendix-PBE- A	B	C
1e	5	80 Seconds	72 Seconds	50 Seconds
1h	8	55 "	47 "	55 "
1i	9	80 "	-	80 "

The increases in surface temperature taking place are attributed to the vapor bubbles growing sufficiently large that they are pressed against the heater surface. The largest size vapor bubble that can be accommodated in the test vessel before contact is made with the walls is about 12 cm in diameter, and correspond to estimates of the size of the bubbles formed at the times given above. The discrepancy noted in PBE-IC Run No. 5 is believed due to the subcooling of the liquid and random agitation imparted by the bubbles.

An interesting question arises as to the mechanism which holds the large vapor bubble away from the heater surface in those cases where it is initially impelled away, in view of the presence of thermocapillary forces which would tend to move such a large vapor bubble toward the heater surface. This behavior was observed in Run No. 2 of PBE-IA-IB-IC and in Run Nos. 5 and 8 of PBE-IB, and is tentatively attributed to the following, pending confirmation by computations to be conducted: Nucleate boiling takes place in the thin liquid layer underlying the large vapor bubble in the vicinity of the heater surface. Because of surface tension the vapor pressure within these bubbles is larger than that in the large vapor bubble. As soon as contact is made between these coalescence takes place, and the large vapor pressure of the small bubble impels its vapor in a jet-like action into the large bubble. It is the net sum of the momentum transfer associated with all the nucleating sites beneath the large bubble that counteracts the thermocapillary forces tending to draw the large vapor bubble toward the heater surface.

In assessing the role that buoyancy and its absence in microgravity has on the nucleate boiling heat transfer process it is important to recognize the variability that can take place with different systems. That significant differences can occur between metallic and non-metallic heater surfaces, particularly when the influence of surface roughness is added, is a well-known phenomena among research workers in boiling. Considerable differences in behavior exist even when extreme precautions are taken to achieve reproducible circumstances. An example is given in Figure 6.31, in which the data of Kirk and Merte (1992) and Li and Merte (1993) are presented for nucleate boiling of R-113 at such low velocities on flat surfaces in the upward facing orientation that buoyancy dominates over any forced convection effects. These data were taken separated by a three year interval, with the fabrication of the polished quartz substrate and sputtered gold film separated also

by the three year period. The fabrication techniques followed were as identical as practical, but a change in the heat transfer coefficient of about 30% takes place nevertheless. The Post Flight data for PBE-IA (STS-47) and PBE-IC (STS-60) are included for comparison. These operated with the identical hardware, but were separated by a time period of 18 months, as can be seen from Tables A-II and C-II. These results are between the other two sets of data, with a variability that falls within the uncertainty of $\pm$ 1°C in the absolute measurement of the heater surface temperature. No Post Flight data were obtained for PBE-IB (STS-57). The conclusion to be gained from the above is that a meaningful assessment of how buoyancy or microgravity influence boiling is possible at present only if provision is made for subjecting identical systems, or systems as similar as possible, to the variation of the independent parameter under consideration — gravity in the present case. Because of size limitations for the experimental apparatus, the Pool Boiling Experiment was designed to function in a transient mode, providing up to two (2) minutes maximum operating time for each Run. This is adequate for many purposes, but imposes other limitations, the inability to use metallic substrates for the heater surface, for example. The data of Kirk and Li shown in Figure 6.31, on the other hand, were obtained following steady boiling taking place over an hour. Such is possible only with forced convection, here with a low velocity.

Direct comparisons are given in Figure 6.32 of nucleate pool boiling for identical systems operating in quasi steady state at $a/g = +1$ and at microgravity. A quasi-steady operation occurred in the PBE-IA-IB-IC (STS-47-57-60) only at the high subcooling level and at the two lower levels of heat flux. Even here, it is noted that the data point for PBE-IA (STS-47) at the medium heat flux level (Run No. 2) was obtained with partial dry-out, in Figure A-6b, which resulted in a higher heater surface superheat. Also included in Figure 6.32 are the measurements of Oker and Merte (1973) obtained with R-113 in a 1.4 second drop tower. In this case the gold film heater was facing upward with nucleate boiling at $a/g = +1$ when the test package was released in an environment providing $a/g < 10^{-3}$. With active boiling taking place initially, the system response was sufficiently rapid that steady conditions were achieved in the 1.4 second drop period. In all cases given in Figure 6.32 it is clear that a significant and reproducible degree of enhancement in the boiling process takes place at the lower levels of heat flux with some degree of subcooling. Further measurements are necessary to identify more closely the limits of heat flux and subcooling which precipitate the onset of dryout.

To show more clearly the relationship of the microgravity pool boiling data to the total pool boiling process at $a/g = +1$, a Reference Curve for Pool Boiling at $a/g = +1$ was constructed for R-113, using all available reliable data and correlations. This is plotted in

Figure 6.33, and incudes all the data from Figure 6.32. The nucleate pool boiling part of the Reference Curve was constructed to pass through the data of Kirk and Merte (1992). The uncertainty limit for dryout on flat heater surfaces is indicated as shown, based on the PBE data obtained to date. A significant decrease from what is termed the CHF is to be noted. In the absence of forced convection, imposed by any means, it seems highly unlikely that a phenomena similar to film boiling will take place in microgravity, or if it does, it will be highly system dependent. If a phenomena similar to the minimum heat flux is observed, it is expected to be more a spatially averaged transition between nucleate boiling and complete dryout. The determination of such behavior requires the ability to operate in a steady state mode, for a given system.

A better correlation of the non-boiling natural convection data in Figures 6.32 and 6.33 with the natural convection equation in Figure 6.33, from Lloyd and Moran (1974), would result were the data plotted as heater surface temperature minus the bulk liquid temperature rather than as heater surface superheat. The heater surface — bulk liquid temperature difference is obtained by adding the heater surface superheat and the bulk liquid subcooling. As in Figure 6.32, it is clear in Figure 6.33 that nucleate pool boiling is enhanced considerably in microgravity over that in earth gravity, albeit the maximum possible heat flux level is reduced considerably by the onset of dryout. A line is drawn through the microgravity nucleate boiling data available, and can be extended smoothly into the dryout domain.

Another means sometimes used for comparing nucleate boiling data is on the basis of the heat transfer coefficient as a function of the independent variables of heater surface superheat, heat flux, or bulk liquid subcooling. A disadvantage is that one of the parameters, the heat transfer coefficient, is derived from the parameters of the heater surface superheat and the heat flux, and some information may be lost in dealing with this combination. However, in certain circumstances some insights in the boiling behavior can be gained by the use of the heat transfer coefficient.

Figure 6.34 is a plot of the heat transfer coefficient as a function of the bulk liquid subcooling, using the heat flux to the fluid as a parameter. Only data obtained with the PBE hardware under quasi-steady conditions, both at $a/g = +1$ and in microgravity, are included here, which excludes all data with dry-out. The two conditions of $a/g = +1$ and microgravity are distinguished by open versus filled-in data points. The distinction between non-boiling natural convection at $a/g = +1$, with $h \approx 500$ w/m^{2}k, and nucleate boiling in either $a/g = +1$ or microgravity becomes quite clear in Figure 6.34. At the highest level of heat flux, $q'' = 8$ w/cm^2, steady boiling took place only at $a/g = +1$, while

at the lowest level of heat flux, q" = 2 w/cm^2, only non-boiling convection occurred at a/g = +1, and steady nucleate boiling always took place at microgravity.

The behavior at the intermediate level of heat flux, q" = 4 w/cm^2, was quite inconsistent: At a/g = +1 non-boiling convection always took place at the lower levels of subcooling up to ΔT_{sub} = 4°C, but produced nucleate boiling when the subcooling was increased to ΔT_{sub} = 11°C. This is believed to be related to the pressure effect on homogeneous nucleation referred to earlier in connection with nucleation in microgravity. Only in PBE-IB (STS-57) did steady boiling occur in microgravity at q" = 4 w/cm^2 for all levels of subcooling. For PBE-IA and -IC steady boiling occurred only at the highest level of subcooling, with dry-out taking place as subcooling was decreased.

The quasi-steady heat transfer coefficients from PBE-IA-IB-IC (STS-47-57-60) at a/g = +1 and in microgravity are presented in Figure 6.35 as a function of the heat flux to the fluid, for the highest level of subcooling, ΔT_{sub} = 11°C. For additional comparison of the effects of subcooling, composite data for low subcooling levels are included, from Figure 6.34. This means that the specific data points from Run Nos. 1, 2, 3 only are given here. The discrepancy between the two data at a/g = +1 for the highest heat flux level must be given proper interpretation, even though they apply to the same hardware: Heating took place in PBE-IC (STS-60) for only 5 seconds, while in PBE-IA (STS-47) the heat transfer coefficient increased from the early value of h = 2100 w/m^{2}k to a steady value of h = 2450 w/m^{2}k following heating for 55 seconds. The same presumably would have taken place with PBE-IC (STS-60), and the results would demonstrate complete reproducibility, even though separated by a time interval of 18 months. Reproducibility can also be demonstrated for the six (6) data points with high subcooling in microgravity. The data point labeled partial dryout is for PBE-IA (STS-47) (Run No. 2), and the dryout may be observed in Figure A-6b. This phenomena of "steady" spatial dryout was unique among all the testing that took place in microgravity. Using a procedure to be described below, the heat transfer coefficient over the nucleate boiling portion of the heater surface was determined from measurement of the fractional dry area with a value of h = 1600 w/m^{2}k, which puts it in agreement with the other results. The plot of Figure 6.35 further demonstrates the enhancement that takes place with nucleate boiling in microgravity over earth gravity at this level of subcooling. Whether such can be concluded with a satisfactory degree of confidence for lower levels of subcooling must await experimentation with smaller variations in bulk liquid subcooling. A straight line extrapolation curve is drawn through the microgravity data, labeled "Prediction Curve" here, to indicate the potential for performance at higher levels of heat flux were some means provided to prevent premature

dry-out. One realistic possibility for implementation of this would be by the use of low velocity forced convection.

As described previously, the mean fluid heat transfer coefficients computed from the measured mean heater surface temperatures are plotted in Figures 1a — 1i of Appendices A, B, C for each of the respective Runs of the matrix. A definite relationship exists between the transient mean heater surface temperature and the heat transfer coefficient. These serve to indicate, qualitatively at present, the modes of heat transfer between the heater surface and fluid: conduction to the liquid; nucleate boiling; conduction to the vapor phase (termed dryout); and combinations of the three forgoing mechanisms based on the fractional part of the heater surface over which each is acting. For the time being the conduction heat transfer mode to the liquid is being neglected in the interest of simplicity. For the heat flux levels used to date, nucleation and its propagation across the heater surface take place early in the process, so that the major part of the heat transfer surface is either covered by vapor or influenced by the nucleate boiling phenomenon itself. In future cases where the heat flux levels are sufficiently low that relatively smaller portions of the heater surface are influenced by the presence of either nucleating sites or significant amounts of vapor, the heat transfer to the stagnant liquid regions then could be incorporated.

For those circumstances where a portion of the heating surface is dry during boiling in microgravity, a procedure is used by which the mean heat transfer coefficient is computed for that portion of the heater surface on which nucleate boiling is taking place, using measurements of the overall mean heat transfer coefficient and the fractional dry area of the heater surface. The procedure is described in Appendix E, and involve several simplifying assumptions, also included in Appendix E. The most severe one under certain circumstances is that the ratio of the mean superheat over the nucleate boiling portion of the heater surface to that over the entire heater surface is approximately unity. In the process of evaluating the fractional dry heater area from the digitized images, using commercial image analyzing software, it was found that defining the dry-out portion of the heater surface requires a certain element of human interpretation, since the automatic measurements based on a defined gray scale in conjunction with the processing software available tended to produce much larger fractional dry areas than was deemed reasonable. Nucleating sites produce light shaded areas similar to dry areas, but make significant contribution to the heat transfer, and must be discounted in the area evaluation.

The time domains within each Run of PBE-IA-IB-IC (STS-47-57-60) over which measurements of the dry fraction of the heater surface were made are tabulated in Table IV of Appendices A, B, C, respectively. Following these, for each of these time domains the

heater surface dry fraction and mean temperature are plotted in Figures 10--i, the wet fraction and mean heat transfer coefficient are plotted in Figures 10--ii, the microgravity boiling heat transfer coefficient computed from Equation (E.12) is added to these latter two quantities in Figures 10--iii, and sample images are given in Figures 10--iv.

The net results in Figures 10 of Appendices A, B, C are condensed in Table XVI in terms of the following for each time domain in each Run: Range of mean heater surface temperatures covered; Range of fractional dry heater surface area; Range of mean heat transfer coefficient (w/m^2k); and range of microgravity boiling heat transfer coefficient computed from Equation (E.12). For each time domain in each Run the values listed for the ranges are corresponding ones in the order given. All of the results are transient in nature in that variations with time take place, and where single values are given represent short term steady states. These transients, consisting of progressive dry-out or rewetting, can be viewed as taking place in a transition from complete nucleate boiling to complete dry-out, termed the transition boiling domain at $a/g = +1$. On subtracting the saturation temperature from each mean heater surface temperature T_s in Table XVI, the resulting mean heater surface superheat can be multiplied by the corresponding mean heat transfer coefficient in Table XVI to provide a mean heater surface heat flux. These are all plotted on Figure 6.36, on which are superimposed the $a/g = +1$ Reference curve of Figure 6.33 and the steady microgravity boiling data. It is seen to be possible to construct approximate composite microgravity pool boiling curves at this time, one for low levels of subcooling and one for the higher level of cooling, which bear some resemblance to the Reference Curve, albeit over a wider spread in the heater surface superheat.

Run No.	Secti	PBE-IA				PBE-IB				PBE-IC			
		Ts(°C)	x(dry)	h(mean)	h(boil)	Ts(°C)	x(dry)	h(mean)	h(boil)	Ts(°C)	x(dry)	h(mean)	h(boil)
1	1	87-110	.20-.45	1700-900	2100-1700	87-108	.10-.30	1900-1100	2000-1500	90	0.15	1750	2000
	2					110-130	.35-.40	900	1500				
	3					135-125	.30-.20	500-1000	1000-1200				
	4					125-118	.20-.25	1050-1150	1200-1400				
2	1	88	0.3	1200	1600	90-82	.25-0.0	1000-1750	1300-1750	85	0.15	1600	1850
	2	88	0.25	1300	1600	82	0	1750	1750				
	3	87	0.2	1200	1600								
3	1	76	0.1	1200	1250	78	0.15	900	1100	78	0.3	1000	1250
	2	75-78	.05-.25	1200-900	1250-1000	78	0.15	900	1100	75	0.15	1000	1100
4	1	90-140	.50-.80	1000-300	1700-1500	85-160	.30-.80	900-200	1000-700	87-110	.50-.70	900-350	1700-1500
	2									180	0.9	200	2000
5	1	100	0.6	500	1200	80	0.02	1370	1380	100	0.7	350	1200
	2	120-138	.60-.80	300	1000	79-120	.03-.80	1500-300	1500	110-130	.60-.90	400-200	1000-2500
6	1	80-70	.60-.30	400-800	1000	73	0.04	1200	1250	70	0	1000	1000
	2												
7	1	90-115	.55-.75	900-400	1600	80-130	.30-.80	750-250	1200	90-120	.75-.60	800-300	1750
	2												
8	1	98-107	0.65	400	1200	78	0.05	1250	1250	96	0.65	400	1200
	2	130	0.9	200	2000								
9	1	80-68	.70-.10	500-1200	1300					67	0	1000	1000
	2	70-85	.20-.90	800-100	1100					66	0	1000	1000

Table XVI. Measurement summary of transient dry-out and rewetting on heater surface in microgravity. PBE-IA-IB-IC (STS-47-57-60).

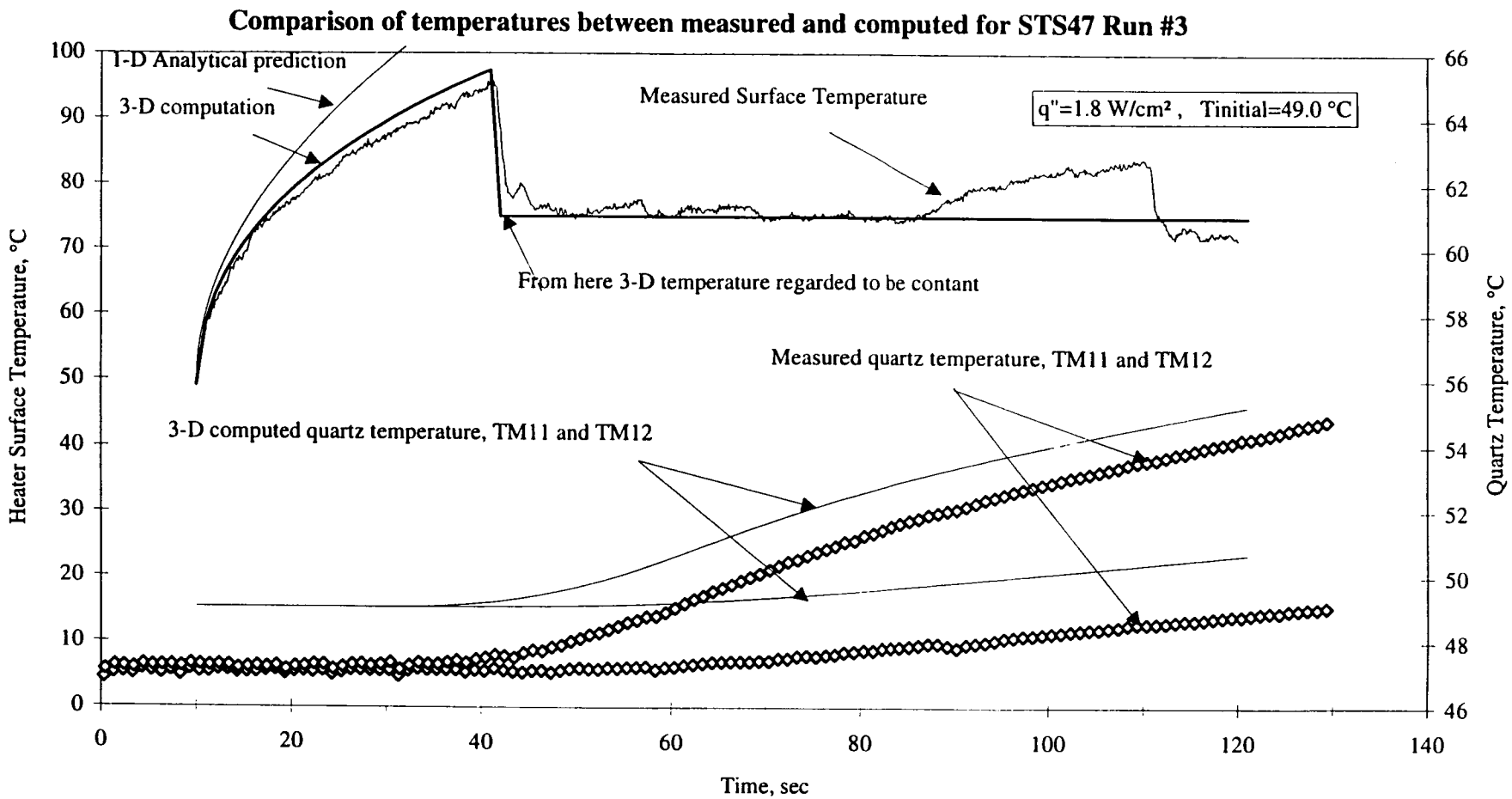

Figure 6.1. Comparison of 1 - D and 3 - D predicted temperatures with measurements. PBE-IA (STS-47). Run No. 3. $q''_T = 1.8$ w/cm^2, $\Delta T_{sub} = 10.9$°C.

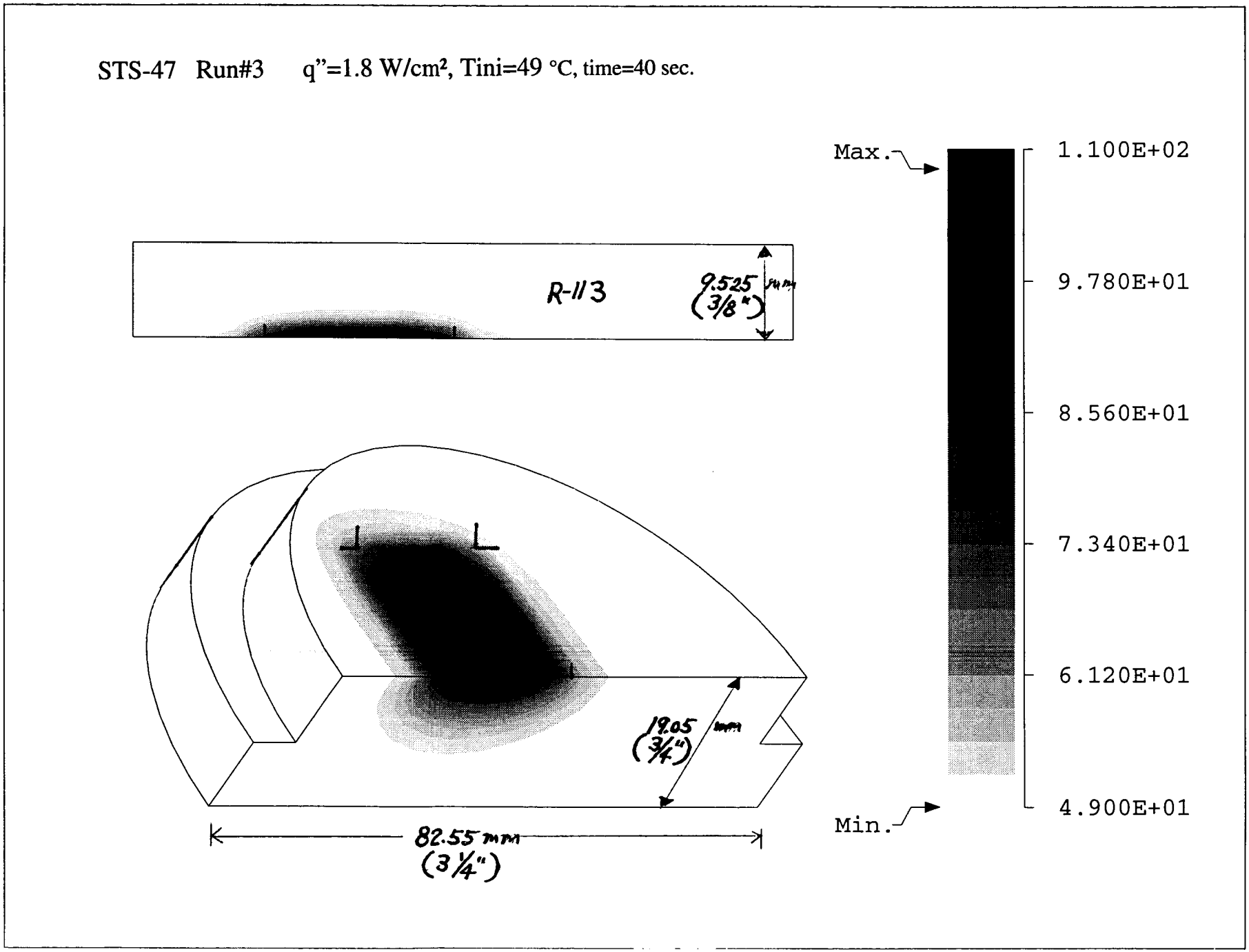

Figure 6.2. Isometric plot of 3 - D temperature distribution in quartz substrate at 40 seconds. PBE-IA (STS-47). Run No. 3.

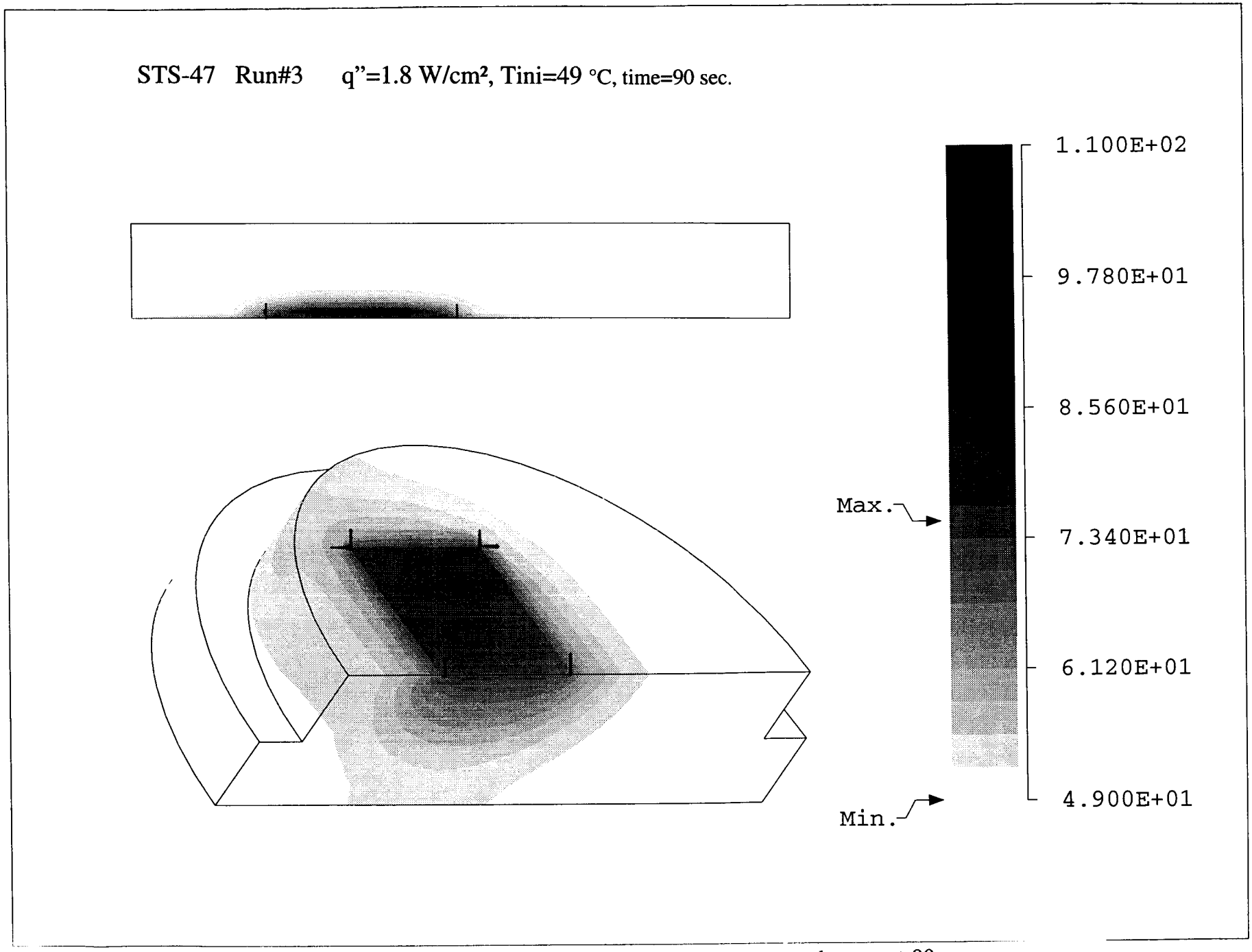

Figure 6.3. Isometric plot of 3 - D temperature distribution in quartz substrate at 90

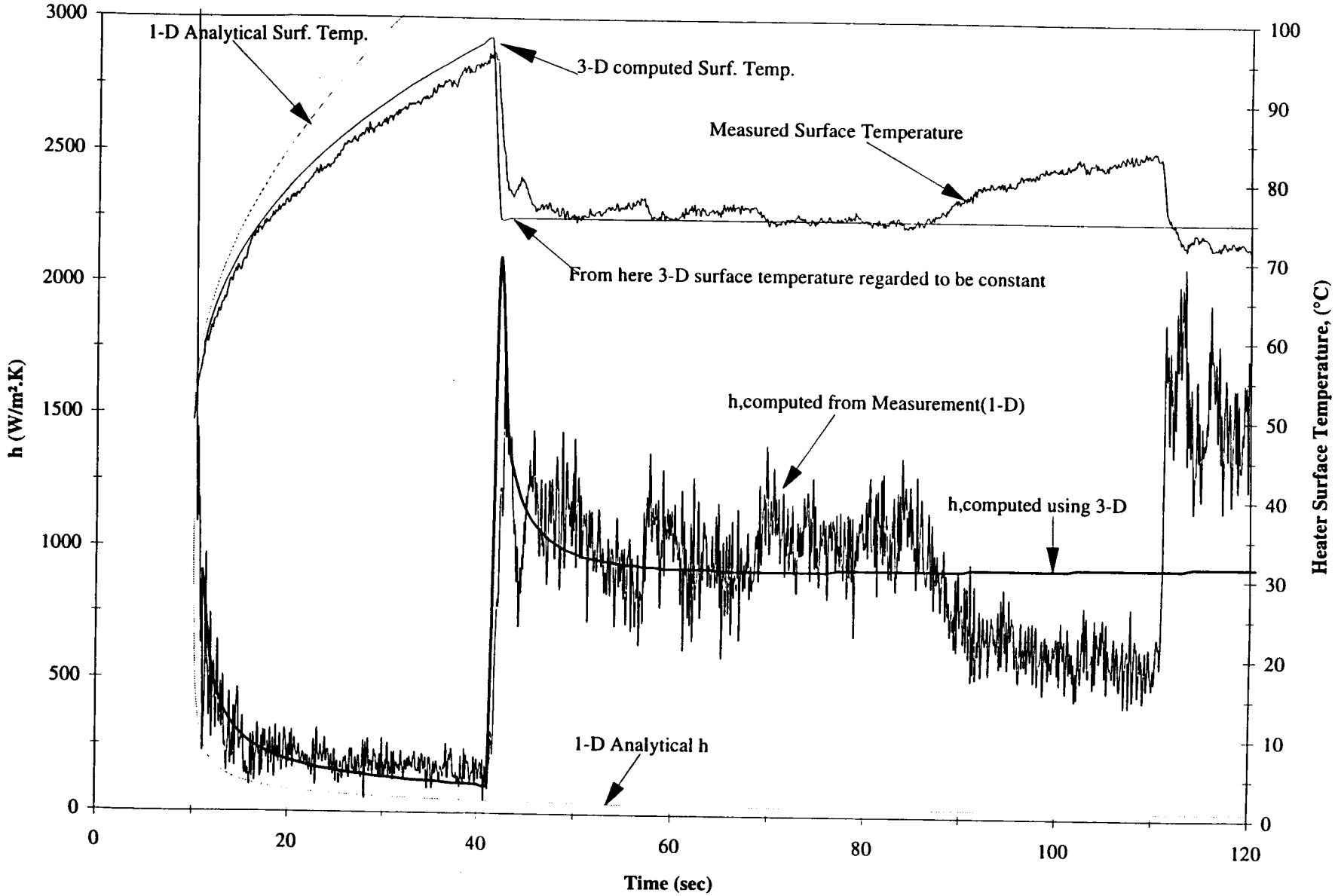

Figure 6.4. Comparison of fluid heat transfer coefficients computed from measured mean heater surface temperatures using 1 - D finite difference and 3-D finite element models. PBE-IA (STS-47). Run No. 3.

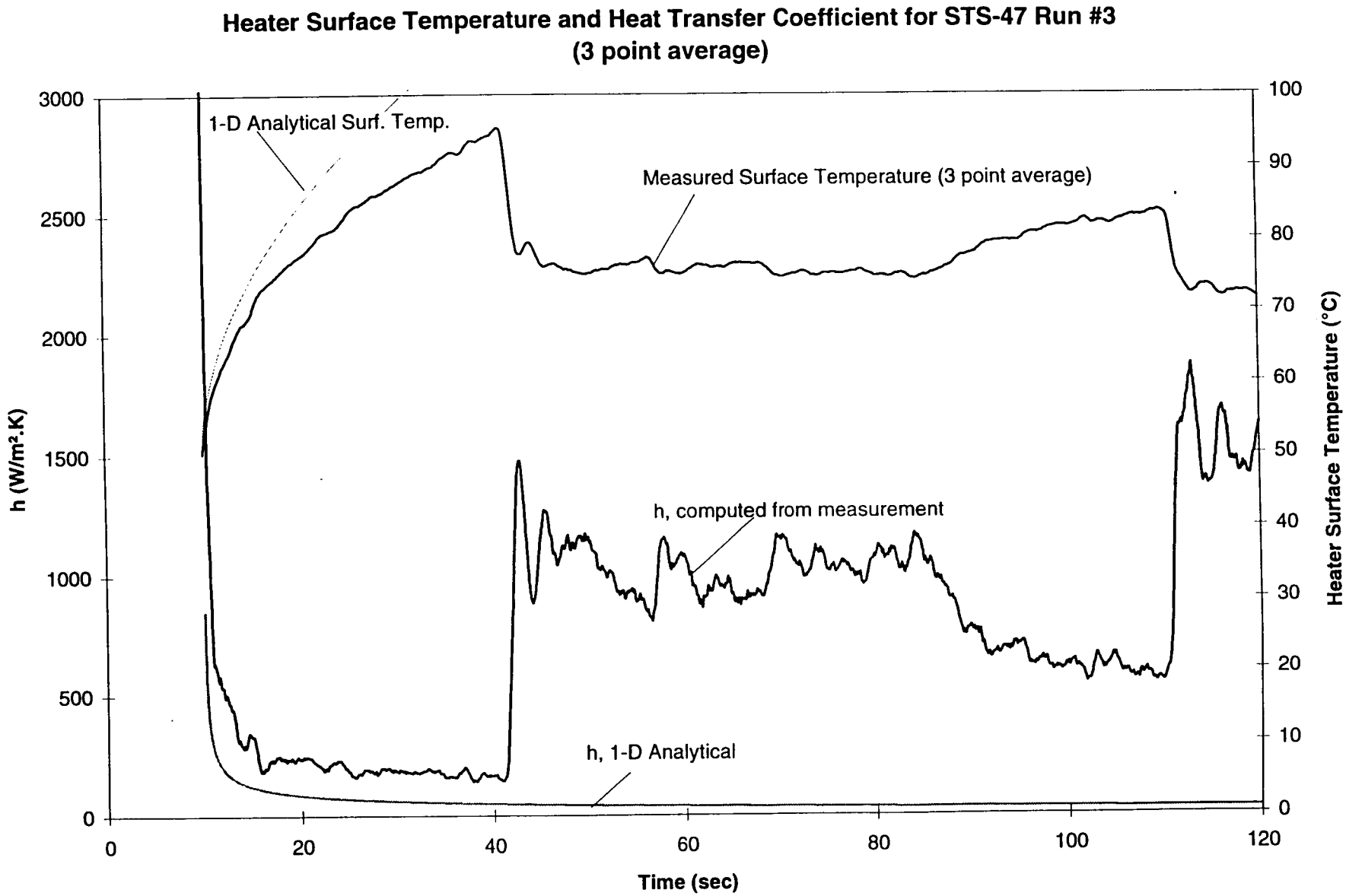

Figure 6.5. Measured heater surface temperature filtered by averaging three (3) consecutive measurement points sequentially. PBE-IA (STS-47). Run No. 3.

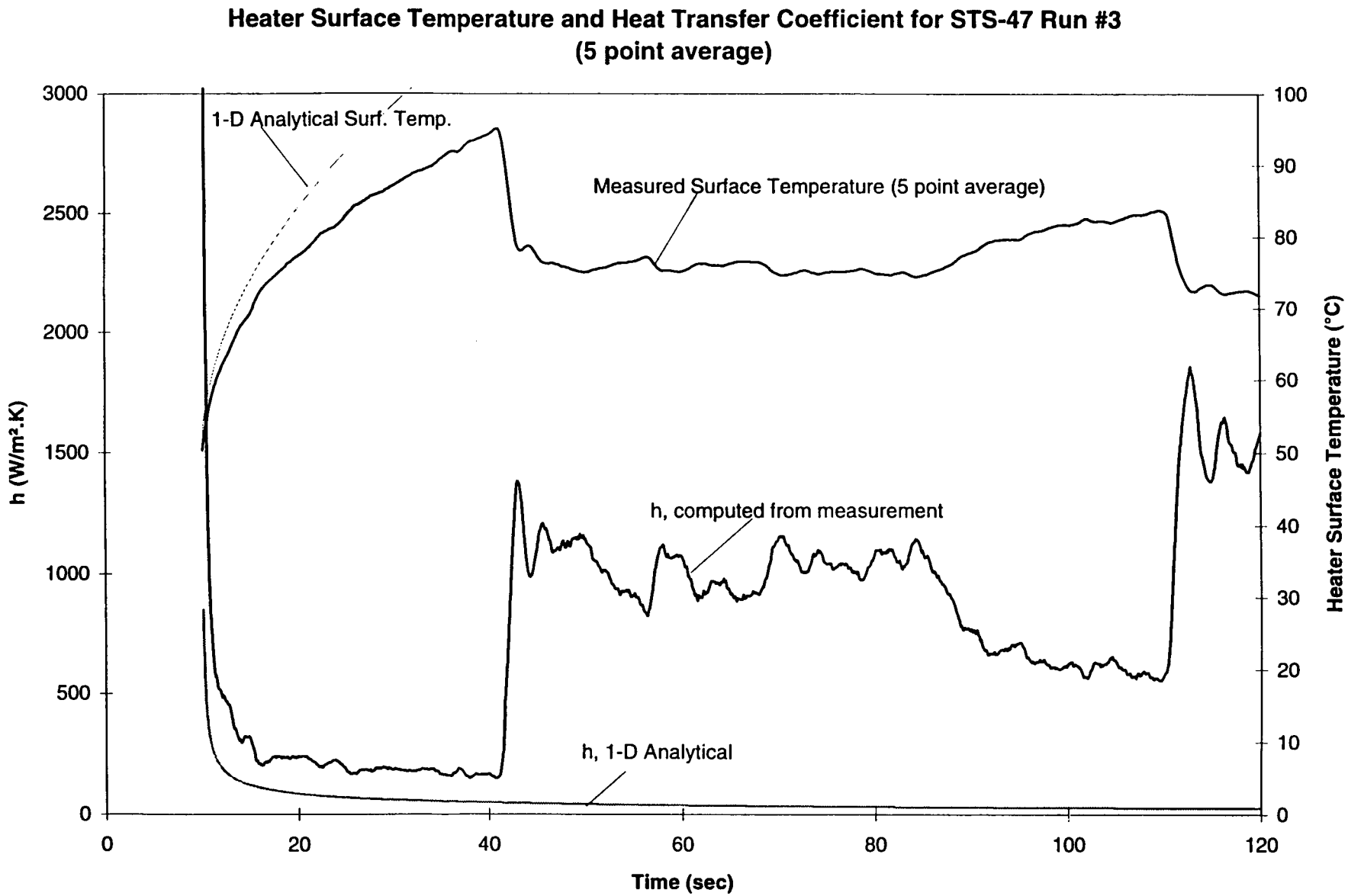

Figure 6.6. Measured heater surface temperature filtered by averaging five (5) consecutive measurement points sequentially. PBE-IA (STS-47). Run No. 3.

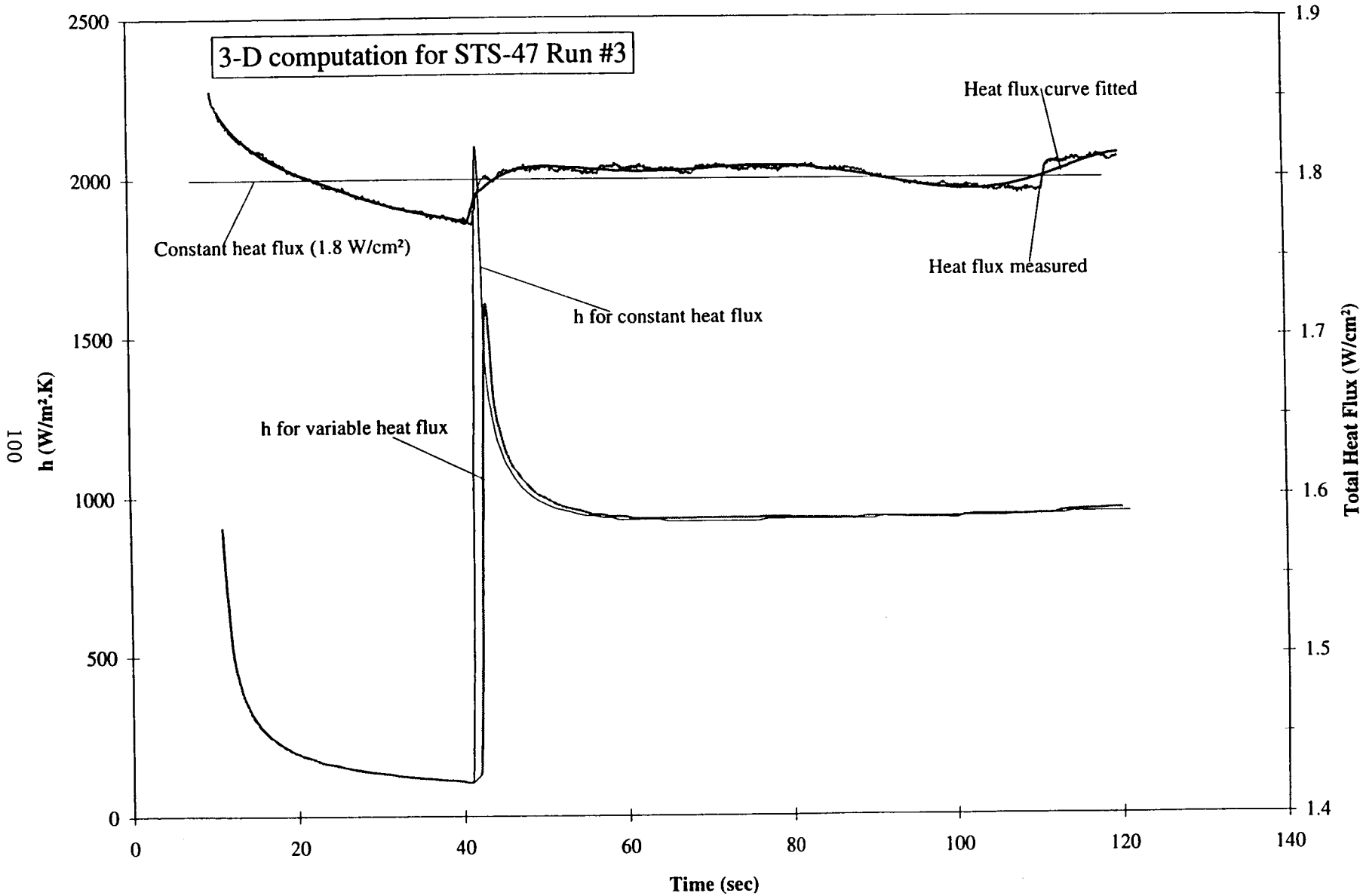

Figure 6.7. Comparison of the fluid heat transfer coefficients obtained by taking the input heat flux as constant or variable. PBE-IA (STS-47). Run No. 3.

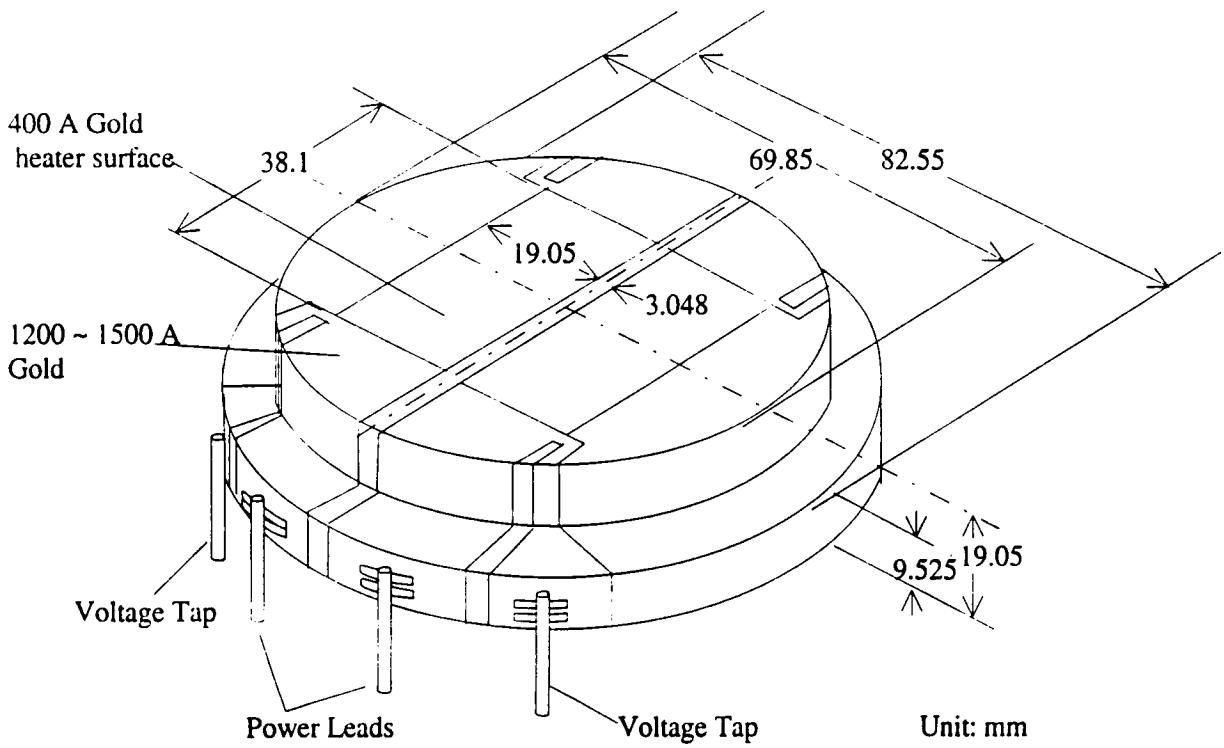

Figure 6.8. Layout of gold film heater surfaces on quartz substrate.

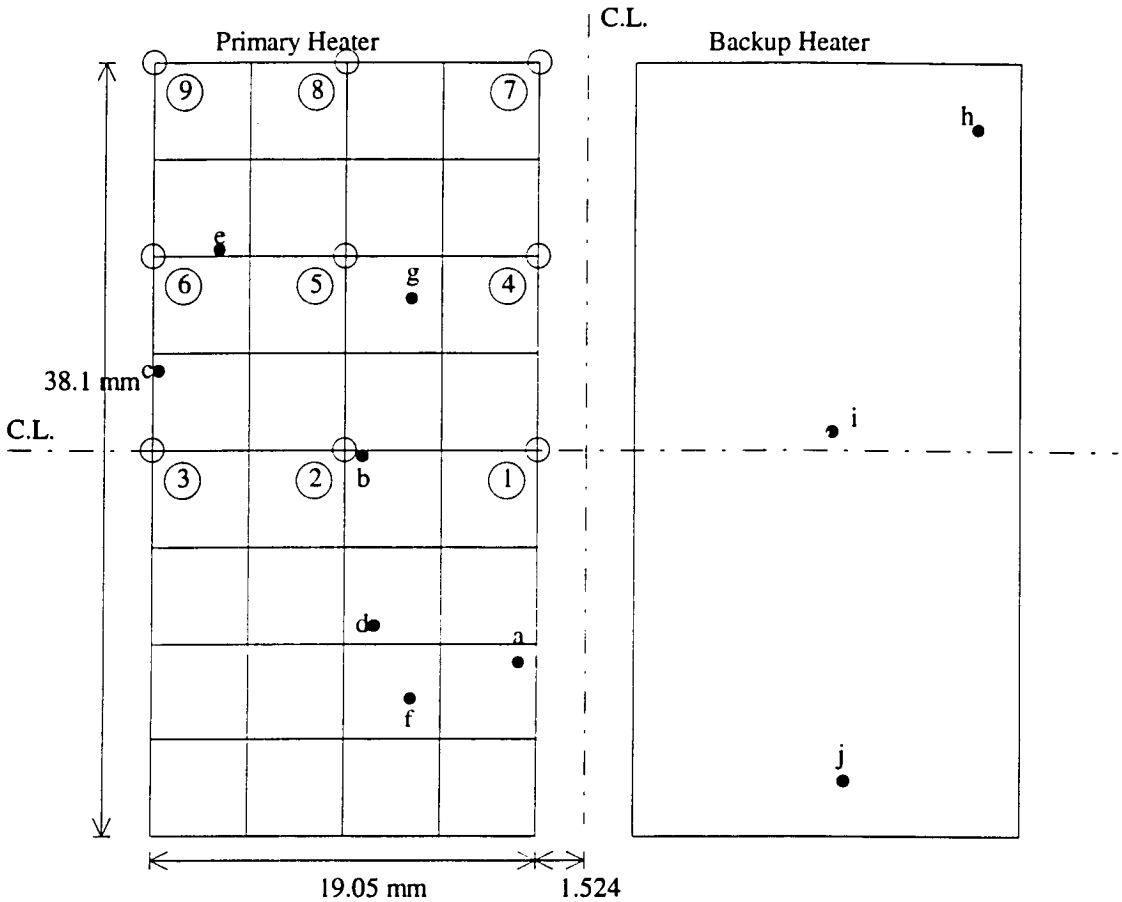

Site Location

Primary Heater

Site a
: STS47 Run#1,4,& 7
STS60 Run#1,4,& 7

Site b
: STS47 Run#2,5
STS60 Run#2,5

Site c
: STS47 Run#3

Site d
: STS47 Run#6

Not possible to determine
STS47 Run#8 & 9

Site e
: STS60 Run#3

Site f
: STS60 Run#6
STS60 Run#8

Site g
: STS60 Run#9

Site Location

Backup Heater

Site h
: STS57 Run#1,4,& 7

Site i
: STS57 Run#2

Site j
: STS57 Run#3

Not possible to determine
STS57 Run# 5,6,8 &9

Figure 6.9. Layout of heater surfaces from underside, with 3-D finite element grid and nucleation sites superimposed. PBE-IA-IB-IC. (STS-47-57-60).

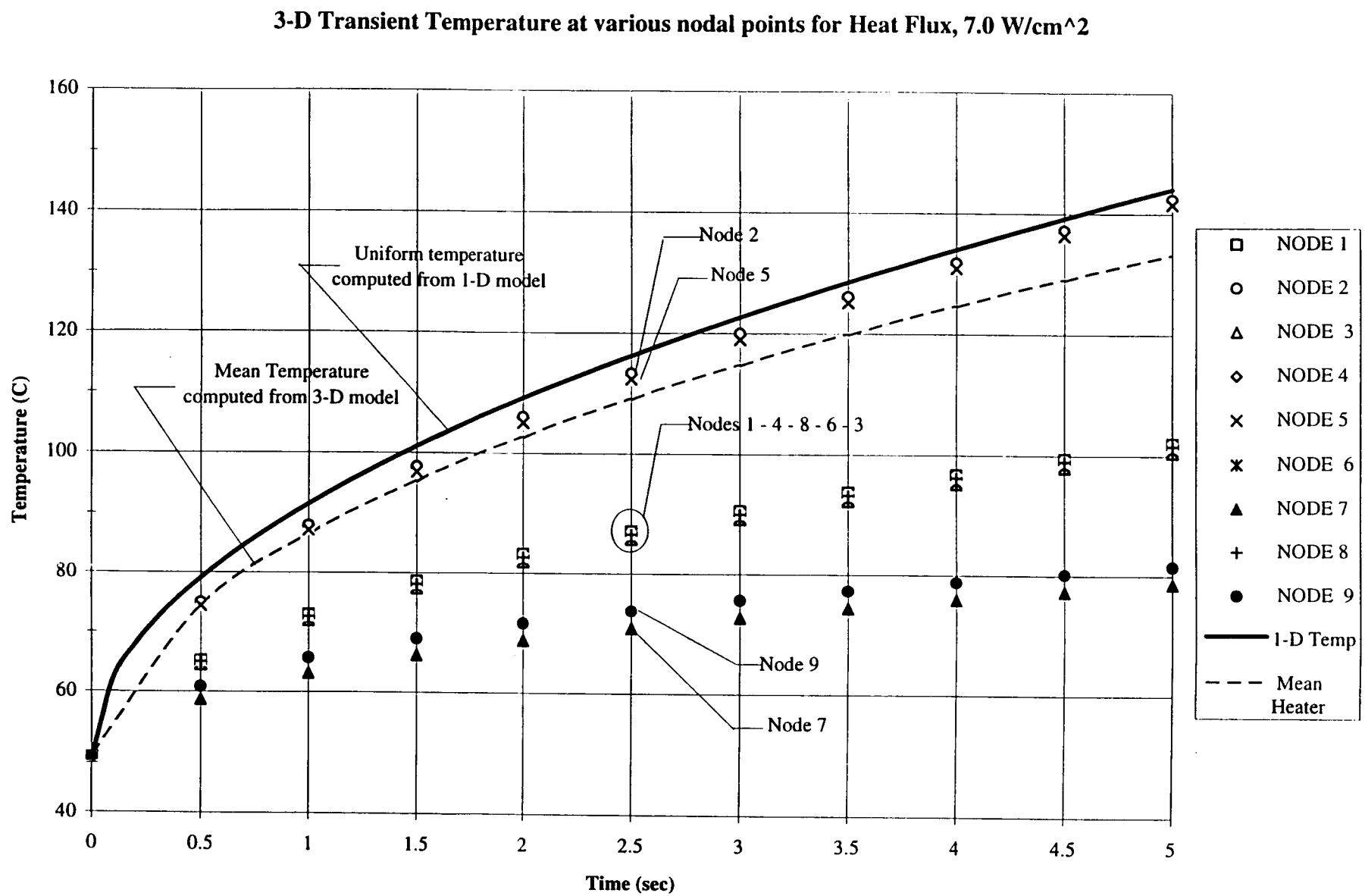

Figure 6.10. Heater surface temperature at Nodes of Figure 6.9 computed with 3 - D finite element model of PBE heater geometry. $q_T'' = 7.0$ w/cm^2. Run Nos. 1-3.

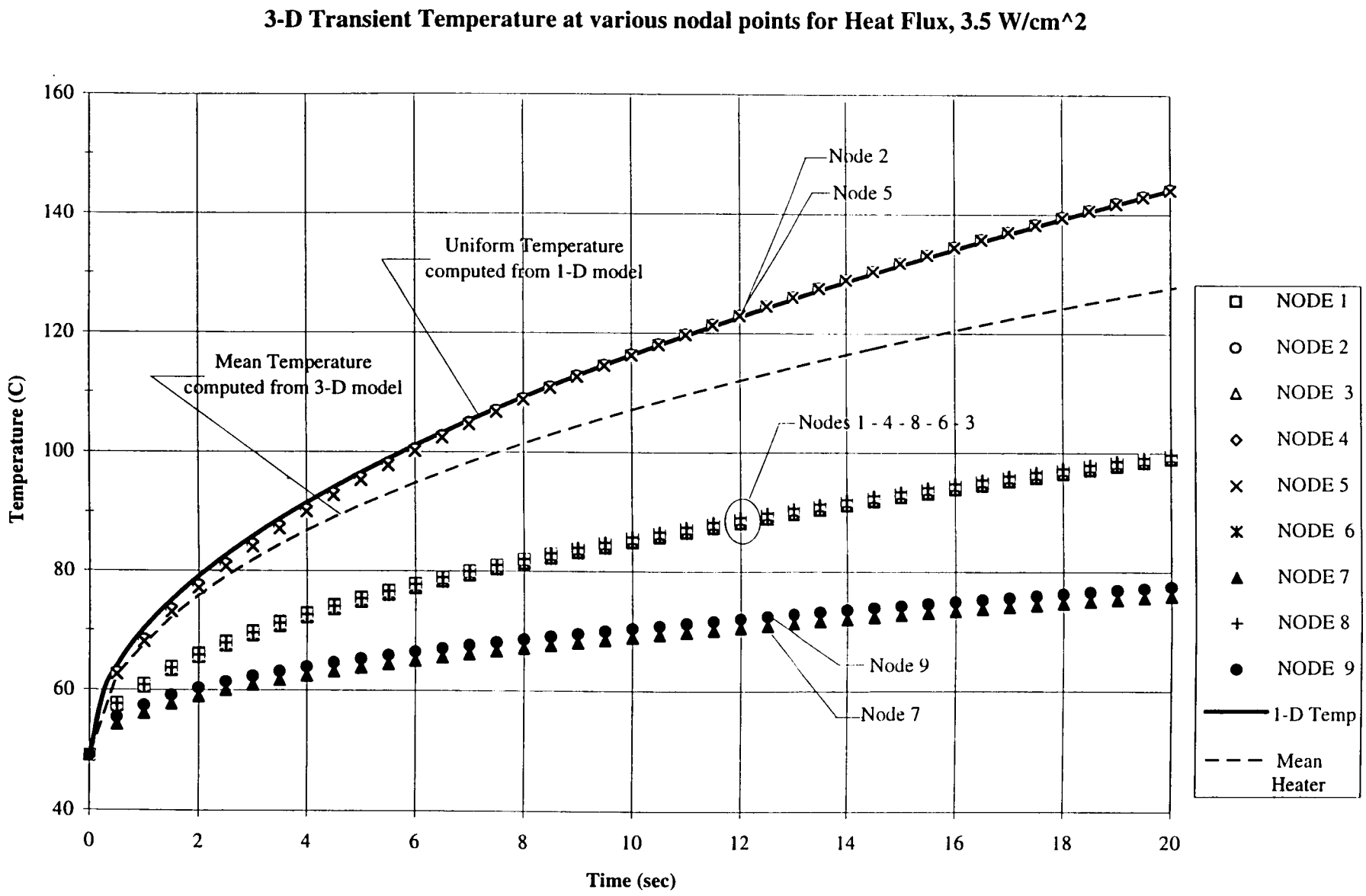

Figure 6.11. Heater surface temperature at Nodes of Figure 6.9 computed with 3-D finite element model PBE heater geometry. $q''_T = 3.5$ w/cm^2. Run Nos. 4-6.

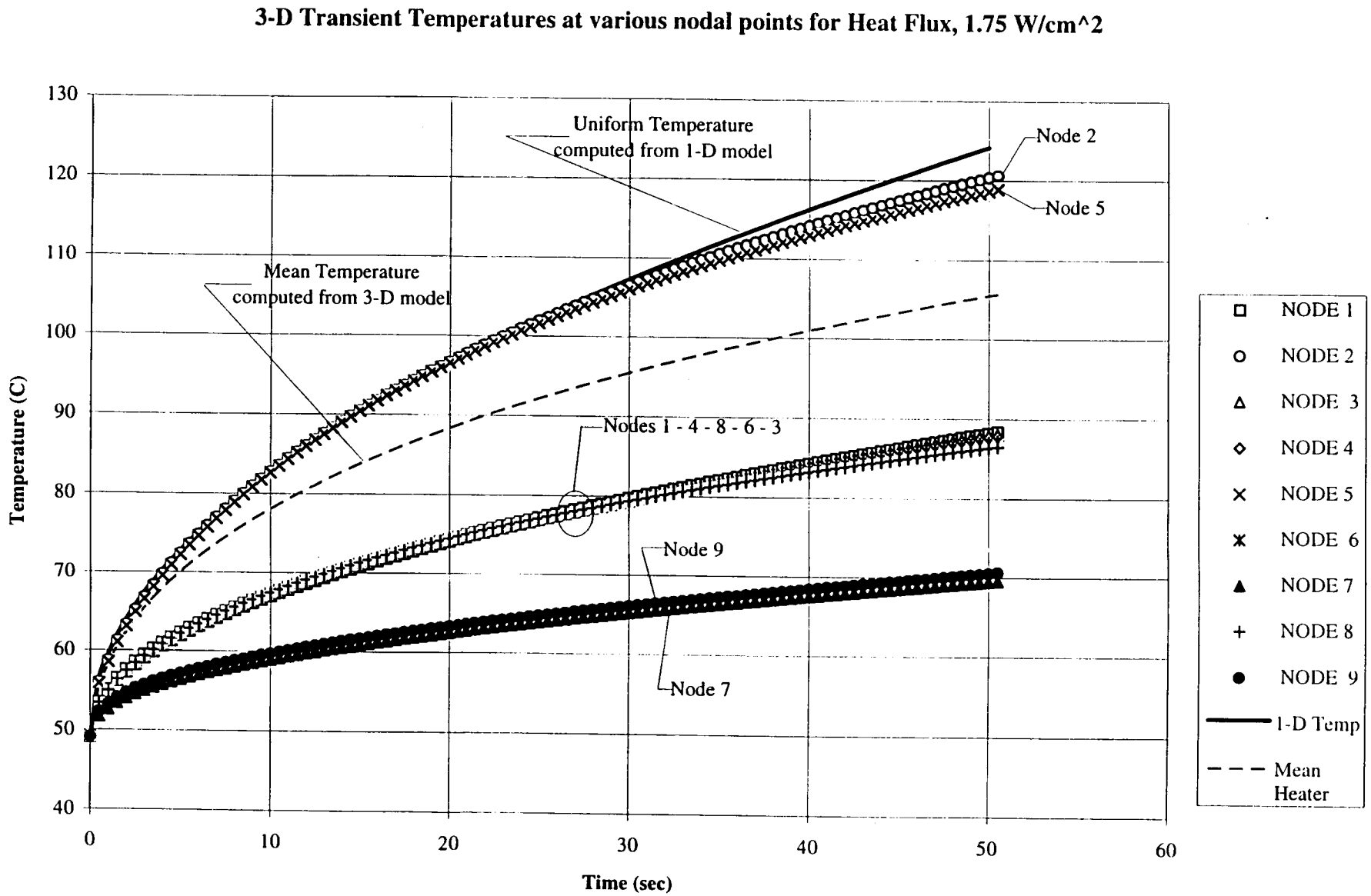

Figure 6.12. Heater surface temperature at Nodes of Figure 6.9 computed with 3 - D finite element model of PBE heater geometry. $q''_T = 1.75$ w/cm^2. Run Nos. 7-9.

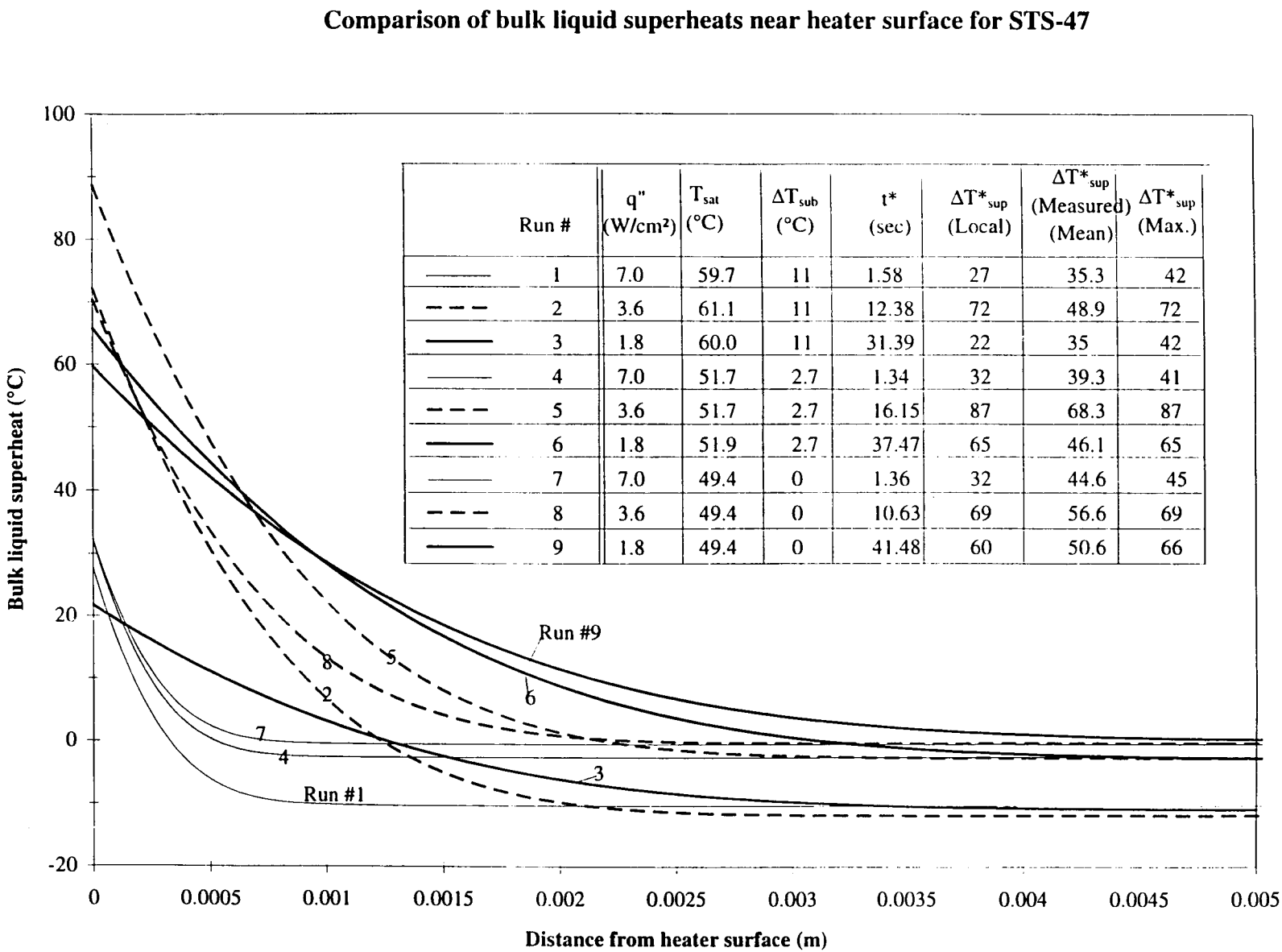

Run #	q" (W/cm²)	T_{sat} (°C)	ΔT_{sub} (°C)	t* (sec)	ΔT^*_{sup} (Local)	ΔT^*_{sup} (Measured) (Mean)	ΔT^*_{sup} (Max.)
1	7.0	59.7	11	1.58	27	35.3	42
2	3.6	61.1	11	12.38	72	48.9	72
3	1.8	60.0	11	31.39	22	35	42
4	7.0	51.7	2.7	1.34	32	39.3	41
5	3.6	51.7	2.7	16.15	87	68.3	87
6	1.8	51.9	2.7	37.47	65	46.1	65
7	7.0	49.4	0	1.36	32	44.6	45
8	3.6	49.4	0	10.63	69	56.6	69
9	1.8	49.4	0	41.48	60	50.6	66

Figure 6.13. Local R-113 temperature distribution at nucleation at heater surface sites indicated on Figure 6.9. PBE-IA (STS-47).

Comparison of bulk liquid superheats near heater surface for STS-57

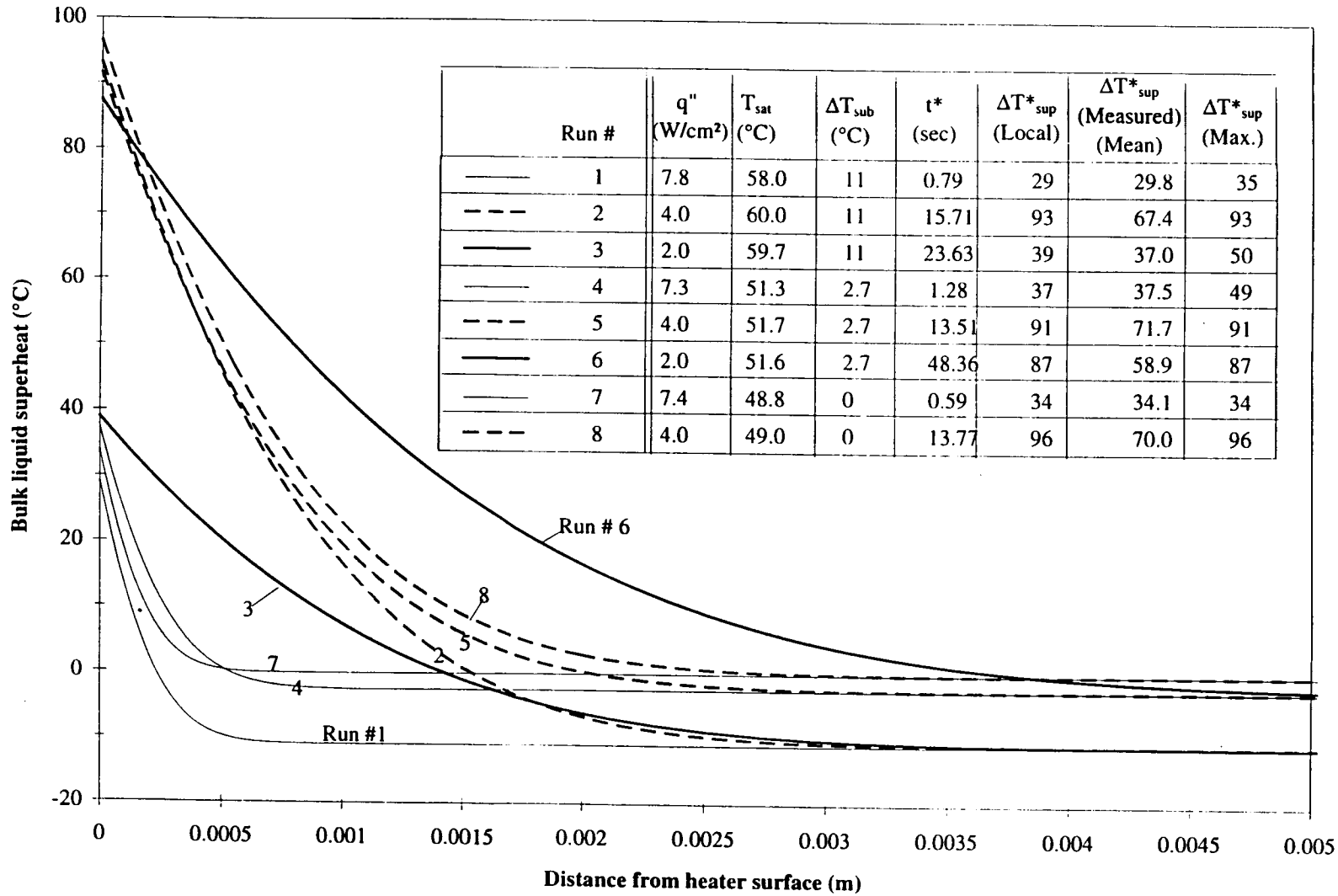

Run #	q" (W/cm²)	T_{sat} (°C)	ΔT_{sub} (°C)	t* (sec)	ΔT^*_{sup} (Local)	ΔT^*_{sup} (Measured) (Mean)	ΔT^*_{sup} (Max.)
1	7.8	58.0	11	0.79	29	29.8	35
2	4.0	60.0	11	15.71	93	67.4	93
3	2.0	59.7	11	23.63	39	37.0	50
4	7.3	51.3	2.7	1.28	37	37.5	49
5	4.0	51.7	2.7	13.51	91	71.7	91
6	2.0	51.6	2.7	48.36	87	58.9	87
7	7.4	48.8	0	0.59	34	34.1	34
8	4.0	49.0	0	13.77	96	70.0	96

Figure 6.14. Local R-113 temperature distribution at nucleation at heater surface sites indicated on Figure 6.9. PBE-IB (STS-57).

Comparison of bulk liquid superheats near heater surface for STS-60

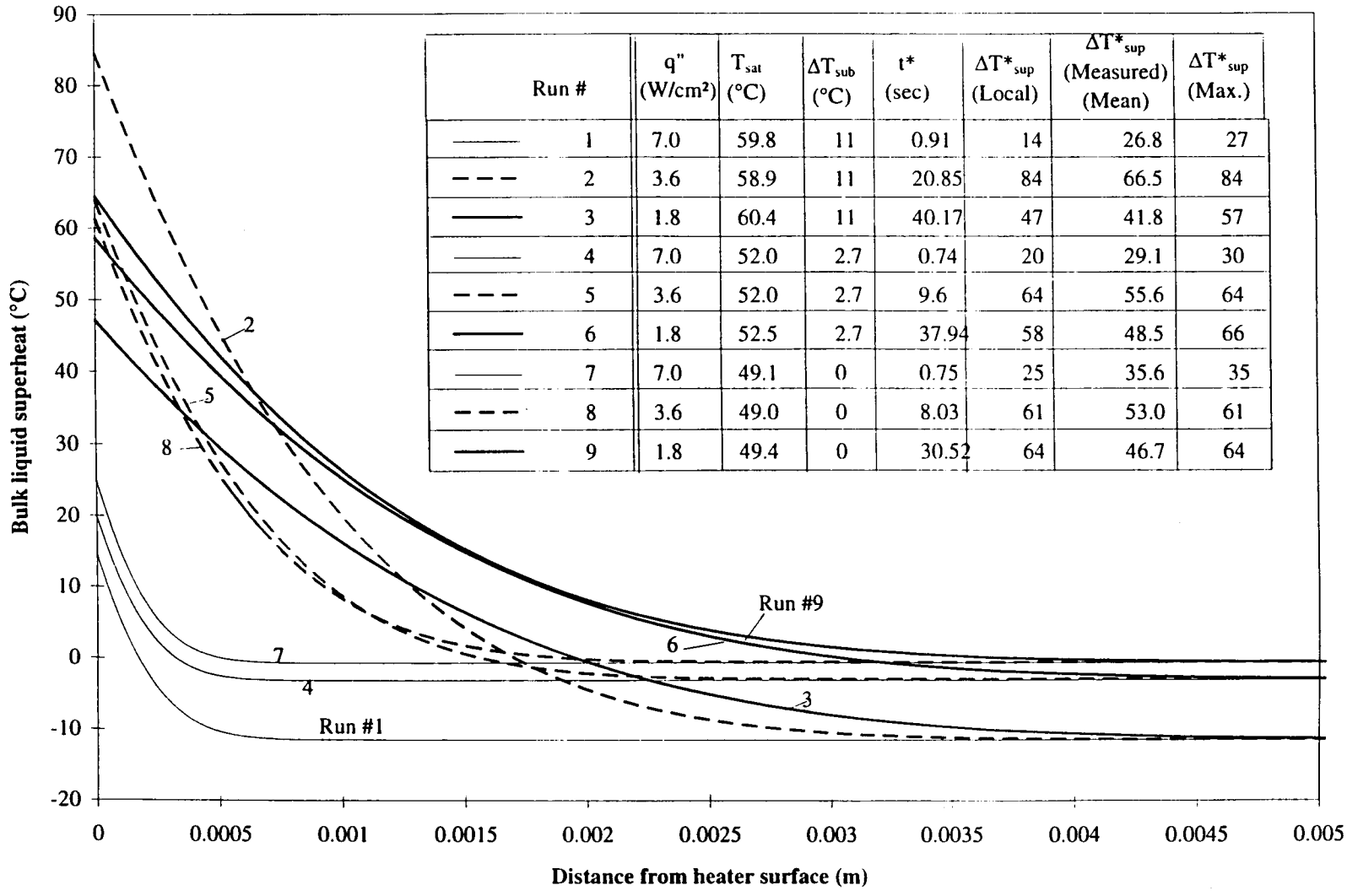

Run #	q" (W/cm²)	T_{sat} (°C)	ΔT_{sub} (°C)	t* (sec)	ΔT^*_{sup} (Local)	ΔT^*_{sup} (Measured) (Mean)	ΔT^*_{sup} (Max.)
1	7.0	59.8	11	0.91	14	26.8	27
2	3.6	58.9	11	20.85	84	66.5	84
3	1.8	60.4	11	40.17	47	41.8	57
4	7.0	52.0	2.7	0.74	20	29.1	30
5	3.6	52.0	2.7	9.6	64	55.6	64
6	1.8	52.5	2.7	37.94	58	48.5	66
7	7.0	49.1	0	0.75	25	35.6	35
8	3.6	49.0	0	8.03	61	53.0	61
9	1.8	49.4	0	30.52	64	46.7	64

Figure 6.15. Local R-113 temperature distributions at nucleation at heater surface sites indicated on Figure 6.9. PBE-IC (STS-60).

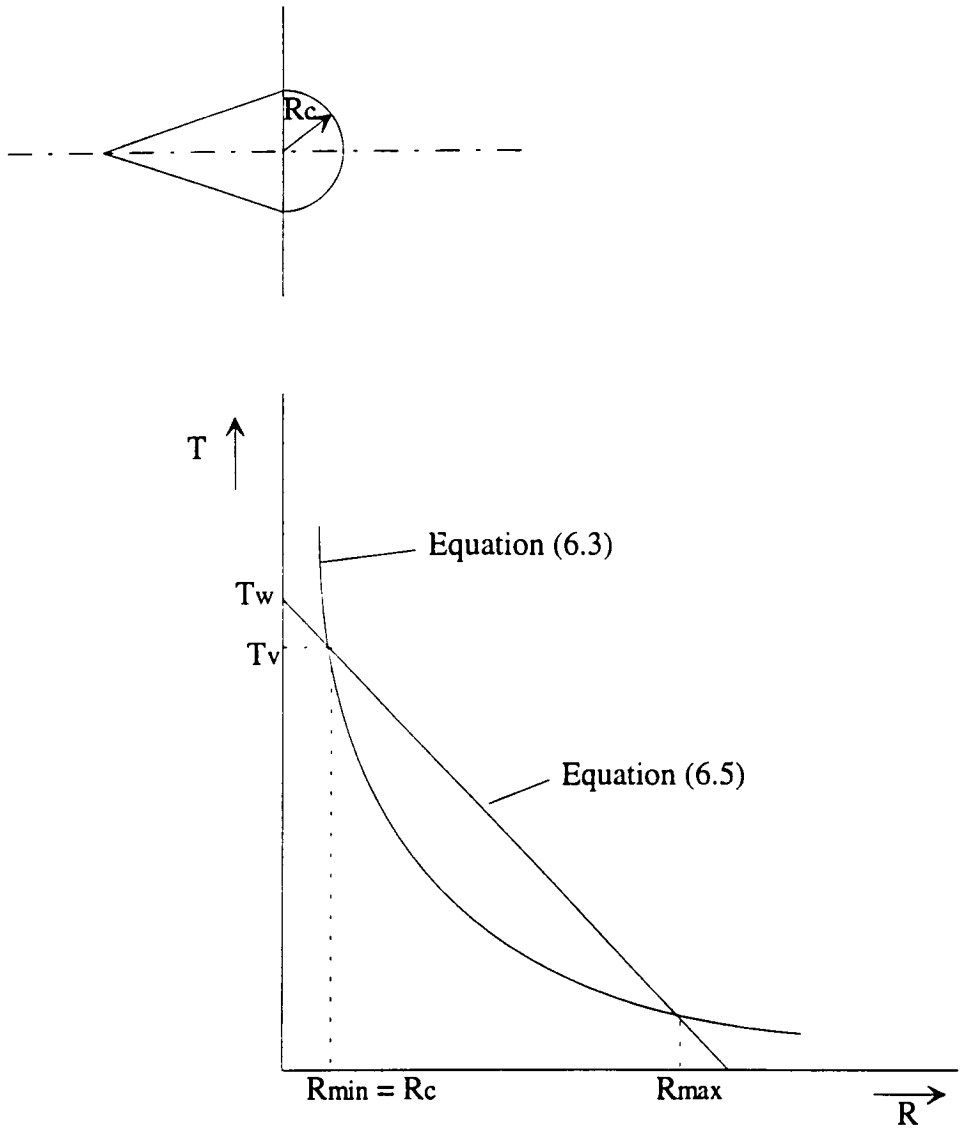

Figure 6.16. Schematic for development of heterogeneous nucleation.

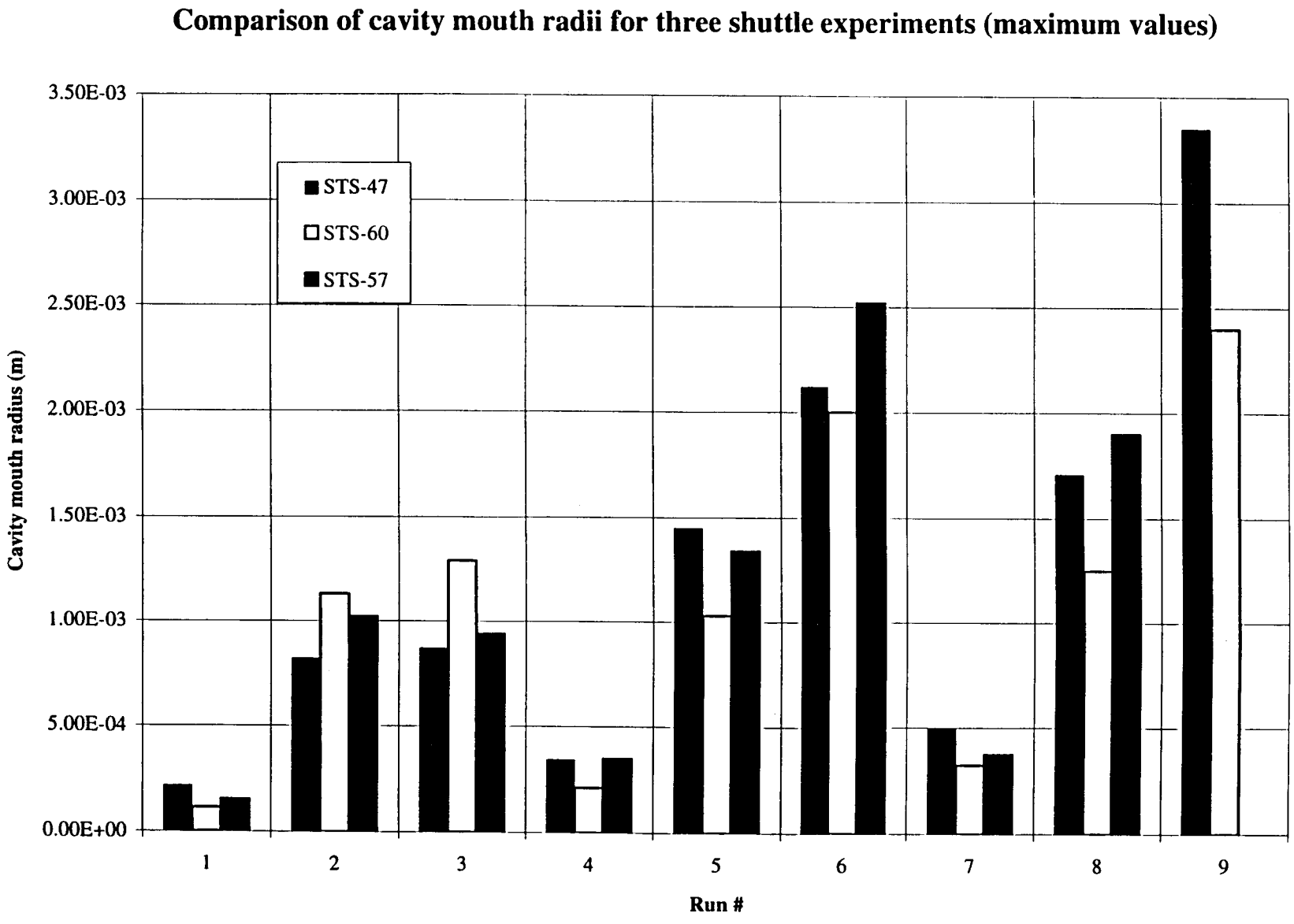

Figure 6.17. Values of maximum critical size nucleation cavities computed from measured heater surface superheats of the PBE in GAS.

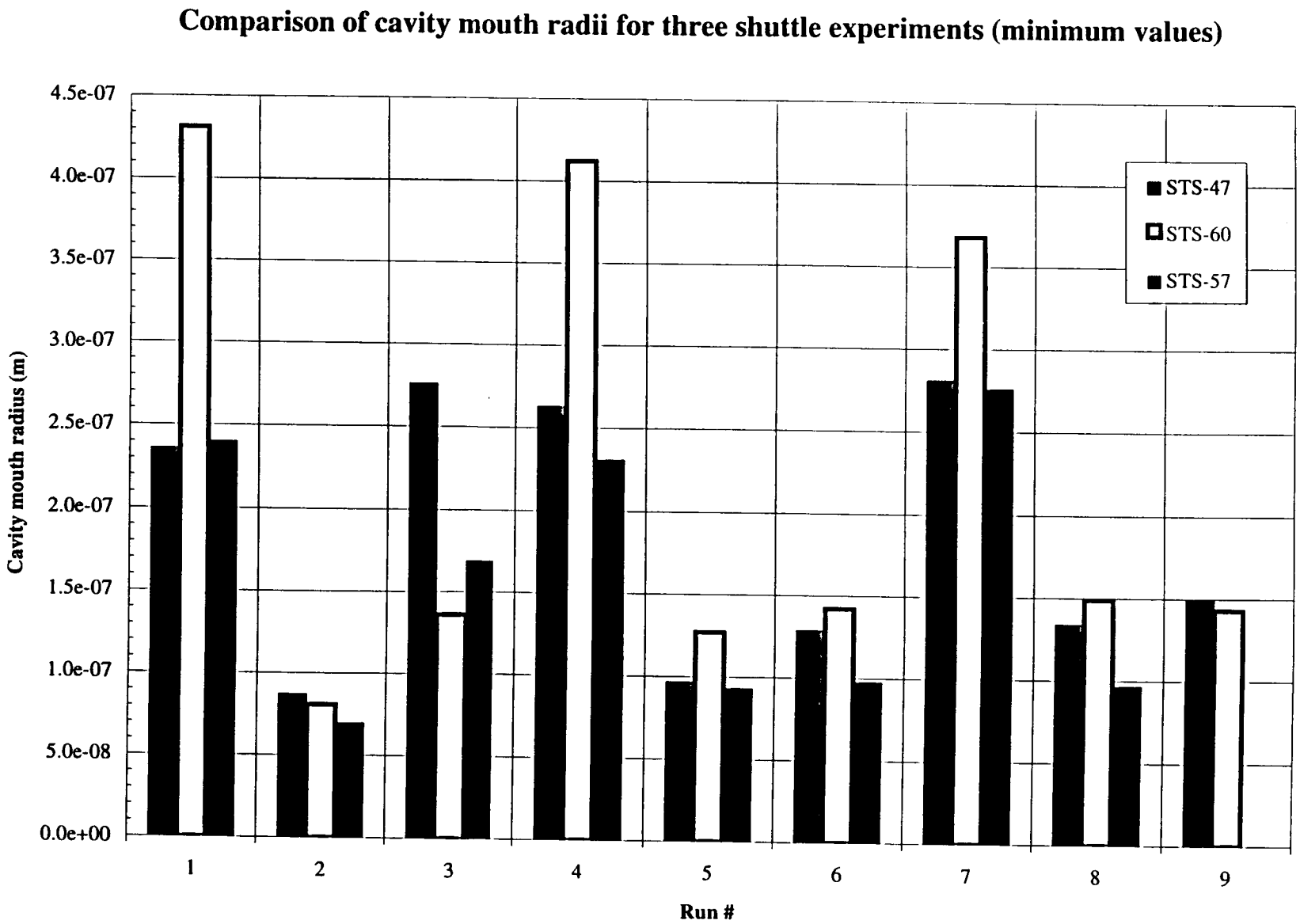

Figure 6.18. Values of minimum critical size nucleation cavities computed from measured heater surface superheats of the PBE in GAS.

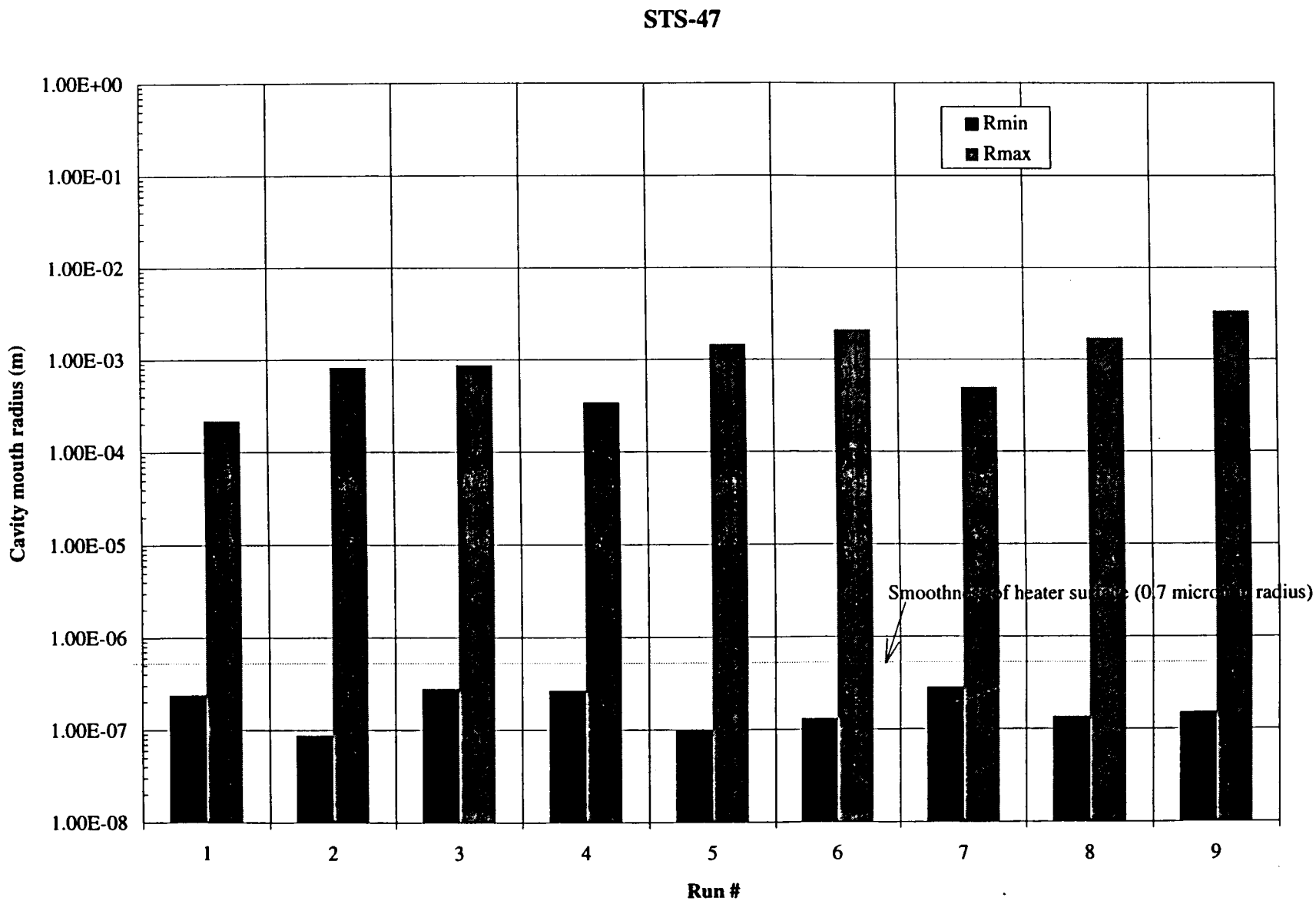

Figure 6.19. Values of maximum and minimum critical size nucleation cavities computed from measured heater surface superheats of PBE-IA (STS-47).

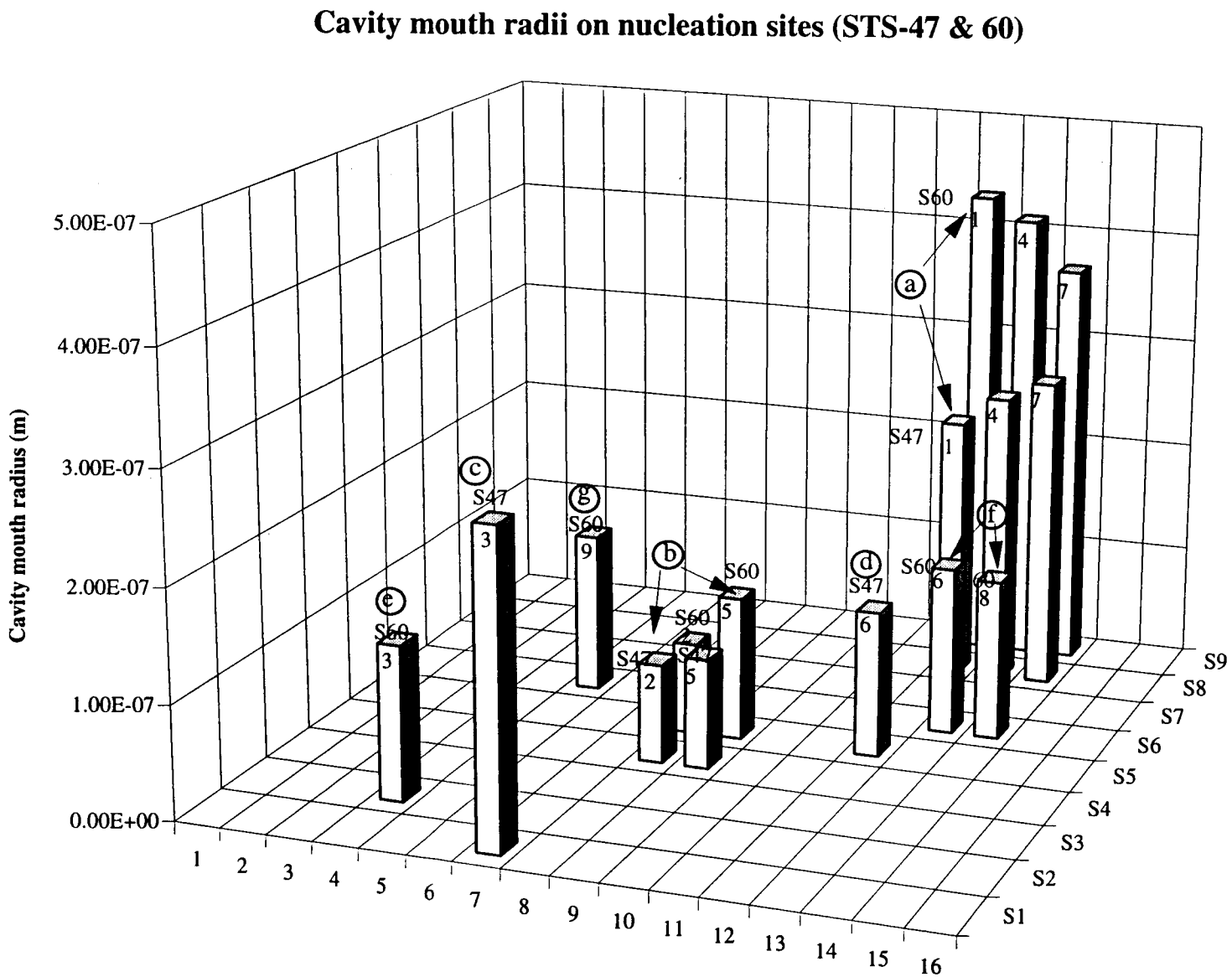

Figure 6.20. Values of minimum critical size nucleation cavities superimposed at physical locations of nucleation for PBE-IA and -IC (STS-47 and -60).

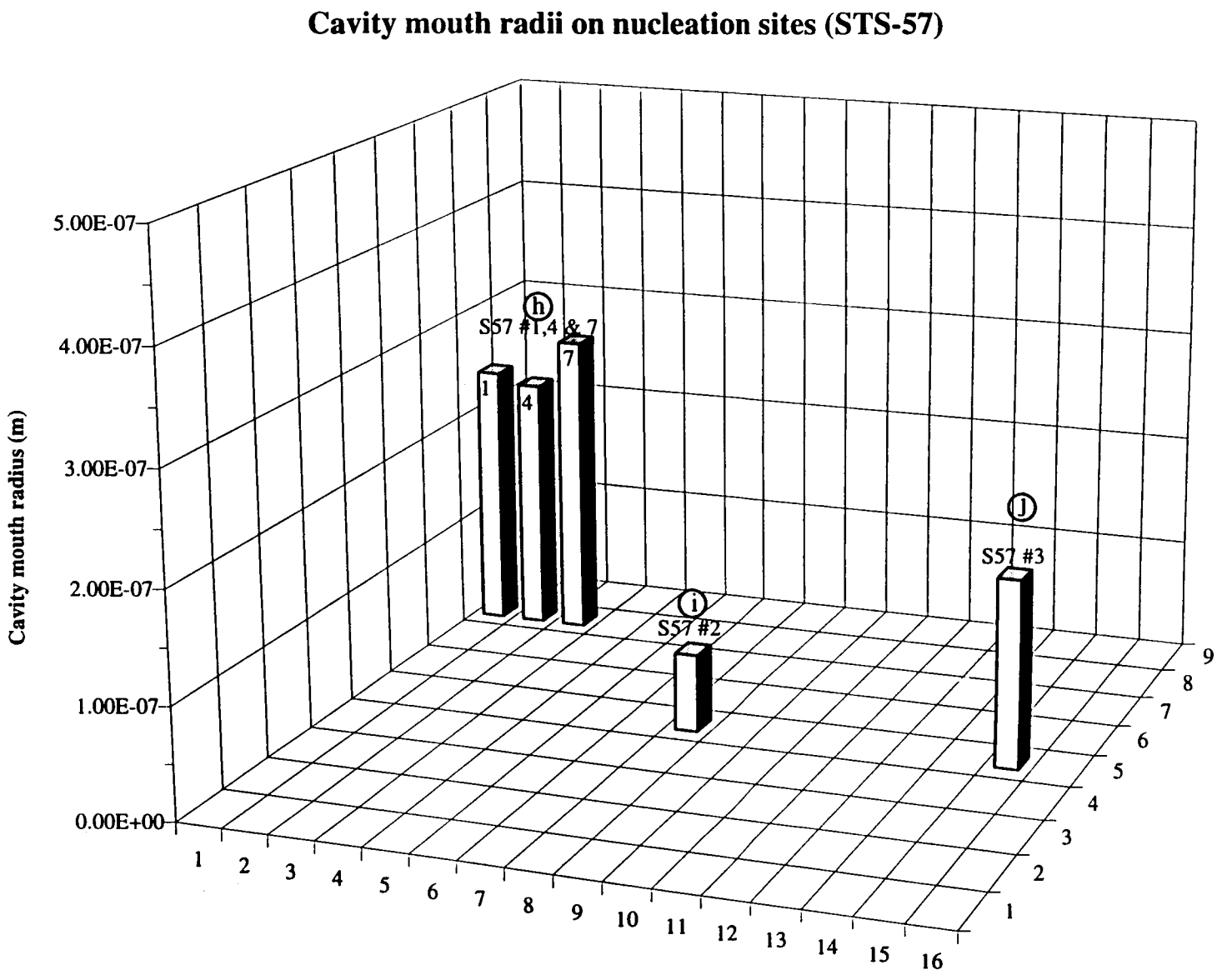

Figure 6.21. Values of minimum critical size nucleation cavities superimposed at physical locations of nucleation for PBE-IB (STS-57).

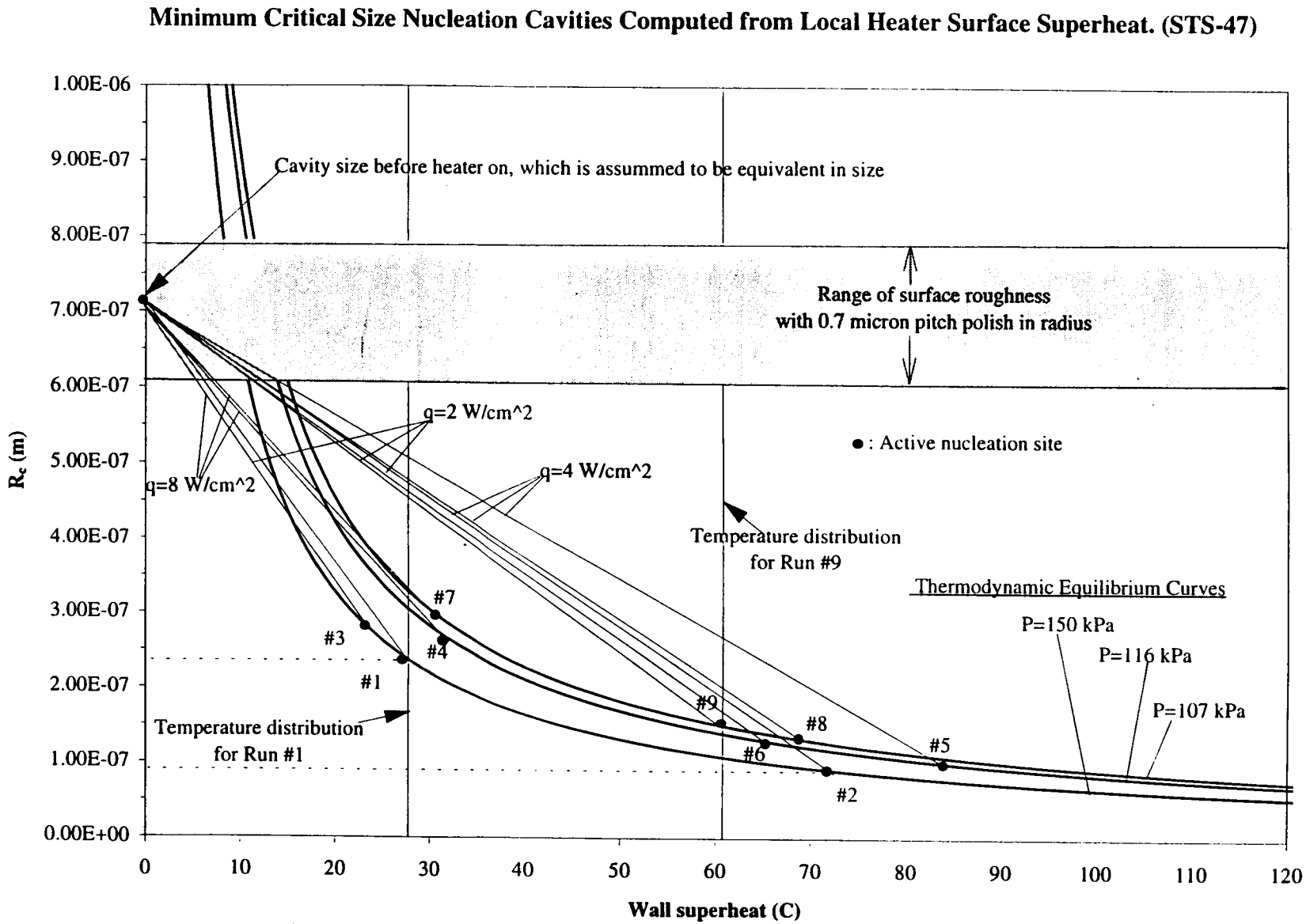

Figure 6.22. Relationship between minimum critical size nucleation cavities computed from measured heater surface superheat and typical grit size used for polishing the heater surface, and liquid temperature distribution at nucleation. PBE-IA (STS-47).

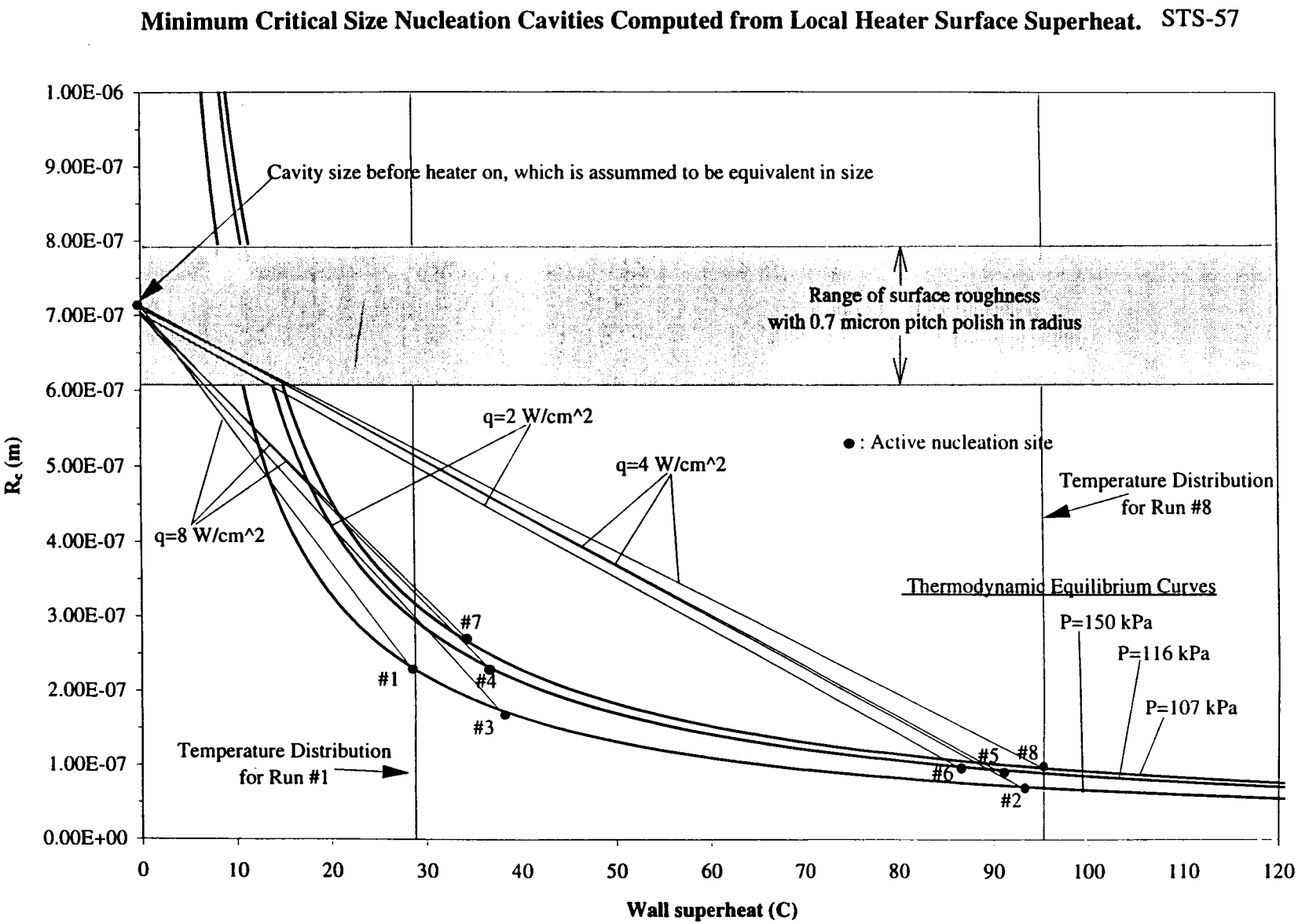

Figure 6.23. Relationship between minimum critical size nucleation cavities computed from measured heater surface superheat and typical grit size used for polishing the heater surface, and liquid temperature distribution at nucleation. PBE-IB (STS-57).

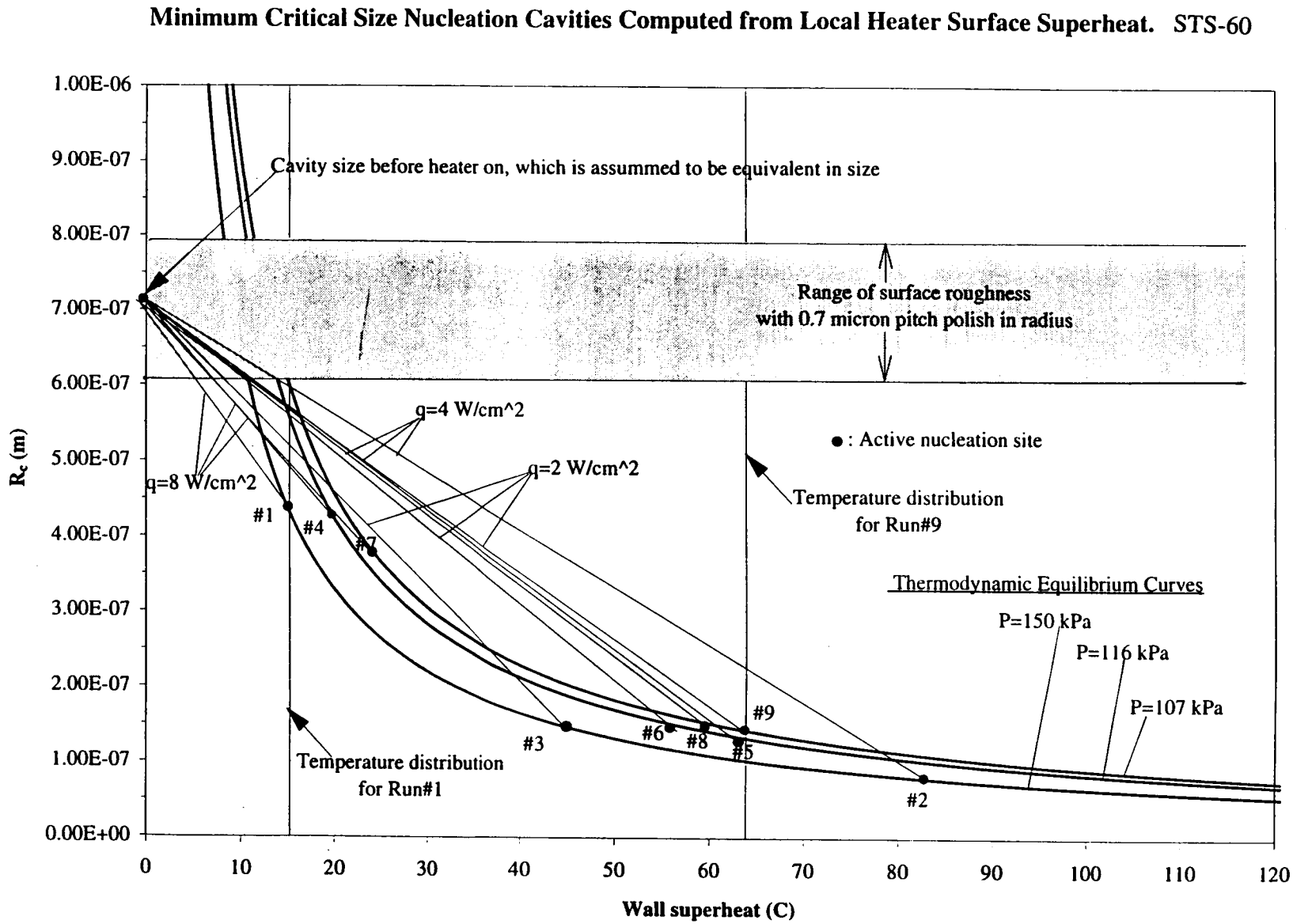

Figure 6.24. Relationship between minimum critical size nucleation cavities computed from measured heater surface superheat and typical grit size used for polishing the heater surface, and liquid temperature distribution at nucleation. PBE-IC (STS-60).

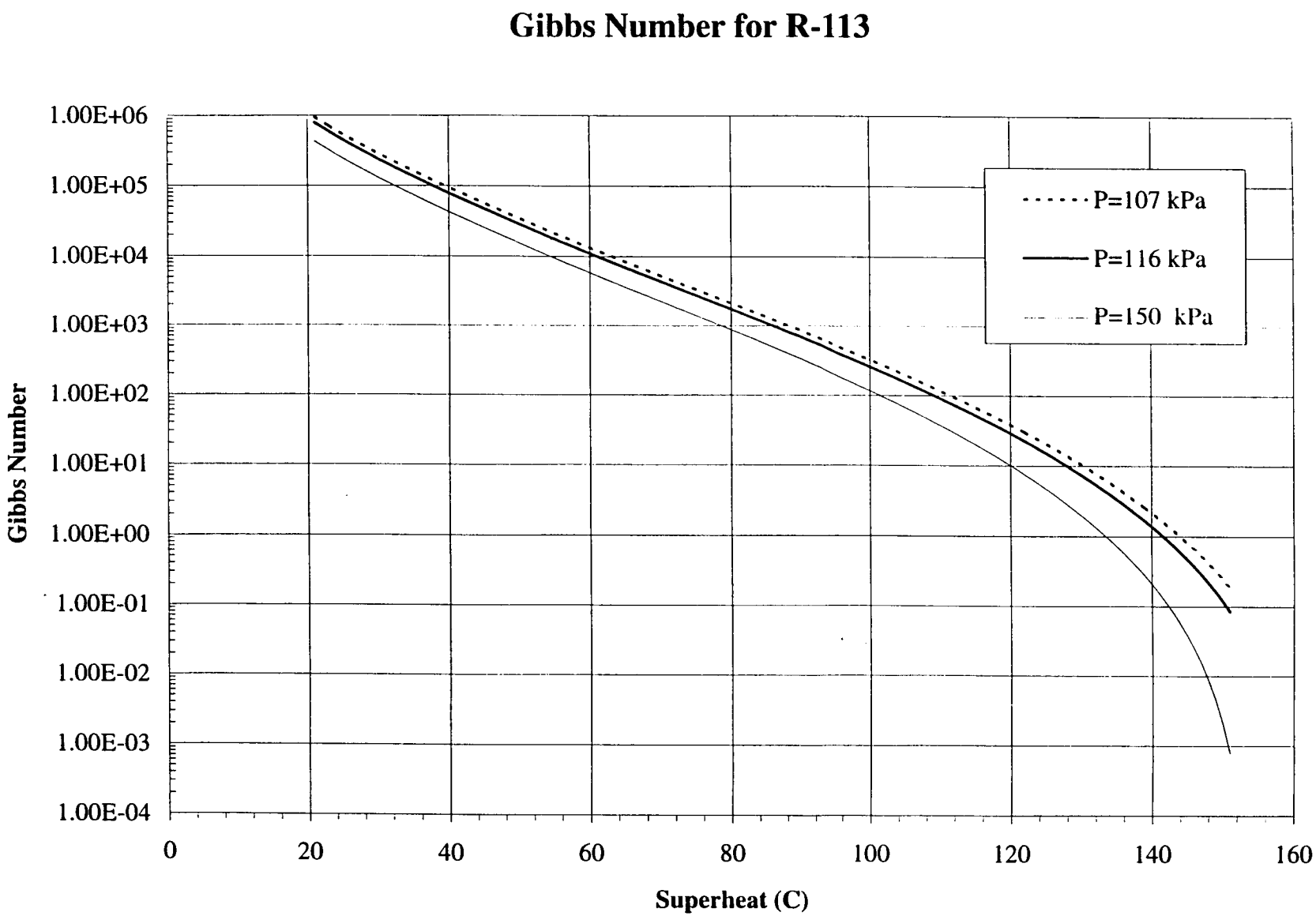

Figure 6.25. Gibbs Number for R-113.

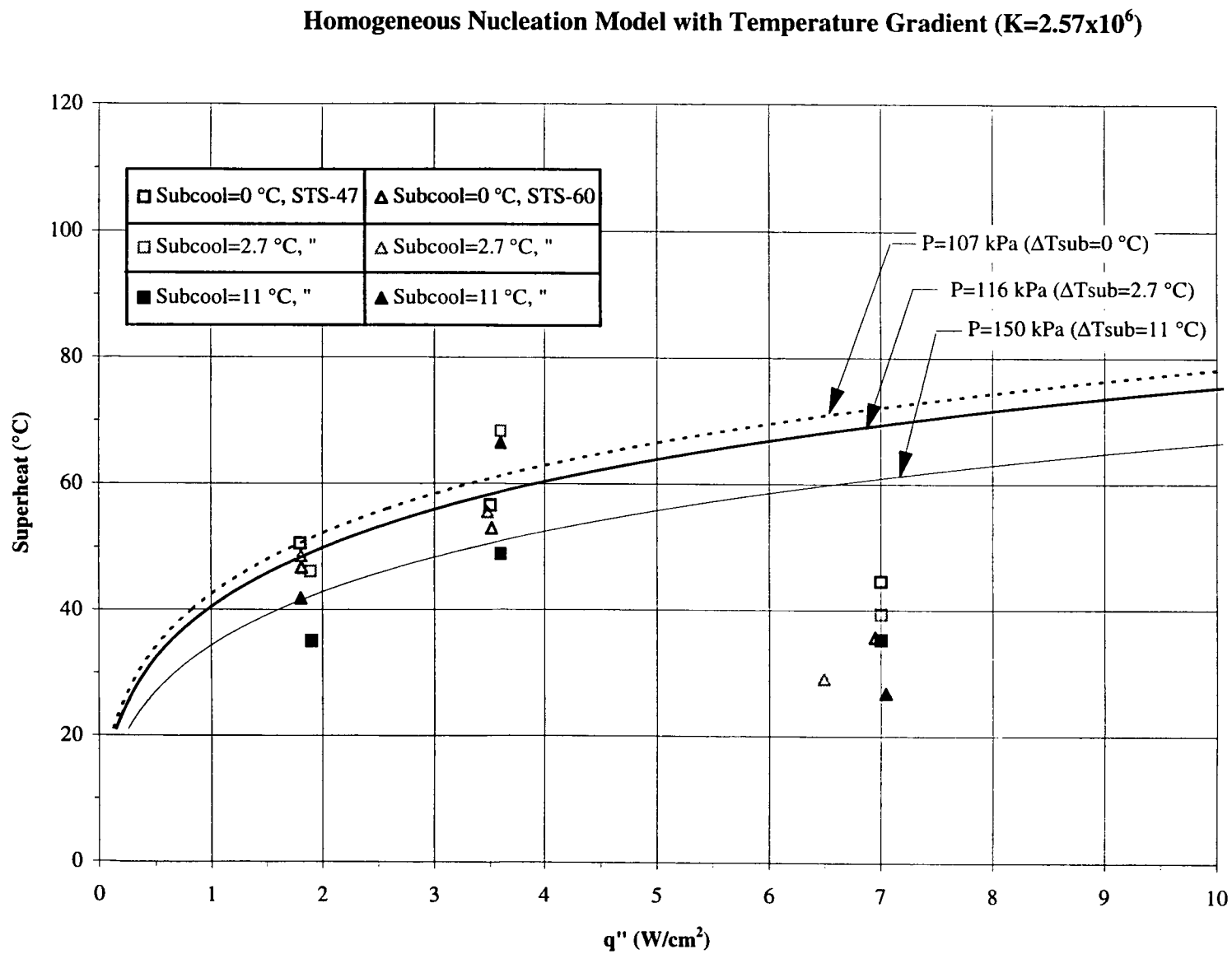

Figure 6.26. Homogeneous nucleation model for R-113 with transient heating in microgravity. Nucleation measurements with PBE-IA - IC (STS-47 -60). K* evaluated for PBE-IA. Run No. 9.

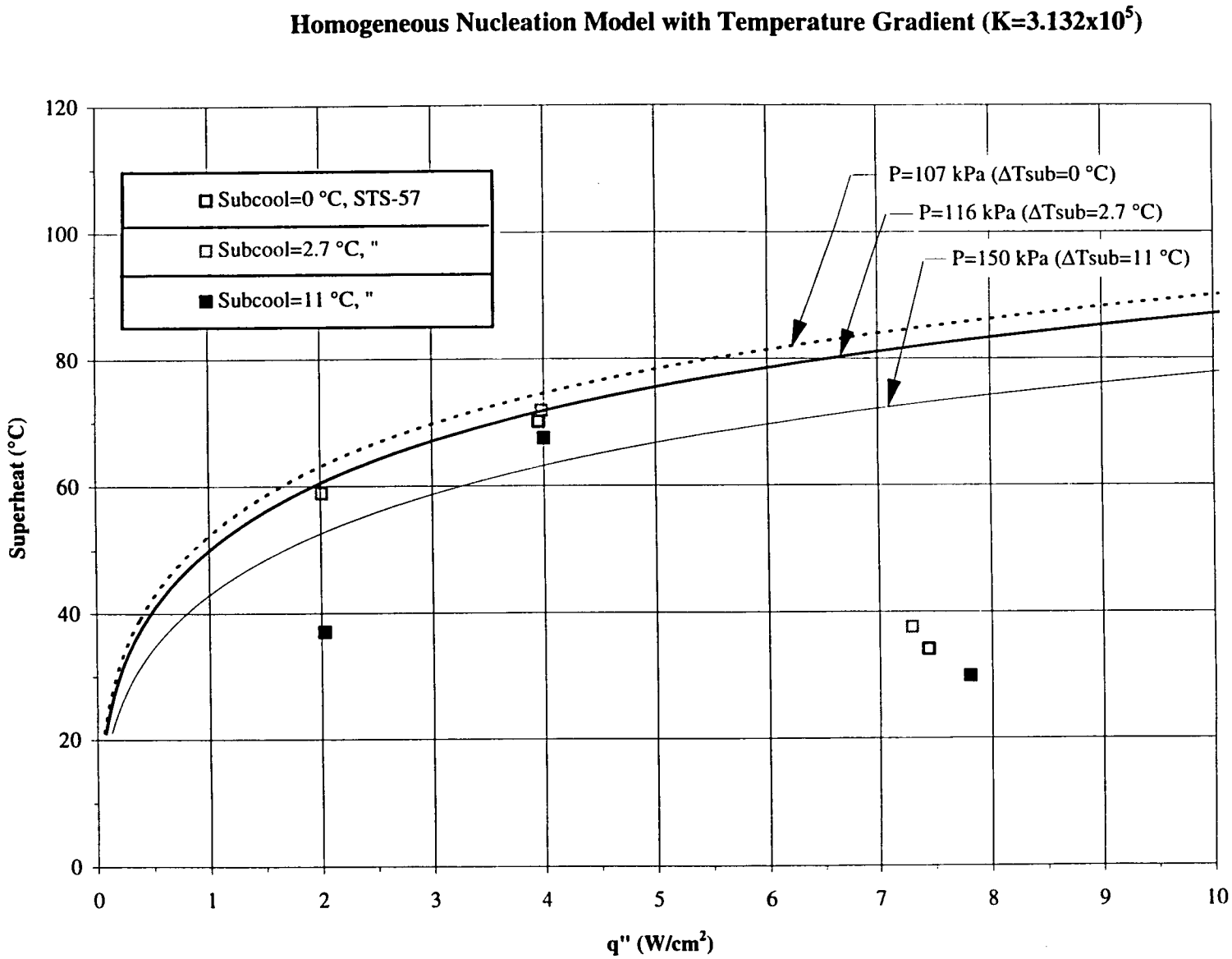

Figure 6.27. Homogeneous nucleation model for R-113 with transient heating in microgravity. Nucleation measurements with PBE-IB (STS-57). K* evaluated for PBE-IB. Run No. 5.

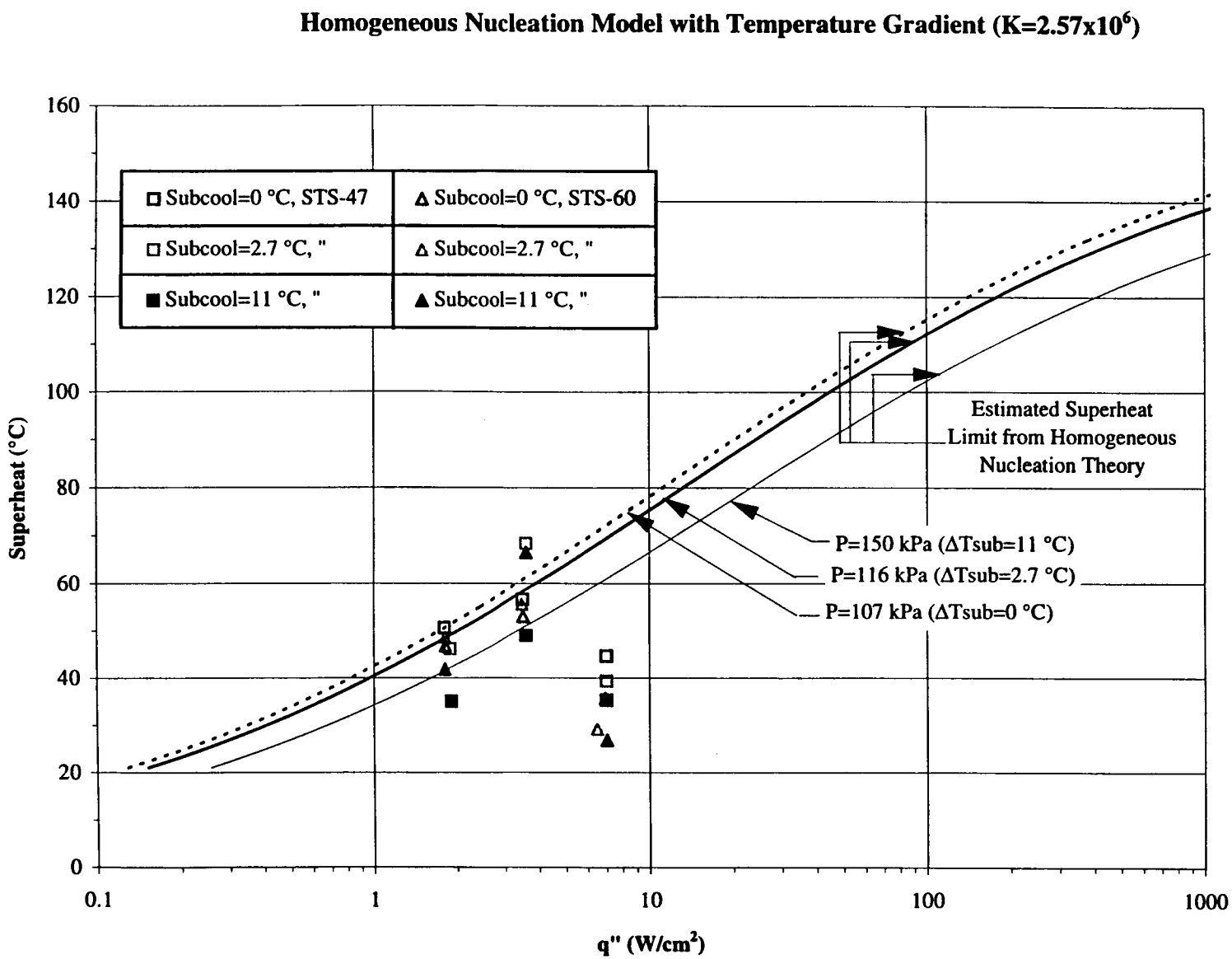

Figure 6.28. Semi-log plot. Homogeneous nucleation model for R-113 with transient heating in microgravity. Measurements with PBE-IA -IC (STS-47-60). K* evaluated for PBE-IA. Run No. 9.

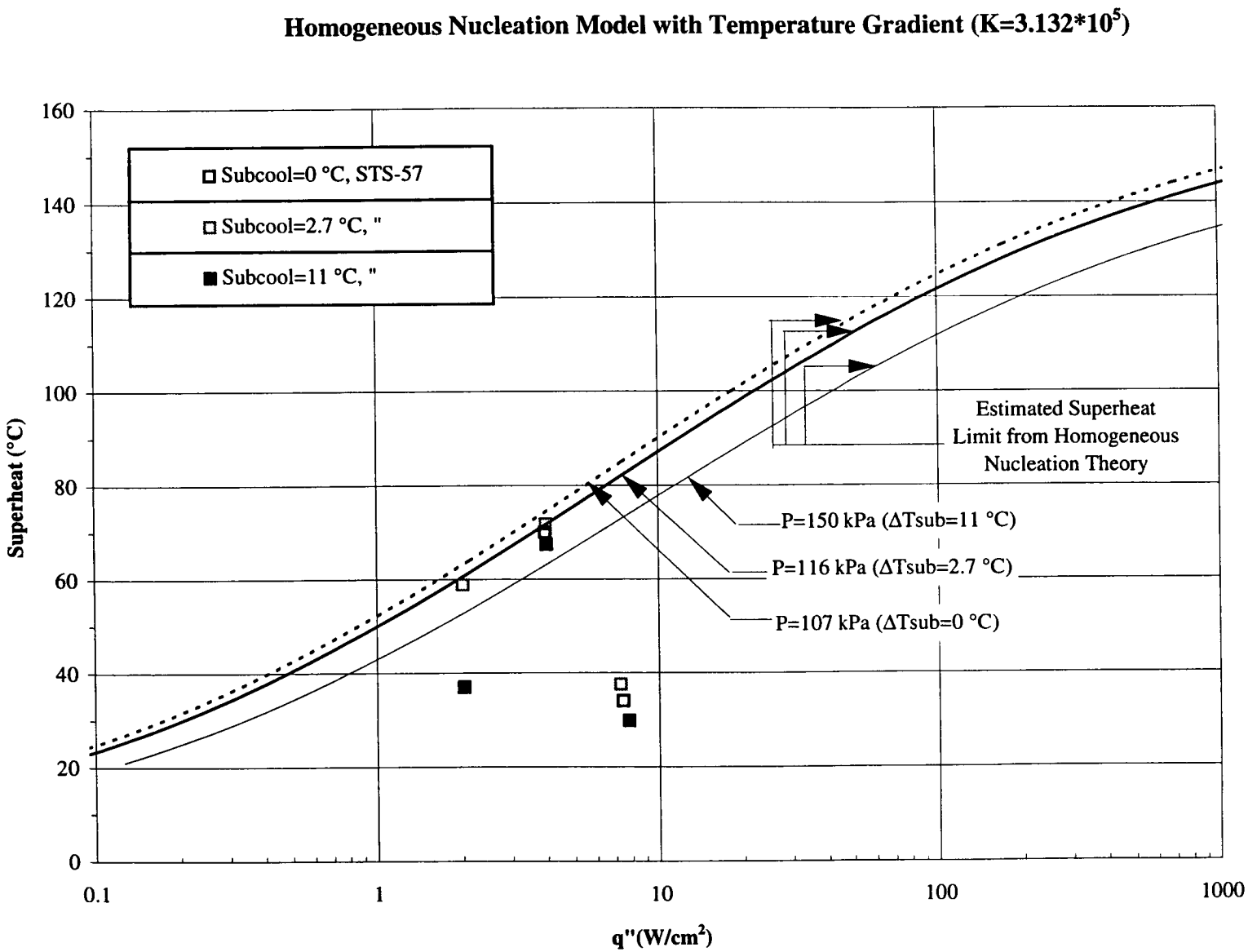

Figure 6.29. Semi-log plot. Homogeneous nucleation model for R-113 with transient heating in microgravity. Measurements with PBE-IB (STS-57). K* evaluated for PBE-IB. Run No. 5.

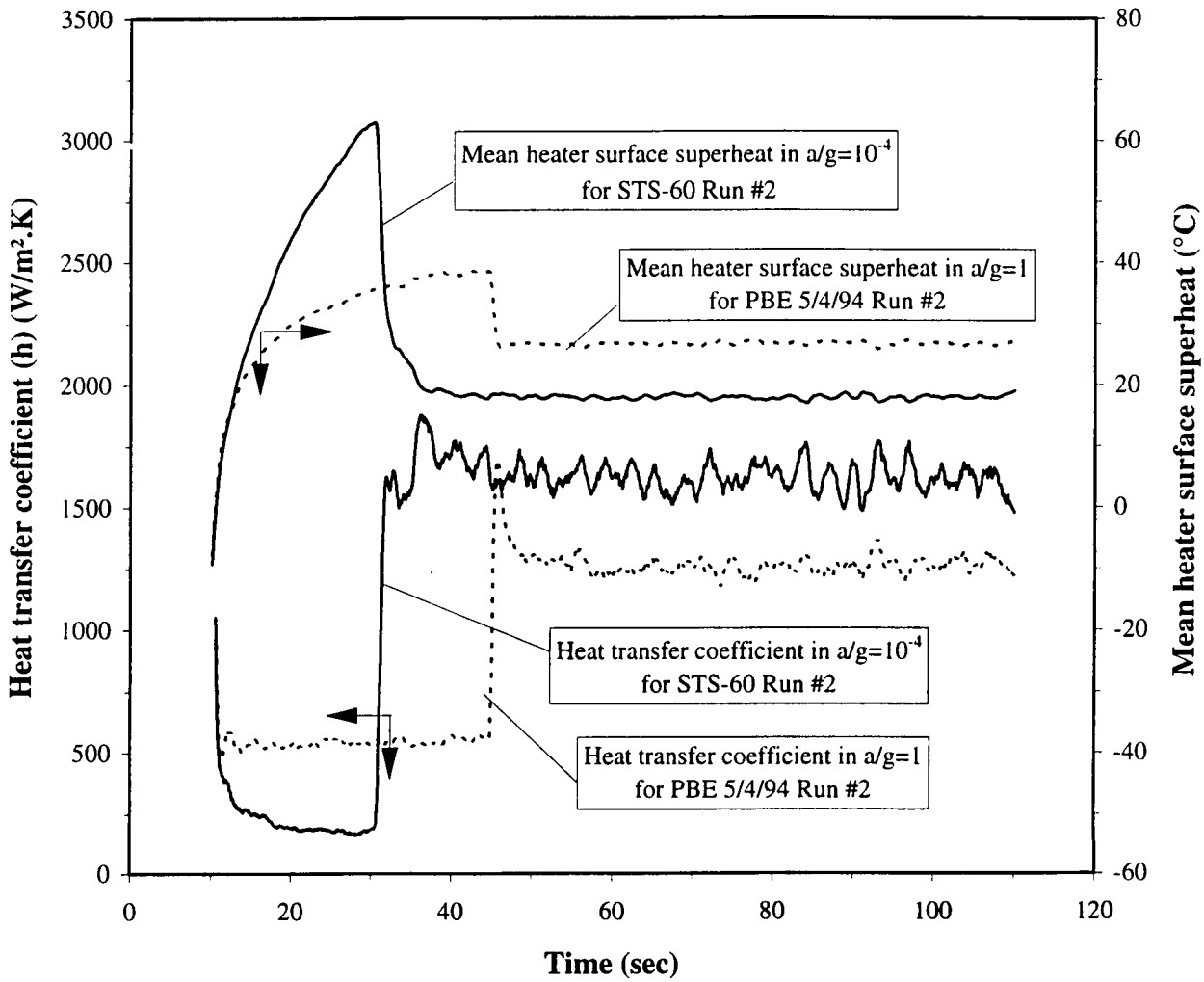

Figure 6.30. Comparison of measured mean heater surface superheat and derived heat transfer coefficient between Space Flight and a/g = +1 Post Flight Test. PBE-IC (STS-60). Run No. 2.

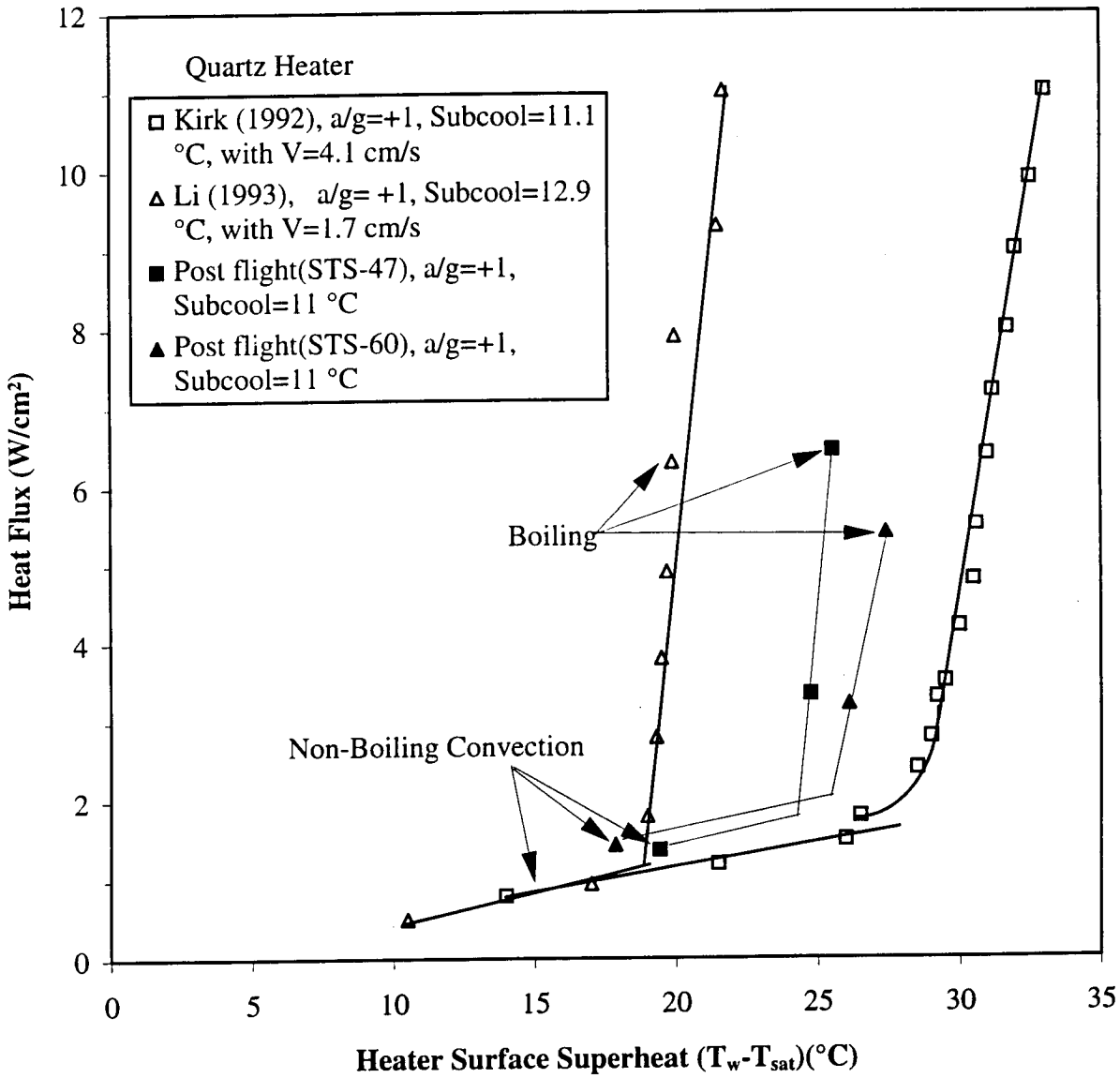

Figure 6.31. Comparison of Post Flight nucleate pool boiling data with other R-113 data at a/g = +1 to demonstrate variability with different systems of gold films on quartz substrates.

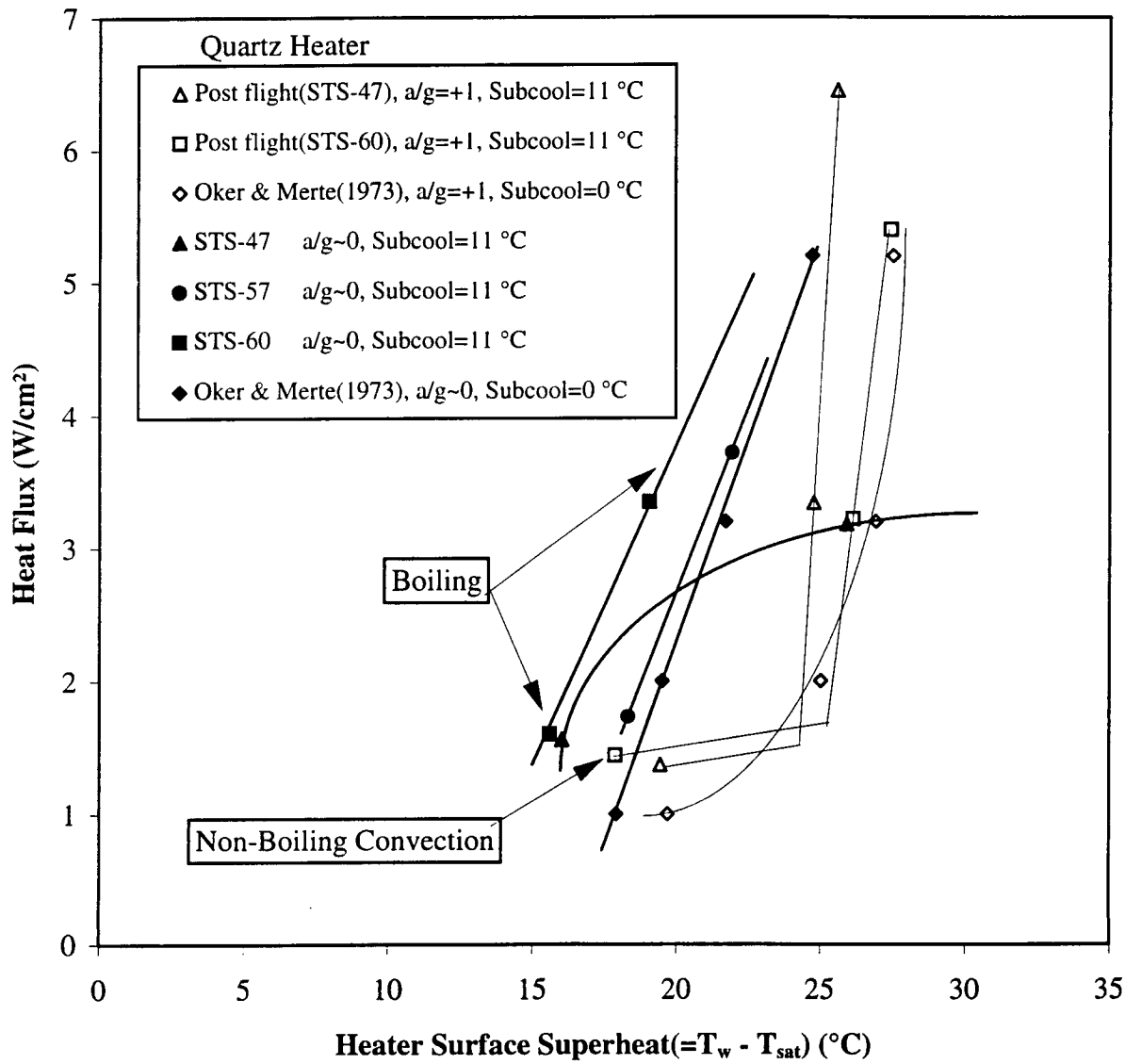

Figure 6.32. Direct comparisons of nucleate pool boiling of R-113 between identical systems at a/g = +1 and approximate microgravity conditions.

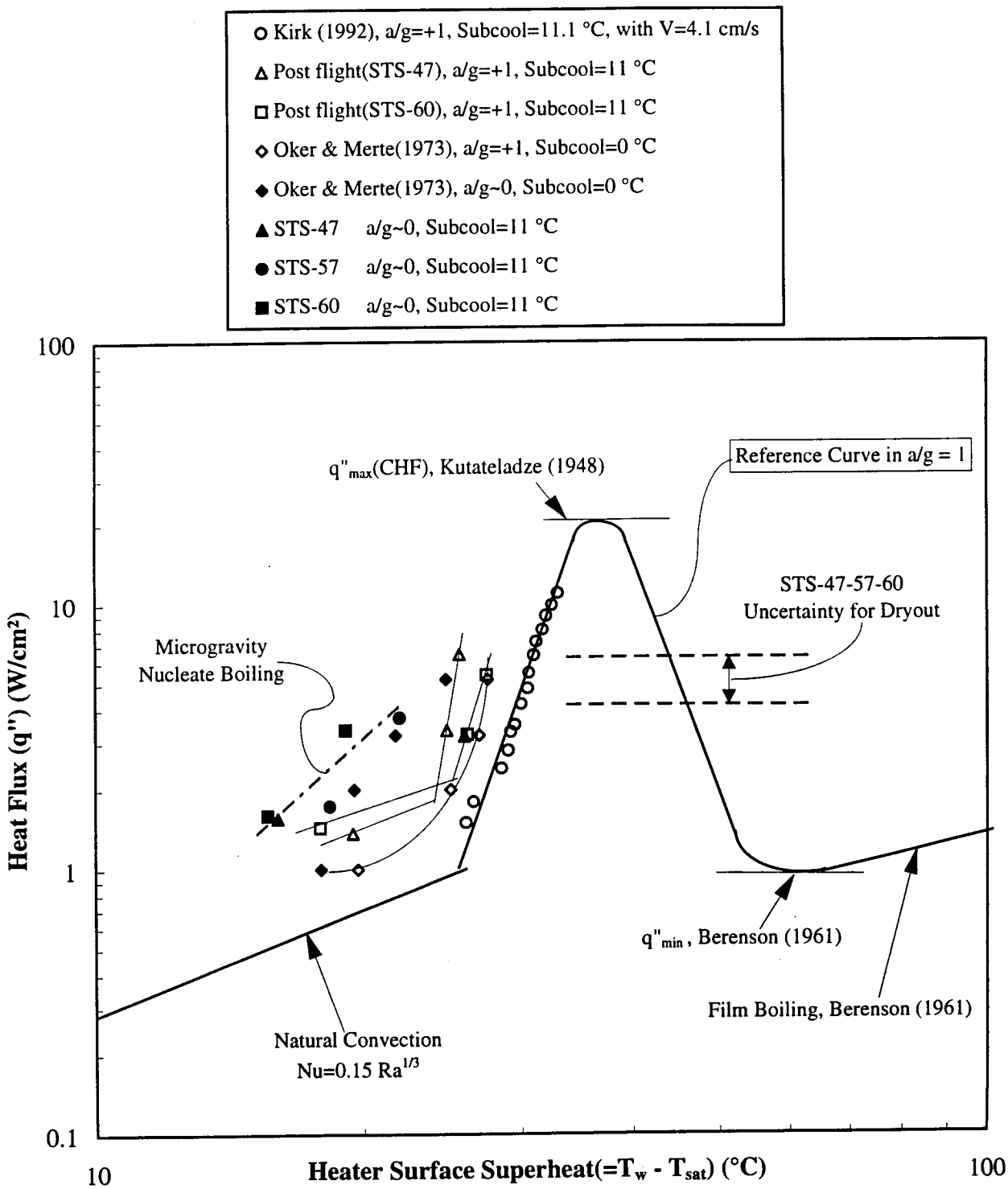

Figure 6.33. Comparison of nucleate pool boiling data in microgravity with a Pool Boiling Reference Curve for R-113 at a/g = +1.

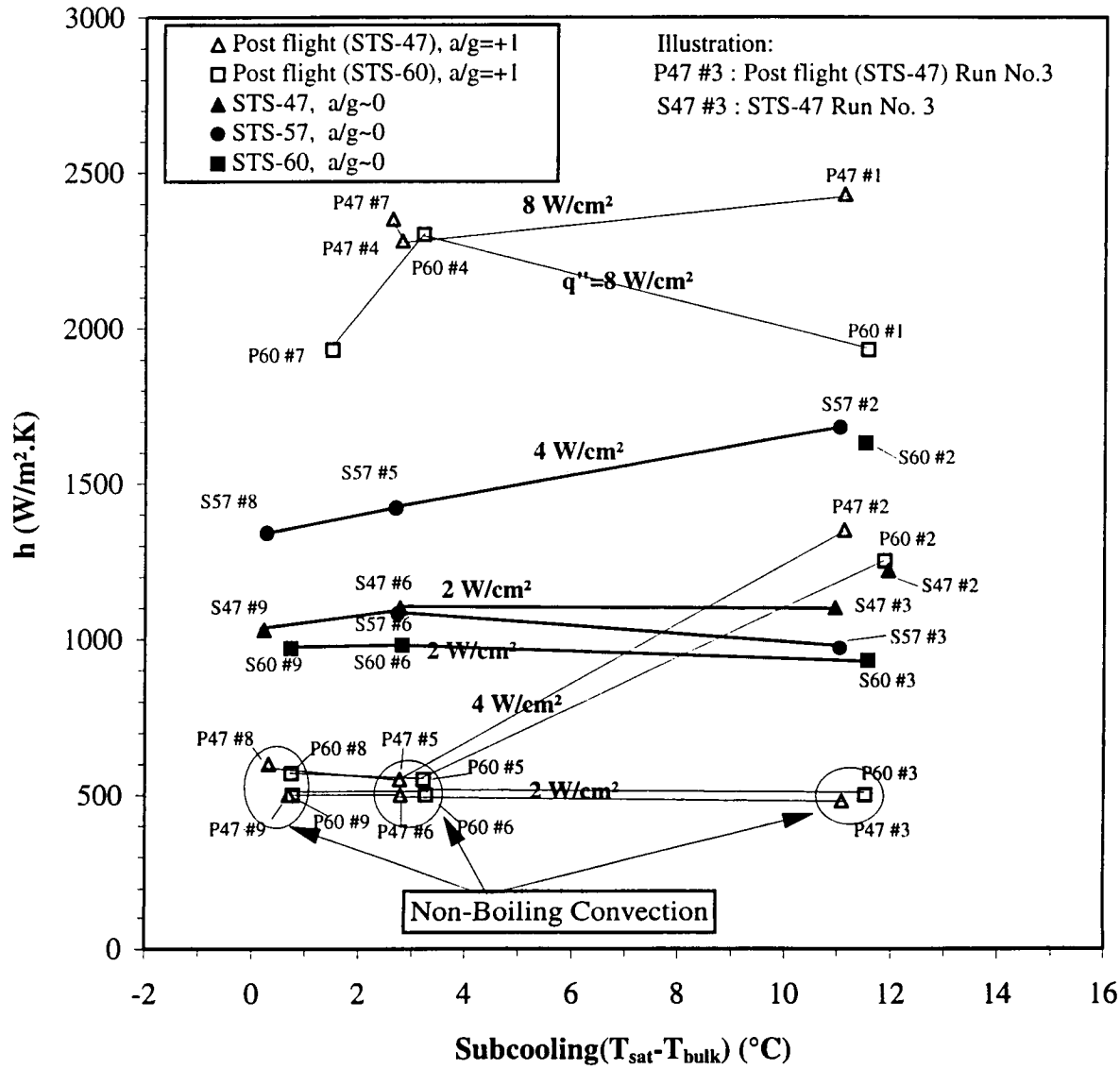

Figure 6.34. All heat transfer coefficient data obtained with PBE-IA-IB-IC (STS-47-57-60) under quasi-steady conditions, both at a/g = +1 and in microgravity.

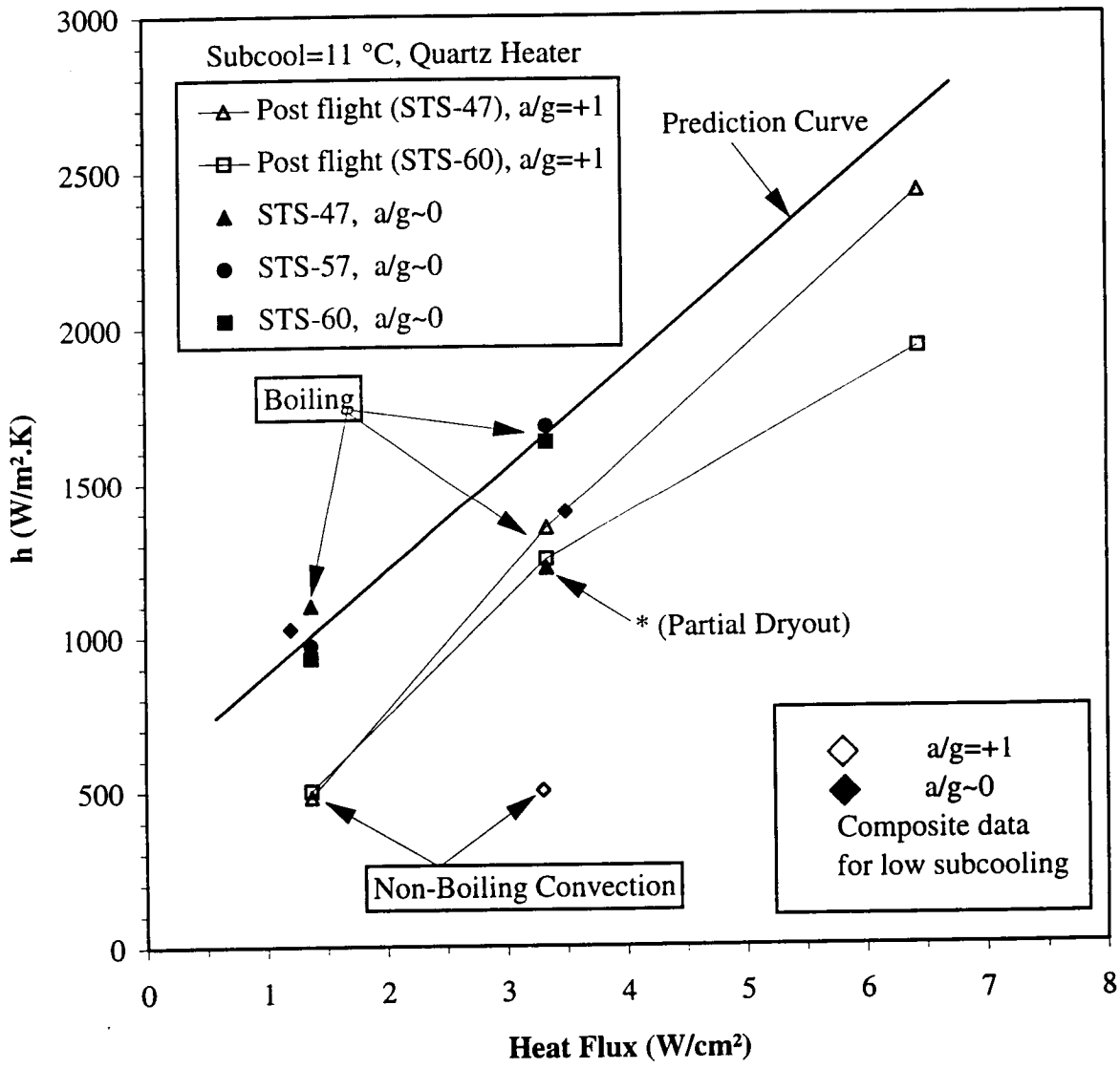

Figure 6.35. Quasi-steady heat transfer coefficient data as a function of heat flux to fluid, for high subcooling level.

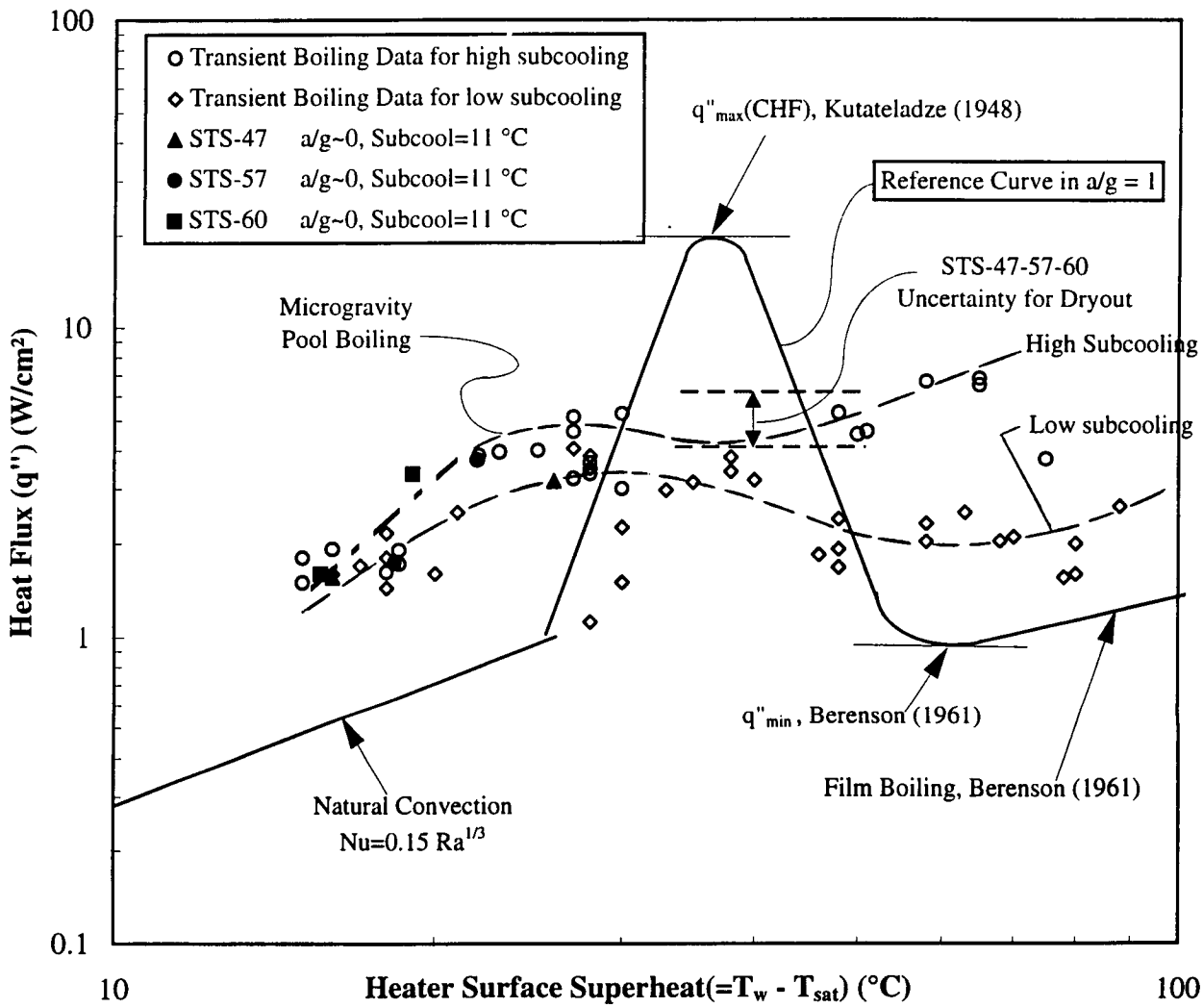

Figure 6.36. Approximate composite microgravity pool boiling curves for R-113 from steady and transient measurements on PBE-IA-IB-IC (STS-47-57-60).

7. CONCLUSIONS AND RECOMMENDATIONS

When considered historically over a sufficiently long period of time, the study of a subject as complex as nucleate boiling can be viewed as a continuing evolutionary process. The understanding of the various elements which constitute nucleate boiling has been enhanced considerably as a result of improvements in measurement capabilities, and the use of microgravity is another step in this direction.

With the completion of one phase of this study of pool boiling in microgravity, represented by the current work, statements can be made as to what has been learned and discovered:

a. The absence of buoyancy and the associated single phase natural convection permits the attainment of homogeneous nucleation at low levels of heat flux.

b. The high liquid superheats obtained at nucleation produce an extremely dynamic and unusual initial vapor bubble growth under certain conditions in microgravity which appears to be associated with an instability problem, and which results in an unusual interfacial behavior.

c. In certain circumstances where rapid expansion of the boiling front takes place, vapor bubbles appear to be formed both within the residual liquid microlayer remaining on the surface as this front passes by, and in advance of the boiling front.

d. It appears that long term steady-state nucleate boiling can take place on a flat heater surface in microgravity with a wetting liquid under conditions in which a large vapor bubble somewhat removed from the heater surface is formed, which acts as a thermal sink to remove the nucleating bubbles from the heater surface.

e. The steady nucleate boiling heat transfer is significantly enhanced in microgravity compared to that in earth gravity.

f. Related to (d) above, surface tension has an important role in producing dryout and/or rewetting on a heated surface. The circumstances describing this remain to be explored further, but the heat flux at which dryout occurs is considerably less in microgravity than in earth gravity.

g. Using the quasi-steady data obtained during the periods in which some significant portions of the heater surface were dried out it was possible to construct two distinct composite approximate microgravity pool boiling curves for R-113, one for the higher level of subcooling and one for the lower level of subcooling. This is compared with a Reference Curve for pool boiling at $a/g = +1$,

constructed from all available data and correlations deemed to reasonably represent the circumstances present. The microgravity pool boiling curves bear some resemblance to the Reference Curve, although the maximum heat flux is reduced considerably, and the difference between the maximum heat flux and the minimum (film boiling) heat flux is also reduced considerably.

Based on the experience gained during the conduct of the experimentation and in the analysis of the results, a number of recommendations can be set forth for further experiments in microgravity using the same hardware with minor revisions. These are listed below, but in no particular order of importance:

i. A film or video camera having both higher framing speeds and higher resolution would be desirable for studying the early bubble dynamics of the energetic growth cases in detail.

ii. Repeat tests at subcooling levels between 2 and 11°C at heat flux levels between 4 and 8 w/cm^2 to determine more precisely the upper limits of nucleate pool boiling enhancement.

iii. Conduct experiments at considerably lower levels of heat flux at low or zero levels of subcooling to determine the lower limits of heat flux, if any, of nucleate pool boiling and nucleate pool boiling enhancement.

iv. Repeat tests at high levels of subcooling to determine if the dryout heat flux can be increased.

v. Energize both heaters, either simultaneously and/or sequentially, with identical or different levels of heat flux to study interactions and coalescences of vapor bubbles in microgravity. The latter constitutes an important area for modeling of bubble dynamics.

References

Avedisian, C.T., (1985), "The Homogeneous Nucleation Limits of Liquids," J. Phys. Chem. Ref. Data, Vol. 14, No. 3, pp. 695-729.

Cole, R., (1974), "Boiling Nucleation," in Advances in Heat Transfer, Vol. 10, Ed. by J.P. Hartnett and T. F. Irvine, Jr., Academic Press, NY, pp. 85-166.

Ervin, J.S. and Merte, H., Jr., (1991), "A Fundamental Study of Nucleate Pool Boiling under Microgravity," Report No. UM-MEAM-91-08, Department of Mechanical Engineering and Applied Mechanics, University of Michigan, Ann Arbor, MI., Final Report on NASA Grant NAG3-663.

Ervin, J.S., Merte, H., Keller, R.B., Kirk, K., (1992), "Transient Pool Boiling in Microgravity". Int. J. Heat Mass Transfer, Vol. 35, pp. 659-674.

Fisher, J.C., (1948), "The Fracture of Liquids," J. of Applied Physics, 19, November, pp. 1062-1068.

Griffith, P., Wallis, J.D., (1960), "The Role of Surface Conditions in Nucleate Boiling," Chem. Eng. Prog. Symp., Vol. 56, No. 30, pp. 49.

Hsu, Y.Y., (1962), "On the Size Range of Active Nucleation Cavities on a Heating Surface," Trans. ASME, J. Heat Transfer, 84C, pp. 207.

Iida, Y., Okuyama, K., Sakurai, K., (1993), "Peculiar Bubble Generation on a Film Heater Submerged in Ethyl Alcohol and Imposed a High Heating Rate over 10^7 k/s," Tech. Note, Int. J. Heat Mass Transfer, 36, No. 10, pp. 2699-2701.

Iida, Y., Okuyama, K., Sakurai, K., (1994), "Boiling Nucleation on a Very Small Film Heater Subjected to Extremely Rapid Heating," Int. J. Heat Mass Transfer, 37, 17, pp. 2771-2780.

Lee, Ho Sung and Merte, H., Jr., (1993), "Vapor Bubble Dynamics in Microgravity," Report No. UM-MEAM-93-10, Department of Mechanical Engineering and Applied Mechanics, University of Michigan, Ann Arbor, MI., Pool Boiling Experiment Report on NASA Contract NAS3-25812.

Lloyd, J.R., Moran, W.R., (1974), "Natural Convection Adjacent to Horizontal Surface of Various Planforms," Trans. ASME, J. Heat Transfer 96C, 4, pp. 443-447.

Mastroianni, M.J., Stahl, R.F., and Sheldon, P.N., (1978), "Physical and Thermodynamic Properties of 1, 1, 2 - Trifluorotrichloroethane (R-113)," J. of Chemical and Engineering Data, 23, 2, pp. 113-118.

Kirk, K. M., Merte, H., Jr., (1992), A Study of the Relative Effects of Buoyancy and Liquid Momentum in Forced Convection Nucleate Boiling," Report No.UM-MEAM-92-

06, Department of Mechanical Engineering and Applied Mechanics, University of Michigan, Ann MI., Final Report on NASA Grant NAG3-1310.

Li, L., Merte, H., Jr., (1993) "Bubble Dyanics and Forced Convection Boiling Heat Transfer with Low Velocity," Report No. UM-MEAM-93-09, Department of Mechanical Engineering and Applied Mechanics, University of Michigan, Ann Arbor, MI., Report on Forced Convection Boiling in Microgravity to NASA, Grant NAG3-1310.

Merte, Herman Jr., (1992), "Pool Boiling Experiment," Report No. UM-MEAM-91-19, Department of Mechanical Engineering and Applied Mechanics, University of Michigan, Ann Arbor, Michigan, Status Report for period 2/1/91 - 9/30/91 to NASA Lewis Research Center on Contract NAS3-25812.

Merte, H., Jr., Lee, H.S., Keller, R.B., (1994), "Report on Pool Boiling Experiment Prototype Model Flown on STS-47 (PBE-IA)," NASA Contract NAS 3-25812, Report No. UM-MEAM-94-09, June 1994, Department of Mechanical Engineering and Applied Mechanics, The University of Michigan.

Monti, R., Langbein, D., Favier, J.J., (1987), "Influence of Residual Accelerations on Fluid Physics and Materials Science Experiments," Chapter XVIII in "Fluid Sciences and Materials Science in Space-A European Perspective," Ed. by H.U. Walter, Springer-Verlag, New York.

Skripov, V.P., (1974), "Metastable Liquids," Halsted Press.

Volmer, M., (1939), "Kinetics of Phase Change," Steinkopff.

Weinzierl, A., and Straub, J., (1982), "Nucleate Pool Boiling in Microgravity Environment," Proceedings of the 7th International Heat Transfer Conference, September 6-10, 1982, Munich.

Kutateladze, S. S., (1948), "On the Tansition to Film Boiling Under Natural Convection," Kotloturbrostroenie, No. 3, p. 10.

Berenson, P. J., (1961), "Film Boiling Heat Transfer for a Horizontal Surface," J. Heat Transfer, Vol. 83, p. 351.

Appendix A. PBE-IA (STS-47). Experimental Results

		Page No. A-
1.	Table A-I. Test matrix for PBE-IA (STS-47). (Prototype Hardware)	2
2.	Table A-II. Measured parameters at a/g = -1, a/g = +1, and Space Flight	3
3.	Table A-III. Summary of relatively larger acceleration excursions during PBE-IA (STS-47).	5
4.	Figures A-1a — A-1i. Mean heater surface temperature and derived heat transfer coefficient. PBE-IA (STS-47). Run Nos. 1-9	6-14
5.	Figures A-2a — A-2i. Heat flux input. PBE-IA (STS-47). Run Nos. 1-9.	15-23
6.	Figures A-3a — A-3i. System pressure and fluid side mean heat flux. PBE-IA (STS-47). Run Nos. 1-9.	24-32
7.	Figures A-4a — A-4i. Measured fluid temperatures near primary heater and far field bulk liquid. PBE-IA (STS-47). Run Nos. 1-9.	33-41
8.	Figures A-5a — A-5i. Measured fluid temperatures near secondary heater and heater underside. PBE-IA (STS-47). Run Nos. 1-9	42-50
9.	Figures A-6a — A-6i. Selected Photographic Images. PBE-IA (STS-47). Run Nos. 1-9.	51-68
10.	Figure A-7. Nucleation Delay Time. Comparisons with ground testing and drop tower correlation. PBE-IA (STS-47).	69
11.	Figure A-8. Mean heater surface nucleation superheat. Comparisons with ground testing. PBE-IA (STS-47).	70
12.	Figures A-9a — A-9i. Comparisons of bubble growth measurements with several models. PBE-IA (STS-47). Run Nos. 1-9.	71-79
13.	Table A-IV. Index for heater surface dry fraction measurements and computation of microgravity nucleate boiling heat transfer coefficients. PBE-IA (STS-47).	80
14.	Figures A-10a — A-10i. Development of microgravity boiling heat transfer coefficients from heater surface dry fraction and mean heat transfer coefficients. PBE-IA (STS-47) Run Nos. 1-9.	81-140
15.	Figures A-11a — A-11i. a/g = +1 Post flight test. Mean heater surface temperature and derived heat transfer coefficient. PBE-IA (STS-47). Run Nos. 1-9.	141-149
16.	Figures A-12a — A-12i. a/g = +1 Postflight test. Heat flux input. PBE-IA. (STS-47). Run Nos. 1-9.	150-158
17.	Figures A-13a — A-13i. a/g = +1. Postflight test. System pressure and heat flux into fluid. PBE-IA (STS-47). Run Nos. 1-9.	159-167

PBE Prototype System Test Matrix (STS-47)

RUN NO.	HEAT FLUX W/CM^2	SUBCOOLING (°F)	HEATER POWER ON/OFF (SEC)	10 FPS ON/OFF (SEC)	100 FPS ON/OFF (SEC)	STIRRER START (SEC)	REPRESS. START (SEC)	TOTAL TEST TIME (SEC)
1	8	20 ± 2	10--70	15--80	10--15	65-	-	80
2	4	20 ± 2	10--100	10--15, 25--130	15--25	-	-	130
3	2	20 ± 2	10--120	20--30, 50--130	30--50	110-	-	130
4	8	5 ± 1	10--55	15--65	10--15	50-	-	65
5	4	5 ± 1	10--100	10--15, 25--105	15--25	-	-	105
6	2	5 ± 1	10--105	20--30, 50--115	30--50	-	-	115
7	8	0.5 ± 0.4	10--40	15--55	10--15	-	45-	55
8	4	0.5 ± 0.4	10--70	10--15, 25--80	15--25	65-	-	80
9	2	0.5 ± 0.4	10--115	10--30, 50--125	30--50	105-	-	125

Table A-I. Test matrix for PBE-IA (STS-47). (Prototype Hardware).

Test Matrix for Pool boiling-STS-47

a/g -1 experiment based on date 4/28/92
a/g 0 experiment based on date 9/11/92 STS-47
a/g -1 experiment based on date 12/22/92
a/g+1 experiment based on data 11/4/92

Run#	Date of Experiment	Flight system	Gravit a/g	Heat Flux, W/cm^ Nom.	Heat Flux, W/cm^ Actual	Subcool,oF Nom.o	Subcool,oF Actual oF	Tbulk oC	Sys.Press kPa	Tsat oC	T*wall oC	T*sup oC	t* time sec	100pps On-Off	Remark
1	4/28/92	Prototype	-1	8.00	6.70	20	21.00	49.44	153.48	61.11	93	31.89	1.20	0 -- 5	
	9/11/92	Prototype	0	8.00	7.00	20	18.50	49.44	149.00	59.72	95	35.28	1.58	0 -- 5	
	12/22/92	Prototype	-1	8.00	6.22	20	19.94	49.42	152.99	60.50	77	16.50	0.54	0 -- 5	
	11/4/92	Prototype	1	8.00	7.02	20	20.02	48.31	147.89	59.43	93	33.57	2.10	0 -- 5	
2	4/28/92	Prototype	-1	4.00	3.65	20	19.80	49.00	151.55	60.00	81	21.00	2.68	5 --15	
	9/11/92	Prototype	0	4.00	3.60	20	21.50	49.17	154.44	61.11	110	48.89	12.38	5 --15	
	12/22/92	Prototype	-1	4.00	3.37	20	19.92	49.28	152.31	60.35	100	39.65	8.50	5 --15	
	11/4/92	Prototype	1	4.00	3.56	20.00	20.00	48.14	147.07	59.25	101	41.75	51.20	5 --15	
3	4/28/92	Prototype	-1	2.00	1.78	20	21.00	49.44	154.44	61.11	89	27.89	23.40	20 -- 40	
	9/11/92	Prototype	0	2.00	1.80	20	19.70	49.06	151.20	60.00	95	35.00	31.39	20 -- 40	
	12/22/92	Prototype	-1	2.00	1.80	20	20.28	49.56	154.30	60.83	102	41.17	90.00	20 -- 40	
	11/4/92	Prototype	1	2.00	1.81	20	19.95	48.49	148.51	59.57				20 -- 40	No Nucleation
4	4/28/92	Prototype	-1	8.00	6.50	5	5.30	49.00	116.87	51.94	91	39.06	1.10	0 -- 5	
	9/11/92	Prototype	0	8.00	7.00	5	4.80	49.00	115.83	51.67	91	39.33	1.34	0 -- 5	
	12/22/92	Prototype	-1	8.00	6.30	5	4.22	49.08	115.21	51.43	75	23.57	0.50	0 -- 5	
	11/4/92	Prototype	1	8.00	7.05	5	5.05	47.81	112.04	50.62	94	43.38	1.90	0 -- 5	
5	4/28/92	Prototype	-1	4.00	3.40	5	5.40	49.22	117.21	52.22	102	49.78	8.70	5 --15	
	9/11/92	Prototype	0	4.00	3.60	5	5.00	48.89	115.83	51.67	120	68.33	16.15	5 --15	
	12/22/92	Prototype	-1	4.00	3.38	5	4.93	49.04	116.52	51.78	109	57.22	12.70	5 --15	
	11/4/92	Prototype	1	4.00	3.54	5	4.98	47.92	112.32	50.69				5 --15	No Nucleation

Page 2 of 2

Table A-II. Measured parameters at a/g = -1, a/g = +1, and Space Flight.

Run#	Date of Experiment	Flight system	Gravit a/g	Heat Flux, W/cm^ Nom.	Actual	Subcool,oF Nom.o	Actual oF	Tbulk oC	Sys.Press kPa	Tsat oC	T*wall oC	T*sup oC	t* time sec	100pps On-Off	
6	4/28/92	Prototype	-1	2.00	1.76	5	4.70	49.06	115.83	51.67	87	35.33	34.30	20 -- 40	
	9/11/92	Prototype	0	2.00	1.82	5	5.00	49.17	116.52	51.94	98	46.06	37.47	20 -- 40	
	12/22/92	Prototype	-1	2.00	1.77	5	4.95	49.25	117.35	52.00				20 -- 40	No Nucleation
	11/4/92	Prototype	1	2.00	1.81	5	5.01	48.04	112.87	50.82				20 -- 40	No Nucleation
7	4/28/92	Prototype	-1	8.00	6.70	0.50	1.20	48.78	106.87	49.44	93	43.56	1.18	0 -- 5	
	9/11/92	Prototype	0	8.00	7.00	0.50	1.00	48.89	106.87	49.44	94	44.56	1.36	0 -- 5	
	12/22/92	Prototype	-1	8.00	6.42	0.50	4.92	48.79	115.56	51.52	86	34.48	1.00	0 -- 5	
	11/4/92	Prototype	1	8.00	7.06	0.50	4.74	47.51	110.32	50.14	91	40.86	1.90	0 -- 5	
8	4/28/92	Prototype	-1	4.00	3.50	0.50	1.40	48.67	106.87	49.44	101	51.56	9.30	5 --15	
	9/11/92	Prototype	0	4.00	3.50	0.50	0.70	49.06	106.87	49.44	106	56.56	10.63	5 --15	
	12/22/92	Prototype	-1	4.00	3.42	0.50	0.45	49.09	107.63	49.34	111	61.66	14.50	5 --15	
	11/4/92	Prototype	1	4.00	3.55	0.50	0.56	47.42	101.90	47.73				5 --15	No Nucleation
9	4/28/92	Prototype	-1	2.00	1.80	0.50	1.00	48.72	106.18	49.28	99	49.72	65.90	20 -- 40	
	9/11/92	Prototype	0	2.00	1.80	0.50	0.40	49.22	106.87	49.44	100	50.56	41.48	20 -- 40	
	12/22/92	Prototype	-1	2.00	1.76	0.50	0.41	49.05	107.42	49.28	89	39.72	27.00	20 -- 40	
	11/4/92	Prototype	1	2.00	1.81	0.50	1.23	47.49	103.42	48.17				20 -- 40	No Nucleation

Table A-II. Continued.

Notes: (1) Accelerometer units are given as micro-g's.

(2) Heating in each run begins at t = 10 sec.

RUN #	Time, sec	Plots	Max value			Uncertainty (Noise)	Comments
			x	y	z		
1		no	50	52	50	2.40E+01	
2		no	76	77	50	2.40E+01	
3		no	51	77	50	2.40E+01	
4		no	101	77	75	2.40E+01	
5	98.3	yes	**179**	52	**348**	2.40E+01	
5	98.4	yes	51	**103**	50	2.40E+01	
6	89.9	yes	51	52	**273**	2.40E+01	
6	90.1	yes	51	**258**	50	2.40E+01	
6	90.2	yes	**254**	52	50	2.40E+01	
7		no	76	77	75	2.40E+01	
8	4.9	yes	**306**	52	75	2.40E+01	
8	5	yes	51	**103**	75	2.40E+01	
9	48.1	yes	51	**103**	50	2.40E+01	
9	60.4	yes	**281**	52	75	2.40E+01	

Table A-III. Summary of relatively larger acceleration excursions during PBE-IA (STS-47).

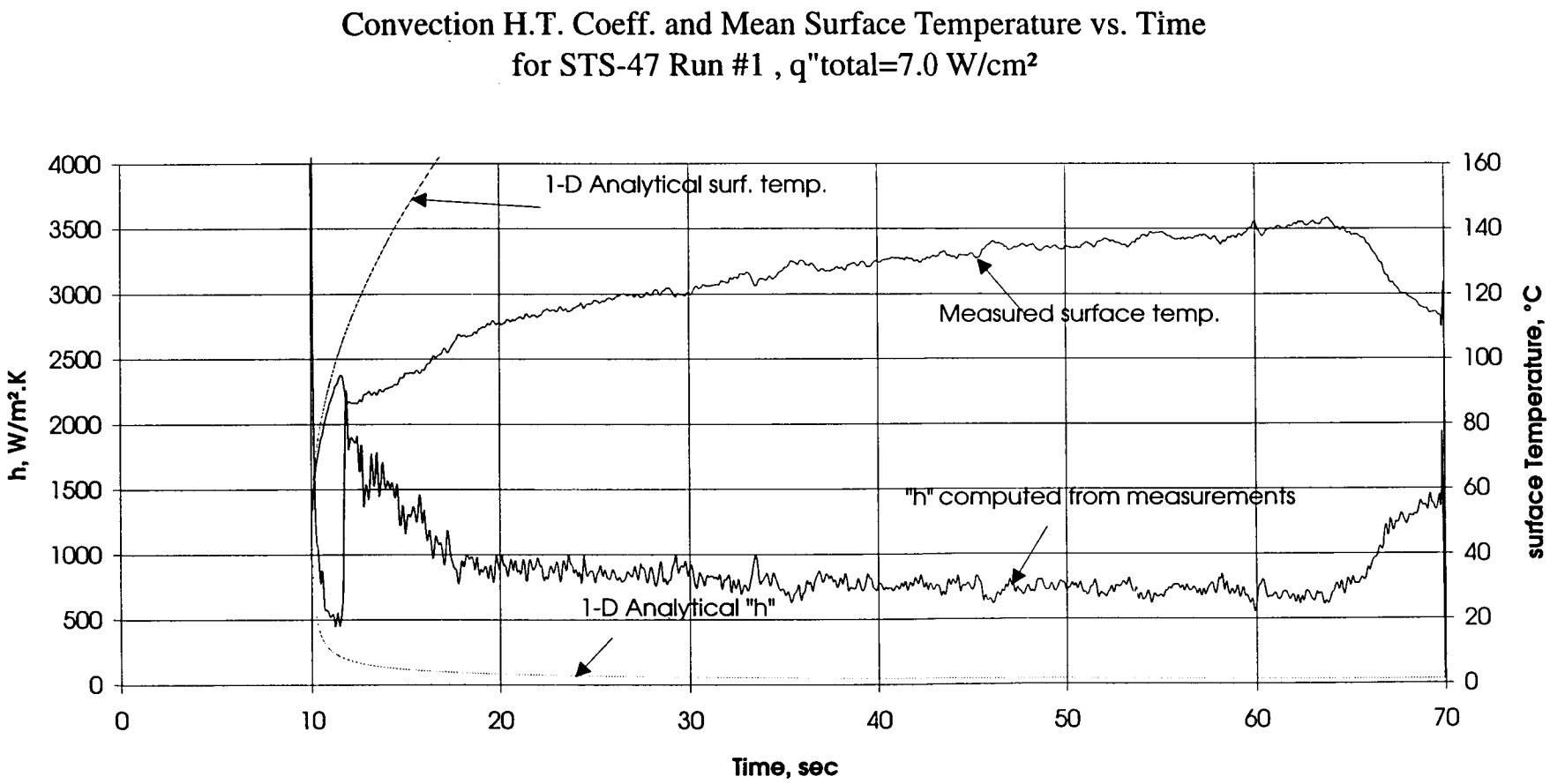

Figure A-1a. Mean heater surface temperature and derived heat transfer coefficient. PBE-IA (STS-47). Run No. 1.

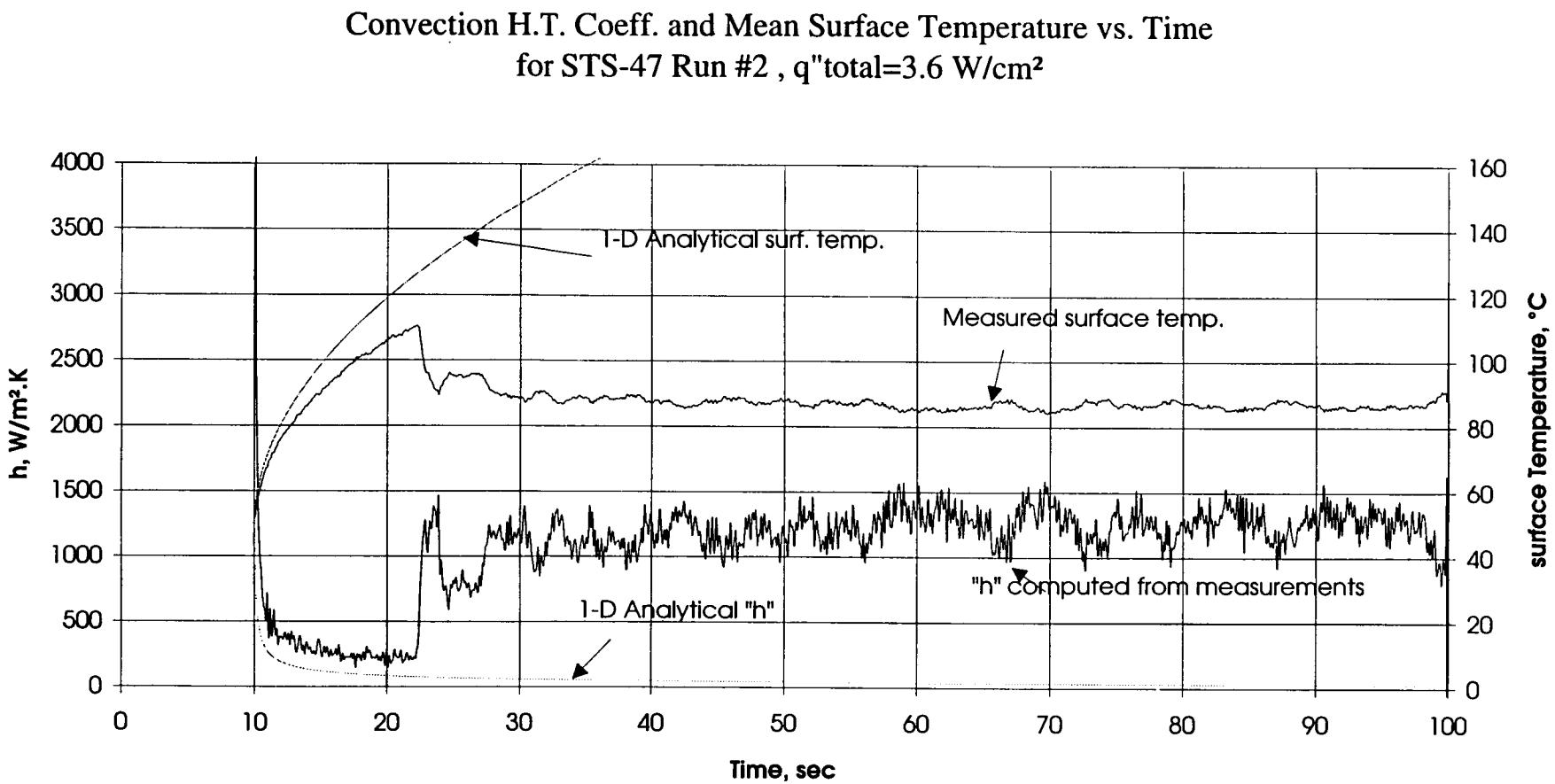

Figure A-1b. Mean heater surface temperature and derived heat transfer coefficient. PBE-IA (STS-47). Run No. 2.

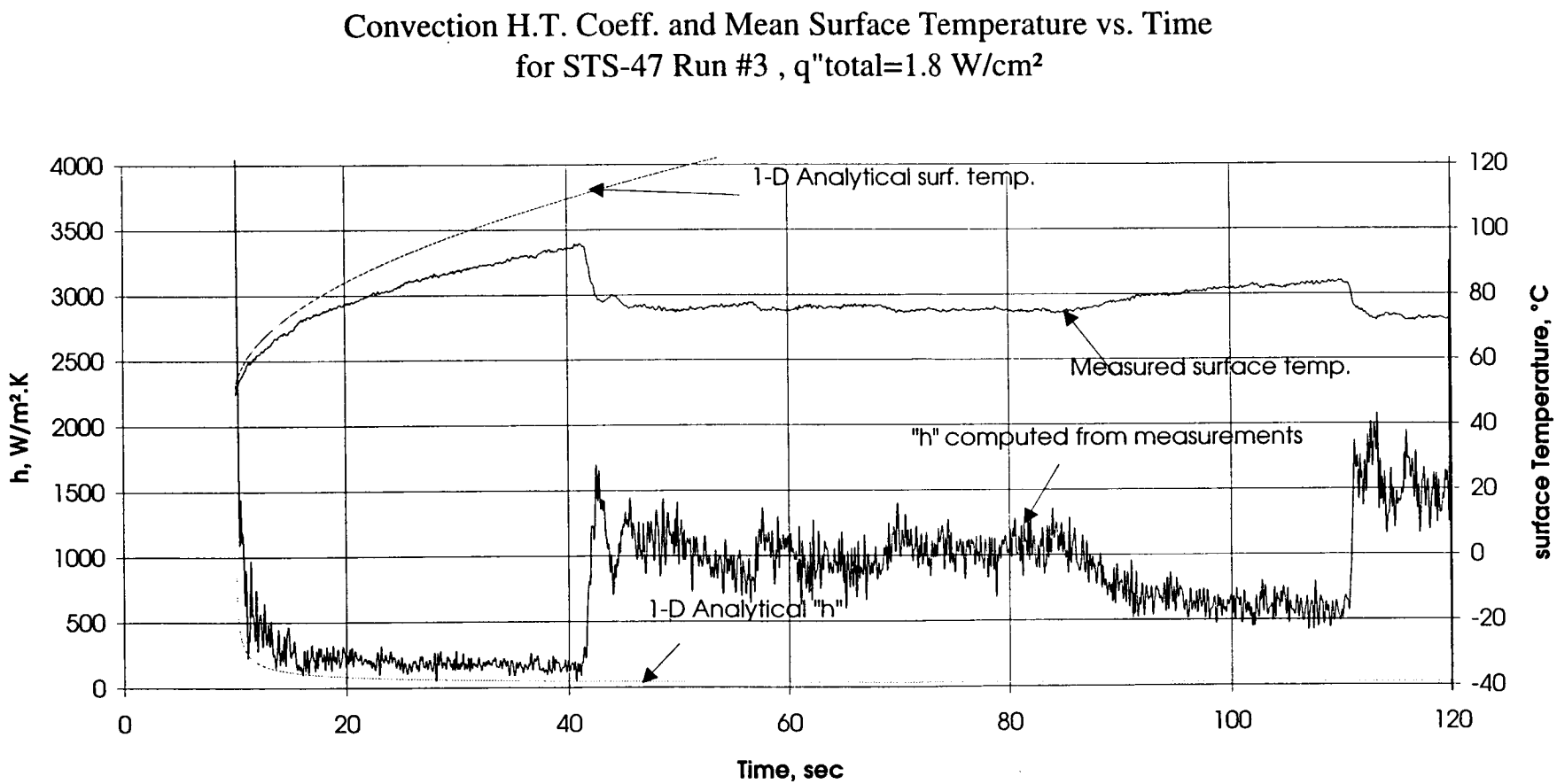

Figure A-1c. Mean heater surface temperature and derived heat transfer coefficient. PBE-IA (STS-47). Run No. 3.

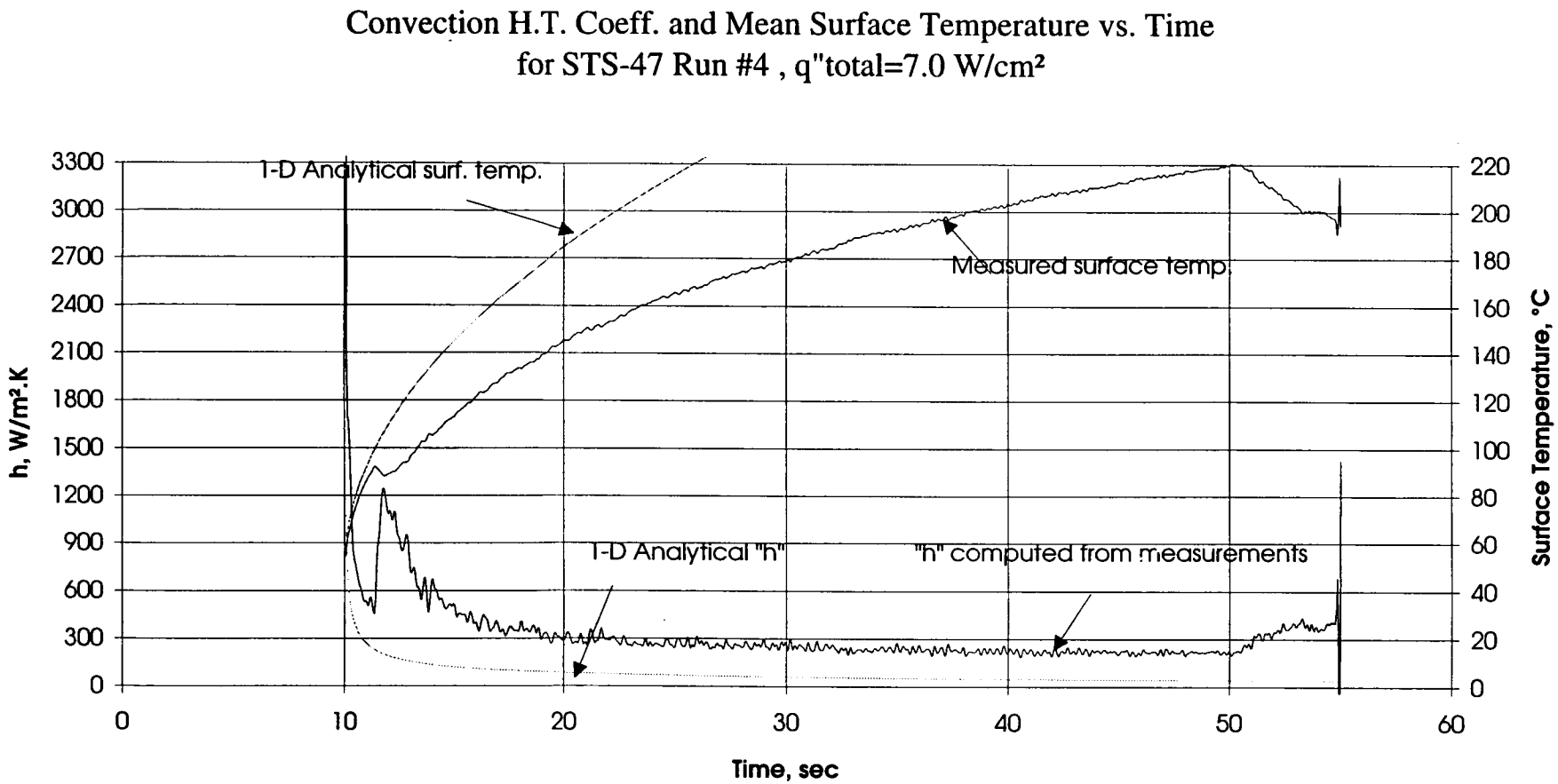

Figure A-1d. Mean heater surface temperature and derived heat transfer coefficient. PBE-IA (STS-47). Run No. 4.

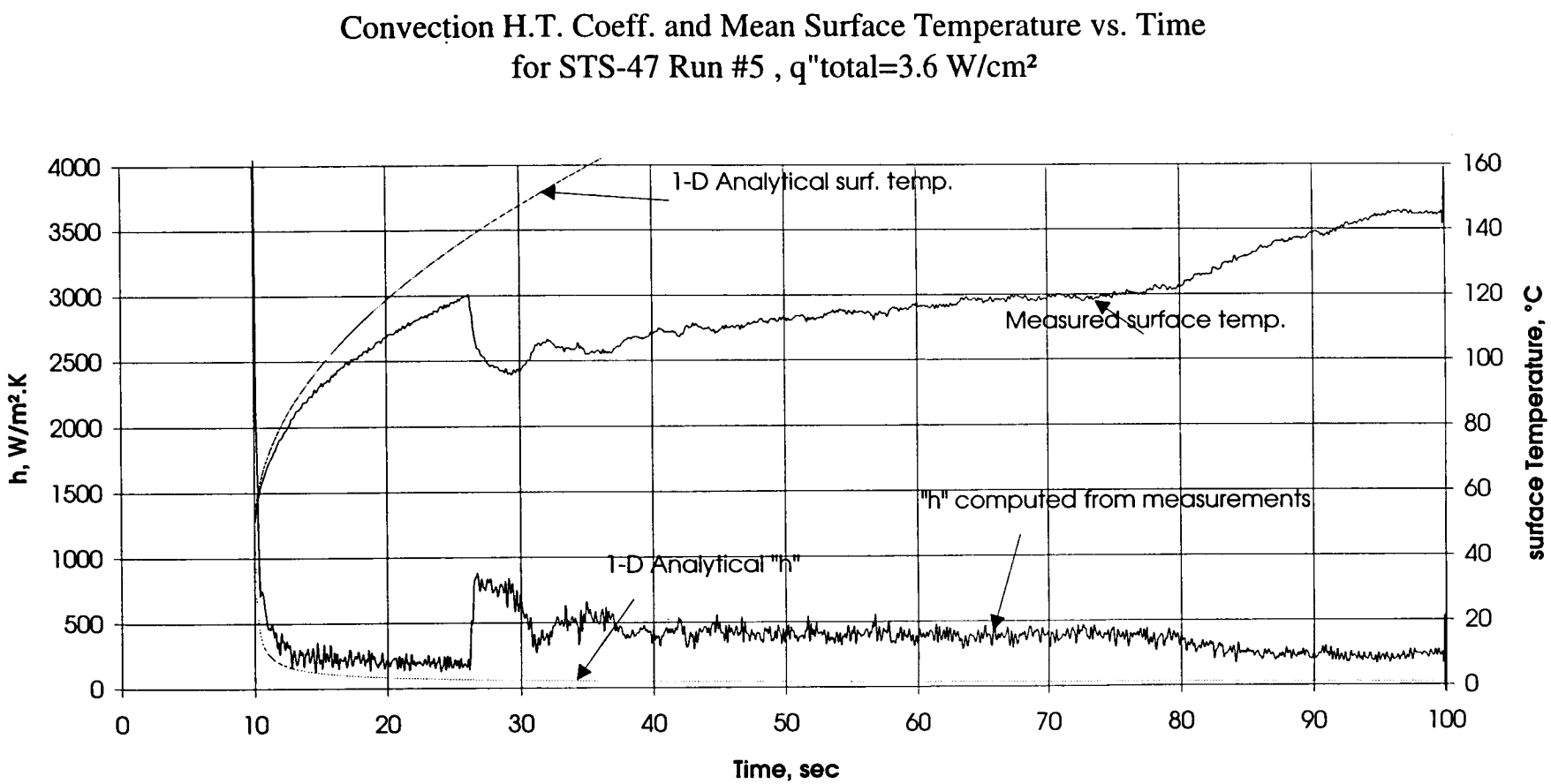

Figure A-1e. Mean heater surface temperature and derived heat transfer coefficient. PBE-IA (STS-47). Run No. 5.

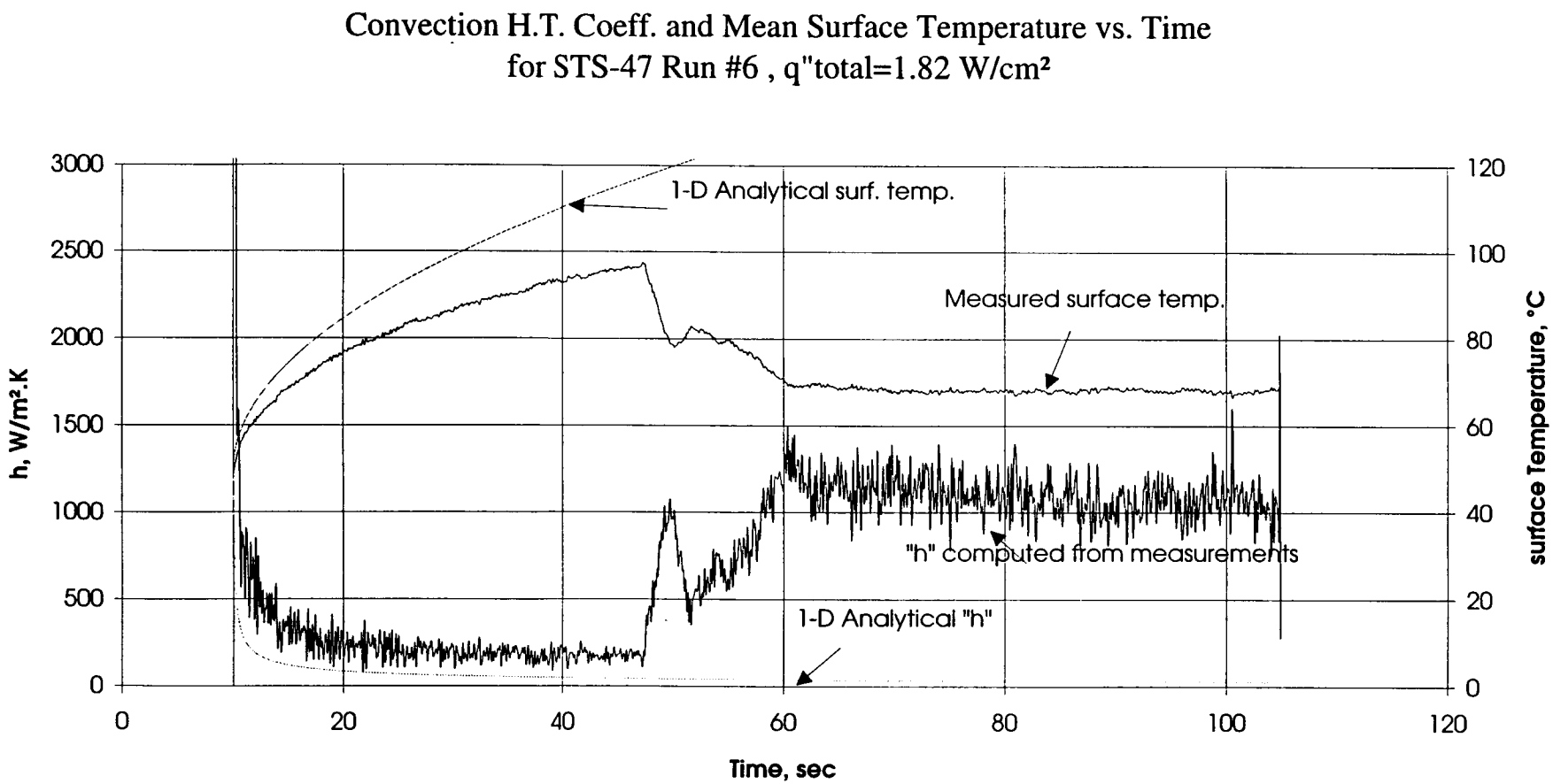

Figure A-1f. Mean heater surface temperature and derived heat transfer coefficient. PBE-IA (STS-47). Run No. 6.

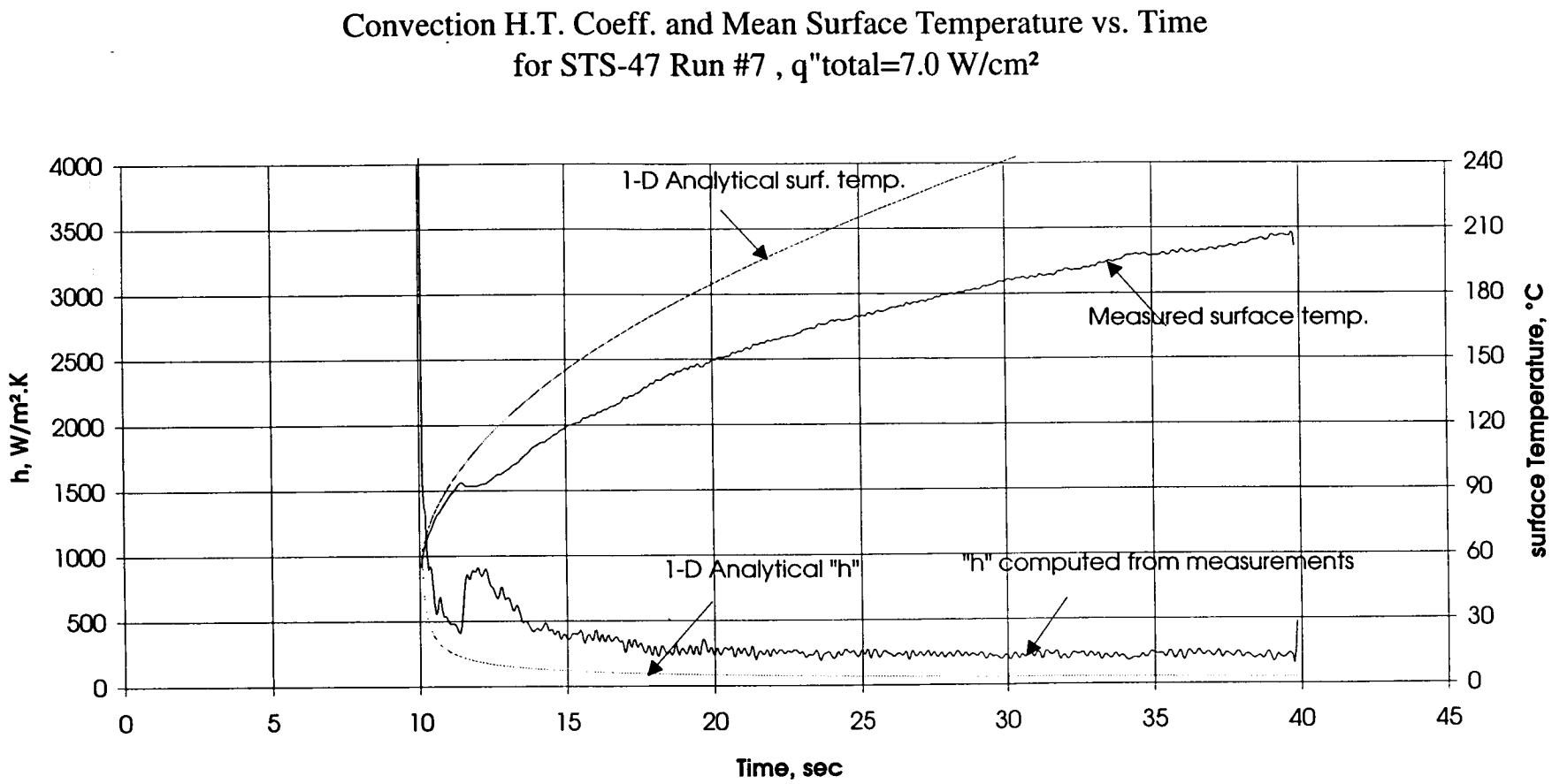

Figure A-1g. Mean heater surface temperature and derived heat transfer coefficient. PBE-IA (STS-47). Run No. 7.

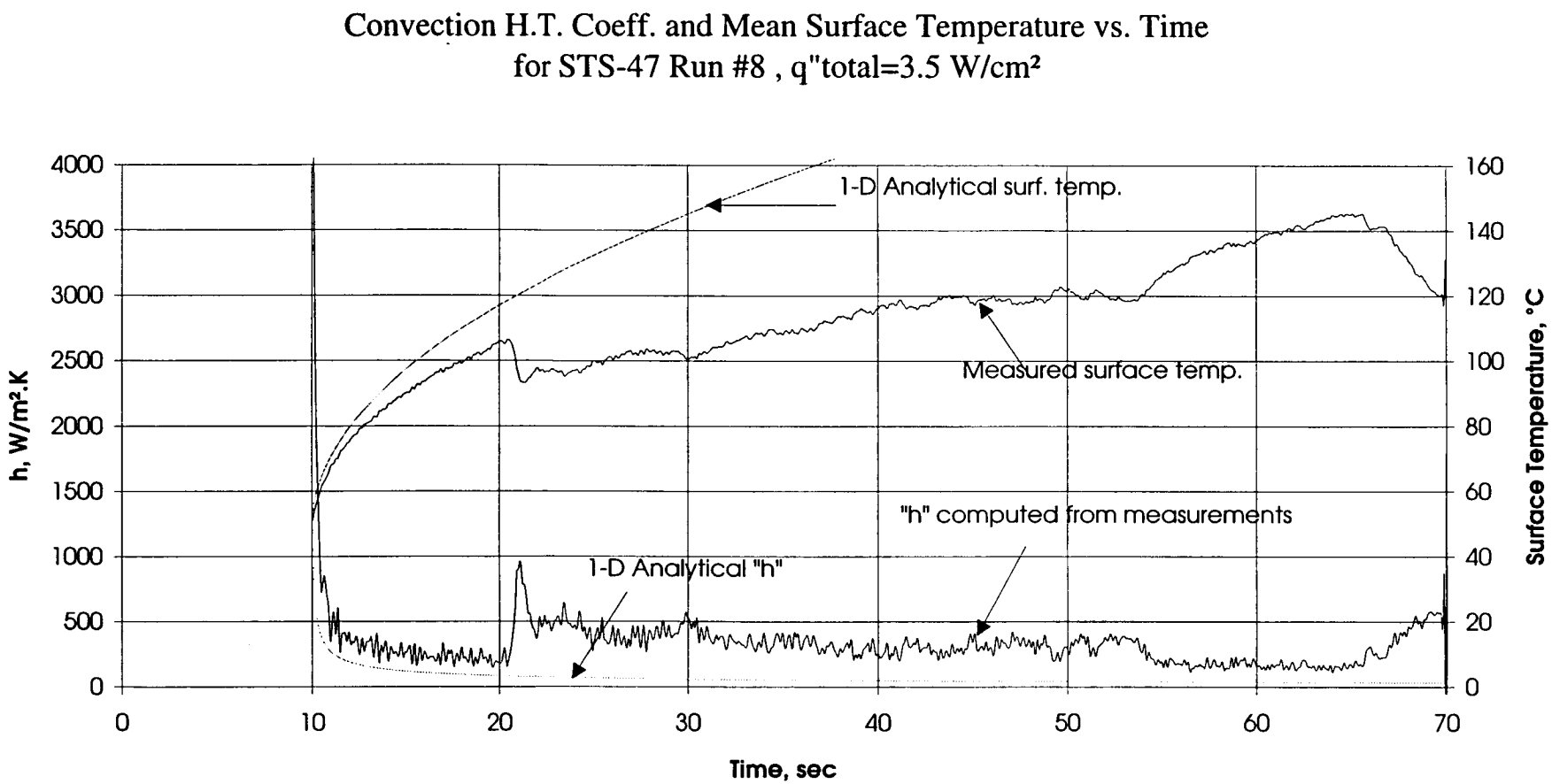

Figure A-1h. Mean heater surface temperature and derived heat transfer coefficient. PBE-IA (STS-47). Run No. 8.

Convection H.T. Coeff. and Mean Surface Temperature vs. Time
for STS-47 Run #9 , q"total=1.8 W/cm²

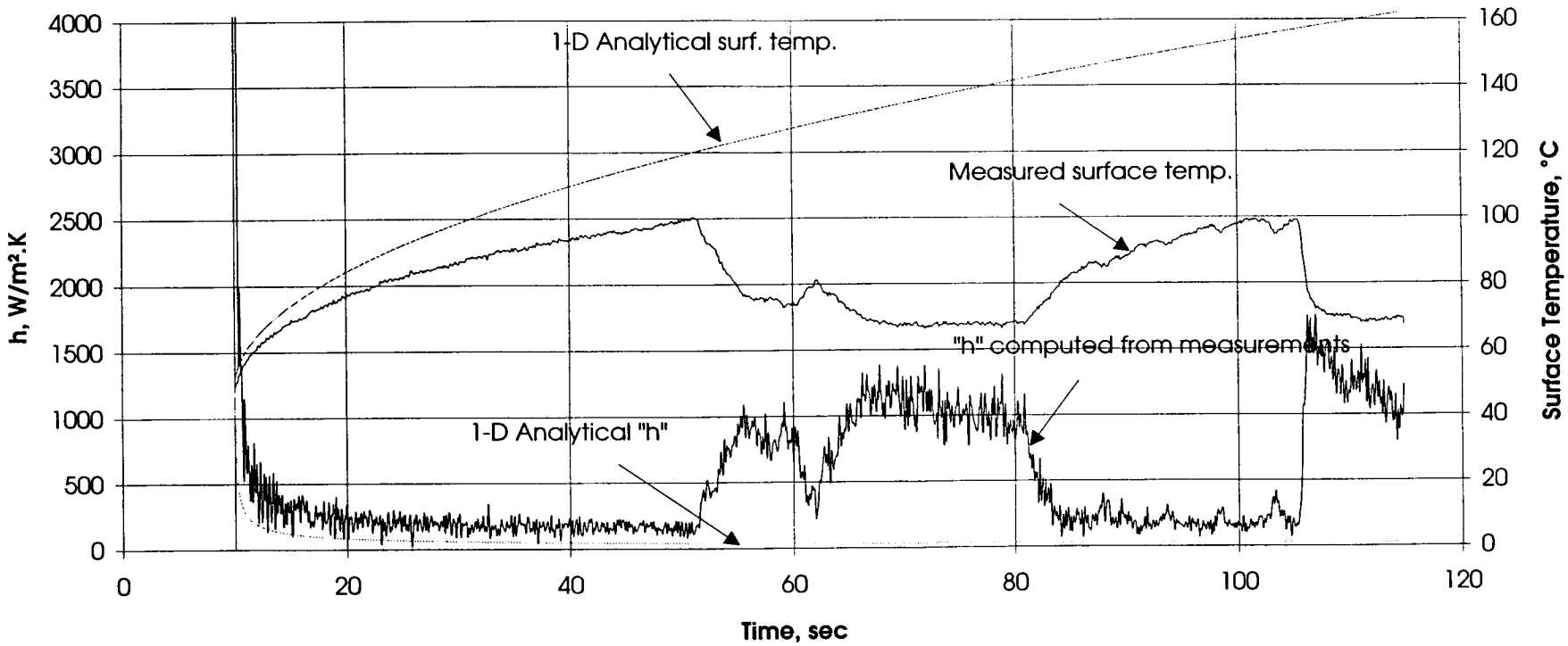

Figure A-1i. Mean heater surface temperature and derived heat transfer coefficient. PBE-IA (STS-47). Run No. 9.

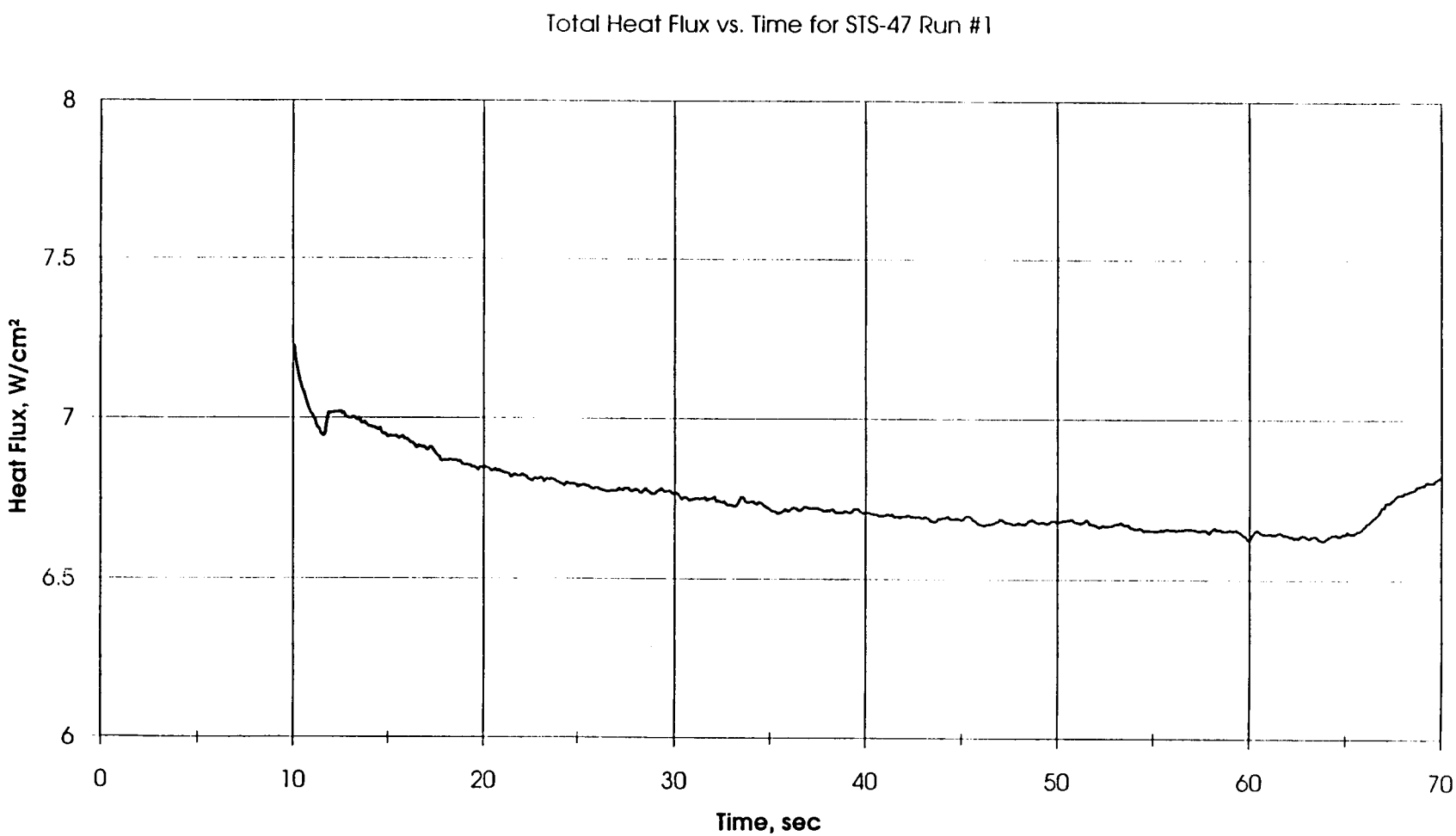

Figure A-2a. Heat flux input. PBE-IA (STS-47). Run No. 1.

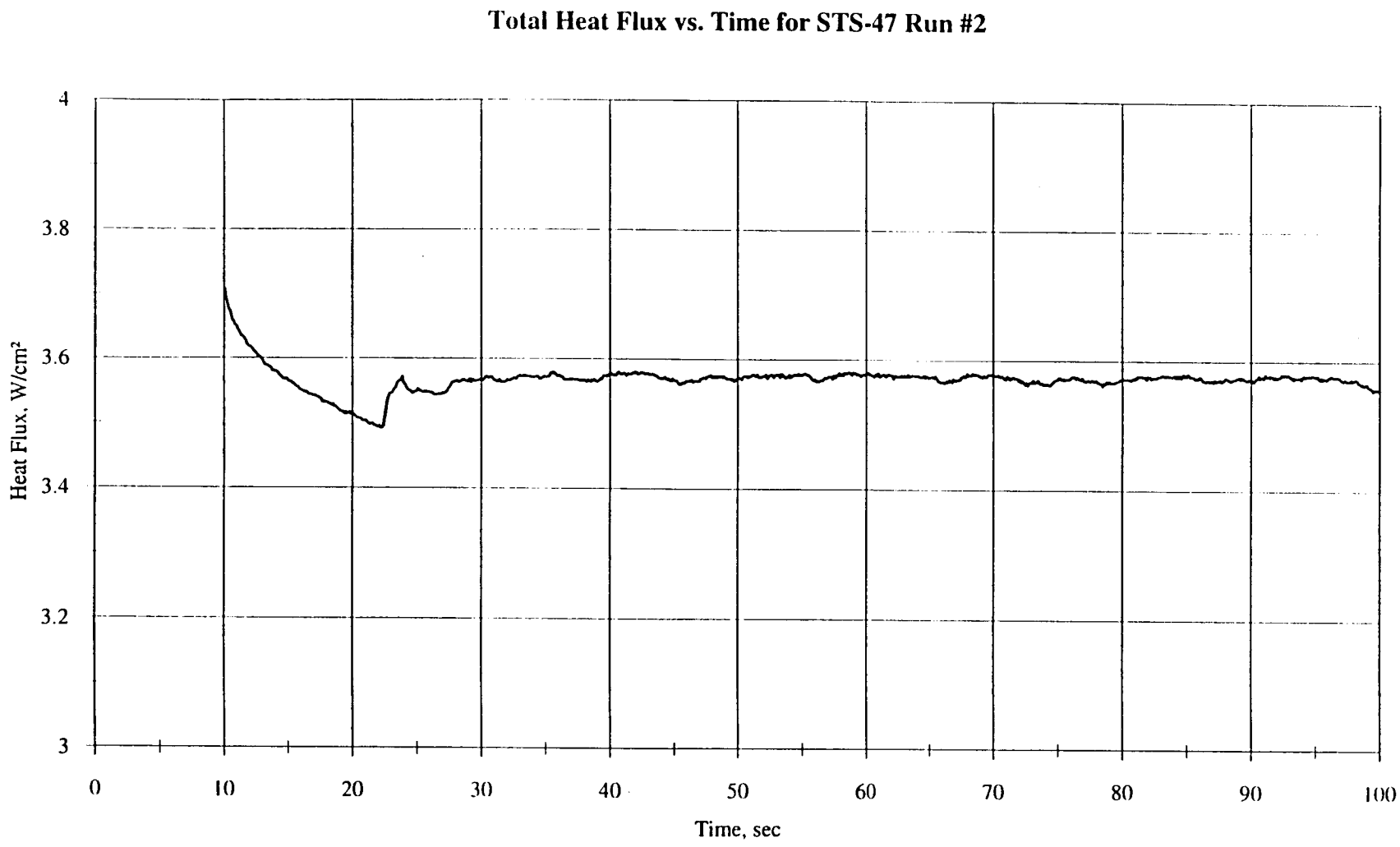

Figure A-2b. Heat flux input. PBE-IA (STS-47). Run No. 2.

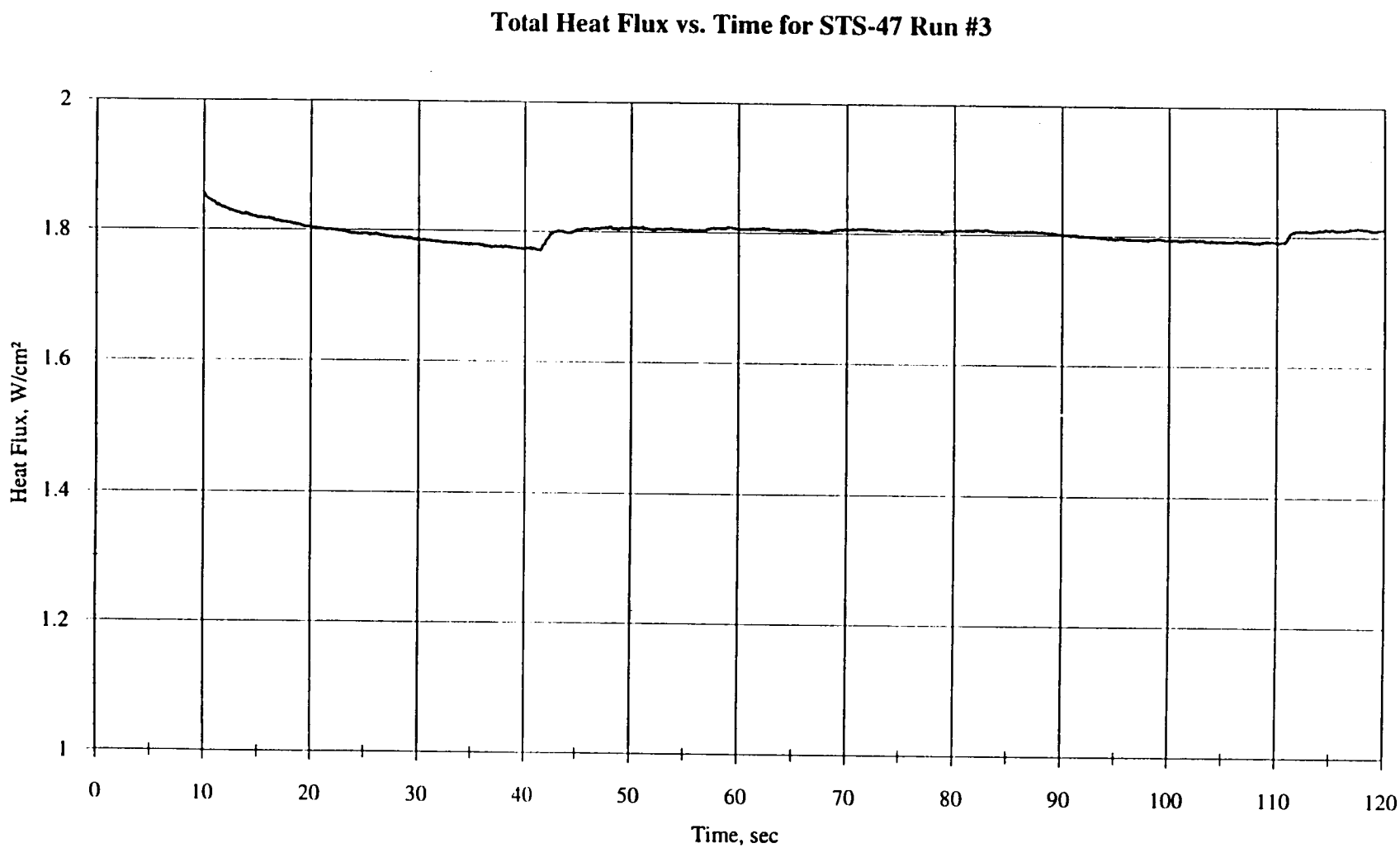

Figure A-2c. Heat flux input. PBE-IA (STS-47). Run No. 3.

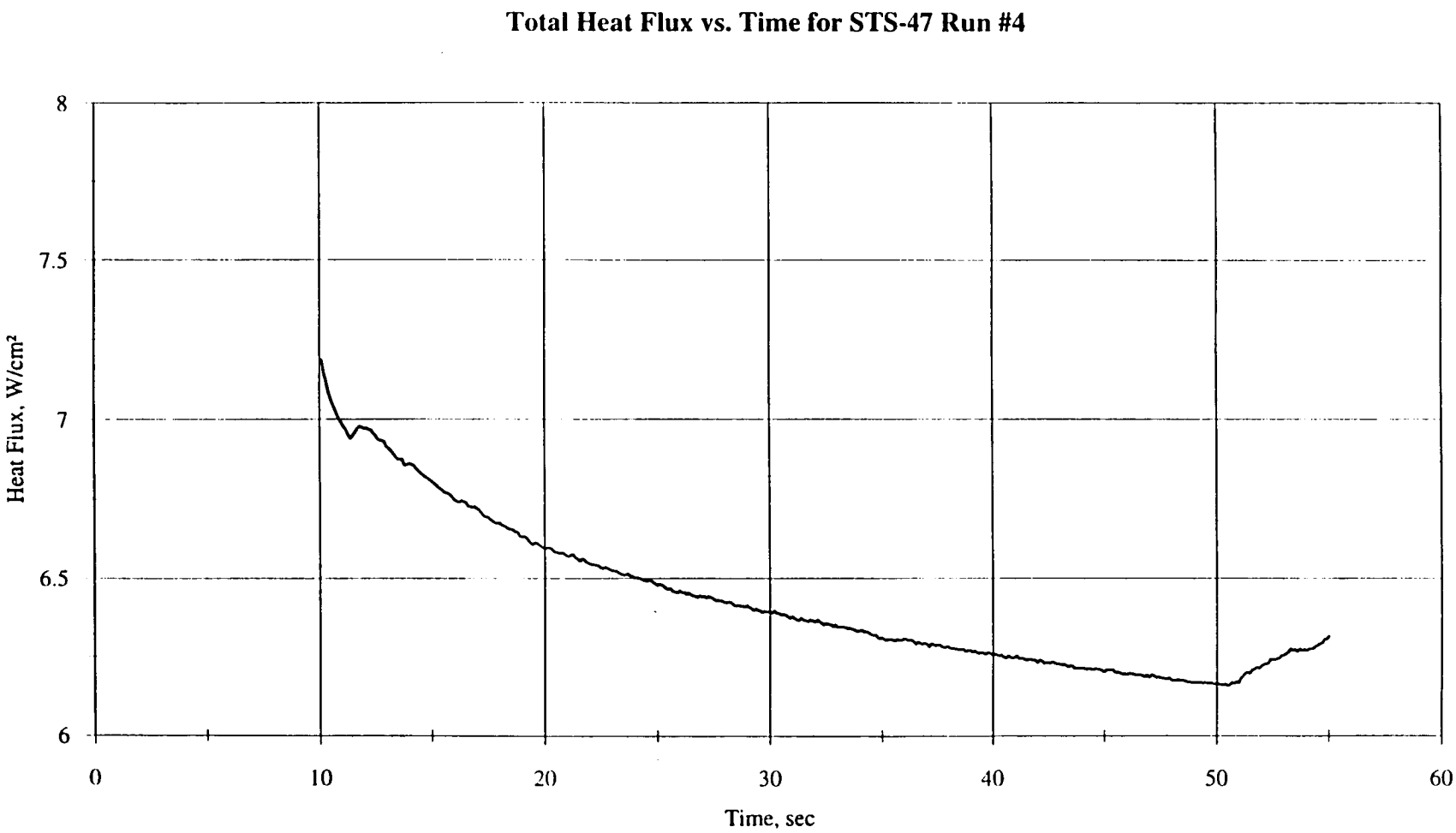

Figure A-2d. Heat flux input. PBE-IA (STS-47). Run No. 4.

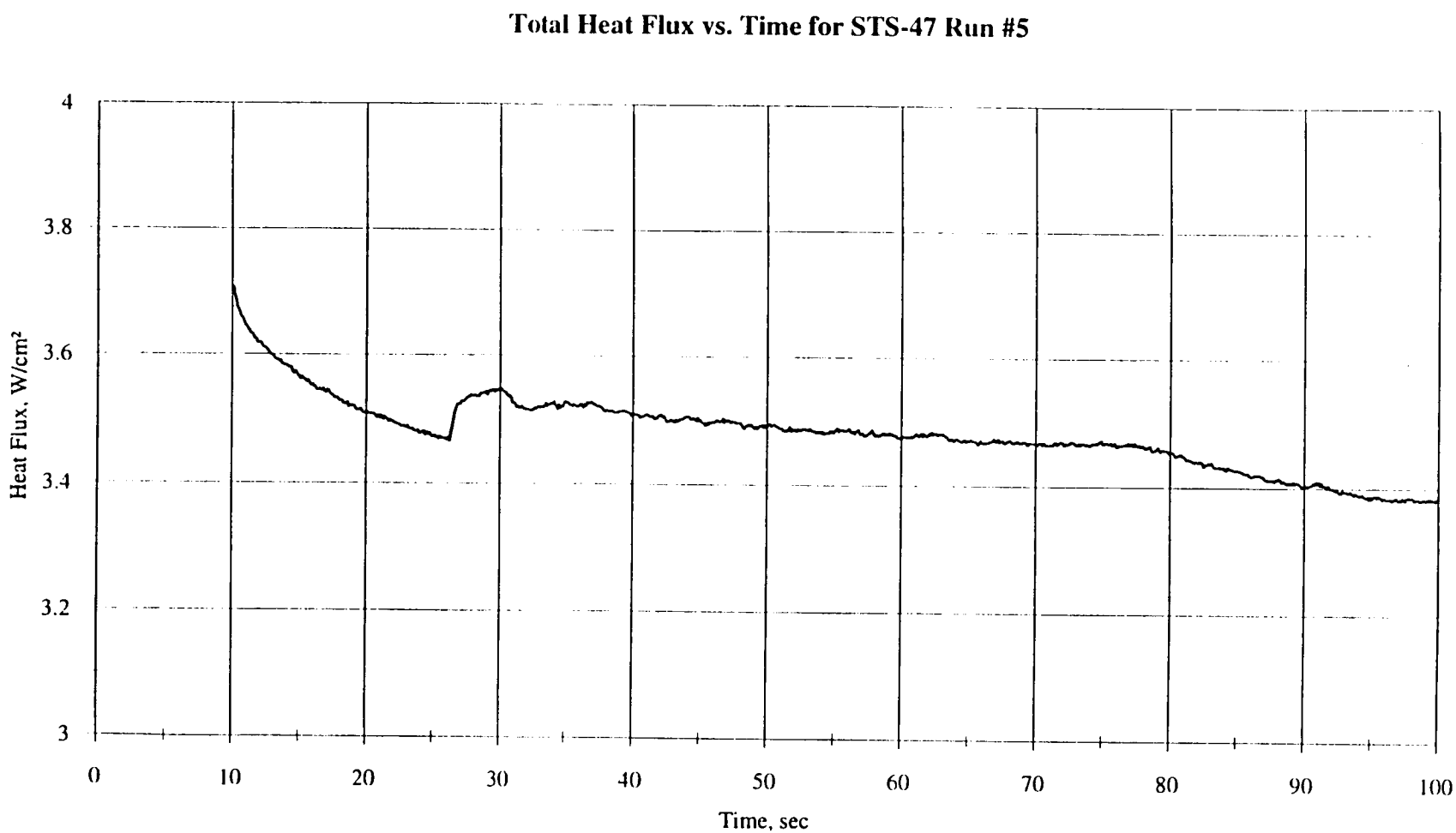

Figure A-2e. Heat flux input. PBE-IA (STS-47). Run No. 5.

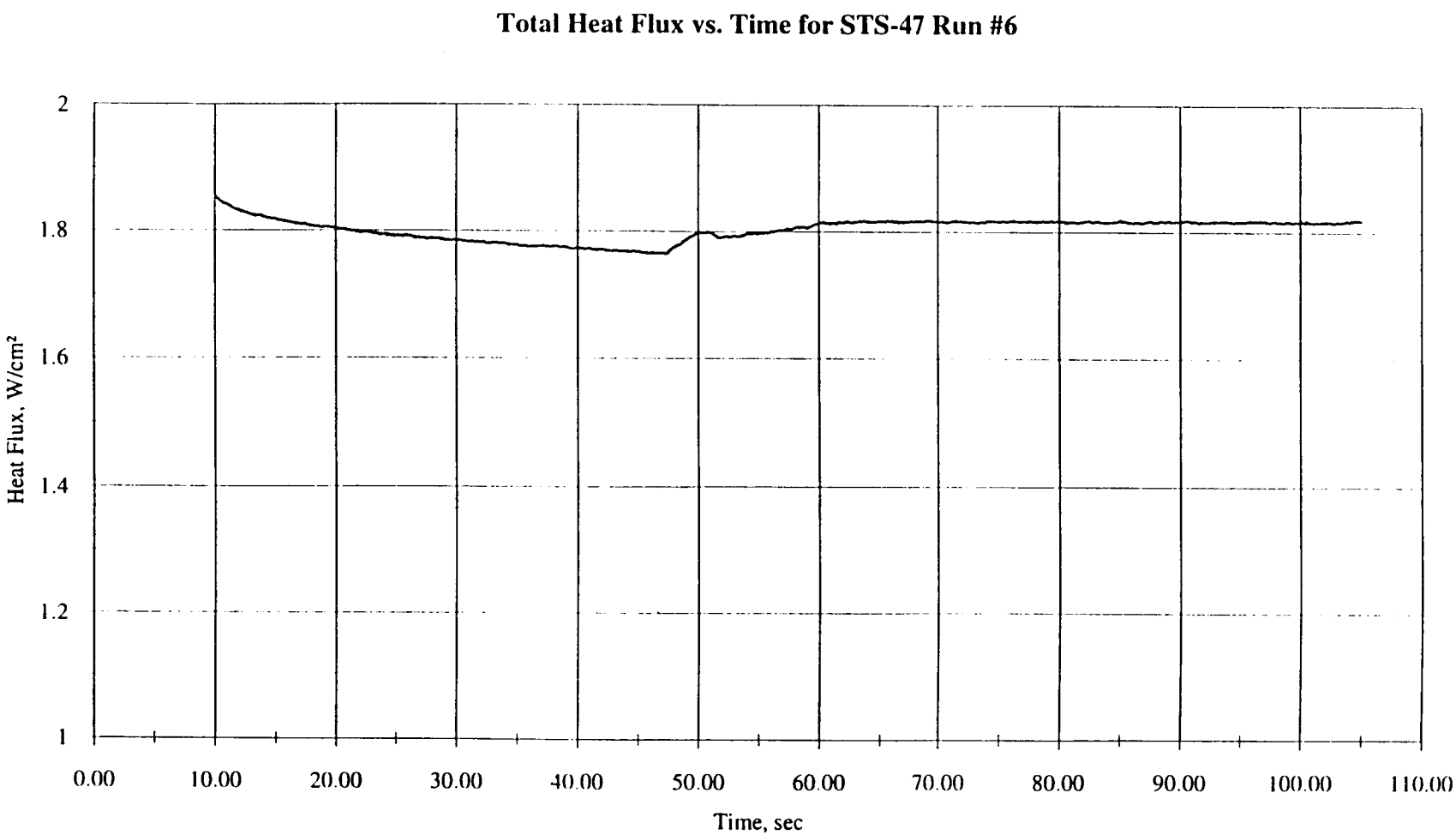

Figure A-2f. Heat flux input. PBE-IA (STS-47). Run No. 6.

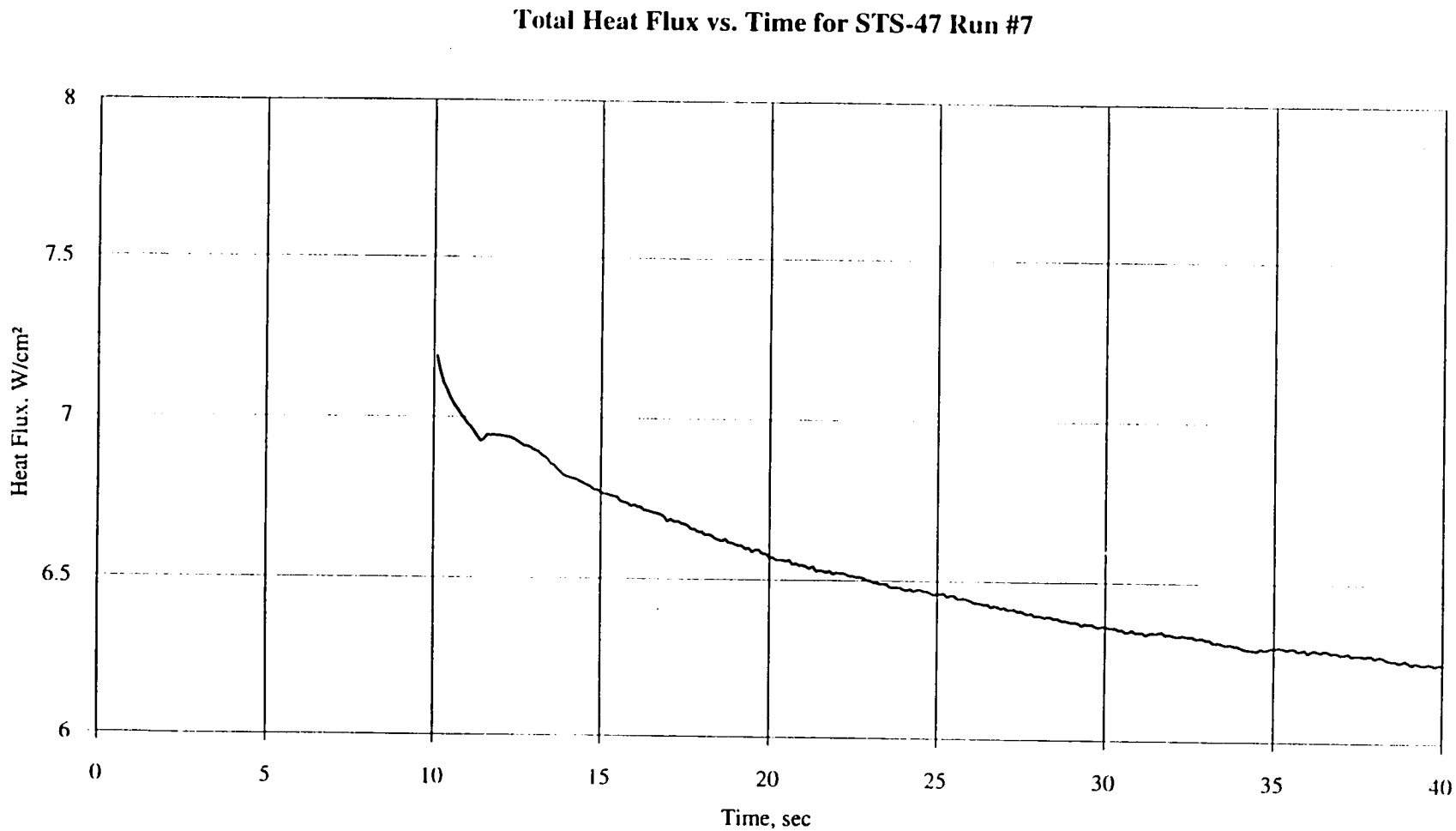

Figure A-2g. Heat flux input. PBE-IA (STS-47). Run No. 7.

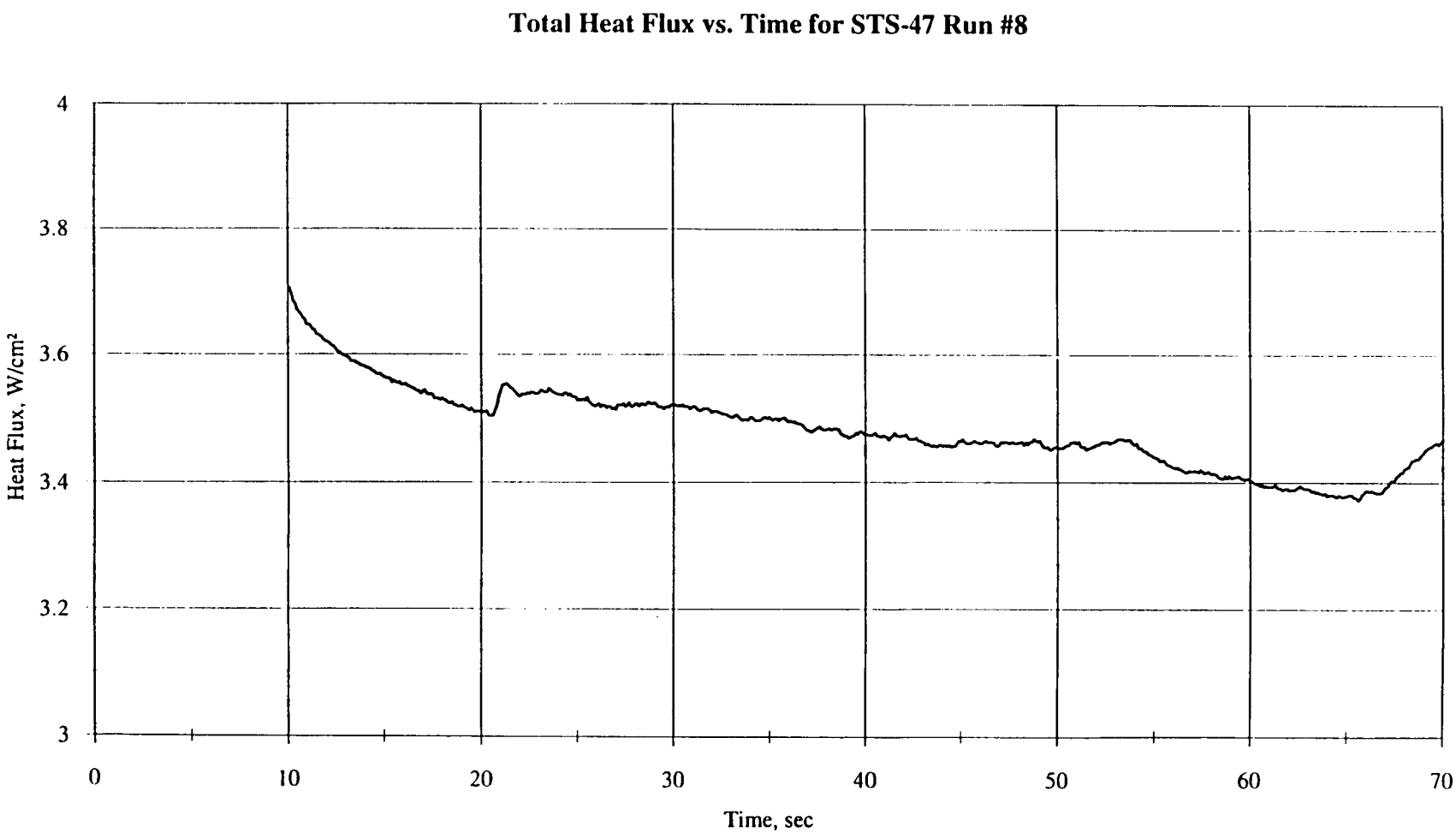

Figure A-2h. Heat flux input. PBE-IA (STS-47). Run No. 8.

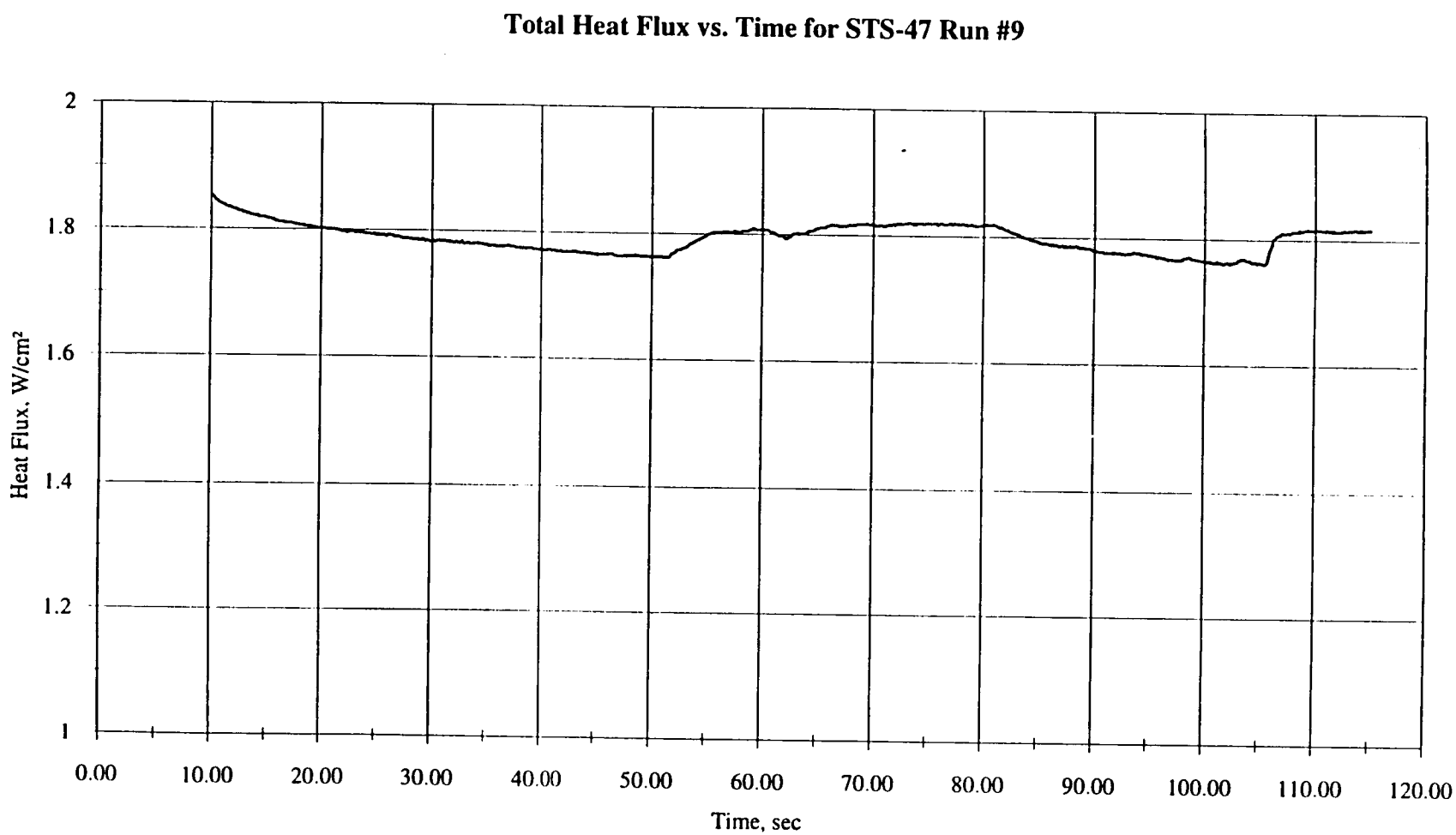

Figure A-2i. Heat flux input. PBE-IA (STS-47). Run No. 9.

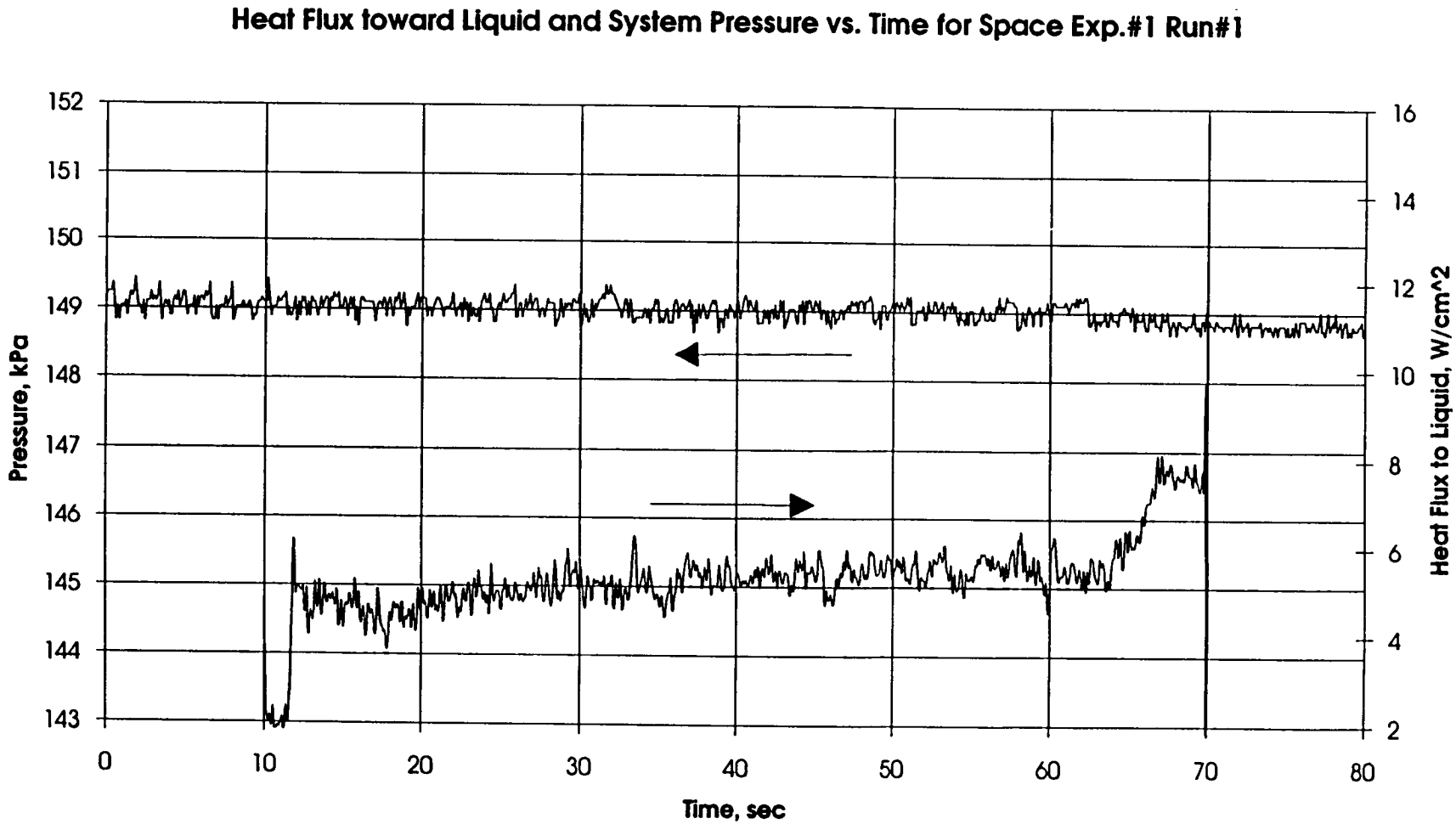

Figure A-3a. System pressure and fluid side mean heat flux. PBE-IA (STS-47). Run No. 1.

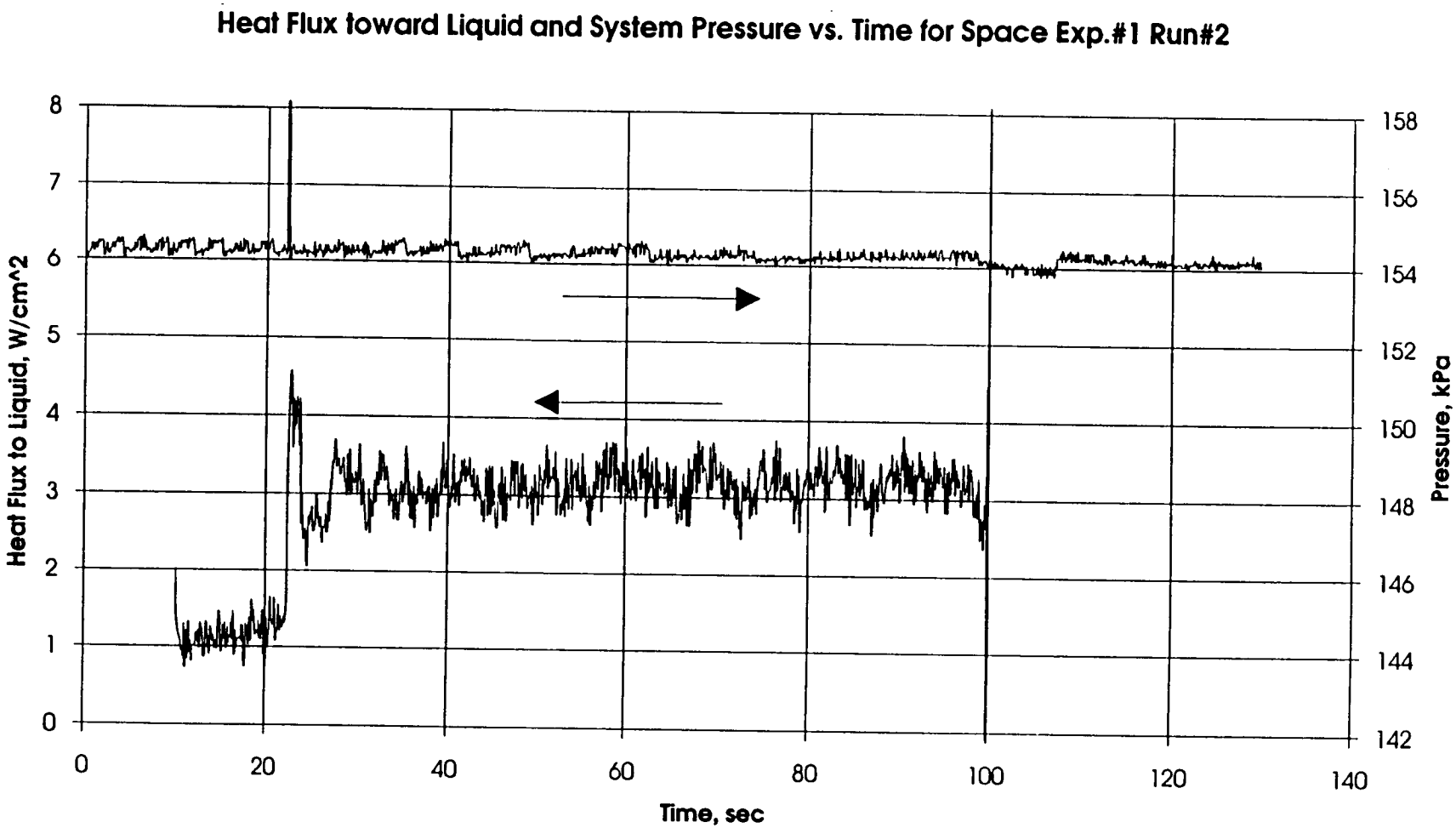

Figure A-3b. System pressure and fluid side mean heat flux. PBE-IA (STS-47). Run No. 2.

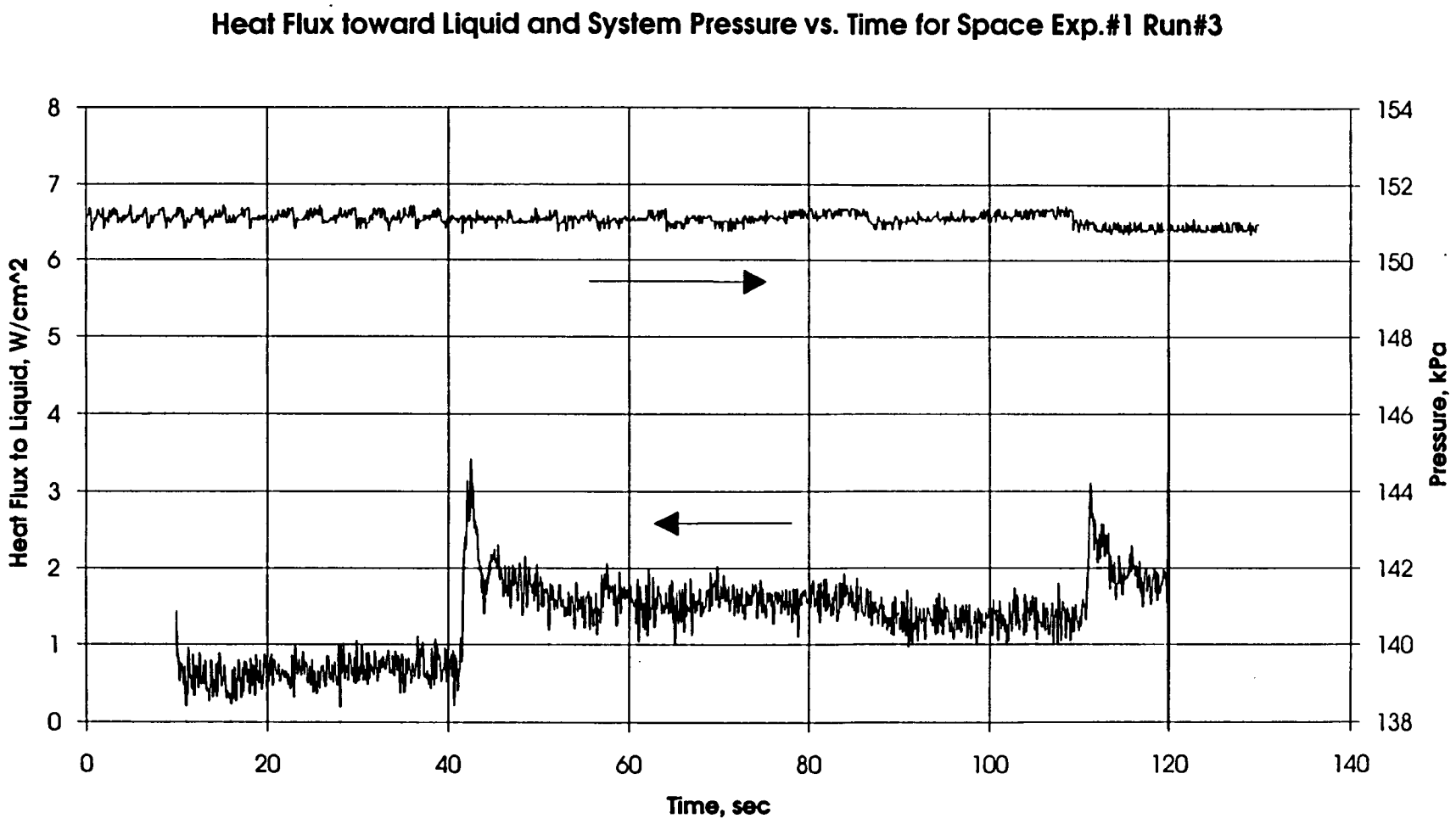

Figure A-3c. System pressure and fluid side mean heat flux. PBE-IA (STS-47). Run No. 3.

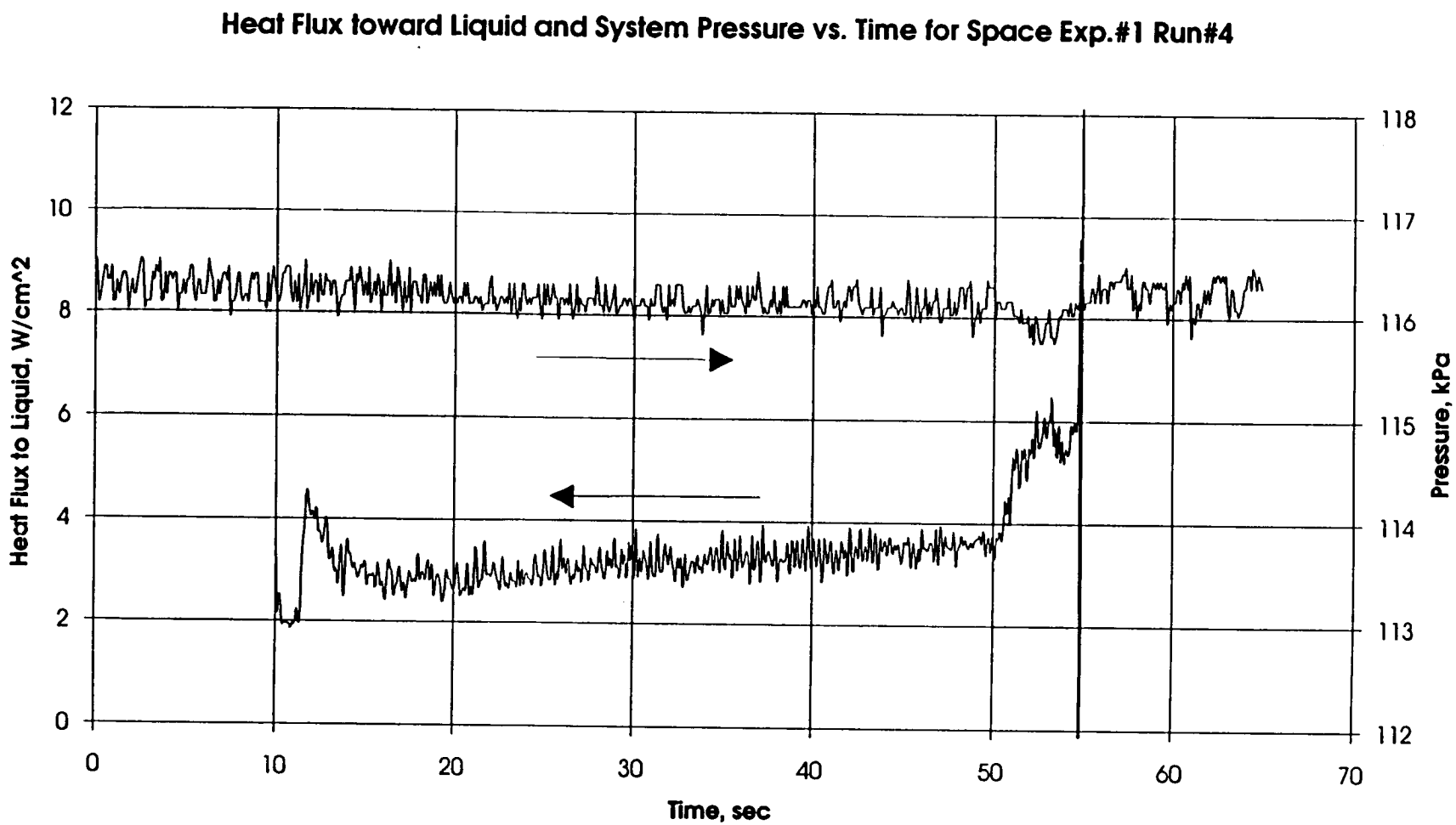

Figure A-3d. System pressure and fluid side mean heat flux. PBE-IA (STS-47). Run No. 4.

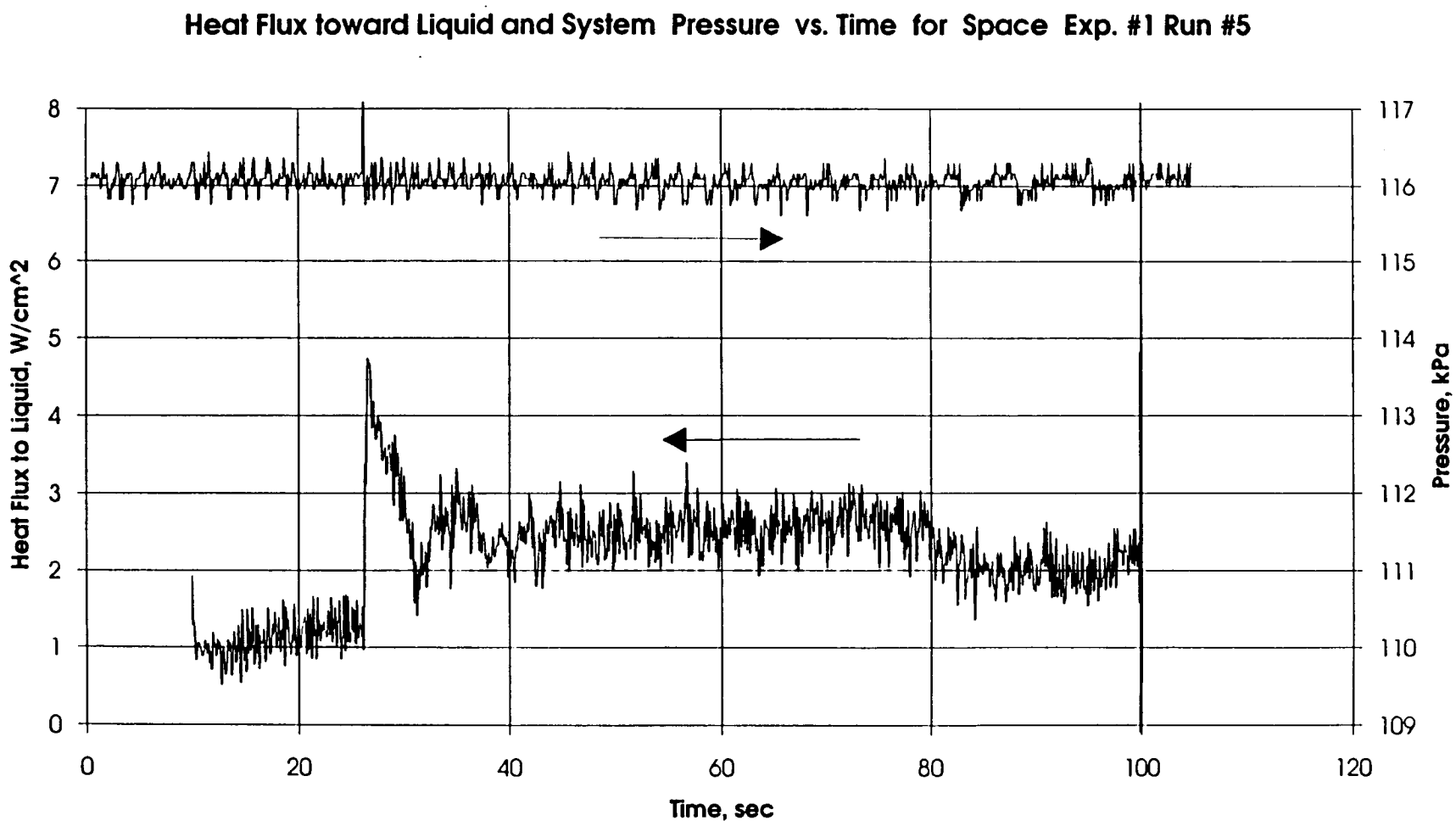

Figure A-3e. System pressure and fluid side mean heat flux. PBE-IA (STS-47). Run No. 5.

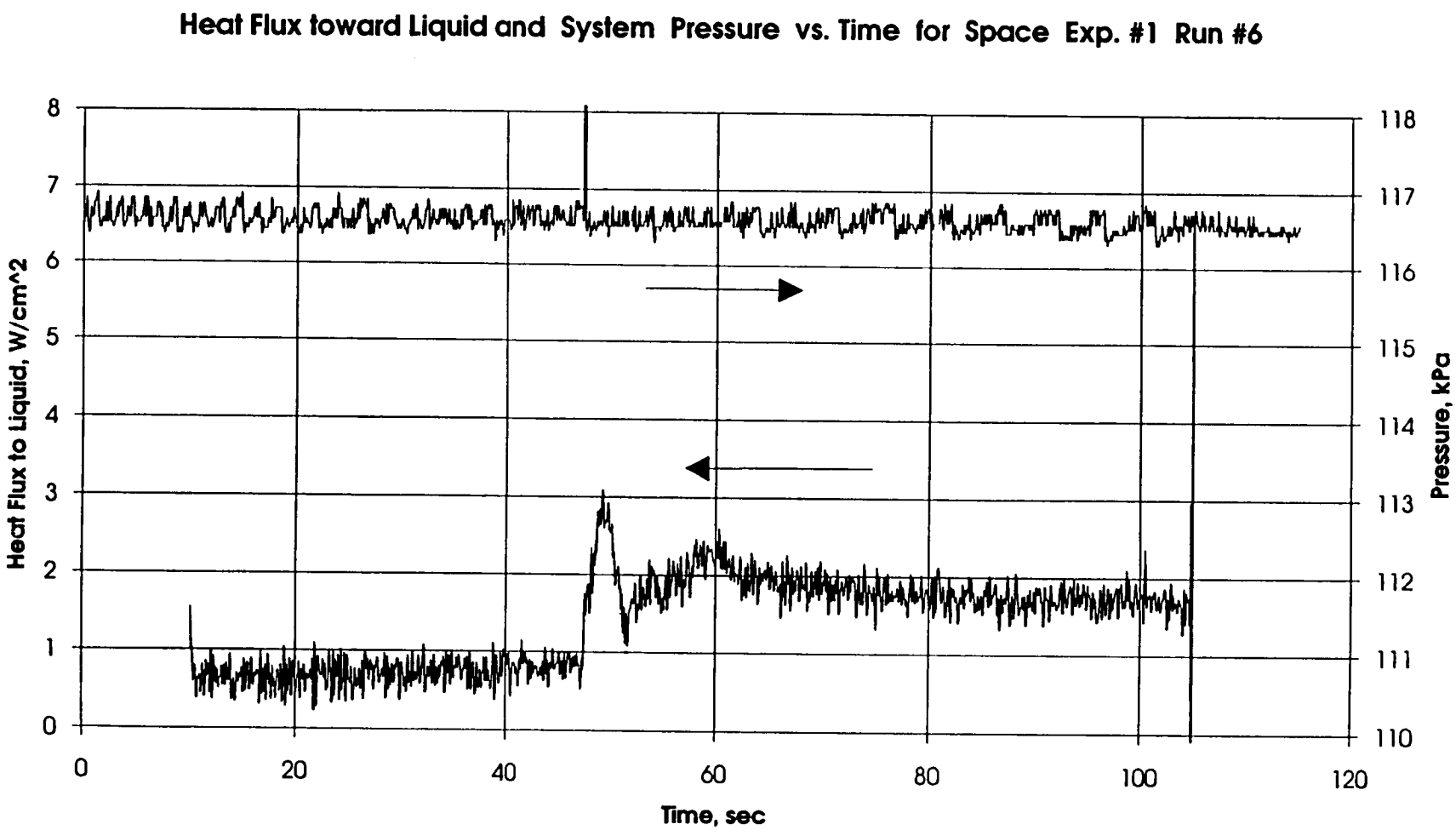

Figure A-3f. System pressure and fluid side mean heat flux. PBE-IA (STS-47). Run No. 6.

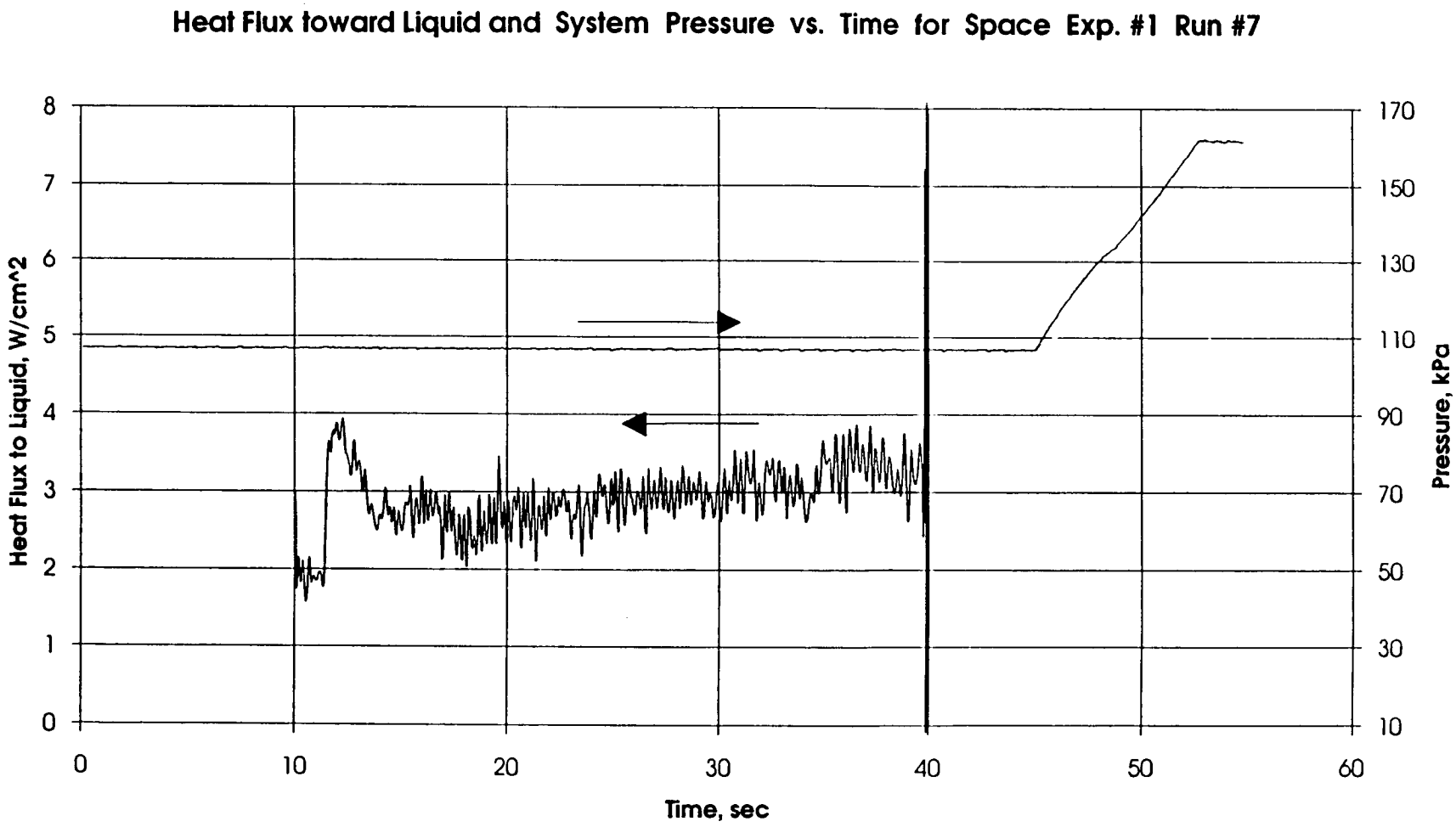

Figure A-3g. System pressure and fluid side mean heat flux. PBE-IA (STS-47). Run No. 7.

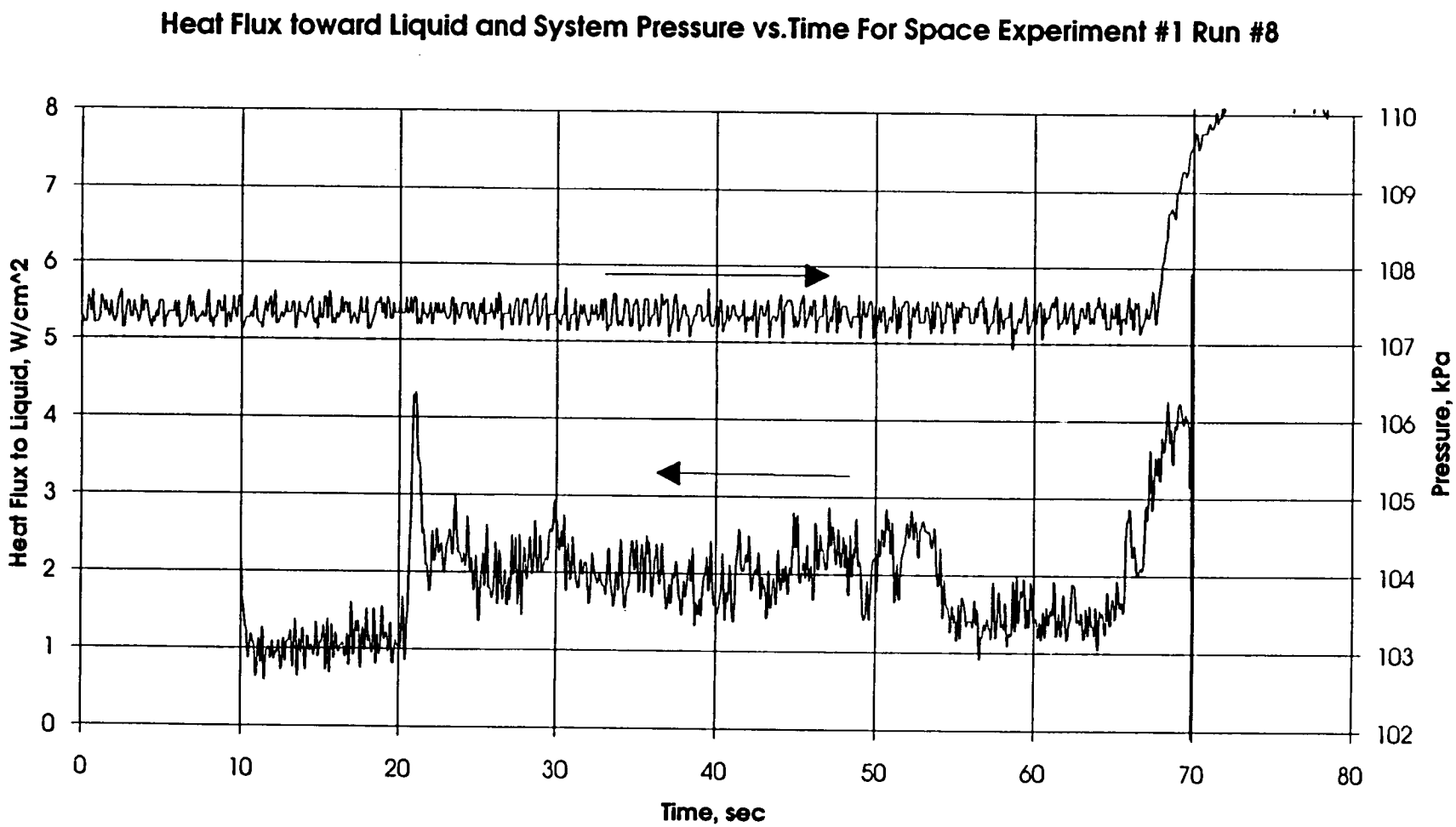

Figure A-3h. System pressure and fluid side mean heat flux. PBE-IA (STS-47). Run No. 8.

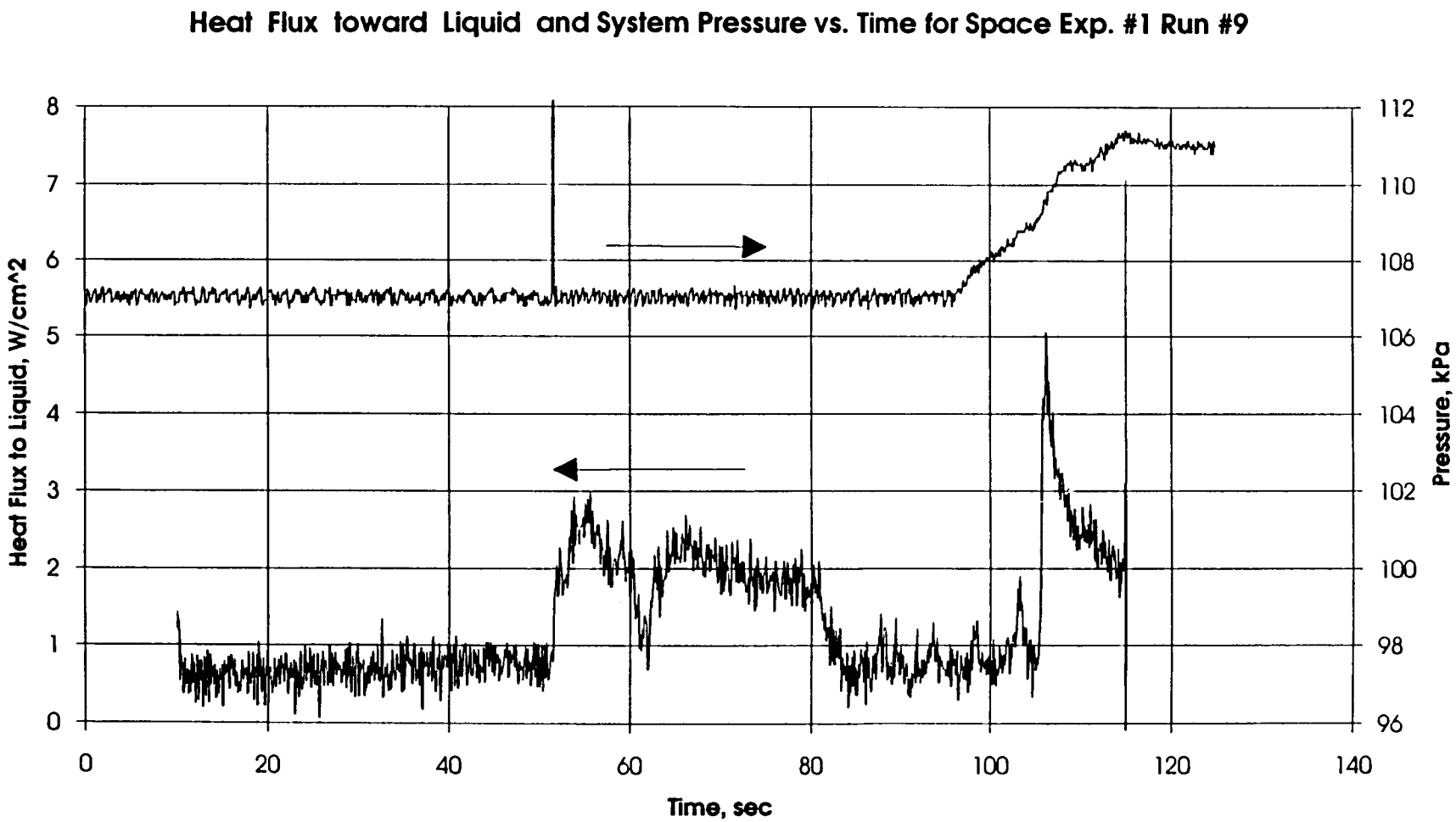

Figure A-3i. System pressure and fluid side mean heat flux. PBE-IA (STS-47). Run No. 9.

A. Mean Heater Surface Temperature

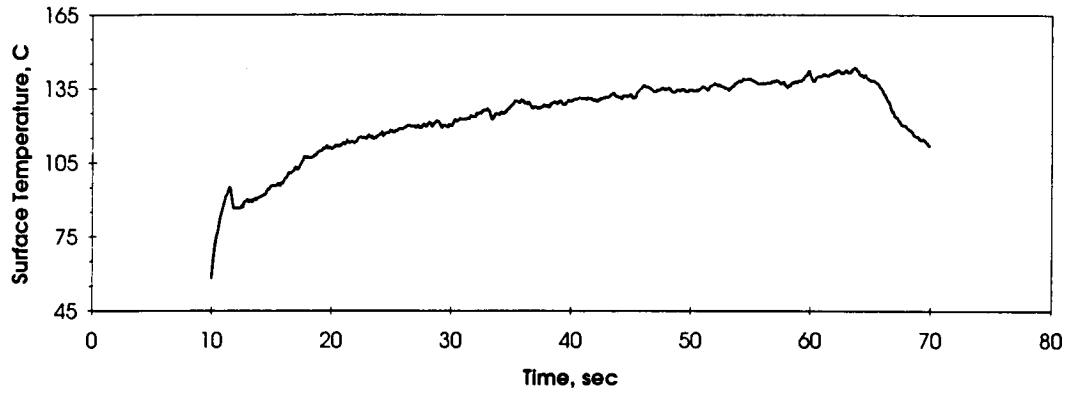

B. Local Fluid Temperatures

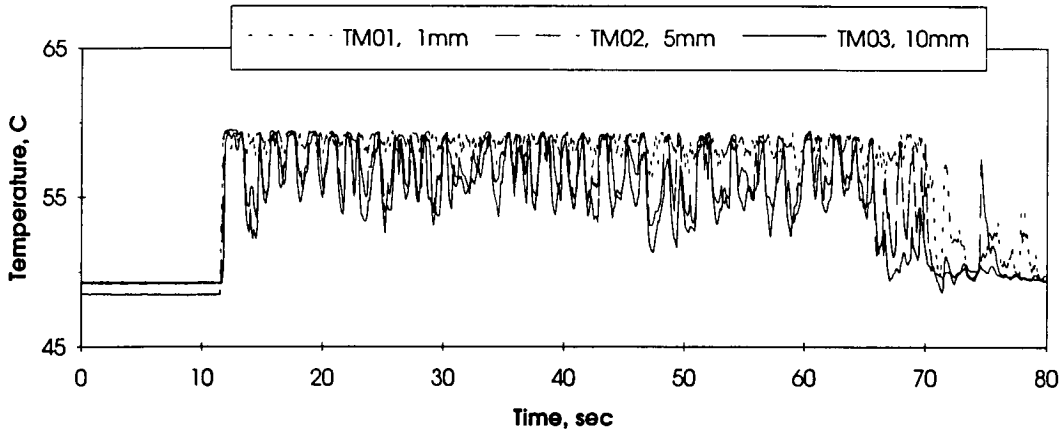

C. Far Field Bulk Temperatures

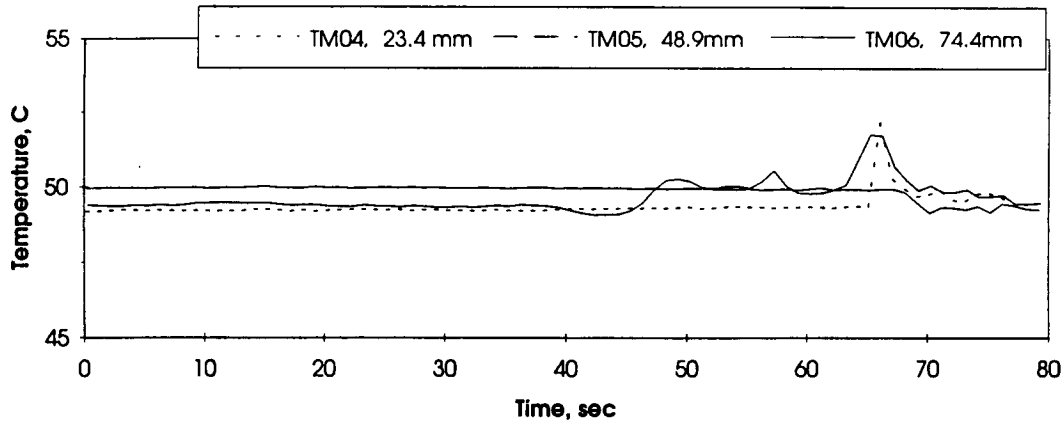

FIGURE : MEASURED FLUID TEMPERATURES **STS 47 - RUN#1**

HEAT FLUX	SUBCOOLING (F)	HEATER POWER ON/OFF	100 FPS ON/OFF	STIRRER START	REPRESS START	TOTAL TEST TIME
8	20 ± 2	10-70 sec.	10-15 sec.	65 sec.	----------	80 sec.

Figure A-4a. Measured fluid temperatures near primary heater and far field bulk liquid. PBE-IA (STS-47). Run No. 1.

A. Mean Heater Surface Temperature

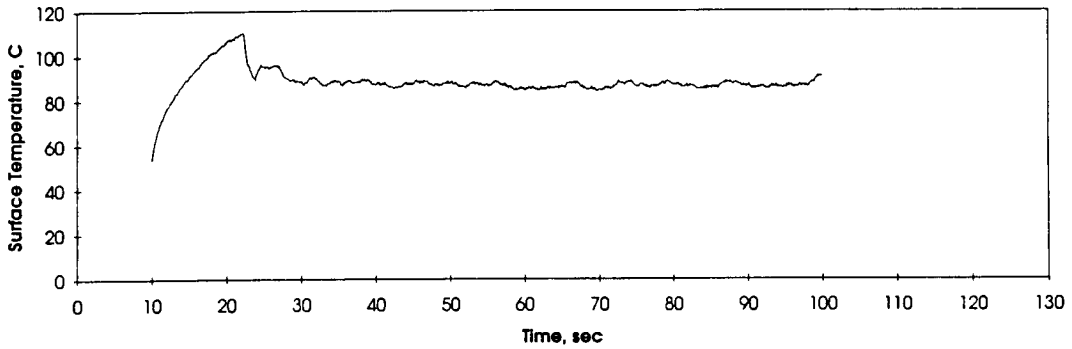

B. Local Fluid Temperatures

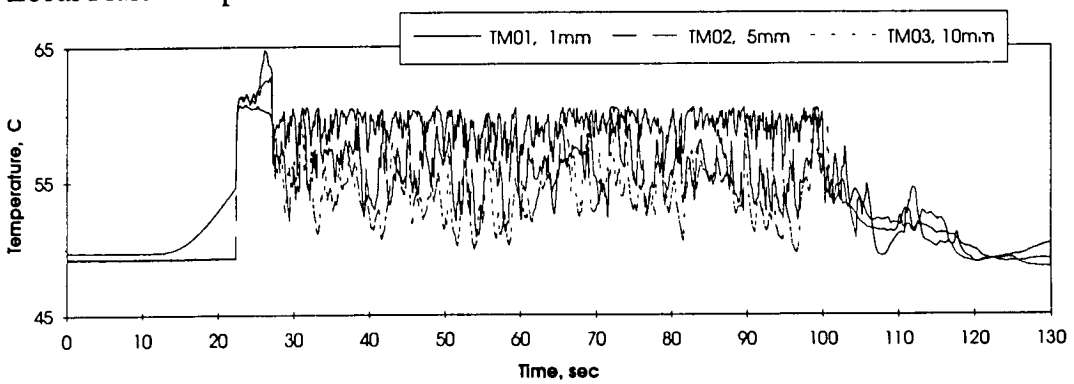

C. Far Field Bulk Temperatures

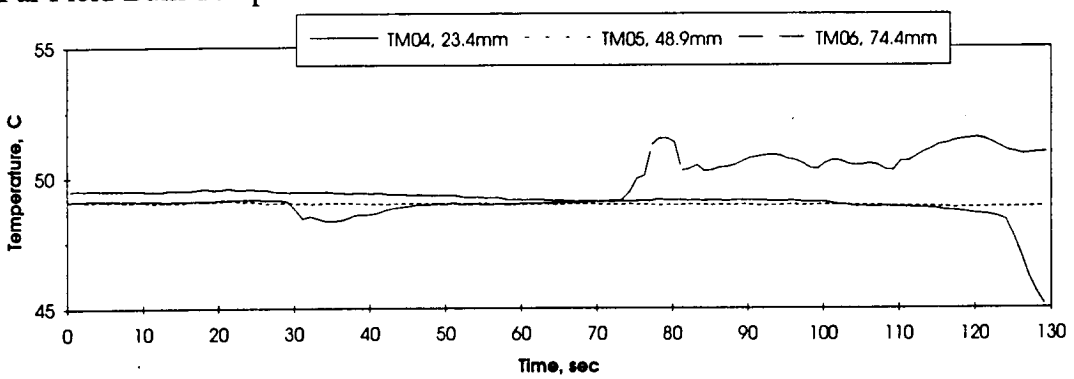

FIGURE : MEASURED FLUID TEMPERATURES **STS 47 - RUN#2**

HEAT FLUX	SUBCOOLING (F)	HEATER POWER ON/OFF	100 FPS ON/OFF	STIRRER START	REPRESS START	TOTAL TEST TIME
4	20 ± 2	10-100 sec.	15-25 sec.	-----	----------	130 sec.

Figure A-4b. Measured fluid temperatures near primary heater and far field bulk liquid. PBE-IA (STS-47). Run No. 2.

A. Mean Heater Surface Temperature

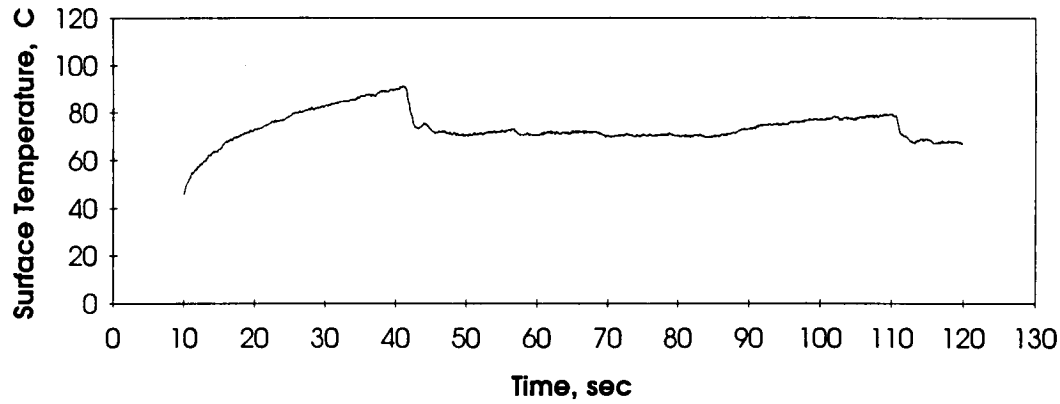

B. Local Fluid Temperatures

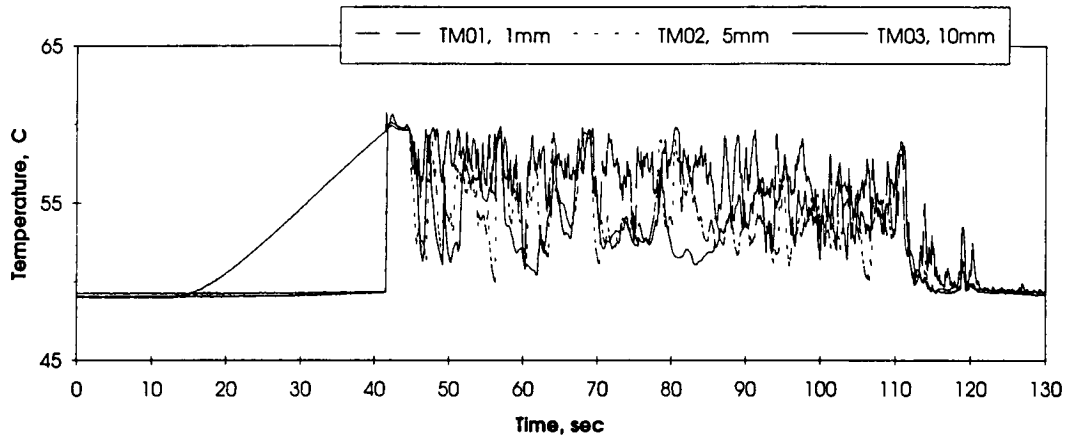

C. Far Field Bulk Temperatures

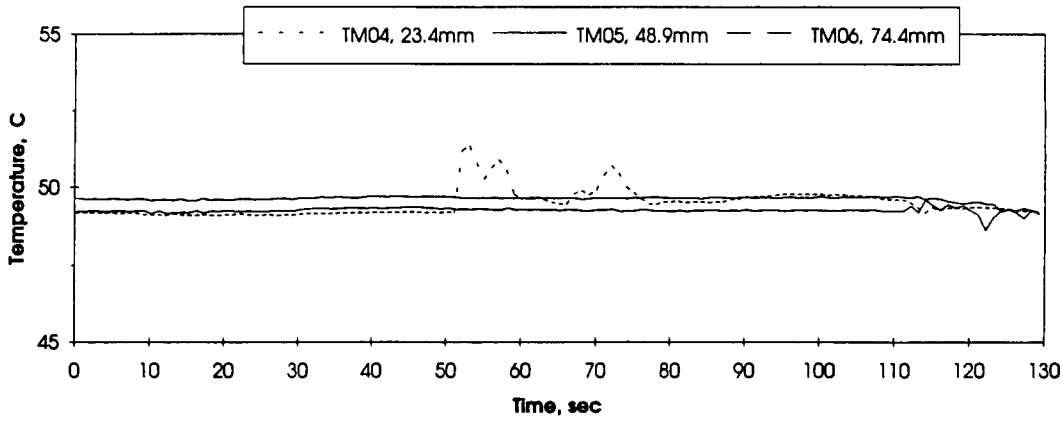

FIGURE : MEASURED FLUID TEMPERATURES **STS 47 - RUN#3**

HEAT FLUX	SUBCOOLING (F)	HEATER POWER ON/OFF	100 FPS ON/OFF	STIRRER START	REPRESS START	TOTAL TEST TIME
2	20 ± 2	10-120 sec.	30-50 sec.	110 sec.	----------	130 sec.

Figure A-4c. Measured fluid temperatures near primary heater and far field bulk liquid. PBE-IA (STS-47). Run No. 3.

A. Mean Heater Surface Temperature

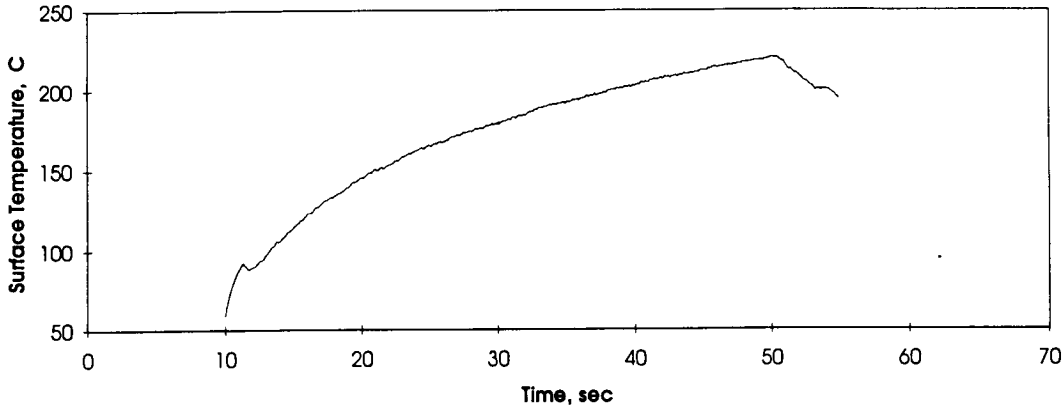

B. Local Fluid Temperatures

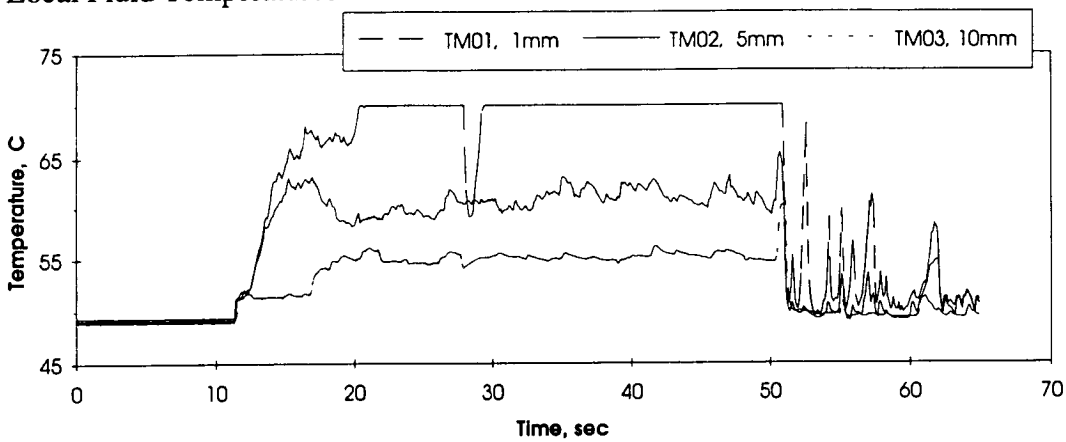

C. Far Field Bulk Temperatures

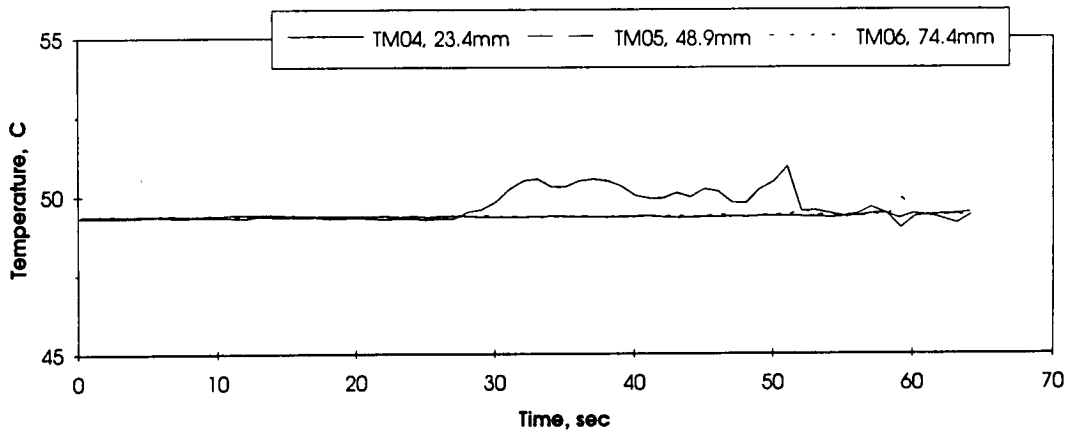

FIGURE : MEASURED FLUID TEMPERATURES **STS 47 - RUN#4**

HEAT FLUX	SUBCOOLING (F)	HEATER POWER ON/OFF	100 FPS ON/OFF	STIRRER START	REPRESS START	TOTAL TEST TIME
8	05 ± 1	10-55 sec.	10-15 sec.	50 sec.	----------	65 sec.

Figure A-4d. Measured fluid temperatures near primary heater and far field bulk liquid. PBE-IA (STS-47). Run No. 4.

A. Mean Heater Surface Temperature

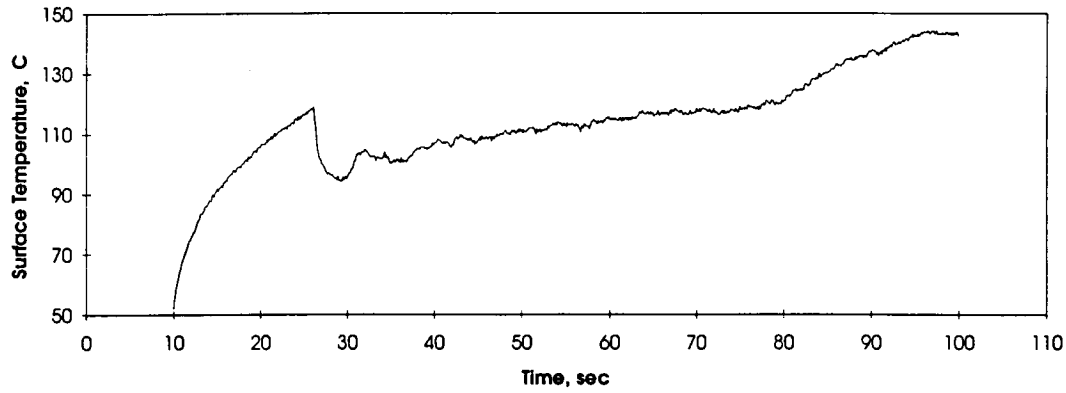

B. Local Fluid Temperatures

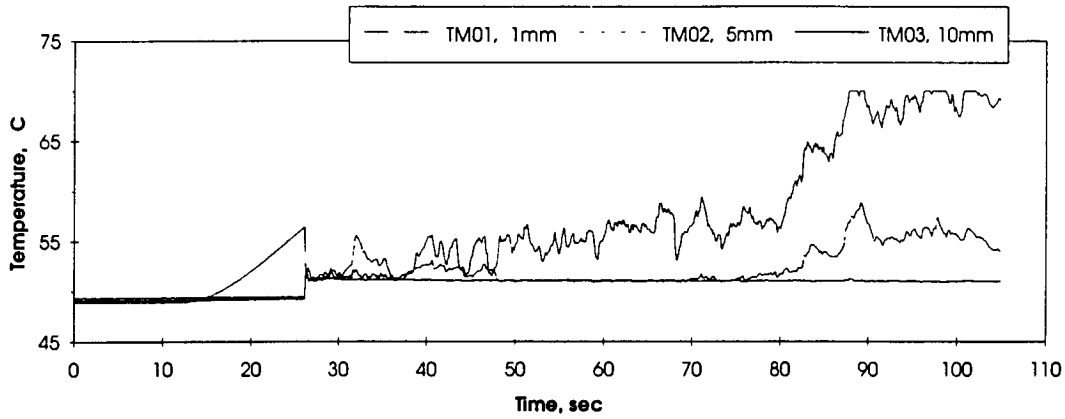

C. Far Field Bulk Temperatures

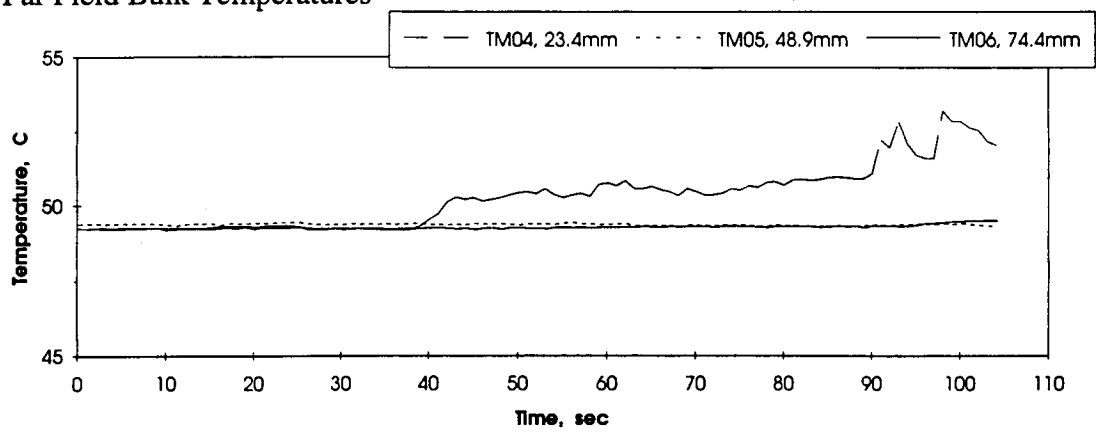

FIGURE : MEASURED FLUID TEMPERATURES **STS 47 - RUN#5**

HEAT FLUX	SUBCOOLING (F)	HEATER POWER ON/OFF	100 FPS ON/OFF	STIRRER START	REPRESS START	TOTAL TEST TIME
4	5 ± 1	10-100 sec.	15-25 sec.	--------	----------	105 sec.

Figure A-4e. Measured fluid temperatures near primary heater and far field bulk liquid. PBE-IA (STS-47). Run No. 5.

A. Mean Heater Surface Temperature

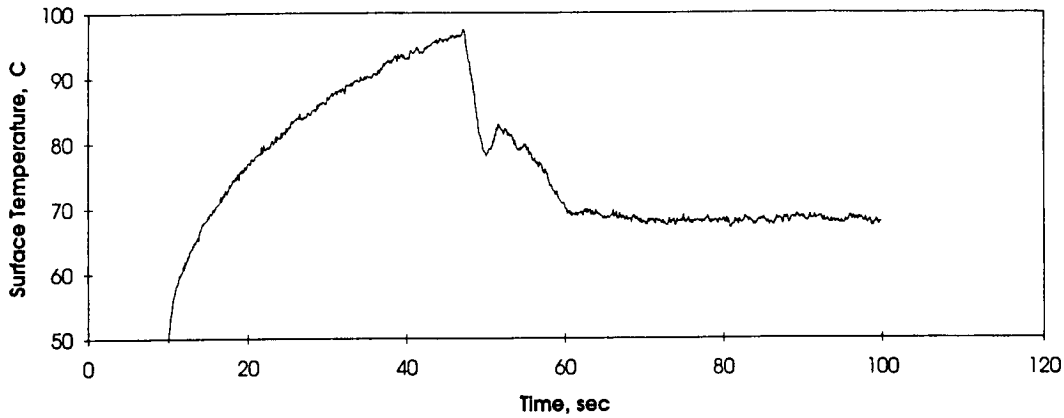

B. Local Fluid Temperatures

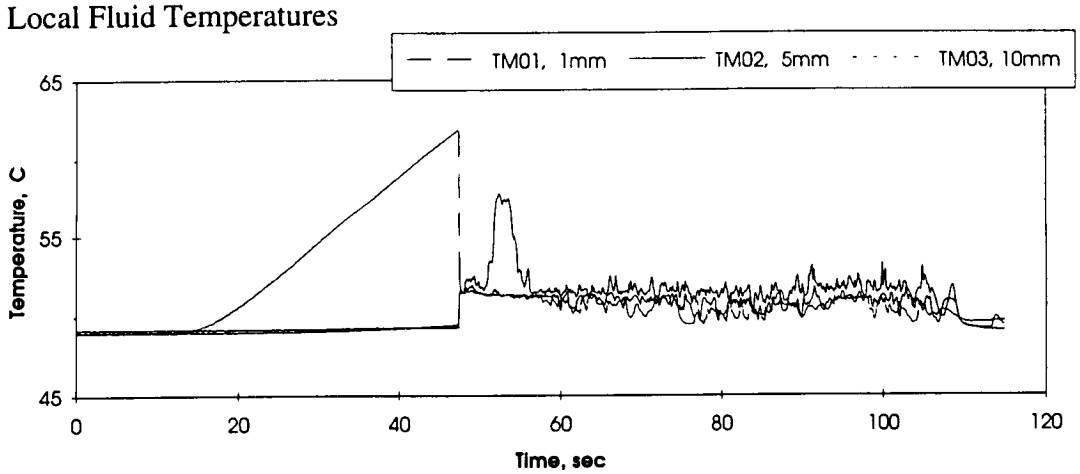

C. Far Field Bulk Temperatures

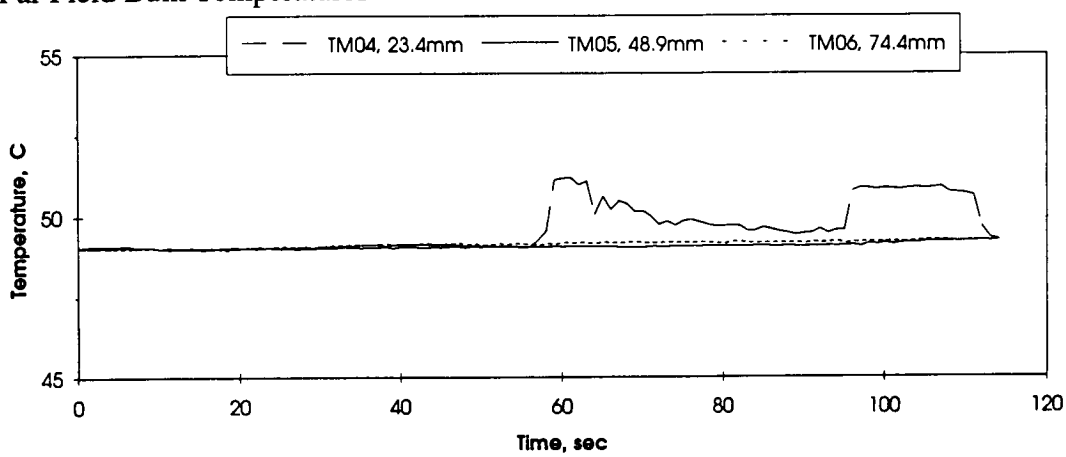

FIGURE : MEASURED FLUID TEMPERATURES **STS 47 - RUN#6**

HEAT FLUX	SUBCOOLING (F)	HEATER POWER ON/OFF	100 FPS ON/OFF	STIRRER START	REPRESS START	TOTAL TEST TIME
2	5 ± 1	10-105 sec.	30-50 sec.	--------	----------	115 sec.

Figure A-4f. Measured fluid temperatures near primary heater and far field bulk liquid. PBE-IA (STS-47). Run No. 6.

A. Mean Heater Surface Temperature

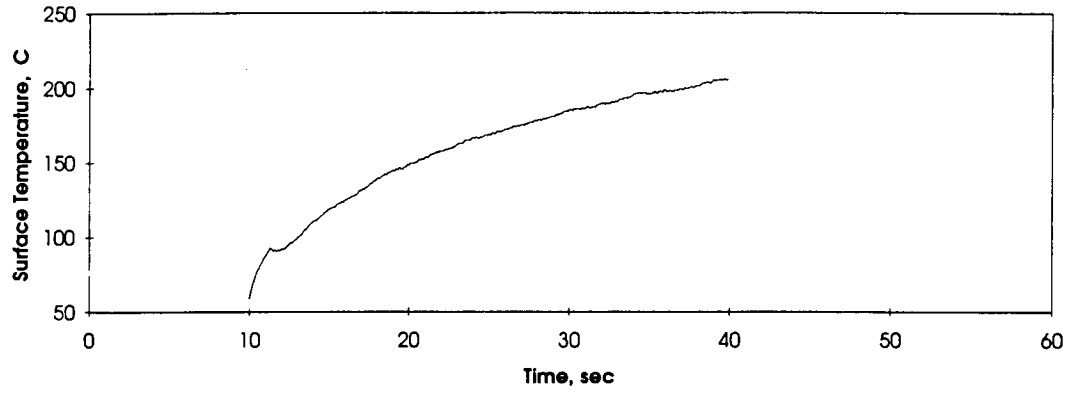

B. Local Fluid Temperatures

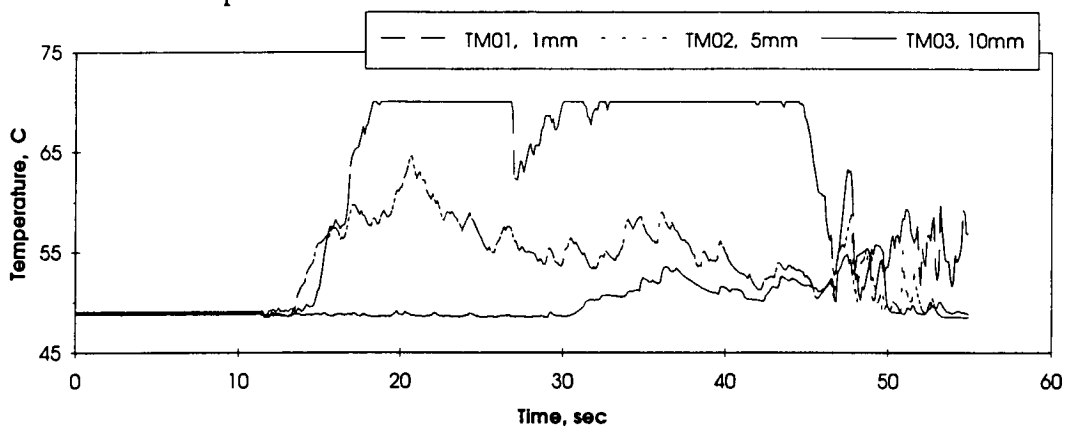

C. Far Field Bulk Temperatures

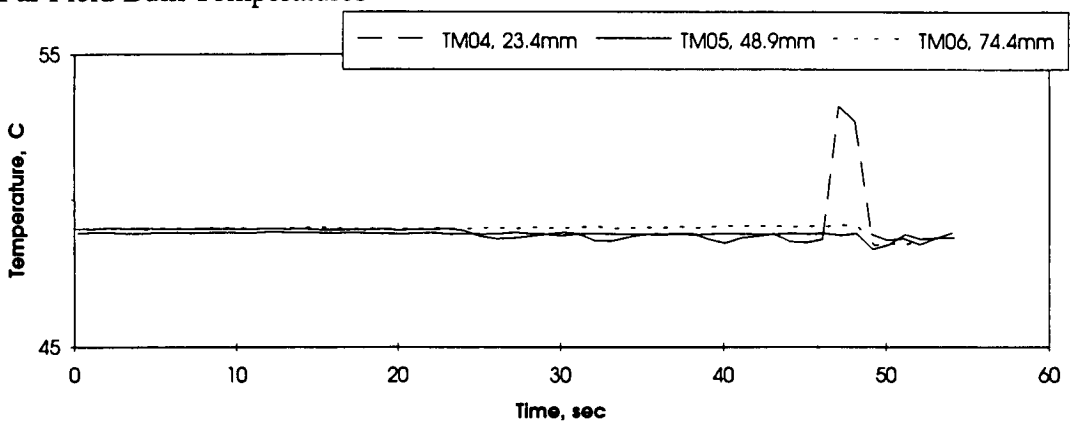

FIGURE : MEASURED FLUID TEMPERATURES **STS 47 - RUN#7**

HEAT FLUX	SUBCOOLING (F)	HEATER POWER ON/OFF	100 FPS ON/OFF	STIRRER START	REPRESS START	TOTAL TEST TIME
8	.5 ± .4	10-40 sec.	10-15 sec.	--------	45 sec.	55 sec.

Figure A-4g. Measured fluid temperatures near primary heater and far field bulk liquid. PBE-IA (STS-47). Run No. 7.

A. Mean Heater Surface Temperature

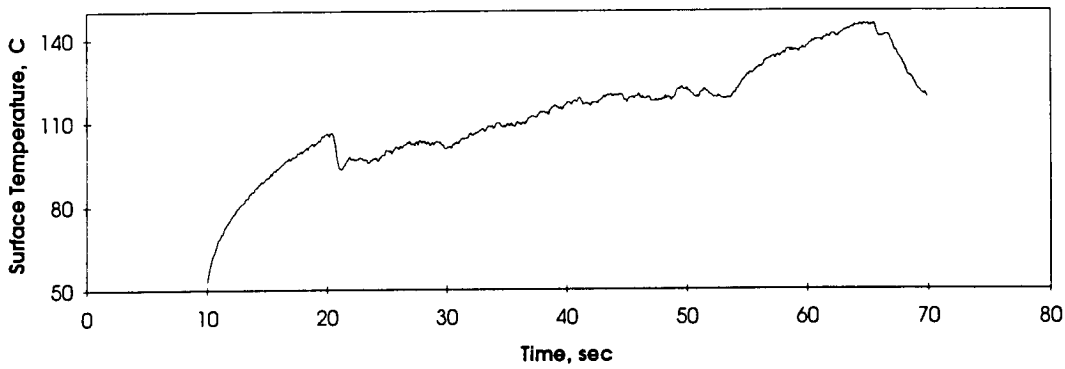

B. Local Fluid Temperatures

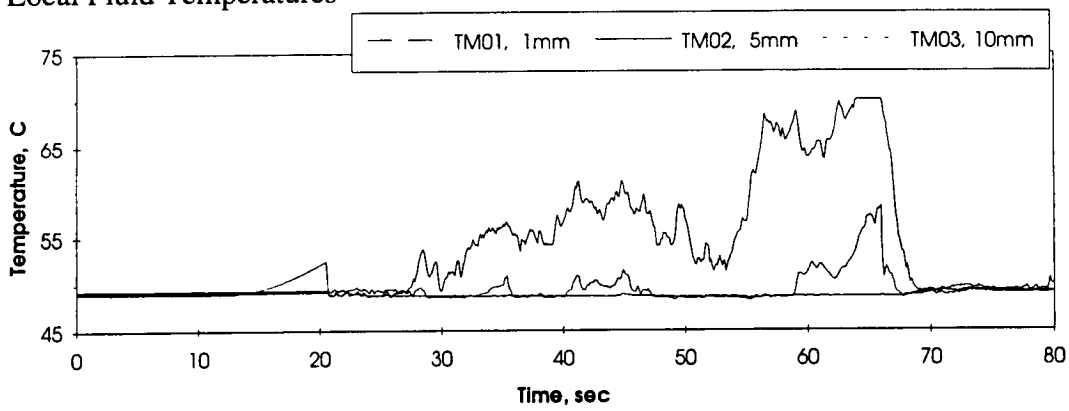

C. Far Field Bulk Temperatures

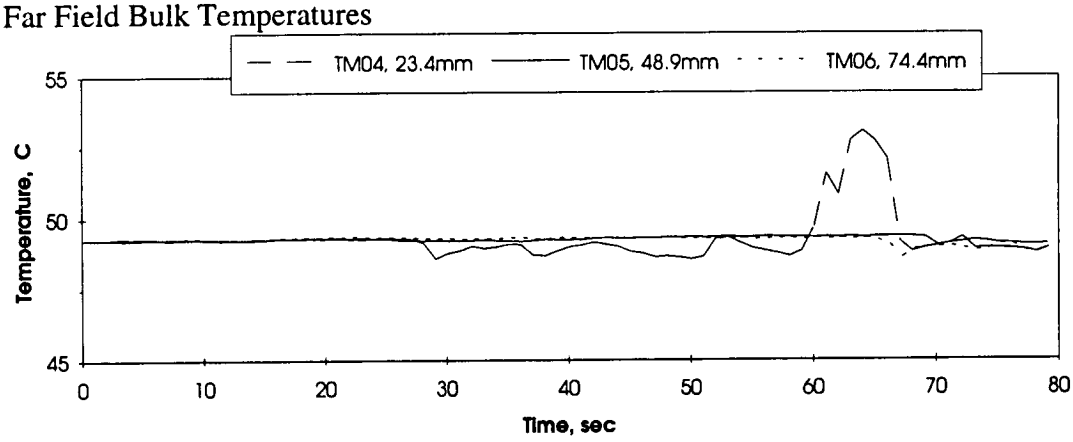

FIGURE : MEASURED FLUID TEMPERATURES **STS 47 - RUN#8**

HEAT FLUX	SUBCOOLING (F)	HEATER POWER ON/OFF	100 FPS ON/OFF	STIRRER START	REPRESS START	TOTAL TEST TIME
4	.5 ± .4	10-70 sec.	15-25 sec.	65 sec.	--------	80 sec.

Figure A-4h. Measured fluid temperatures near primary heater and far field bulk liquid. PBE-IA (STS-47). Run No. 8.

A. Mean Heater Surface Temperature

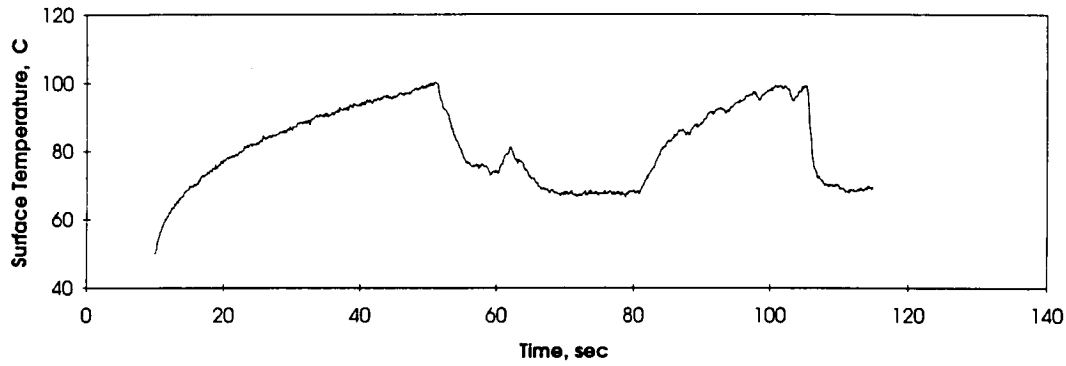

B. Local Fluid Temperatures

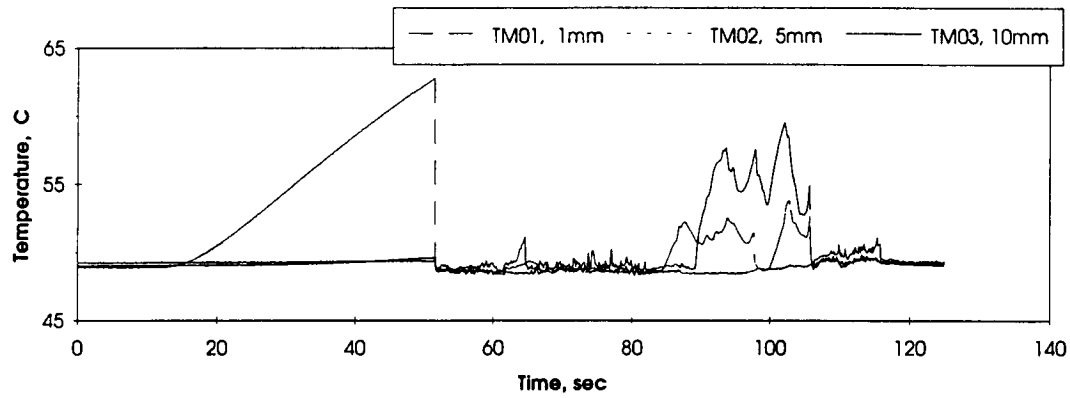

C. Far Field Bulk Temperatures

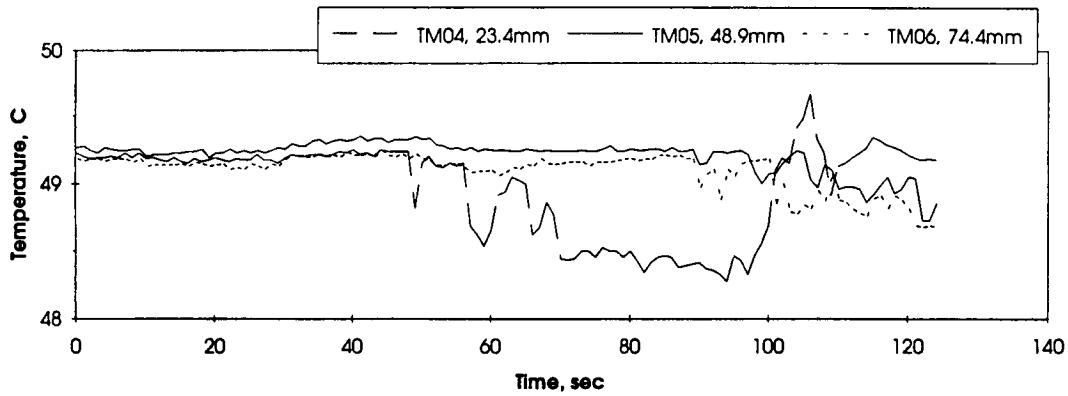

FIGURE : MEASURED FLUID TEMPERATURES **STS 47 - RUN#9**

HEAT FLUX	SUBCOOLING (F)	HEATER POWER ON/OFF	100 FPS ON/OFF	STIRRER START	REPRESS START	TOTAL TEST TIME
2	.5 ± .4	10-115 sec.	30-50 sec.	105 sec.	--------	125 sec.

Figure A-4i. Measured fluid temperatures near primary heater and far field bulk liquid. PBE-IA (STS-47). Run No. 9.

A. Mean Heater Surface Temperature

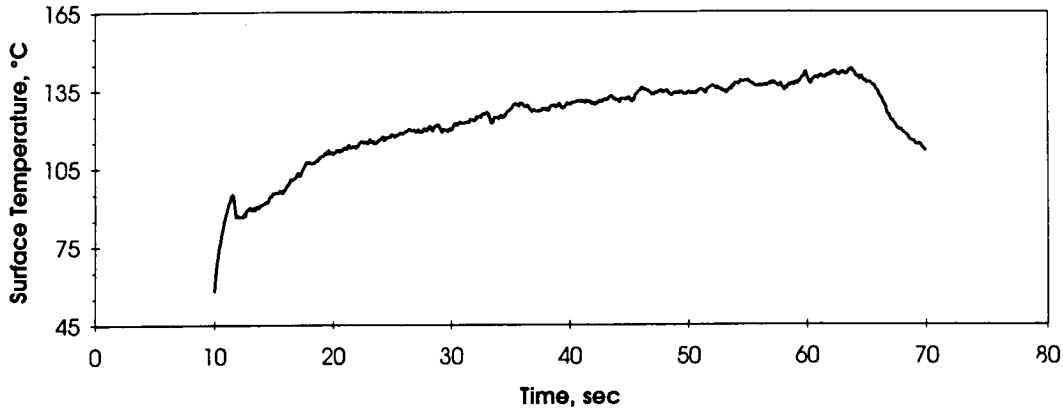

D.

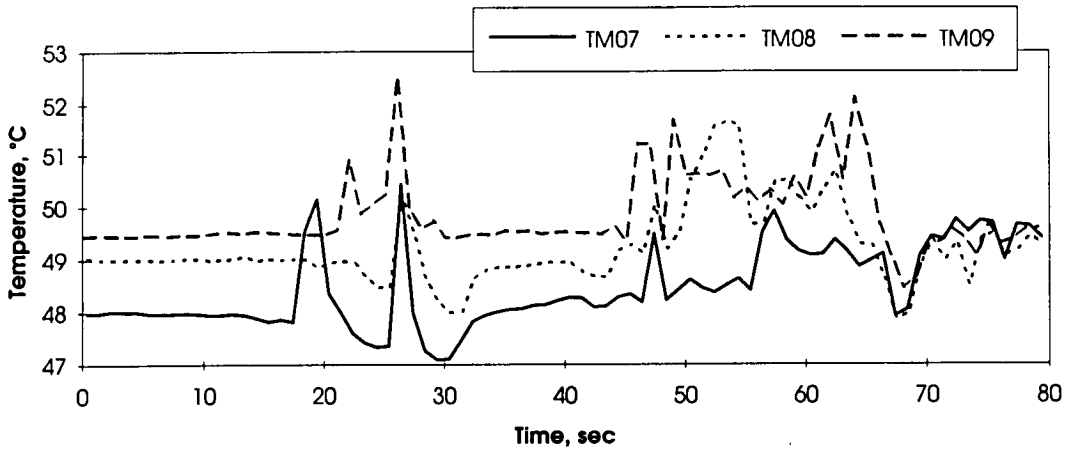

E.

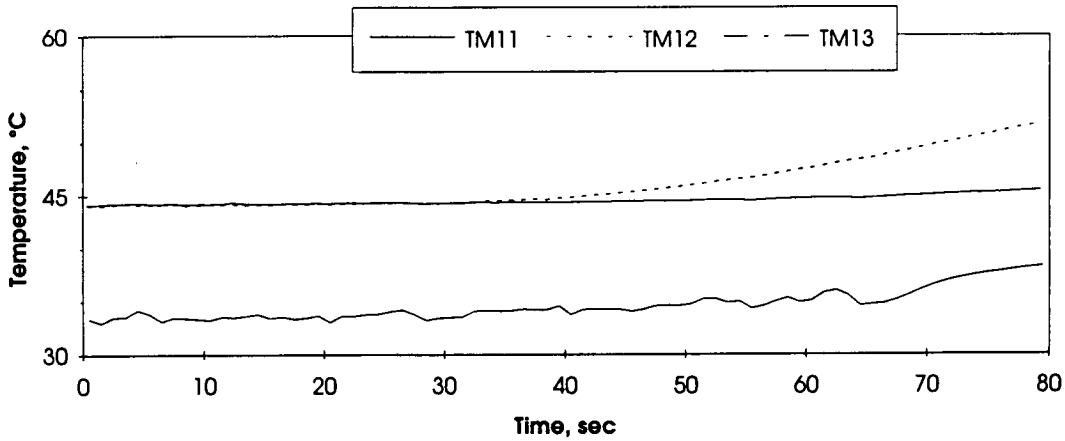

FIGURE : MEASURED HEATER-UNDERSIDE TEMPERATURES **STS 47 - RUN #1**

HEAT FLUX	SUBCOOLING (F)	HEATER POWER ON/OFF	100 FPS ON/OFF	STIRRER START	REPRESS START	TOTAL TEST TIME
8	20 ± 2	10-70 sec.	10-15 sec.	65 sec.	----------	80 sec.

Figure A-5a. Measured fluid temperatures near secondary heater and heater underside. PBE-IA (STS-47). Run No. 1.

A. Mean Heater Surface Temperature

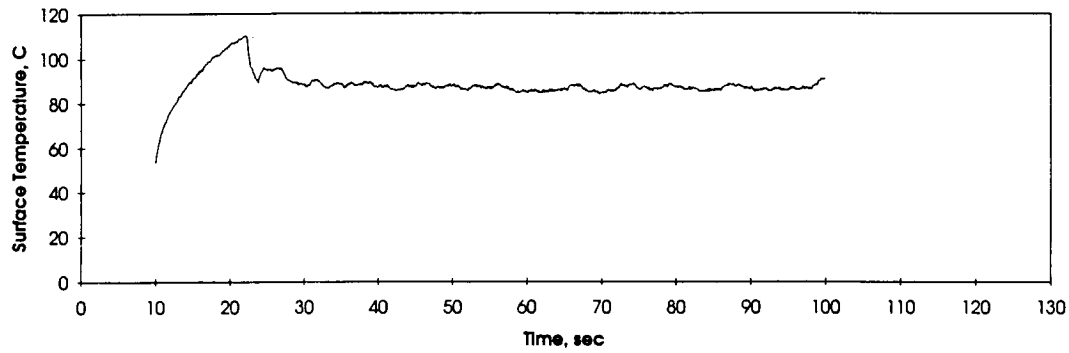

D.

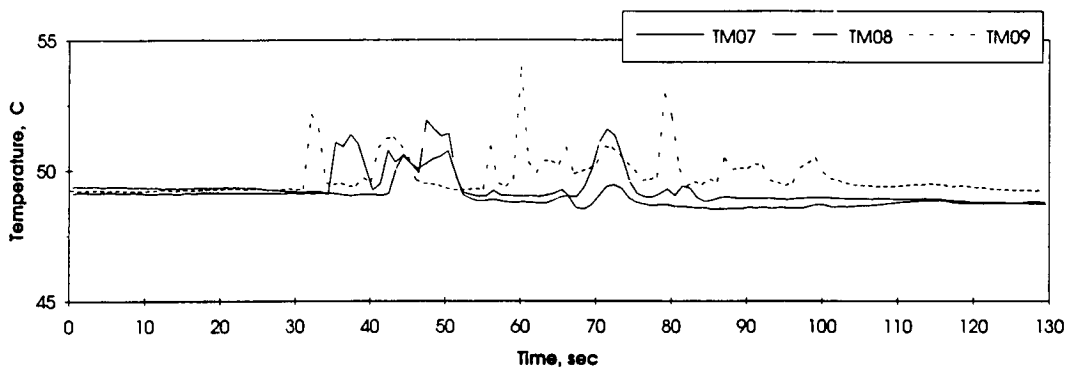

E.

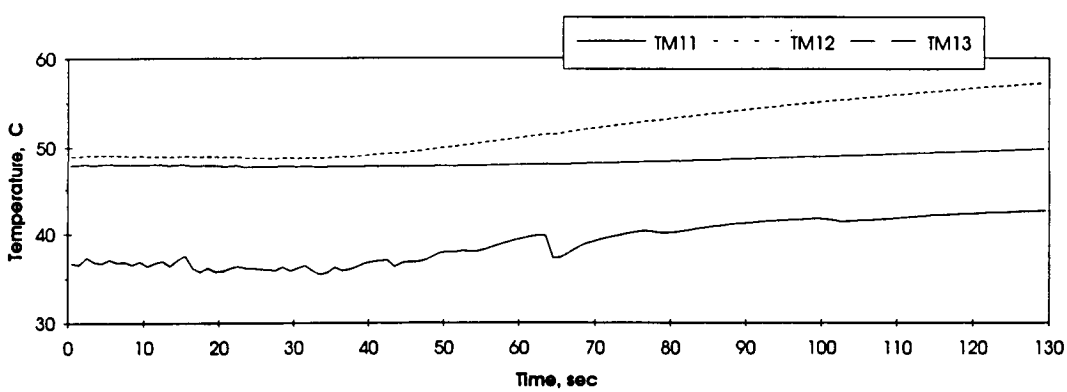

FIGURE : MEASURED HEATER-UNDERSIDE TEMPERATURES **STS 47 - RUN #2**

HEAT FLUX	SUBCOOLING (F)	HEATER POWER ON/OFF	100 FPS ON/OFF	STIRRER START	REPRESS START	TOTAL TEST TIME
4	20 ± 2	10-100 sec.	15-25 sec.	-------	----------	130 sec.

Figure A-5b. Measured fluid temperatures near secondary heater and heater underside. PBE-IA (STS-47). Run No. 2.

A. Mean Heater Surface Temperature

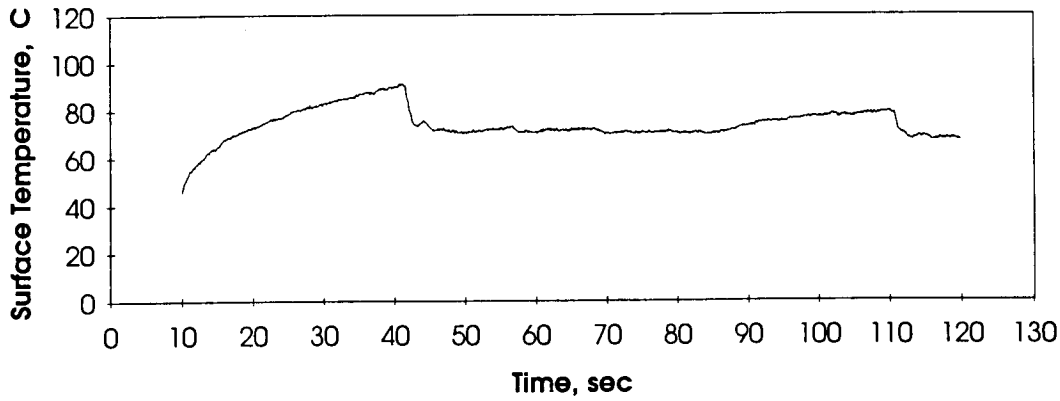

D.

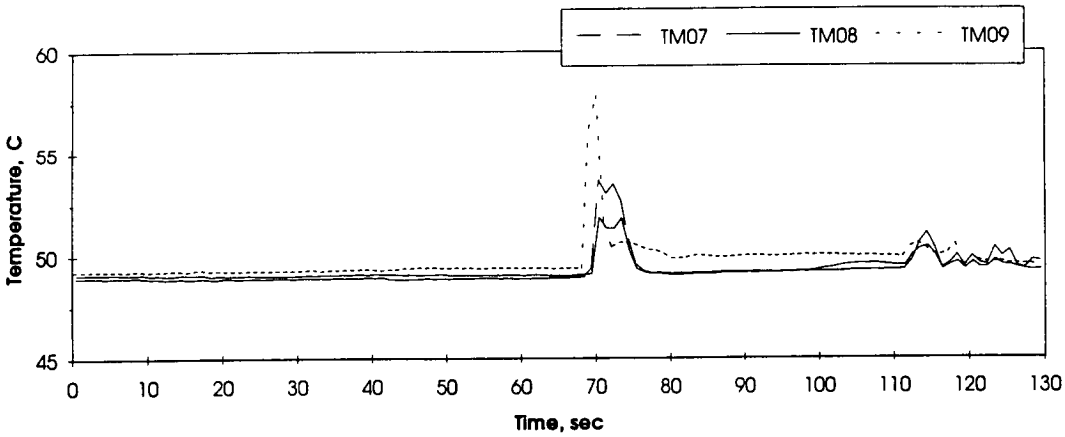

E.

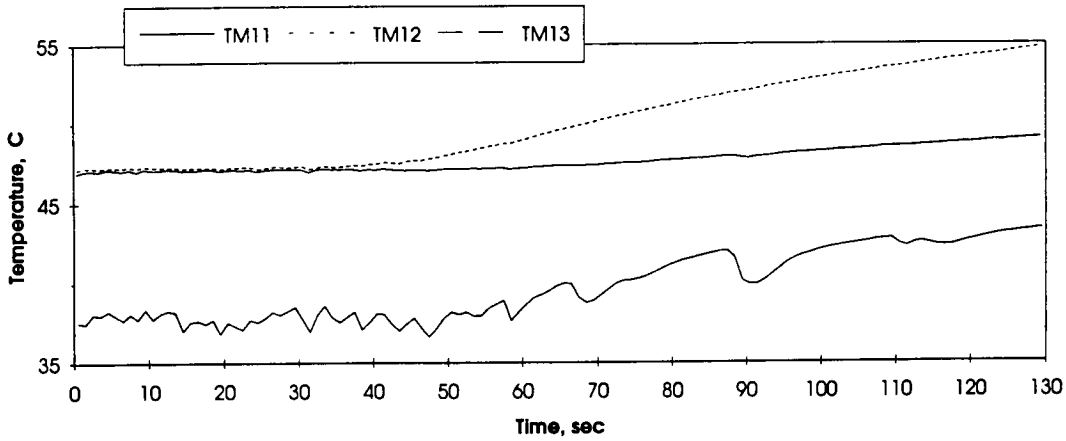

FIGURE : MEASURED HEATER-UNDERSIDE TEMPERATURES **STS 47 - RUN #3**

HEAT FLUX	SUBCOOLING (F)	HEATER POWER ON/OFF	100 FPS ON/OFF	STIRRER START	REPRESS START	TOTAL TEST TIME
2	20 ± 2	10-120 sec.	30-50 sec.	110 sec.	----------	130 sec.

Figure A-5c. Measured fluid temperatures near secondary heater and heater underside. PBE-IA (STS-47). Run No. 3.

A. Mean Heater Surface Temperature

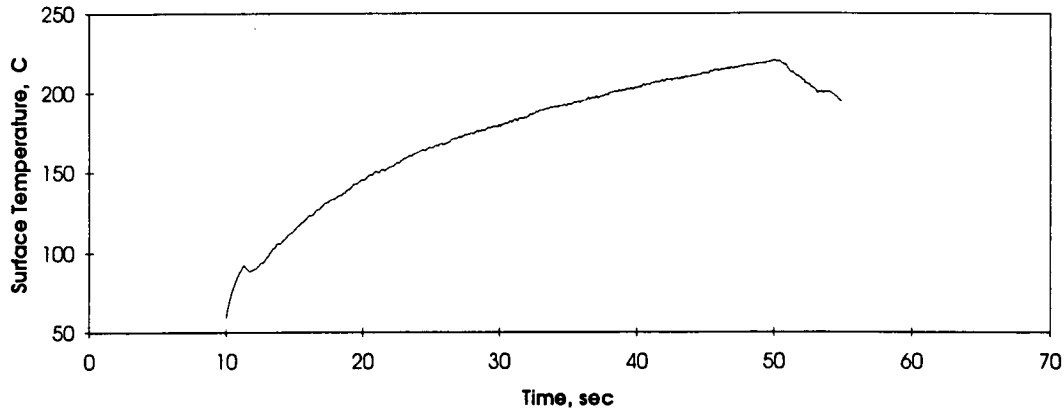

D.

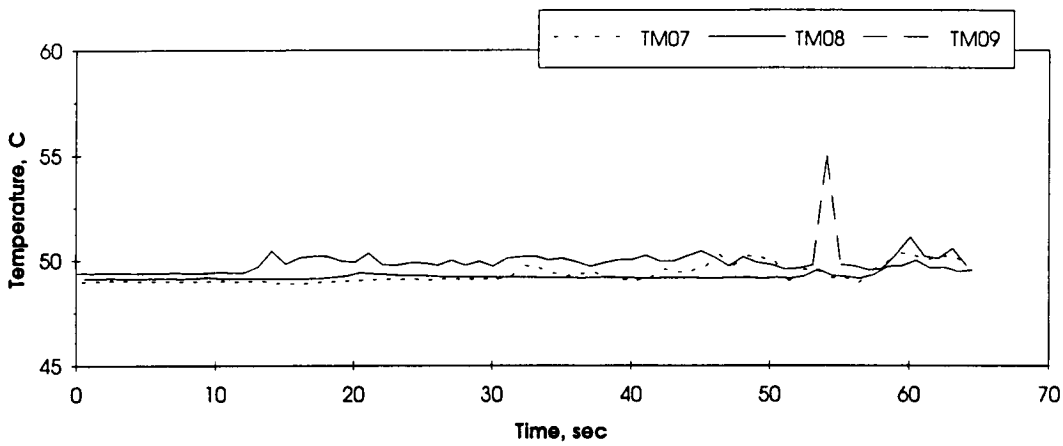

E.

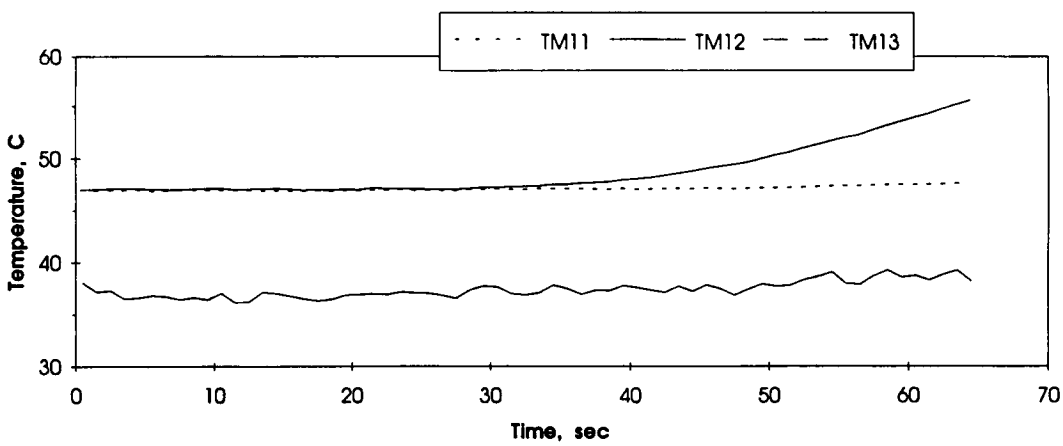

FIGURE : MEASURED HEATER-UNDERSIDE TEMPERATURES **STS 47 - RUN #4**

HEAT FLUX	SUBCOOLING (F)	HEATER POWER ON/OFF	100 FPS ON/OFF	STIRRER START	REPRESS START	TOTAL TEST TIME
8	5 ± 1	10-55 sec.	10-15 sec.	50 sec.	----------	65 sec.

Figure A-5d. Measured fluid temperatures near secondary heater and heater underside. PBE-IA (STS-47). Run No. 4.

A. Mean Heater Surface Temperature

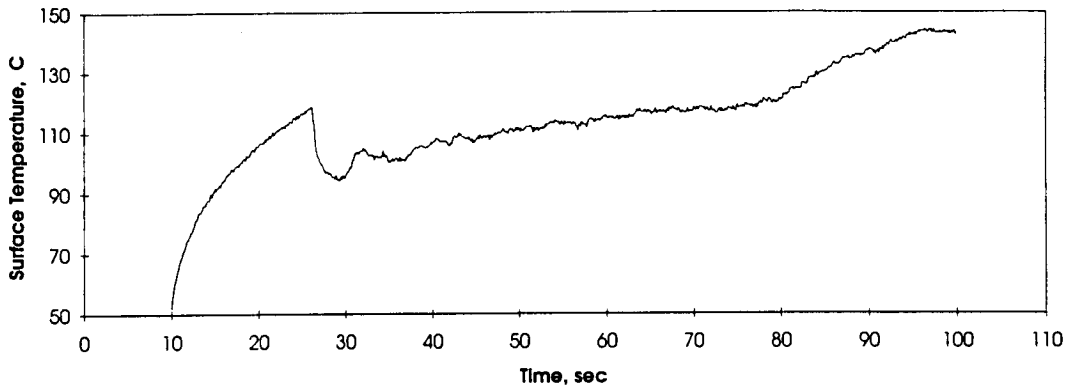

D.

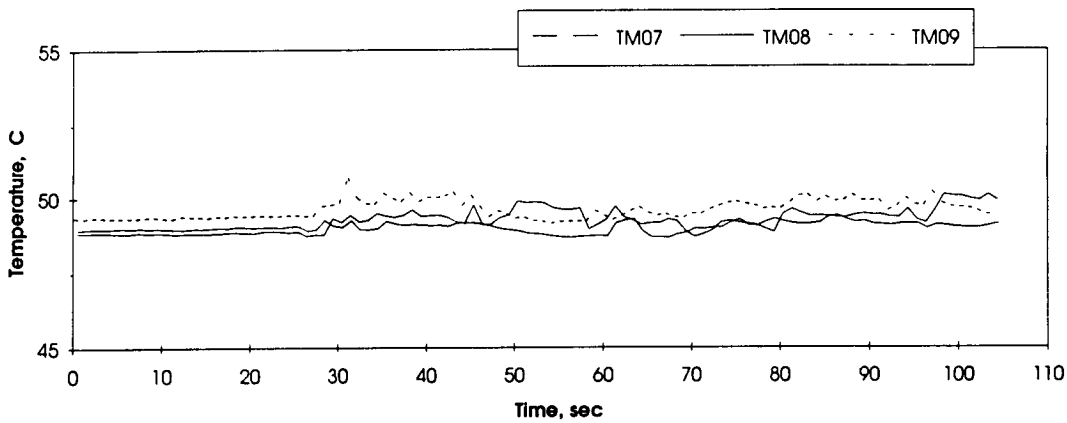

E.

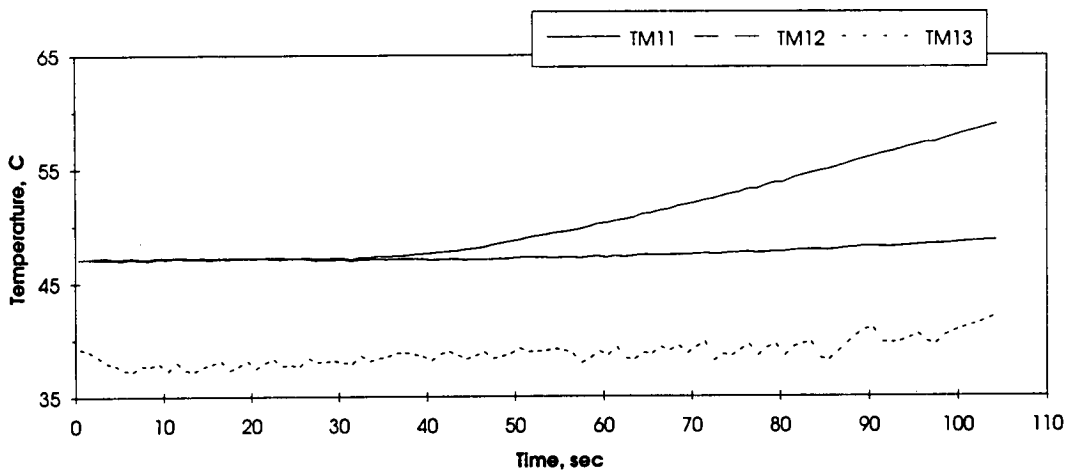

FIGURE : MEASURED HEATER-UNDERSIDE TEMPERATURES **STS 47 - RUN #5**

HEAT FLUX	SUBCOOLING (F)	HEATER POWER ON/OFF	100 FPS ON/OFF	STIRRER START	REPRESS START	TOTAL TEST TIME
4	5 ± 1	10-100 sec.	15-25 sec.	--------	----------	105 sec.

Figure A-5e. Measured fluid temperatures near secondary heater and heater underside. PBE-IA (STS-47). Run No. 5.

A. Mean Heater Surface Temperature

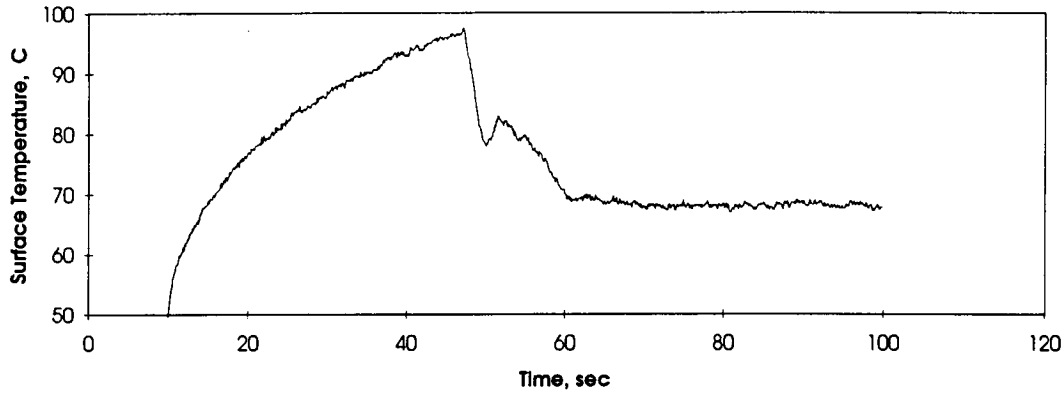

D.

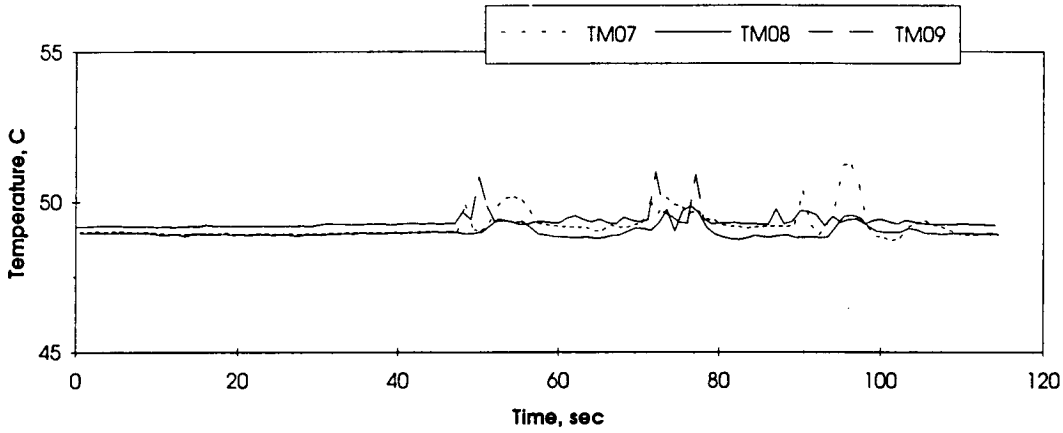

E.

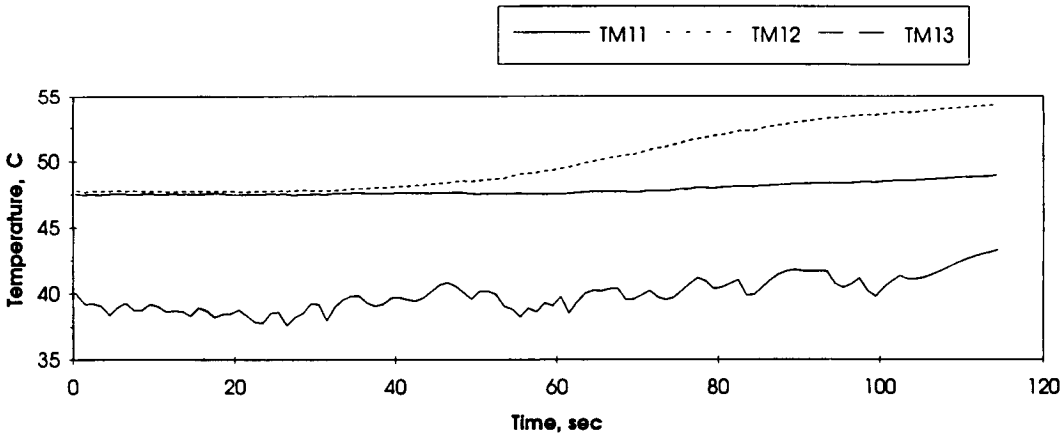

FIGURE : MEASURED HEATER-UNDERSIDE TEMPERATURES **STS 47 - RUN #6**

HEAT FLUX	SUBCOOLING (F)	HEATER POWER ON/OFF	100 FPS ON/OFF	STIRRER START	REPRESS START	TOTAL TEST TIME
2	5 ± 1	10-105 sec.	30-50 sec.	--------	----------	115 sec.

Figure A-5f. Measured fluid temperatures near secondary heater and heater underside. PBE-IA (STS-47). Run No. 6.

A. Mean Heater Surface Temperature

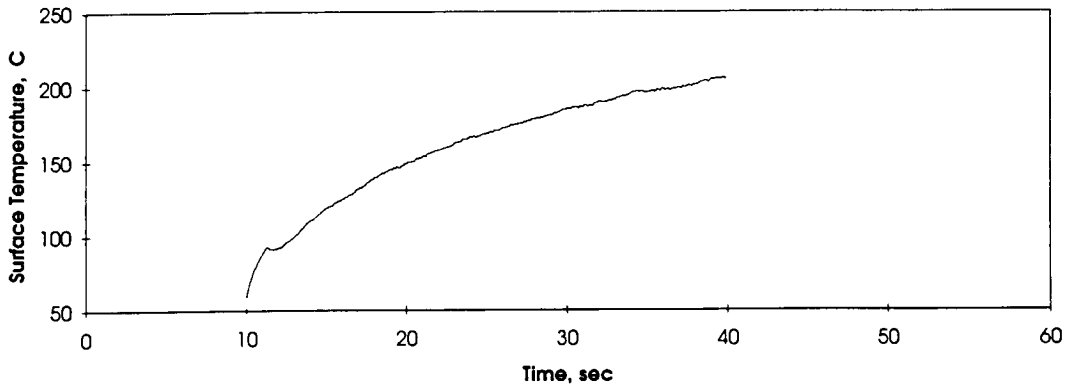

D.

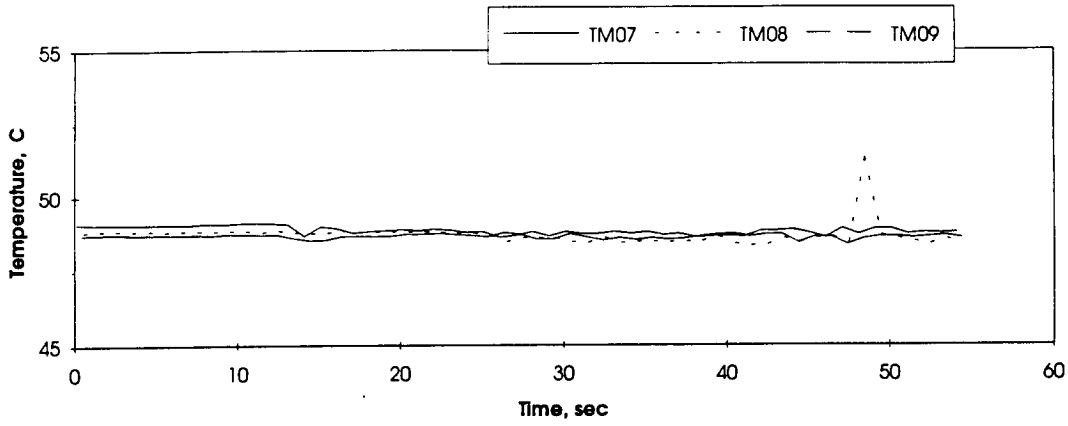

E.

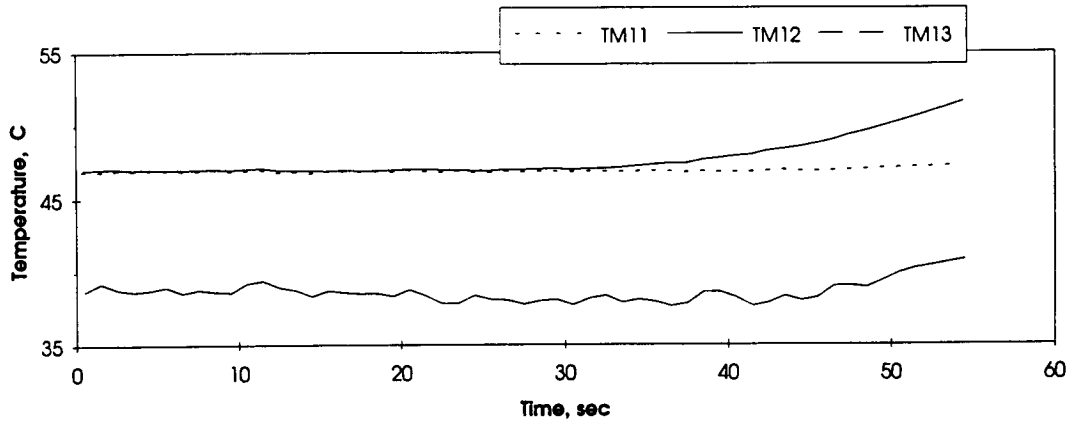

FIGURE : MEASURED HEATER-UNDERSIDE TEMPERATURES **STS 47 - RUN #7**

HEAT FLUX	SUBCOOLING (F)	HEATER POWER ON/OFF	100 FPS ON/OFF	STIRRER START	REPRESS START	TOTAL TEST TIME
8	.5 ± .4	10-40 sec.	10-15 sec.	--------	45 sec.	55 sec.

Figure A-5g. Measured fluid temperatures near secondary heater and heater underside. PBE-IA (STS-47). Run No. 7.

A. Mean Heater Surface Temperature

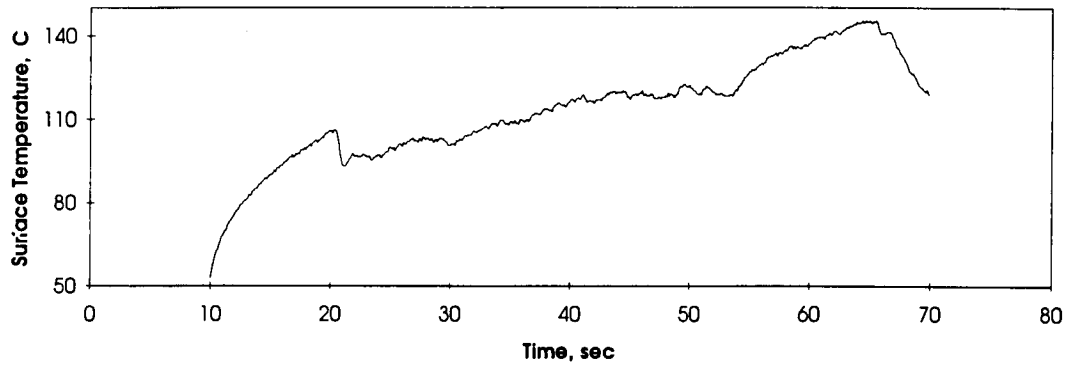

D.

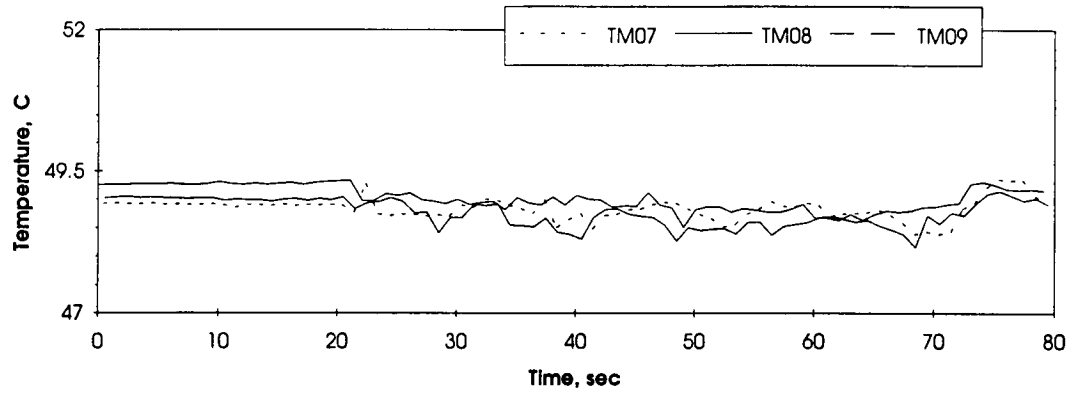

E.

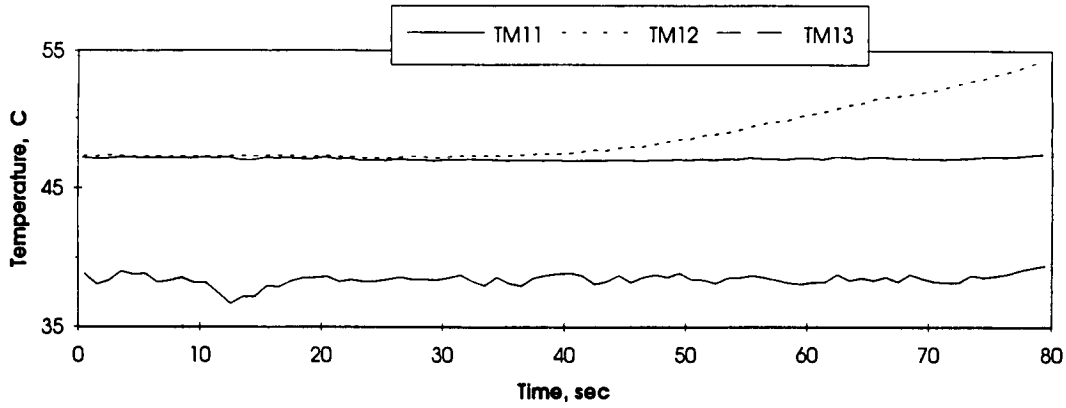

FIGURE : MEASURED HEATER-UNDERSIDE TEMPERATURES **STS 47 - RUN #8**

HEAT FLUX	SUBCOOLING (F)	HEATER POWER ON/OFF	100 FPS ON/OFF	STIRRER START	REPRESS START	TOTAL TEST TIME
4	.5 ± .4	10-70 sec.	15-25 sec.	65 sec.	--------	80 sec.

Figure A-5h. Measured fluid temperatures near secondary heater and heater underside. PBE-IA (STS-47). Run No. 8.

A. Mean Heater Surface Temperature

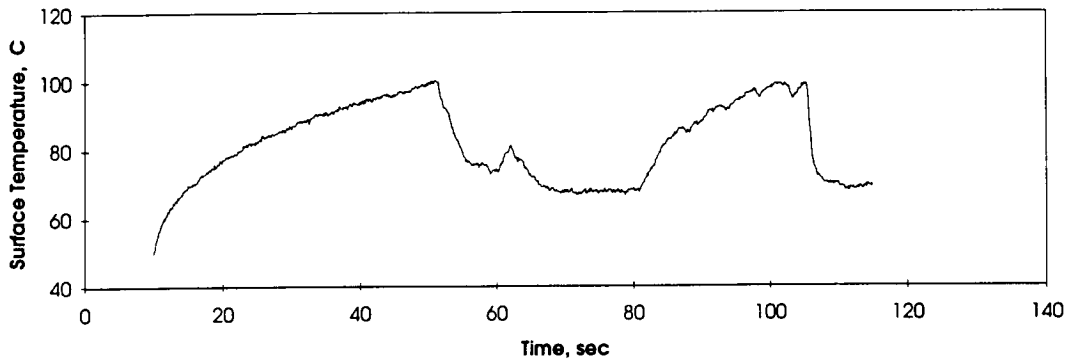

D.

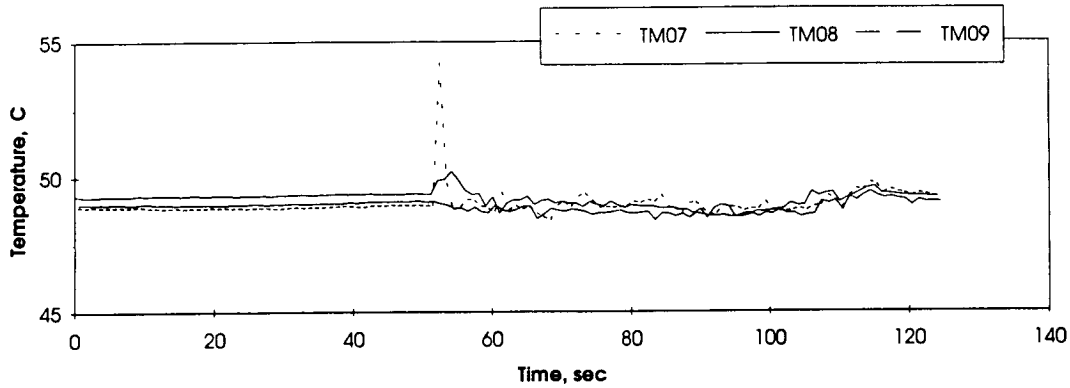

E.

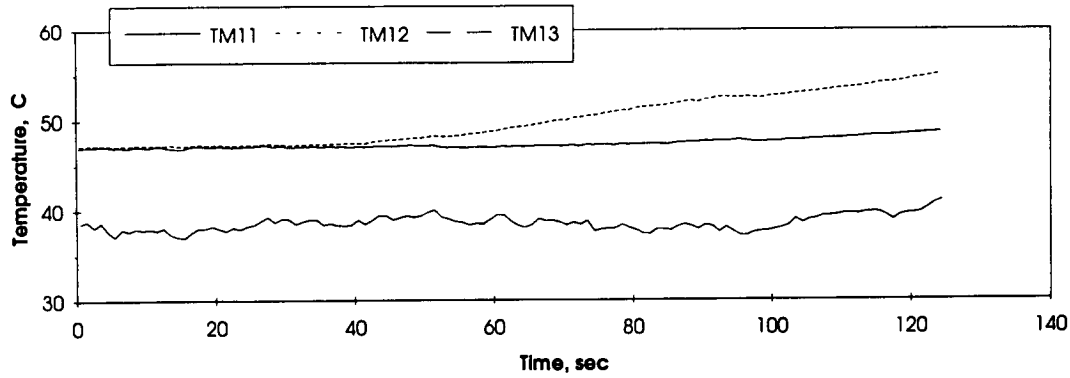

FIGURE : MEASURED HEATER-UNDERSIDE TEMPERATURES **STS 47 - RUN #9**

HEAT FLUX	SUBCOOLING (F)	HEATER POWER ON/OFF	100 FPS ON/OFF	STIRRER START	REPRESS START	TOTAL TEST TIME
2	.5 ± .4	10-115 sec.	30-50 sec.	105 sec.	--------	125 sec.

Figure A-5i. Measured fluid temperatures near secondary heater and heater underside. PBE-IA (STS-47). Run No. 9.

STS-47 Run #1

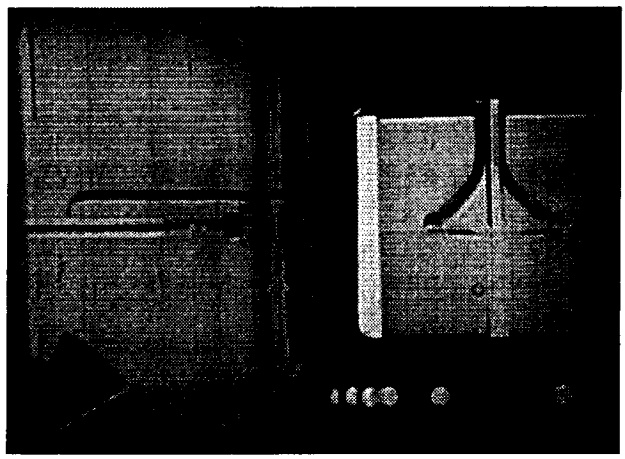

Frame#0158 time=11.58 sec.

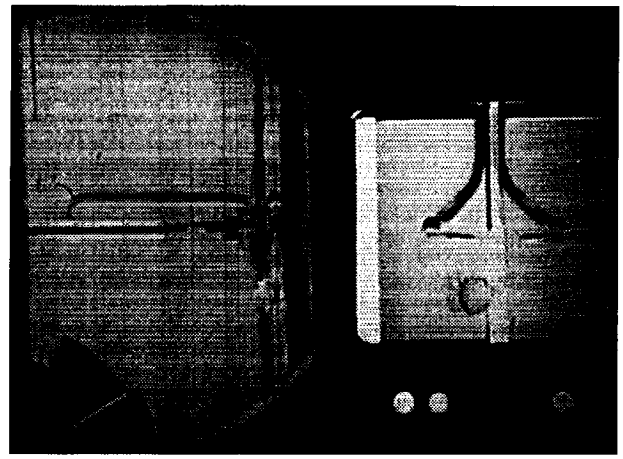

Frame#0161 time=11.60 sec.

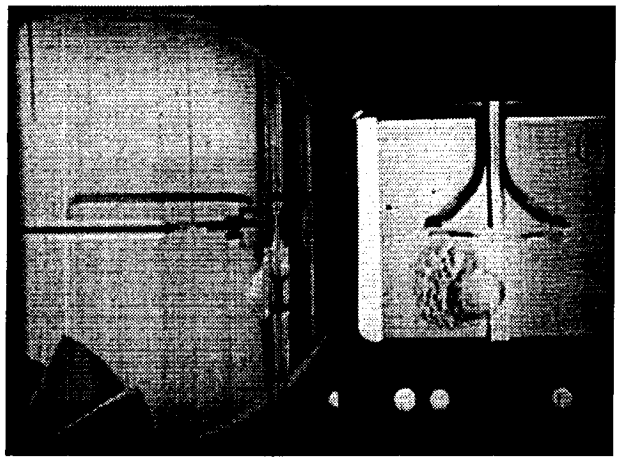

Frame#0163 time=11.62 sec.

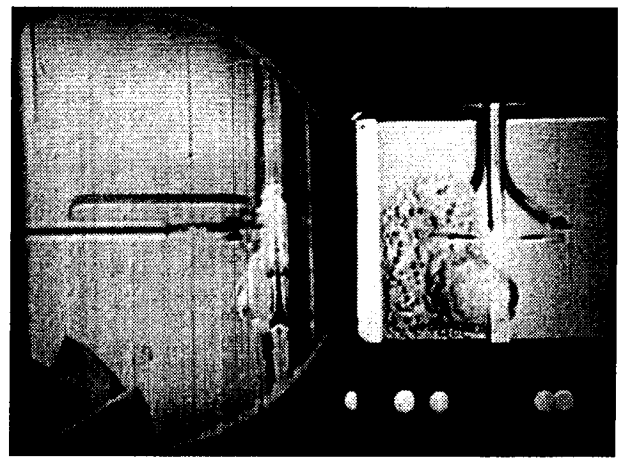

Frame#0166 time=11.65 sec.

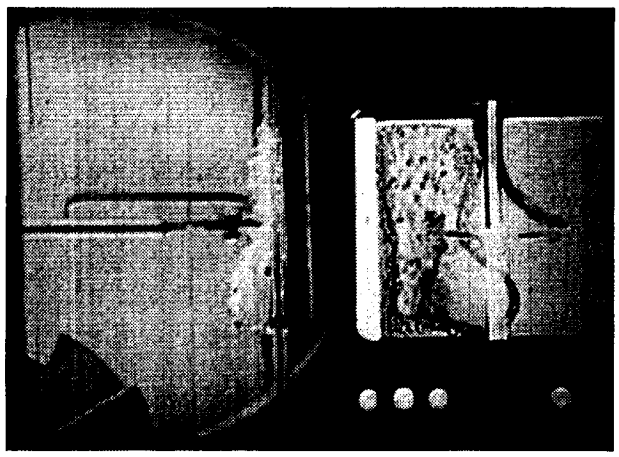

Frame#0169 time=11.68 sec.

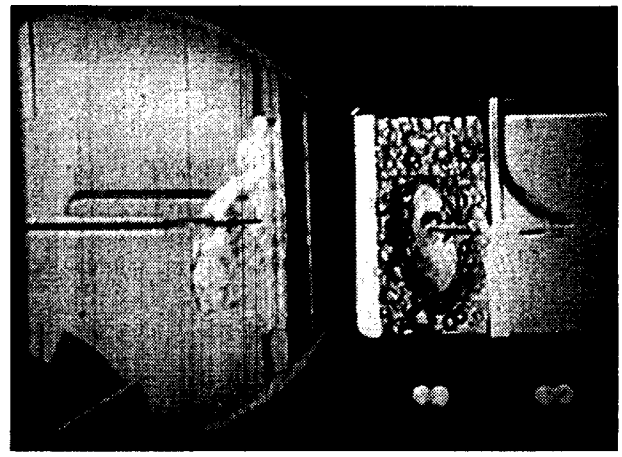

Frame#0194 time=11.93 sec.

Figure A-6a. Selected Photographic Images. PBE-IA (STS-47). Run No. 1.

STS-47 Run #1

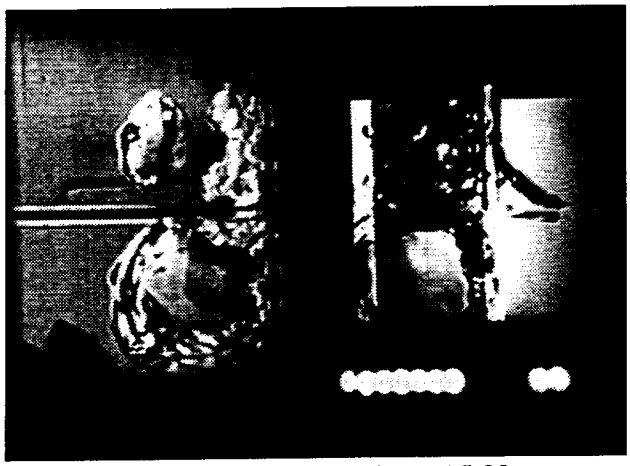

Frame#0511 time=15.09 sec.

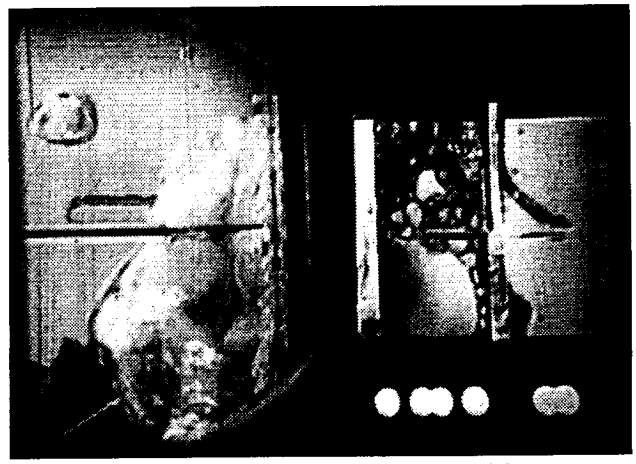

Frame#0000 time=17.20 sec.

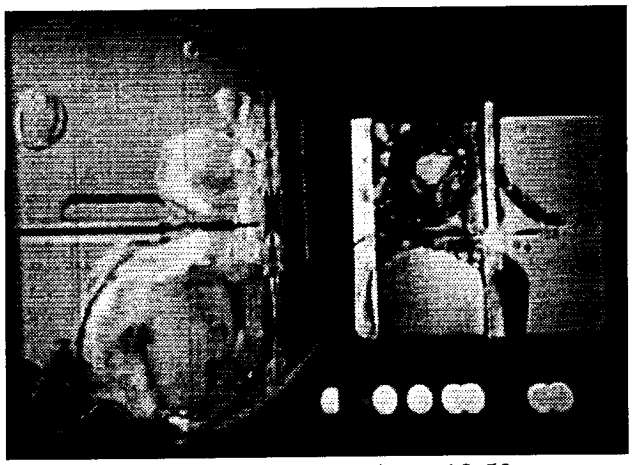

Frame#0013 time=18.50 sec.

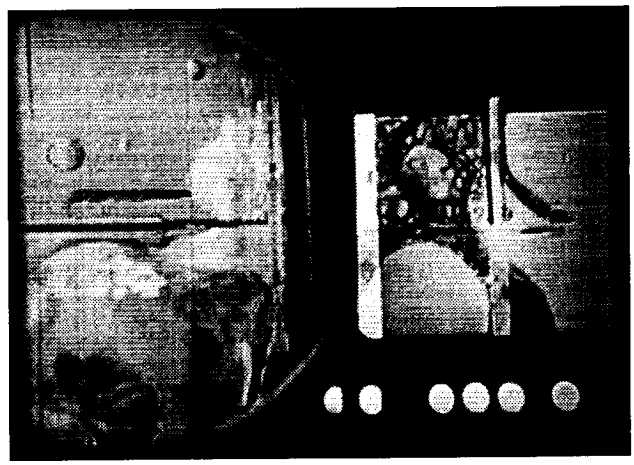

Frame#0742 time=36.98 sec.

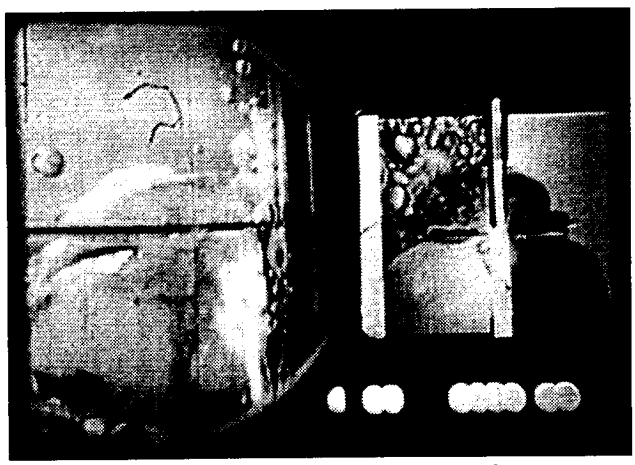

Frame#0859 time=48.67 sec.

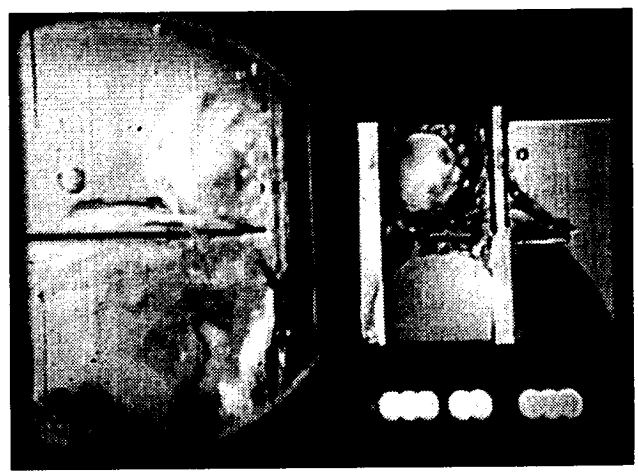

Frame#0970 time=59.77 sec.

Figure A-6a. Continued.

STS-47 Run #2

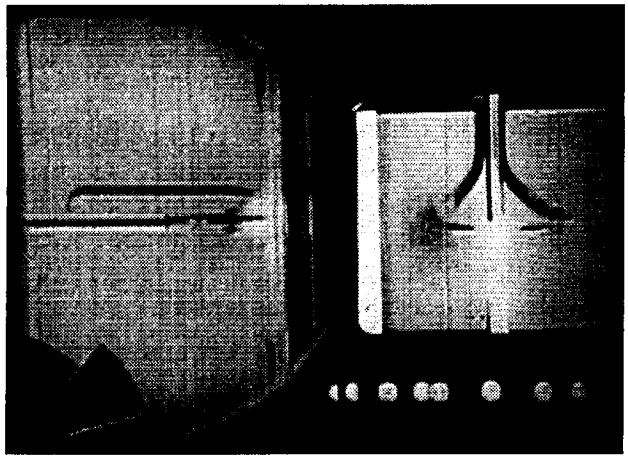

Frame#0783 time=22.38 sec.

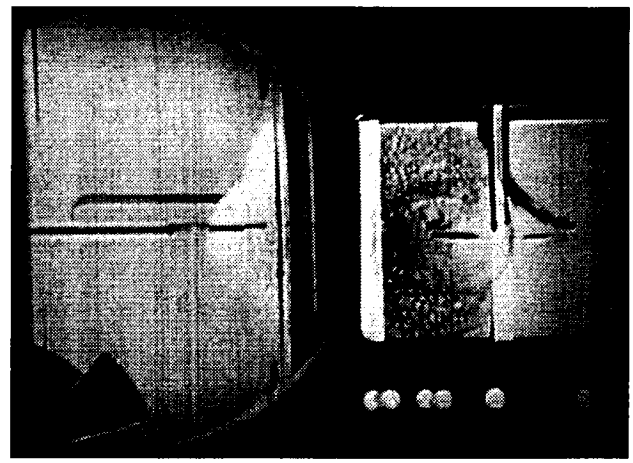

Frame#0784 time=22.39 sec.

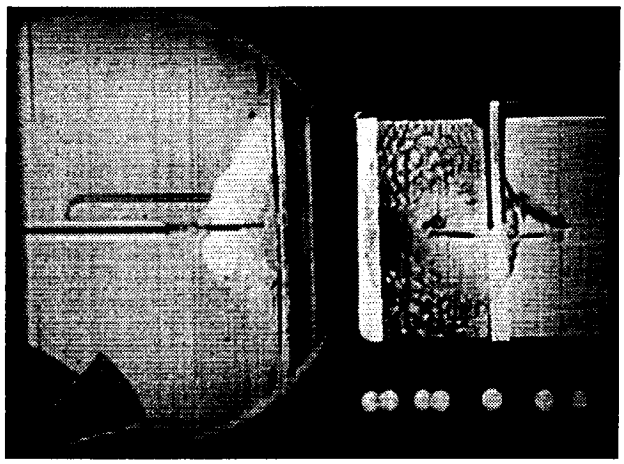

Frame#0785 time=22.40 sec.

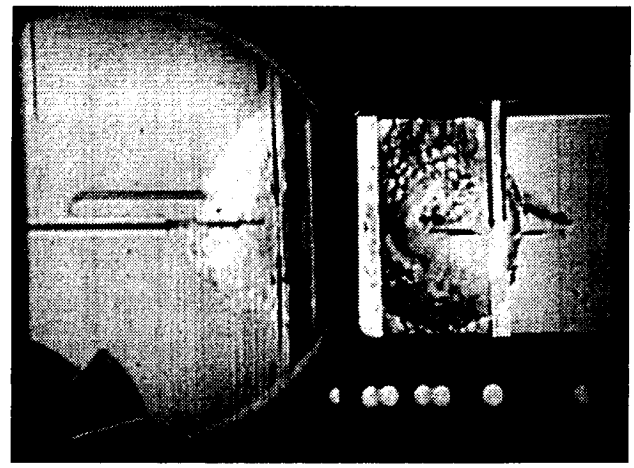

Frame#0786 time=22.41 sec.

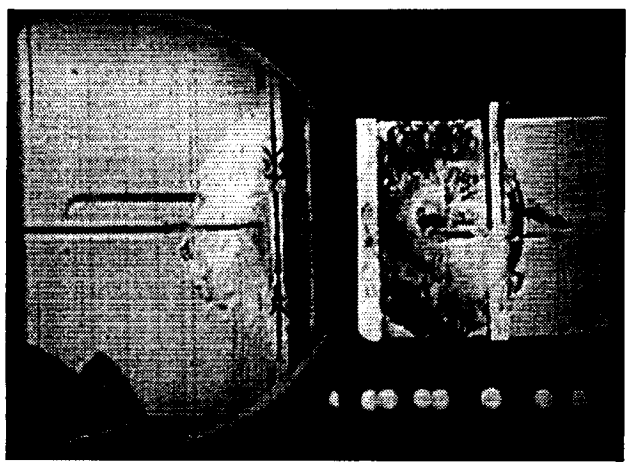

Frame#0787 time=22.42 sec.

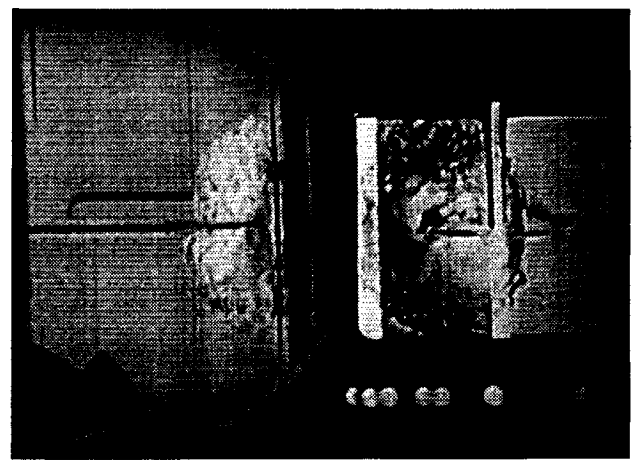

Frame#0788 time=22.43 sec.

Figure A-6b. Selected Photographic Images. PBE-IA (STS-47). Run No. 2.

STS-47 Run #2

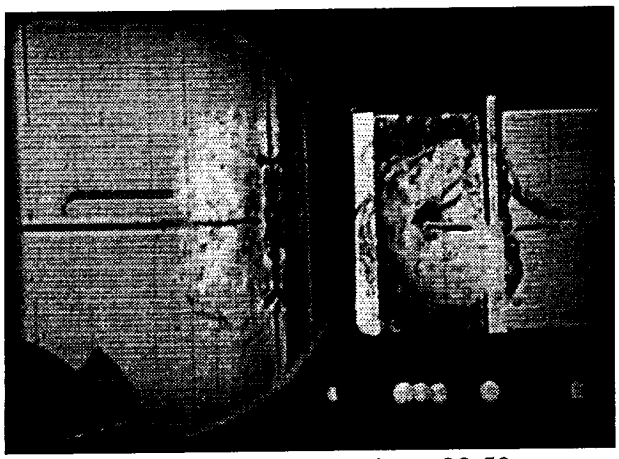

Frame#0795 time=22.50 sec.

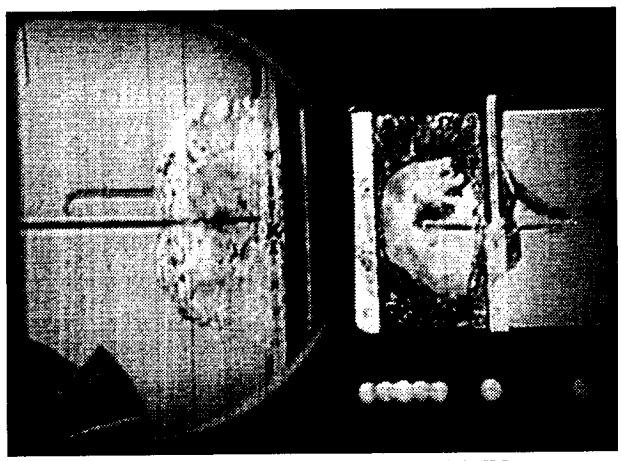

Frame#0817 time=22.72 sec.

Frame#0952 time=24.06 sec.

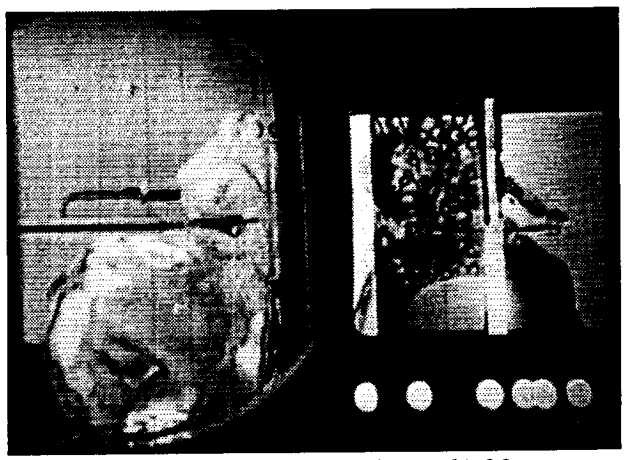

Frame#0385 time=61.93 sec.

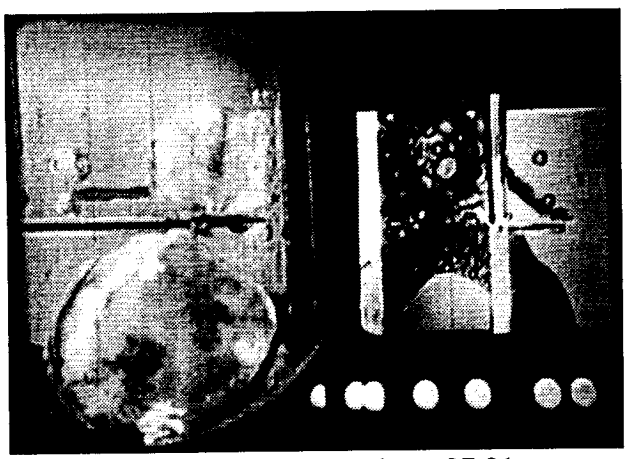

Frame#0744 time=97.81 sec.

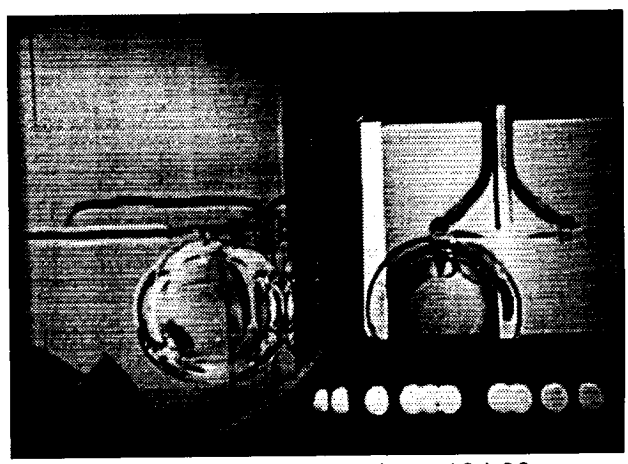

Frame#1016 time=124.99 sec.

Figure A-6b. Continued.

STS-47 Run #3

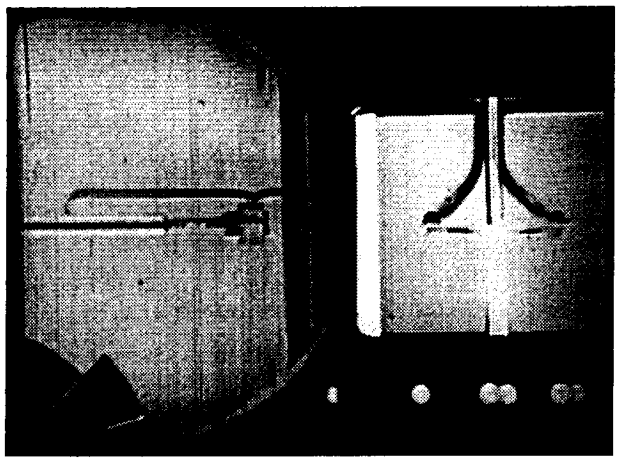

Frame#1233 time=41.39 sec.

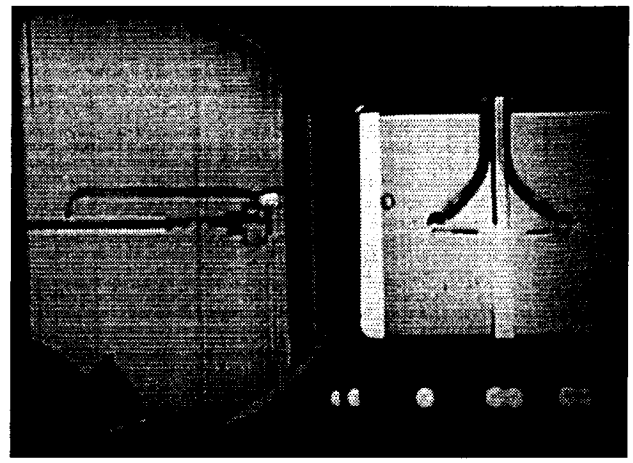

Frame#1236 time=41.42 sec.

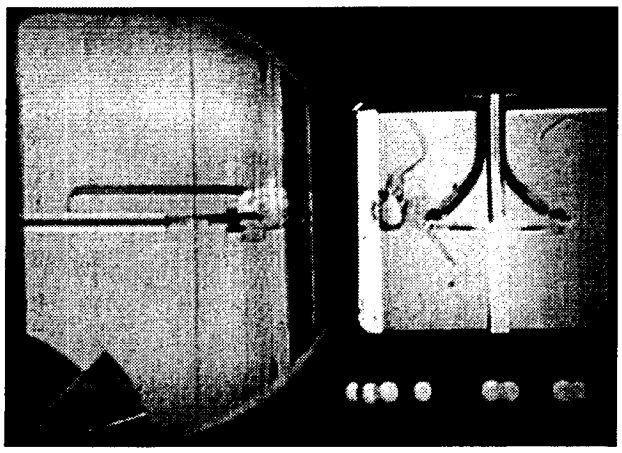

Frame#1258 time=41.64 sec.

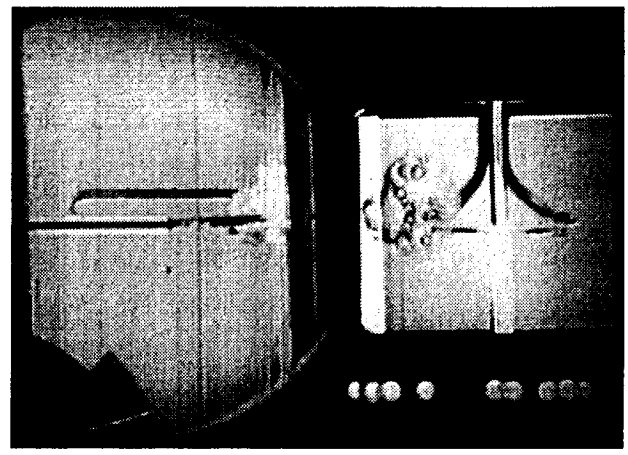

Frame#1259 time=41.65 sec.

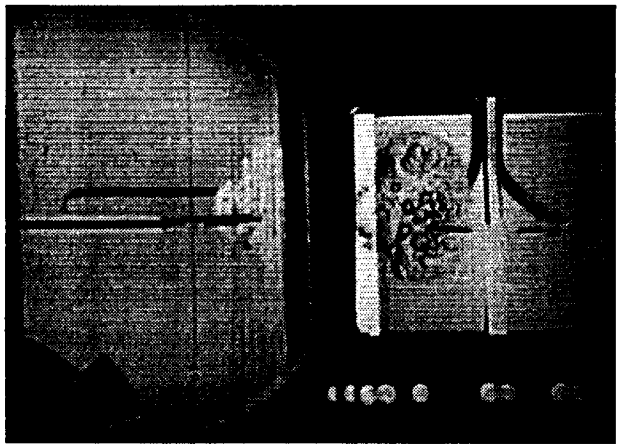

Frame#1260 time=41.66 sec.

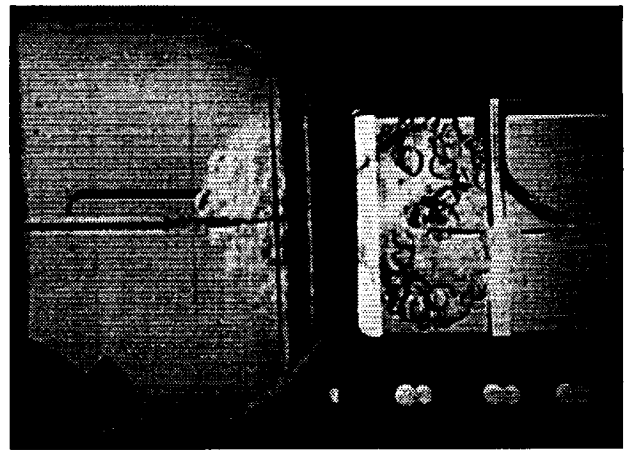

Frame#1264 time=41.70 sec.

Figure A-6c. Selected Photographic Images. PBE-IA (STS-47). Run No. 3.

STS-47 Run #3

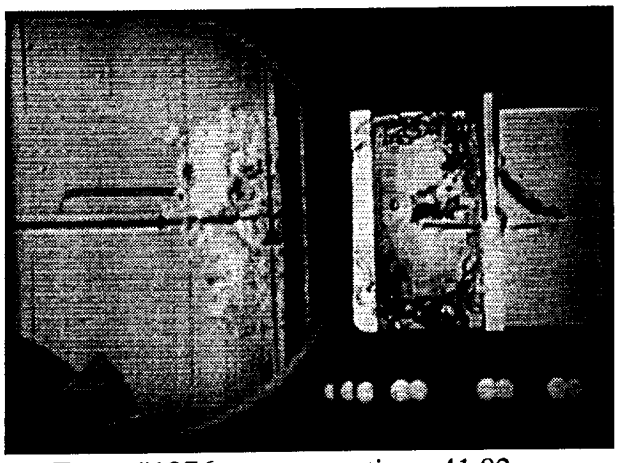

Frame#1276 time=41.82 sec.

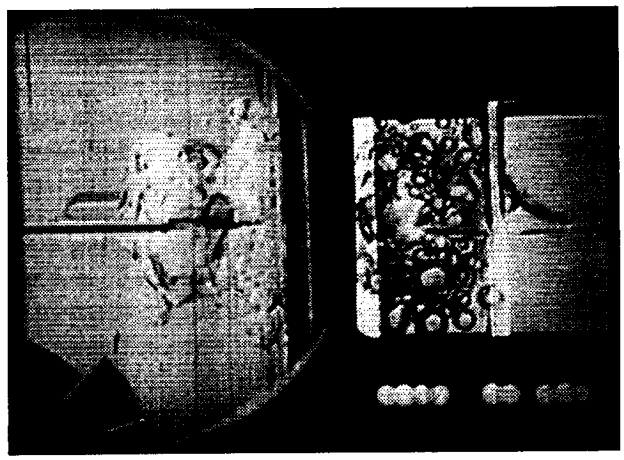

Frame#1408 time=43.13 sec.

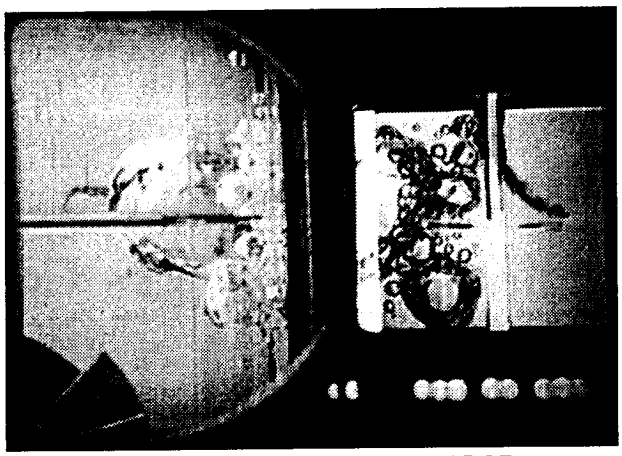

Frame#1623 time=45.27 sec.

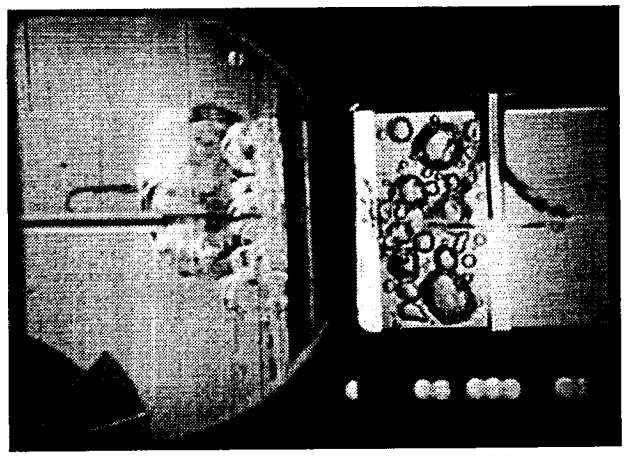

Frame#1877 time=47.80 sec.

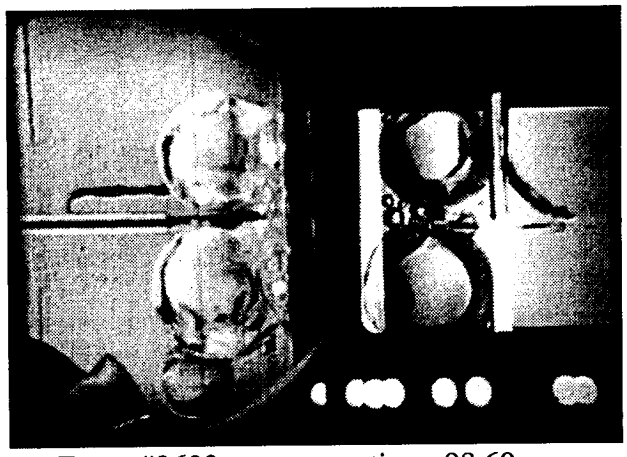

Frame#2603 time=98.60 sec.

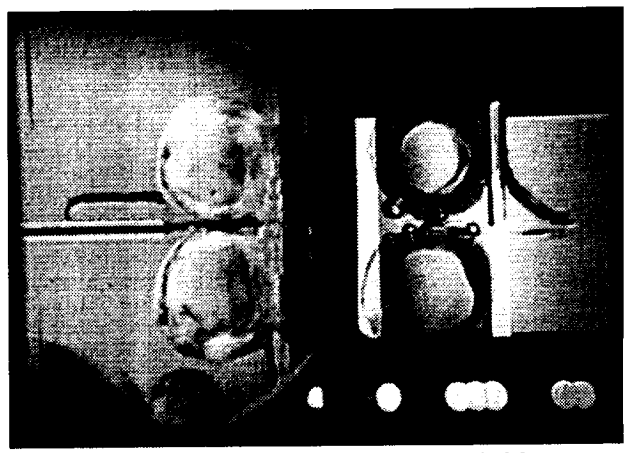

Frame#2717 time=110.00 sec.

Figure A-6c. Continued.

STS-47 Run #4

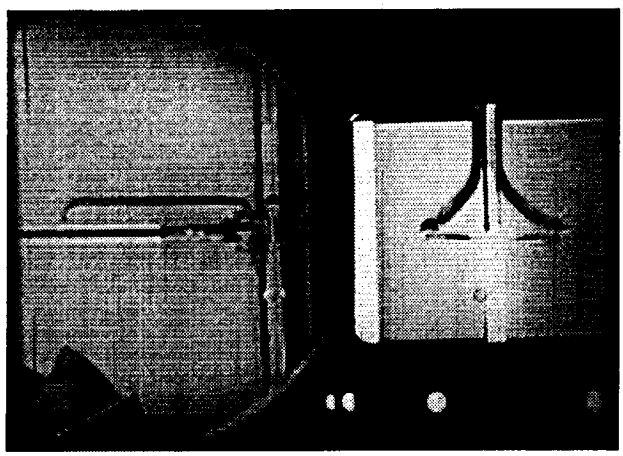

Frame#0134 time=11.34 sec.

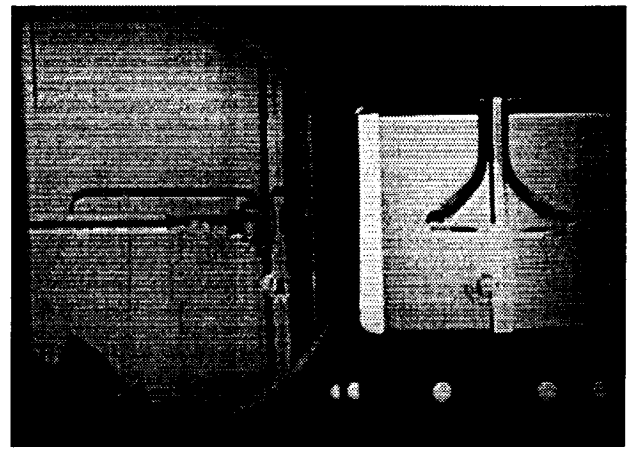

Frame#0135 time=11.35 sec.

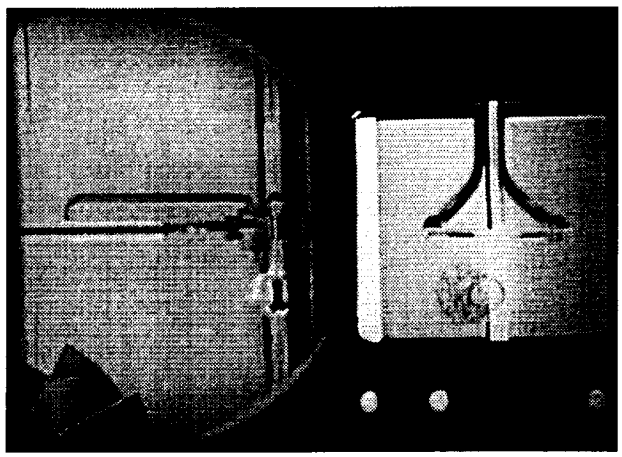

Frame#0136 time=11.36 sec.

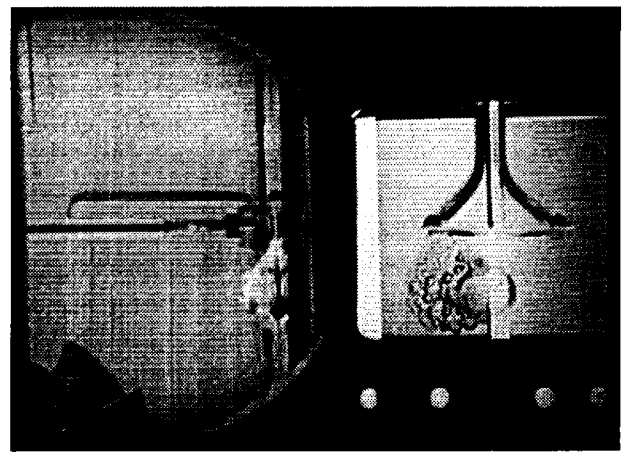

Frame#0137 time=11.37 sec.

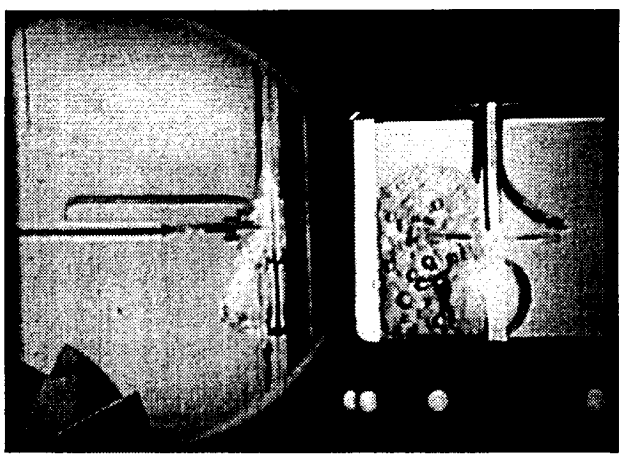

Frame#0140 time=11.40 sec.

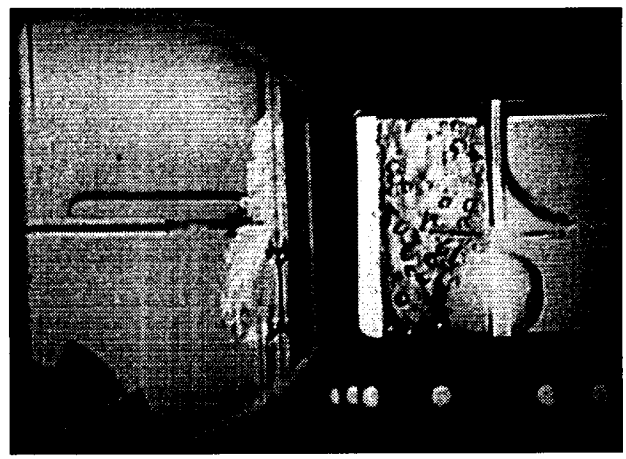

Frame#0143 time=11.43 sec.

Figure A-6d. Selected Photographic Images. PBE-IA (STS-47). Run No. 4.

STS-47 Run #4

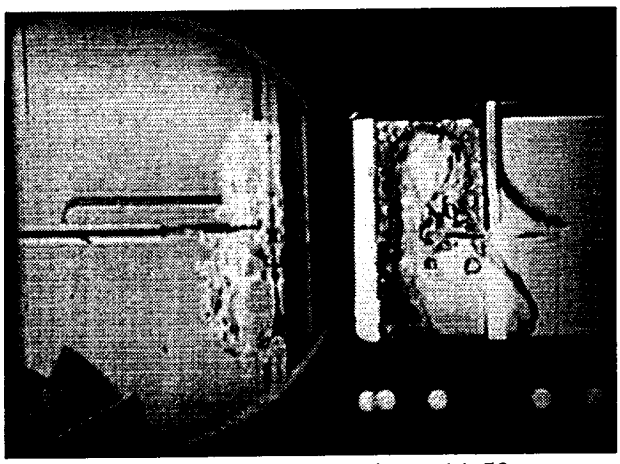

Frame#0153 time=11.53 sec.

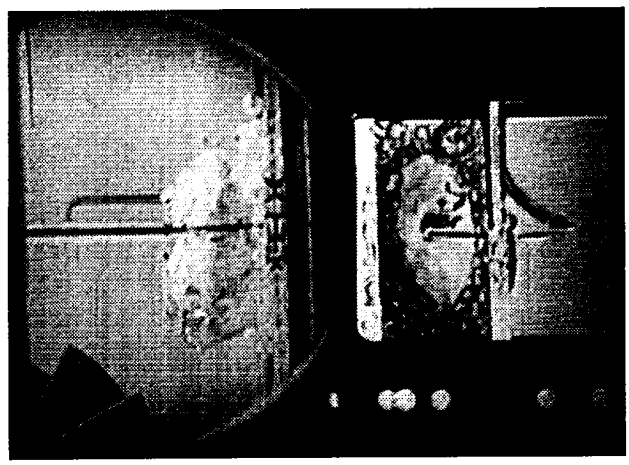

Frame#0179 time=11.79 sec.

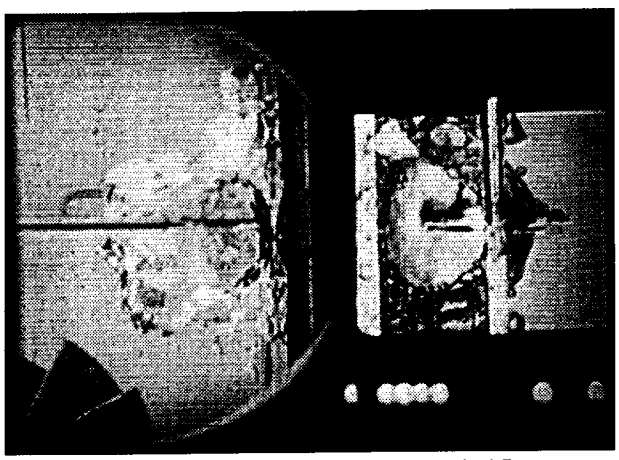

Frame#0245 time=12.45 sec.

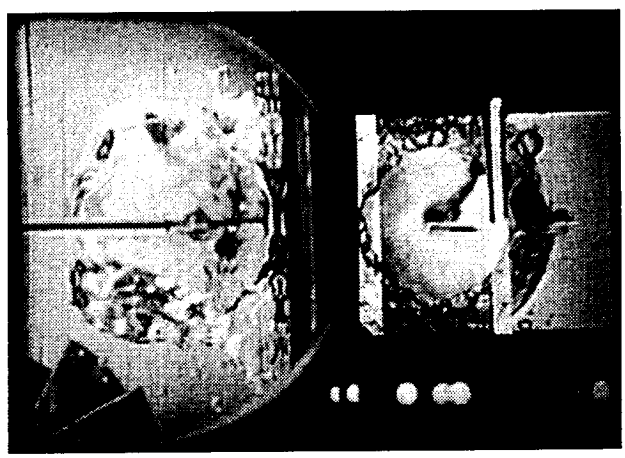

Frame#0423 time=14.22 sec.

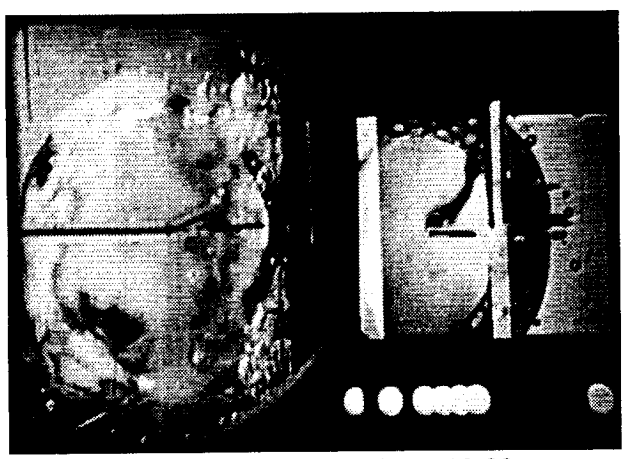

Frame#0567 time=19.82 sec.

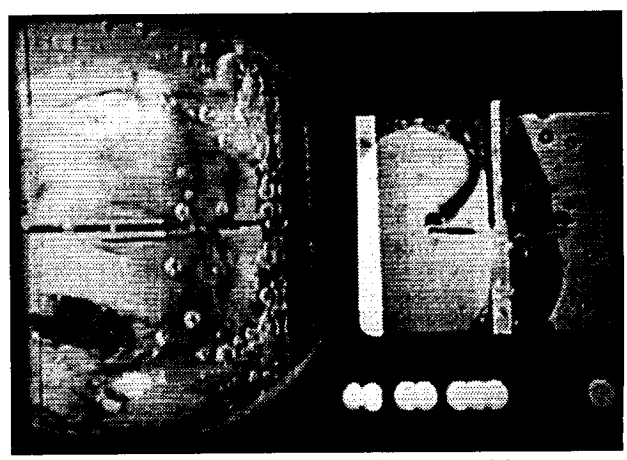

Frame#0092 time=29.00 sec.

Figure A-6d. Continued.

STS-47 Run #5

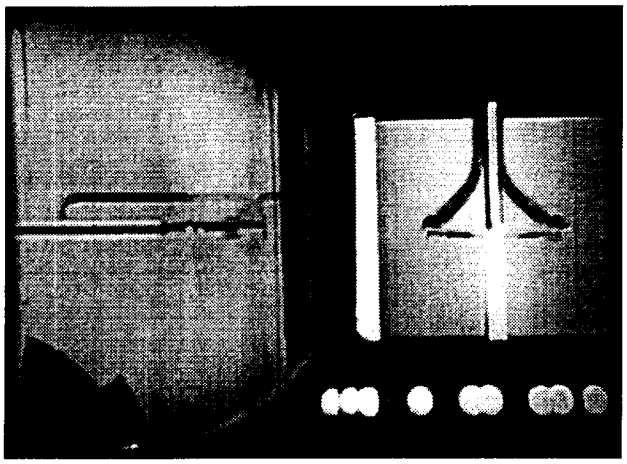

Frame#2098 time=26.15 sec.

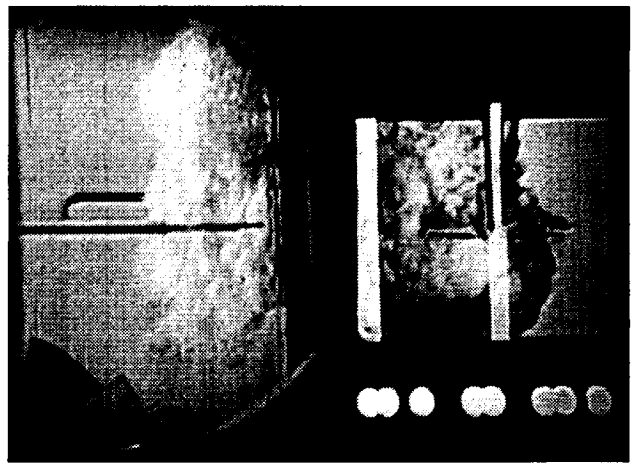

Frame#2099 time=26.25 sec.

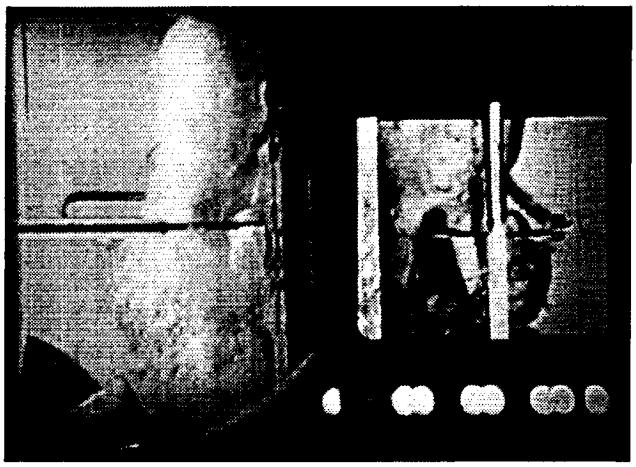

Frame#2100 time=26.35 sec.

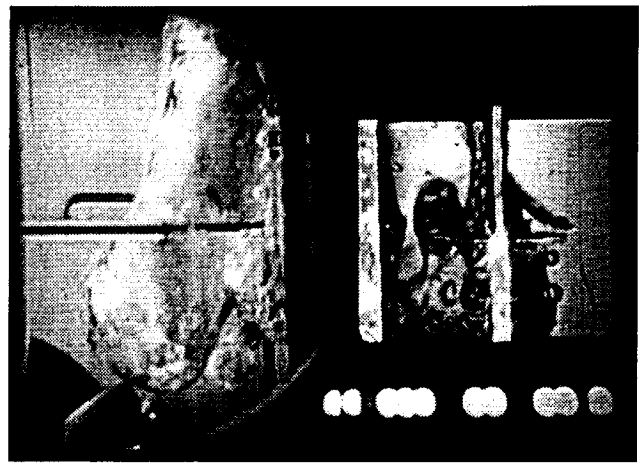

Frame#2102 time=26.55 sec.

Frame#2104 time=26.75 sec.

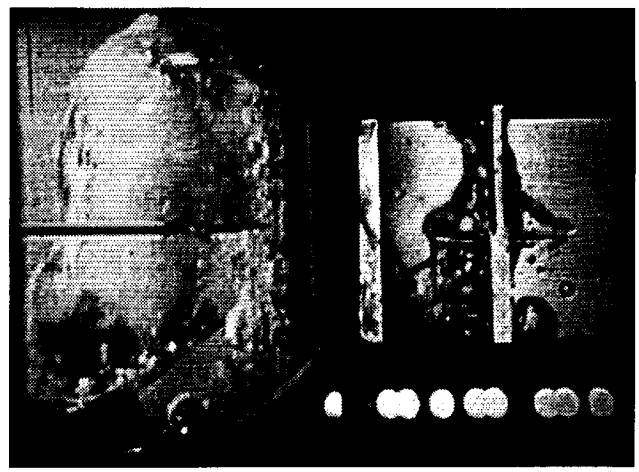

Frame#2108 time=27.15 sec.

Figure A-6e. Selected Photographic Images. PBE-IA (STS-47). Run No. 5.

STS-47 Run #5

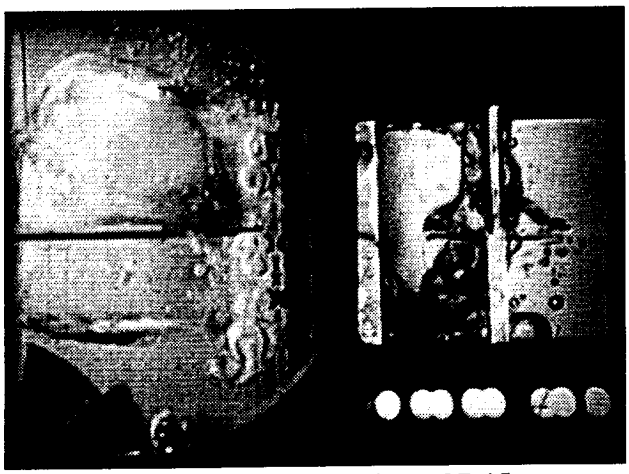

Frame#2111 time=27.45 sec.

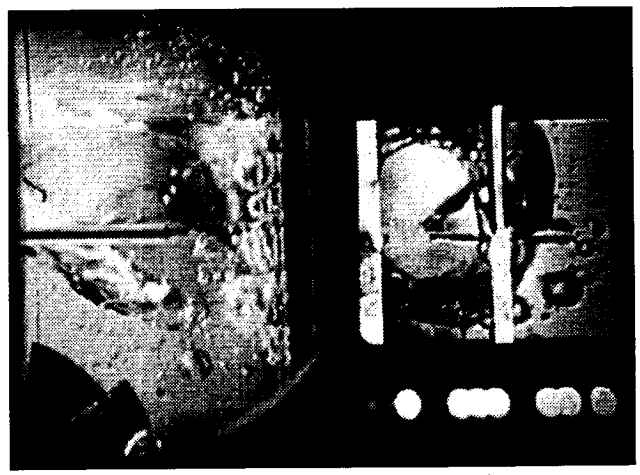

Frame#2119 time=28.25 sec.

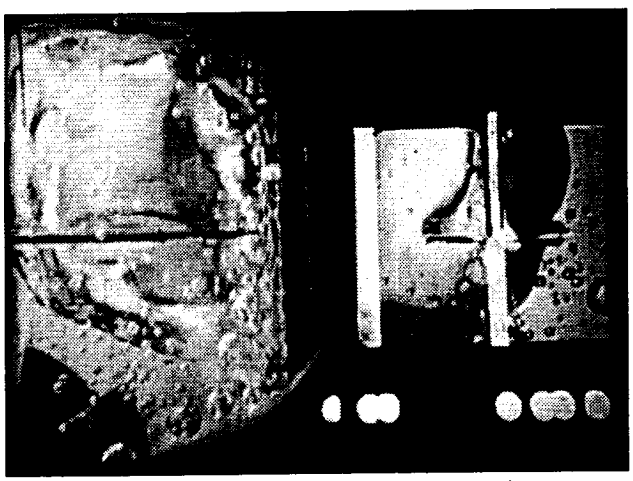

Frame#2144 time=30.75 sec.

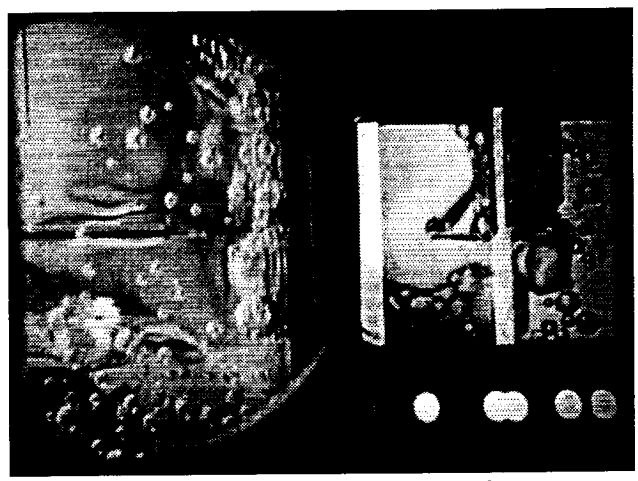

Frame#2250 time=41.36 sec.

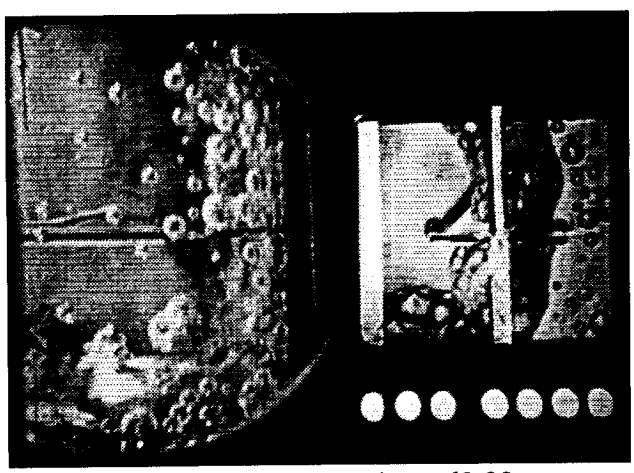

Frame#2465 time=62.88 sec.

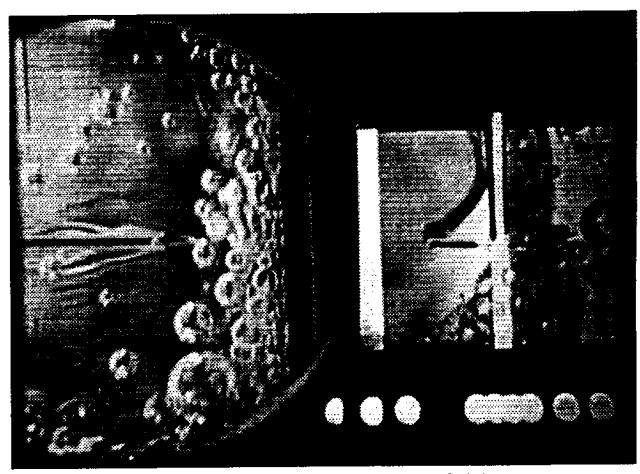

Frame#2708 time=86.22 sec.

Figure A-6e. Continued.

STS-47 Run #6

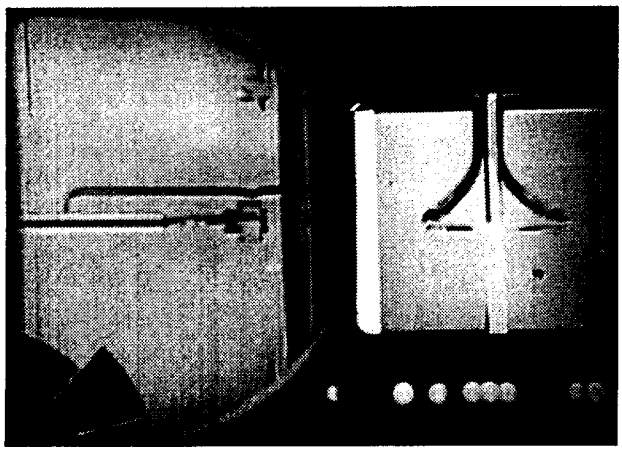

Frame#1843 time=47.46 sec.

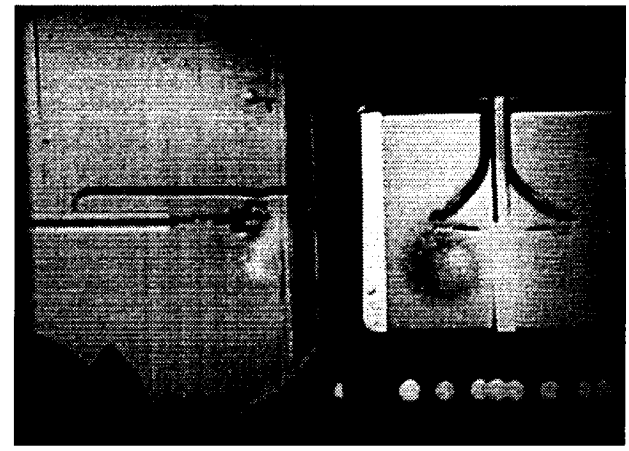

Frame#1844 time=47.47 sec.

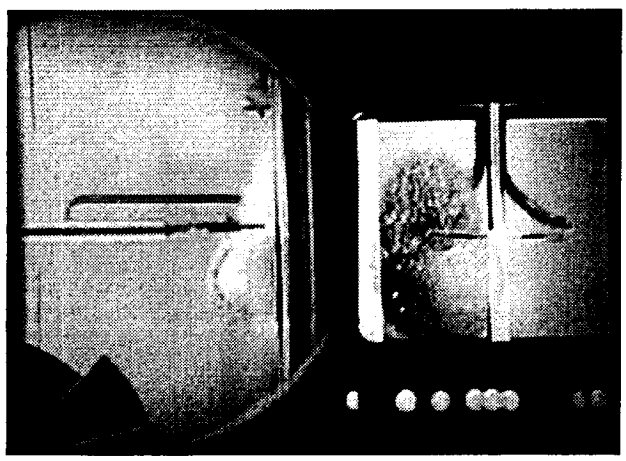

Frame#1845 time=47.48 sec.

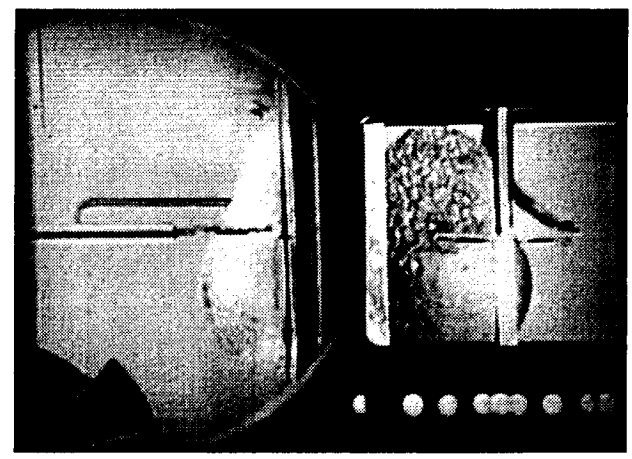

Frame#1846 time=47.49 sec.

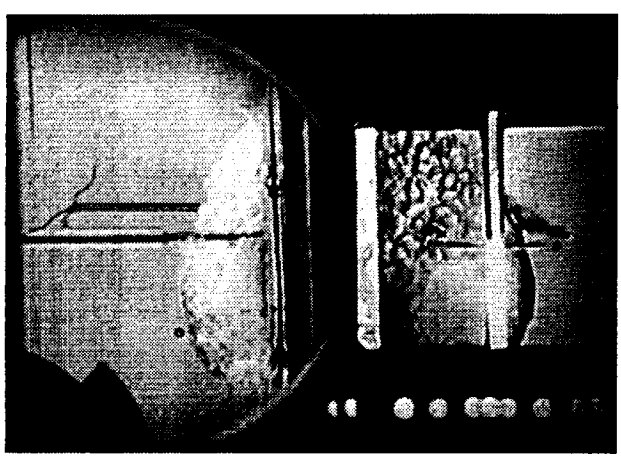

Frame#1848 time=47.51 sec.

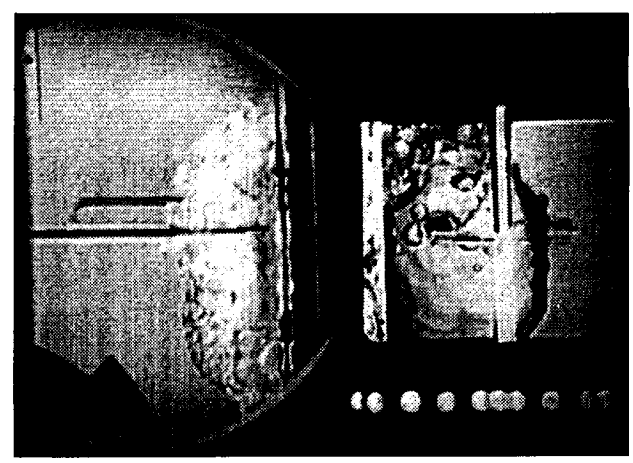

Frame#1854 time=47.57 sec.

Figure A-6f. Selected Photographic Images. PBE-IA (STS-47). Run No. 6.

STS-47 Run #6

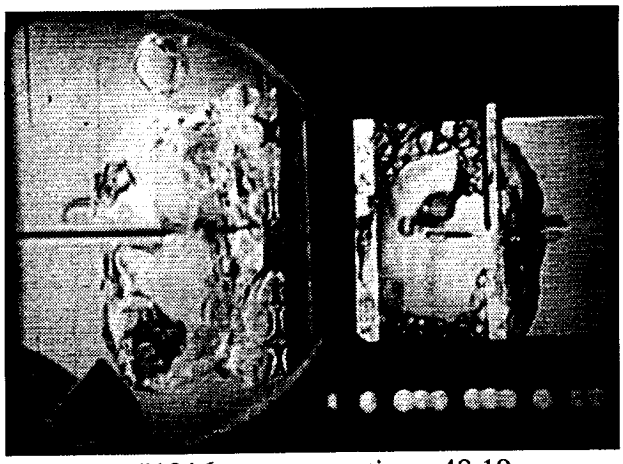

Frame#1916 time=48.19 sec.

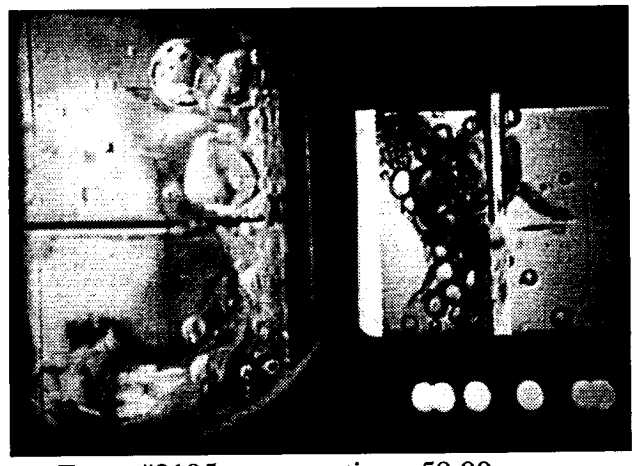

Frame#2195 time=58.00 sec.

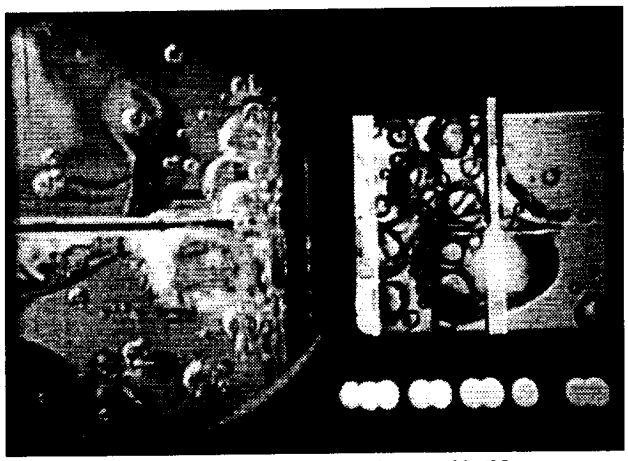

Frame#2300 time=68.52 sec.

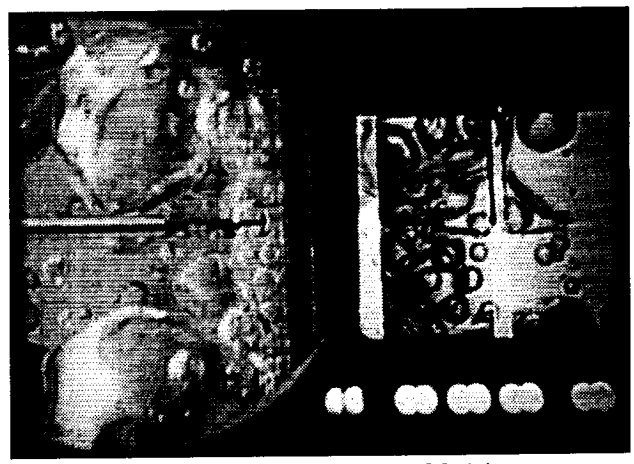

Frame#2416 time=80.14 sec.

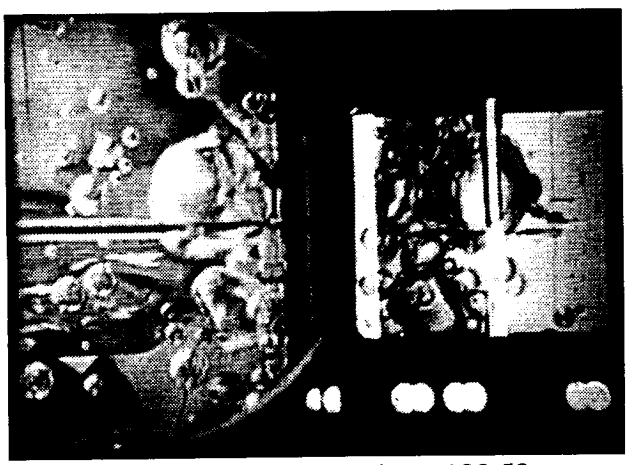

Frame#2620 time=100.58 sec.

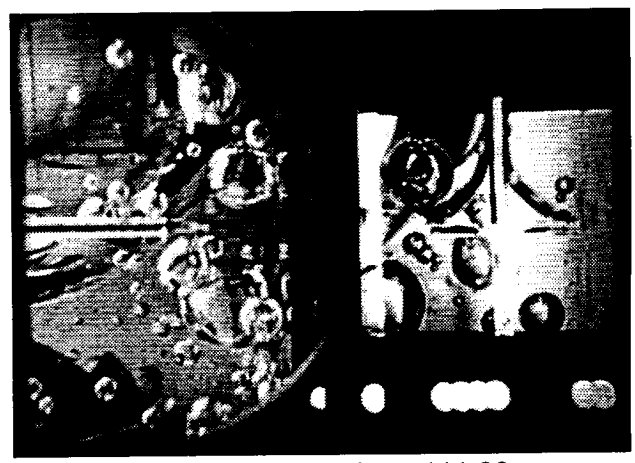

Frame#2726 time=111.20 sec.

Figure A-6f. Continued.

STS-47 Run #7

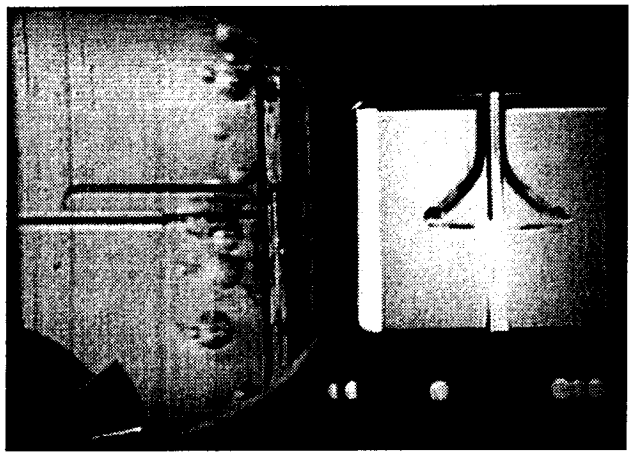

Frame#0164 time=11.34 sec.

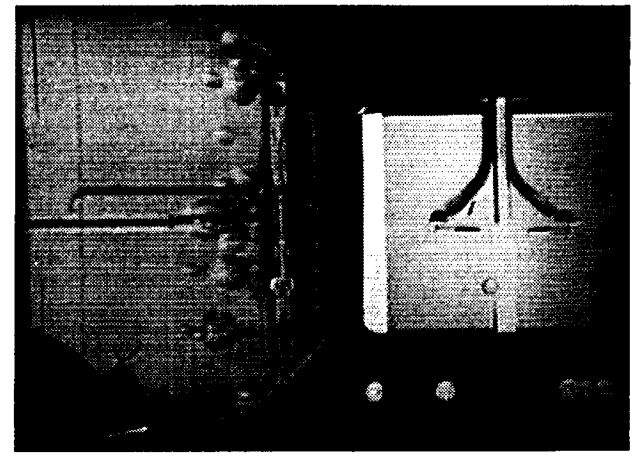

Frame#0166 time=11.36 sec.

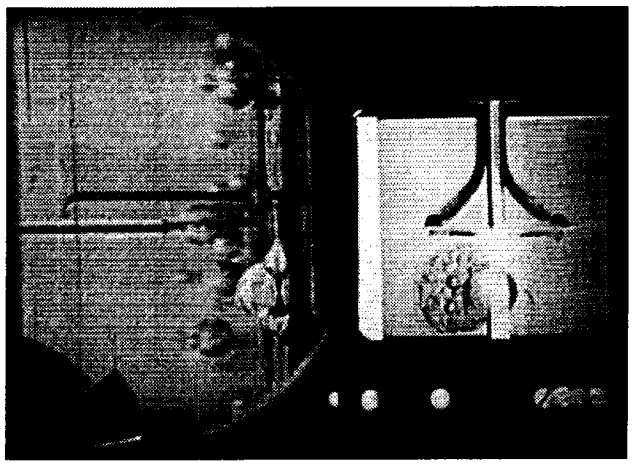

Frame#0169 time=11.39 sec.

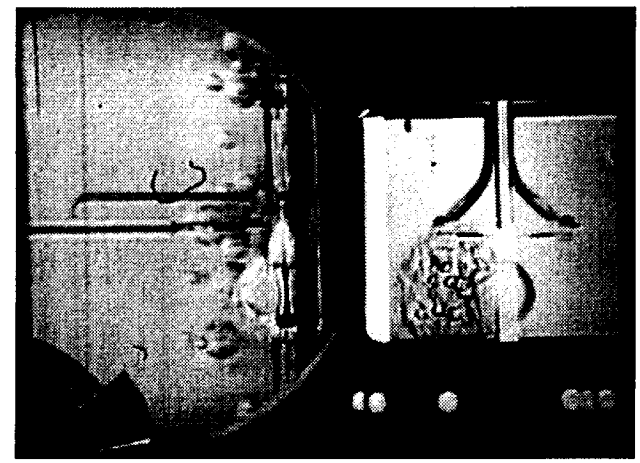

Frame#0170 time=11.40 sec.

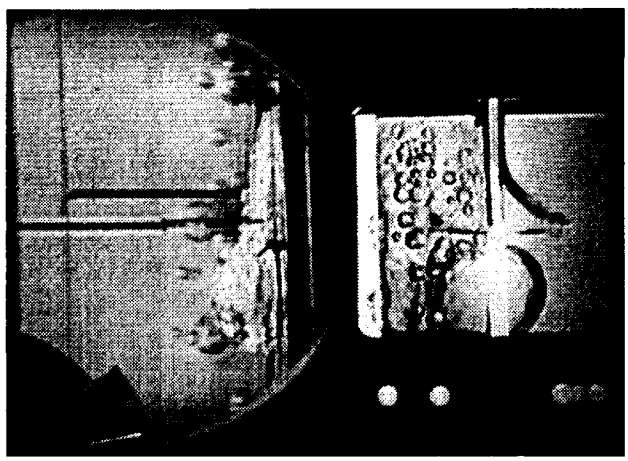

Frame#0174 time=11.44 sec.

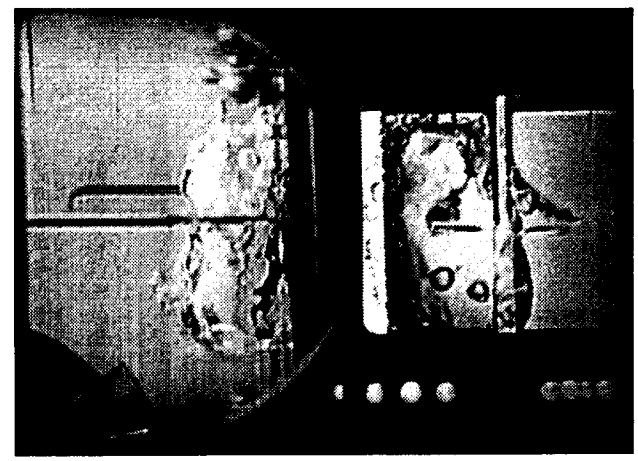

Frame#0201 time=11.71 sec.

Figure A-6g. Selected Photographic Images. PBE-IA (STS-47). Run No. 7.

STS-47 Run #7

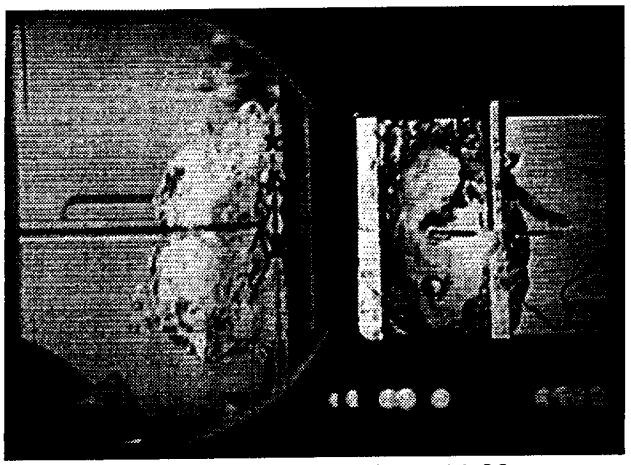

Frame#0213 time=11.83 sec.

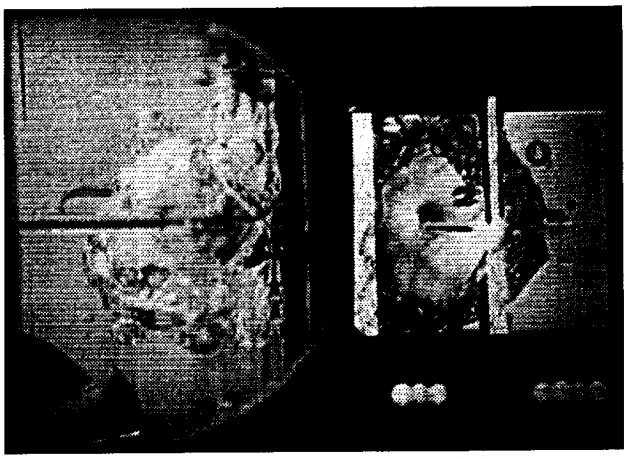

Frame#0256 time=12.24 sec.

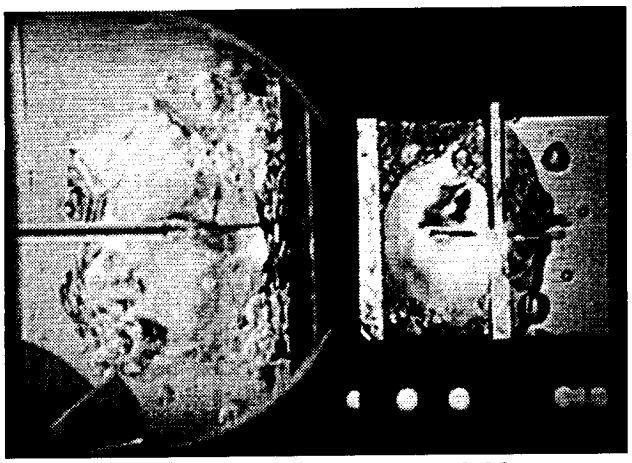

Frame#0323 time=12.92 sec.

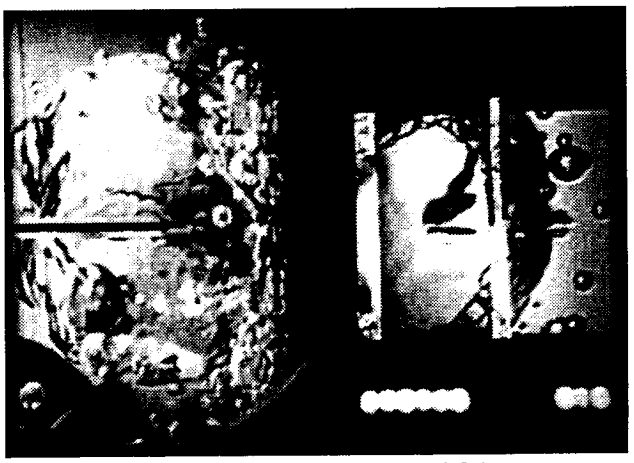

Frame#0536 time=15.04 sec.

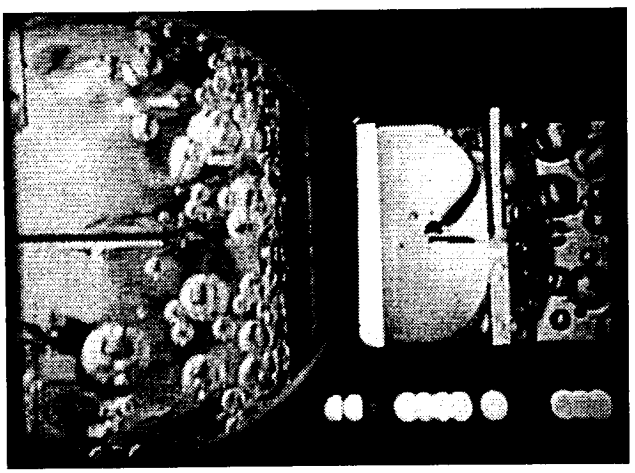

Frame#0650 time=25.10 sec.

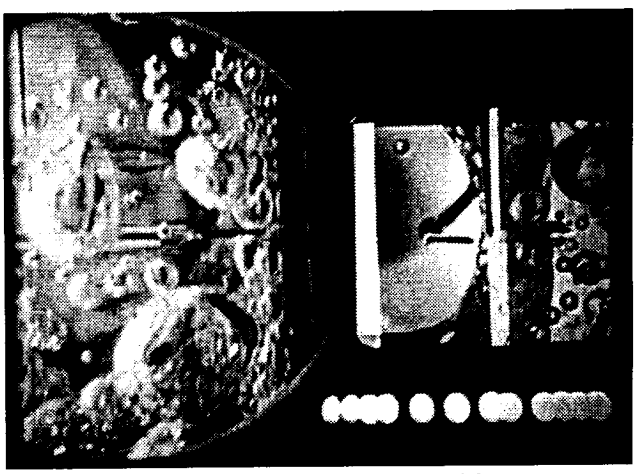

Frame#0841 time=44.23 sec.

Figure A-6g. Continued.

STS-47 Run #8

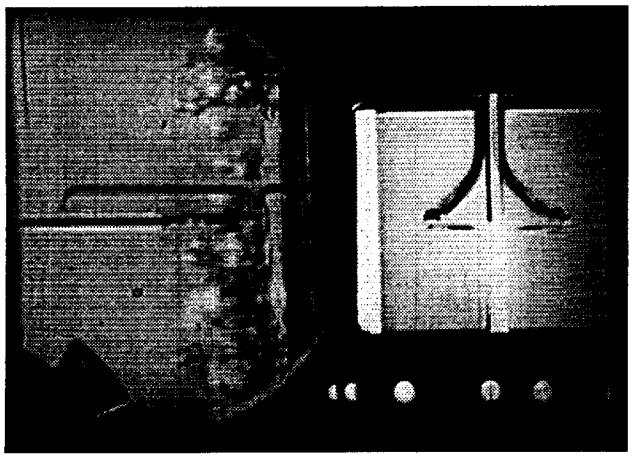

Frame#0611 time=20.63 sec.

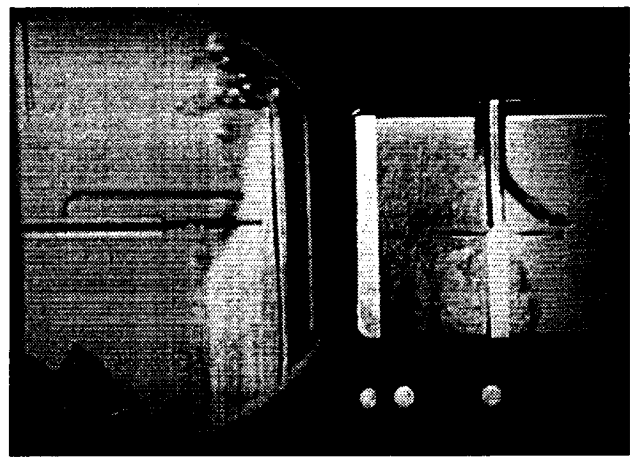

Frame#0612 time=20.64 sec.

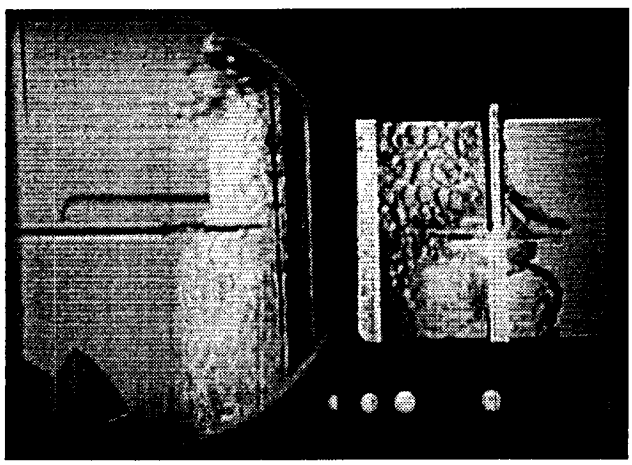

Frame#0614 time=20.66 sec.

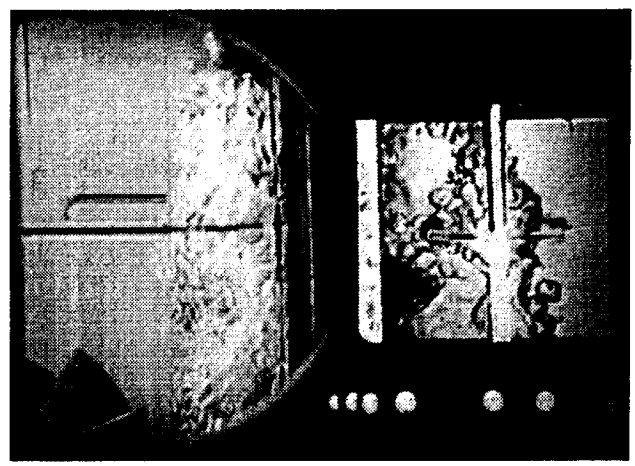

Frame#0619 time=20.71 sec.

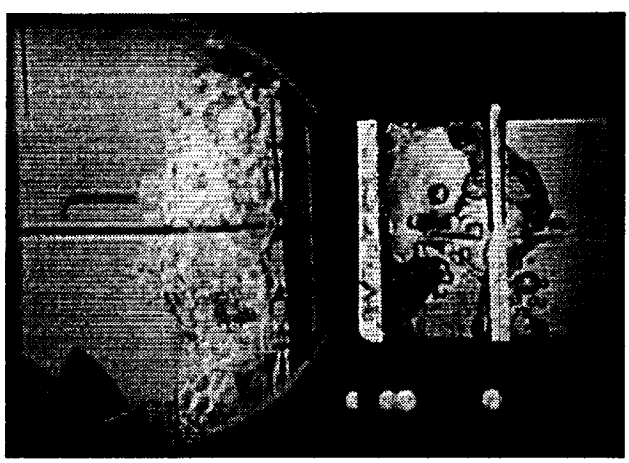

Frame#0624 time=20.76 sec.

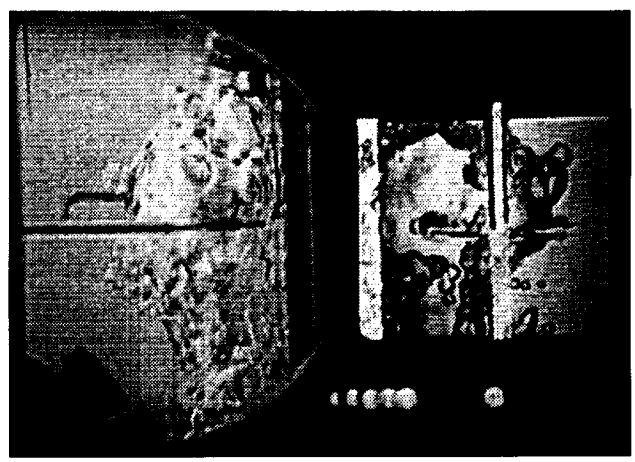

Frame#0634 time=20.86 sec.

Figure A-6h. Selected Photographic Images. PBE-IA (STS-47). Run No. 8.

STS-47 Run #8

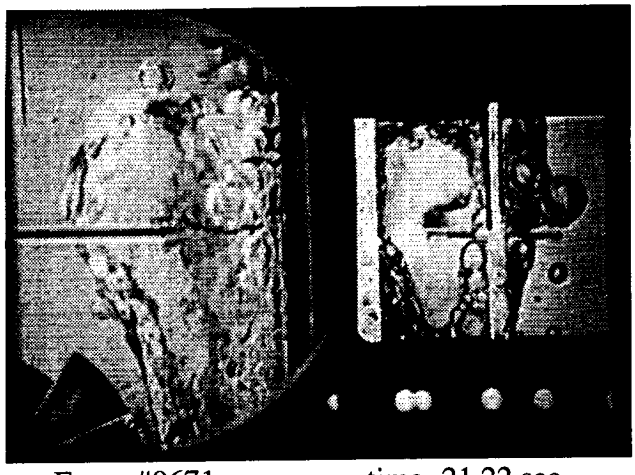

Frame#0671 time=21.22 sec.

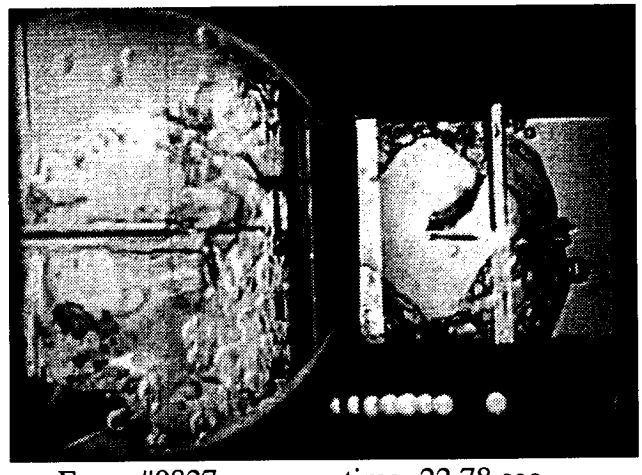

Frame#0827 time=22.78 sec.

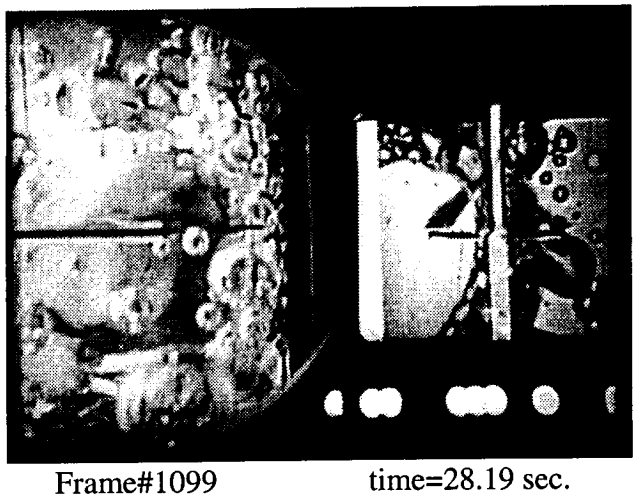

Frame#1099 time=28.19 sec.

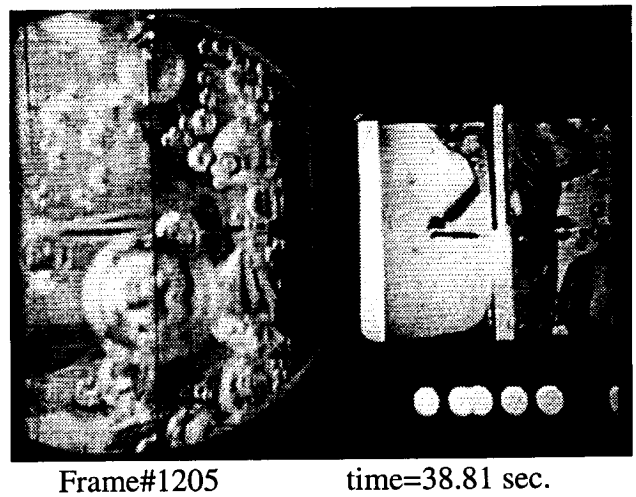

Frame#1205 time=38.81 sec.

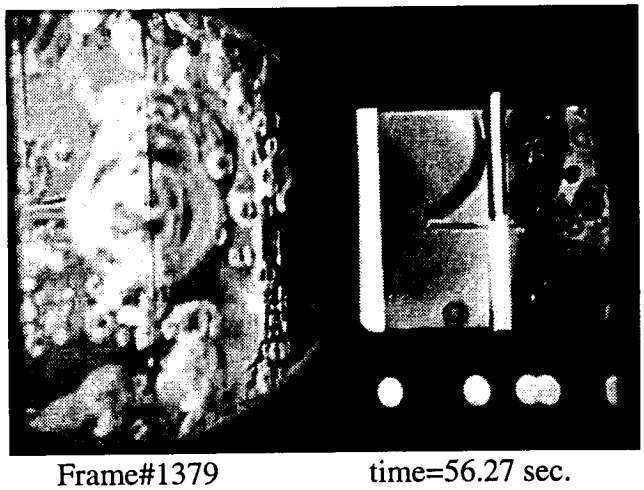

Frame#1379 time=56.27 sec.

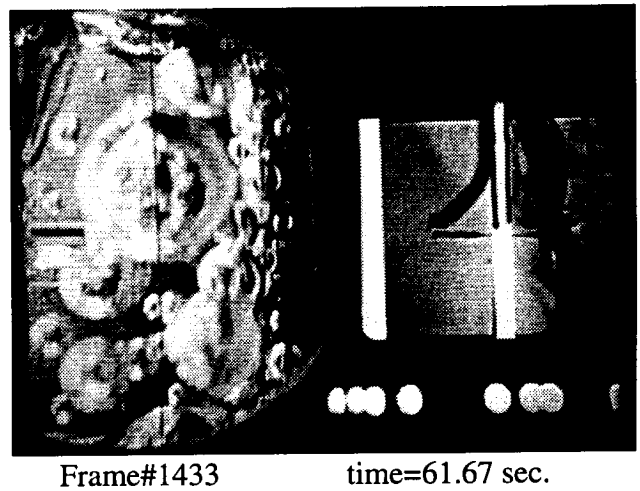

Frame#1433 time=61.67 sec.

Figure A-6h. Continued.

STS-47 Run #9

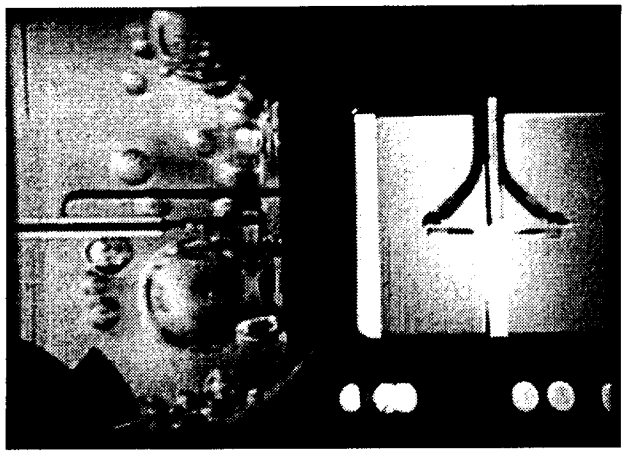

Frame#2229 time=51.48 sec.

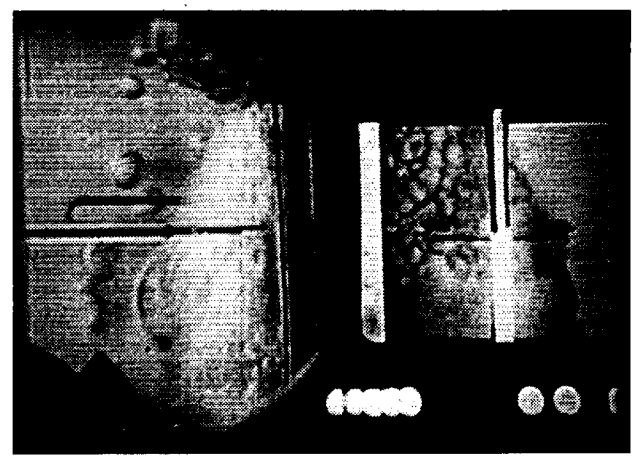

Frame#2230 time=51.58 sec.

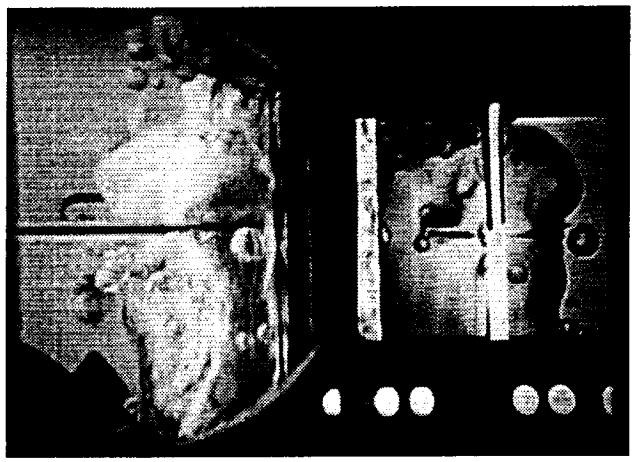

Frame#2232 time=51.78 sec.

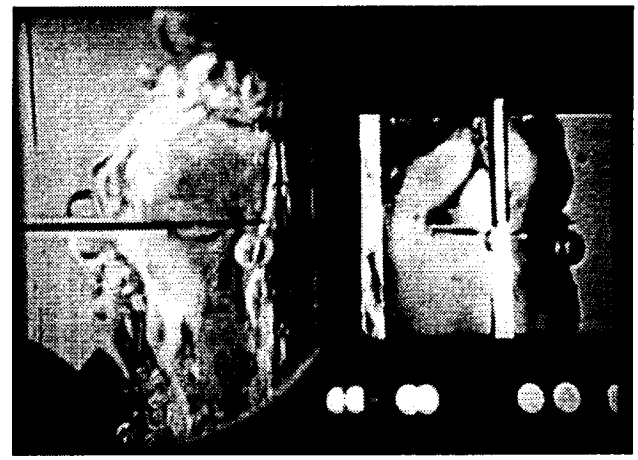

Frame#2234 time=51.98 sec.

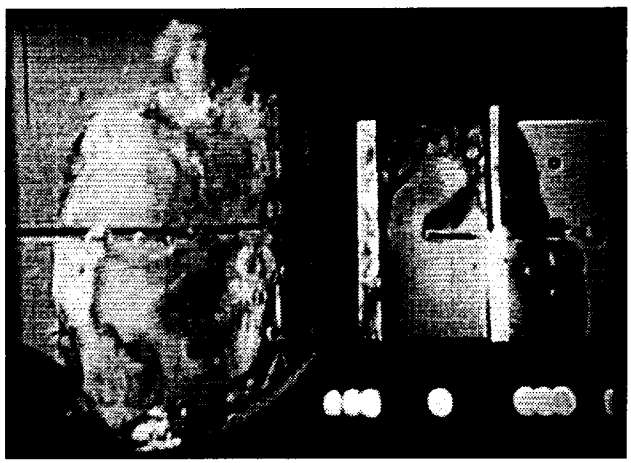

Frame#2238 time=52.39 sec.

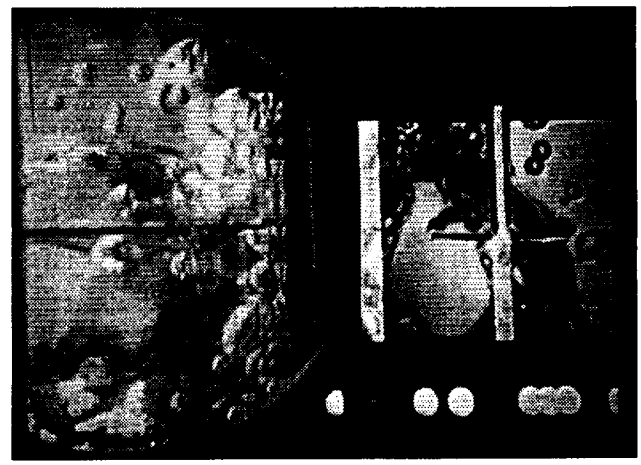

Frame#2256 time=54.19 sec.

Figure A-6i. Selected Photographic Images. PBE-IA (STS-47). Run No. 9.

STS-47 Run #9

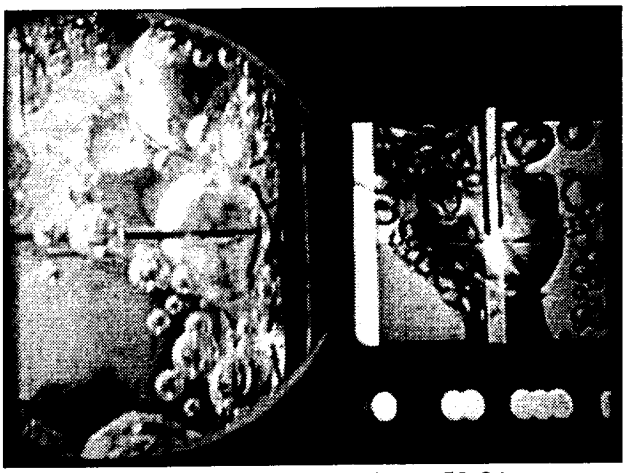

Frame#2302 time=58.81 sec.

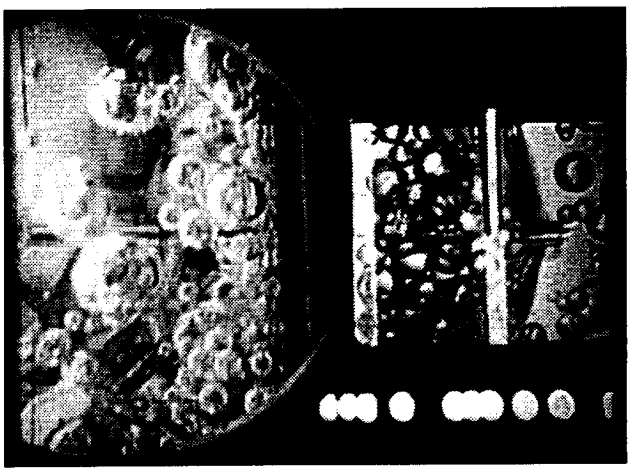

Frame#2407 time=69.34 sec.

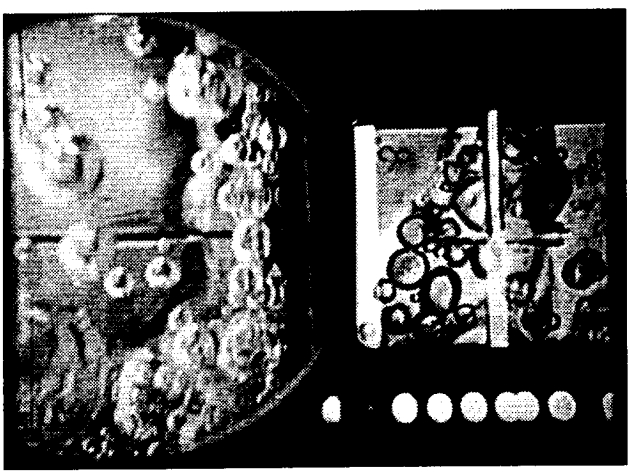

Frame#2495 time=78.18 sec.

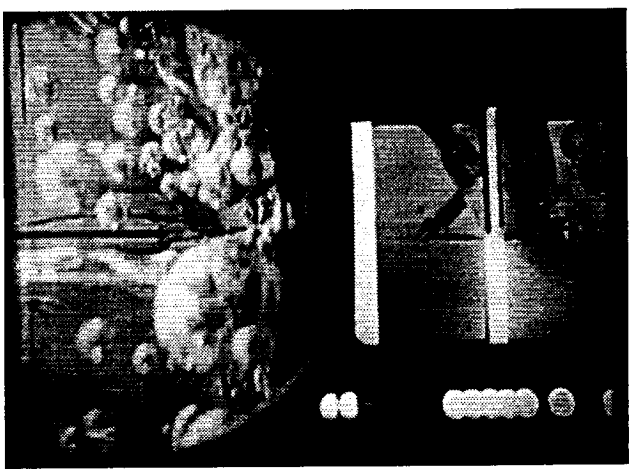

Frame#2607 time=89.42 sec.

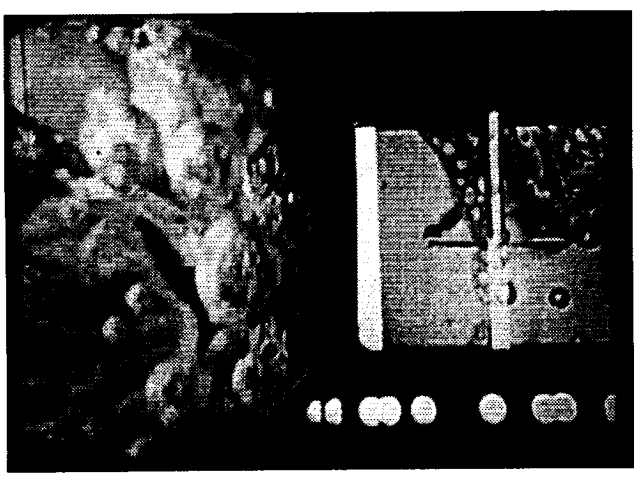

Frame#2743 time=103.07 sec.

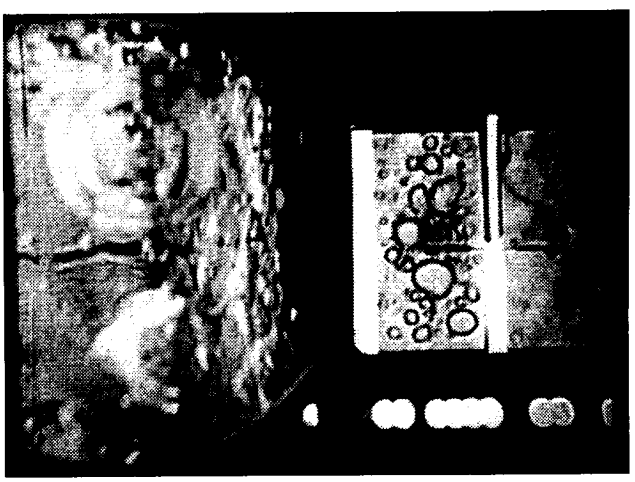

Frame#2828 time=111.63 sec.

Figure A-6i. Continued.

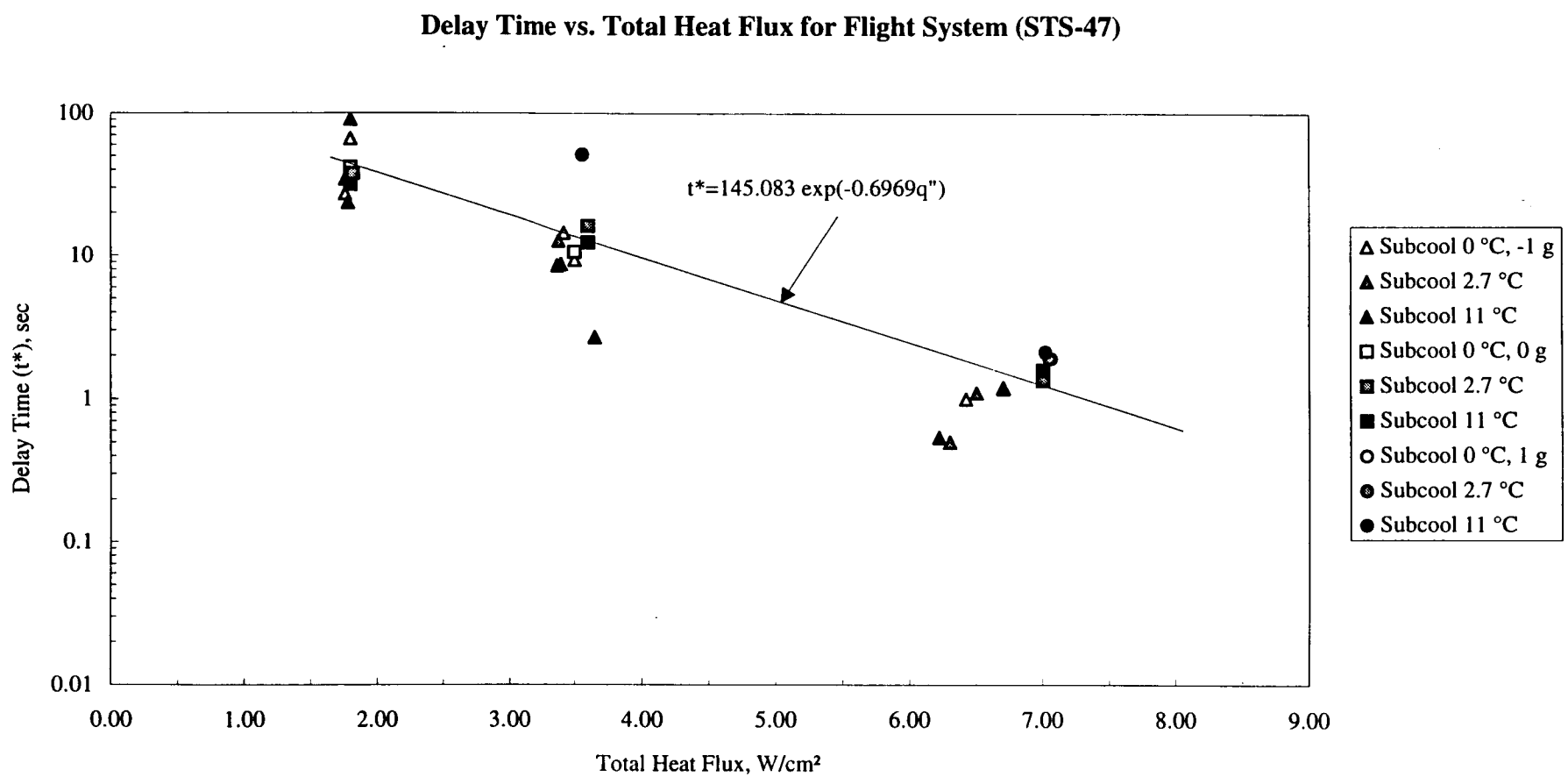

Figure A-7. Nucleation Delay Time. Comparisons with ground testing and drop tower correlation. PBE-IA (STS-47).

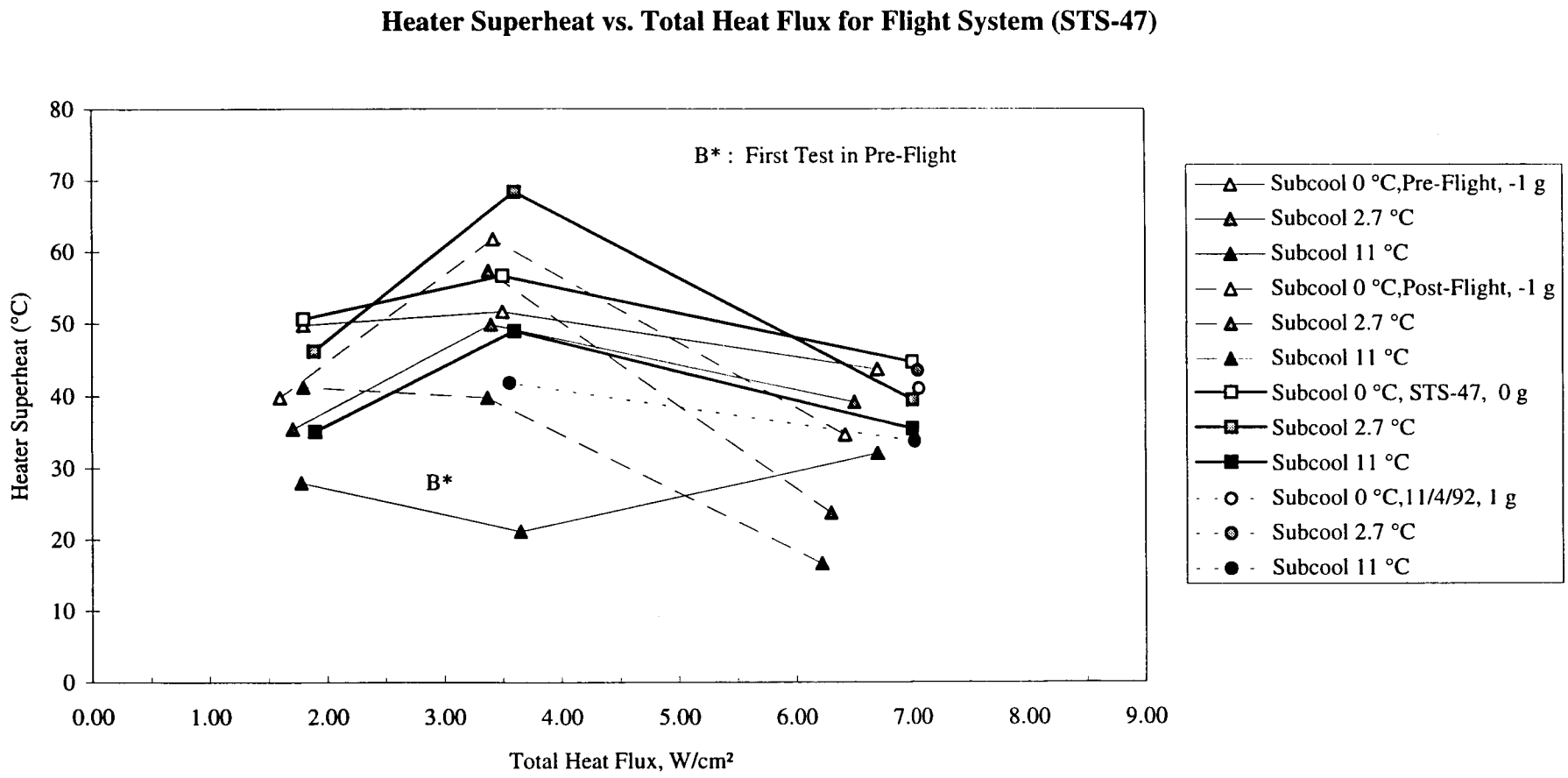

Figure A-8. Mean heater surface nucleation superheat. Comparisons with ground testing. PBE-IA (STS-47).

Comparison of Numerical Computation of Bubble growth with Experiment and Temperature Profile at Nucleation for STS-47 Run #1 (q"=7 W/cm²; T_{sat}=59.72 °C; P=149 kPa;ΔT_{sub}=10.28 °C; t*=1.58 sec)

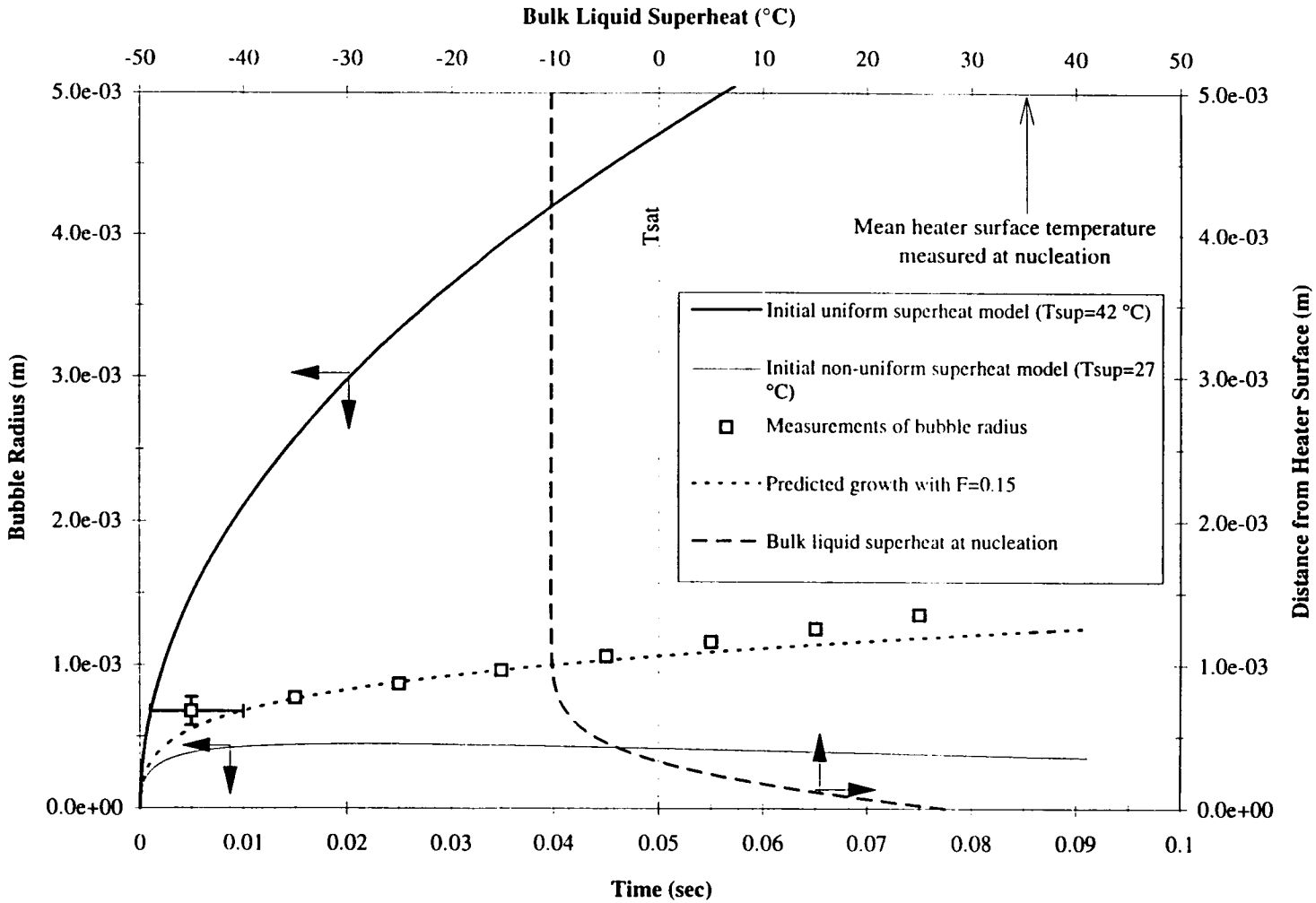

Figure A-9a. Comparisons of bubble growth measurements with several models. PBE-IA (STS-47). Run No. 1.

Comparison of Numerical Computation of Bubble growth with Experiment and Temperature Profile at Nucleation for STS-47 Run #2 (q"=3.6 W/cm²; T_{sat}=61.1 °C; P=154.4 kPa; ΔTsub=11.9 °C; t*=12.38 sec)

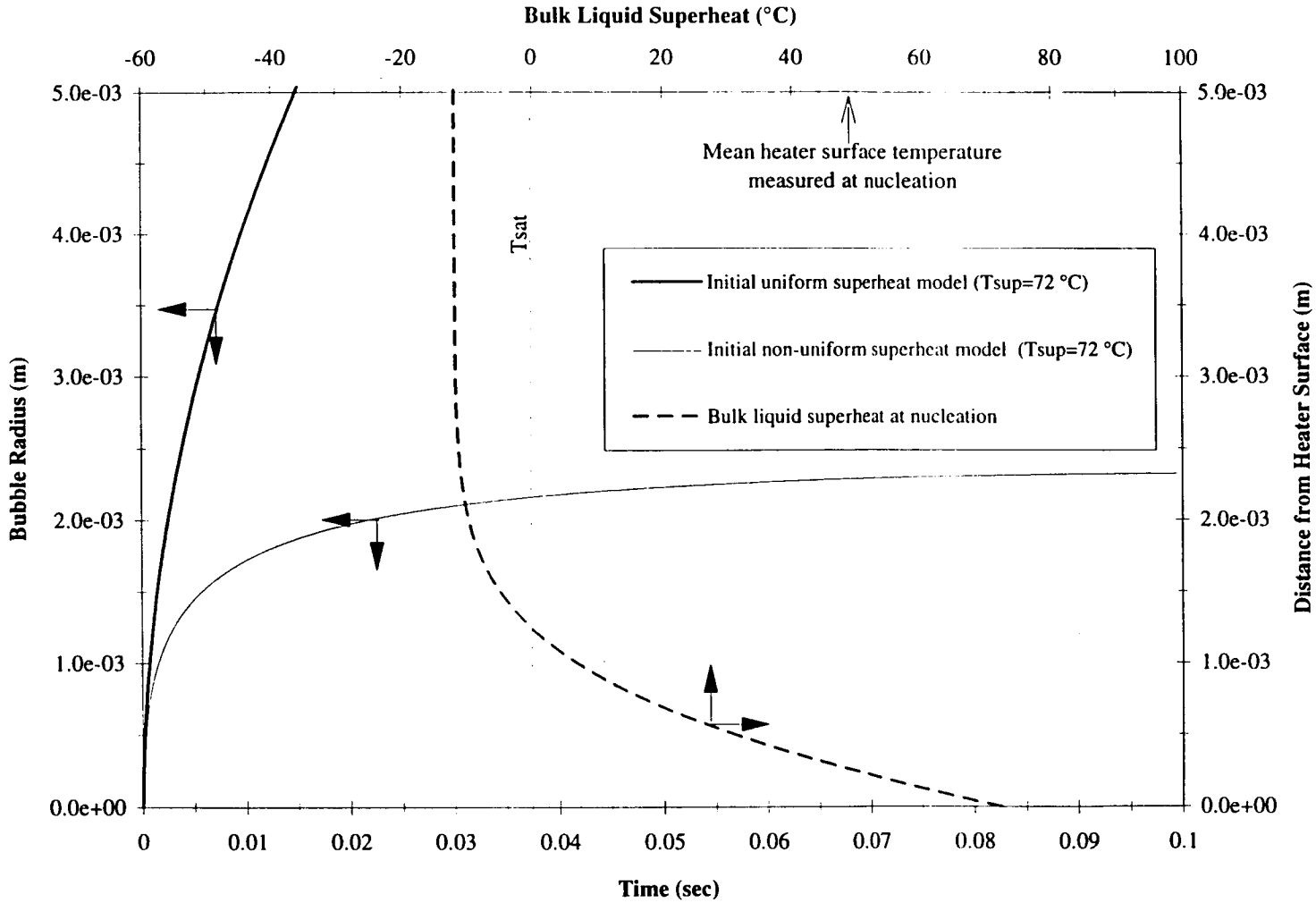

Figure A-9b. Comparisons of bubble growth measurements with several models. PBE-IA (STS-47). Run No. 2.

Comparison of Numerical Computation of Bubble growth with Experiment and Temperature Profile at Nucleation for STS-47 Run #3 (q"=1.8 W/cm²; T_{sat}=60.0 °C; P=151 kPa; ΔTsub=10.9 °C; t*=31.39 sec)

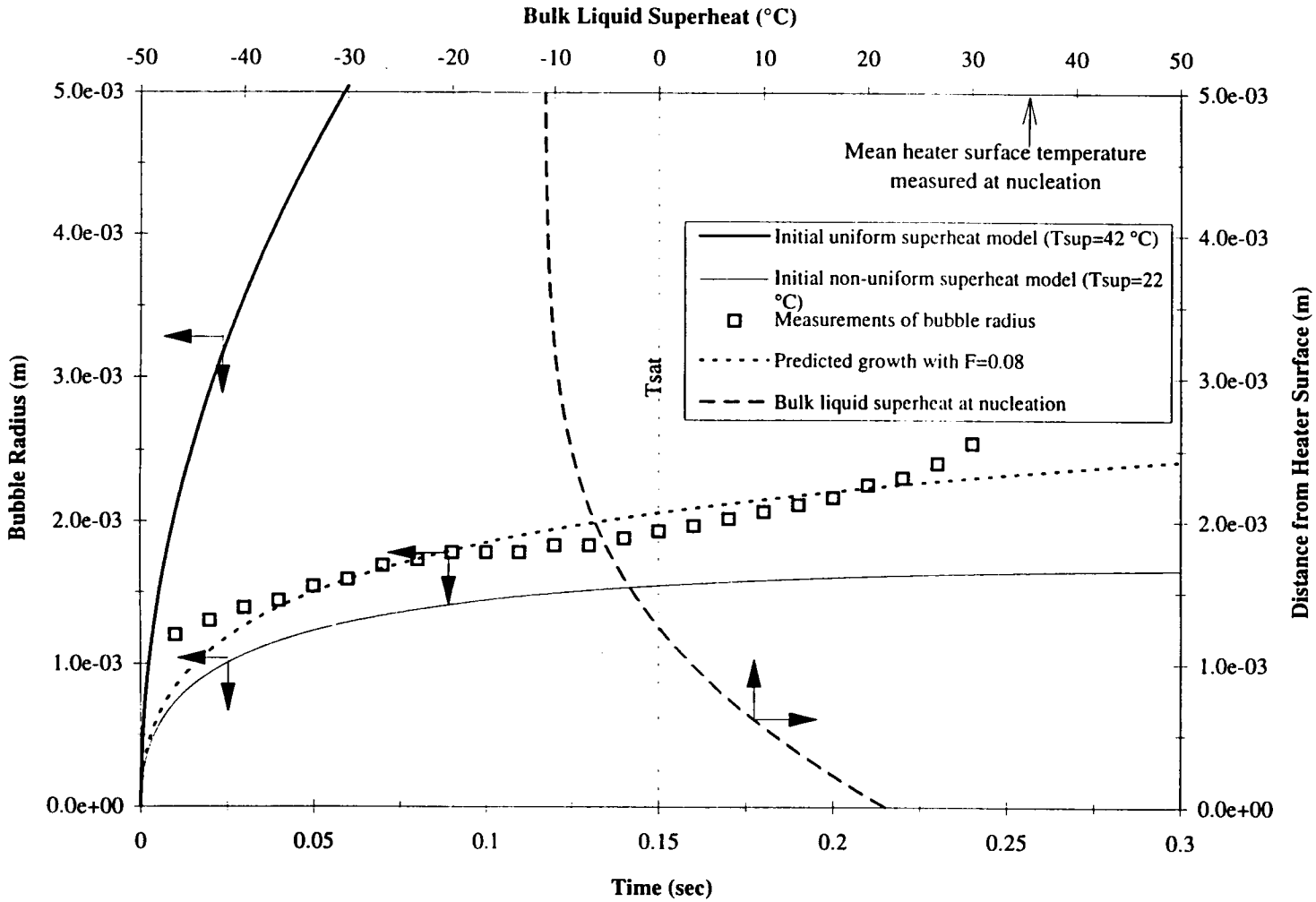

Figure A-9c. Comparisons of bubble growth measurements with several models. PBE-IA (STS-47). Run No. 3.

Comparison of Numerical Computation of Bubble growth with Experiment and Temperature Profile at Nucleation for STS-47 Run #4 (q"=7 W/cm²; T_{sat}=51.67 °C; P=115.8 kPa; ΔTsub=2.7 °C; t*=1.34 sec)

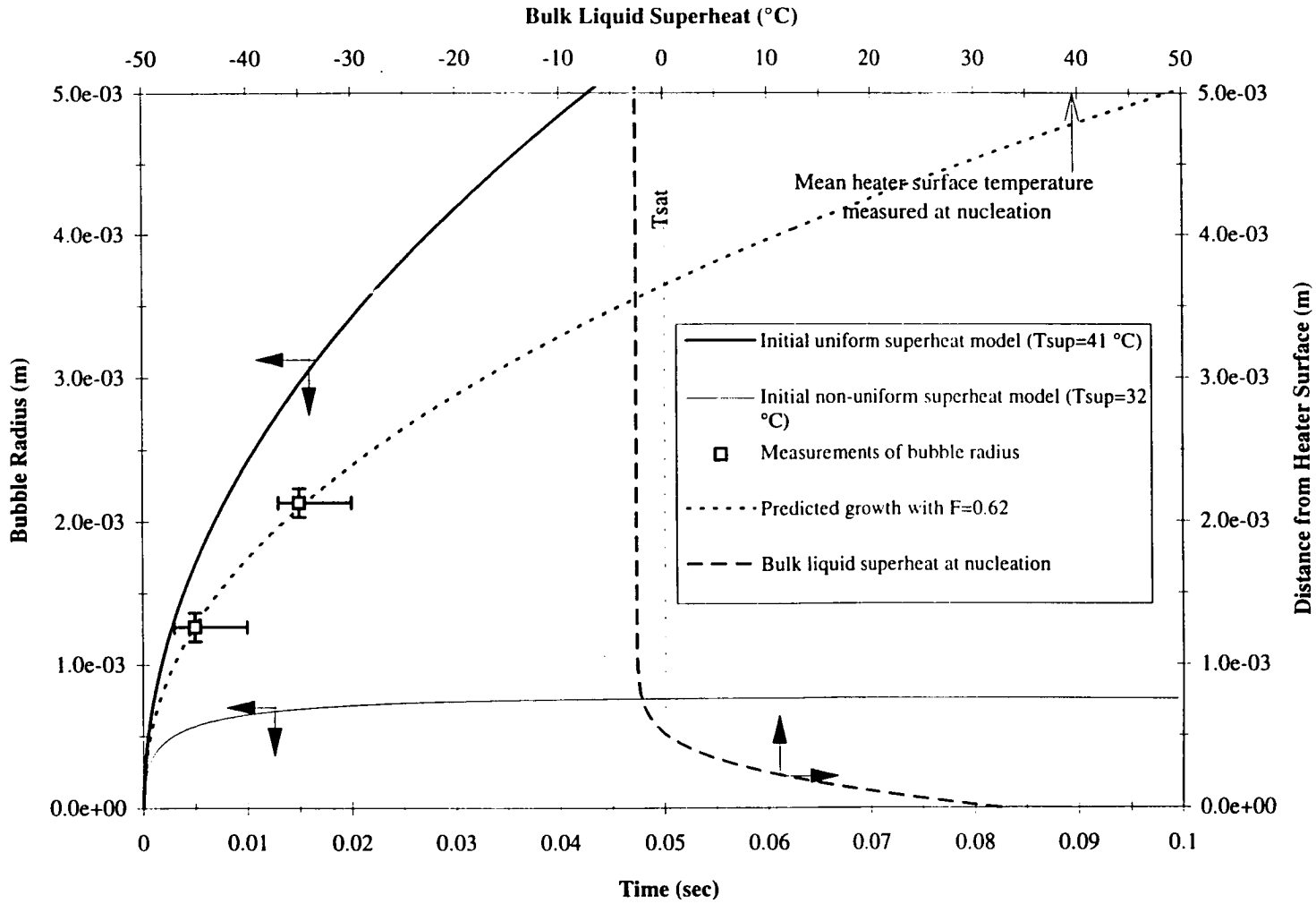

Figure A-9d. Comparisons of bubble growth measurements with several models. PBE-IA (STS-47). Run No. 4.

Comparison of Numerical Computation of Bubble growth with Experiment and Temperature Profile at Nucleation for STS-47 Run #5 (q"=3.6 W/cm²; T_{sat}=51.67 °C; P=115.8 kPa; ΔTsub=2.8 °C; t*=16.15 sec)

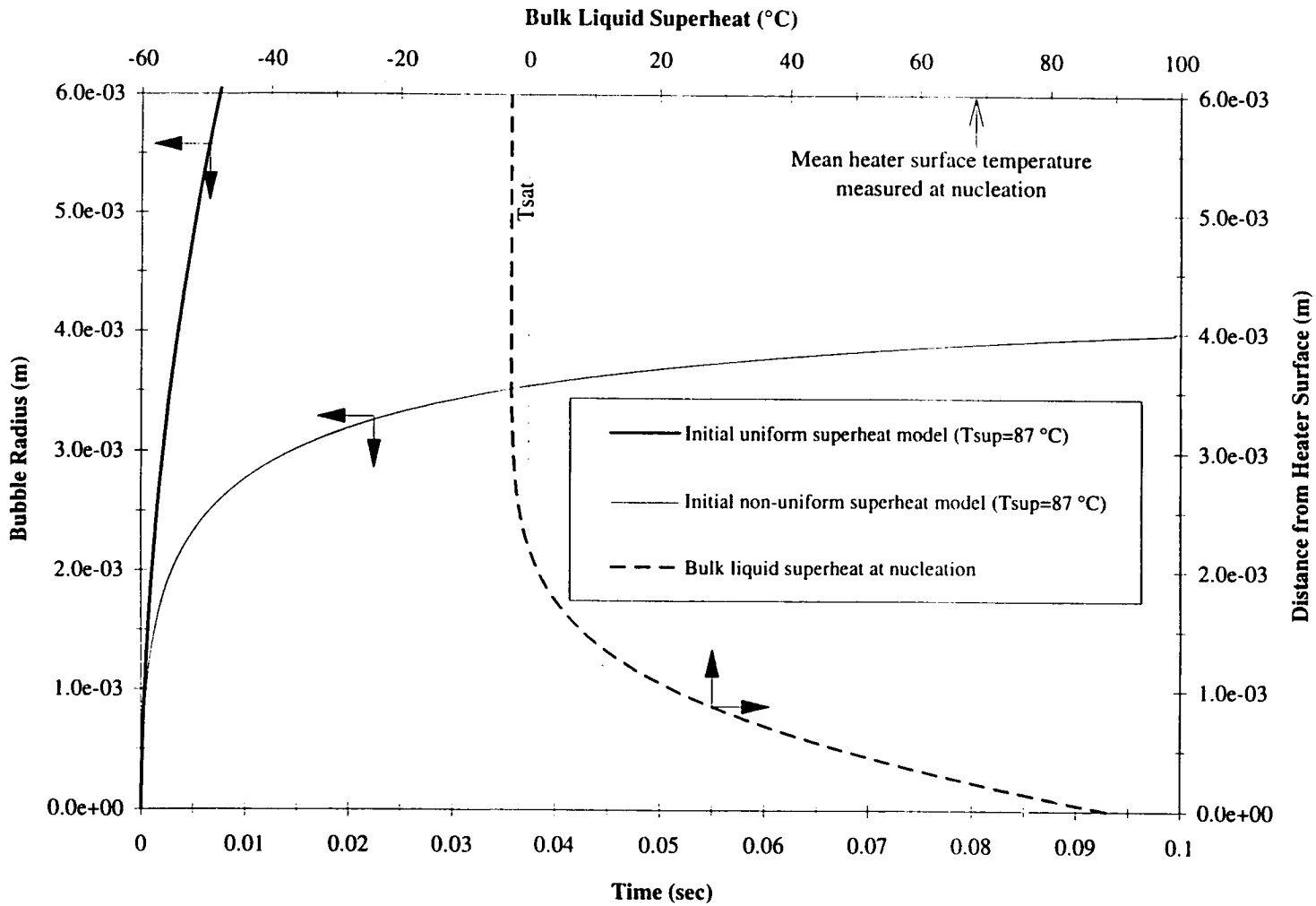

Figure A-9e. Comparisons of bubble growth measurements with several models. PBE-IA (STS-47). Run No. 5.

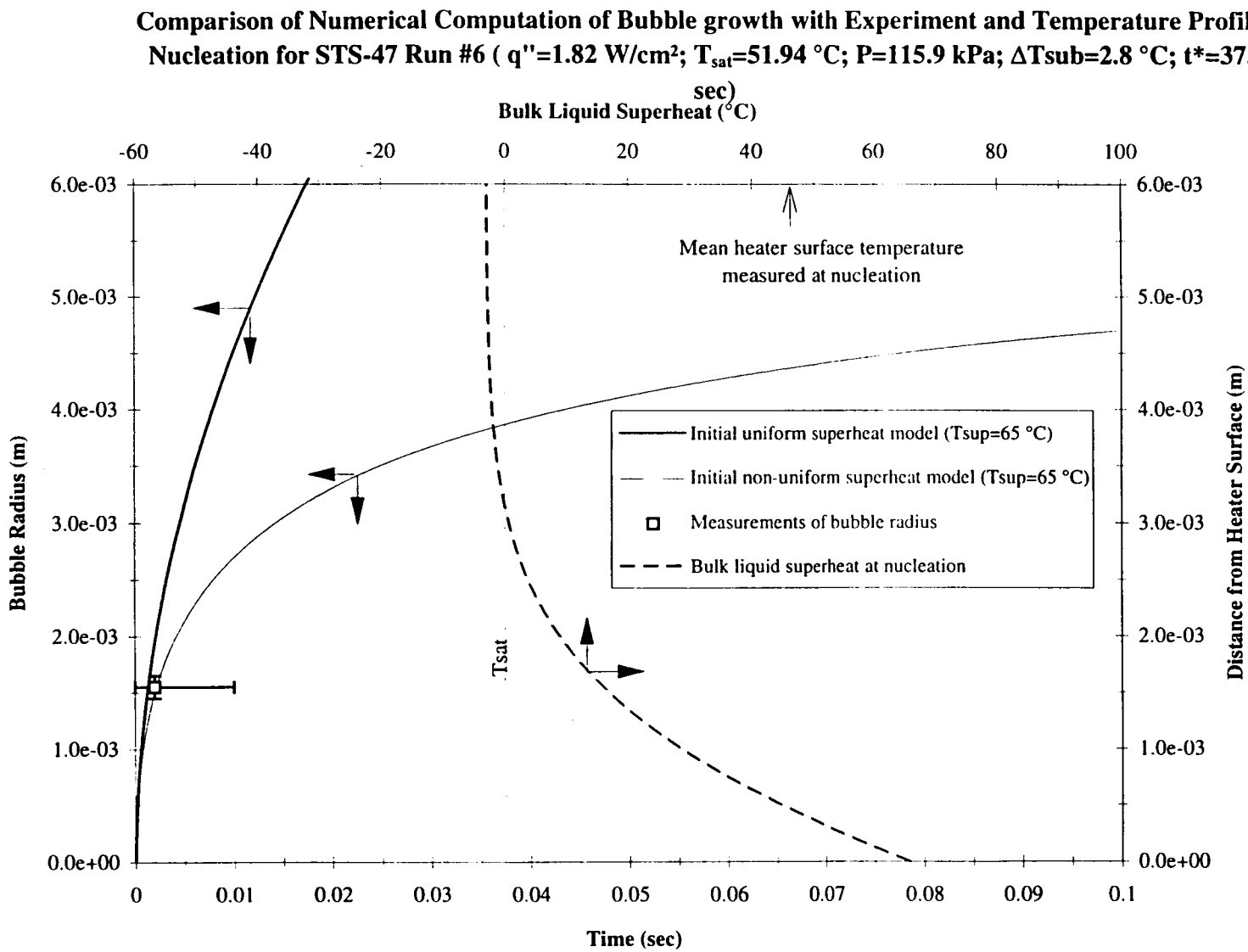

Figure A-9f. Comparisons of bubble growth measurements with several models. PBE-IA (STS-47). Run No. 6.

Comparison of Numerical Computation of Bubble growth with Experiment and Temperature Profile at Nucleation for STS-47 Run #7 (q"=7 W/cm²; T_{sat}=49.44 °C; P=106.87 kPa; ΔT_{sub}=0.6 °C; t*=1.36 sec)

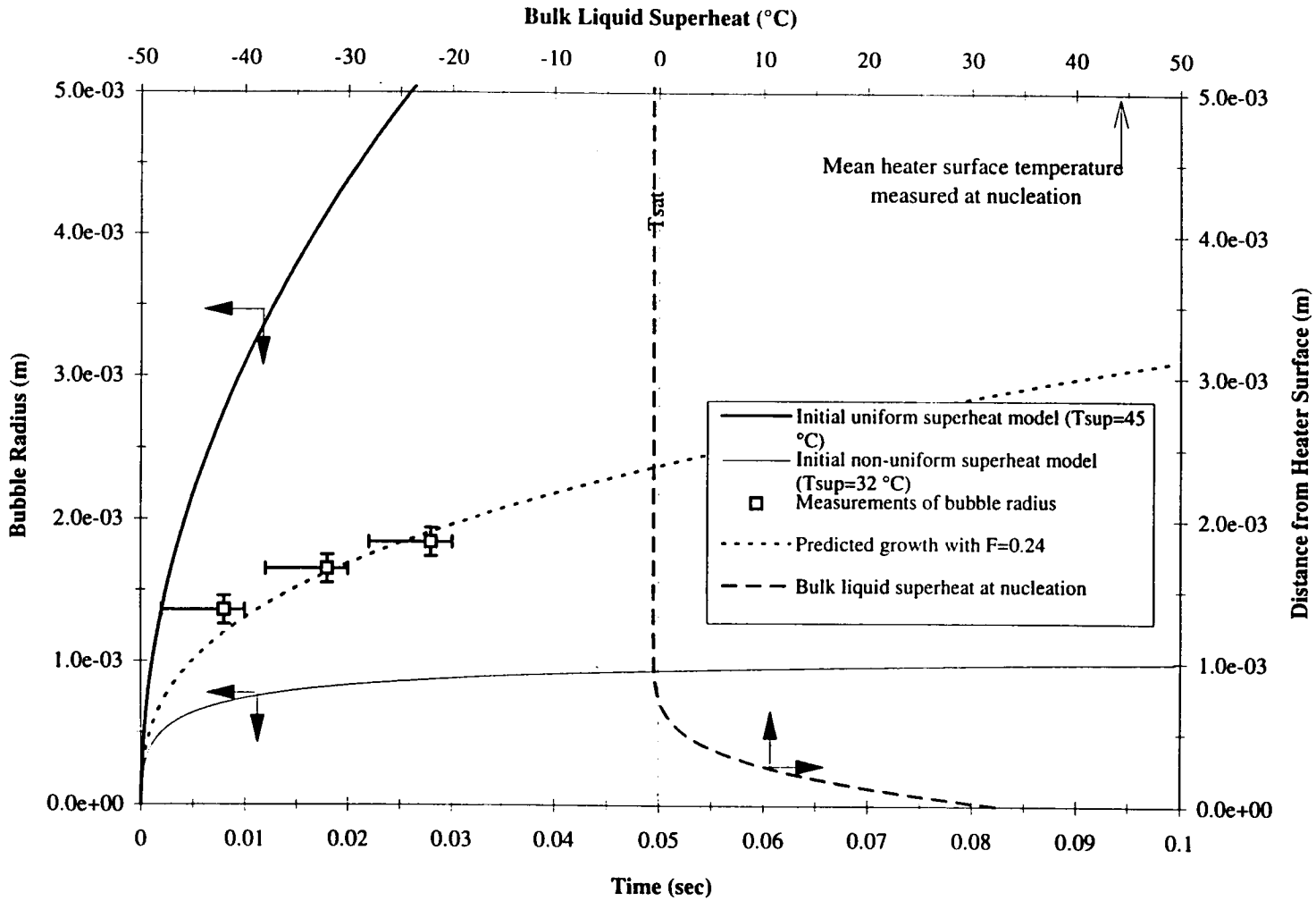

Figure A-9g. Comparisons of bubble growth measurements with several models. PBE-IA (STS-47). Run No. 7.

Comparison of Numerical Computation of Bubble growth with Experiment and Temperature Profile at Nucleation for STS-47 Run #8 (q"=3.5 W/cm²; T_{sat}=49.44 °C; P=106.87 kPa; ΔT_{sub}=0.4 °C; t*=10.63 sec)

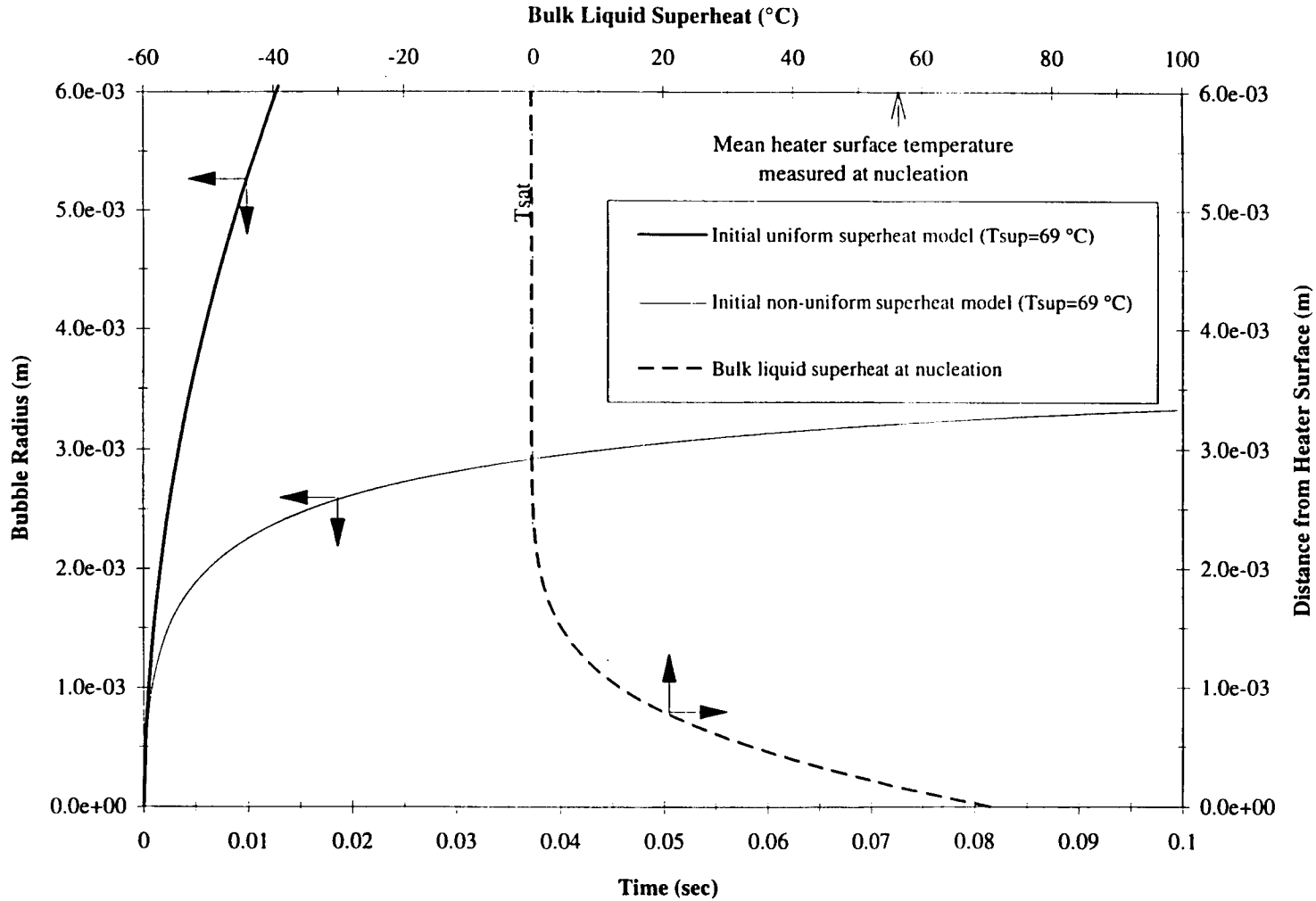

Figure A-9h. Comparisons of bubble growth measurements with several models. PBE-IA (STS-47). Run No. 8.

Comparison of Numerical Computation of Bubble growth with Experiment and Temperature Profile at Nucleation for STS-47 Run #9 (q"=1.8 W/cm²; T_{sat}=49.44 °C; P=106.9 kPa; ΔT_{sub}=0.2 °C; t*=41.48 sec)

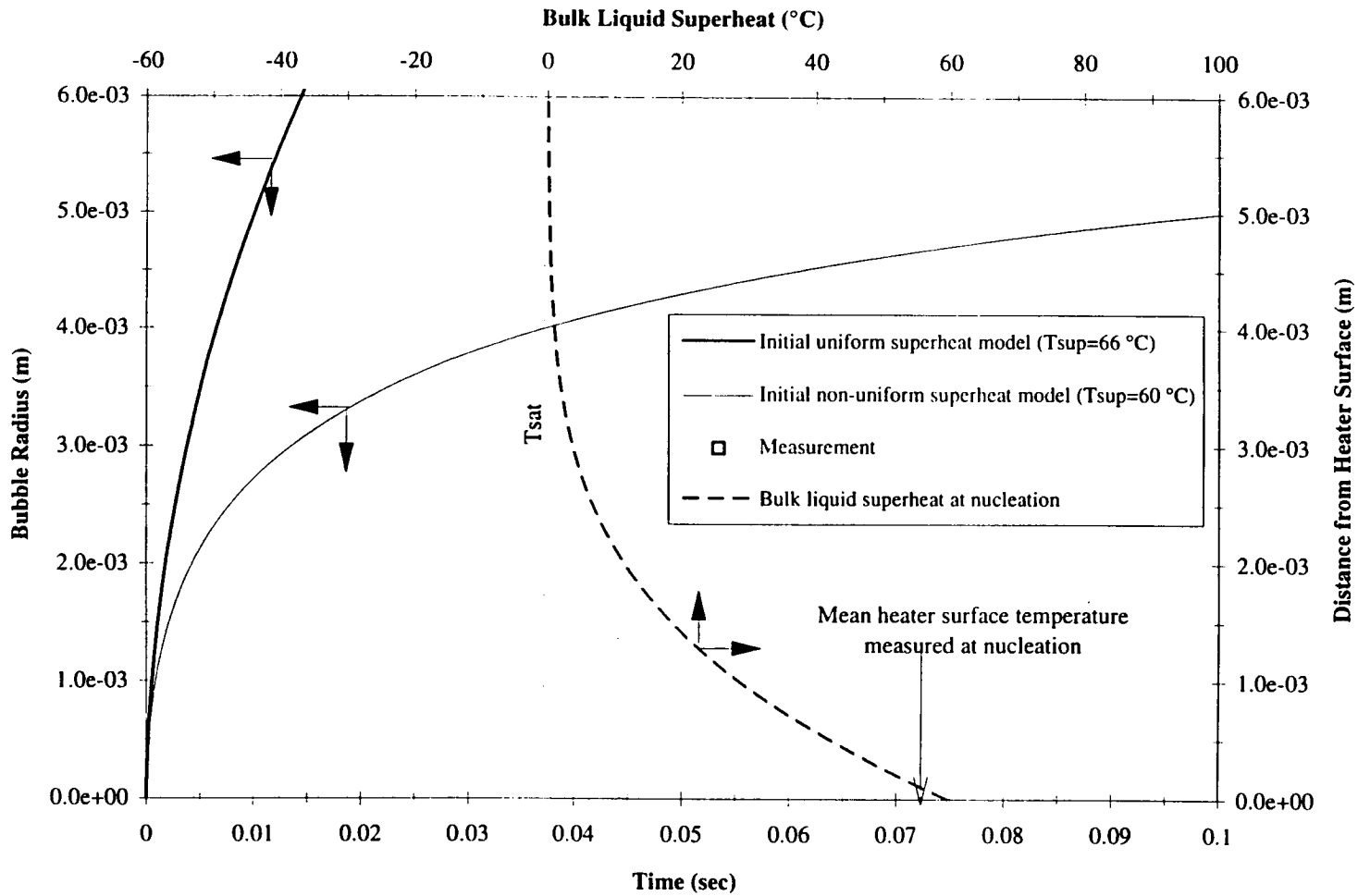

Figure A-9i. Comparisons of bubble growth measurements with several models. PBE-IA (STS-47). Run No. 9.

Run #	10 FPS	100 FPS	Nucleation	Range	Rate	Total # Frames	Analysis # Frames	Notes	Data Storage
1	15-80	10-15	11.7	nuc-20	10/100fps	550	150	JLP	OD3-B
2	10--15	15--25	22.2	23-30	10/100 fps	520	200	JAJ	OD3-B
	25-130			65-75	10	100	100	JAJ	OD3-B
				95-100	10	50	50	JAJ	OD3-B
3	20--30	30--50	41.2	42-50	100 fps	300	80	R	OD1-B
	50--130			85-90	10	50	50	R	OD1-B
4	15-65	10-15	11.4	nuc.--20	both	450	134	JLP	OD4-A
5	10-15	15-25	26.0	26-35	10fps	90	90	JLP	OD4-A
	25-105			70-90	10 fps	200	200	JLP	OD4-A
6	20--30	30--50	47.3	nuc.--65	both	450	120	R	OD1-B
	50--115								
7	15-55	10-15	11.3	nuc.--15	100 fps	400	186	JLP	OD4-A
8	10--15	15--25	20.3	nuc.--35	both	600	206	JLP	OD4-A
	25--80			50-60	10	100	100		
9	10-30	30-50	51.0	51-70	10	190	190	R	OD1-B
	50-125			80-90	10	100	100	R	OD1-B

**Note: All times are relative to ZERO. Heater power is active at 10 sec;

Table A-IV. Index for heater surface dry fraction measurements and computation of microgravity nucleate boiling heat transfer coefficients. PBE-IA (STS-47).

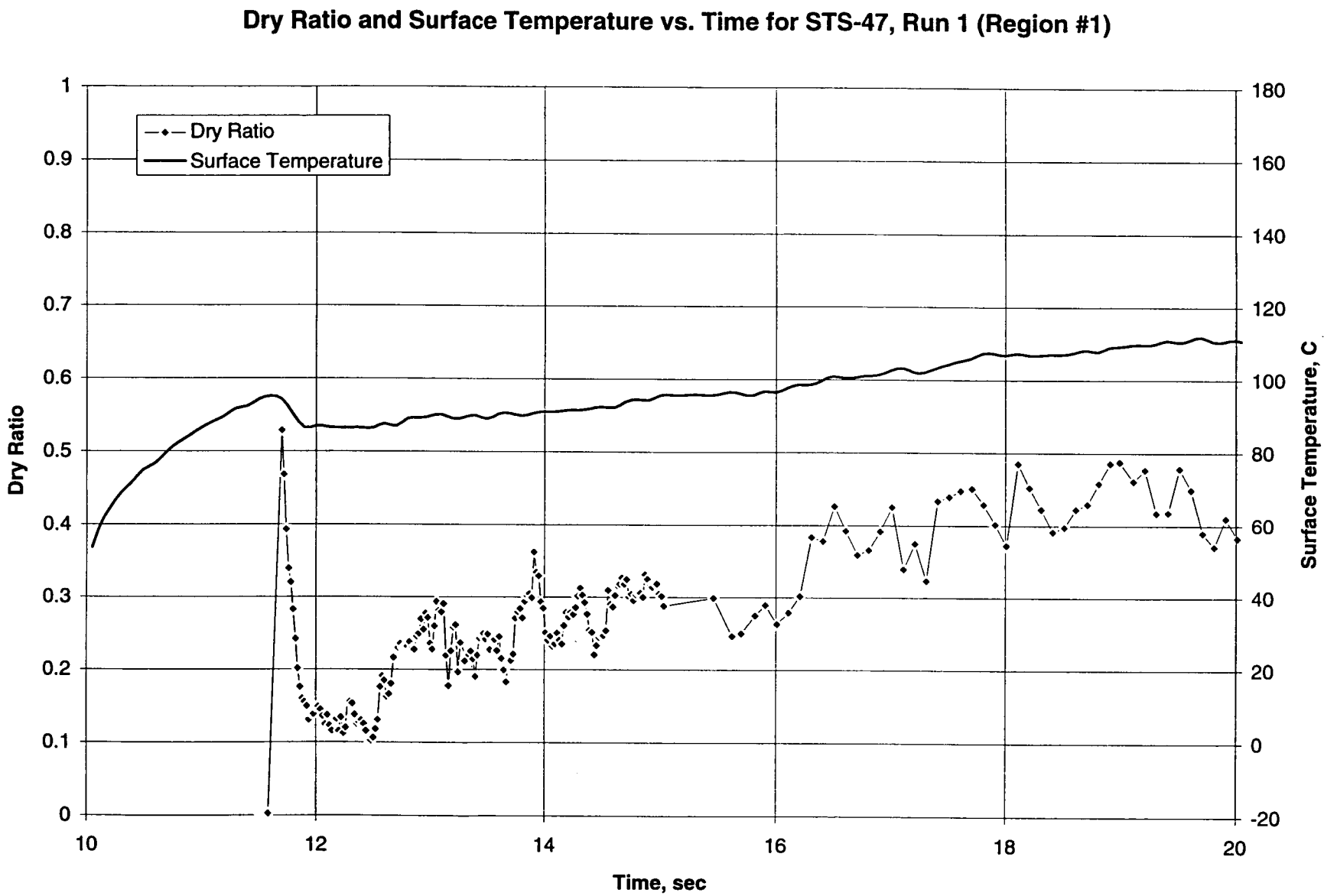

Figure A-10a-1-i. Heater surface dry fraction and mean temperature. PBE-IA (STS-47). Run No. 1. Time interval: 11.5 - 20.0 seconds.

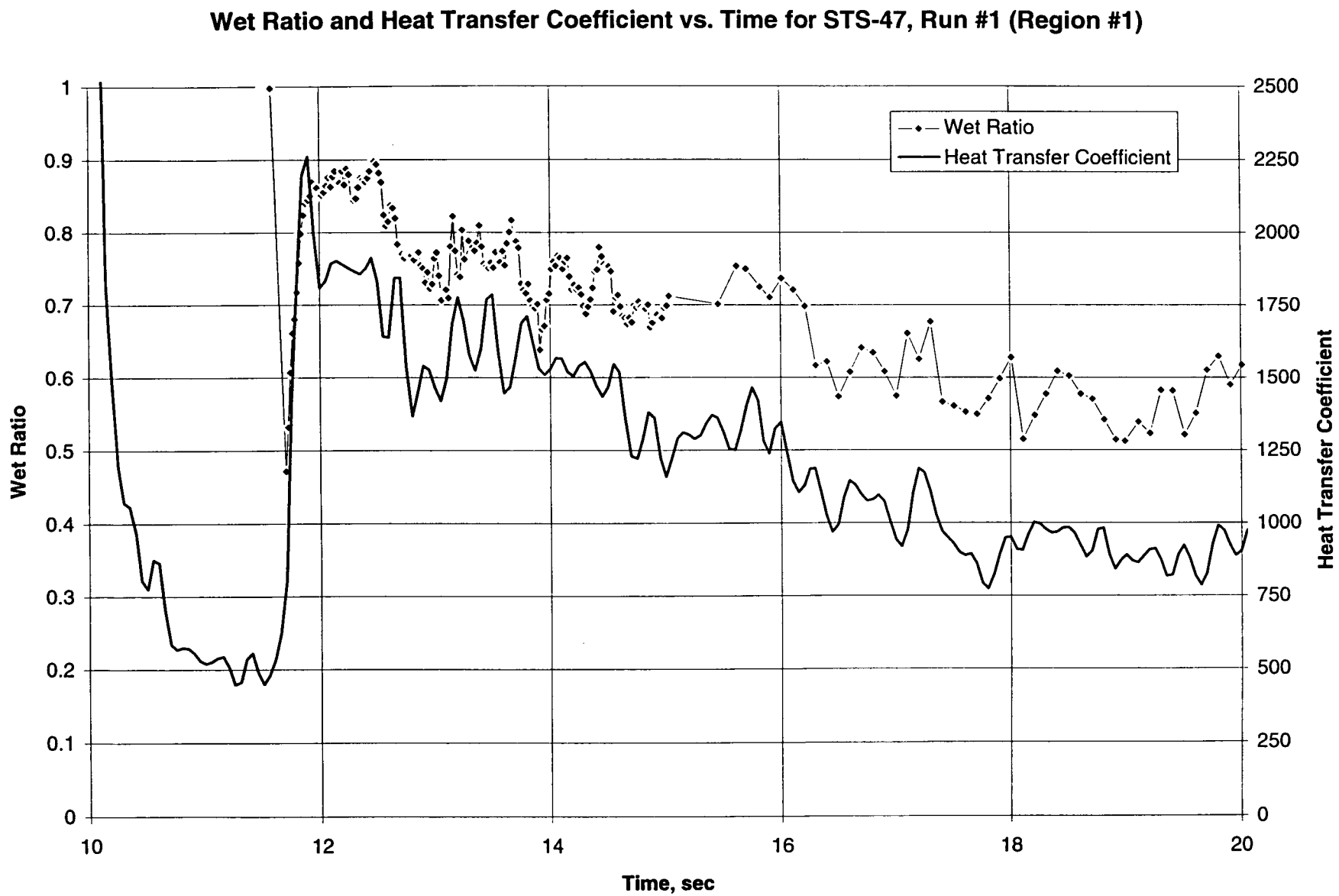

Figure A-10a-1-ii. Heater surface wet fraction and mean heat transfer coefficients. PBE-IA (STS-47). Run No. 1. Time interval: 11.5 - 20.0 seconds.

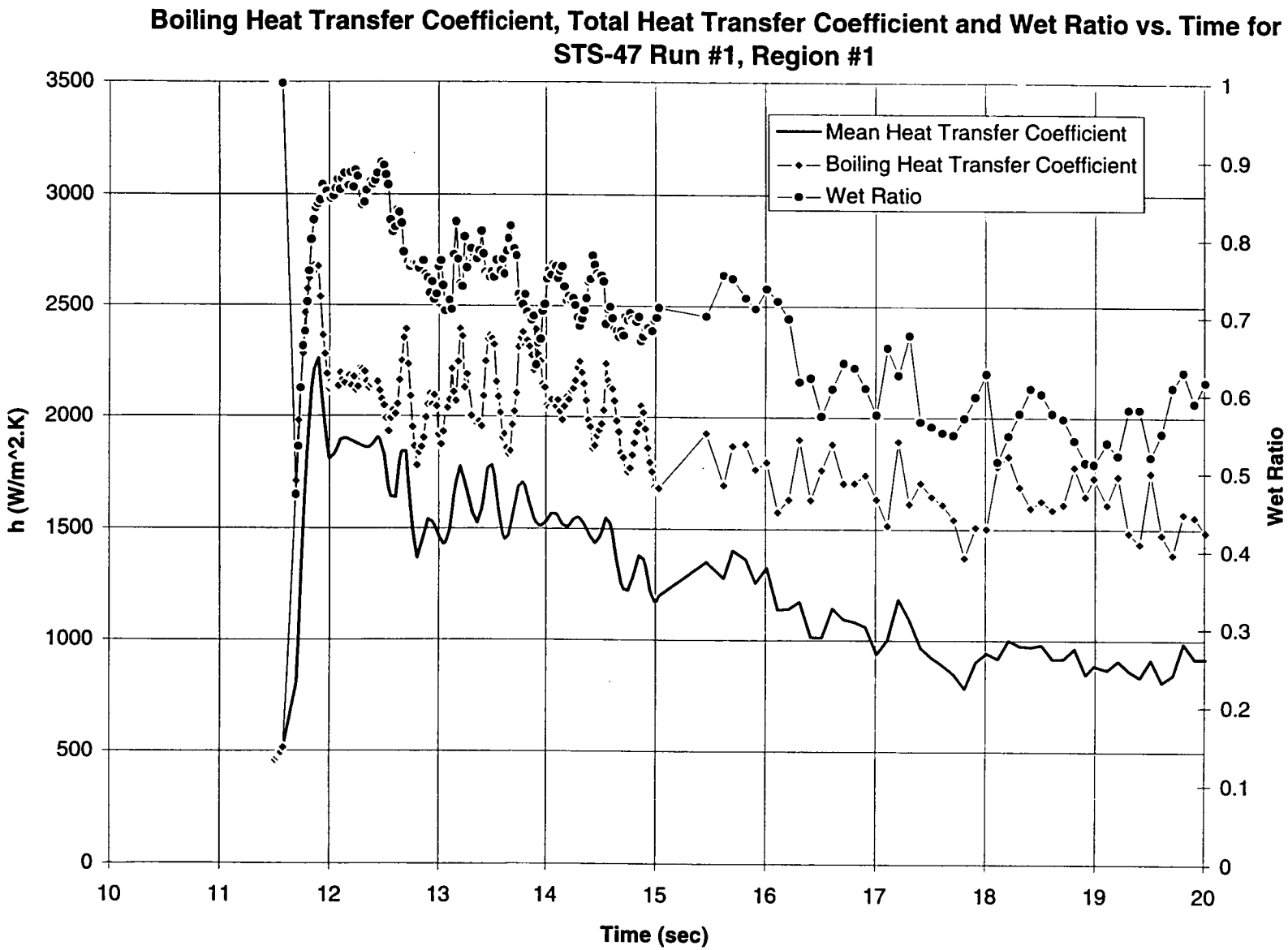

Figure A-10a-1-iii. Development of microgravity boiling heat transfer coefficient. PBE-IA (STS-47). Run No. 1. Time interval: 11.5 - 20.0 seconds.

STS-47 Run #1

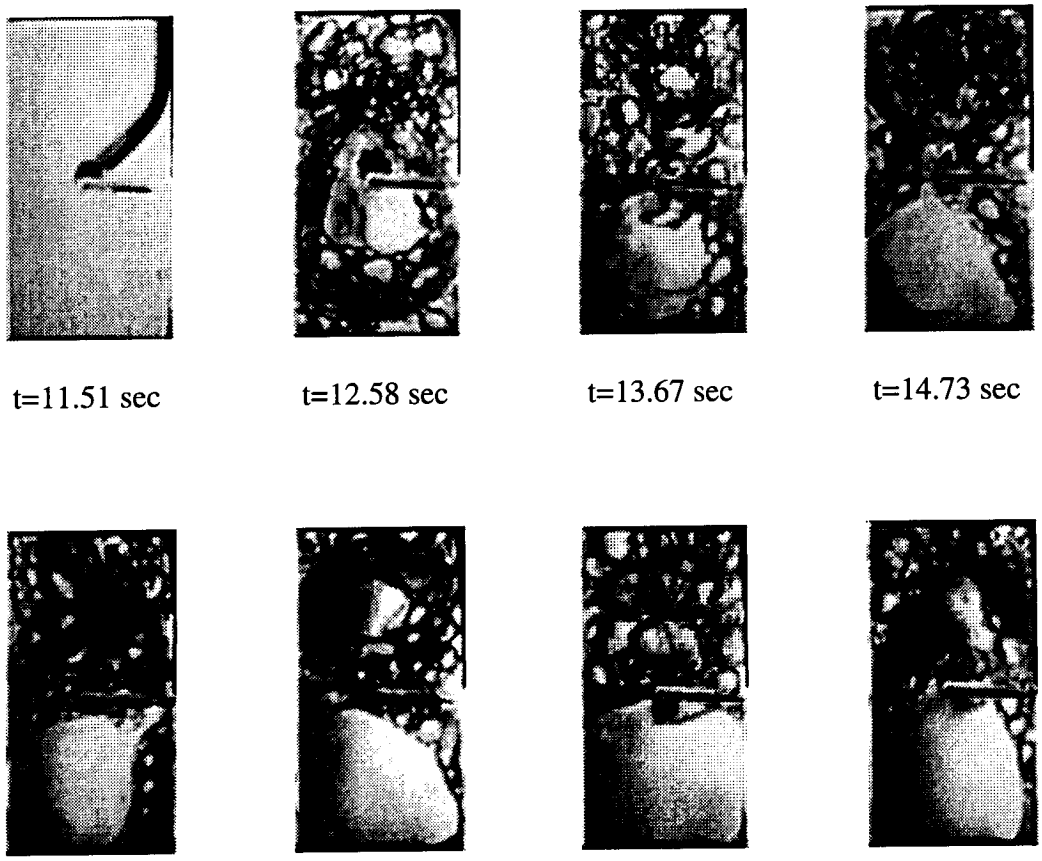

Figure A-10a-1-iv. Sample images showing dryout/rewetting. PBE-IA (STS-47). Run No. 1. Time interval: 11.5 - 20.0 seconds.

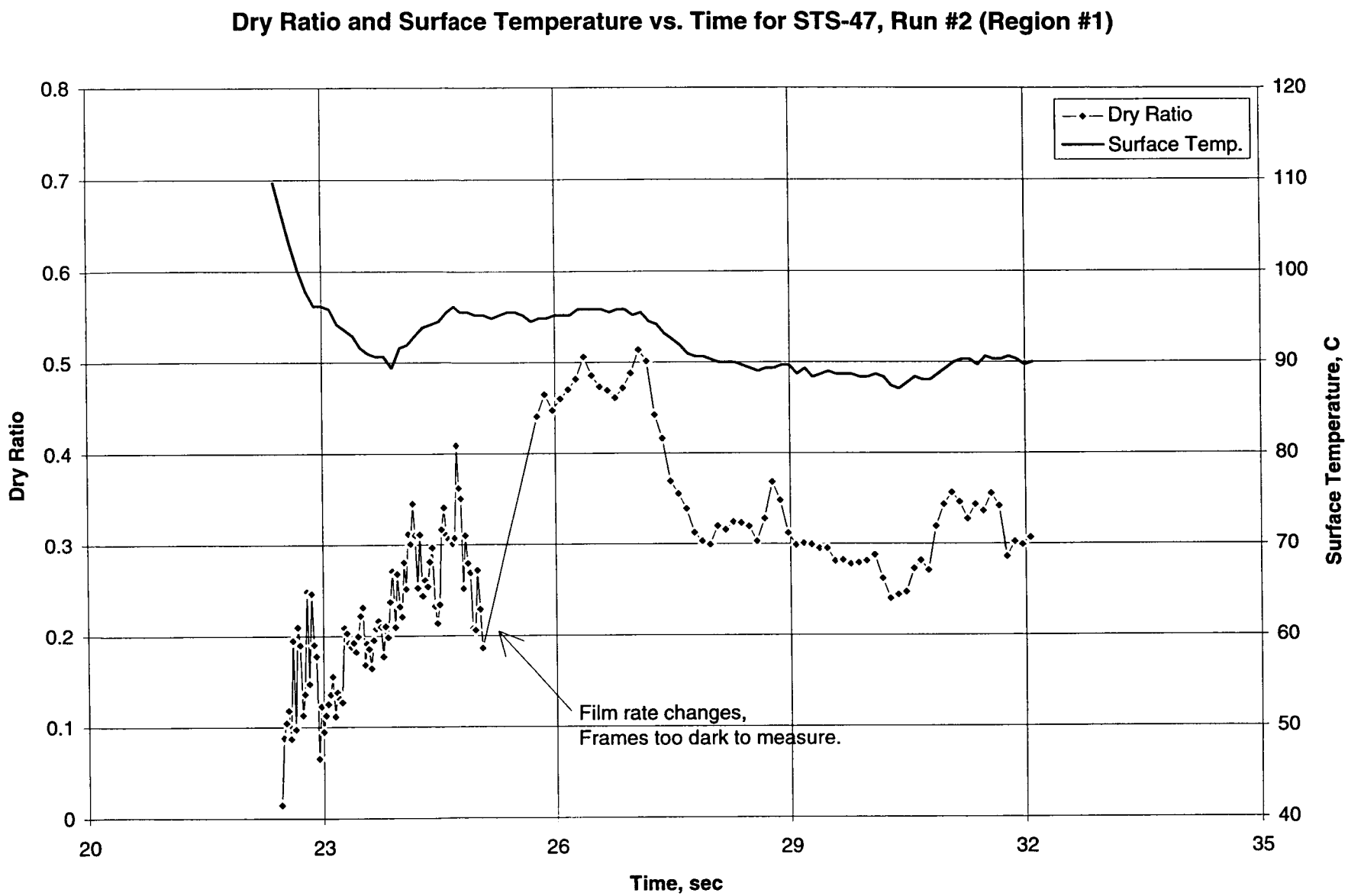

Figure A-10b-1-i. Heater surface dry fraction and mean temperature. PBE-IA (STS-47). Run No. 2. Time interval: 22.5 - 32.0 seconds.

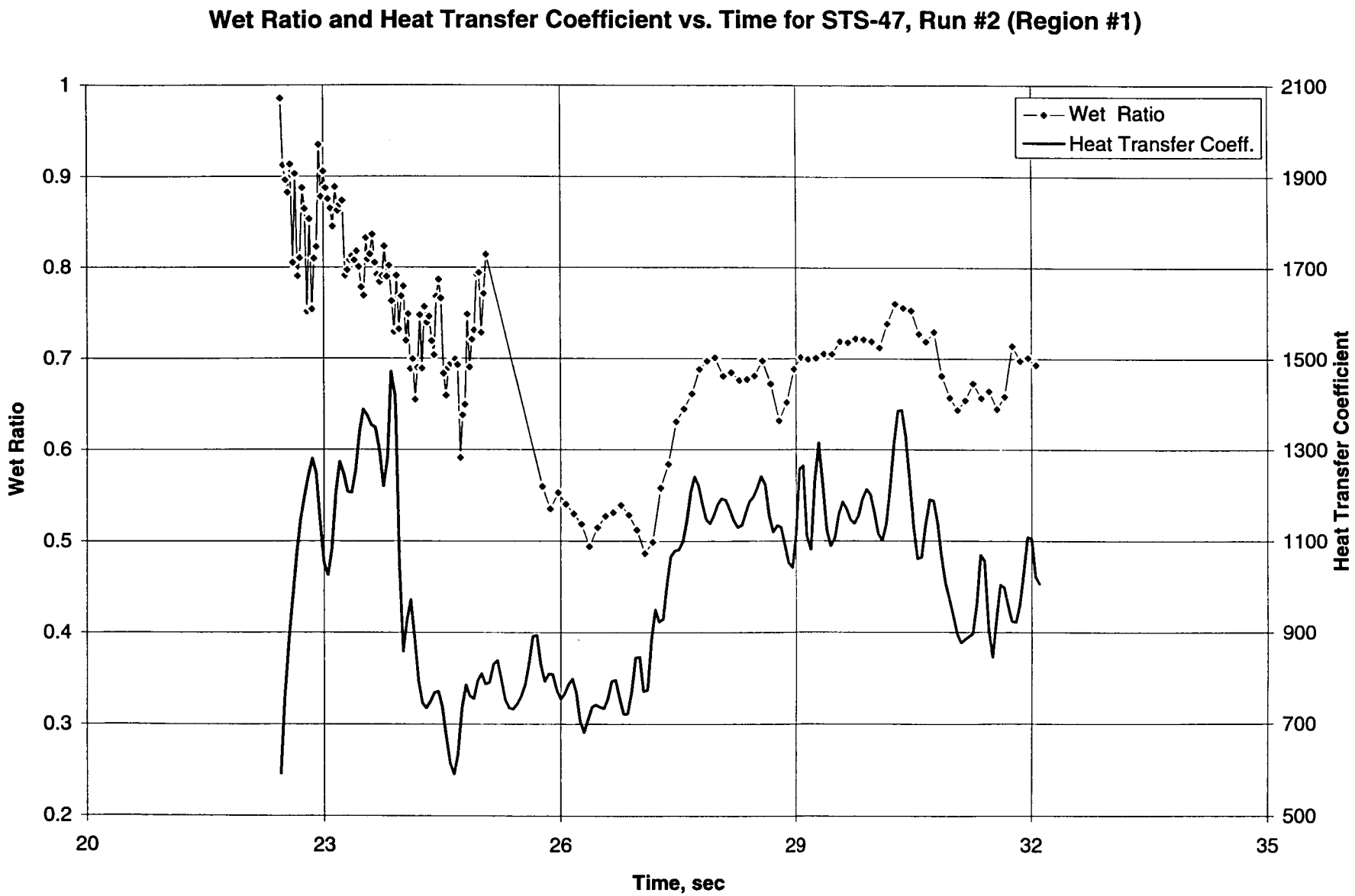

Figure A-10b-1-ii. Heater surface wet fraction and mean heat transfer coefficients. PBE-IA (STS-47). Run No. 2. Time interval: 22.5 - 32.0 seconds.

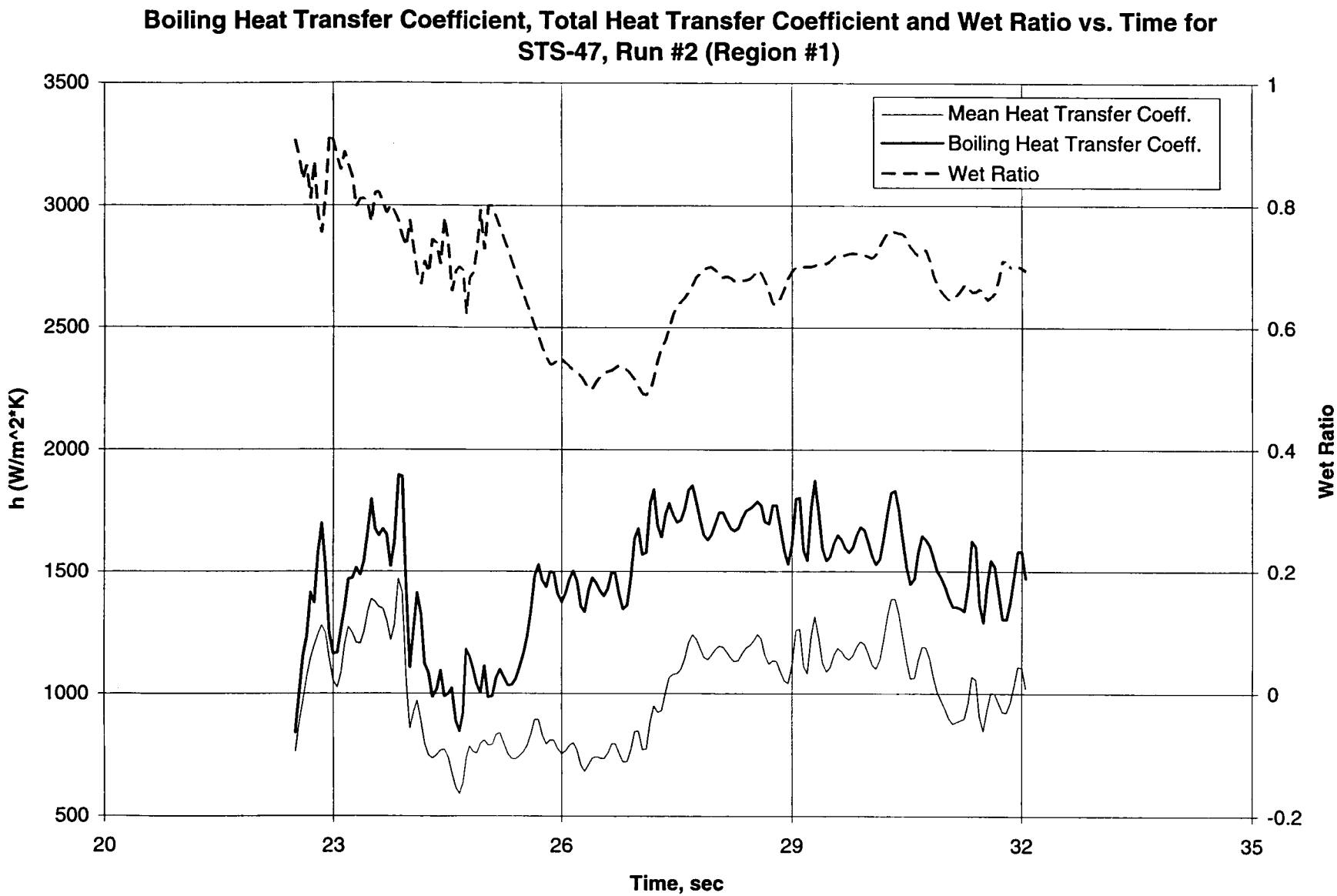

Figure A-10b-1-iii. Development of microgravity boiling heat transfer coefficient. PBE-IA (STS-47). Run No. 2. Time interval: 22.5 - 32.0 seconds.

STS-47 Run #2 (Region #1)

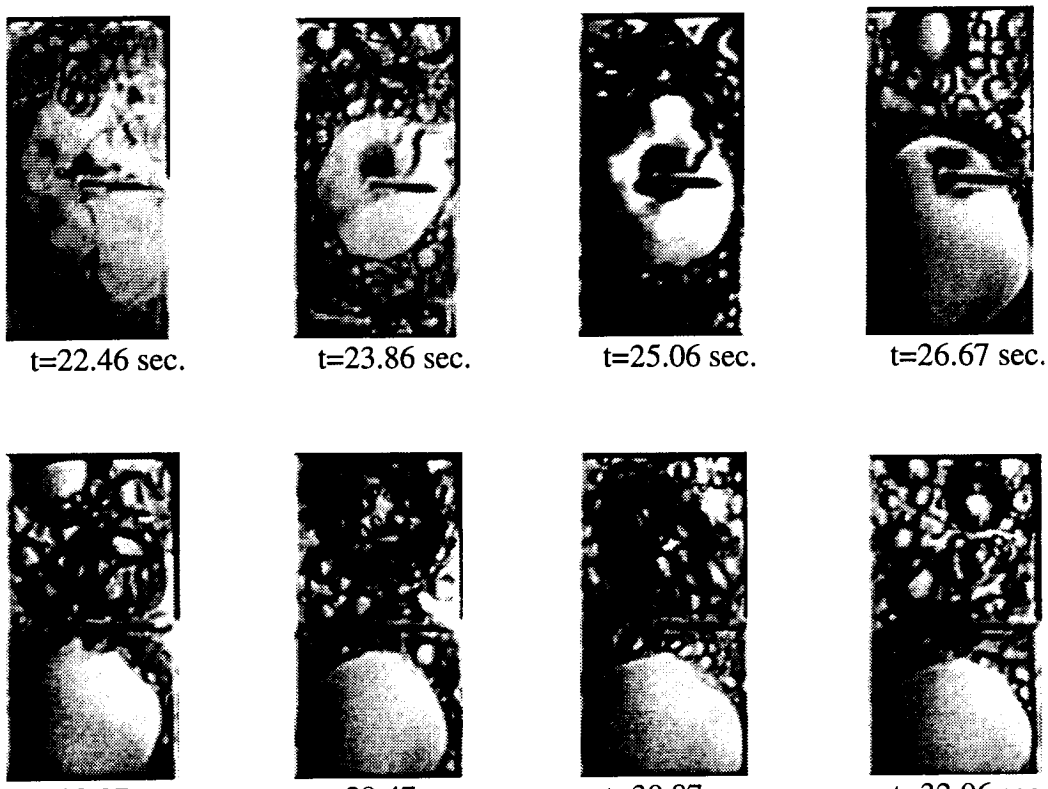

Figure A-10b-1-iv. Sample images showing dryout/rewetting. PBE-IA (STS-47). Run No. 2. Time interval: 22.5 - 32.0 seconds.

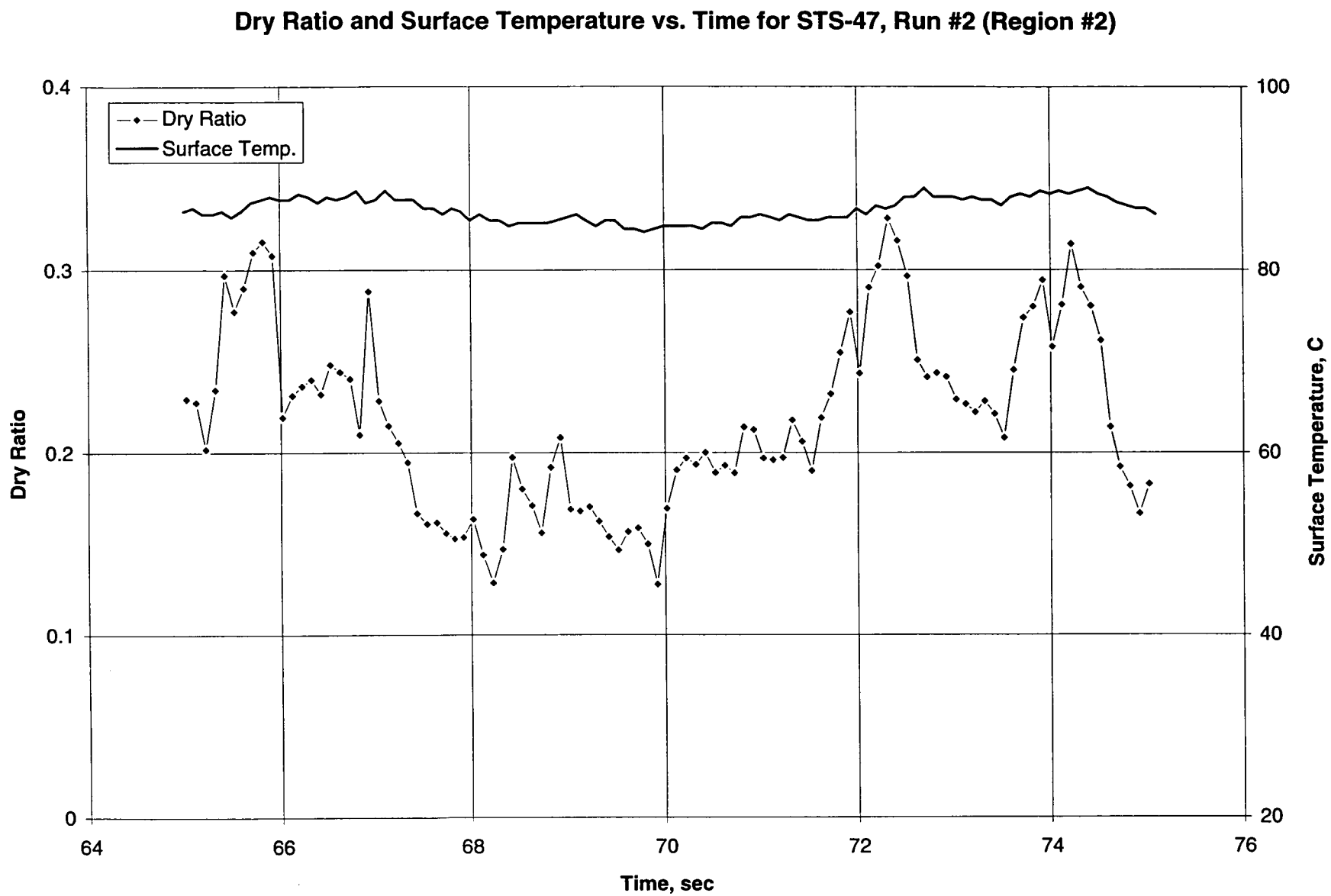

Figure A-10b - 2-i. Heater surface dry fraction and mean temperature. PBE-IA (STS-47). Run No. 2. Time interval: 65 - 75 seconds.

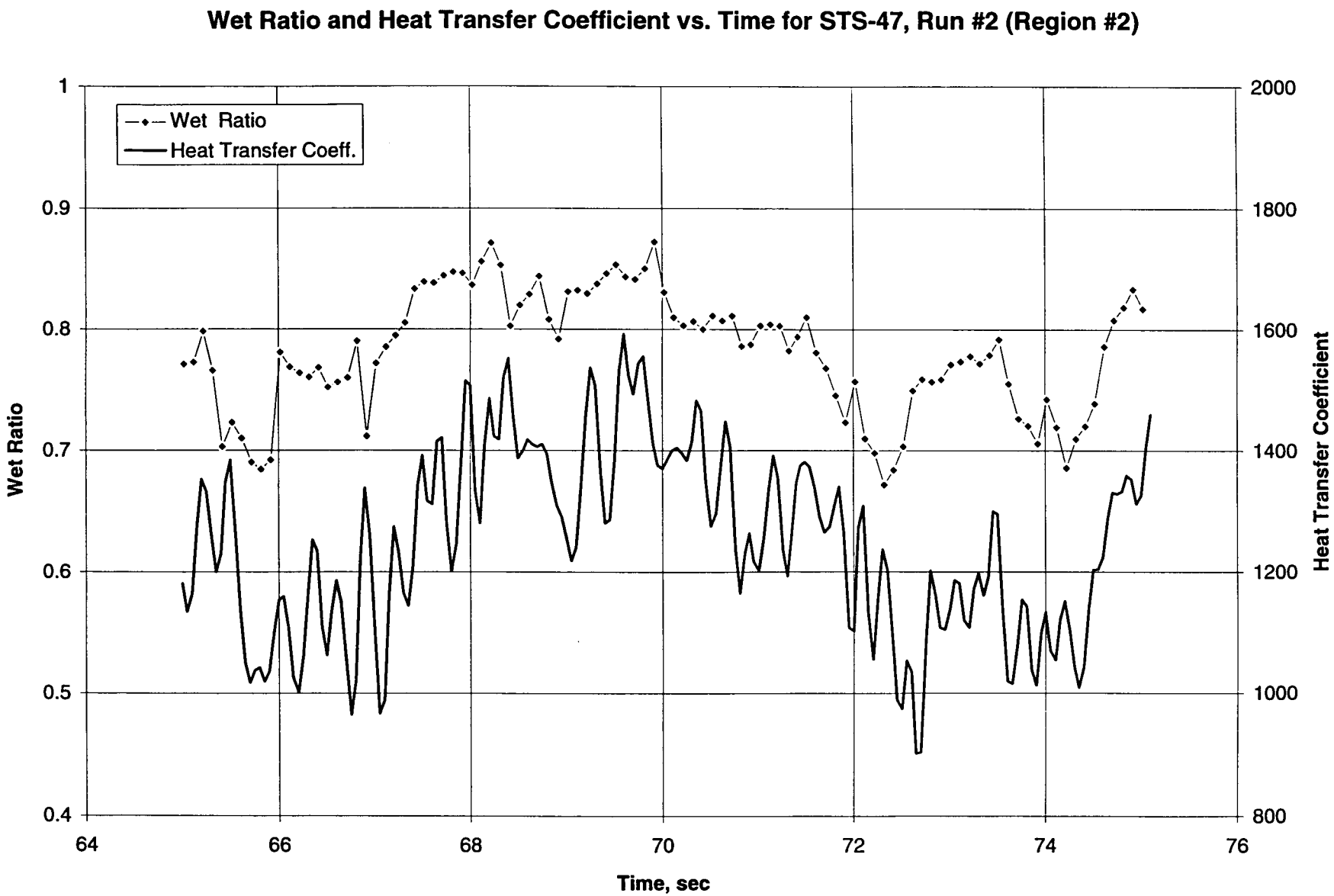

Figure A-10b-2-ii. Heater surface wet fraction and mean heat transfer coefficients. PBE-IA (STS-47). Run No. 2. Time interval: 65 - 75 seconds.

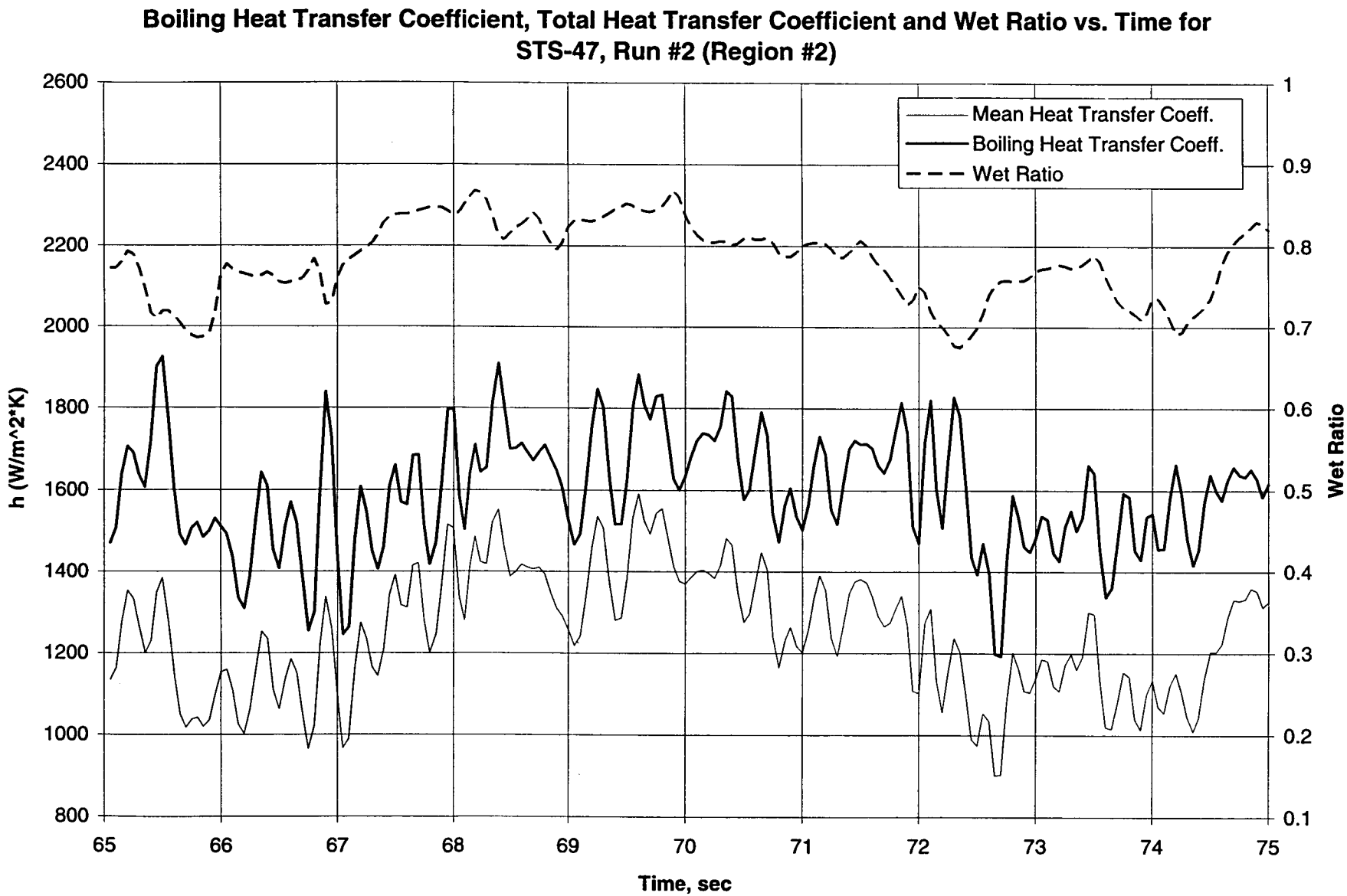

Figure A-10b-2-iii. Development of microgravity boiling heat transfer coefficient. PBE-IA (STS-47). Run No. 2. Time interval: 65 - 75 seconds).

STS-47 Run #2 (Region #2)

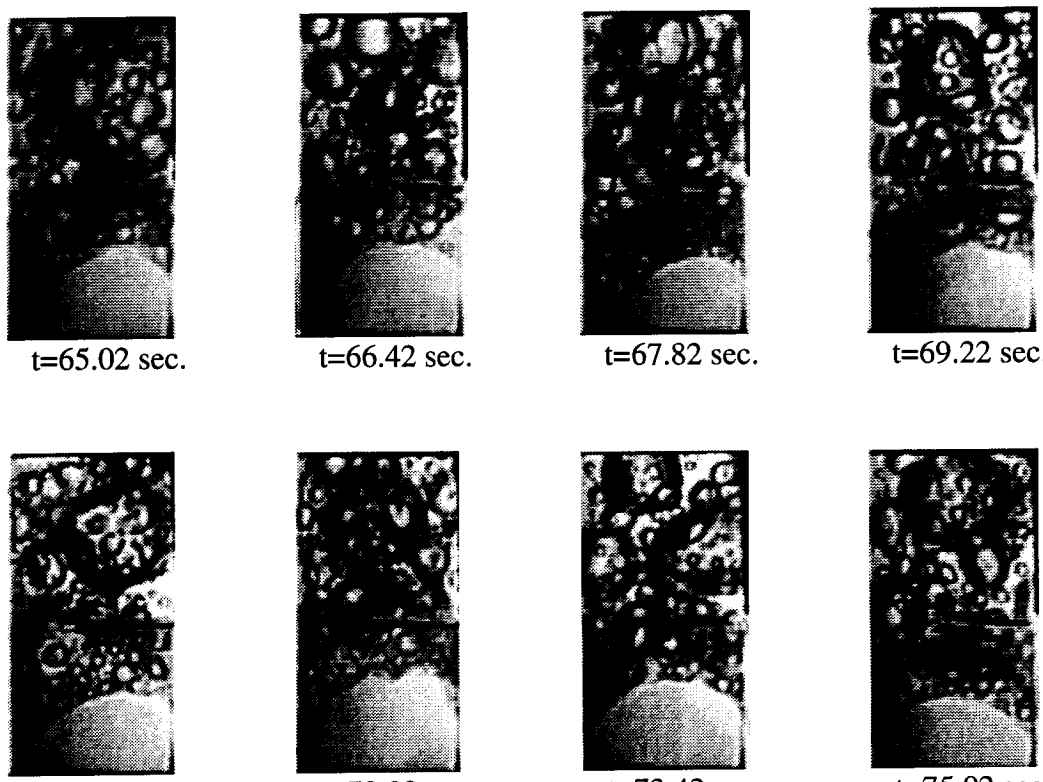

Figure A-10b-2-iv. Sample images showing dryout/rewetting. PBE-IA (STS-47). Run No. 2. Time interval: 65 - 75 seconds.

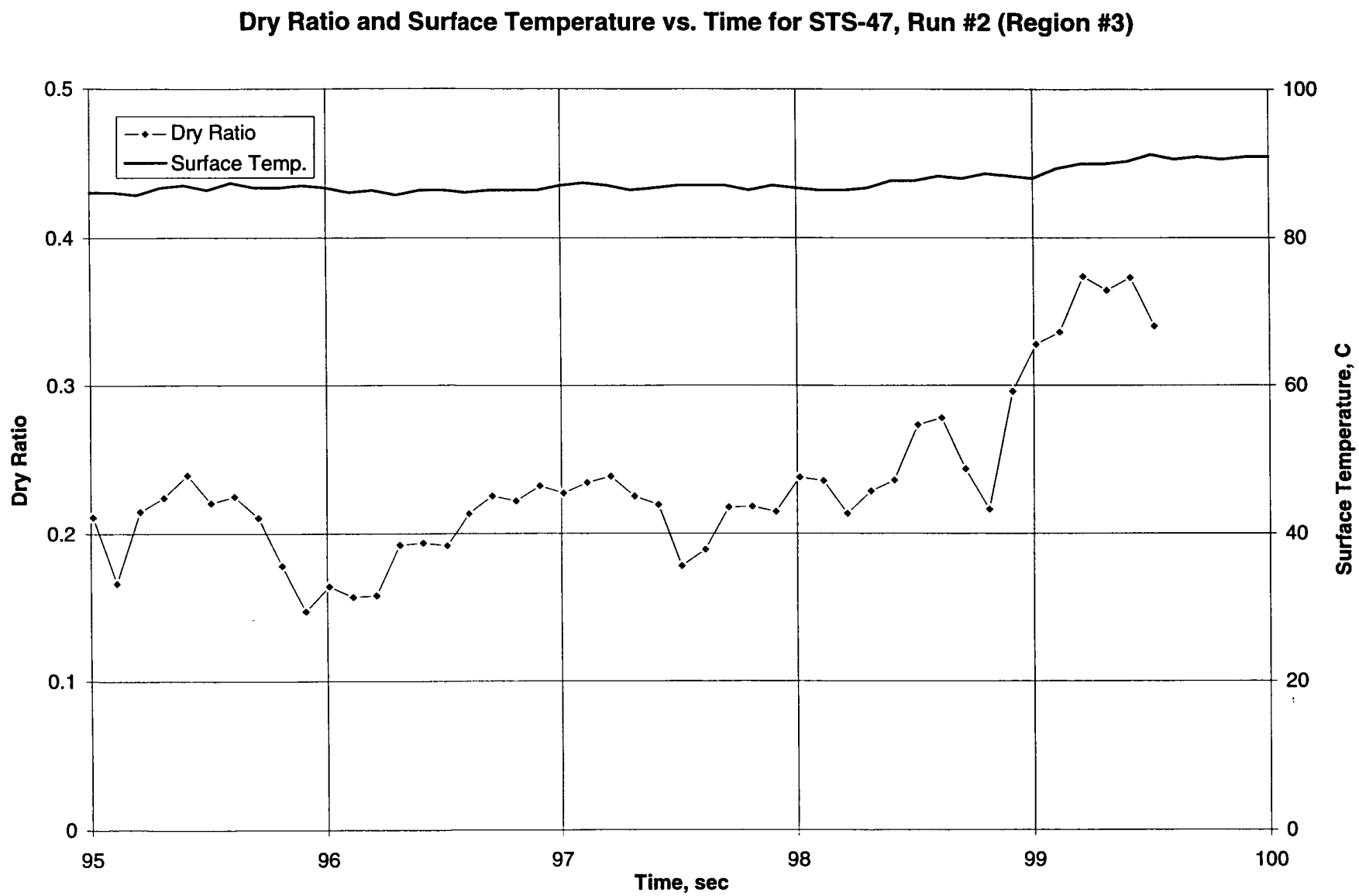

Figure A-10b-3-i. Heater surface dry fraction and mean temperature. PBE-IA (STS-47). Run No. 2. Time interval: 95.0 - 99.5 seconds.

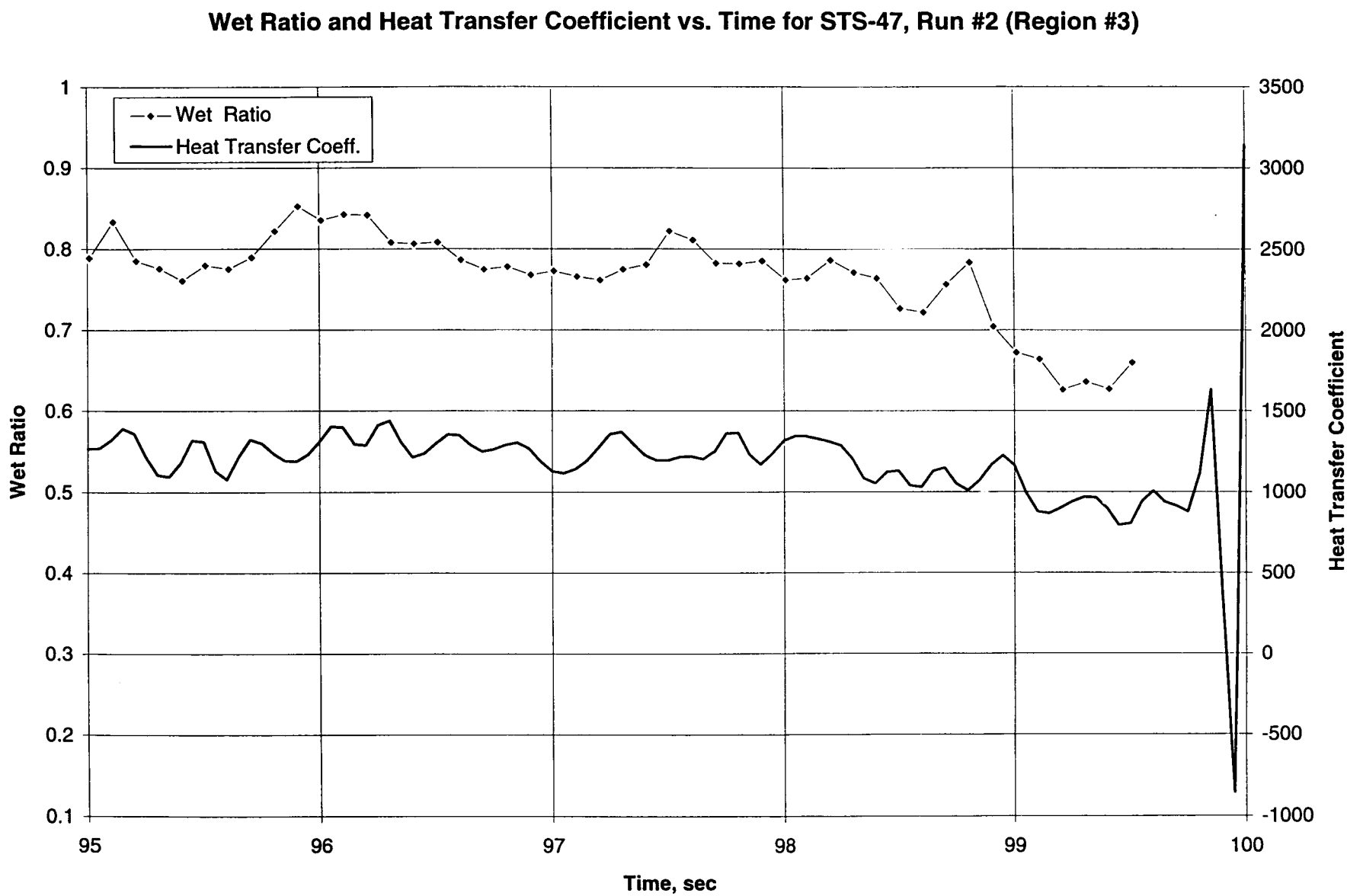

Figure A-10b-3-ii. Heater surface wet fraction and mean heat transfer coefficients. PBE-IA (STS-47). Run No. 2. Time interval: 95.0 - 99.5 seconds.

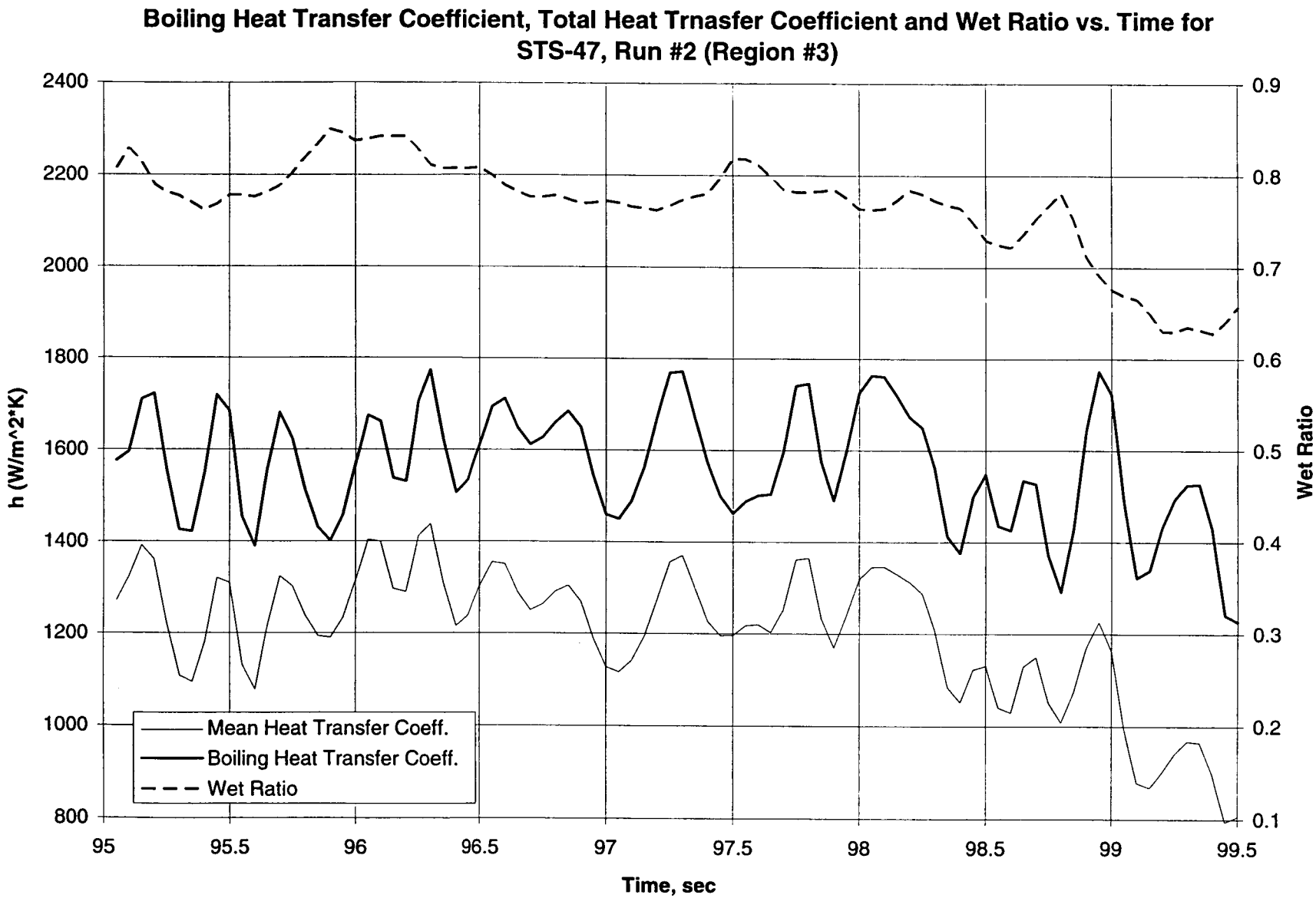

Figure A-10b-3-iii. Development of microgravity boiling heat transfer coefficient. PBE-IA (STS-47). Run No. 2. Time interval: 95.0 - 99.5 seconds.

STS-47 Run #2 (Region #3)

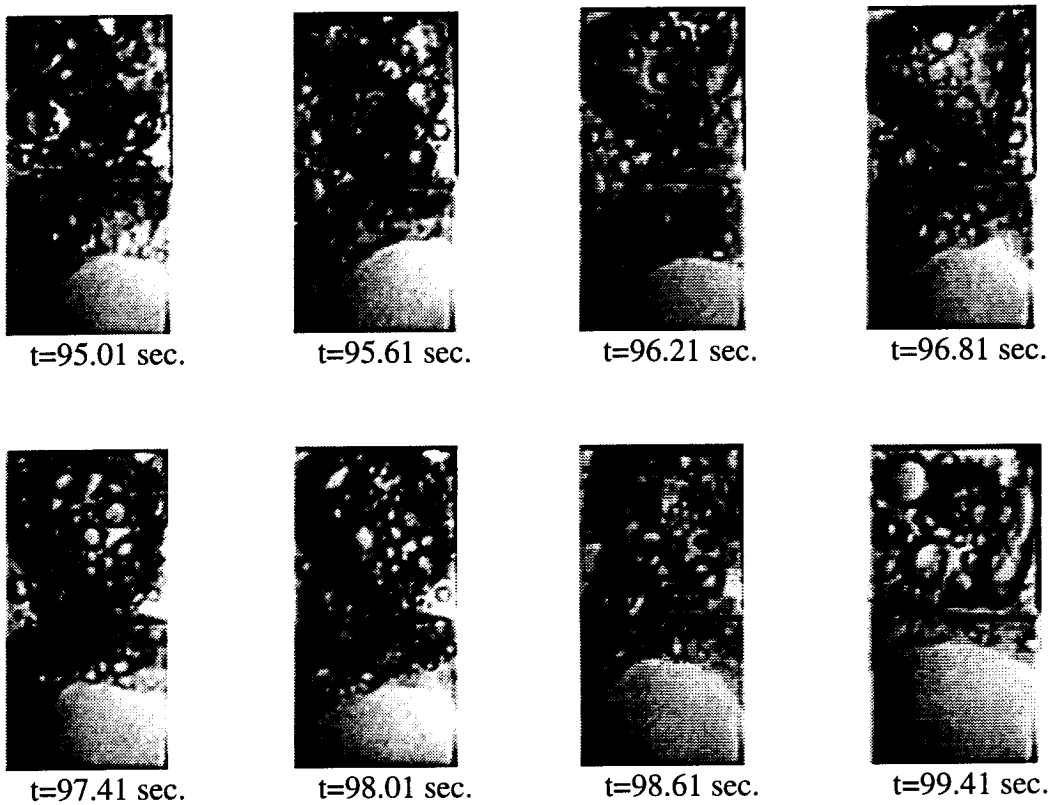

Figure A-10b-3-iv. Sample images showing dryout/rewetting. PBE-IA (STS-47). Run No. 2. Time interval: 95.0 - 99.5 seconds.

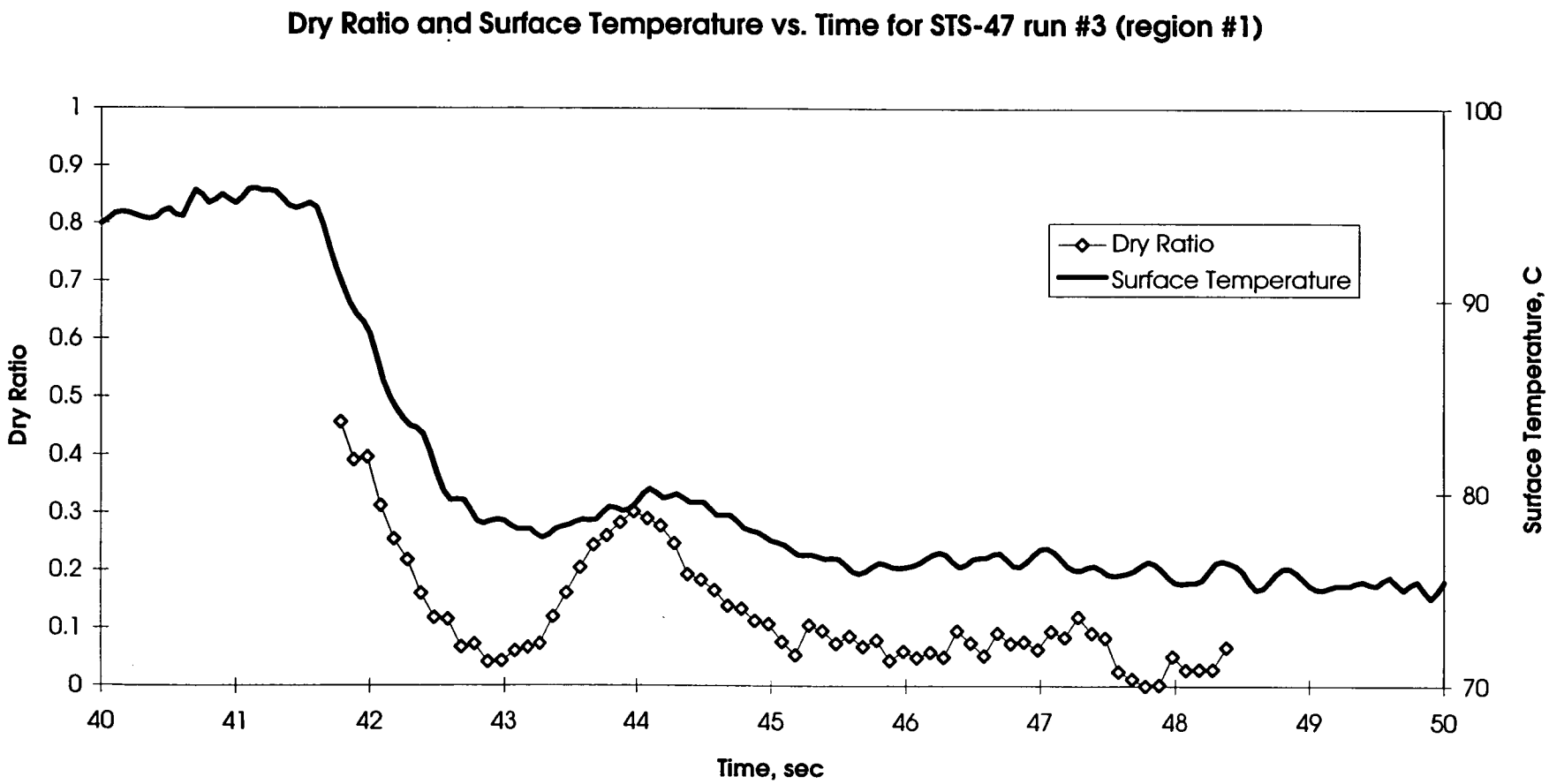

Figure A-10c-1-i. Heater surface dry fraction and mean temperature. PBE-IA (STS-47). Run No. 3. Time interval: 41.5 - 48.5 seconds.

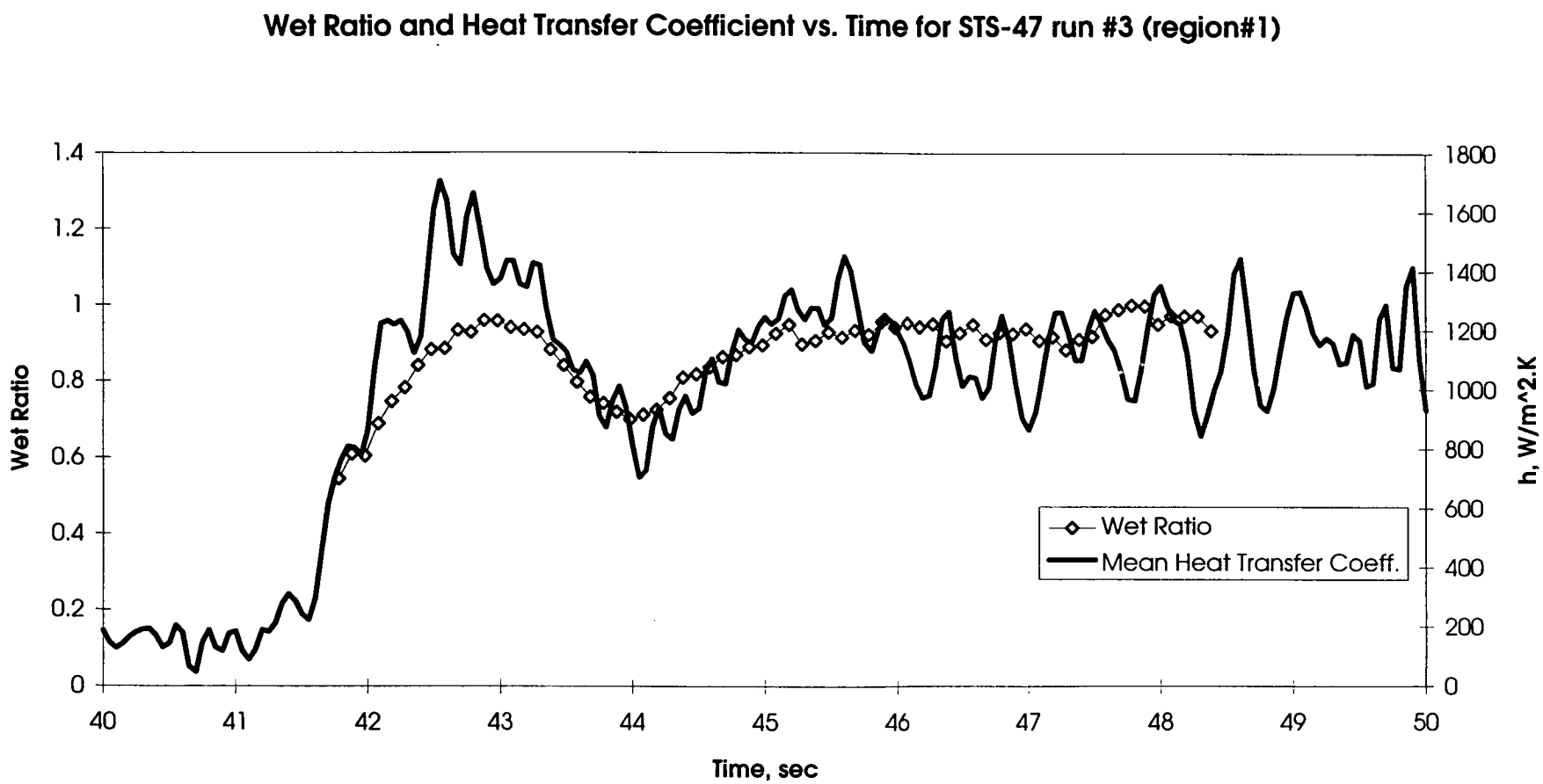

Figure A-10c-1-ii. Heater surface wet fraction and mean heat transfer coefficients. PBE-IA (STS-47). Run No. 3. Time interval: 41.5 - 48.5 seconds.

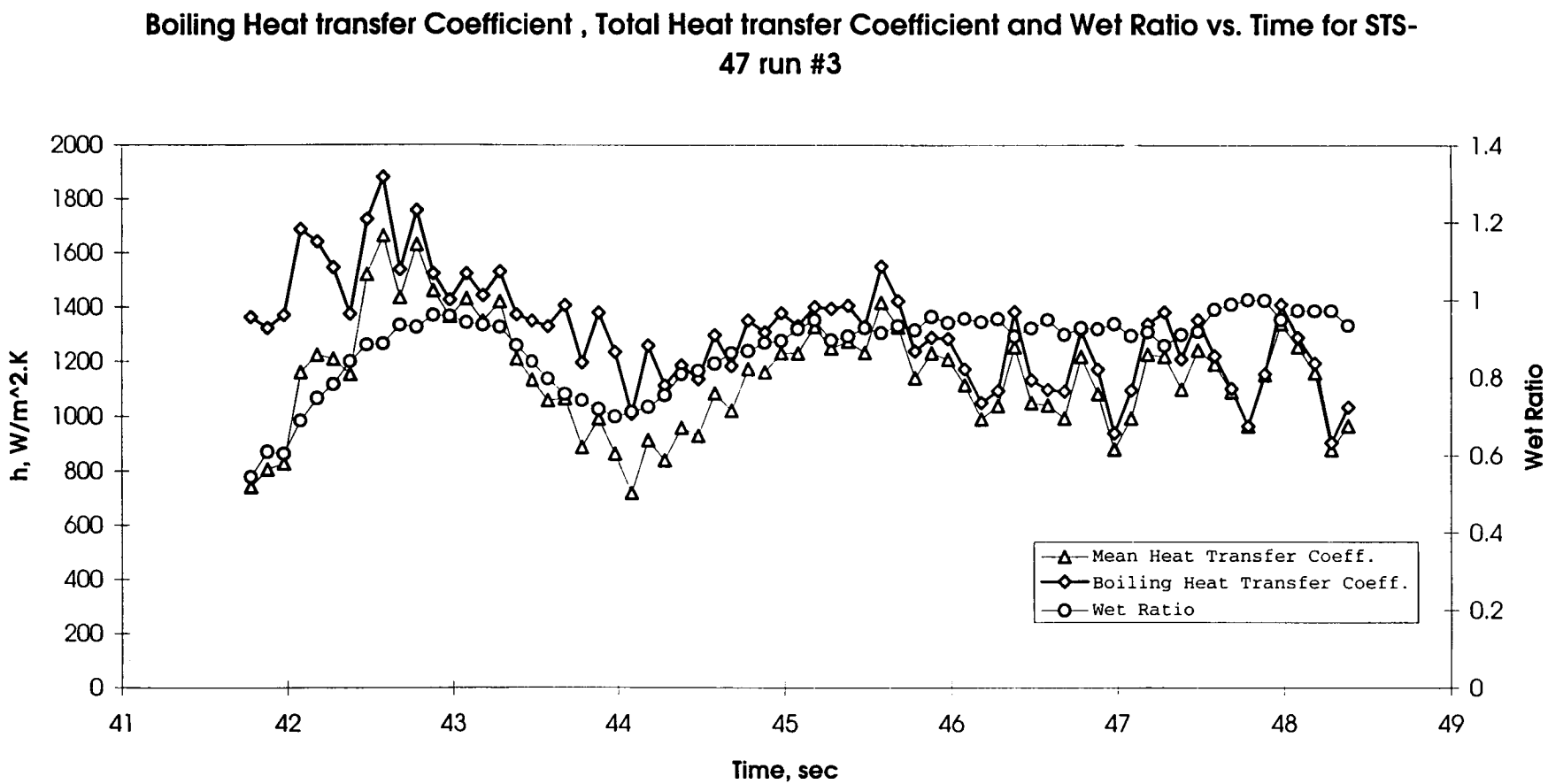

Figure A-10c-1-iii. Development of microgravity boiling heat transfer coefficient. PBE-IA (STS-47). Run No. 3. Time interval: 41.5 - 48.5 seconds.

STS-47 Run #3, Region 1

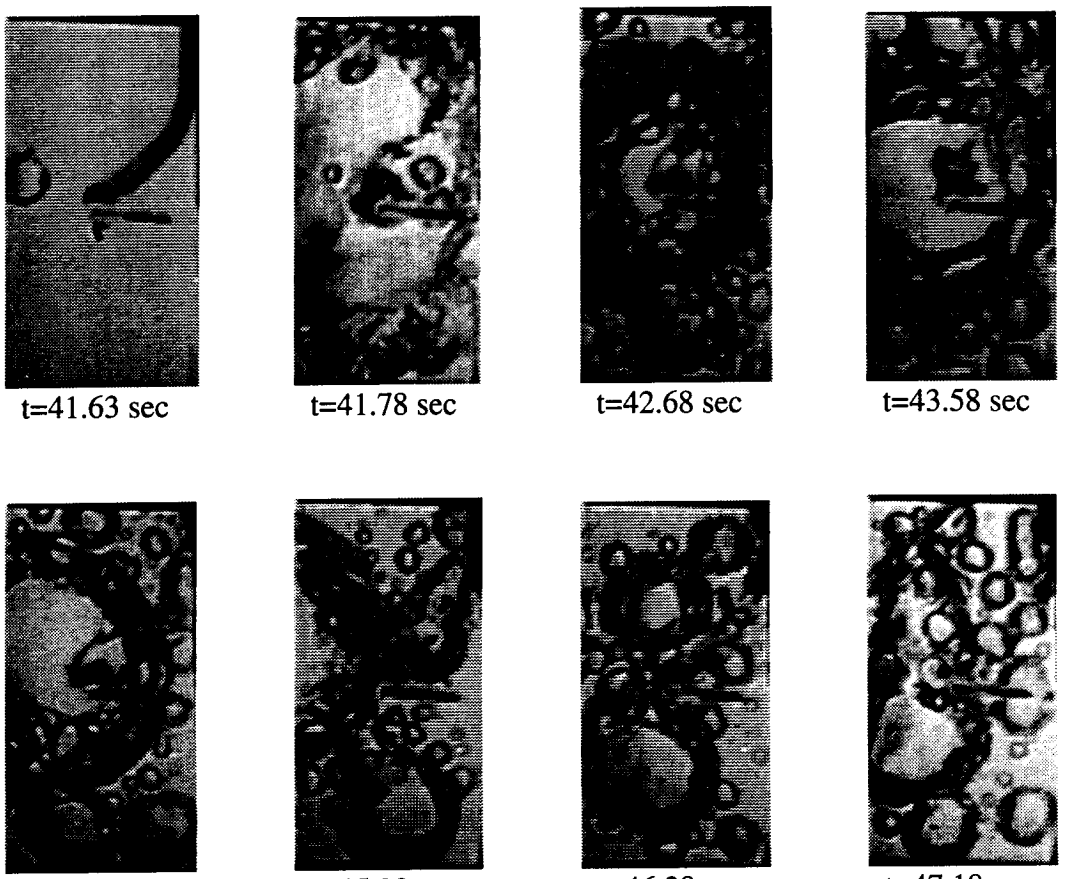

Figure A-10c-1-iv. Sample images showing dryout/rewetting. PBE-IA (STS-47). Run No. 3. Time interval: 41.5 - 48.5 seconds.

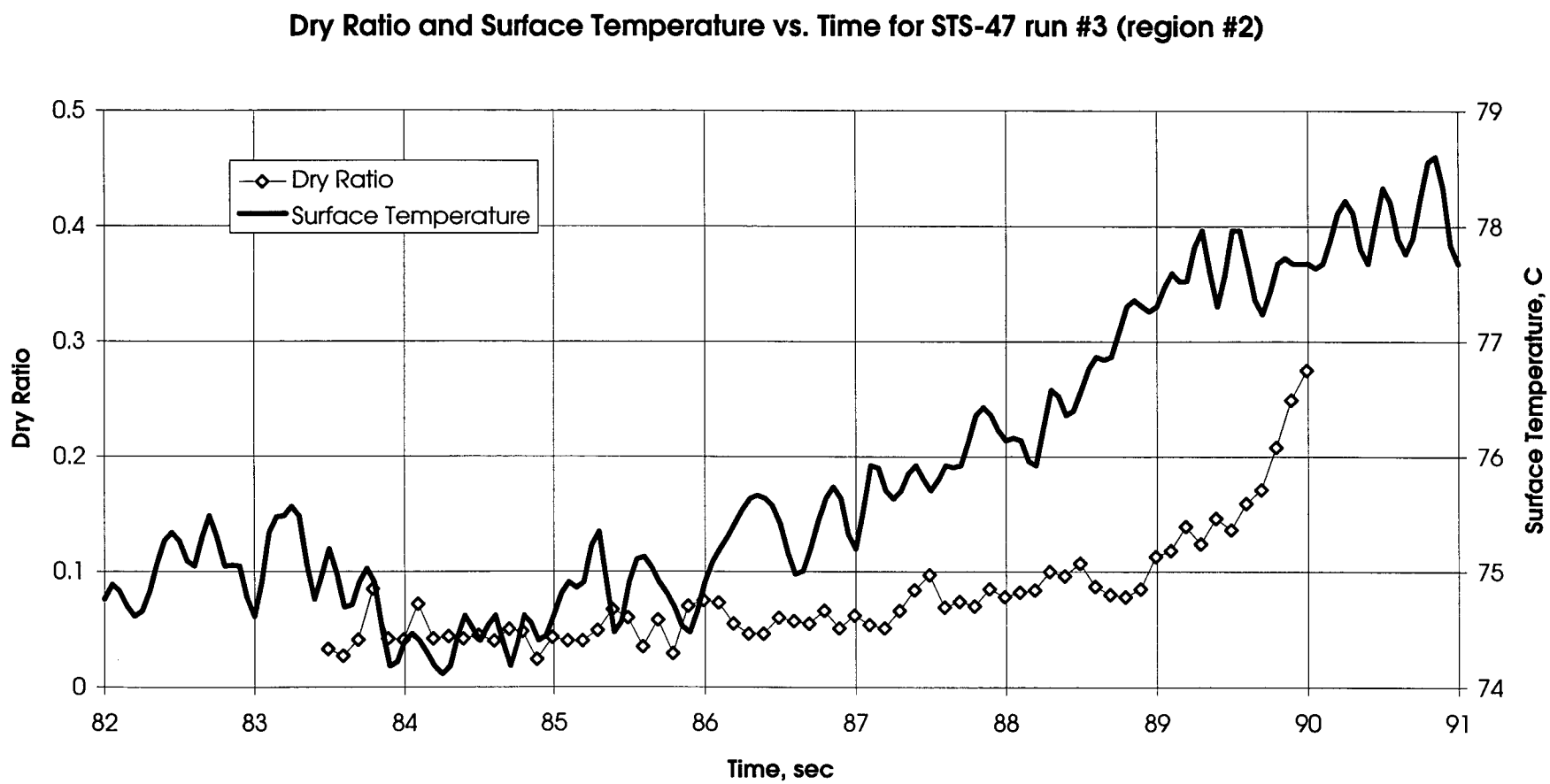

Figure A-10c-2-i. Heater surface dry fraction and mean temperature. PBE-IA (STS-47). Run No. 3. Time interval: 83.5 - 90.0 seconds.

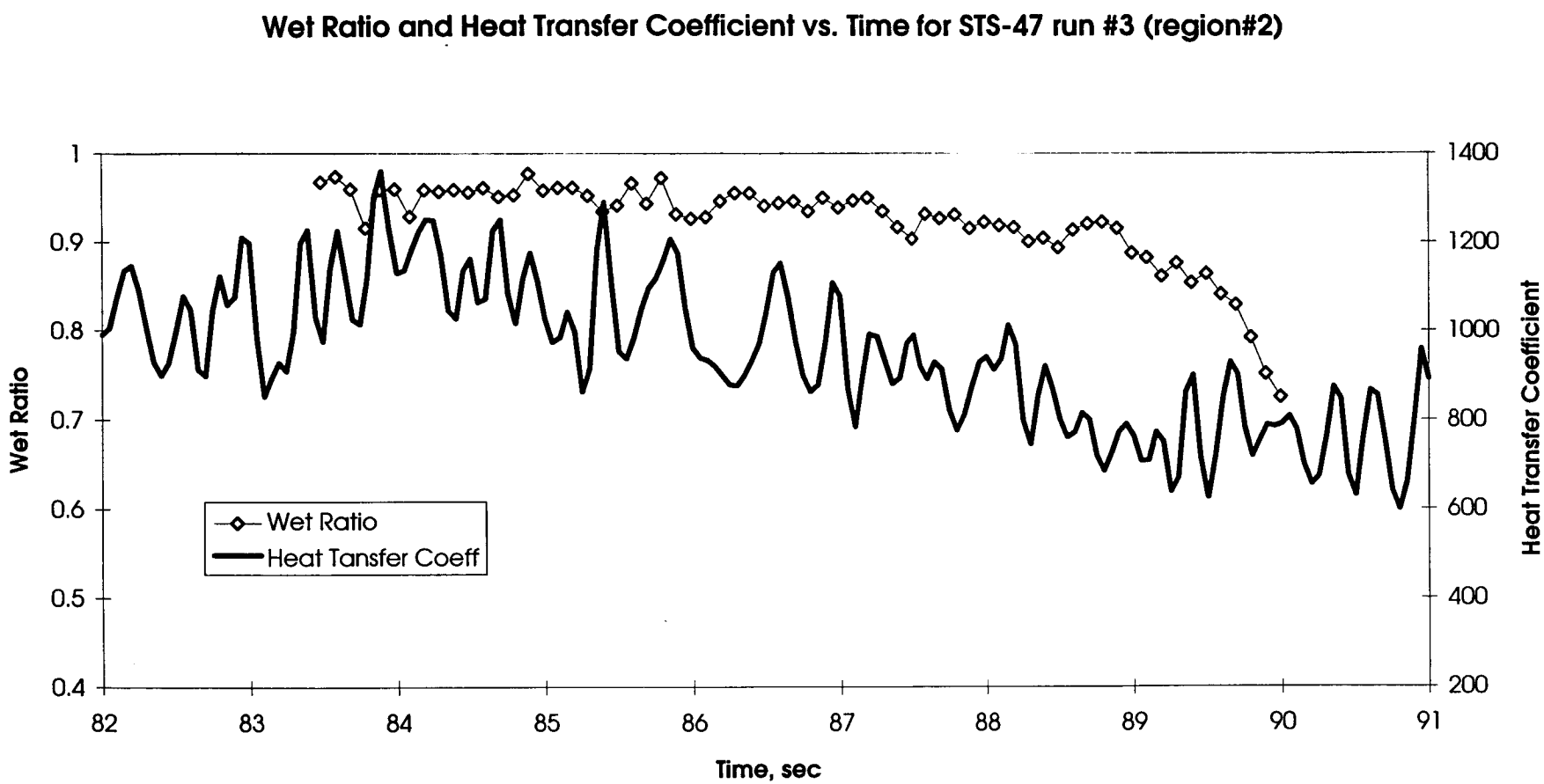

Figure A-10c-2-ii. Heater surface wet fraction and mean heat transfer coefficients. PBE-IA (STS-47). Run No. 3. Time interval: 83.5 - 90.0 seconds.

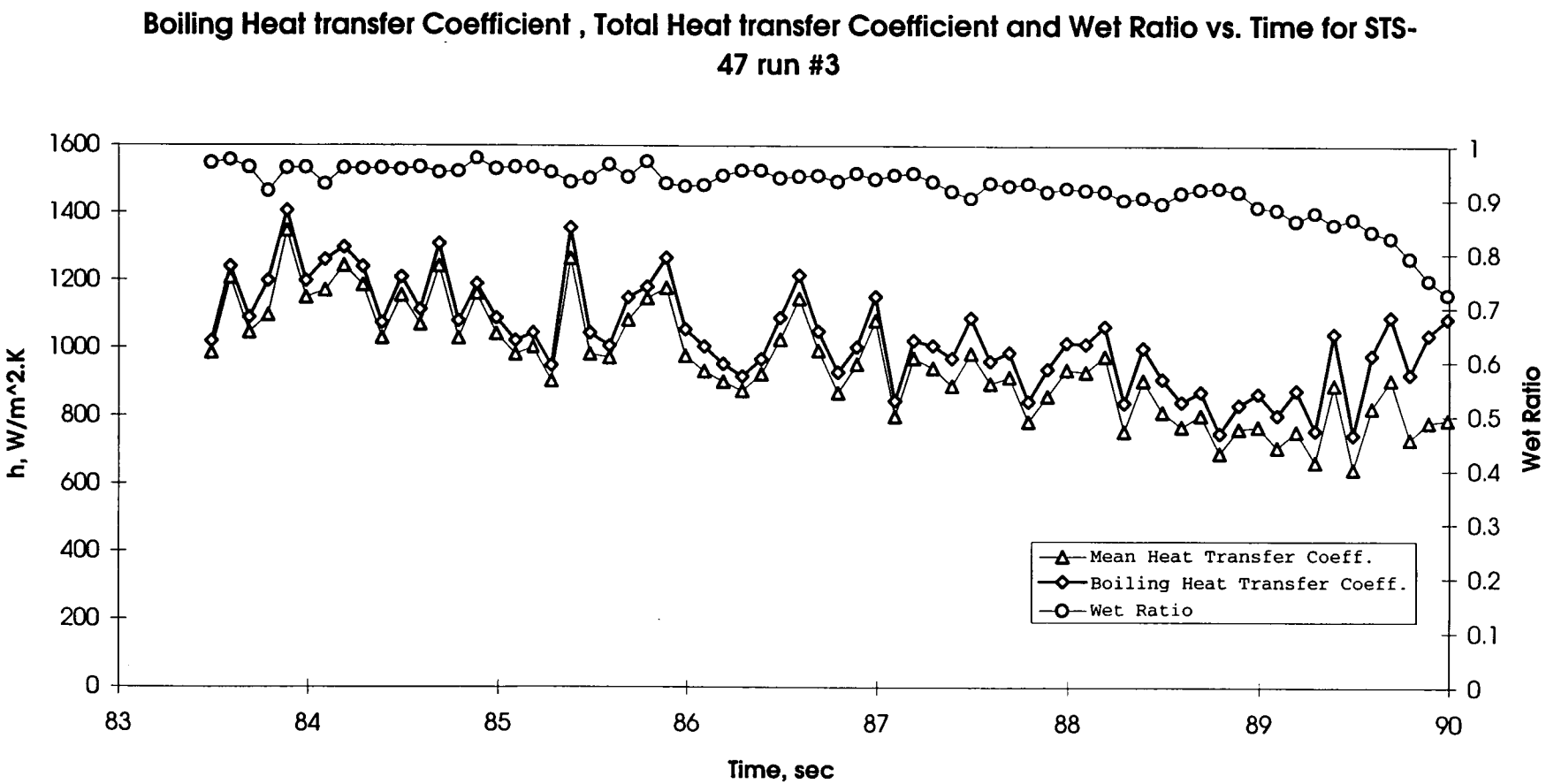

Figure A-10c-2-iii. Development of microgravity boiling heat transfer coefficient. PBE-IA (STS-47). Run No. 3. Time interval: 83.5 - 90.0 seconds.

STS-47 Run #3, Region 2

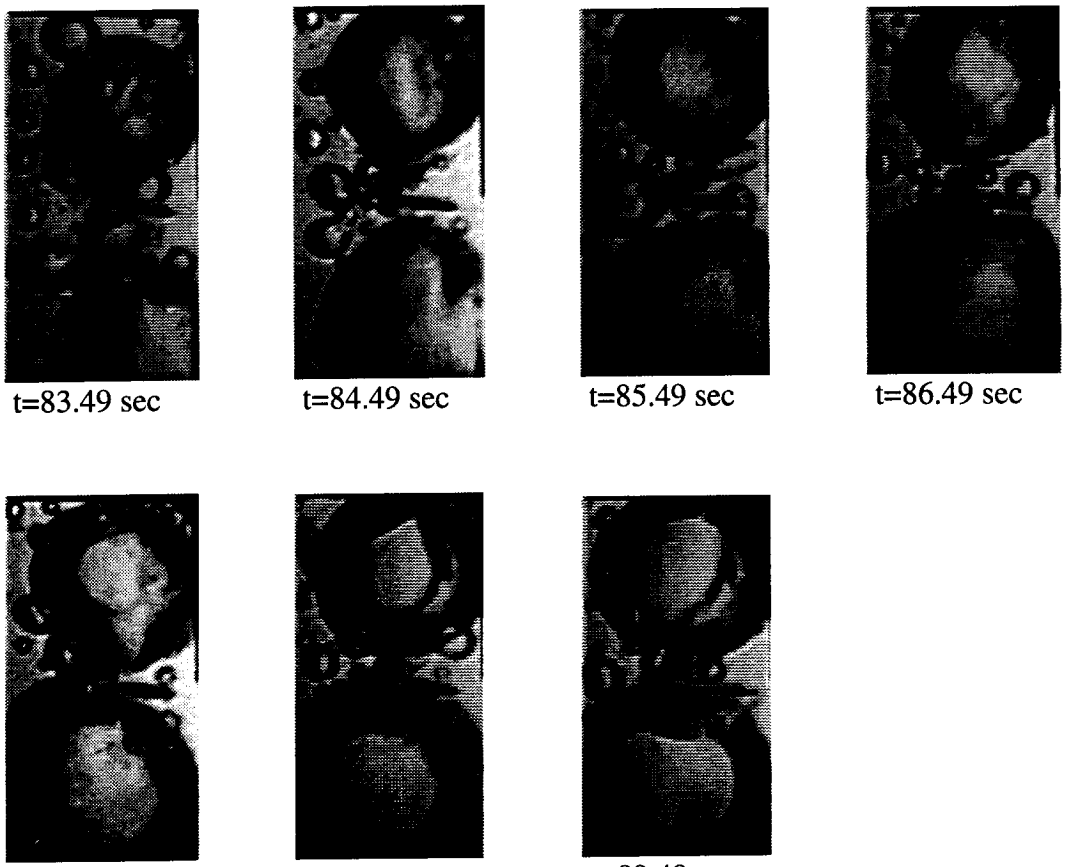

Figure A-10c-2-iv. Sample images showing dryout/rewetting. PBE-IA (STS-47). Run No. 3. Time interval: 83.5 - 90.0 seconds.

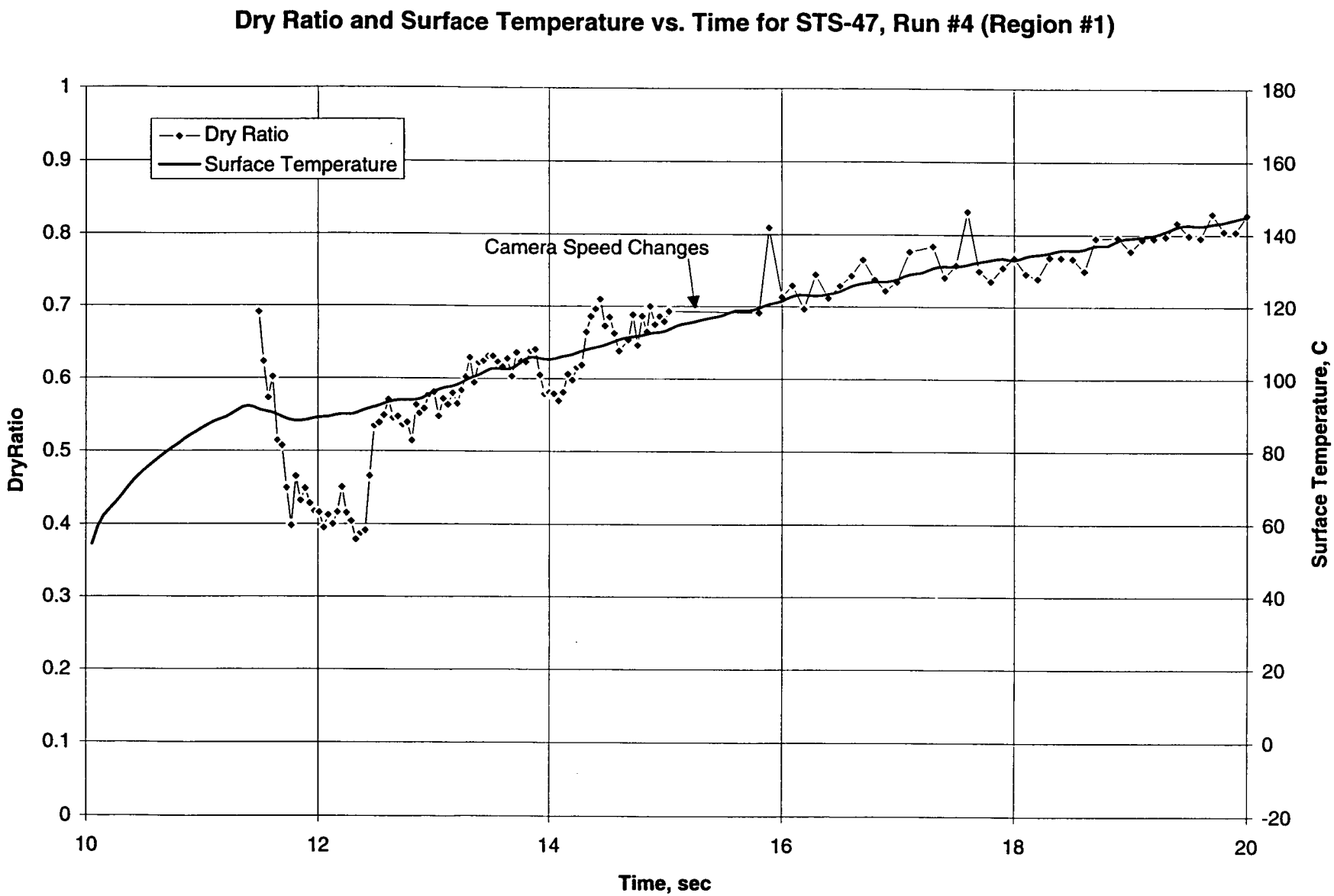

Figure A-10d-1-i. Heater surface dry fraction and mean temperature. PBE-IA (STS-47). Run No. 4. Time interval: 11.4 - 20.0 seconds.

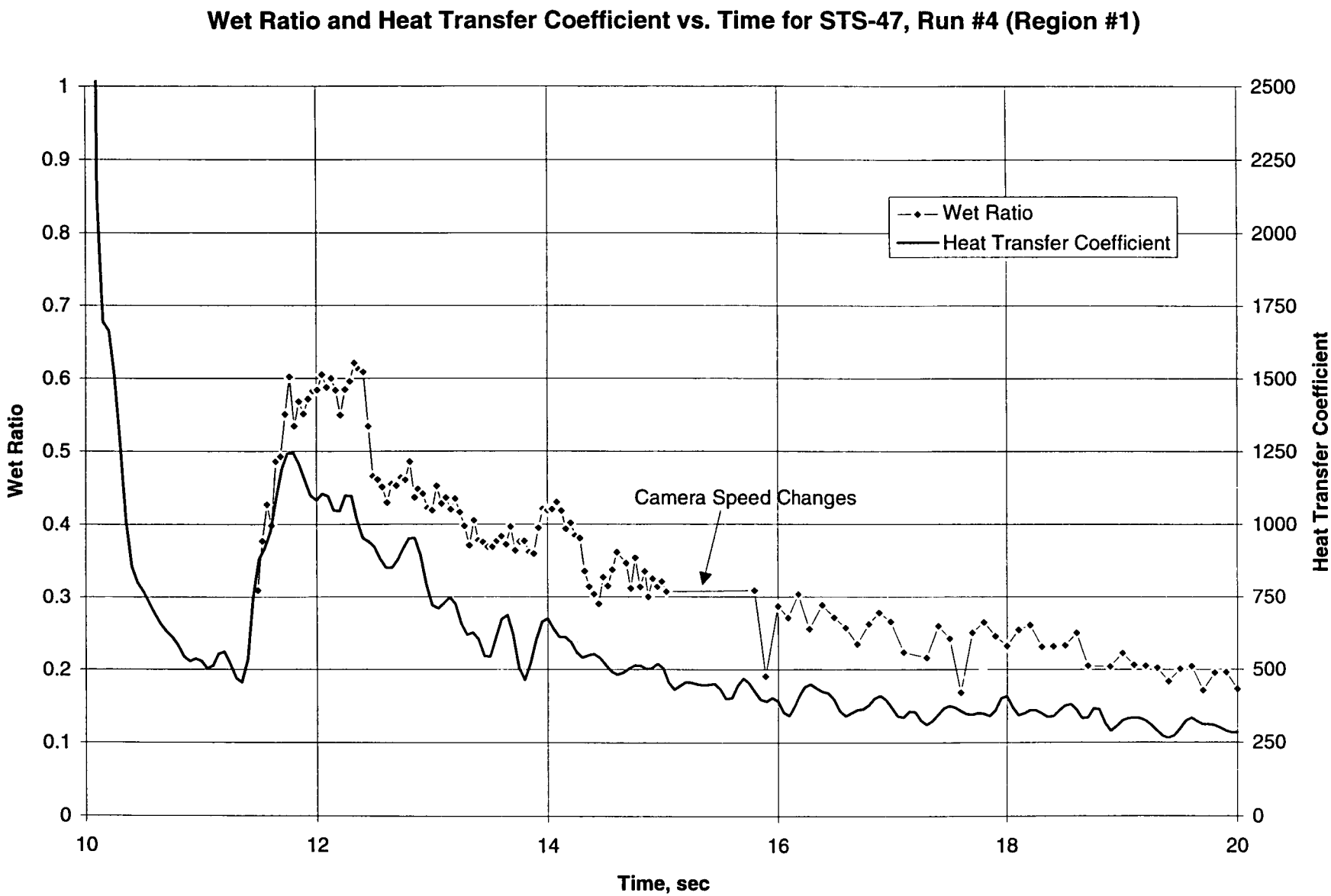

Figure A-10d-1-ii. Heater surface wet fraction and mean heat transfer coefficients. PBE-IA (STS-47). Run No. 4. Time interval: 11.4 - 20.0 seconds.

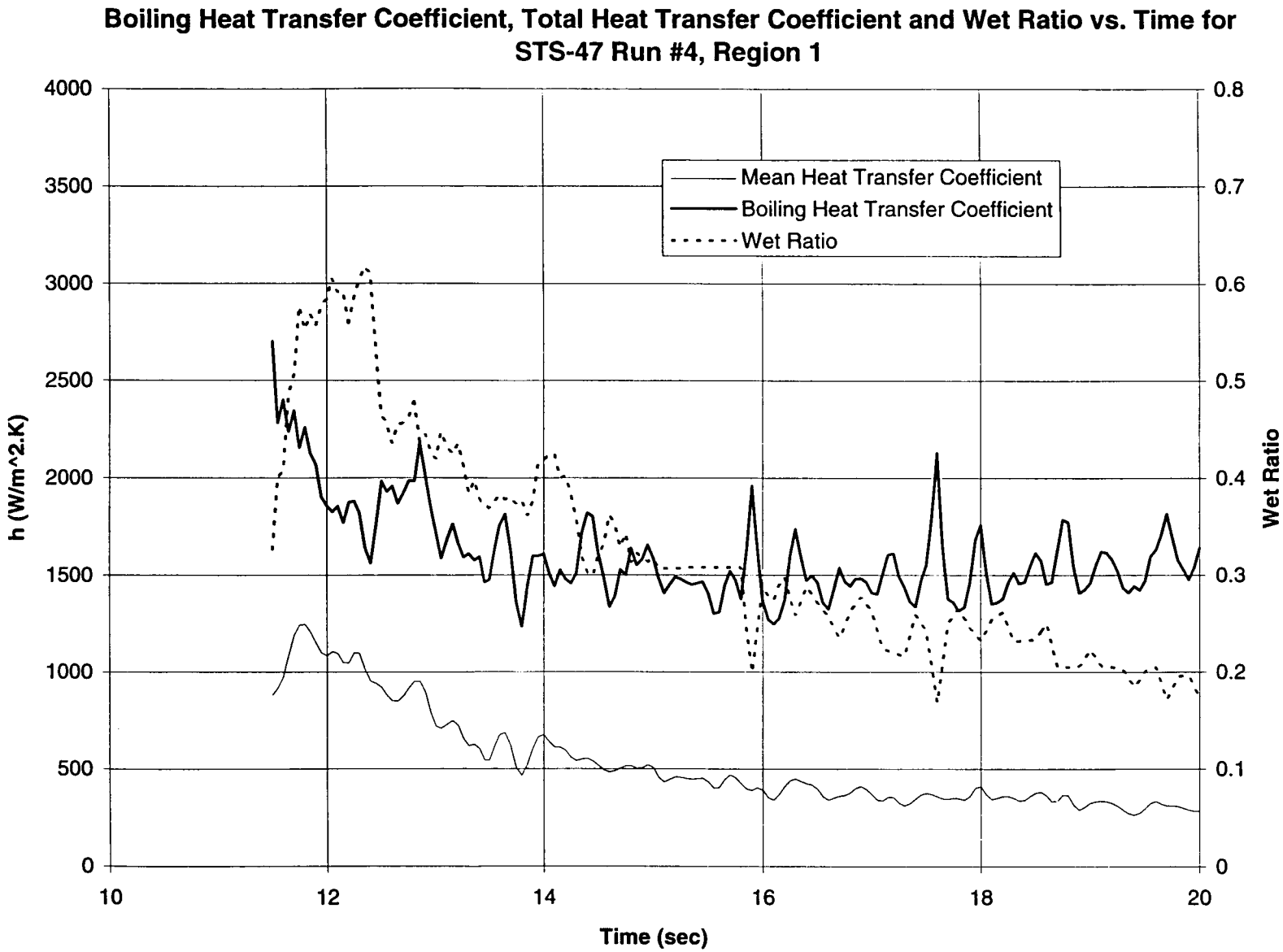

Figure A-10d-1-iii. Development of microgravity boiling heat transfer coefficient. PBE-IA (STS-47). Run No. 4. Time interval: 11.4 - 20.0 seconds.

STS-47 Run #4

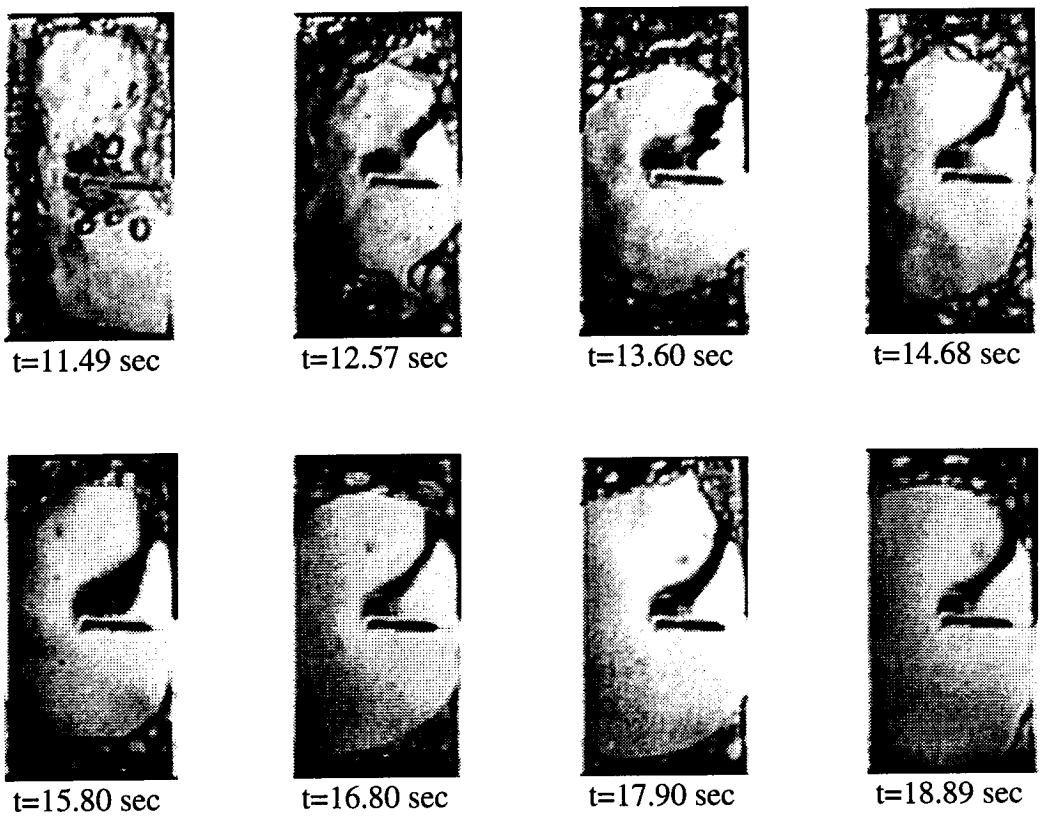

Figure A-10d-1-iv. Sample images showing dryout/rewetting. PBE-IA (STS-47). Run No. 4. Time interval: 11.4 - 20.0 seconds.

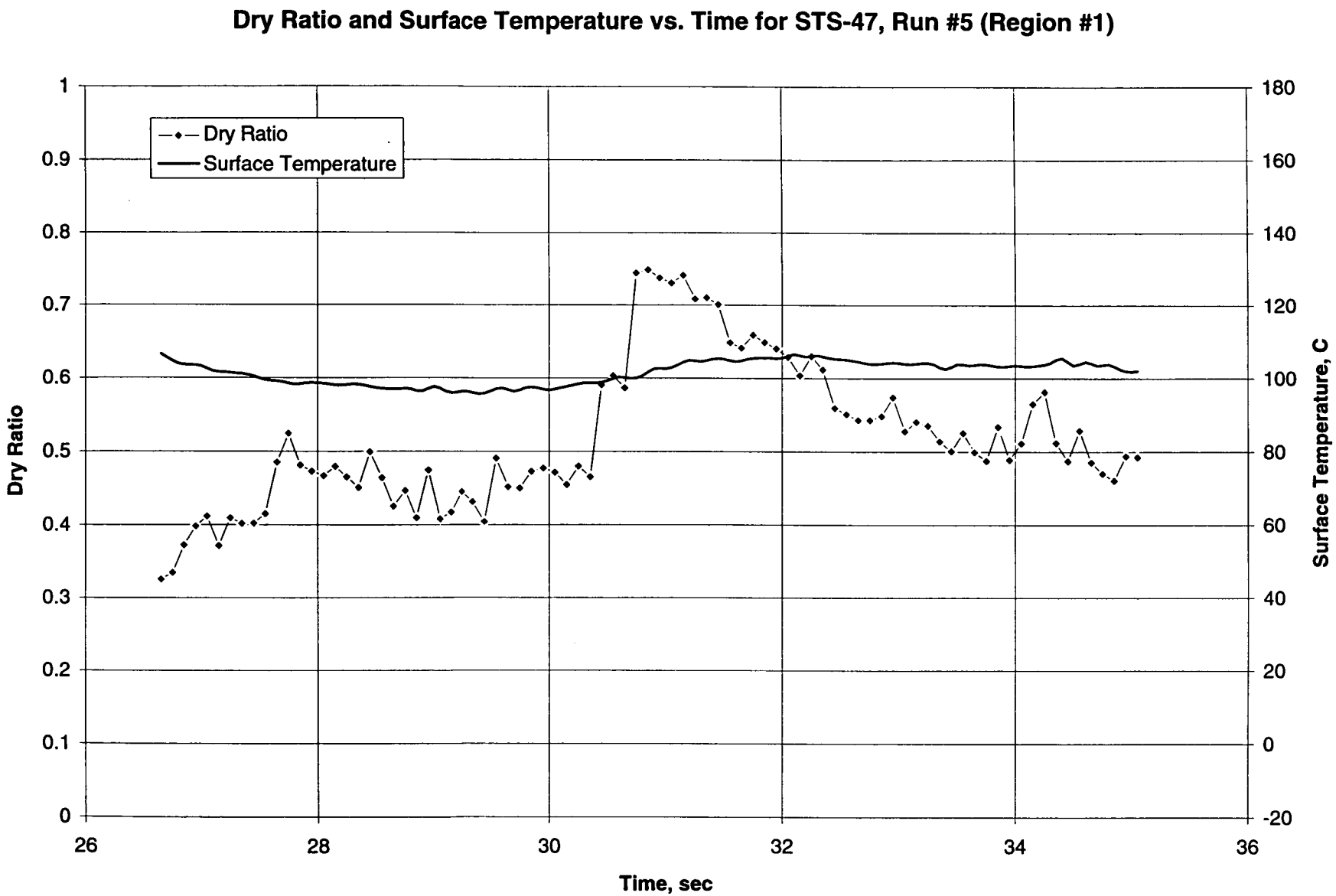

Figure A-10e-1-i. Heater surface dry fraction and mean temperature. PBE-IA (STS-47). Run No. 5. Time interval: 26.5 - 35.0 seconds.

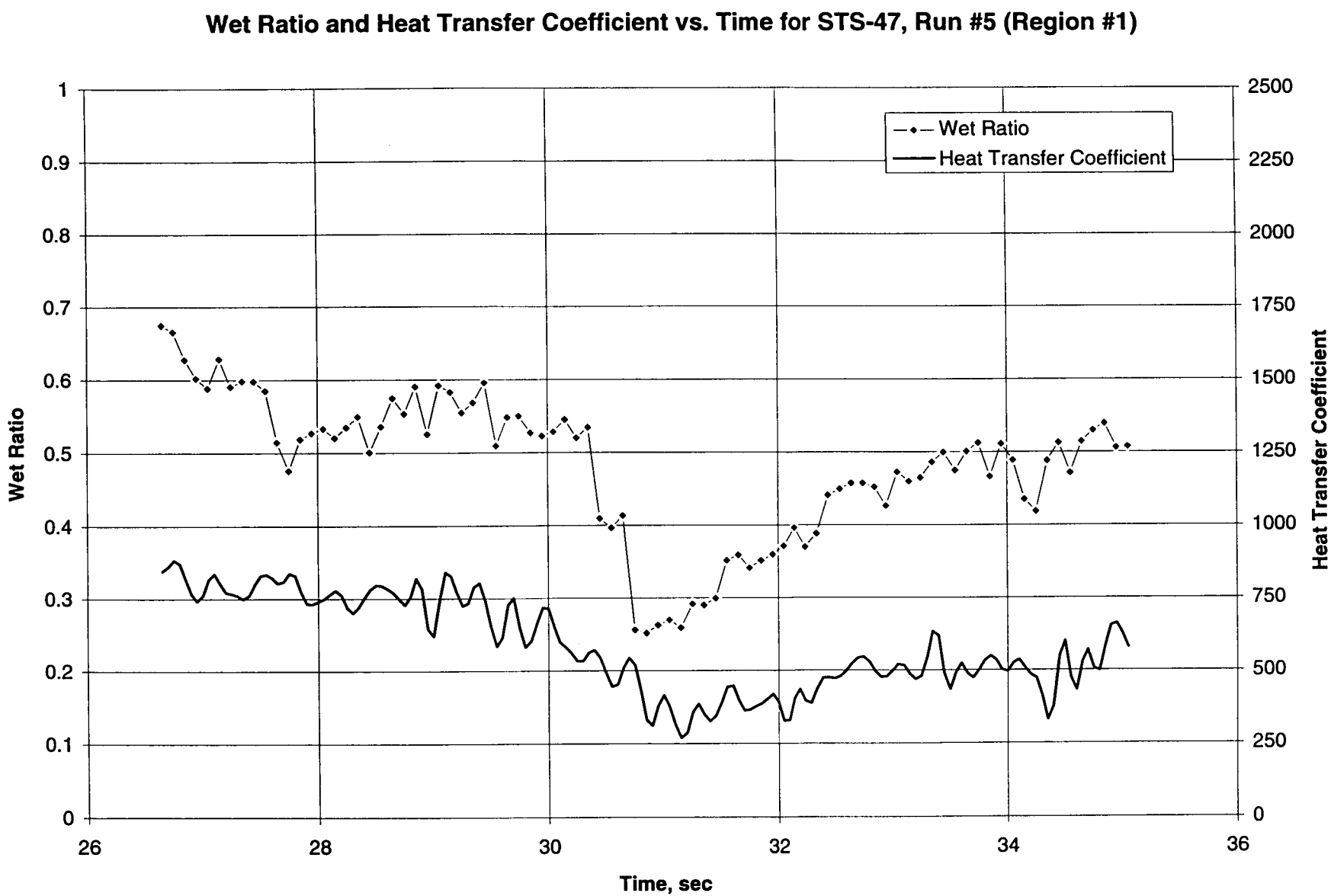

Figure A-10e-1-ii. Heater surface wet fraction and mean heat transfer coefficients. PBE-IA (STS-47). Run No. 5. Time interval: 26.5 - 35.0 seconds.

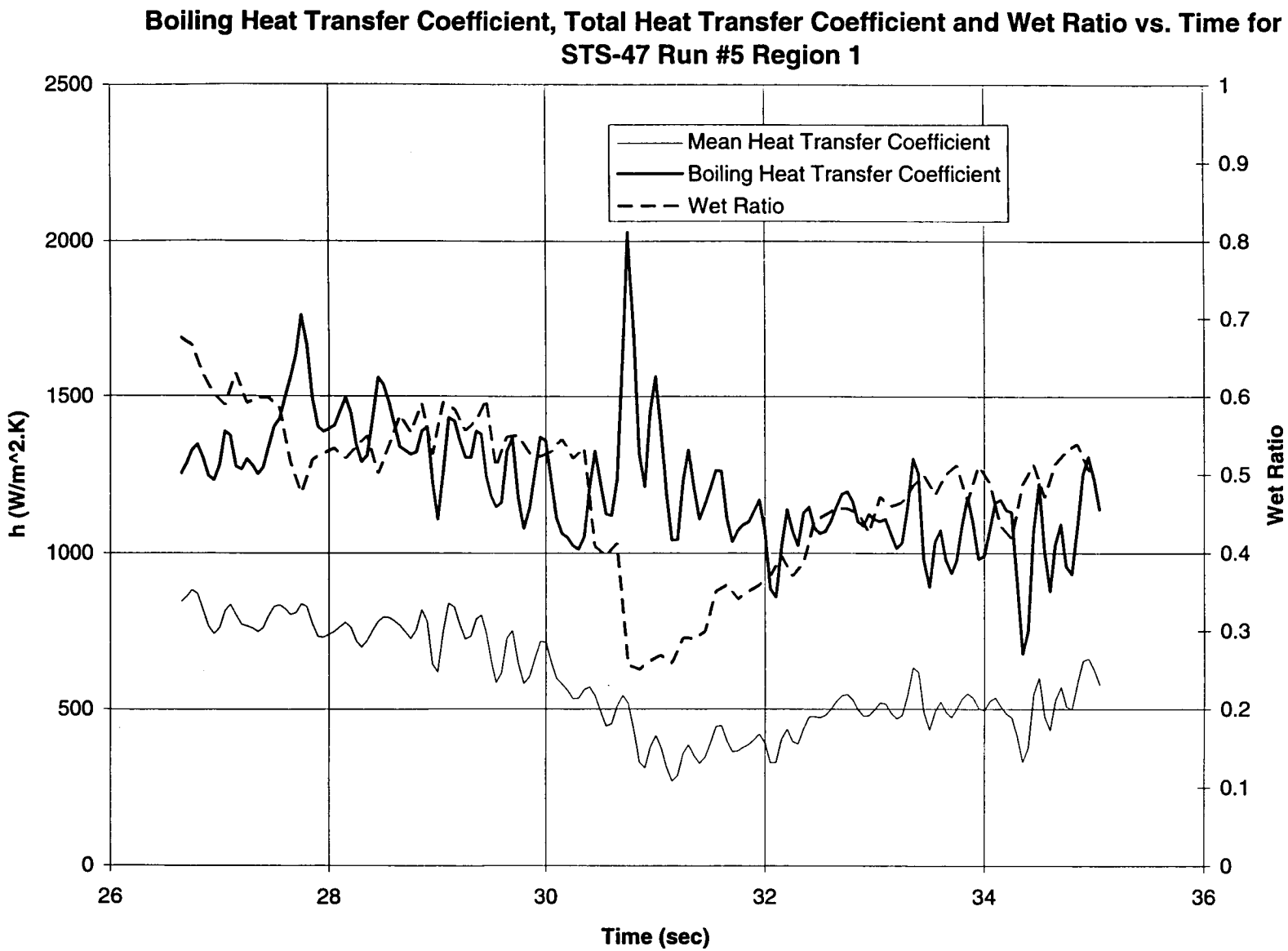

Figure A-10e-1-iii. Development of microgravity boiling heat transfer coefficient. PBE-IA (STS-47). Run No. 5. Time interval: 26.5 - 35.0 seconds.

STS-47 Run #5, Region 1

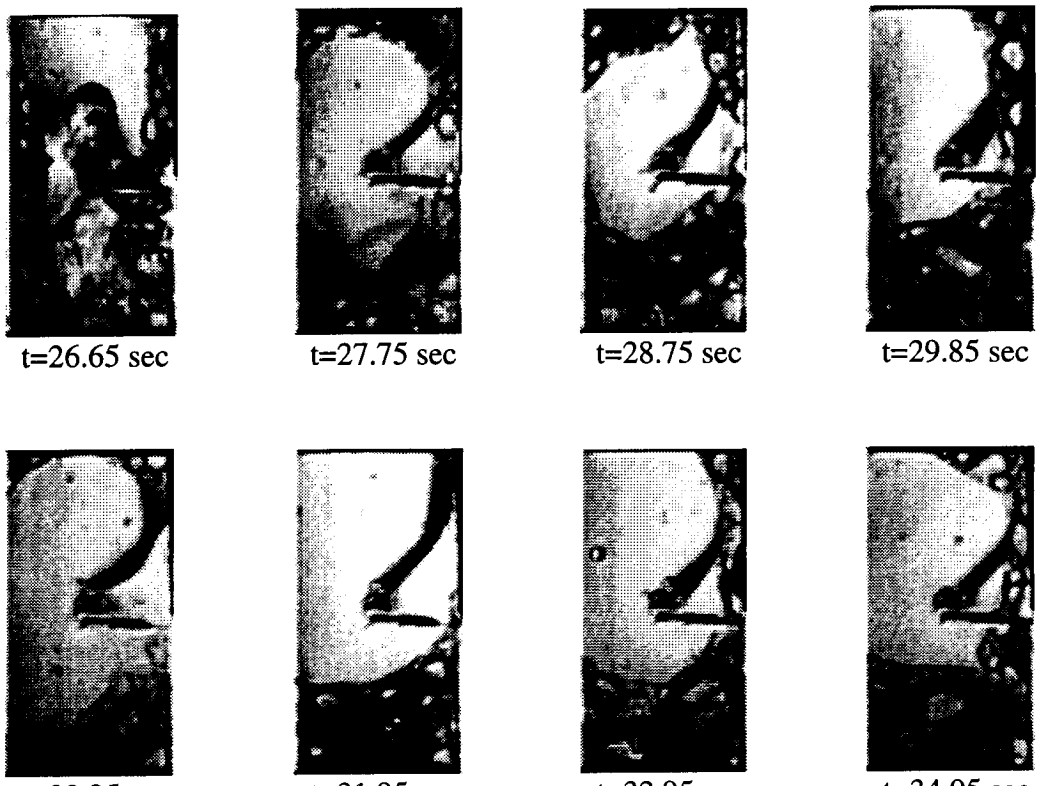

Figure A-10e-1-iv. Sample images showing dryout/rewetting. PBE-IA (STS-47). Run No. 5. Time interval: 26.5 - 35.0 seconds.

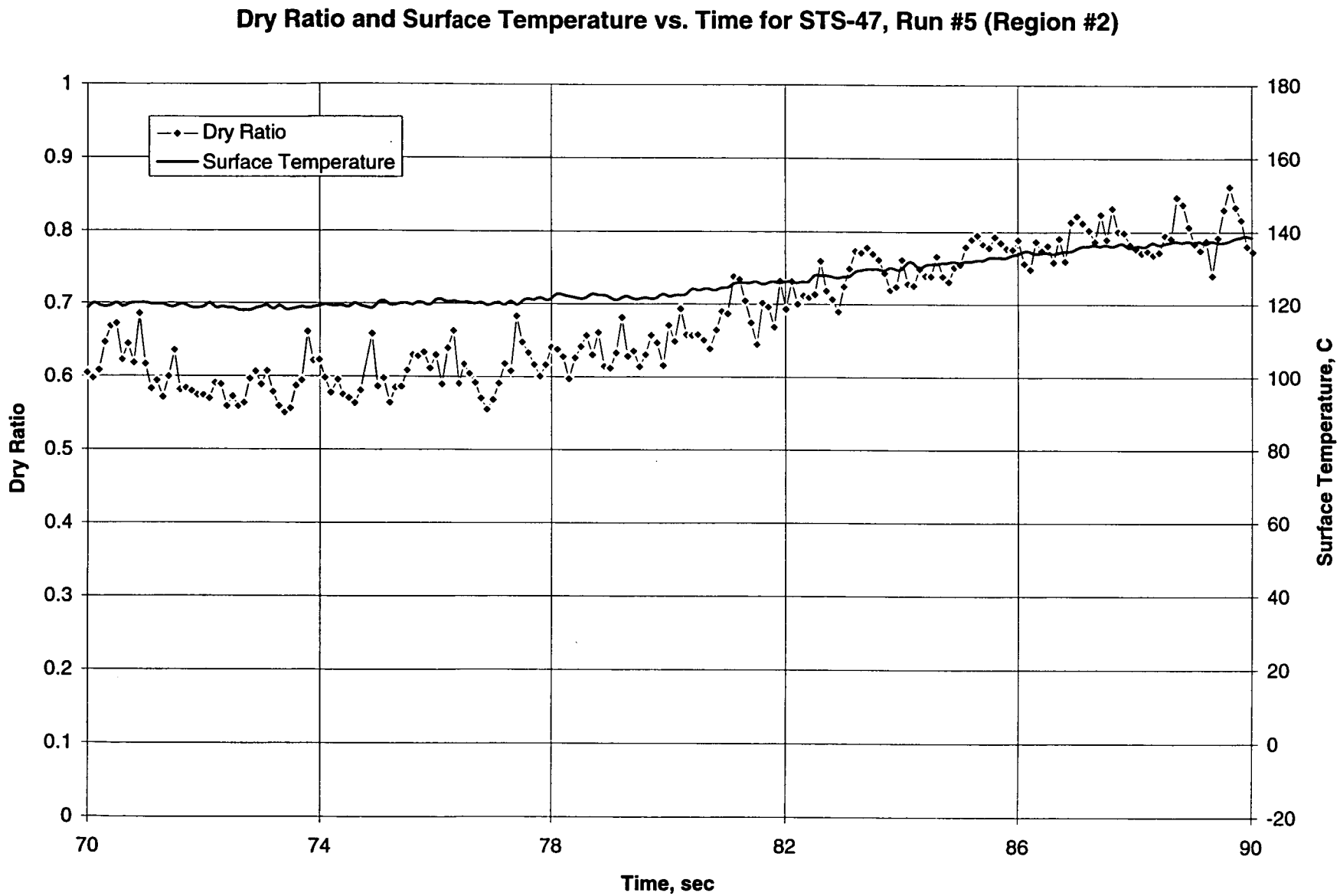

Figure A-10-e-2-i. Heater surface dry fraction and mean temperature. PBE-IA (STS-47). Run No. 5. Time interval: 70.0 - 90.0 seconds.

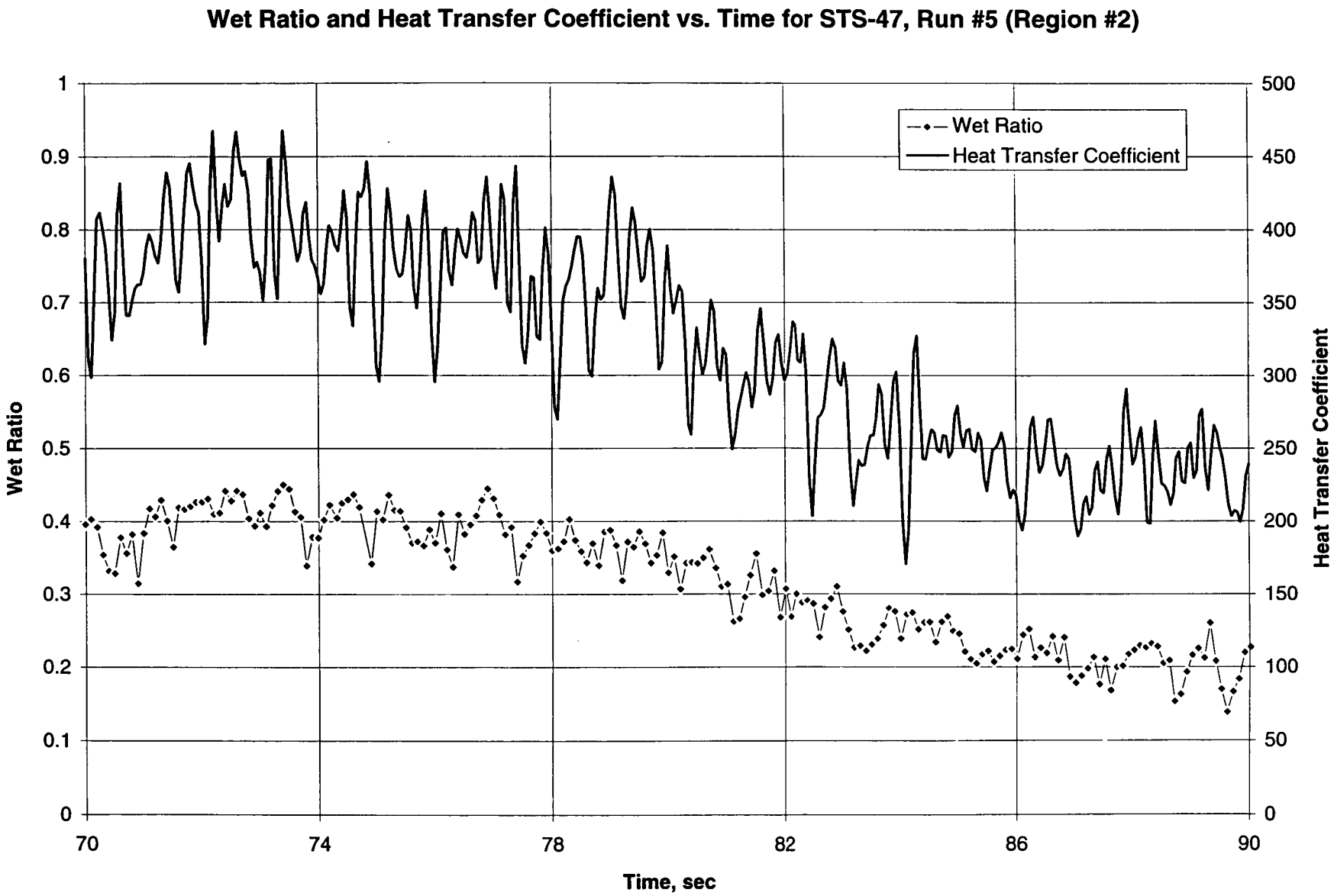

Figure A-10e-2-ii. Heater surface wet fraction and mean heat transfer coefficients. PBE-IA (STS-47). Run No. 5. Time interval: 70.0 - 90.0 seconds.

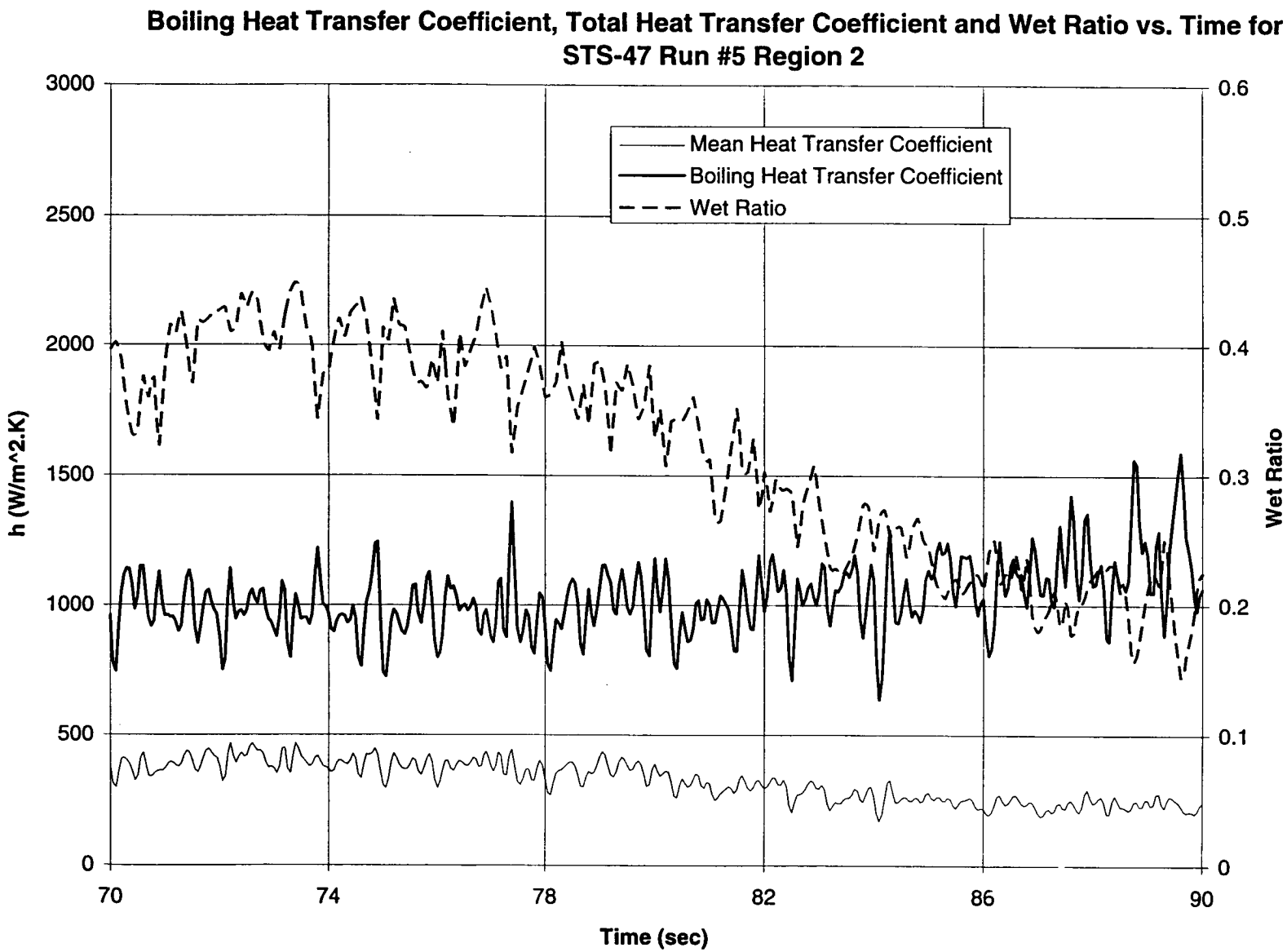

Figure A-10e-2-iii. Development of microgravity boiling heat transfer coefficient. PBE-IA (STS-47). Run No. 5. Time interval: 70.0 - 90.0 seconds.

STS-47 Run #5, Region 2

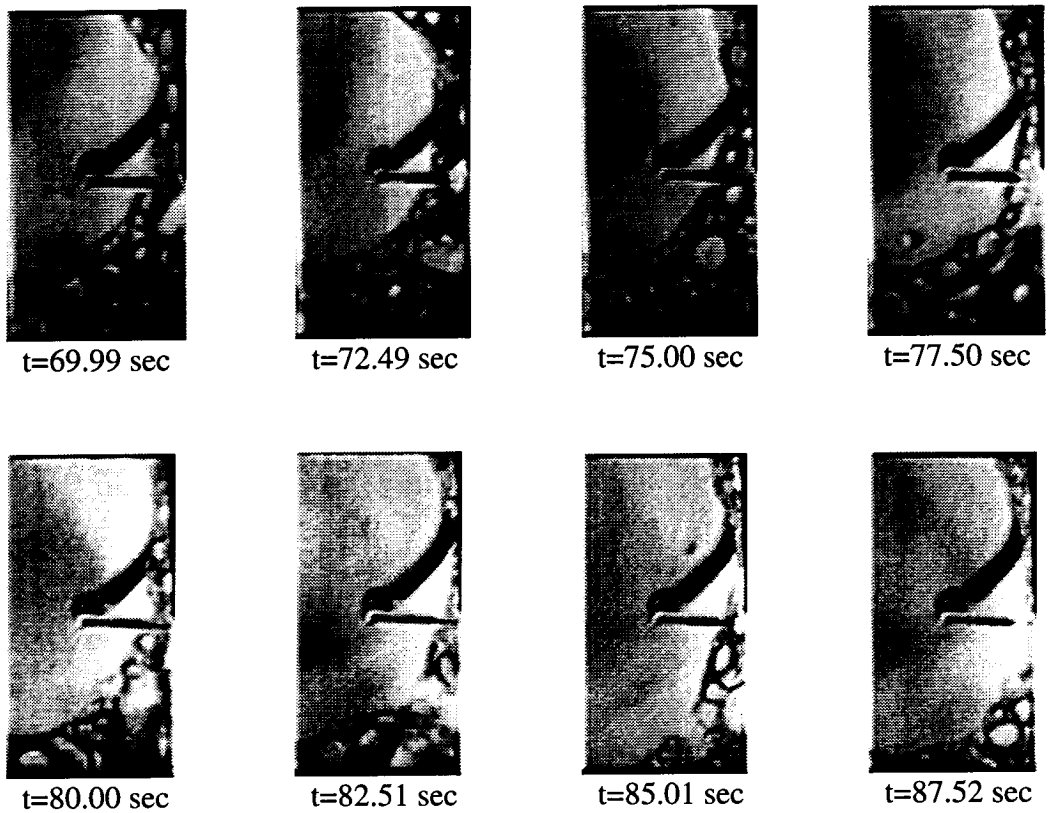

Figure A-10e-2-iv. Sample images showing dryout/rewetting. PBE-IA (STS-47). Run No. 5. Time interval: 70.0 - 90.0 seconds.

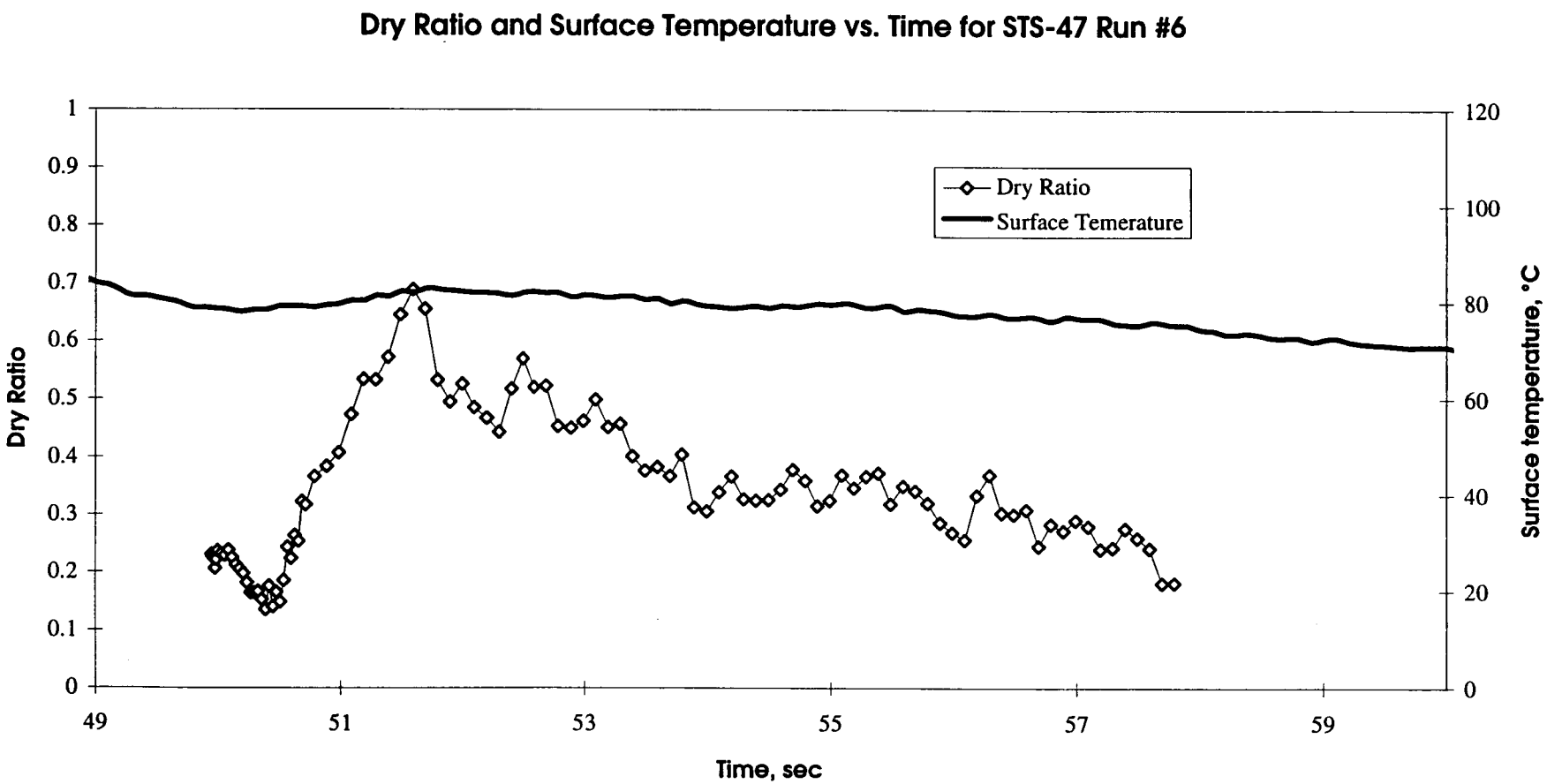

Figure A-10f-1-i. Heater surface dry fraction and mean temperature. PBE-IA (STS-47). Run No. 6. Time interval: 50 - 58 seconds.

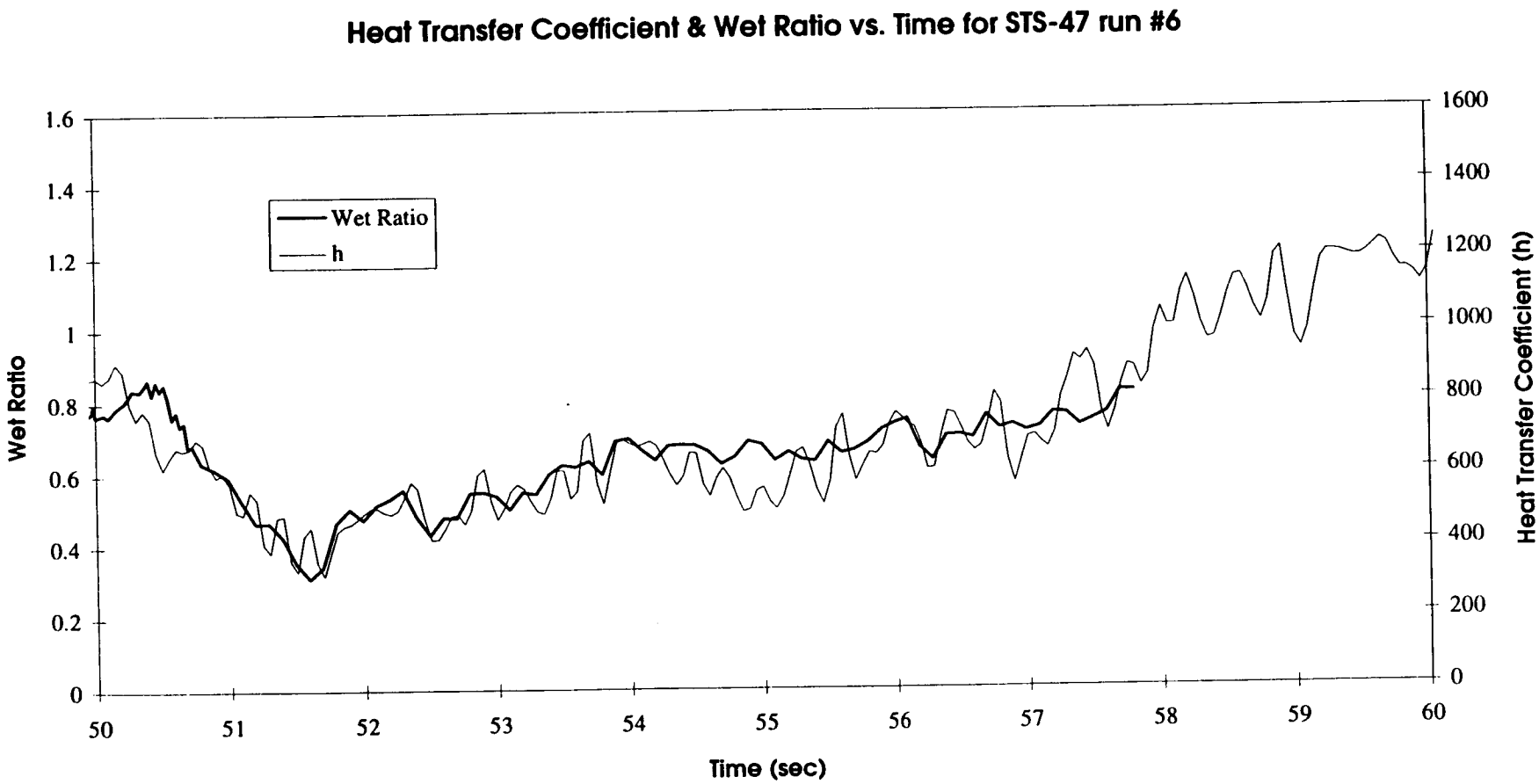

Figure A-10f-1-ii. Heater surface wet fraction and mean heat transfer coefficients. PBE-IA (STS-47). Run No. 6. Time interval: 50 - 58 seconds.

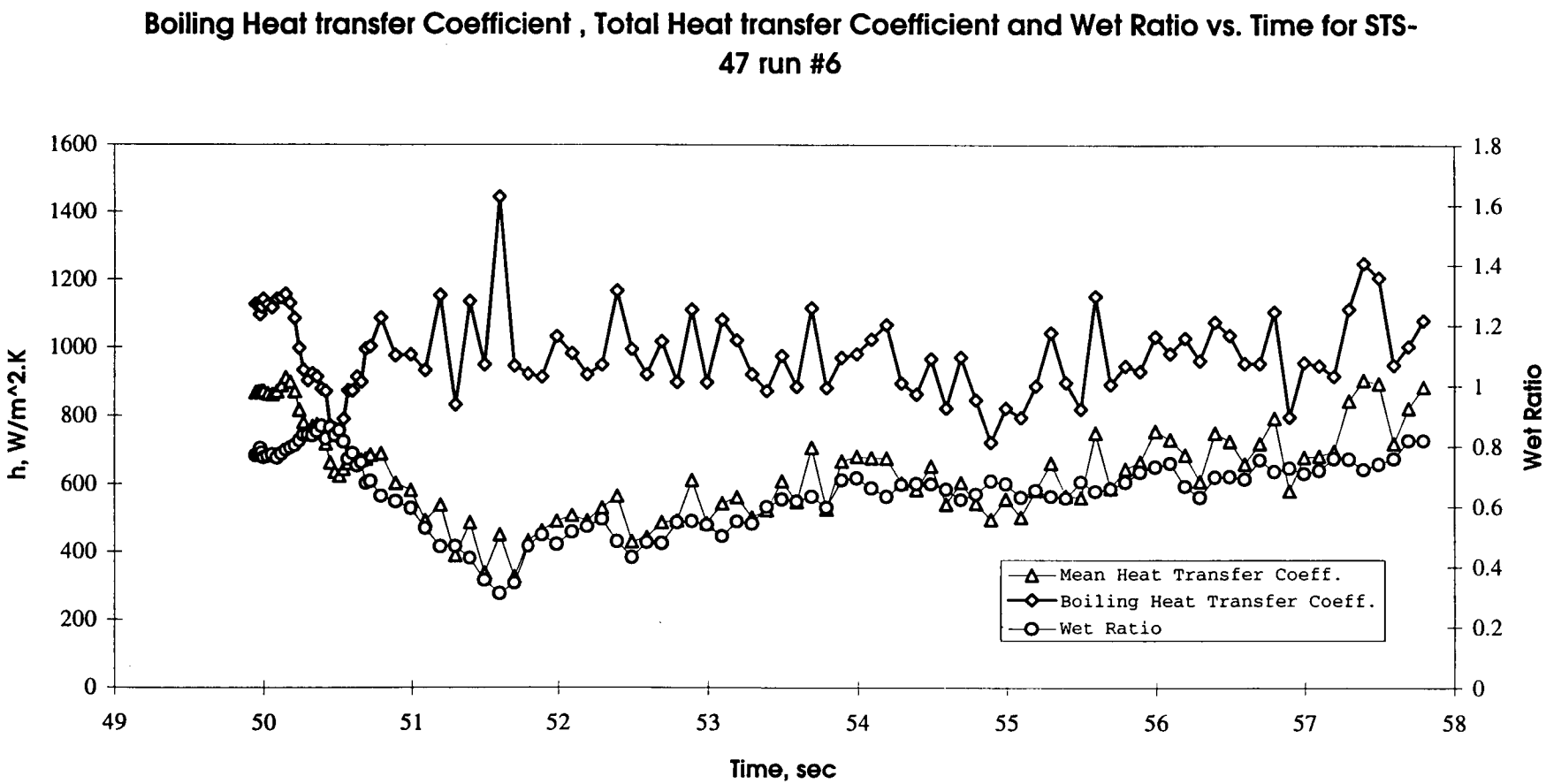

Figure A-10f-1-iii. Development of microgravity boiling heat transfer coefficient. PBE-IA (STS-47). Run No. 6. Time interval: 50 - 58 seconds.

STS-47 Run # 6

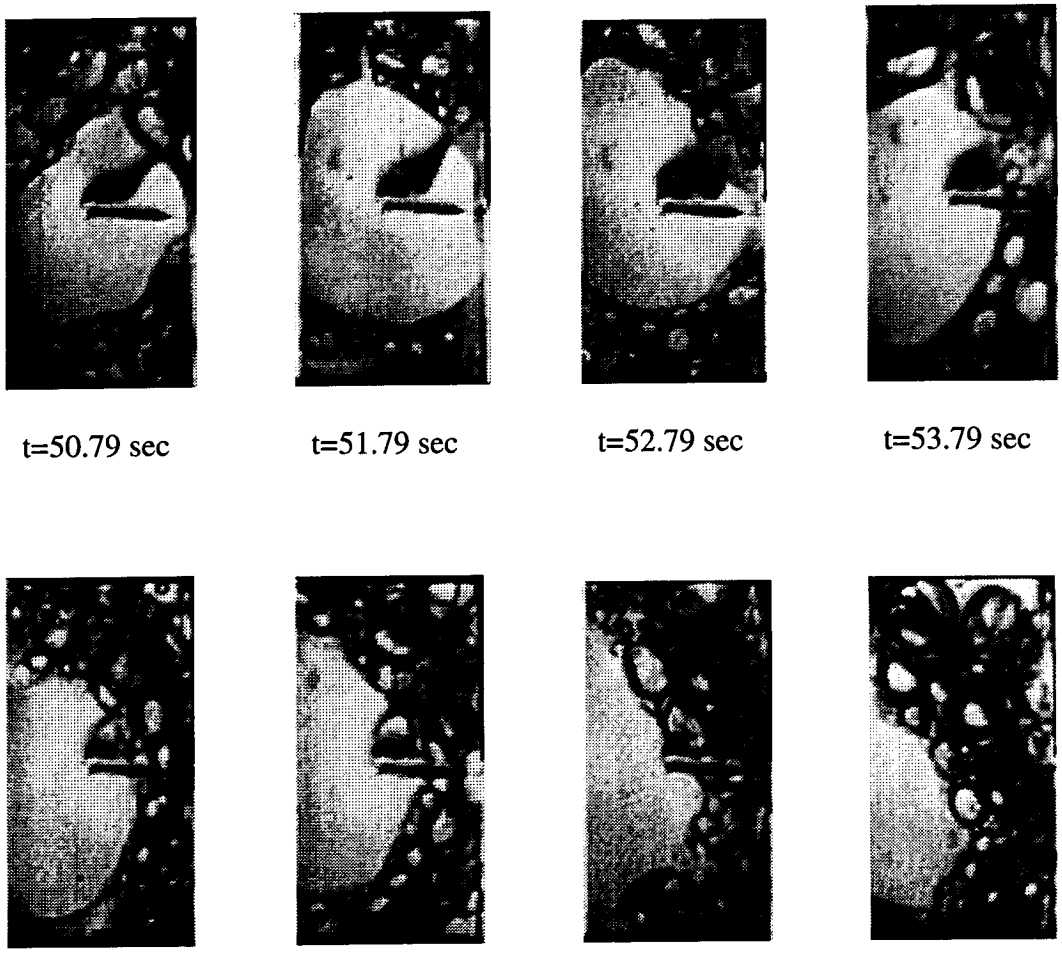

Figure A-10f-1-iv. Sample images showing dryout/rewetting. PBE-IA (STS-47). Run No. 6. Time interval: 50 - 58 seconds.

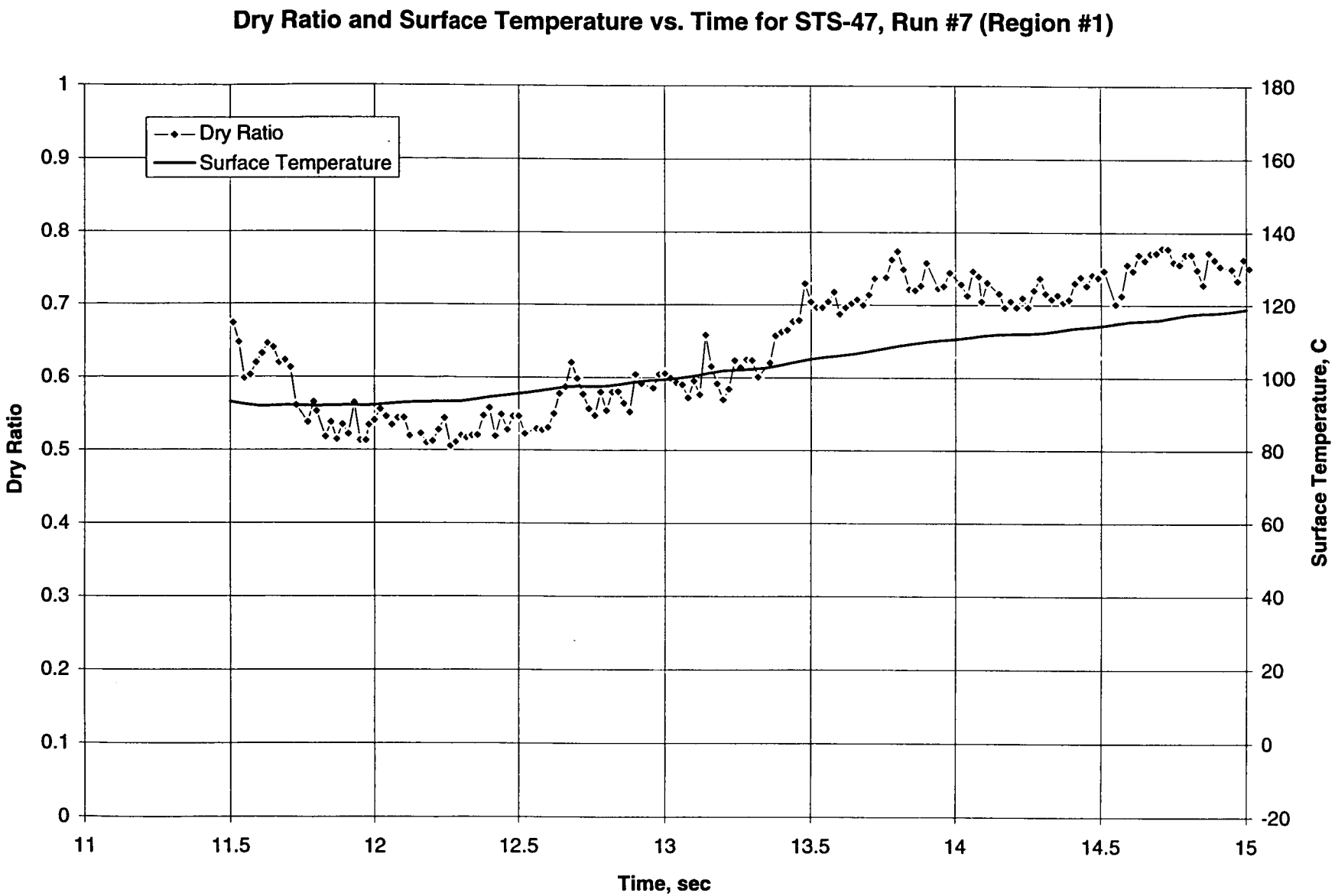

Figure A-10g-1-i. Heater surface dry fraction and mean temperature. PBE-IA (STS-47). Run No. 7. Time interval: 11.5 - 15.0 seconds.

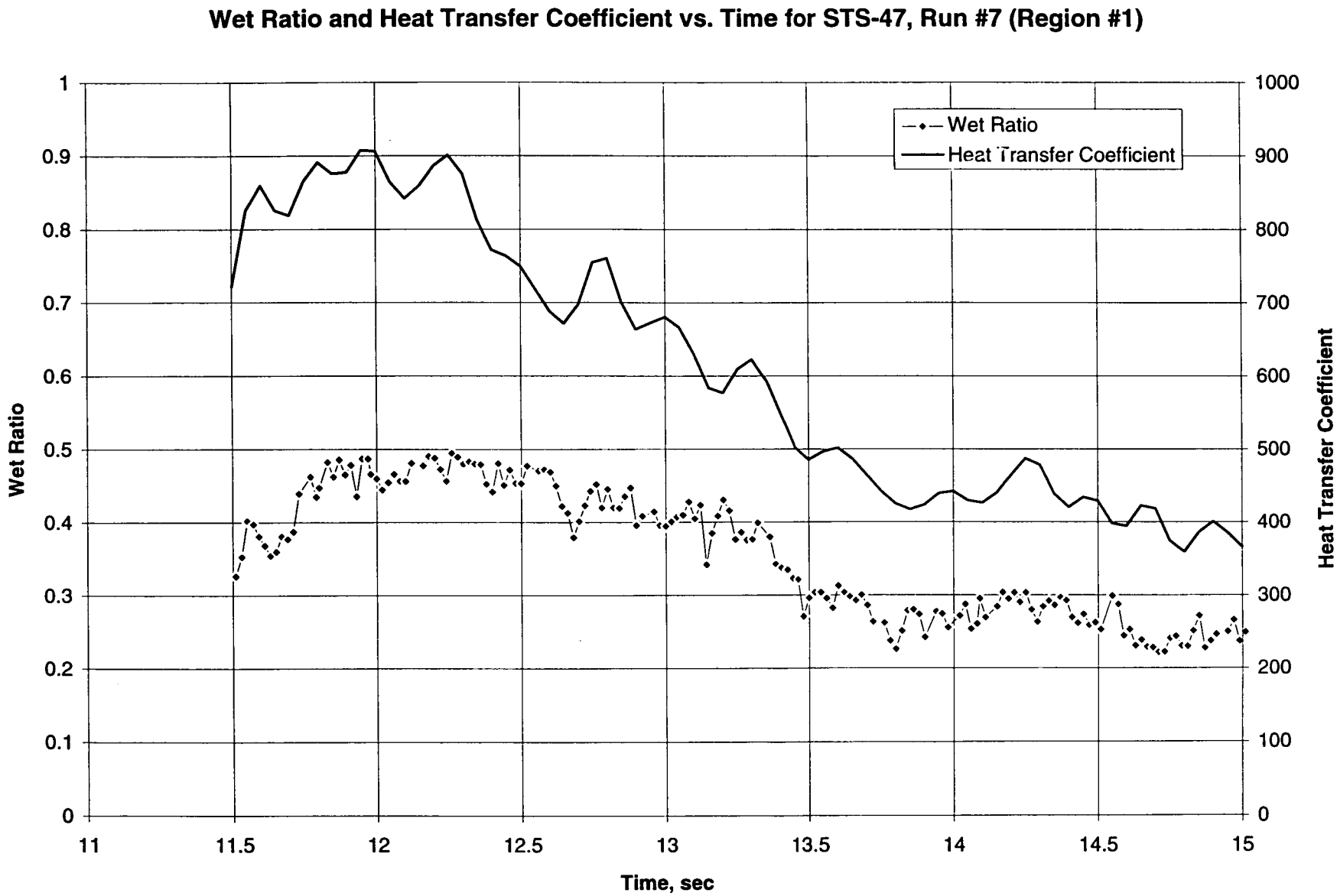

Figure A-10g-1-ii. Heater surface wet fraction and mean heat transfer coefficients. PBE-IA (STS-47). Run No. 7. Time interval: 11.5 - 15.0 seconds.

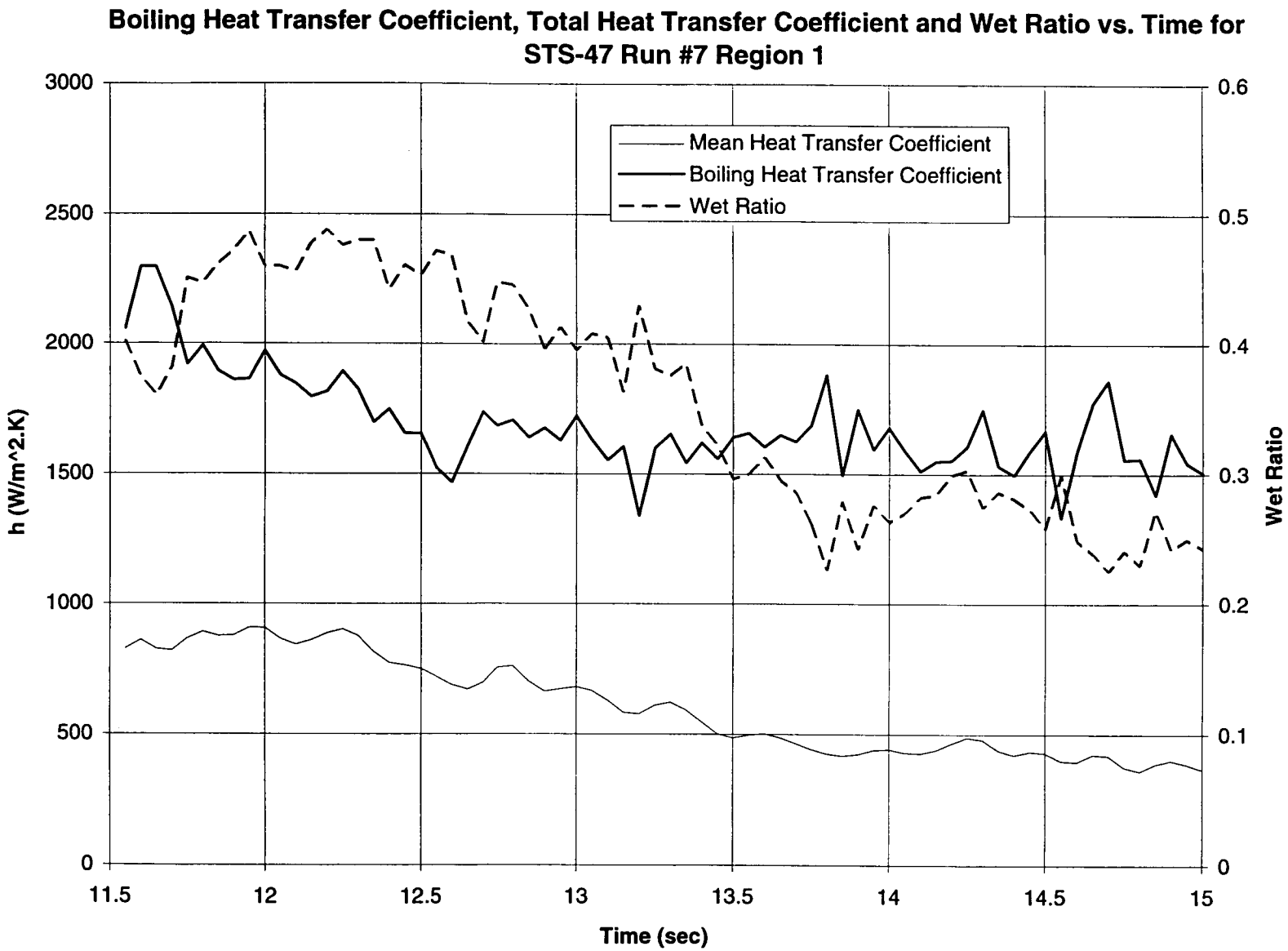

Figure A-10g-1-iii. Development of microgravity boiling heat transfer coefficient. PBE-IA (STS-47). Run No. 7 Time interval: 11.5 - 15.0 seconds.

STS-47 Run #7

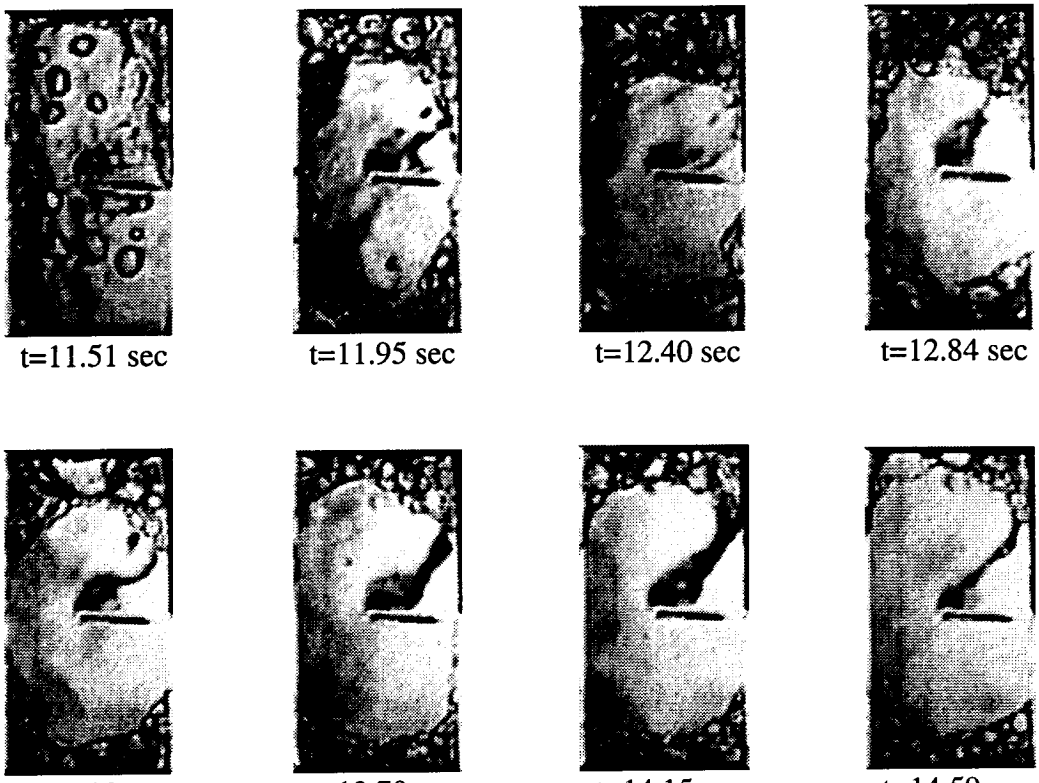

Figure A-10g-1-iv. Sample images showing dryout/rewetting. PBE-IA (STS-47). Run No. 7. Time interval: 11.5 - 15.0 seconds.

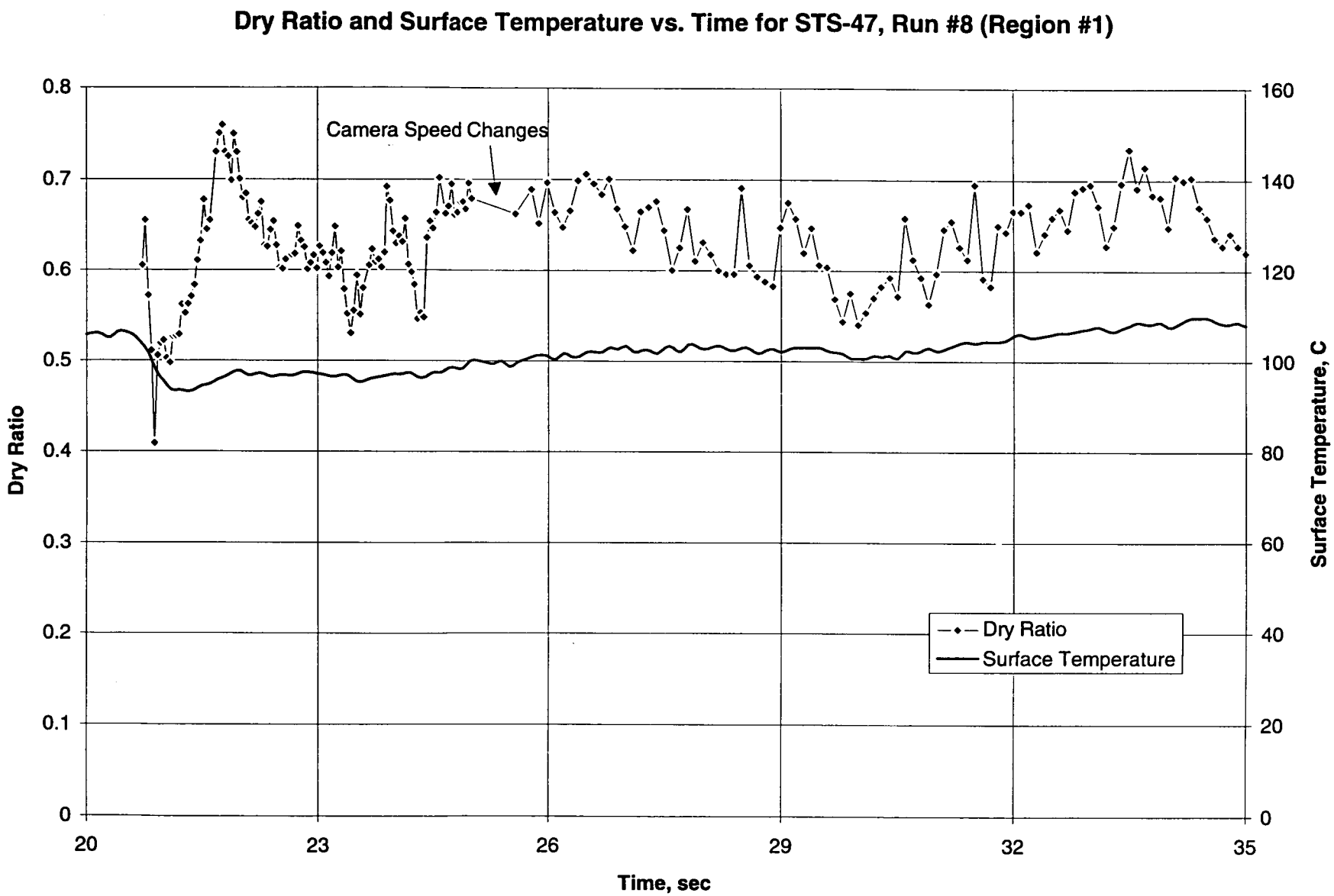

Figure A-10h-1-i. Heater surface dry fraction and mean temperature. PBE-IA (STS-47). Run No. 8. Time interval: 21 - 35 seconds.

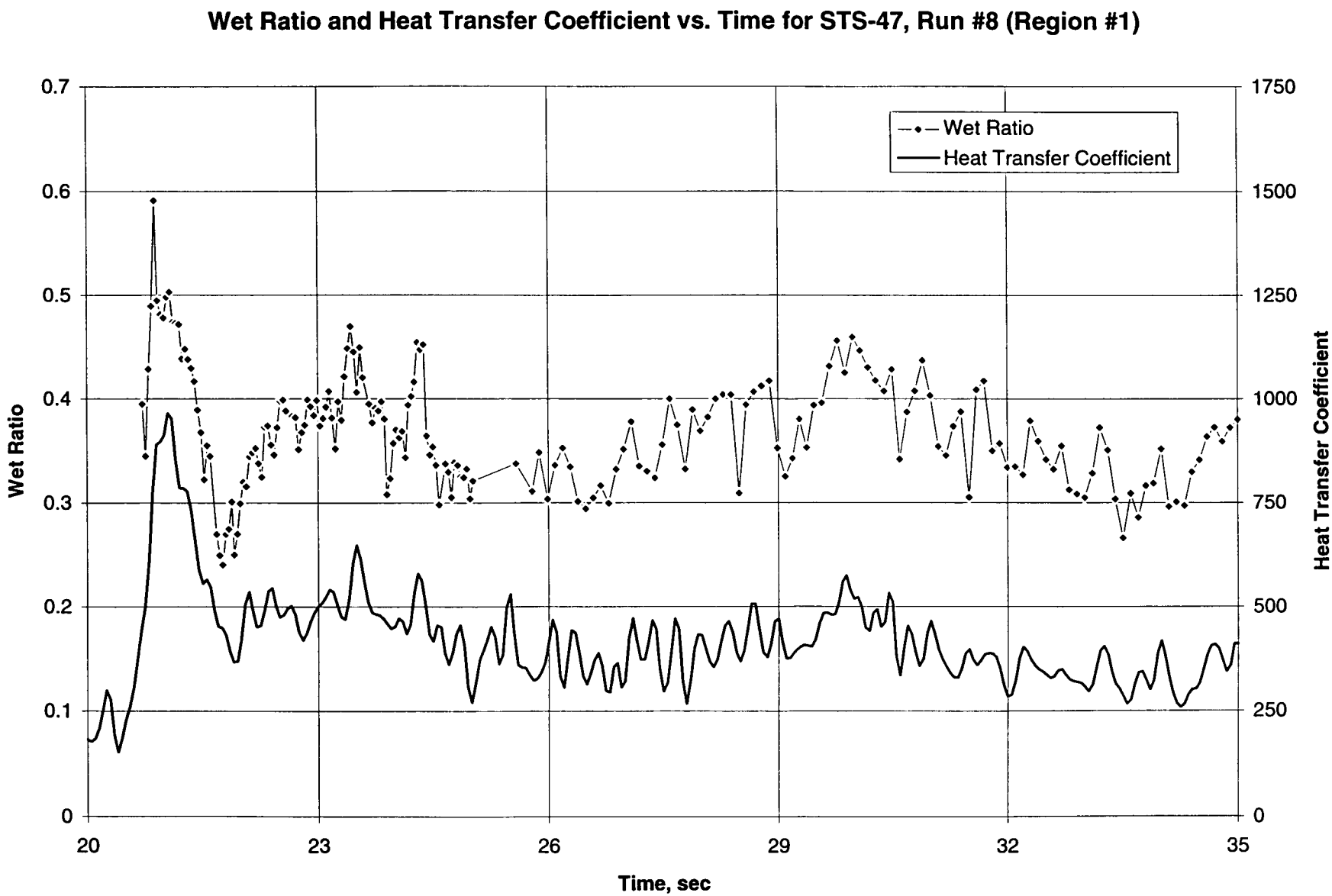

Figure A-10h-1-ii. Heater surface wet fraction and mean heat transfer coefficients. PBE-IA (STS-47). Run No. 8. Time interval: 21 - 35 seconds.

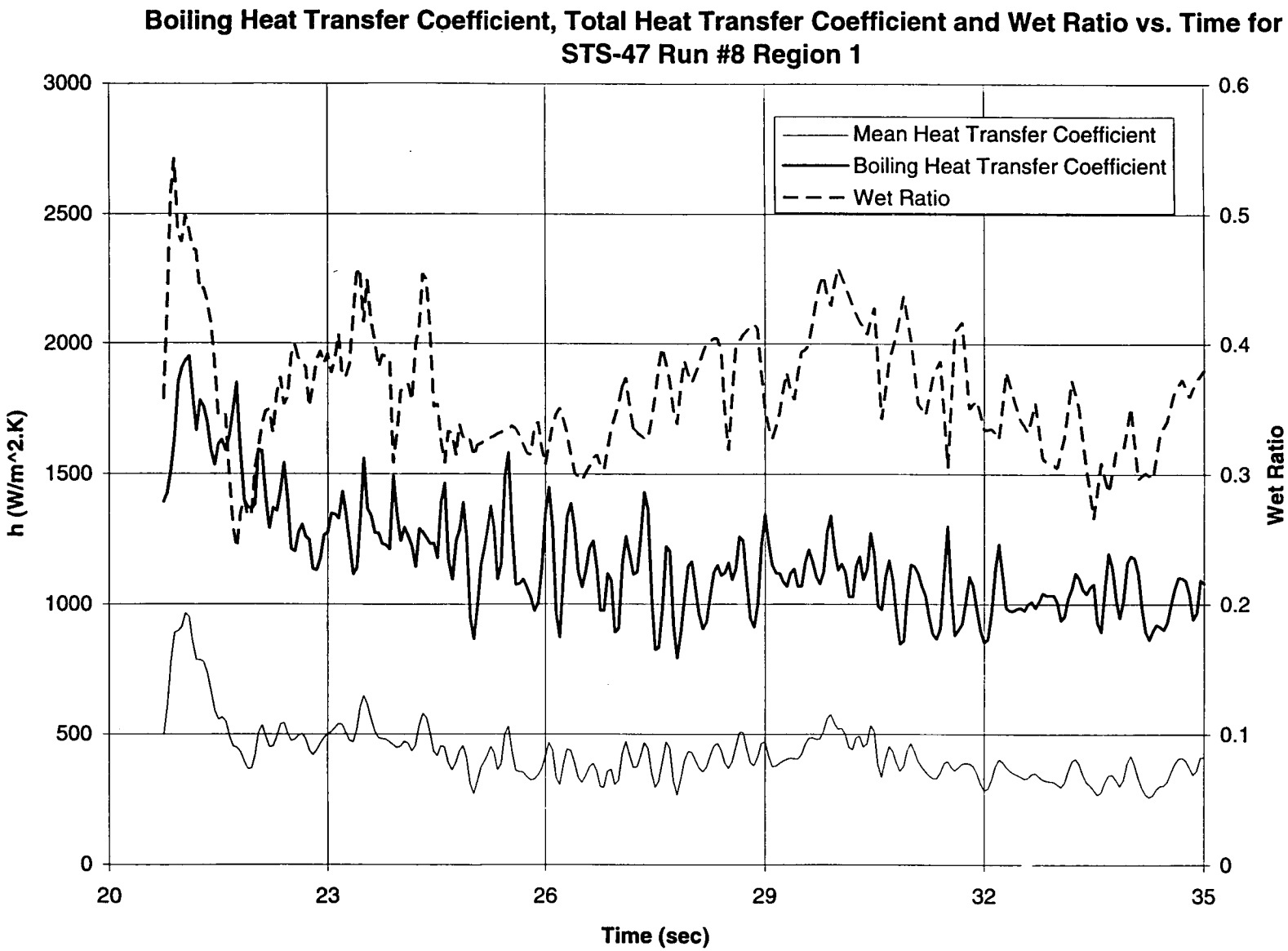

Figure A-10h-1-iii. Development of microgravity boiling heat transfer coefficient. PBE-IA (STS-47). Run No. 8. Time interval: 21 - 35 seconds.

STS-47 Run #8, Region1

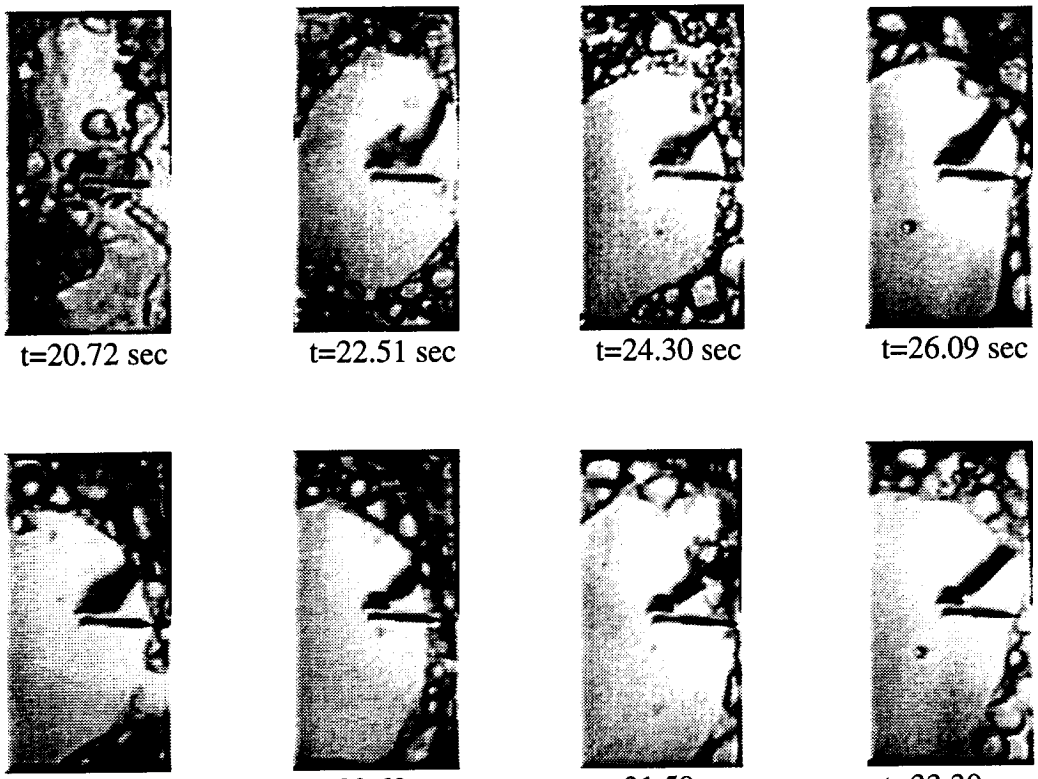

Figure A-10h-1-iv. Sample images showing dryout/rewetting. PBE-IA (STS-47). Run No. 8. Time interval: 21 - 35 seconds.

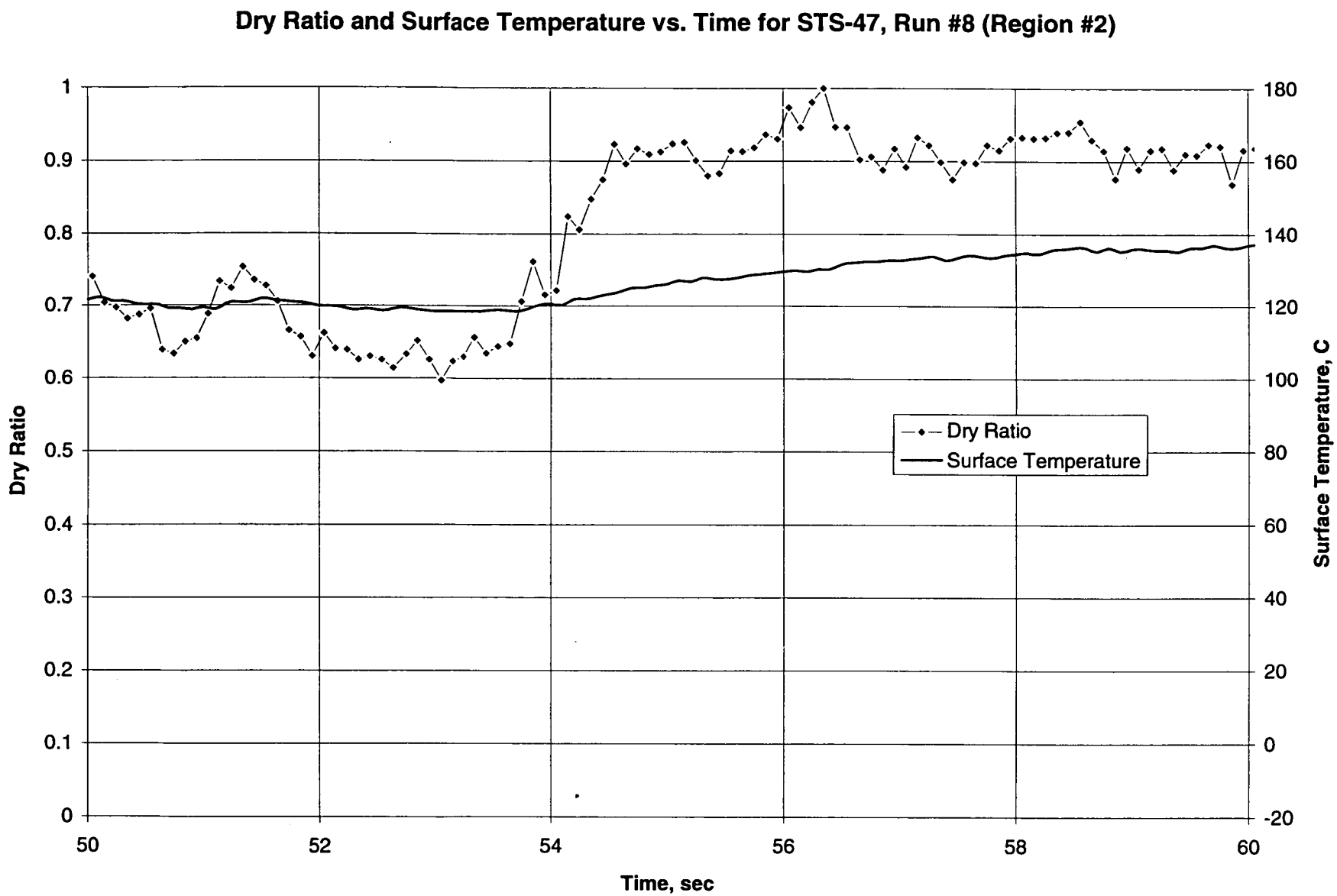

Figure A-10h-2-i. Heater surface dry fraction and mean temperature. PBE-IA (STS-47). Run No. 8. Time interval: 50 - 60 seconds.

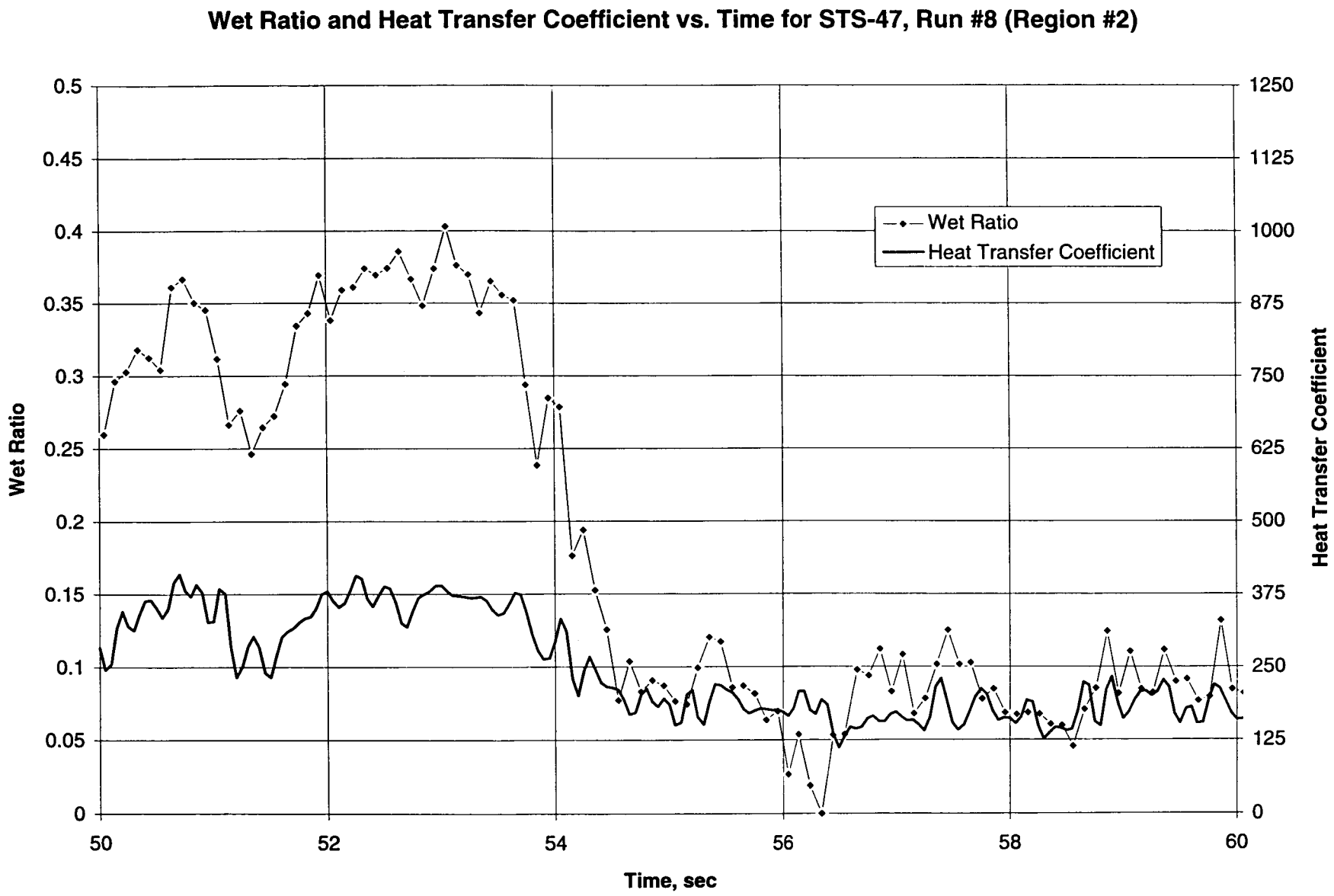

Figure A-10h-2-ii. Heater surface wet fraction and mean heat transfer coefficients. PBE-IA (STS-47). Run No. 8. Time interval: 50 - 60 seconds.

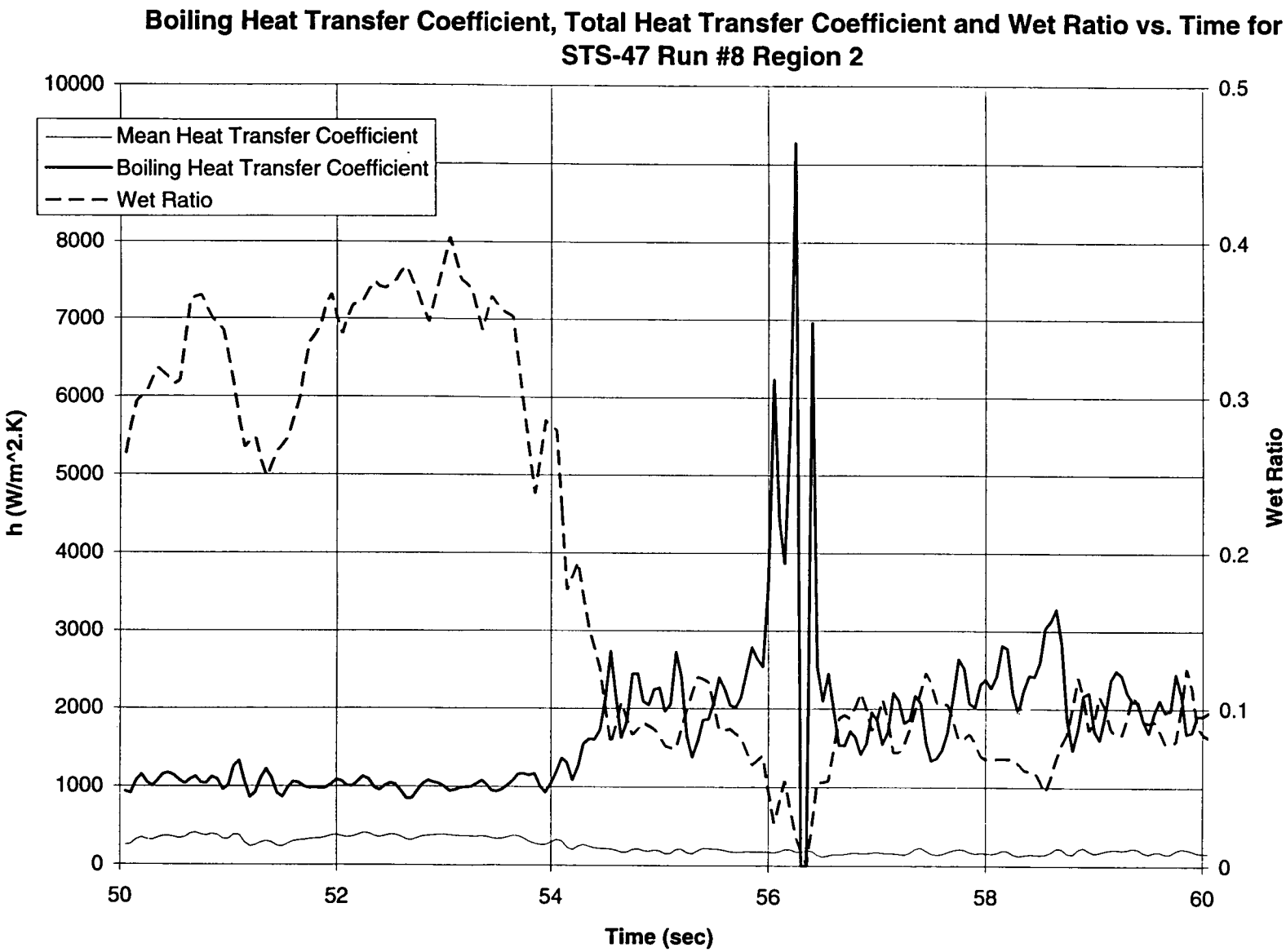

Figure A-10h-2-iii. Development of microgravity boiling heat transfer coefficient. PBE-IA (STS-47). Run No. 8. Time interval: 50 - 60 seconds.

STS-47 Run #8, Region 2

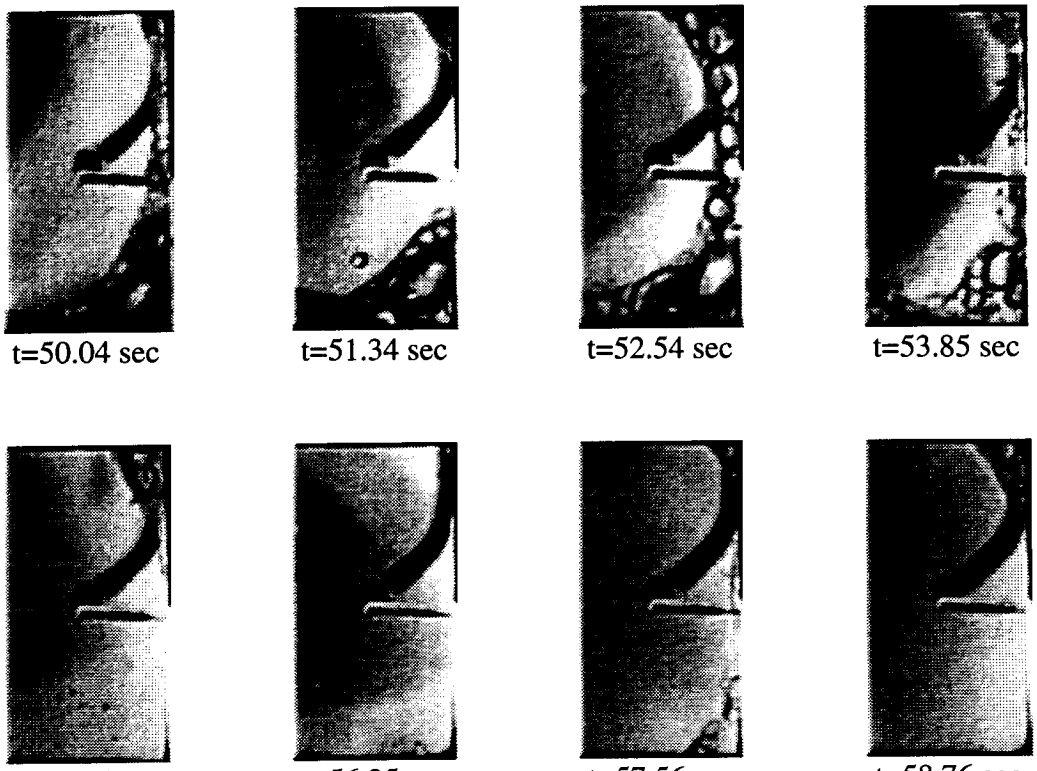

Figure A-10h-2-iv. Sample images showing dryout/rewetting. PBE-IA (STS-47). Run No. 8. Time interval: 50 - 60 seconds.

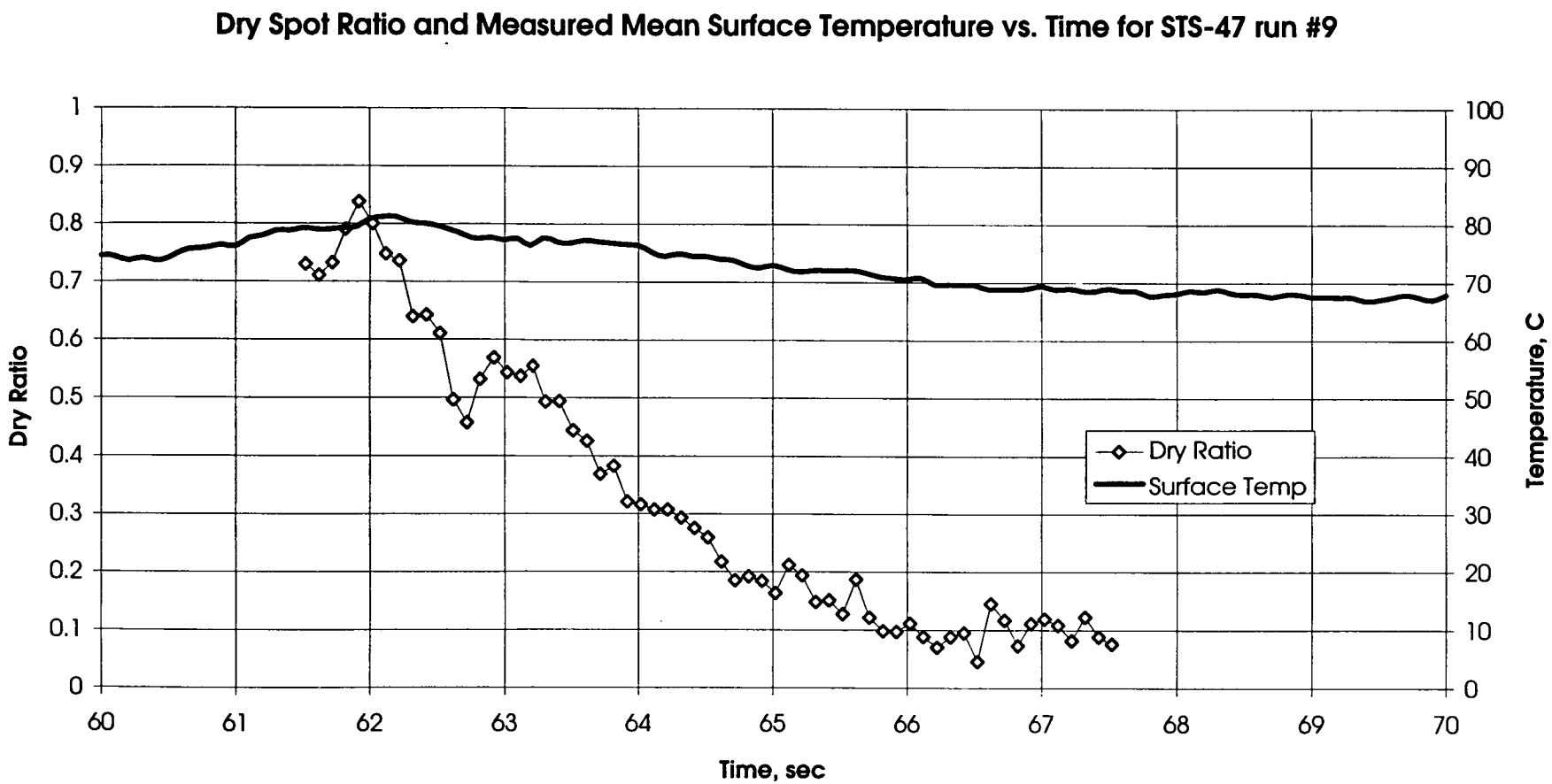

Figure A-10i-1-i. Heater surface dry fraction and mean temperature. PBE-IA (STS-47). Run No. 9. Time interval: 61.5 - 67.5 seconds.

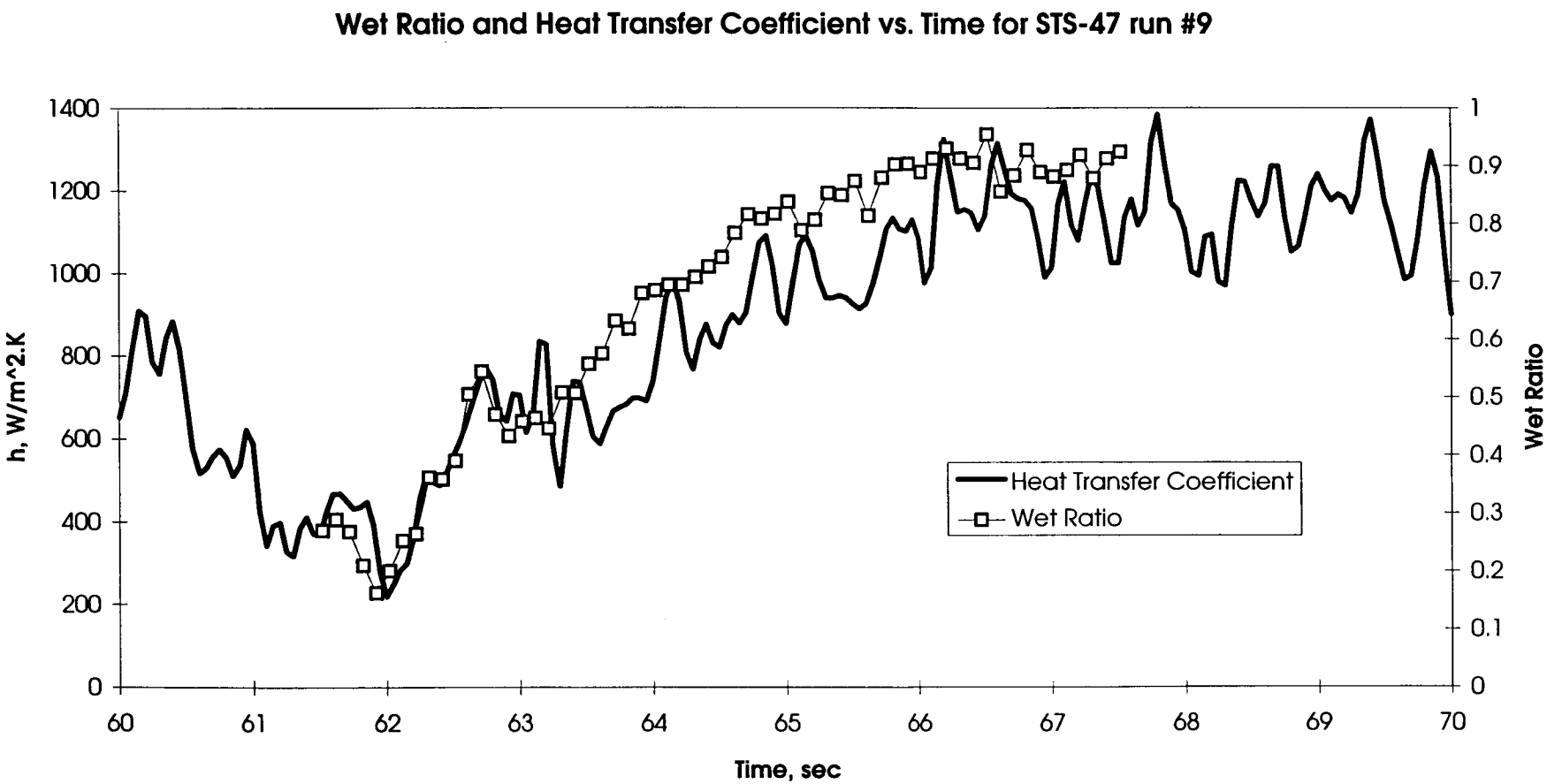

Figure A-10i-1-ii. Heater surface wet fraction and mean heat transfer coefficients. PBE-IA (STS-47). Run No. 9. Time interval: 61.5 - 67.5 seconds.

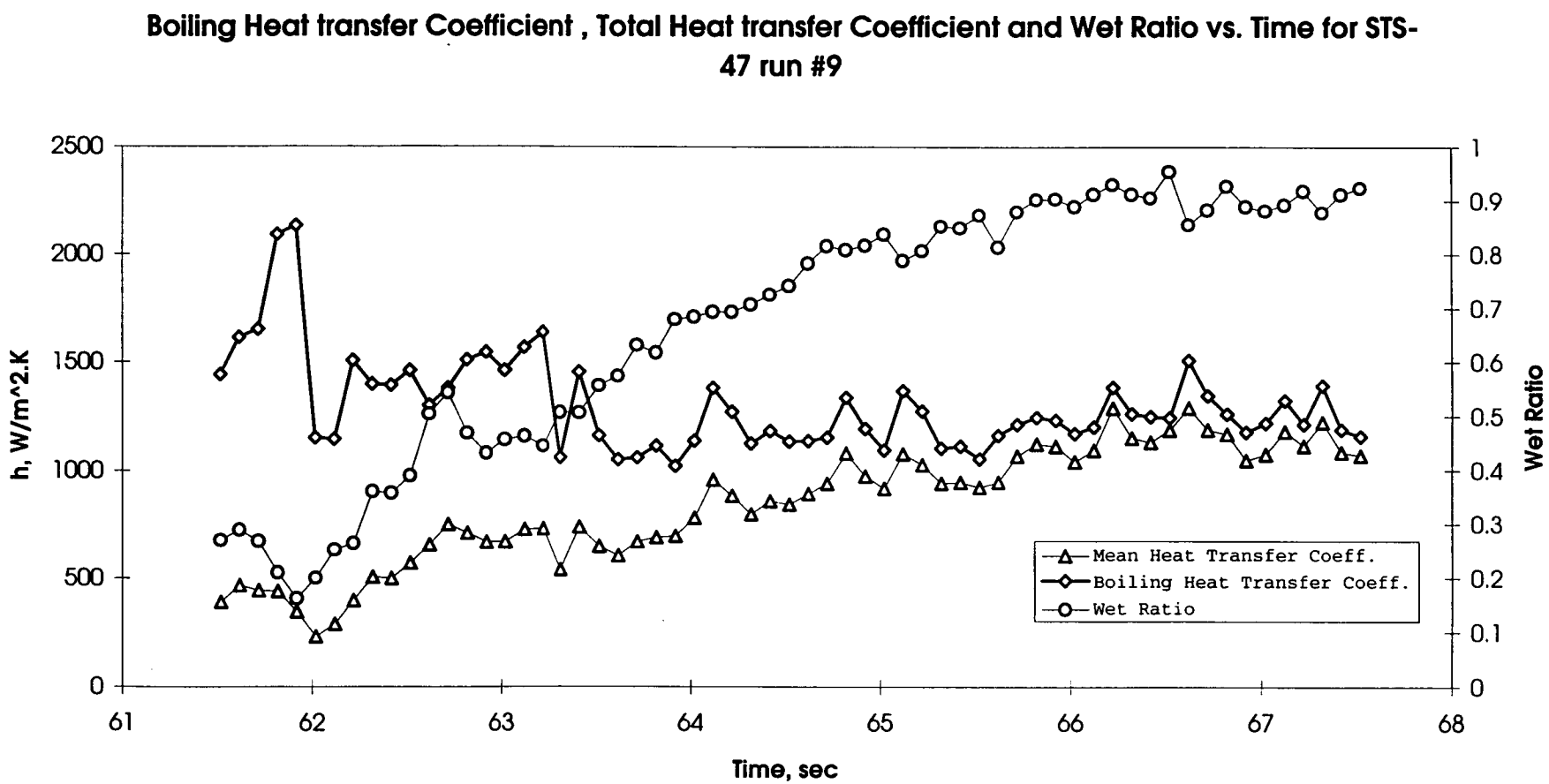

Figure A-10i-1-iii. Development of microgravity boiling heat transfer coefficient. PBE-IA (STS-47). Run No. 9. Time interval: 61.5 - 67.5 seconds.

STS-47 Run # 9 (S1)

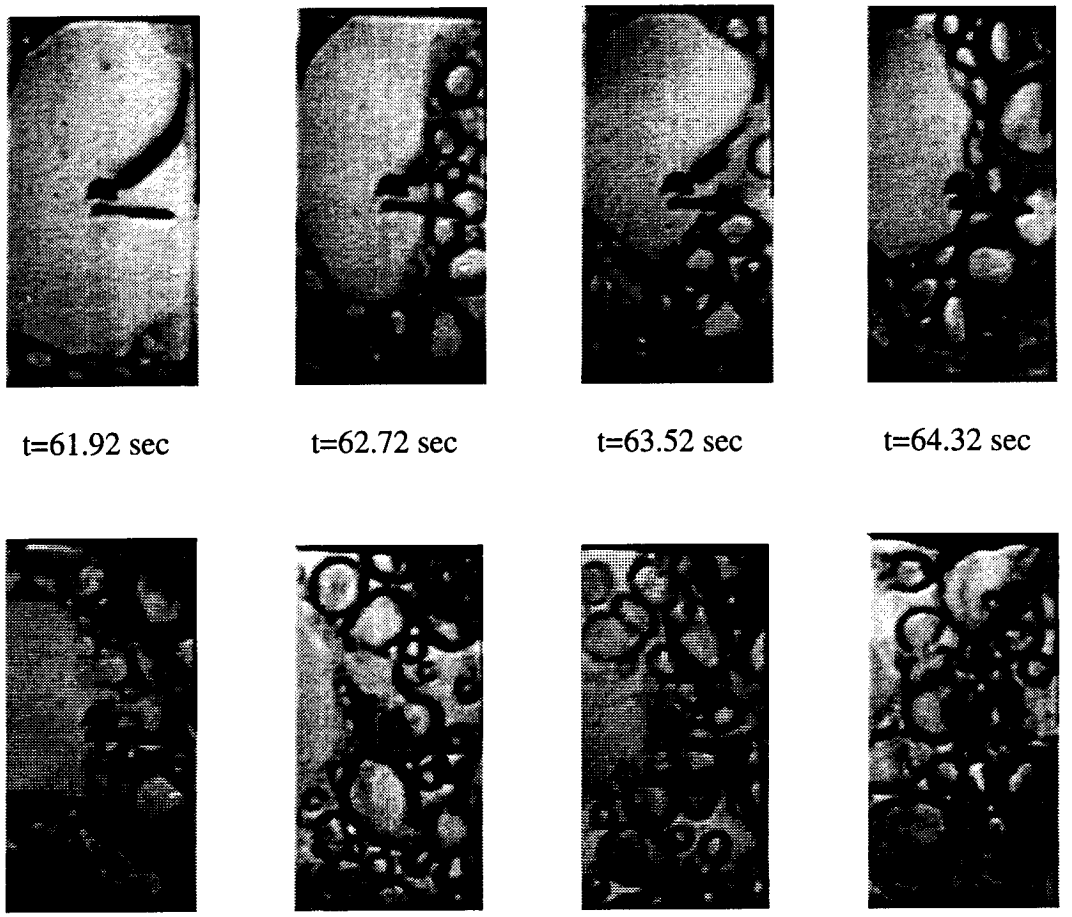

Figure A-10i-1-iv. Sample images showing dryout/rewetting. PBE-IA (STS-47). Run No. 9. Time interval: 61.5 - 67.5 seconds.

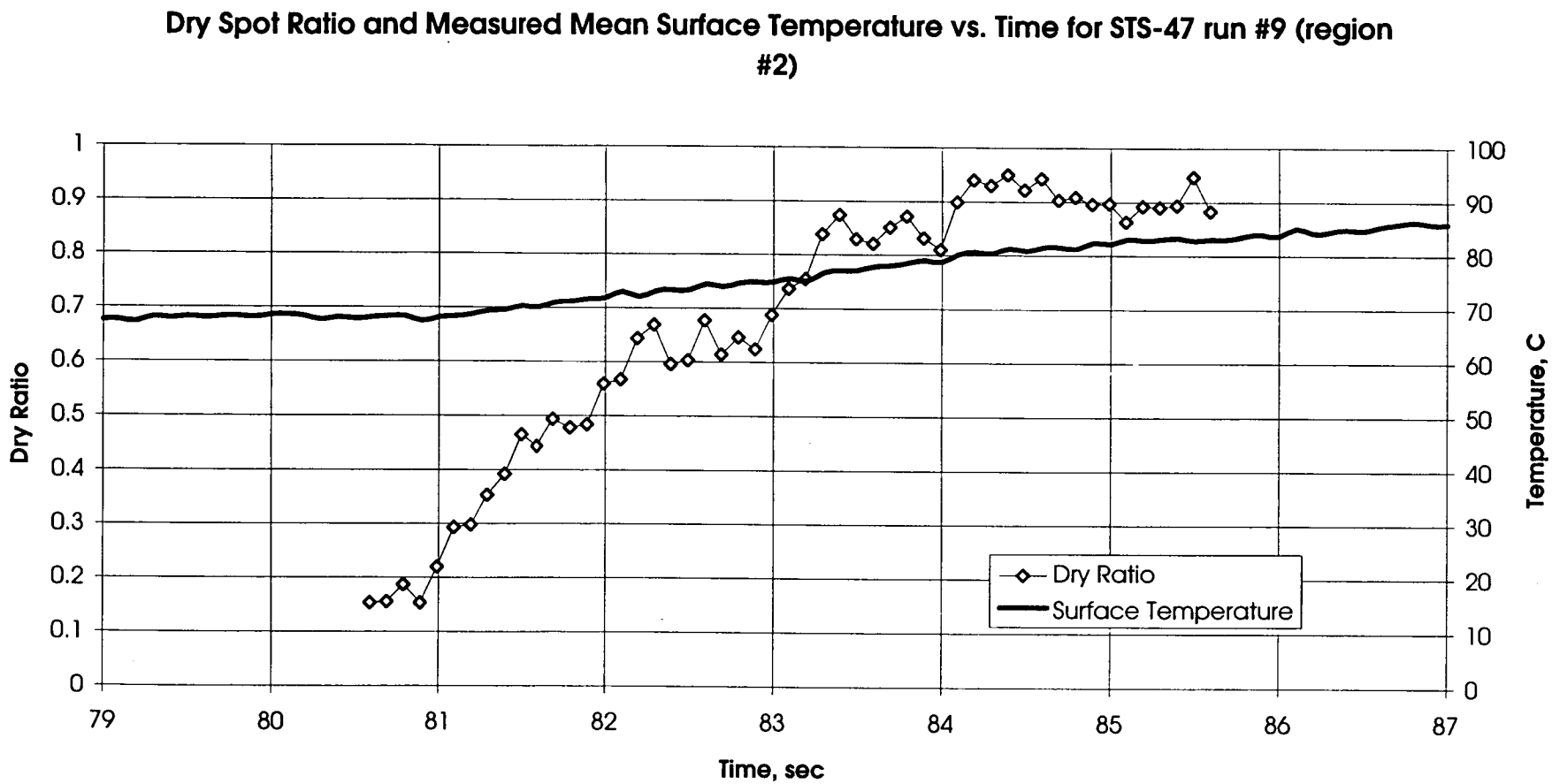

Figure A-10i-2-i. Heater surface dry fraction and mean temperature. PBE-IA (STS-47). Run No. 9. Time interval: 80.5 - 85.5 seconds.

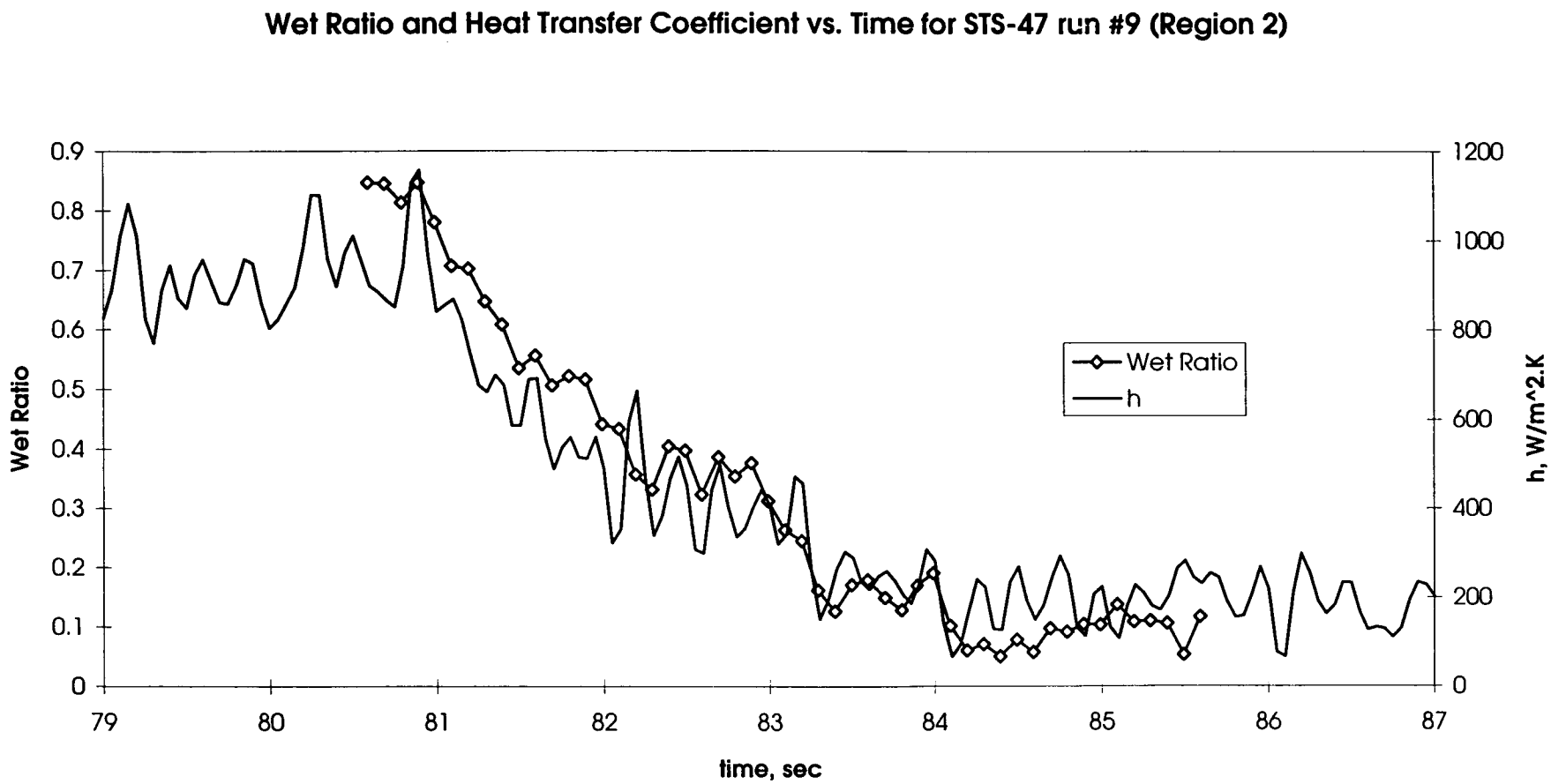

Figure A-10i-2-ii. Heater surface wet fraction and mean heat transfer coefficients. PBE-IA (STS-47). Run No. 9. Time interval: 80.5 - 85.5 seconds.

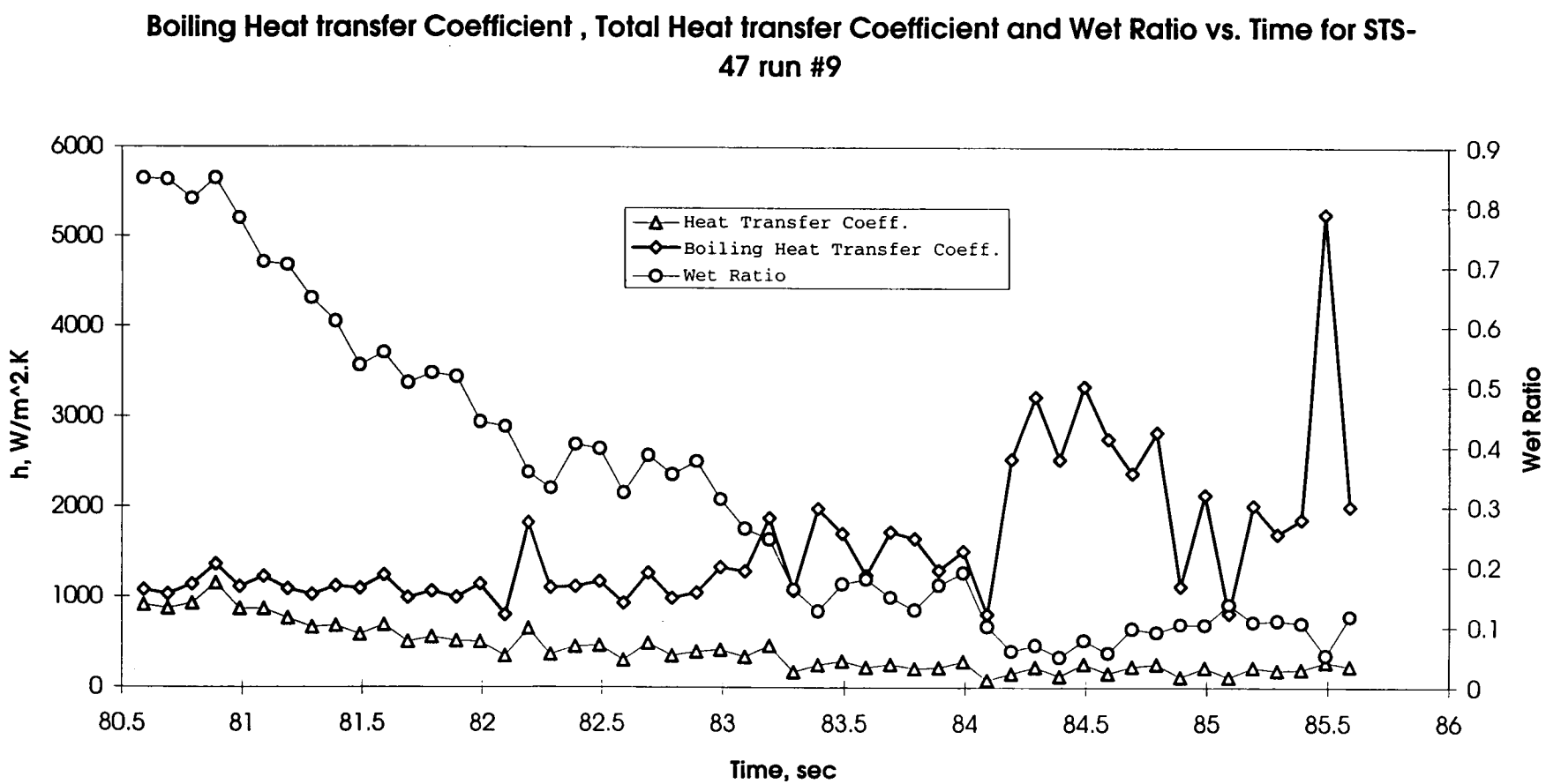

Figure A-10i-2-iii. Development of microgravity boiling heat transfer coefficient PBE-IA (STS-47). Run No. 9. Time interval: 80.5 - 85.5 seconds.

STS-47 Run #9 (S2)

t=80.59 sec

t=81.19 sec

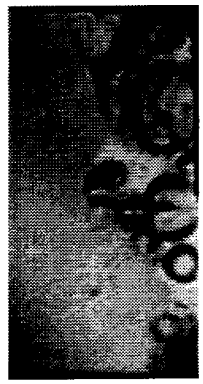

t=81.79 sec

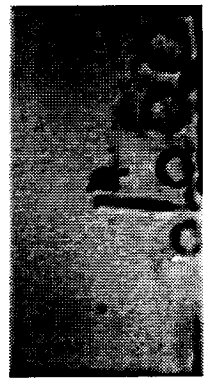

t=82.39 sec

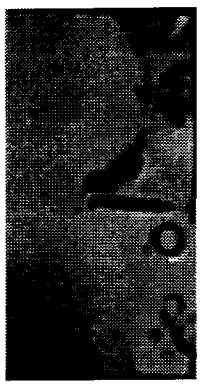

t=82.99 sec

t=83.59 sec

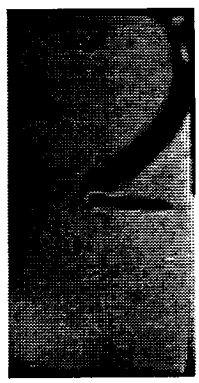

t=84.19 sec

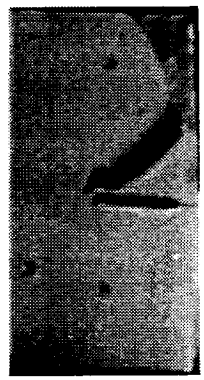

t=84.79 sec

Figure A-10i-2-iv. Sample images showing dryout/rewetting. PBE-IA (STS-47). Run No. 9. Time interval: 80.5 - 85.5 seconds.

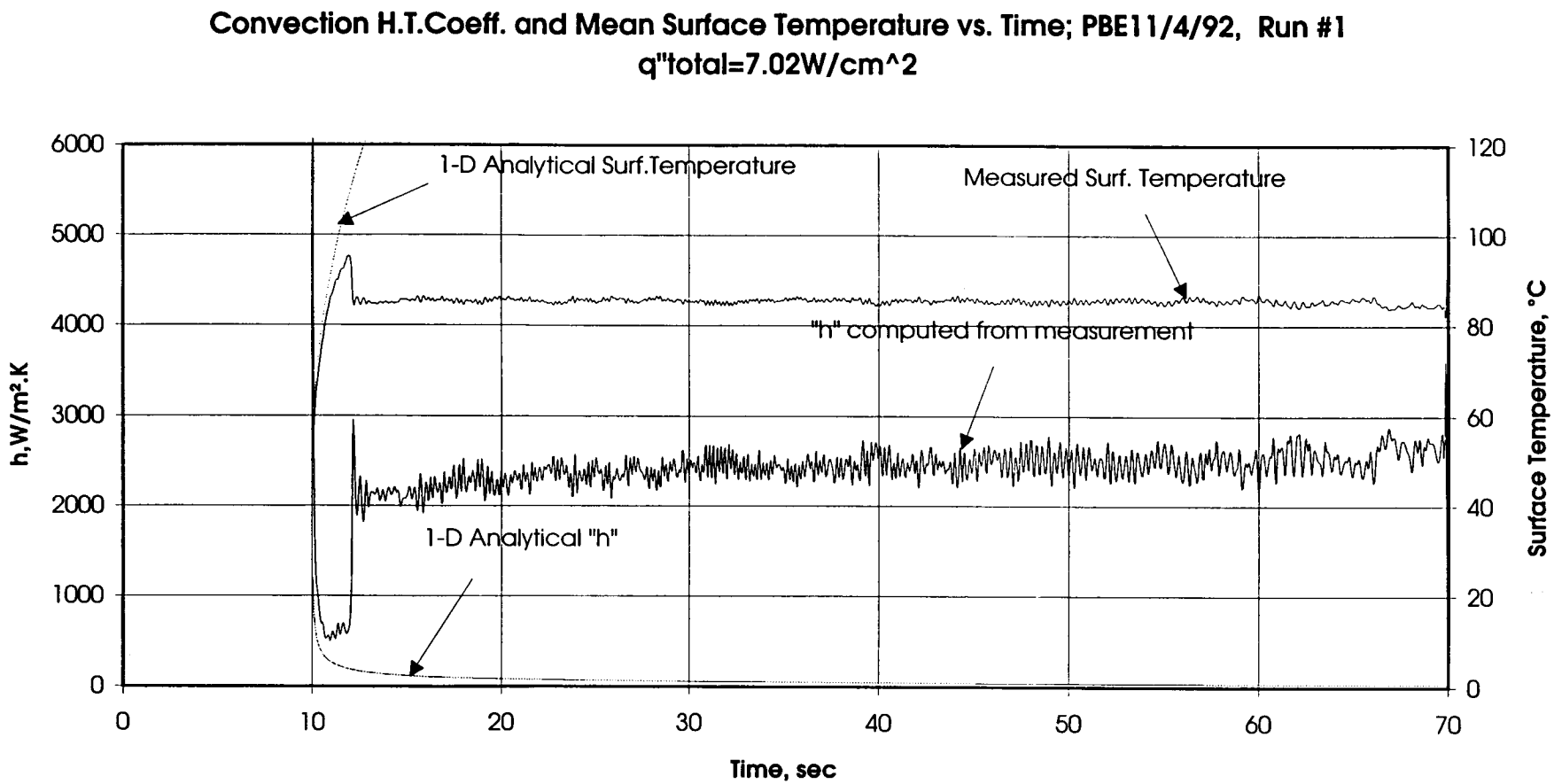

Figure A-11a. a/g = +1 Postflight test. Mean heater surface temperature and derived heat transfer coefficient. PBE-IA (STS-47). Run No. 1.

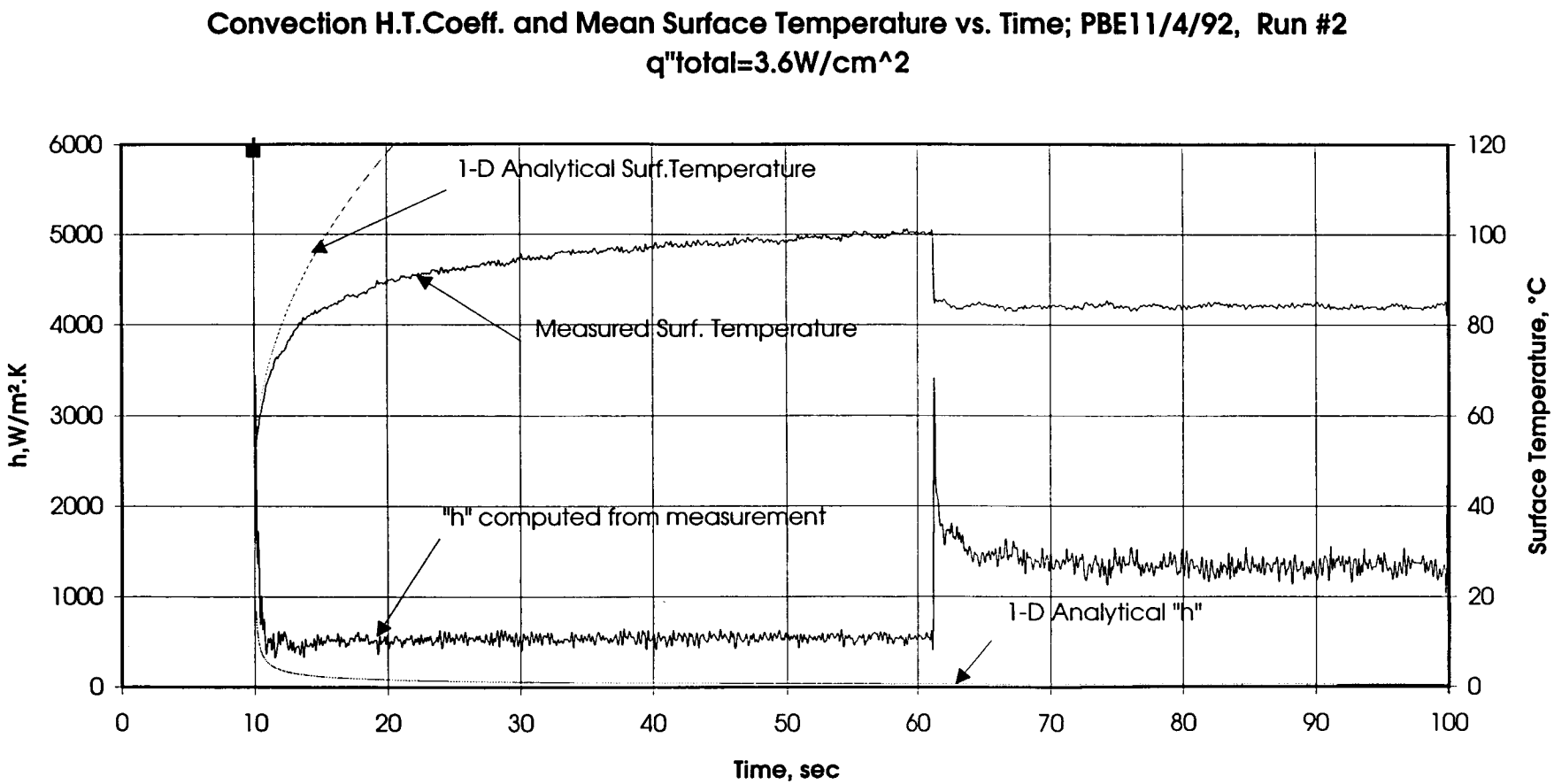

Figure A-11b. a/g = +1 Postflight test. Mean heater surface temperature and derived heat transfer coefficient. PBE-IA (STS-47). Run No. 2.

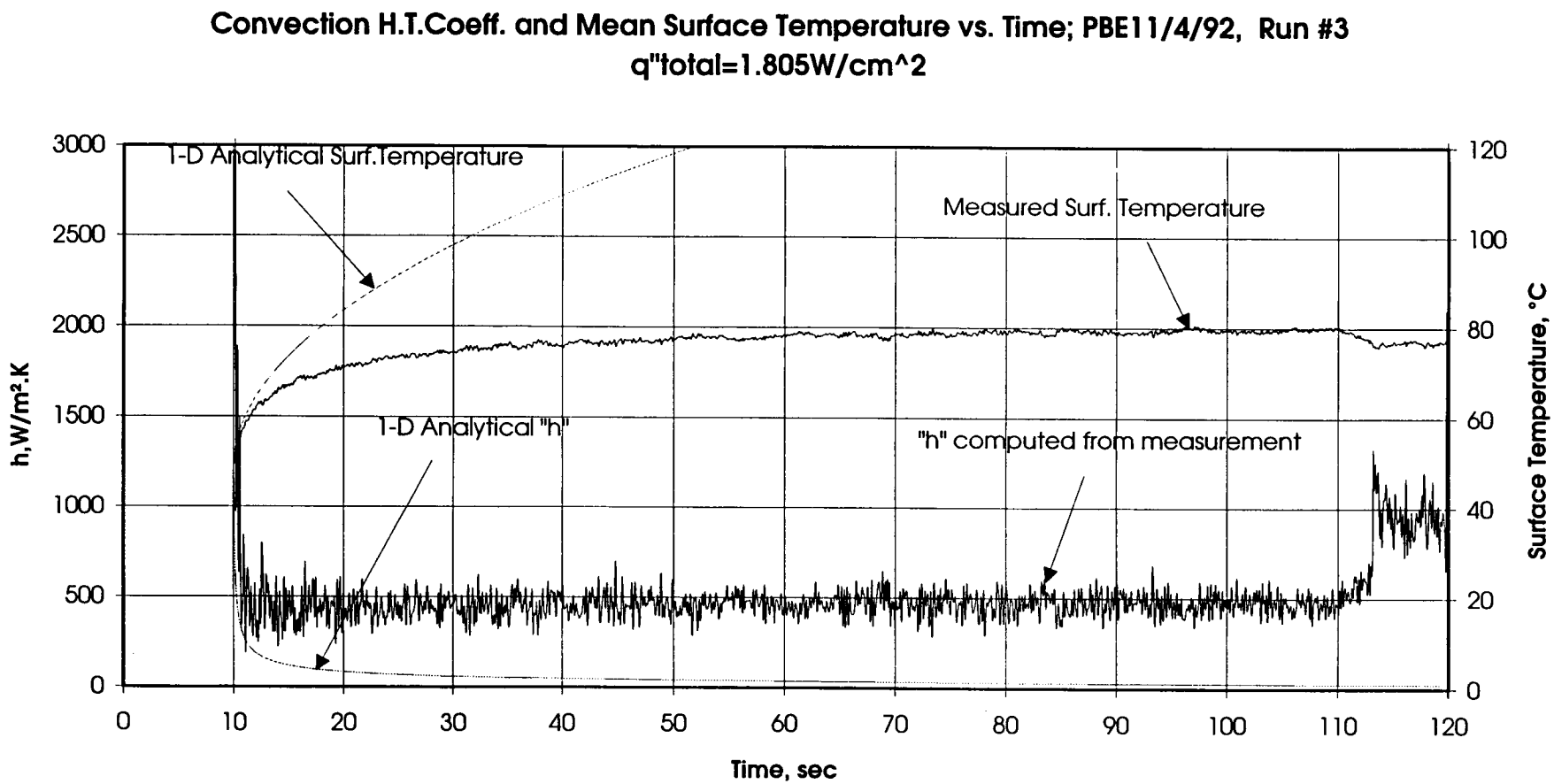

Figure A-11c. a/g = +1 Postflight test. Mean heater surface temperature and derived heat transfer coefficient. PBE-IA (STS-47). Run No. 3.

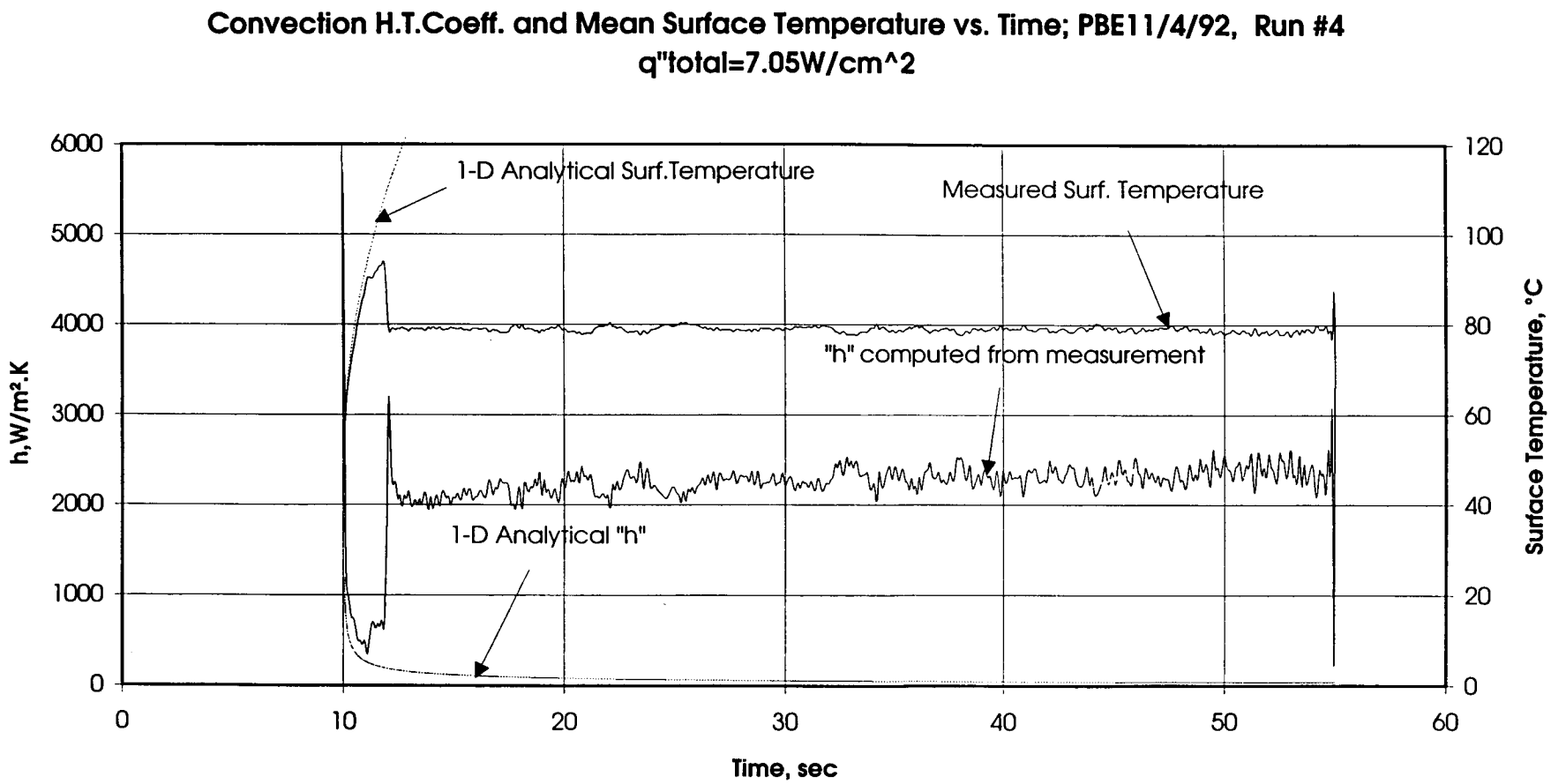

Figure A-11d. a/g = +1 Postflight test. Mean heater surface temperature and derived heat transfer coefficient. PBE-IA (STS-47). Run No. 4.

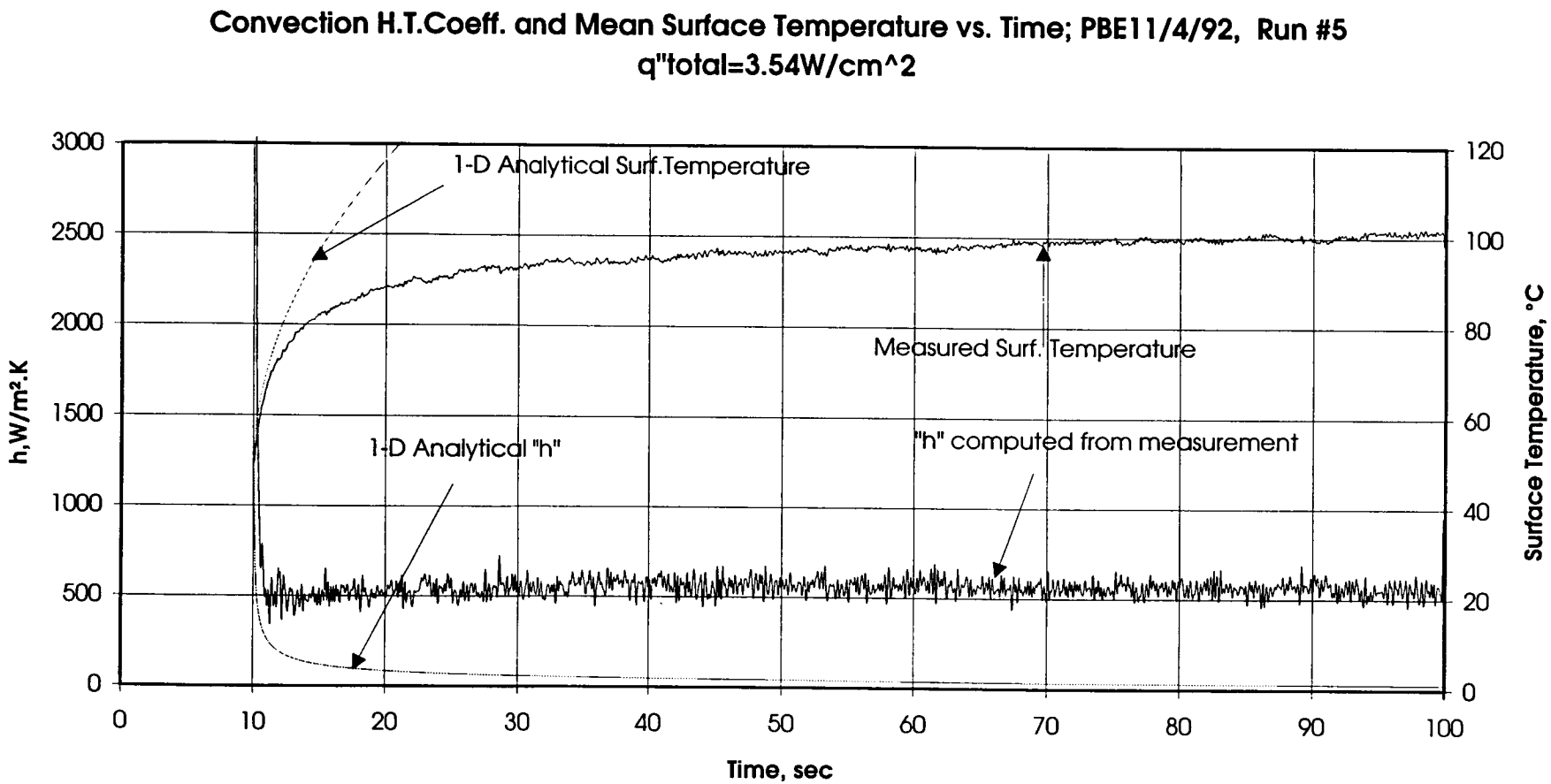

Figure A-11e. a/g = +1 Postflight test. Mean heater surface temperature and derived heat transfer coefficient. PBE-IA (STS-47). Run No. 5.

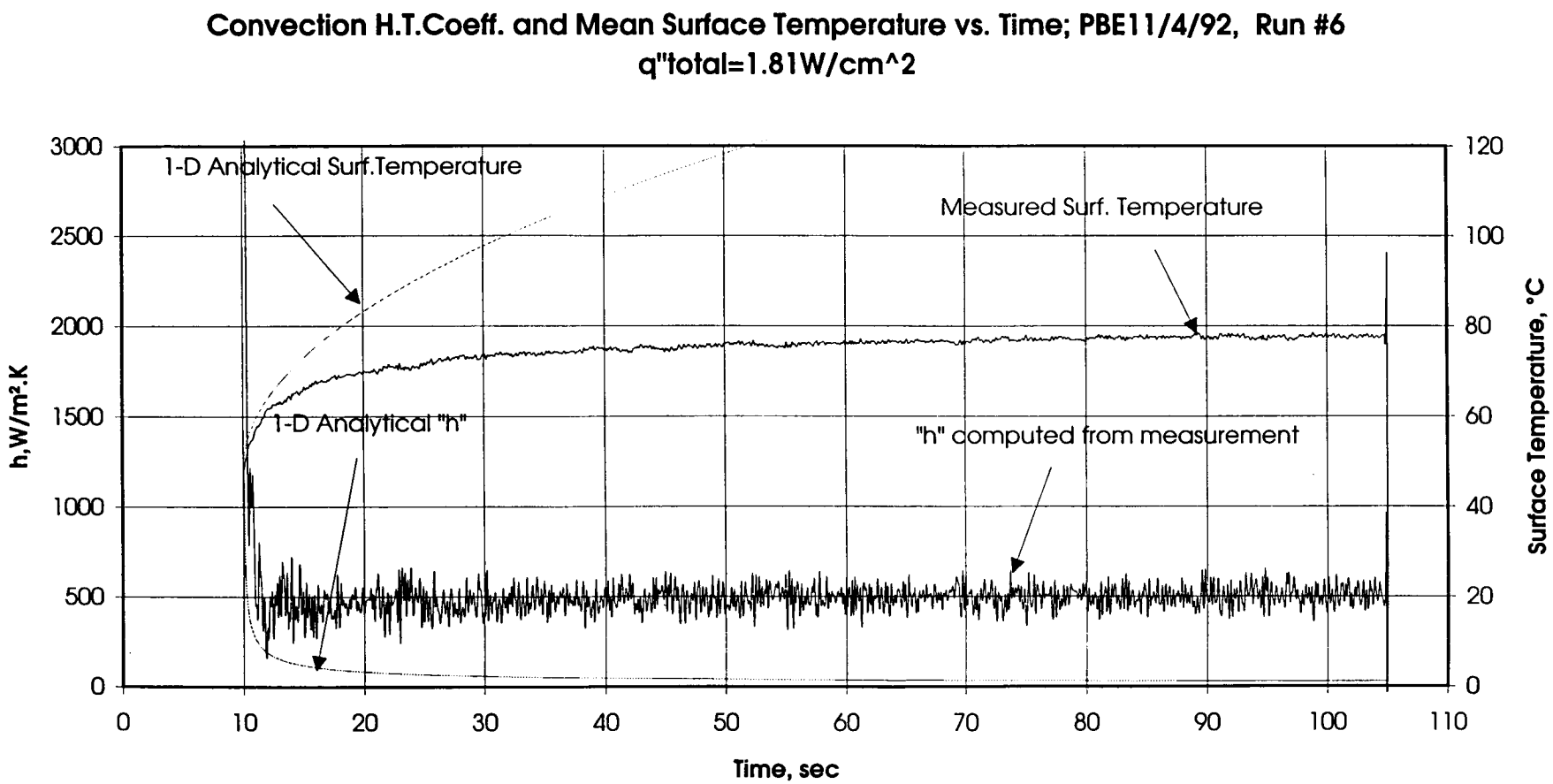

Figure A-11f. a/g = +1 Postflight test. Mean heater surface temperature and derived heat transfer coefficient. PBE-IA (STS-47). Run No. 6.

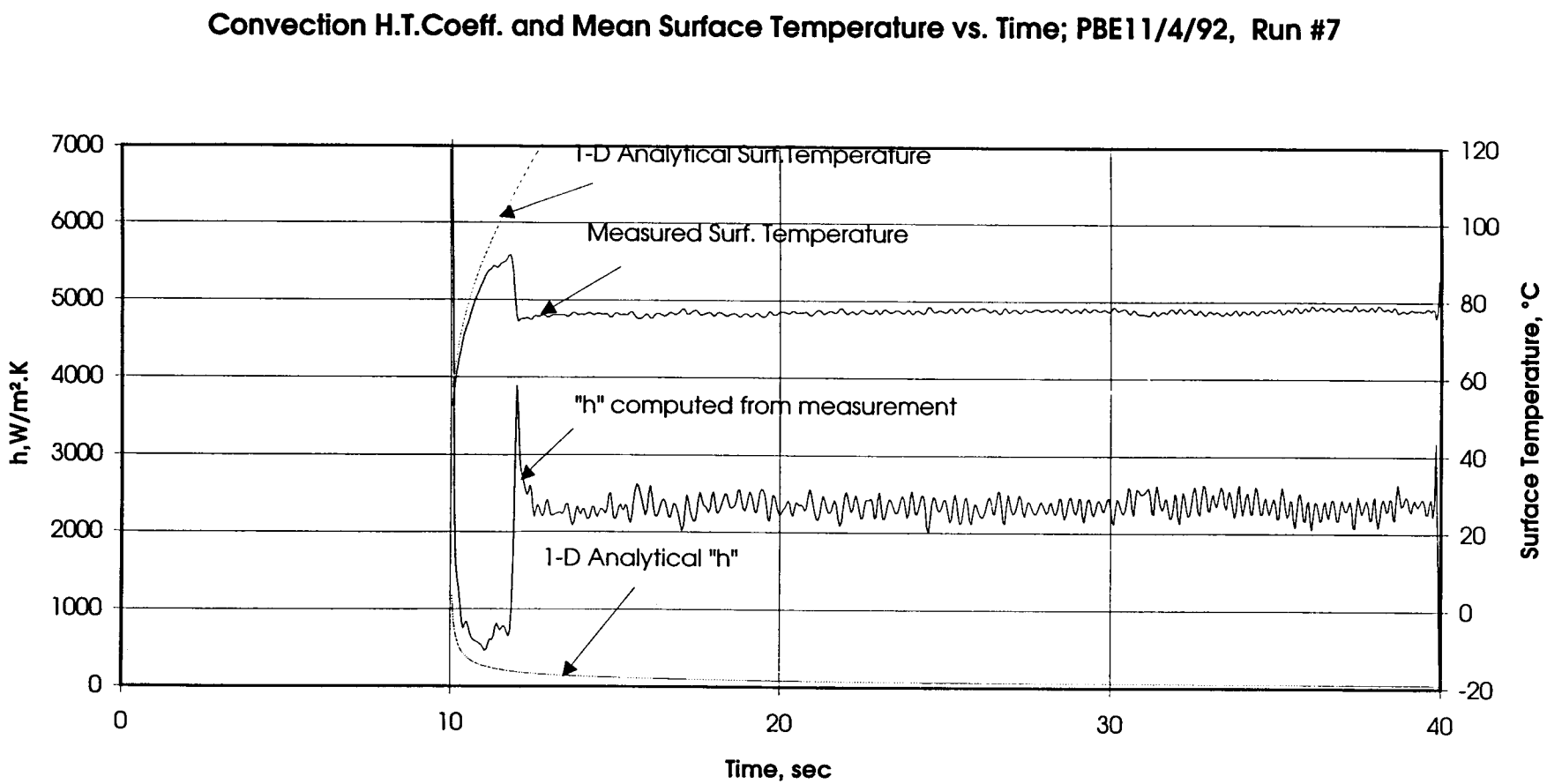

Figure A-11g. a/g = +1 Postflight test. Mean heater surface temperature and derived heat transfer coefficient. PBE-IA (STS-47). Run No. 7.

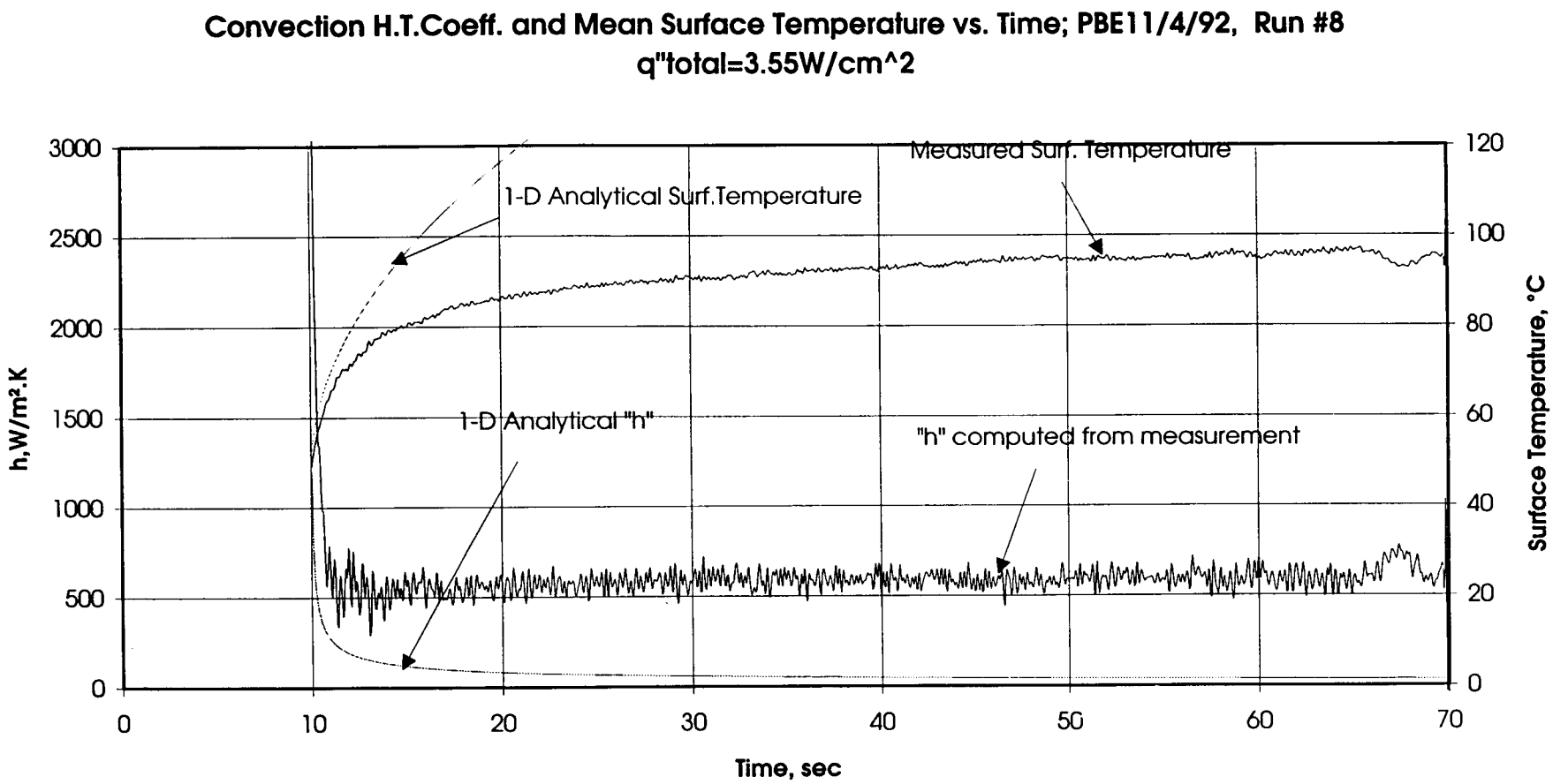

Figure A-11h. a/g = +1 Postflight test. Mean heater surface temperature and derived heat transfer coefficient. PBE-IA (STS-47). Run No. 8.

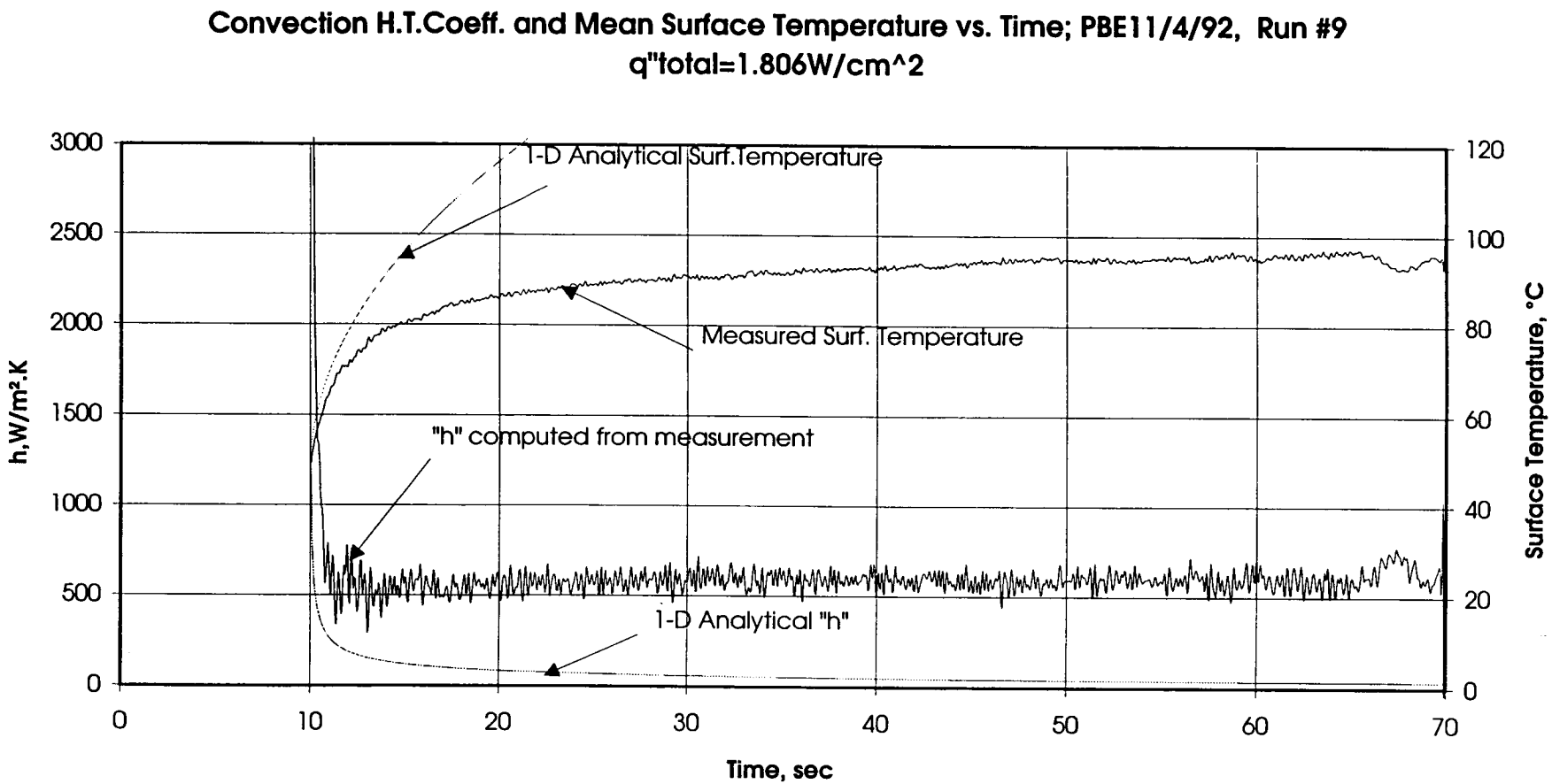

Figure A-11i. a/g = +1 Postflight test. Mean heater surface temperature and derived heat transfer coefficient. PBE-IA (STS-47). Run No. 9.

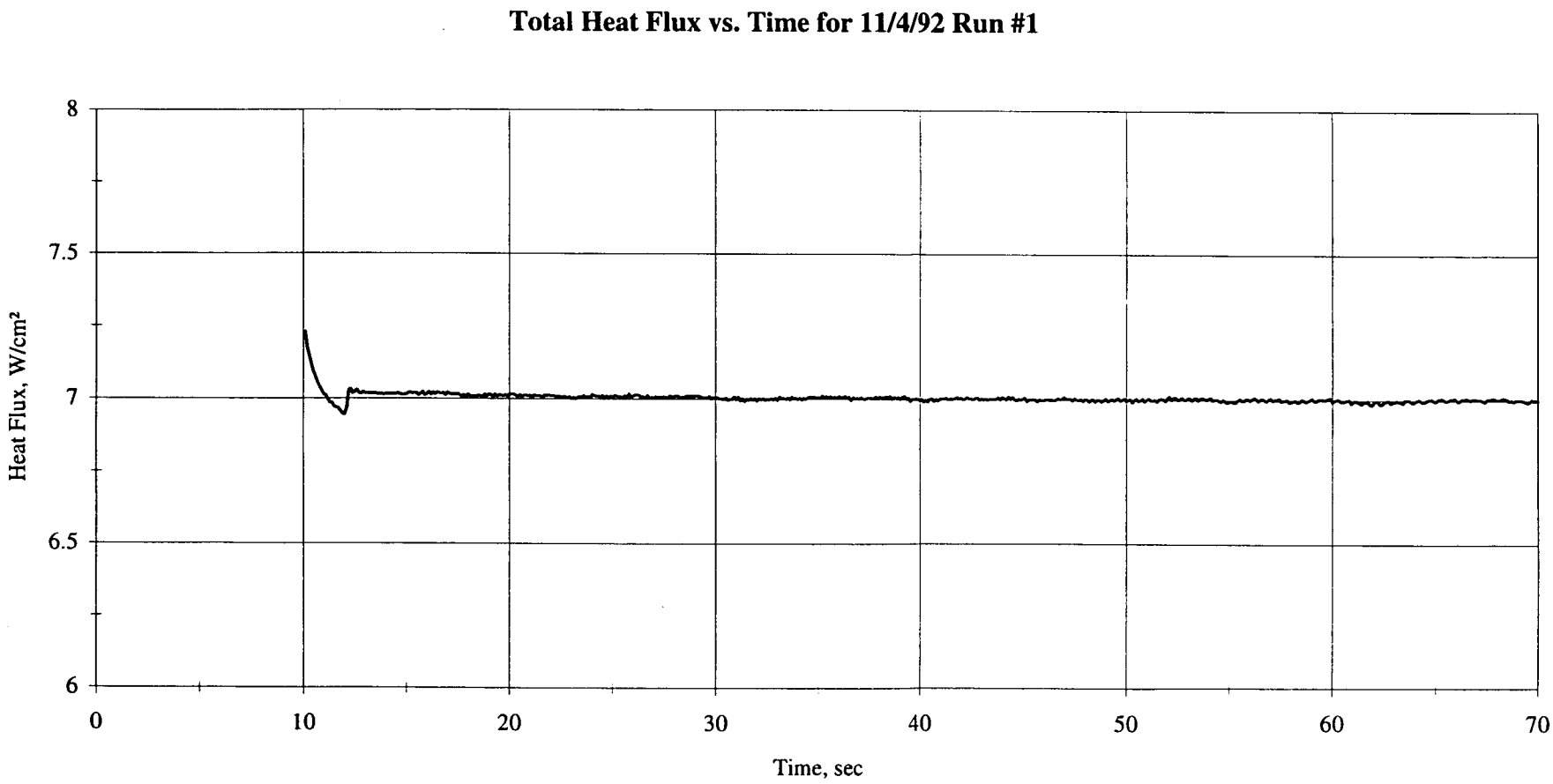

Figure A-12a. a/g = +1 Postflight test. Heat flux input. PBE-IA (STS-47). Run No. 1.

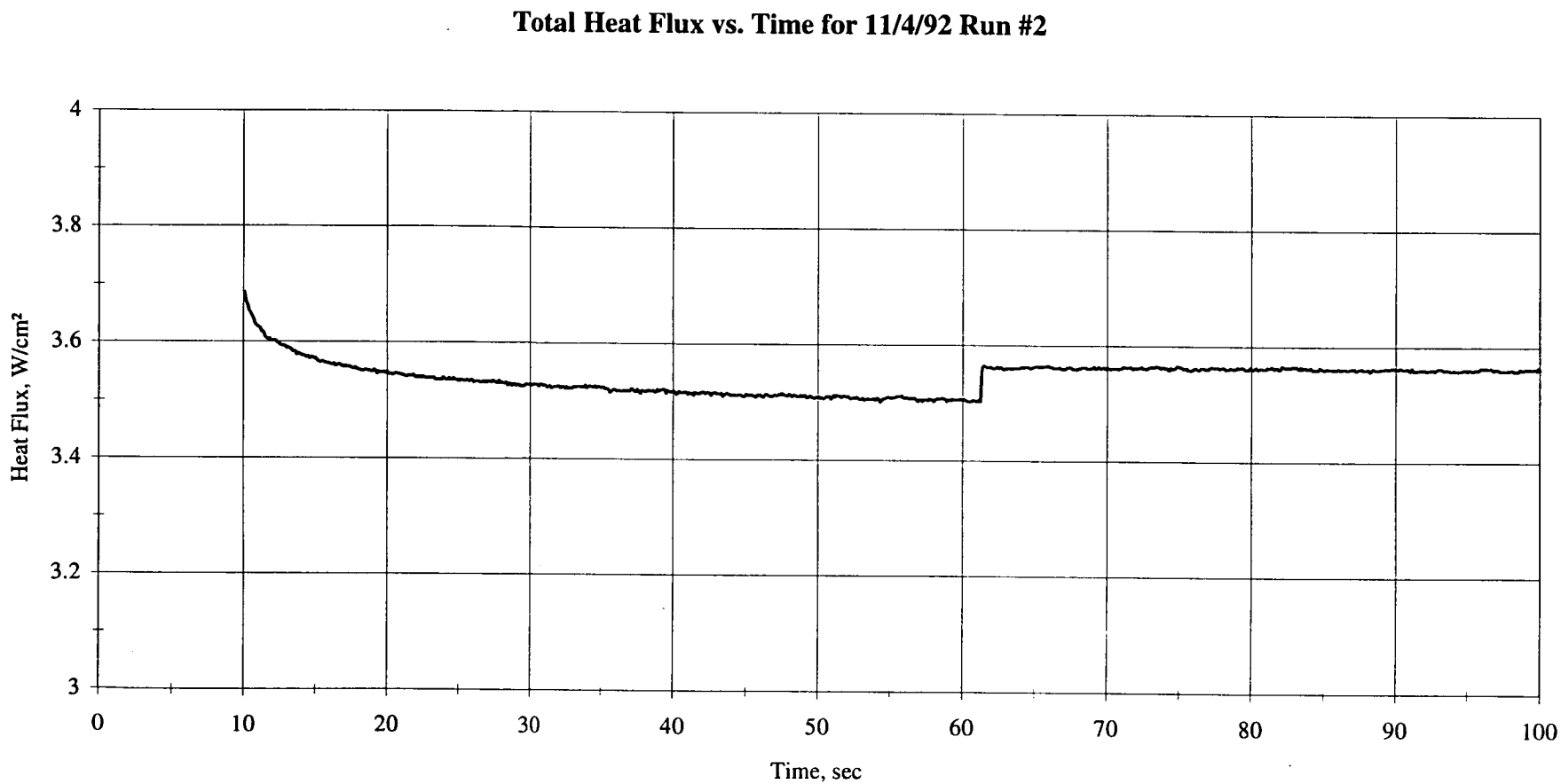

Figure A-12b. a/g = +1 Postflight test. Heat flux input. PBE-IA (STS-47). Run No. 2.

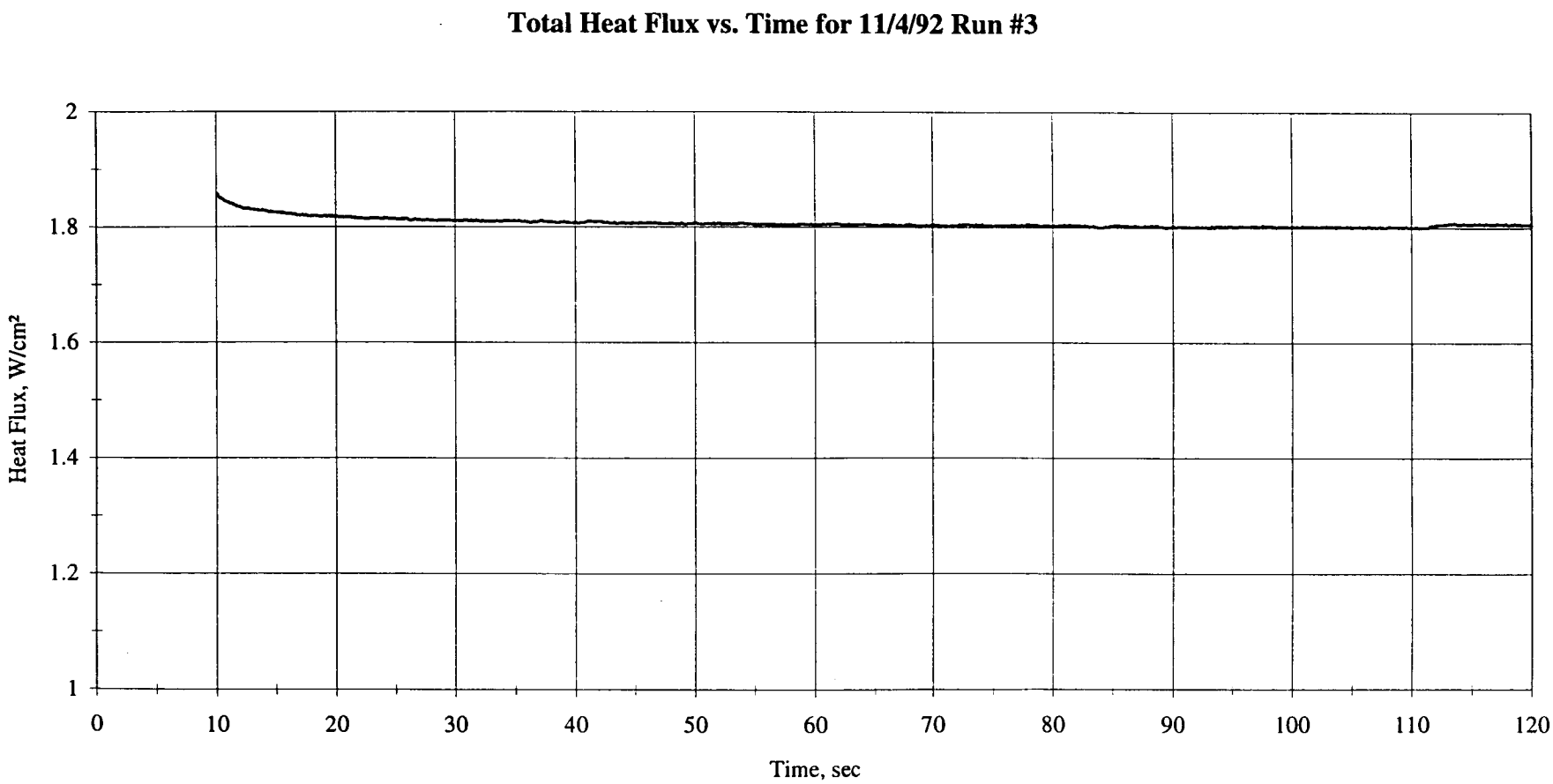

Figure A-12c. a/g = +1 Postflight test. Heat flux input. PBE-IA (STS-47). Run No. 3.

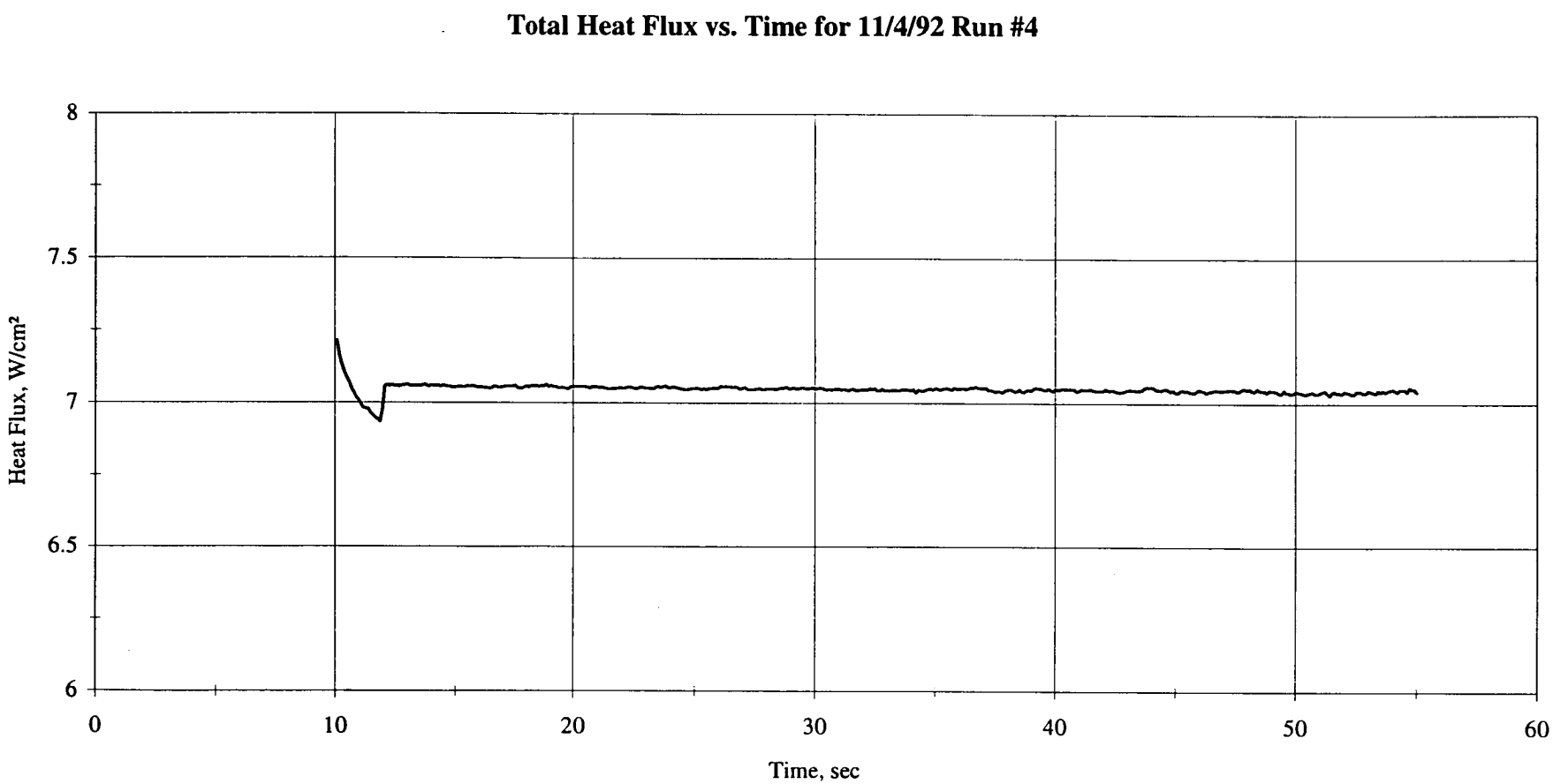

Figure A-12d. a/g = +1 Postflight test. Heat flux input. PBE-IA (STS-47). Run No. 4.

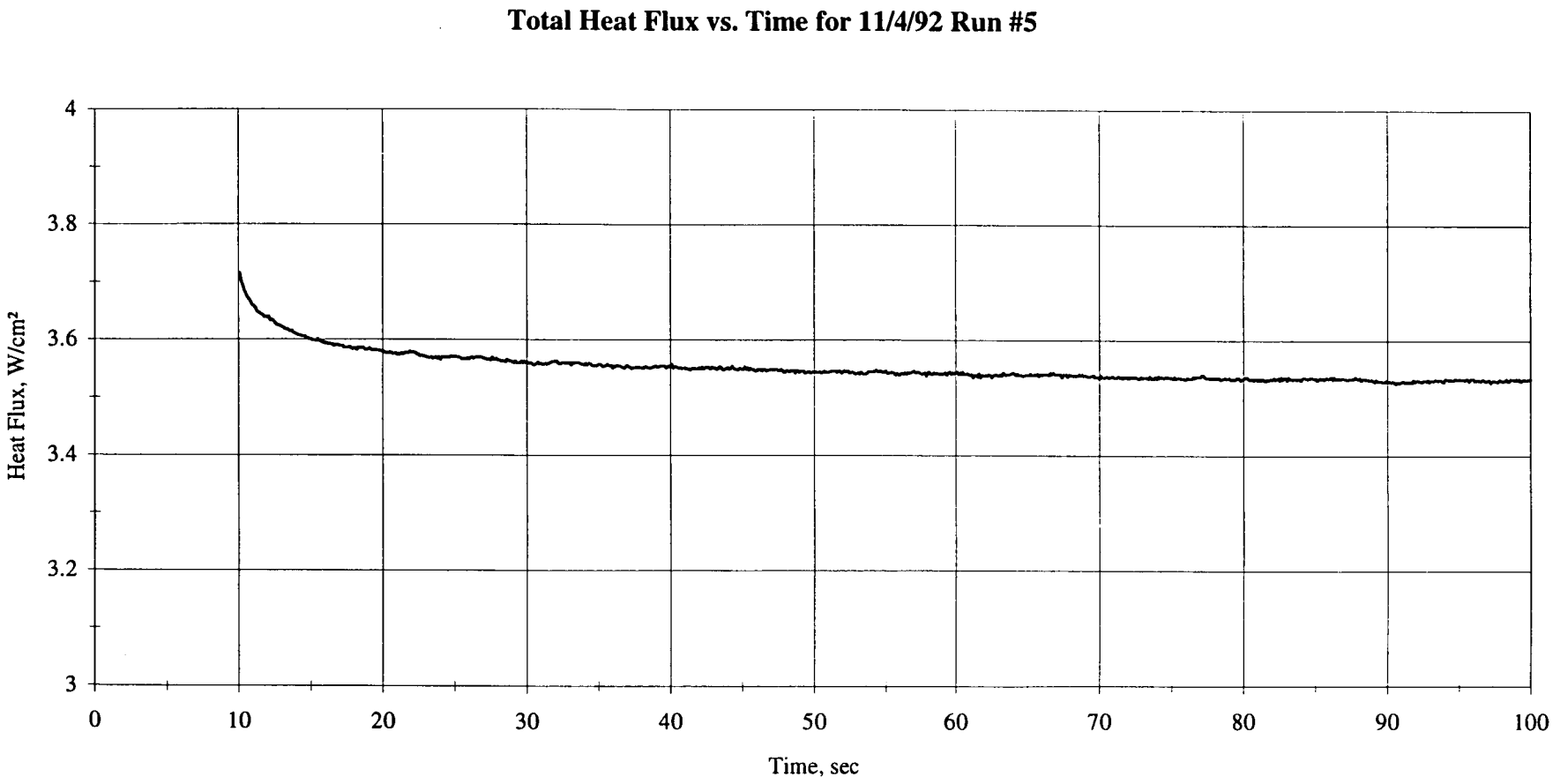

Figure A-12e. a/g = +1 Postflight test. Heat flux input. PBE-IA (STS-47). Run No. 5.

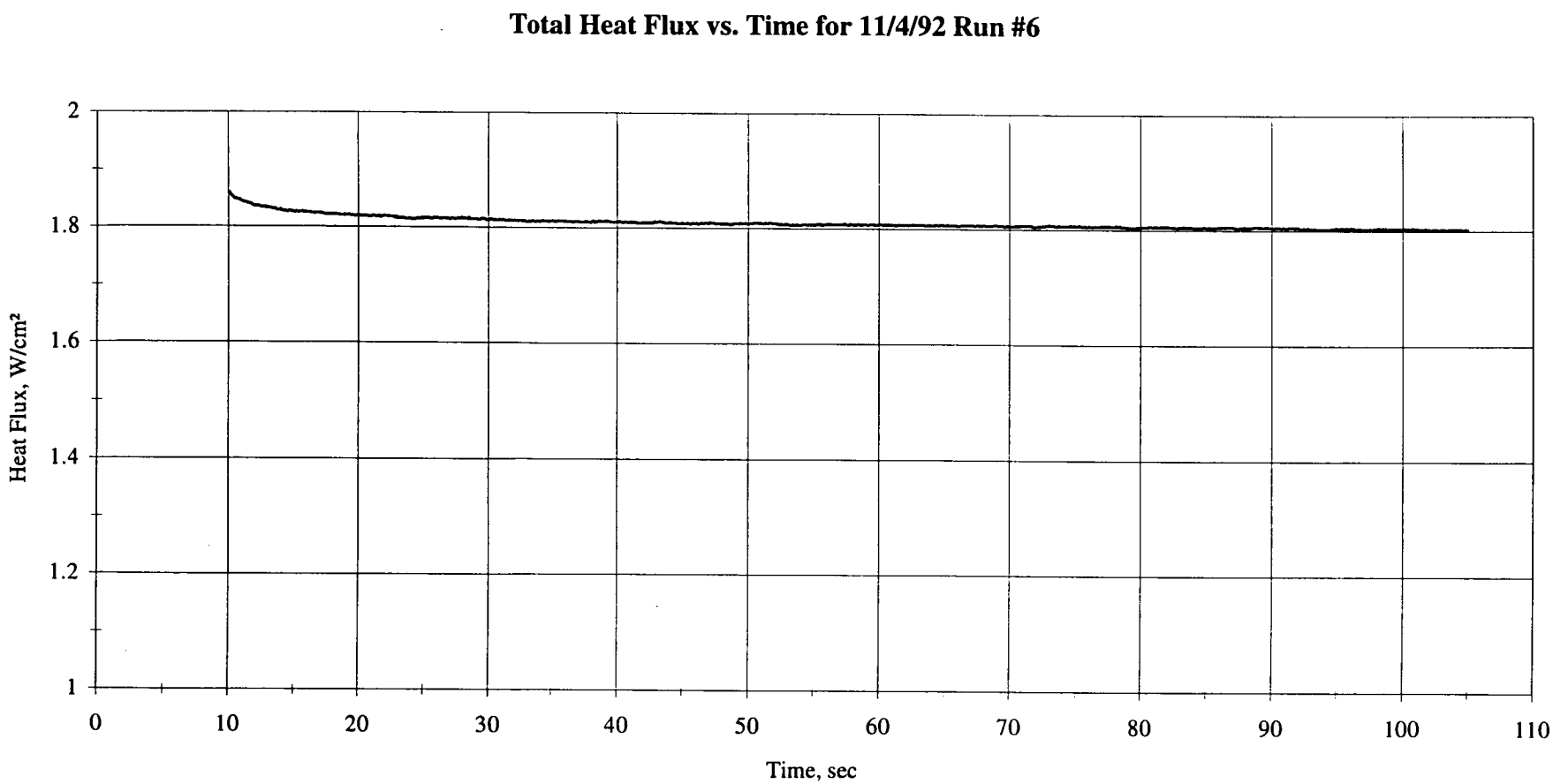

Figure A-12f. a/g = +1 Postflight test. Heat flux input. PBE-IA (STS-47). Run No. 6.

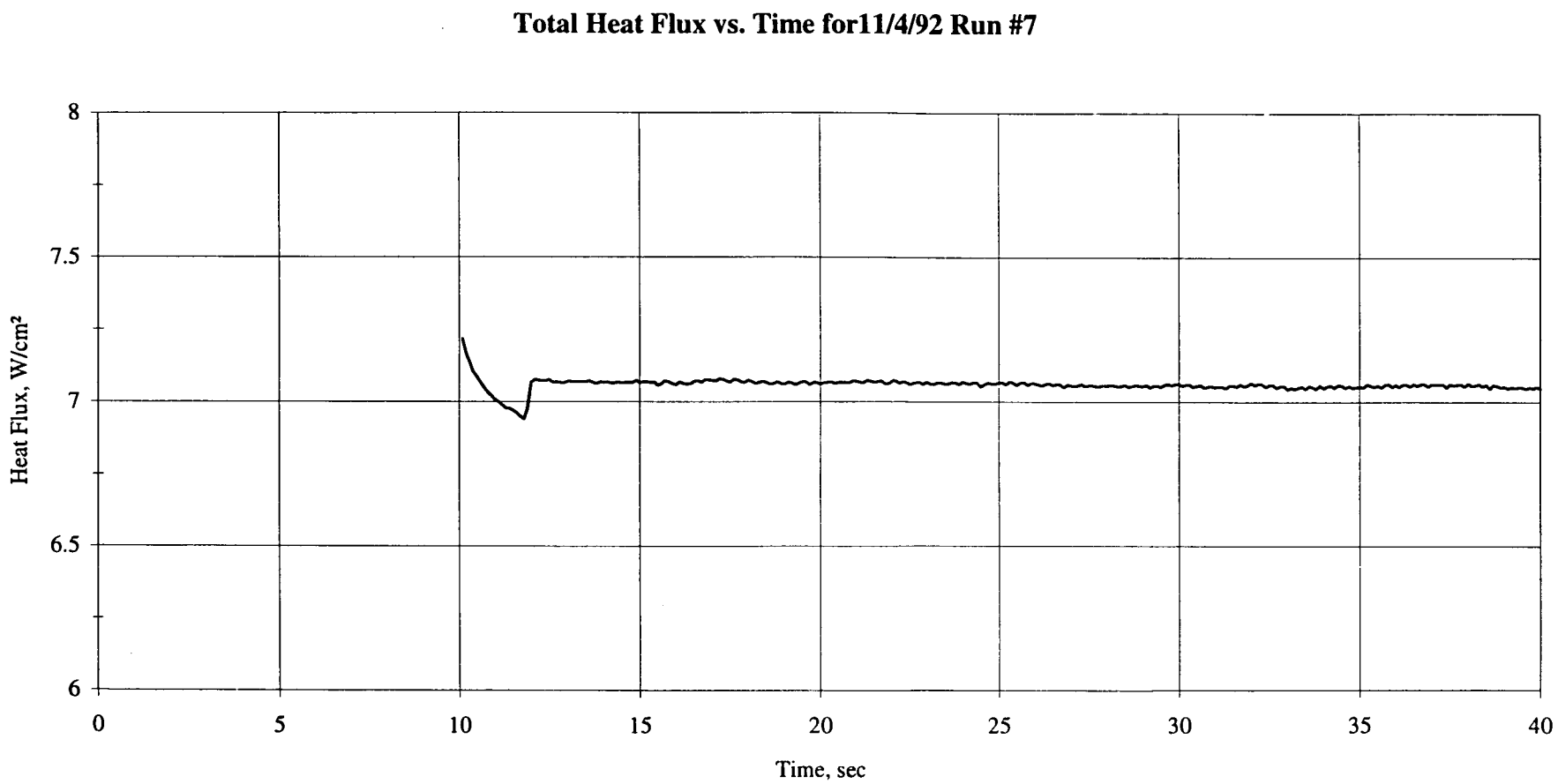

Figure A-12g. a/g = +1 Postflight test. Heat flux input. PBE-IA (STS-47). Run No. 7.

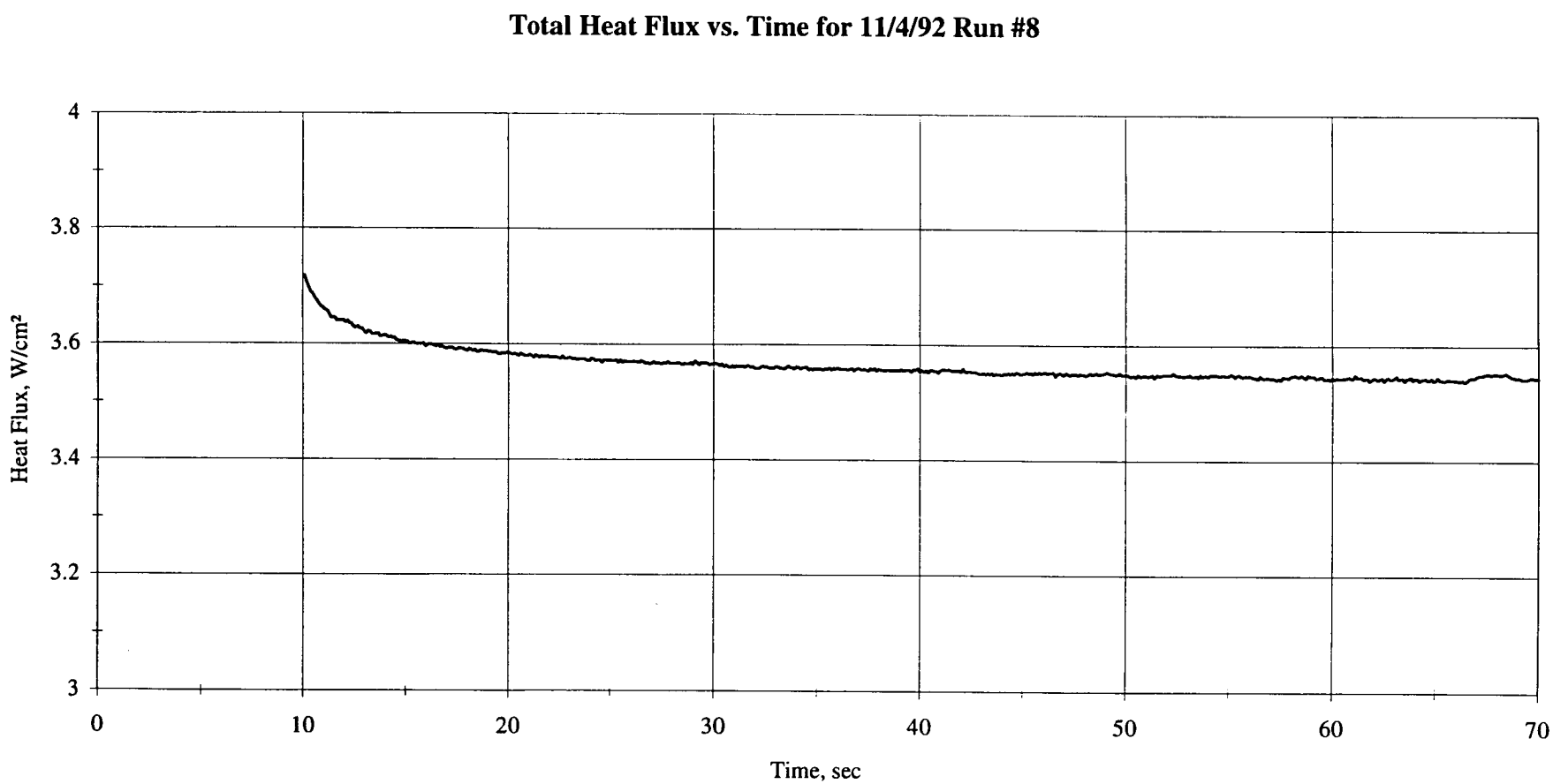

Figure A-12h. a/g = +1 Postflight test. Heat flux input. PBE-IA (STS-47). Run No. 8.

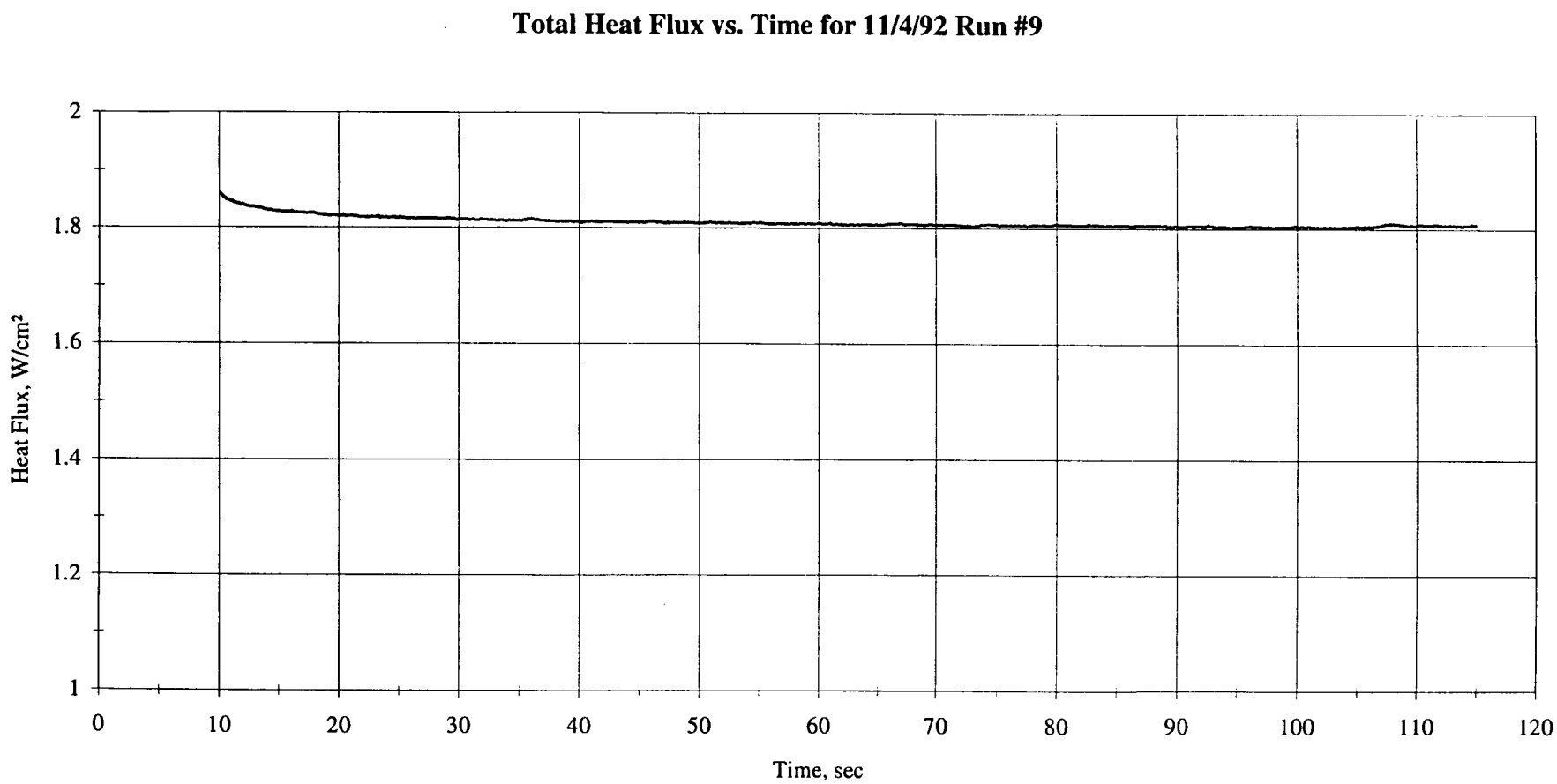

Figure A-12i. a/g = +1 Postflight test. Heat flux input. PBE-IA (STS-47). Run No. 9.

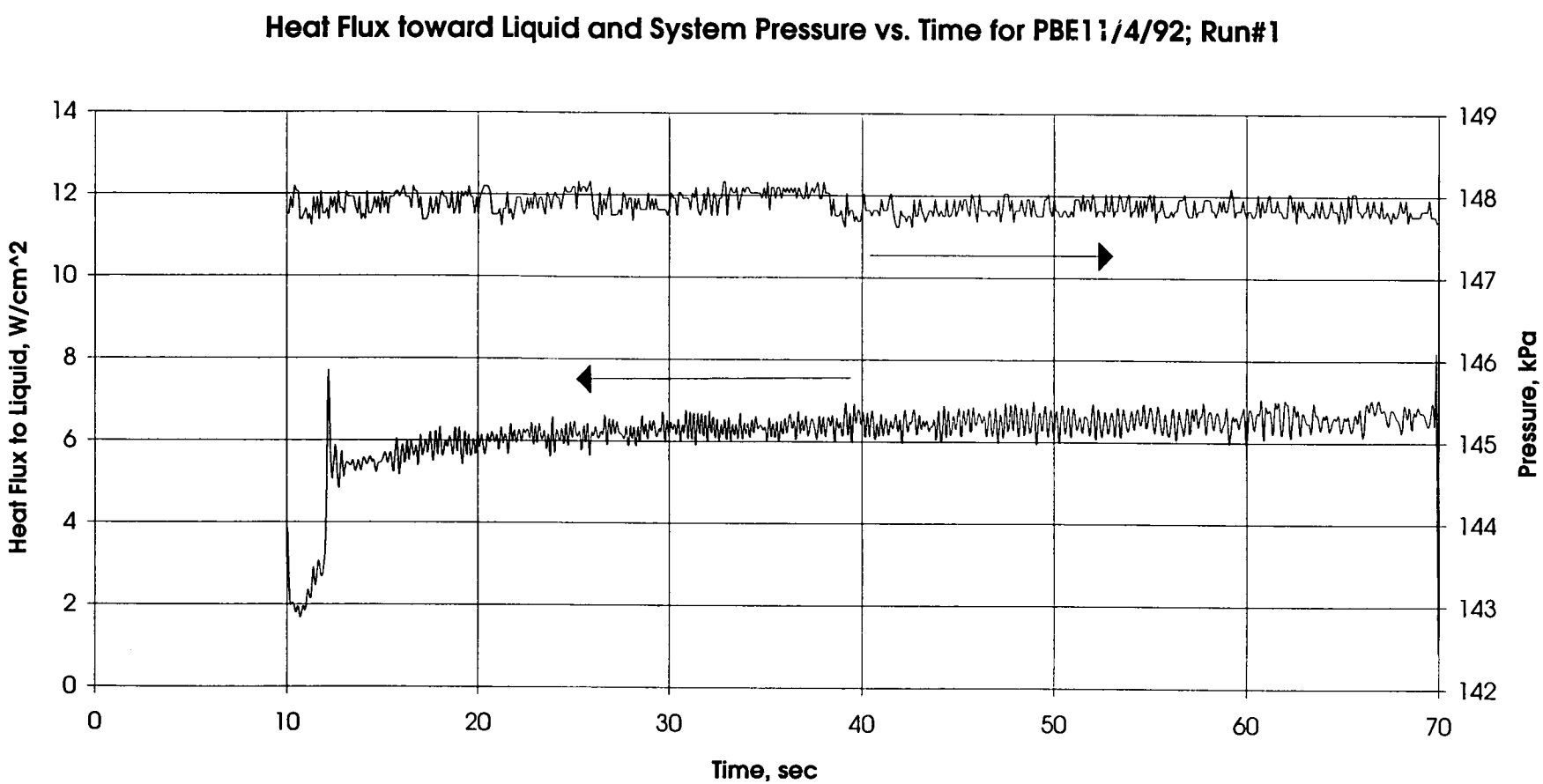

Figure A-13a. a/g = +1 Postflight test. System pressure and heat flux into fluid. PBE-IA (STS-47). Run No. 1.

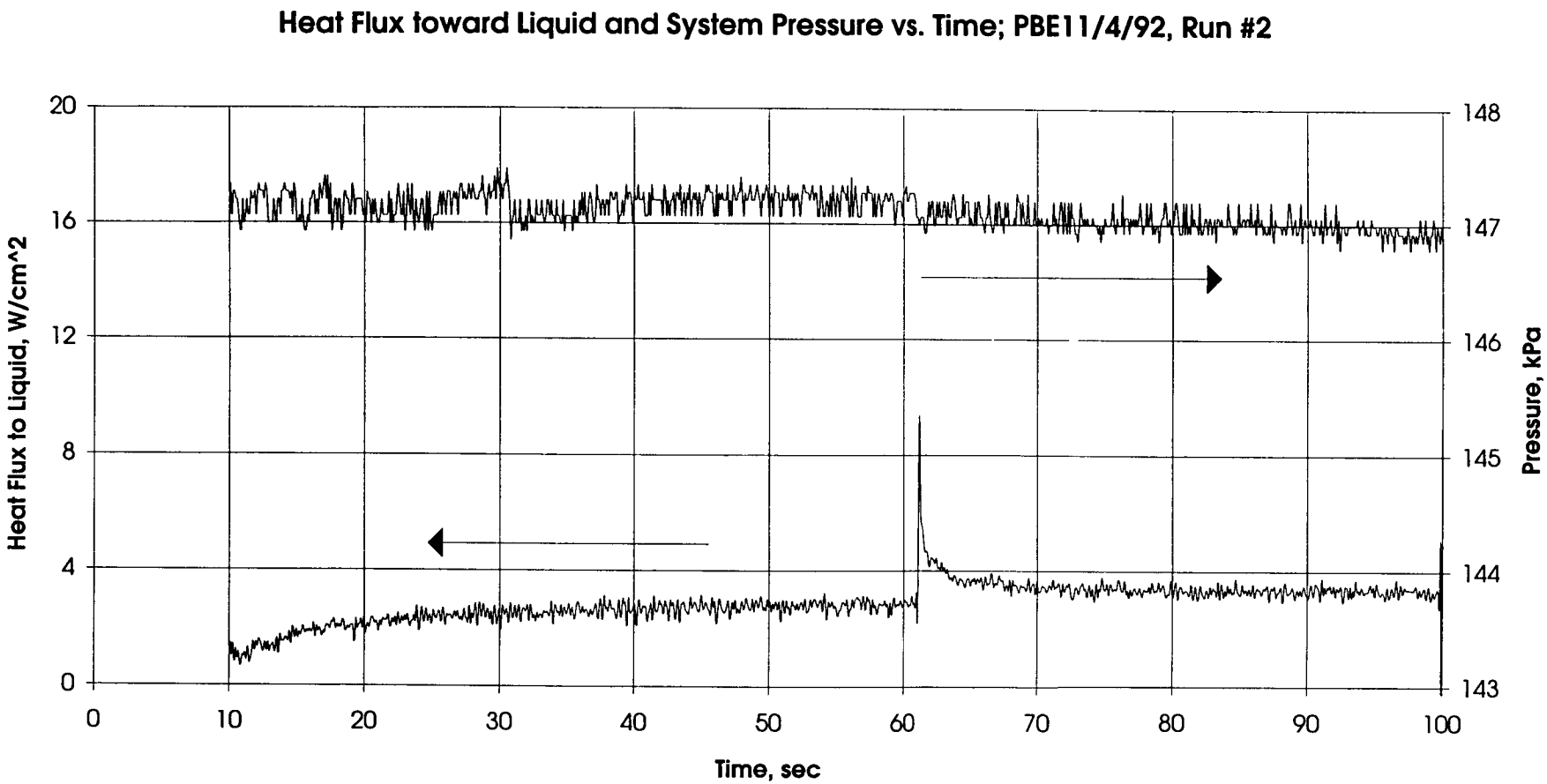

Figure A-13b. a/g = +1 Postflight test. System pressure and heat flux into fluid. PBE-IA (STS-47). Run No. 2.

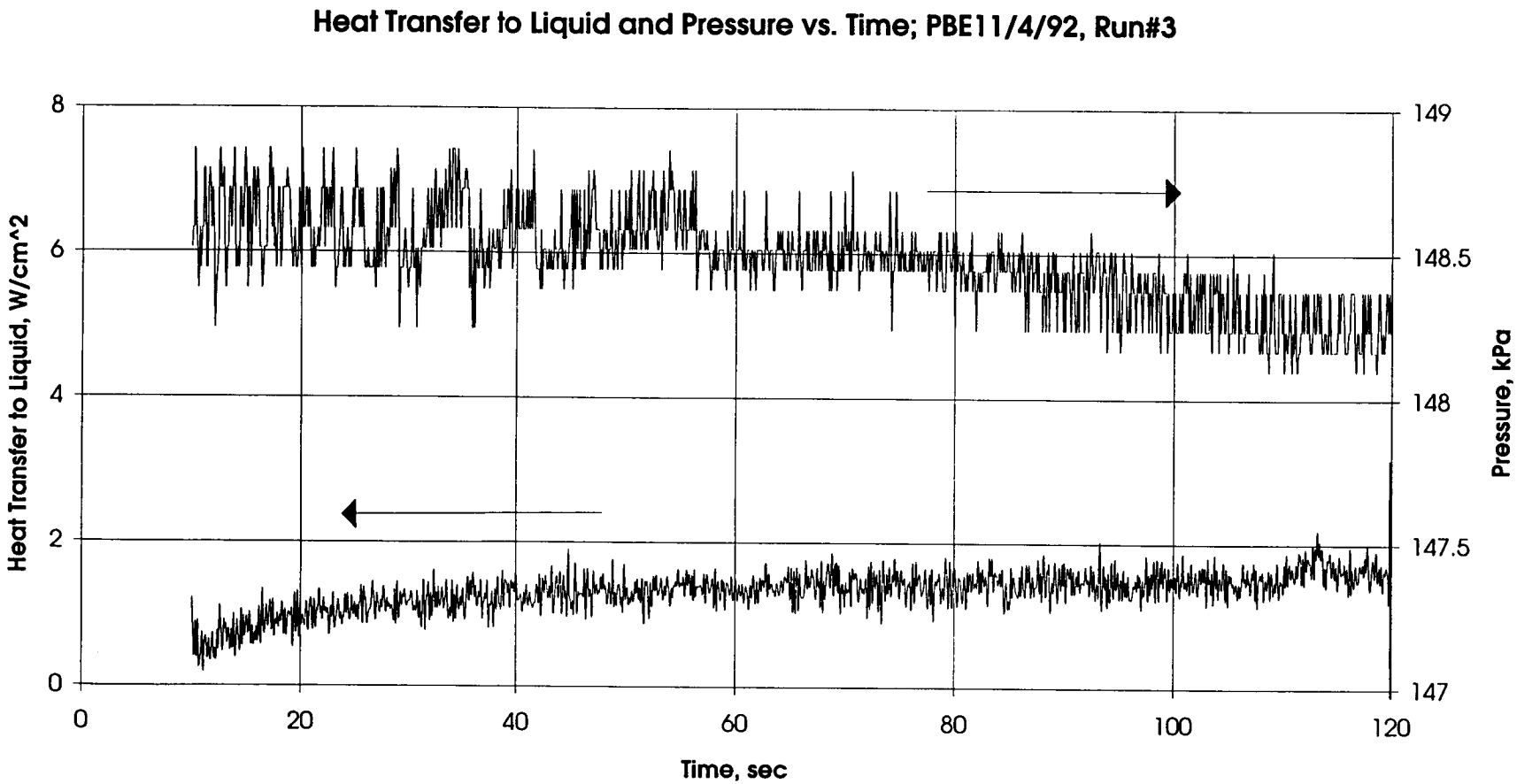

Figure A-13c. a/g = +1 Postflight test. System pressure and heat flux into fluid. PBE-IA (STS-47). Run No. 3.

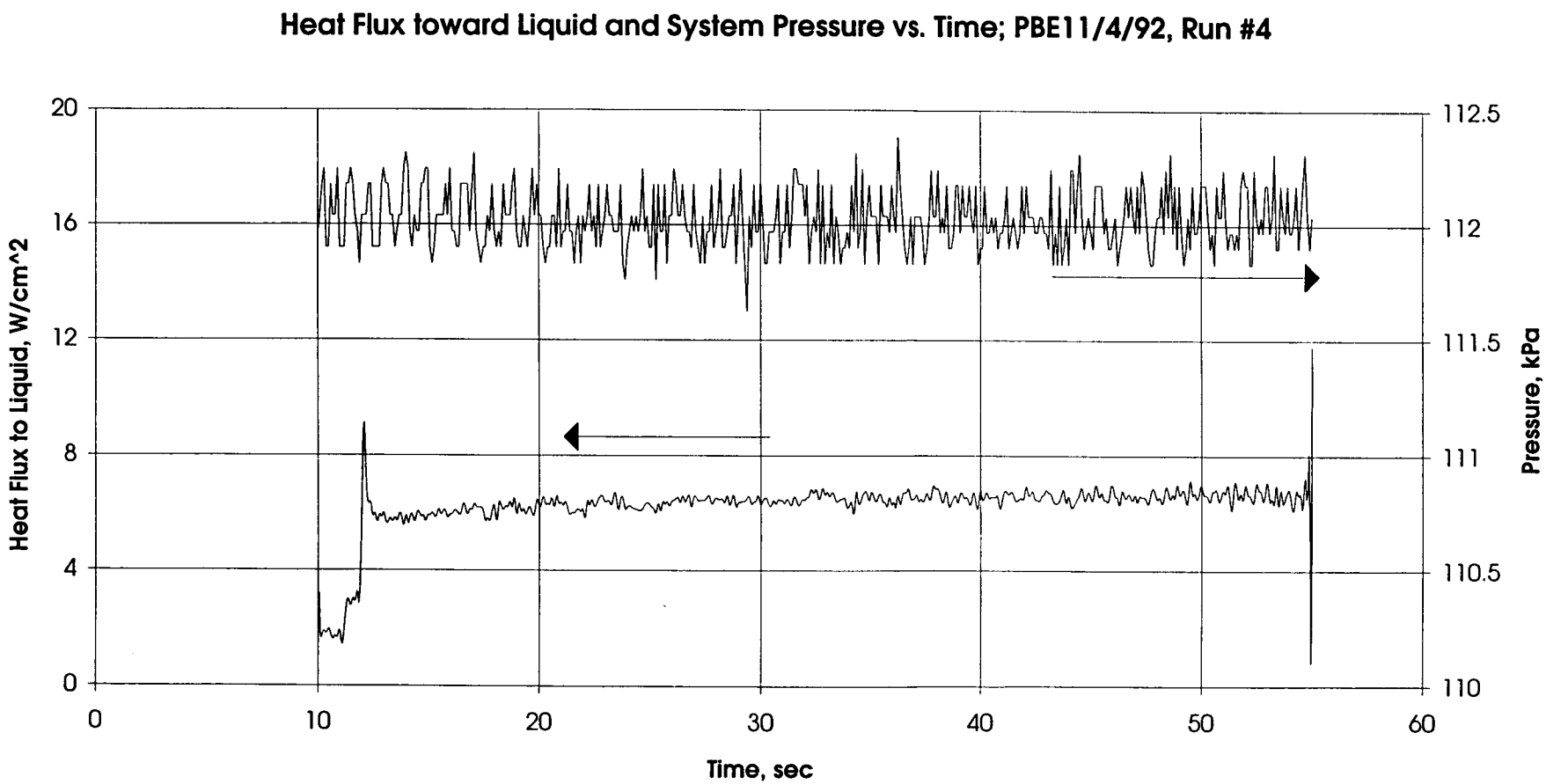

Figure A-13d. a/g = +1 Postflight test. System pressure and heat flux into fluid. PBE-IA (STS-47). Run No. 4.

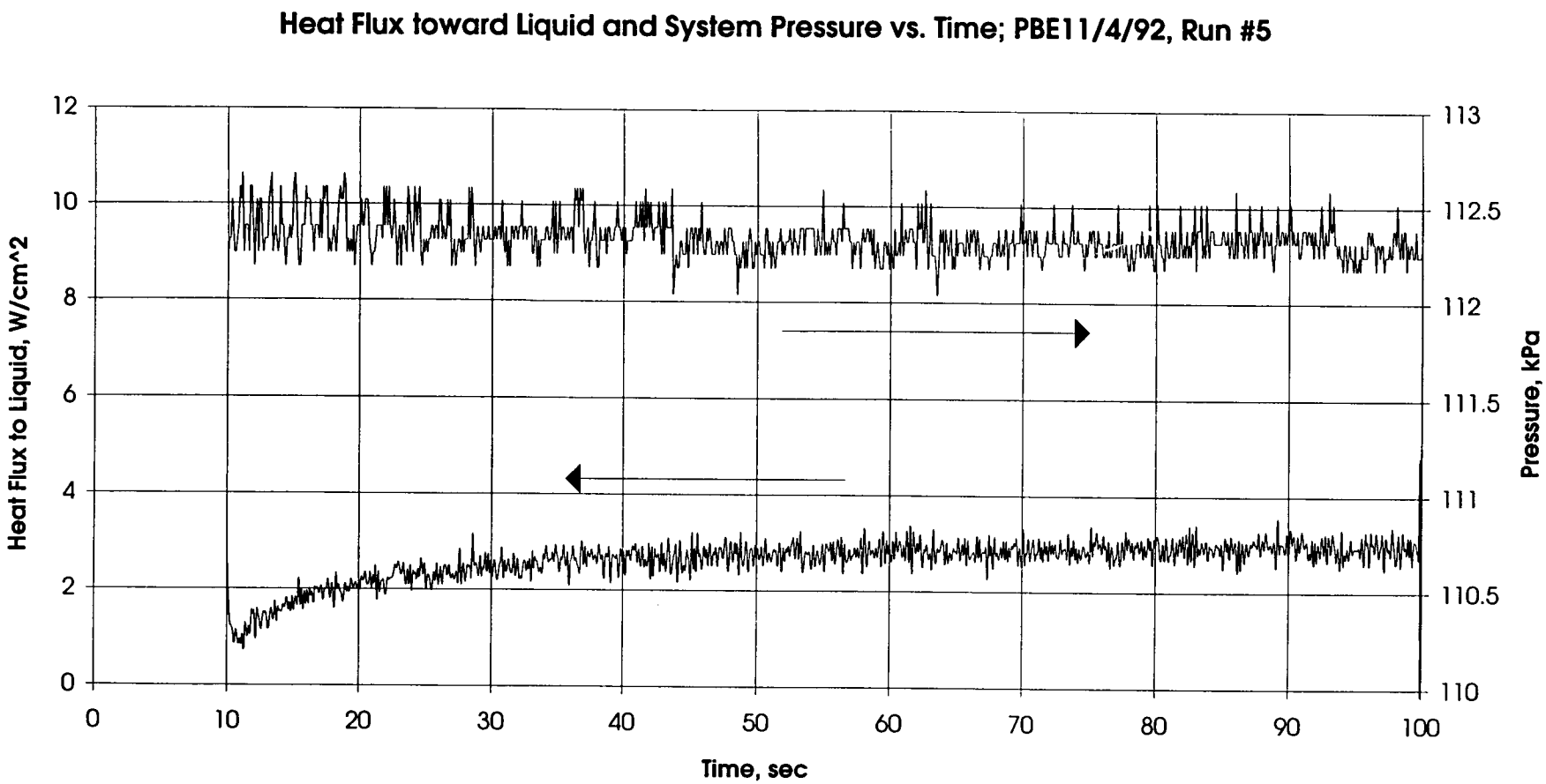

Figure A-13e. a/g = +1 Postflight test. System pressure and heat flux into fluid. PBE-IA (STS-47). Run No. 5.

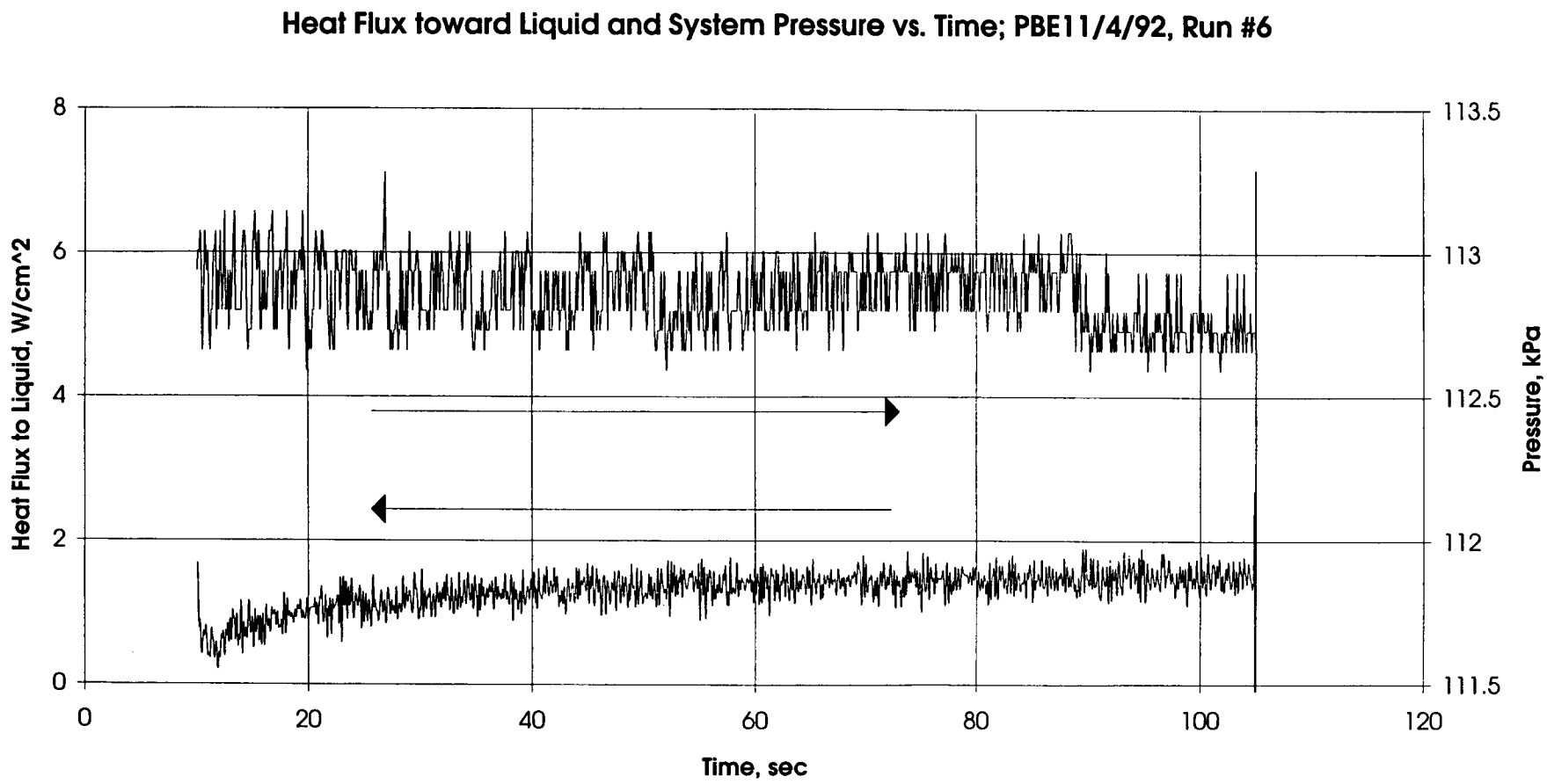

Figure A-13f. a/g = +1 Postflight test. System pressure and heat flux into fluid. PBE-IA (STS-47). Run No. 6.

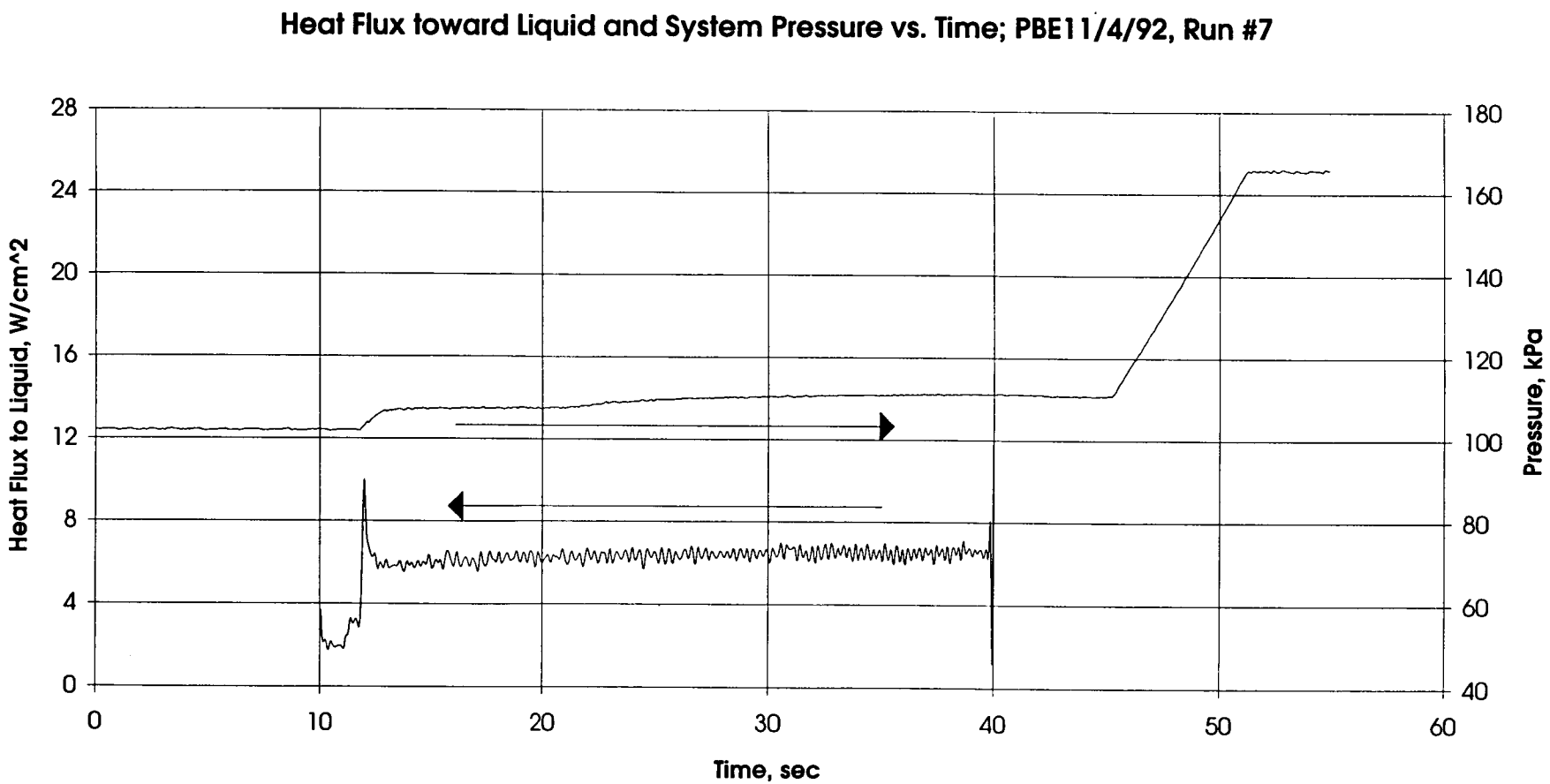

Figure A-13g. a/g = +1 Postflight test. System pressure and heat flux into fluid. PBE-IA (STS-47). Run No. 7.

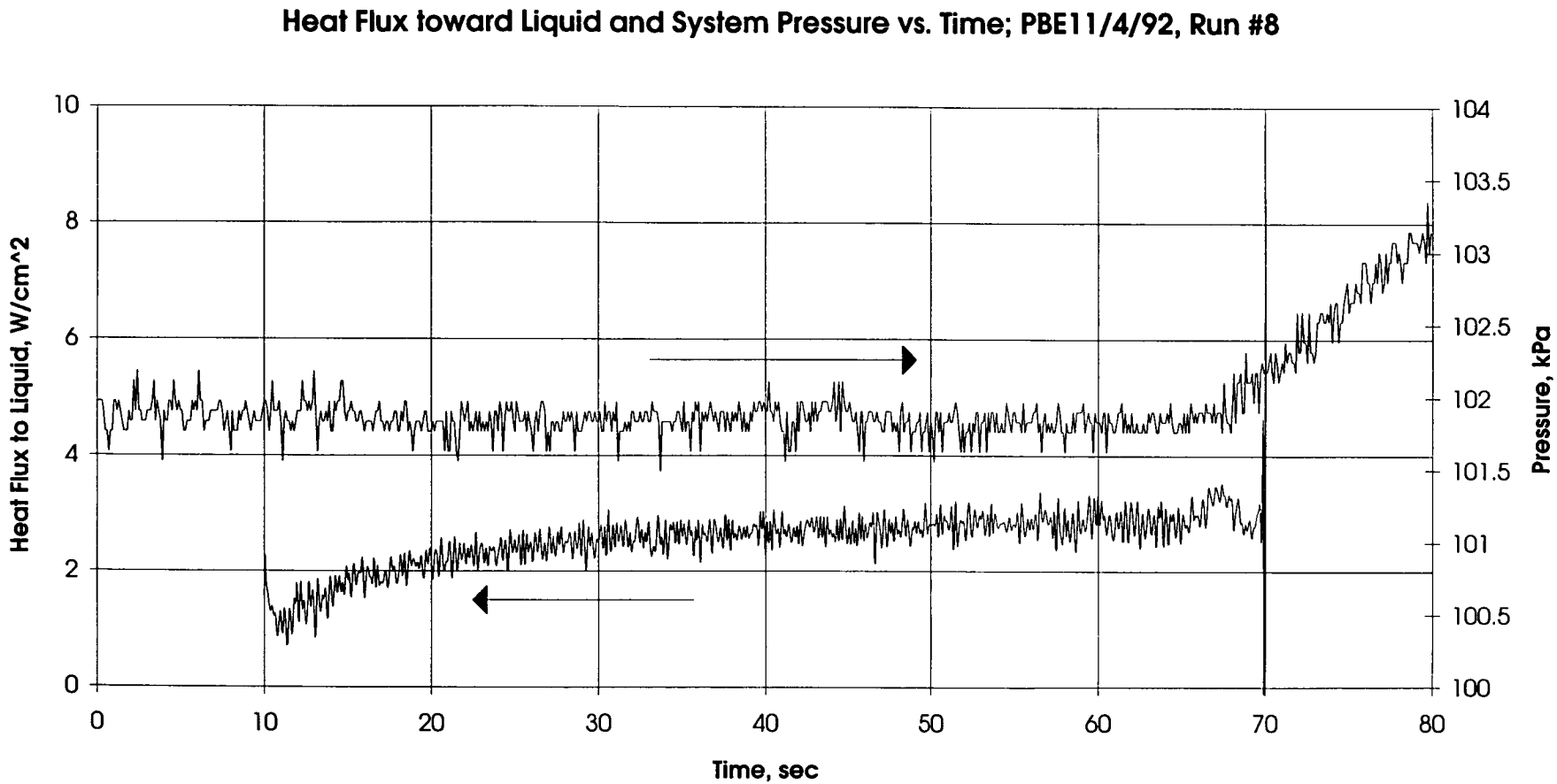

Figure A-13h. a/g = +1 Postflight test. System pressure and heat flux into fluid. PBE-IA (STS-47). Run No. 8.

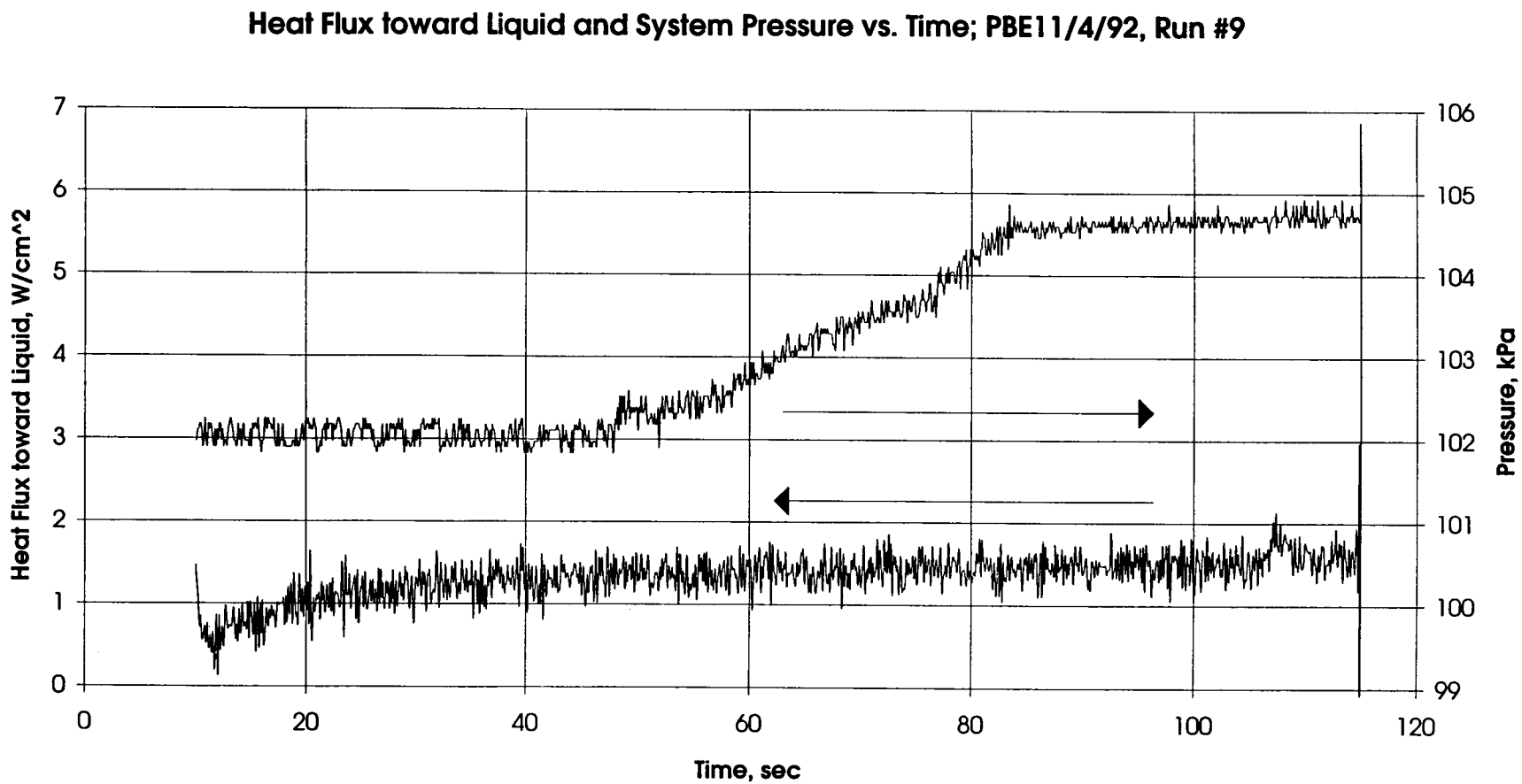

Figure A-13i. a/g = +1 Postflight test. System pressure and heat flux into fluid. PBE-IA (STS-47). Run No. 9.

Appendix B. PBE-IB (STS-57). Experimental Results

		Page No. B-
1.	Table B-I. Test matrix for PBE-IB (STS-57). (Prototype Hardware)	2
2.	Table B-II. Measured parameters at a/g = -1, a/g = +1, and Space Flight	3
3.	Table B-III. Summary of relatively larger acceleration excursions during PBE-IB (STS-57).	5
4.	Figures B-1a — B-1i. Mean heater surface temperature and derived heat transfer coefficient. PBE-IB (STS-57). Run Nos. 1-9	6-14
5.	Figures B-2a — B-2i. Heat flux input. PBE-IB (STS-57). Run Nos. 1-9.	15-23
6.	Figures B-3a — B-3i. System pressure and fluid side mean heat flux. PBE-IB (STS-57). Run Nos. 1-9.	24-32
7.	Figures B-4a — B-4h. Measured fluid temperatures near primary heater and far field bulk liquid. PBE-IB (STS-57). Run Nos. 1-8.	33-41
8.	Figures B-5a — B-5h. Measured fluid temperatures near secondary heater and heater underside. PBE-IB (STS-57). Run Nos. 1-8	42-50
9.	Figures B-6a — B-6i. Selected Photographic Images. PBE-IB (STS-57). Run Nos. 1-9.	51-68
10.	Figure B-7. Nucleation Delay Time. Comparisons with ground testing and drop tower correlation. PBE-IB (STS-57).	69
11.	Figure B-8. Mean heater surface nucleation superheat. Comparisons with ground testing. PBE-IB (STS-57).	70
12.	Figures B-9a — B-9h. Comparisons of bubble growth measurements with several models. PBE-IB (STS-57). Run Nos. 1-8.	71-78
13.	Table B-IV. Index for heater surface dry fraction measurements and computation of microgravity nucleate boiling heat transfer coefficients. PBE-IB (STS-57).	79
14.	Figures B-10a — B-10h. Development of microgravity boiling heat transfer coefficients from heater surface dry fraction and mean heat transfer coefficients. PBE-IB (STS-57) Run Nos. 1-8.	80-132

PBE Flight System Test Matrix (STS-57)

RUN NO.	HEAT FLUX W/CM^2	SUBCOOLING (°F)	HEATER POWER ON/OFF (SEC)	10 FPS ON/OFF (SEC)	100 FPS ON/OFF (SEC)	STIRRER START (SEC)	REPRESS. START (SEC)	TOTAL TEST TIME (SEC)
1	8	20 ± 2	10--70	15--80	10--15	55-	-	80
2	4	20 ± 2	10--110	10--15, 25--135	15--25	-	-	135
3	2	20 ± 2	10--120	20--30, 50--130	30--50	110-	-	130
4	8	5 ± 1	10--55	15--65	10--15	45-	-	65
5	4	5 ± 1	10--100	10--15, 25--105	15--25	90-	-	105
6	2	5 ± 1	10--85	20--30, 50--100	30--50	-	-	100
7	8	0.5 ± 0.4	10--35	15--65	10--15	-	45-	65
8	4	0.5 ± 0.4	10--70	10--15, 25--80	15--25	60-	-	80
9	2	0.5 ± 0.4	10--115	10--30, 50--125	30--50	95-	-	125

December1,1992
Version 1.0

Table B-I. Test matrix for PBE-IB (STS-57). (Prototype Hardware).

Test Matrix for Pool boiling - STS-57

a/g -1 experiment based on date 1/22/93
a/g 0 experiment based on date 6/ 2 /93
a/g -1 experiment based on date 9/30/93

Run#	Date of Experiment	Flight system	Gravit a/g	Heat Flux, W/cm^ Nom.	Actual	Subcool,oF Nom.o	Actual of	Tbulk oC	Sys.Press kPa	Tsat oC	T*wall oC	T*sup oC	t* time sec	100fps On-Off	Remark
1	1/22/93	Flight Syste	-1	8.00	7.023	20	19.87	49.46	152.95	60.5	86.60	26.10	0.74	0 – 5	
	6/2/93	Flight Syste	0	8.00	7.804	20	19.83	46.96	141.66	57.98	87.81	29.83	0.79	0 – 5	
	9/30/93	Flight Syste	-1	8.00	7.024	20	19.87	49.86	155.00	60.9	86.45	25.55	0.62	0 – 5	
2	1/22/93	Flight Syste	-1	4.00	3.725	20	19.94	49.31	152.46	60.39	119.35	58.96	12.27	5 – 15	
	6/2/93	Flight Syste	0	4.00	3.999	20	19.86	49.04	151.00	60.07	127.46	67.39	15.71	5 – 15	
	9/30/93	Flight Syste	-1	4.00	3.727	20	19.92	49.32	152.47	60.39	126.14	65.75	17.11	5 – 15	
3	1/22/93	Flight Syste	-1	2.00	1.982	20	19.92	49.62	153.85	60.69				20 – 40	No Nucleation
	6/2/93	Flight Syste	0	2.00	2.027	20	19.85	48.66	149.26	59.69	96.69	37.00	23.63	20 – 40	
	9/30/93	Flight Syste	-1	2.00	1.983	20	19.84	50.05	155.65	61.07				20 – 40	No Nucleation
4	1/22/93	Flight Syste	-1	8.00	7.126	5	4.92	49.09	116.67	51.82	91.10	39.28	0.89	0 – 5	
	6/2/93	Flight Syste	0	8.00	7.287	5	4.88	48.61	114.79	51.32	88.86	37.54	1.28	0 – 5	
	9/30/93	Flight Syste	-1	8.00	7.119	5	4.91	48.66	115.05	51.39	82.09	30.70	0.55	0 – 5	
5	1/22/93	Flight Syste	-1	4.00	3.742	5	4.89	49.18	116.97	51.90	112.56	60.66	10.00	5 – 15	
	6/2/93	Flight Syste	0	4.00	3.978	5	4.84	49.00	116.17	51.69	123.44	71.75	13.51	5 – 15	
	9/30/93	Flight Syste	-1	4.00	3.737	5	4.90	49.48	118.11	52.20	124.77	72.57	16.05	5 -- 15	
6	1/22/93	Flight Syste	-1	2.00	1.993	5	4.96	49.22	117.27	51.98				20 – 40	No Nucleation
	6/2/93	Flight Syste	0	2.00	2.012	5	4.93	48.87	115.89	51.61	110.47	58.86	48.36	20 – 40	
	9/30/93	Flight Syste	-1	2.00	1.995	5	4.88	49.01	116.30	51.72				20 -- 40	No Nucleation

Table B-II. Measured parameters at a/g = -1, a/g = +1, and Space Flight.

Page 2 of 2

Run#	Date of Experiment	Flight system	Gravit a/g	Heat Flux, W/cm^ Nom.	Actual	Subcool,oF Nom.o	Actual o	Tbulk oC	Sys.Press kPa	Tsat oC	T*wall oC	T*sup oC	t* time sec	100pps On-Off	Remark
7	1/22/93	Flight Syste	-1	8.00	7.32	0.50	0.38	49.01	107.21	49.22	93.09	43.87	0.92	0 -- 5	
	6/2/93	Flight Syste	0	8.00	7.433	0.50	0.32	48.59	105.63	48.77	82.83	34.06	0.59	0 -- 5	
	9/30/93	Flight Syste	-1	8.00	7.312	0.50	0.43	49.11	107.65	49.35	83.07	33.72	0.55	0 -- 5	
8	1/22/93	Flight Syste	-1	4.00	3.788	0.50	0.37	48.94	106.97	49.15	97.96	48.81	6.56	5 -- 15	
	6/2/93	Flight Syste	0	4.00	3.953	0.50	0.50	48.73	106.45	49.01	119.04	70.03	13.77	5 -- 15	
	9/30/93	Flight Syste	-1	4.00	3.799	0.50	0.41	49.10	107.59	49.33	129.02	79.69	19.41	5 -- 15	
9	1/22/93	Flight Syste	-1	2.00	1.98	0.50	0.34	49.05	107.29	49.24	107.60	58.36	57.07	20 -- 40	
	6/2/93	Flight Syste	0	2.00	1.961	0.50	1.64	48.61	108.28	49.52				20 -- 40	No Data
	9/30/93	Flight Syste	-1	2.00	1.983	0.50	0.43	49.30	108.34	49.54	114.43	64.89	83.28	20 -- 40	

Table B-II. Continued.

RUN #	Time, sec	Plots	Max Value			Uncertainty (Noise)	Comments
			x	y	z		
1		no	50	50	26	2.40E+01	
2		no	50	50	51	2.40E+01	
3		no	25	50	51	2.40E+01	
4		no	25	50	51	2.40E+01	
5		no	50	49	51	2.40E+01	
6		no	50	50	26	2.40E+01	
7		no	25	50	26	2.40E+01	
8	12.8	yes	**98**	25	25	2.40E+01	
8	69.5	yes	50	**100**	**178**	2.40E+01	
9		no	50	25	26	2.40E+01	

Notes: (1) Accelerometer units are given as micro-g's.

(2) Heating in each run begins at t = 10 sec.

Table B-III. Summary of relatively larger acceleration excursions during PBE-IB (STS-57).

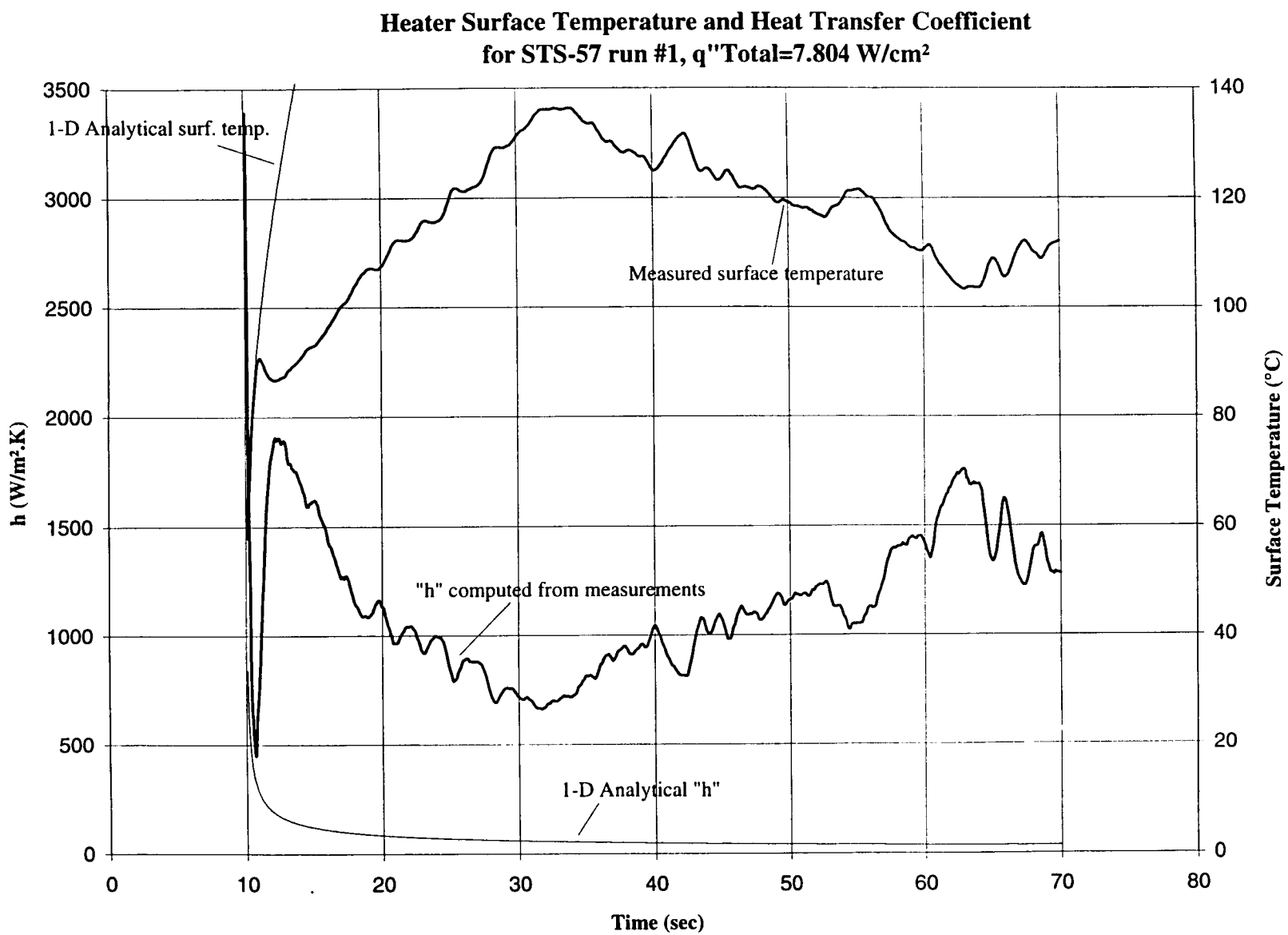

Figure B-1a. Mean heater surface temperature and derived heat transfer coefficient. PBE-IB (STS-57). Run No. 1.

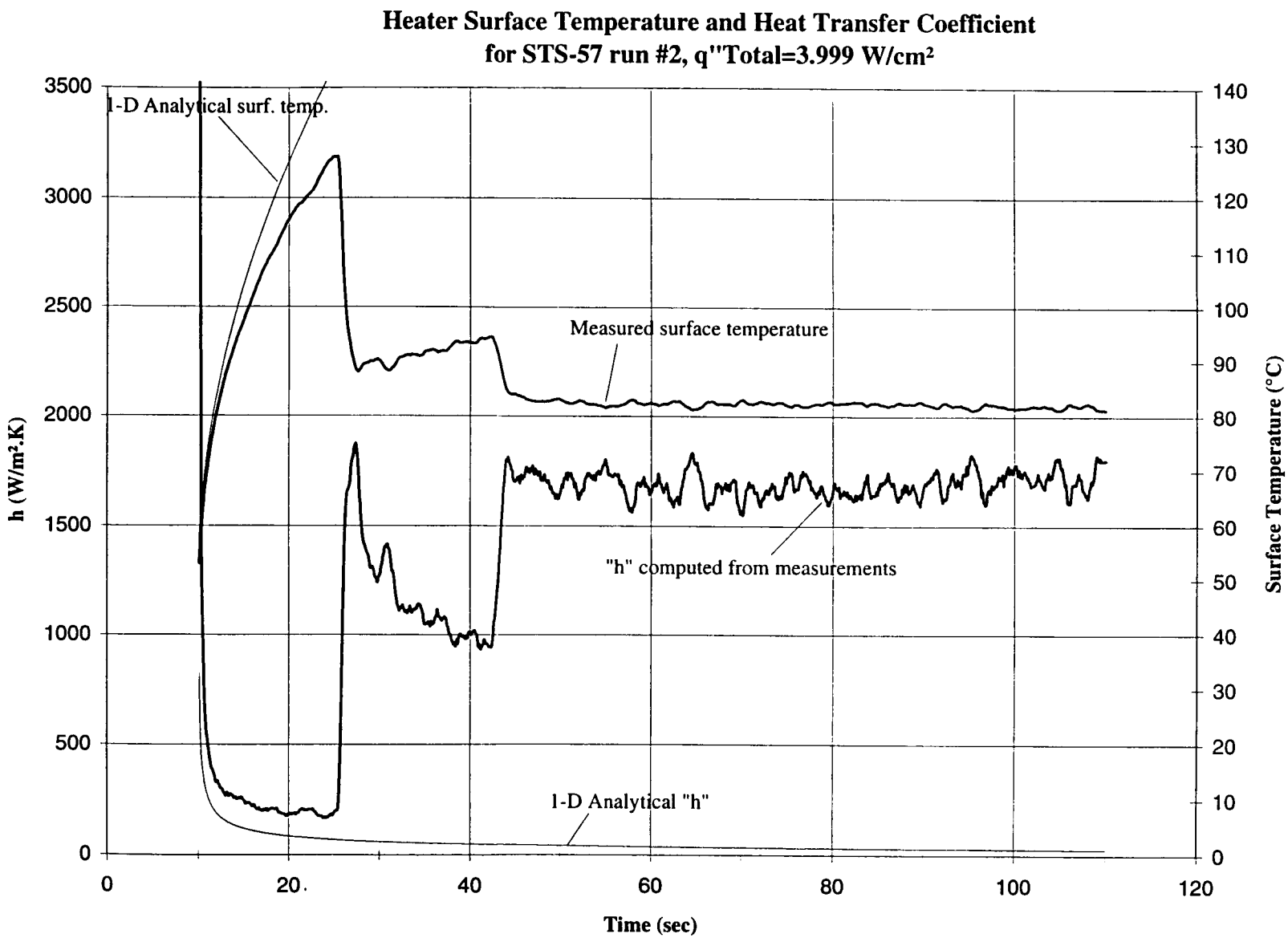

Figure B-1b. Mean heater surface temperature and derived heat transfer coefficient. PBE-IB (STS-57). Run No. 2.

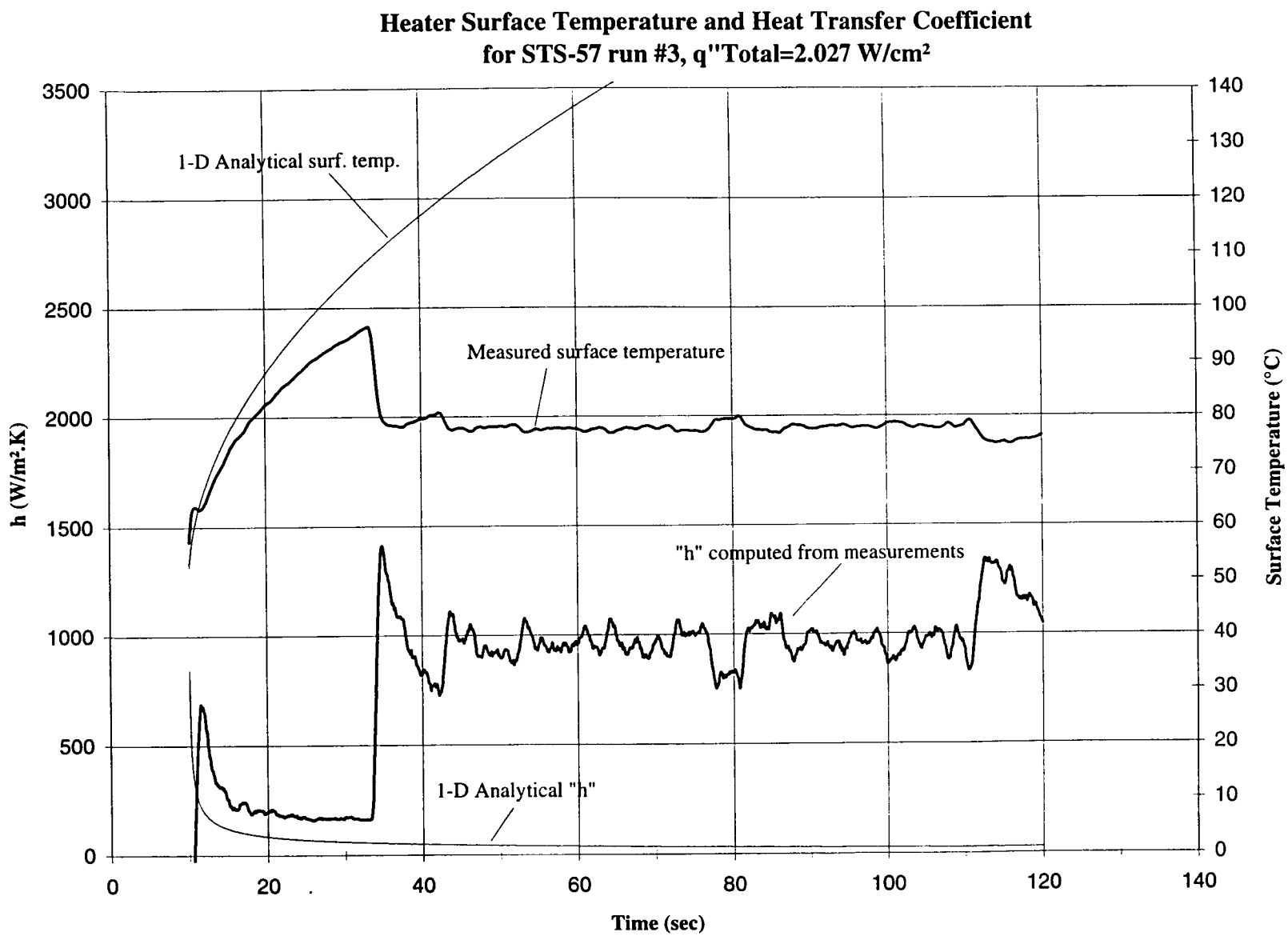

Figure B-1c. Mean heater surface temperature and derived heat transfer coefficient. PBE-IB (STS-57). Run No. 3.

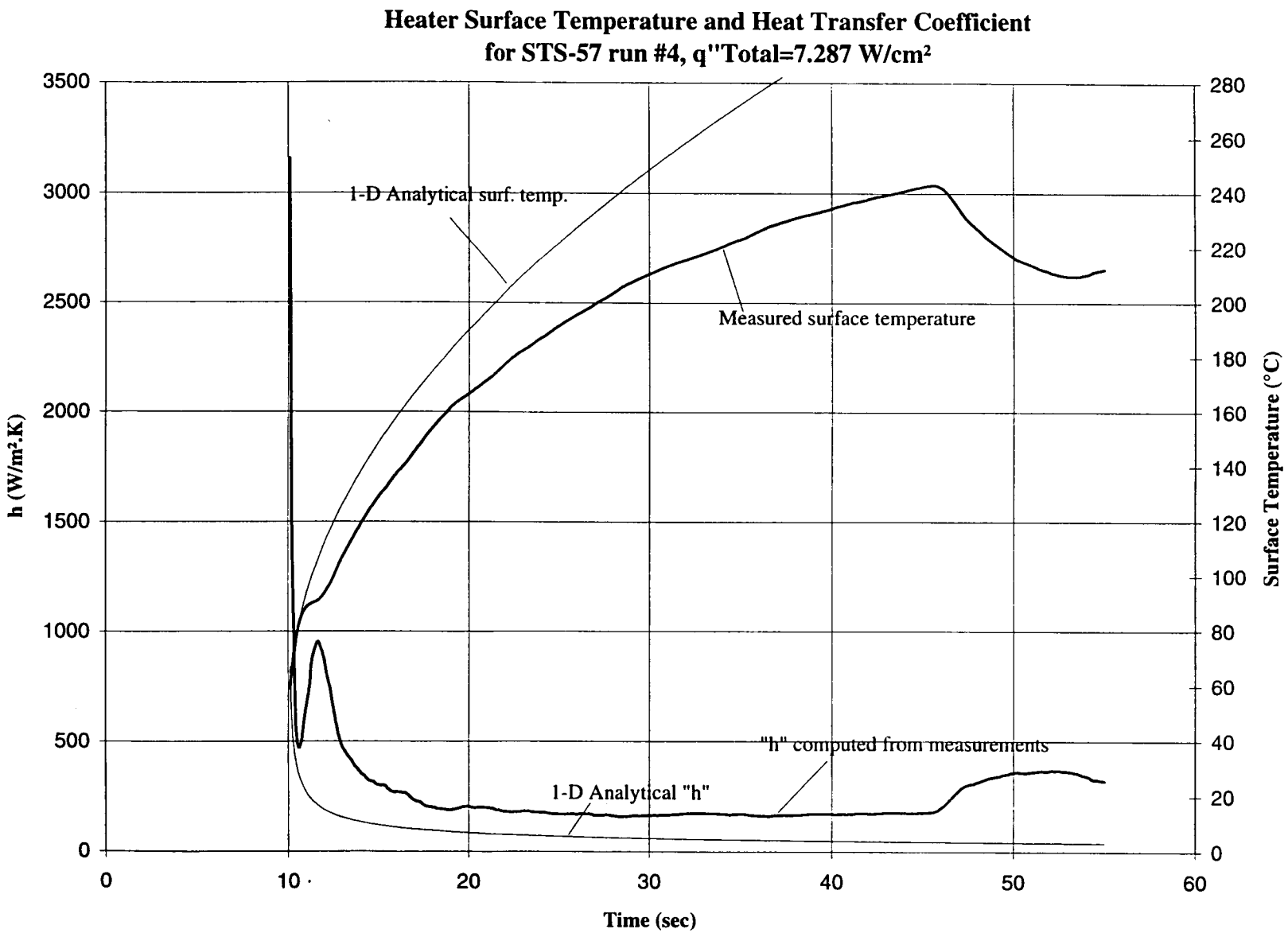

Figure B-1d. Mean heater surface temperature and derived heat transfer coefficient. PBE-IB (STS-57). Run No. 4.

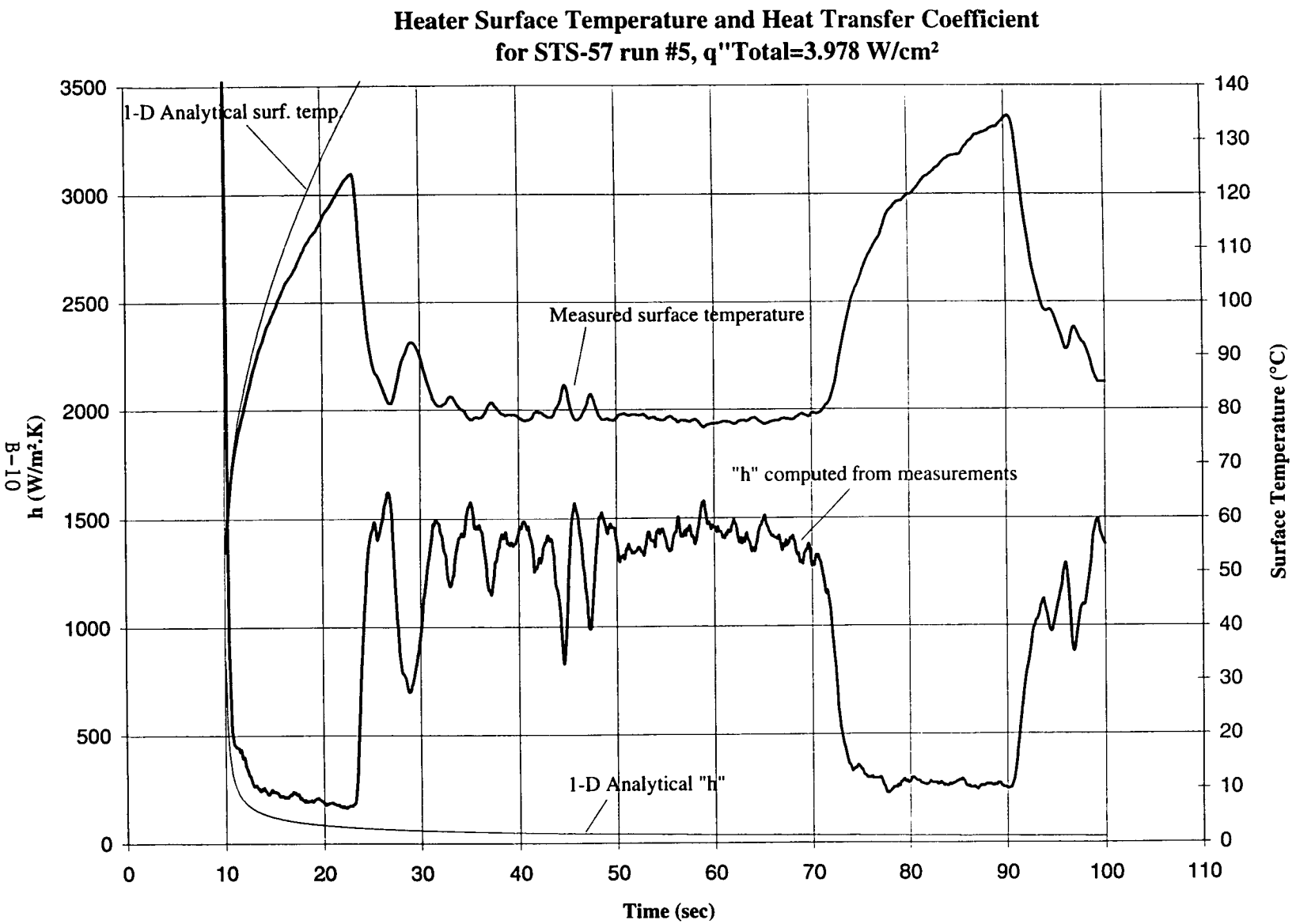

Figure B-1e. Mean heater surface temperature and derived heat transfer coefficient. PBE-IB (STS-57). Run No. 5.

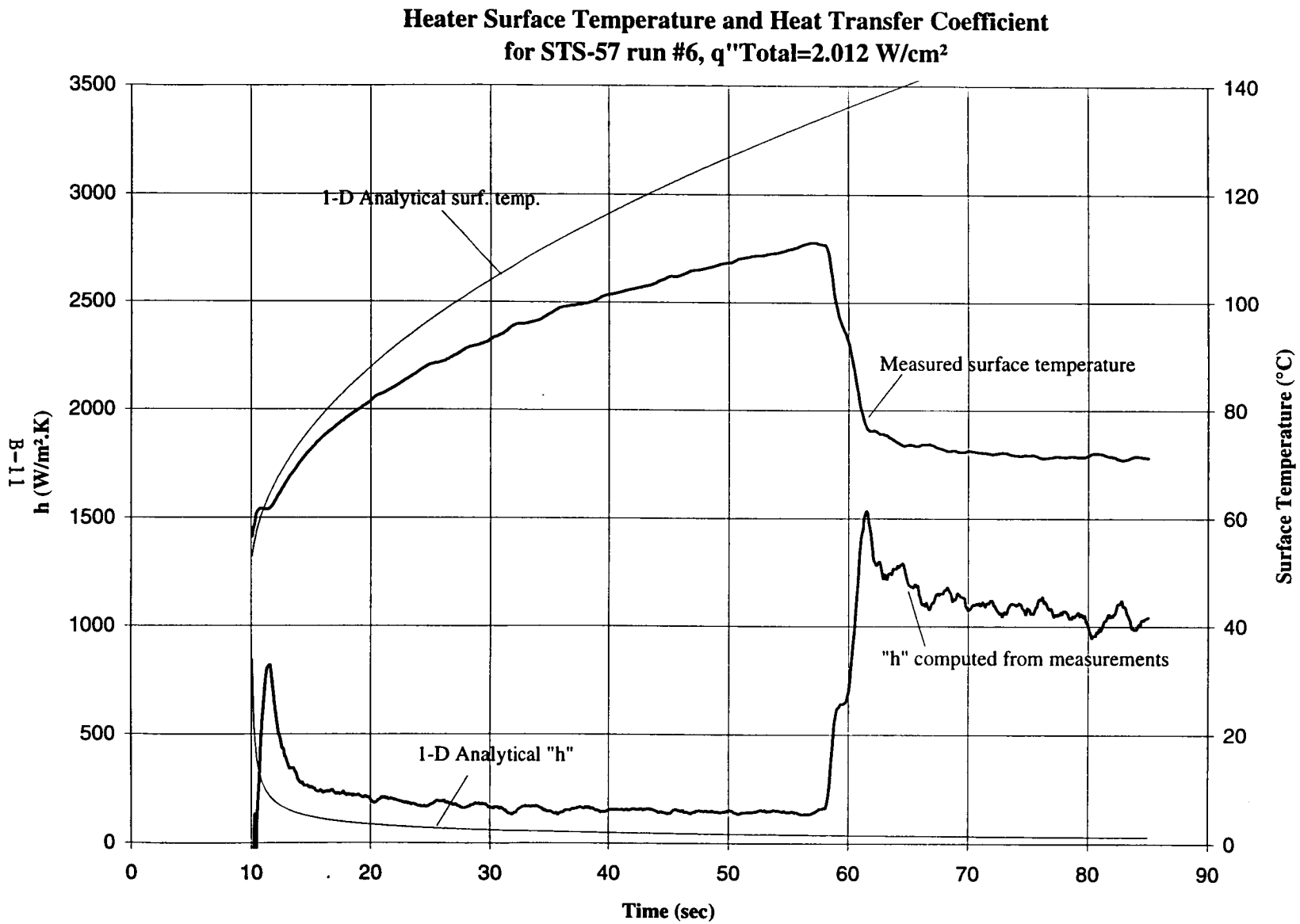

Figure B-1f. Mean heater surface temperature and derived heat transfer coefficient. PBE-IB (STS-57). Run No. 6.

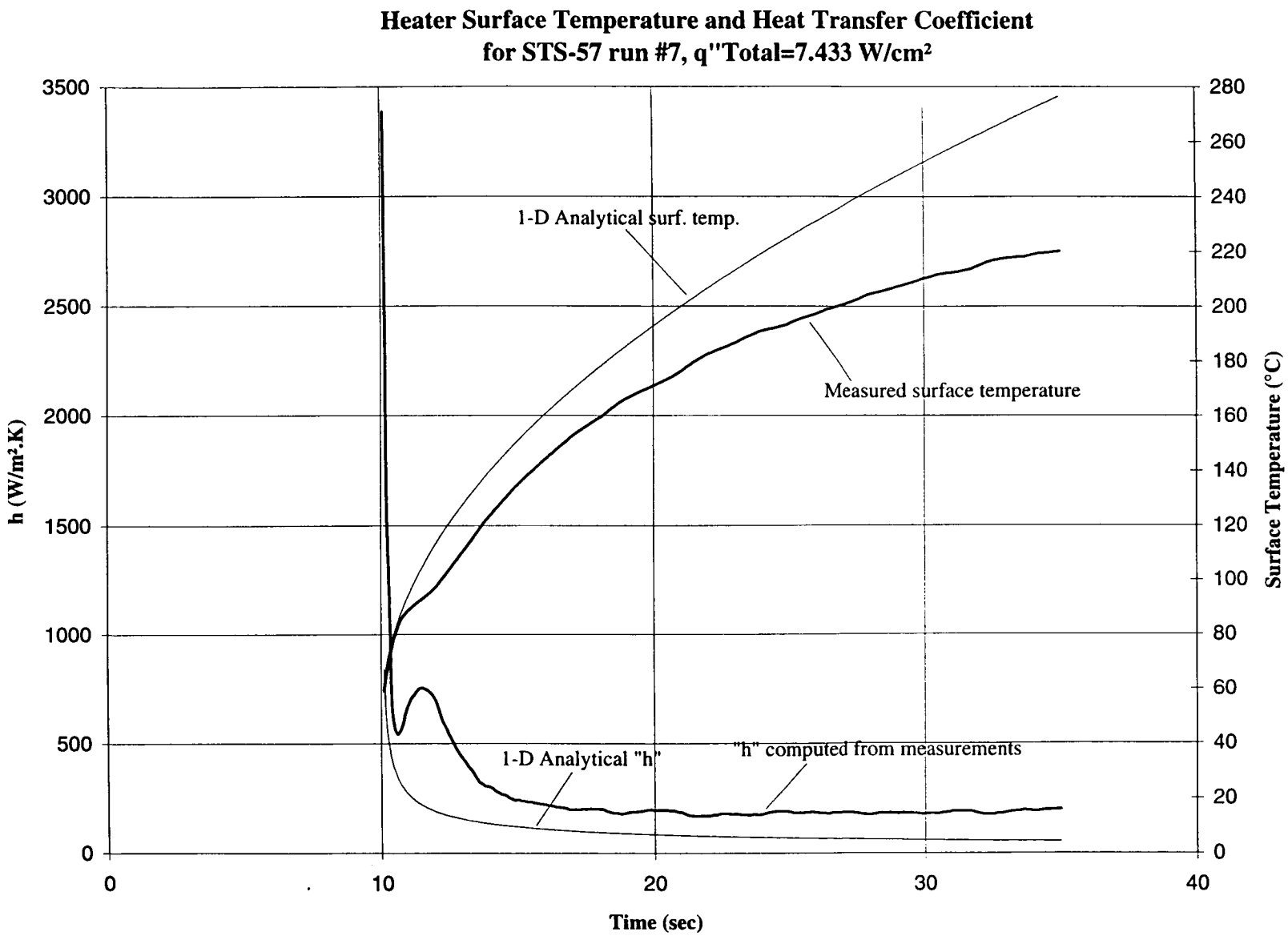

Figure B-1g. Mean heater surface temperature and derived heat transfer coefficient. PBE-IB (STS-57). Run No. 7.

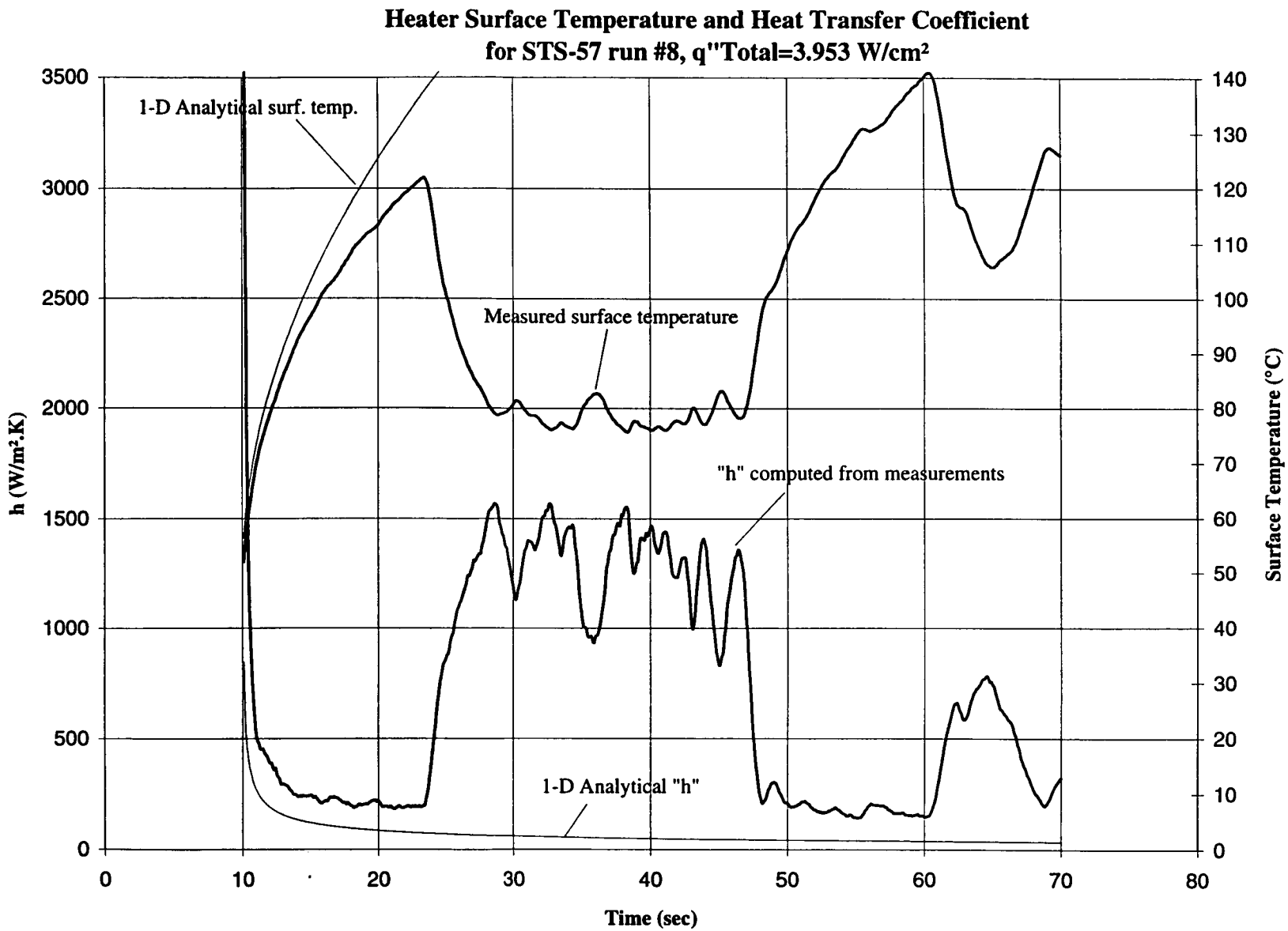

Figure B-1h. Mean heater surface temperature and derived heat transfer coefficient. PBE-IB (STS-57). Run No. 8.

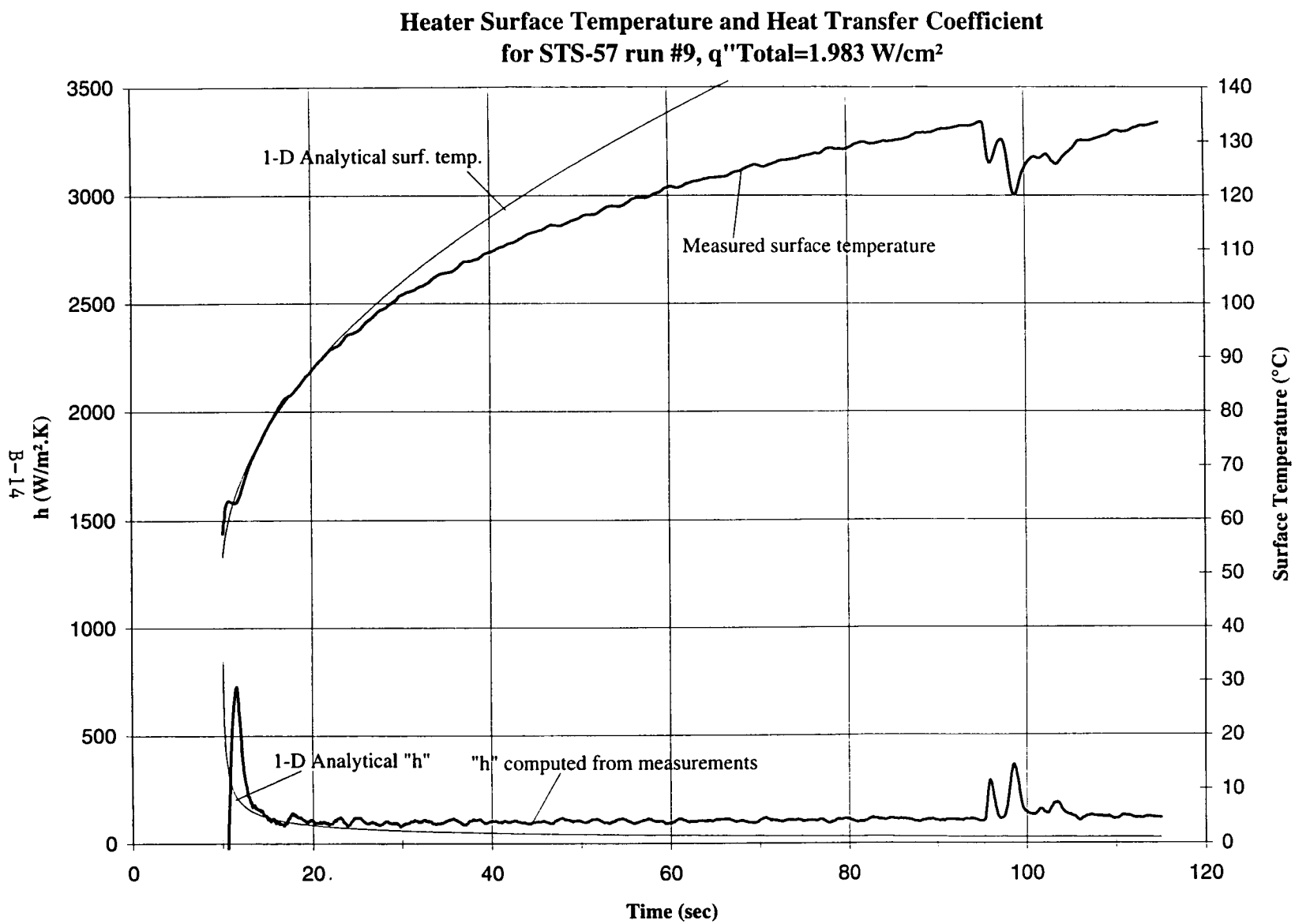

Figure B-1i. Mean heater surface temperature and derived heat transfer coefficient. PBE-IB (STS-57). Run No. 9.

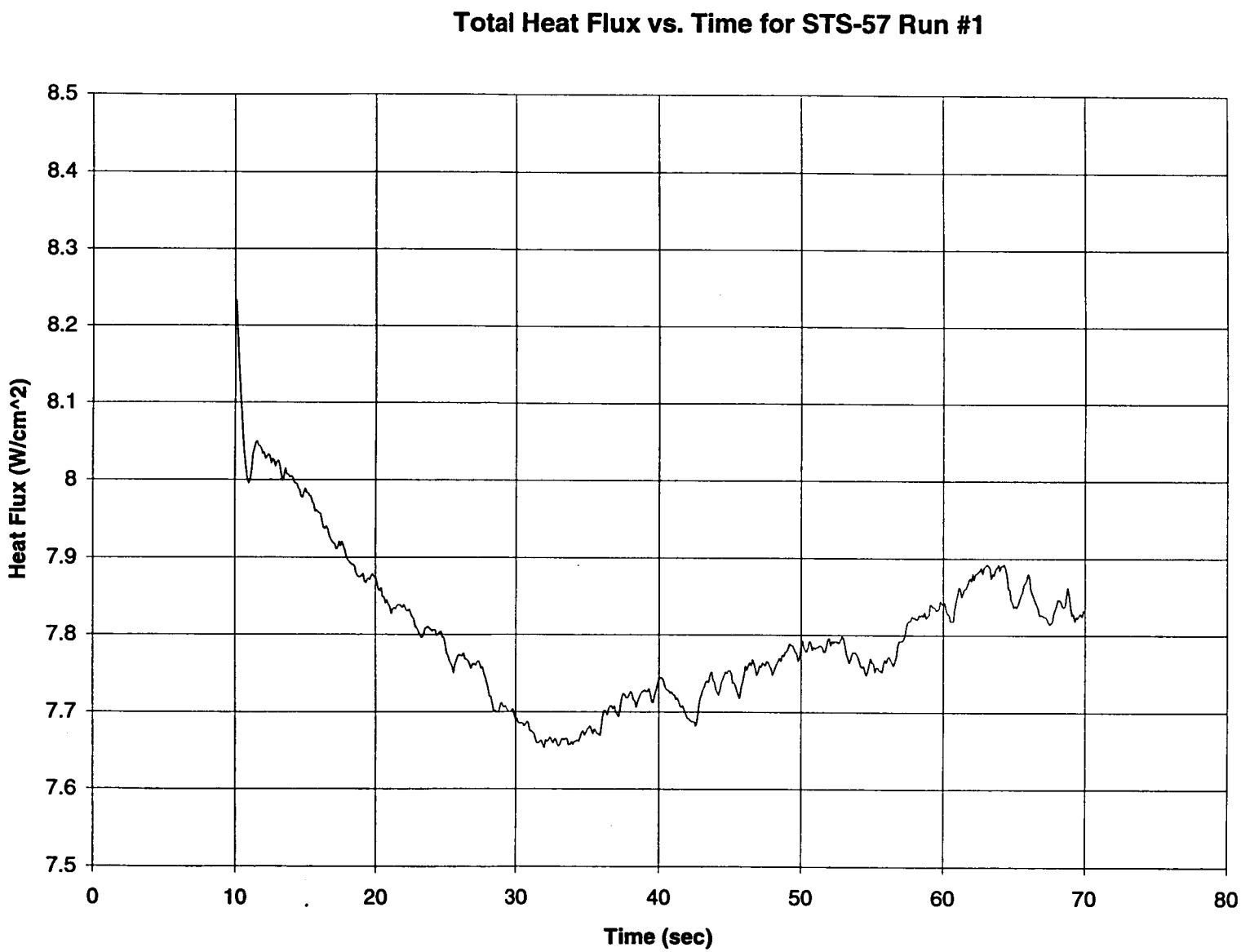

Figure B-2a. Heat flux input. PBE-IB (STS-57). Run No. 1.

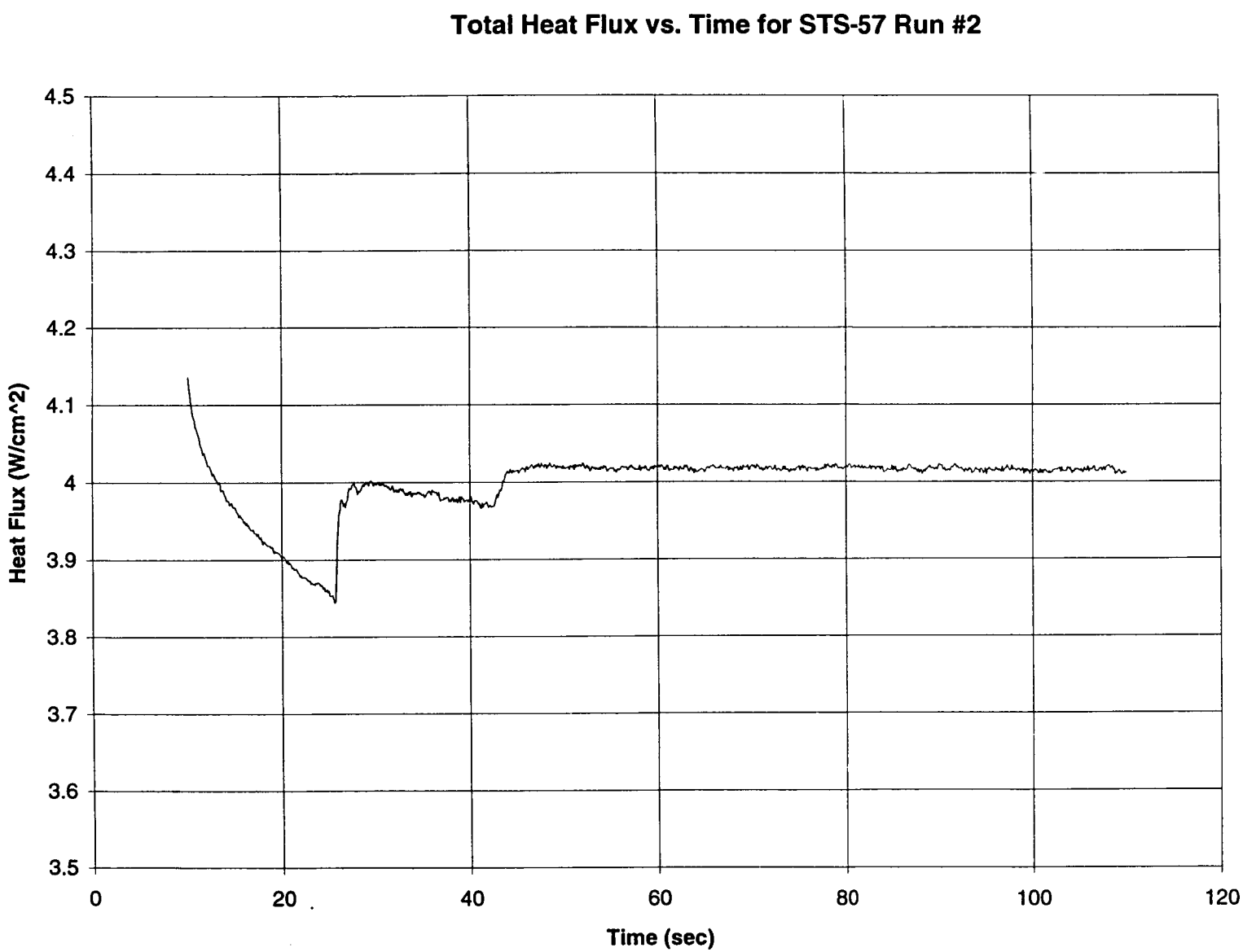

Figure B-2b. Heat flux input. PBE-IB (STS-57). Run No. 2.

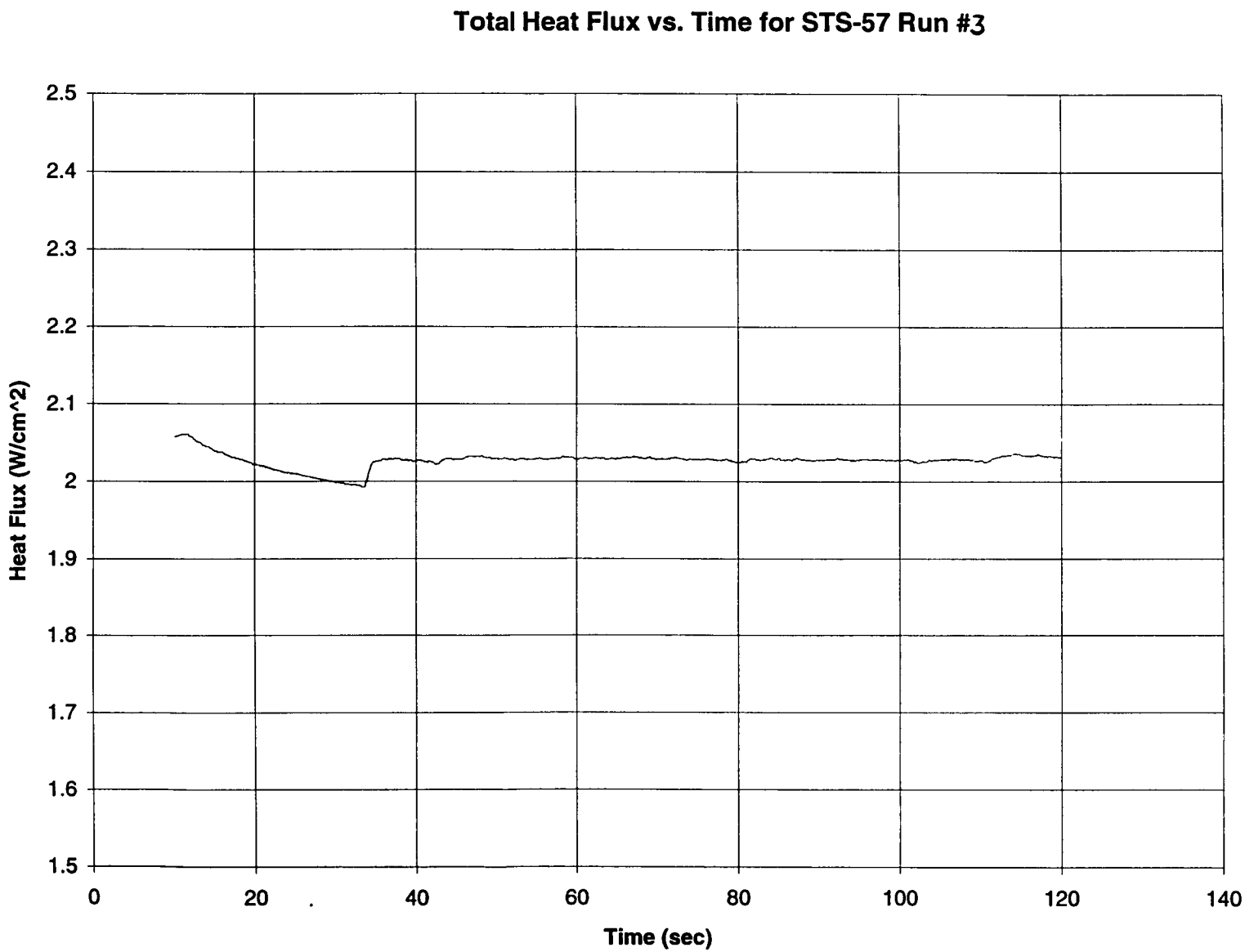

Figure B-2c. Heat flux input. PBE-IB (STS-57). Run No. 3.

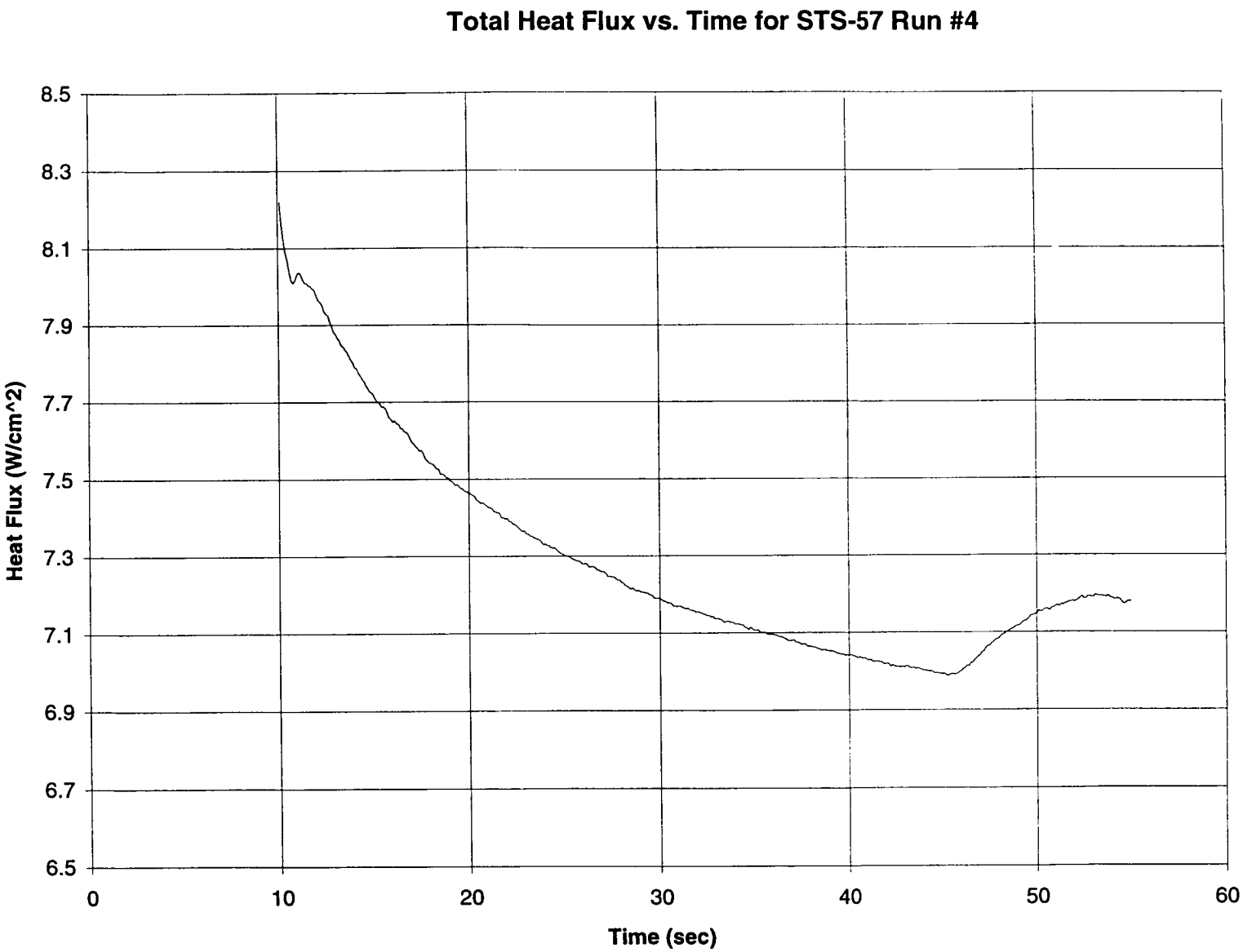

Figure B-2d. Heat flux input. PBE-IB (STS-57). Run No. 4.

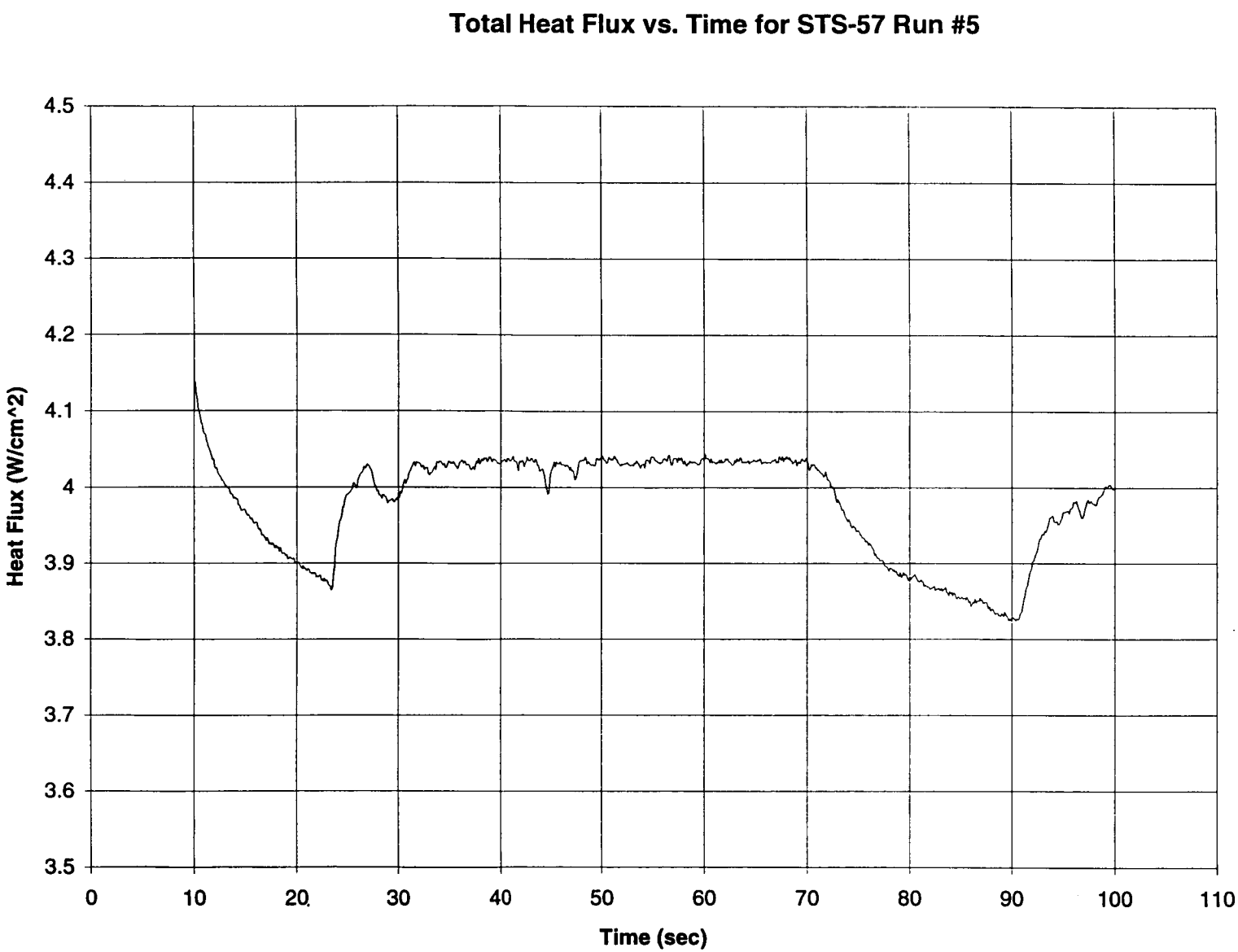

Figure B-2e. Heat flux input. PBE-IB (STS-57). Run No. 5.

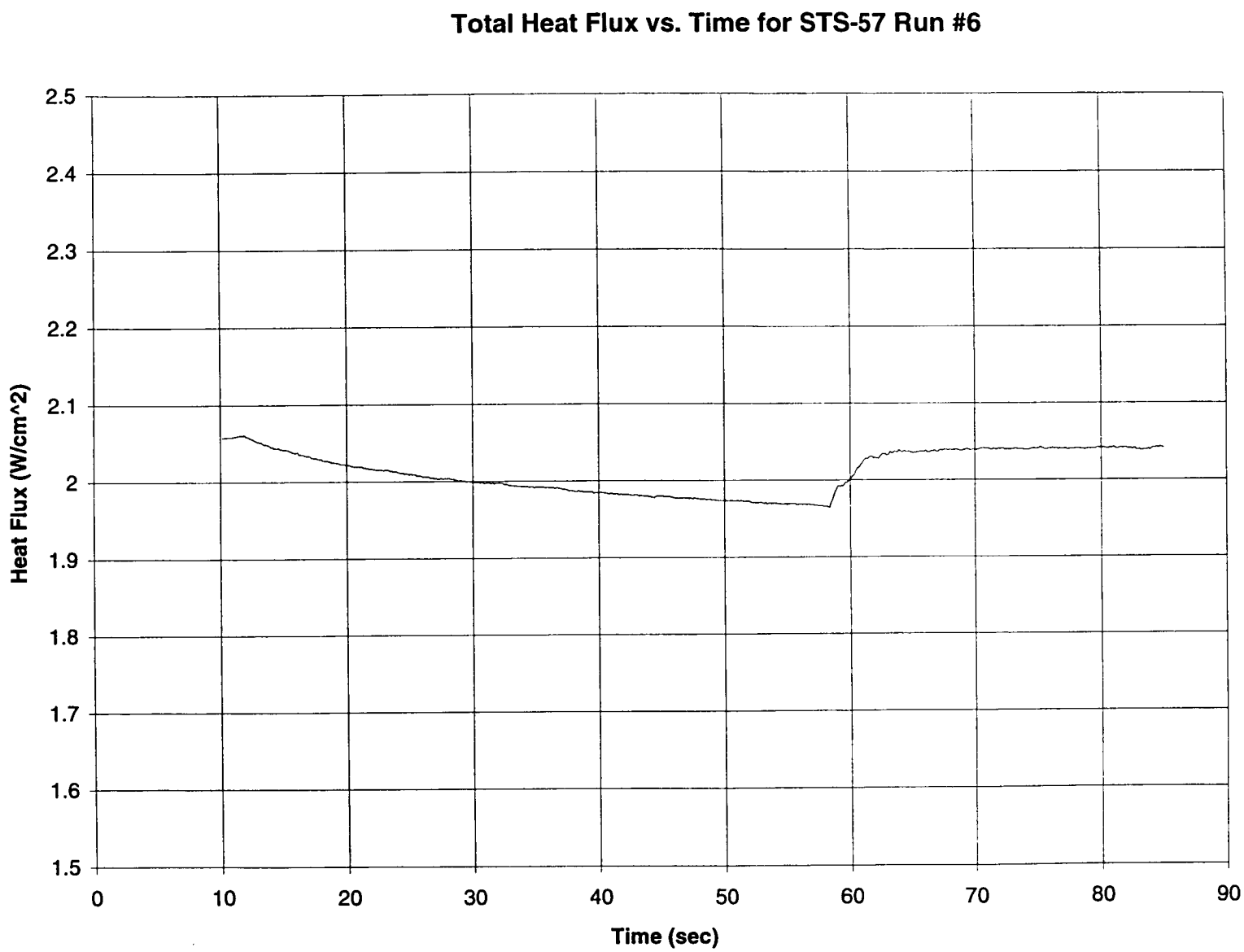

Figure B-2f. Heat flux input. PBE-IB (STS-57). Run No. 6.

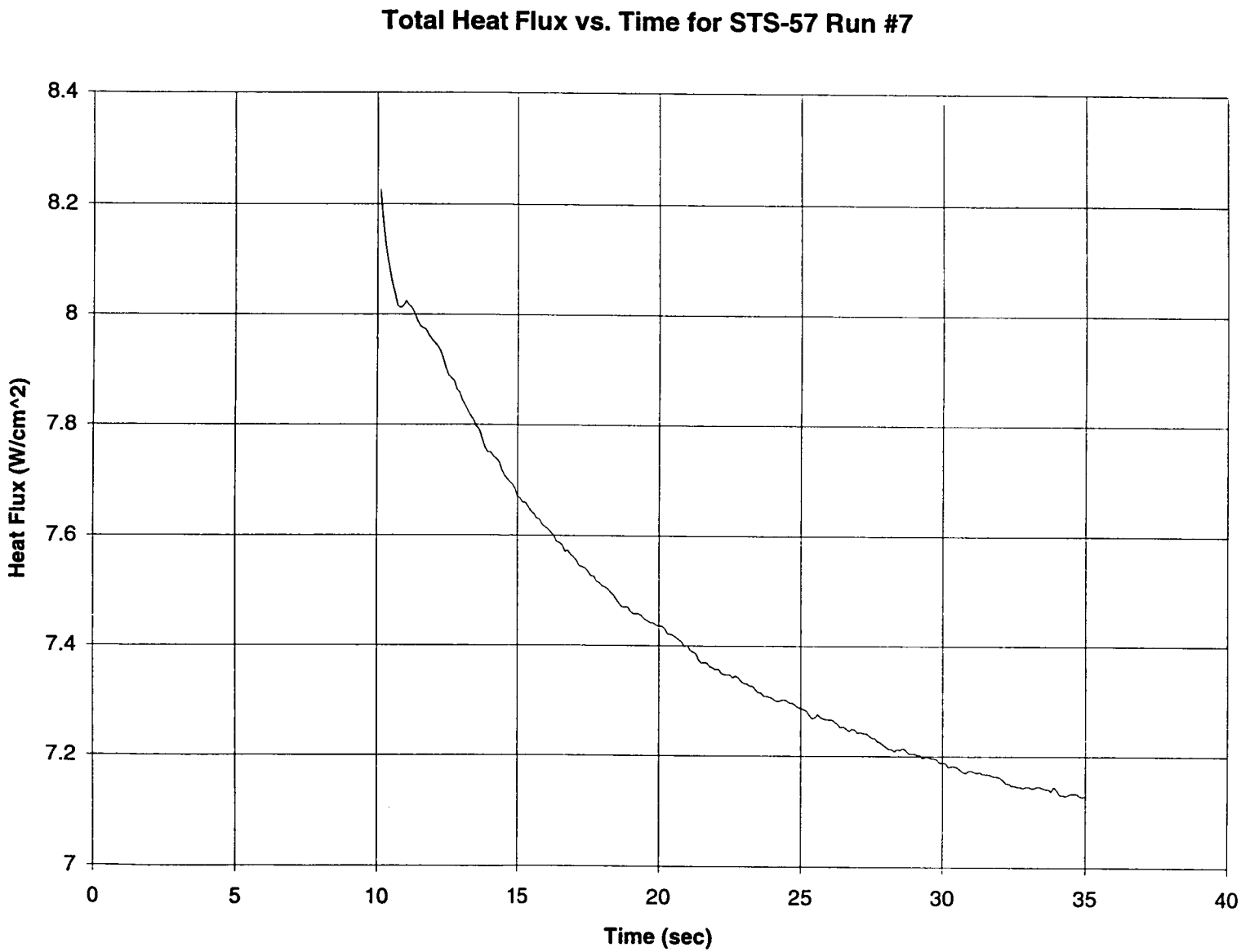

Figure B-2g. Heat flux input. PBE-IB (STS-57). Run No. 7.

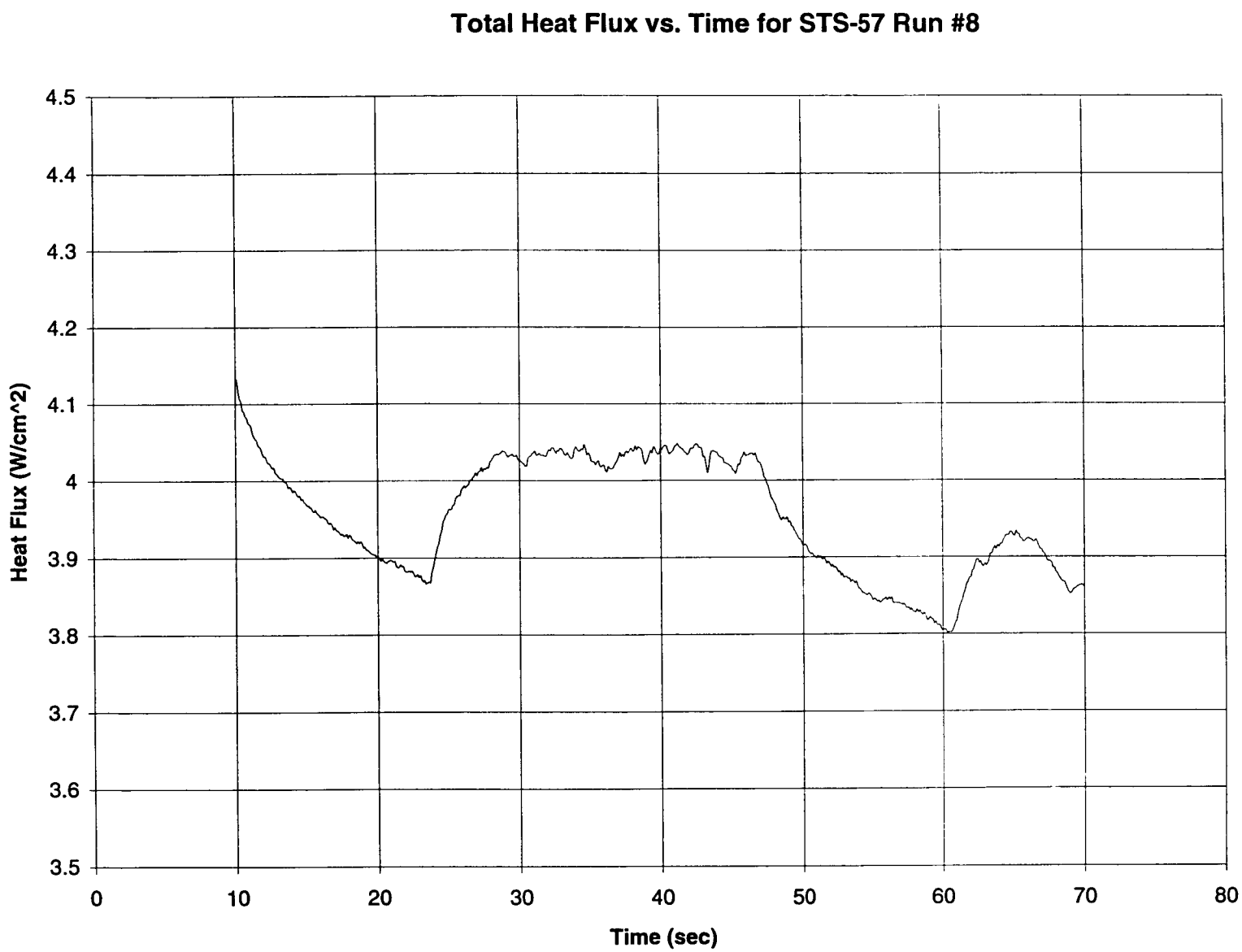

Figure B-2h. Heat flux input. PBE-IB (STS-57). Run No. 8.

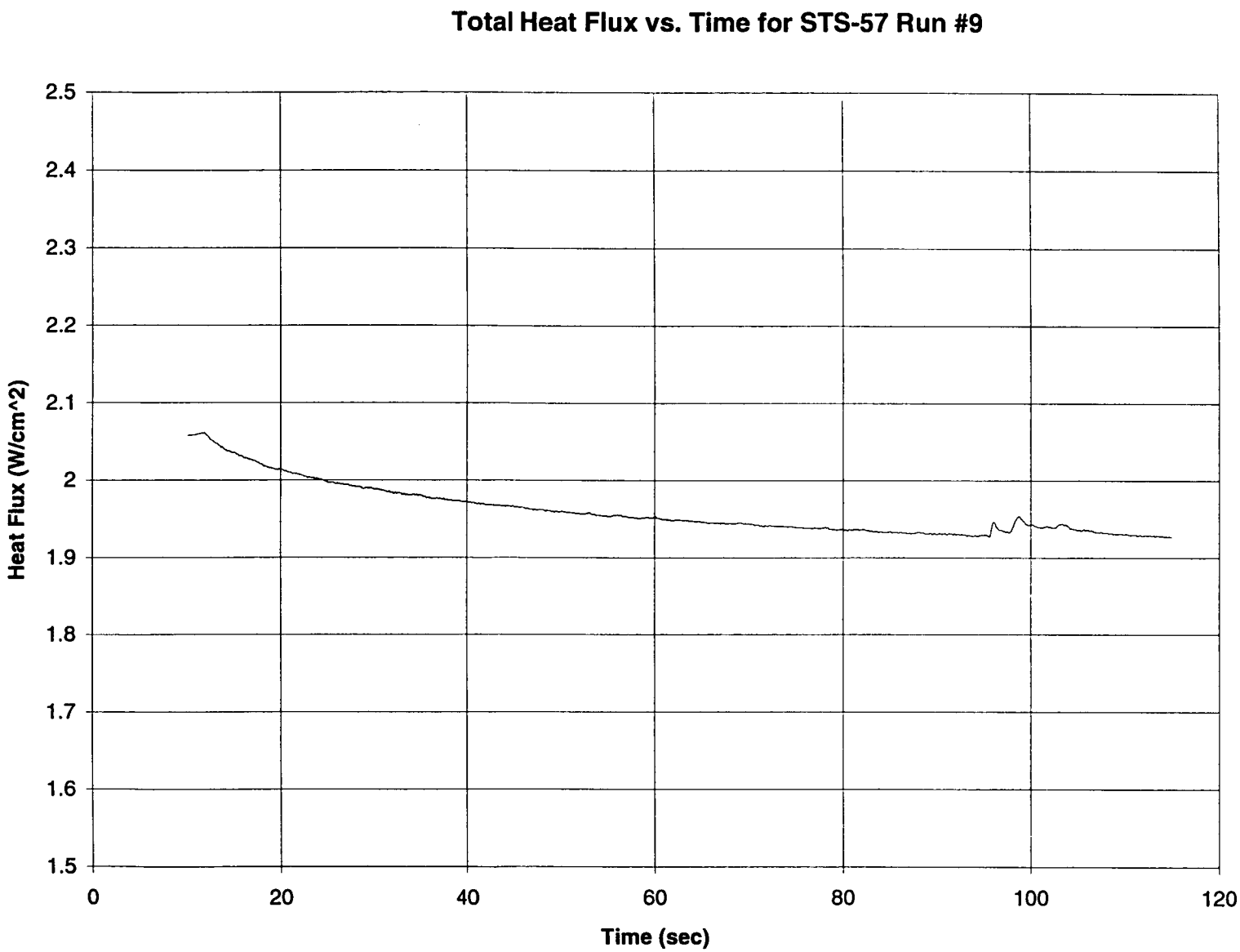

Figure B-2i. Heat flux input. PBE-IB (STS-57). Run No. 9.

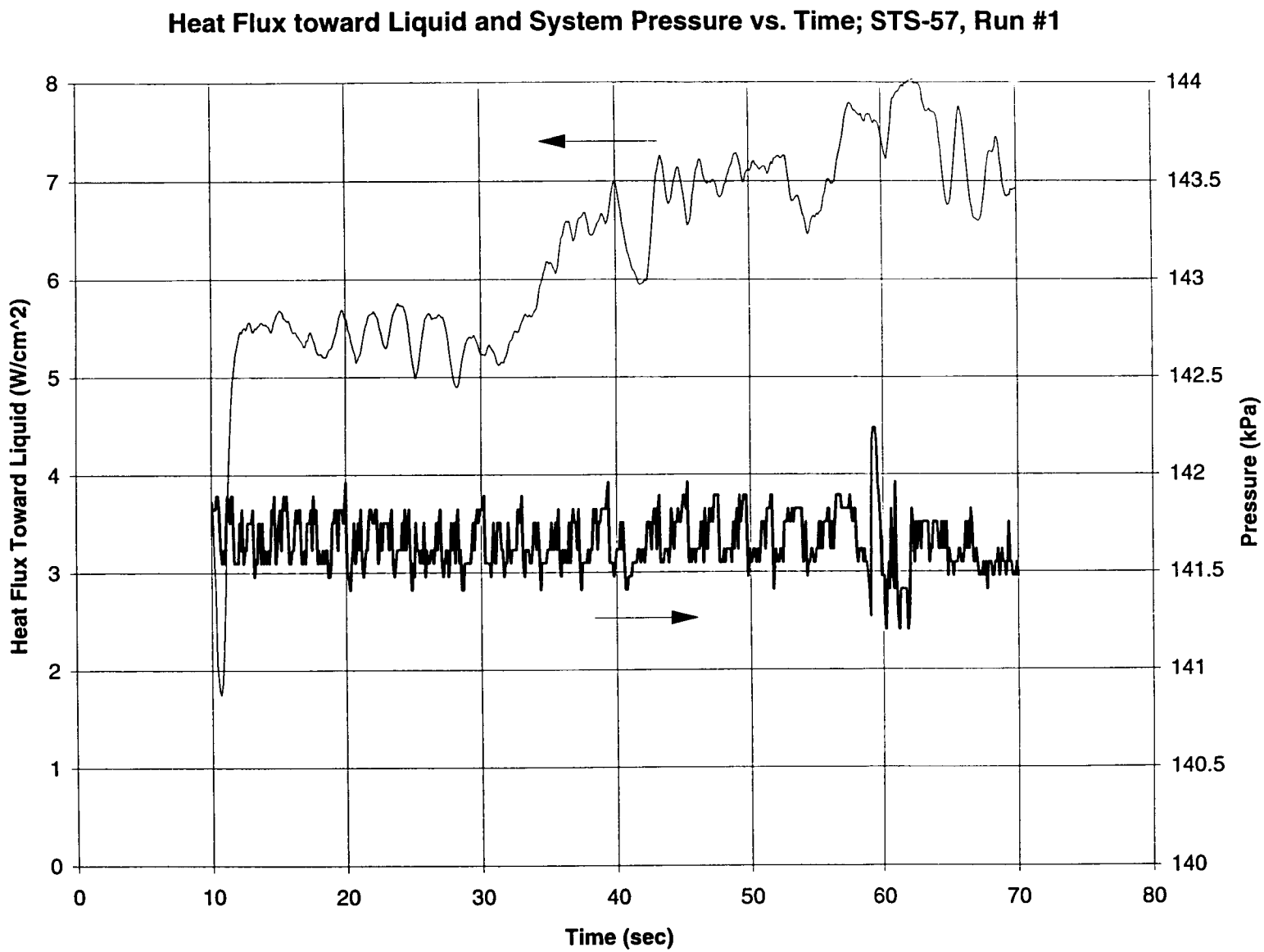

Figure B-3a. System pressure and fluid side mean heat flux. PBE-IB (STS-57). Run No. 1.

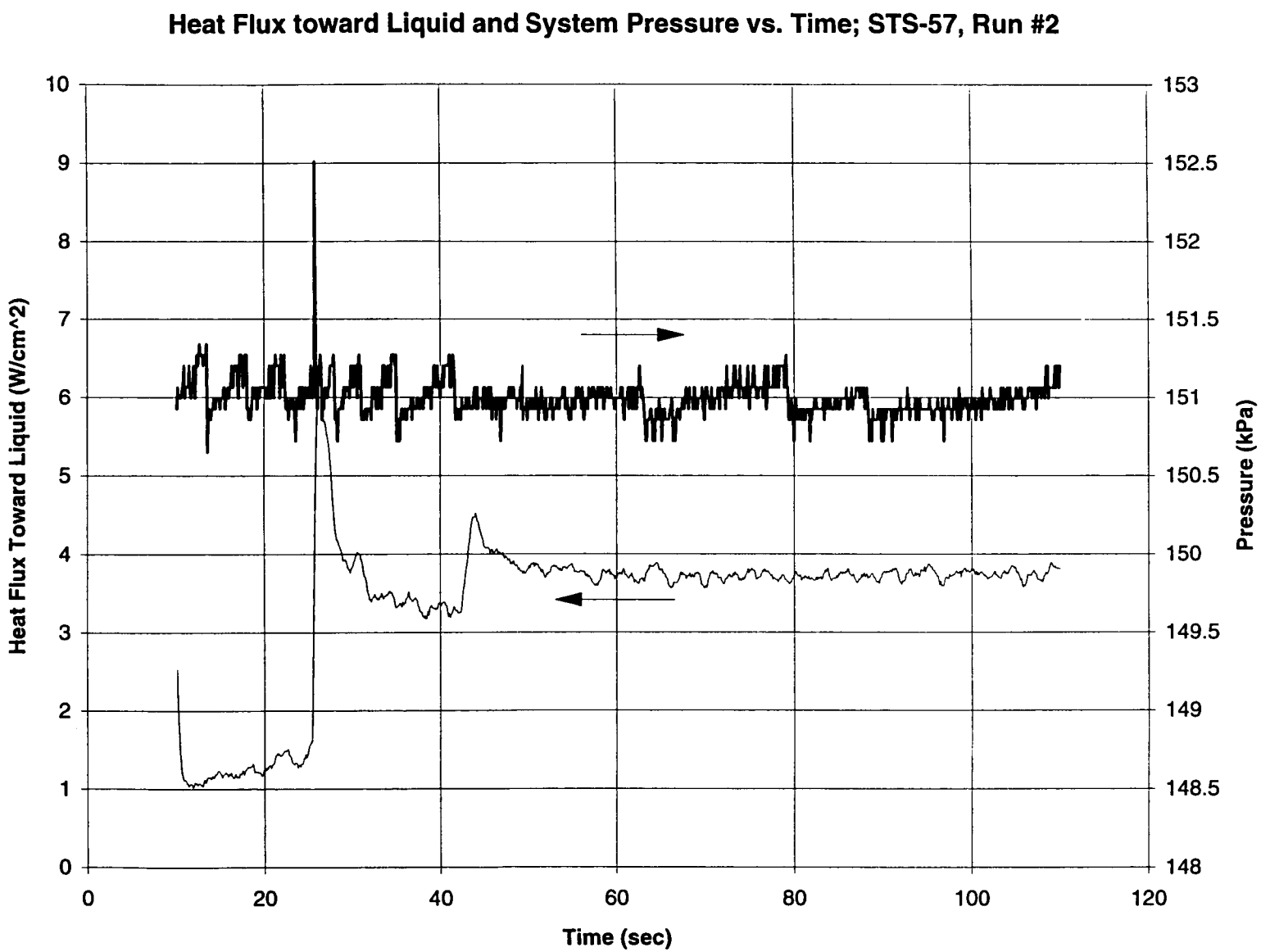

Figure B-3b. System pressure and fluid side mean heat flux. PBE-IB (STS-57). Run No. 2.

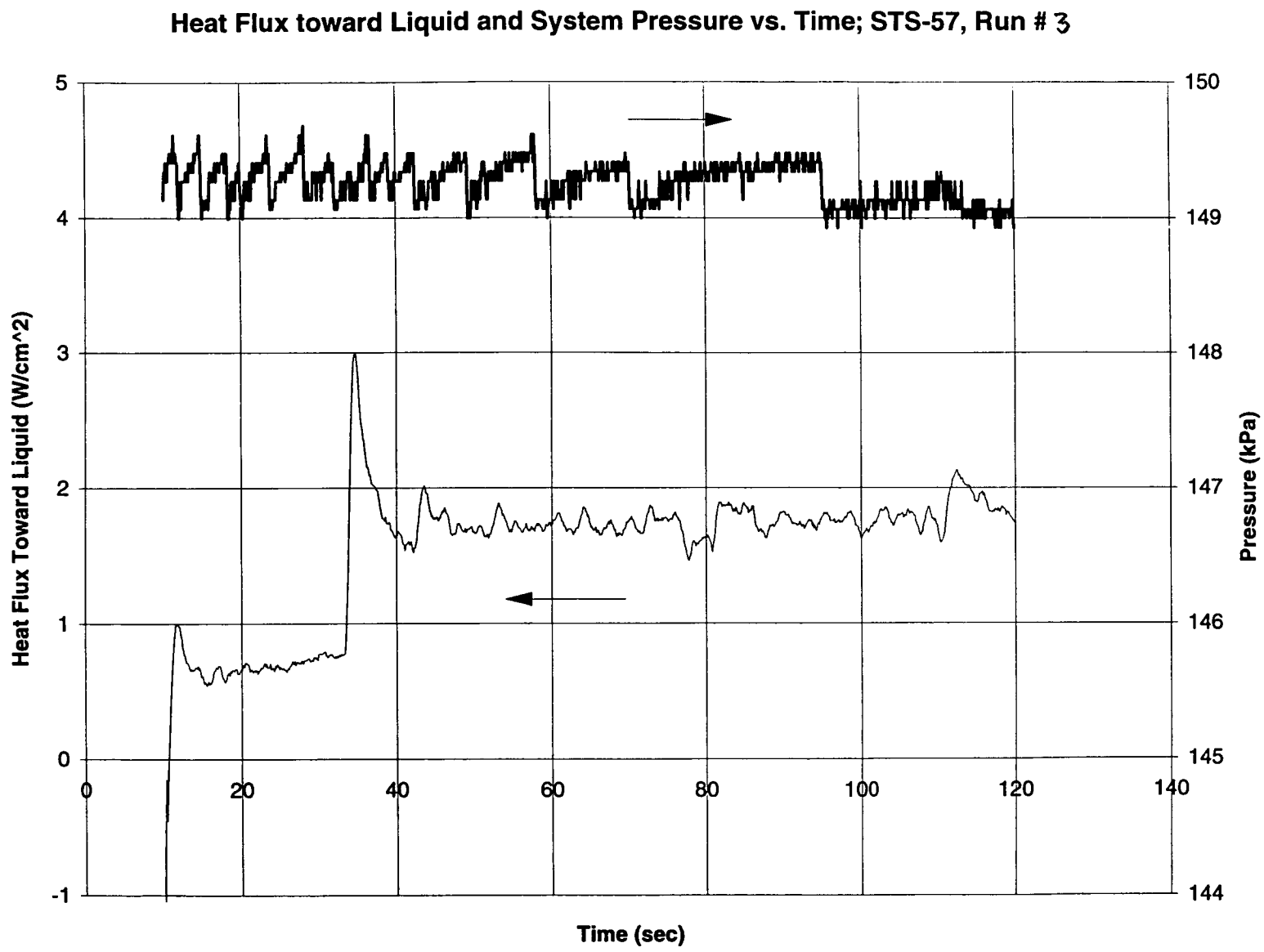

Figure B-3c. System pressure and fluid side mean heat flux. PBE-IB (STS-57). Run No. 3.

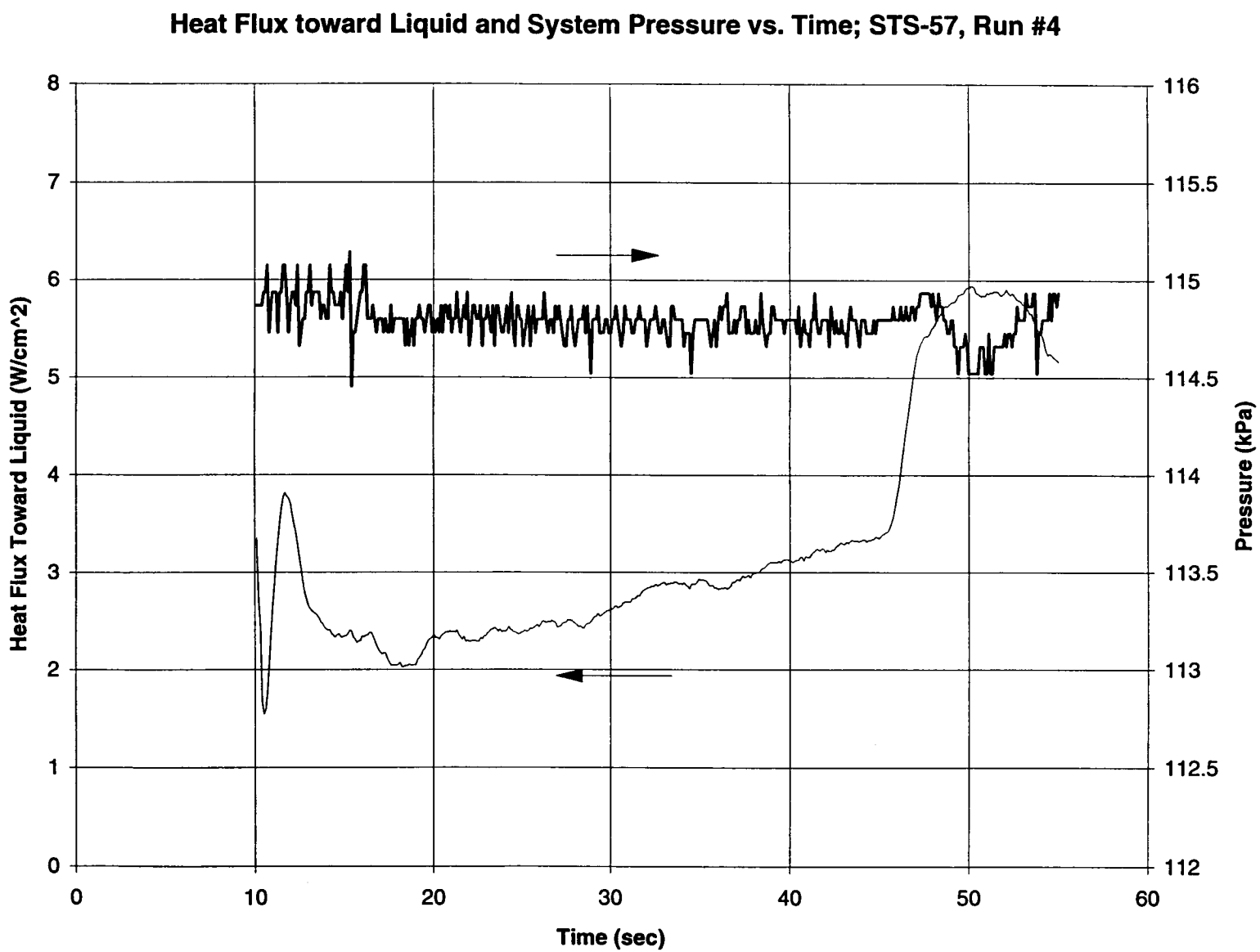

Figure B-3d. System pressure and fluid side mean heat flux. PBE-IB (STS-57). Run No. 4.

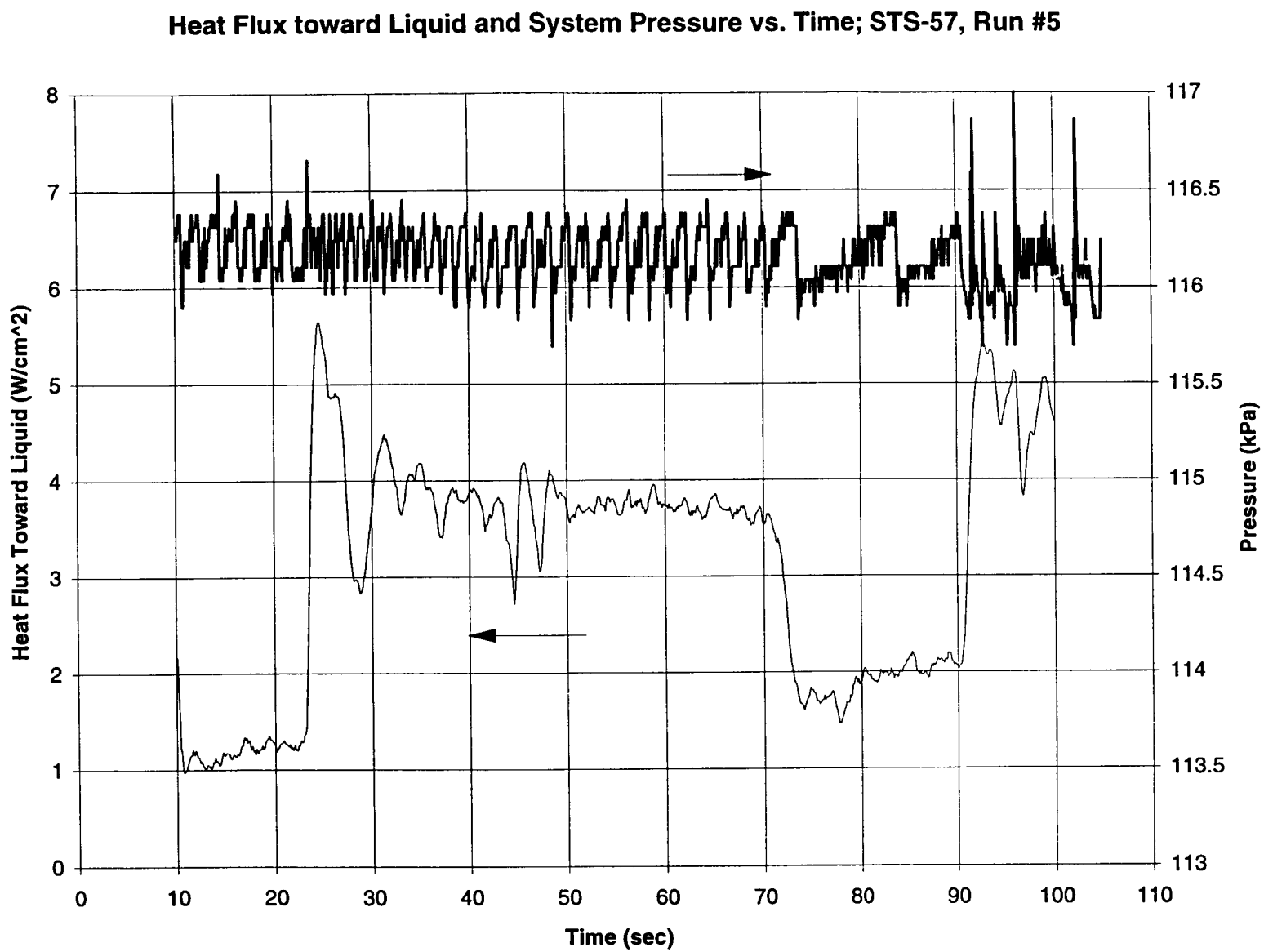

Figure B-3e. System pressure and fluid side mean heat flux. PBE-IB (STS-57). Run No. 5.

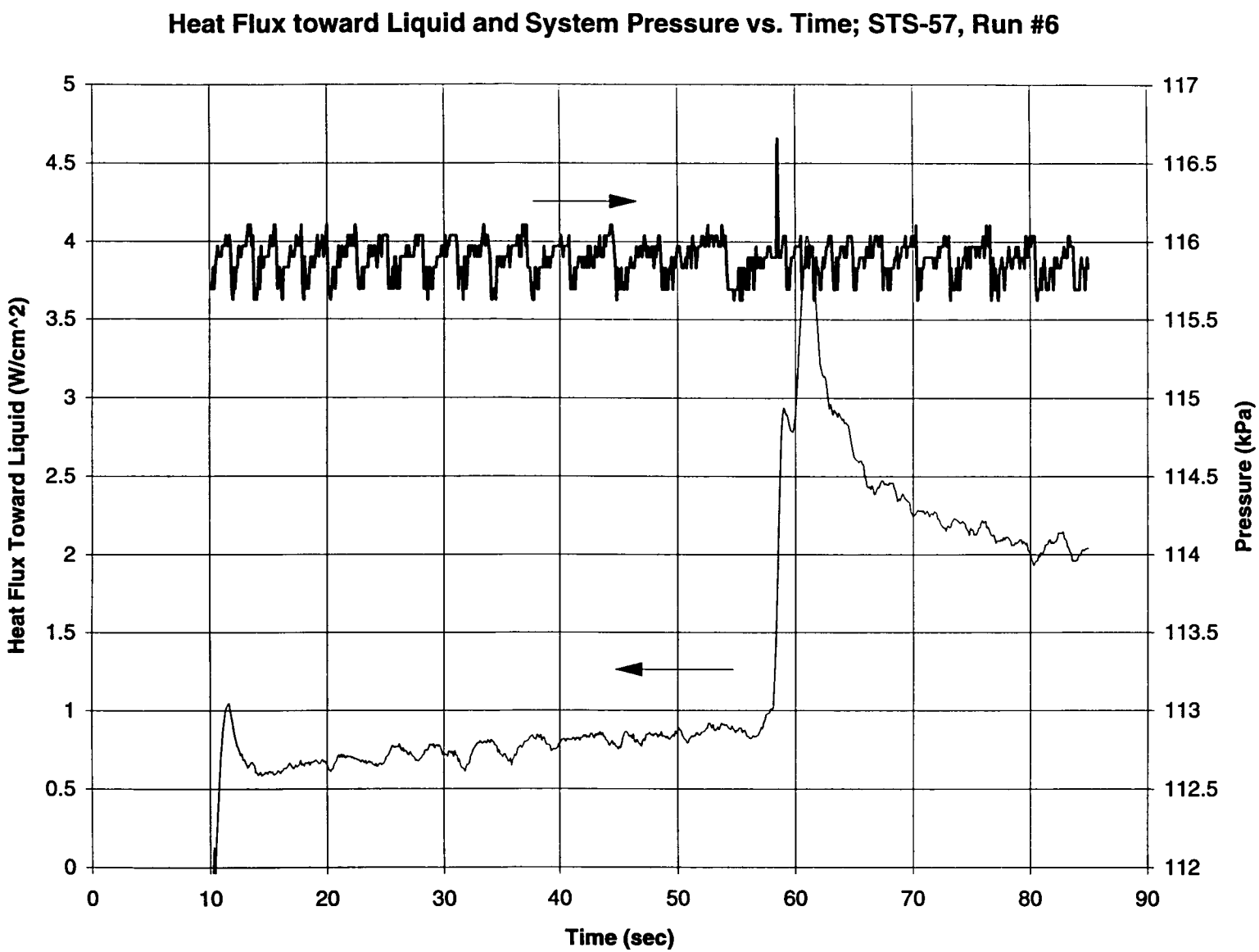

Figure B-3f. System pressure and fluid side mean heat flux. PBE-IB (STS-57). Run No. 6.

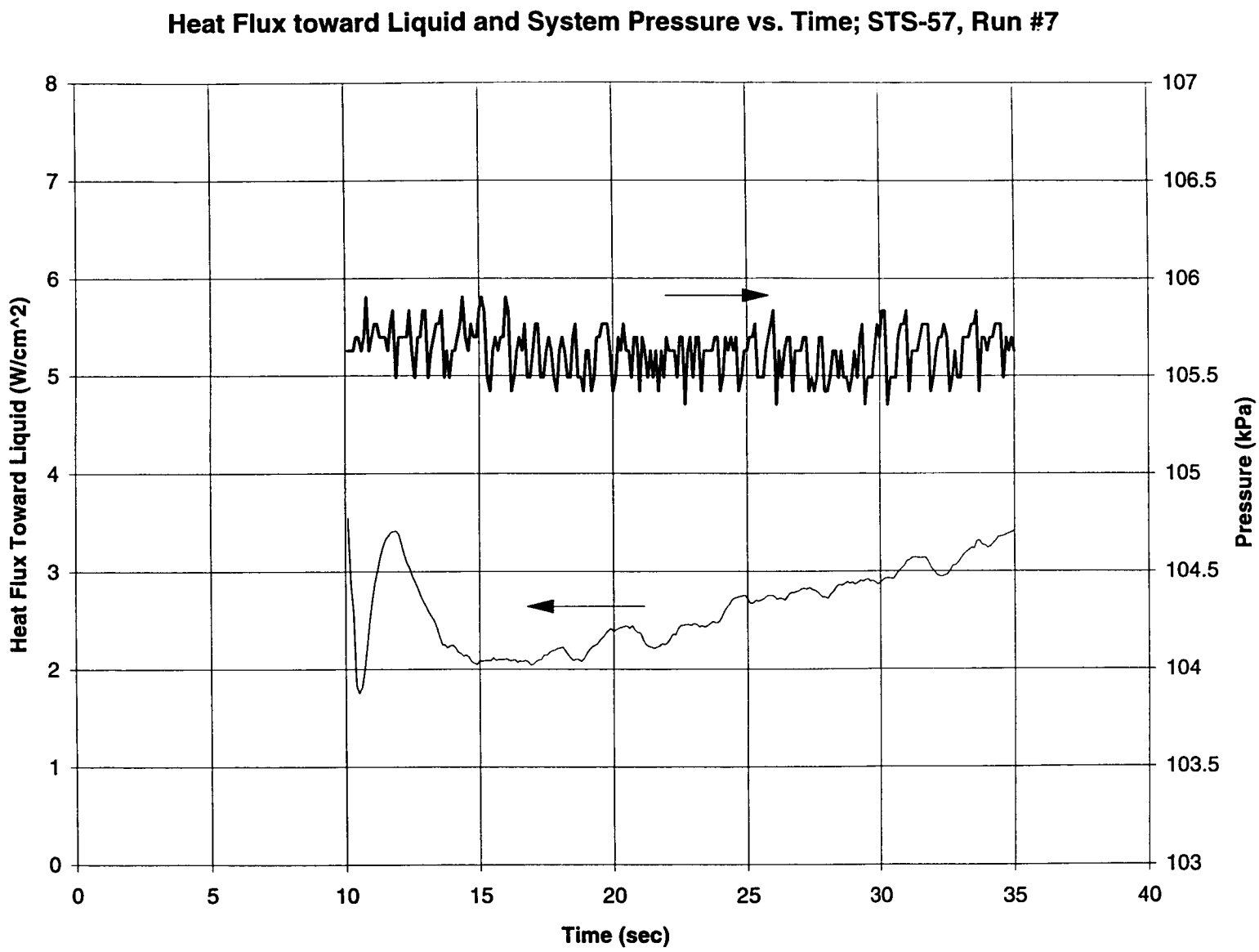

Figure B-3g. System pressure and fluid side mean heat flux. PBE-IB (STS-57). Run No. 7.

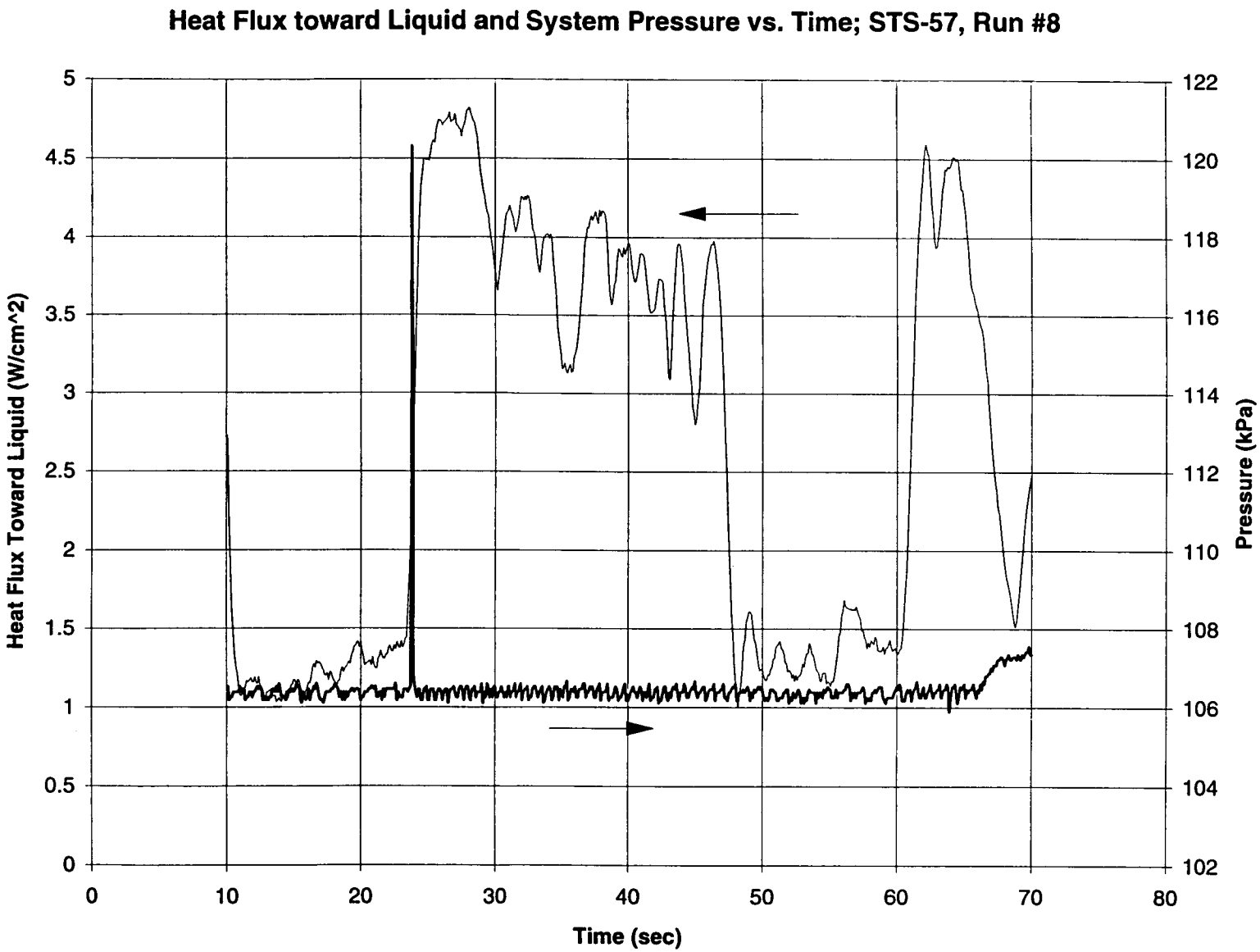

Figure B-3h. System pressure and fluid side mean heat flux. PBE-IB (STS-57). Run No. 8.

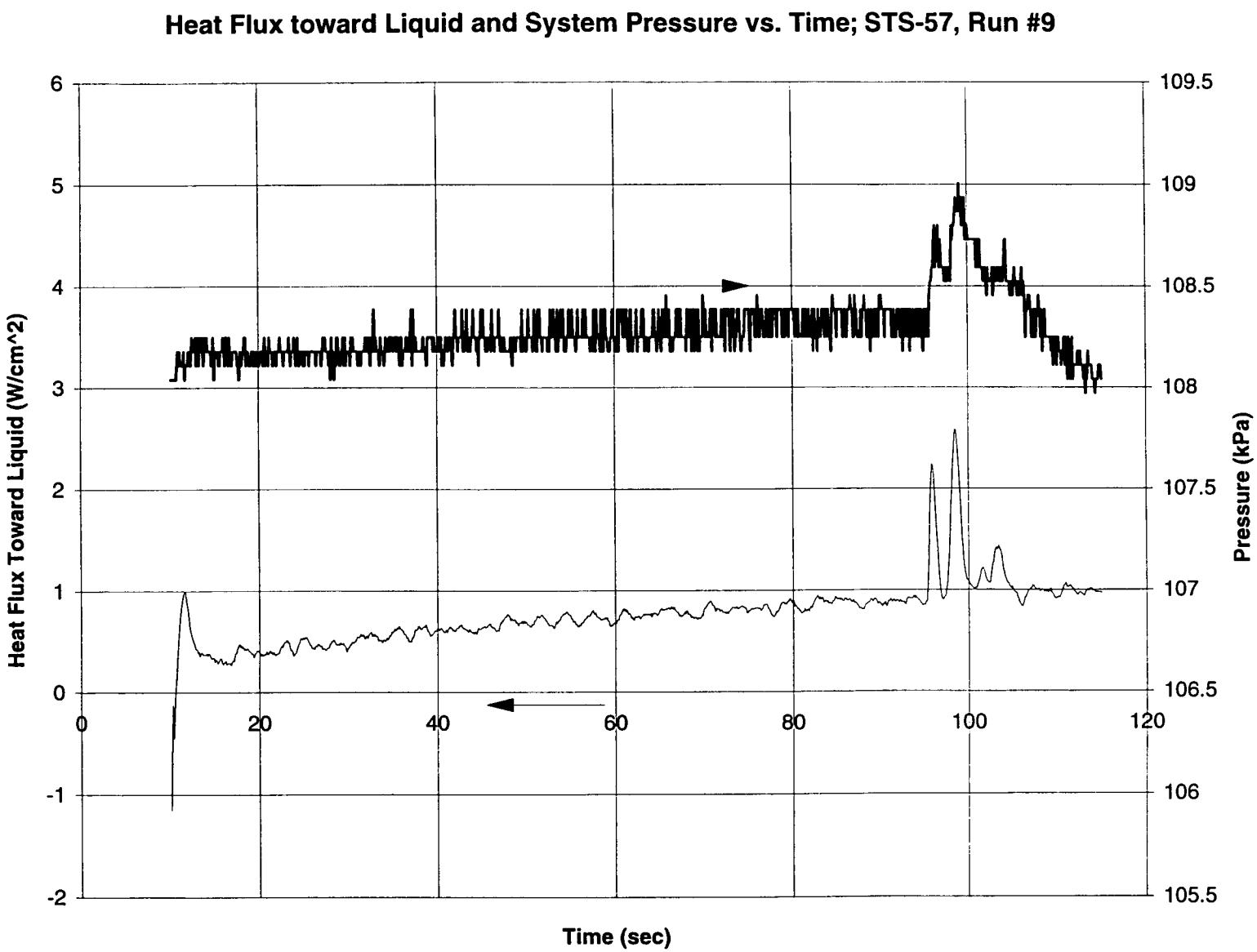

Figure B-3i. System pressure and fluid side mean heat flux. PBE-IB (STS-57). Run No. 9.

A. Mean Surface Heater Temperature

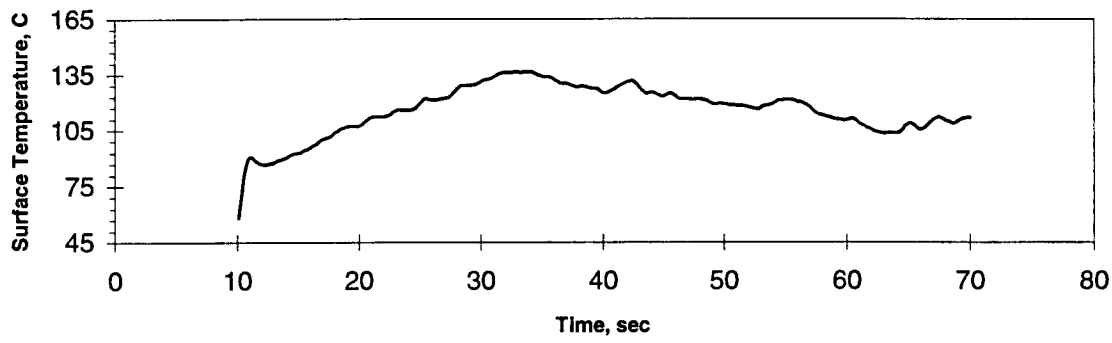

B. Local Fluid Temperatures

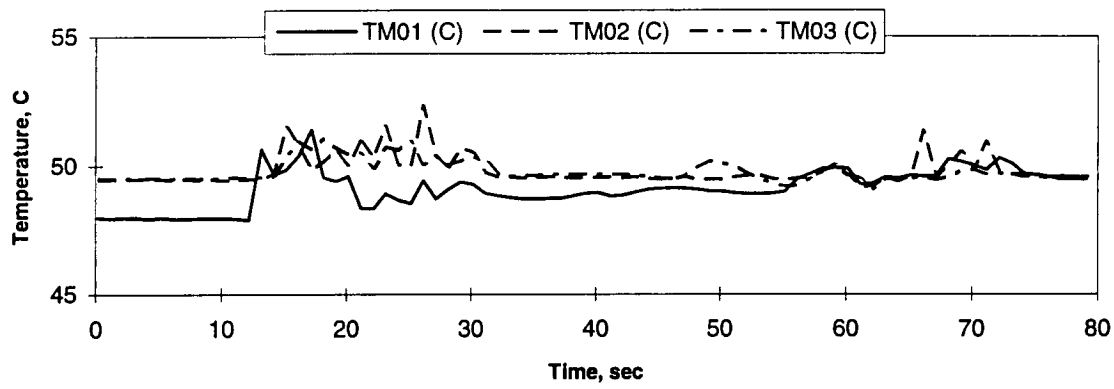

C. Far Field Bulk Temperatures

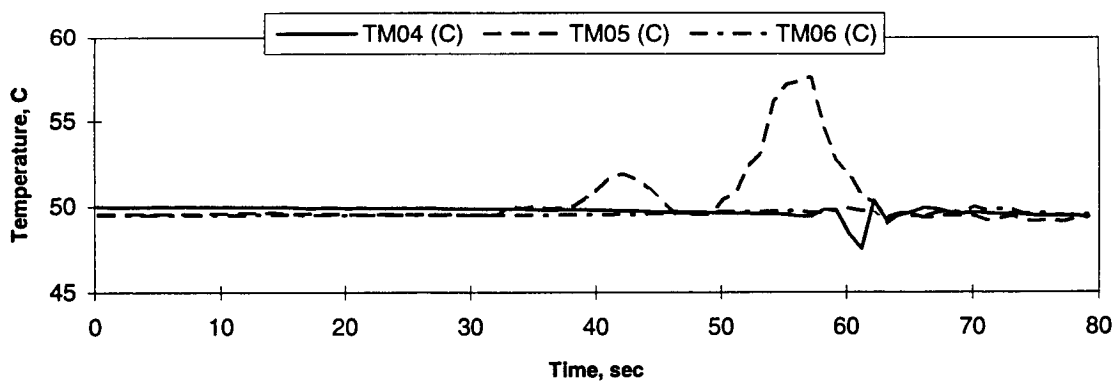

FIGURE: Measured Fluid Temperatures **STS 57 - Run #1**

Heat Flux	Subcooling (F)	Heater Power On/Off	100 FPS On/Off	Stirrer Start	Repress Start	Total Test Time
8	20 ± 2	10-70 sec.	10-15 sec.	55 sec.	------	80 sec.

Figure B-4a. Measured fluid temperatures near primary heater and far field bulk liquid. PBE-IB (STS-57). Run No. 1.

A. Mean Heater Surface Temperature

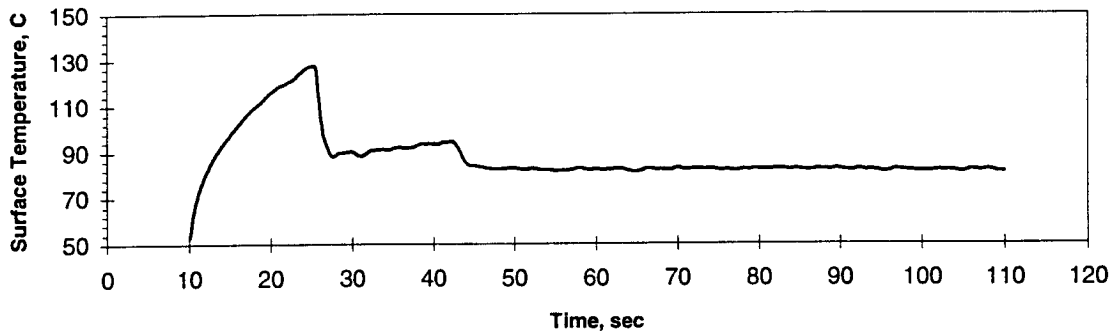

B. Local Fluid Temperatures

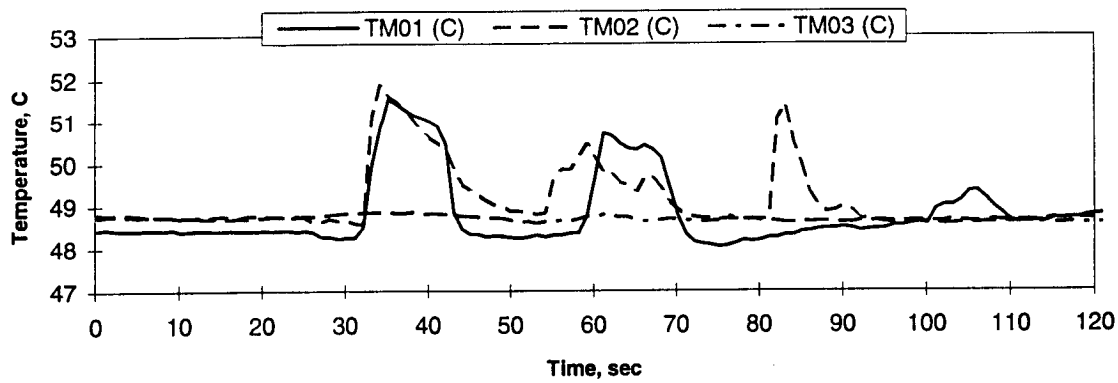

C. Far Field Bulk Temperatures

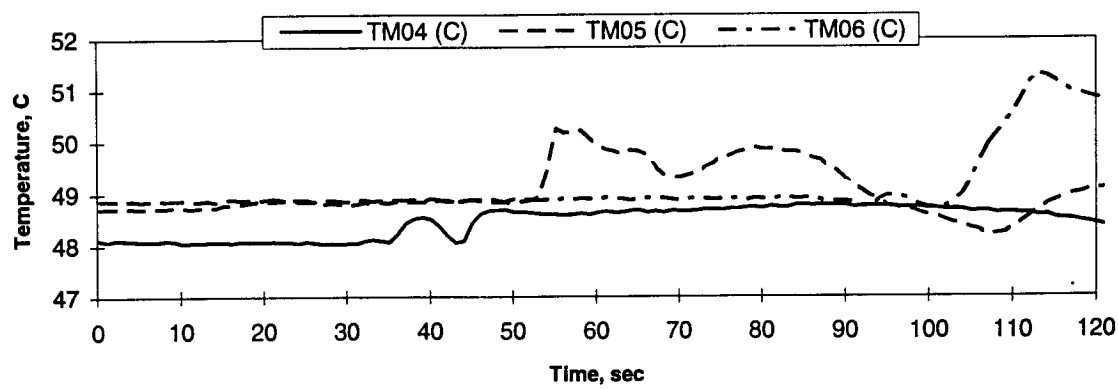

FIGURE: Measured Fluid Temperatures **STS 57 - Run #2**

Heat Flux	Subcooling (F)	Heater Power On/Off	100 FPS On/Off	Stirrer Start	Repress Start	Total Test Time
4	20 ± 2	10-110 sec.	15-25 sec.	------	------	135 sec.

Figure B-4b. Measured fluid temperatures near primary heater and far field bulk liquid. PBE-IB (STS-57). Run No. 2.

A. Mean Heater Surface Temperature

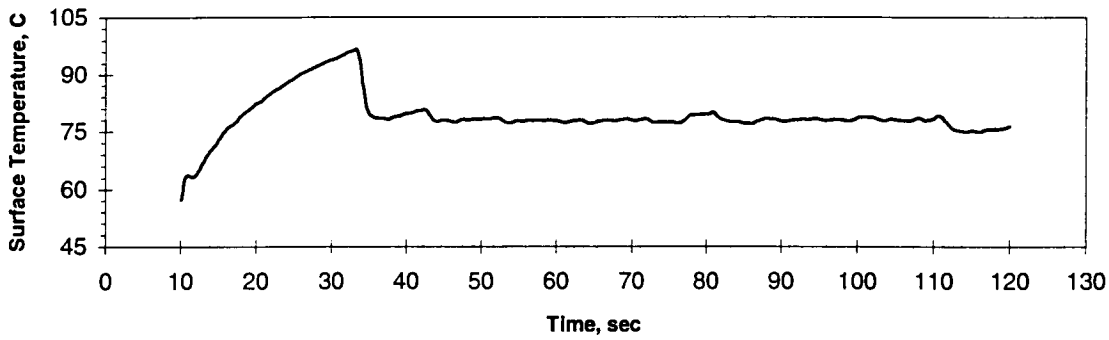

B. Local Fluid Temperatures

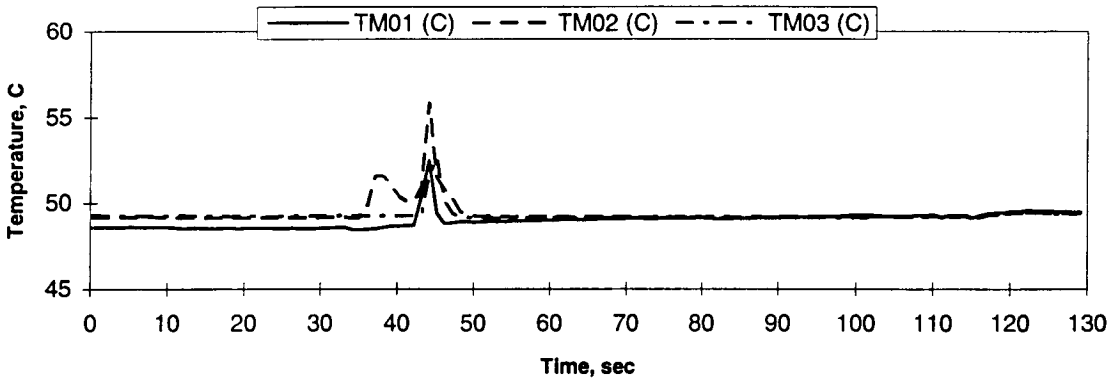

C. Far Field Bulk Temperatures

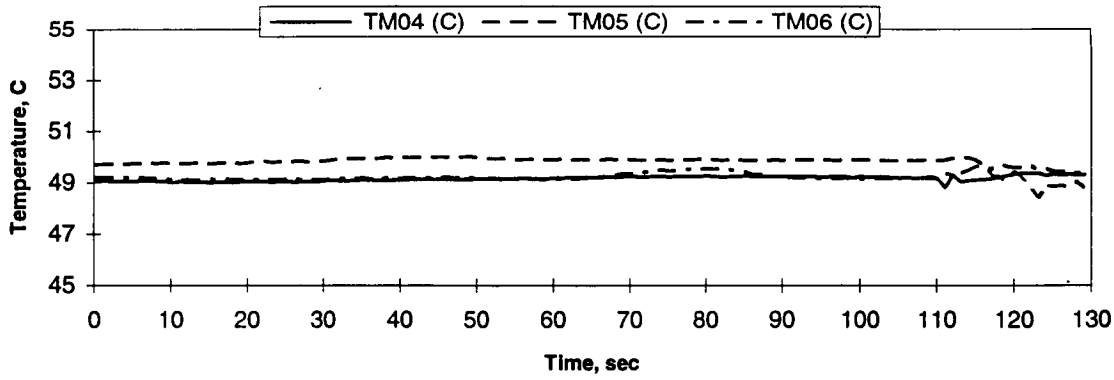

FIGURE: Measured Fluid Temperatures **STS 57 - Run #3**

Heat Flux	Subcooling (F)	Heater Power On/Off	100 FPS On/Off	Stirrer Start	Repress Start	Total Test Time
2	20 ± 2	10-120 sec.	30-50 sec.	110 sec.	------	130 sec.

Figure B-4c. Measured fluid temperatures near primary heater and far field bulk liquid. PBE-IB (STS-57). Run No. 3.

A. Mean Heater Surface Temperature

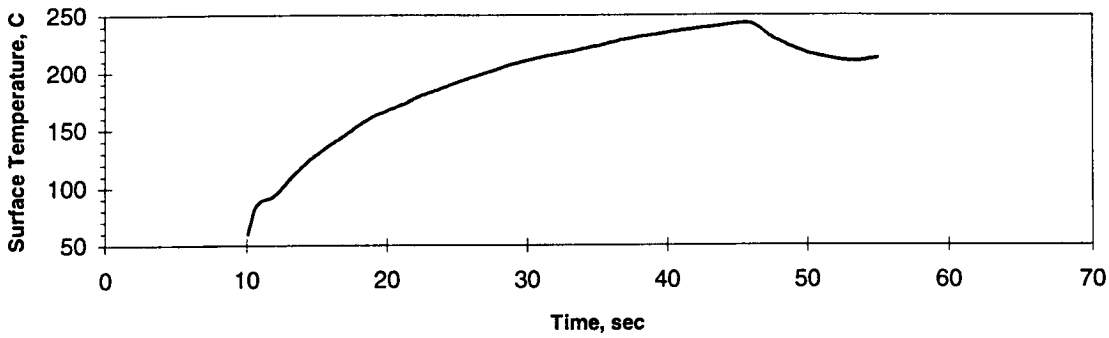

B. Local Fluid Temperatures

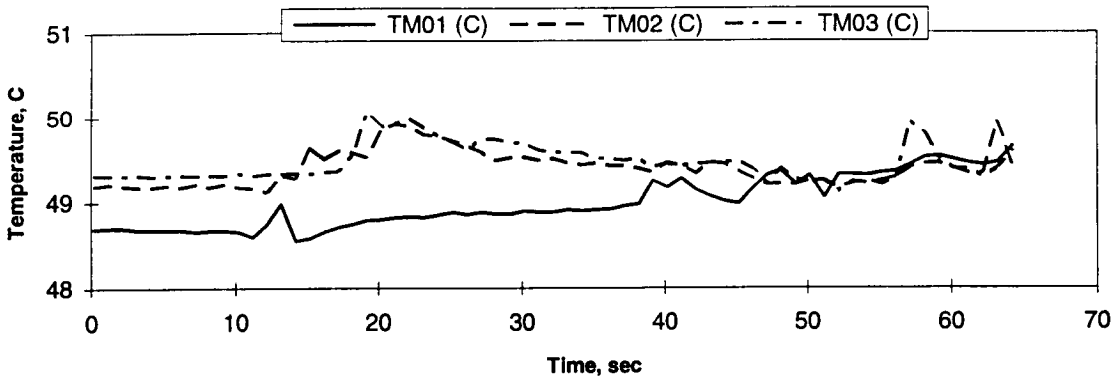

C. Far Field Bulk Temperatures

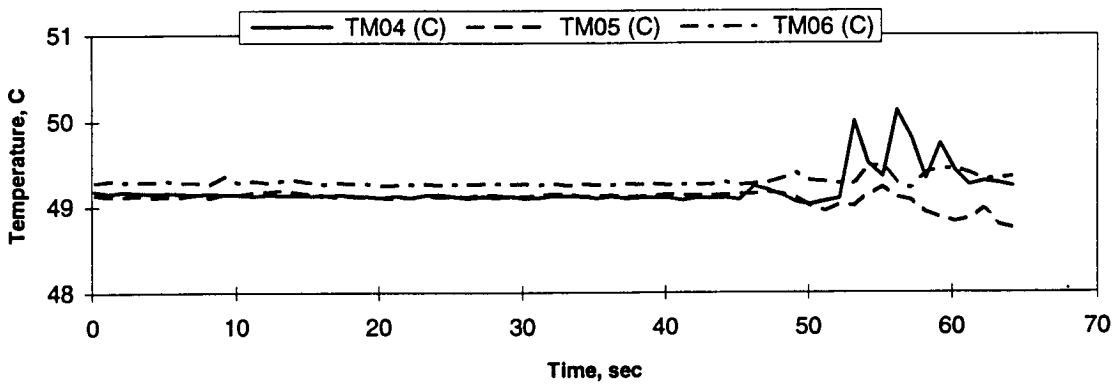

FIGURE: Measured Fluid Temperatures **STS 57 - Run #4**

Heat Flux	Subcooling (F)	Heater Power On/Off	100 FPS On/Off	Stirrer Start	Repress Start	Total Test Time
8	5 ± 1	10-55 sec.	10-15 sec.	45 sec.	------	65 sec.

Figure B-4d. Measured fluid temperatures near primary heater and far field bulk liquid. PBE-IB (STS-57). Run No. 4.

A. Mean Heater Surface Temperature

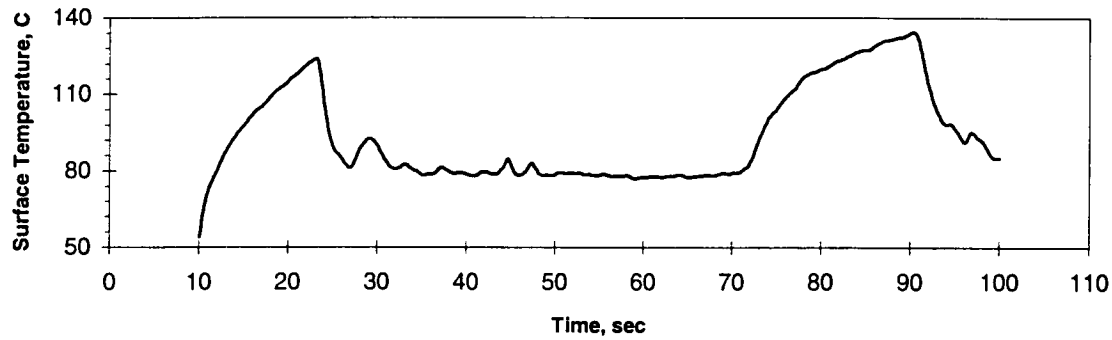

B. Local Fluid Temperatures

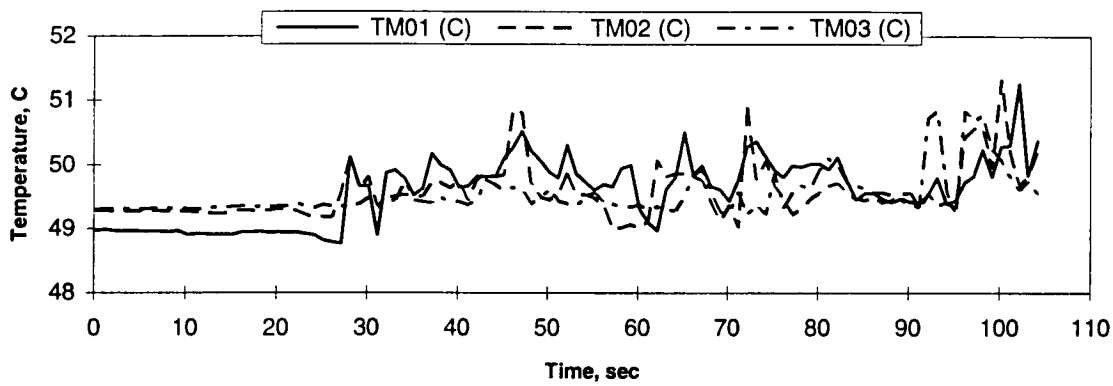

C. Far Field Bulk Temperatures

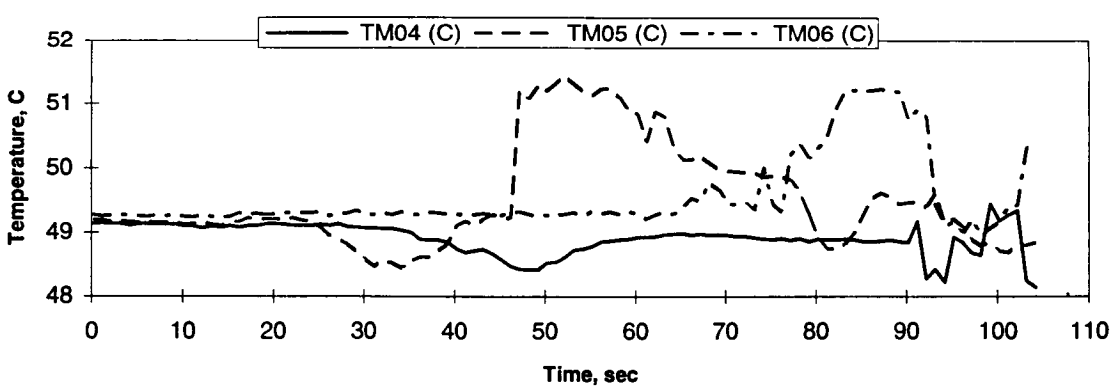

FIGURE: Measured Fluid Temperatures **STS 57 - Run #5**

Heat Flux	Subcooling (F)	Heater Power On/Off	100 FPS On/Off	Stirrer Start	Repress Start	Total Test Time
4	5 ± 1	10-100 sec.	15-25 sec.	90 sec.	------	105 sec.

Figure B-4e. Measured fluid temperatures near primary heater and far field bulk liquid. PBE-IB (STS-57). Run No. 5.

A. Mean Heater Surface Temperature

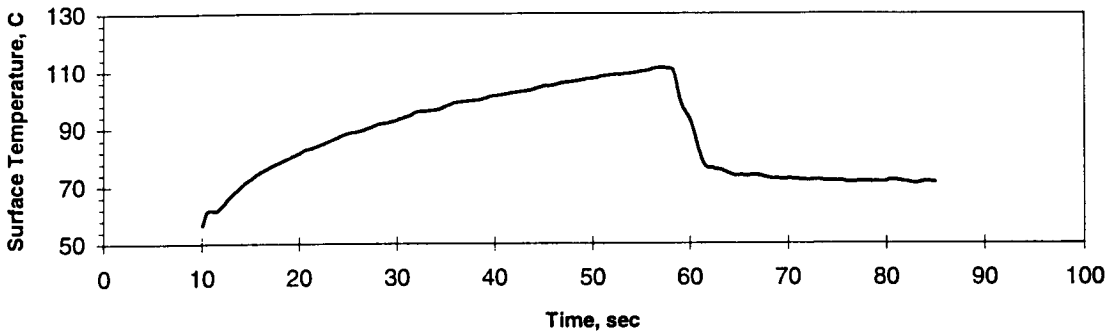

B. Local Fluid Temperatures

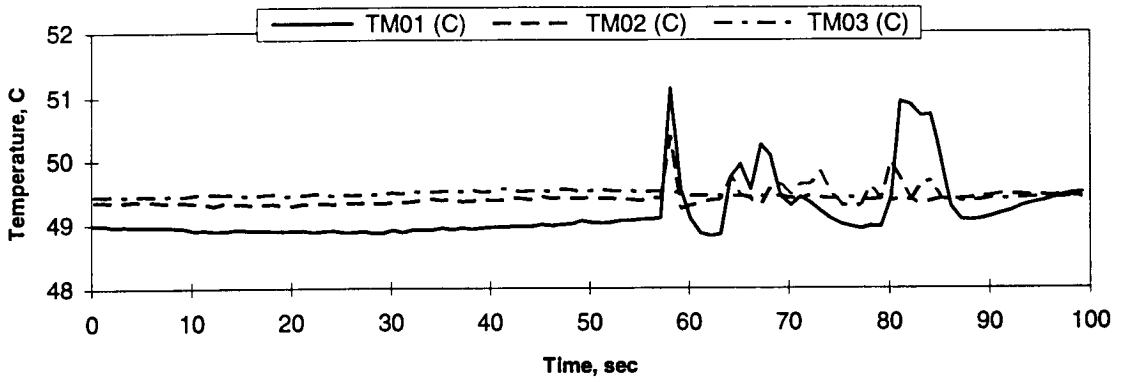

C. Far Field Bulk Temperatures

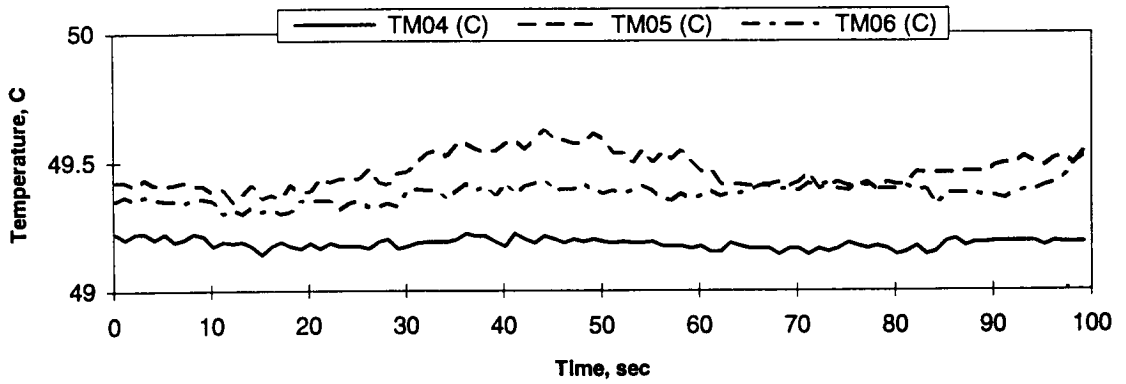

FIGURE: Measured Fluid Temperatures **STS 57 - Run #6**

Heat Flux	Subcooling (F)	Heater Power On/Off	100 FPS On/Off	Stirrer Start	Repress Start	Total Test Time
2	5 ± 1	10-85 sec.	30-50 sec.	------	------	100 sec.

Figure B-4f. Measured fluid temperatures near primary heater and far field bulk liquid. PBE-IB (STS-57). Run No. 6.

A. Mean Heater Surface Temperature

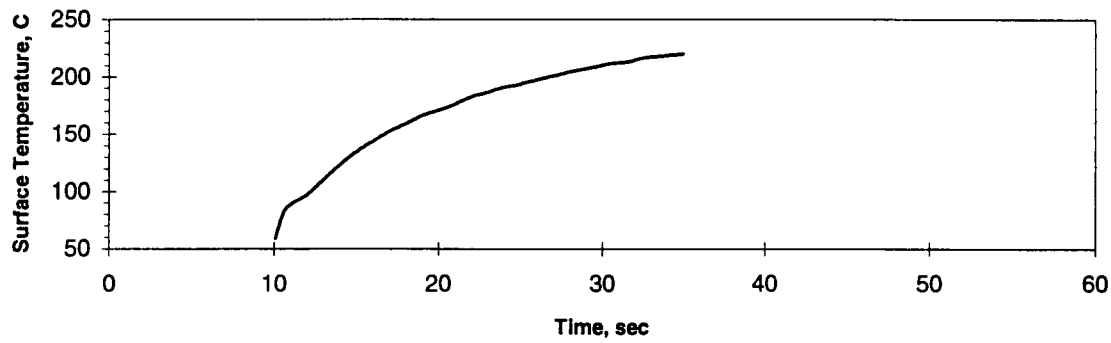

B. Local Fluid Temperatures

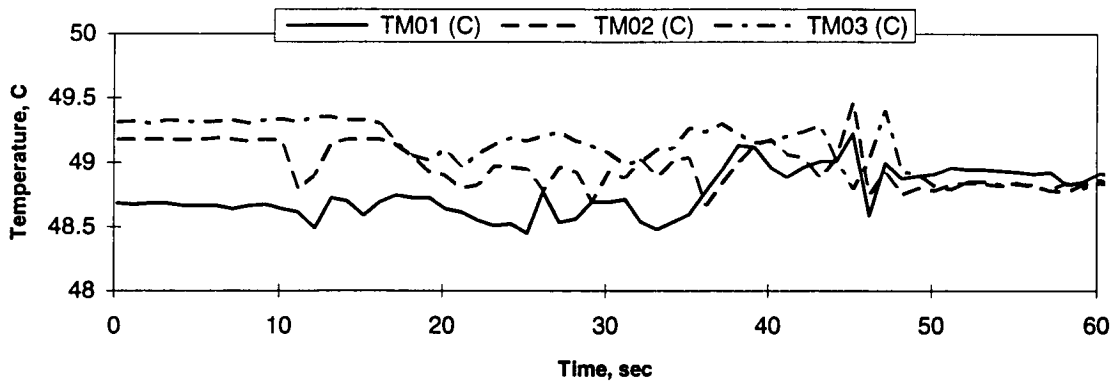

C. Far Field Bulk Temperatures

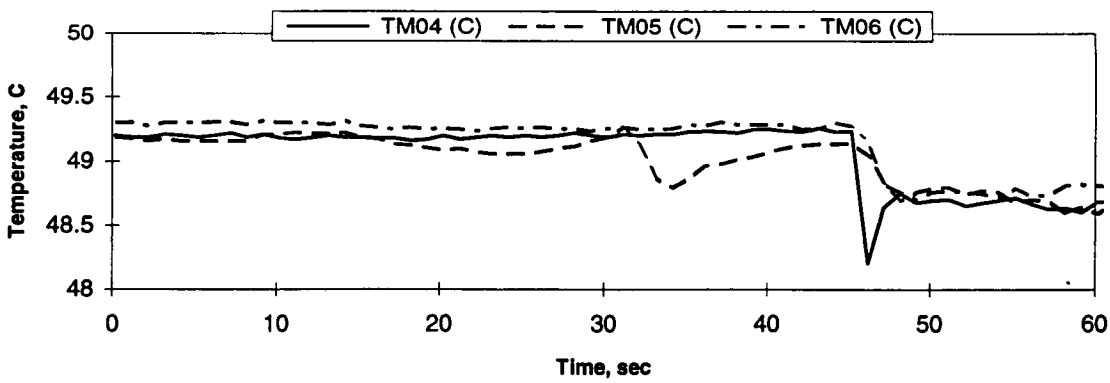

FIGURE: Measured Fluid Temperatures **STS 57 - Run #7**

Heat Flux	Subcooling (F)	Heater Power On/Off	100 FPS On/Off	Stirrer Start	Repress Start	Total Test Time
8	0.5 ± 0.4	10-35 sec.	10-15 sec.	------	45 sec.	65 sec.

Figure B-4g. Measured fluid temperatures near primary heater and far field bulk liquid. PBE-IB (STS-57). Run No. 7.

A. Mean Heater Surface Temperature

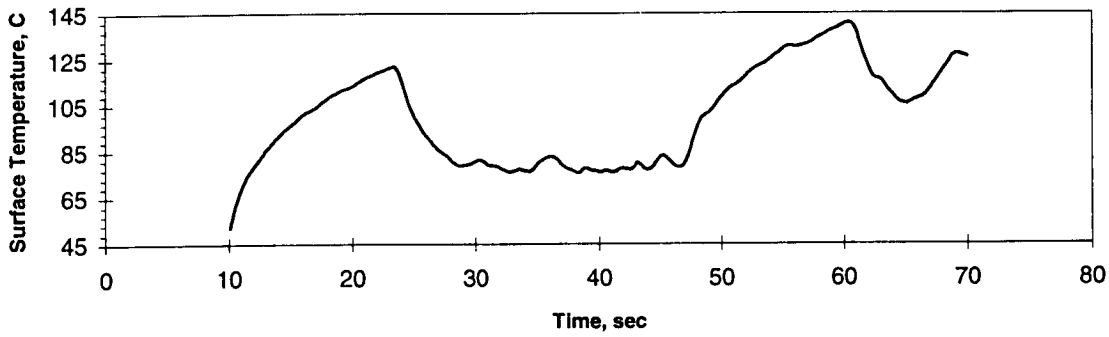

B. Local Fluid Temperatures

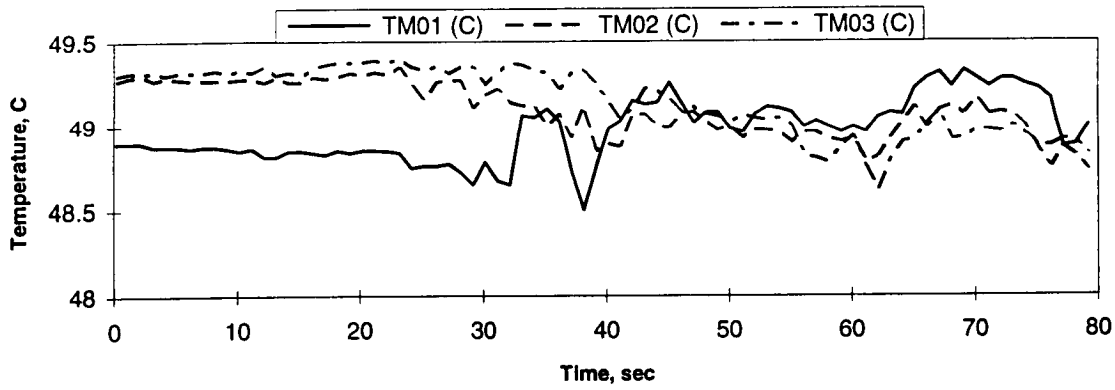

C. Far Field Bulk Temperatures

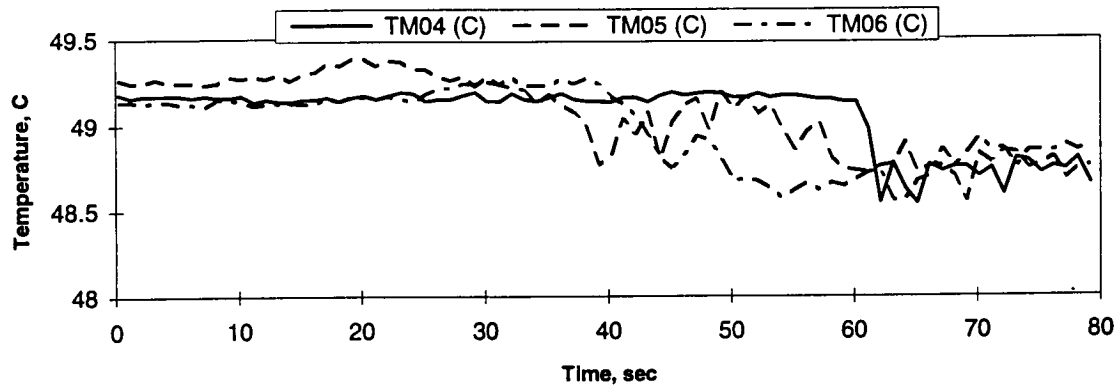

FIGURE: Measured Fluid Temperatures **STS 57 - Run #8**

Heat Flux	Subcooling (F)	Heater Power On/Off	100 FPS On/Off	Stirrer Start	Repress Start	Total Test Time
4	0.5 ± 0.4	10-70 sec.	15-25 sec.	60 sec.	------	80 sec.

Figure B-4h. Measured fluid temperatures near primary heater and far field bulk liquid. PBE-IB (STS-57). Run No. 8.

A. Mean Heater Surface Temperature

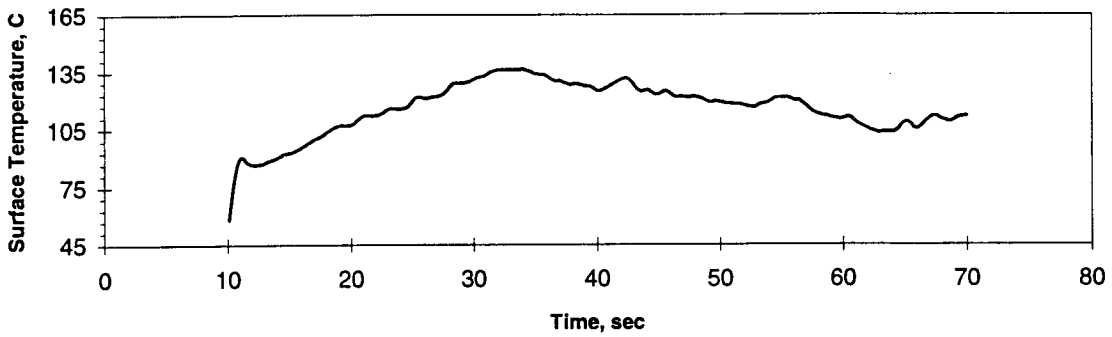

D.

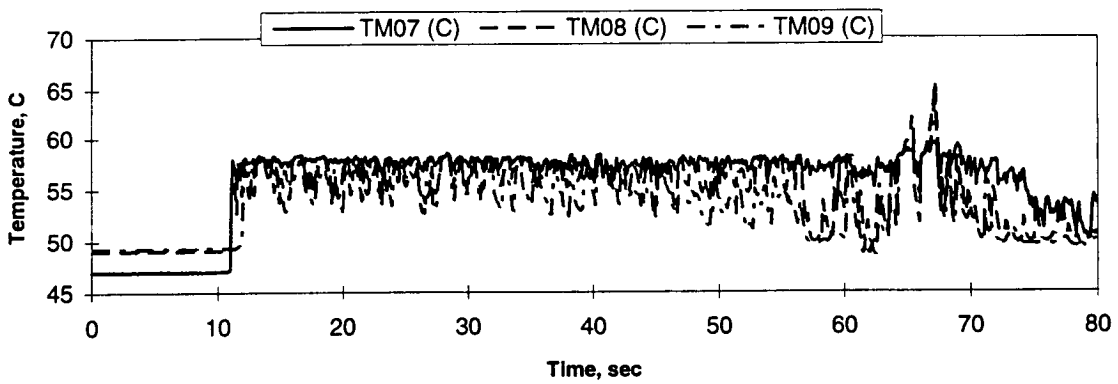

E.

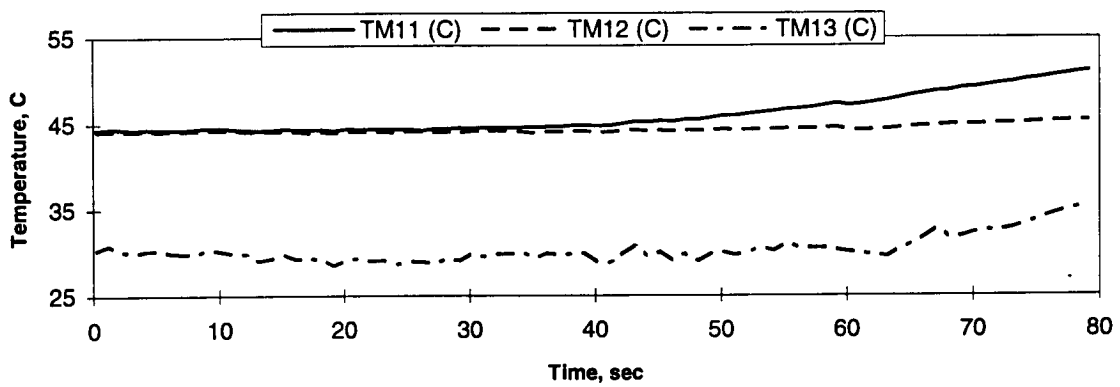

FIGURE: Measured Heater-Underside Temperatures **STS 57 - Run #1**

Heat Flux	Subcooling (F)	Heater Power On/Off	100 FPS On/Off	Stirrer Start	Repress Start	Total Test Time
8	20 ± 2	10-70 sec.	10-15 sec.	55 sec.	------	80 sec.

Figure B-5a. Measured fluid temperatures near secondary heater and heater underside. PBE-IB (STS-57). Run No. 1.

A. Mean Heater Surface Temperature

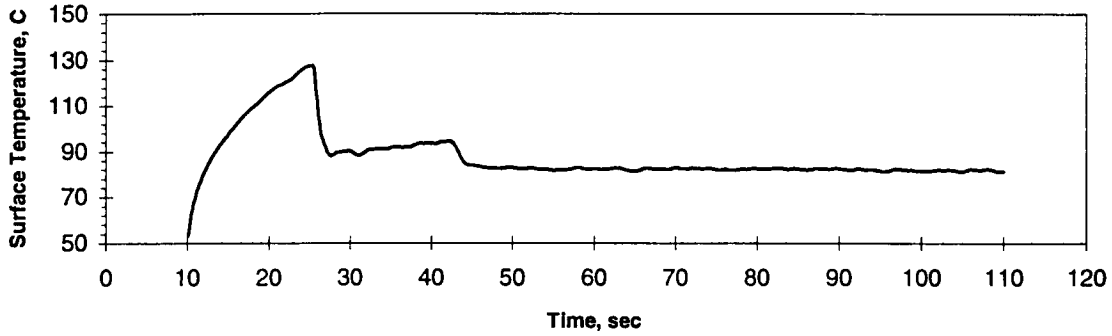

D.

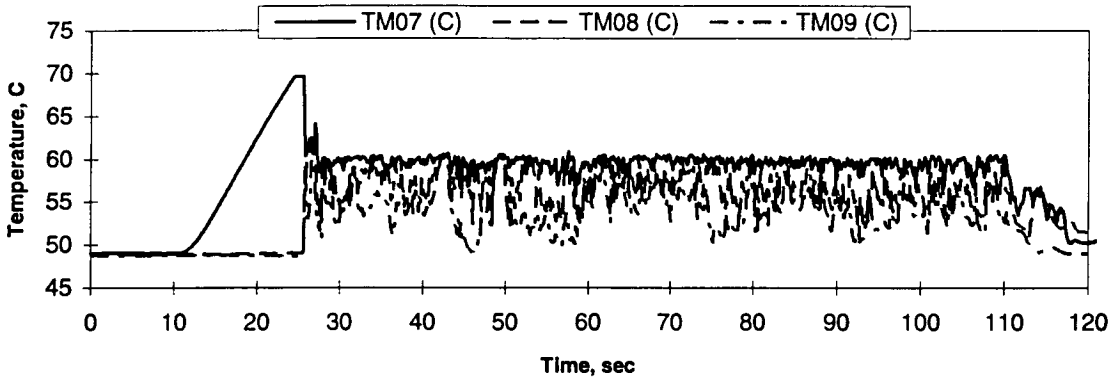

E.

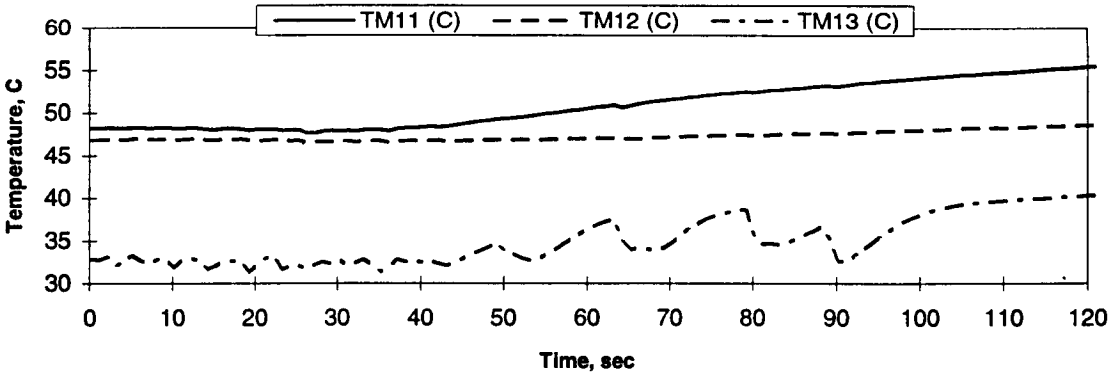

FIGURE: Measured Heater-Underside Temperatures **STS 57 - Run #2**

Heat Flux	Subcooling (F)	Heater Power On/Off	100 FPS On/Off	Stirrer Start	Repress Start	Total Test Time
4	20 ± 2	10-110 sec.	15-25 sec.	------	------	135 sec.

Figure B-5b. Measured fluid temperatures near secondary heater and heater underside. PBE-IB (STS-57). Run No. 2.

A. Mean Heater Surface Temperature

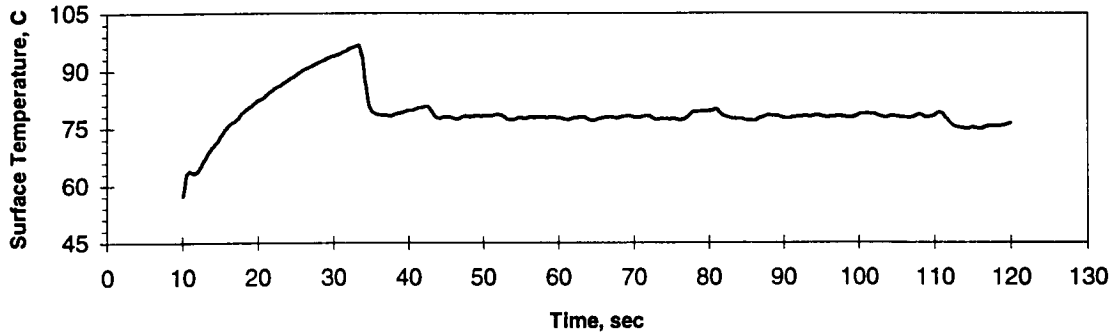

D.

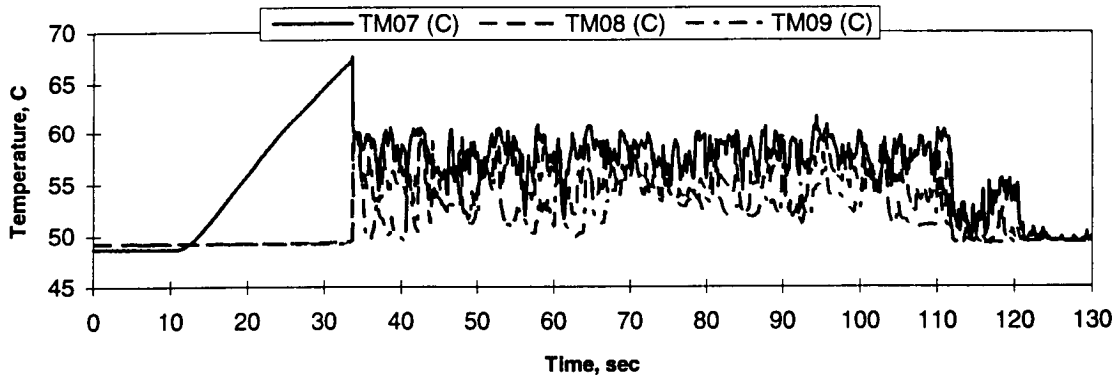

E.

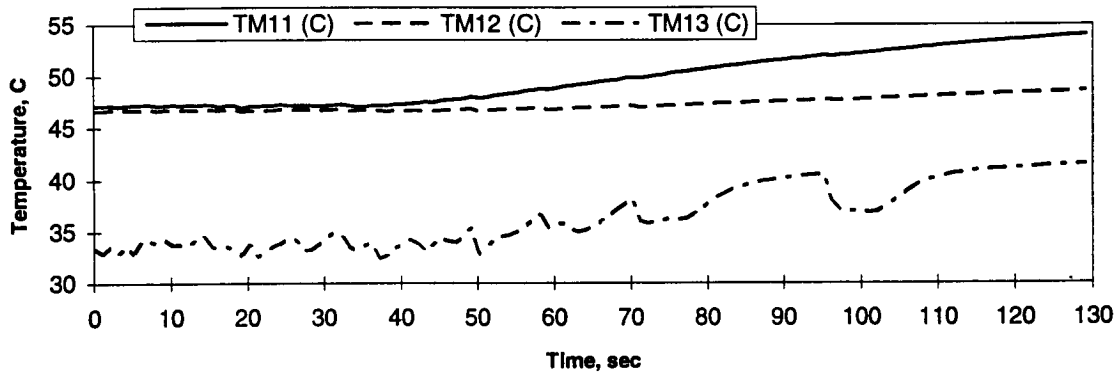

FIGURE: Measured Heater-Underside Temperatures **STS 57 - Run #3**

Heat Flux	Subcooling (F)	Heater Power On/Off	100 FPS On/Off	Stirrer Start	Repress Start	Total Test Time
2	20 ± 2	10-120 sec.	30-50 sec.	110 sec.	------	130 sec.

Figure B-5c. Measured fluid temperatures near secondary heater and heater underside. PBE-IB (STS-57). Run No. 3

A. Mean Heater Surface Temperature

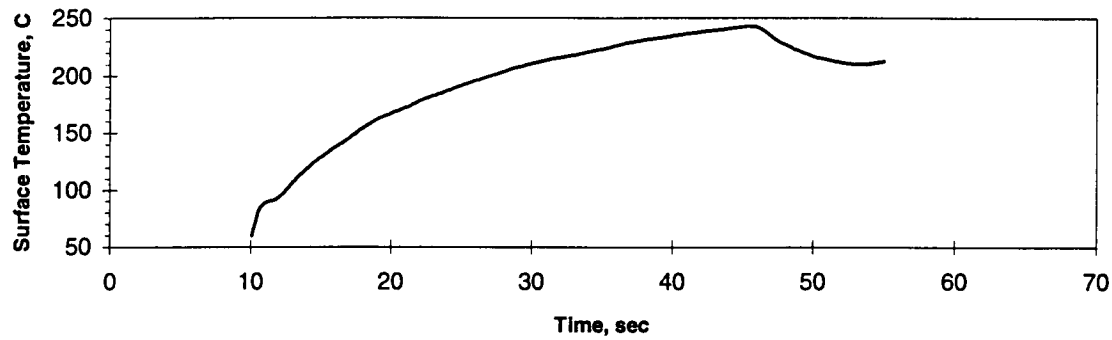

D.

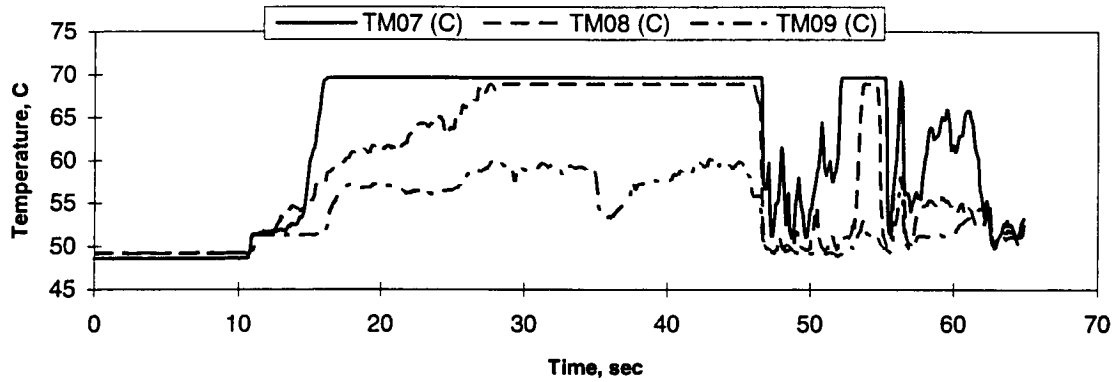

E.

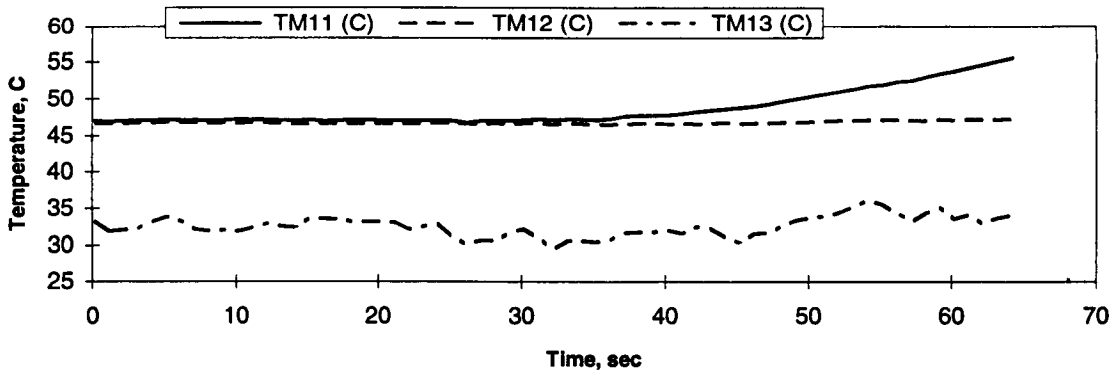

FIGURE: Measured Heater-Underside Temperatures **STS 57 - Run #4**

Heat Flux	Subcooling (F)	Heater Power On/Off	100 FPS On/Off	Stirrer Start	Repress Start	Total Test Time
8	5 ± 1	10-55 sec.	10-15 sec.	45 sec.	------	65 sec.

Figure B-5d. Measured fluid temperatures near secondary heater and heater underside. PBE-IB (STS-57). Run No. 4.

A. Mean Heater Surface Temperature

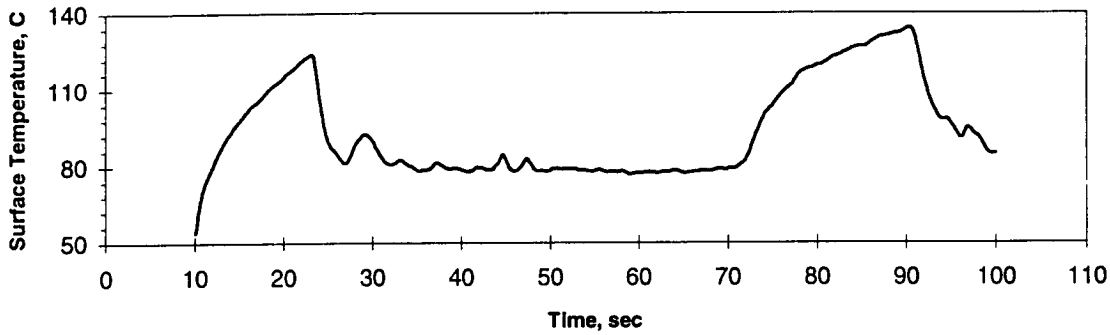

D.

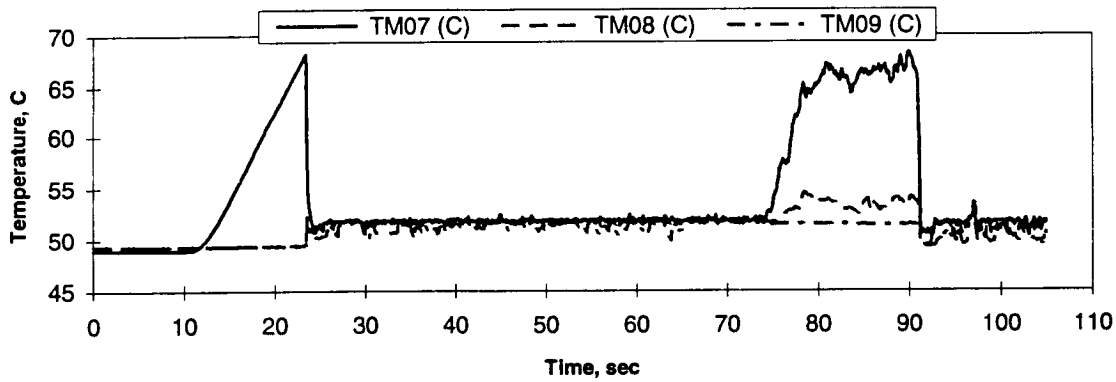

E.

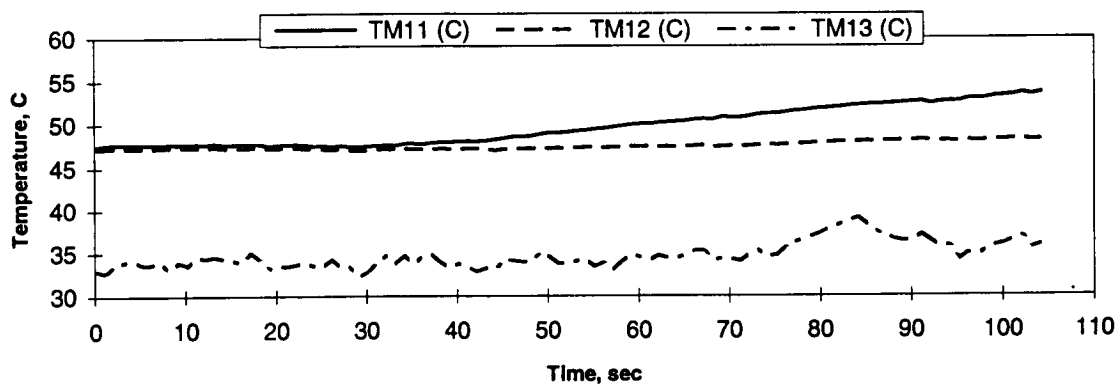

FIGURE: Measured Heater-Underside Temperatures **STS 57 - Run #5**

Heat Flux	Subcooling (F)	Heater Power On/Off	100 FPS On/Off	Stirrer Start	Repress Start	Total Test Time
4	5 ± 1	10-100 sec.	15-25 sec.	90 sec.	------	105 sec

Figure B-5e. Measured fluid temperatures near secondary heater and heater underside. PBE-IB (STS-57). Run No. 5.

A. Mean Heater Surface Temperature

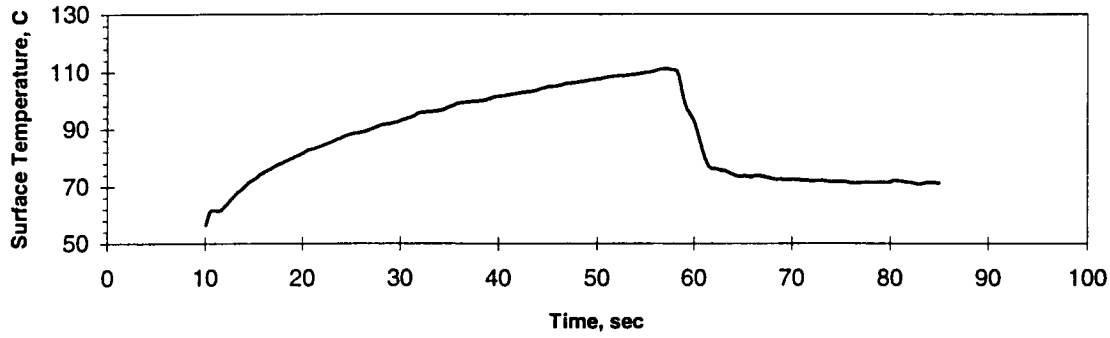

D.

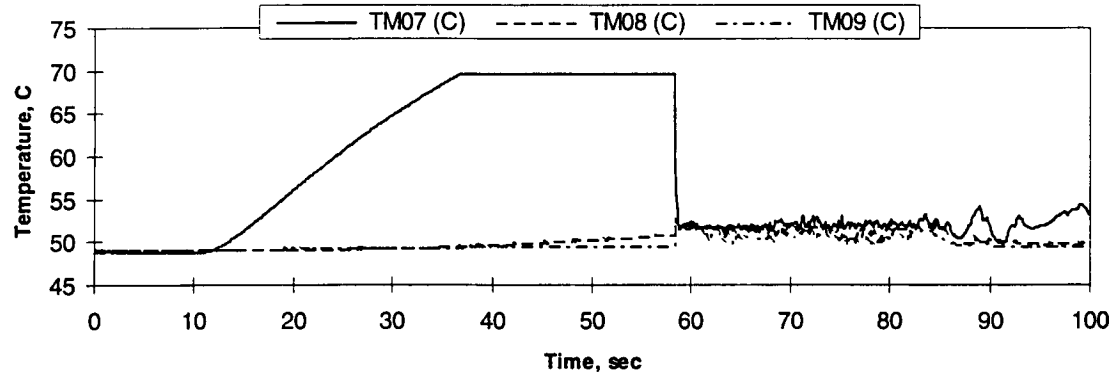

E.

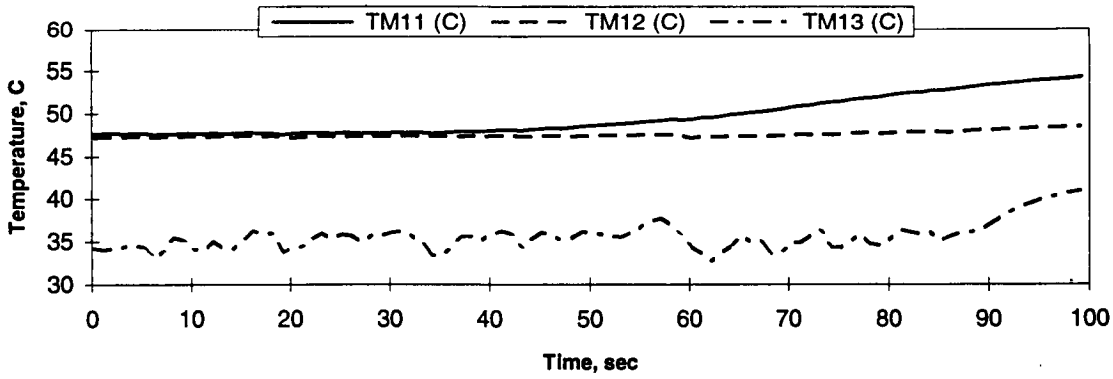

FIGURE: Measured Heater-Underside Temperatures **STS 57 - Run #6**

Heat Flux	Subcooling (F)	Heater Power On/Off	100 FPS On/Off	Stirrer Start	Repress Start	Total Test Time
2	5 ± 1	10-85 sec.	30-50 sec.	------	------	100 sec.

Figure B-5f. Measured fluid temperatures near secondary heater and heater underside. PBE-IB (STS-57). Run No. 6.

A. Mean Heater Surface Temperature

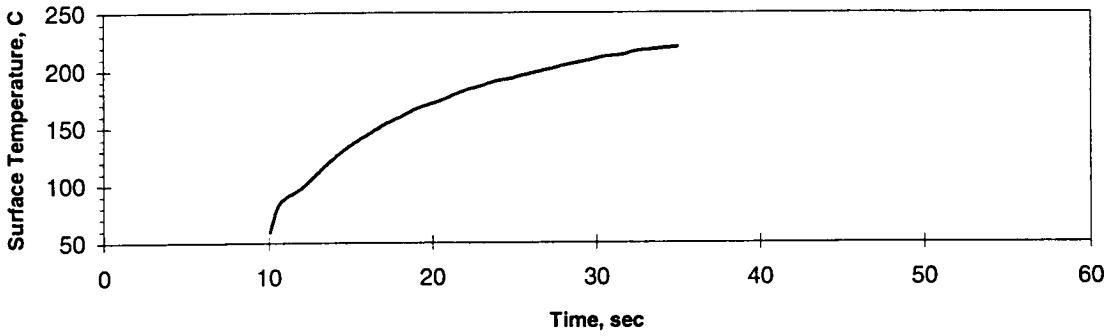

D.

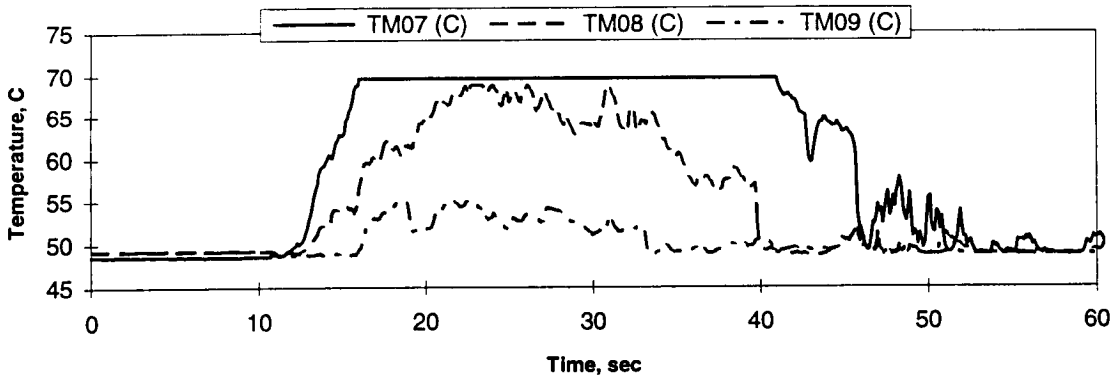

E.

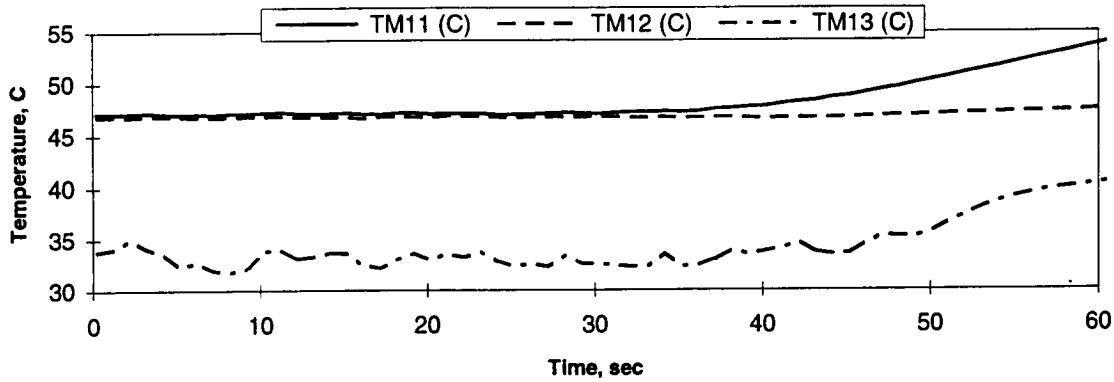

FIGURE: Measured Heater-Underside Temperatures **STS 57 - Run #7**

Heat Flux	Subcooling (F)	Heater Power On/Off	100 FPS On/Off	Stirrer Start	Repress Start	Total Test Time
8	0.5 ± 0.4	10-35 sec.	10-15 sec.	------	45 sec.	65 sec.

Figure B-5g. Measured fluid temperatures near secondary heater and heater underside. PBE-IB (STS-57). Run No. 7.

A. Mean Heater Surface Temperature

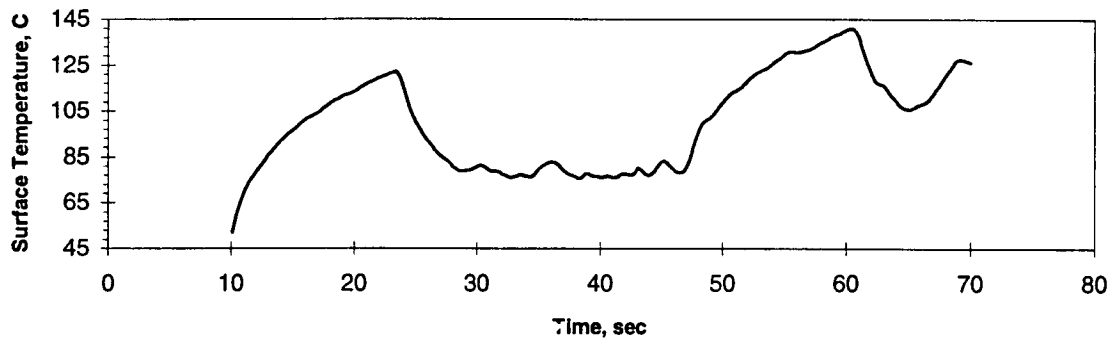

D.

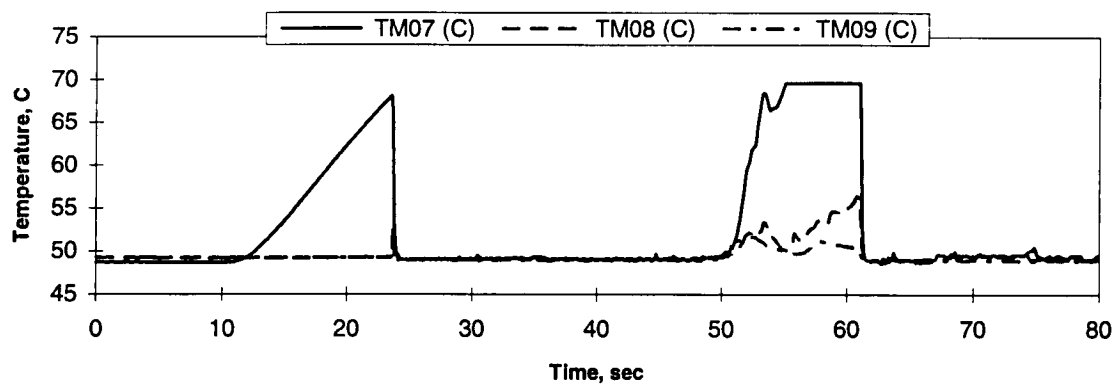

E.

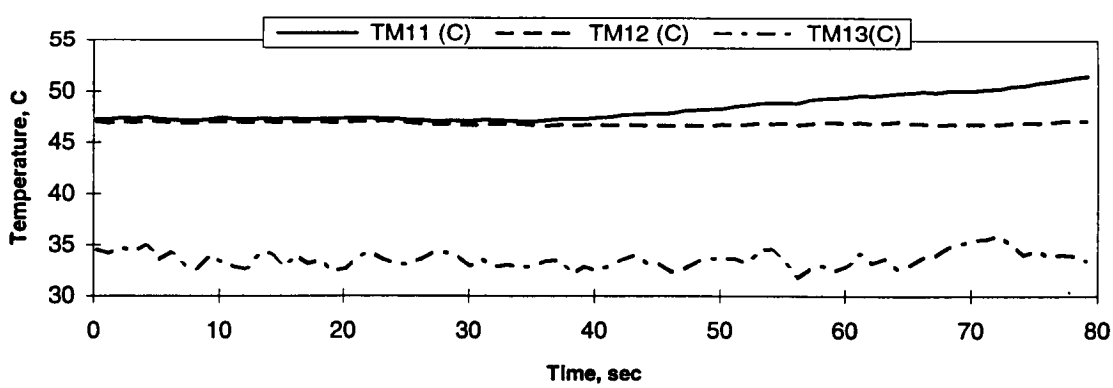

FIGURE: Measured Heater-Underside Temperatures **STS 57 - Run #8**

Heat Flux	Subcooling (F)	Heater Power On/Off	100 FPS On/Off	Stirrer Start	Repress Start	Total Test Time
4	0.5 ± 0.4	10-70 sec.	15-25 sec.	60 sec.	------	80 sec.

Figure B-5h. Measured fluid temperatures near secondary heater and heater underside. PBE-IB (STS-57). Run No. 8.

STS-57 Run #1

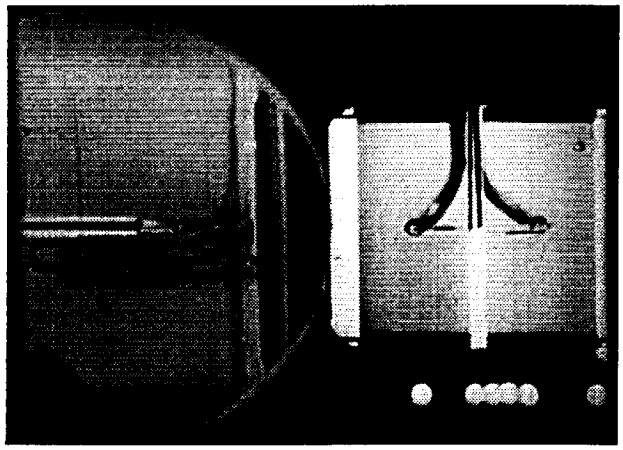

Frame#0080 time=10.79 sec.

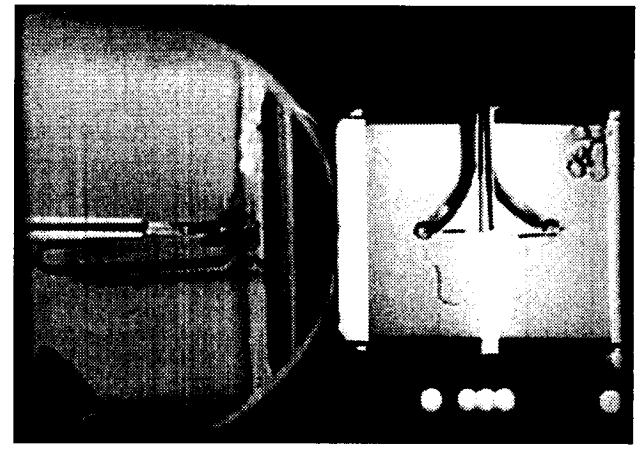

Frame#0093 time=10.92 sec.

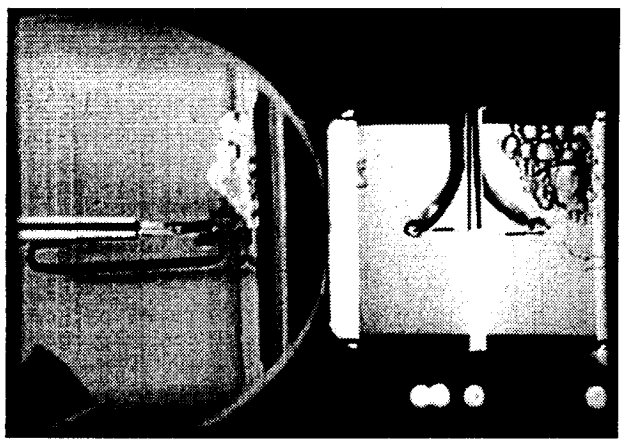

Frame#0105 time=11.04 sec.

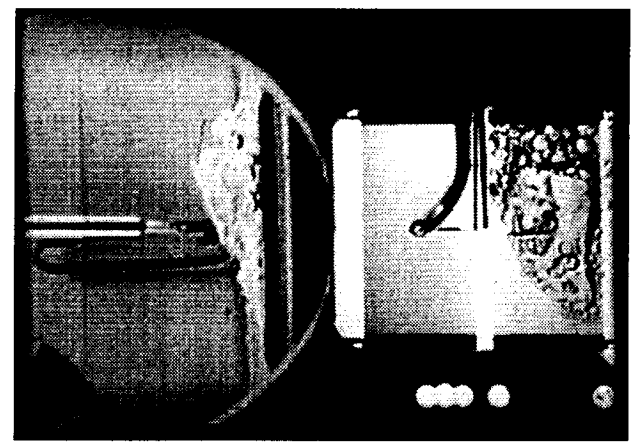

Frame#0117 time=11.16 sec.

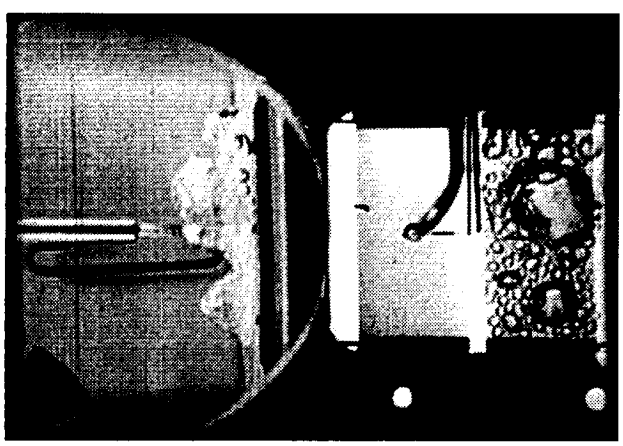

Frame#0129 time=11.28 sec.

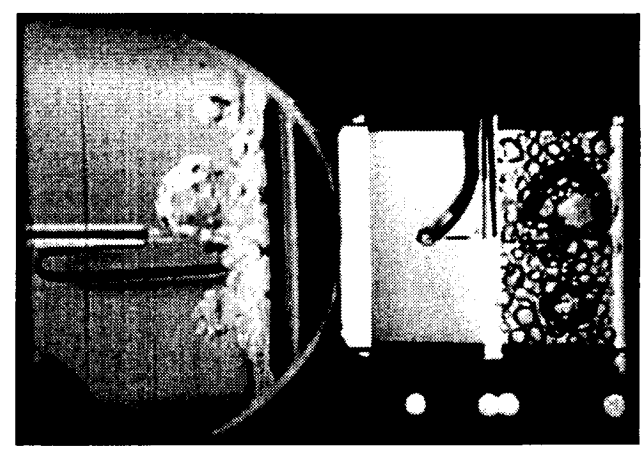

Frame#0141 time=11.40 sec.

Figure B-6a. Selected Photographic Images. PBE-IB (STS-57). Run No. 1.

STS-57 Run #1

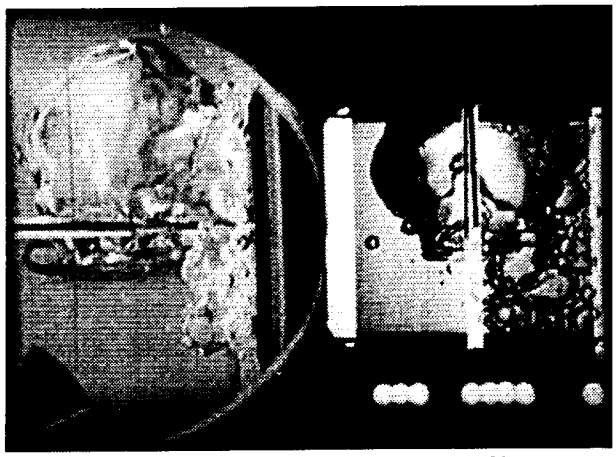

Frame#0372 time=14.63 sec.

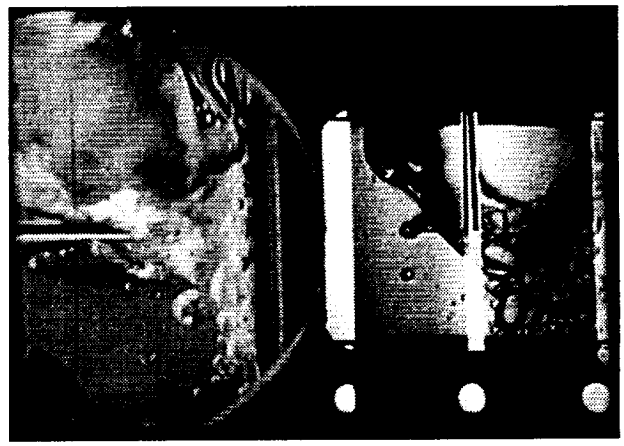

Frame#0484 time=20.32 sec.

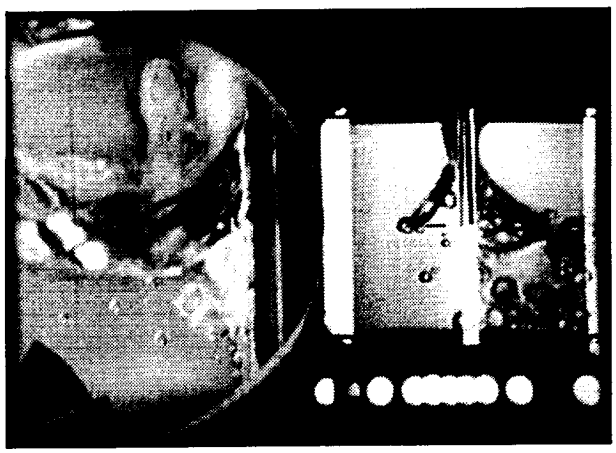

Frame#0634 time=34.29 sec.

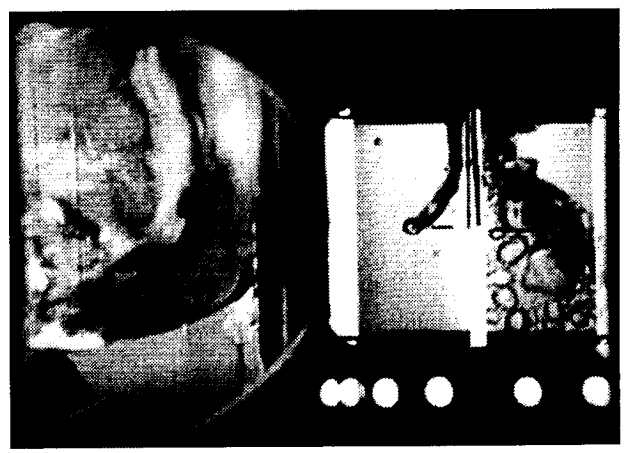

Frame#0742 time=43.61 sec.

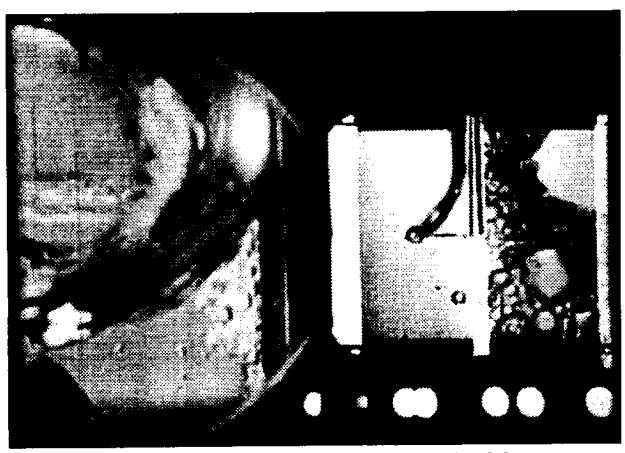

Frame#0850 time=52.93 sec.

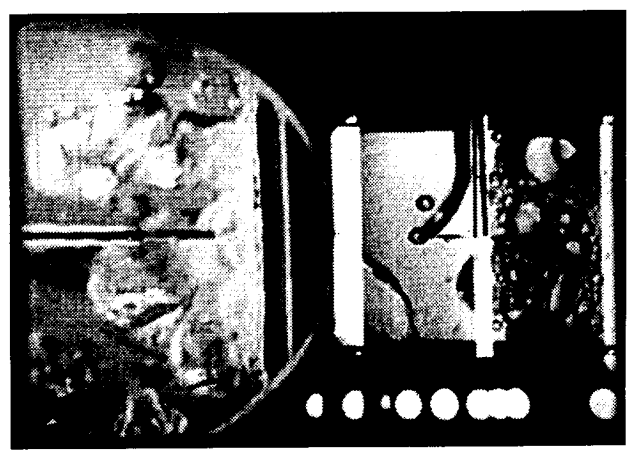

Frame#0923 time=62.94 sec.

Figure B-6a. Continued.

STS-57 Run #2

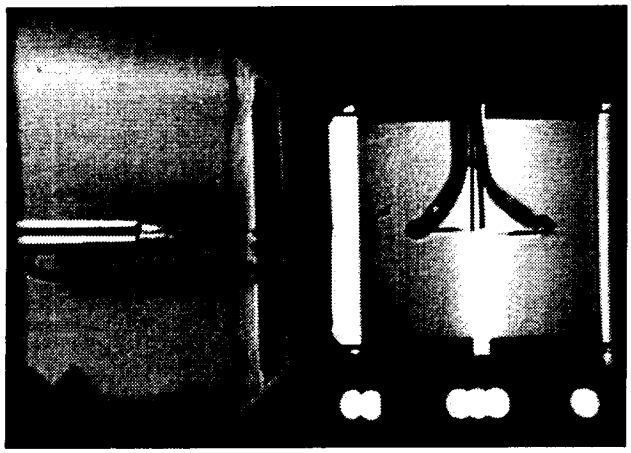

Frame#1071 time=25.64 sec.

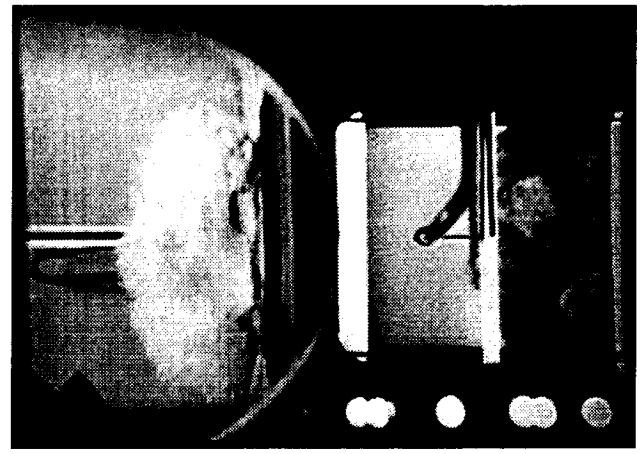

Frame#1072 time=25.71 sec.

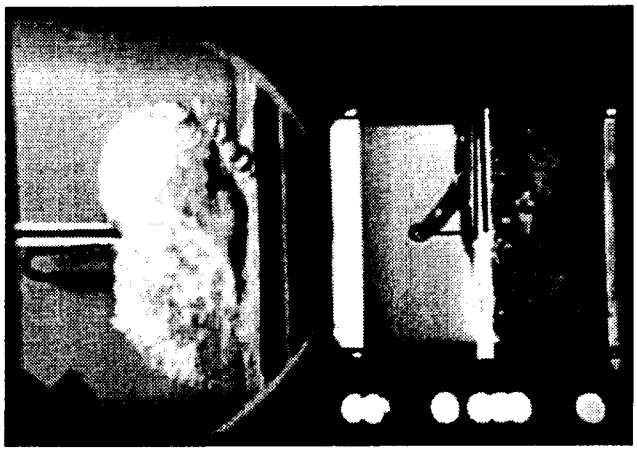

Frame#1073 time=25.82 sec.

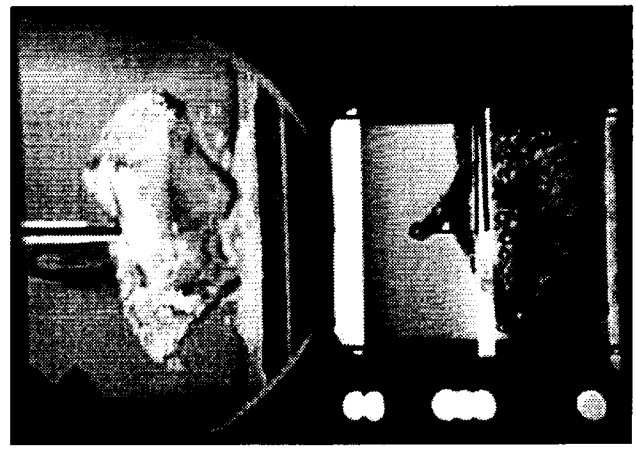

Frame#1074 time=25.92 sec.

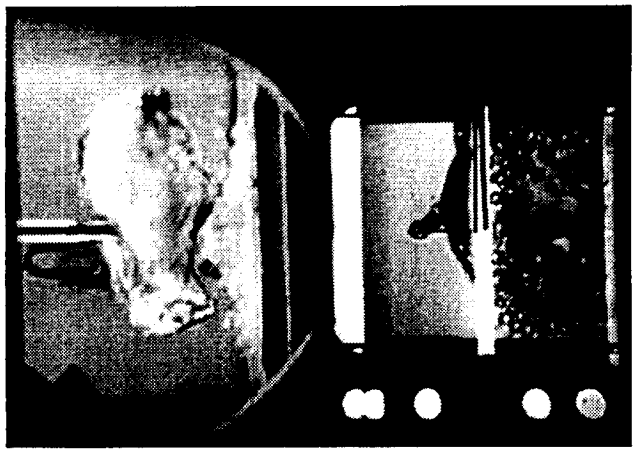

Frame#1075 time=26.01 sec.

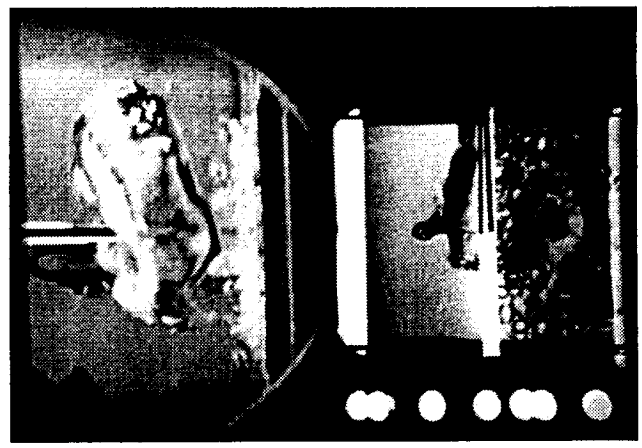

Frame#1076 time=26.11 sec.

Figure B-6b. Selected Photographic Images. PBE-IB (STS-57). Run No. 2.

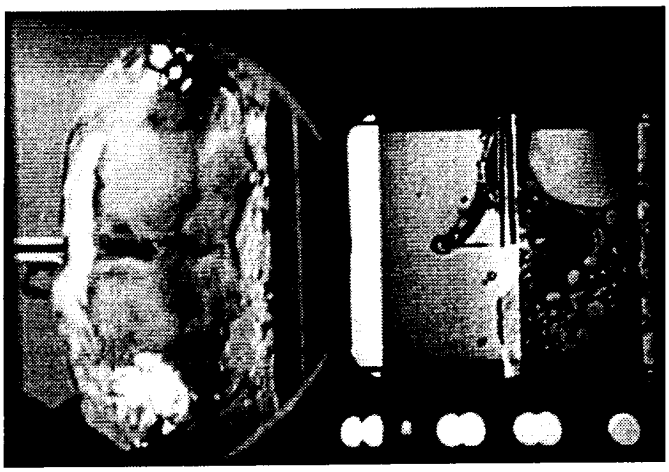

Run #2 Frame#1237 time=42.38 sec

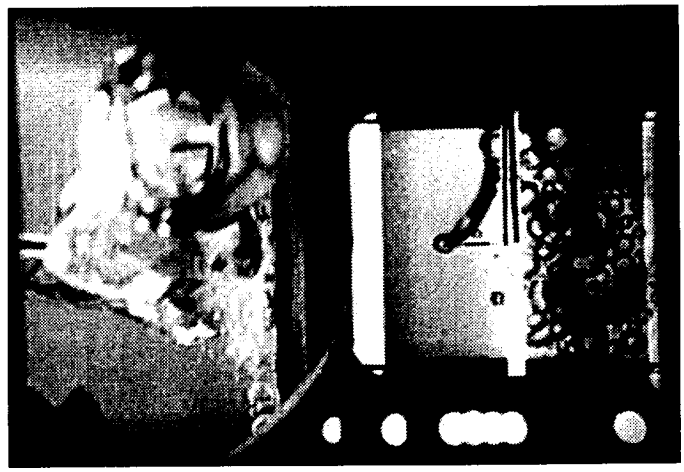

Run #2 Frame#1397 time=57.28 sec

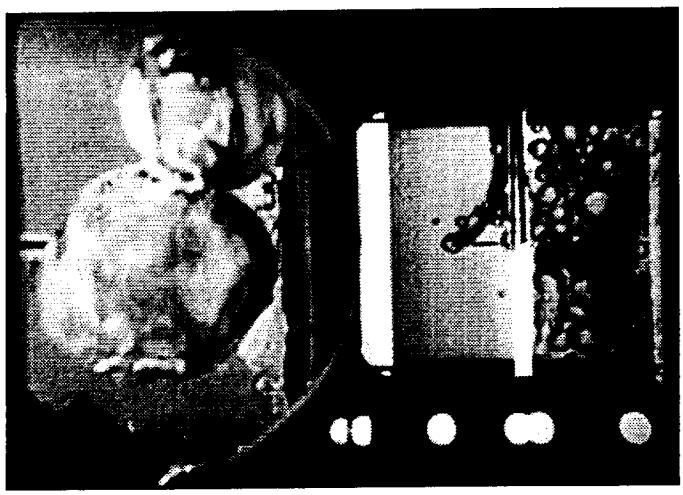

Run #2 Frame#1557 time=72.84 sec

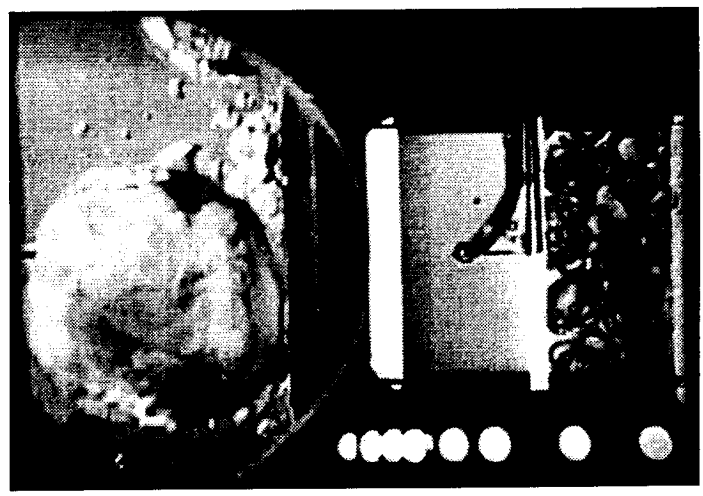

Run #2 Frame#1717 time=88.42 sec

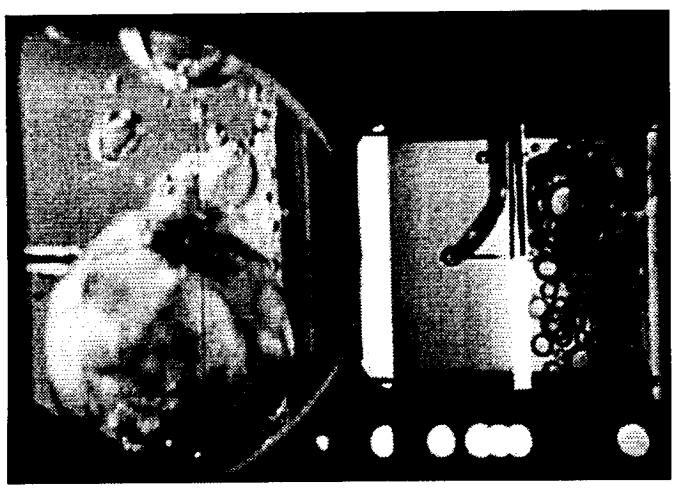

Run #2 Frame#1877 time=104.00 sec

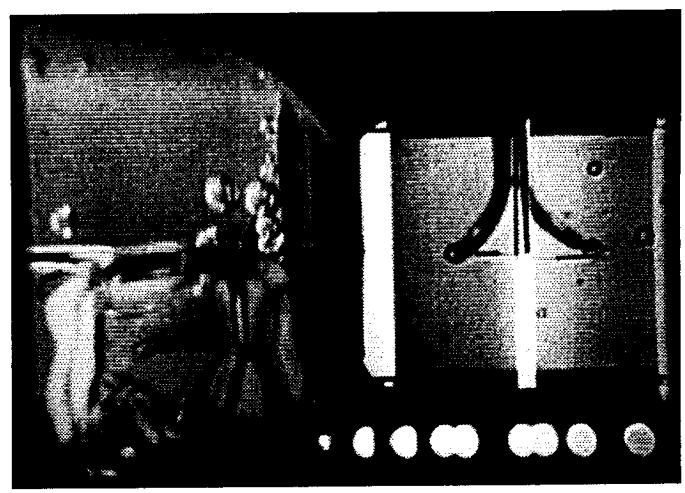

Run #2 Frame#2037 time=119.57 sec

Figure B-6b. Continued.

STS-57 Run #3

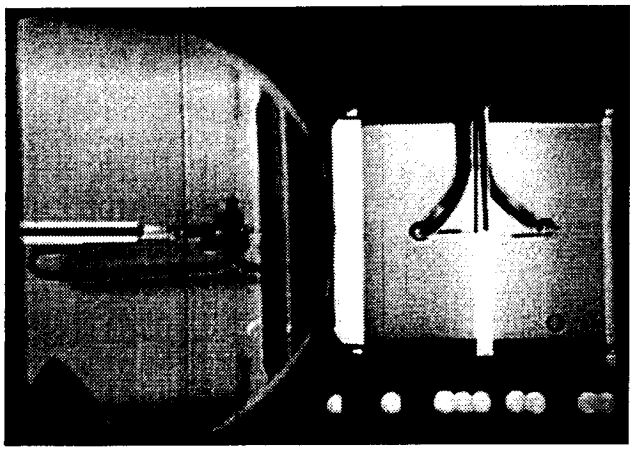

Frame#0454 time=33.63 sec.

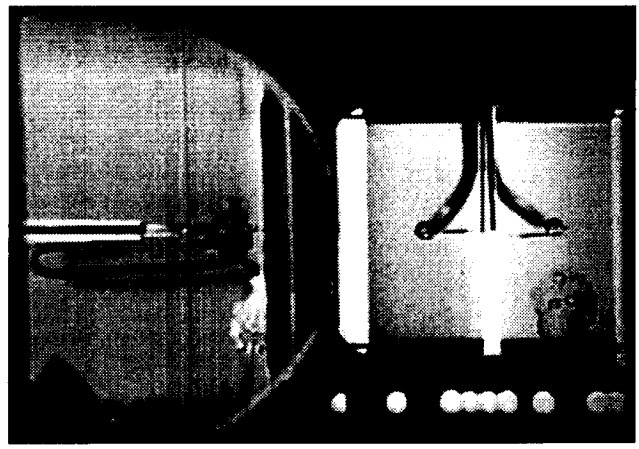

Frame#0456 time=33.65 sec.

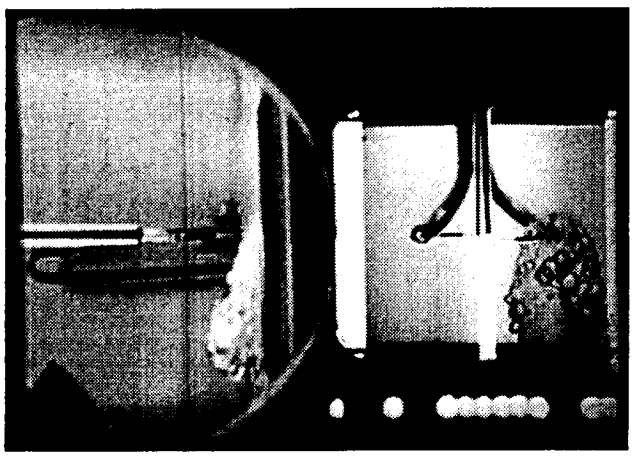

Frame#0458 time=33.67 sec.

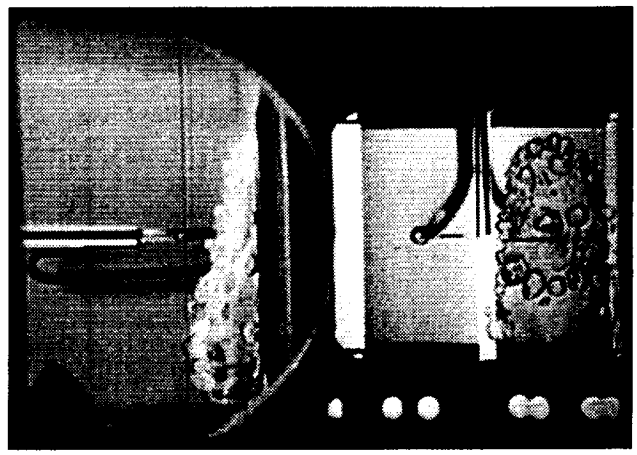

Frame#0462 time=33.71 sec.

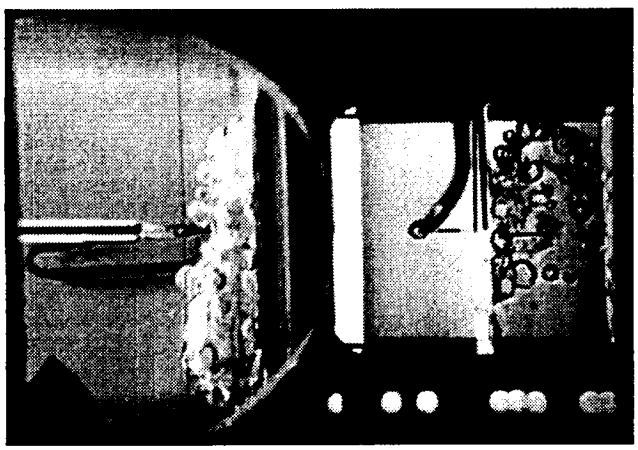

Frame#0466 time=33.75 sec.

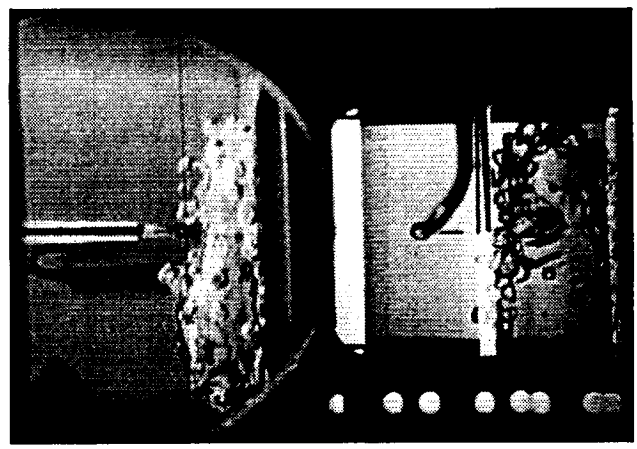

Frame#0470 time=33.79 sec.

Figure B-6c. Selected Photographic Images. PBE-IB (STS-57). Run No. 3.

STS-57 Run #3

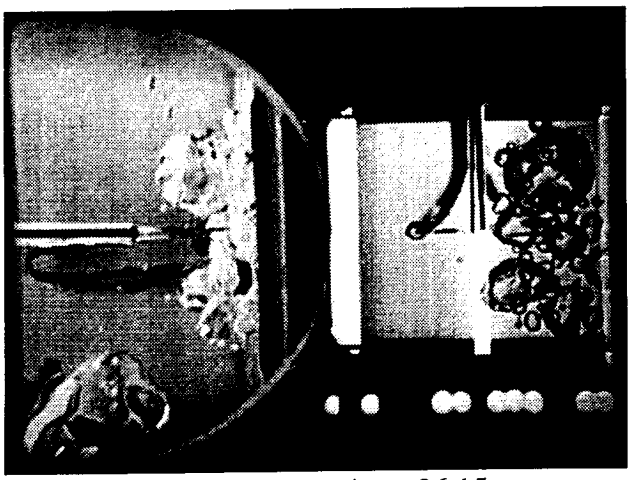

Frame#0706 time=36.15 sec.

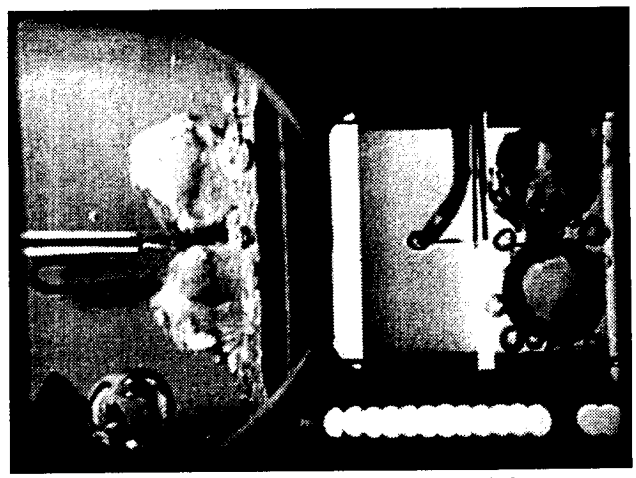

Frame#2123 time=50.95 sec.

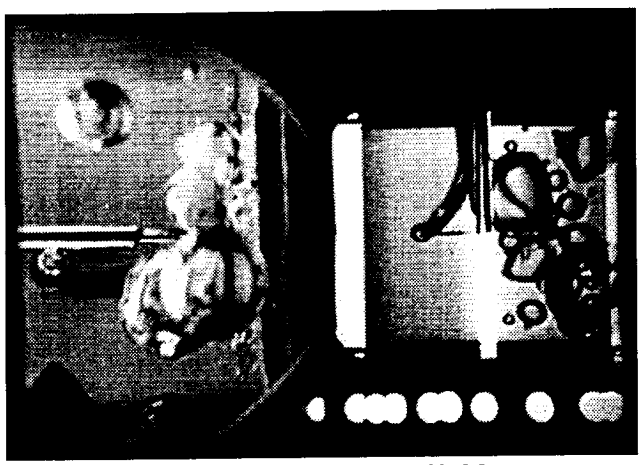

Frame#2318 time=69.93 sec.

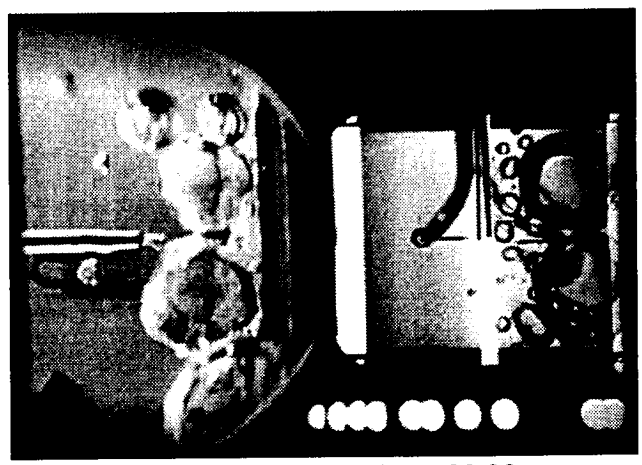

Frame#2513 time=88.92 sec.

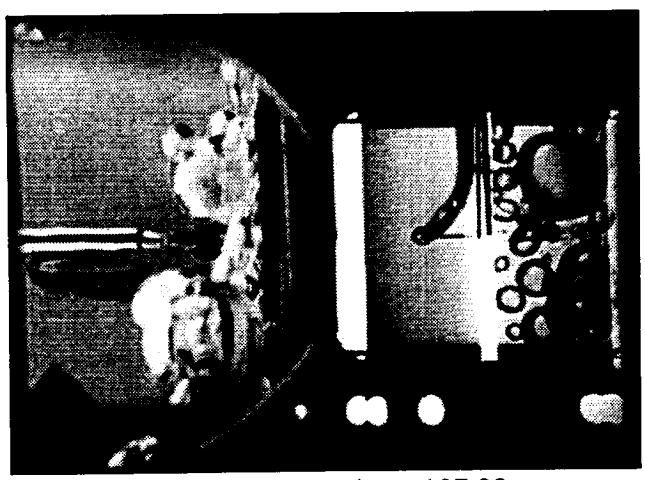

Frame#2708 time=107.92 sec.

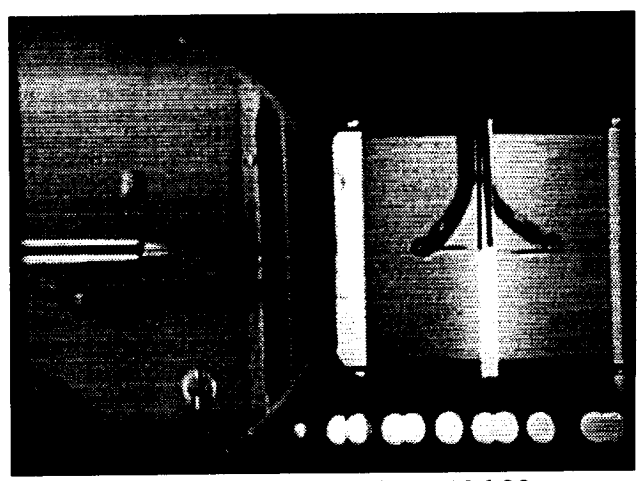

Frame#2903 time=126.93 sec.

Figure B-6c. Continued.

STS-57 Run #4

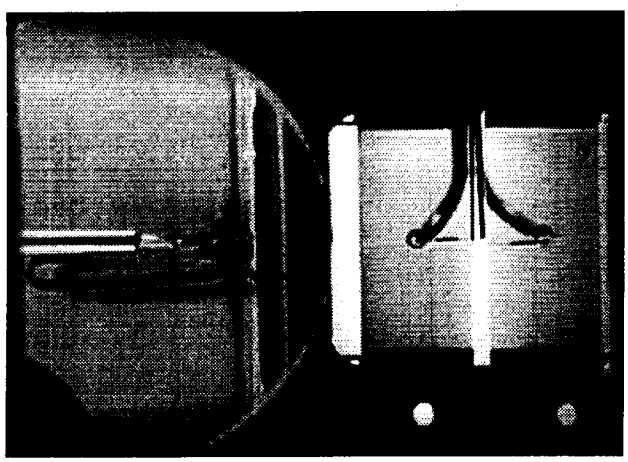

Frame#0063 time=11.28 sec.

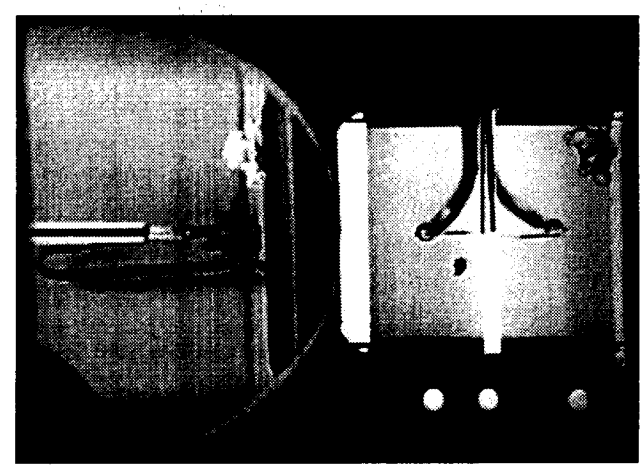

Frame#0071 time=11.44 sec.

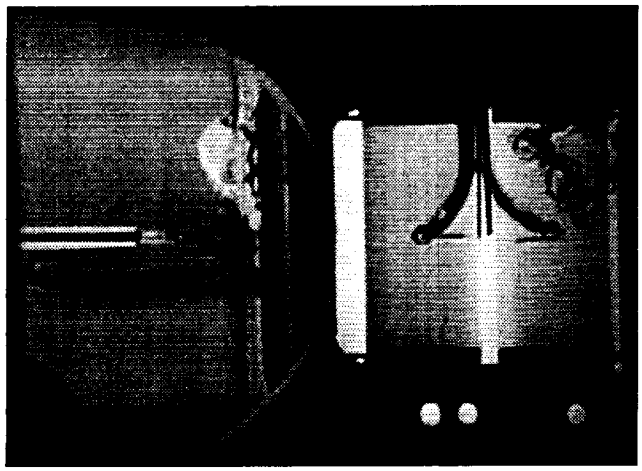

Frame#0079 time=11.60 sec.

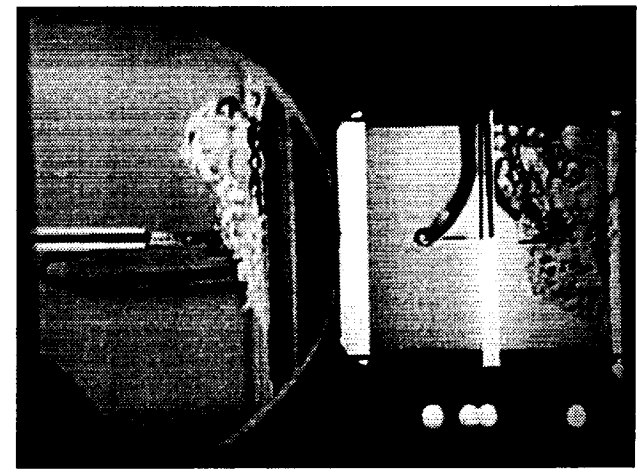

Frame#0087 time=11.88 sec.

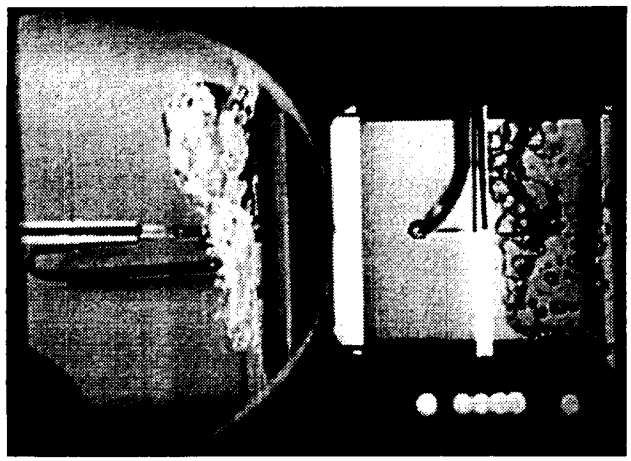

Frame#0093 time=11.88 sec.

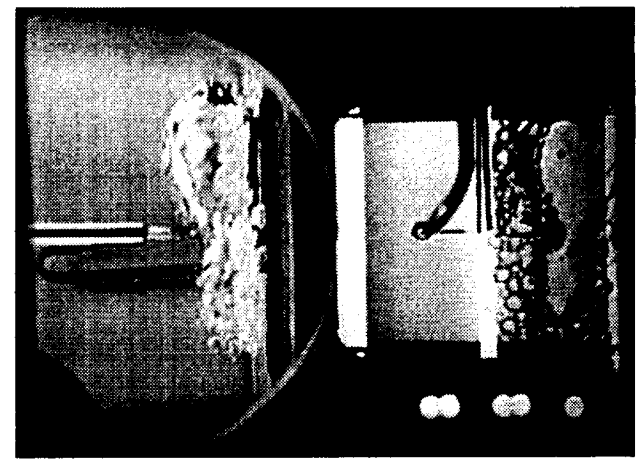

Frame#0101 time=12.04 sec.

Figure B-6d. Selected Photographic Images. PBE-IB (STS-57). Run No. 4.

STS-57 Run #4

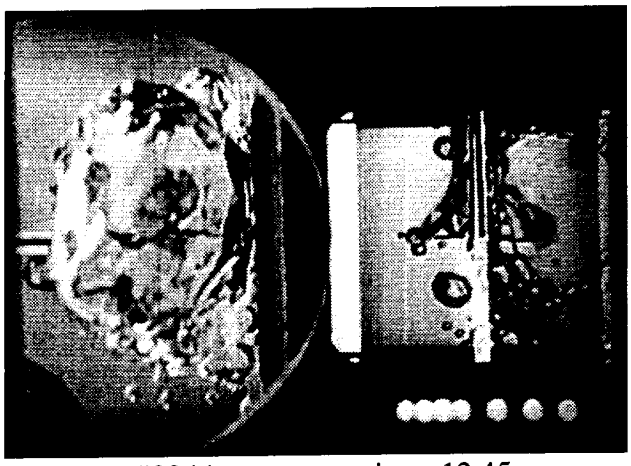

Frame#0244 time=12.45 sec.

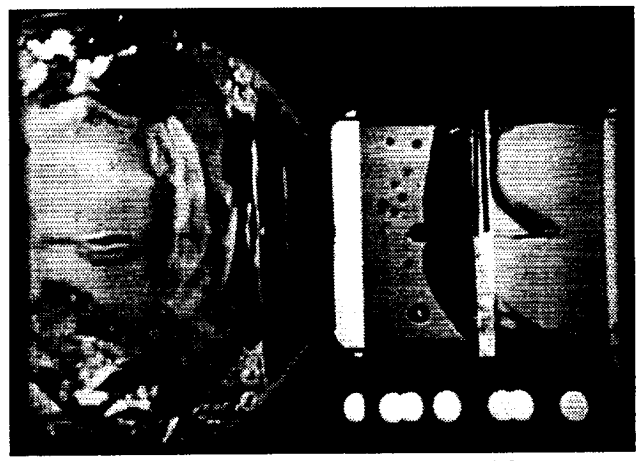

Frame#0615 time=24.46 sec.

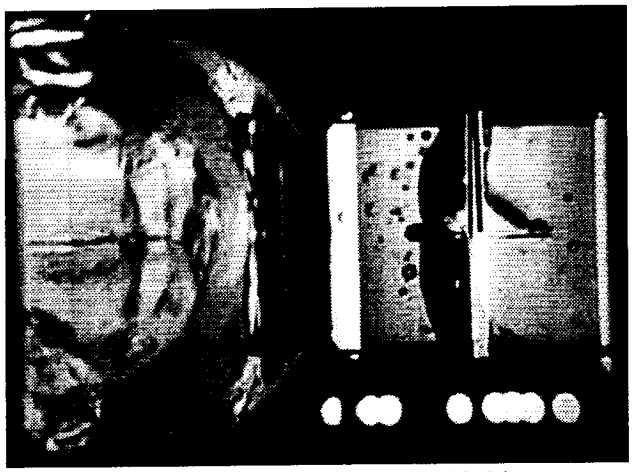

Frame#0758 time=38.39 sec.

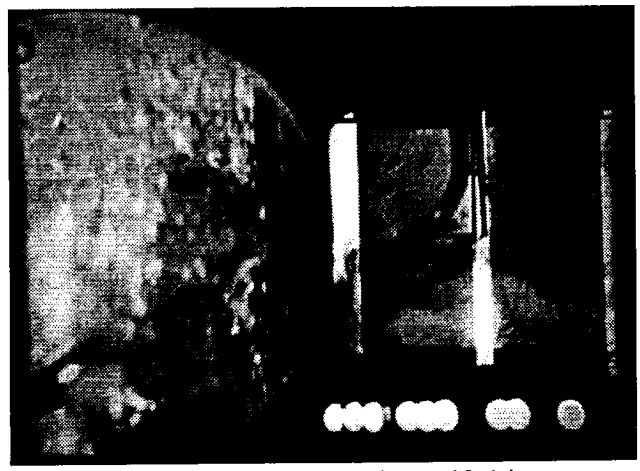

Frame#0858 time=48.14 sec.

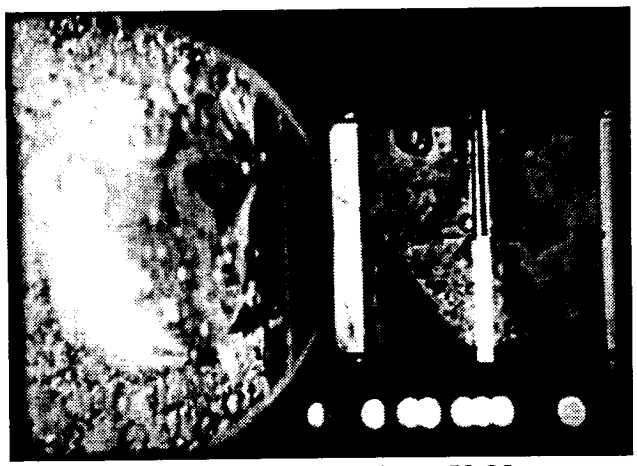

Frame#0962 time=58.28 sec.

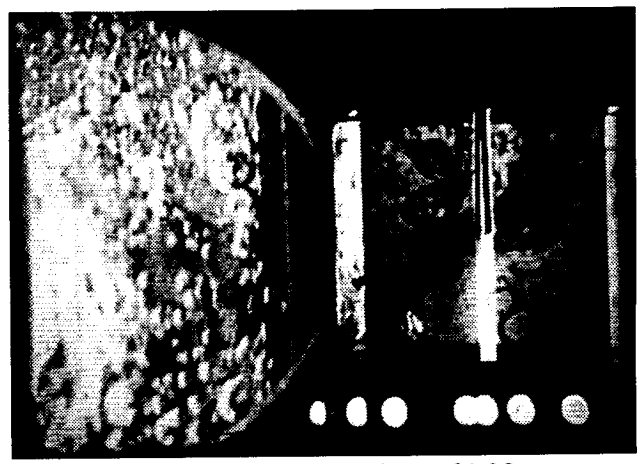

Frame#1021 time=64.02 sec.

Figure B-6d. Continued.

STS-57 Run #5

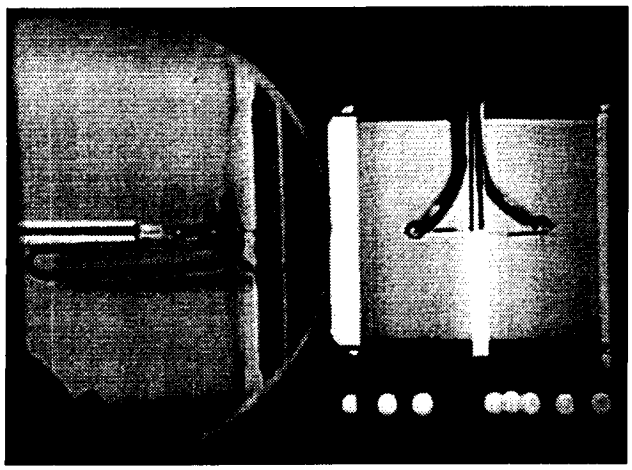

Frame#0894 time=23.51 sec.

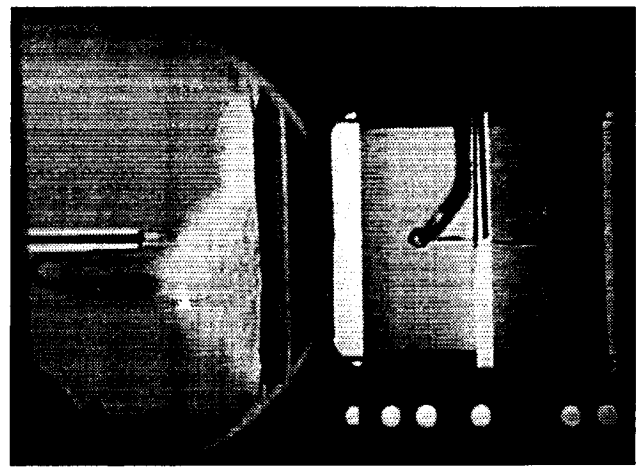

Frame#0895 time=23.52 sec.

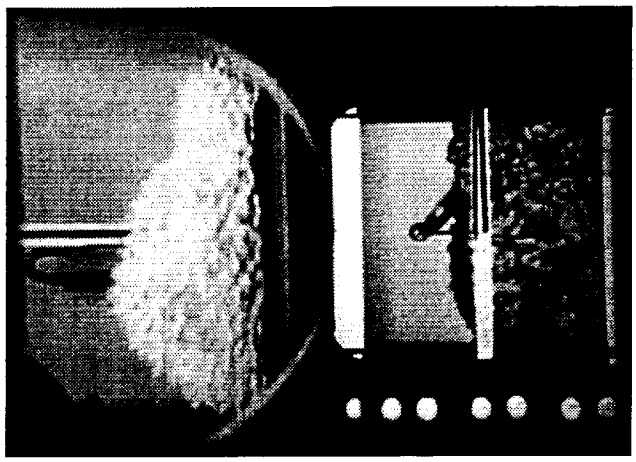

Frame#0897 time=23.54 sec.

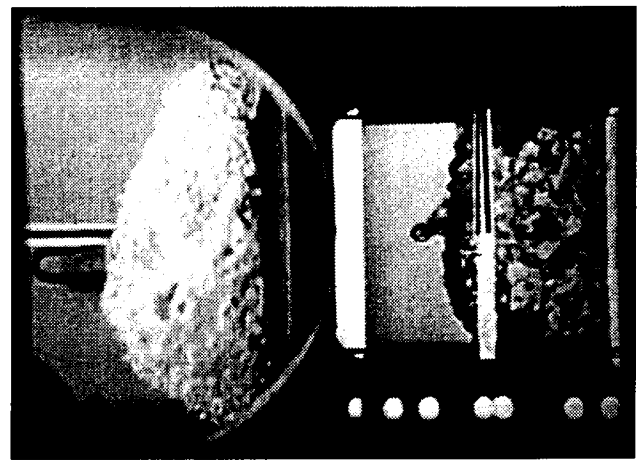

Frame#0899 time=23.56 sec.

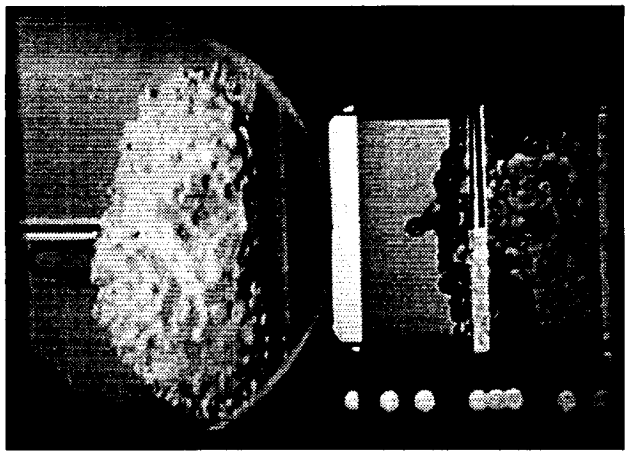

Frame#0901 time=23.58 sec.

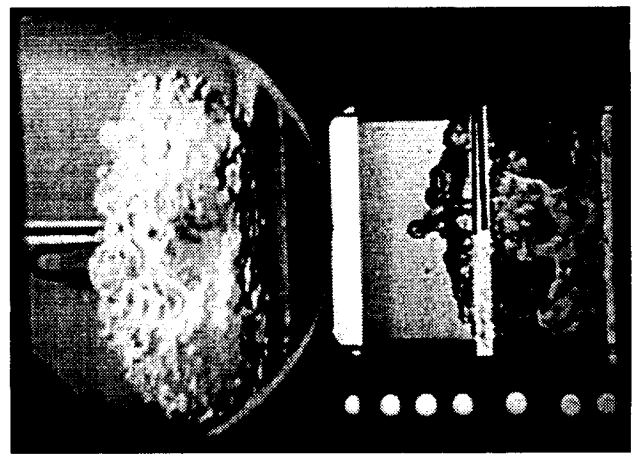

Frame#0905 time=23.62 sec.

Figure B-6e. Selected Photographic Images. PBE-IB (STS-57). Run No. 5.

STS-57 Run #5

Frame#0967 time=24.39 sec.

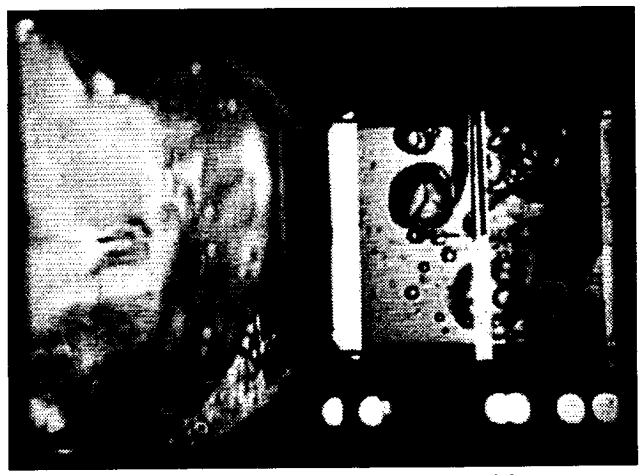

Frame#1171 time=35.66 sec.

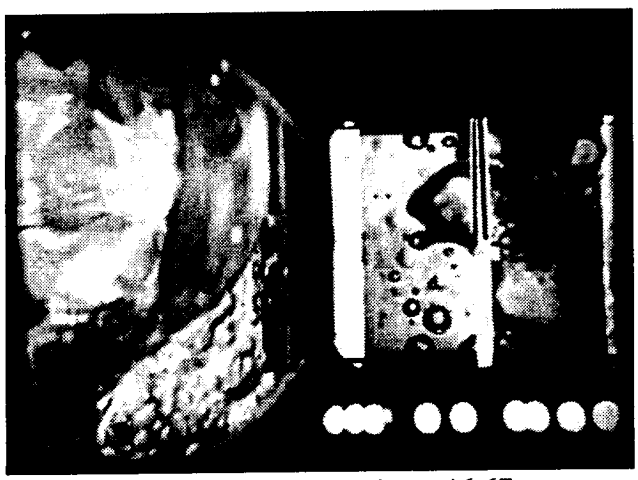

Frame#1284 time=46.67 sec.

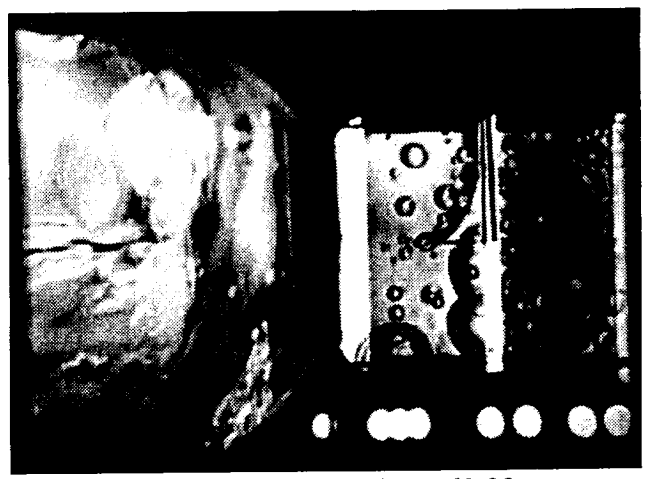

Frame#1421 time=60.02 sec.

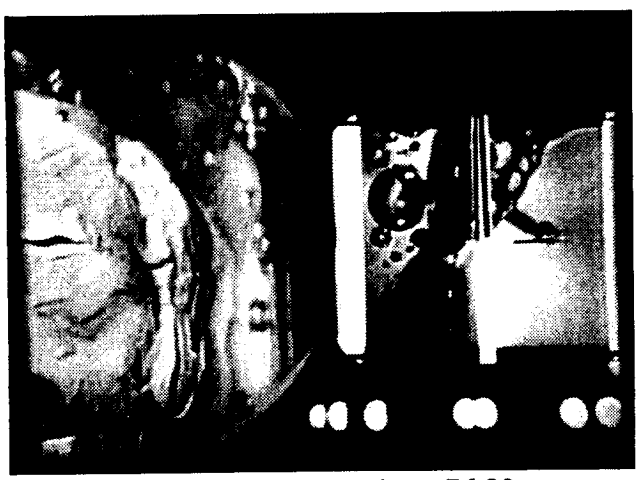

Frame#1593 time=76.80 sec.

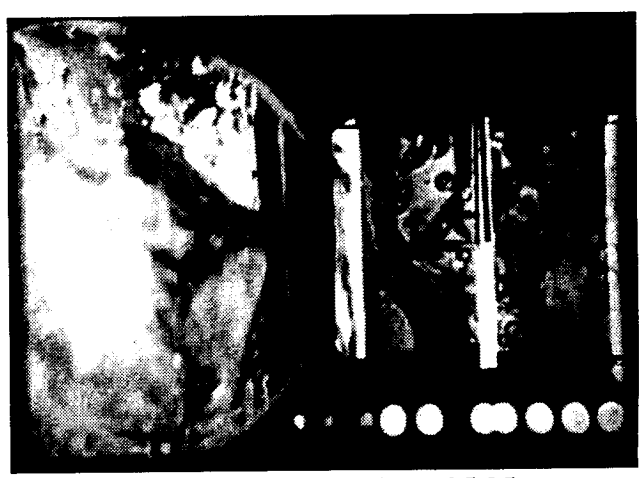

Frame#1782 time=95.25 sec.

Figure B-6e. Continued.

STS-57 Run #6

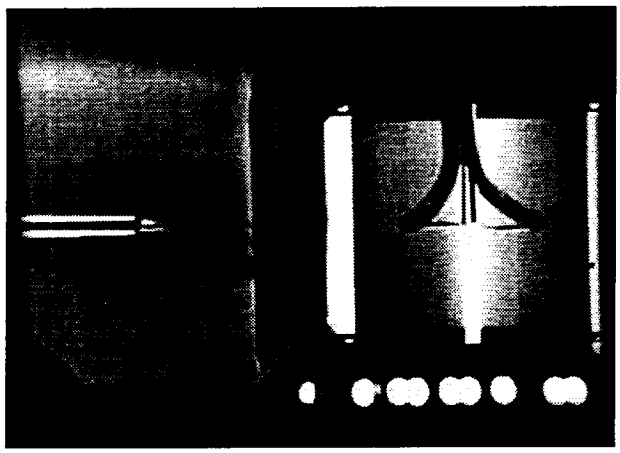

Frame#2195 time=58.26 sec.

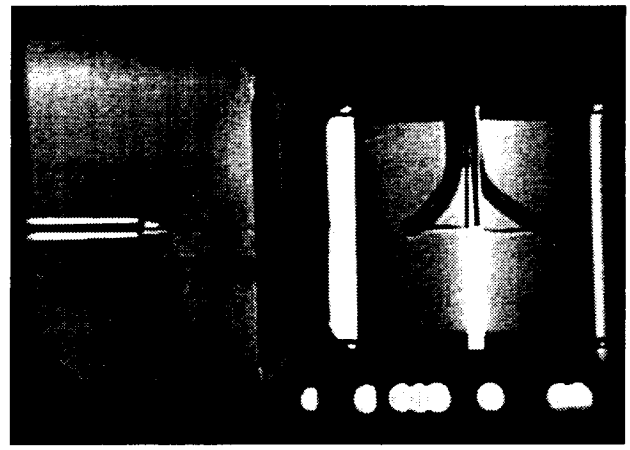

Frame#2196 time=58.36 sec.

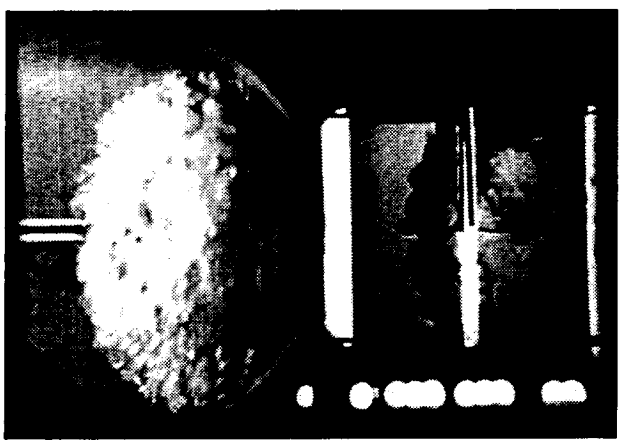

Frame#2197 time=58.46 sec.

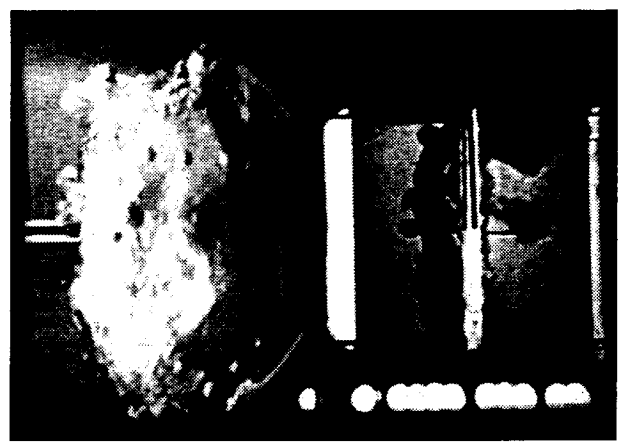

Frame#2198 time=58.55 sec.

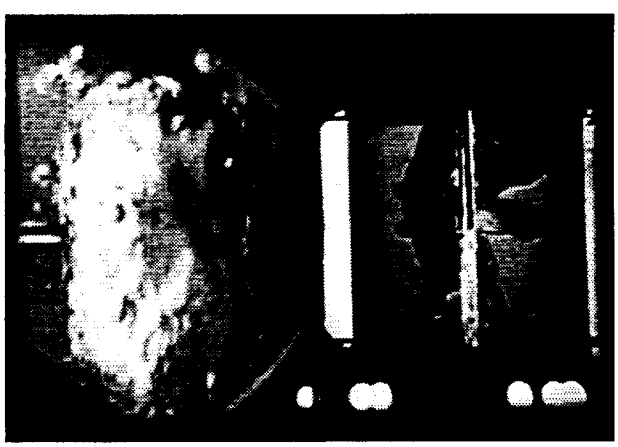

Frame#2199 time=58.65 sec.

Frame#2200 time=58.75 sec.

Figure B-6f. Selected Photographic Images. PBE-IB (STS-57). Run No. 6.

STS-57 Run #6

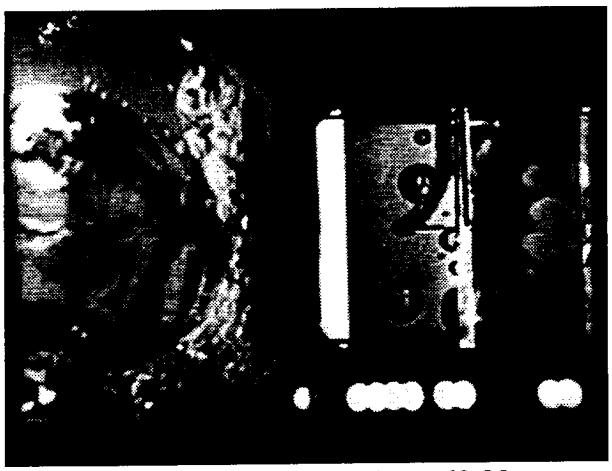

Frame#2221 time=60.80 sec.

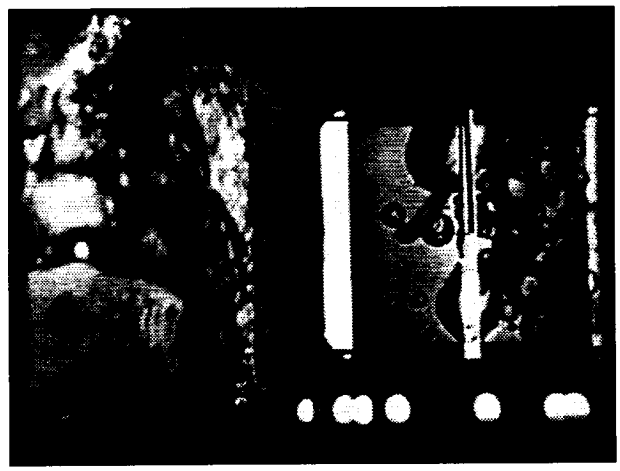

Frame#2291 time=67.64 sec.

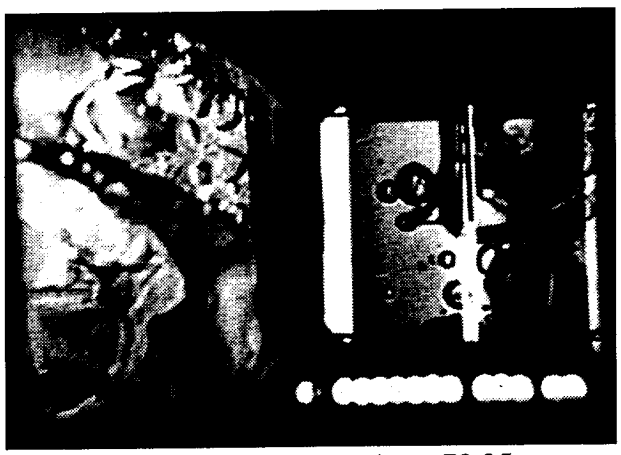

Frame#2329 time=72.35 sec.

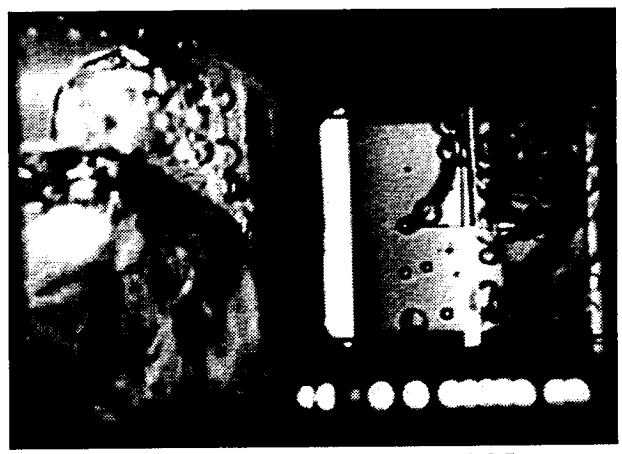

Frame#2366 time=74.95 sec.

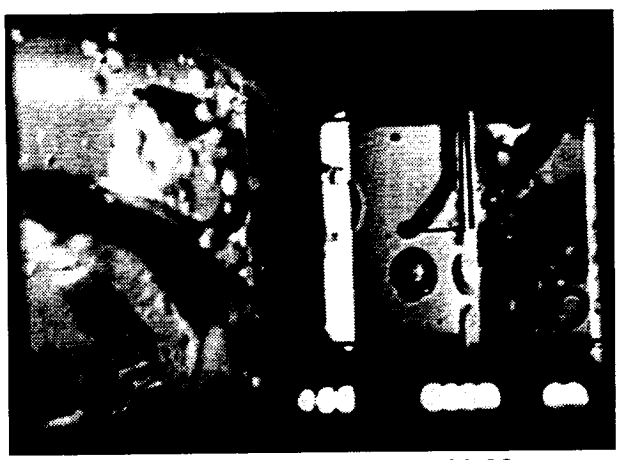

Frame#2515 time=82.28 sec.

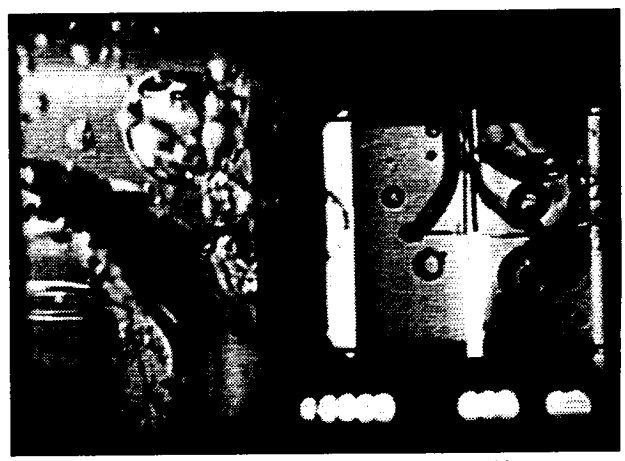

Frame#2601 time=89.50 sec.

Figure B-6f. Continued.

STS-57 Run #7

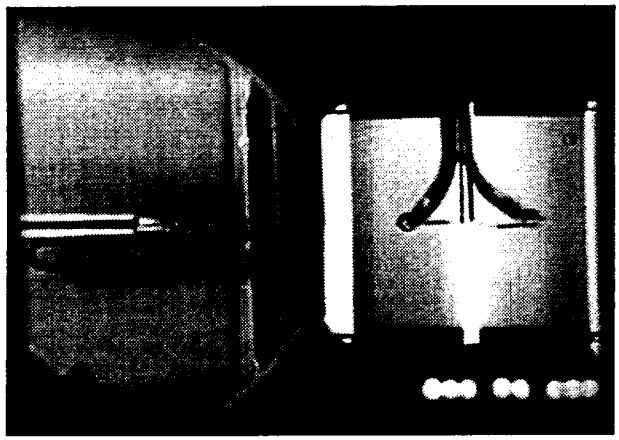

Frame#0057 time=10.59 sec.

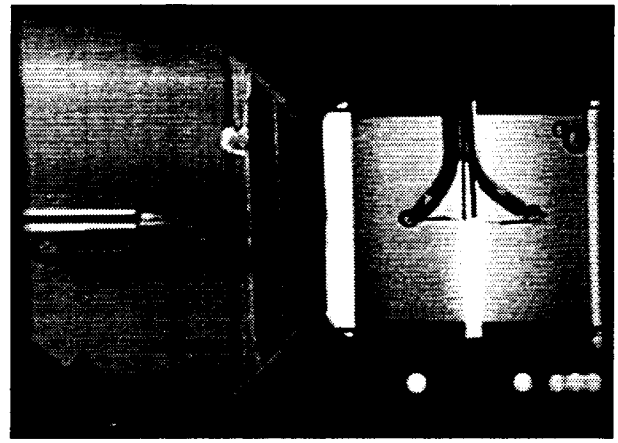

Frame#0063 time=10.65 sec.

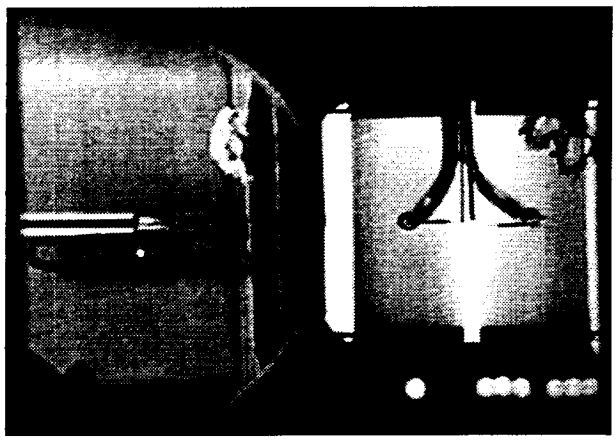

Frame#0069 time=10.71 sec.

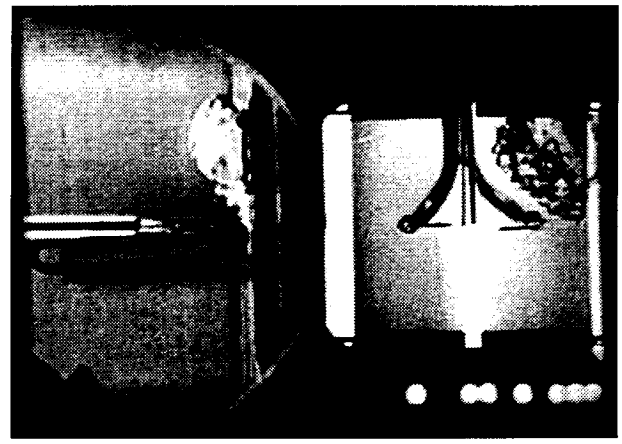

Frame#0075 time=10.77 sec.

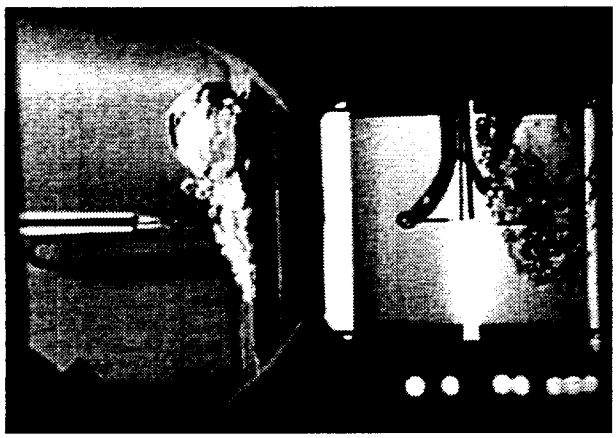

Frame#0081 time=10.83 sec.

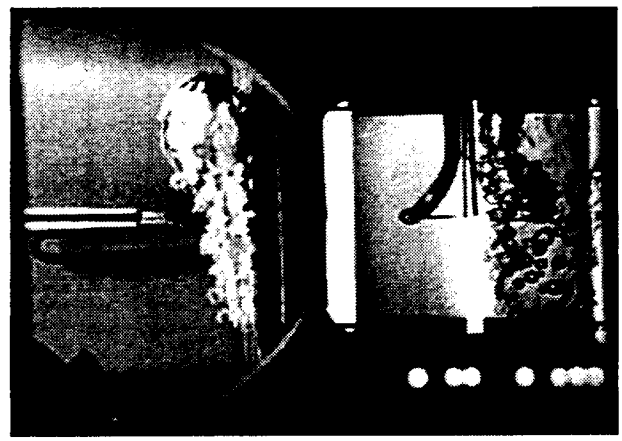

Frame#0087 time=10.89 sec.

Figure B-6g. Selected Photographic Images. PBE-IB (STS-57). Run No. 7.

STS-57 Run #7

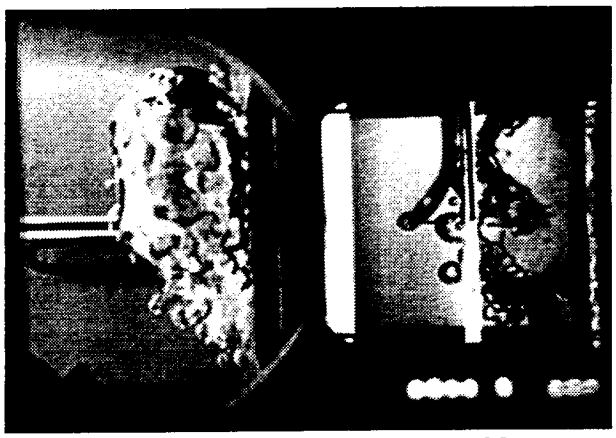

Frame#0120 time=11.22 sec.

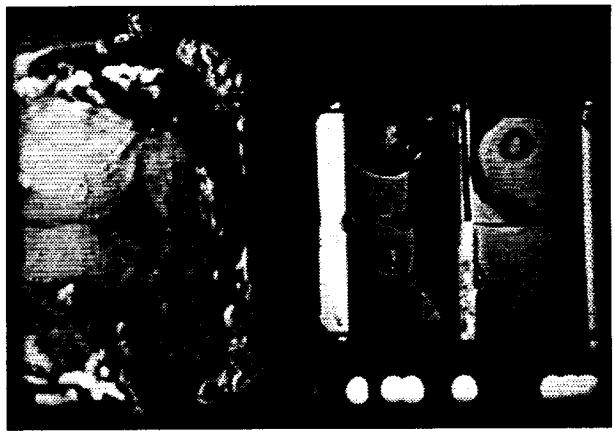

Frame#0538 time=17.12 sec.

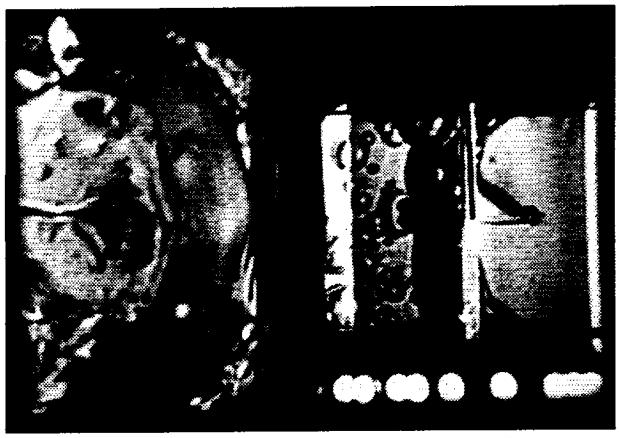

Frame#0644 time=27.46 sec.

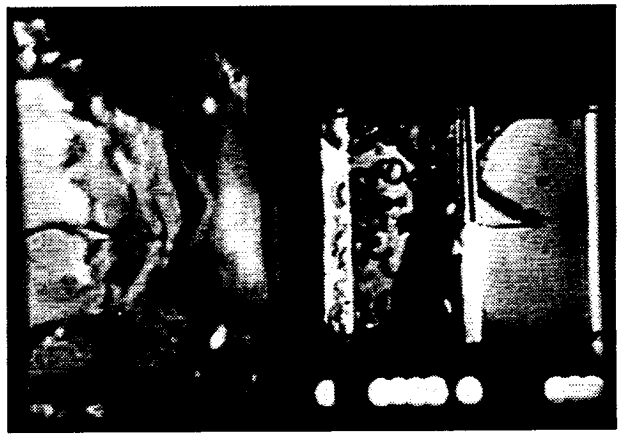

Frame#0725 time=35.36 sec.

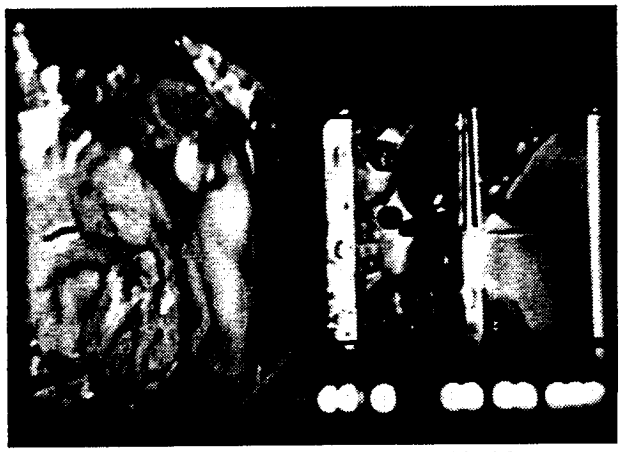

Frame#0809 time=43.55 sec.

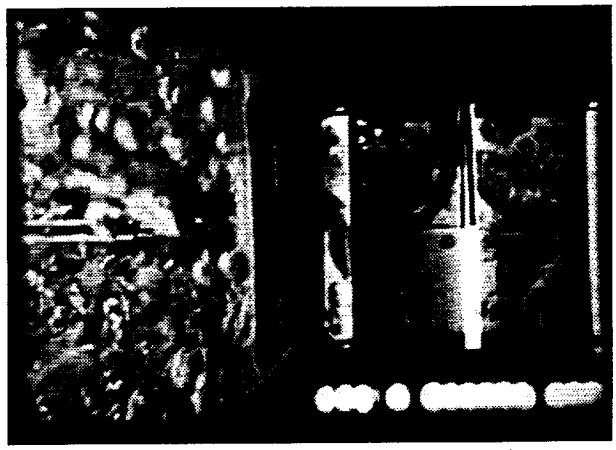

Frame#0852 time=47.75 sec.

Figure B-6g. Continued.

STS-57 Run #8

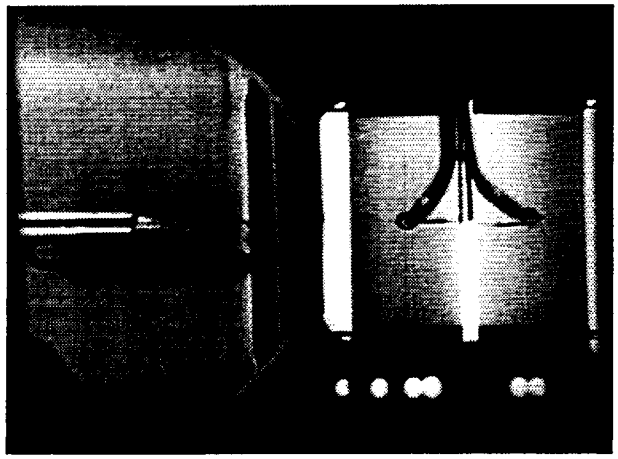

Frame#0920 time=23.77 sec.

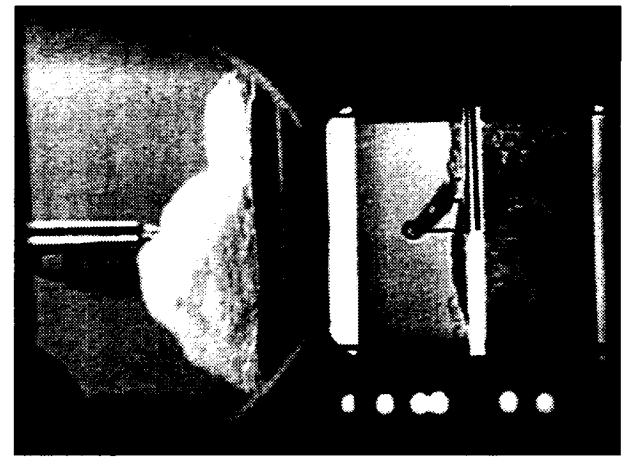

Frame#0921 time=23.78 sec.

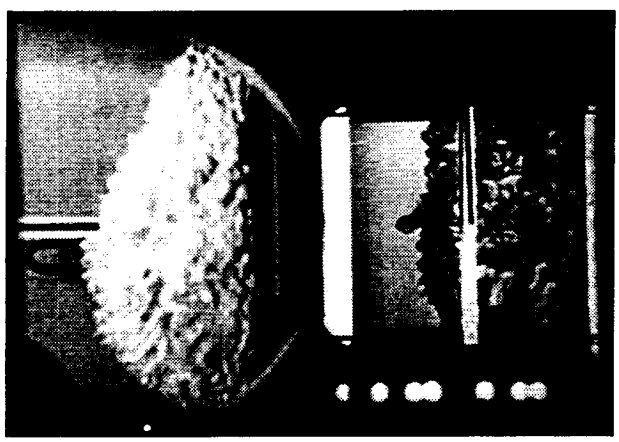

Frame#0924 time=23.81 sec.

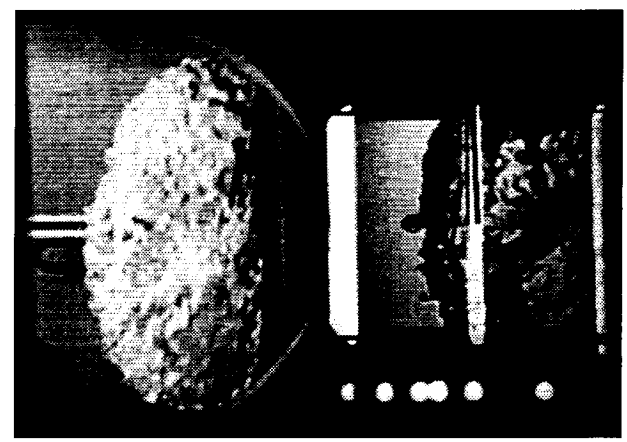

Frame#0927 time=23.84 sec.

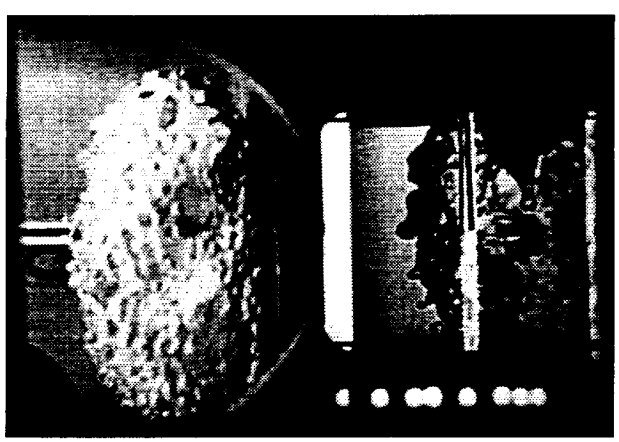

Frame#0930 time=23.87 sec.

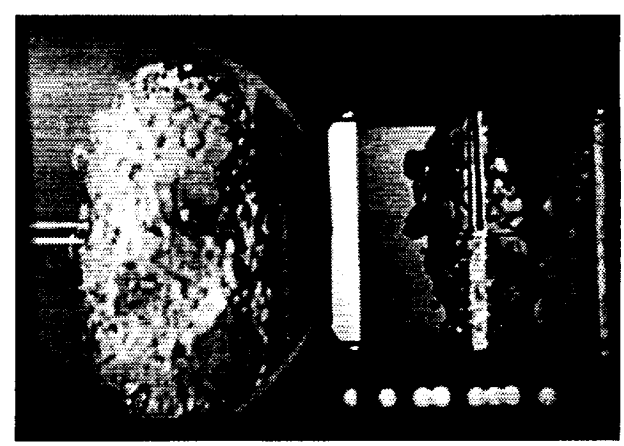

Frame#0933 time=23.90 sec.

Figure B-6h. Selected Photographic Images. PBE-IB (STS-57). Run No. 8.

STS-57 Run #8

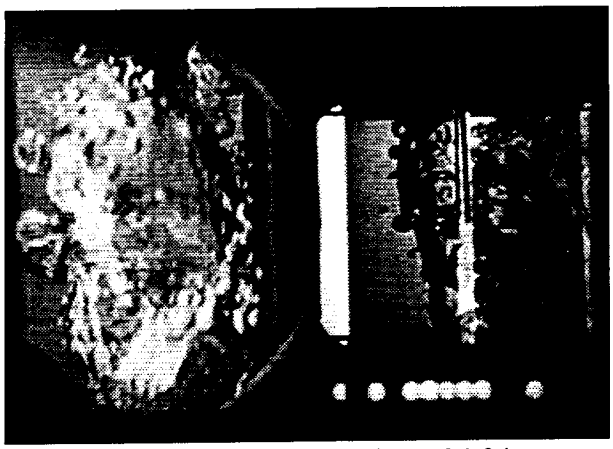

Frame#0947 time=24.04 sec.

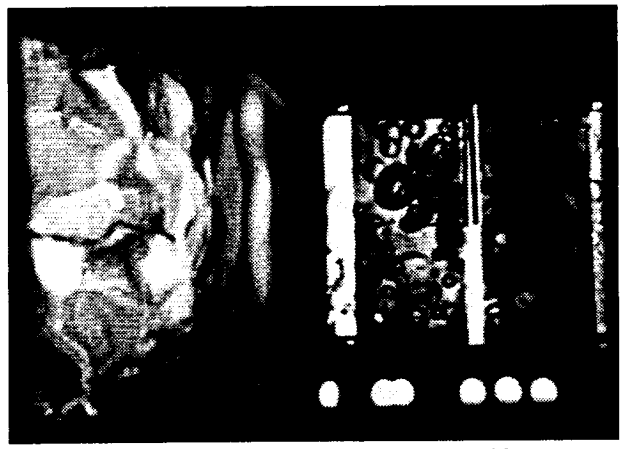

Frame#1157 time=34.42 sec.

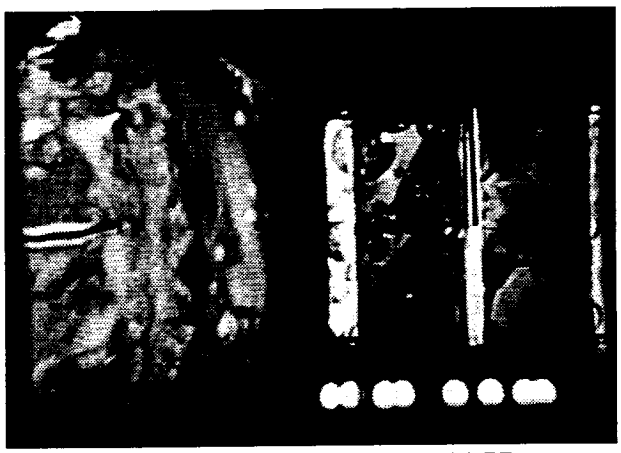

Frame#1263 time=44.77 sec.

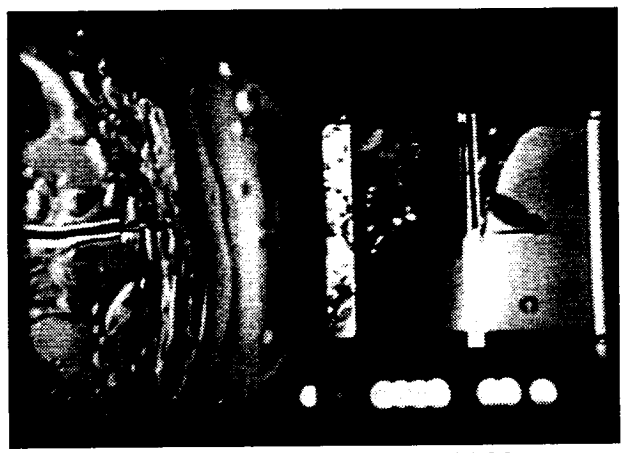

Frame#1376 time=55.82 sec.

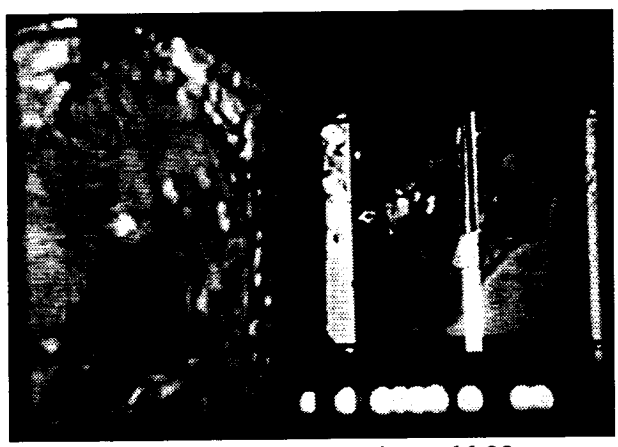

Frame#1481 time=66.09 sec.

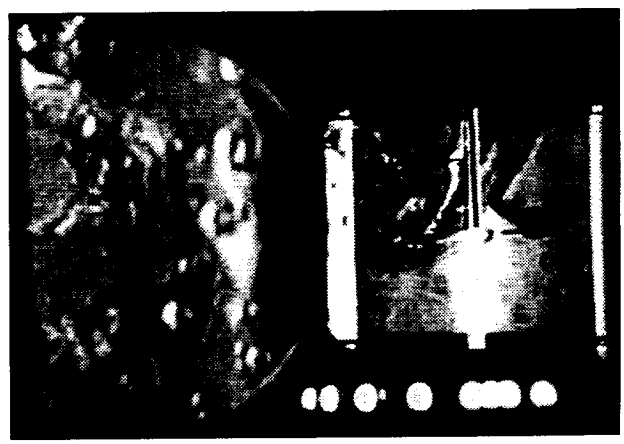

Frame#1596 time=77.34 sec.

Figure B-6h. Continued.

STS-57 Run #9

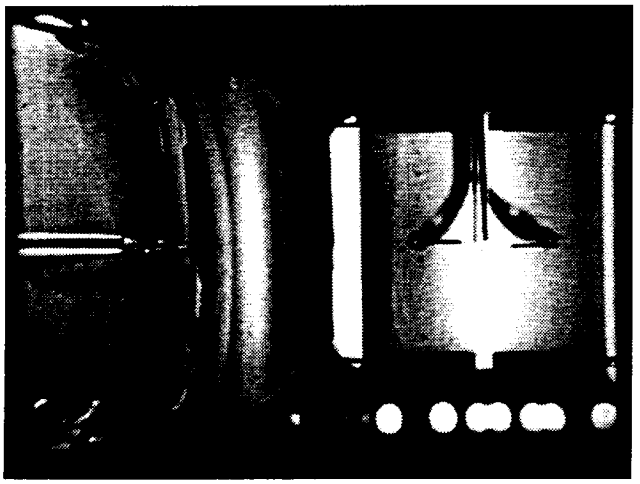

Frame#2672 time=94.93 sec.

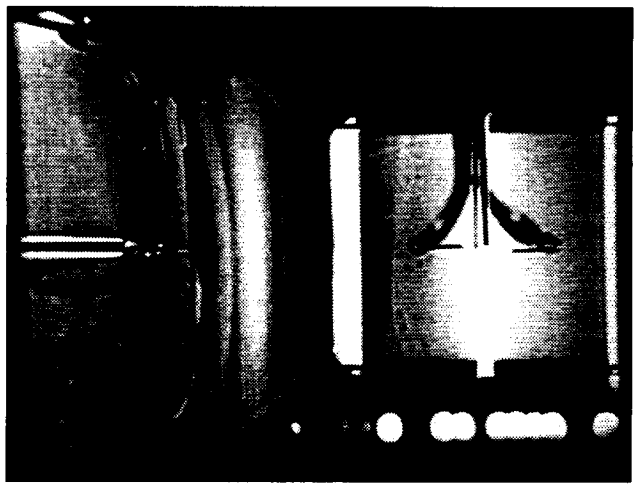

Frame#2673 time=95.03

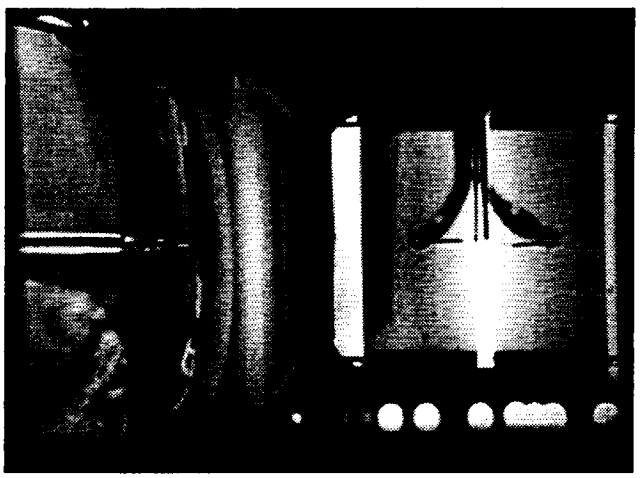

Frame#2675 time=95.23 sec.

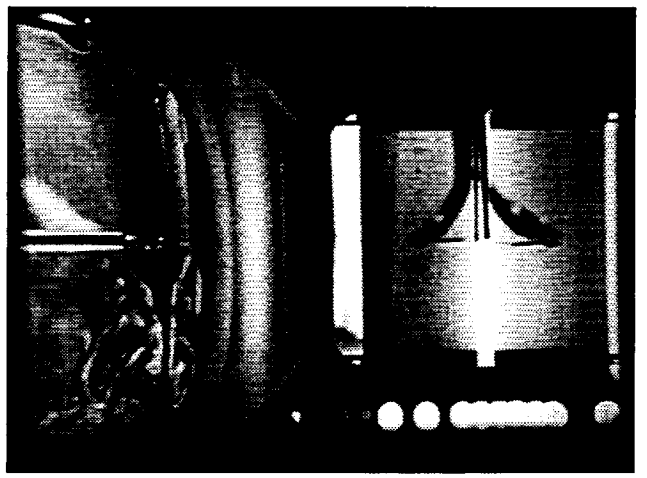

Frame#2677 time=95.43 sec.

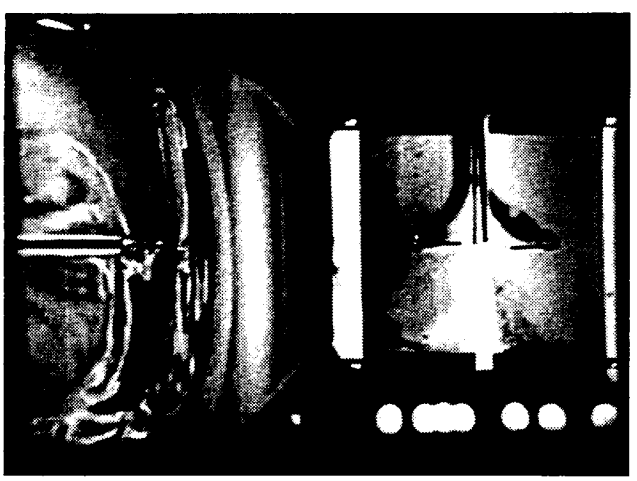

Frame#2679 time=95.62 sec.

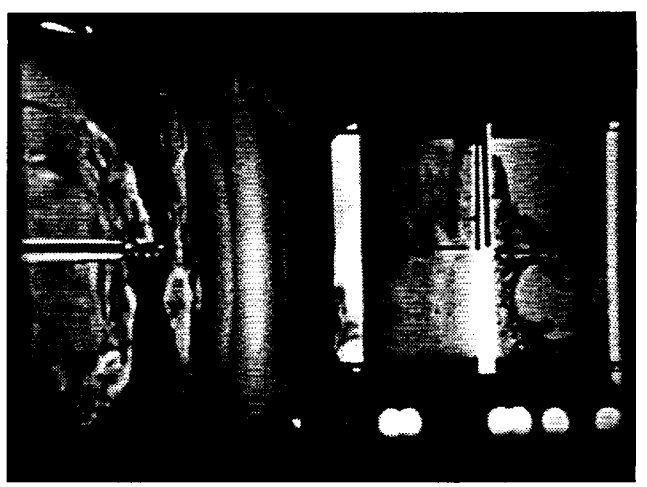

Frame#2681 time=95.82 sec.

Figure B-6i. Selected Photographic Images. PBE-IB (STS-57). Run No. 9.

STS-57 Run #9

Frame#2690 time=96.70 sec.

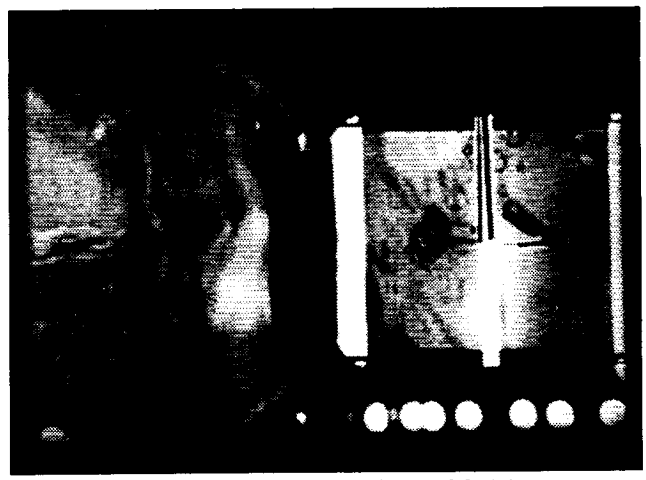

Frame#2715 time=99.14 sec.

Frame#2730 time=100.61 sec.

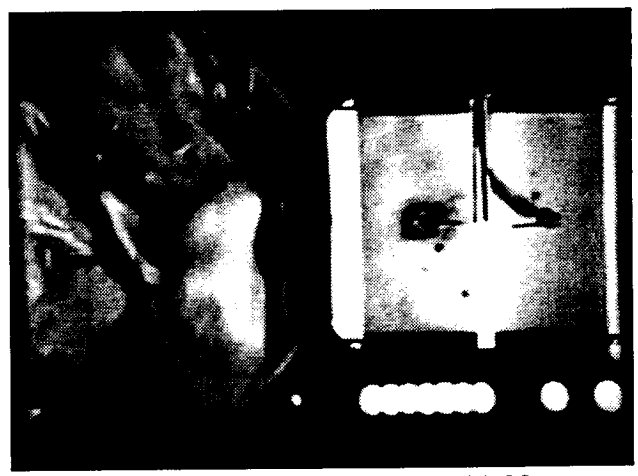

Frame#2745 time=102.08 sec.

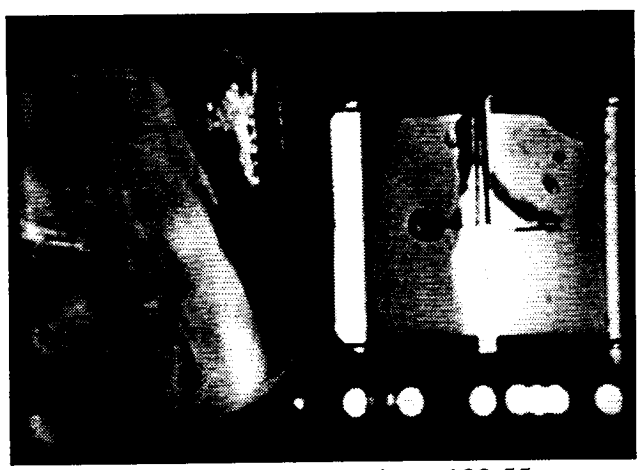

Frame#2760 time=103.55 sec.

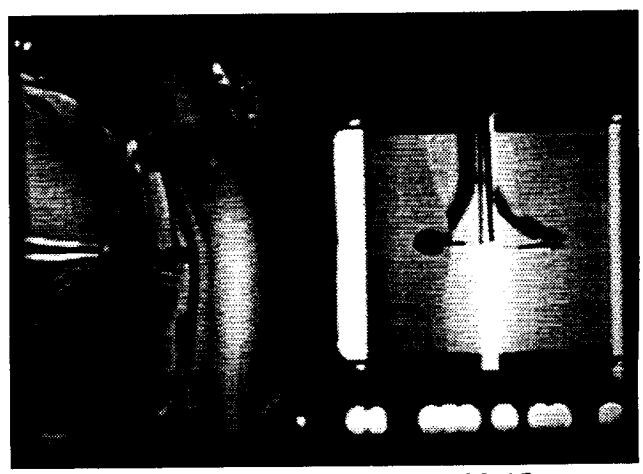

Frame#2810 time=108.45 sec.

Figure B-6i. Continued.

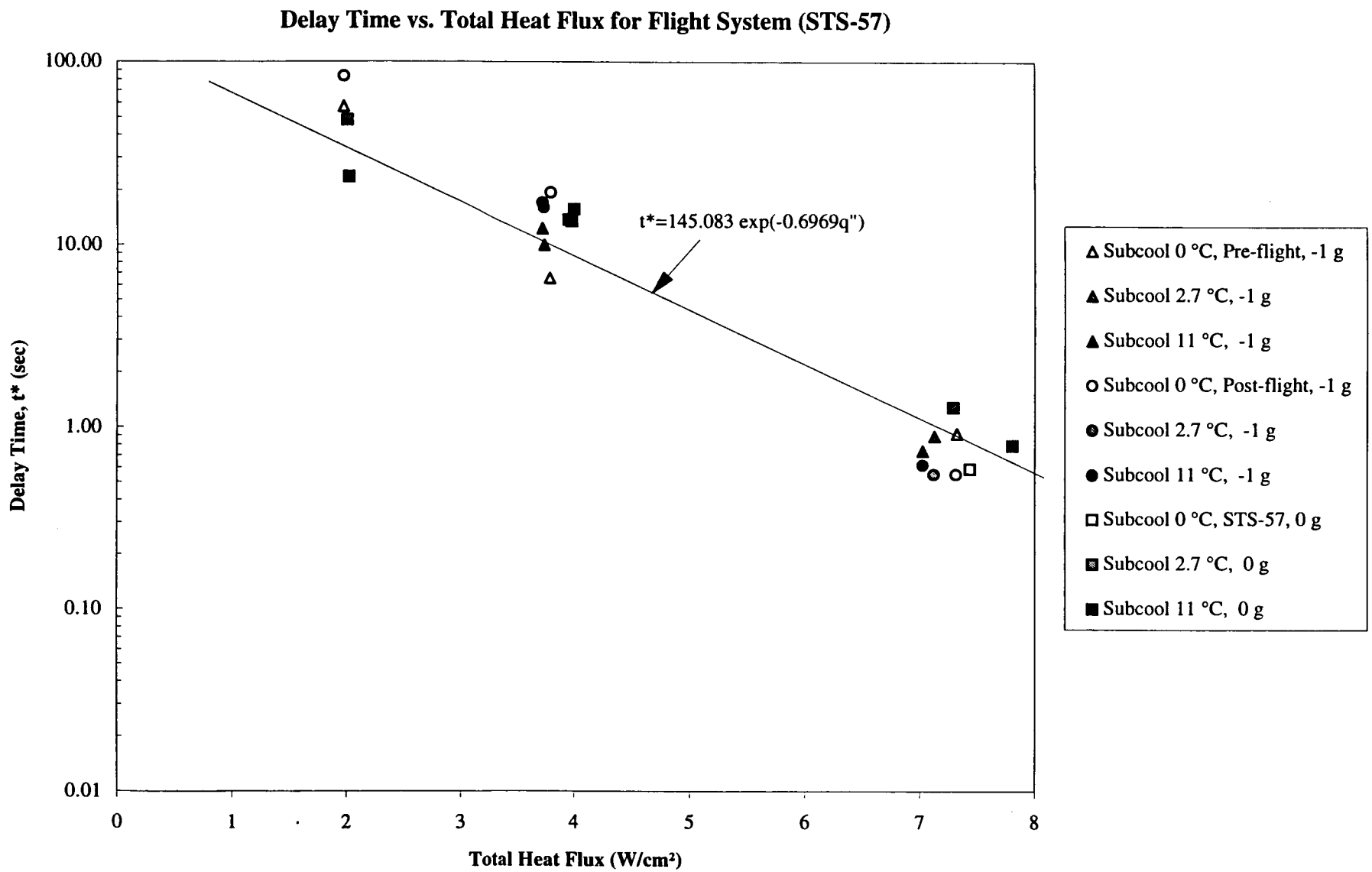

Figure B-7. Nucleation Delay Time. Comparisons with ground testing and drop tower correlation. PBE-IB (STS-57).

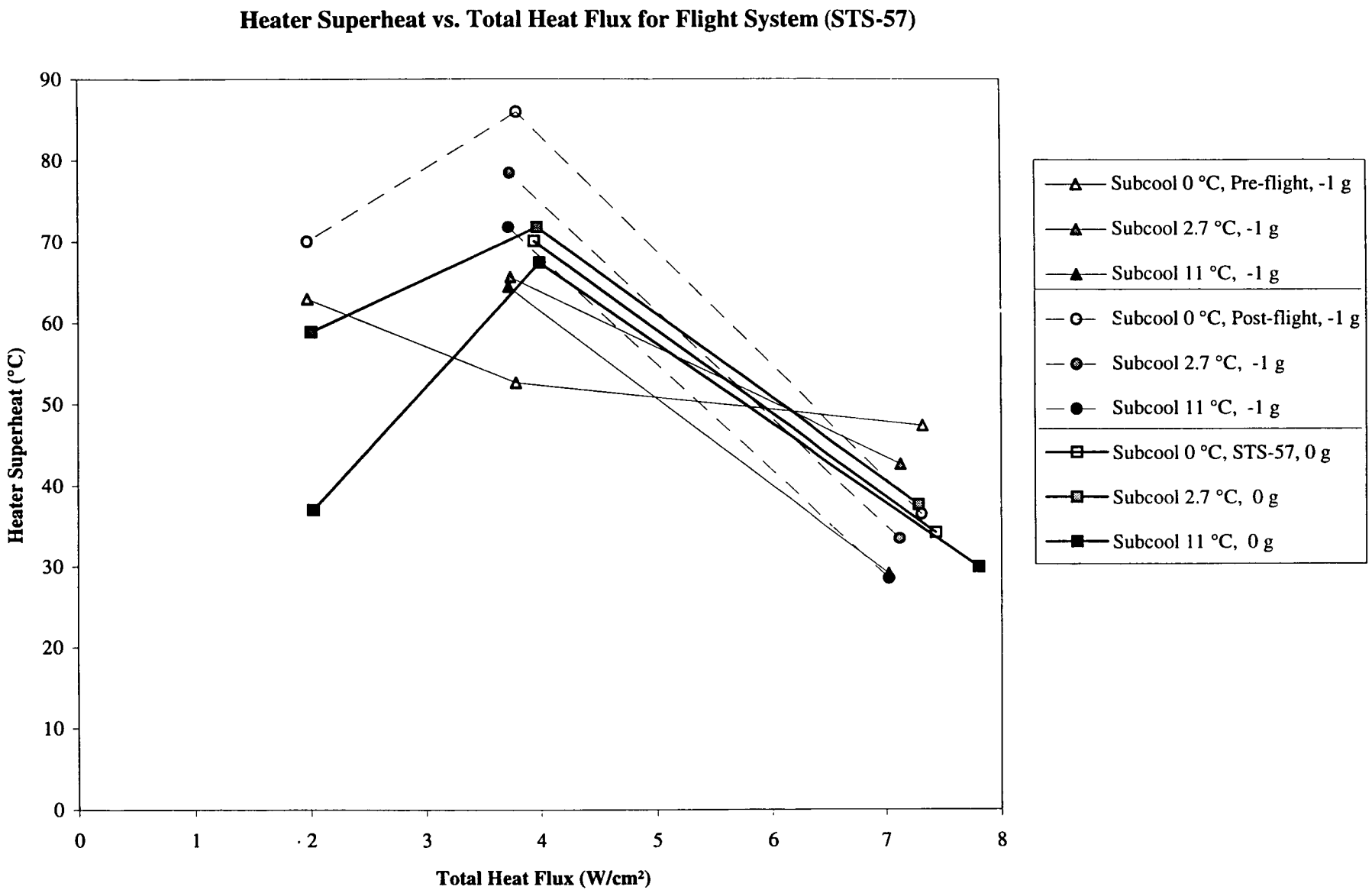

Figure B-8. Mean heater surface nucleation superheat. Comparisons with ground testing. PBE-IB (STS-57).

Comparison of Numerical Computation of Bubble growth with Experiment and Temperature Profile at Nucleation for STS-57 Run #1 (q"=7.8 W/cm²; T_{sat}=58 °C; P=141.66 kPa; ΔT_{sub}=11.0 °C; t*=0.79 sec)

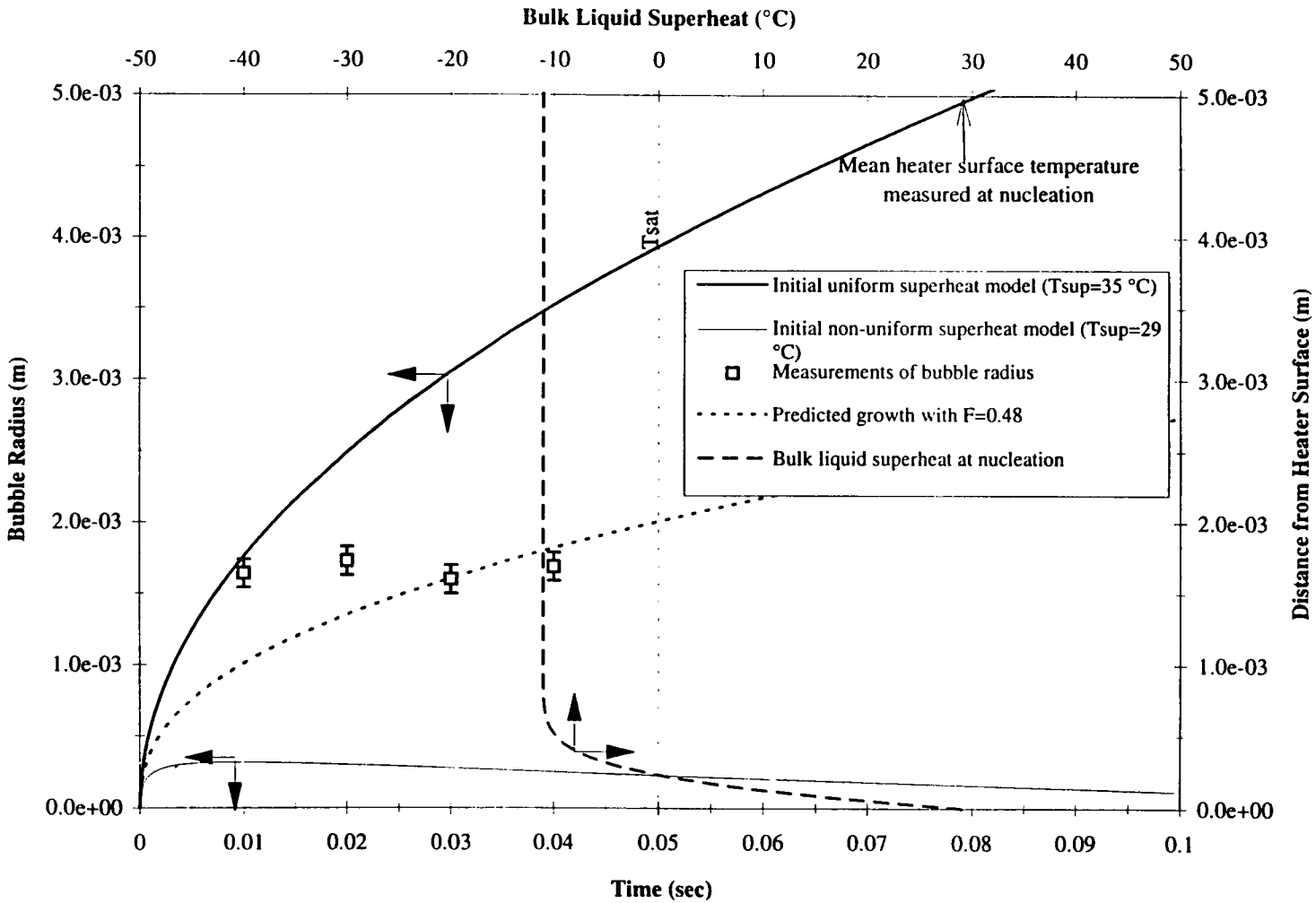

Figure B-9a. Comparisons of bubble growth measurements with several models. PBE-IB (STS-57). Run No. 1.

Comparison of Numerical Computation of Bubble growth with Experiment and Temperature Profile at Nucleation for STS-57 Run #2 (q"=4.0 W/cm²; T_{sat}=60.0 °C; P=151.0 kPa; ΔT_{sub}=11.0 °C; t*=15.71 sec)

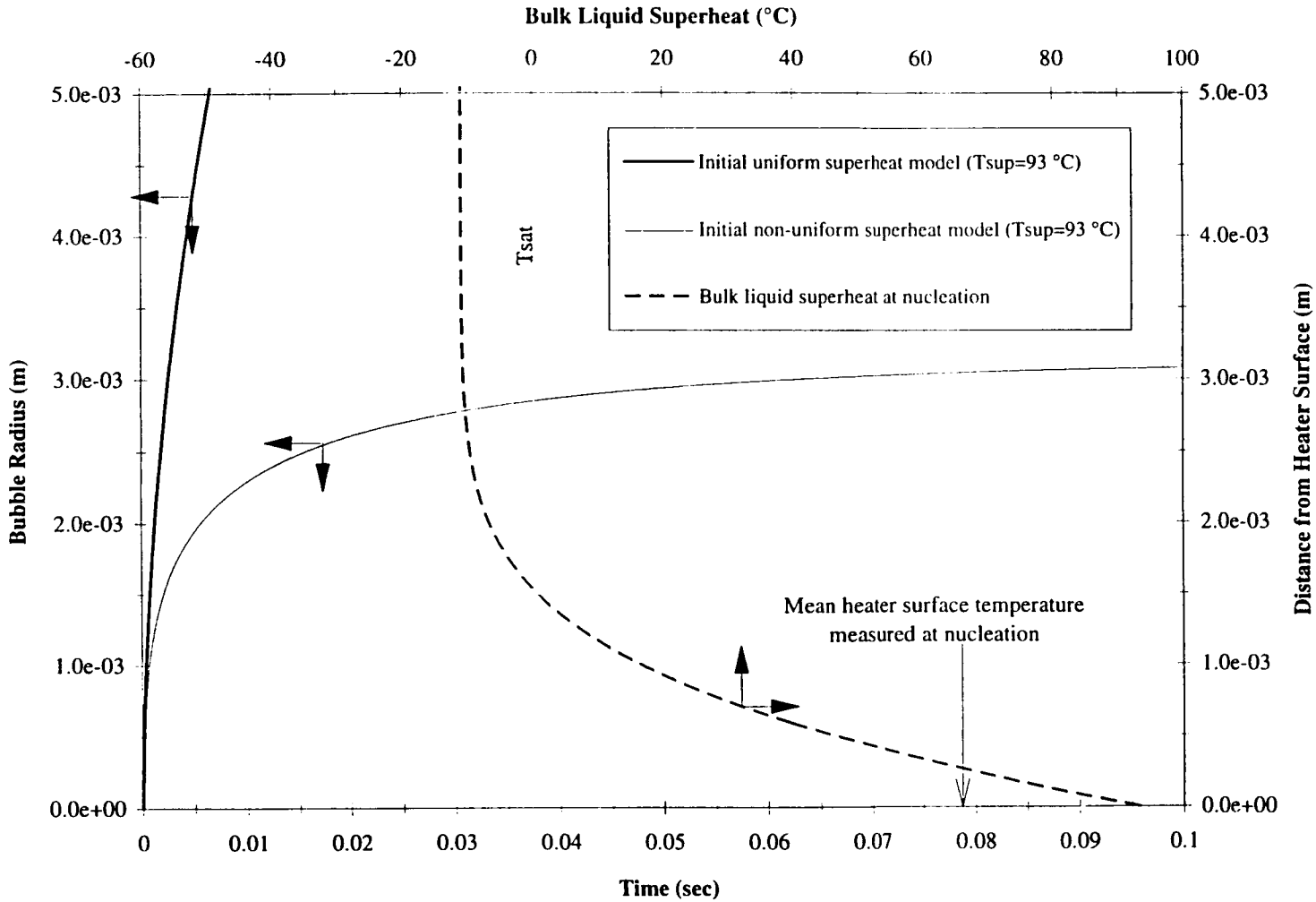

Figure B-9b. Comparisons of bubble growth measurements with several models. PBE-IB (STS-57). Run No. 2.

Comparison of Numerical Computation of Bubble growth with Experiment and Temperature Profile at Nucleation for STS-57 Run #3 (q"=2.0 W/cm²; T_{sat}=59.7 °C; P=149.26 kPa; ΔT_{sub}=11.0 °C; t*=23.63 sec)

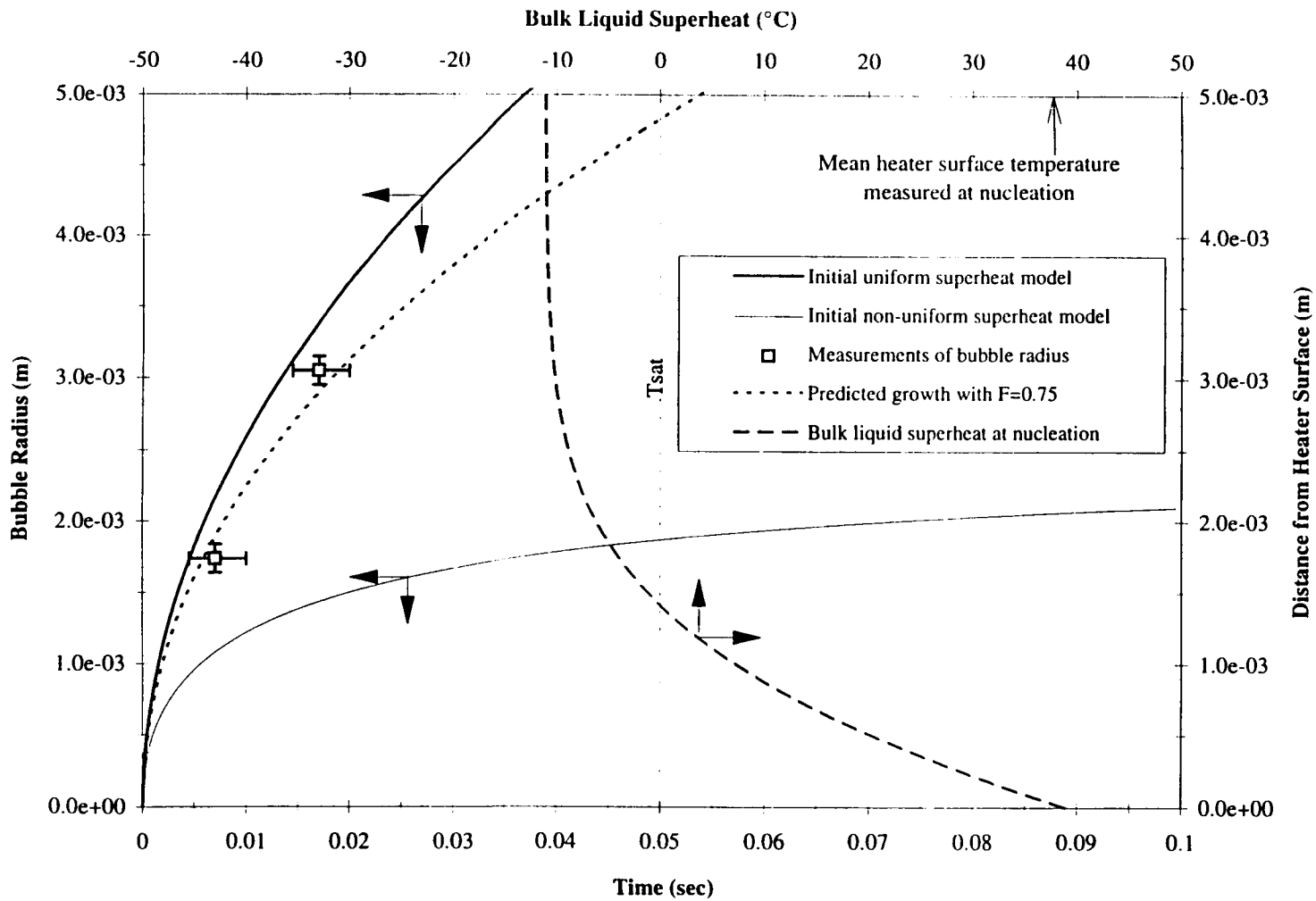

Figure B-9c. Comparisons of bubble growth measurements with several models. PBE-IB (STS-57). Run No. 3.

Comparison of Numerical Computation of Bubble growth with Experiment and Temperature Profile at Nucleation for STS-57 Run #4 (q"=7.28 W/cm²; T_{sat}=51.32 °C; P=114.8 kPa; ΔT_{sub}=2.7 °C; t*=1.28 sec)

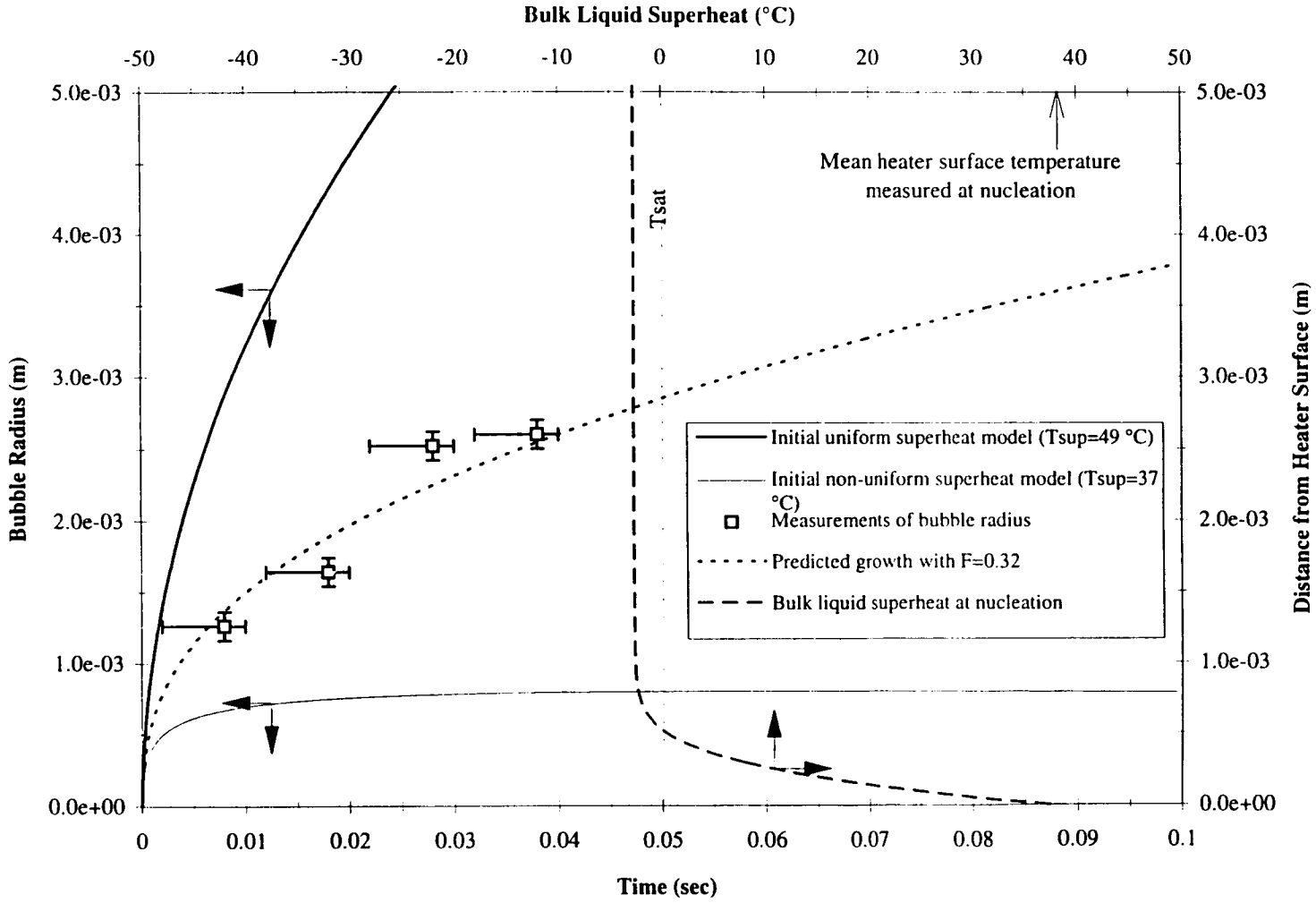

Figure B-9d. Comparisons of bubble growth measurements with several models. PBE-IB (STS-57). Run No. 4.

Comparison of Numerical Computation of Bubble growth with Experiment and Temperature Profile at Nucleation for STS-57 Run #5 (q"=3.98 W/cm²; T_{sat}=51.69 °C; P=116.17 kPa; ΔT_{sub}=2.7 °C; t*=13.51 sec)

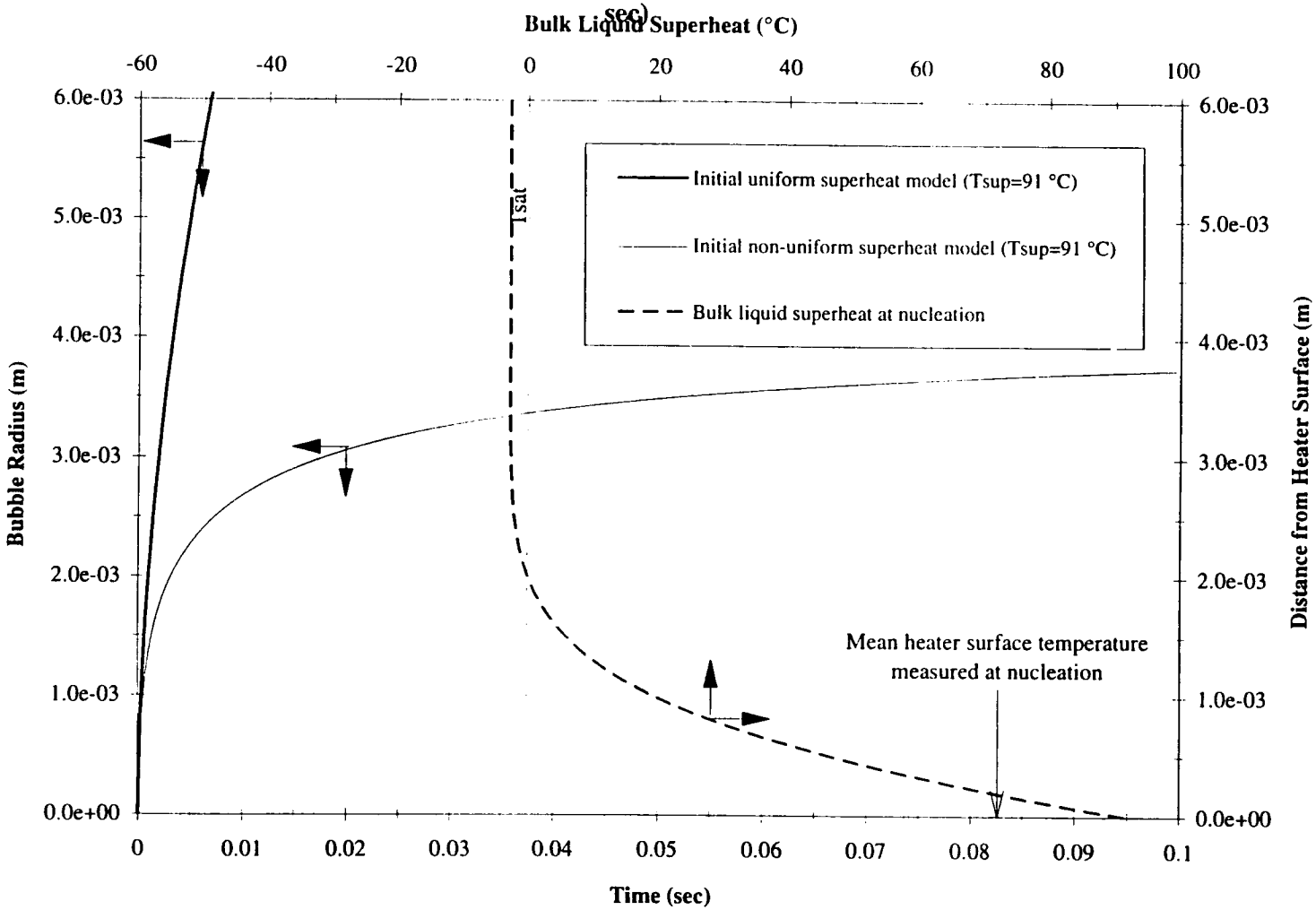

Figure B-9e. Comparisons of bubble growth measurements with several models. PBE-IB (STS-57). Run No. 5.

Comparison of Numerical Computation of Bubble growth with Experiment and Temperature Profile at Nucleation for STS-57 Run #6 (q"=2.0 W/cm²; T_{sat}=51.61 °C; P=116.3 kPa; ΔT_{sub}=2.7 °C; t*=48.36 sec)

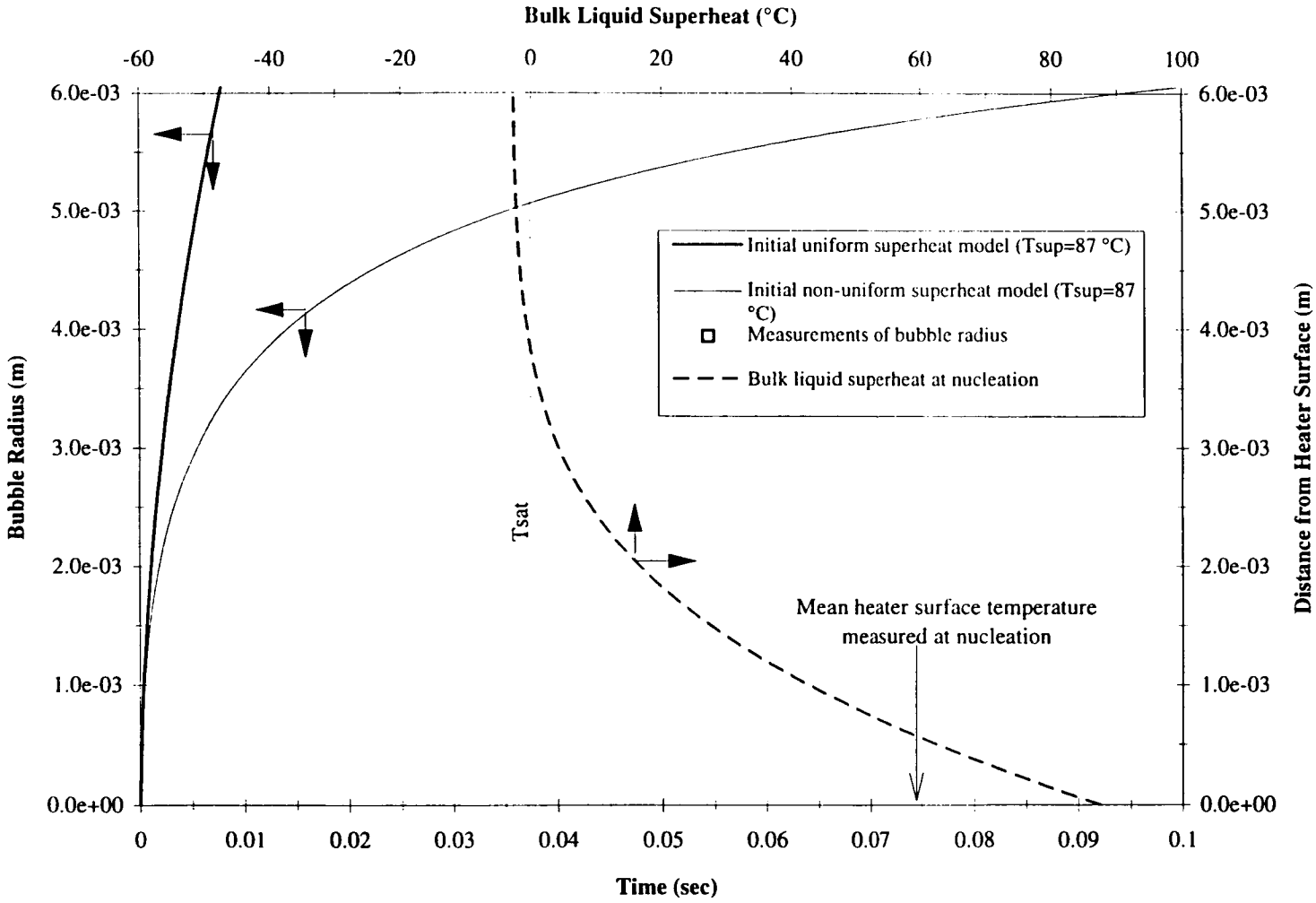

Figure B-9f. Comparisons of bubble growth measurements with several models. PBE-IB (STS-57). Run No. 6.

Comparison of Numerical Computation of Bubble growth with Experiment and Temperature Profile at Nucleation for STS-57 Run #7 (q"=7.433 W/cm²; T_{sat}=48.8 °C; P=105.63 kPa; ΔT_{sub}=0.18 °C; t*=0.59 sec)

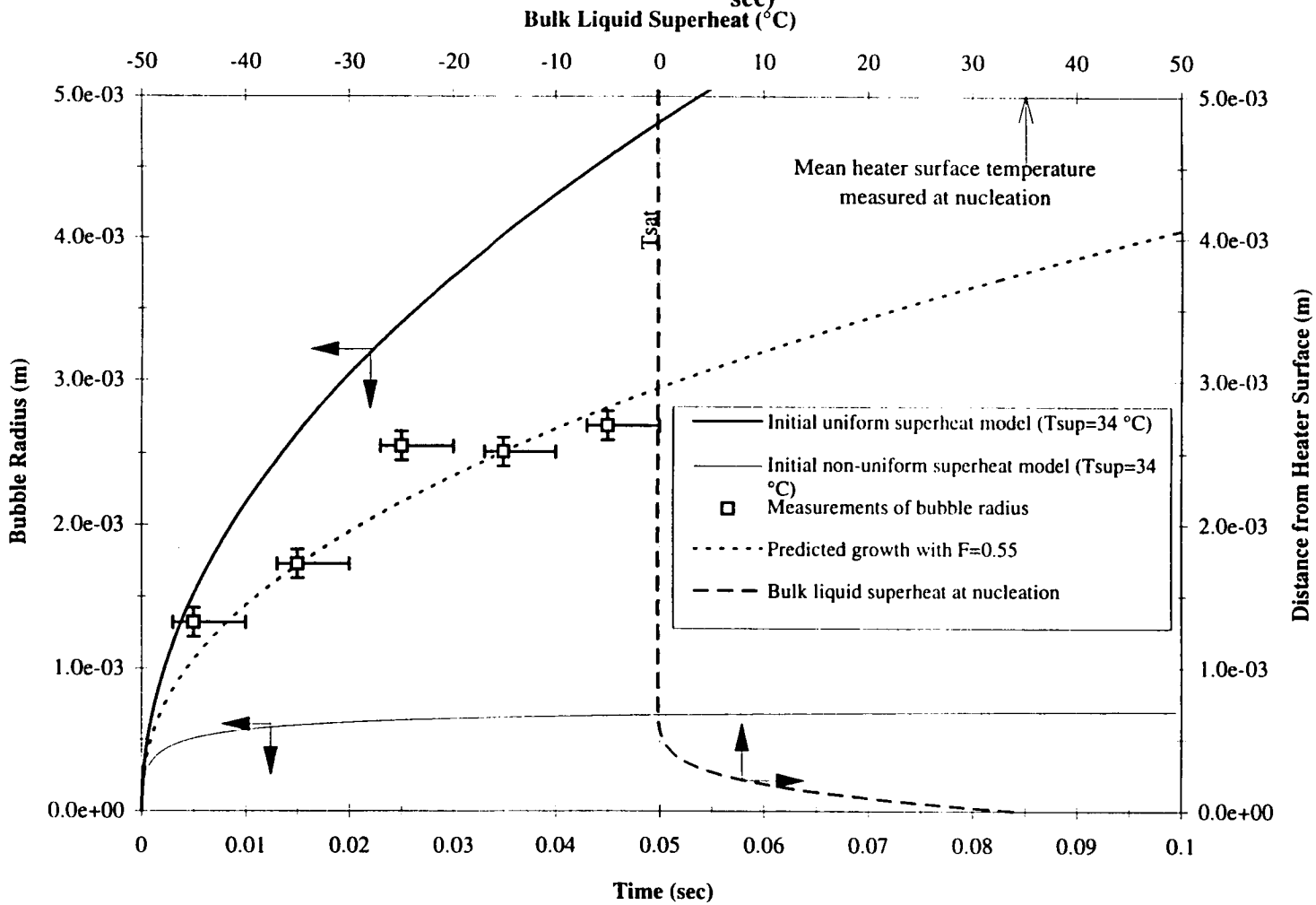

Figure B-9g. Comparisons of bubble growth measurements with several models. PBE-IB (STS-57). Run No. 7.

Comparison of Numerical Computation of Bubble growth with Experiment and Temperature Profile at Nucleation for STS-57 Run #8 (q"=3.95 W/cm²; T_{sat}=49.0 °C; P=106.45 kPa; ΔT_{sub}=0.28 °C; t*=13.77 sec)

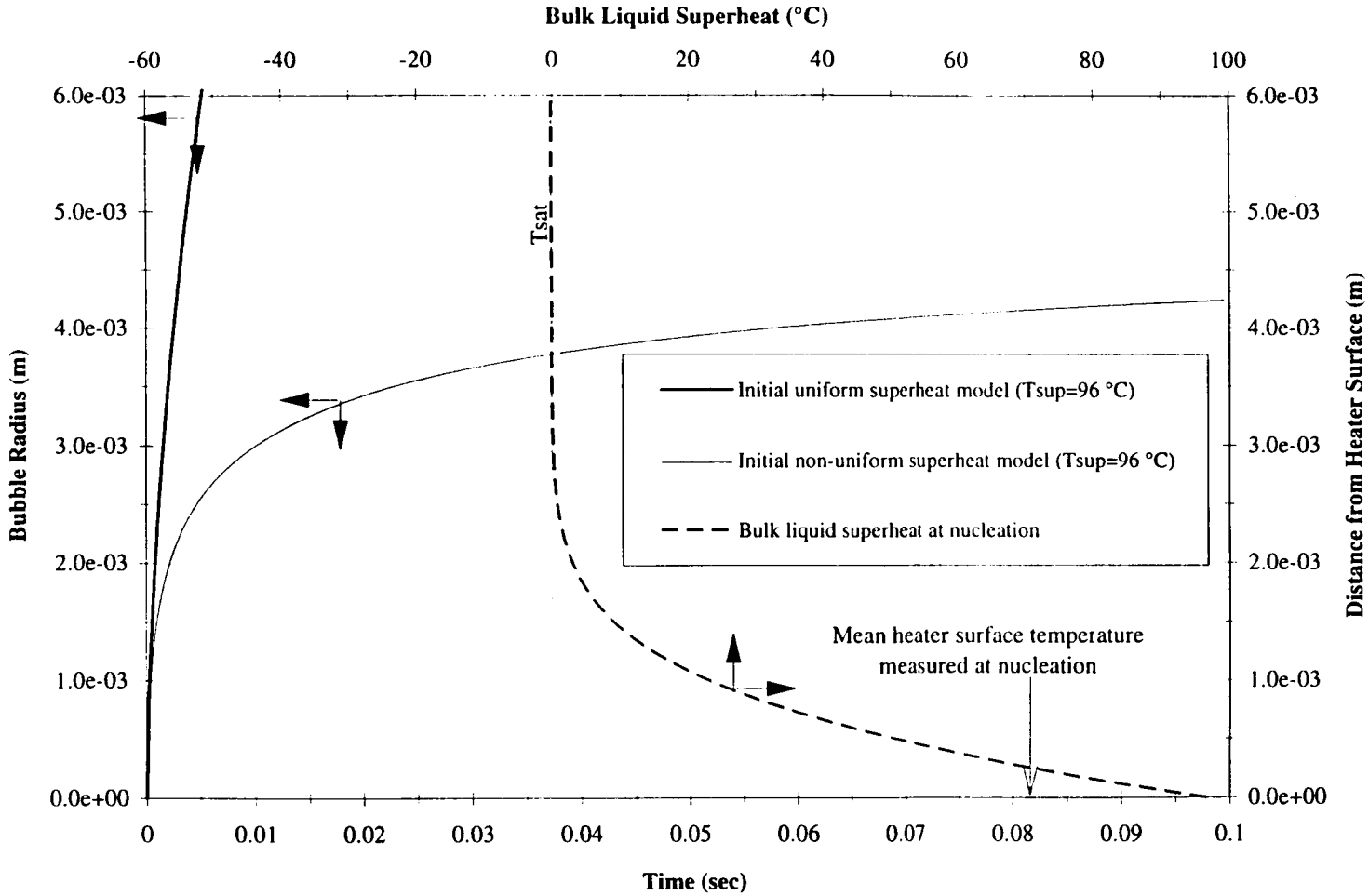

Figure B-9h. Comparisons of bubble growth measurements with several models. PBE-IB (STS-57). Run No. 8.

Run #	10 FPS	100 FPS	Nucleation	Range	Rate	Total # Frames	Analysis # Frames	Notes	Data Storage
1	15-80	10-15	10.79	nuc-20	both	500	200	MSC	OD2-A
				20-30	10 fps	100	100	JAJ	OD2-A
				30-40	10 fps	100	100	JAJ	OD2-A
				40-50	10 fps	100	100	JAJ	OD2-A
2	10--15	15--25	25.71	nuc.--50	10 fps	243	243	JAJ	OD2-B
	25--135			90-100	10 fps	100	100	JAJ	OD2-B
3	20--30	30--50	33.63	nuc.--60	both	1737	200	JAJ	OD2-B
	50--130			70-90	10 fps	200	200	JAJ	OD2-B
4	15-65	10-15	11.28	nuc.--20	both	422	200	JAJ	OD3-B
5	10-15	15-25	23.51	nuc.--50	both	399	200	JAJ	OD3-B
	25-105			60-80	10 fps	200	200	JAJ	OD3-B
6	20--30	30--50	58.36	nuc.--70	both	120	120	JAJ	OD2-A
	50--100			80-85	10 fps	50	50	JAJ	OD2-B
7	15-65	10-15	10.59	nuc.--15	100 fps	441	200	JAJ	OD3-B
8	10--15	15--25	23.77	nuc.--50	both	373	145	JAJ	OD2-B
	25--80								
9	10-30	30-50							
	50-125								

**Note: All times are relative to ZERO. Heater power is active at 10 sec;

Table B-IV. Index for heater surface dry fraction measurements and computation of microgravity nucleate boiling heat transfer coefficients. PBE-IB (STS-57).

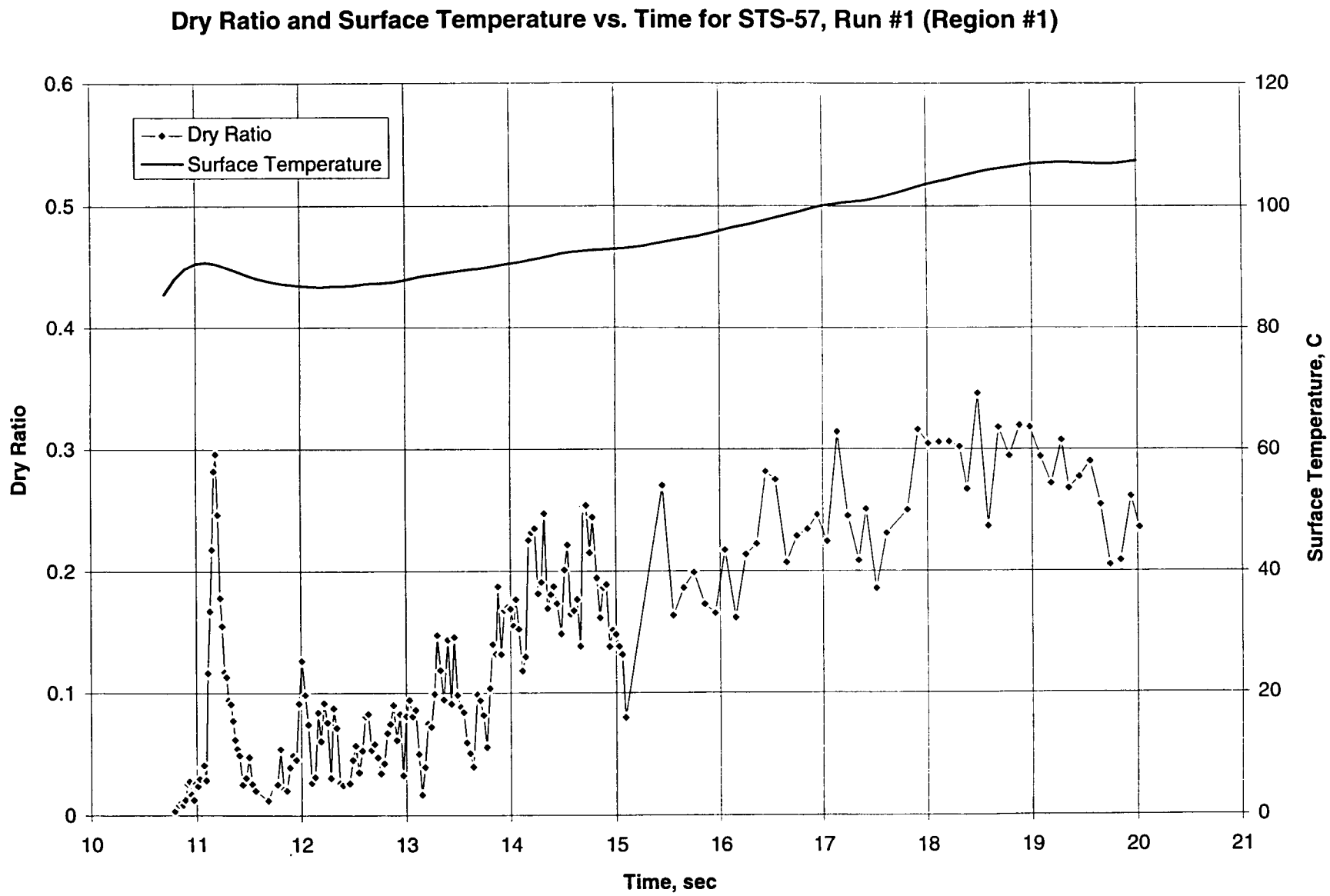

Figure B-10a-1-i. Heater surface dry fraction and mean temperature. PBE-IB (STS-57). Run No. 1. Time interval: 10.8 - 20.0 seconds.

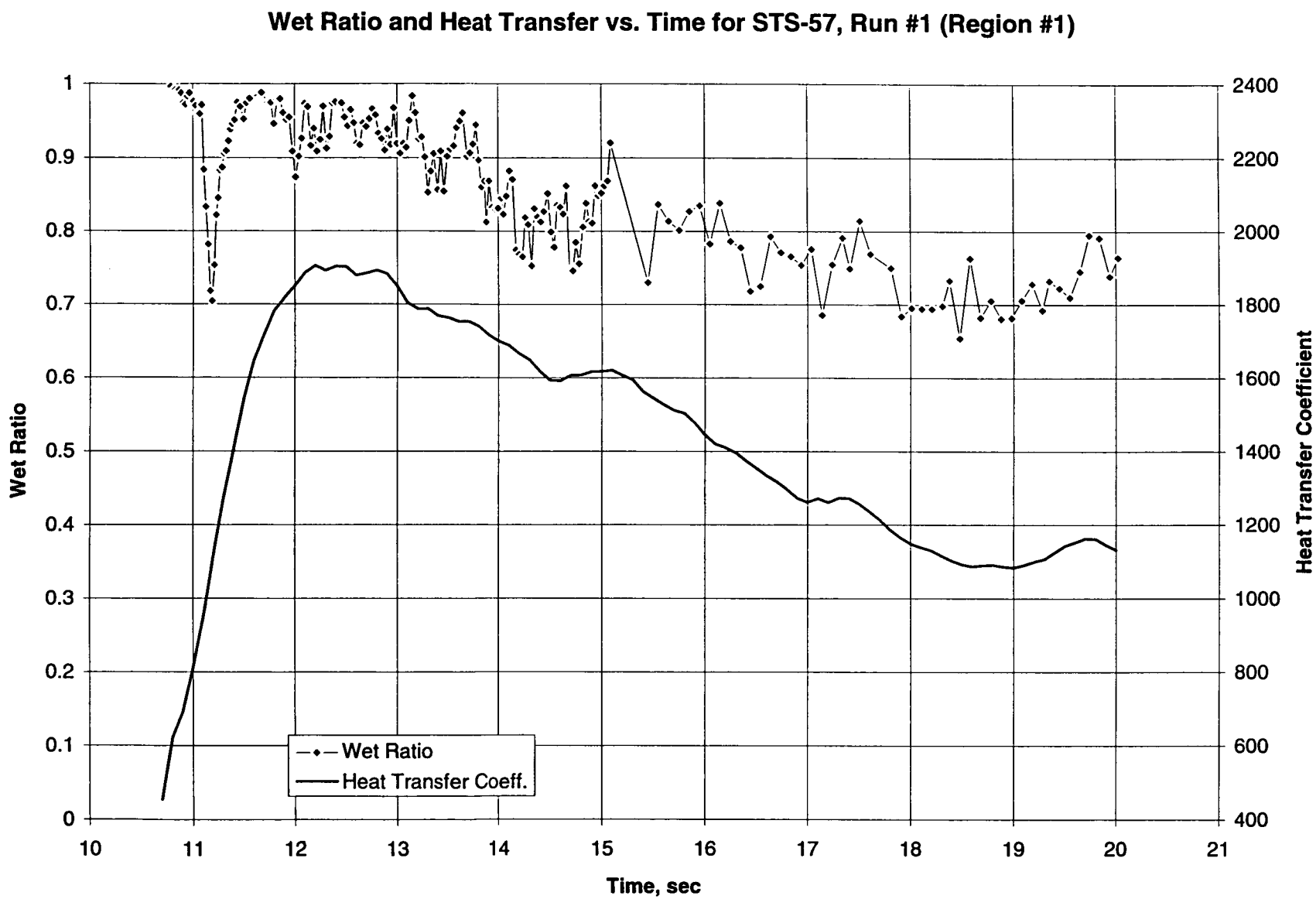

Figure B-10a-1-ii. Heater surface wet fraction and mean heat transfer coefficients. PBE-IB (STS-57). Run No. 1. Time interval: 10.8 - 20.0 seconds.

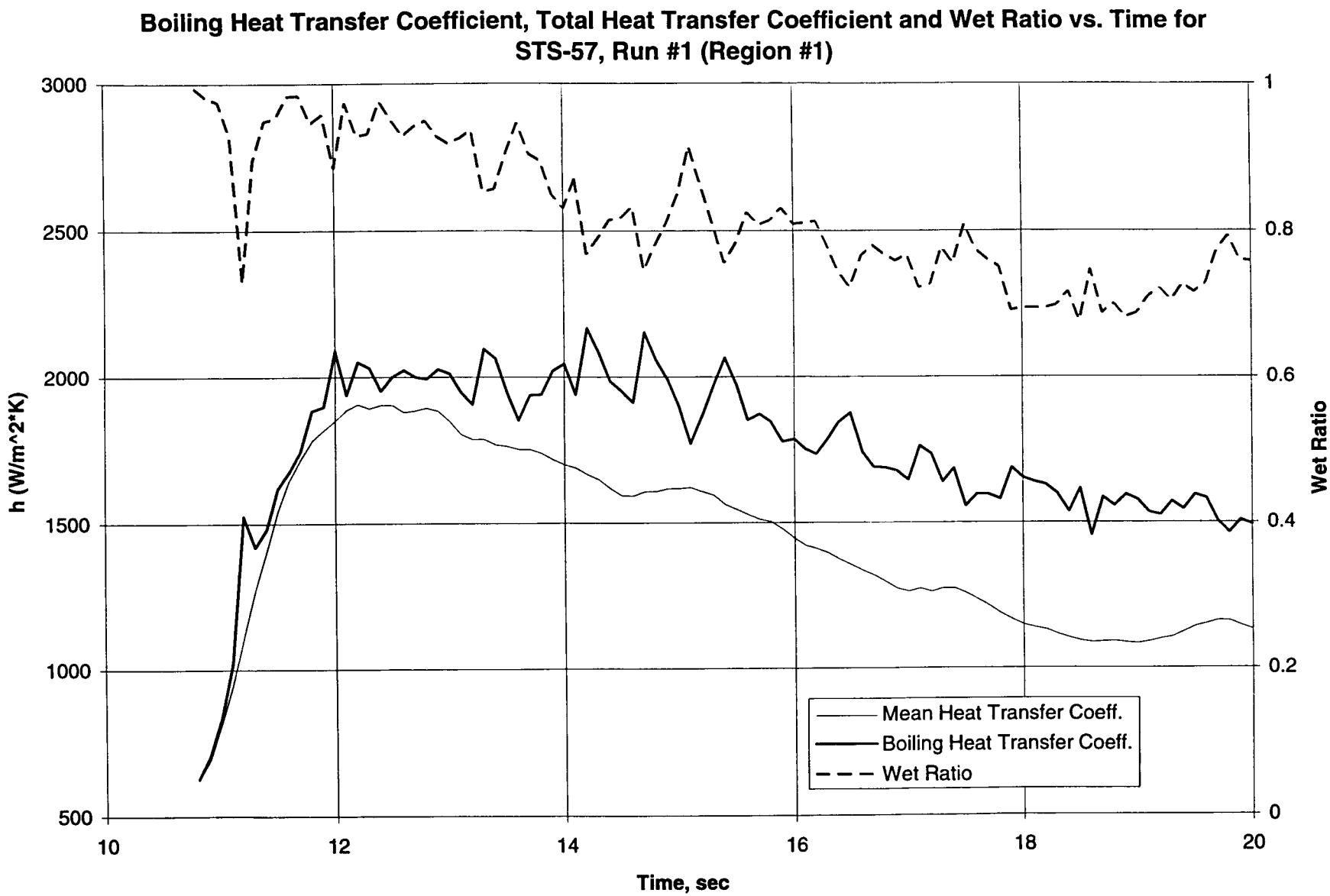

Figure B-10a-1-iii. Development of microgravity boiling heat transfer coefficient. PBE-IB (STS-57). Run No. 1. Time interval: 10.8 - 20.0 seconds.

STS-57 Run #1 (Region #1)

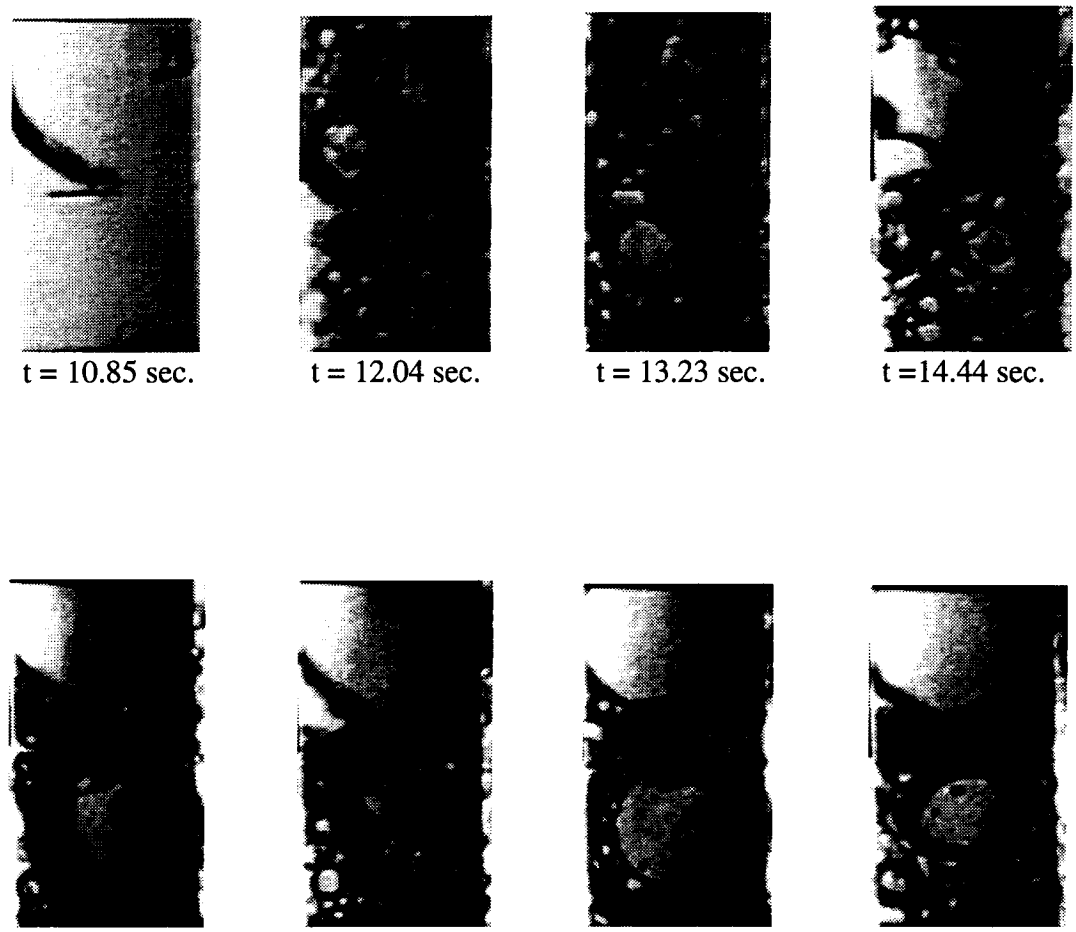

Figure B-10a-1-iv. Sample images showing dryout/rewetting. PBE-IB (STS-57). Run No. 1. Time interval: 10.8 - 20.0 seconds.

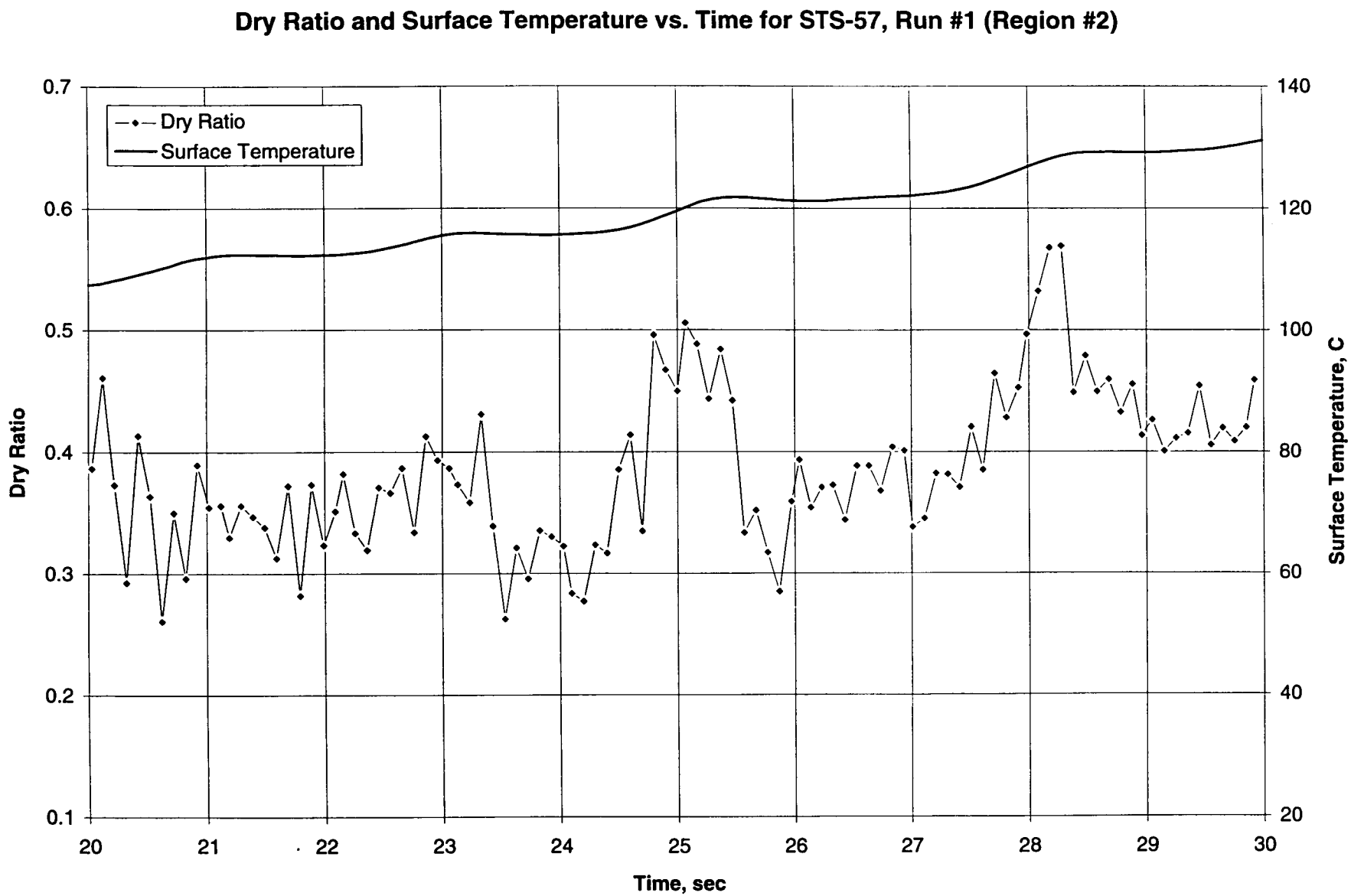

Figure B-10a-2-i. Heater surface dry fraction and mean temperature. PBE-IB (STS-57). Run No. 1. Time interval: 20 - 30 seconds.

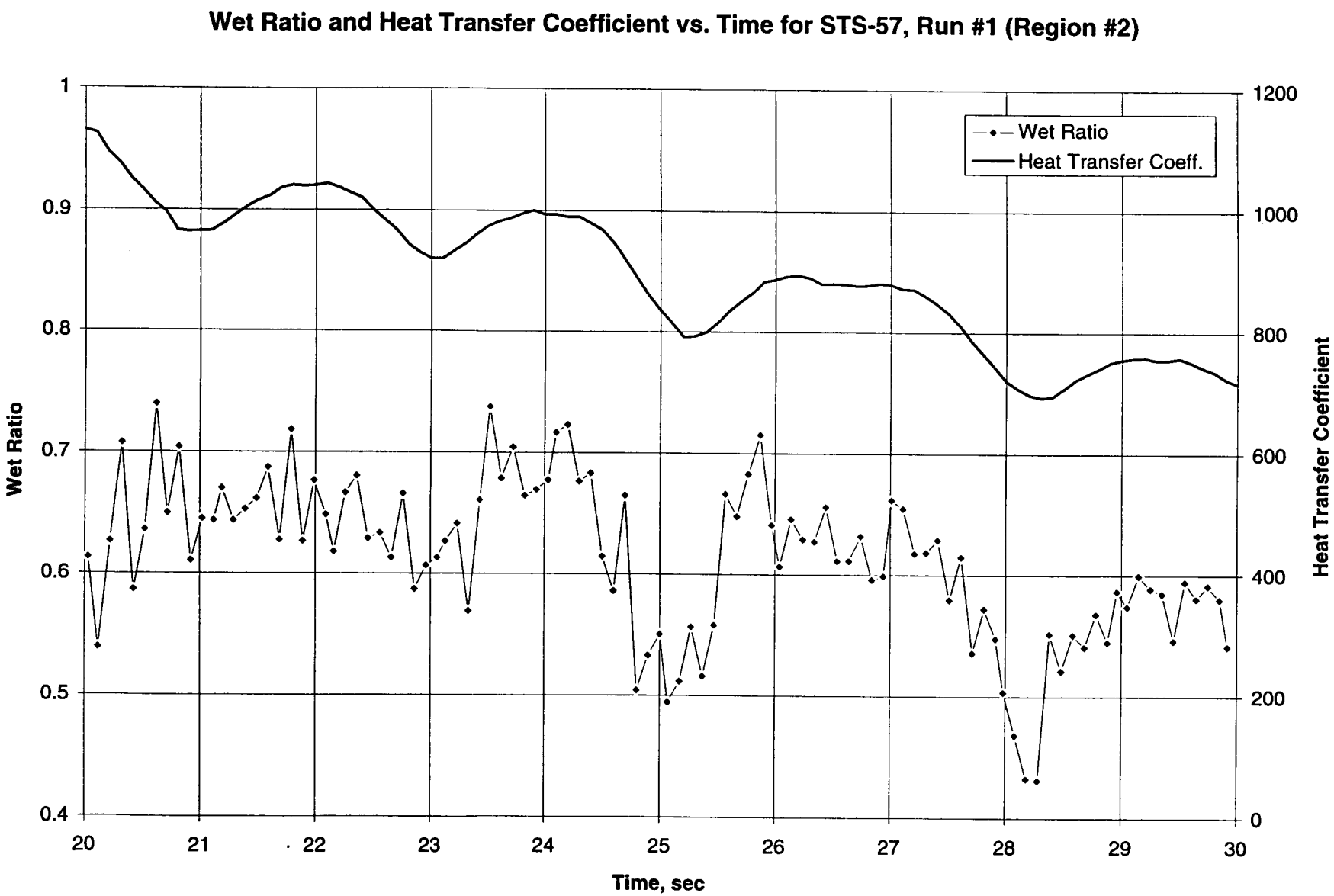

Figure B-10a-2-ii. Heater surface wet fraction and mean heat transfer coefficients. PBE-IB (STS-57). Run No. 1. Time interval: 20 - 30 seconds.

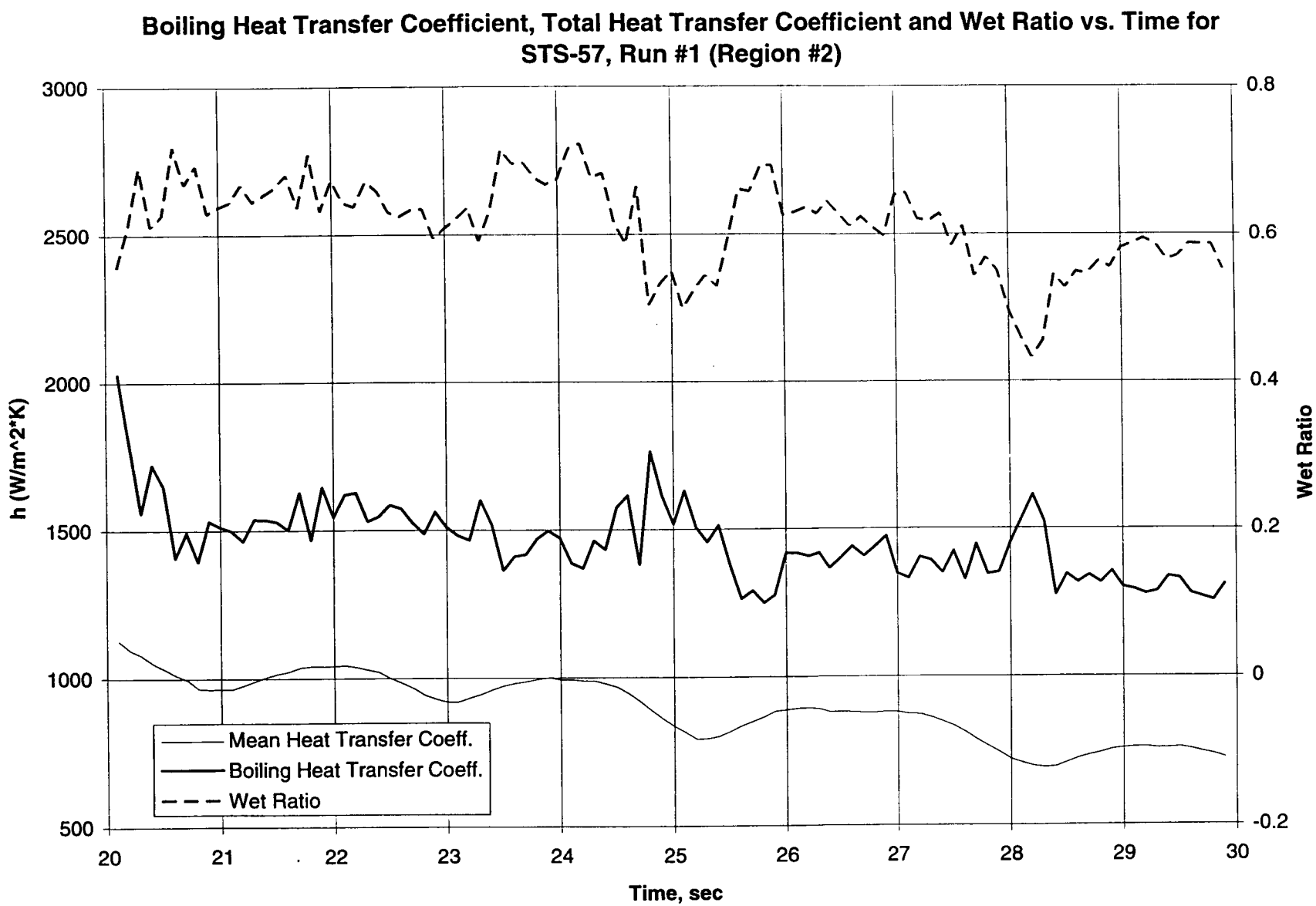

Figure B-10a-2-iii. Development of microgravity boiling heat transfer coefficient. PBE-IB (STS-57). Run No. 1. Time interval: 20 - 30 seconds.

STS-57 Run #1 (Region #2)

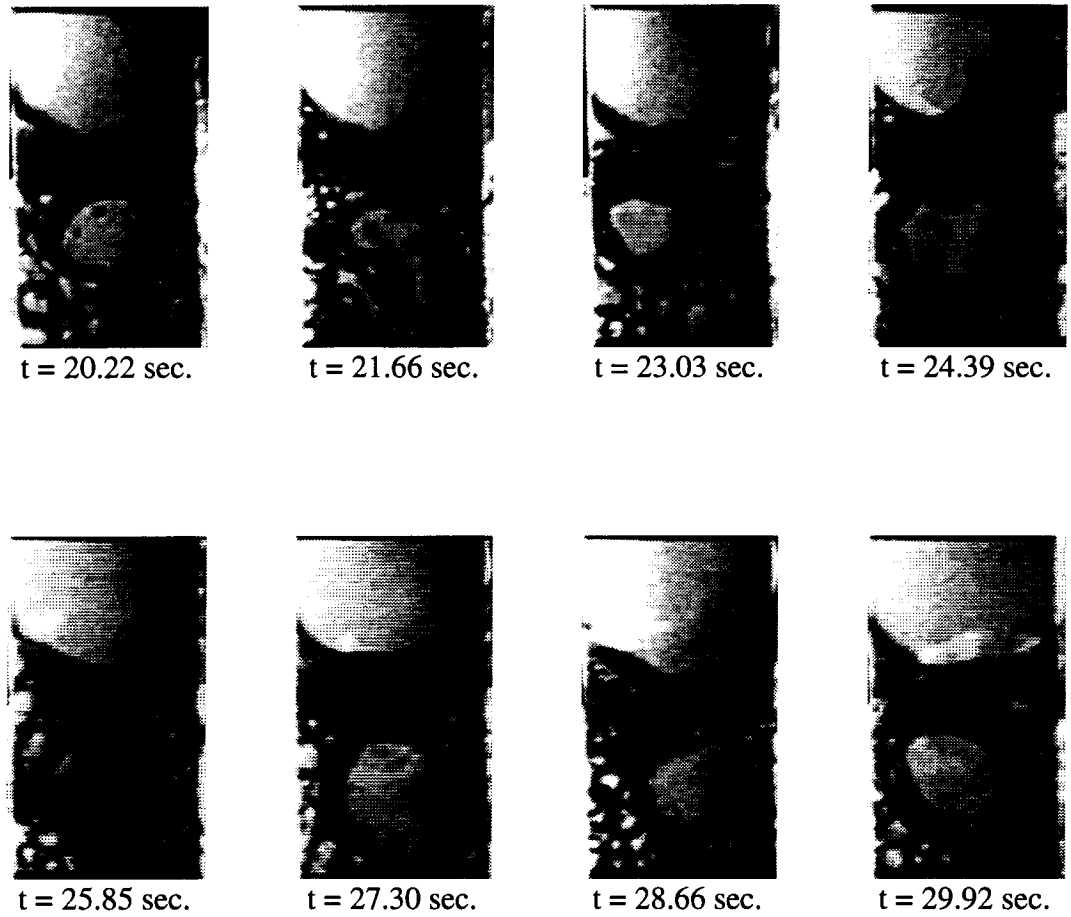

Figure B-10a-2-iv. Sample images showing dryout/rewetting. PBE-IB (STS-57). Run No. 1. Time interval: 20 - 30 seconds.

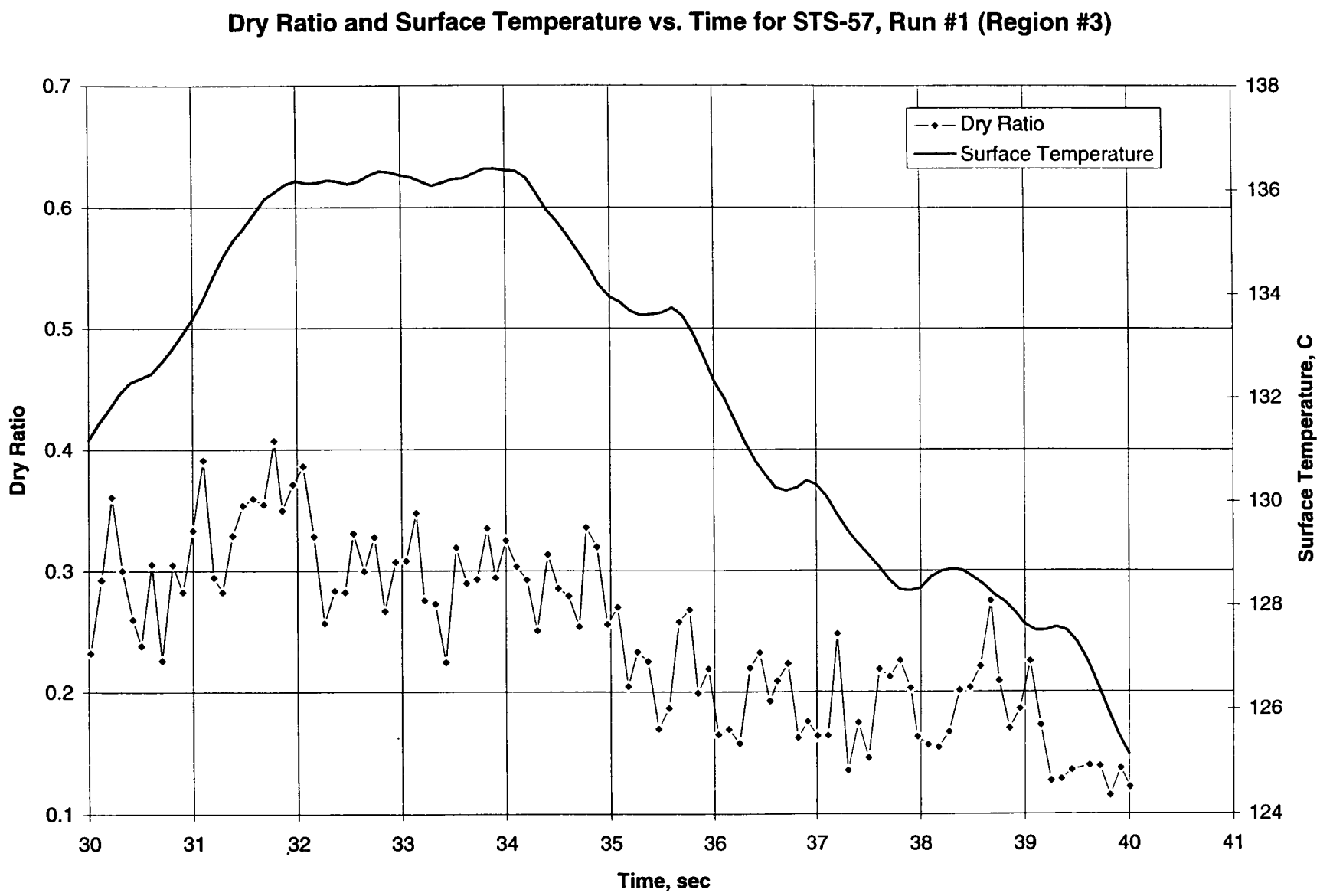

Figure B-10a - 3-i. Heater surface dry fraction and mean temperature. PBE-IB (STS-57). Run No. 1. Time interval: 30 - 40 seconds.

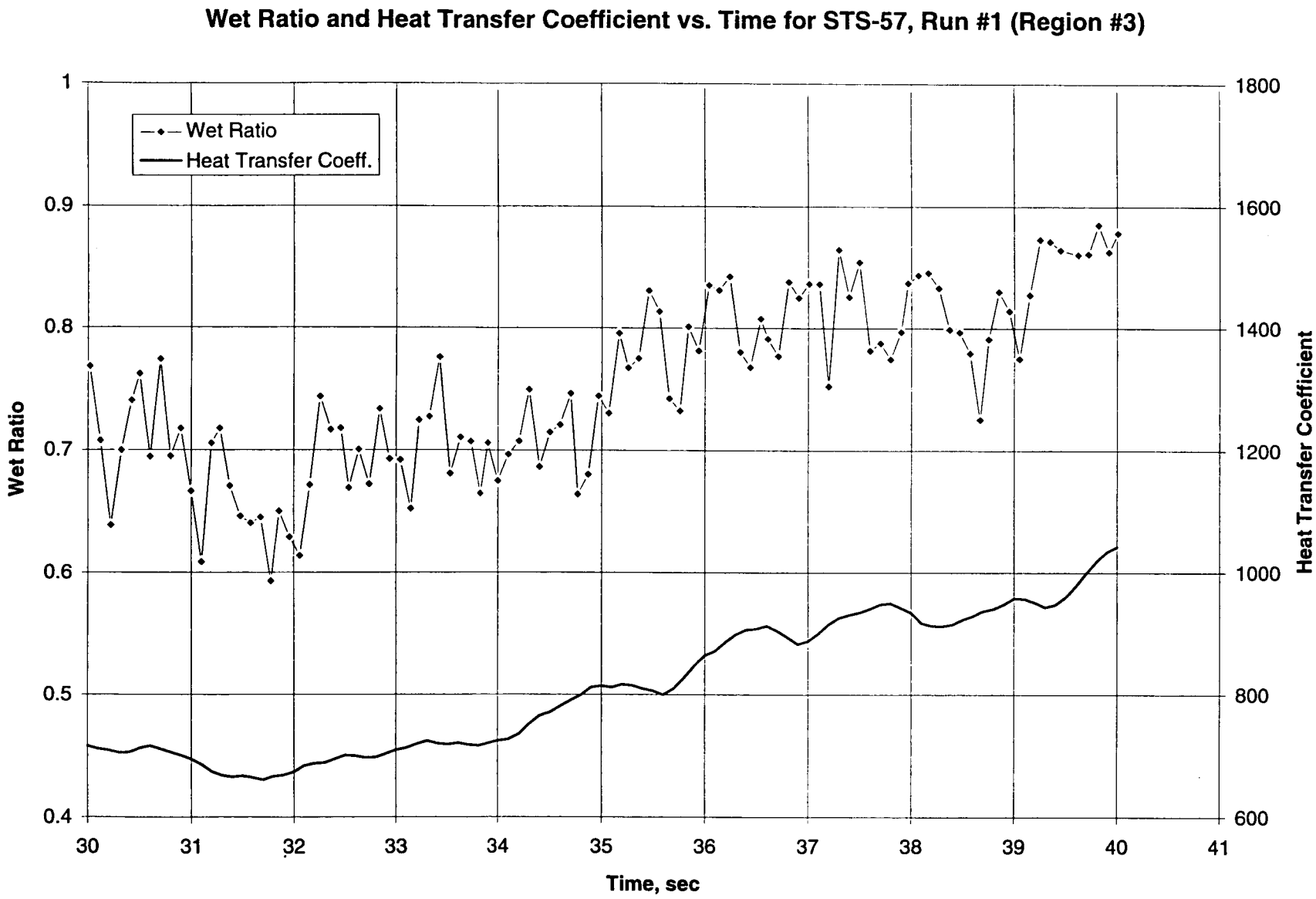

Figure B-10a-3-ii. Heater surface wet fraction and mean heat transfer coefficients. PBE-IB (STS-57). Run No. 1. Time interval: 30 - 40 seconds.

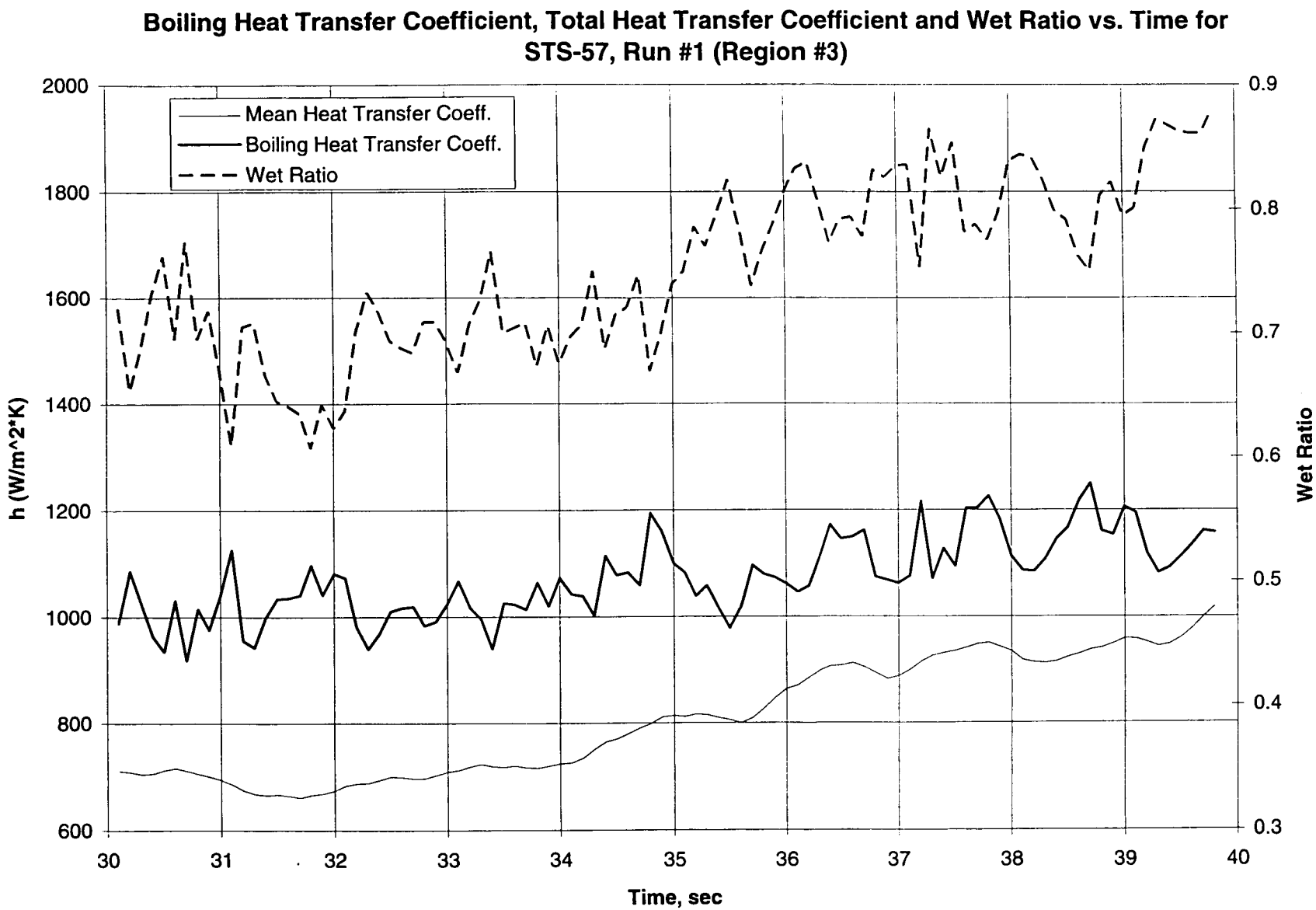

Figure B-10a-3-iii. Development of microgravity boiling heat transfer coefficient. PBE-IB (STS-57). Run No. 1. Time interval: 30 - 40 seconds.

STS-57 Run #1 (Region #3)

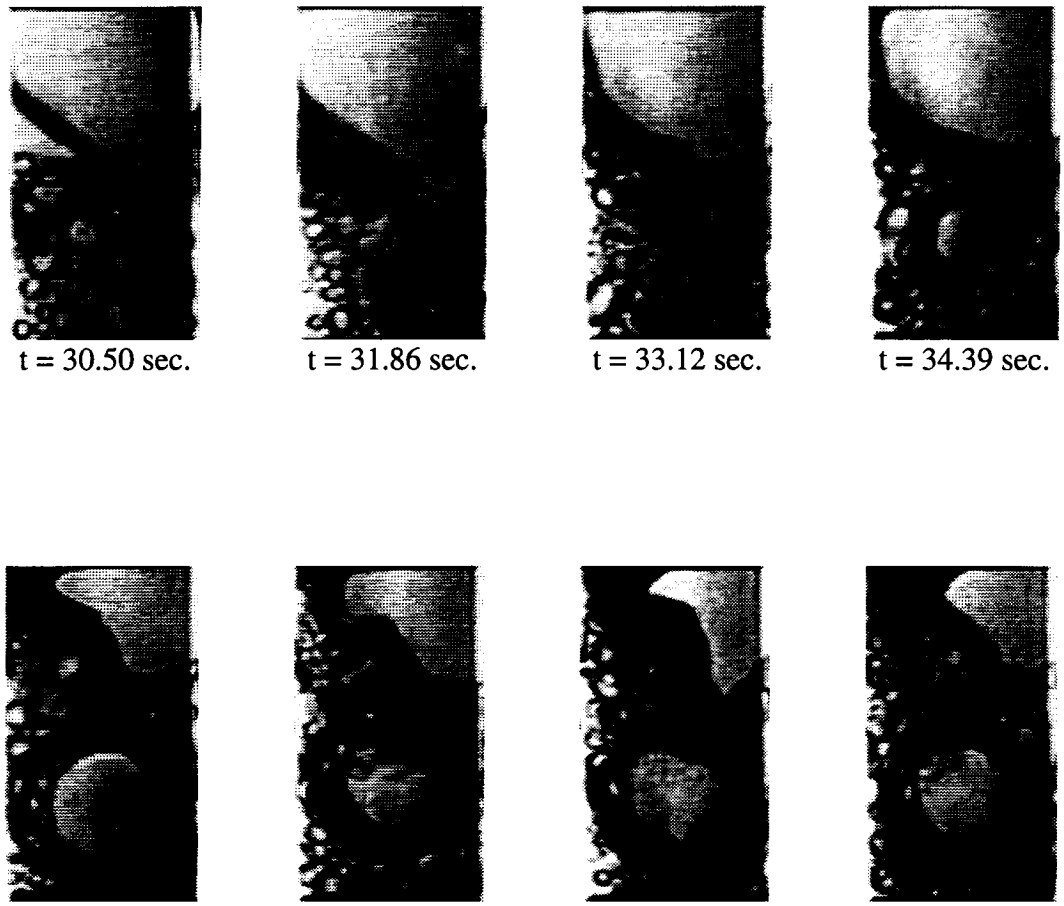

Figure B-10a3-iv. Sample images showing dryout/rewetting. PBE-IB (STS-57). Run No. 1. Time interval: 30 - 40 seconds.

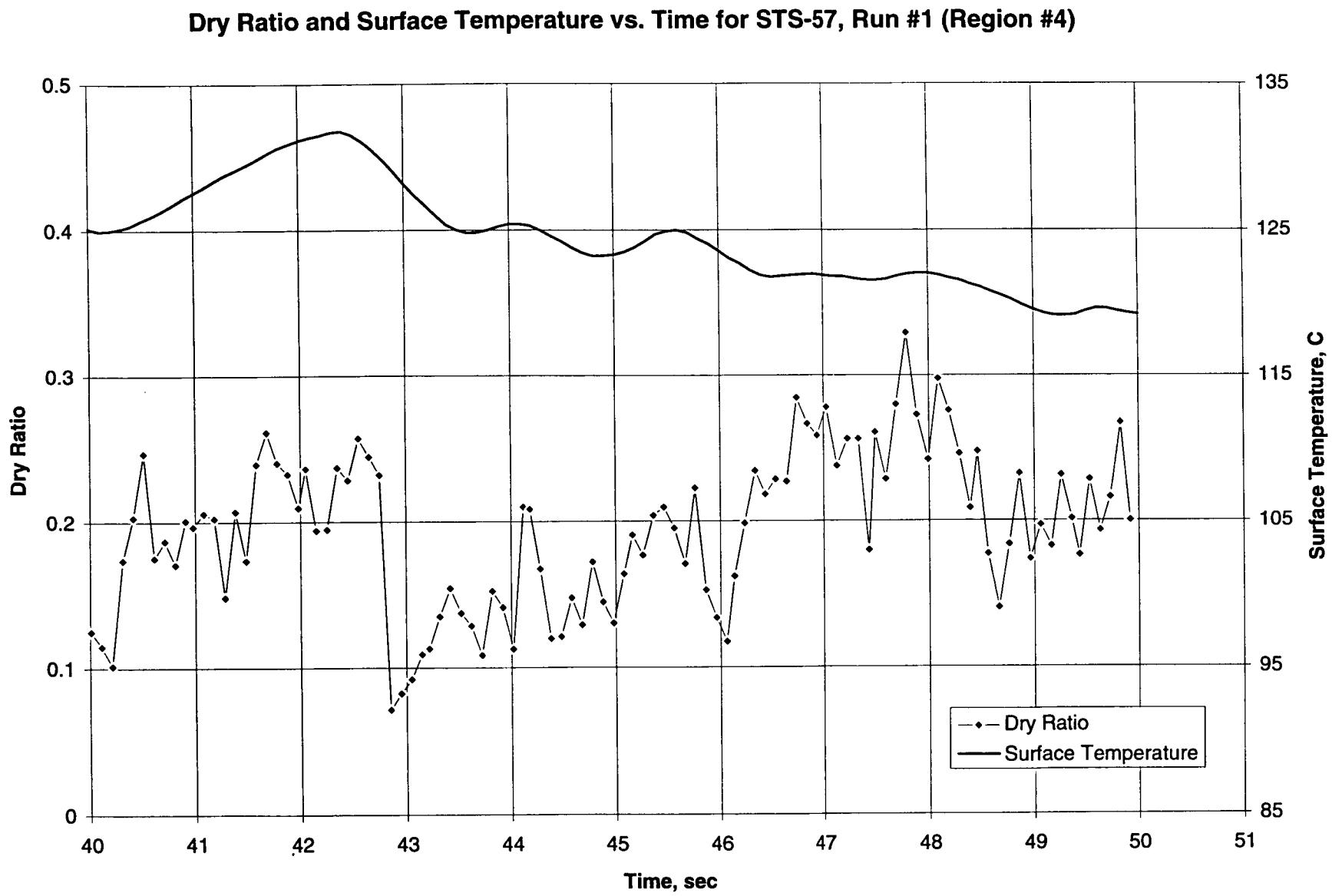

Figure B-10a-4-i. Heater surface dry fraction and mean temperature. PBE-IB (STS-57). Run No. 1. Time interval: 40 - 50 seconds.

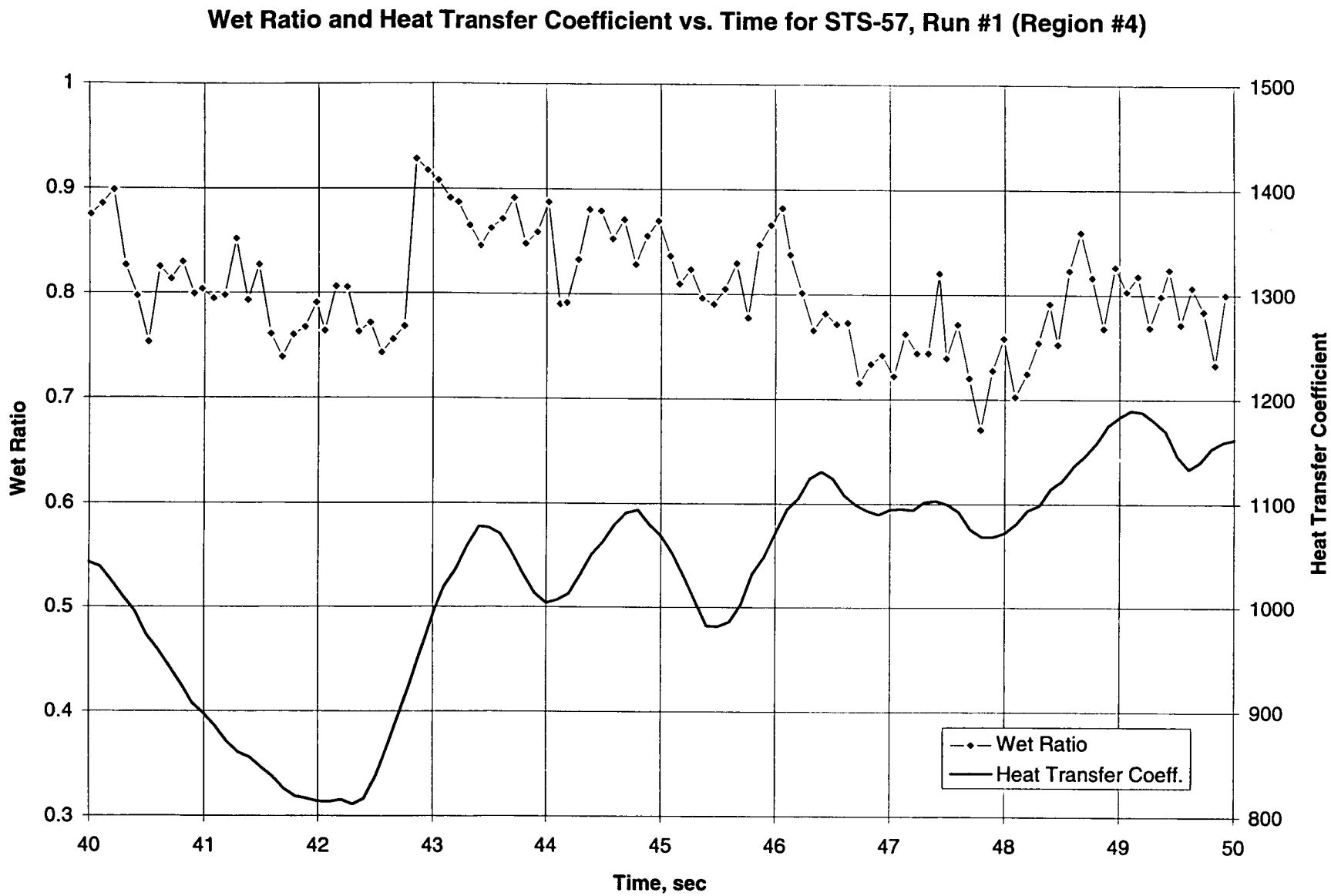

Figure B-10a-4-ii. Heater surface wet fraction and mean heat transfer coefficients. PBE-IB (STS-57). Run No. 1. Time interval: 40 - 50 seconds.

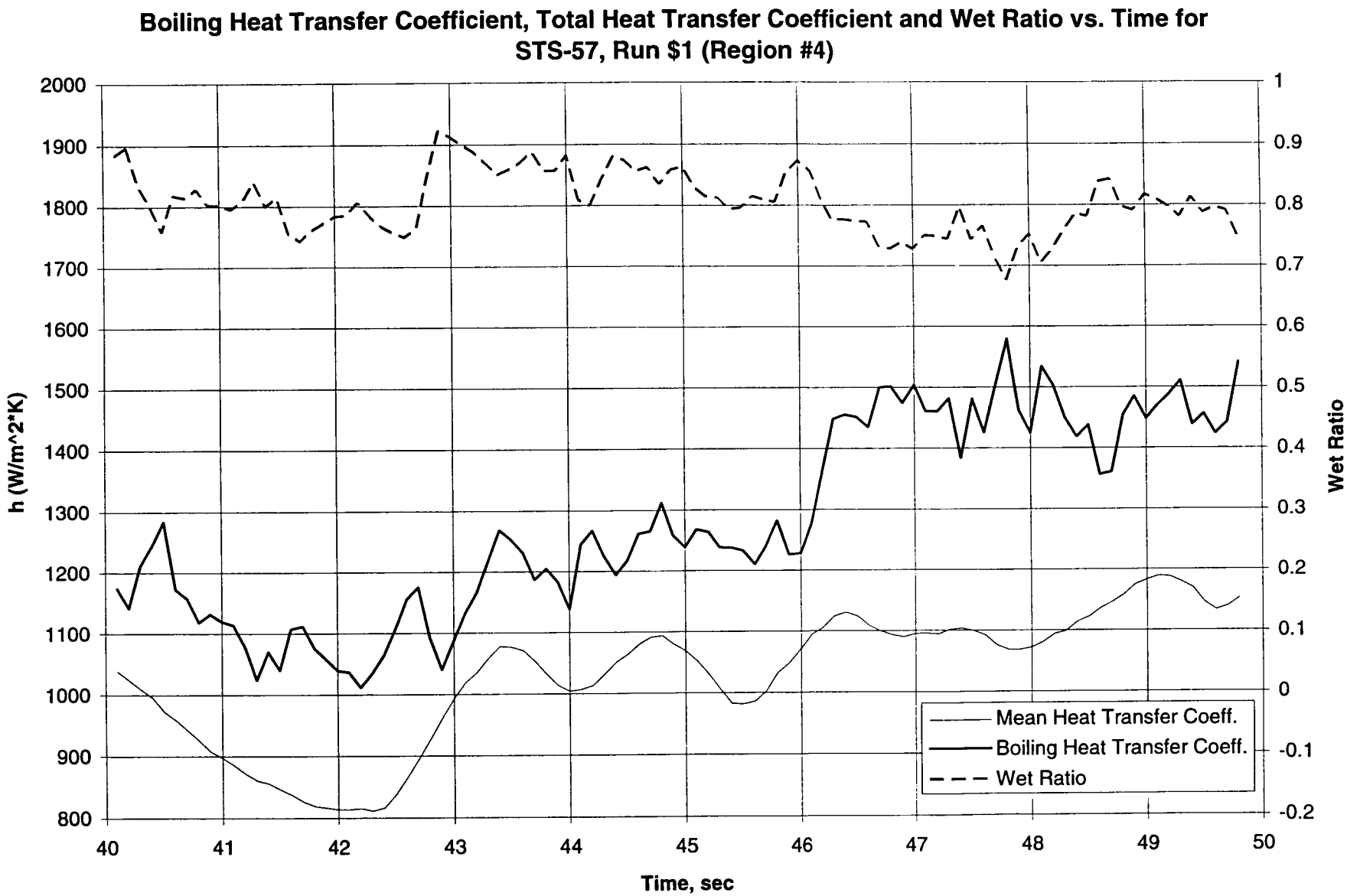

Figure B-10a-4-iii. Development of microgravity boiling heat transfer coefficient. PBE-IB (STS-57). Run No. 1. Time interval: 40 - 50 seconds.

STS-57 Run #1 (Region #4)

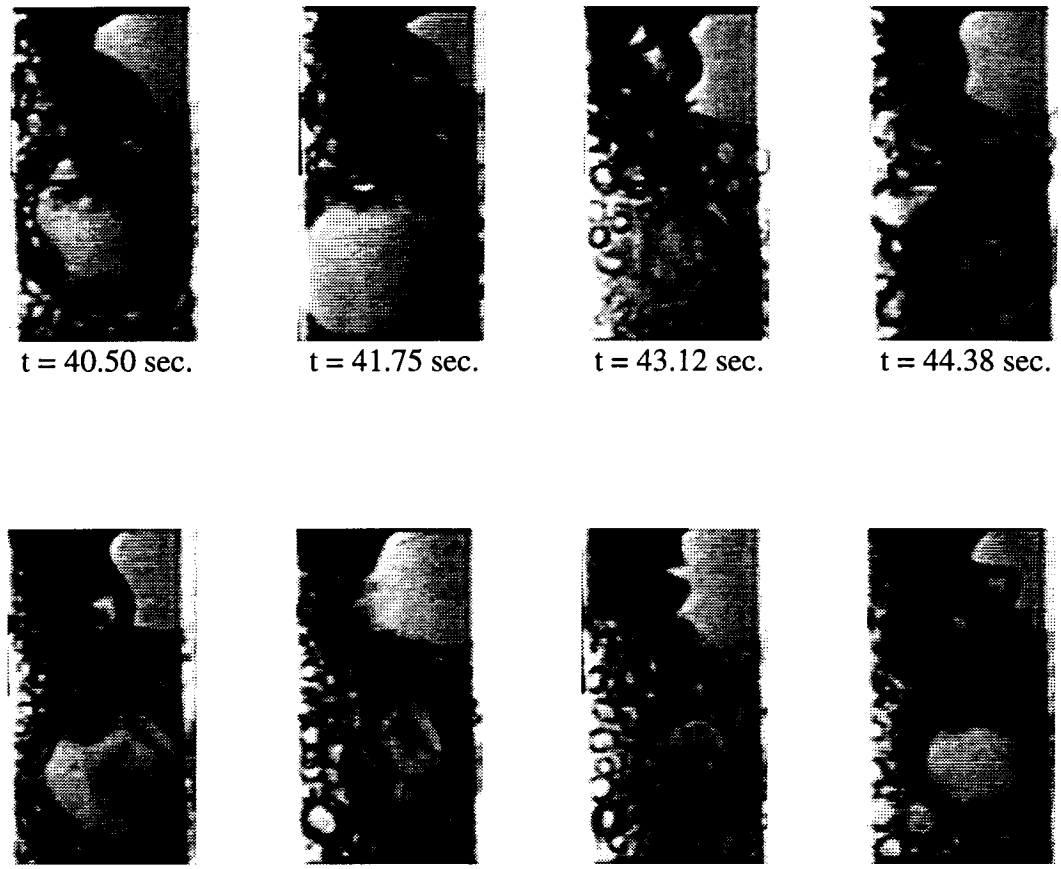

t = 40.50 sec. t = 41.75 sec. t = 43.12 sec. t = 44.38 sec.

t = 45.64 sec. t = 47.00 sec. t = 48.28 sec. t = 49.63 sec.

Figure B-10a-4-iv. Sample images showing dryout/rewetting. PBE-IB (STS-57). Run No. 1. Time interval: 40 - 50 seconds.

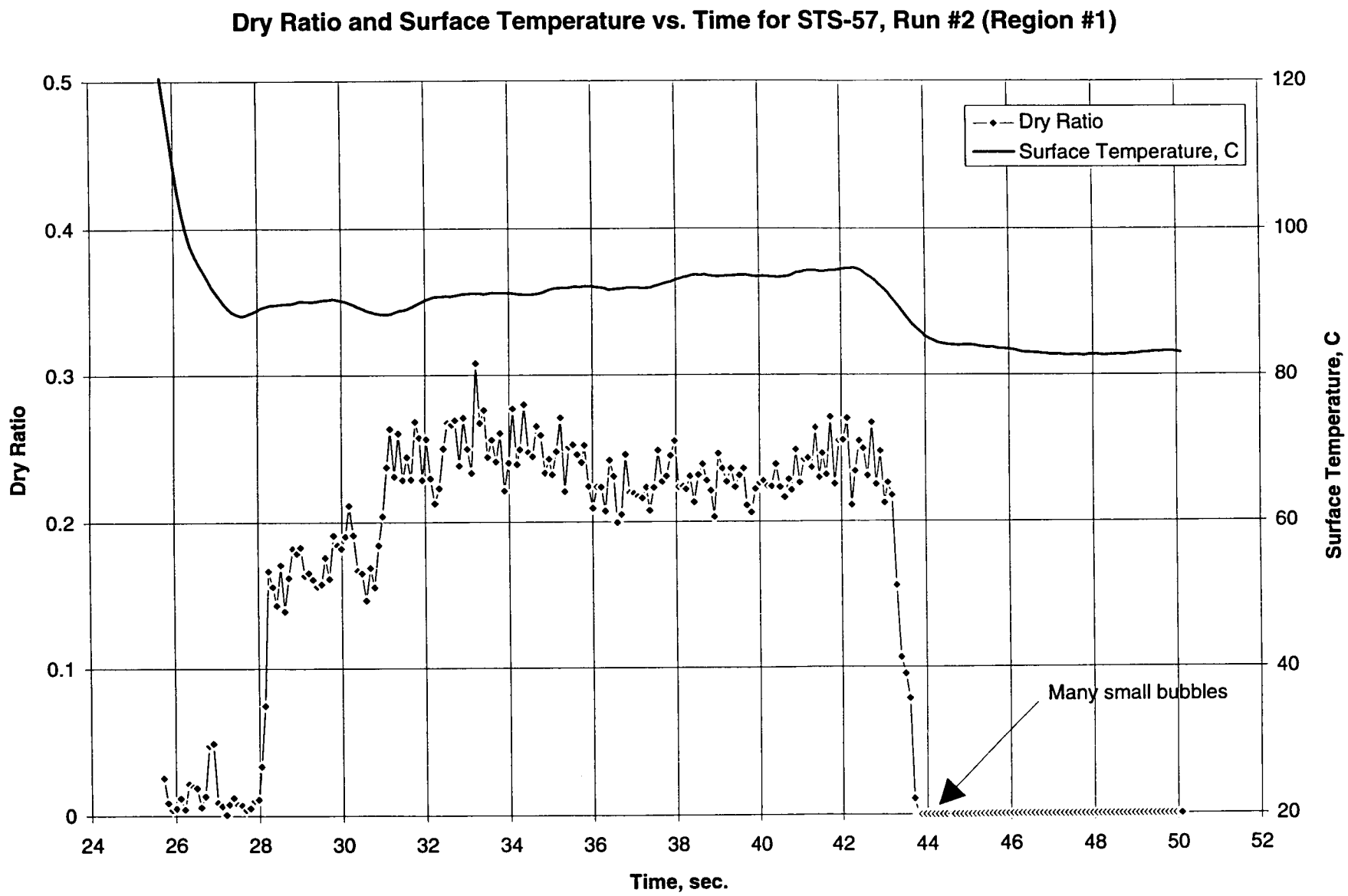

Figure B-10b-1-i. Heater surface dry fraction and mean temperature. PBE-IB (STS-57). Run No. 2. Time interval: 25.8 - 50.0 seconds.

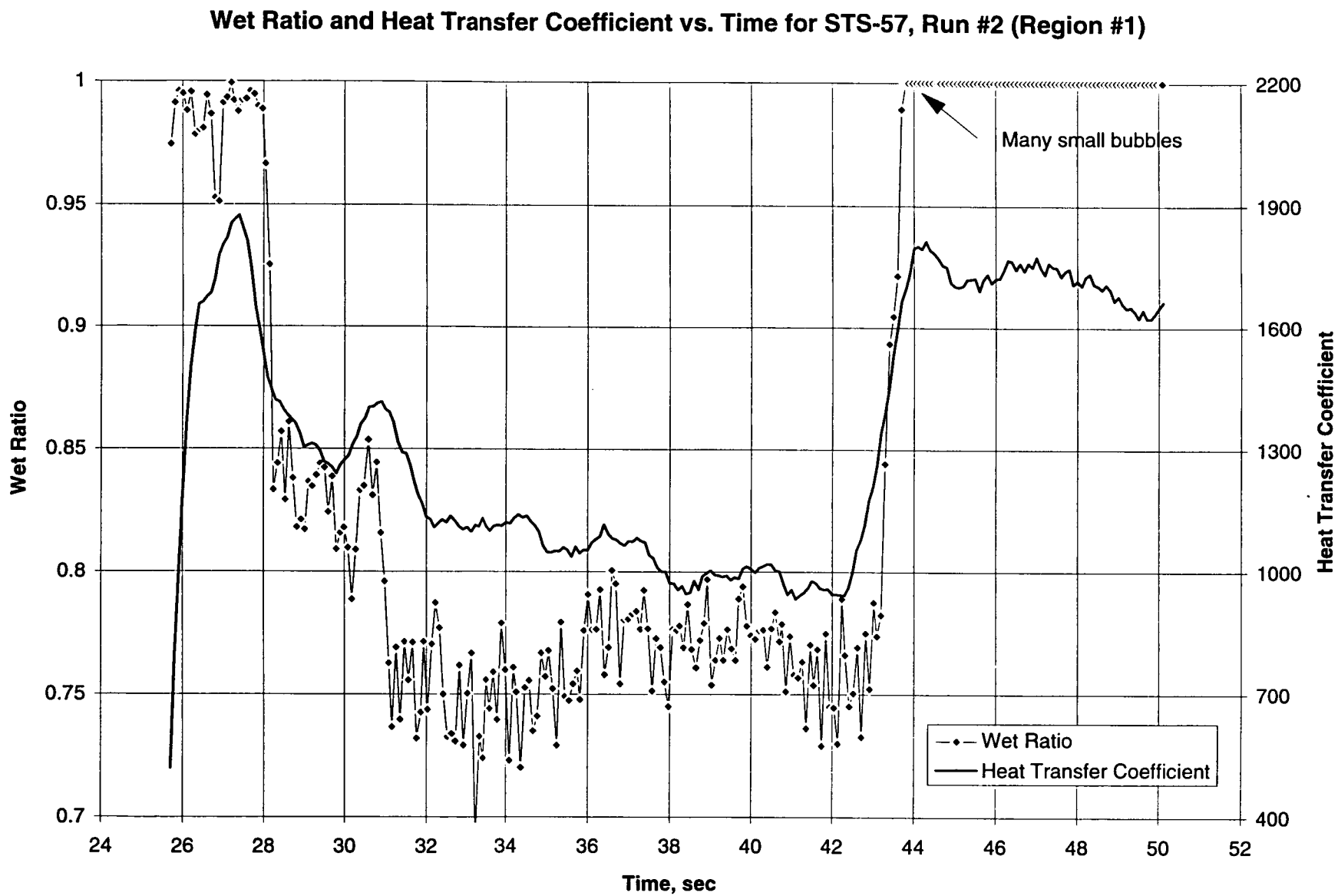

Figure B-10b-1-ii. Heater surface wet fraction and mean heat transfer coefficients. PBE-IB (STS-57). Run No. 2. Time interval: 25.8 - 50.0 seconds.

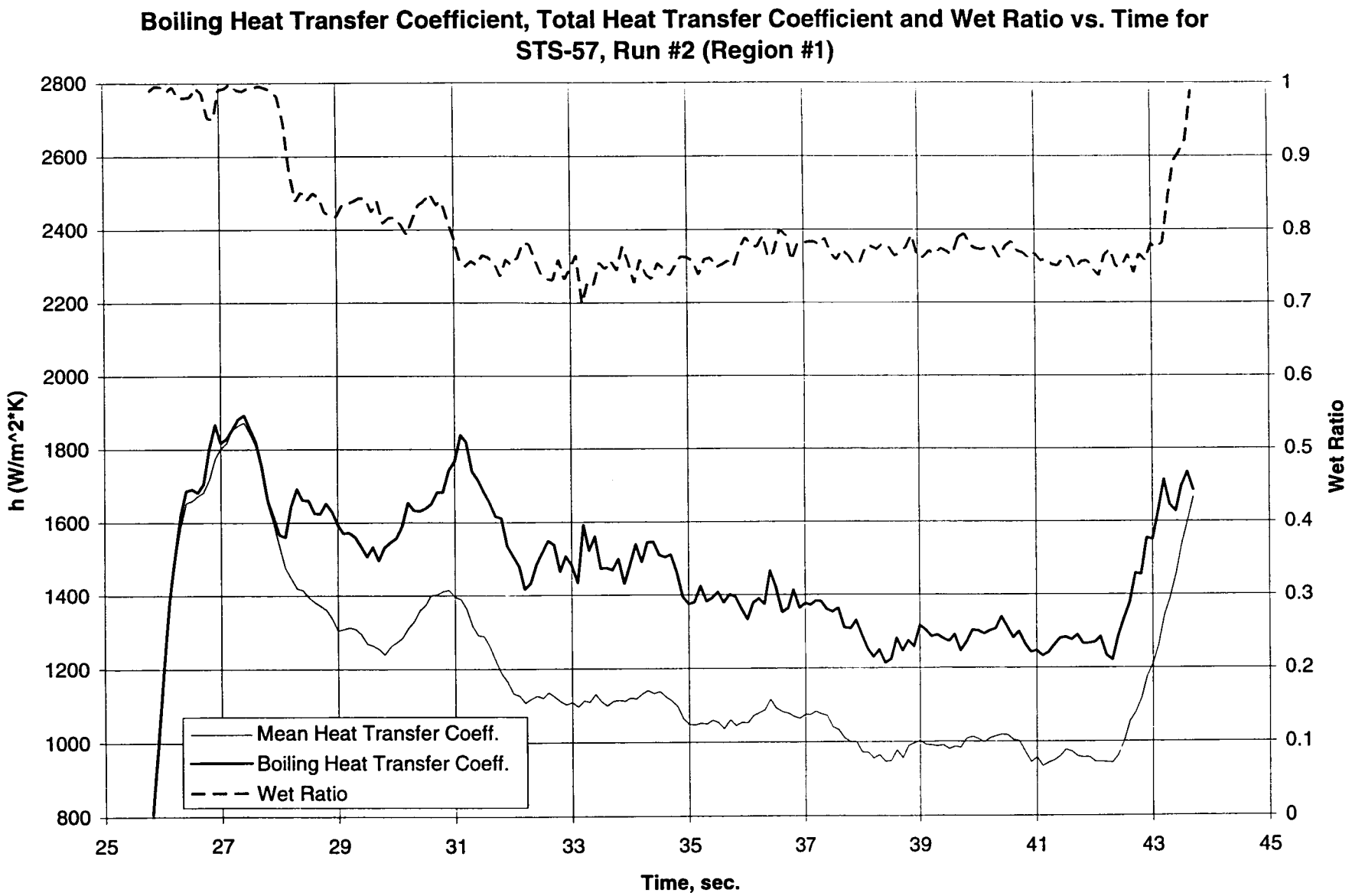

Figure B-10b-1-iii. Development of microgravity boiling heat transfer coefficient. PBE-IB (STS-57). Run No. 2. Time interval: 25.8 - 50.0 seconds.

STS-57 Run #2 (Region #1)

t= 25.71 sec.

t= 29.21 sec.

t= 32.71 sec.

t= 36.21 sec.

t= 39.7 sec.

t= 43.2 sec.

t= 46.65 sec.

t=50.09 sec.

Figure B-10b-1-iv. Sample images showing dryout/rewetting. PBE-IB (STS-57). Run No. 2. Time interval: 25.8 - 50.0 seconds.

STS-57 Run #2 (Region #2) - Bubbles too small for dry spot measurement

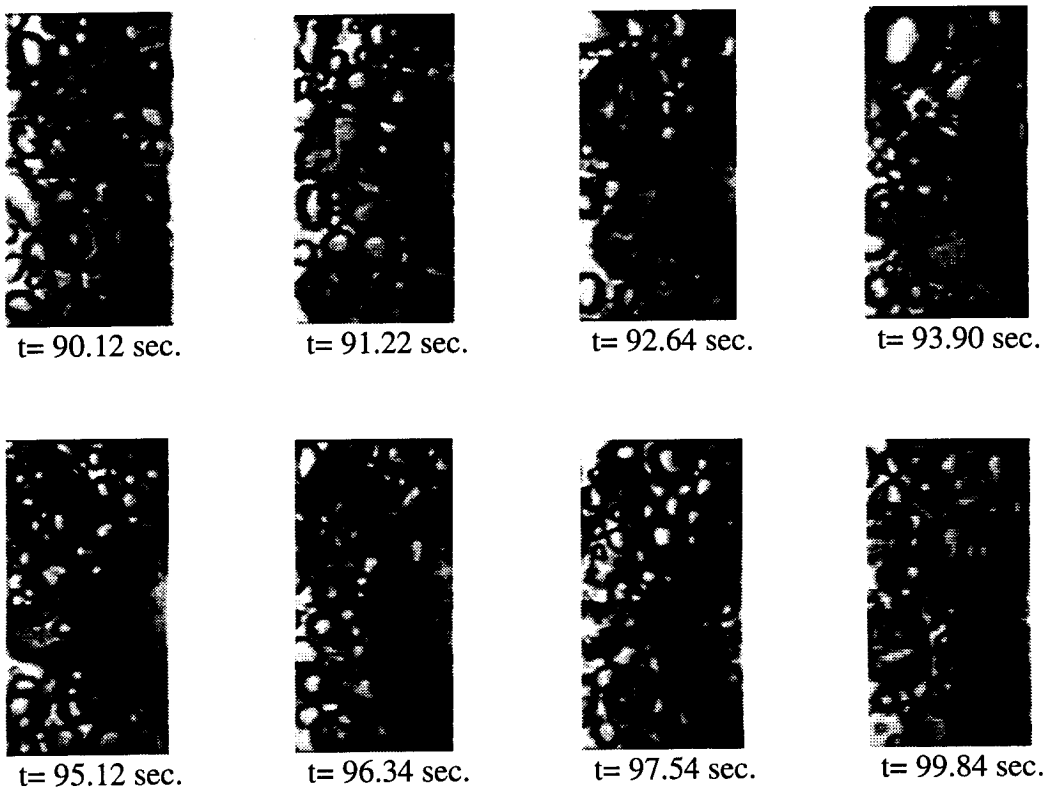

Figure B-10b-2-iv. Sample images. PBE-IB (STS-57). Run No. 2. Time interval: 90 - 100 seconds.

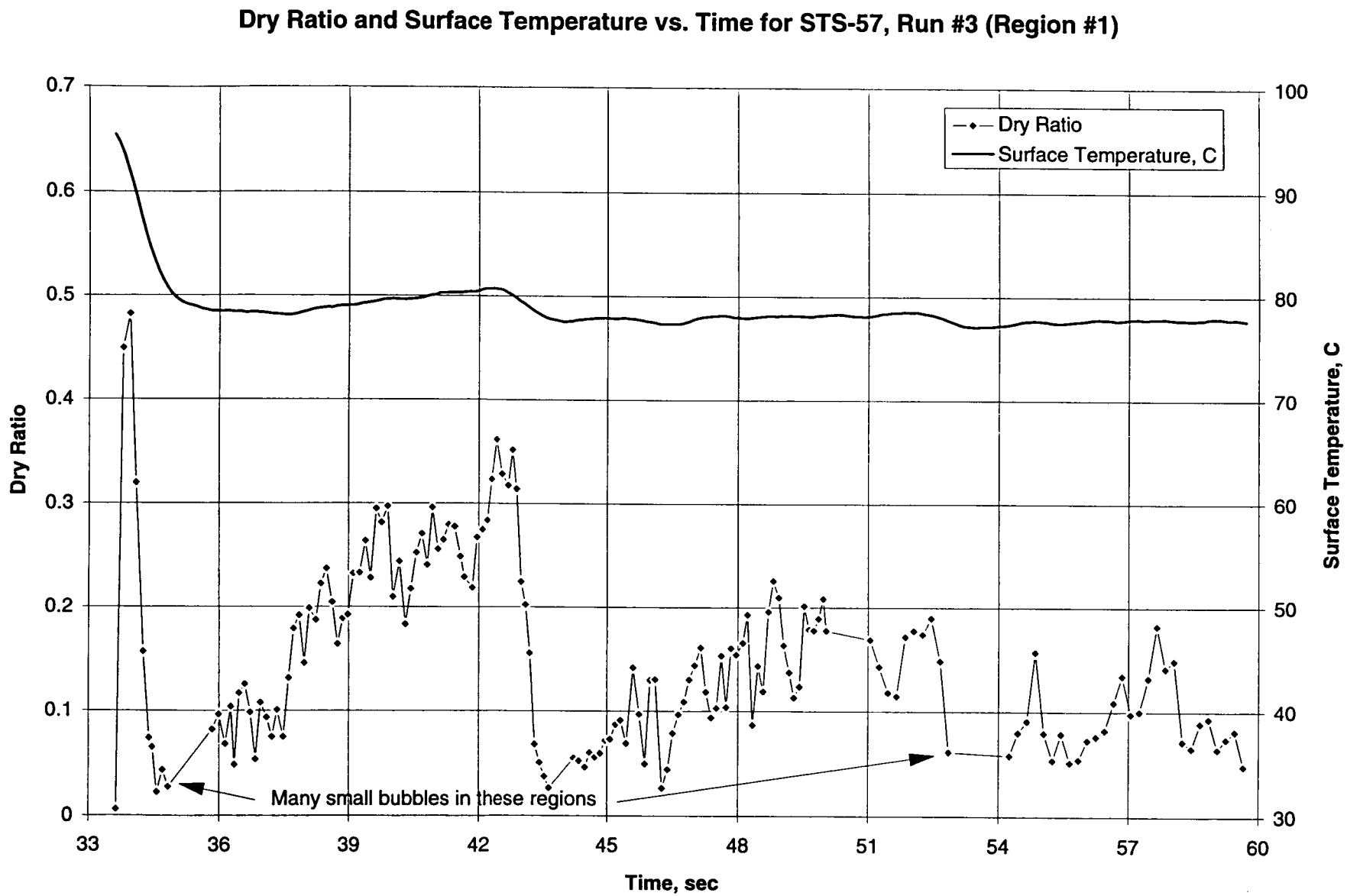

Figure B-10c-1-i. Heater surface dry fraction and mean temperature. PBE-IB (STS-57). Run No. 3. Time interval: 33.6 - 60.0 seconds.

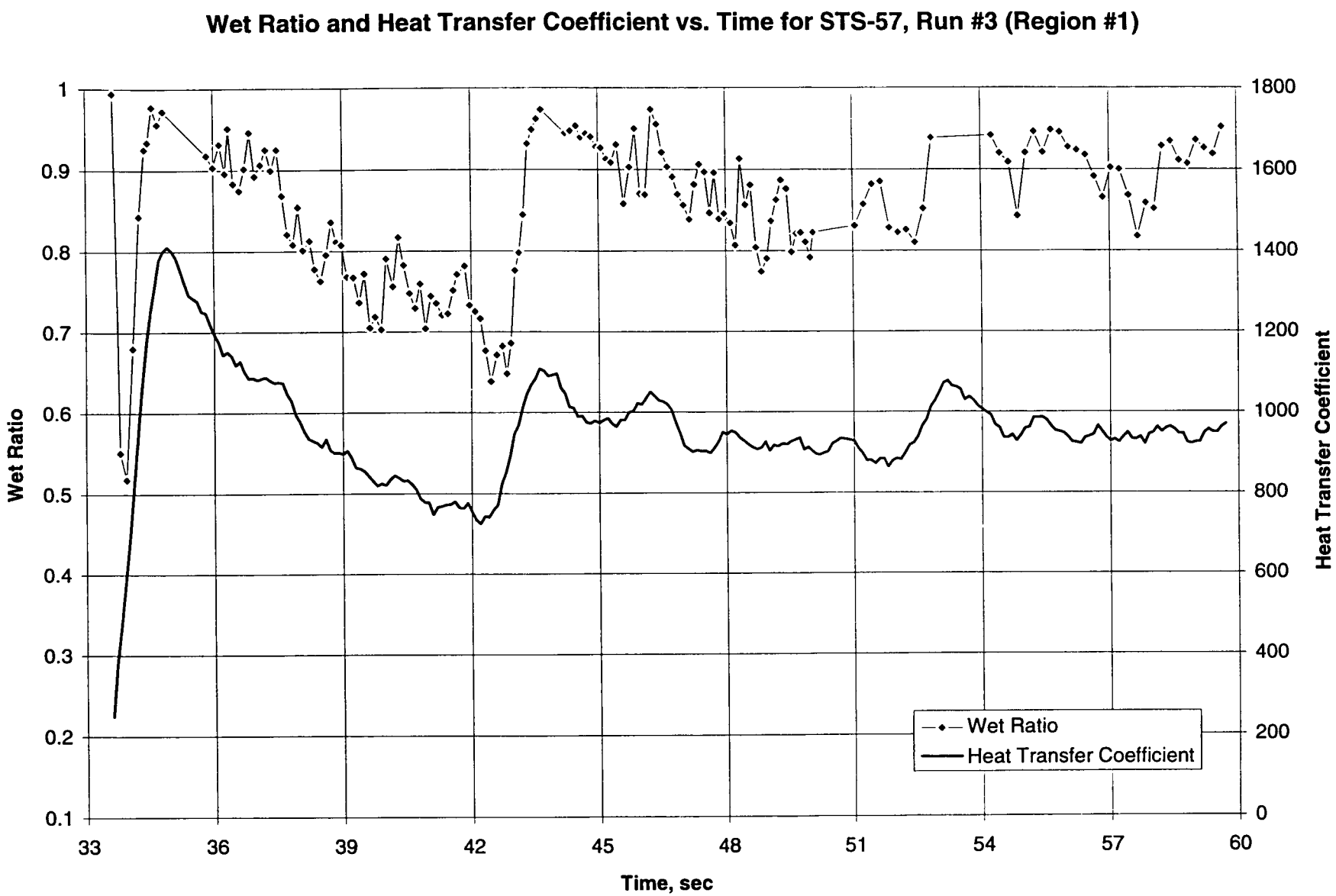

Figure B-10c-1-ii. Heater surface wet fraction and mean heat transfer coefficients. PBE-IB (STS-57). Run No. 3. Time interval: 33.6 - 60.0 seconds.

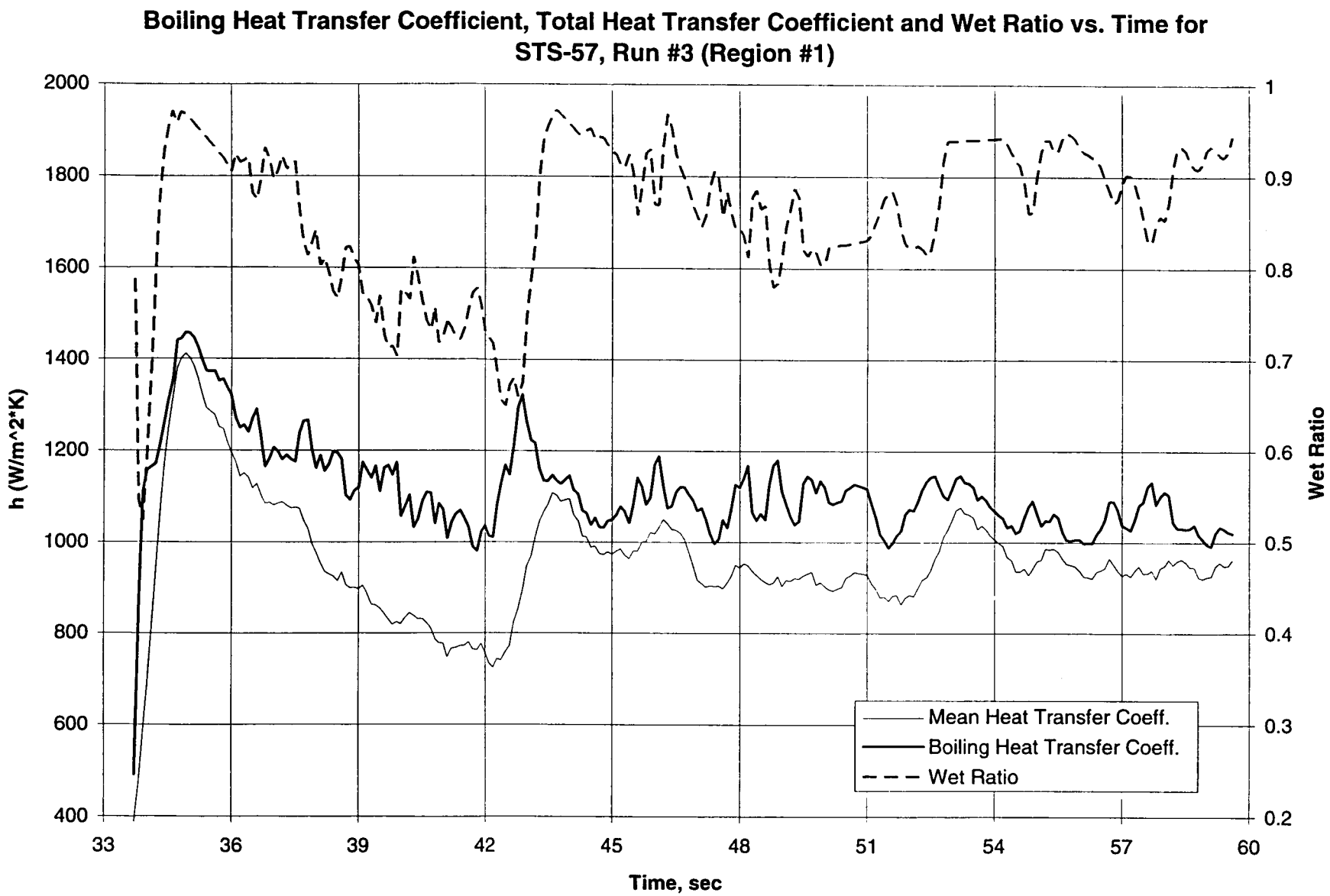

Figure B-10c-1-iii. Development of microgravity boiling heat transfer coefficient. PBE-IB (STS-57). Run No. 3. Time interval: 33.6 - 60.0 seconds.

STS-57 Run #3 (Region #1)

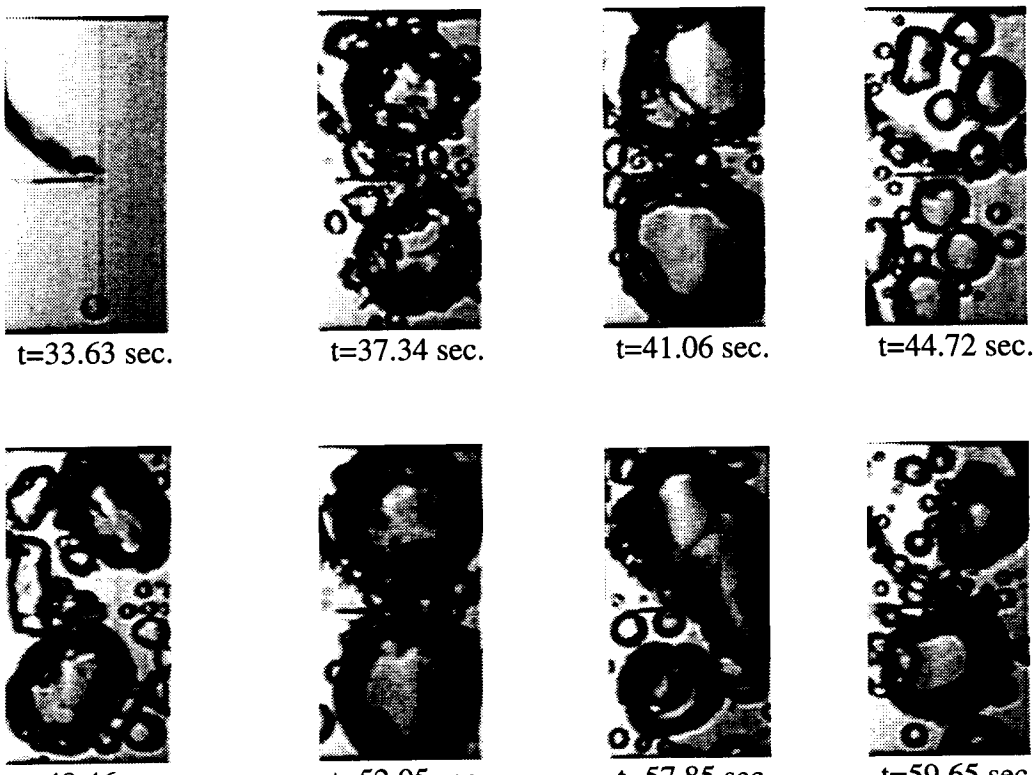

Figure B-10c-1-iv. Sample images showing dryout/rewetting. PBE-IB (STS-57). Run No. 3. Time interval: 33.6 - 60.0 seconds.

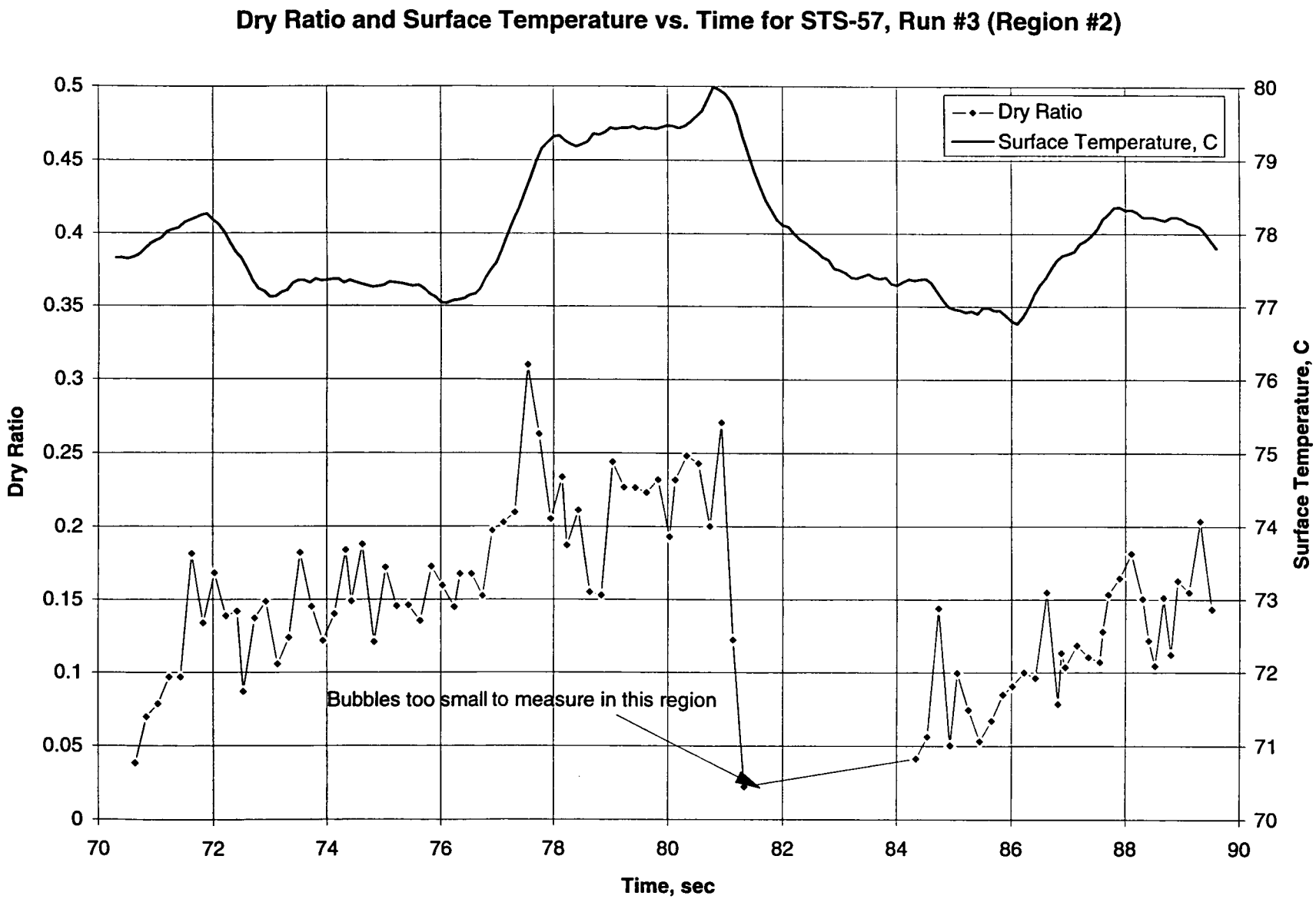

Figure B-10c-2-i. Heater surface dry fraction and mean temperature. PBE-IB (STS-57). Run No. 3. Time interval: 70.6 - 89.5 seconds.

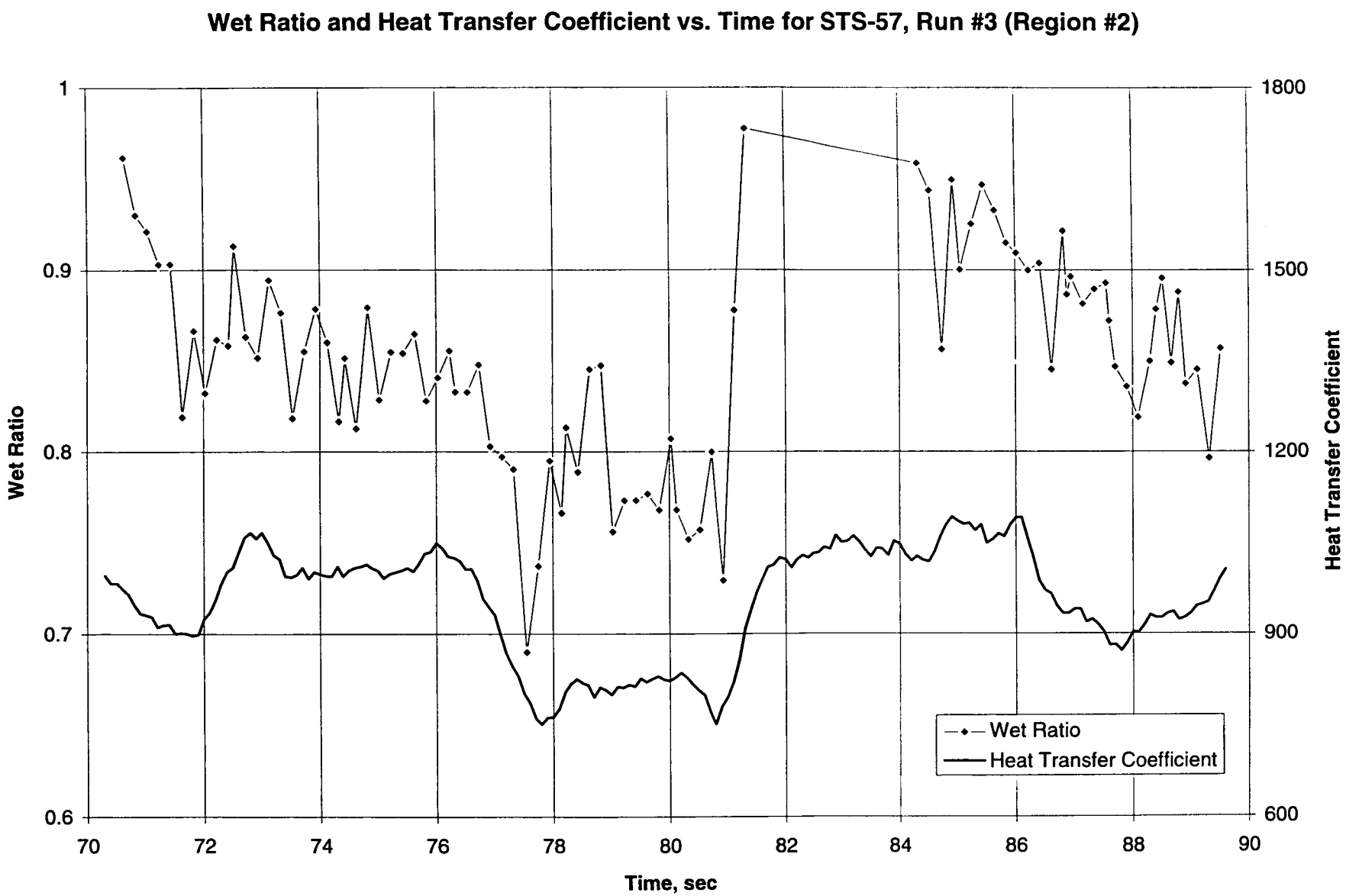

Figure B-10c-2-ii. Heater surface wet fraction and mean heat transfer coefficients. PBE-IB (STS-57). Run No. 3. Time interval: 70.6 - 89.5 seconds.

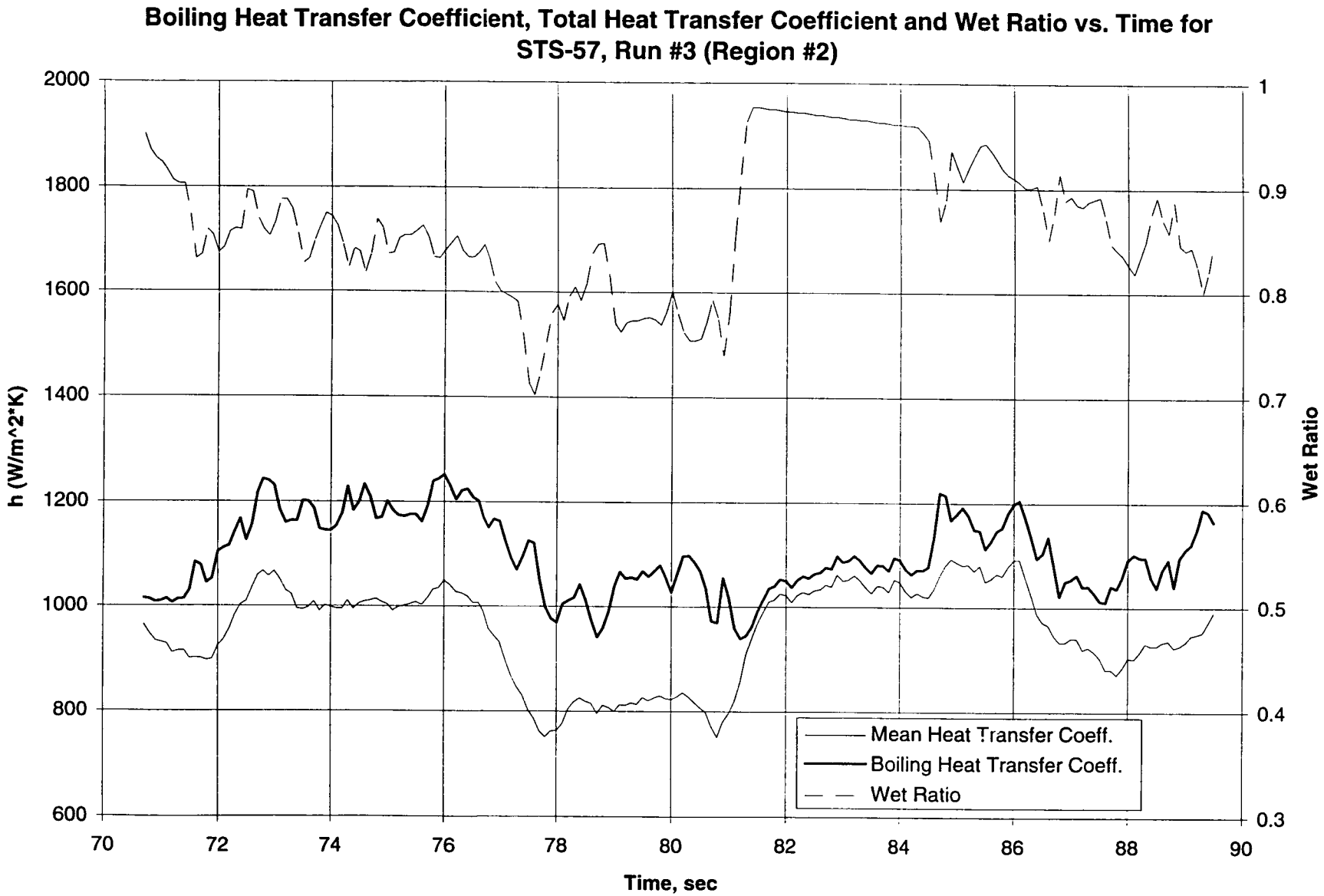

Figure B-10c-2-iii. Development of microgravity boiling heat transfer coefficient. PBE-IB (STS-57). Run No. 3. Time interval: 70.6 - 89.5 seconds.

STS-57 Run #3 (Region #2)

t=70.63 sec.

t=73.33 sec.

t=76.03 sec.

t=78.63 sec.

t=81.33 sec.

t=84.93 sec.

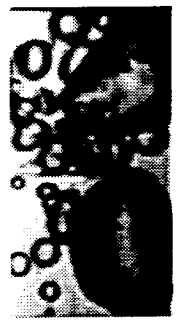
t=87.15 sec.

t=89.52 sec.

Figure B-10c-2-iv. Sample images showing dryout/rewetting. PBE-IB (STS-57). Run No. 3. Time interval: 70.6 - 89.5 seconds.

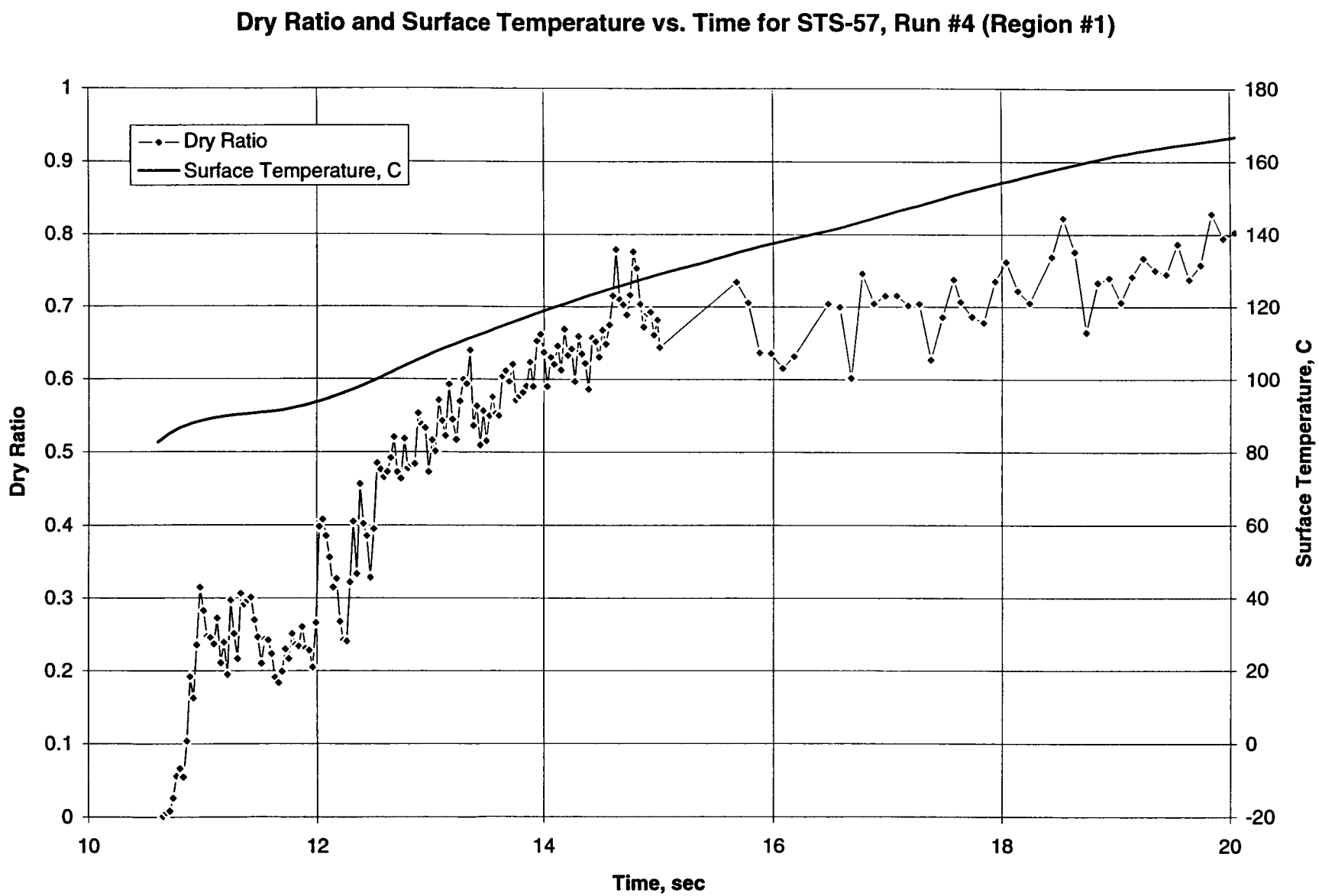

Figure B-10d-1-i. Heater surface dry fraction and mean temperature. PBE-IB (STS-57). Run No. 4. Time interval: 10.6 - 20.0 seconds.

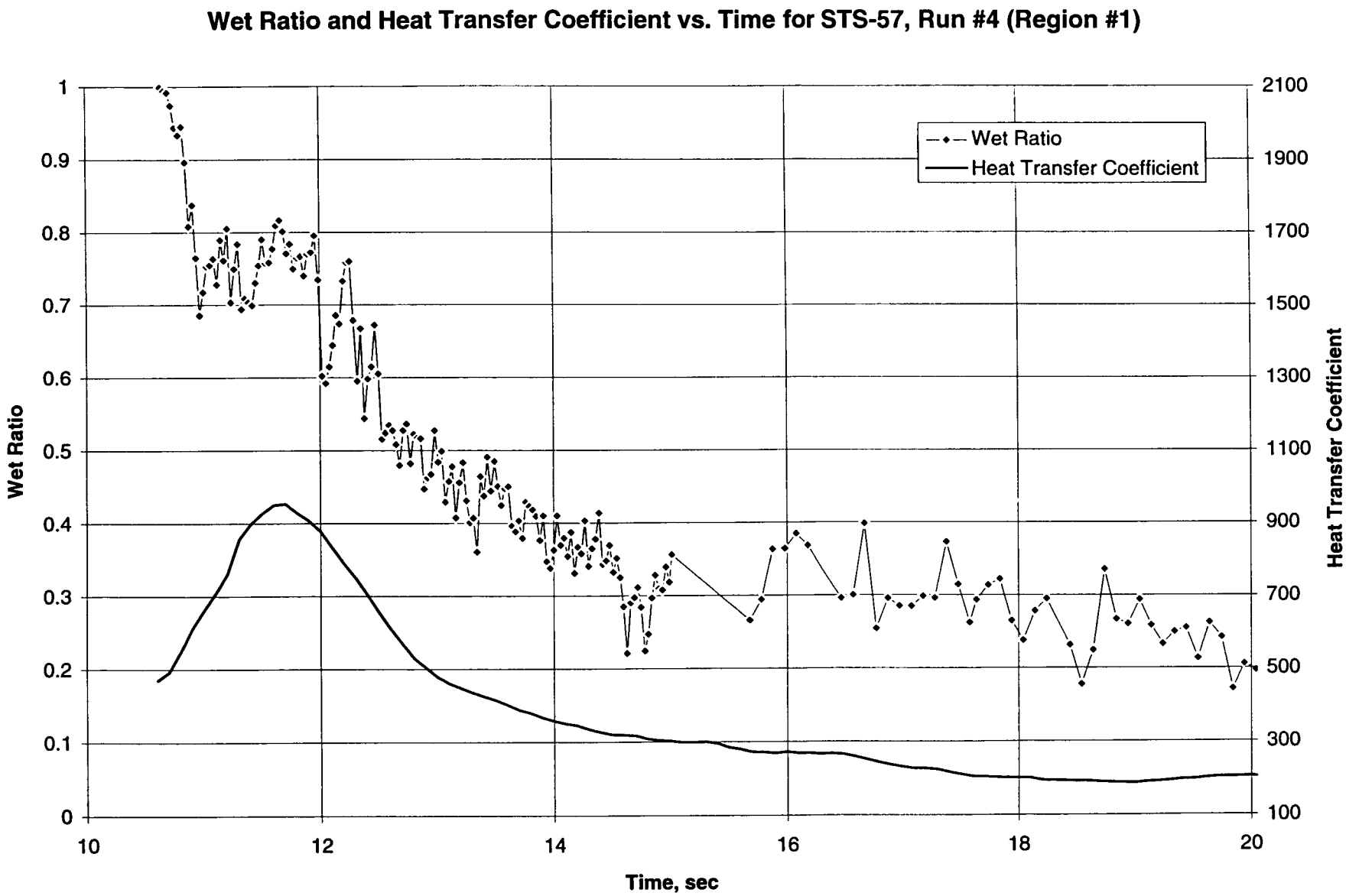

Figure B-10d-1-ii. Heater surface wet fraction and mean heat transfer coefficients. PBE-IB (STS-57). Run No. 4. Time interval: 10.6 - 20.0 seconds.

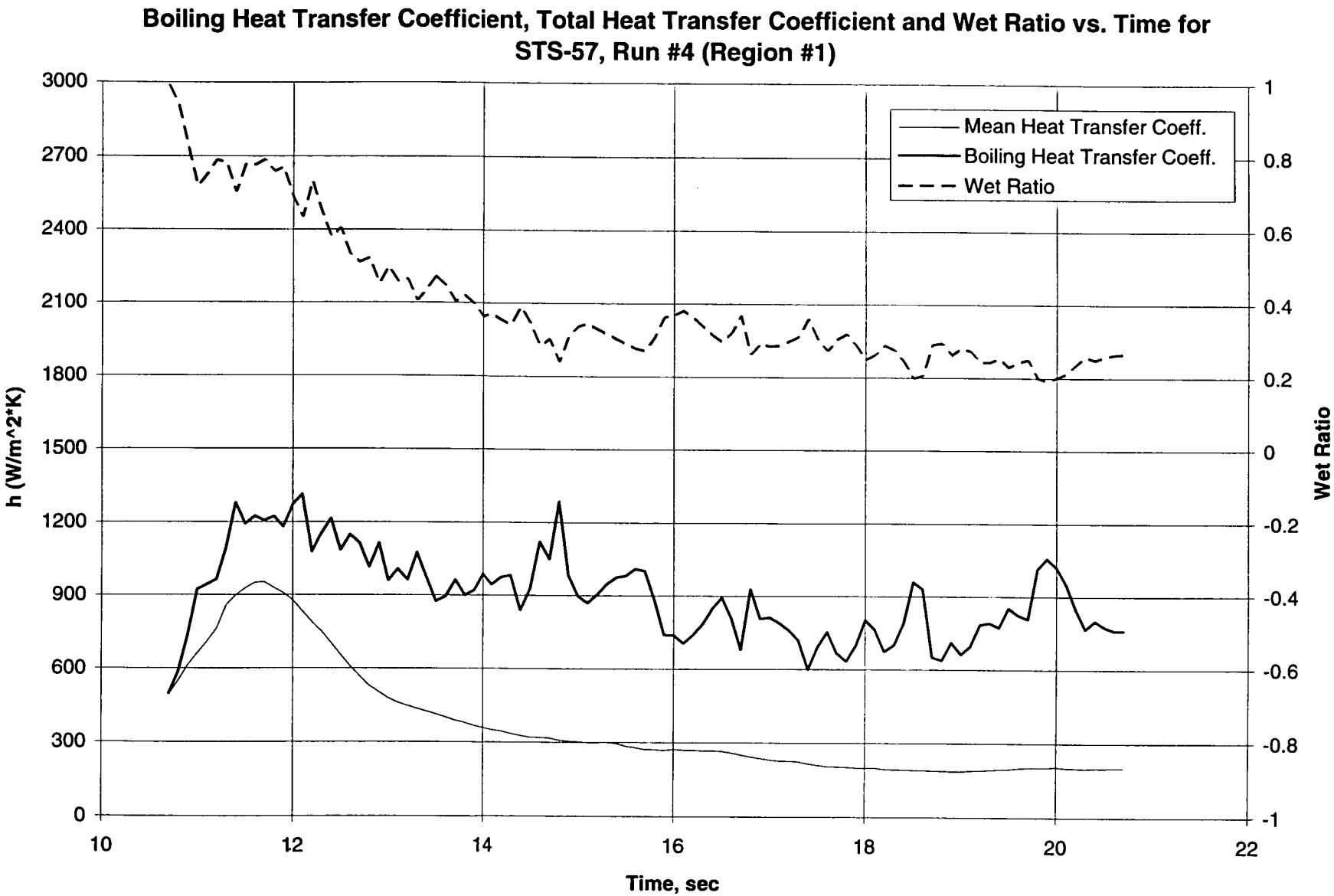

Figure B-10d-1-iii. Development of microgravity boiling heat transfer coefficient. PBE-IB (STS-57). Run No. 4. Time interval: 10.6 - 20.0 seconds.

STS-57 Run #4 (Region #1)

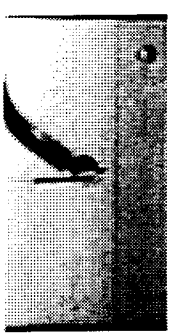
t= 10.64 sec.

t= 11.99 sec.

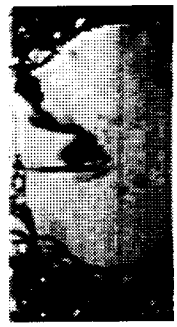
t= 13.31 sec.

t=14.63 sec.

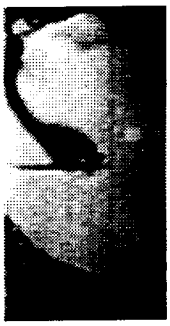
t= 15.98 sec.

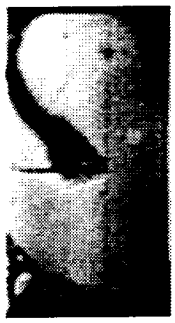
t= 17.28 sec.

t= 18.64 sec.

t= 20.04 sec.

Figure B-10d-1-iv. Sample images showing dryout/rewetting. PBE-IB (STS-57). Run No. 4. Time interval: 10.6 - 20.0 seconds.

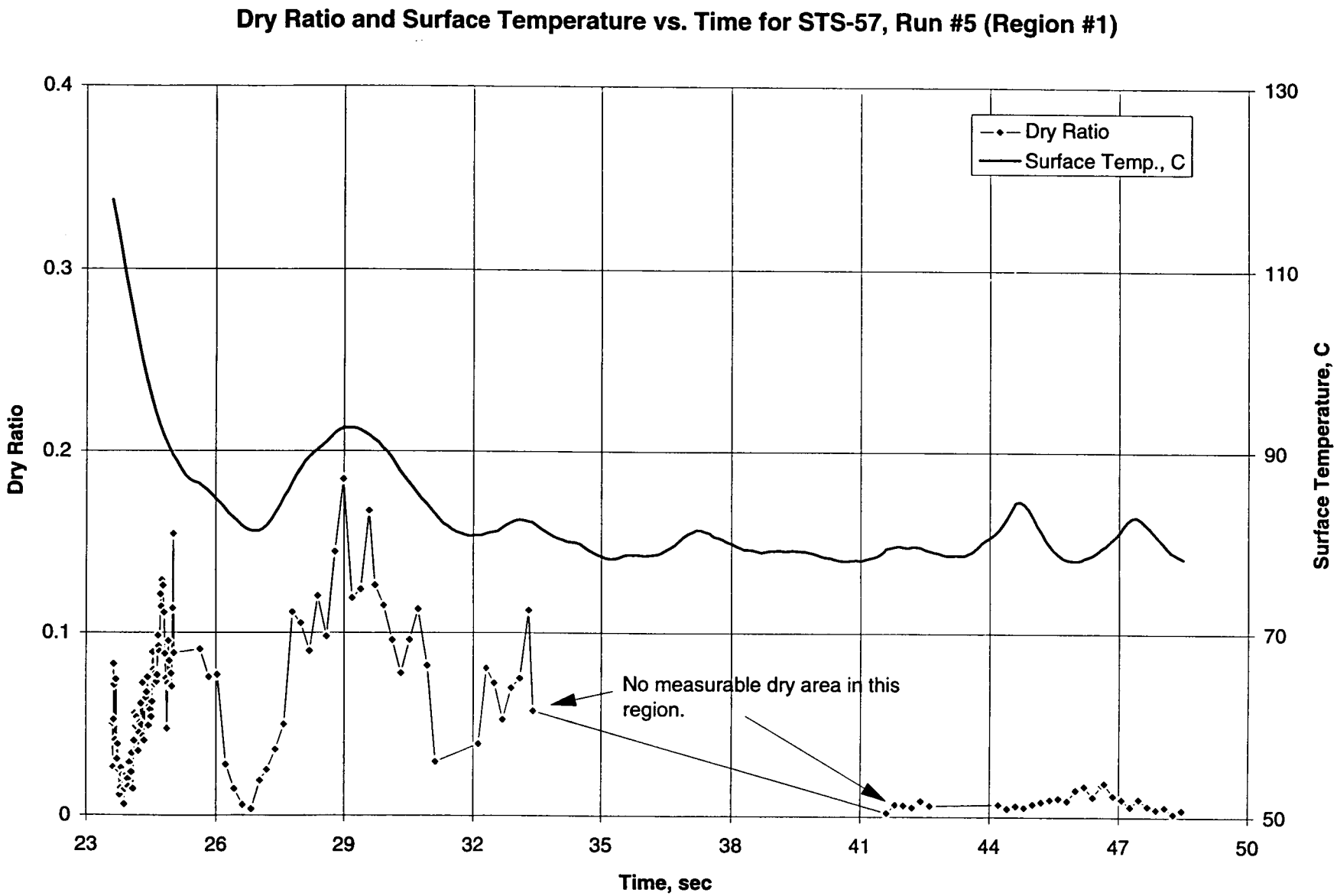

Figure B-10e-1-i. Heater surface dry fraction and mean temperature. PBE-IB (STS-57). Run No. 5. Time interval: 23.5 - 48.5 seconds.

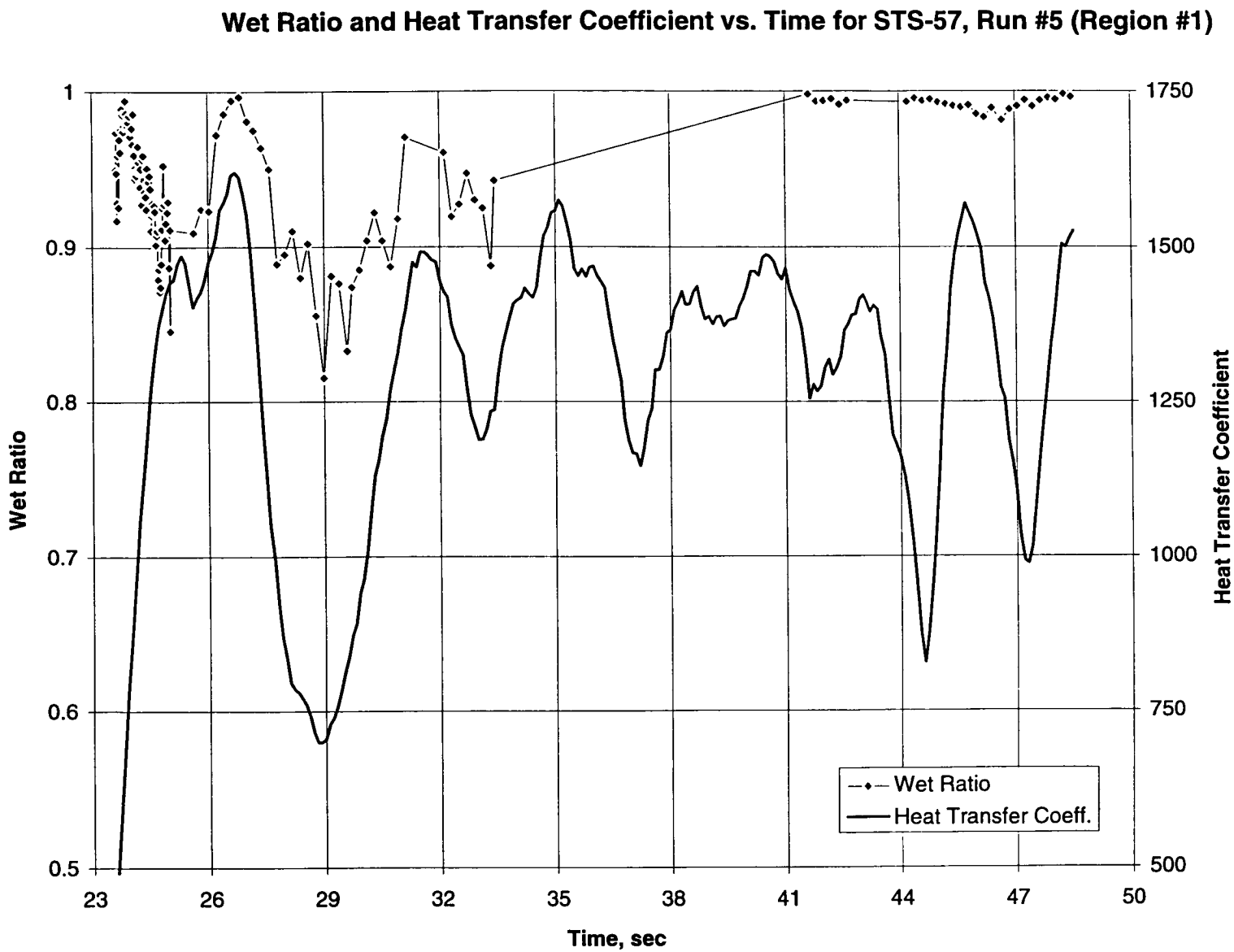

Figure B-10e-1-ii. Heater surface wet fraction and mean heat transfer coefficients. PBE-IB (STS-57). Run No. 5. Time interval: 23.5 - 48.5 seconds.

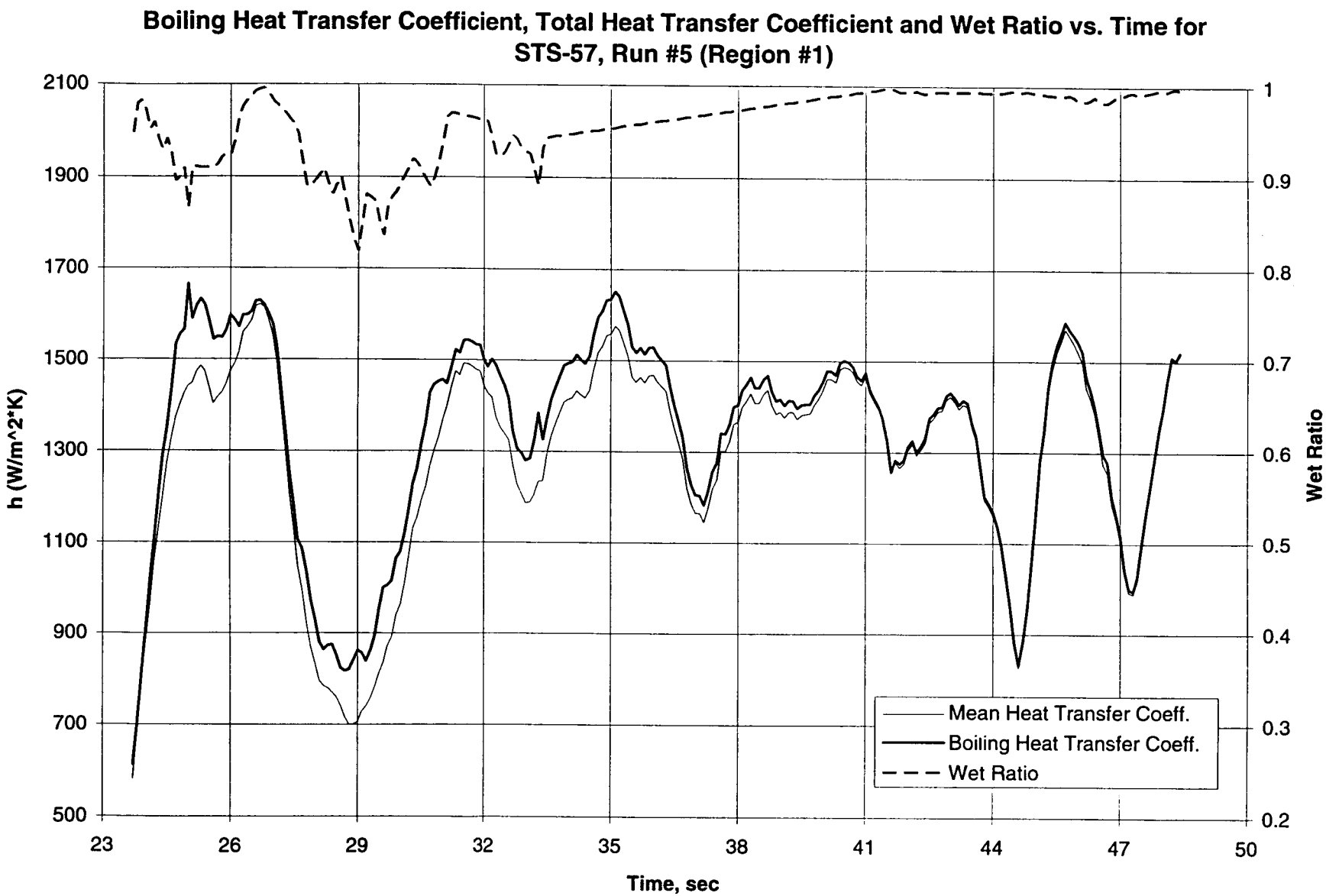

Figure B-10e-1-iii. Development of microgravity boiling heat transfer coefficient. PBE-IB (STS-57). Run No. 5. Time interval: 23.5 - 48.5 seconds.

STS-57 Run #5 (Region #1)

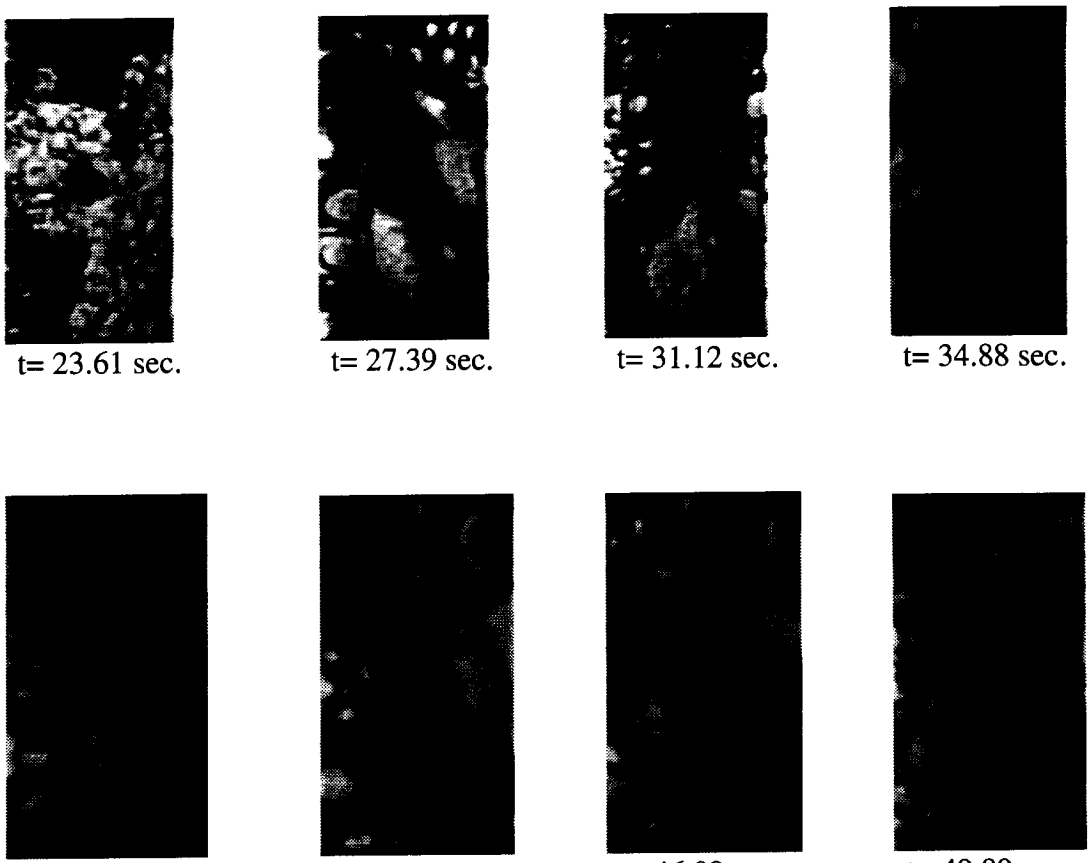

Figure B-10e-1-iv. Sample images showing dryout/rewetting. PBE-IB (STS-57). Run No. 5. Time interval: 23.5 - 48.5 seconds.

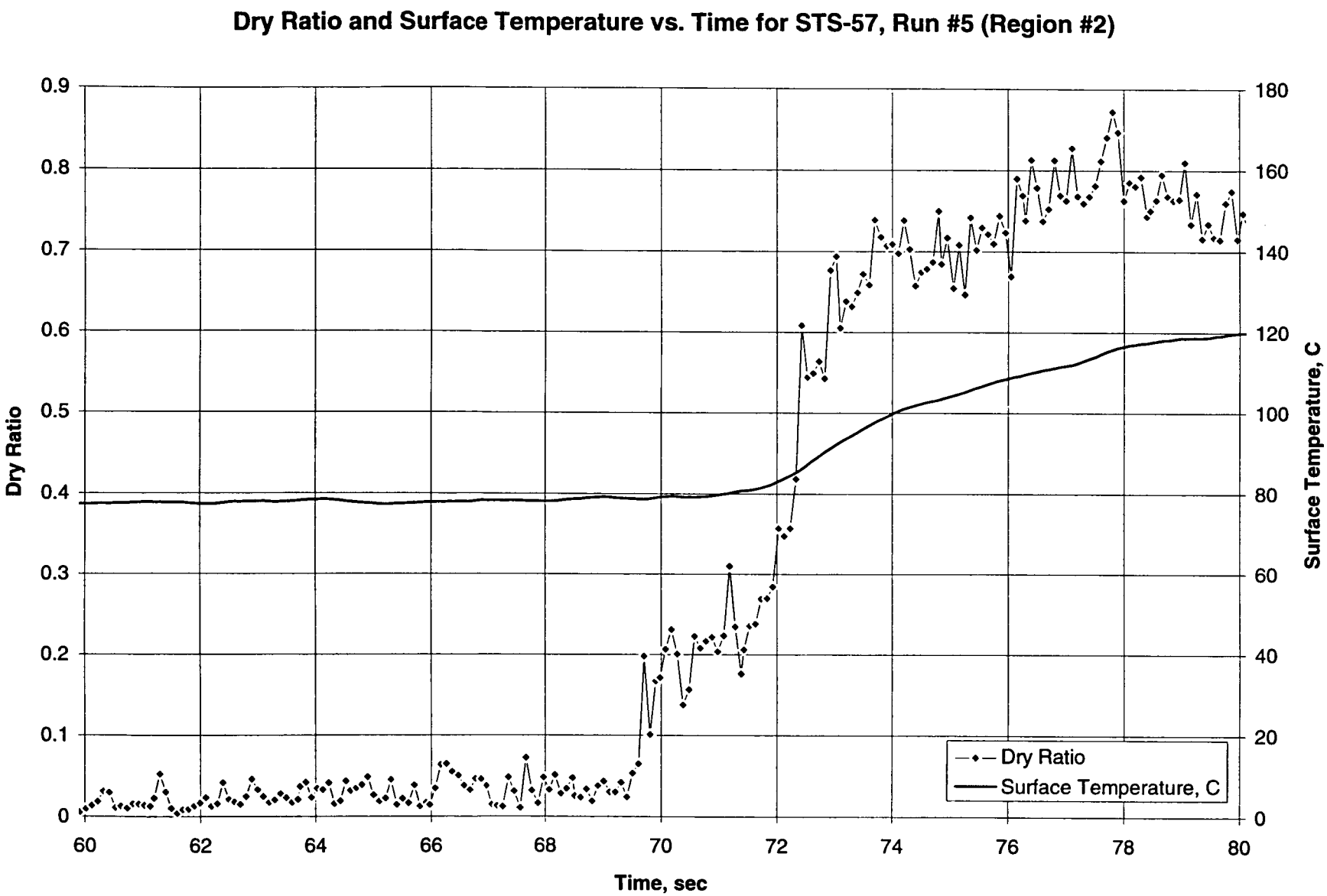

Figure B-10e-2-i. Heater surface dry fraction and mean temperature. PBE-IB (STS-57). Run No.5. Time interval: 60 - 80 seconds.

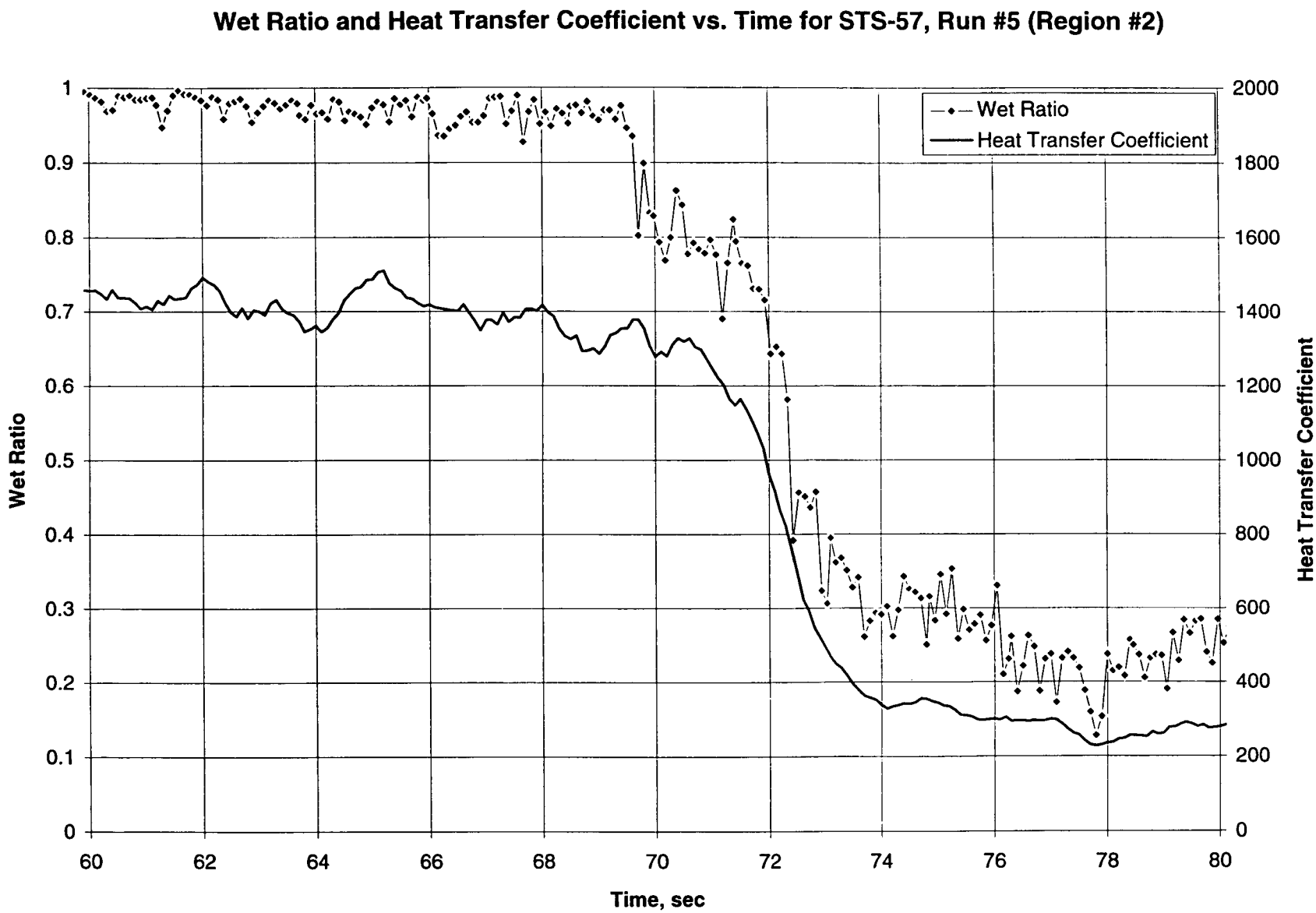

Figure B-10e-2-ii. Heater surface wet fraction and mean heat transfer coefficients. PBE-IB (STS-57). Run No. 5. Time interval: 60 - 80 seconds.

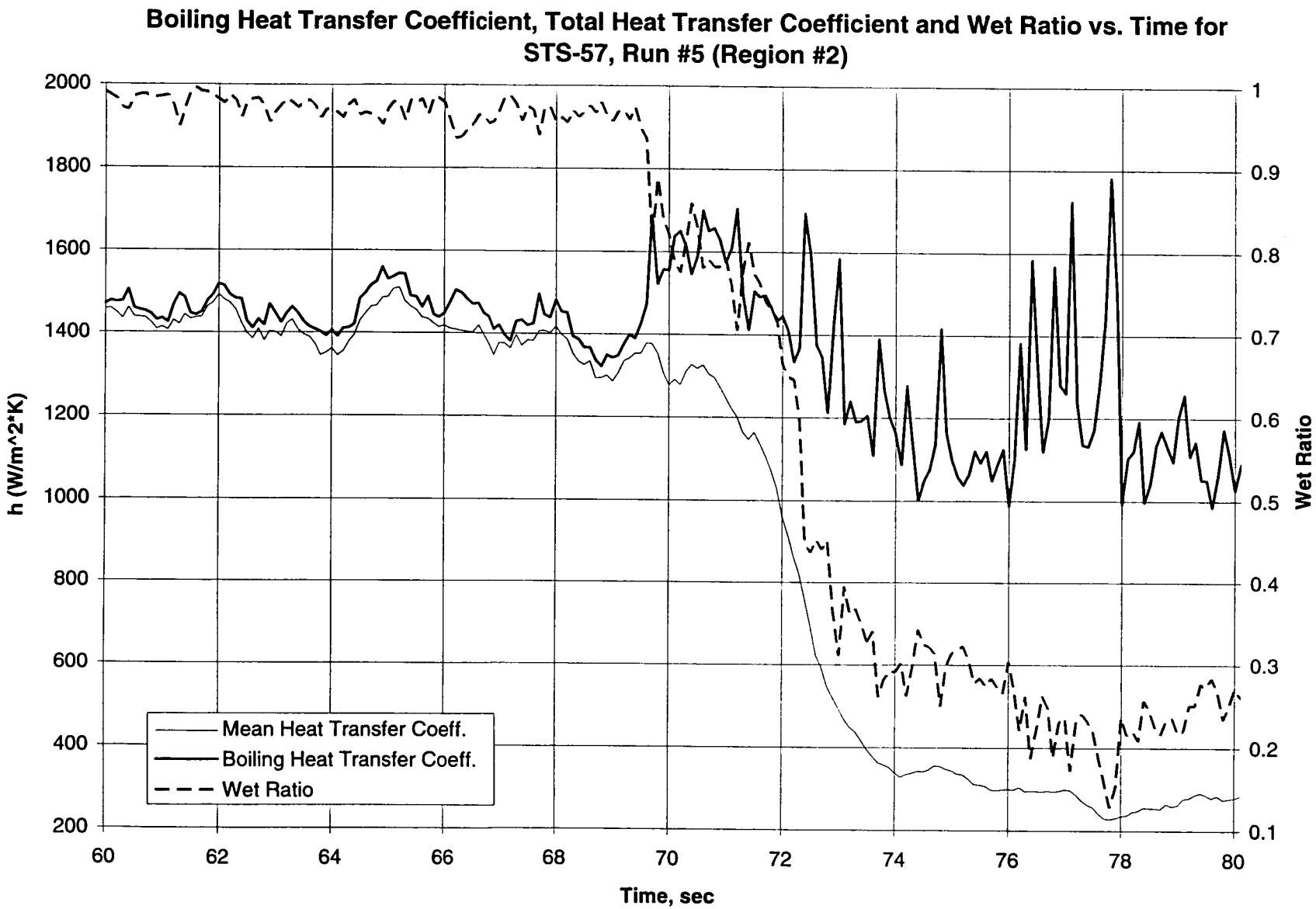

Figure B-10e-2-iii. Development of microgravity boiling heat transfer coefficient. PBE-IB (STS-57). Run No. 5. Time interval: 60 - 80 seconds.

STS-57 Run #5 (Region #2)

t= 51.29 sec.

t= 62.79 sec.

t= 65.71 sec.

t= 68.61 sec.

t= 71.53 sec.

t= 74.50 sec.

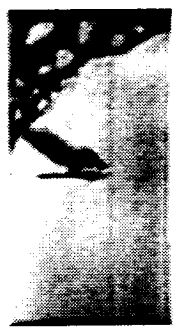

t= 77.40 sec.

t= 80.43 sec.

Figure B-10e-2-iv. Sample images showing dryout/rewetting. PBE-IB (STS-57). Run No. 5. Time interval: 60 - 80 seconds.

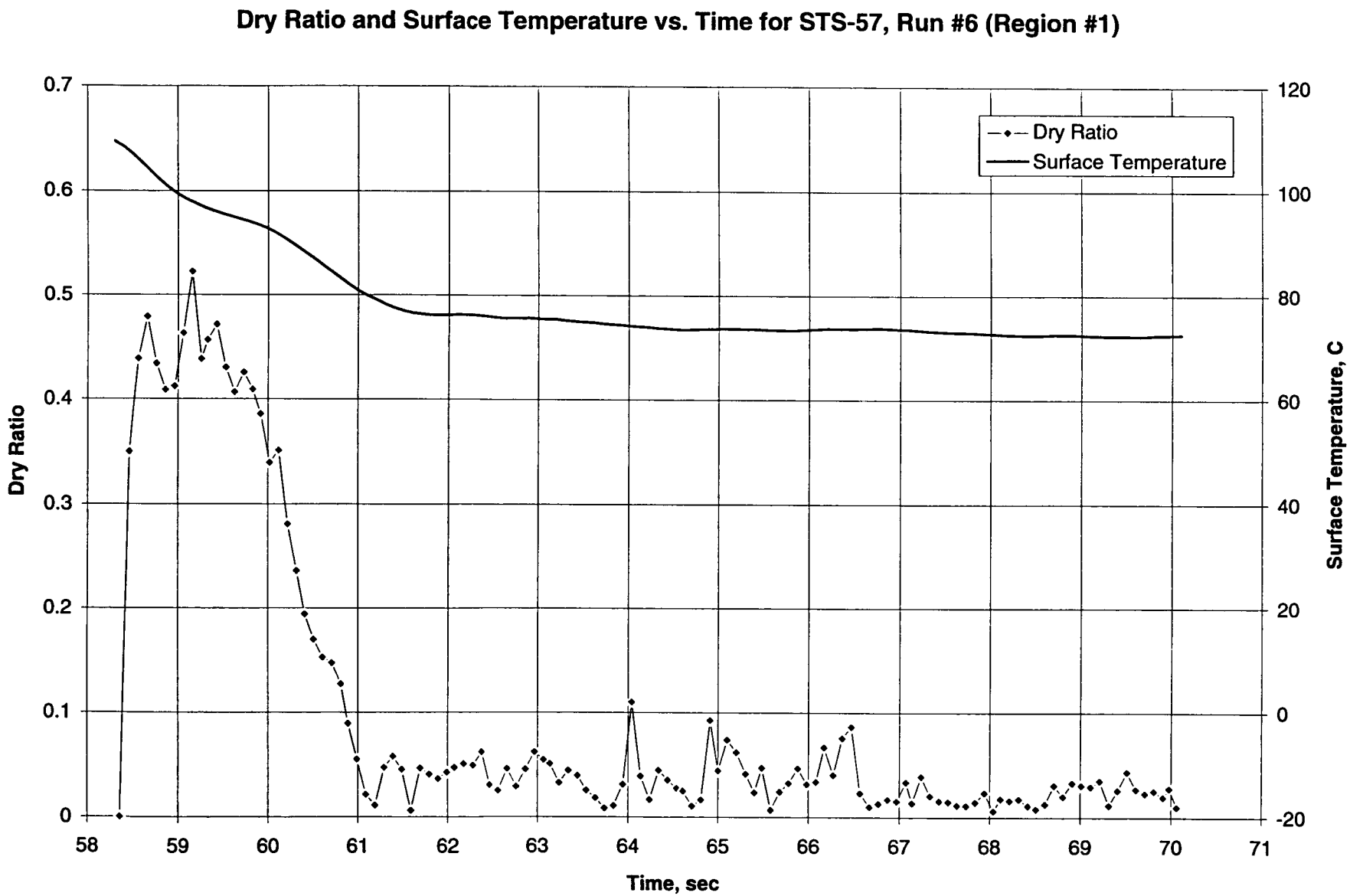

Figure B-10f-1-i. Heater surface dry fraction and mean temperature. PBE-IB (STS-57). Run No. 6. Time interval: 58.4 - 70.0 seconds.

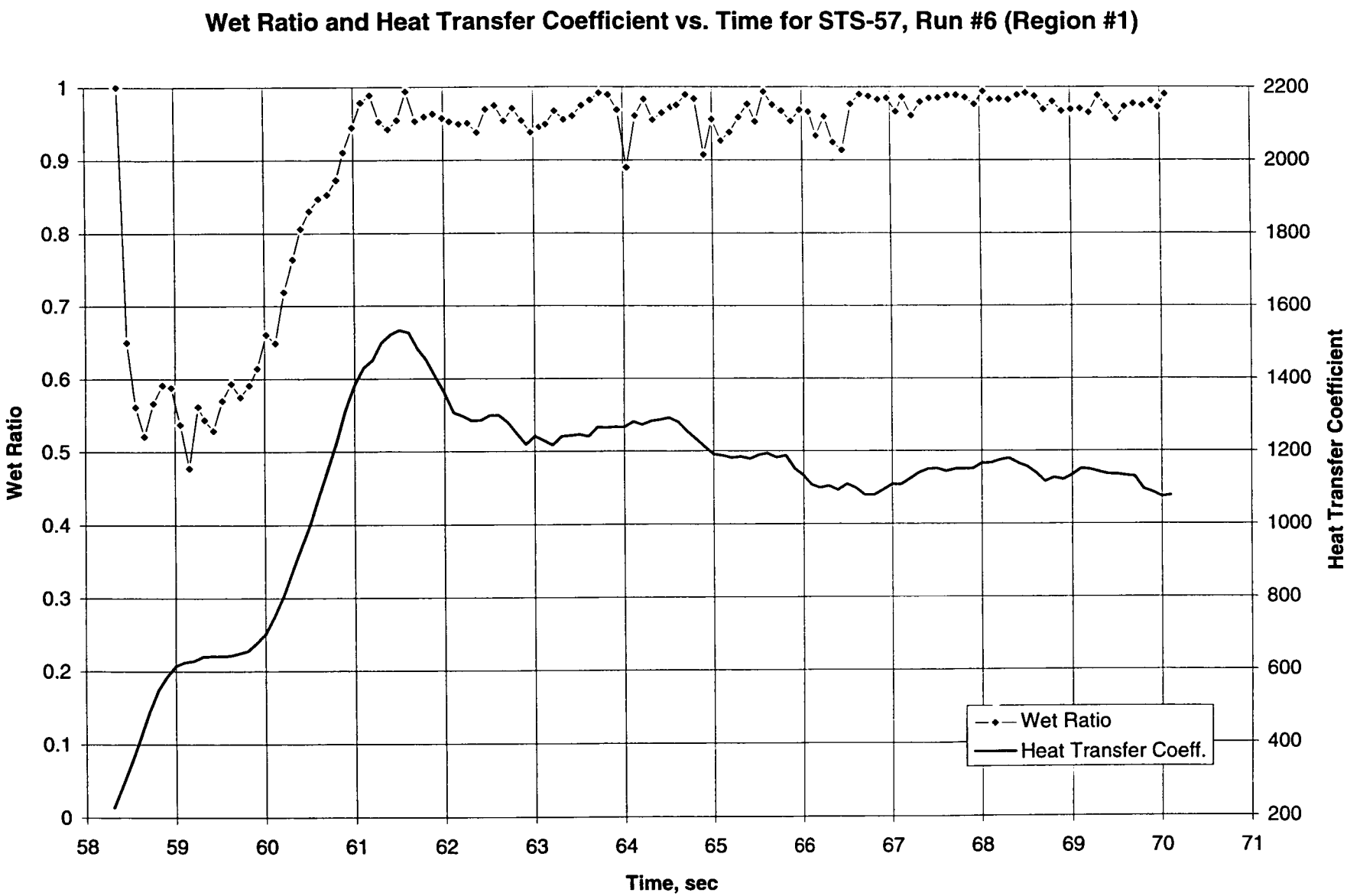

Figure B-10f-1-ii. Heater surface wet fraction and mean heat transfer coefficients. PBE-IB (STS-57). Run No. 6. Time interval: 58.4 - 70.0 seconds.

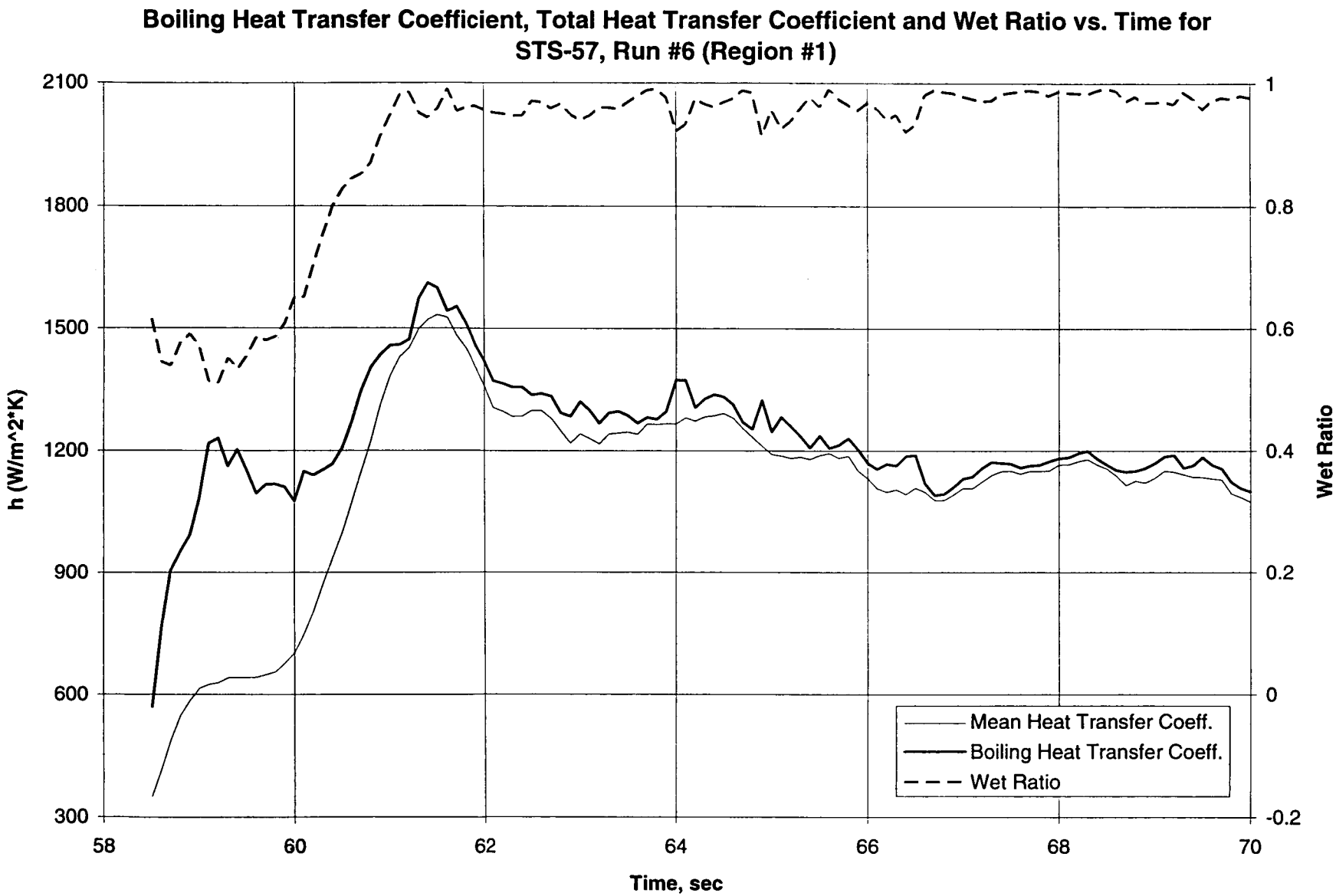

Figure B-10f-1-iii. Development of microgravity boiling heat transfer coefficient. PBE-IB (STS-57). Run No. 6 Time interval: 58.4 - 70.0 seconds.

STS-57 Run #6 (Region #1)

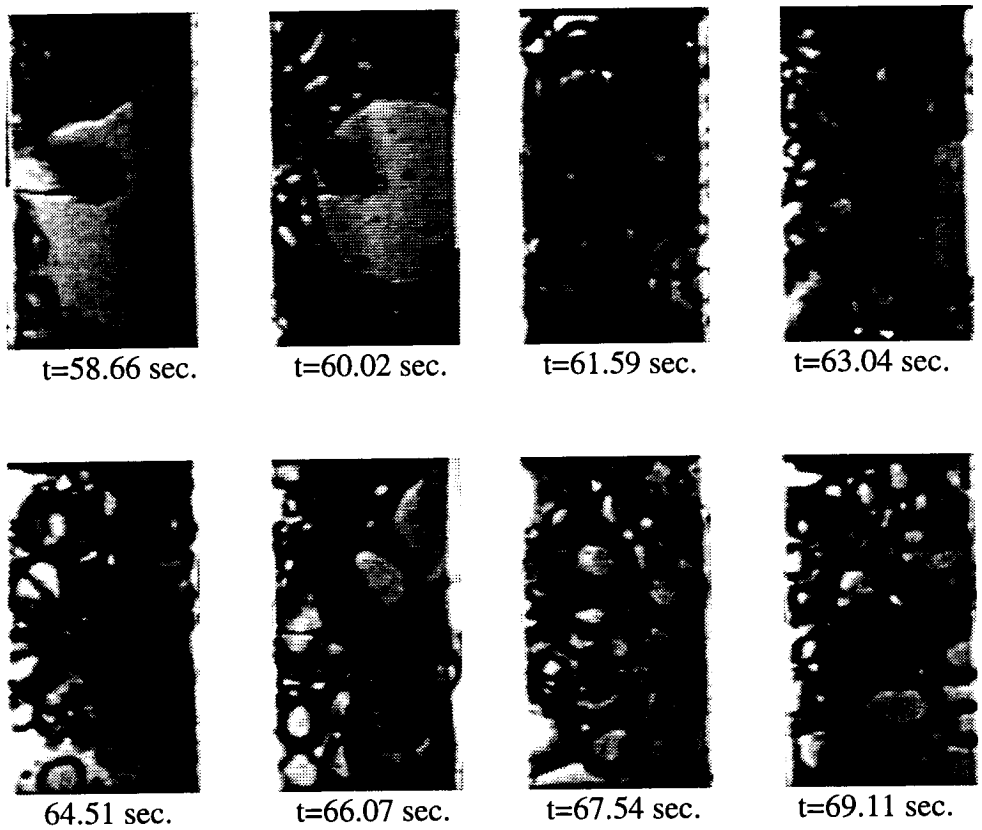

Figure B-10f-1-iv. Sample images showing dryout/rewetting. PBE-IB (STS-57). Run No. 6. Time interval: 58.4 - 70.0 seconds.

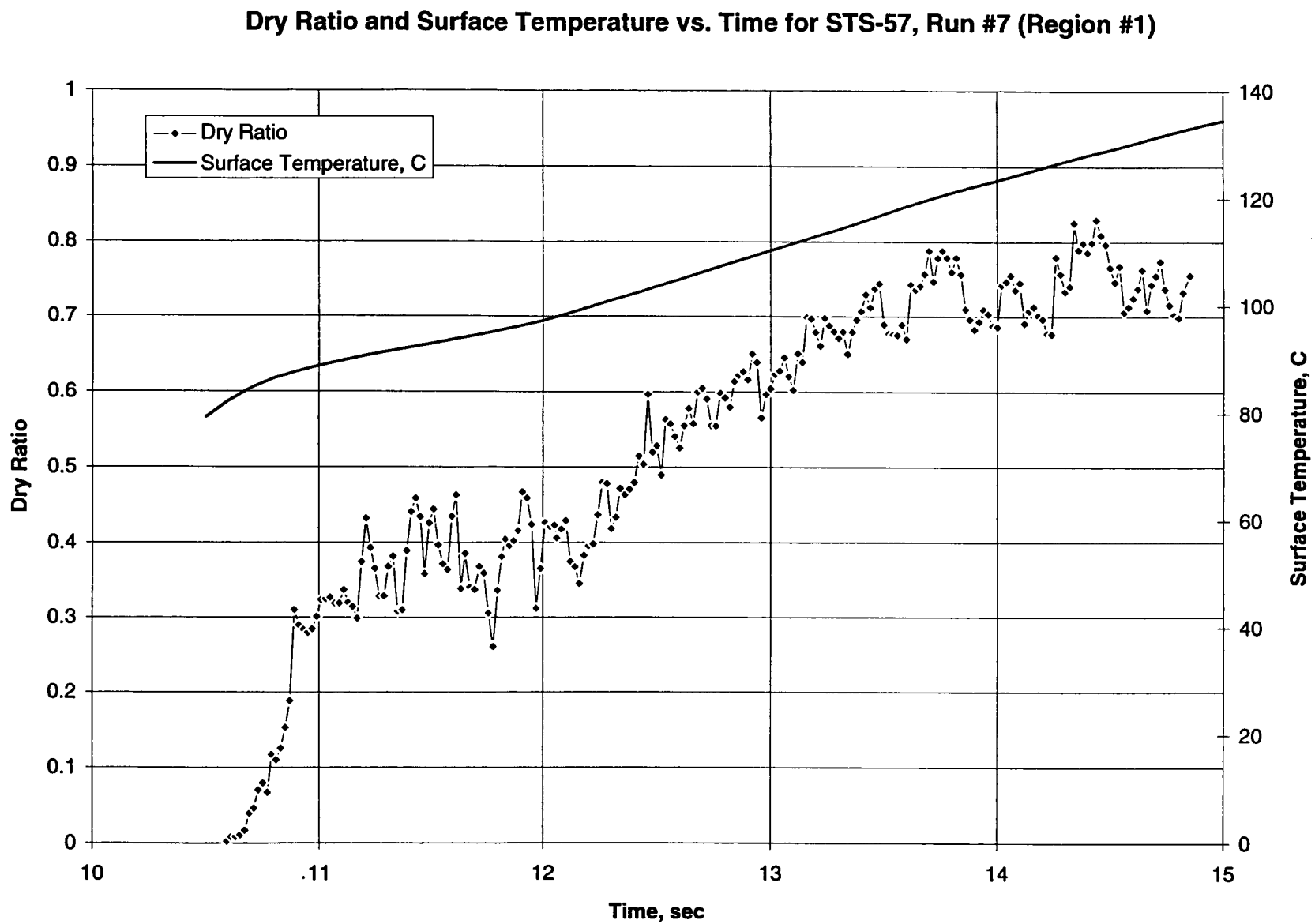

Figure B-10g-1-i. Heater surface dry fraction and mean temperature. PBE-IB (STS-57). Run No. 7. Time interval: 10.6 - 14.8 seconds.

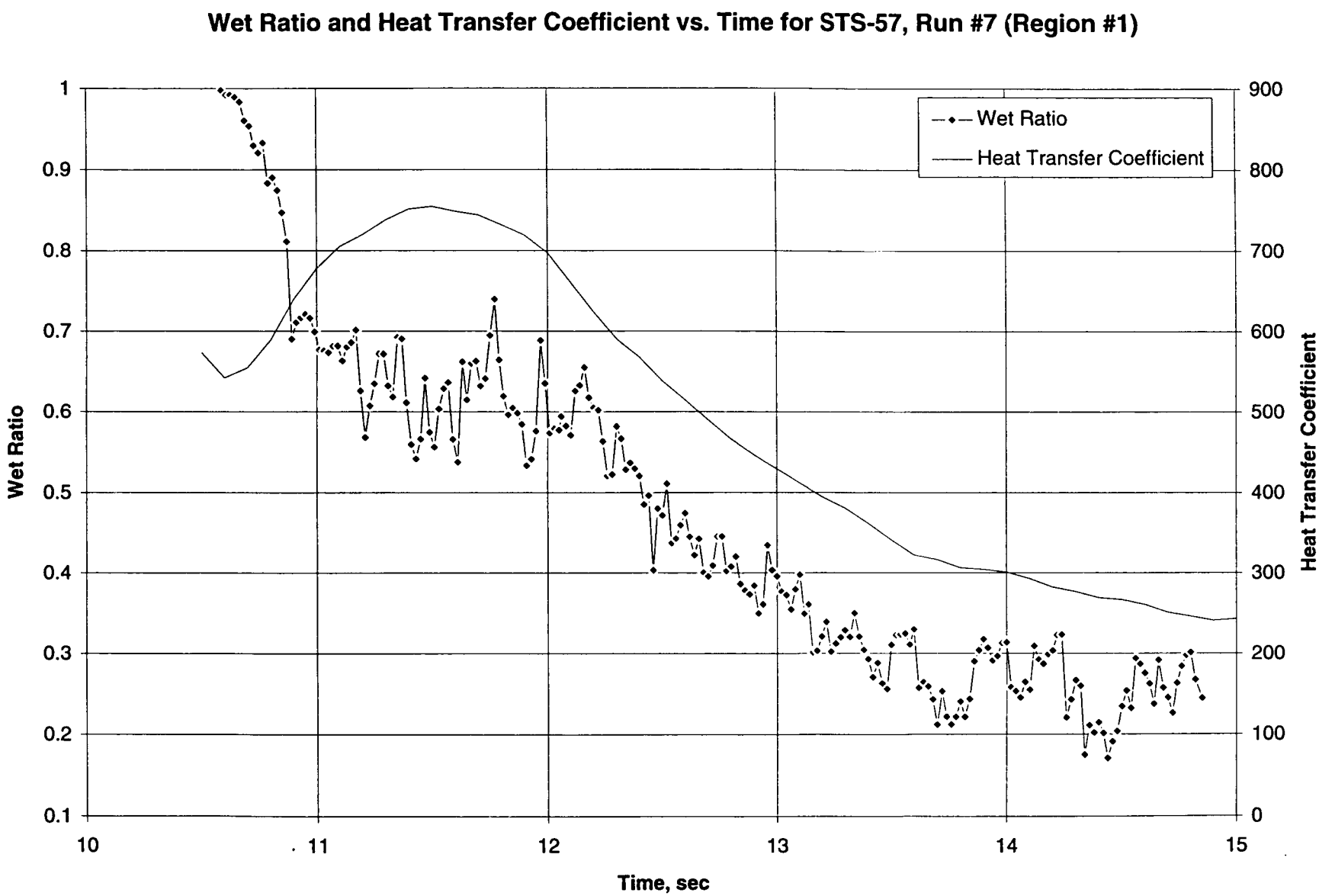

Figure B-10g-1-ii. Heater surface wet fraction and mean heat transfer coefficients. PBE-IB (STS-57). Run No. 7. Time interval: 10.6 - 14.8 seconds.

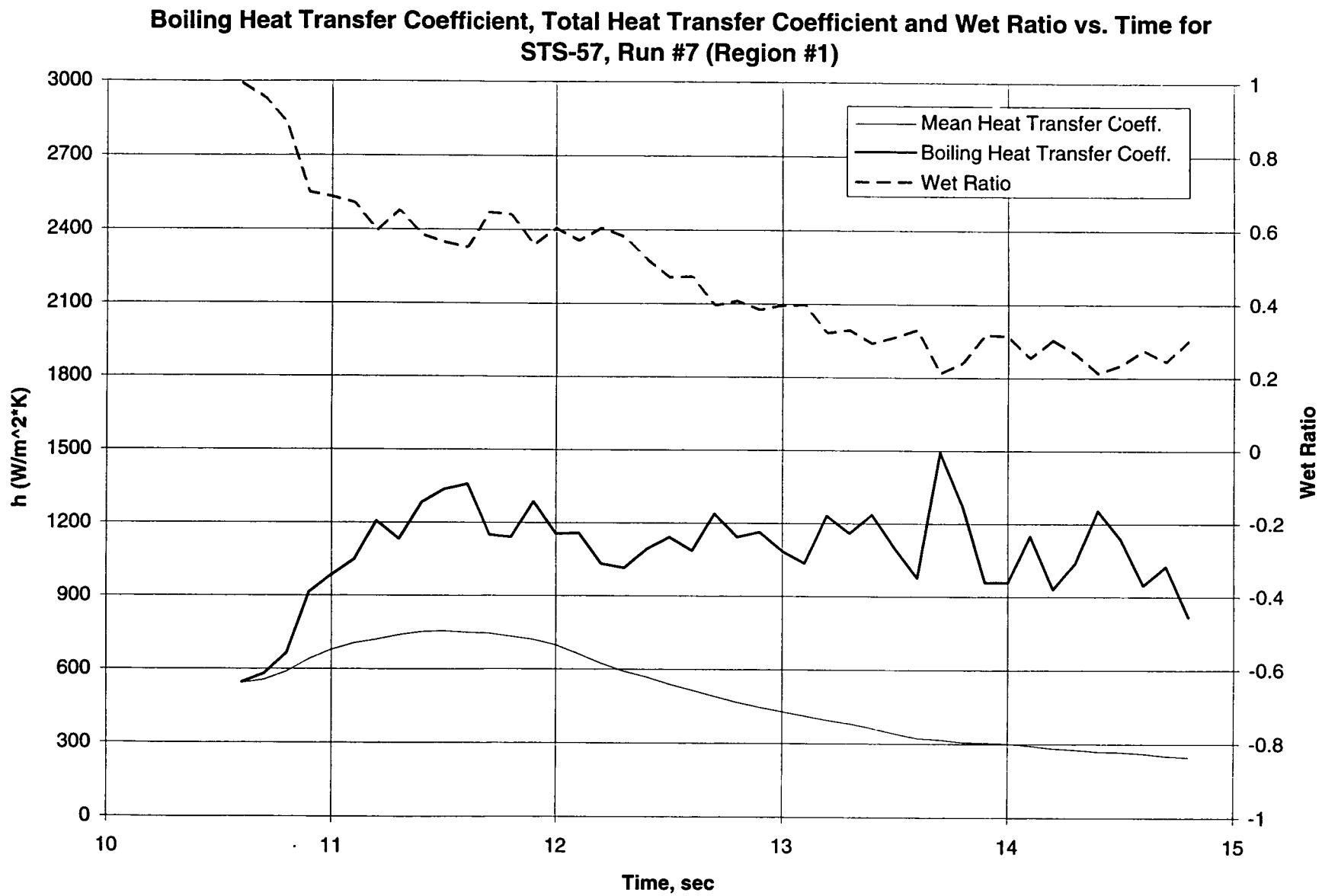

Figure B-10g-1-iii. Development of microgravity boiling heat transfer coefficient. PBE-IB (STS-57). Run No. 7. Time interval: 10.6 - 14.8 seconds.

STS-57 Run #7 (Region #1)

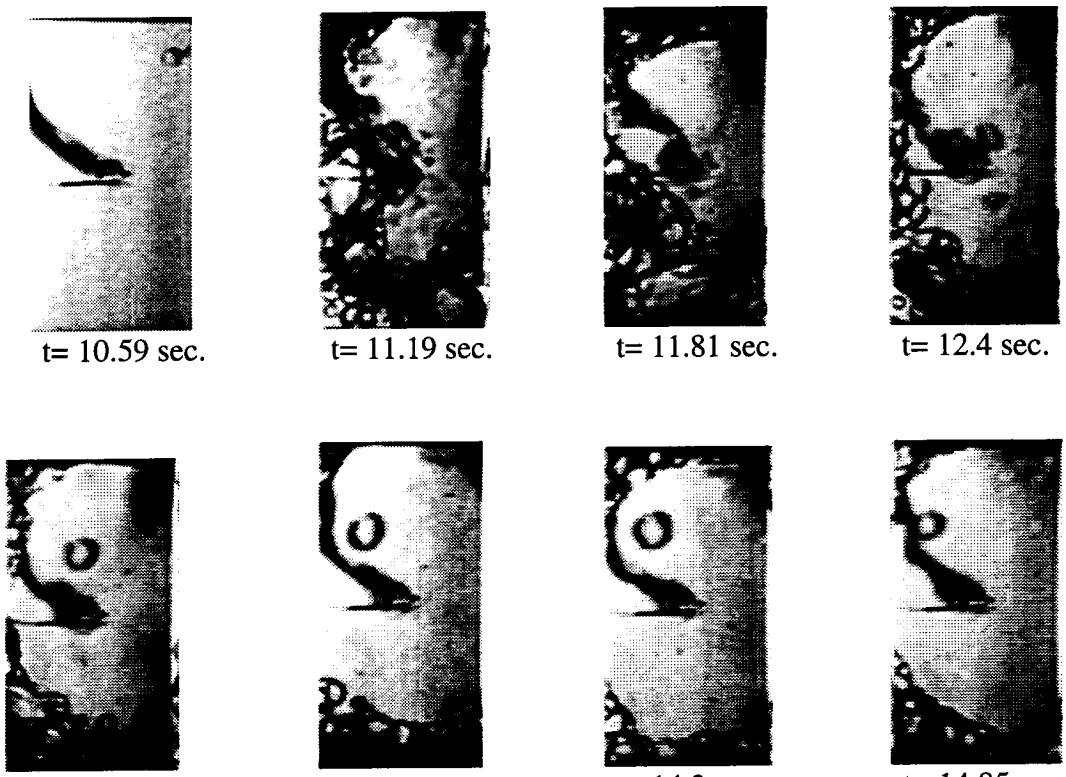

Figure B-10g-1-iv. Sample images showing dryout/rewetting. PBE-IB (STS-57). Run No. 7. Time interval: 10.6 - 14.8 seconds.

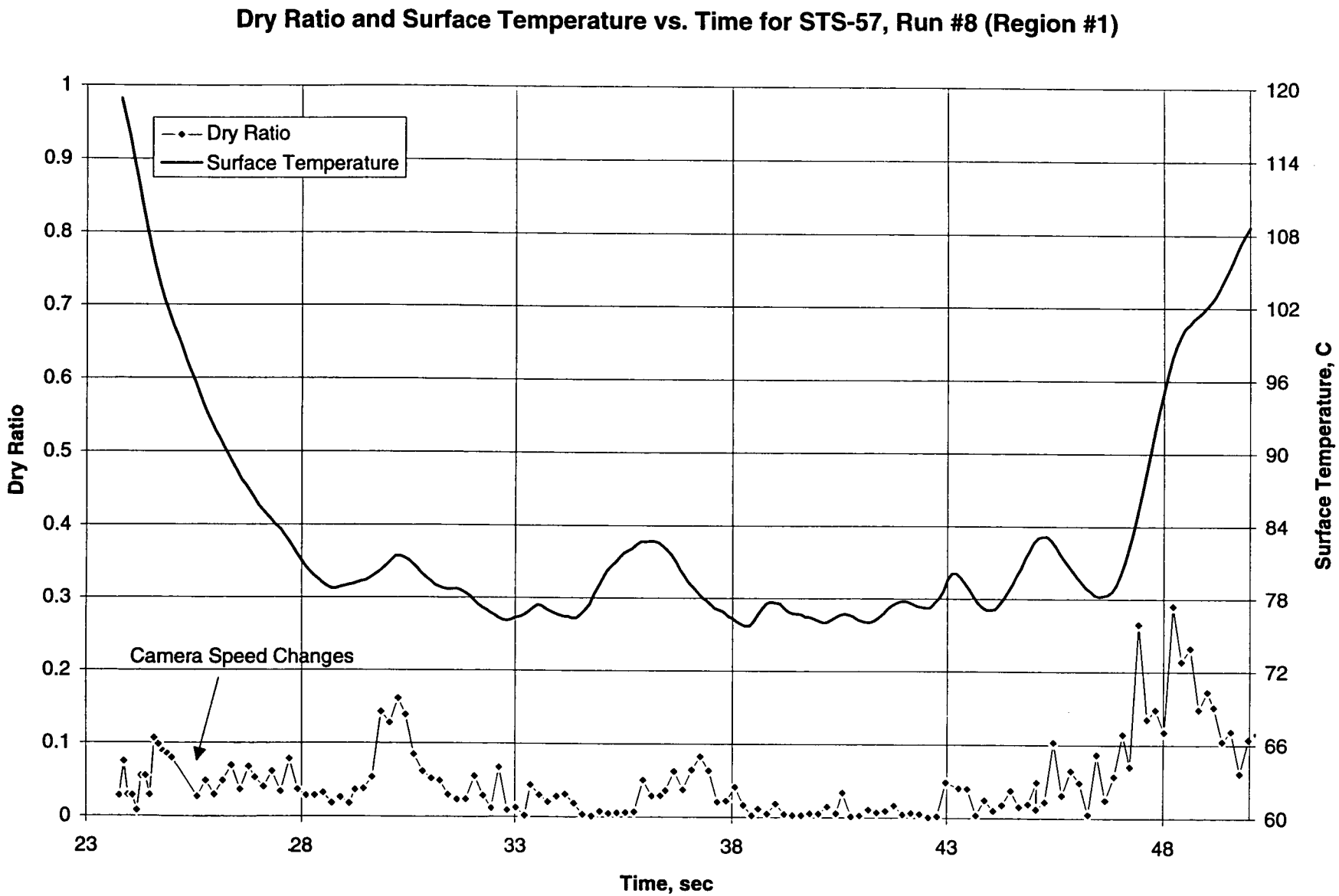

Figure B-10h-1-i. Heater surface dry fraction and mean temperature. PBE-IB (STS-57). Run No. 8. Time interval: 23.8 - 50.0 seconds.

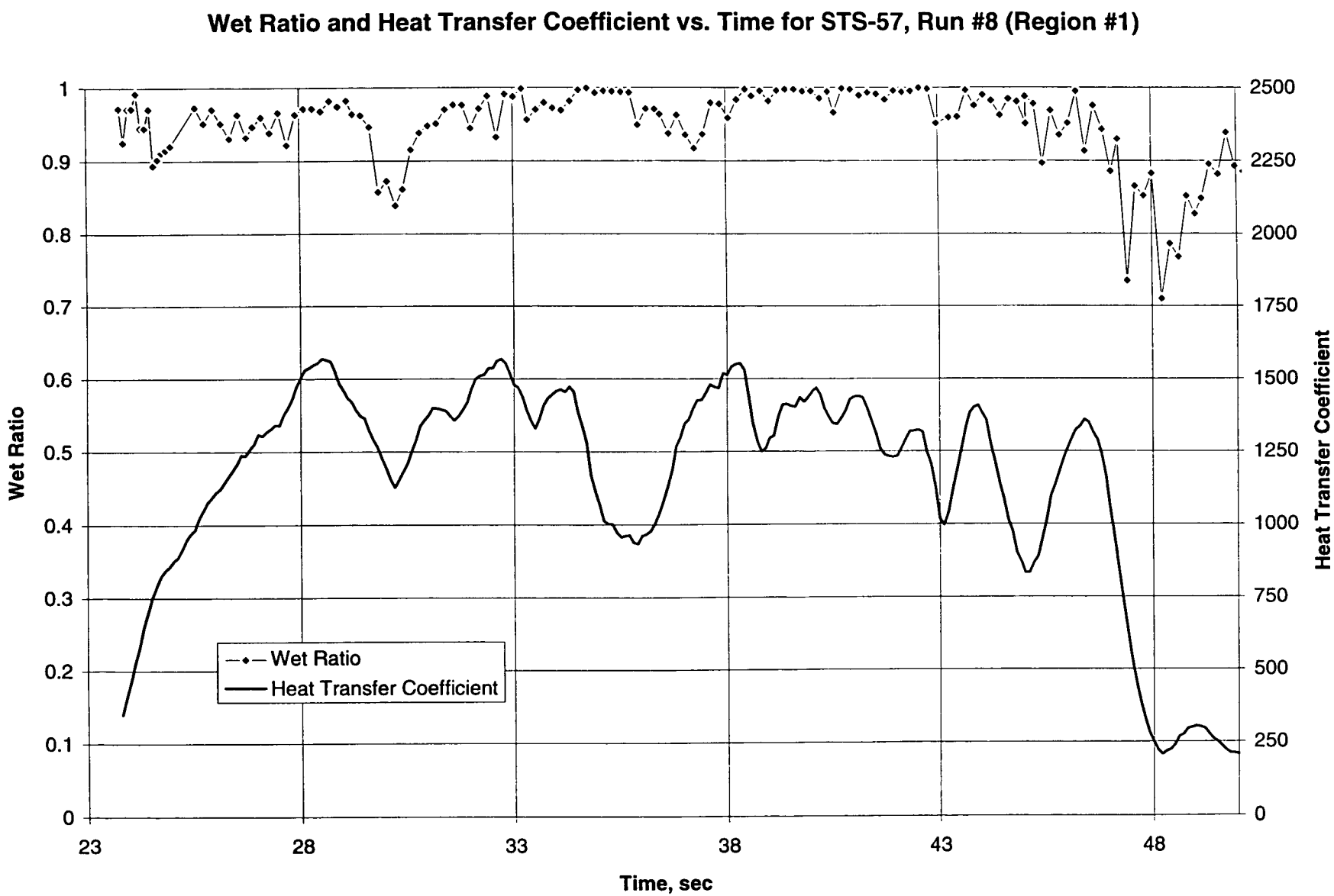

Figure B-10h-1-ii. Heater surface wet fraction and mean heat transfer coefficients. PBE-IB (STS-57). Run No. 8. Time interval: 23.8 - 50.0 seconds.

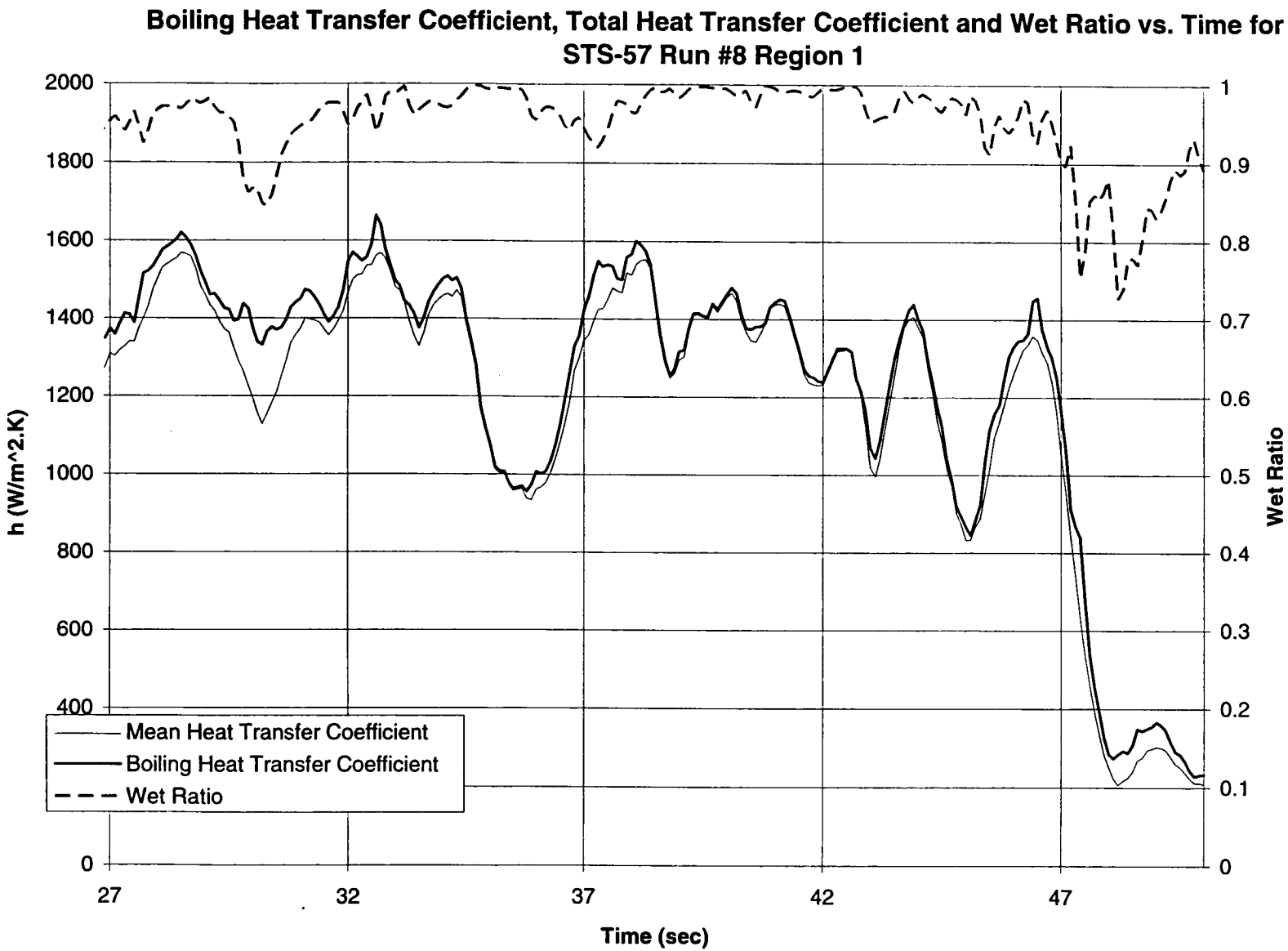

Figure B-10h-1-iii. Development of microgravity boiling heat transfer coefficient. PBE-IB (STS-57). Run No. 8. Time interval: 23.8 - 50.0 seconds.

STS-57 Run#8, Region#1

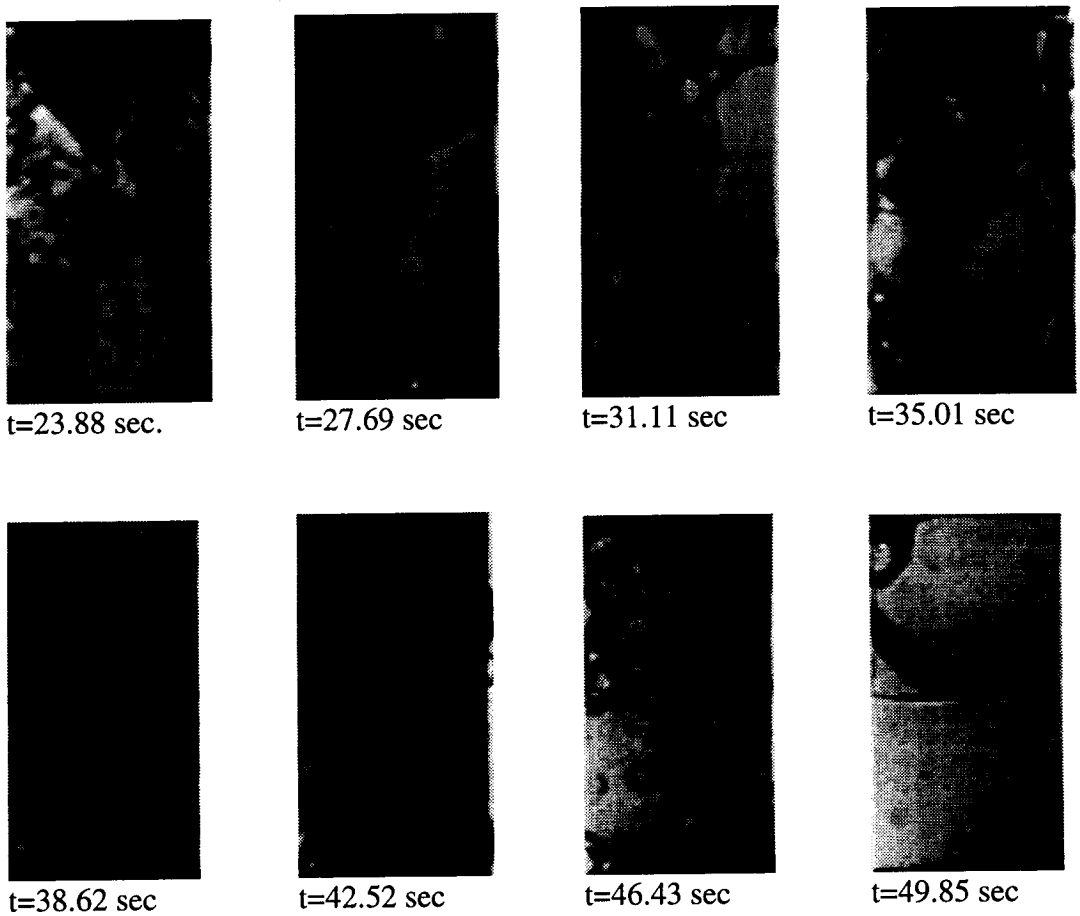

Figure B-10h-1-iv. Sample images showing dryout/rewetting. PBE-IB (STS-57). Run No. 8. Time interval: 23.8 - 50.0 seconds.

Appendix C. PBE-IC (STS-60). Experimental Results

		Page No. C-
1.	Table C-I. Test matrix for PBE-IC (STS-60). (Prototype Hardware)	2
2.	Table C-II. Measured parameters at a/g = -1, a/g = +1, and Space Flight	3
3.	Table C-III. Summary of relatively larger acceleration excursions during PBE-IC (STS-60).	5
4.	Figures C-1a — C-1i. Mean heater surface temperature and derived heat transfer coefficient. PBE-IC (STS-60). Run Nos. 1-9	6-14
5.	Figures C-2a — C-2i. Heat flux input. PBE-IC (STS-60). Run Nos. 1-9.	15-23
6.	Figures C-3a — C-3i. System pressure and fluid side mean heat flux. PBE-IC (STS-60). Run Nos. 1-9.	24-32
7.	Figures C-4a — C4i. Measured fluid temperatures near primary heater and far field bulk liquid. PBE-IC (STS-60). Run Nos. 1-9.	33-41
8.	Figures C-5a — C-5i. Measured fluid temperatures near secondary heater and heater underside. PBE-IC (STS-60). Run Nos. 1-9	42-50
9.	Figures C-6a — C-6i. Selected Photographic Images. PBE-IC (STS-60). Run Nos. 1-9.	51-70
10.	Figure C-7. Nucleation Delay Time. Comparisons with ground testing and drop tower correlation. PBE-IC (STS-60).	71
11.	Figure C-8. Mean heater surface nucleation superheat. Comparisons with ground testing. PBE-IC (STS-60).	72
12.	Figures C-9a — C-9i. Comparisons of bubble growth measurements with several models. PBE-IC (STS-60). Run Nos. 1-9.	73-82
13.	Table C-IV. Index for heater surface dry fraction measurements and computation of microgravity nucleate boiling heat transfer coefficients. PBE-IC (STS-60).	83
14.	Figures C-10a — C-10i. Development of microgravity boiling heat transfer coefficients from heater surface dry fraction and mean heat transfer coefficients. PBE-IC (STS-60) Run Nos. 1-9.	84-135
15.	Figures C-11a — C-11i. a/g = +1 Post flight test. Mean heater surface temperature and derived heat transfer coefficient. PBE-IC (STS-60). Run Nos. 1-9.	136-144
16.	Figures C-12a — C-12i. a/g = +1 Postflight test. Heat flux input. PBE-IC. (STS-60). Run Nos. 1-9.	145-153
17.	Figures C-13a — C-13i. a/g = +1. Postflight test. System pressure and heat flux into fluid. PBE-IC (STS-60). Run Nos. 1-9.	154-162

PBE Prototype System Test Matrix (STS-60)

RUN NO.	HEAT FLUX W/CM^2	SUBCOOLING (°F)	HEATER POWER ON/OFF (SEC)	10 FPS ON/OFF (SEC)	100 FPS ON/OFF (SEC)	STIRRER START (SEC)	REPRESS. START (SEC)	TOTAL TEST TIME (SEC)
1	8	20 ± 2	10--15	13--55	10--13	-	-	55
2	4	20 ± 2	10--110	10--15, 25--130	15--25	-	-	135
3	2	20 ± 2	10--120	20--30, 50--130	30--50	110-	-	130
4	8	5 ± 1	10--55	13--60	10--13	45-	-	60
5	4	5 ± 1	10--100	10--20, 30--105	20--30	90-	-	105
6	2	5 ± 1	10--85	20--30, 50--100	30--50	-	-	100
7	8	0.5 ± 0.4	10--15	25--40	10--25	-	20-	40
8	4	0.5 ± 0.4	10--70	10--15, 25--80	15--25	60-	-	80
9	2	0.5 ± 0.4	10--115	10--40, 60--125	40--60	95-	-	125

June 30,1993

Version 3.0

Table C-I. Test matrix for PBE-IC (STS-60). (Prototype Hardware).

NASA test Matrix for Pool boiling - STS-60

a/g -1 experiment based on date 7/6/93
a/g 0 experiment based on date 2/3 /94
a/g -1 experiment based on date 5/3/94
a/g +1 experiment based on date 5/4/94

Run#	Date of Experiment	Flight system	Gravit a/g	Heat Flux, W/cm^ Nom.	Heat Flux, W/cm^ Actual	Subcool,oF Nom.o	Subcool,oF Actual o	Tbulk oC	Sys.Press kPa	Tsat oC	T*wall oC	T*sup oC	t* time sec	100fps On-Off	Remark
1	7/6/93	Prototype	-1	8.00	6.834	20	20.75	49.46	155.27	60.99	78.73	17.74	0.56	0 – 3	
	2/3/94	Prototype	0	8.00	7.044	20	20.7	48.34	149.96	59.84	91.30	31.46	0.91	0 – 3	
	5/3/94	Prototype	-1	8.00	6.866	20	20.75	49.62	156.01	61.15	83.26	22.11	0.67	0 – 3	
	5/4/94	Prototype	1	8.00	7.03	20	20.81	48.02	148.78	59.58	96.90	37.32	2.26	0 – 3	bubble appeared before film began; time is sudden growth
2	7/6/93	Prototype	-1	4.00	3.365	20	20.74	48.65	151.44	60.17	122.20	62.03	19.53	5 – 15	
	2/3/94	Prototype	0	4.00	3.601	20	20.72	47.43	145.88	58.94	122.70	63.76	20.85	5 – 15	
	5/3/94	Prototype	-1	4.00	3.372	20	20.75	48.38	150.29	59.91	102.39	42.48	7.99	5 – 15	
	5/4/94	Prototype	1	4.00	3.584	20	20.77	48.35	150.18	59.89	97.30	37.41	35.08	5 – 15	
3	7/6/93	Prototype	-1	2.00	1.763	20	20.7	50.09	158.08	61.59	101.13	39.54	59.11	20 – 40	
	2/3/94	Prototype	0	2.00	1.804	20	20.81	48.85	152.55	60.41	99.70	39.29	40.17	20 – 40	
	5/3/94	Prototype	-1	2.00	1.768	20	20.75	49.94	157.53	61.47	99.50	38.03	52.82	20 – 40	
	5/4/94	Prototype	1	2.00	1.811	20	20.74	48.62	151.34	60.14				20 – 40	No Nucleation
4	7/6/93	Prototype	-1	8.00	6.293	5	5.76	49.09	118.45	52.29	69.00	16.71	0.29	0 – 3	
	2/3/94	Prototype	0	8.00	6.491	5	5.8	48.77	117.30	51.99	86.30	34.31	0.74	0 – 3	
	5/3/94	Prototype	-1	8.00	6.327	5	5.81	48.86	117.69	52.09	82.34	30.25	0.65	0 – 3	
	5/4/94	Prototype	1	8.00	7.06	5	5.78	47.93	114.14	51.14	90.90	39.76	0.76	0 – 3	
5	7/6/93	Prototype	-1	4.00	3.366	5	5.76	49.24	119.02	52.44	115.35	62.91	13.56	10 – 20	
	2/3/94	Prototype	0	4.00	3.476	5	5.72	48.88	117.58	52.06	103.80	51.74	9.6	10 – 20	
	5/3/94	Prototype	-1	4.00	3.39	5	5.8	49.32	119.38	52.54	114.89	62.35	14.15	10 – 20	
	5/4/94	Prototype	1	4.00	3.556	5	5.80	47.99	114.39	51.21				10 – 20	No Nucleation

Page 2 of 2

Table C-II. Measured parameters at a/g = -1, a/g = +1, and Space Flight.

Run#	Date of Experiment	Flight system	Gravit a/g	Heat Flux, W/cm^ Nom.	Actual	Subcool,oF Nom.o	Actual o	Tbulk oC	Sys.Press kPa	Tsat oC	T*wall oC	T*sup oC	t* time sec	100pps On-Off	Remark
6	7/6/93	Prototype	-1	2.00	1.775	5	5.8	49.09	118.52	52.31	102.02	49.71	54.04	20 – 40	
	2/3/94	Prototype	0	2.00	1.805	5	5.78	49.28	119.22	52.49	98.50	46.01	37.94	20 – 40	
	5/3/94	Prototype	-1	2.00	1.784	5	5.8	48.9	117.80	52.12	101.74	49.62	57.55	20 – 40	
	5/4/94	Prototype	1	2.00	1.815	5	5.87	47.95	114.40	51.21				20 – 40	No Nucleation
7	7/6/93	Prototype	-1	8.00	6.826	0.50	1.33	48.91	108.74	49.65	83.59	33.94	0.78	0 – 15	
	2/3/94	Prototype	0	8.00	6.948	0.50	1.37	48.35	106.80	49.11	88.10	38.99	0.75	0 – 15	
	5/3/94	Prototype	-1	8.00	6.858	0.50	1.35	48.8	108.38	49.55	78.86	29.31	0.6	0 – 15	
	5/4/94	Prototype	1	8.00	7.083	0.50	2.7	47.49	106.40	48.99	84.80	35.81	0.73	0 – 15	
8	7/6/93	Prototype	-1	4.00	3.412	0.50	1.4	48.87	108.74	49.65	104.17	54.52	9.31	5 – 15	
	2/3/94	Prototype	0	4.00	3.513	0.50	1.28	48.34	106.62	49.05	98.30	49.25	8.03	5 – 15	
	5/3/94	Prototype	-1	4.00	3.428	0.50	1.39	48.85	108.62	49.62	103.43	53.81	8.09	5 – 15	
	5/4/94	Prototype	1	4.00	3.569	0.50	1.33	47.50	103.80	48.24				5 – 15	No Nucleation
9	7/6/93	Prototype	-1	2.00	1.765	0.50	1.39	48.86	108.66	49.63	97.90	48.27	49.95	30 – 50	
	2/3/94	Prototype	0	2.00	1.81	0.50	1.3	48.64	107.70	49.36	93.70	44.34	30.52	30 – 50	
	5/3/94	Prototype	-1	2.00	1.765	0.50	1.4	48.89	108.80	49.67	97.90	48.23	44.13	30 – 50	
	5/4/94	Prototype	1	2.00	1.81	0.50	1.37	47.70	104.57	48.46				30 – 50	No Nucleation

Table C-II. Continued.

Notes: (1) Accelerometer units are given as micro-g's.

(2) Heating in each run begins at t = 10 sec.

RUN #	Time, sec	Plots	Max Value			Uncertainty (Noise)	Comments
			x	y	z	2.40E+01	
1	19.9	yes	26	52	**99**	2.40E+01	
2	30.8	yes	26	39	**99**	2.40E+01	
2	39.8	yes	26	**64**	50	2.40E+01	
2	102	yes	**179**	39	50	2.40E+01	
3	112.3	yes	54	**129**	149	2.40E+01	
3	113.6	yes	**255**	0	**199**	2.40E+01	
4	27.5	yes	**255**	77	0	2.40E+01	
4	28.9	yes	230	**129**	**224**	2.40E+01	
5	19.9	yes	0	13	**100**	2.40E+01	
5	79.7	yes	25	**90**	25	2.40E+01	
5	90.9	yes	**77**	13	0	2.40E+01	
6	39.7	yes	**382**	13	224	2.40E+01	
6	74.1	yes	179	193	**497**	2.40E+01	
6	74.6	yes	128	**219**	348	2.40E+01	
7		no	51	64	50	2.40E+01	
8	15.9	yes	153	**142**	**348**	2.40E+01	
8	17.3	yes	**179**	64	224	2.40E+01	
9	24	yes	0	**90**	25	2.40E+01	
9	76.6	yes	0	39	**75**	2.40E+01	
9	83.2	yes	**77**	39	0	2.40E+01	

Table C-III. Summary of relatively larger acceleration excursions during PBE-IC (STS-60).

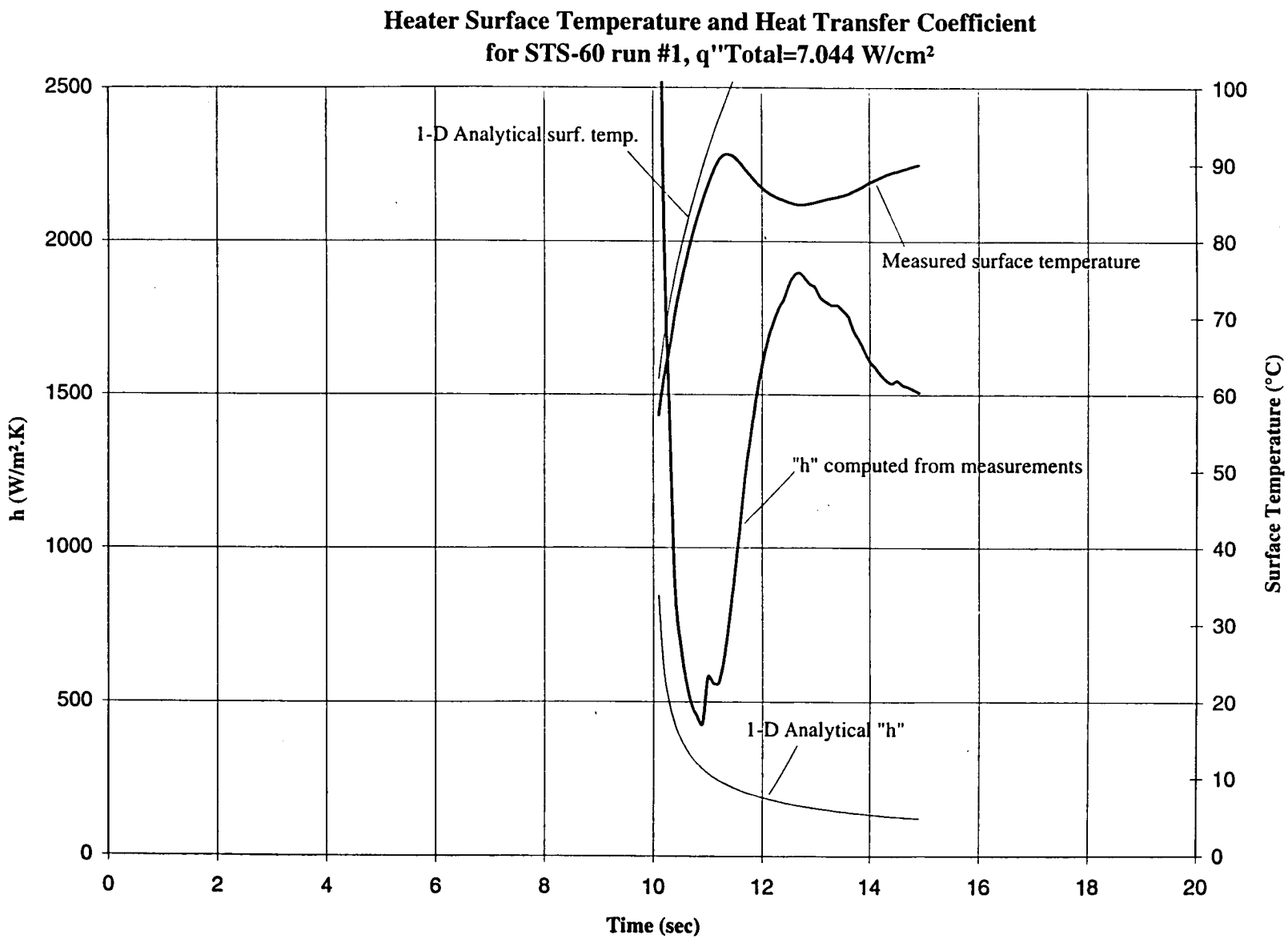

Figure C-1a. Mean heater surface temperature and derived heat transfer coefficient. PBE-IC (STS-60). Run No. 1.

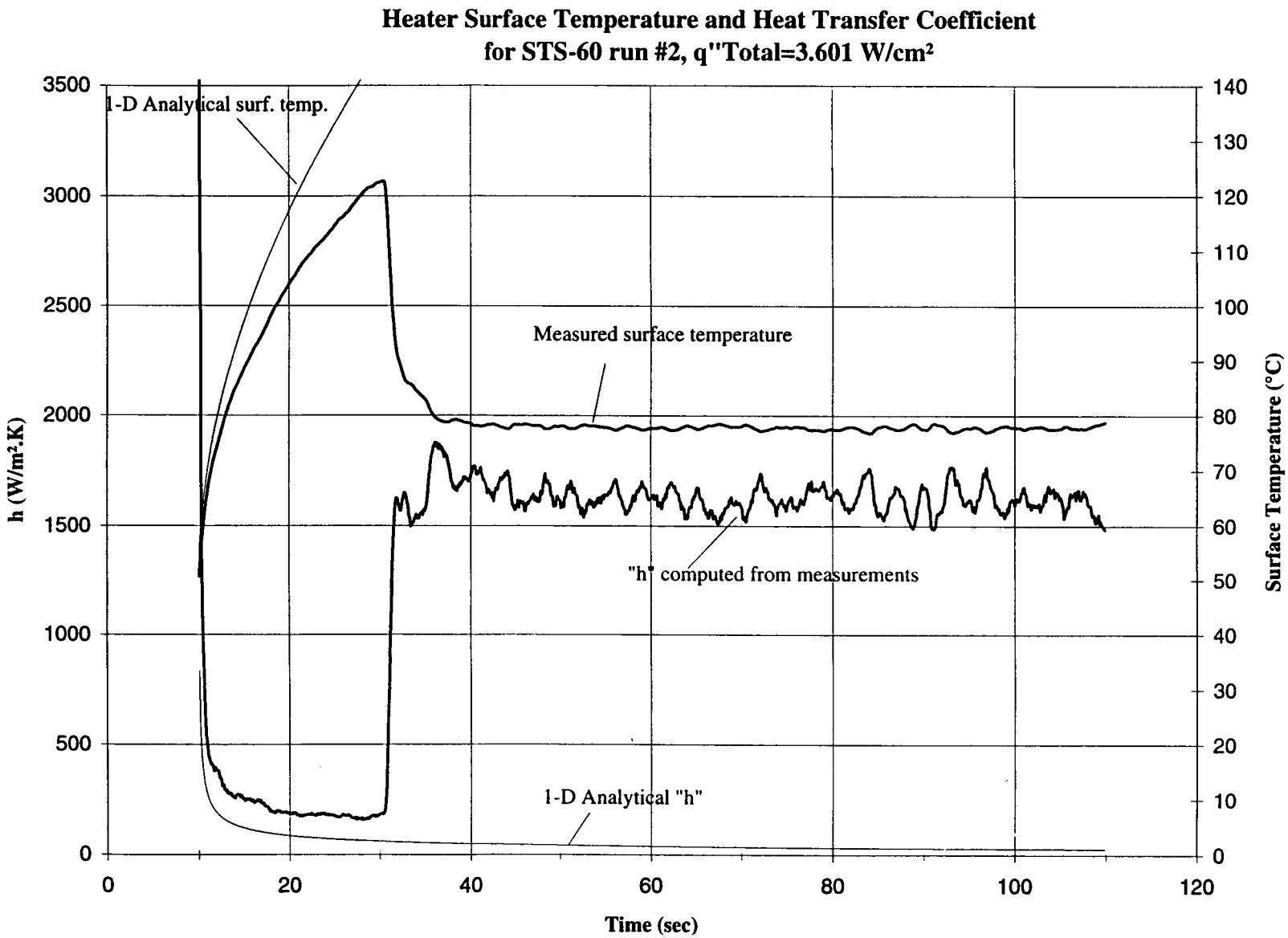

Figure C-1b. Mean heater surface temperature and derived heat transfer coefficient. PBE-IC (STS-60). Run No. 2.

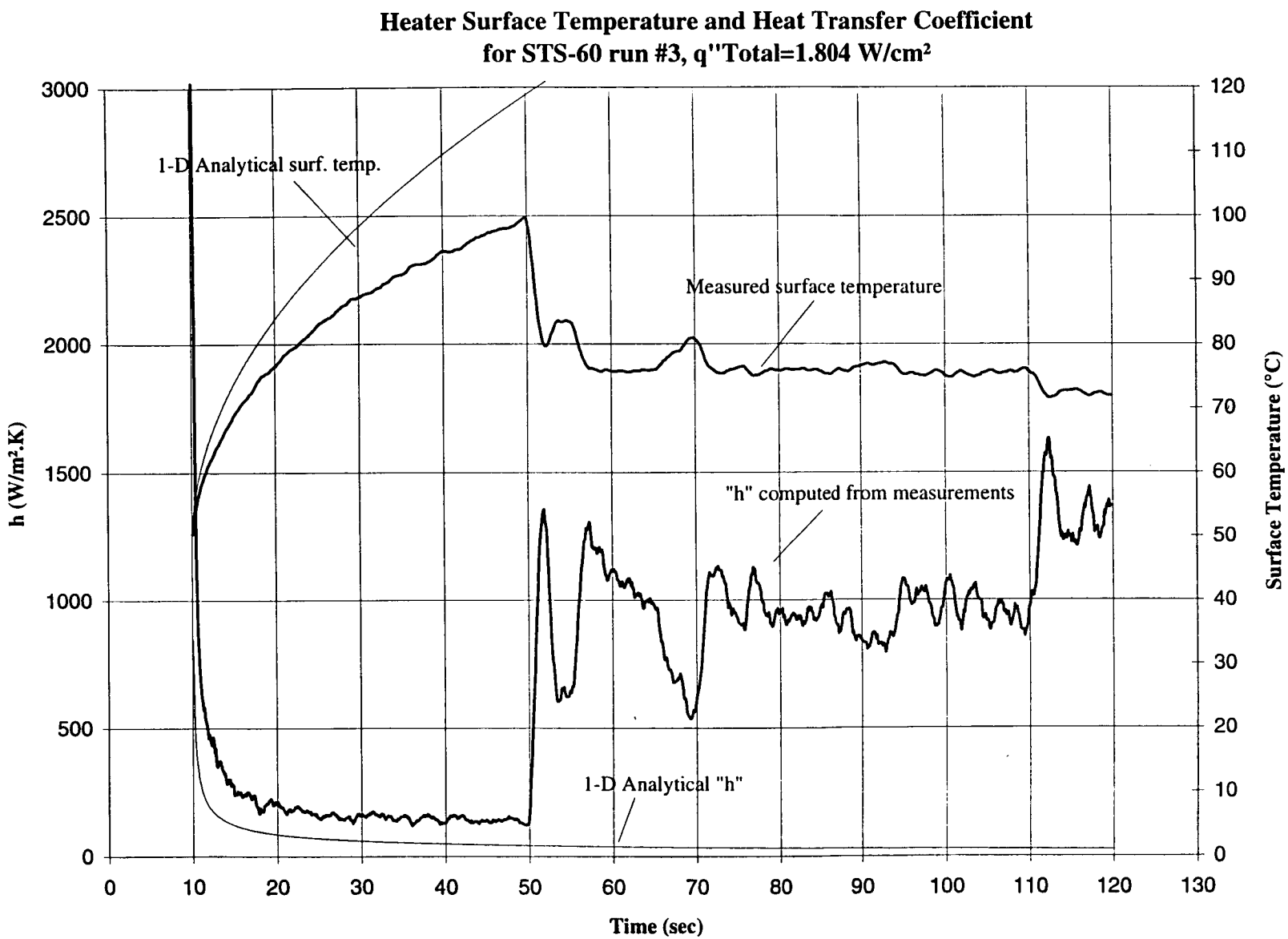

Figure C-1c. Mean heater surface temperature and derived heat transfer coefficient. PBE-IC (STS-60). Run No. 3.

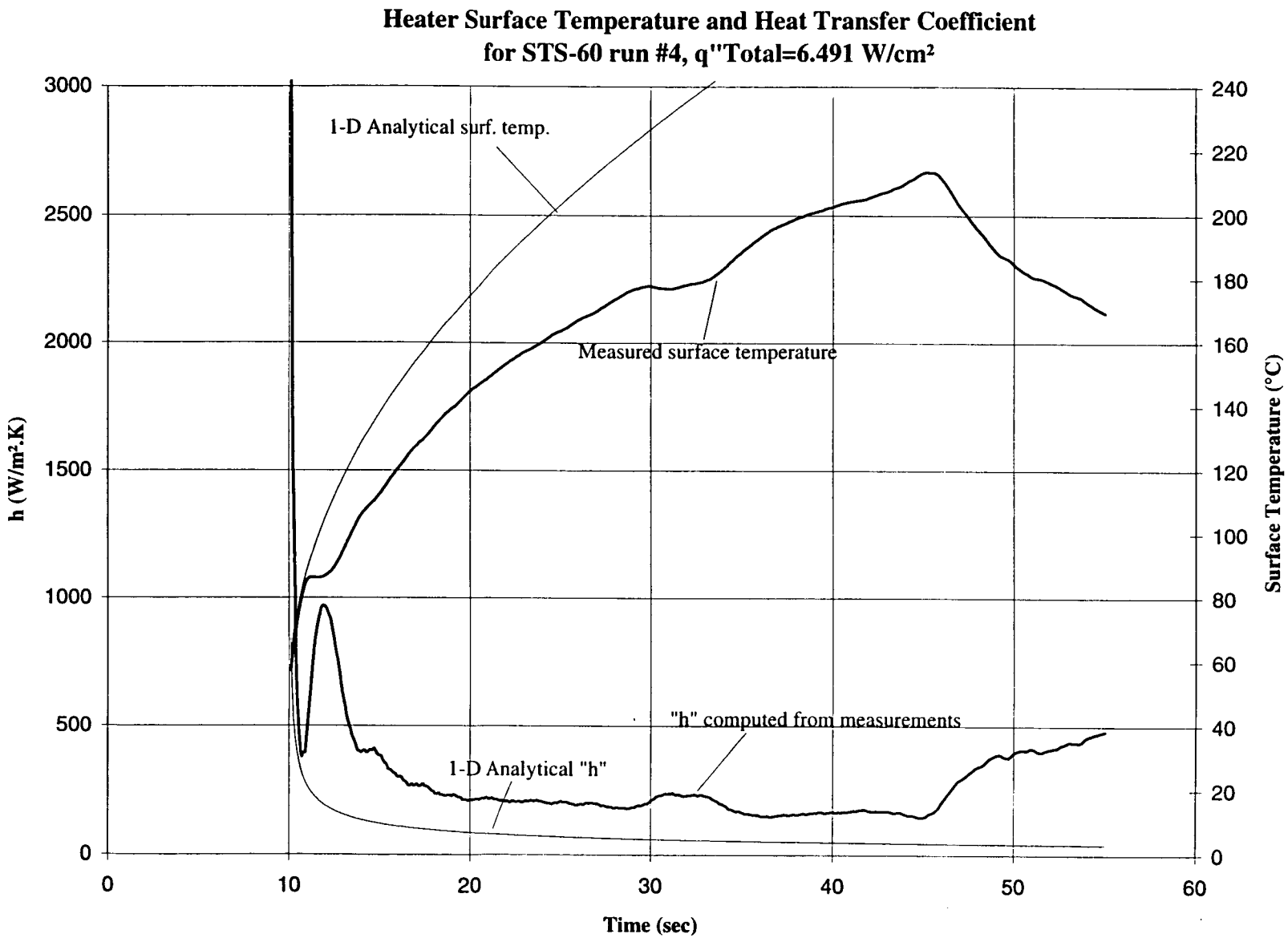

Figure C-1d. Mean heater surface temperature and derived heat transfer coefficient. PBE-IC (STS-60). Run No. 4.

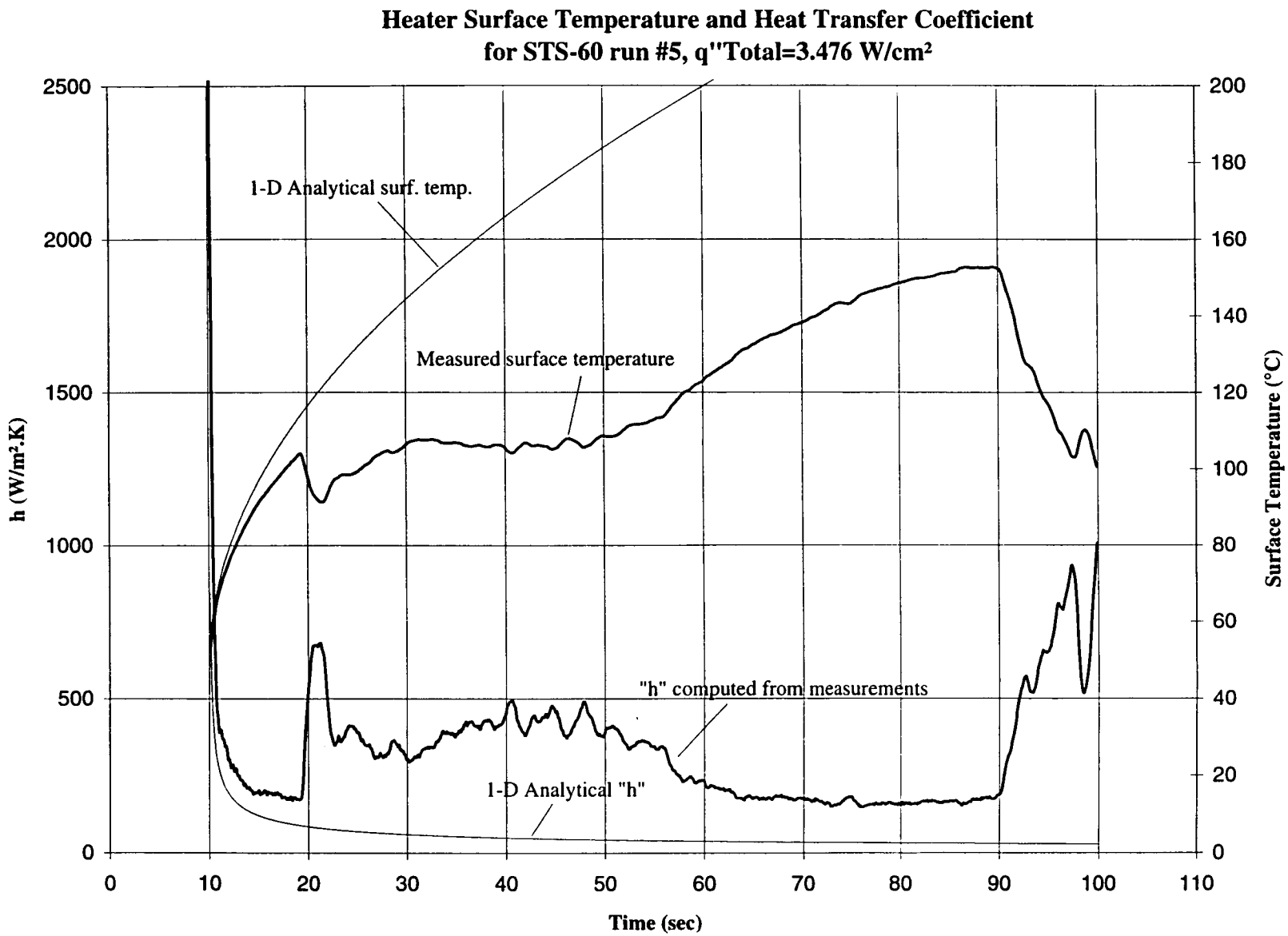

Figure C-1e. Mean heater surface temperature and derived heat transfer coefficient. PBE-IC (STS-60). Run No. 5.

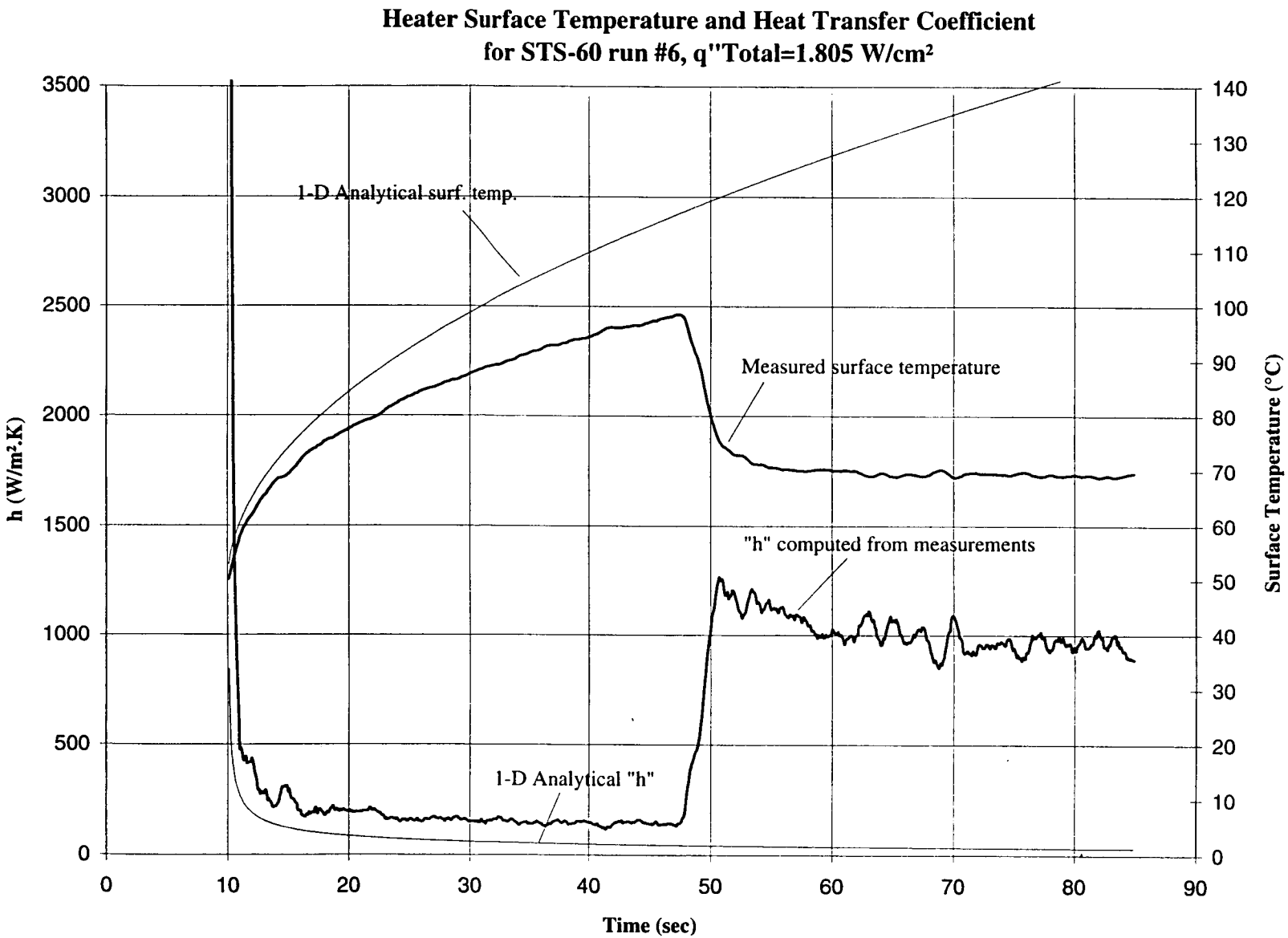

Figure C-1f. Mean heater surface temperature and derived heat transfer coefficient. PBE-IC (STS-60). Run No. 6.

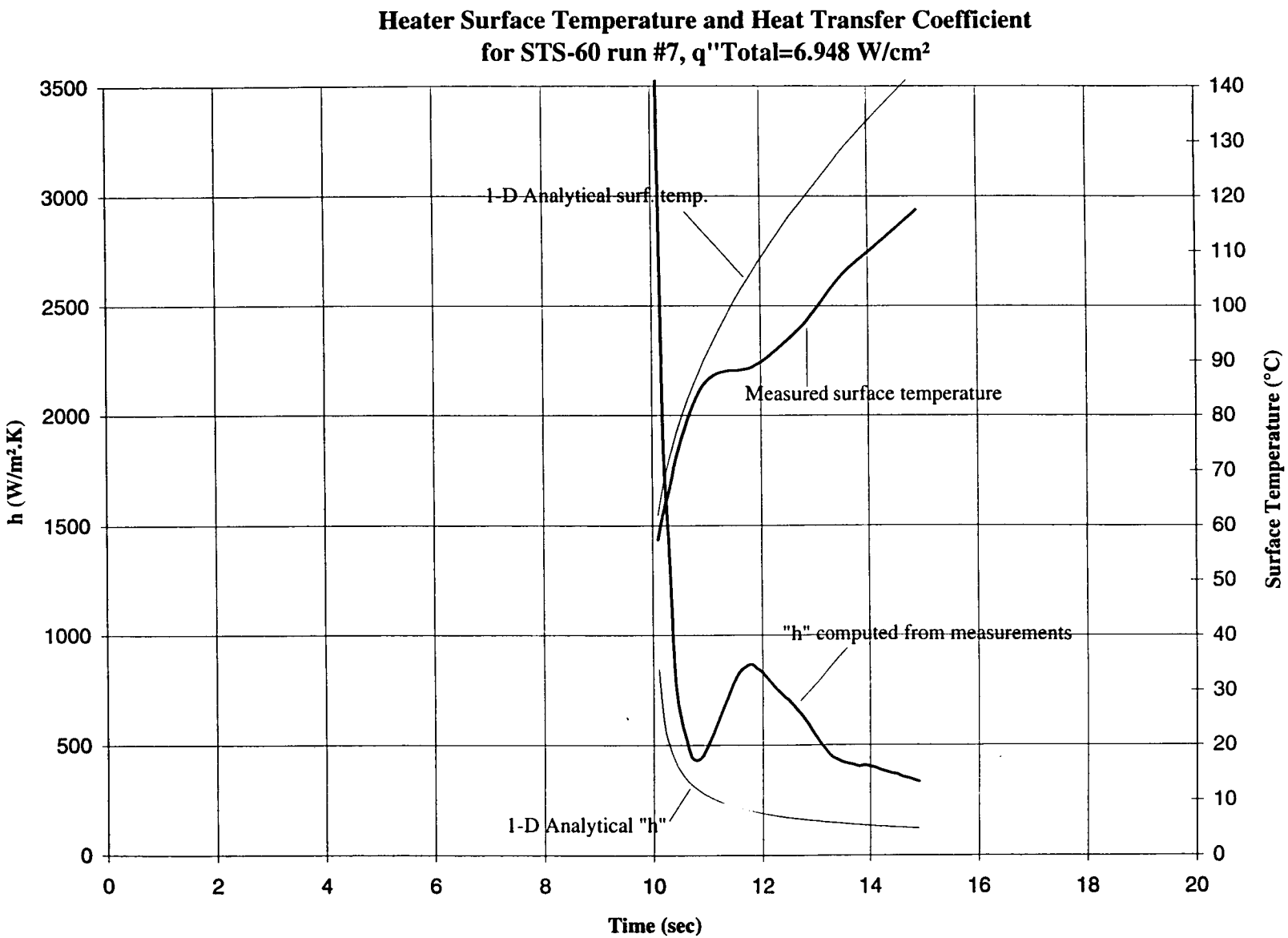

Figure C-1g. Mean heater surface temperature and derived heat transfer coefficient. PBE-IC (STS-60). Run No. 7.

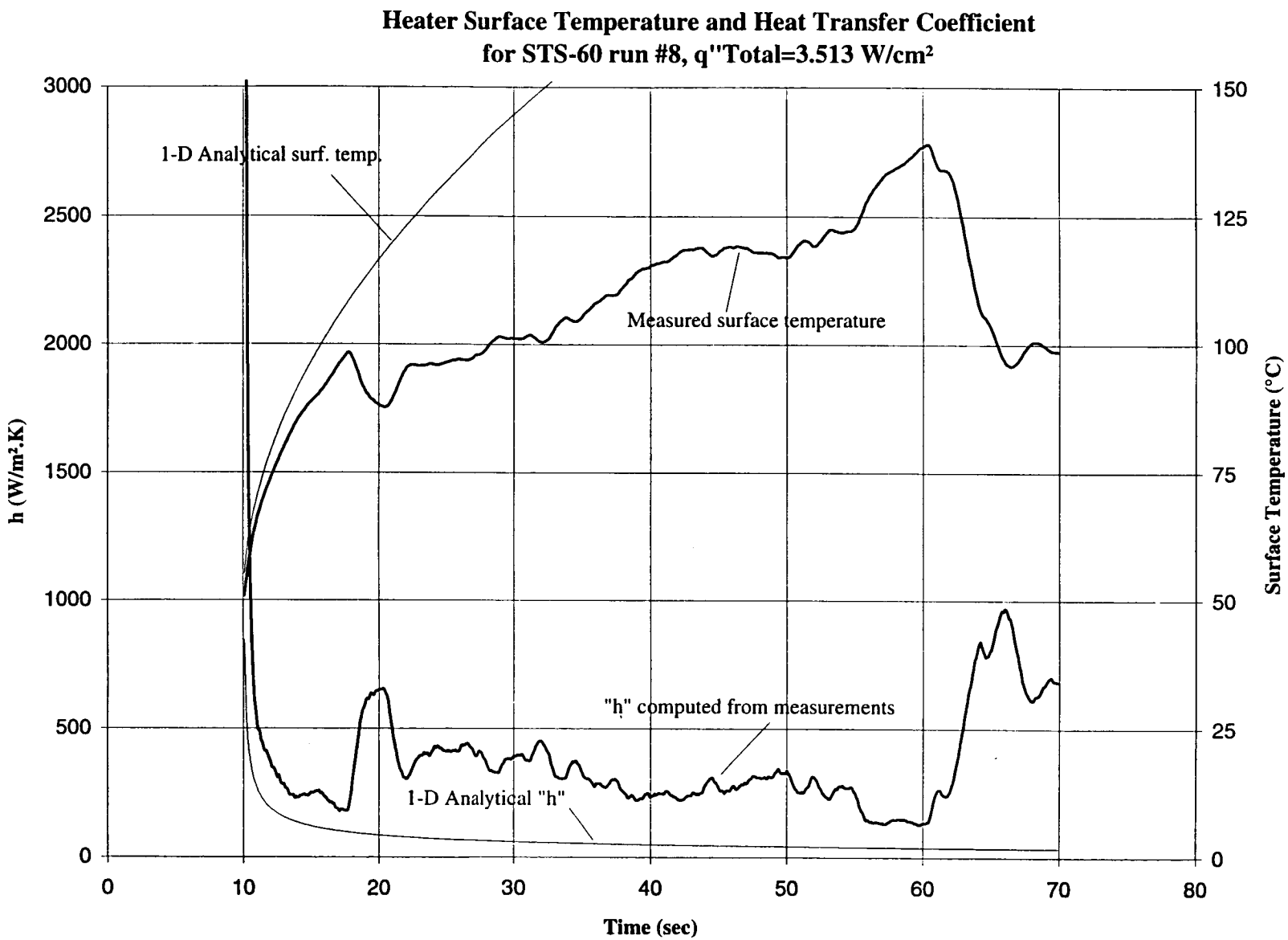

Figure C-1h. Mean heater surface temperature and derived heat transfer coefficient. PBE-IC (STS-60). Run No. 8.

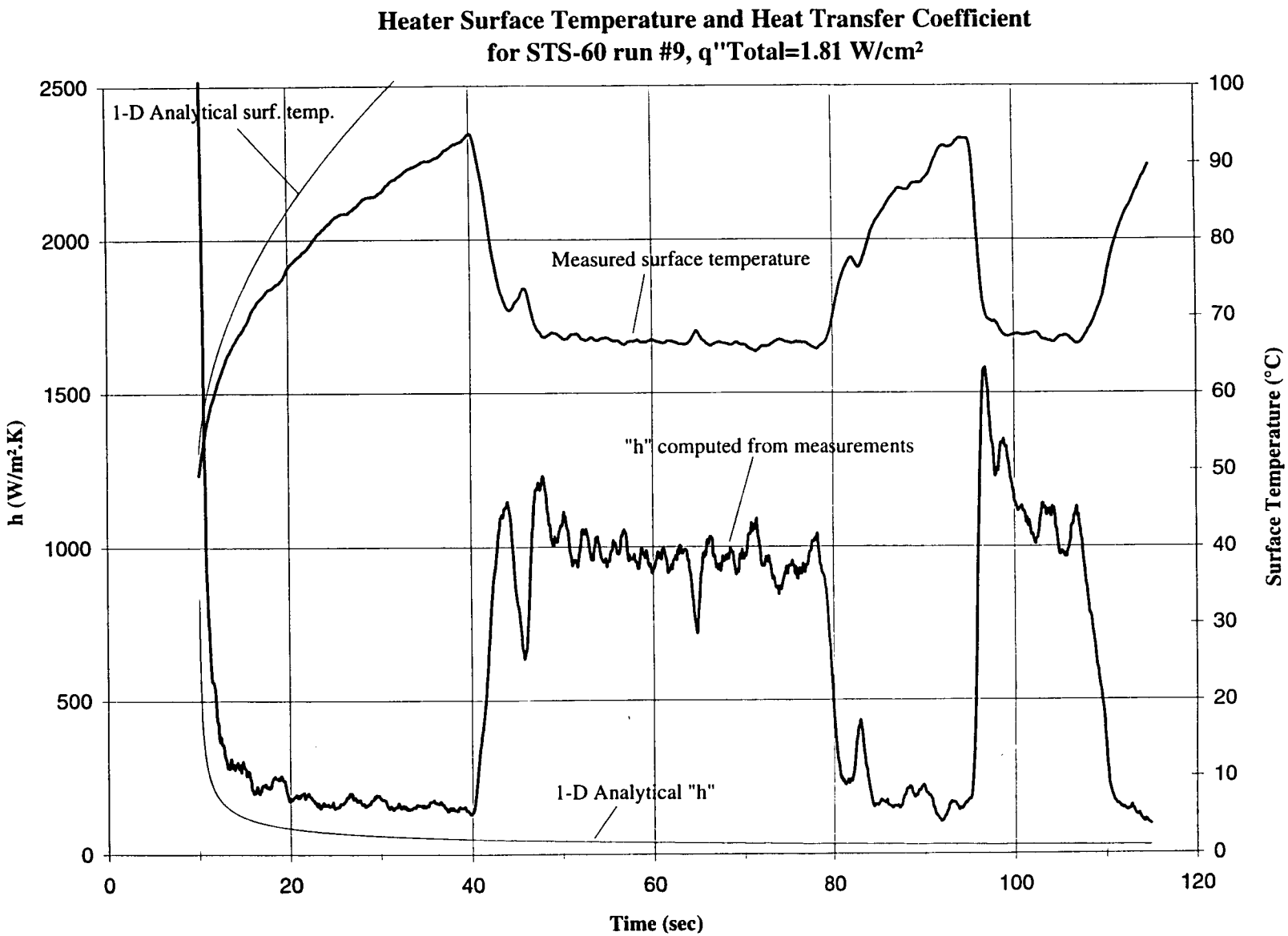

Figure C-1i. Mean heater surface temperature and derived heat transfer coefficient. PBE-IC (STS-60). Run No. 9.

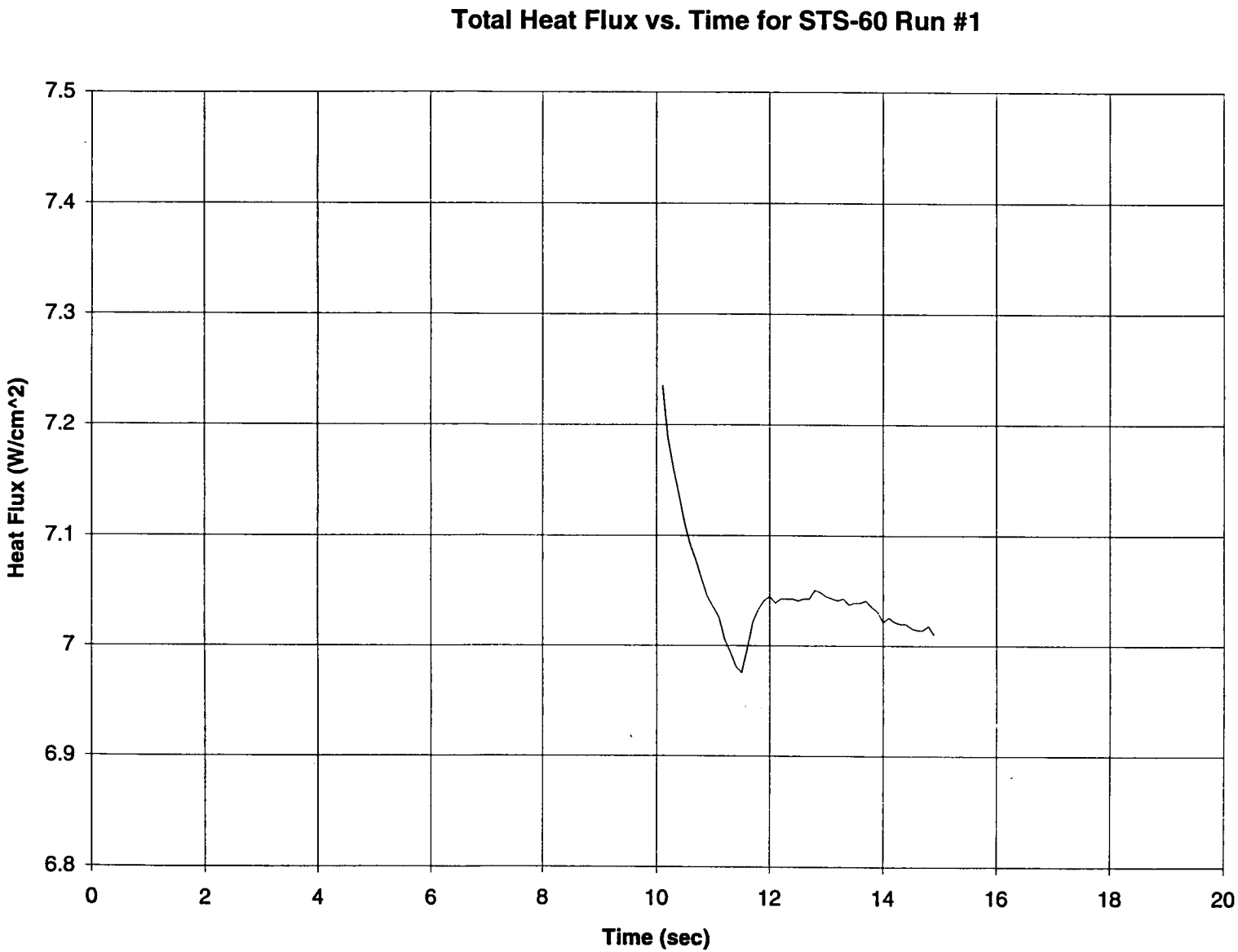

Figure C-2a. Heat flux input. PBE-IC (STS-60). Run No. 1.

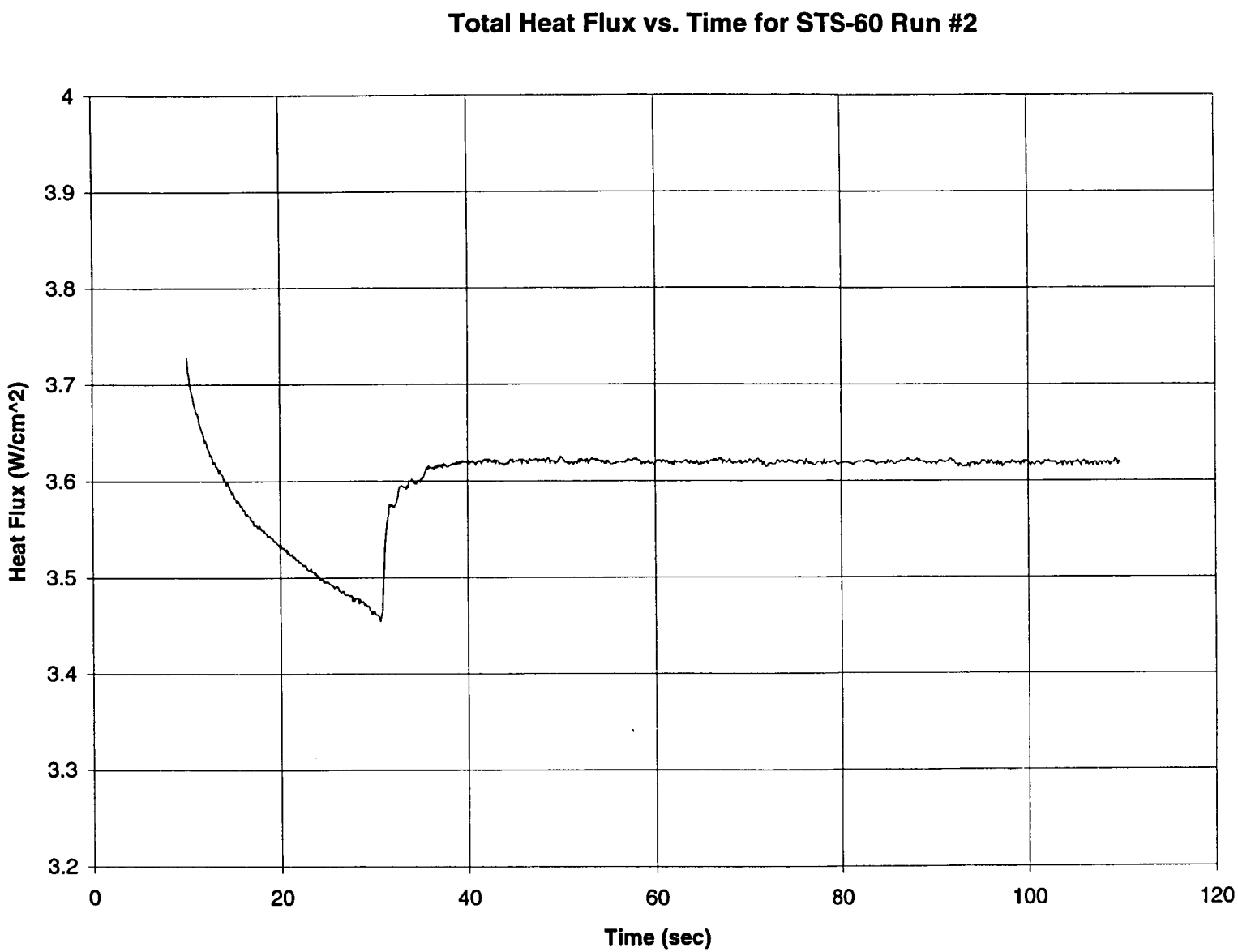

Figure C-2b. Heat flux input. PBE-IC (STS-60). Run No. 2.

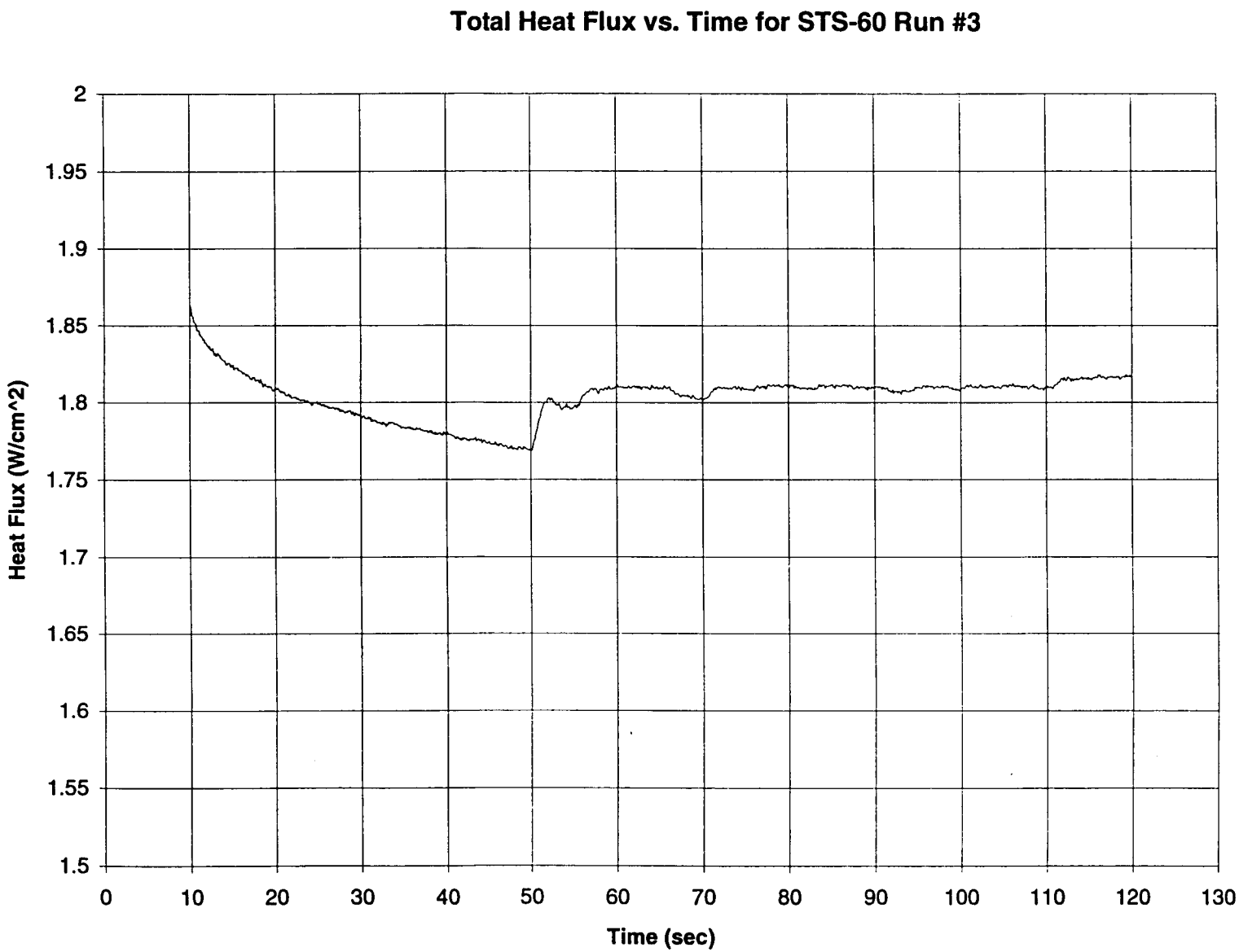

Figure C-2c. Heat flux input. PBE-IC (STS-60). Run No. 3.

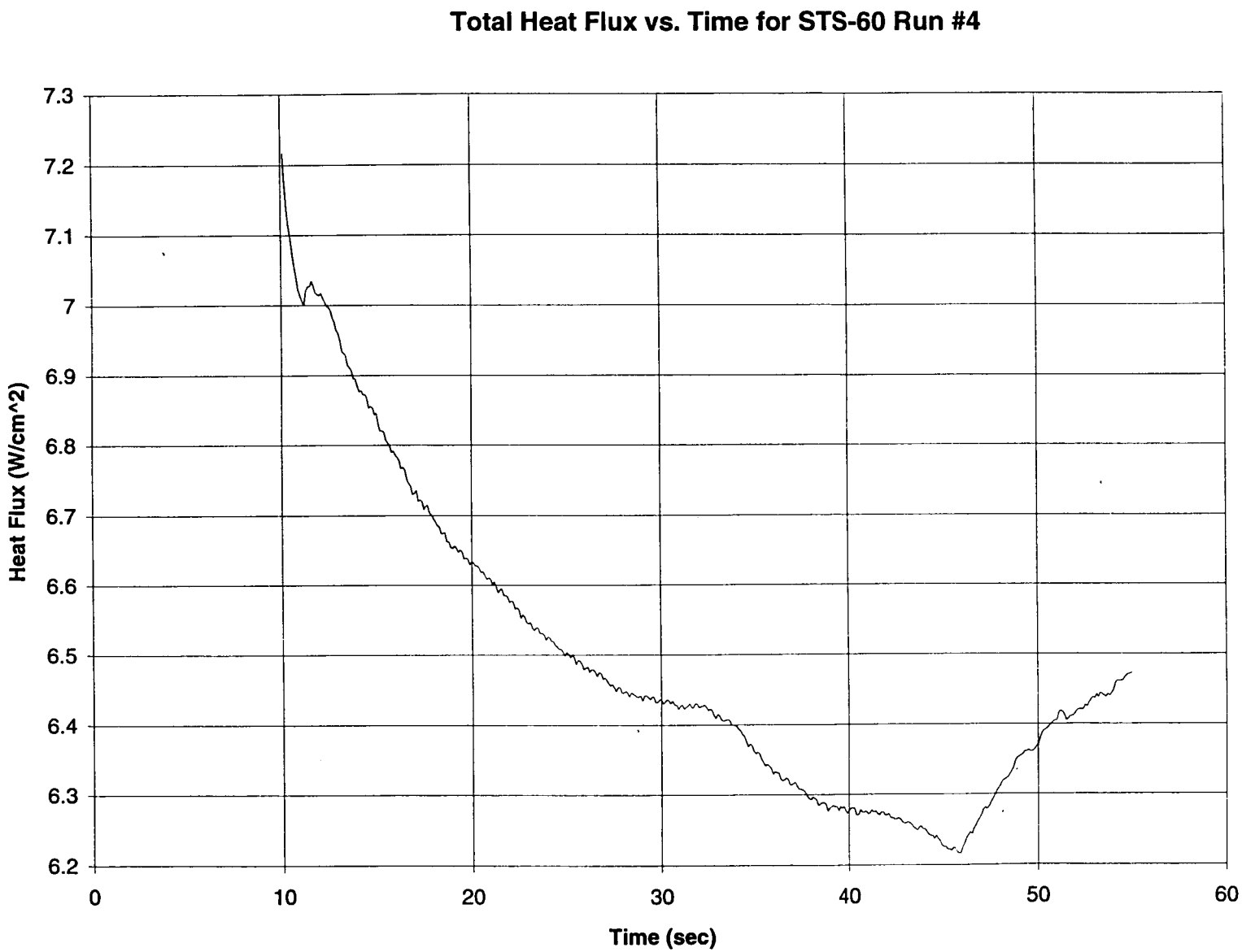

Figure C-2d. Heat flux input. PBE-IC (STS-60). Run No. 4.

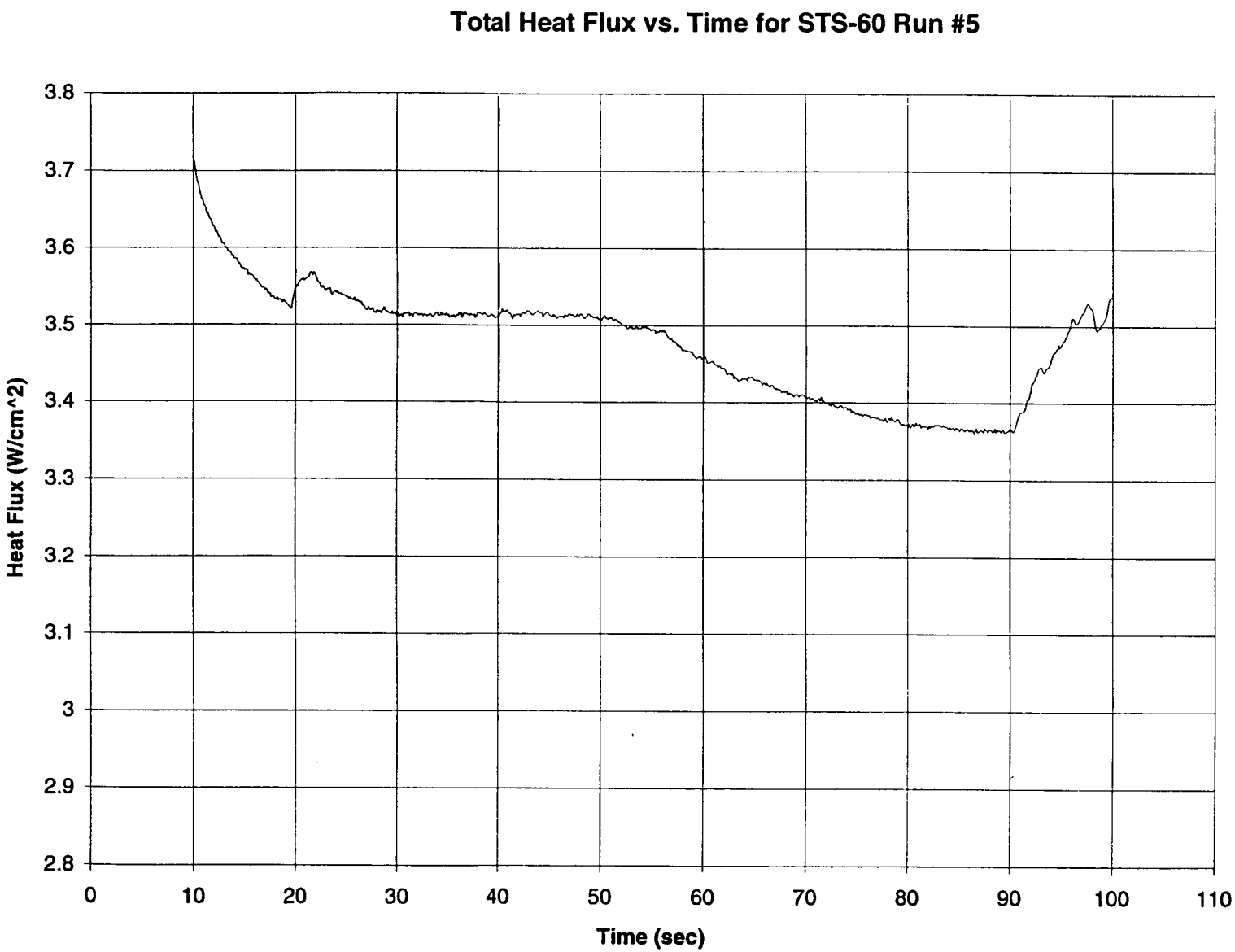

Figure C-2e. Heat flux input. PBE-IC (STS-60). Run No. 5.

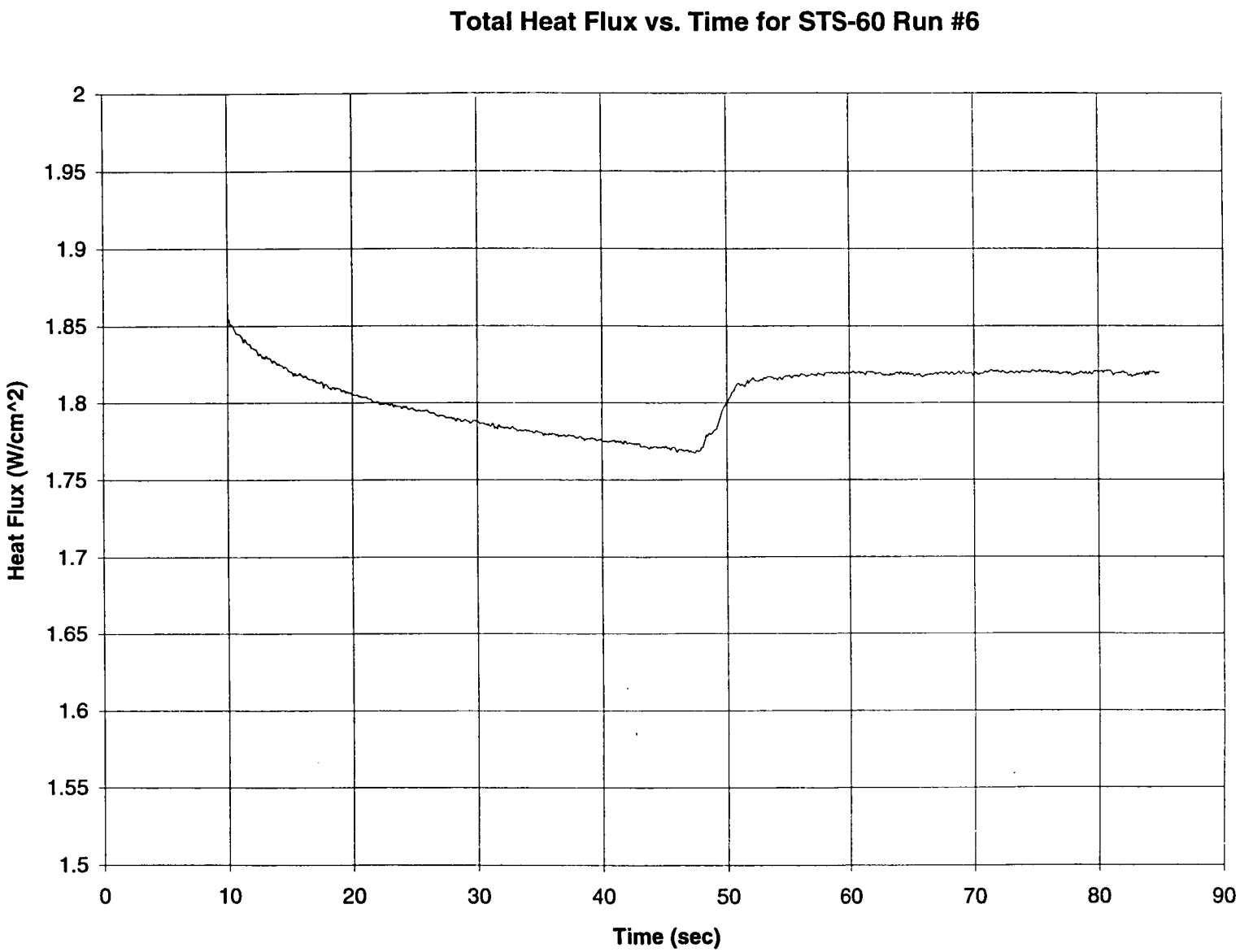

Figure C-2f. Heat flux input. PBE-IC (STS-60). Run No. 6.

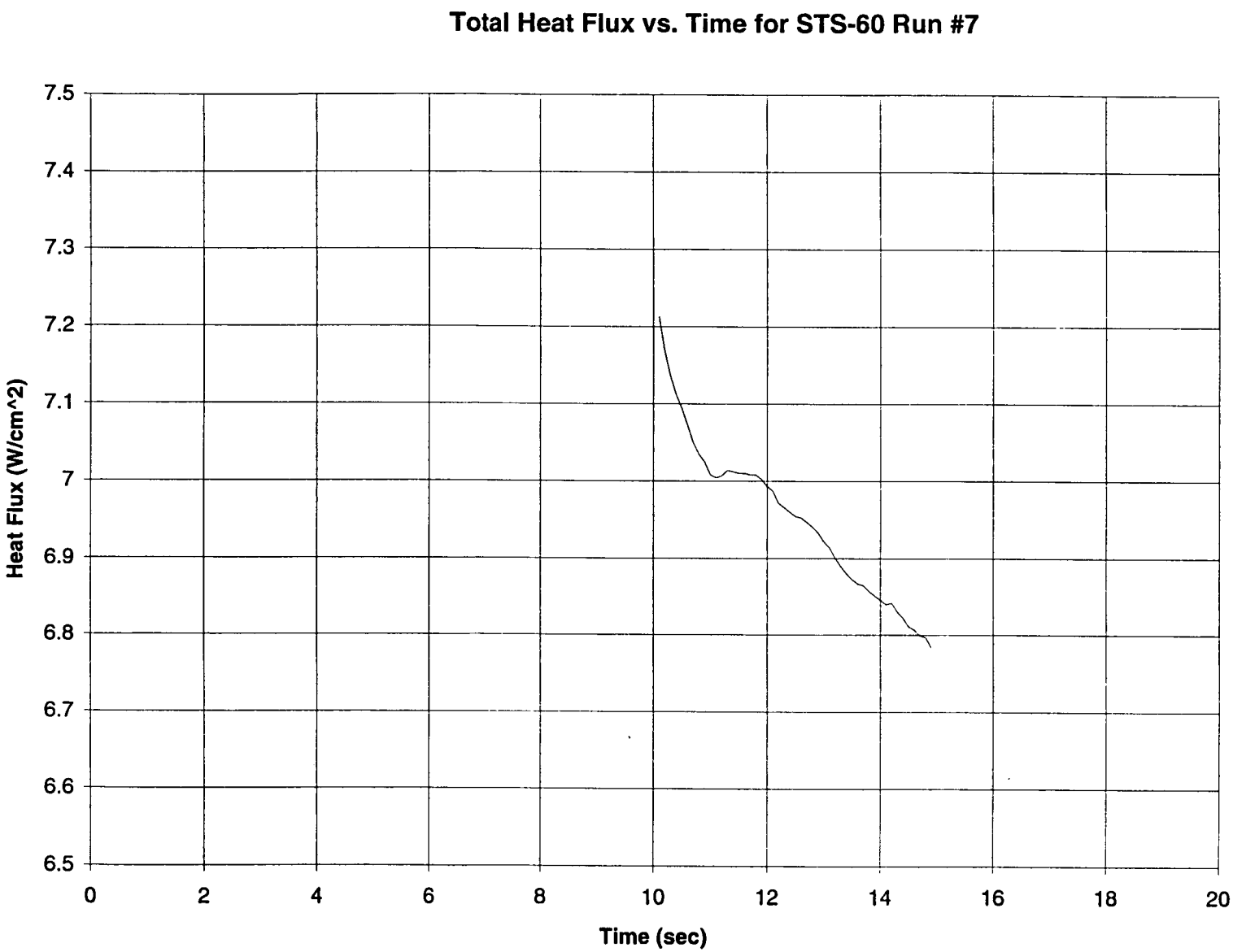

Figure C-2g. Heat flux input. PBE-IC (STS-60). Run No. 7.

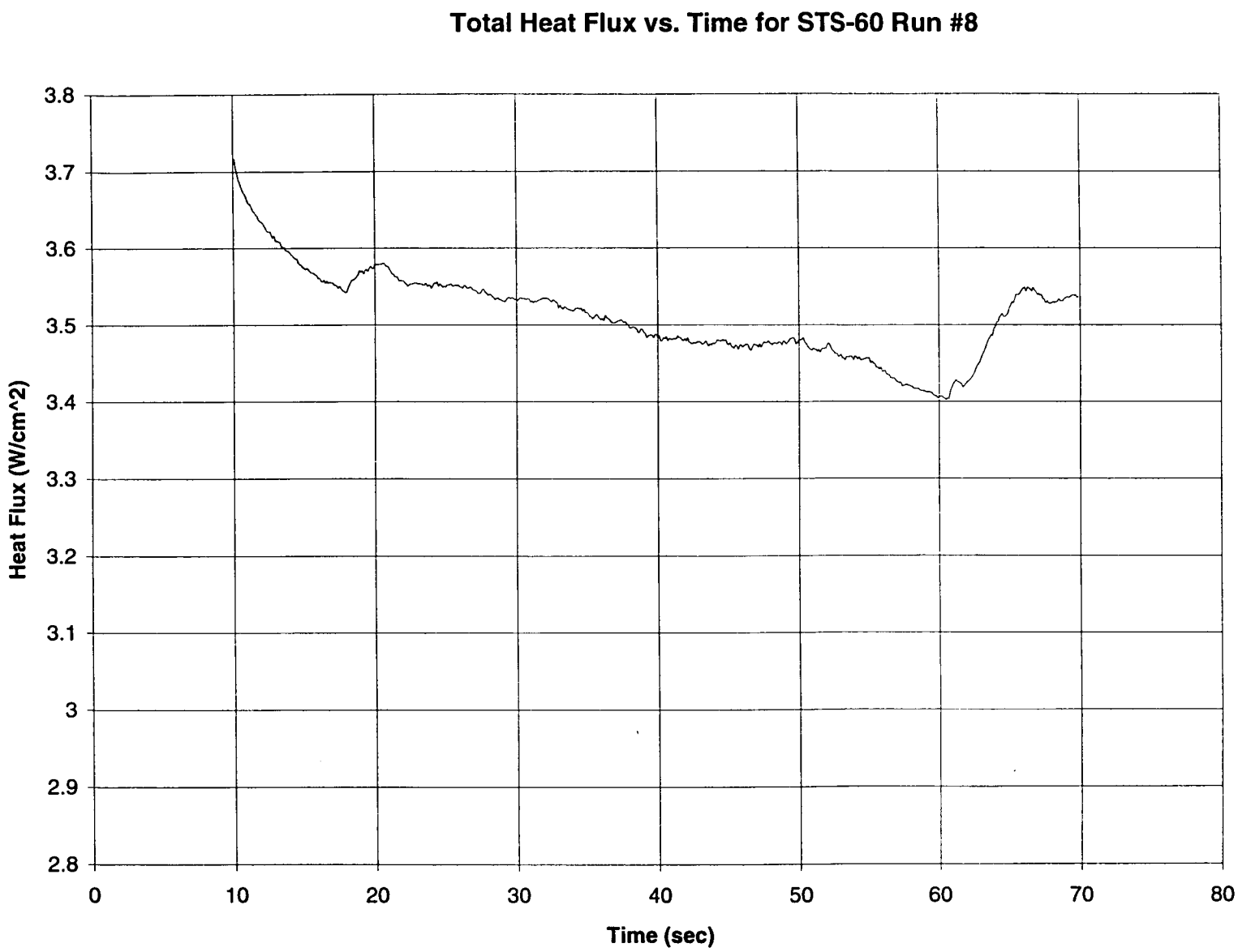

Figure C-2h. Heat flux input. PBE-IC (STS-60). Run No. 8.

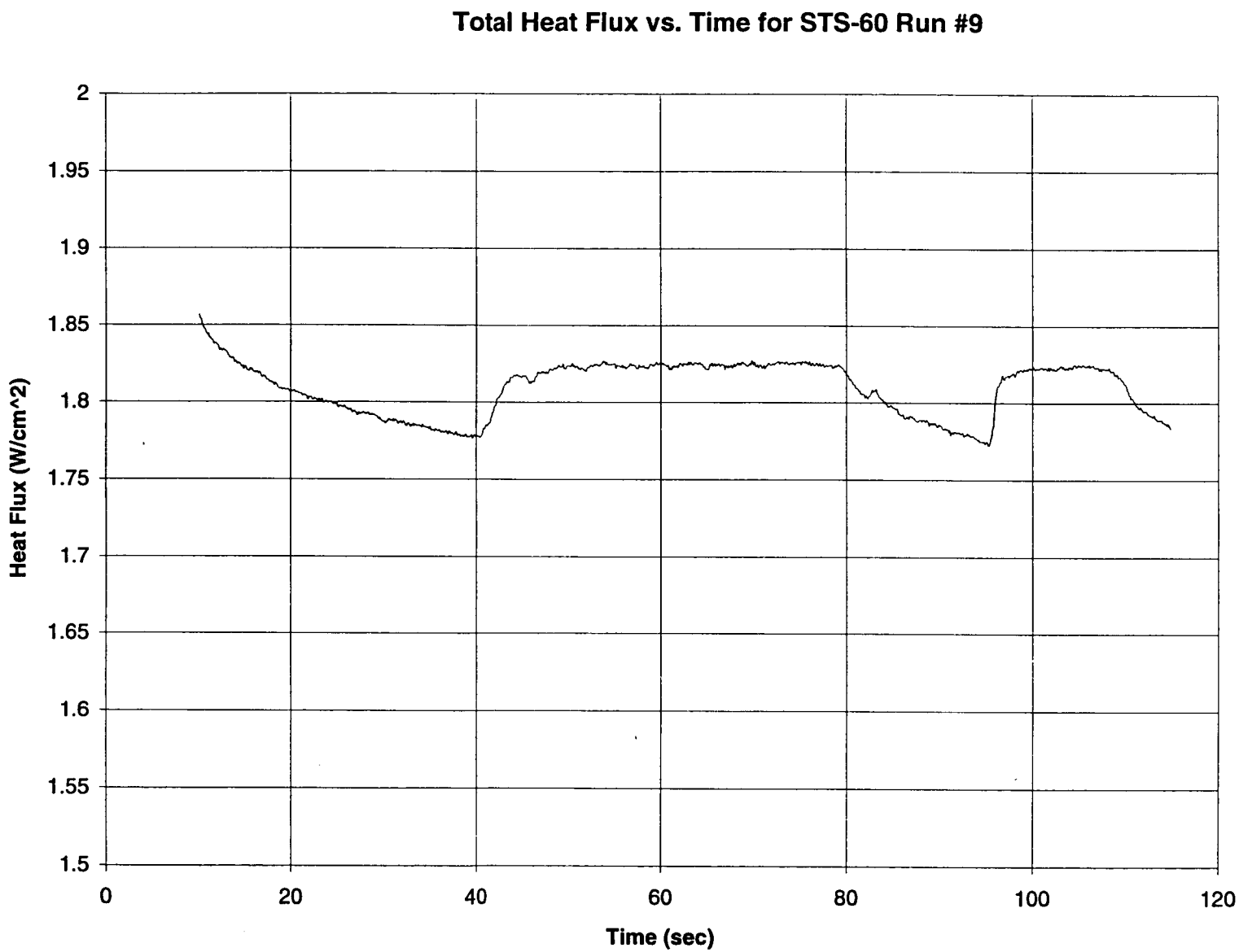

Figure C-2i. Heat flux input. PBE-IC (STS-60). Run No. 9.

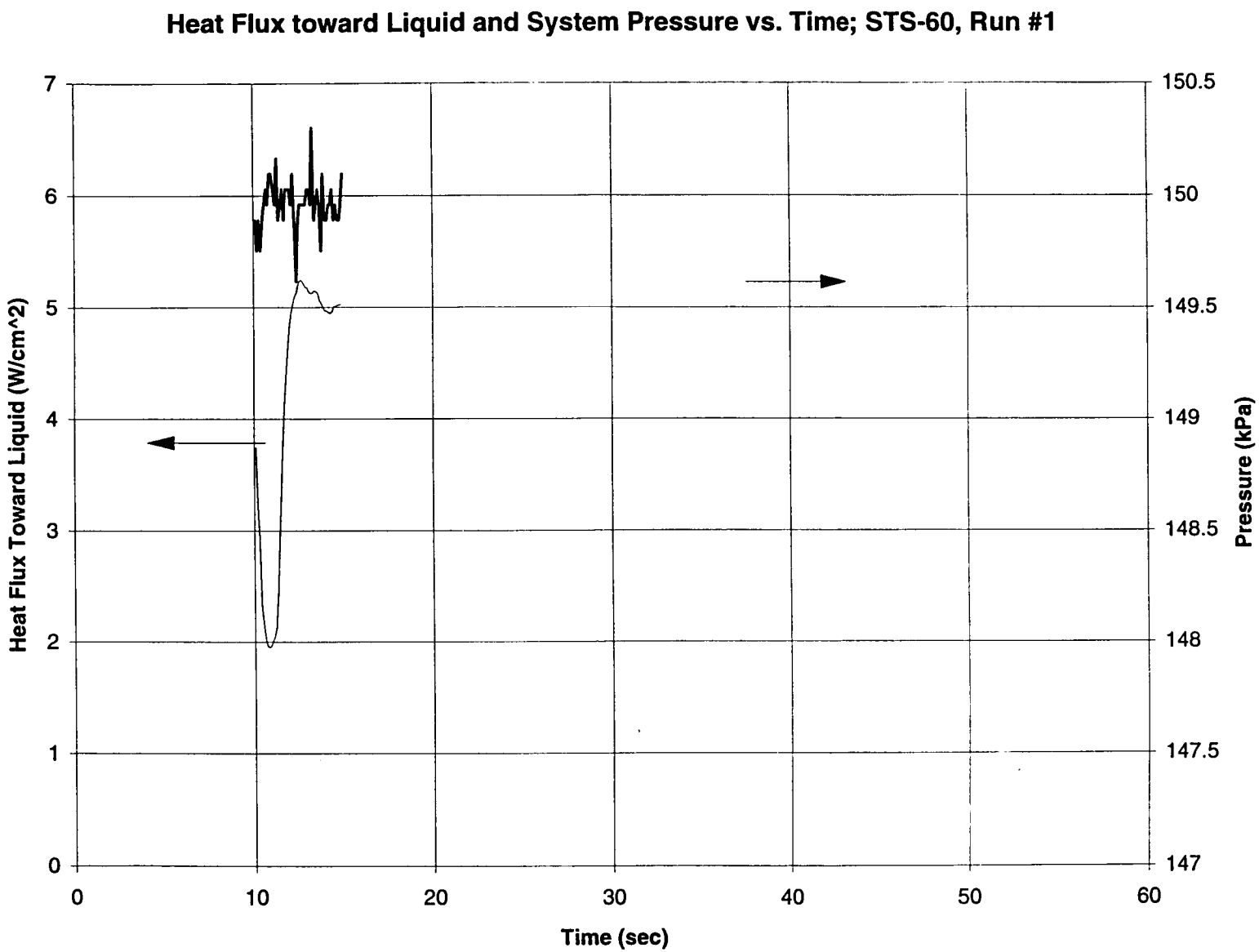

Figure C-3a. System pressure and fluid side mean heat flux. PBE-IC (STS-60). Run No. 1.

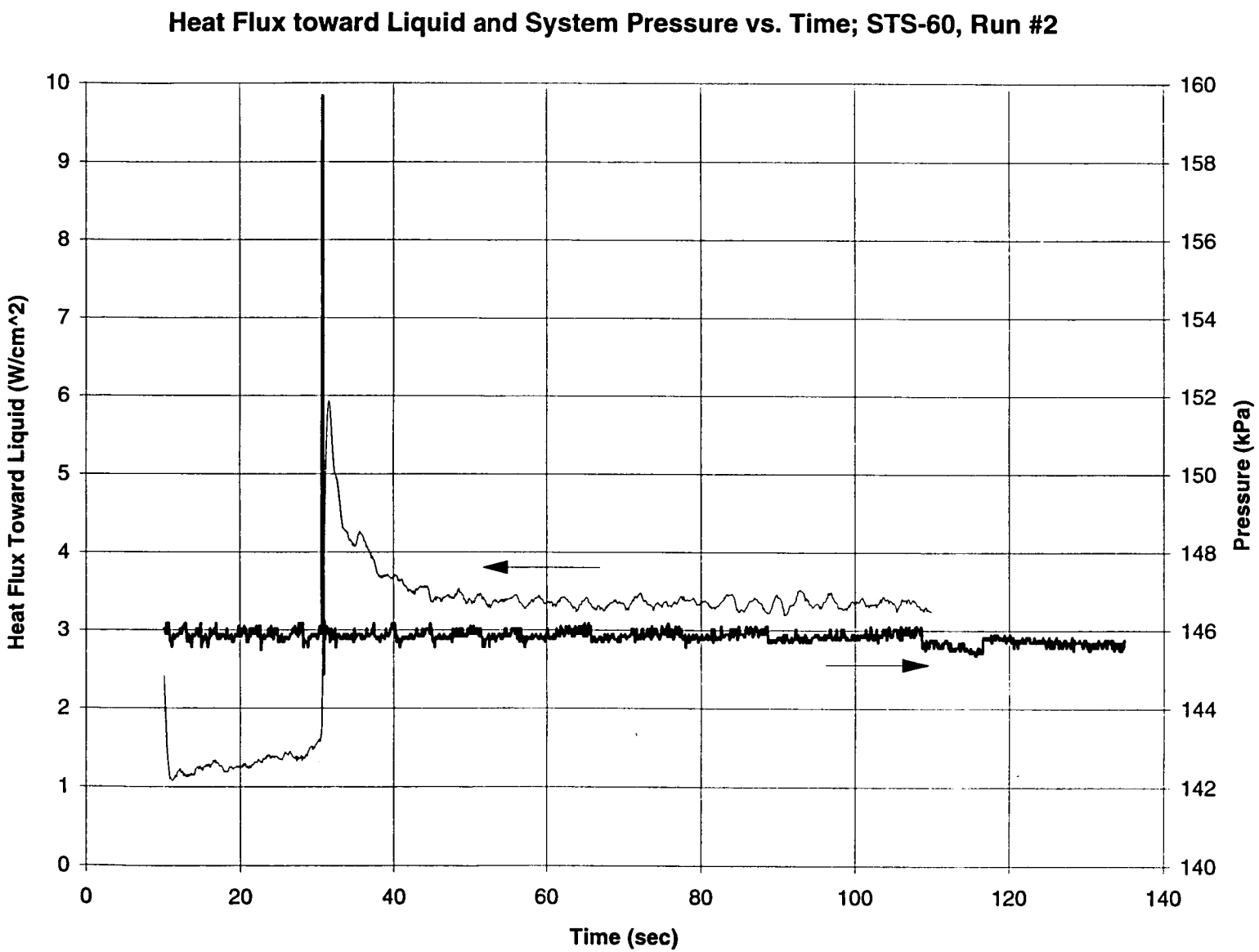

Figure C-3b. System pressure and fluid side mean heat flux. PBE-IC (STS-60). Run No. 2.

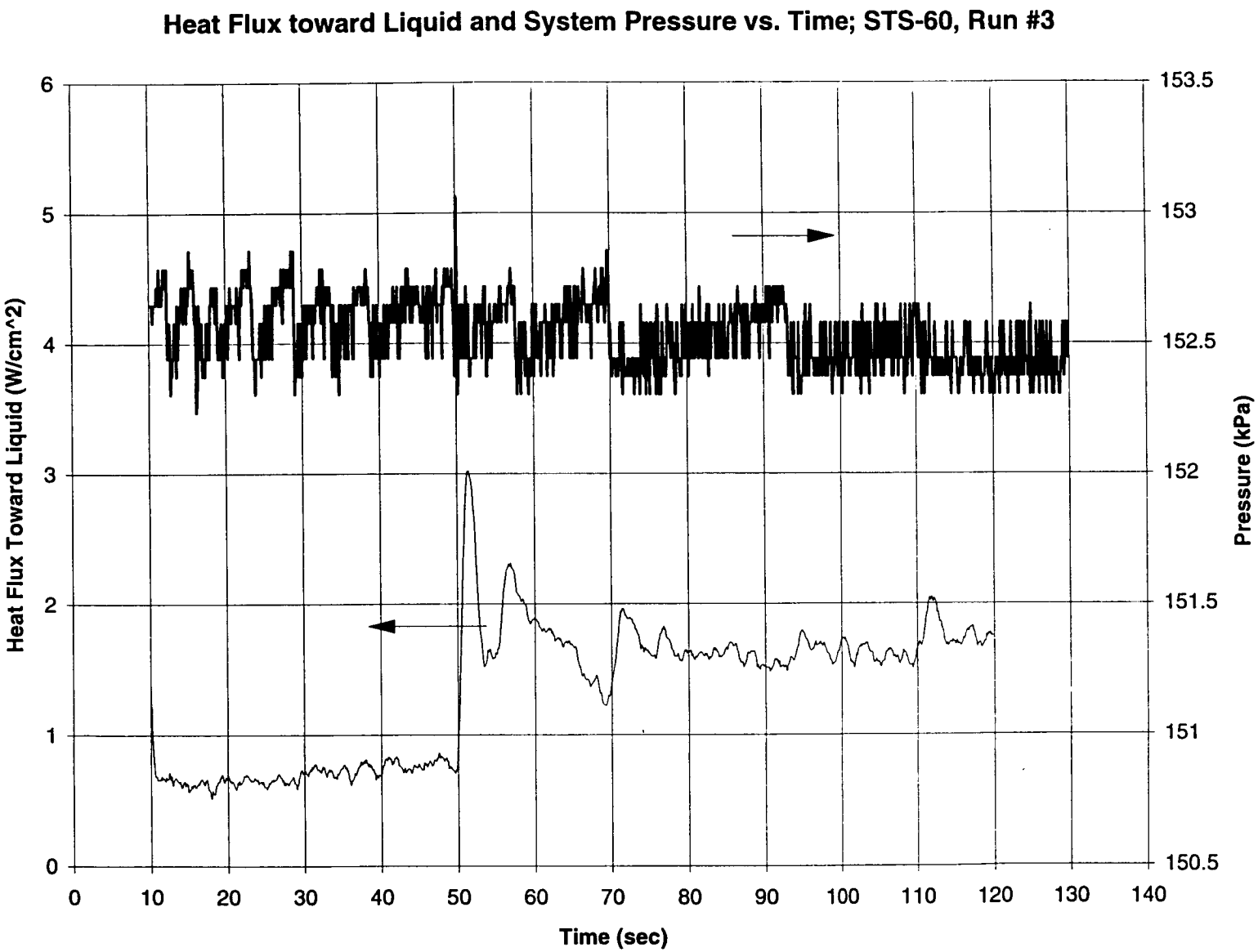

Figure C-3c. System pressure and fluid side mean heat flux. PBE-IC (STS-60). Run No. 3.

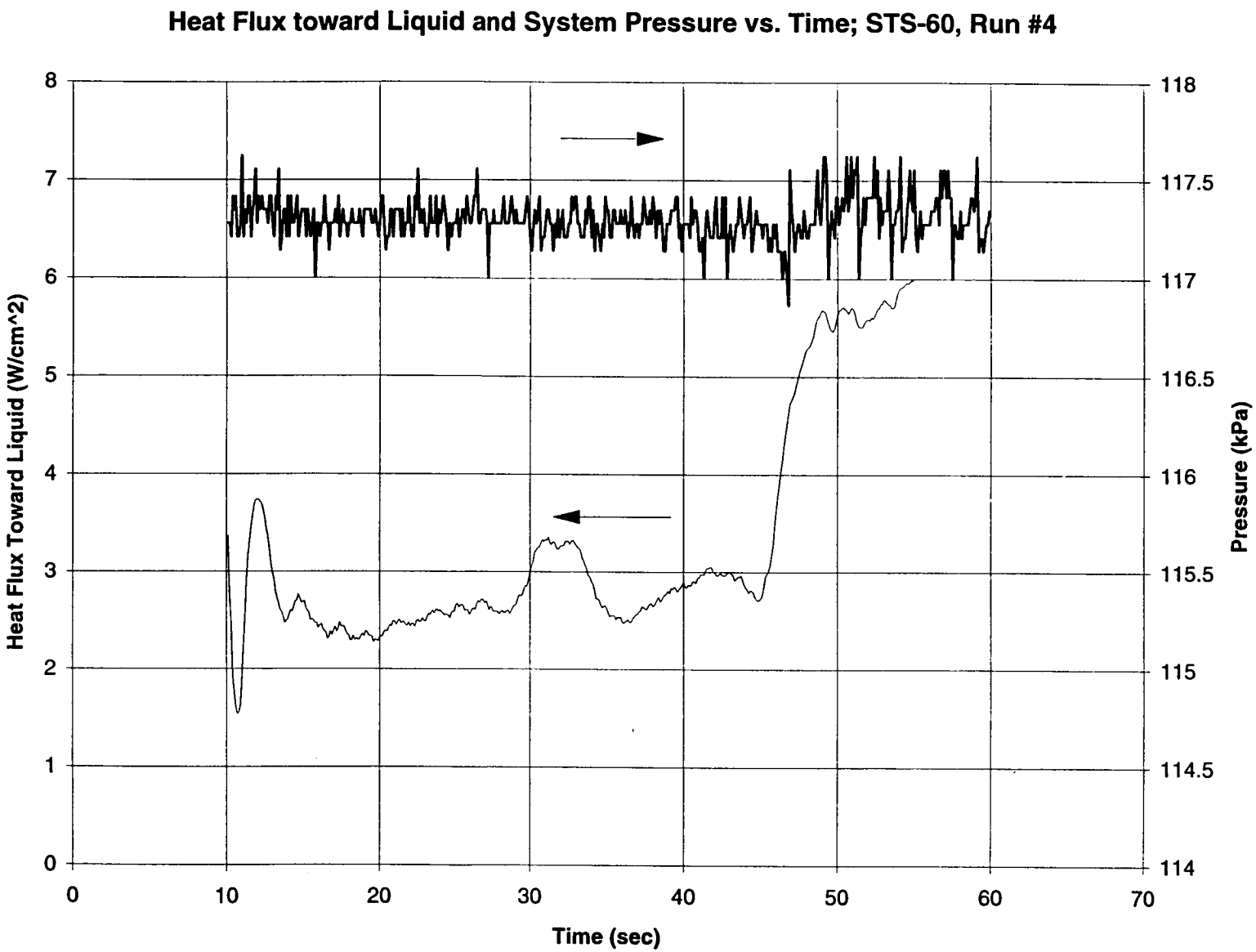

Figure C-3d. System pressure and fluid side mean heat flux. PBE-IC (STS-60). Run No. 4.

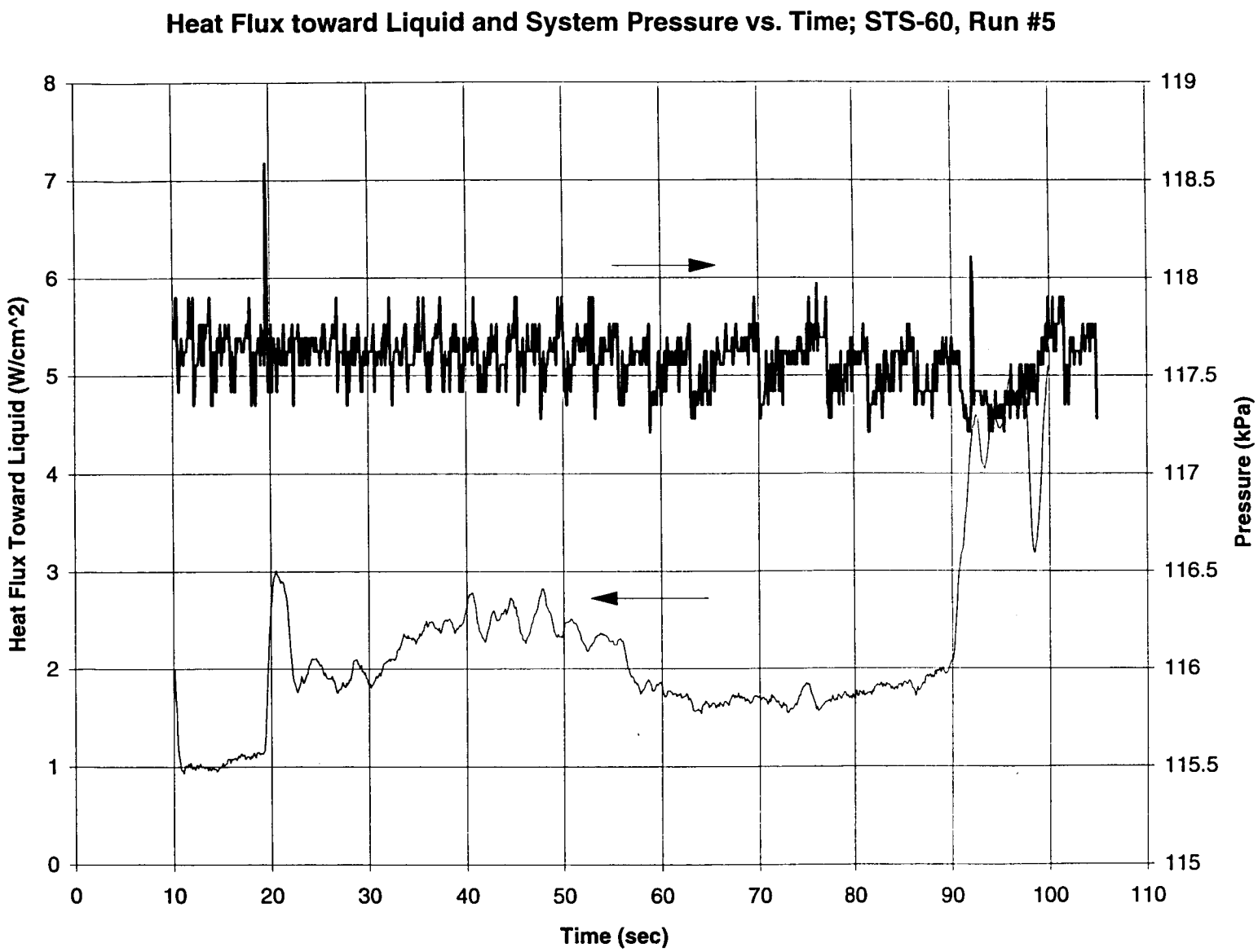

Figure C-3e. System pressure and fluid side mean heat flux. PBE-IC (STS-60). Run No. 5.

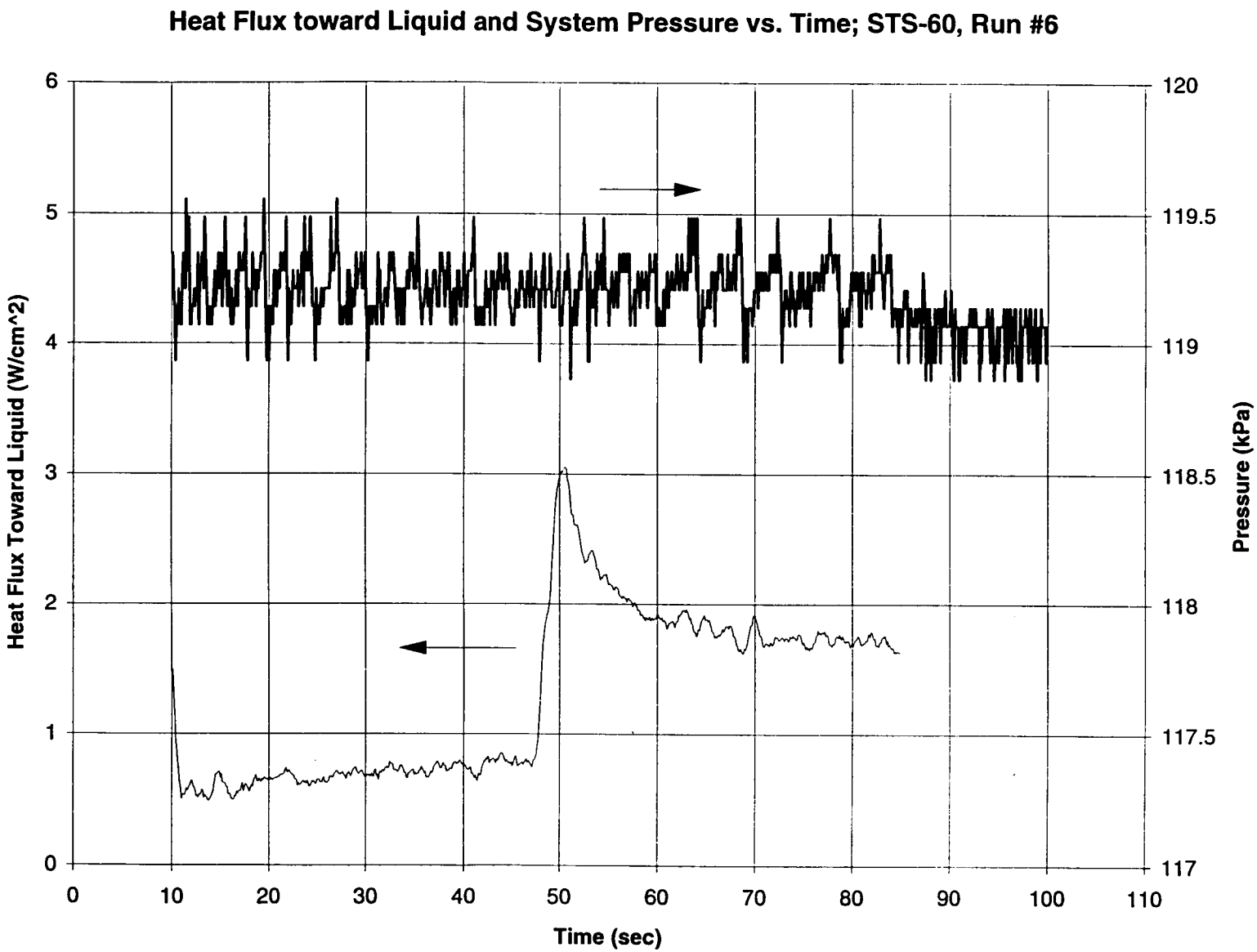

Figure C-3f. System pressure and fluid side mean heat flux. PBE-IC (STS-60). Run No. 6.

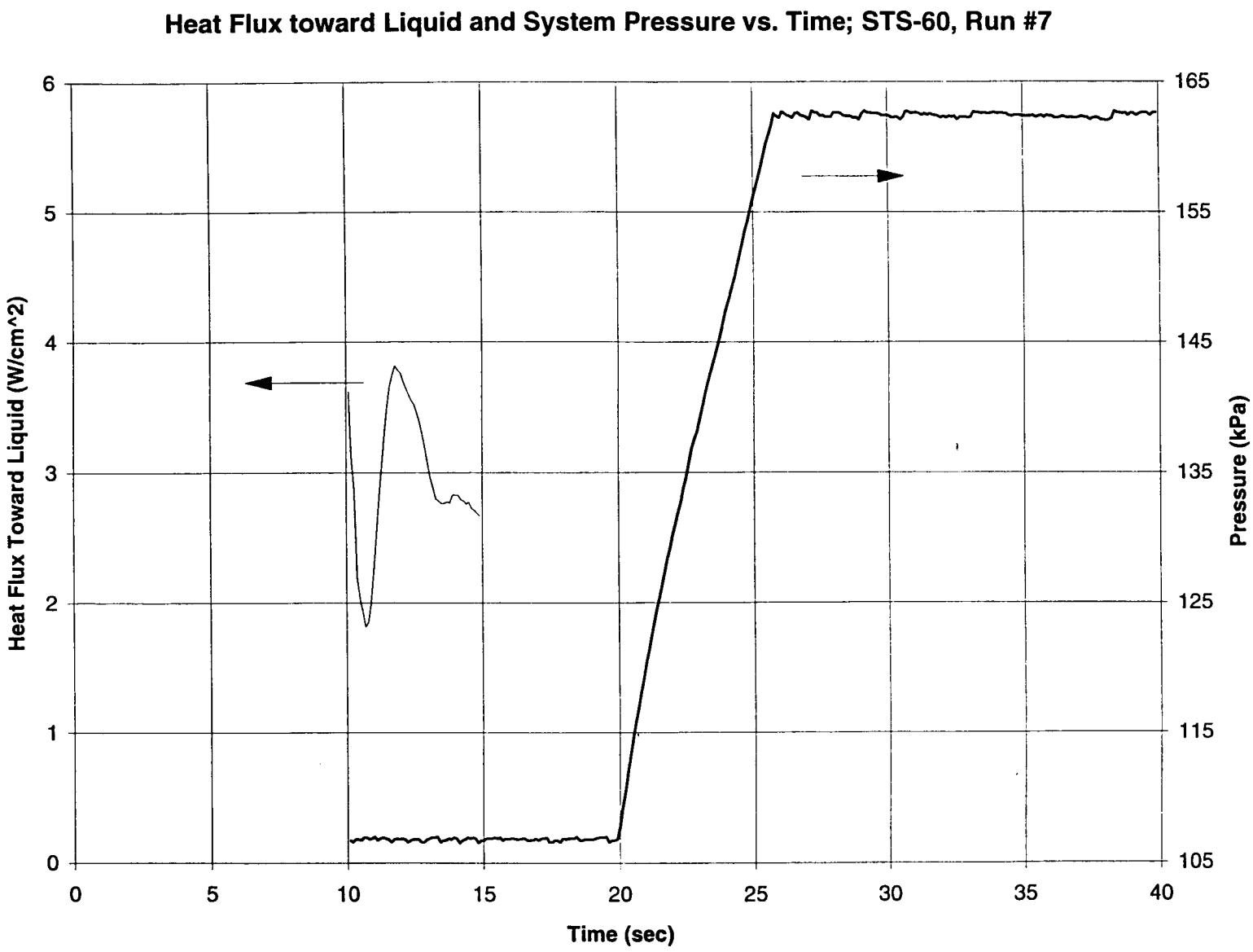

Figure C-3g. System pressure and fluid side mean heat flux. PBE-IC (STS-60). Run No. 7.

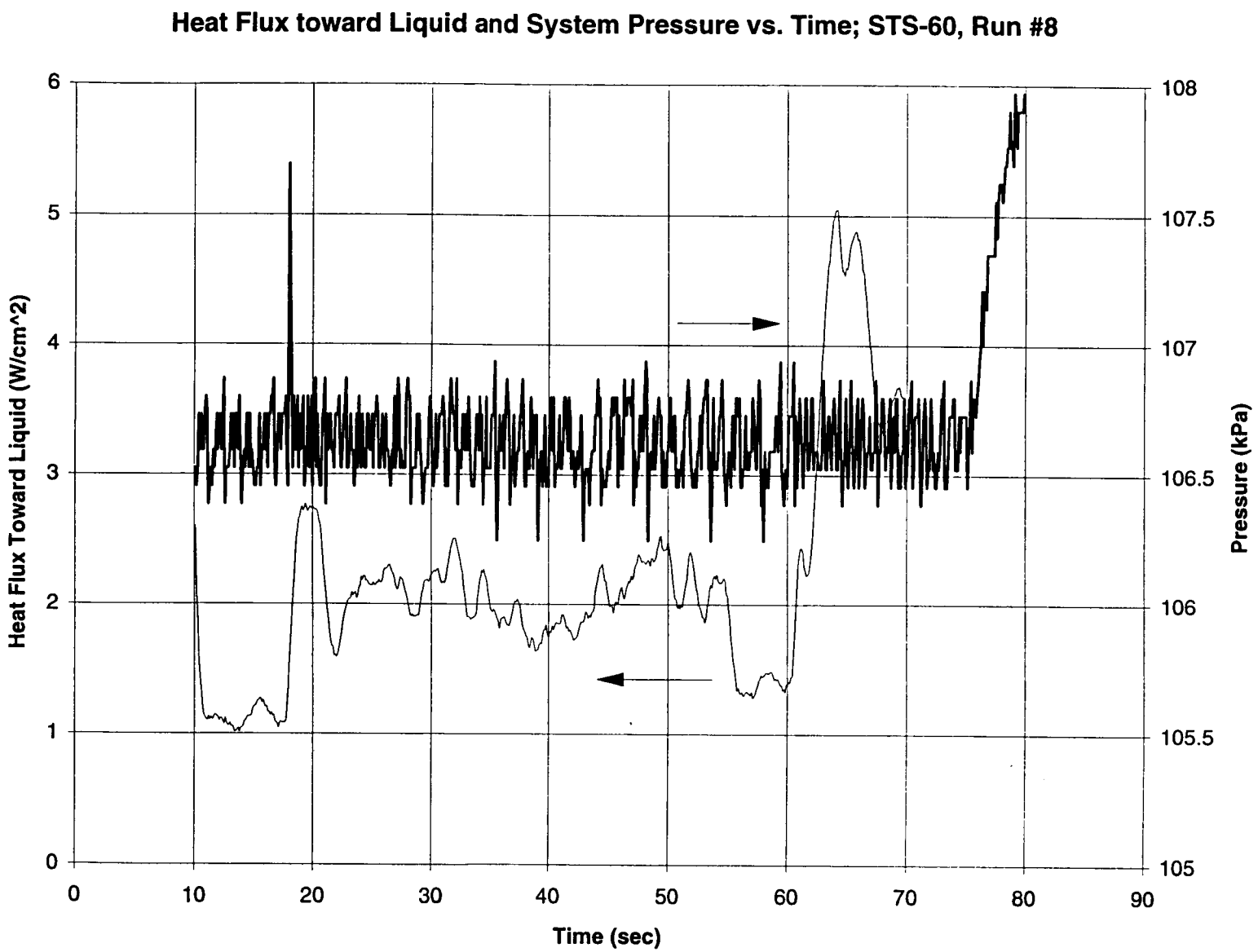

Figure C-3h. System pressure and fluid side mean heat flux. PBE-IC (STS-60). Run No. 8.

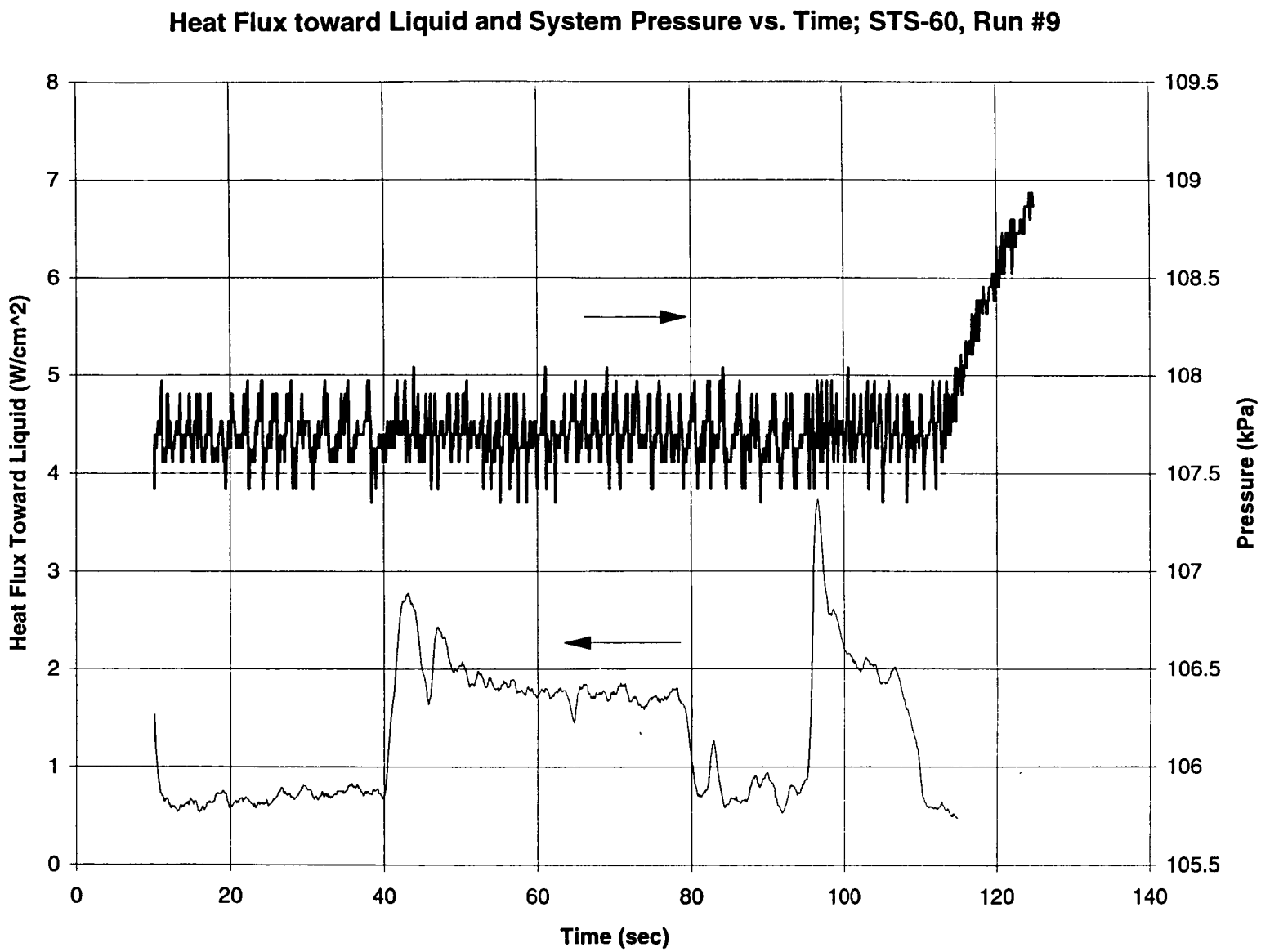

Figure C-3i. System pressure and fluid side mean heat flux. PBE-IC (STS-60). Run No. 9.

A. Mean Heater Surface Temperature

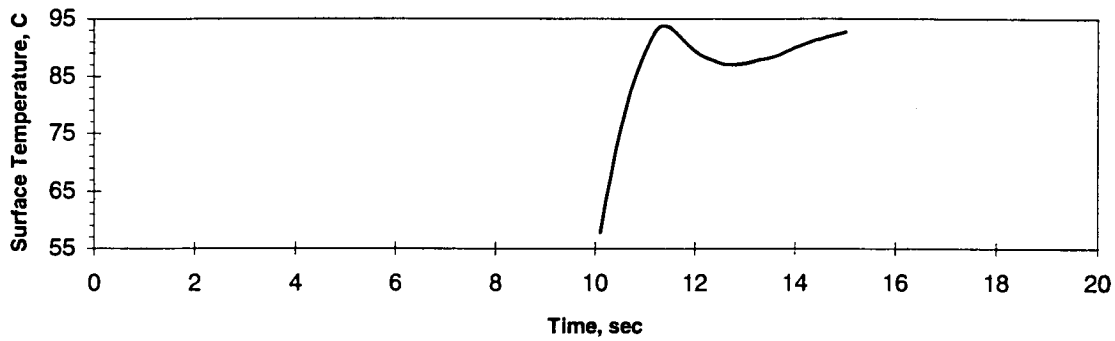

B. Local Fluid Temperatures

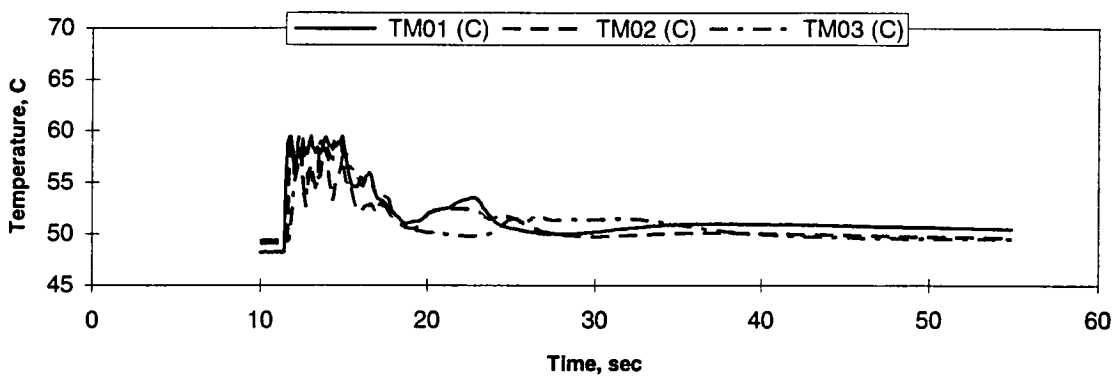

C. Far Field Bulk Temperatures

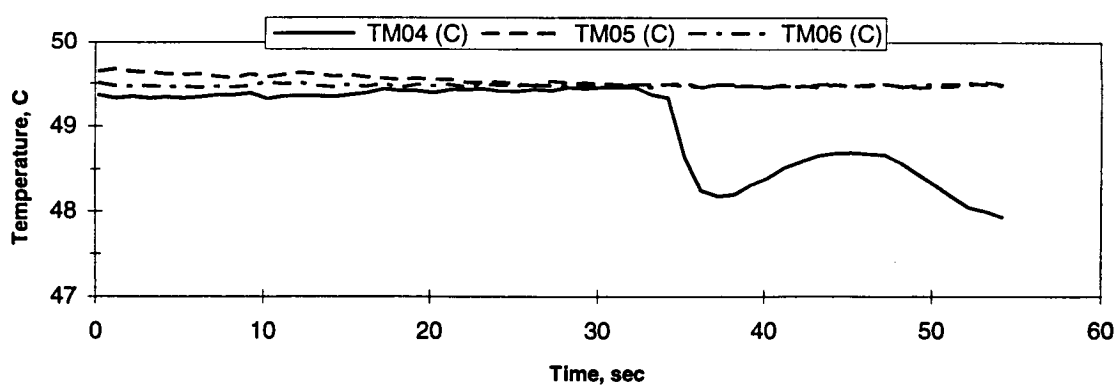

Figure: Measured Fluid Temperatures STS-60 Run #1

Heat Flux	Subcooling (F)	Heater Power On/Off	100 FPS On/Off	Stirrer Start	Repress Start	Total Test Time
8	20 ± 2	10-15 sec.	10-13 sec.	-----	-----	55 sec.

Figure C-4a. Measured fluid temperatures near primary heater and far field bulk liquid. PBE-IC (STS-60). Run No. 1.

A. Mean Heater Surface Temperature

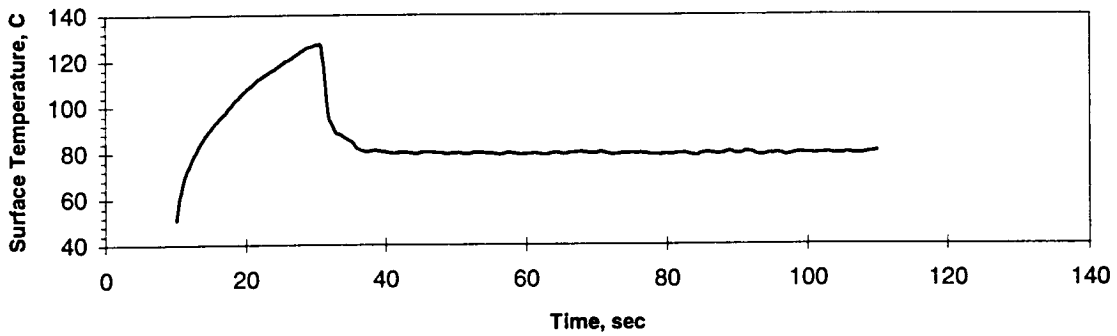

B. Local Fluid Temperatures

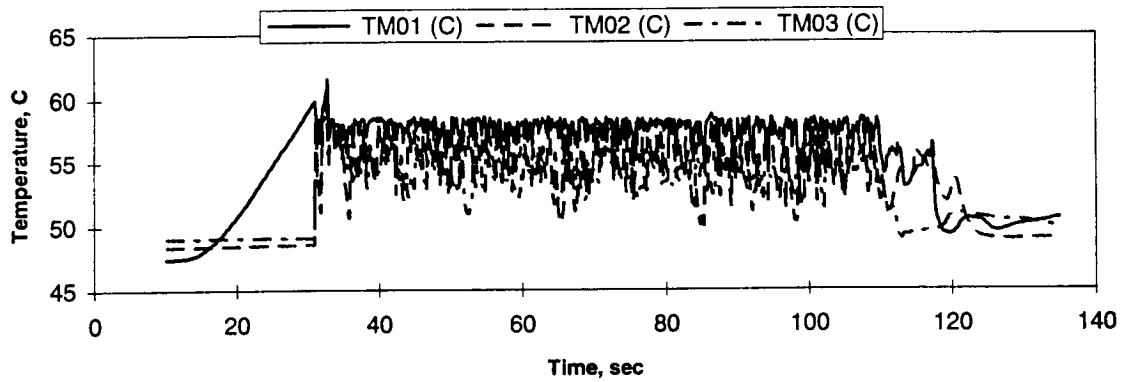

C. Far Field Bulk Temperatures

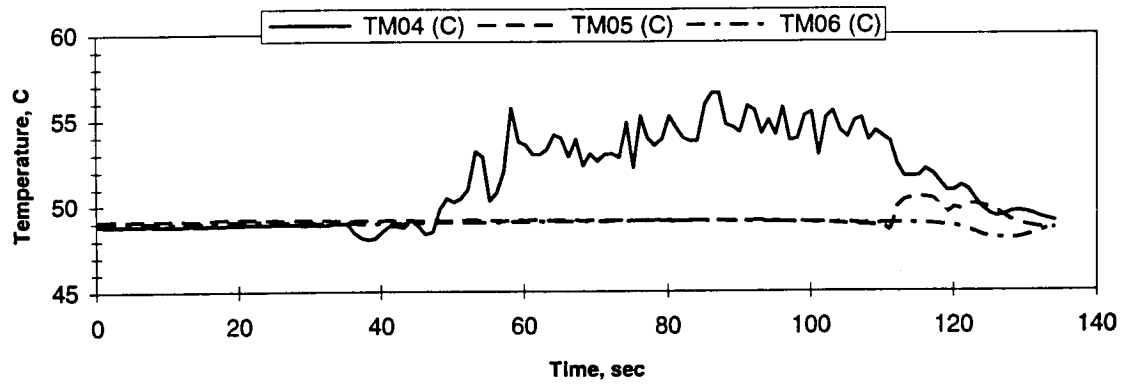

Figure: Measured Fluid Temperatures STS-60 Run #2

Heat Flux	Subcooling (F)	Heater Power On/Off	100 FPS On/Off	Stirrer Start	Repress Start	Total Test Time
4	20 ± 2	10-110 sec.	15-25 sec.	-----	-----	135 sec.

Figure C-4b. Measured fluid temperatures near primary heater and far field bulk liquid. PBE-IC (STS-60). Run No. 2.

A. Mean Heater Surface Temperature

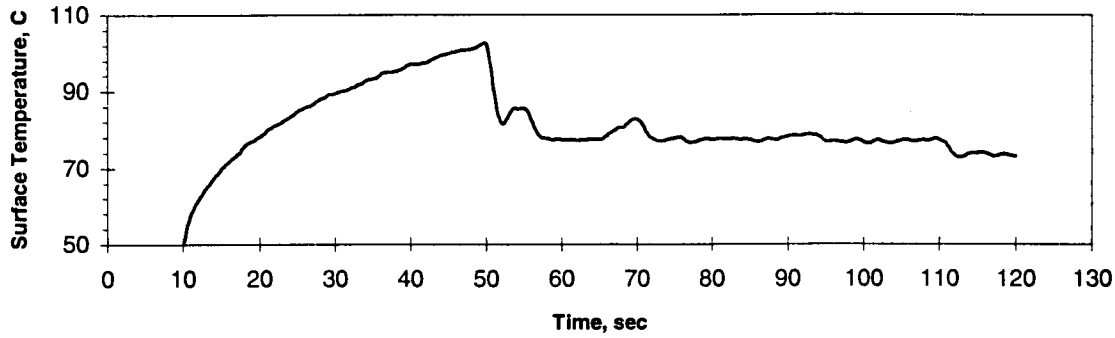

B. Local Fluid Temperatures

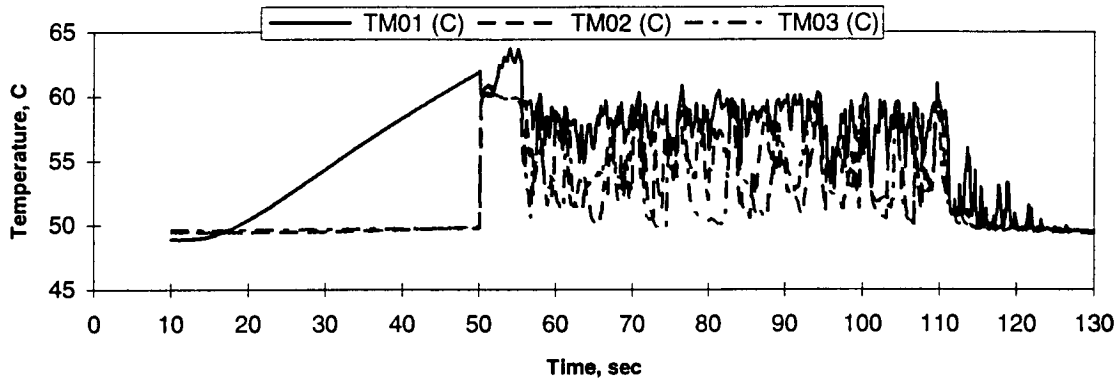

C. Far Field Bulk Temperatures

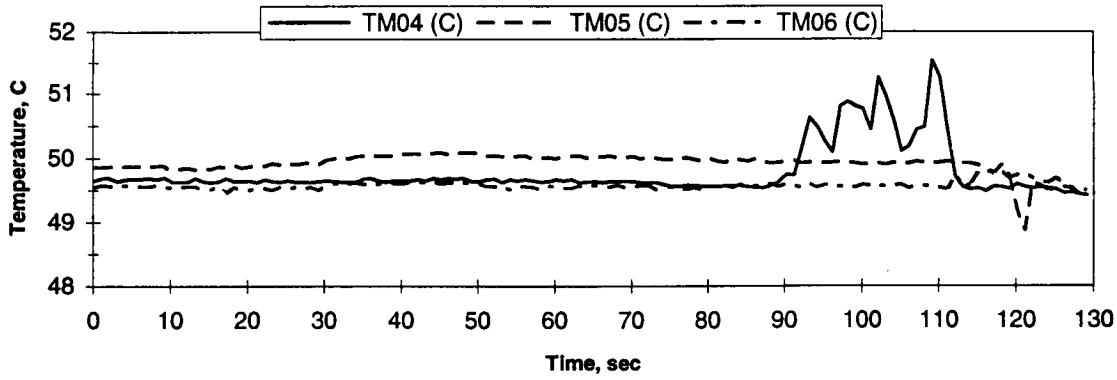

Figure: Measured Fluid Temperatures STS-60 Run #3

Heat Flux	Subcooling (F)	Heater Power On/Off	100 FPS On/Off	Stirrer Start	Repress Start	Total Test Time
2	20 ± 2	10-120 sec.	30-50 sec.	110 sec.	-----	130 sec.

Figure C-4c. Measured fluid temperatures near primary heater and far field bulk liquid. PBE-IC (STS-60). Run No. 3.

A. Mean Heater Surface Temperature

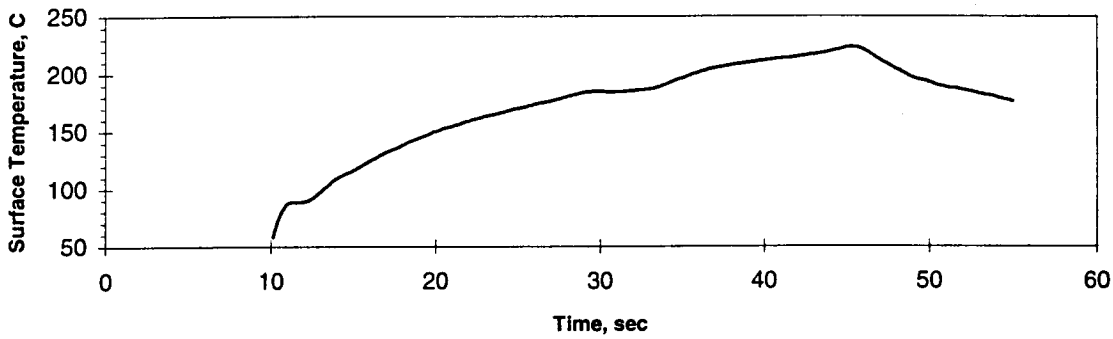

B. Local Fluid Temperatures

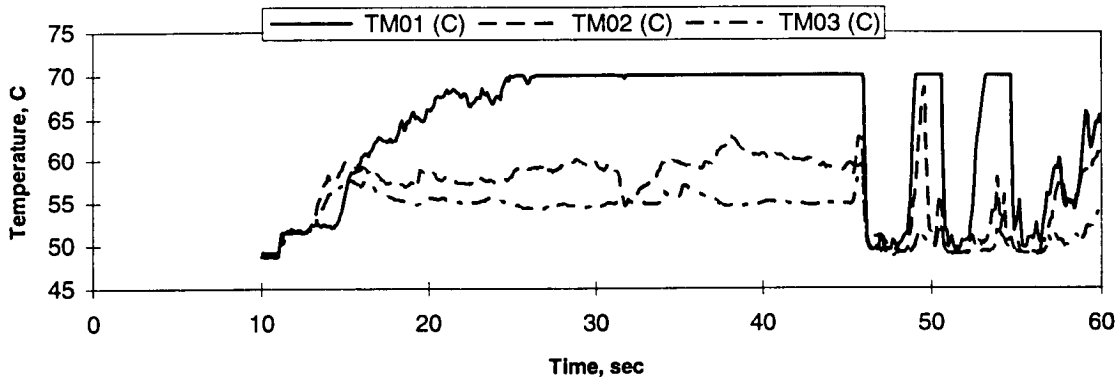

C. Far Field Bulk Temperatures

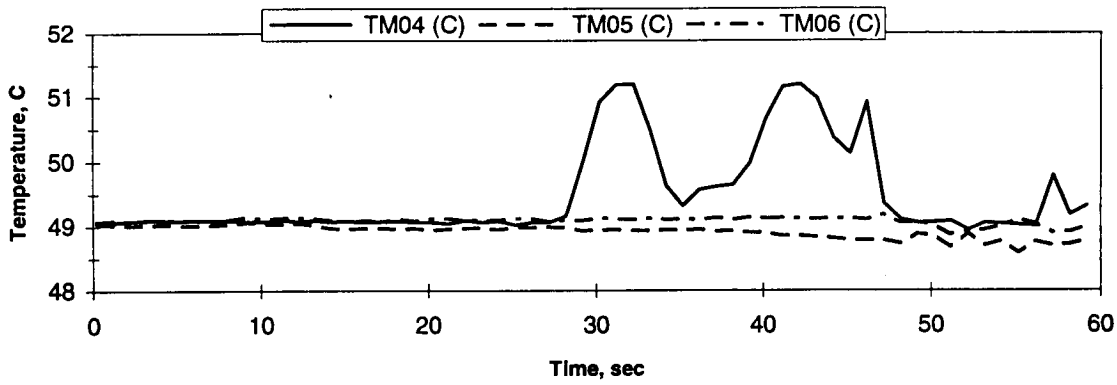

Figure: Measured Fluid Temperatures STS-60 Run #4

Heat Flux	Subcooling (F)	Heater Power On/Off	100 FPS On/Off	Stirrer Start	Repress Start	Total Test Time
8	5 ± 1	10-55 sec.	10-13 sec.	45 sec.	-----	60 sec.

Figure C-4d. Measured fluid temperatures near primary heater and far field bulk liquid. PBE-IC (STS-60). Run No. 4.

A. Mean Heater Surface Temperature

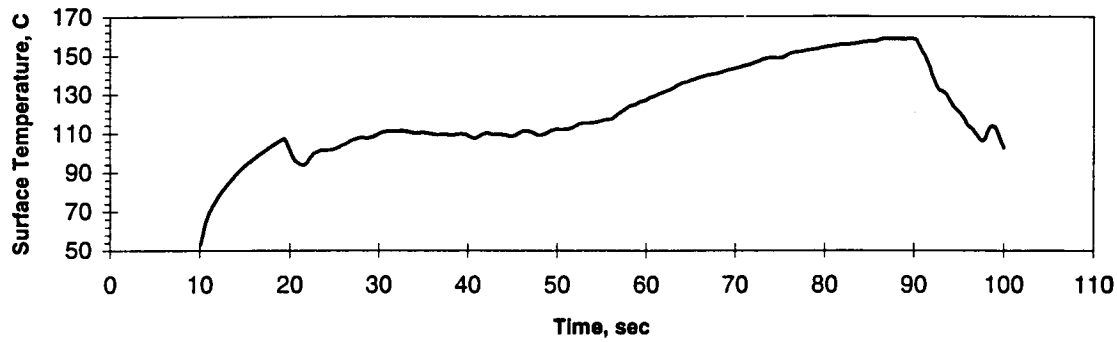

B. Local Fluid Temperatures

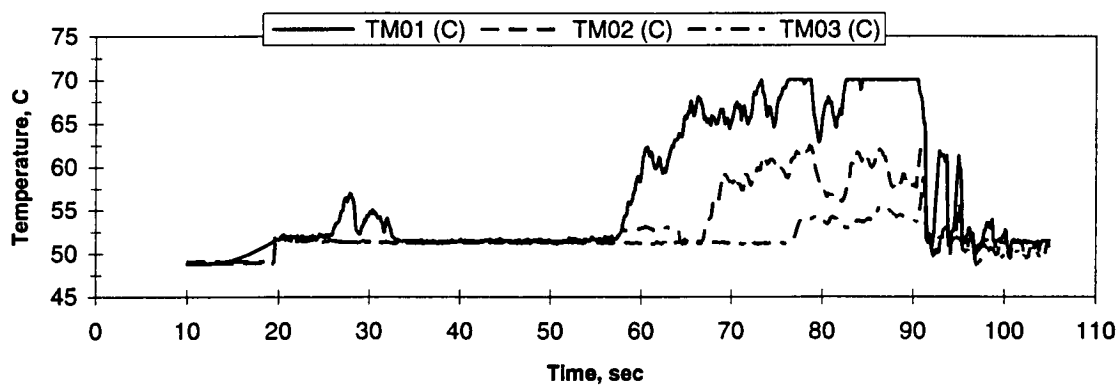

C. Far Field Bulk Temperatures

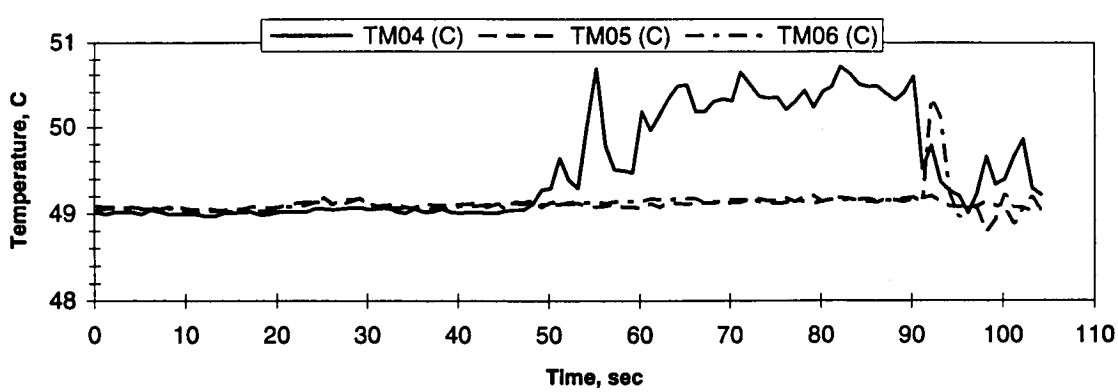

Figure: Measured Fluid Temperatures STS-60 Run #5

Heat Flux	Subcooling (F)	Heater Power On/Off	100 FPS On/Off	Stirrer Start	Repress Start	Total Test Time
4	5 ± 1	10-100 sec.	20-30 sec.	90 sec.	-----	105 sec.

Figure C-4e. Measured fluid temperatures near primary heater and far field bulk liquid. PBE-IC (STS-60). Run No. 5.

A. Mean Heater Surface Temperature

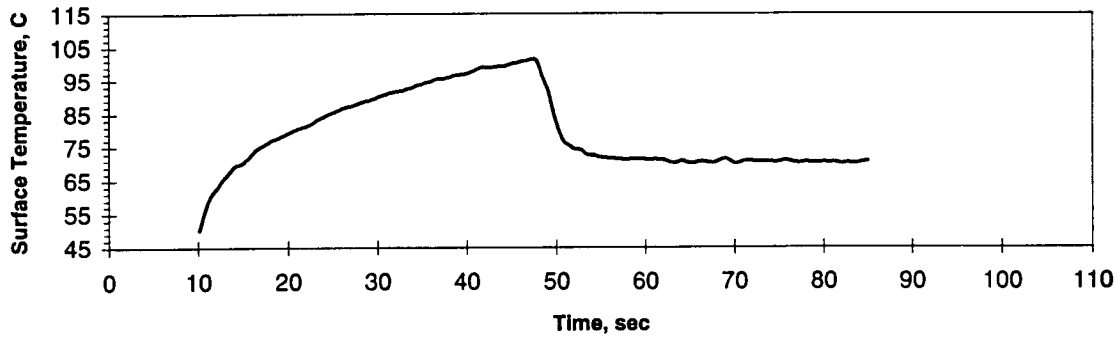

B. Local Fluid Temperatures

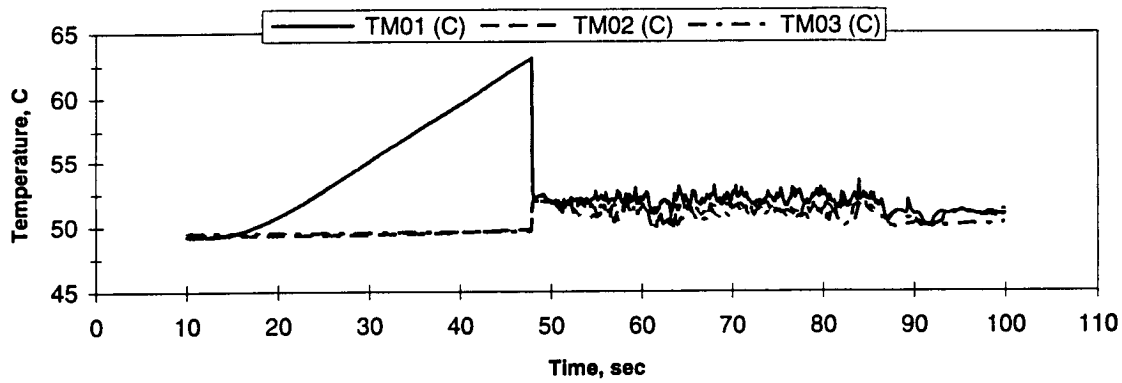

C. Far Field Bulk Temperatures

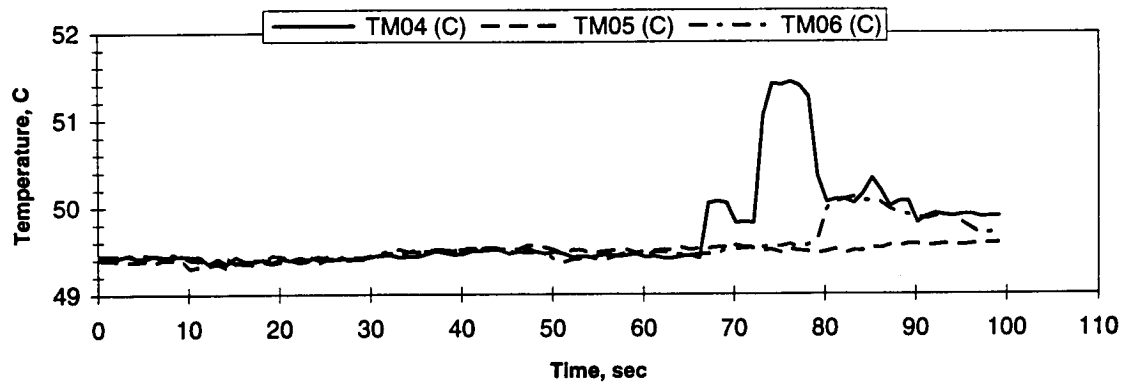

Figure: Measured Fluid Temperatures STS-60 Run #6

Heat Flux	Subcooling (F)	Heater Power On/Off	100 FPS On/Off	Stirrer Start	Repress Start	Total Test Time
2	5 ± 1	10-85 sec.	30-50 sec.	-----	-----	100 sec.

Figure C-4f. Measured fluid temperatures near primary heater and far field bulk liquid. PBE-IC (STS-60). Run No. 6.

A. Mean Heater Surface Temperature

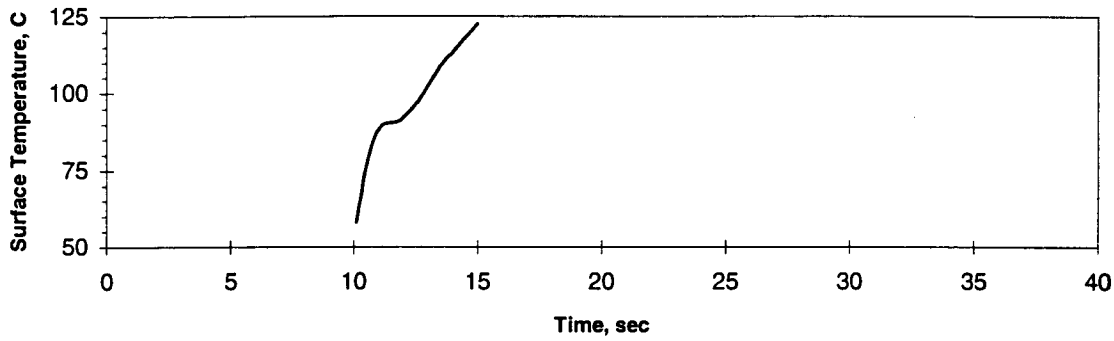

B. Local Fluid Temperatures

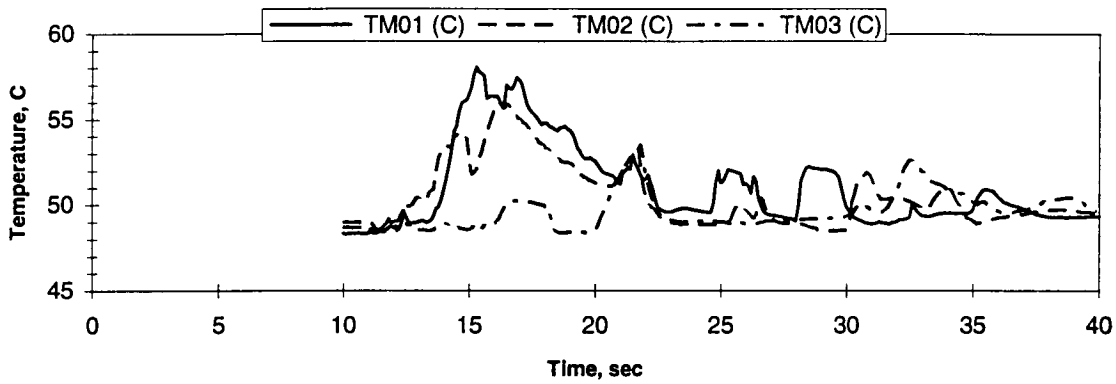

C. Far Field Bulk Temperatures

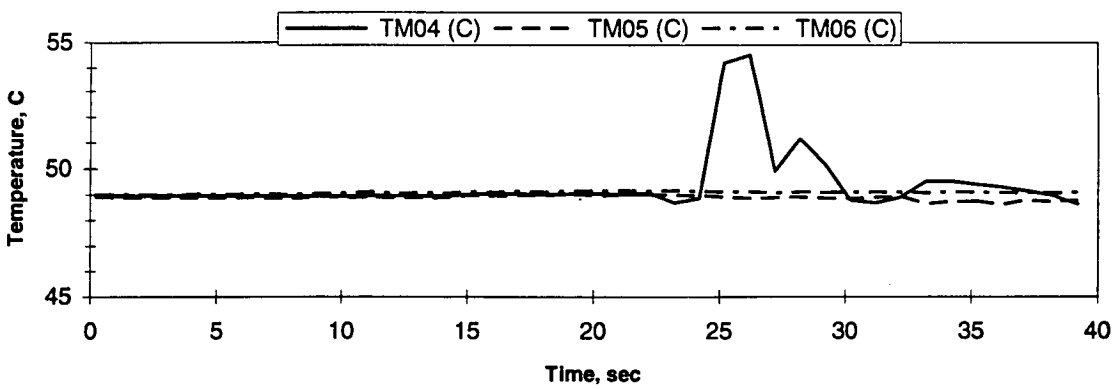

Figure: Measured Fluid Temperatures STS-60 Run #7

Heat Flux	Subcooling (F)	Heater Power On/Off	100 FPS On/Off	Stirrer Start	Repress Start	Total Test Time
8	0.5 ± 0.4	10-15 sec.	10-25 sec.	-----	20 sec.	40 sec.

Figure C-4g. Measured fluid temperatures near primary heater and far field bulk liquid. PBE-IC (STS-60). Run No. 7.

A. Mean Heater Surface Temperature

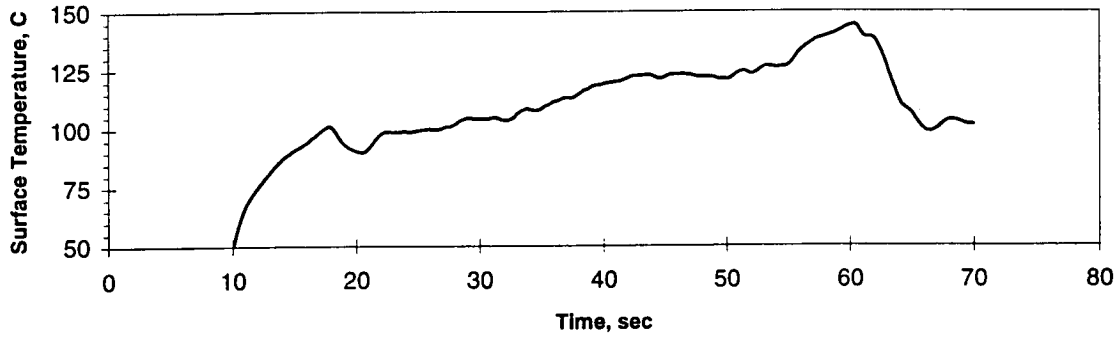

B. Local Fluid Temperatures

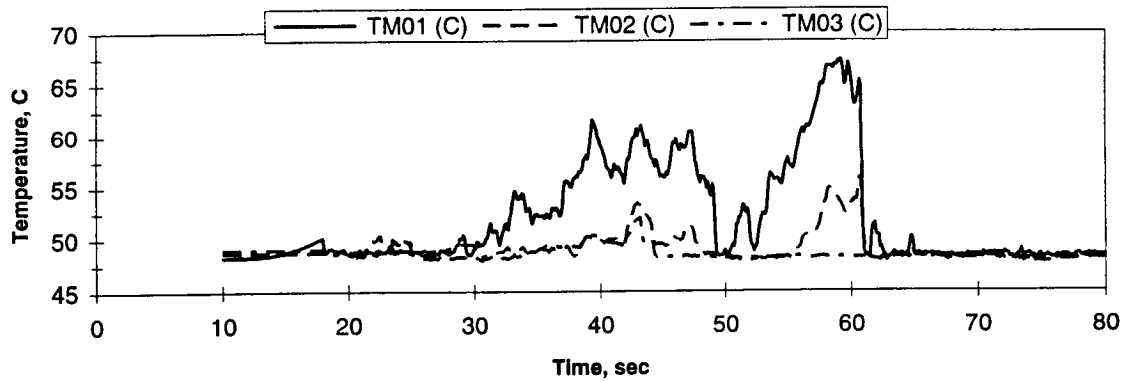

C. Far Field Bulk Temperatures

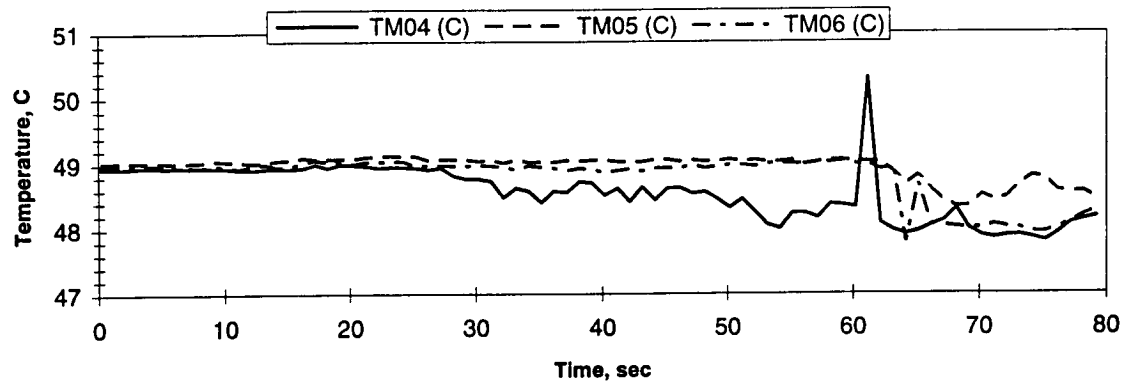

Figure: Measured Fluid Temperatures STS-60 Run #8

Heat Flux	Subcooling (F)	Heater Power On/Off	100 FPS On/Off	Stirrer Start	Repress Start	Total Test Time
4	0.5 ± 0.4	10-70 sec.	15-25 sec.	60 sec.	-----	80 sec.

Figure C-4h. Measured fluid temperatures near primary heater and far field bulk liquid. PBE-IC (STS-60). Run No. 8.

A. Mean Heater Surface Temperature

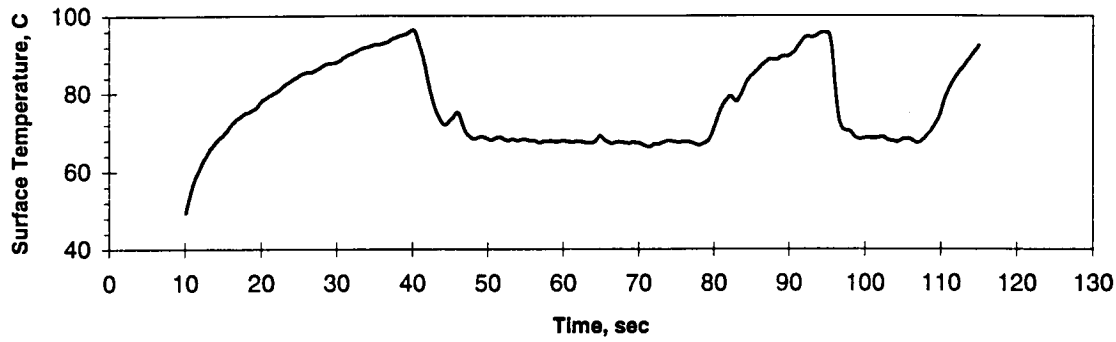

B. Local Fluid Temperatures

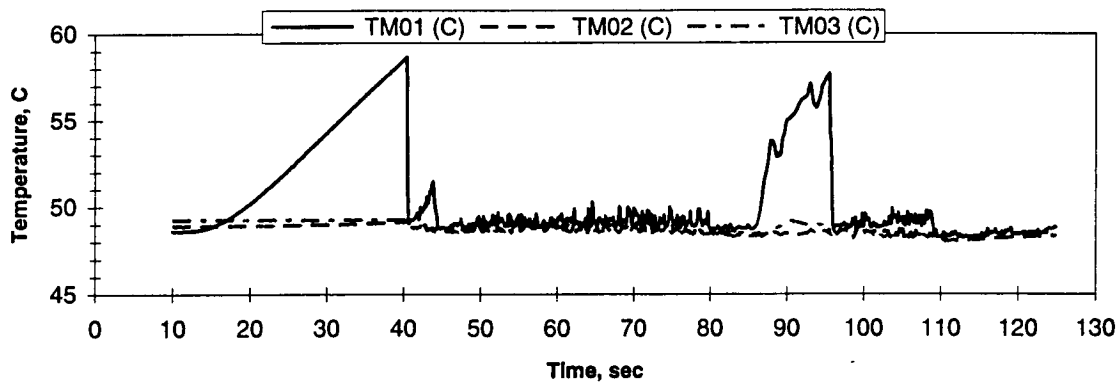

C. Far Field Bulk Temperatures

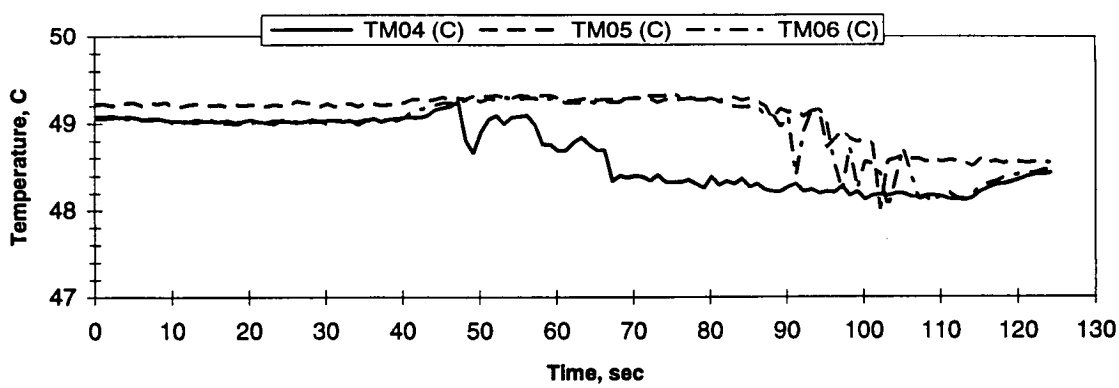

Figure: Measured Fluid Temperatures STS-60 Run #9

Heat Flux	Subcooling (F)	Heater Power On/Off	100 FPS On/Off	Stirrer Start	Repress Start	Total Test Time
2	0.5 ± 0.4	10-110 sec.	40-60 sec.	95 sec.	-----	125 sec.

Figure C-4i. Measured fluid temperatures near primary heater and far field bulk liquid. PBE-IC (STS-60). Run No. 9.

A. Mean Heater Surface Temperature

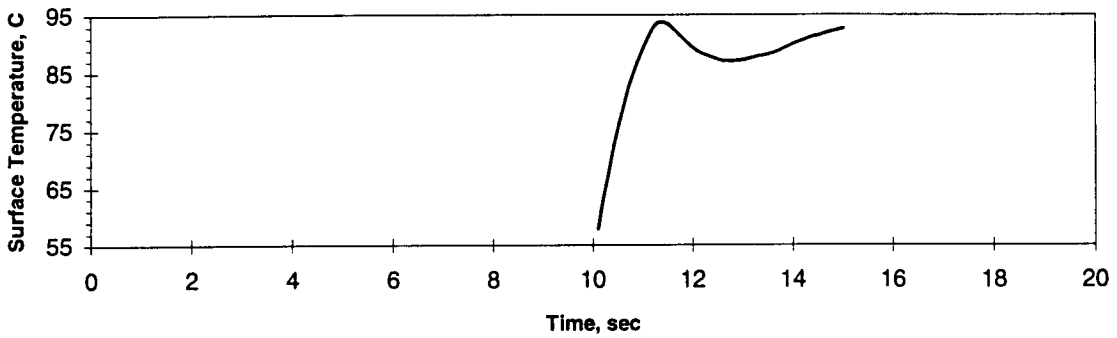

D.

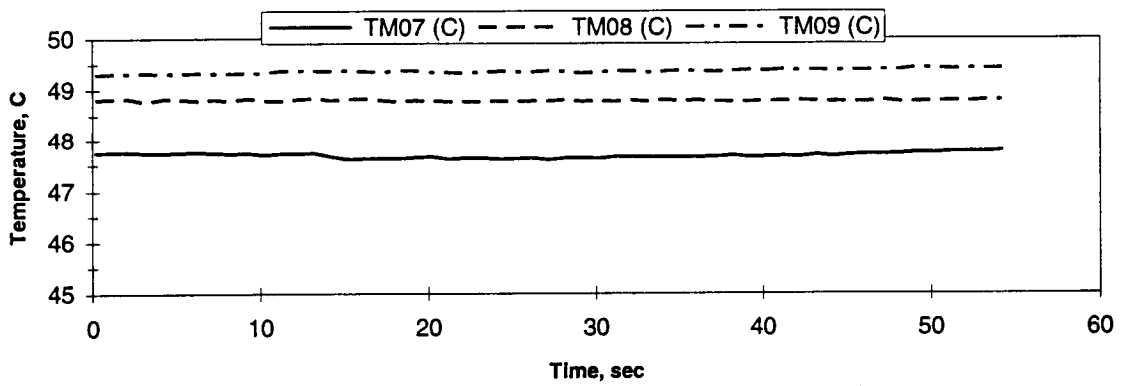

E.

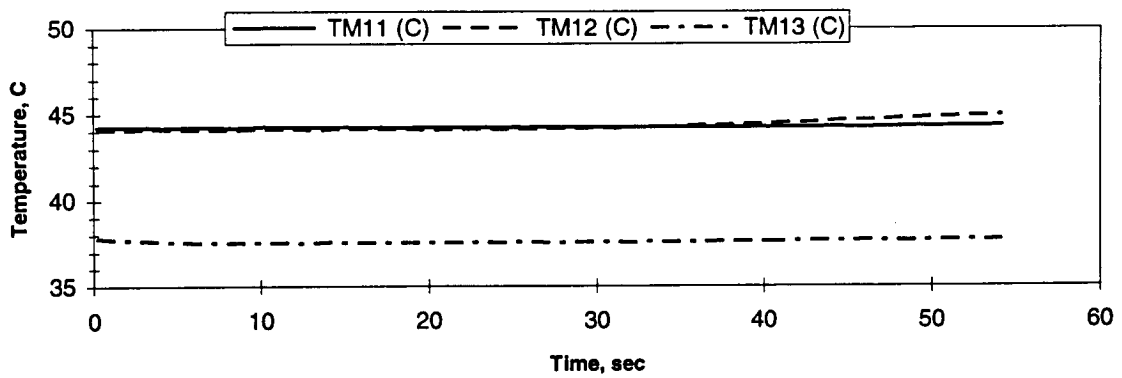

Figure: Measured Heater-Underside Temperatures STS-60 Run #1

Heat Flux	Subcooling (F)	Heater Power On/Off	100 FPS On/Off	Stirrer Start	Repress Start	Total Test Time
8	20 ± 2	10-15 sec.	10-13 sec.	-----	-----	55 sec.

Figure C-5a. Measured fluid temperatures near secondary heater and heater underside. PBE-IC (STS-60). Run No. 1.

A. Mean Heater Surface Temperature

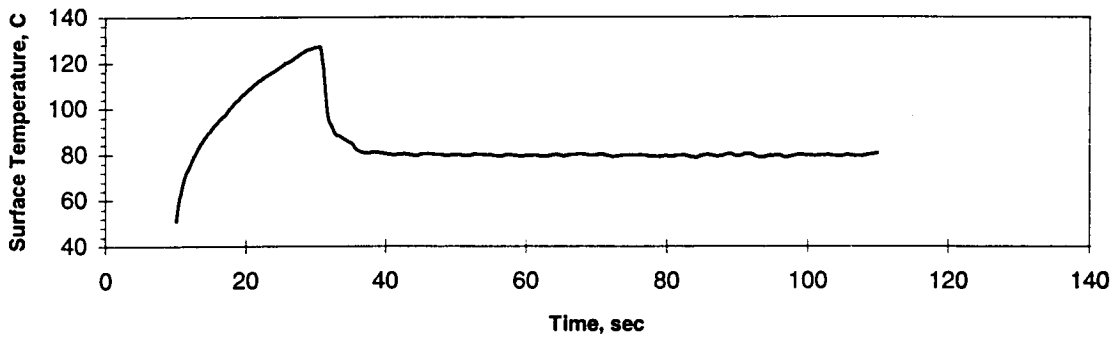

D.

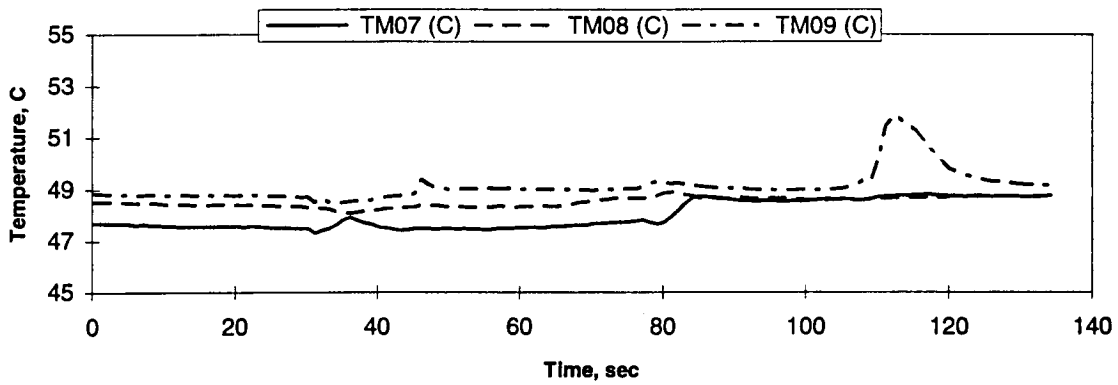

E.

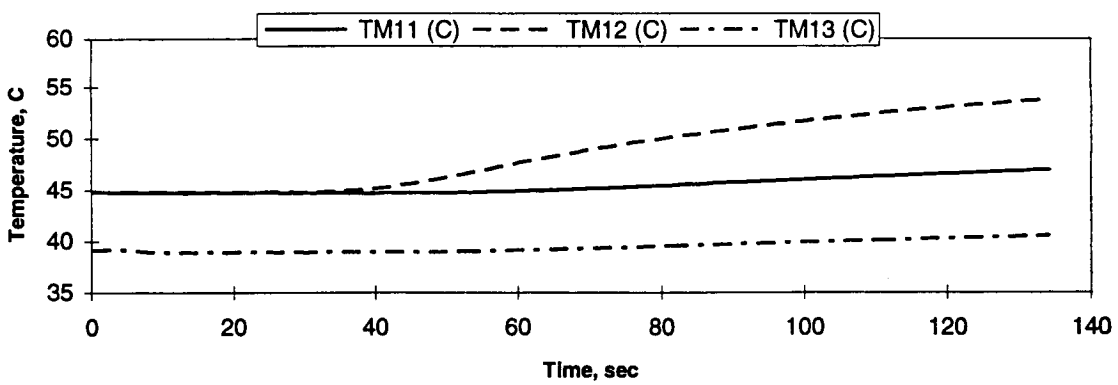

Figure: Measured Heater-Underside Temperatures STS-60 Run #2

Heat Flux	Subcooling (F)	Heater Power On/Off	100 FPS On/Off	Stirrer Start	Repress Start	Total Test Time
4	20 ± 2	10-110 sec.	15-25 sec.	-----	-----	135 sec.

Figure C-5b. Measured fluid temperatures near secondary heater and heater underside. PBE-IC (STS-60). Run No. 2.

A. Mean Heater Surface Temperature

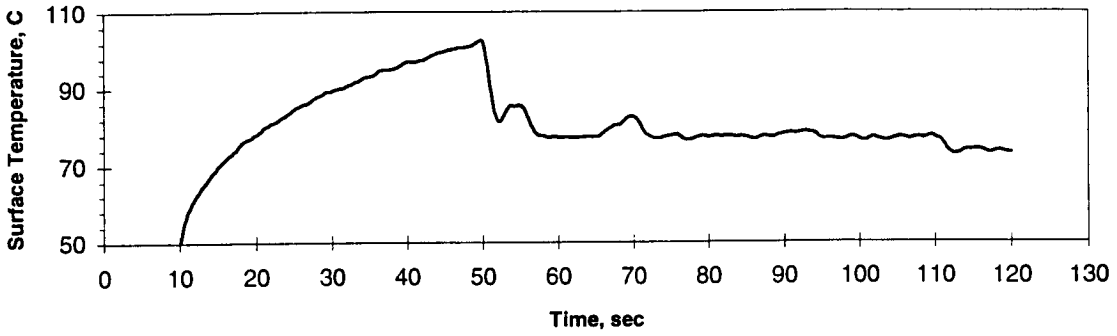

D.

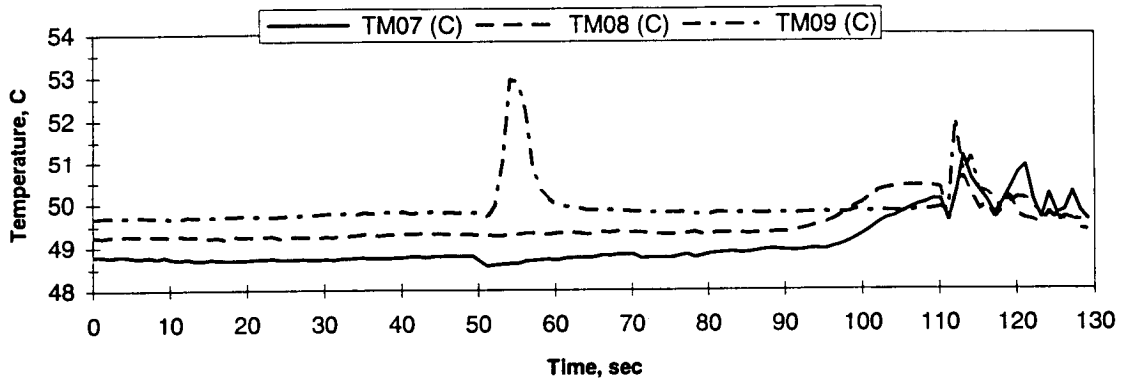

E.

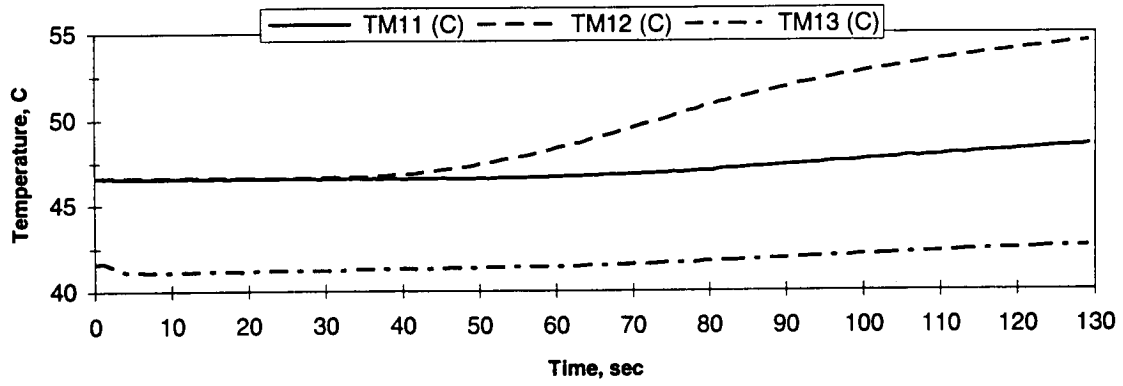

Figure: Measured Heater-Underside Temperatures STS-60 Run #3

Heat Flux	Subcooling (F)	Heater Power On/Off	100 FPS On/Off	Stirrer Start	Repress Start	Total Test Time
2	20 ± 2	10-120 sec.	30-50 sec.	110 sec.	-----	130 sec.

Figure C-5c. Measured fluid temperatures near secondary heater and heater underside. PBE-IC (STS-60). Run No. 3.

A. Mean Heater Surface Temperature

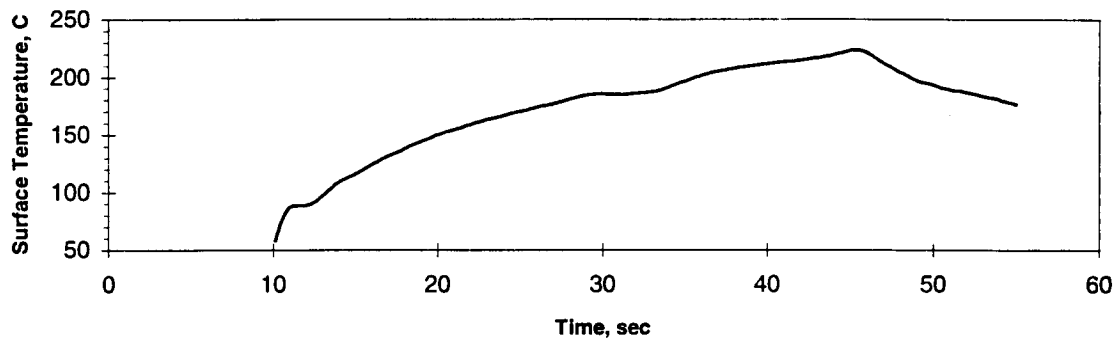

D.

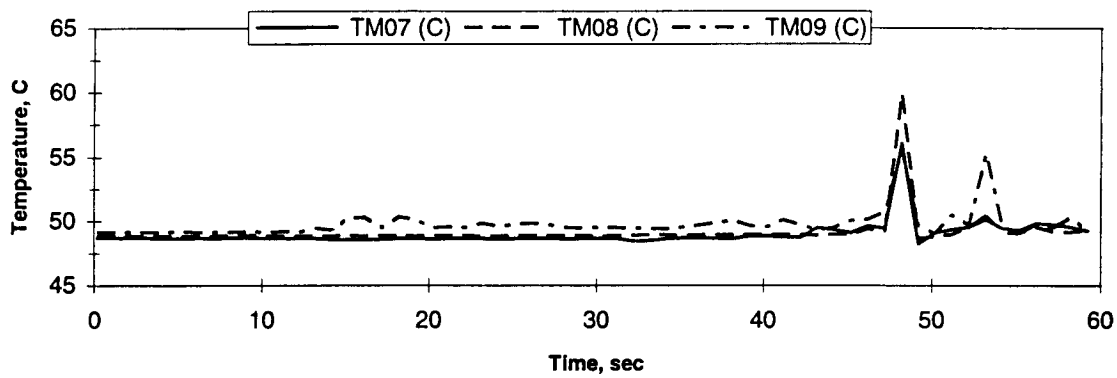

E.

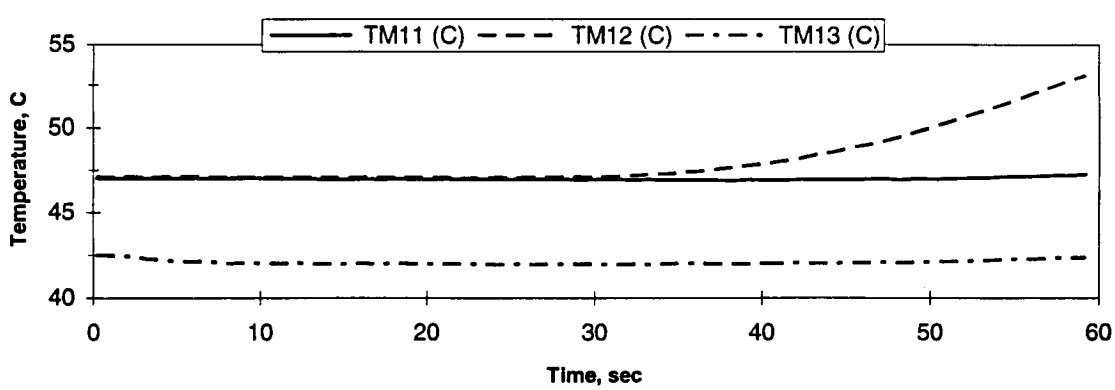

Figure: Measured Heater-Underside Temperatures STS-60 Run #4

Heat Flux	Subcooling (F)	Heater Power On/Off	100 FPS On/Off	Stirrer Start	Repress Start	Total Test Time
8	5 ± 1	10-55 sec.	10-13 sec.	45 sec.	-----	60 sec.

Figure C-5d. Measured fluid temperatures near secondary heater and heater underside. PBE-IC (STS-60). Run No. 4.

A. Mean Heater Surface Temperature

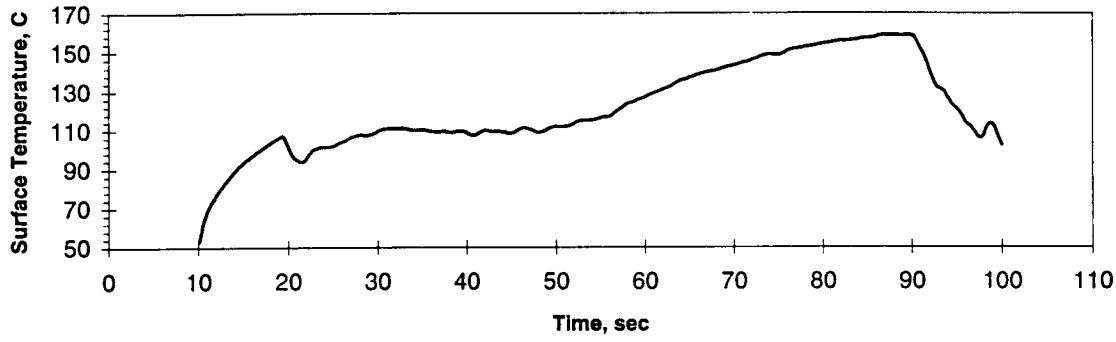

D.

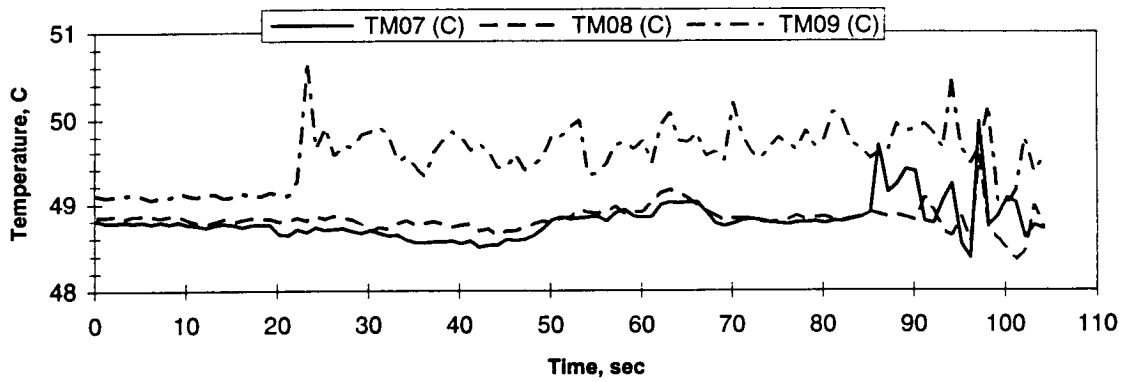

E.

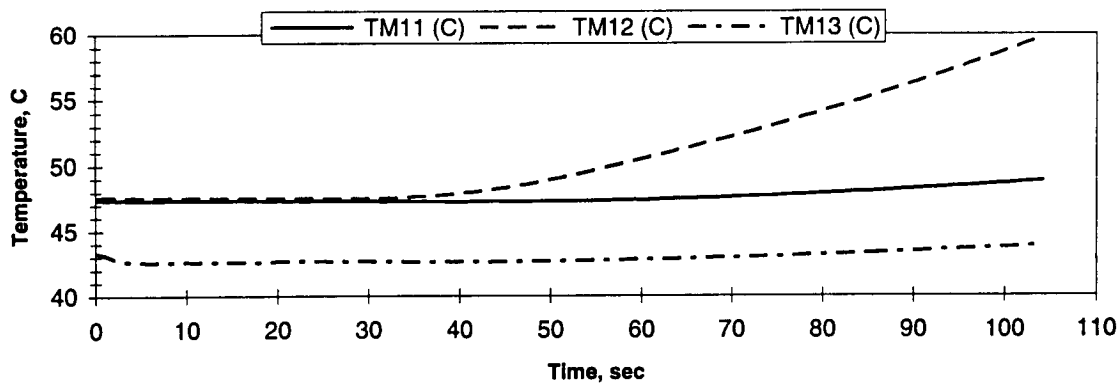

Figure: Measured Fluid Temperatures STS-60 Run #5

Heat Flux	Subcooling (F)	Heater Power On/Off	100 FPS On/Off	Stirrer Start	Repress Start	Total Test Time
4	5 ± 1	10-100 sec.	20-30 sec.	90 sec.	-----	105 sec.

Figure C-5e. Measured fluid temperatures near secondary heater and heater underside. PBE-IC (STS-60). Run No. 5.

A. Mean Heater Surface Temperature

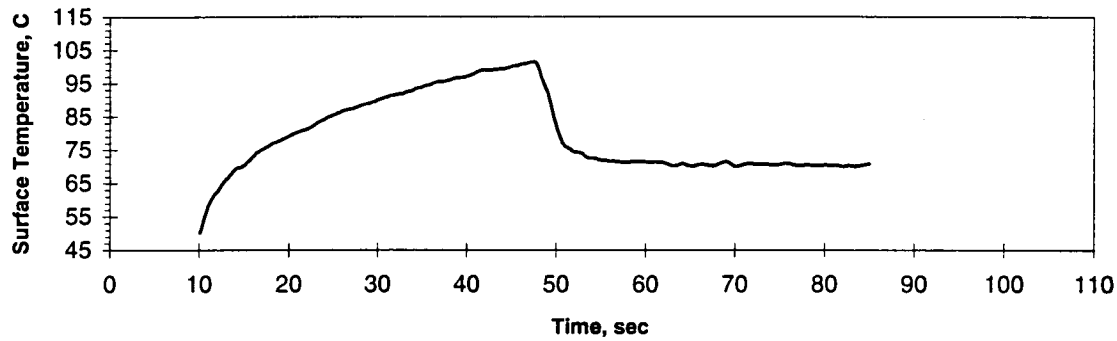

D.

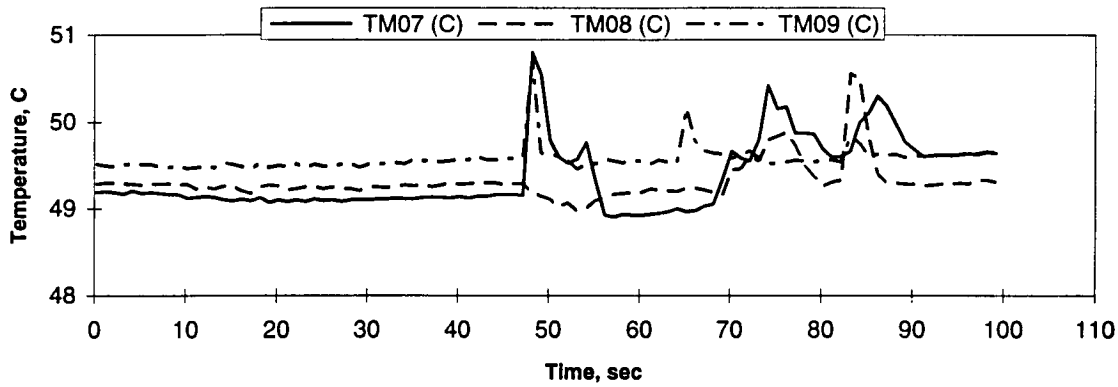

E.

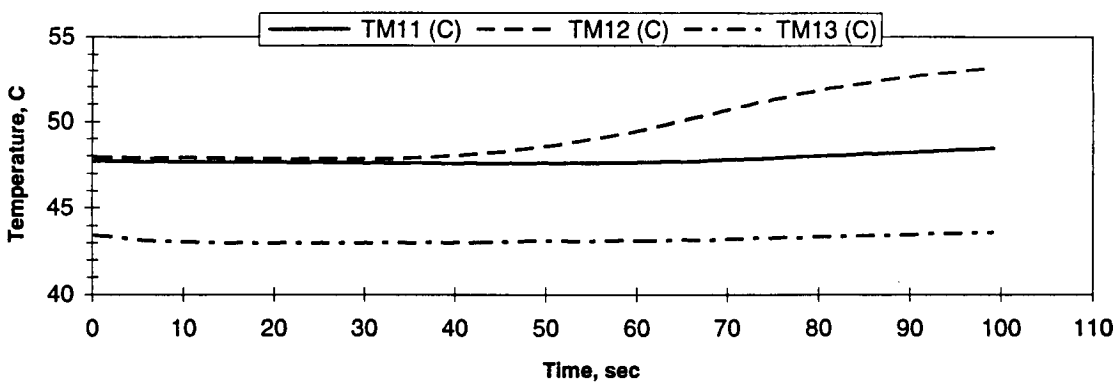

Figure: Measured Fluid Temperatures STS-60 Run #6

Heat Flux	Subcooling (F)	Heater Power On/Off	100 FPS On/Off	Stirrer Start	Repress Start	Total Test Time
2	5 ± 1	10-85 sec.	30-50 sec.	-----	-----	100 sec.

Figure C-5f. Measured fluid temperatures near secondary heater and heater underside. PBE-IC (STS-60). Run No. 6.

A. Mean Heater Surface Temperature

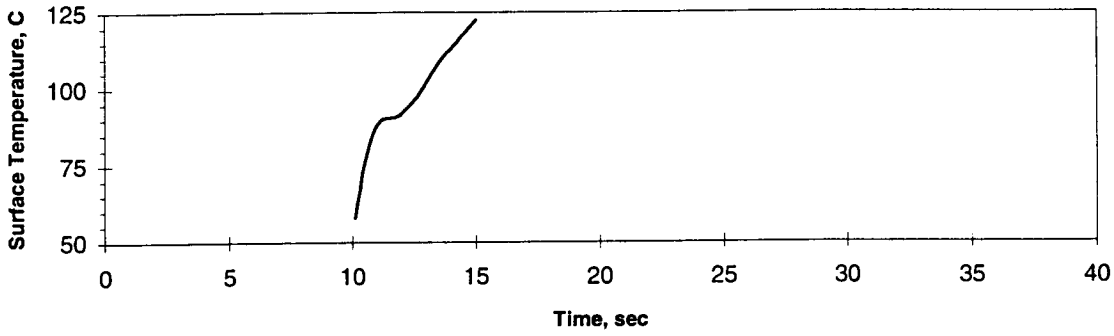

D.

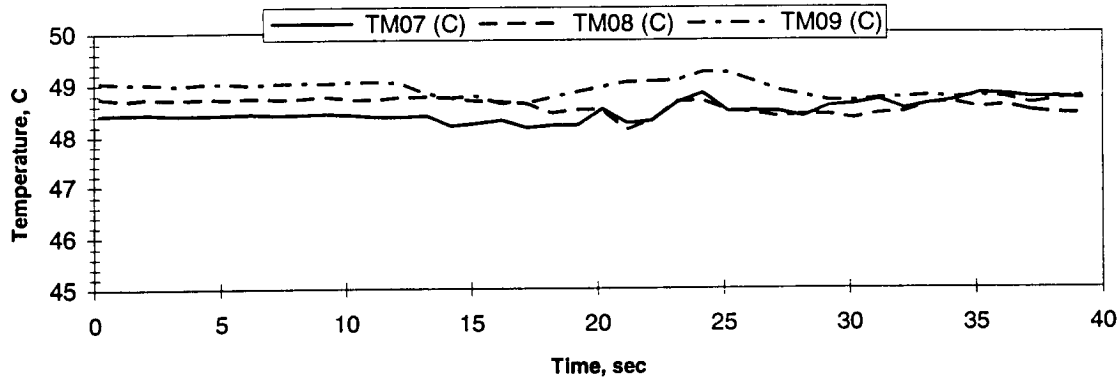

E.

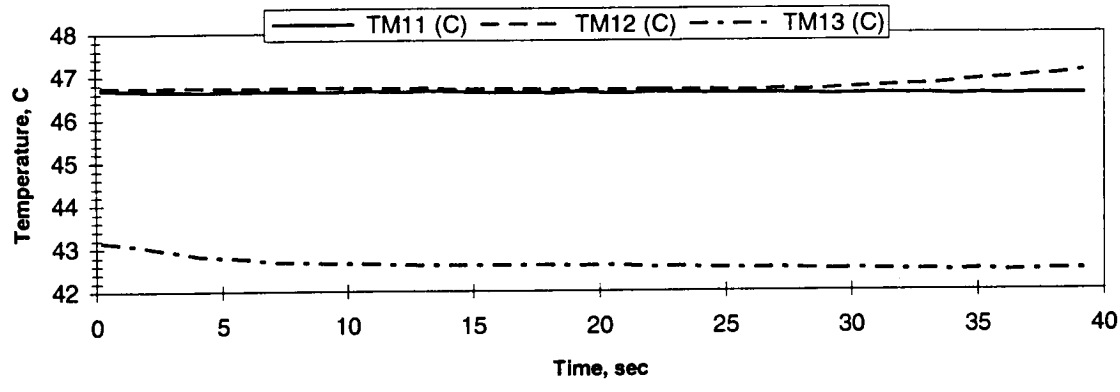

Figure: Measured Heater-Underside Temperatures STS-60 Run #7

Heat Flux	Subcooling (F)	Heater Power On/Off	100 FPS On/Off	Stirrer Start	Repress Start	Total Test Time
8	0.5 ± 0.4	10-15 sec.	10-25 sec.	-----	20 sec.	40 sec.

Figure C-5g. Measured fluid temperatures near secondary heater and heater underside. PBE-IC (STS-60). Run No. 7.

A. Mean Heater Surface Temperature

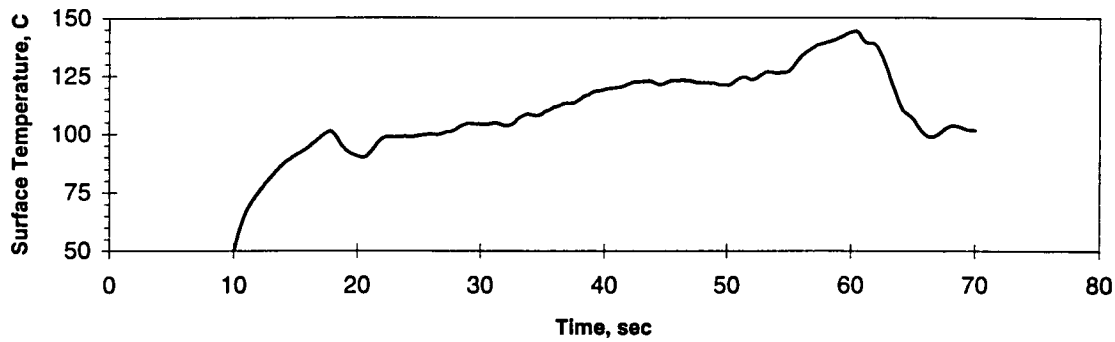

D.

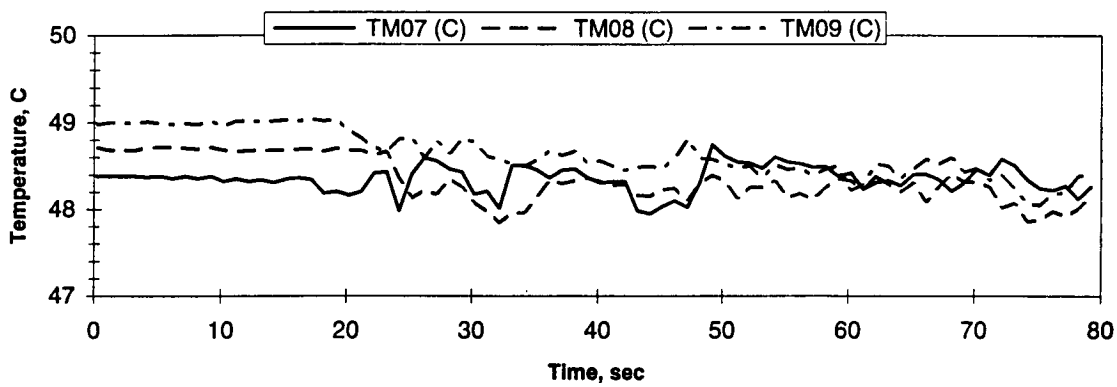

E.

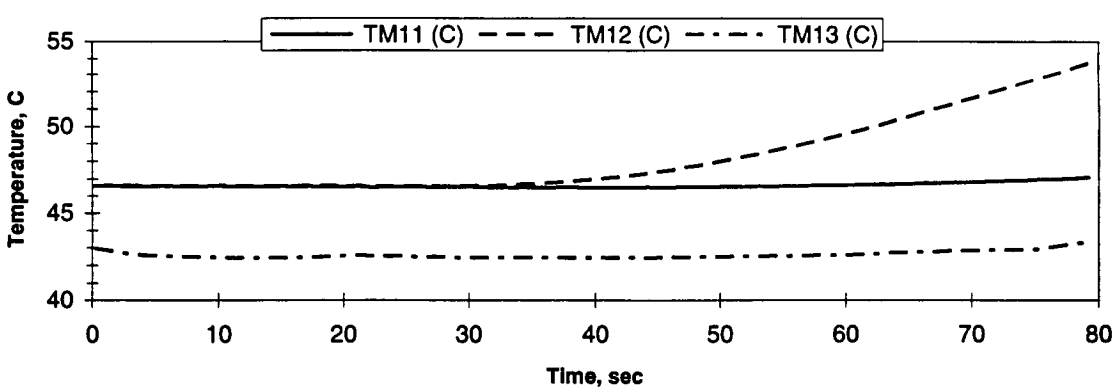

Figure: Measured Fluid Temperatures STS-60 Run #8

Heat Flux	Subcooling (F)	Heater Power On/Off	100 FPS On/Off	Stirrer Start	Repress Start	Total Test Time
4	0.5 ± 0.4	10-70 sec.	15-25 sec.	60 sec.	-----	80 sec.

Figure C-5h. Measured fluid temperatures near secondary heater and heater underside. PBE-IC (STS-60). Run No. 8.

A. Mean Heater Surface Temperature

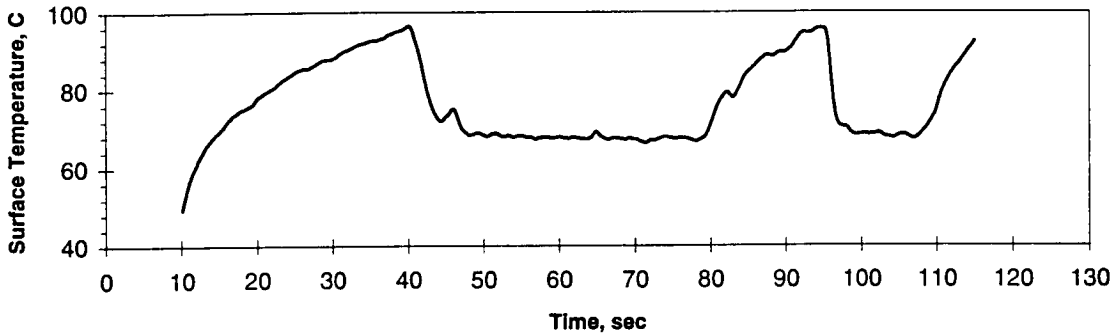

D.

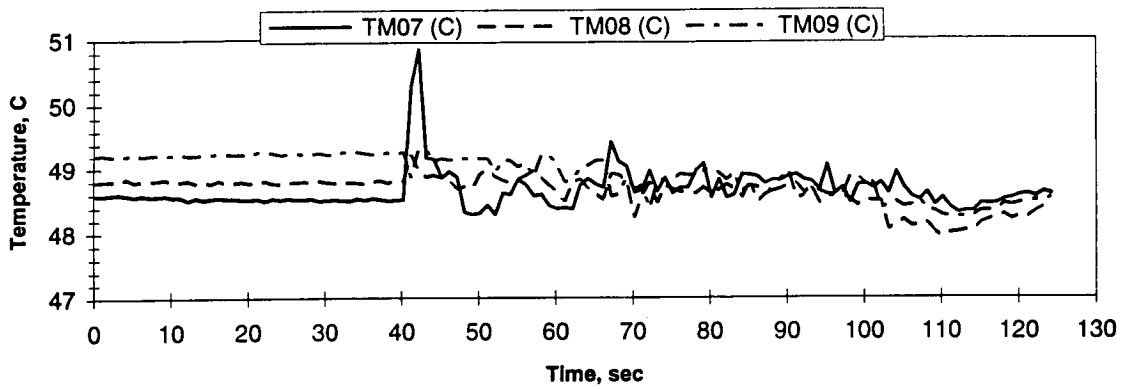

E.

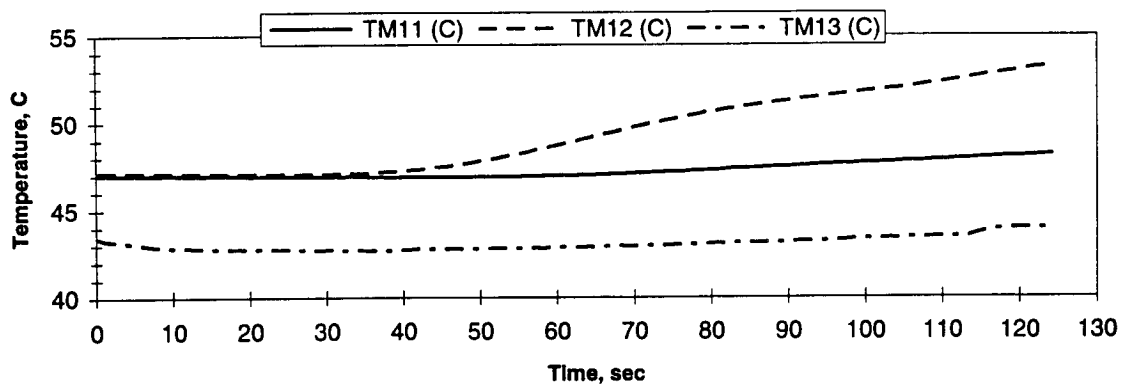

Figure: Measured Fluid Temperatures STS-60 Run #9

Heat Flux	Subcooling (F)	Heater Power On/Off	100 FPS On/Off	Stirrer Start	Repress Start	Total Test Time
2	0.5 ± 0.4	10-110 sec.	40-60 sec.	95 sec.	-----	125 sec.

Figure C-5i. Measured fluid temperatures near secondary heater and heater underside. PBE-IC (STS-60). Run No. 9.

STS-60 Run #1

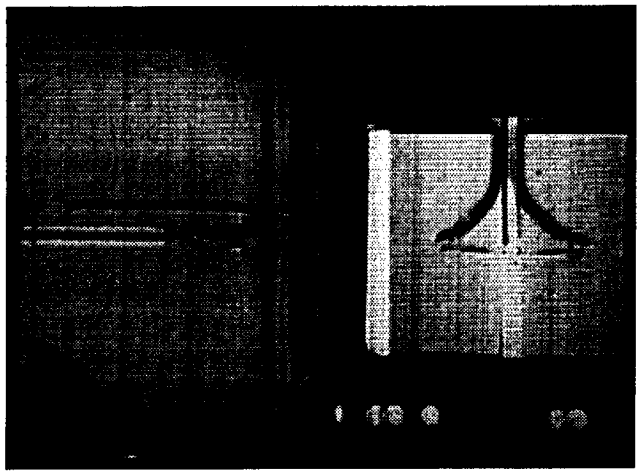

Frame #0088 time= 10.91 sec.

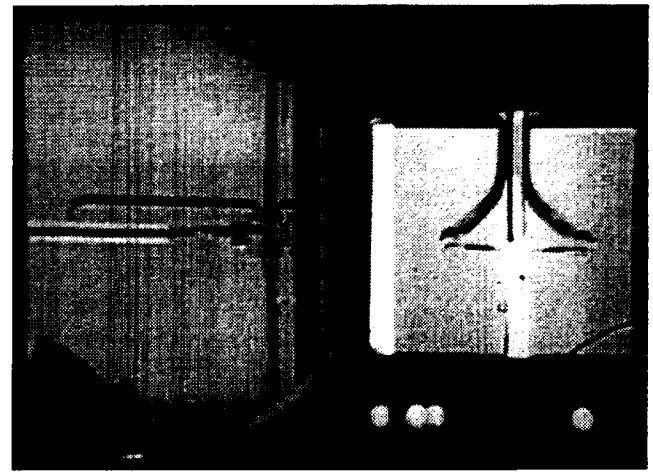

Frame #0101 time= 11.04 sec.

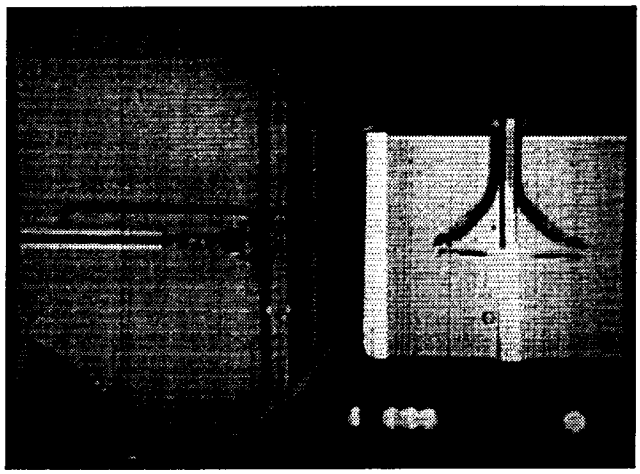

Frame #0114 time= 11.16 sec.

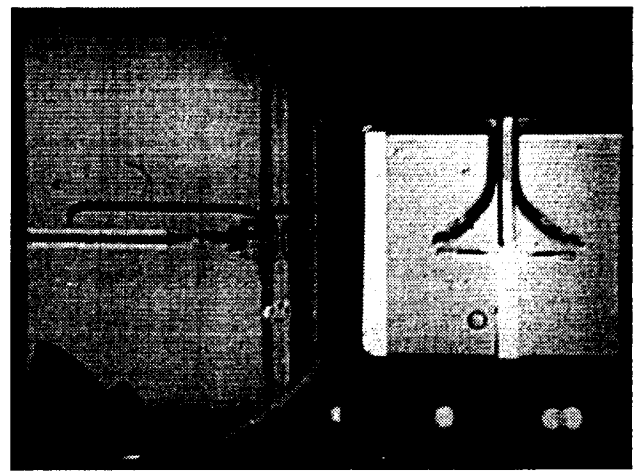

Frame #0129 time= 11.31 sec.

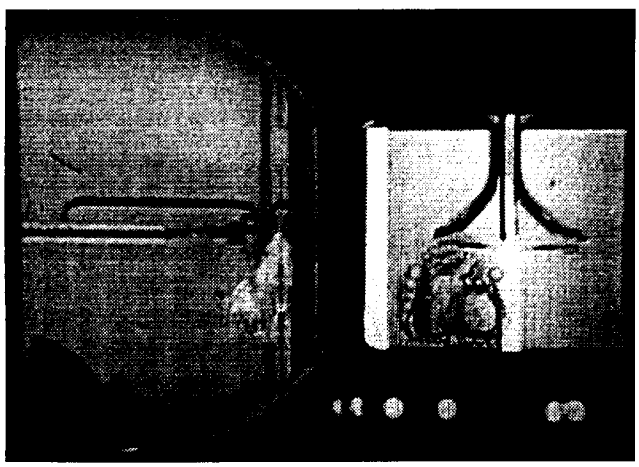

Frame #0149 time= 11.51 sec.

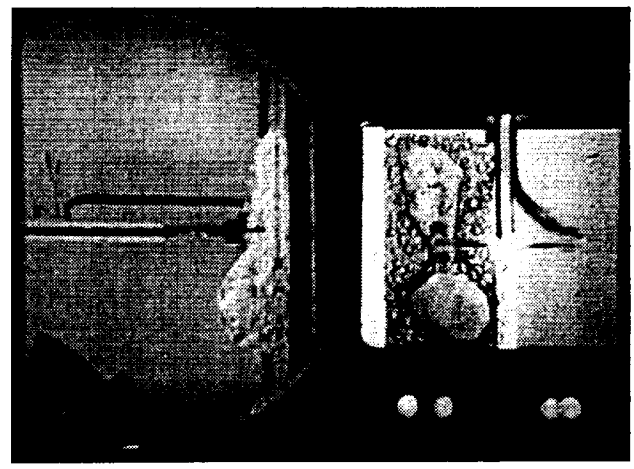

Frame #0159 time= 11.61 sec.

Figure C-6a. Selected Photographic Images. PBE-IC (STS-60). Run No. 1.

STS-60 Run #1

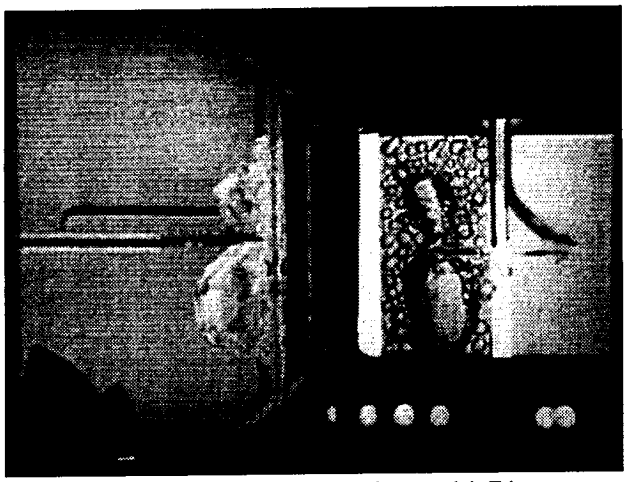

Frame #0169 time= 11.71 sec.

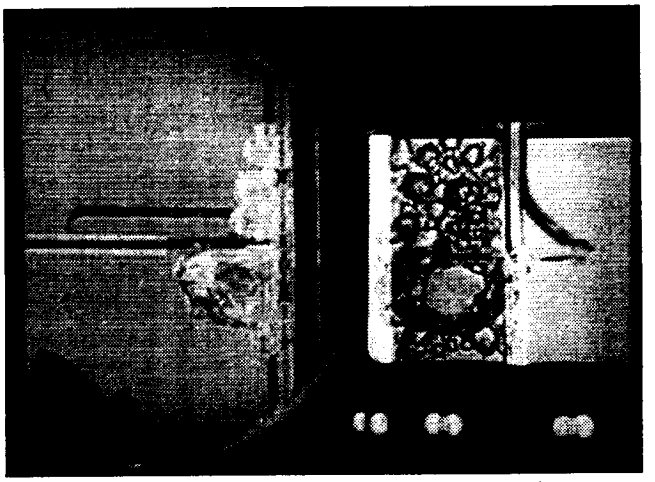

Frame #0203 time= 12.05 sec.

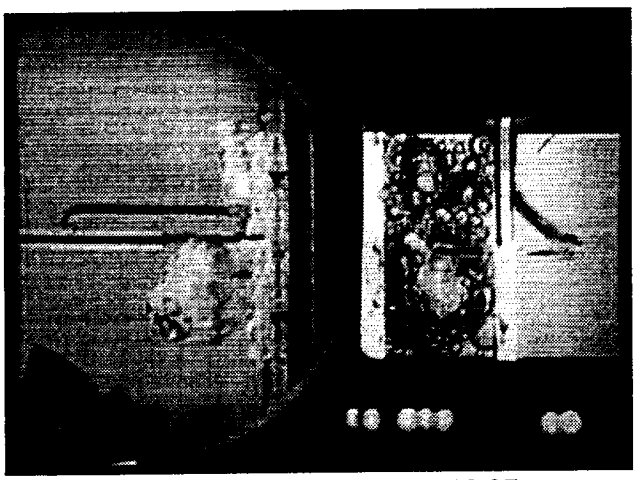

Frame #0235 time= 12.37 sec.

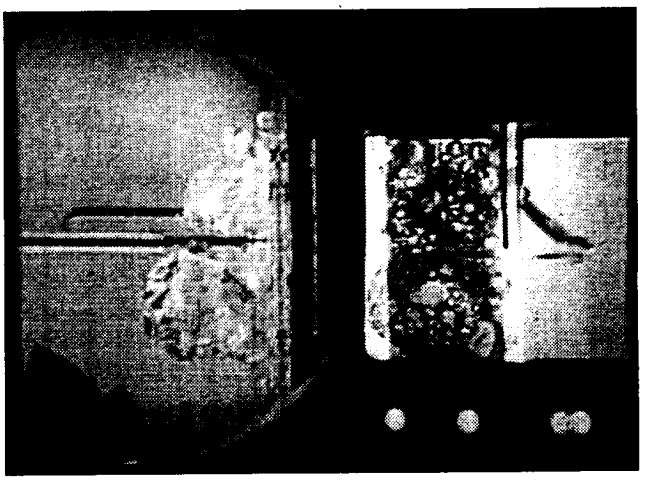

Frame #0271 time= 12.73 sec.

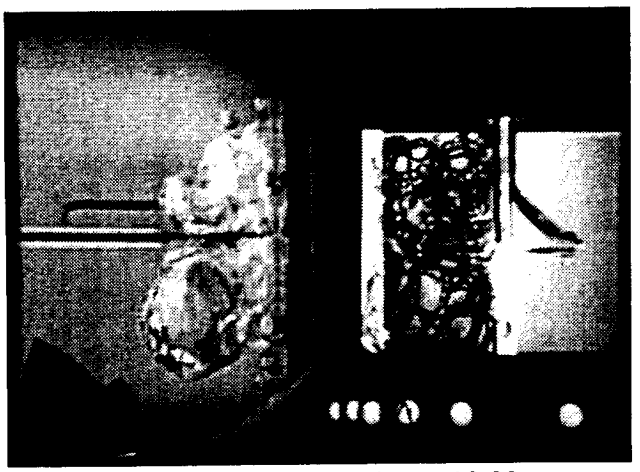

Frame #0301 time= 13.02 sec.

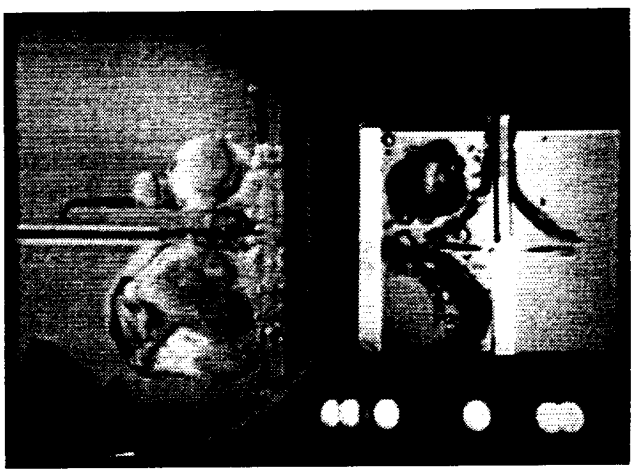

Frame #0340 time= 15.35 sec.

Figure C-6a. Continued.

STS-60 Run #1

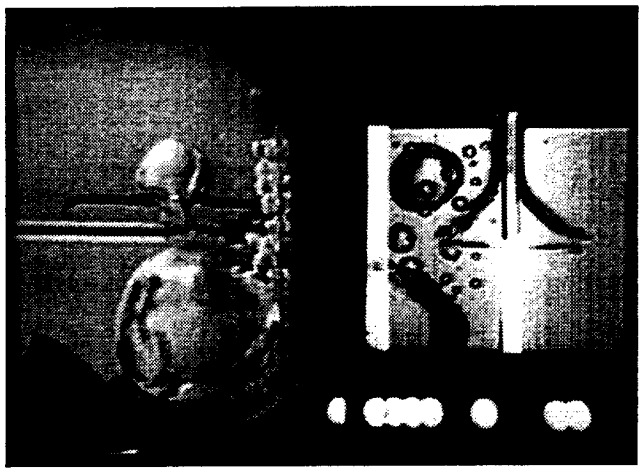

Frame #0350 time= 16.35 sec.

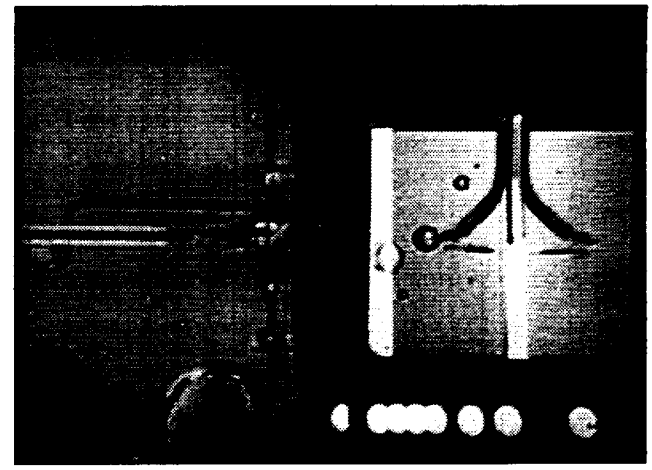

Frame #0427 time= 24.02 sec.

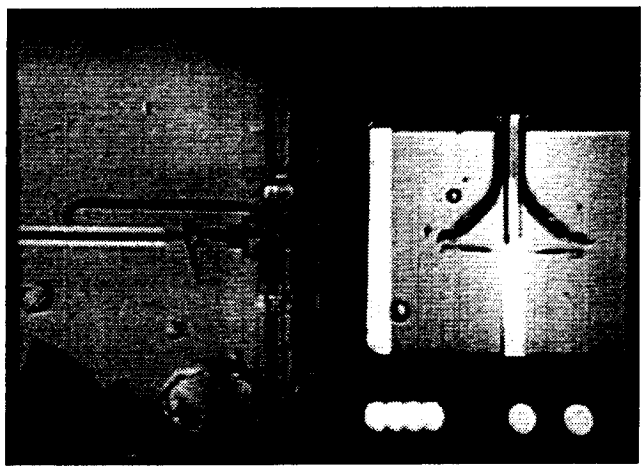

Frame #0504 time= 31.68 sec.

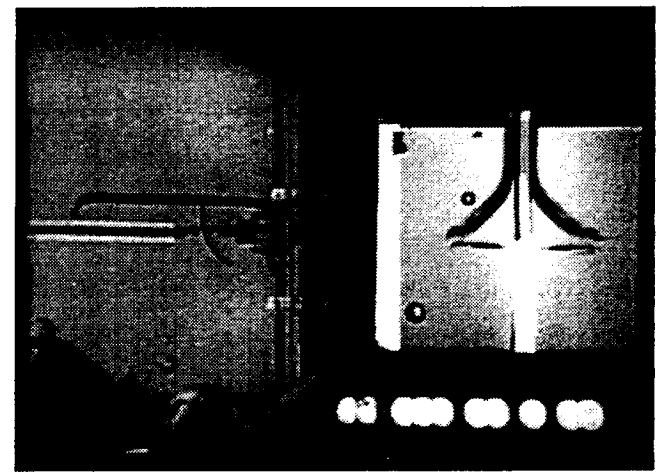

Frame #0581 time= 39.35 sec.

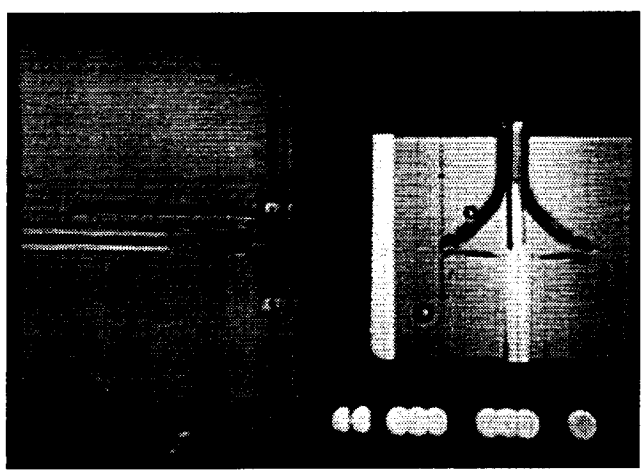

Frame #0658 time= 47.02 sec.

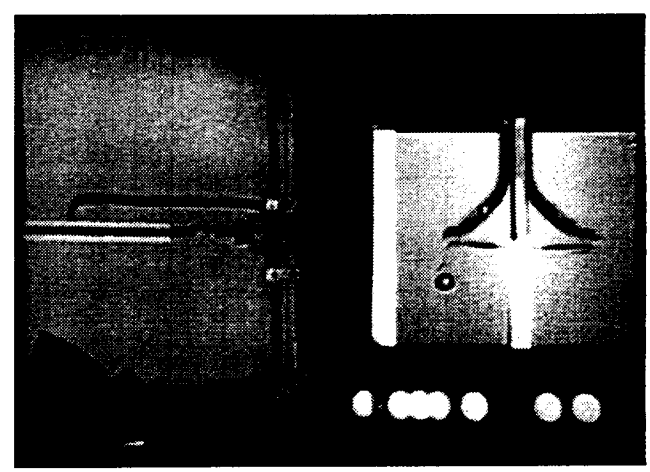

Frame #0735 time= 54.68 sec.

Figure C-6a. Continued.

STS-60 Run #2

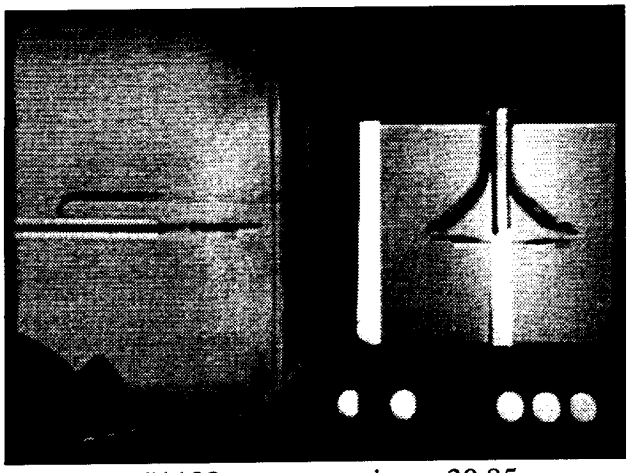

Frame #1122 time= 30.85 sec.

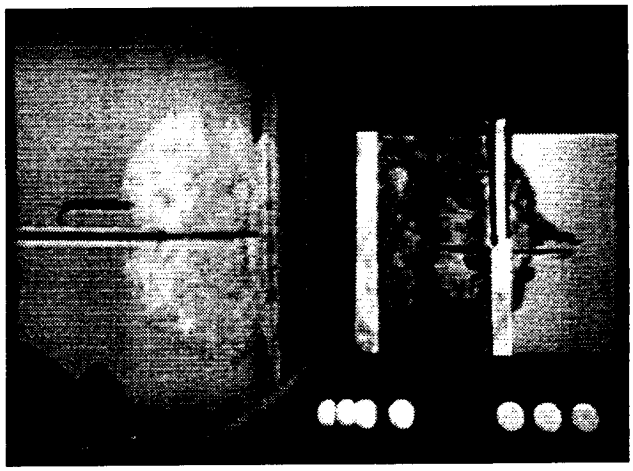

Frame #1123 time= 30.95 sec.

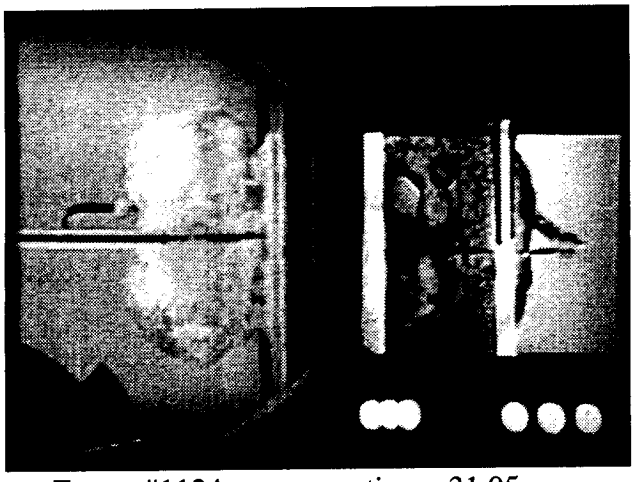

Frame #1124 time= 31.05 sec.

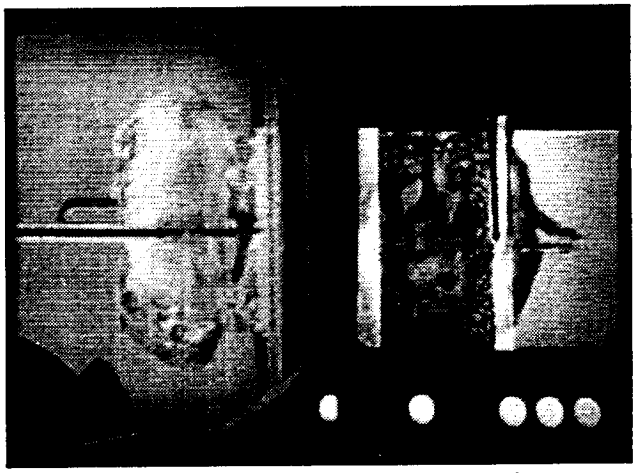

Frame #1125 time= 31.15 sec.

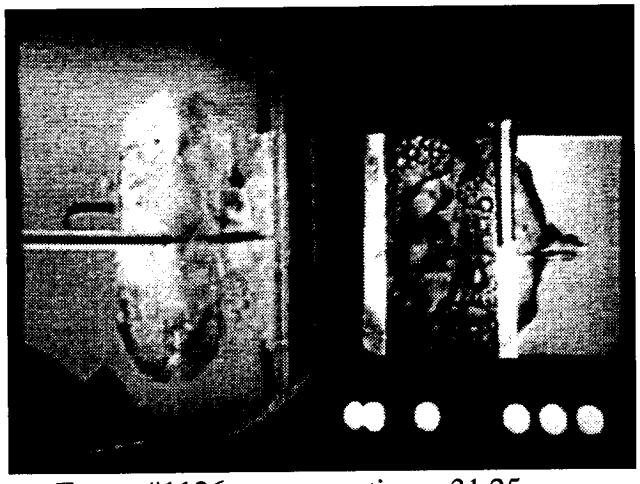

Frame #1126 time= 31.25 sec.

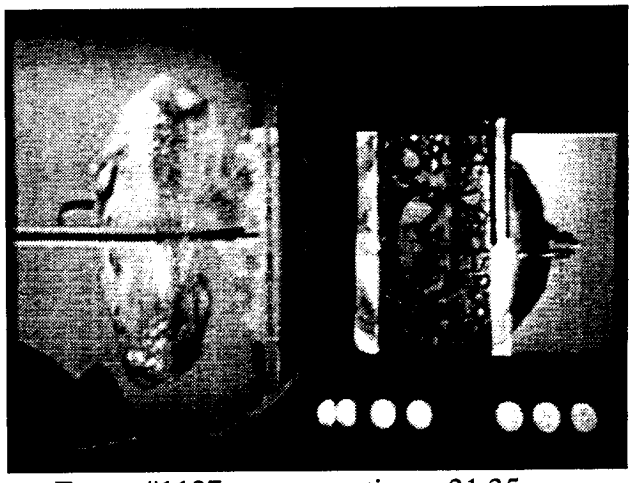

Frame #1127 time= 31.35 sec.

Figure C-6b. Selected Photographic Images. PBE-IC (STS-60). Run No. 2.

STS-60 Run #2

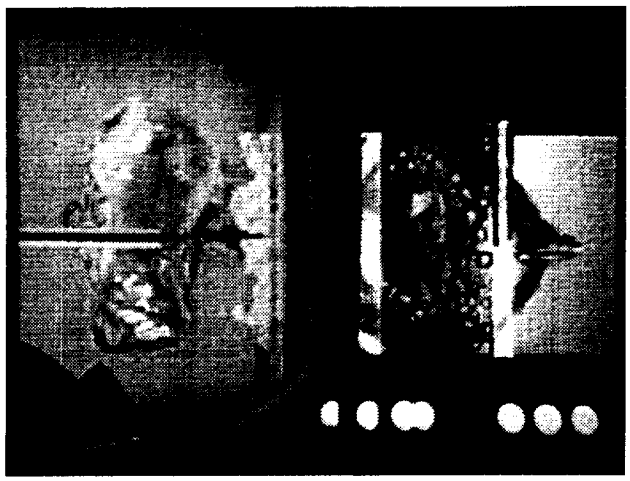

Frame #1129 time= 31.55 sec.

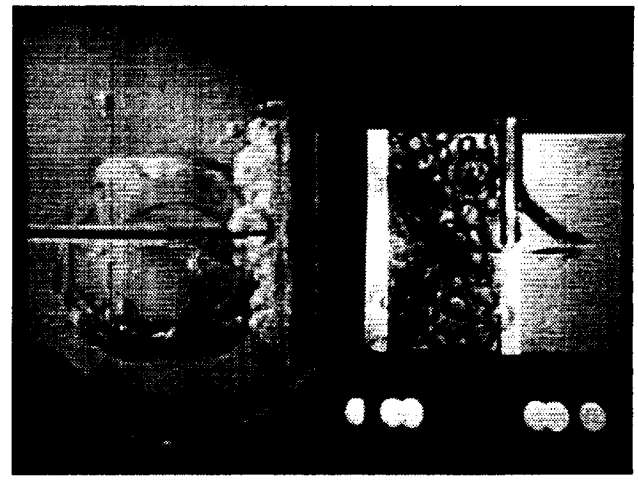

Frame #1329 time= 51.23 sec.

Frame #1429 time= 61.47 sec.

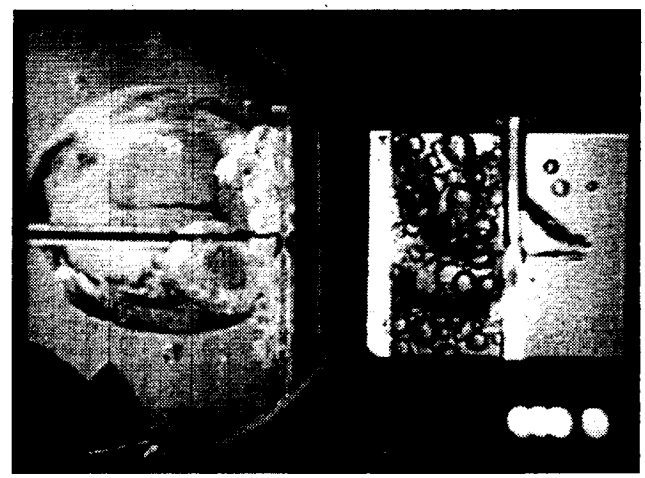

Frame #1529 time= 71.45 sec.

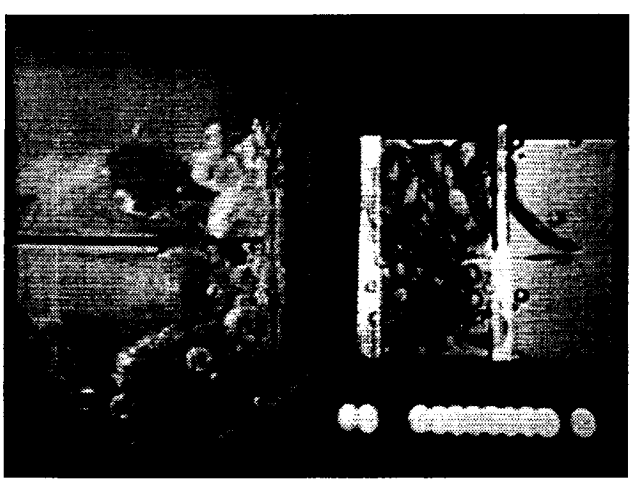

Frame #1729 time= 91.40 sec.

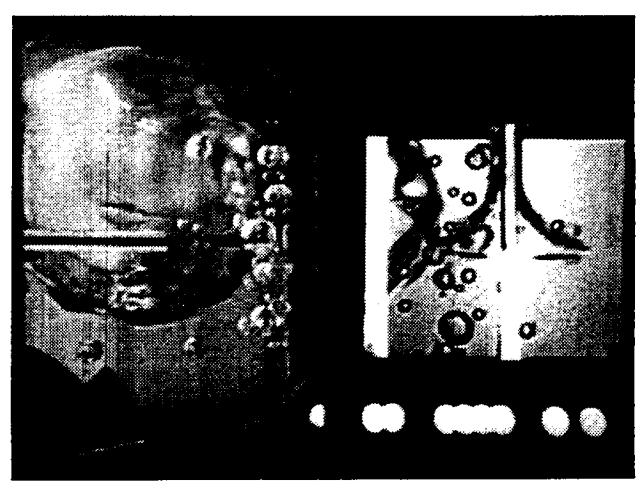

Frame #1929 time= 111.37 sec.

Figure C-6b. Continued.

STS-60 Run #3

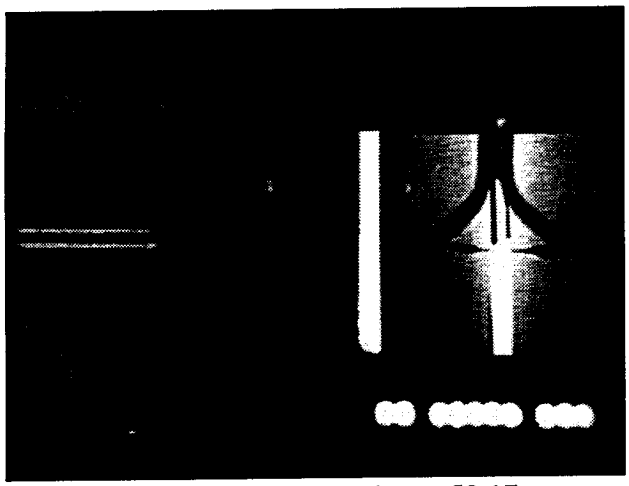

Frame #2112 time= 50.17 sec.

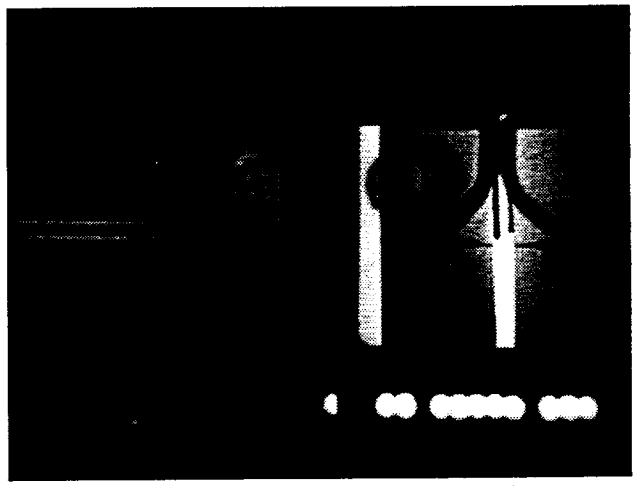

Frame #2113 time= 50.19 sec.

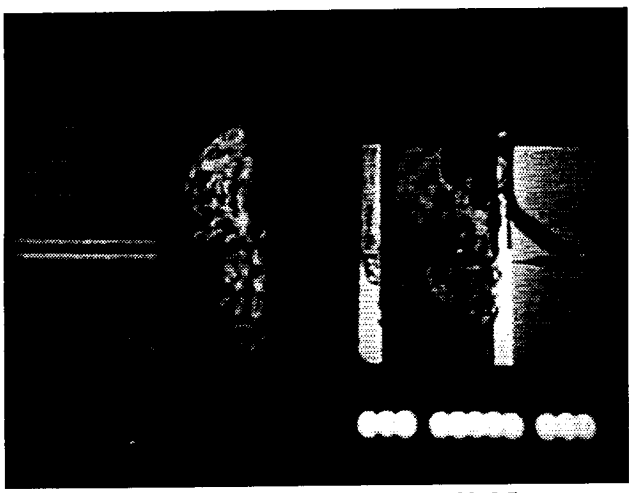

Frame #2116 time= 50.25 sec.

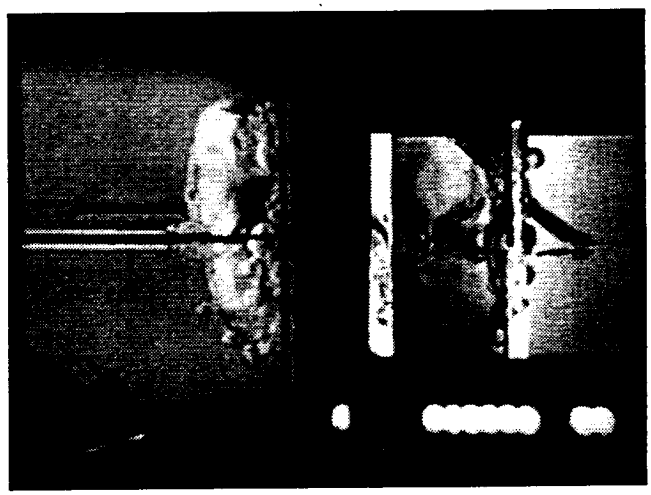

Frame #2119 time= 50.34 sec.

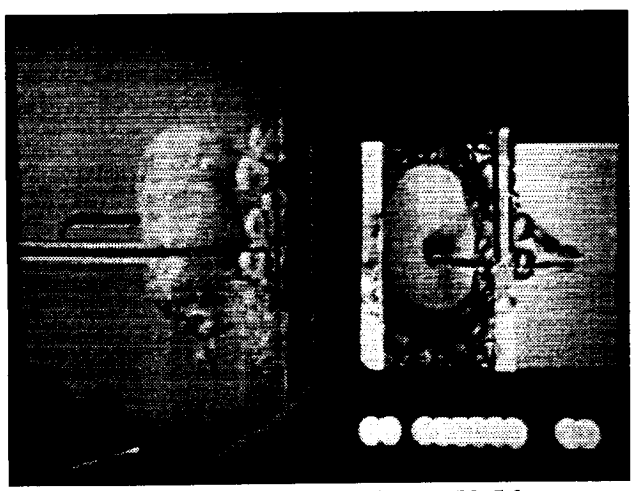

Frame #2122 time= 50.56 sec.

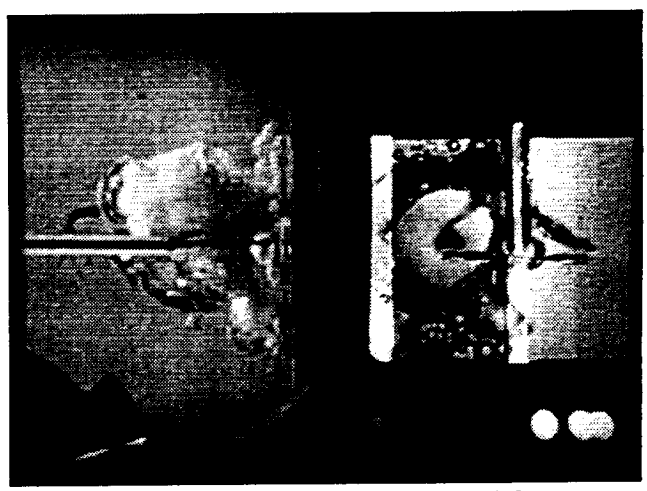

Frame #2125 time= 50.96 sec.

Figure C-6c. Selected Photographic Images. PBE-IC (STS-60). Run No. 3.

STS-60 Run #3

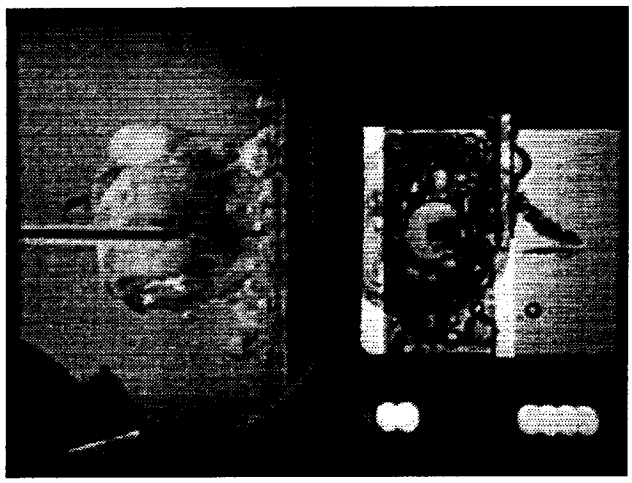

Frame #2130 time= 51.45 sec.

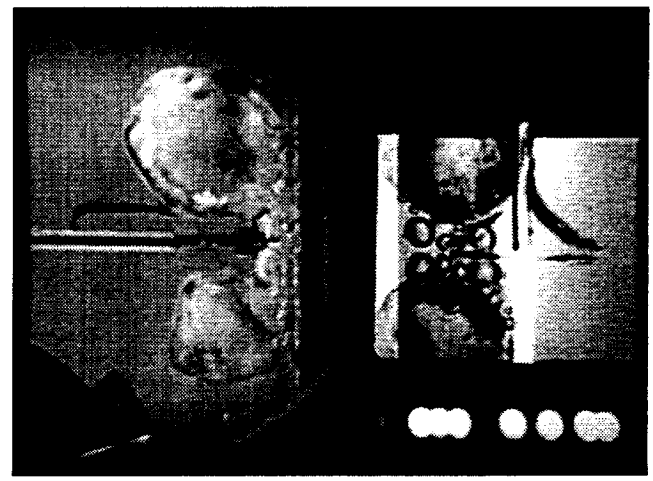

Frame #2250 time= 63.44 sec.

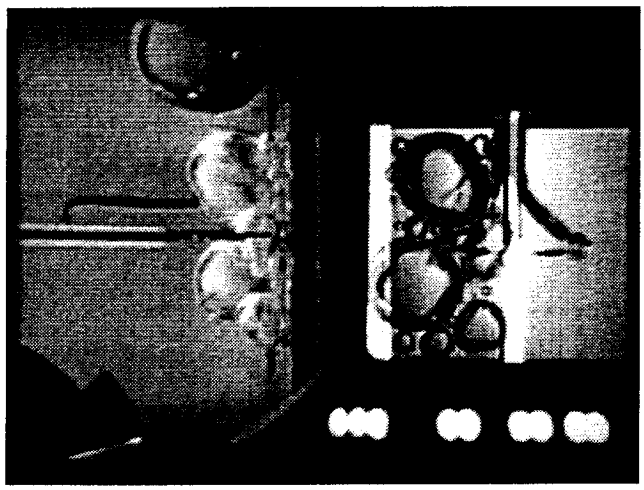

Frame #2370 time= 75.42 sec.

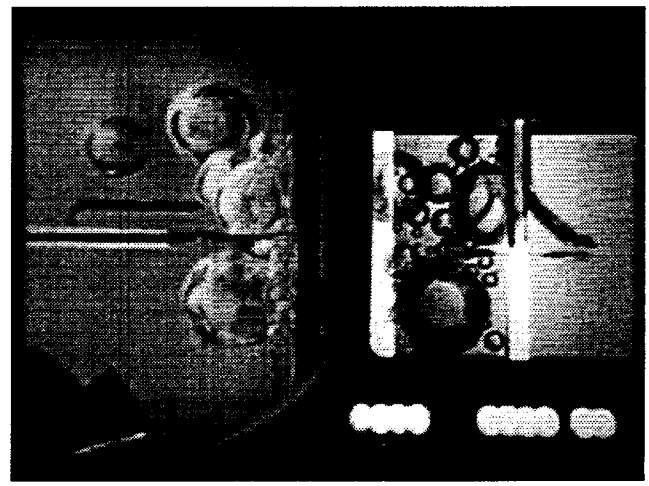

Frame #2490 time=87.40 sec.

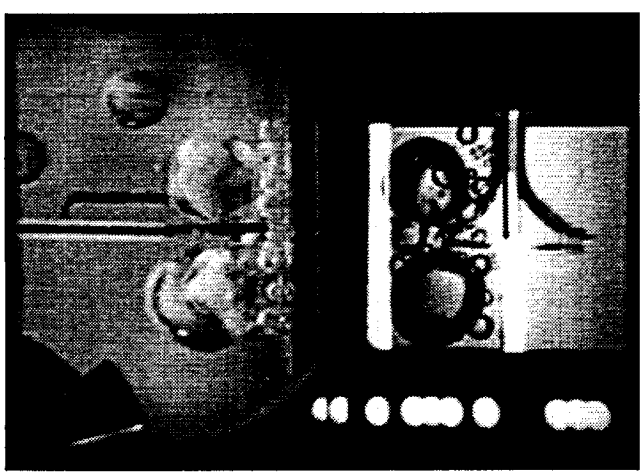

Frame #2610 time= 99.39 sec.

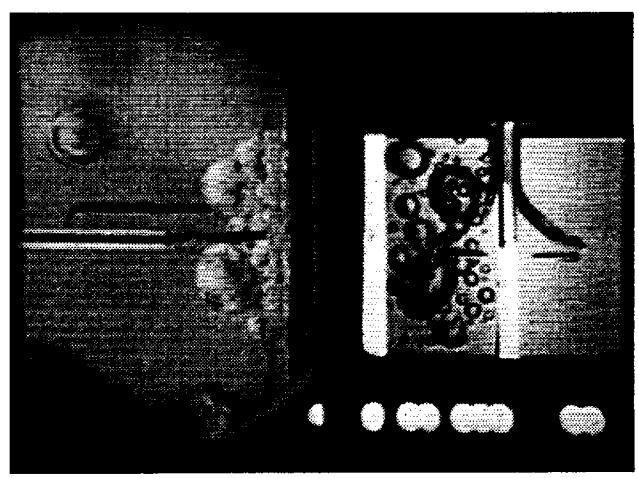

Frame #2725 time= 110.88 sec.

Figure C-6c. Continued.

STS-60 Run #4

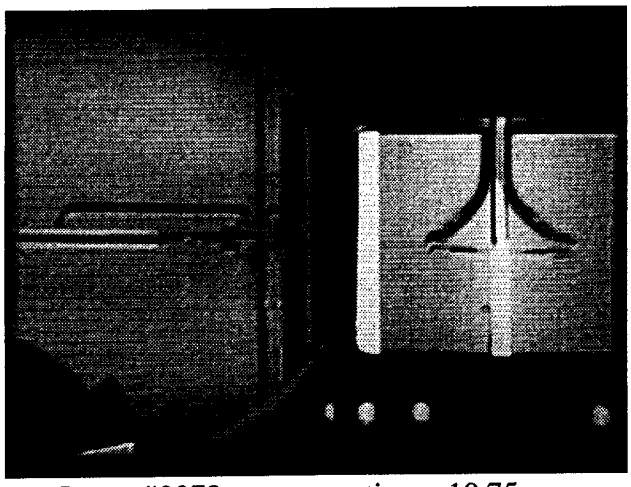

Frame #0072 time= 10.75 sec.

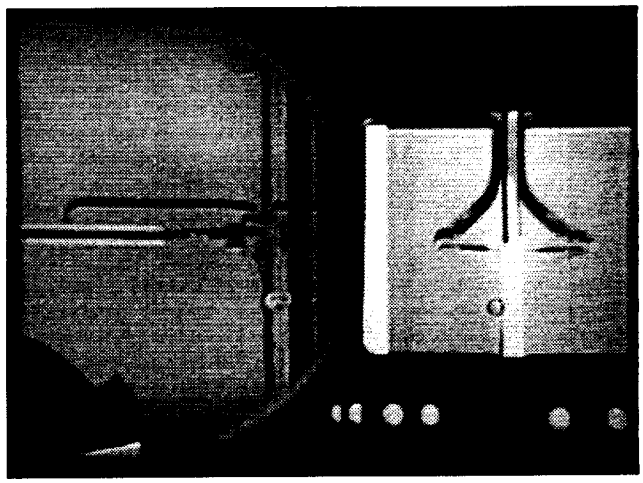

Frame #0085 time= 10.87 sec.

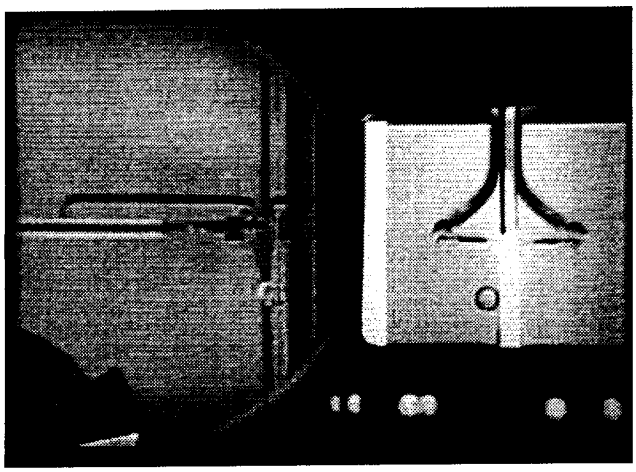

Frame #0098 time= 11.03 sec.

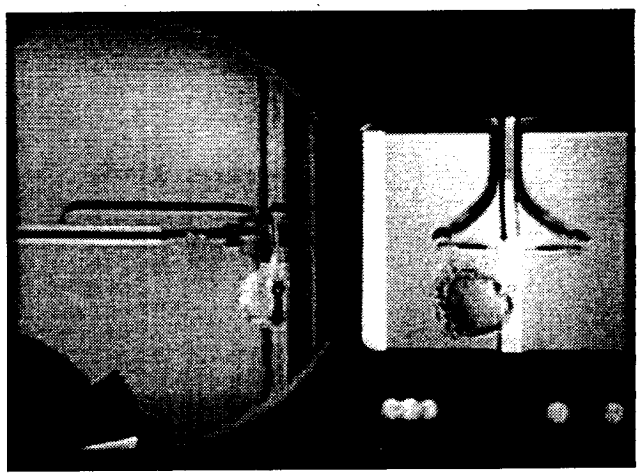

Frame #0111 time= 11.13 sec.

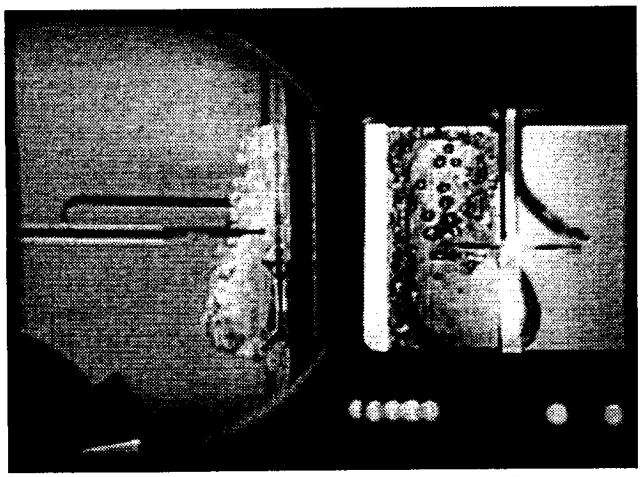

Frame #0124 time= 11.25 sec.

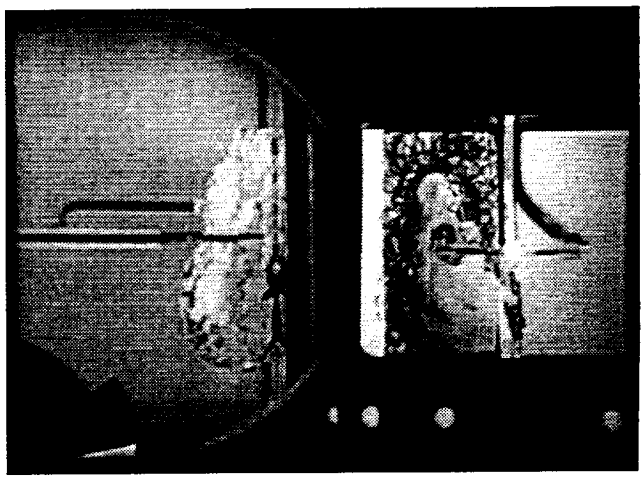

Frame #0137 time= 11.38 sec.

Figure C-6d. Selected Photographic Images. PBE-IC (STS-60). Run No. 4.

STS-60 Run #4

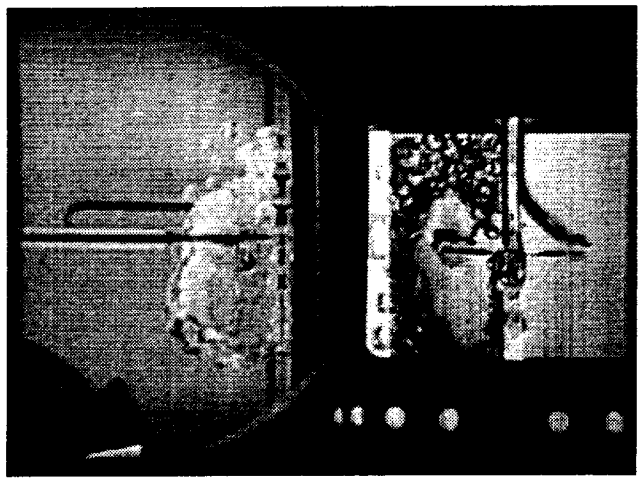

Frame #0150 time= 11.51 sec.

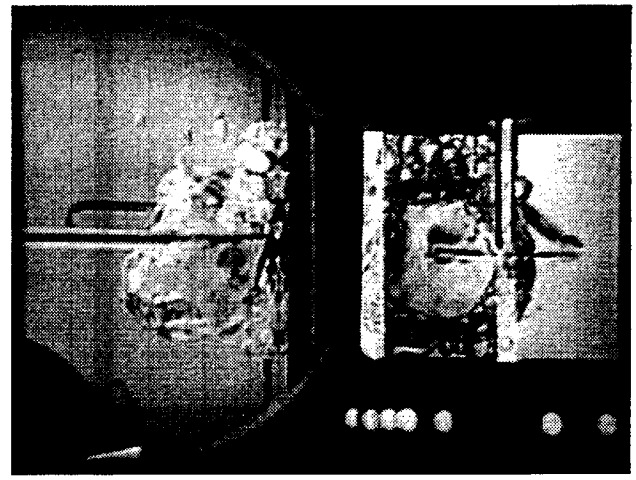

Frame #0188 time= 11.89 sec.

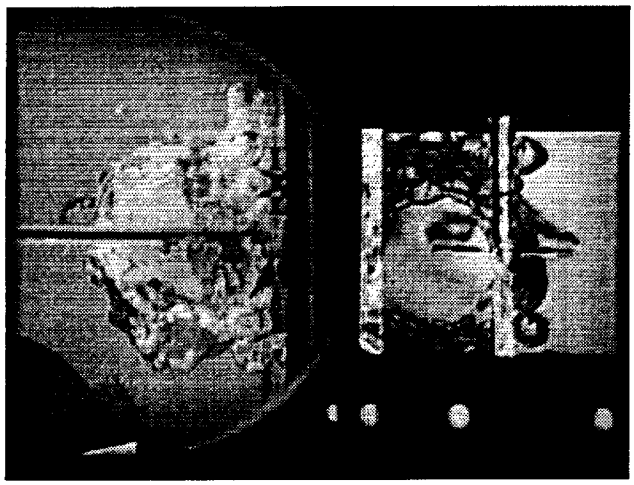

Frame #0265 time= 12.66 sec.

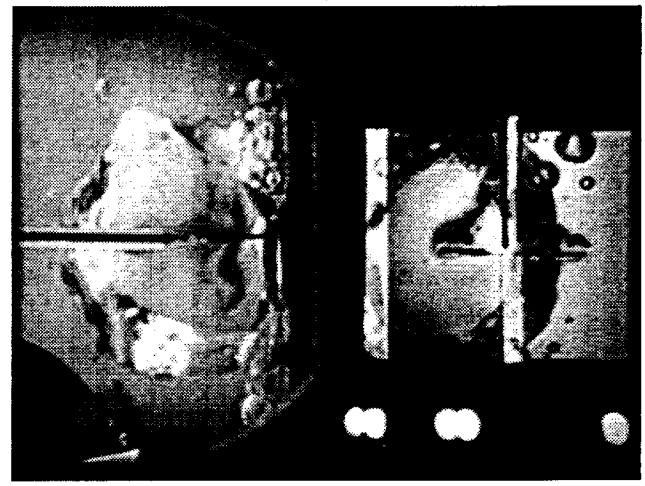

Frame #0325 time= 13.96

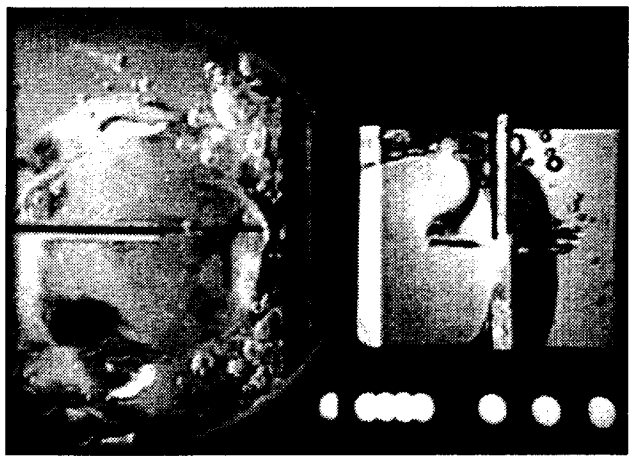

Frame #0400 time= 21.47 sec.

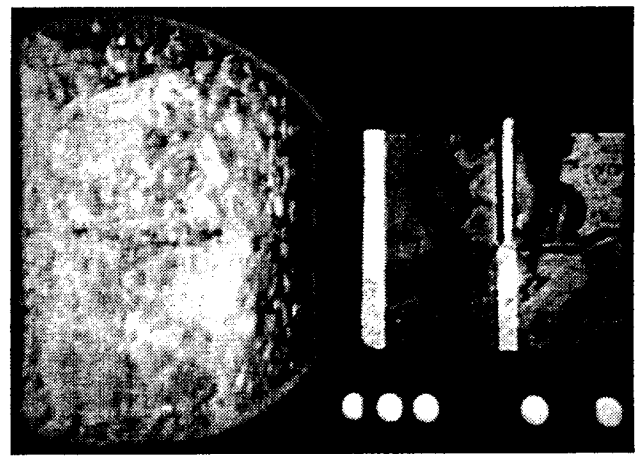

Frame #0703 time= 51.80 sec.

Figure C-6d. Continued.

STS-60 Run #5

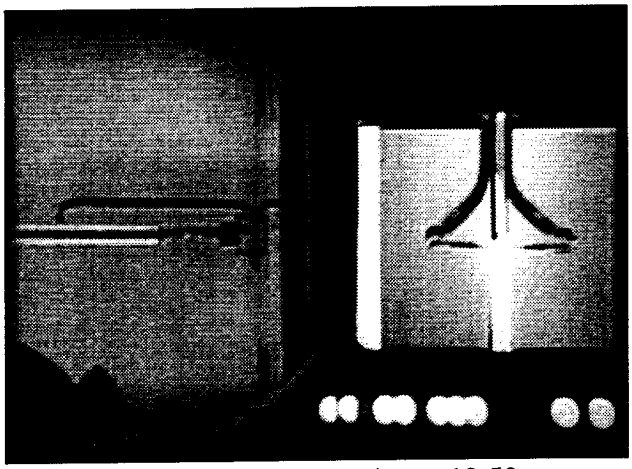

Frame #0095 time= 19.50 sec.

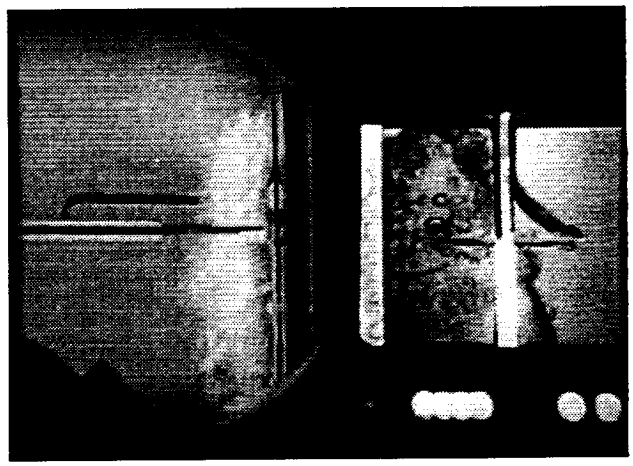

Frame #0096 time= 19.60 sec.

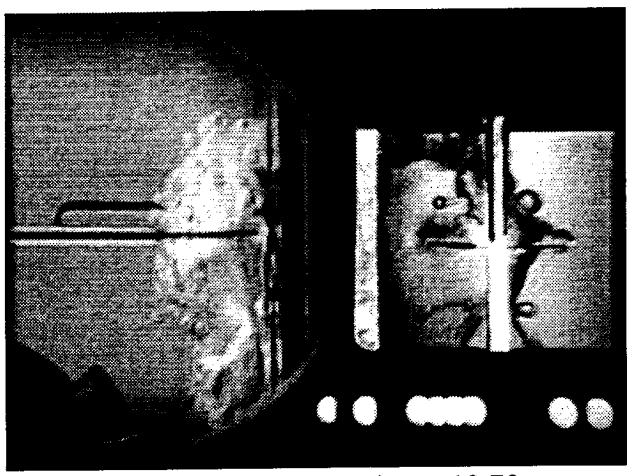

Frame #0097 time= 19.70 sec.

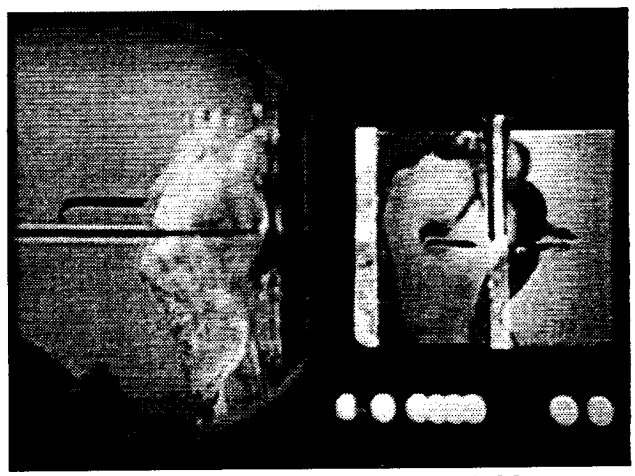

Frame #0098 time= 19.80 sec.

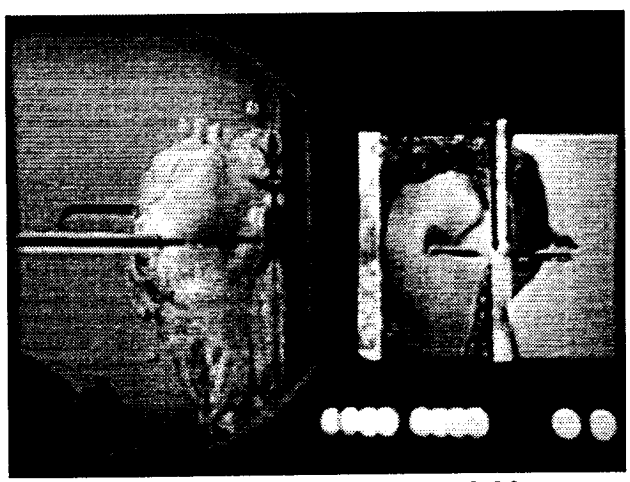

Frame #0099 time= 19.90 sec.

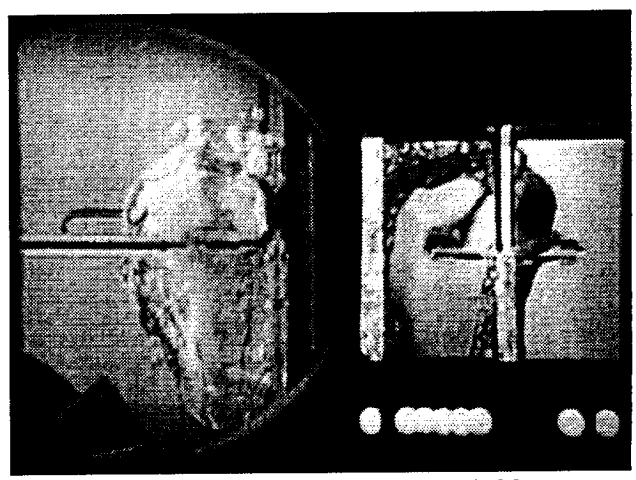

Frame #0100 time= 20.00 sec.

Figure C-6e. Selected Photographic Images. PBE-IC (STS-60). Run No. 5.

STS-60 Run #5

Frame #1095 time= 30.01 sec.

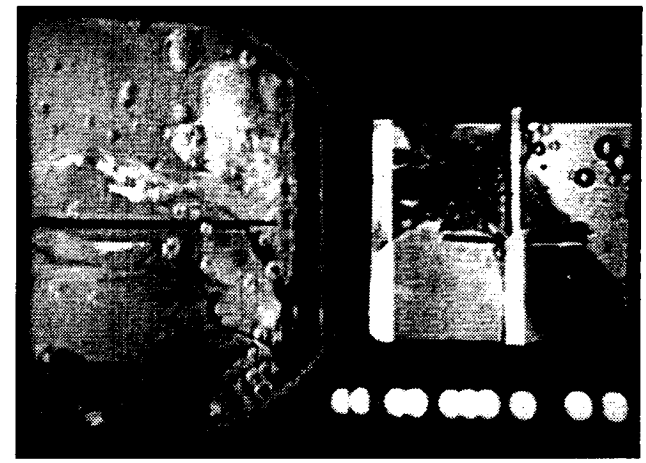

Frame #1210 time=39.98 sec.

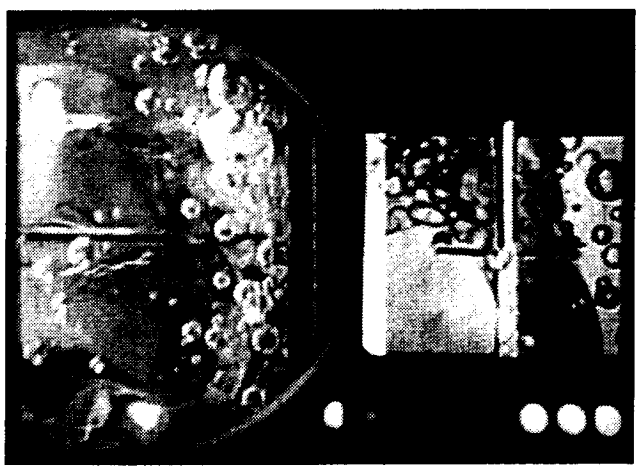

Frame #1320 time= 50.98 sec

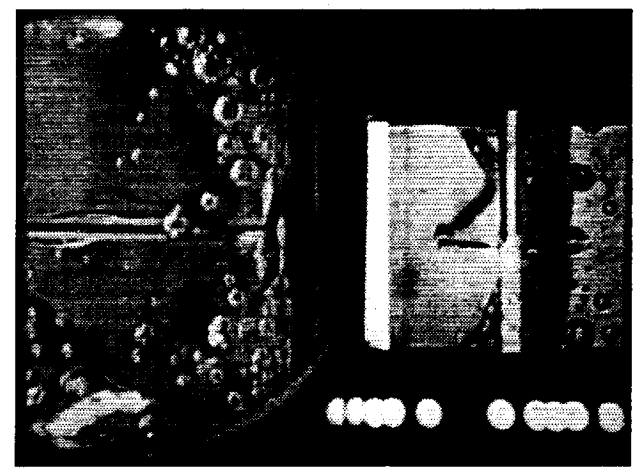

Frame #1430 time= 62.15 sec.

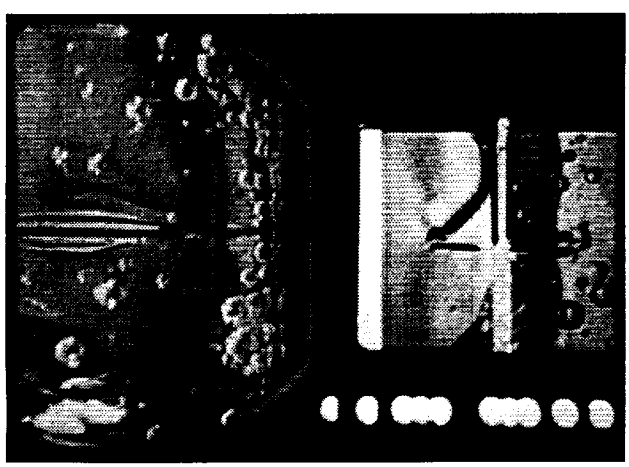

Frame #1650 time= 84.02 sec.

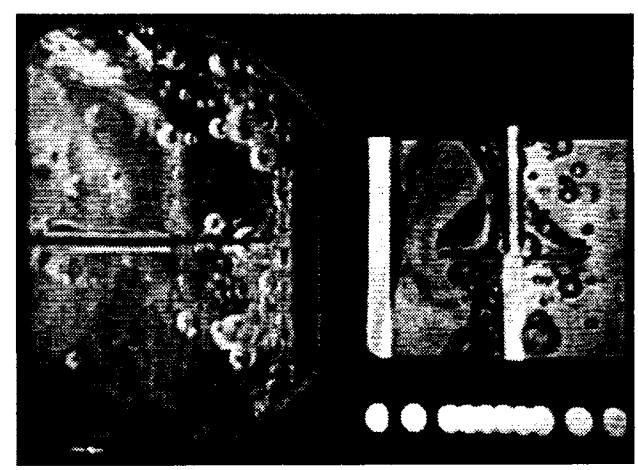

Frame #1720 time= 91.04 sec.

Figure C-6e. Continued.

STS-60 Run #6

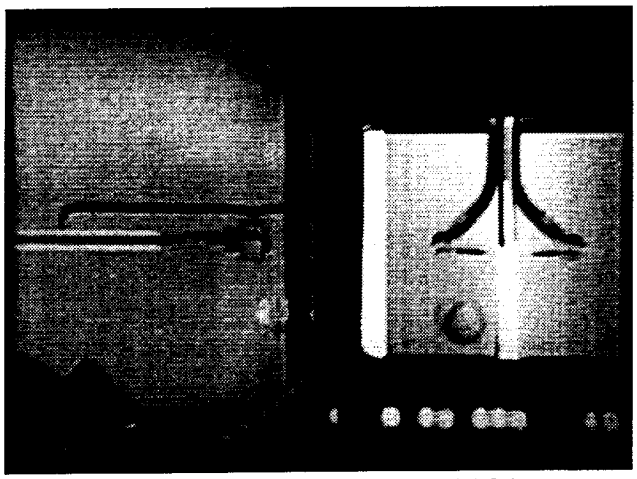

Frame #1888 time= 47.94 sec.

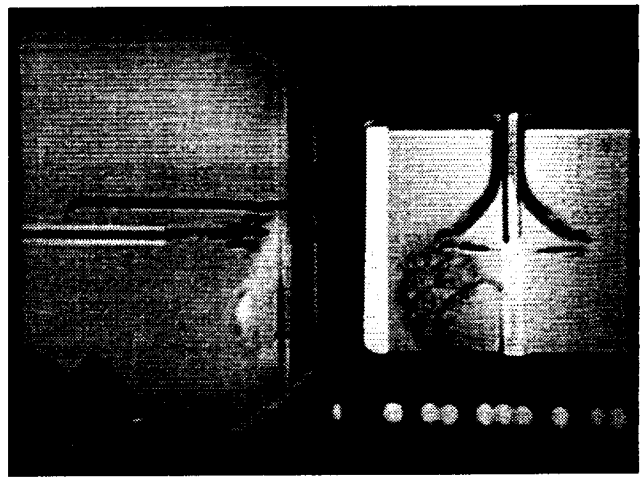

Frame #1889 time= 47.95 sec.

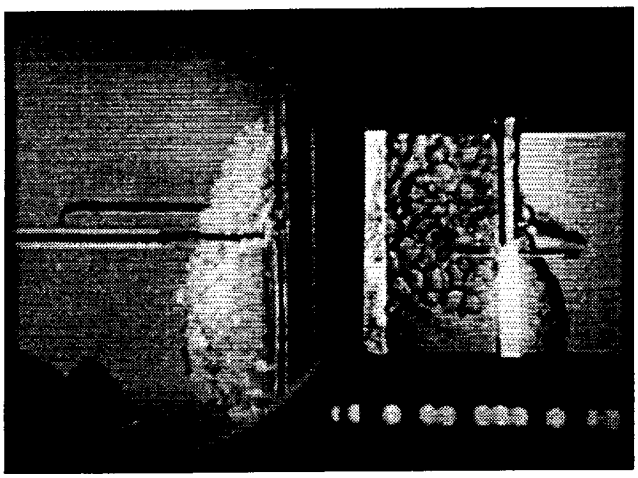

Frame #1893 time= 47.99 sec.

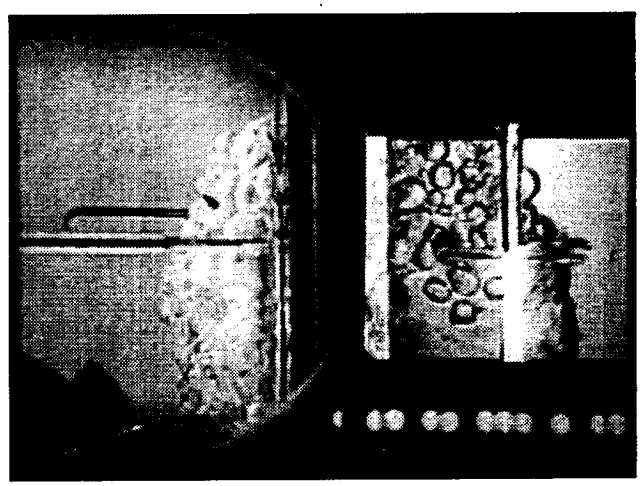

Frame #1897 time= 48.03 sec.

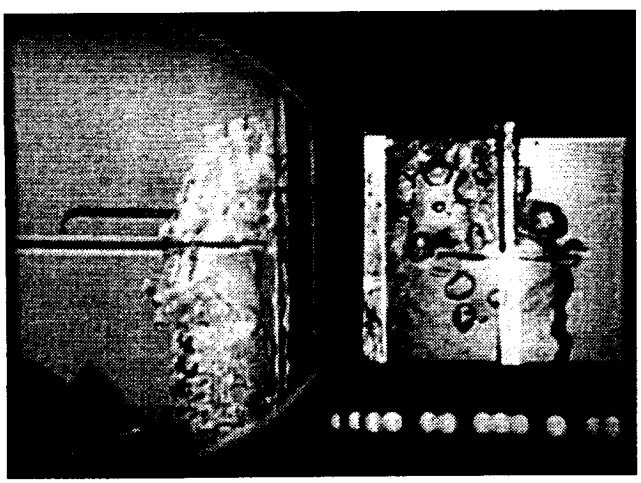

Frame #1901 time= 48.07 sec.

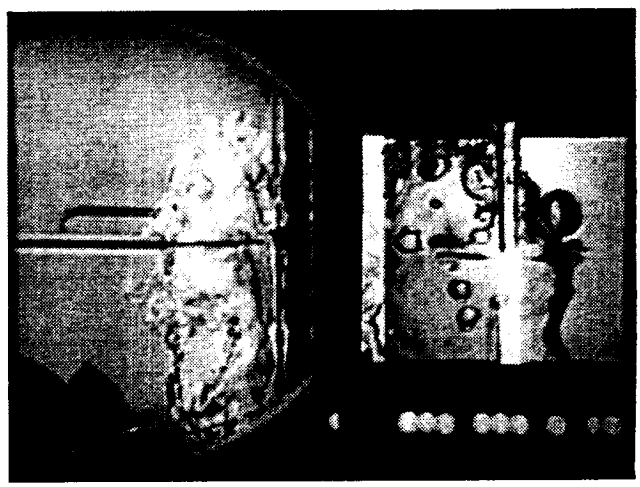

Frame #1905 time=48.11 sec.

Figure C-6f. Selected Photographic Images. PBE-IC (STS-60). Run No. 6.

STS-60 Run #6

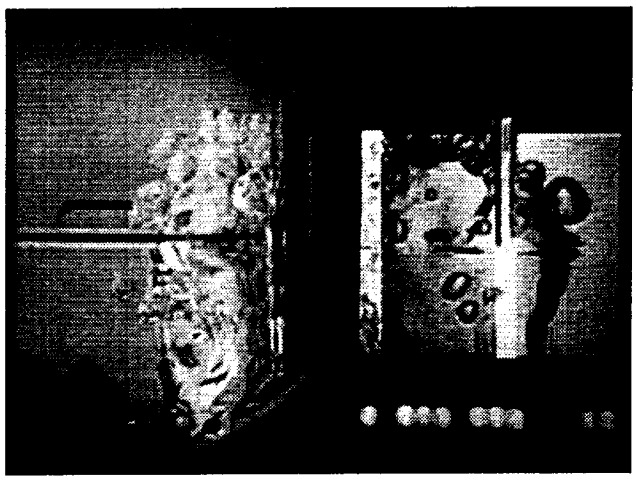

Frame #1910 time= 48.16 sec.

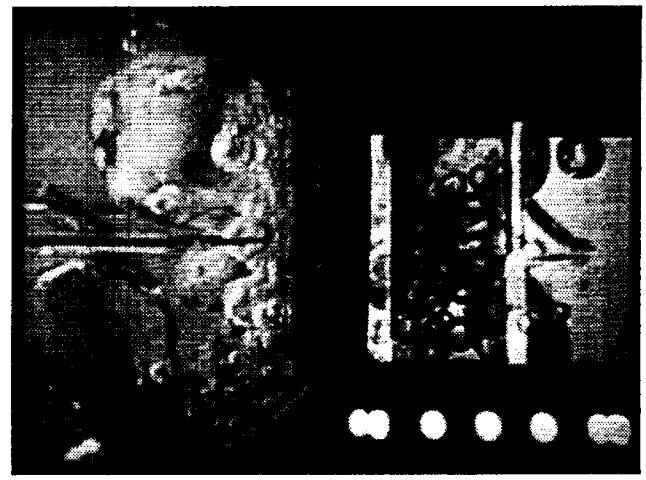

Frame #2180 time= 56.84 sec.

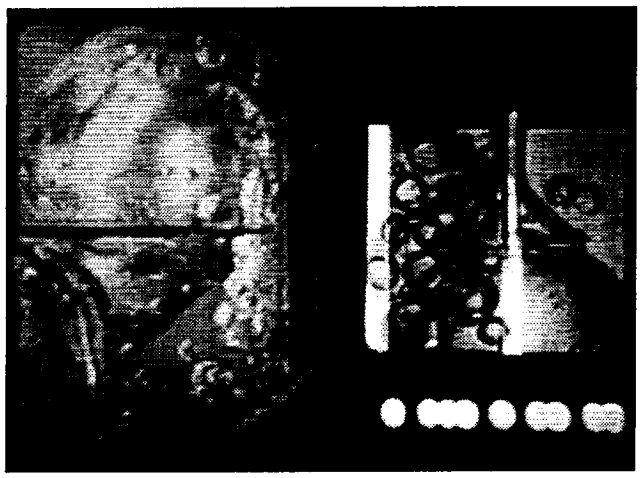

Frame #2270 time= 66.01 sec

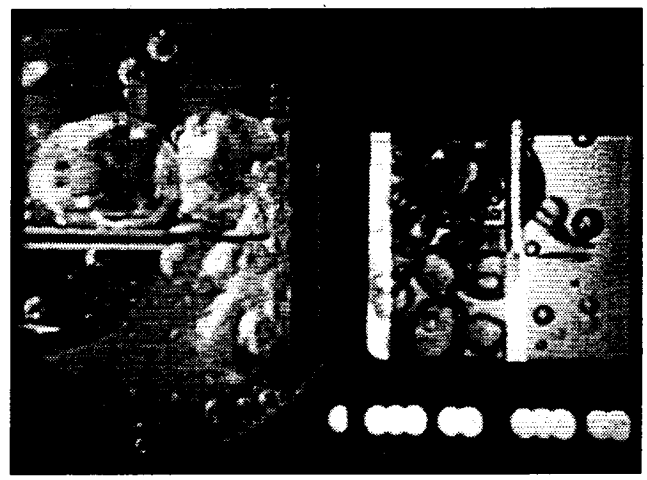

Frame #2370 time= 75.87 sec.

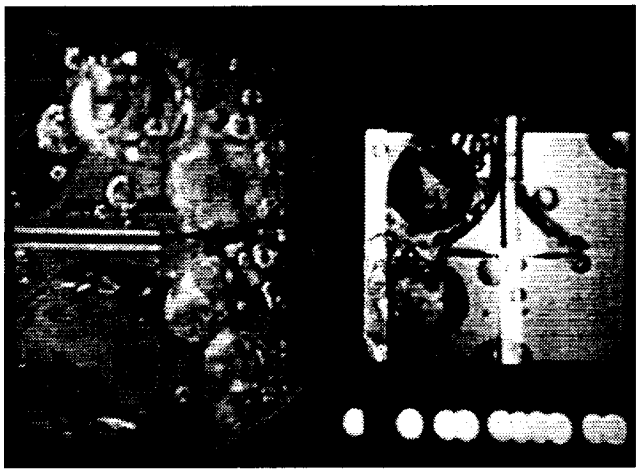

Frame #2470 time= 85.89 sec.

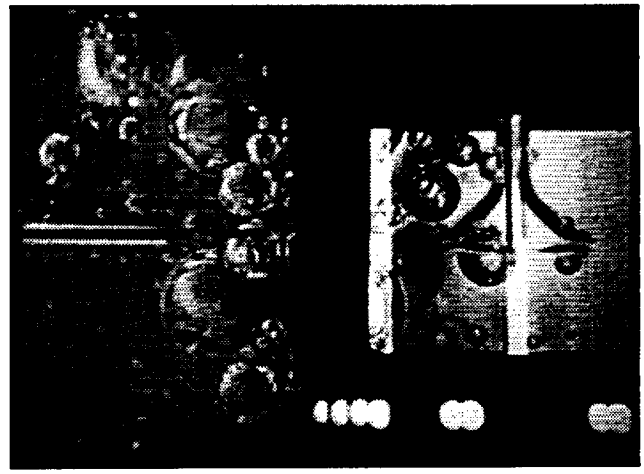

Frame #2570 time= 96.22 sec.

Figure C-6f. Continued.

STS-60 Run #7

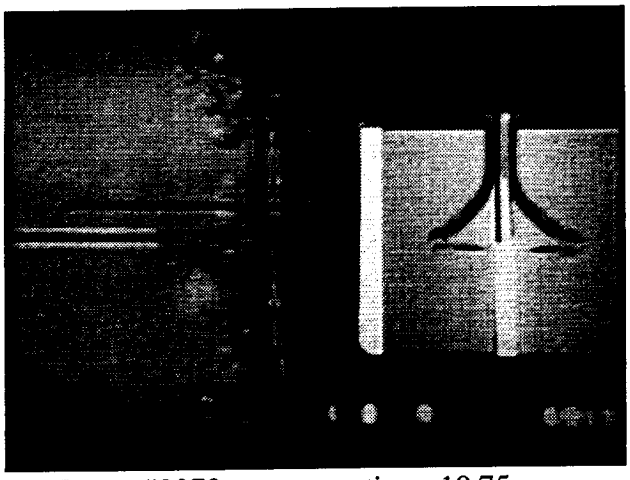

Frame #0070 time=10.75 sec.

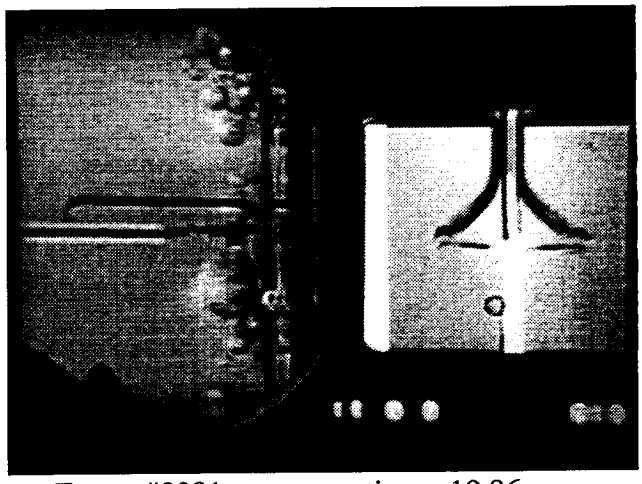

Frame #0081 time= 10.86 sec.

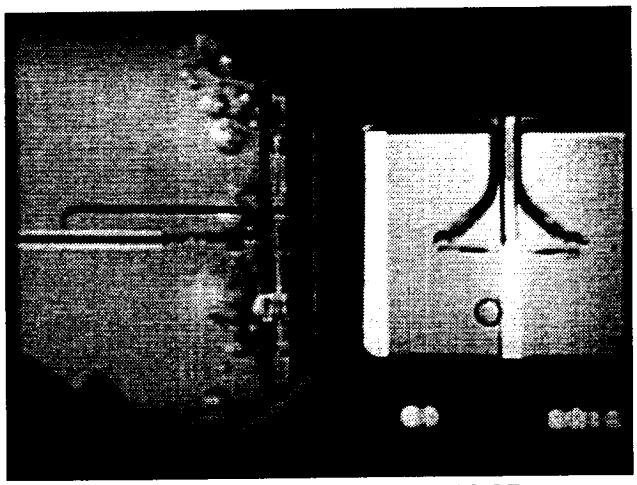

Frame #0092 time= 10.97 sec.

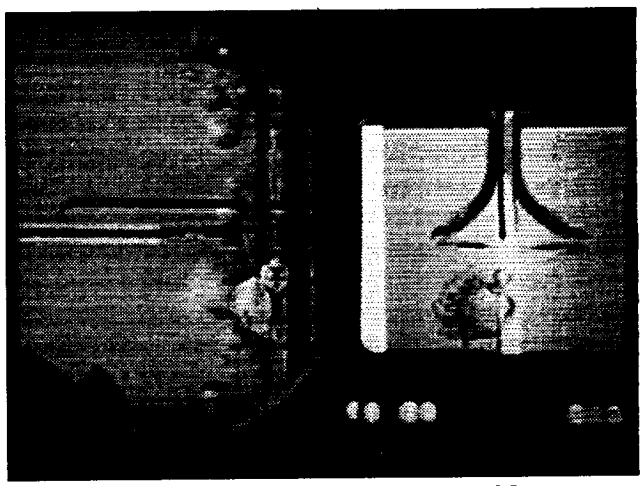

Frame #0103 time= 11.08 sec.

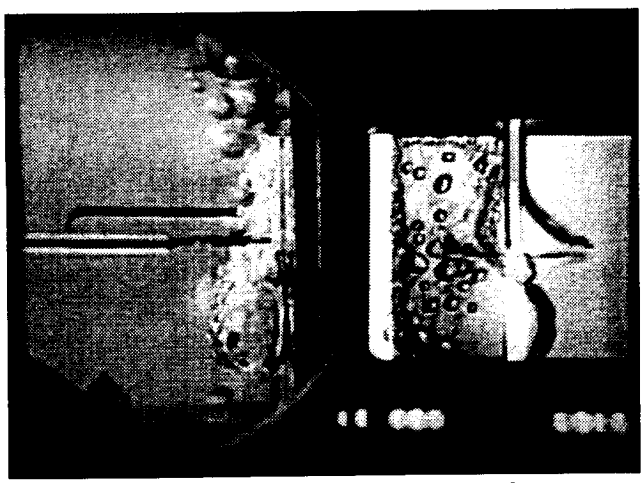

Frame #0114 time= 11.19 sec.

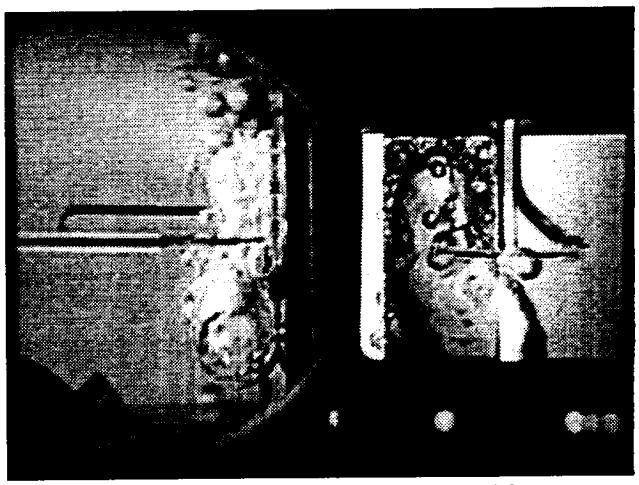

Frame #0125 time= 11.30 sec.

Figure C-6g. Selected Photographic Images. PBE-IC (STS-60). Run No. 7.

STS-60 Run #7

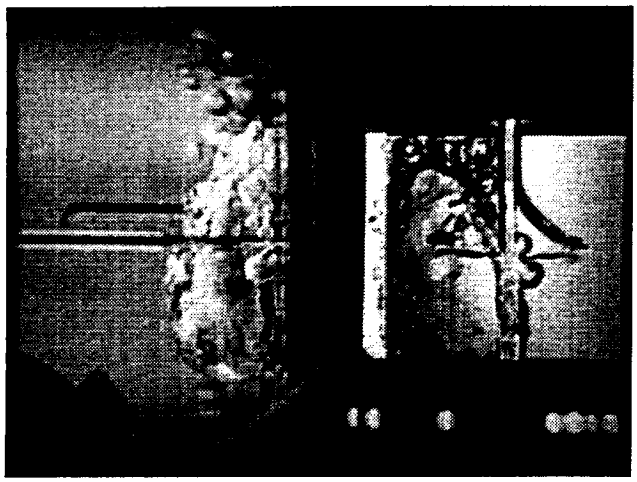

Frame #0136 time= 11.41 sec.

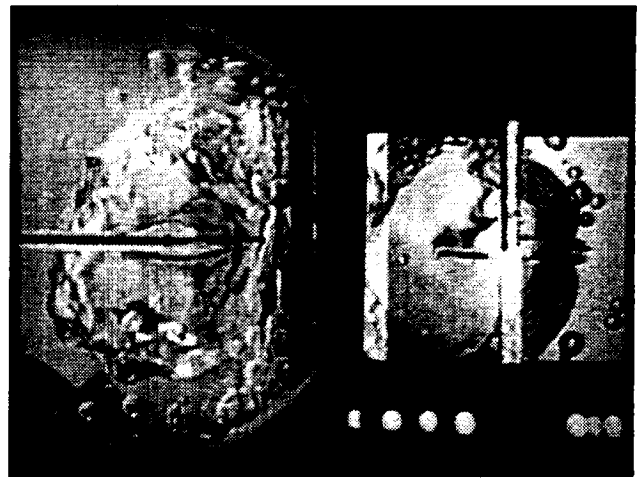

Frame #0336 time= 13.40 sec.

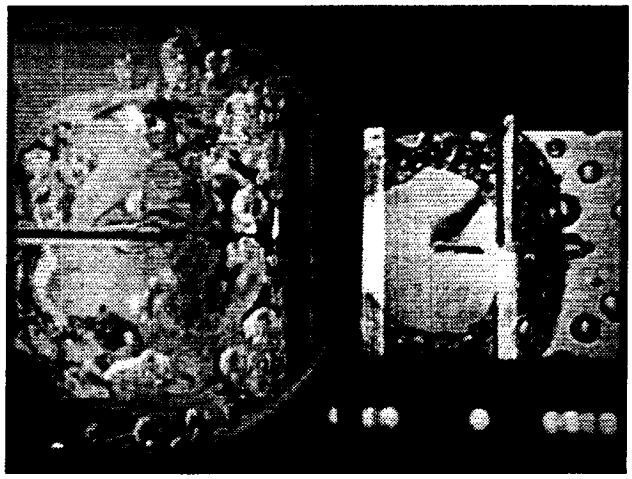

Frame #0536 time= 15.39 sec.

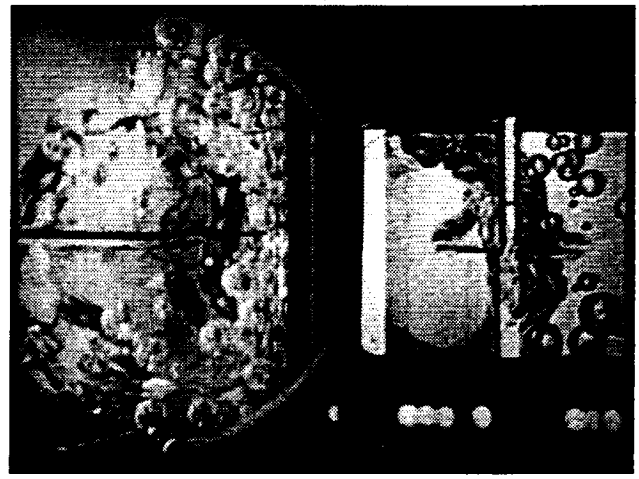

Frame #0736 time= 17.38 sec.

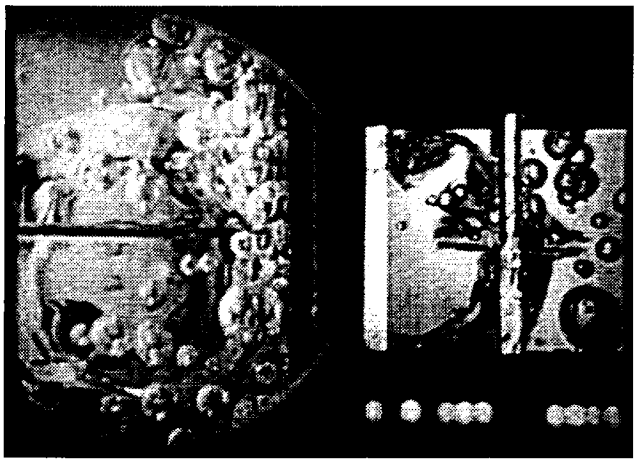

Frame #0936 time= 19.37 sec.

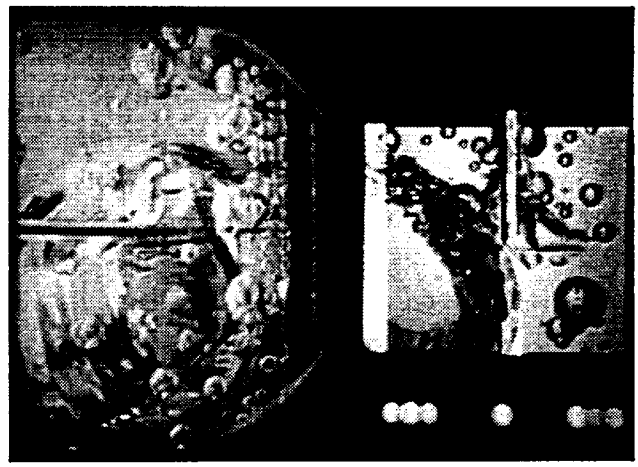

Frame #1136 time= 21.36 sec.

Figure C-6g. Continued.

STS-60 Run #7

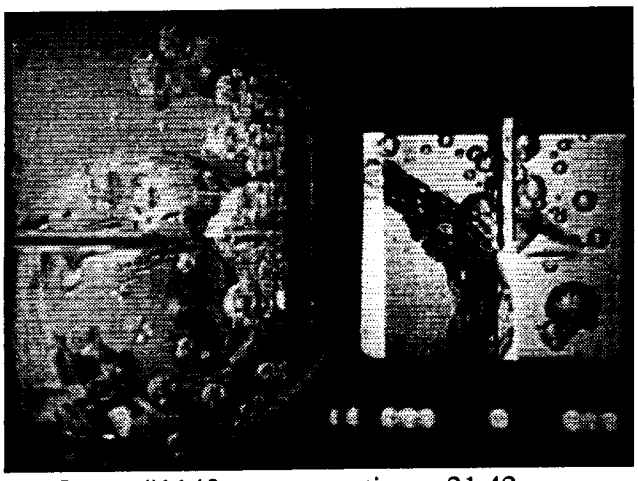

Frame #1143 time= 21.42 sec.

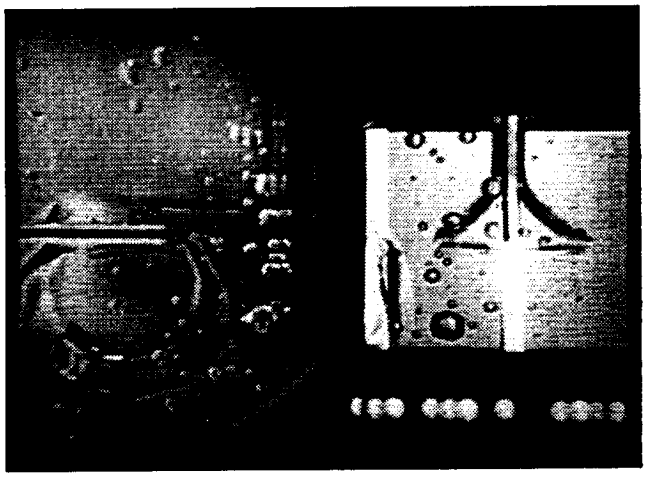

Frame #1504 time= 25.01 sec.

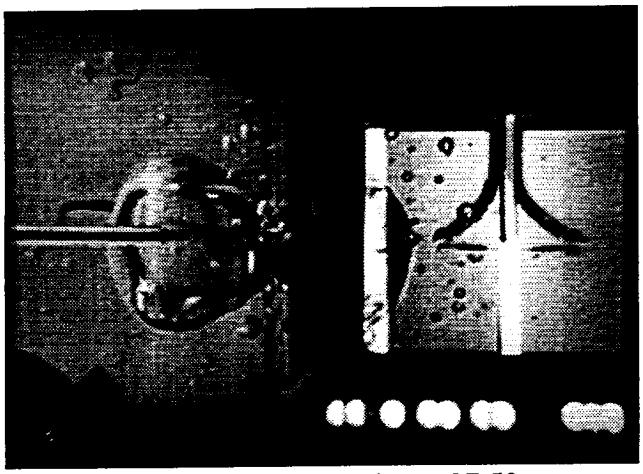

Frame #1544 time= 27.50 sec.

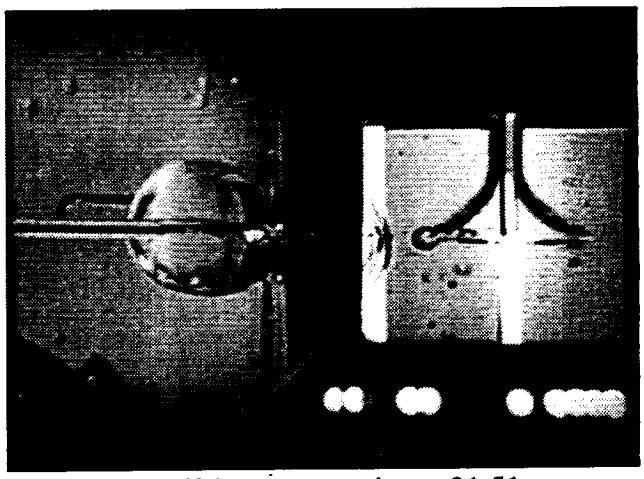

Frame #1584 time= 31.51 sec.

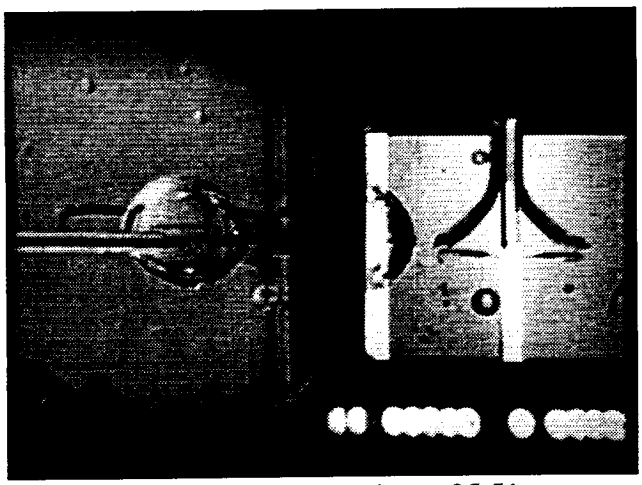

Frame #1624 time= 35.51 sec.

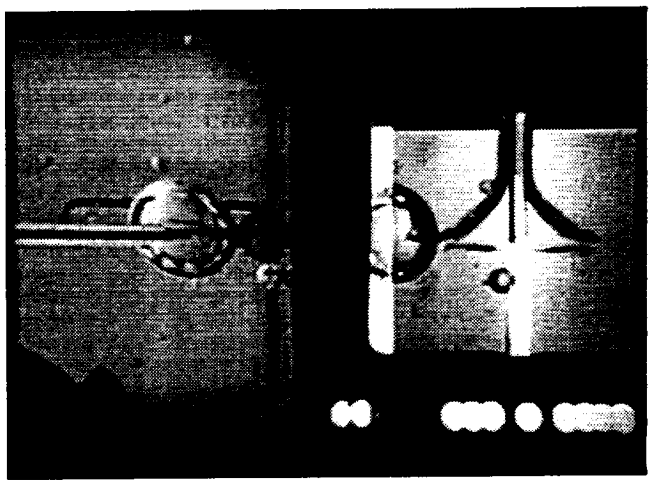

Frame #1664 time= 39.51 sec.

Figure C-6g. Continued.

STS-60 Run #8

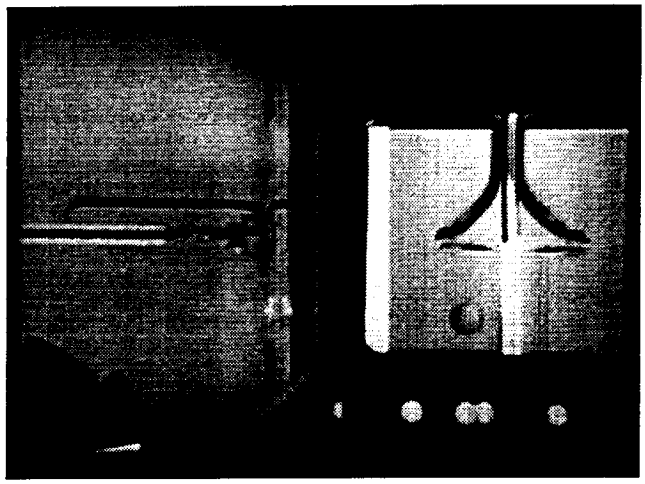

Frame #0342 time= 18.03 sec.

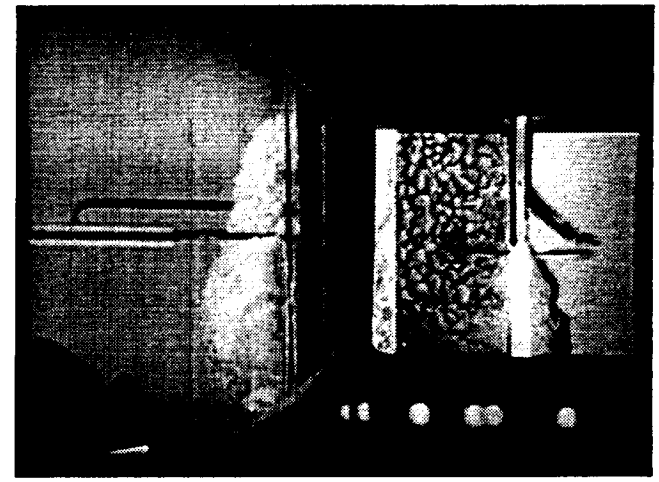

Frame #0346 time= 18.07 sec.

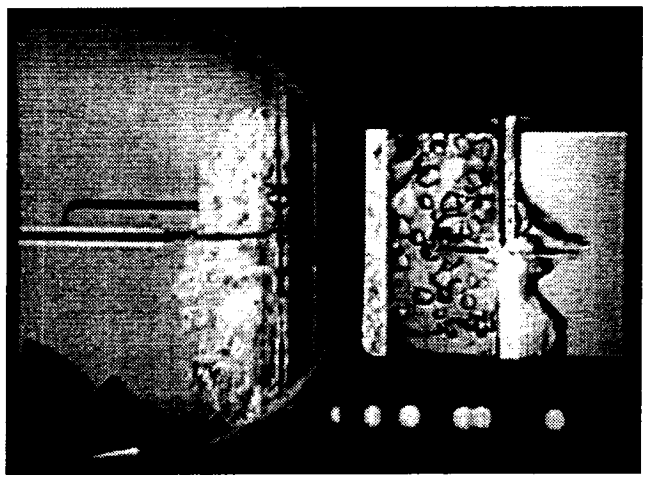

Frame #0350 time= 18.11 sec.

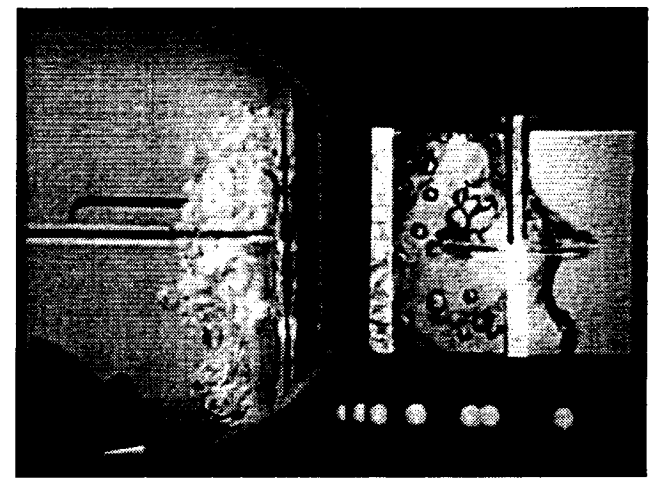

Frame #0354 time= 18.15 sec.

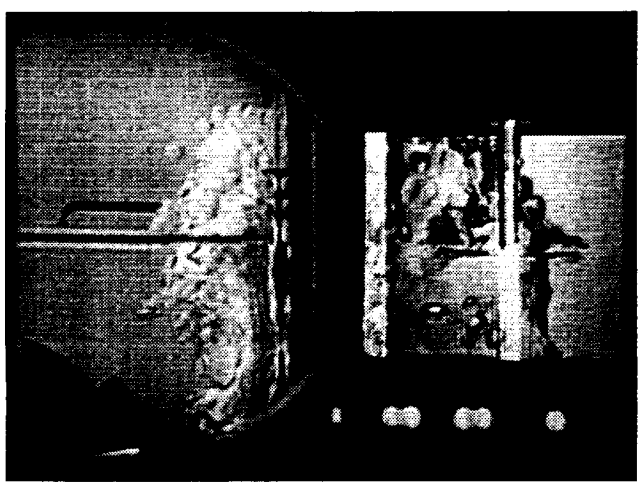

Frame #0358 time= 18.19 sec.

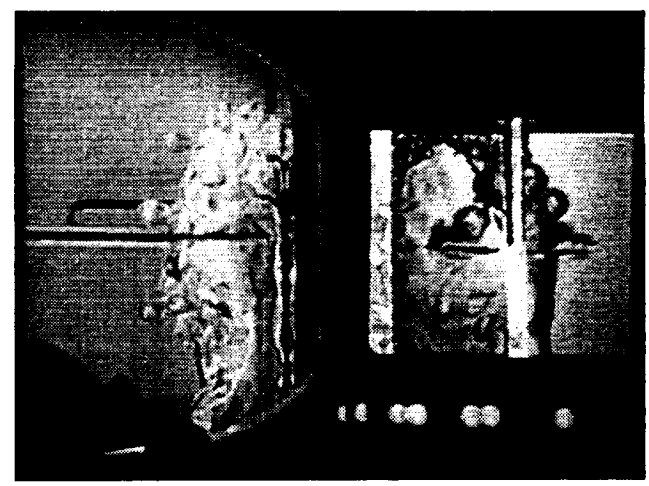

Frame #0362 time= 18.23 sec.

Figure C-6h. Selected Photographic Images. PBE-IC (STS-60). Run No. 8.

STS-60 Run #8

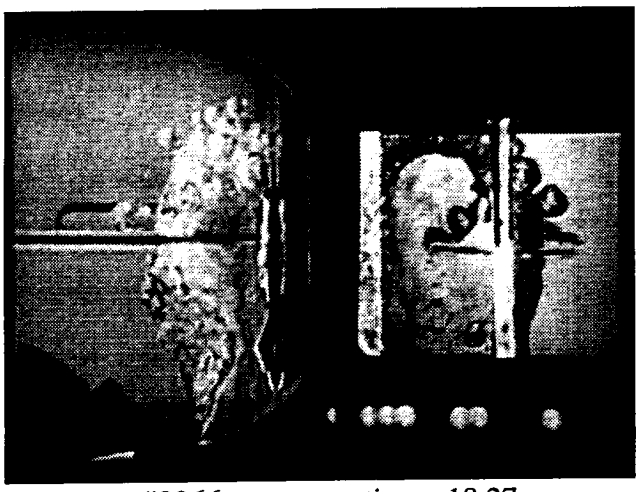

Frame #0366 time= 18.27 sec.

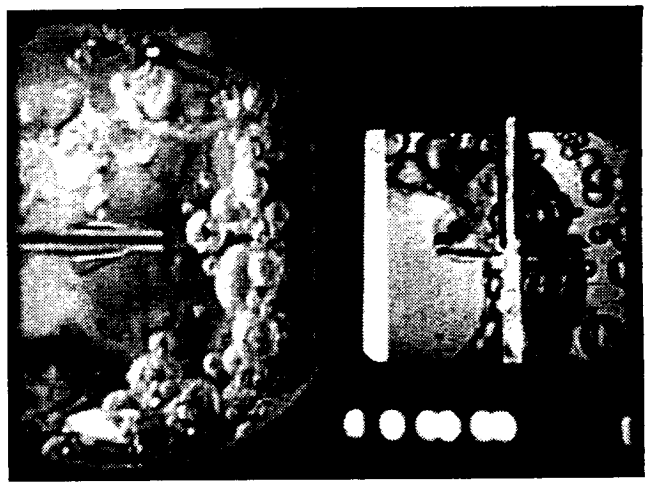

Frame #1080 time=27.48 sec.

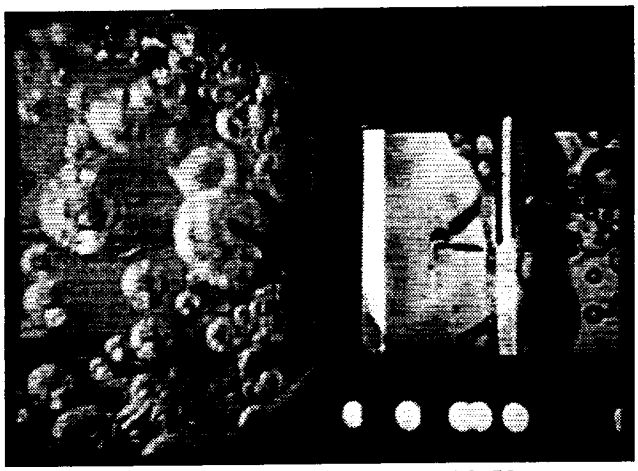

Frame #1190 time= 38.52 sec.

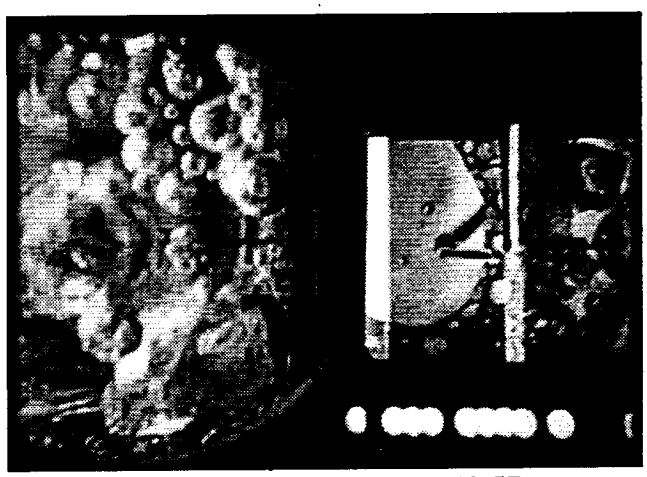

Frame #1300 time= 49.57 sec.

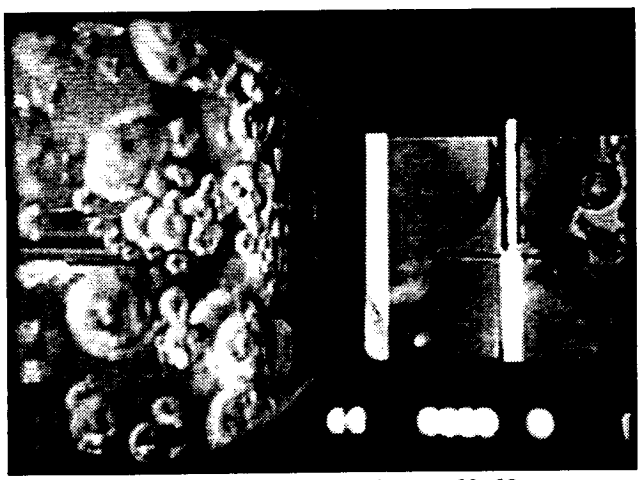

Frame #1410 time= 60.62 sec.

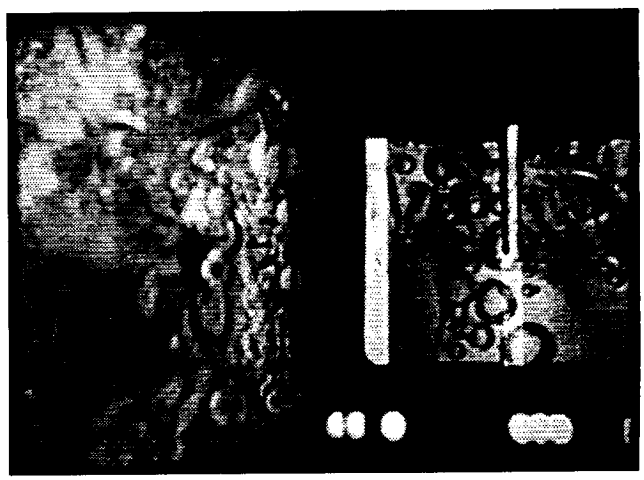

Frame #1520 time= 71.67 sec.

Figure C-6h. Continued.

STS-60 Run #9

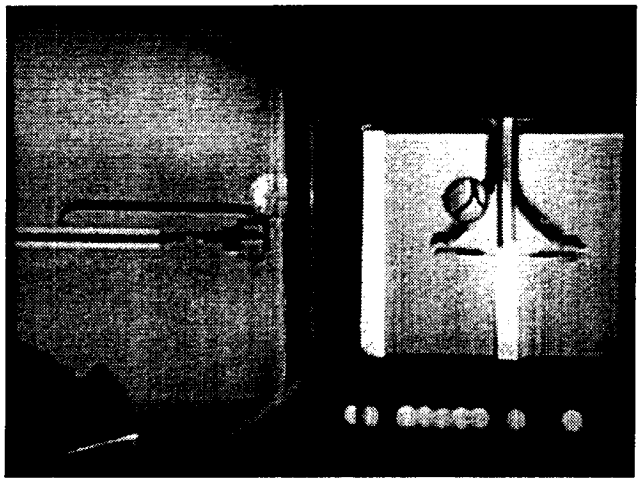

Frame #0341 time= 40.52 sec.

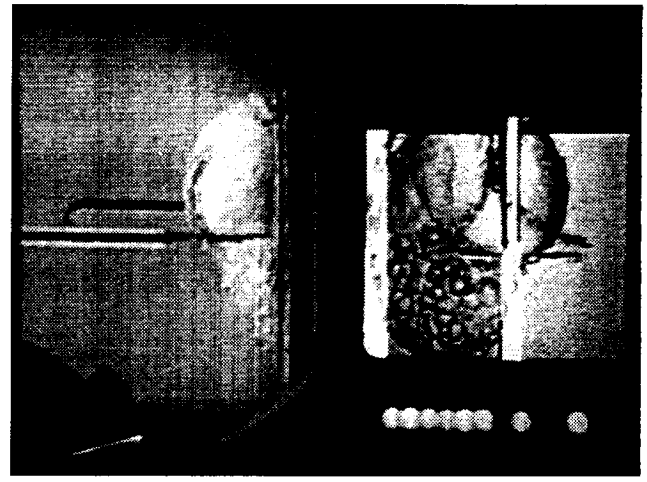

Frame #0345 time= 40.56 sec.

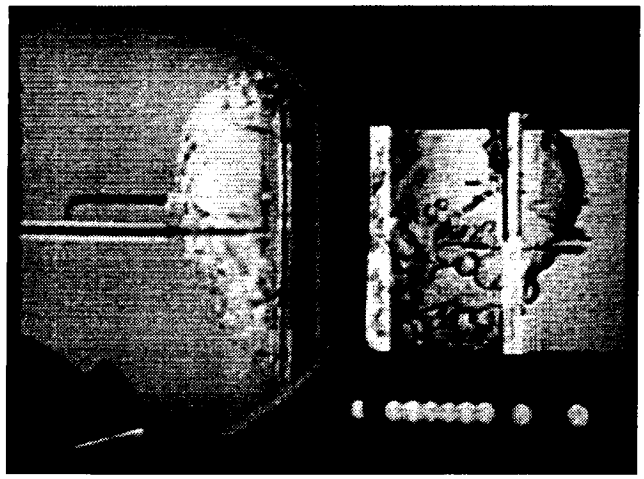

Frame #0349 time= 40.60 sec.

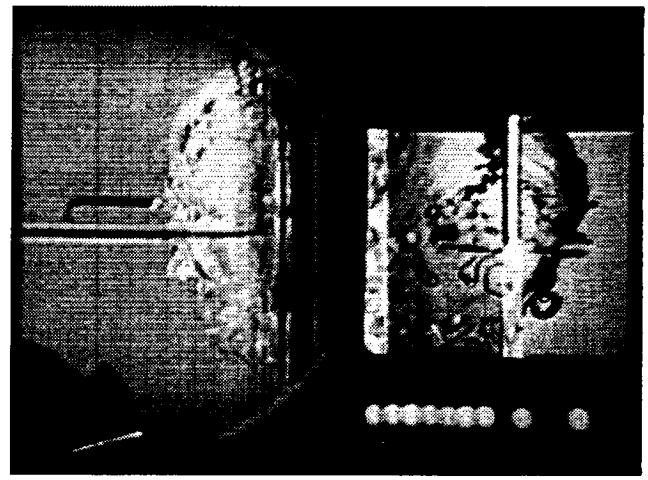

Frame #0353 time= 40.64 sec.

Frame #0357 time= 40.68 sec.

Frame #0361 time= 40.72 sec.

Figure C-6i. Selected Photographic Images. PBE-IC (STS-60). Run No. 9.

STS-60 Run #9

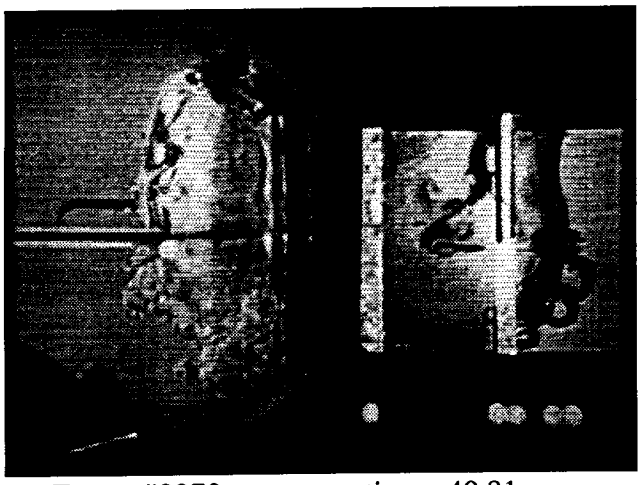

Frame #0370 time= 40.81 sec.

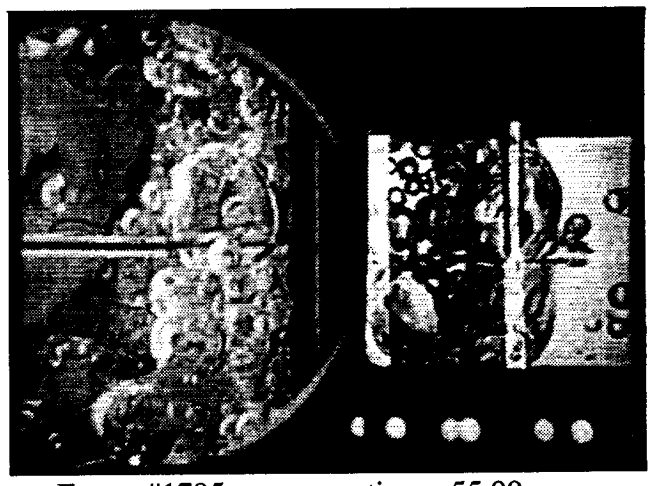

Frame #1795 time= 55.00 sec.

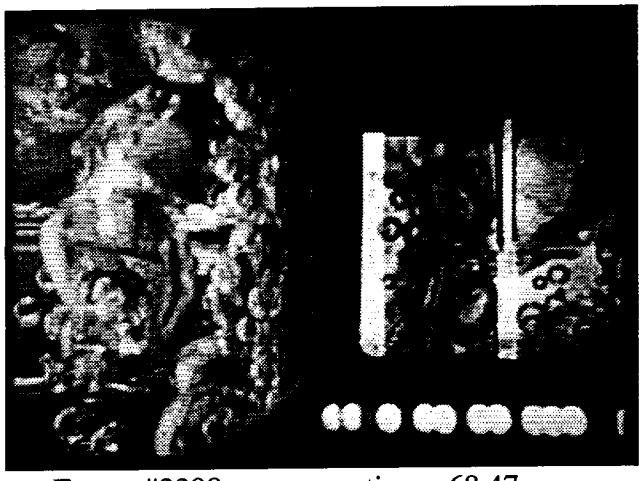

Frame #2398 time= 68.47 sec.

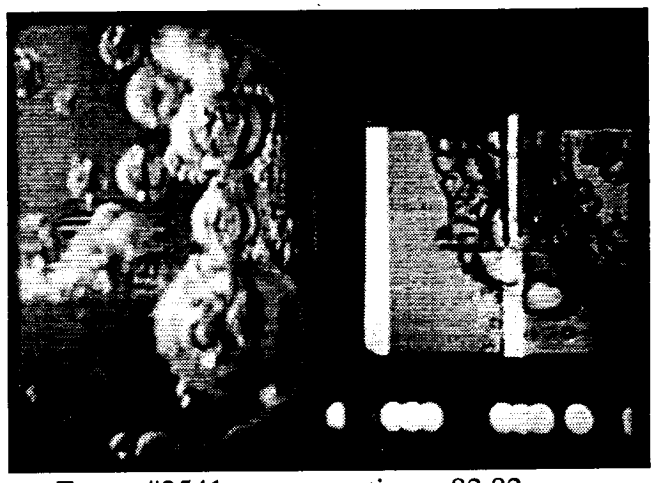

Frame #2541 time= 82.82 sec.

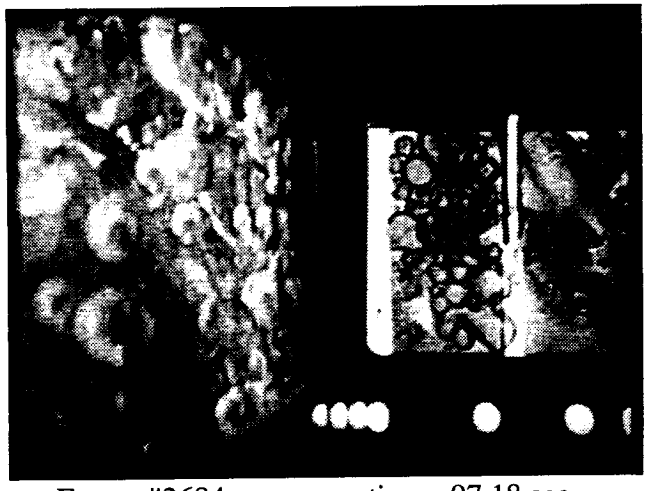

Frame #2684 time= 97.18 sec.

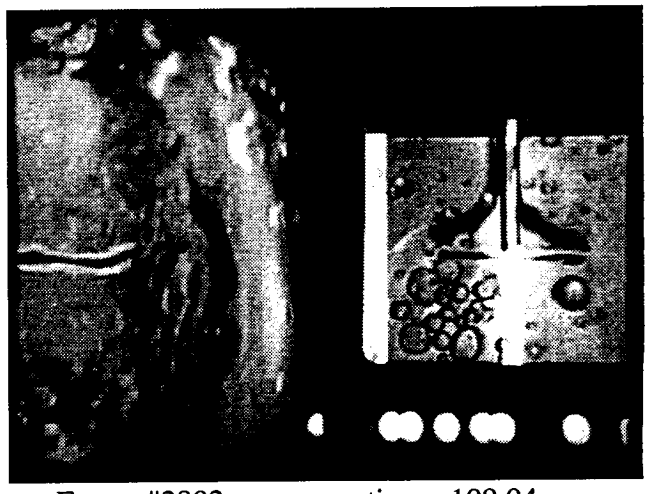

Frame #2802 time= 109.04 sec.

Figure C-6i. Continued.

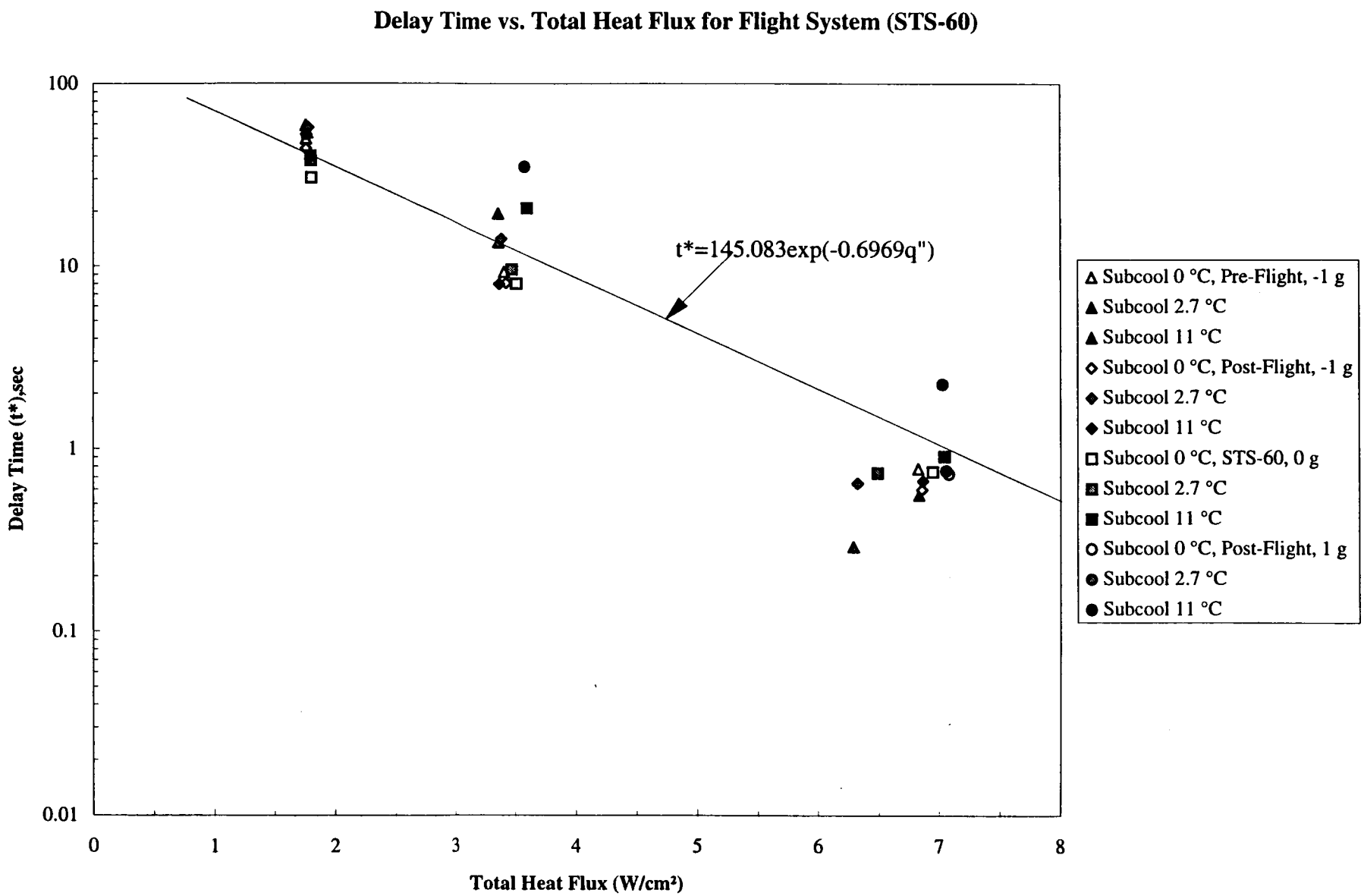

Figure C-7. Nucleation Delay Time. Comparisons with ground testing and drop tower correlation. PBE-IC (STS-60).

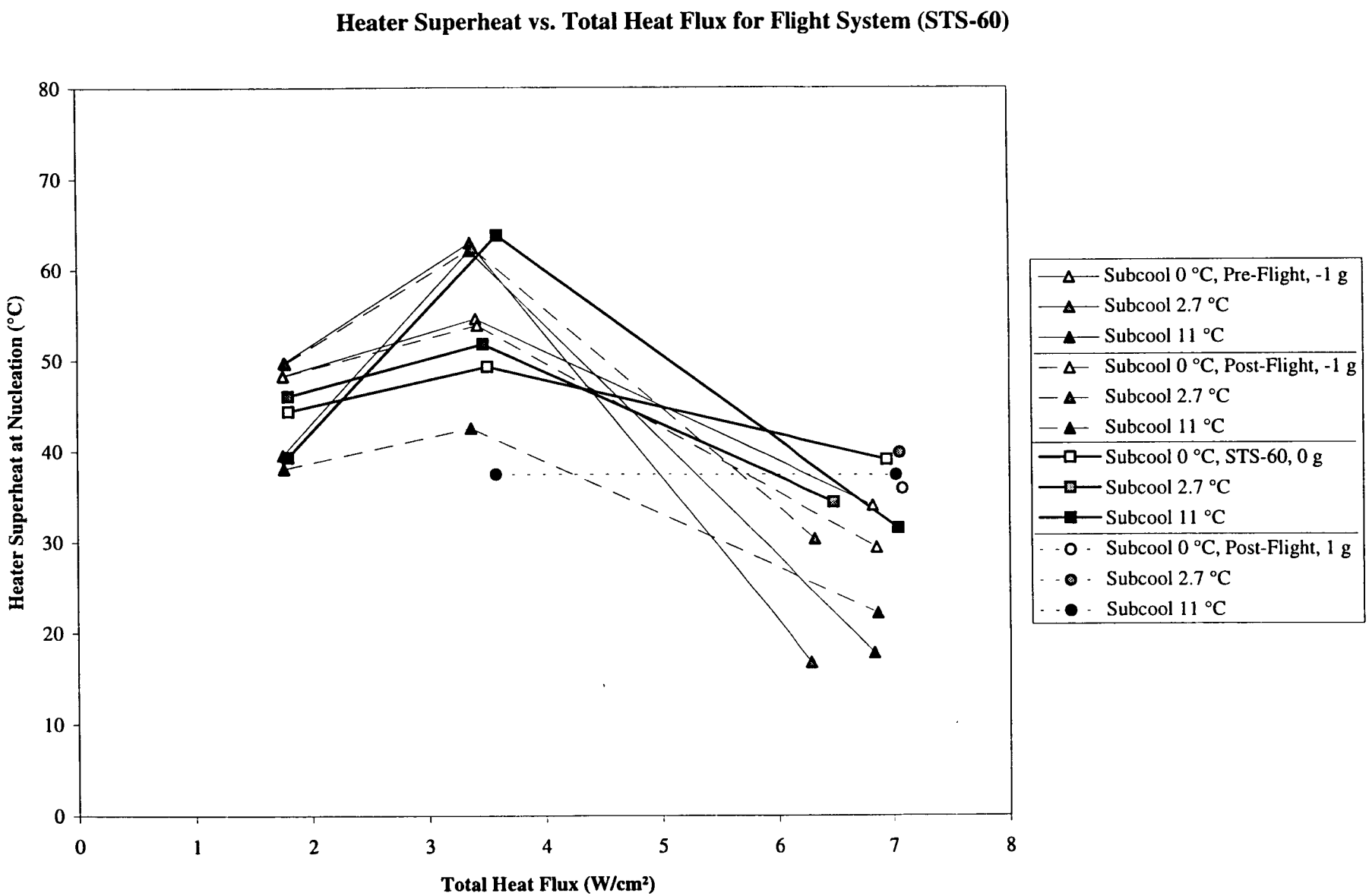

Figure C-8. Mean heater surface nucleation superheat. Comparisons with ground testing. PBE-IC (STS-60).

Comparison of Numerical Computation of Bubble growth with Experiment and Temperature Profile at Nucleation for STS-60 Run #1 (q"=7 W/cm²; T_{sat}=59.84 °C; P=149.9 kPa; ΔT_{sub}=11.5 °C; t*=0.91 sec)

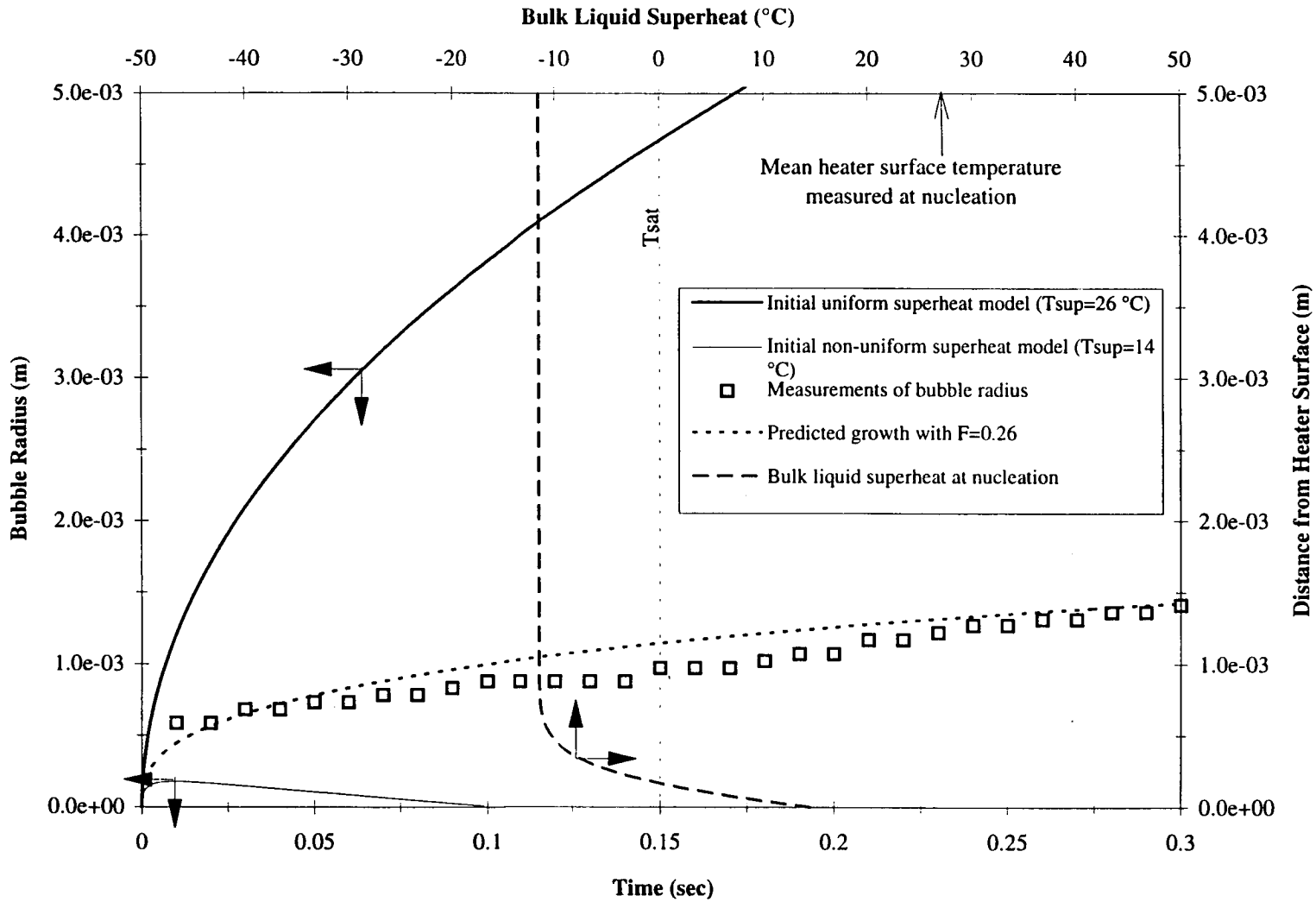

Figure C-9a. Comparisons of bubble growth measurements with several models. PBE-IC (STS-60). Run No. 1.

Comparison of Numerical Computation of Bubble growth with Experiment and Temperature Profile at Nucleation for STS-60 Run #2 (q"=3.6 W/cm²; T_{sat}=58.9 °C; P=145.88 kPa; ΔT_{sub}=11.5 °C; t*=20.85 sec)

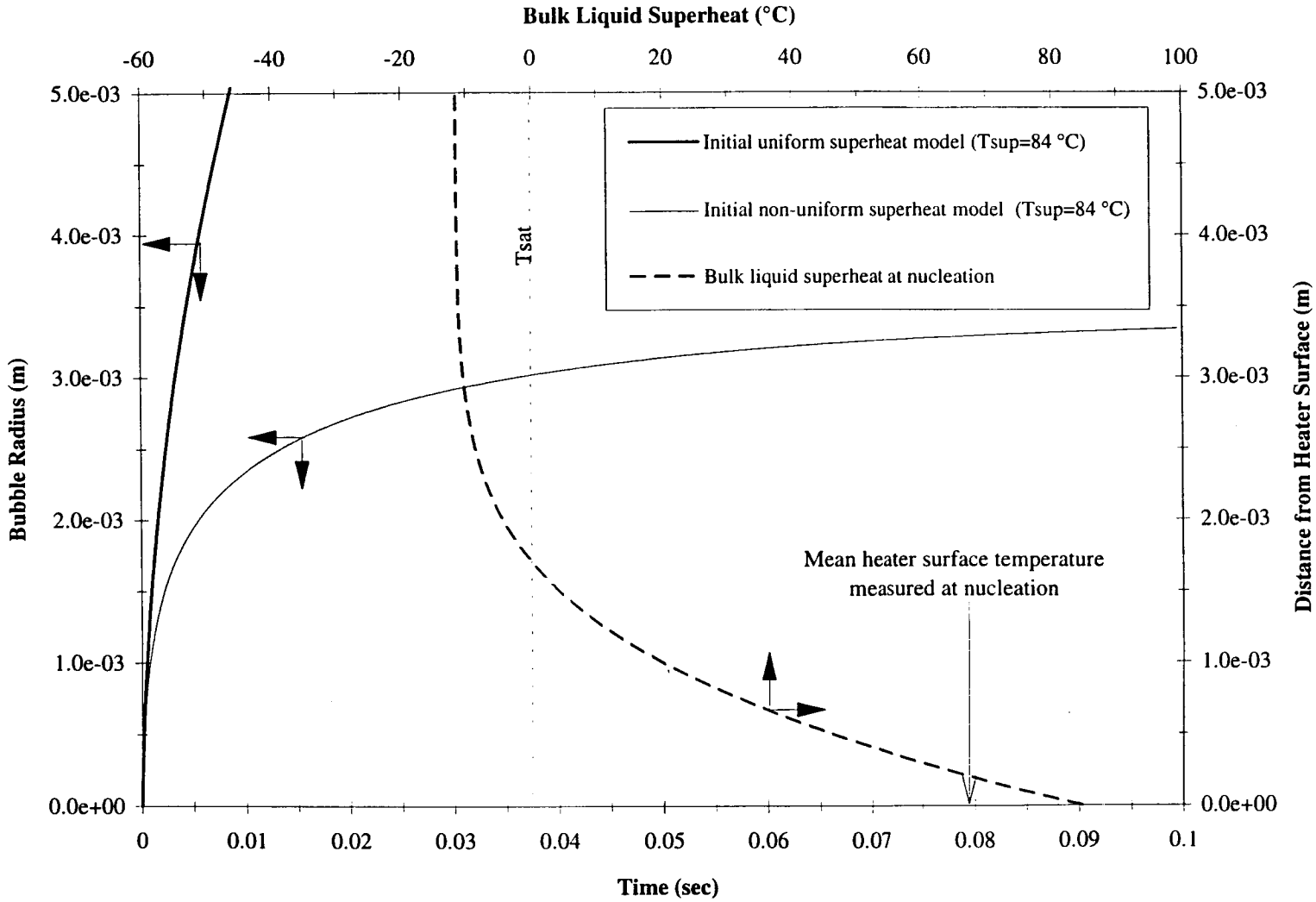

Figure C-9b. Comparisons of bubble growth measurements with several models. PBE-IC (STS-60). Run No. 2.

Comparison of Numerical Computation of Bubble growth with Experiment and Temperature Profile at Nucleation for STS-60 Run #3 (q"=1.8 W/cm²; T_{sat}=60.4 °C; P=152.55 kPa; ΔT_{sub}=11.5 °C; t*=40.17 sec)

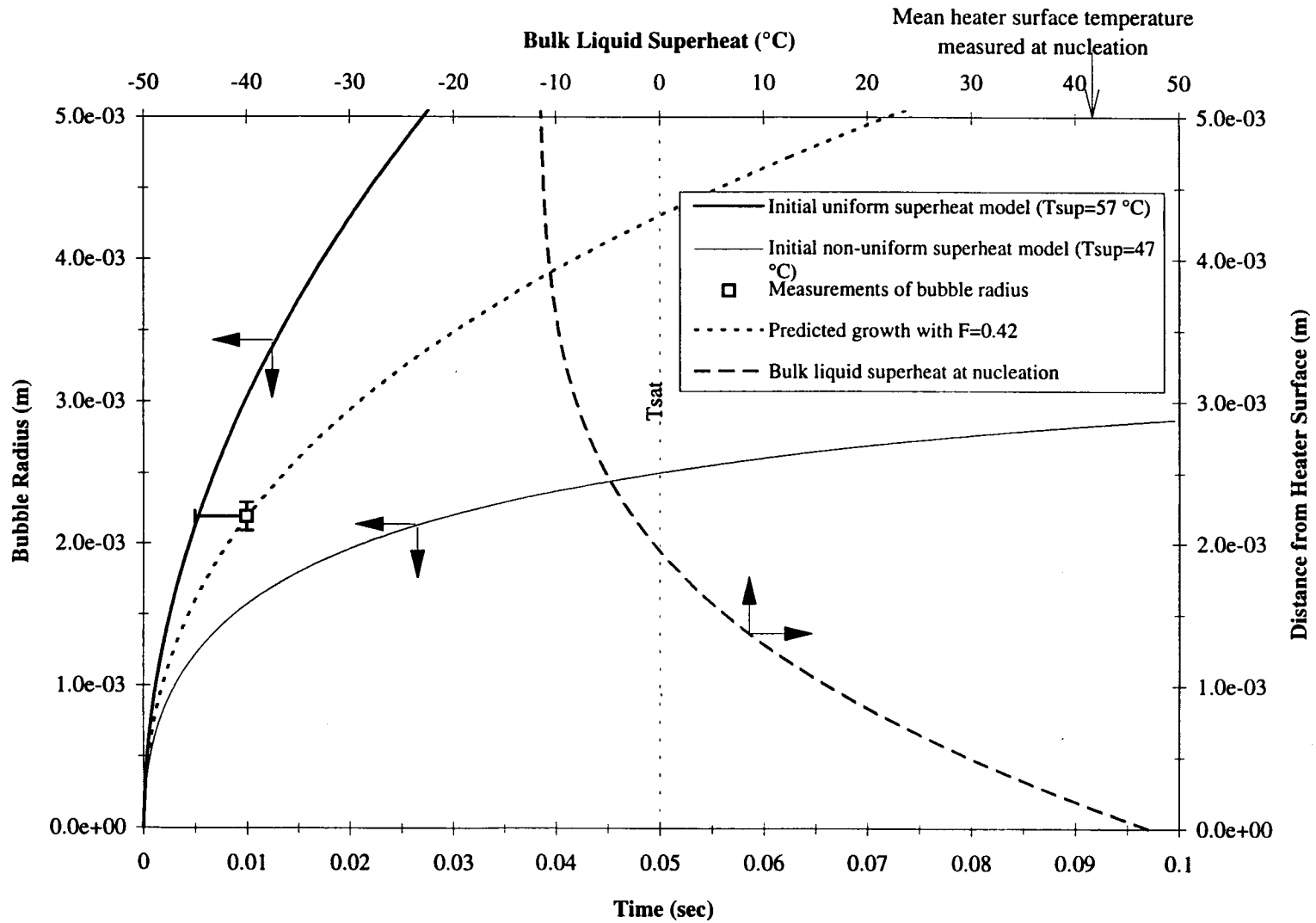

Figure C-9c. Comparisons of bubble growth measurements with several models. PBE-IC (STS-60). Run No. 3.

Comparison of Numerical Computation of Bubble growth with Experiment and Temperature Profile at Nucleation for STS-60 Run #4 (q"=6.5 W/cm²; T_{sat}=52 °C; P=117.3 kPa; ΔT_{sub}=3.2 °C; t*=0.74 sec)

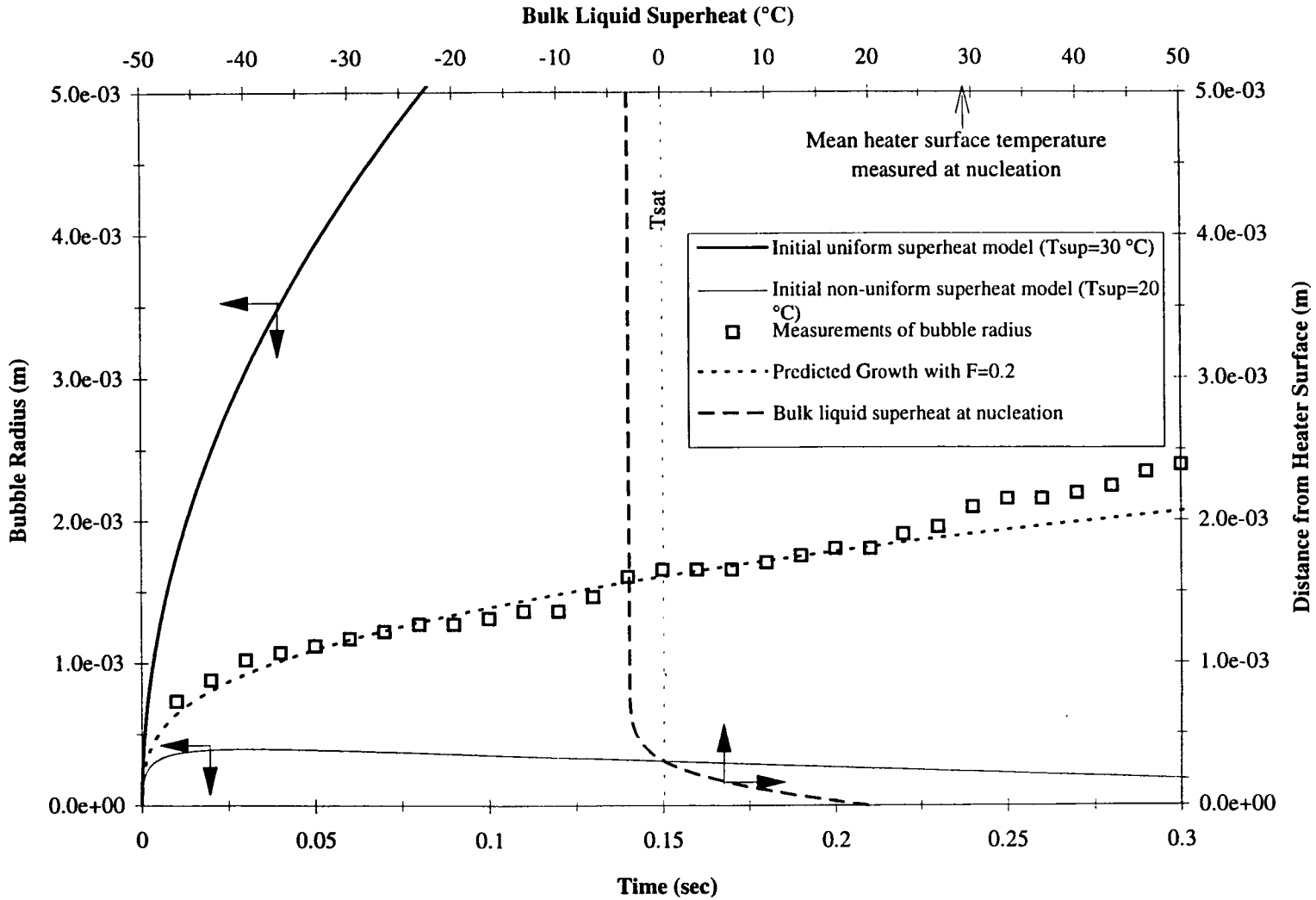

Figure C-9d. Comparisons of bubble growth measurements with several models. PBE-IC (STS-60). Run No. 4.

Comparison of Numerical Computation of Bubble growth with Experiment and Temperature Profile at Nucleation for STS-60 Run #5 (q"=3.47 W/cm²; T_{sat}=52 °C; P=117.58 kPa; ΔT_{sub}=3.2 °C; t*=9.6 sec)

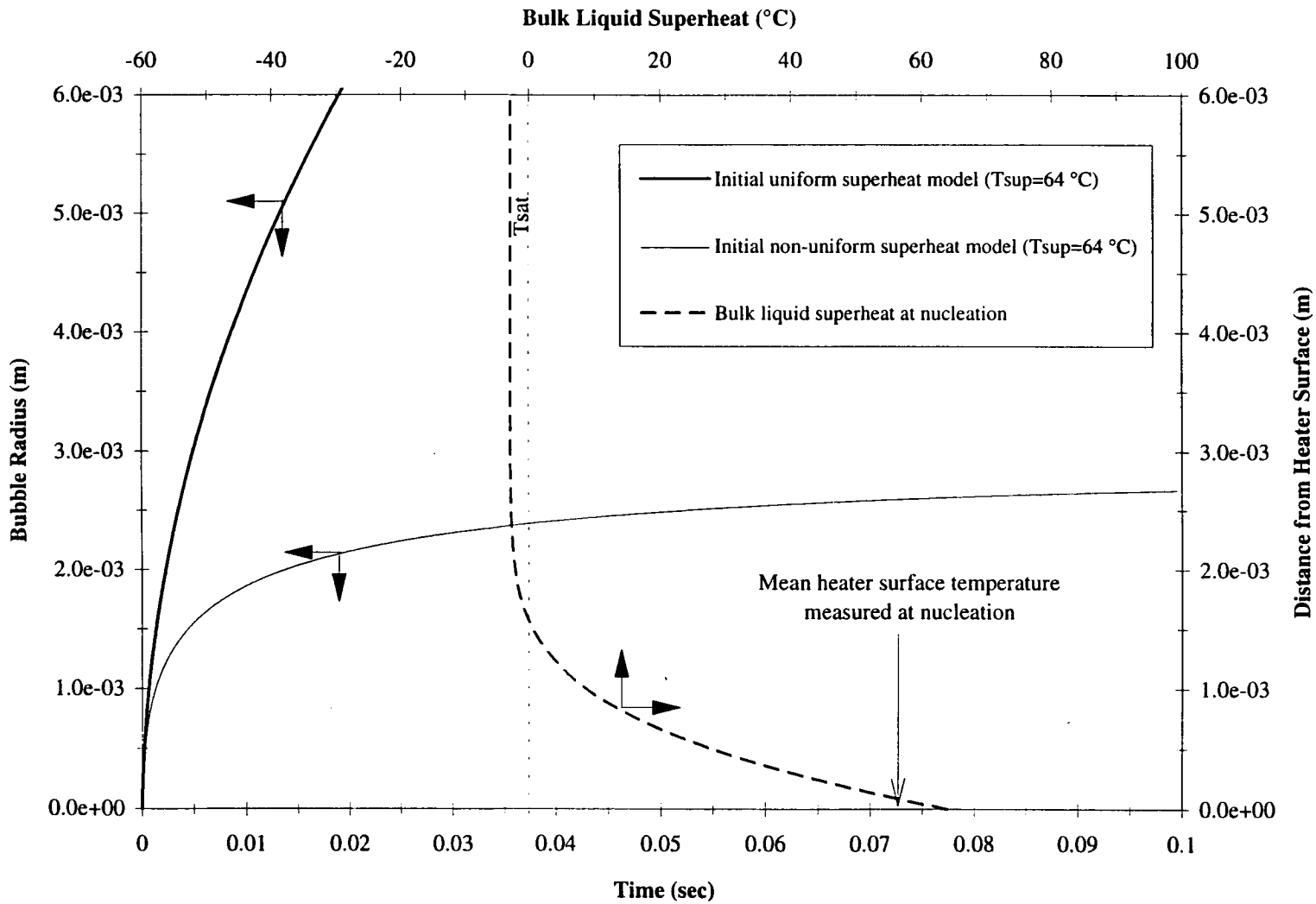

Figure C-9e. Comparisons of bubble growth measurements with several models. PBE-IC (STS-60). Run No. 5.

Comparison of Numerical Computation of Bubble growth with Experiment and Temperature Profile at Nucleation for STS-60 Run #6 (q"=1.8 W/cm²; T_{sat}=52.5 °C; P=119.2 kPa; ΔT_{sub}=3.2 °C; t*=37.94 sec)

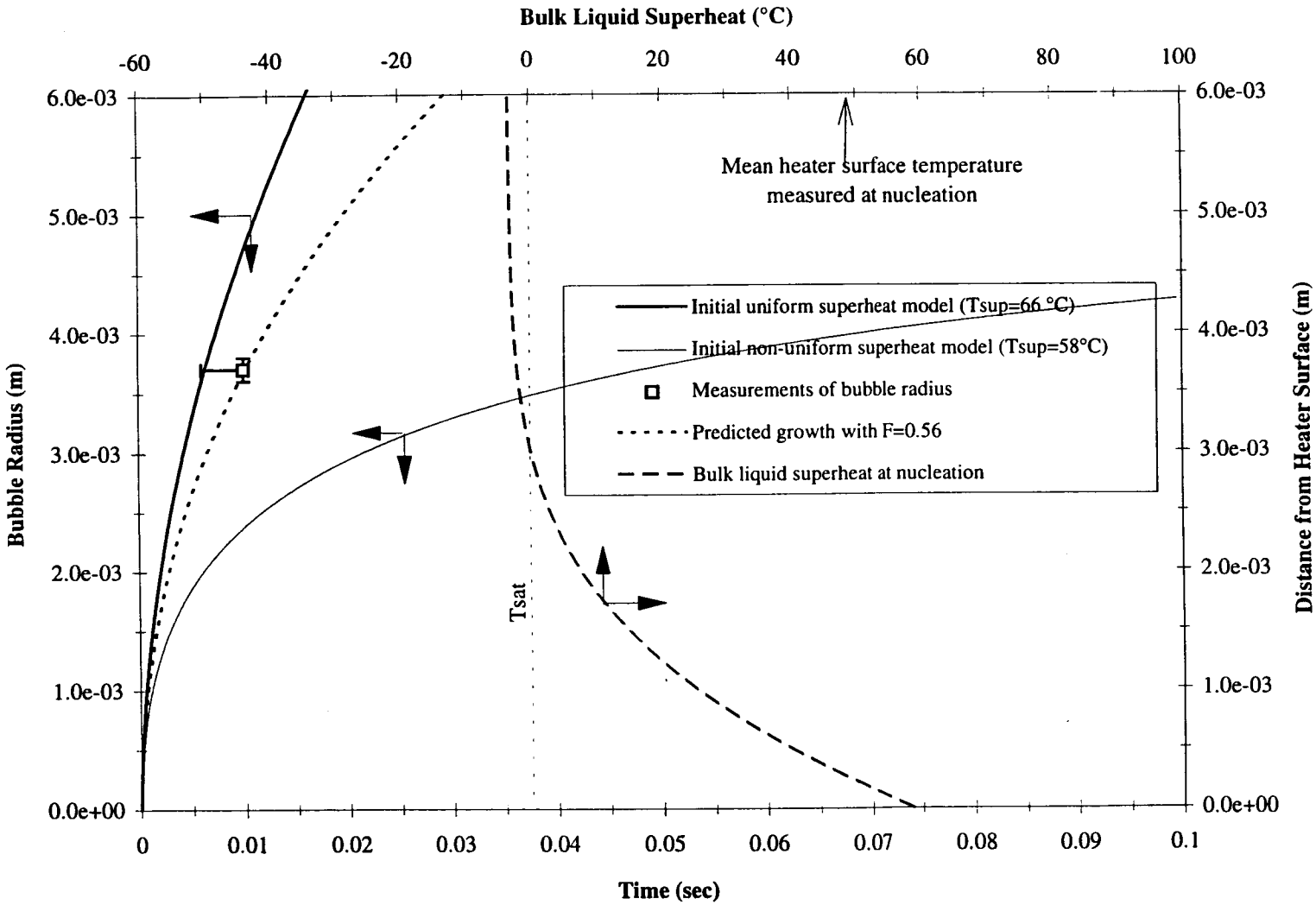

Figure C-9f. Comparisons of bubble growth measurements with several models. PBE-IC (STS-60). Run No. 6.

Comparison of Numerical Computation of Bubble growth with Experiment and Temperature Profile at Nucleation for STS-60 Run #7 (q"=6.95 W/cm²; T_{sat}=49.11 °C; P=106.8 kPa; ΔT_{sub}=0.76 °C; t*=0.75 sec)

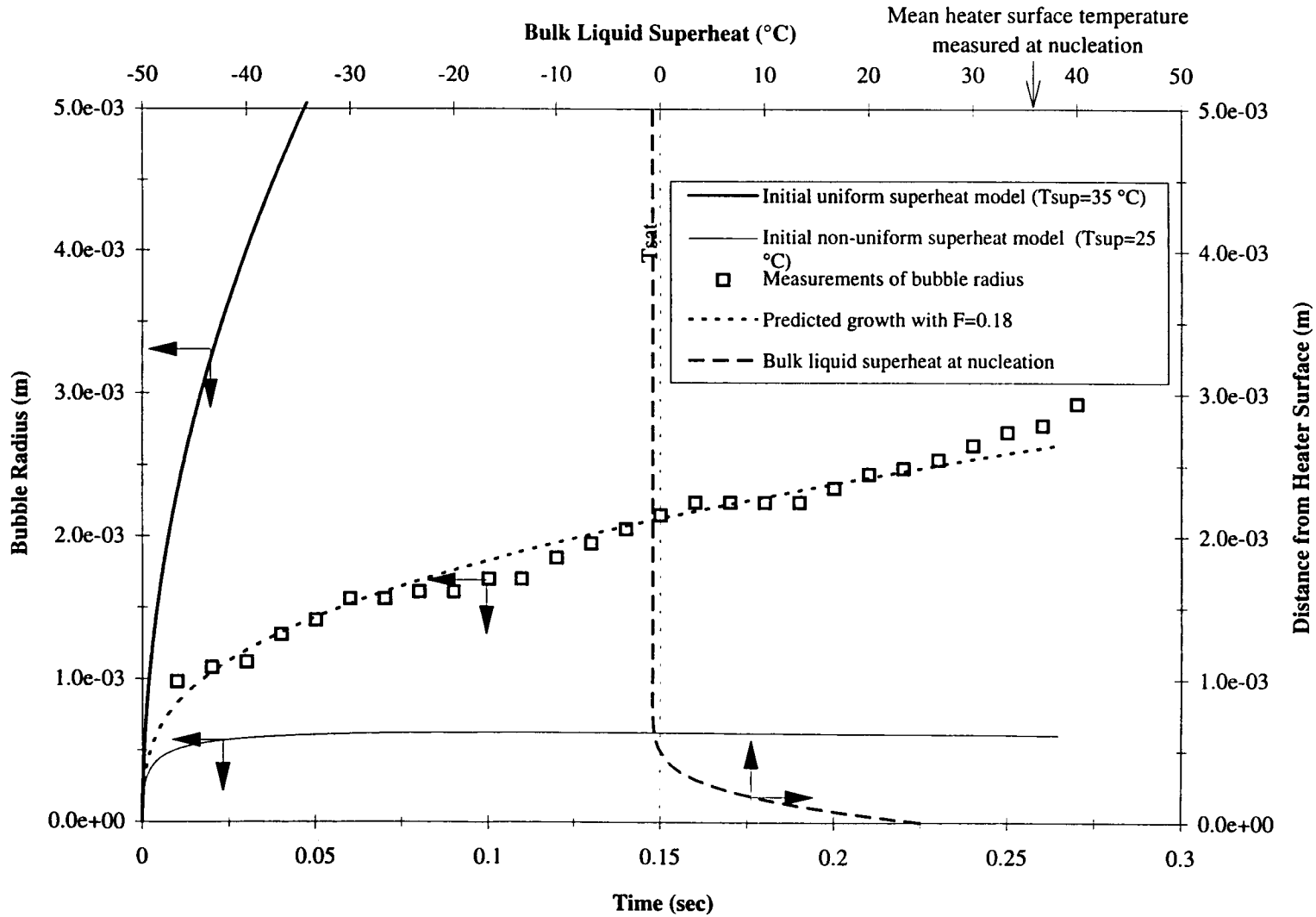

Figure C-9g-1. Comparisons of bubble growth measurements with several models. PBE-IC (STS-60). Run No. 7.

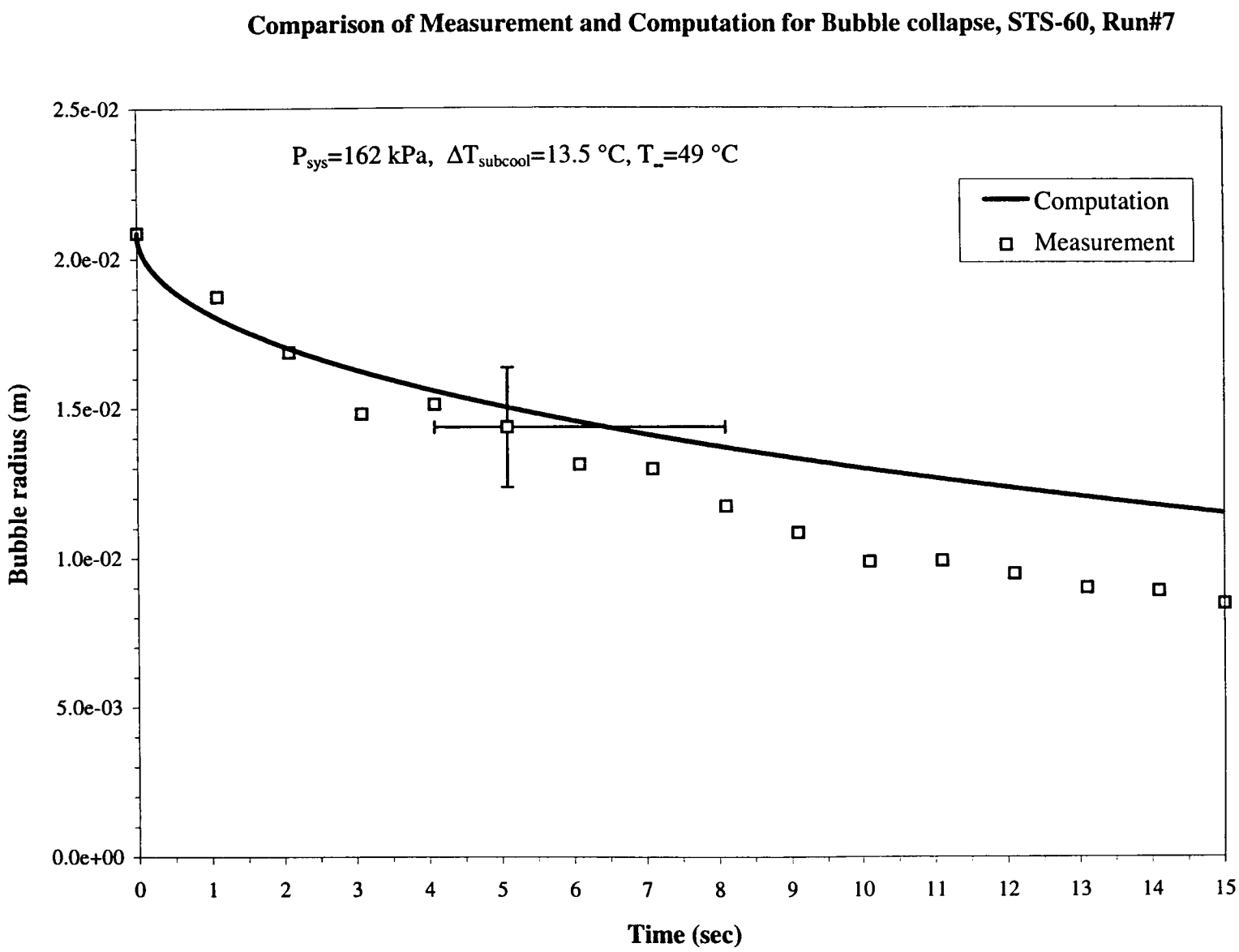

Figure C-9g-2. Comparisons of bubble collapse measurements following pressurization with computation from model. PBE-IC (STS-60). Run No. 7.

Comparison of Numerical Computation of Bubble growth with Experiment and Temperature Profile at Nucleation for STS-60 Run #8 (q"=3.5 W/cm²; T_{sat}=49.05 °C; P=106.62 kPa; ΔT_{sub}=0.71 °C; t*=8.03 sec)

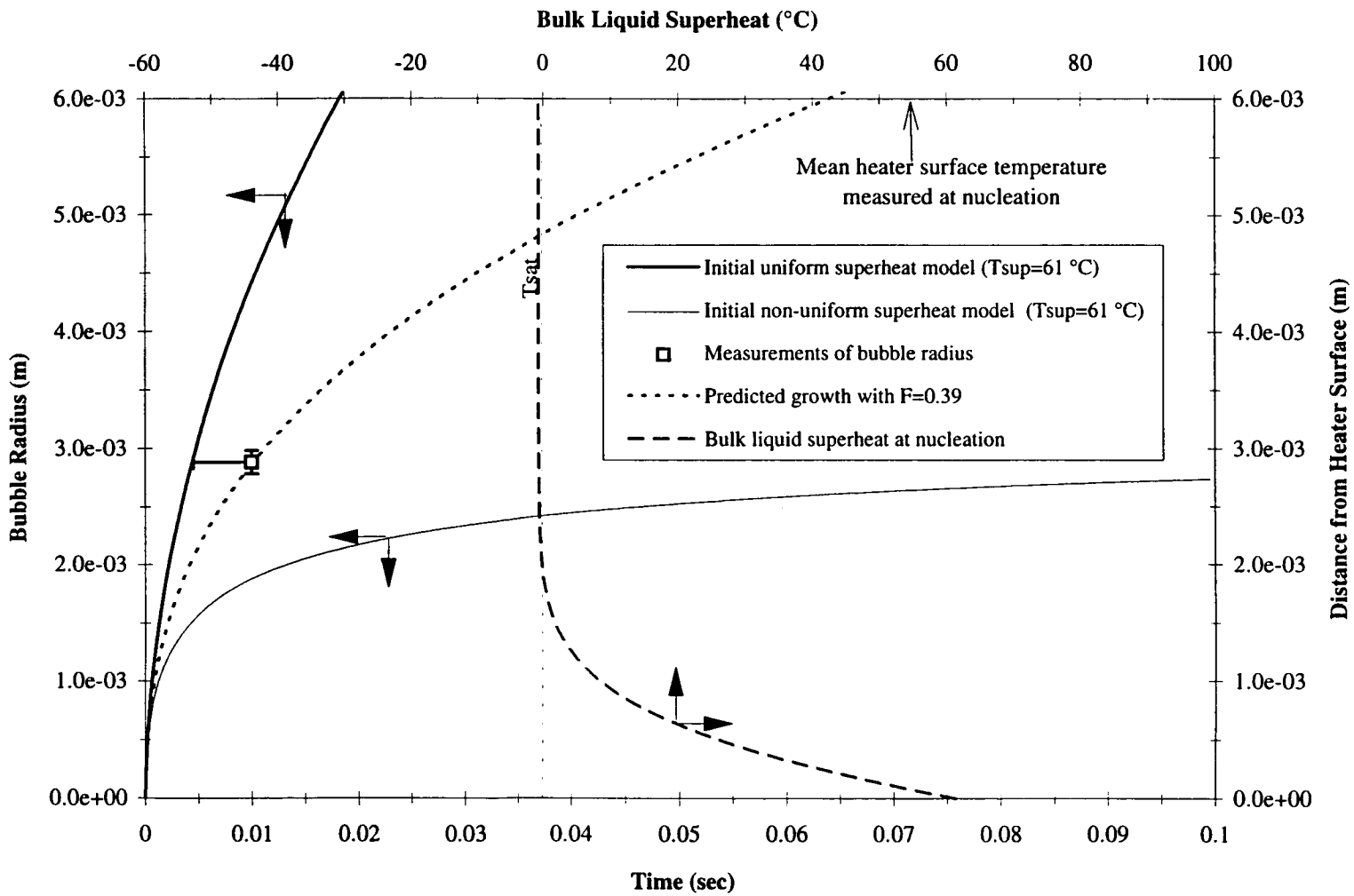

Figure C-9h. Comparisons of bubble growth measurements with several models. PBE-IC (STS-60). Run No. 8.

Comparison of Numerical Computation of Bubble growth with Experiment and Temperature Profile at Nucleation for STS-60 Run #9 (q"=1.81 W/cm²; T_{sat}=49.4 °C; P=107.7 kPa; ΔT_{sub}=0.72 °C; t*=30.52 sec)

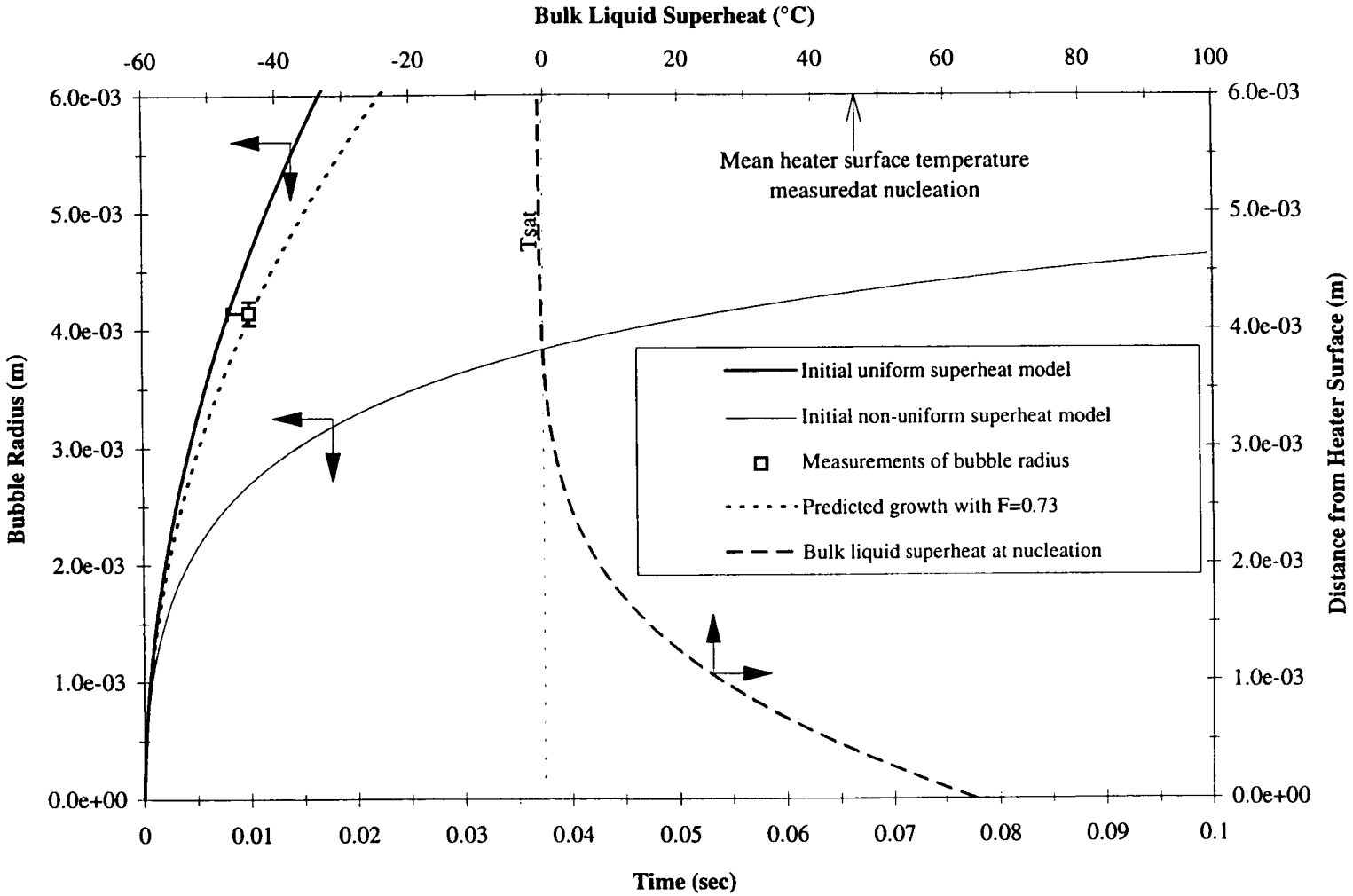

Figure C-9i. Comparisons of bubble growth measurements with several models. PBE-IC (STS-60). Run No. 9.

Run #	10 FPS	100 FPS	Nucleation	Range	Rate	Total # Frames	Analysis # Frames	Notes	Data Storage
1	13--55	10--13	10.91	nuc.--15	both	229	183	JLP	OD5-A
2	10--15	15--25	30.85	nuc.--50	10 fps	192	187	JLP	OD5-A
	25--135			80--100	10 fps	200	201	JLP	OD5-A
3	20--30	30--50	50.17	nuc.--80	10 fps	298	208	JLP	OD5-A
	50--130			90--115	10 fps	250	203	JLP	OD5-A
4	13--60	10--13	10.74	nuc.--15	both	226	188	YHJ	OD5-A
				27--35	10 fps	80	81	YHJ	OD5-A
5	10--20	20--30	19.6	nuc.--30	both	1004	201	YHJ	OD5-B
	30--105			50--65		150	149	YHJ	OD5-B
6	20--30	30--50	47.94	nuc.--70	both	406	224	YHJ	OD5-A
	50--100								
7	25--40	10--25	10.75	nuc.--20	100 fps	925	99	YHJ	OD5-B
8	10--15	15--25	18.03	nuc.--30	both	747	123	HEB	OD5-B
	25--80								
9	10--40	40--60	40.52	nuc.--60	100 fps	1948	203	HEB	OD5-B
	60--125			60--80	10 fps	200	195	HEB	OD5-B

**Note: All times are relative to ZERO. Heater power is active at 10 sec;

Table C-IV. Index for heater surface dry fraction measurements and computation of microgravity nucleate boiling heat transfer coefficients. PBE-IC (STS-60).

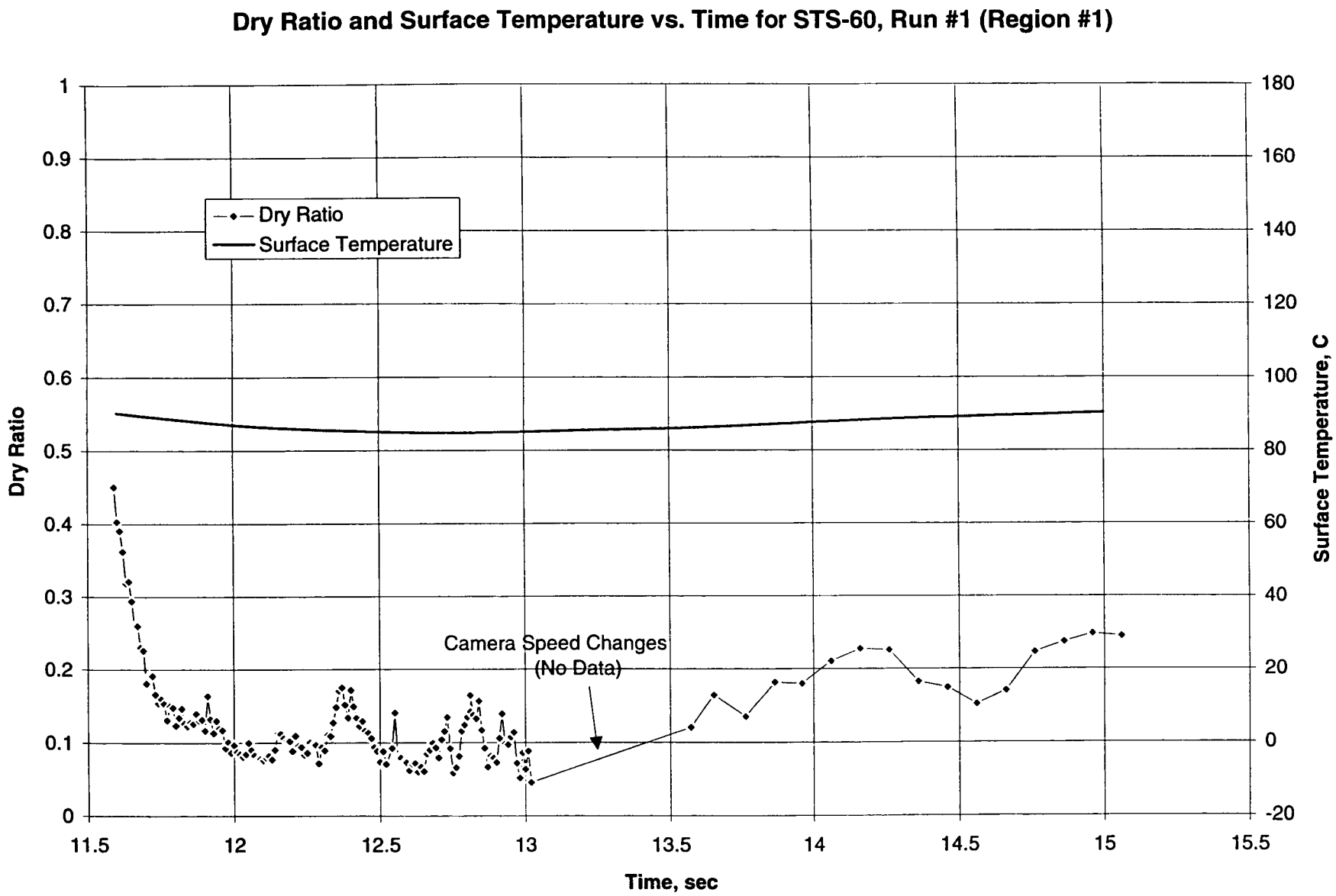

Figure C-10a-1-i. Heater surface dry fraction and mean temperature. PBE-IC (STS-60). Run No. 1. Time interval: 11.6 - 15.1 seconds.

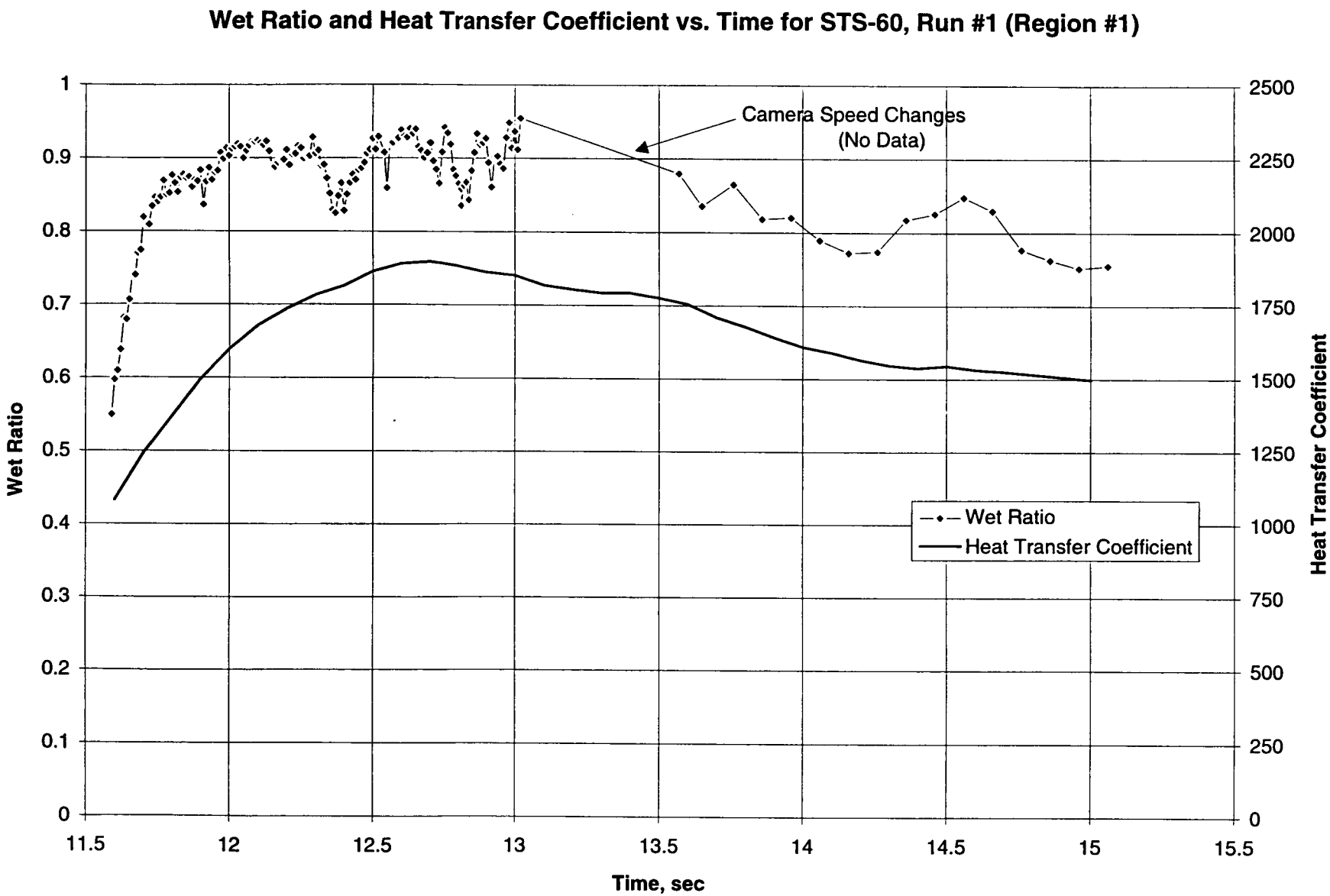

Figure C-10a-1-ii. Heater surface wet fraction and mean heat transfer coefficients. PBE-IC (STS-60). Run No. 1. Time interval: 11.6 - 15.1 seconds.

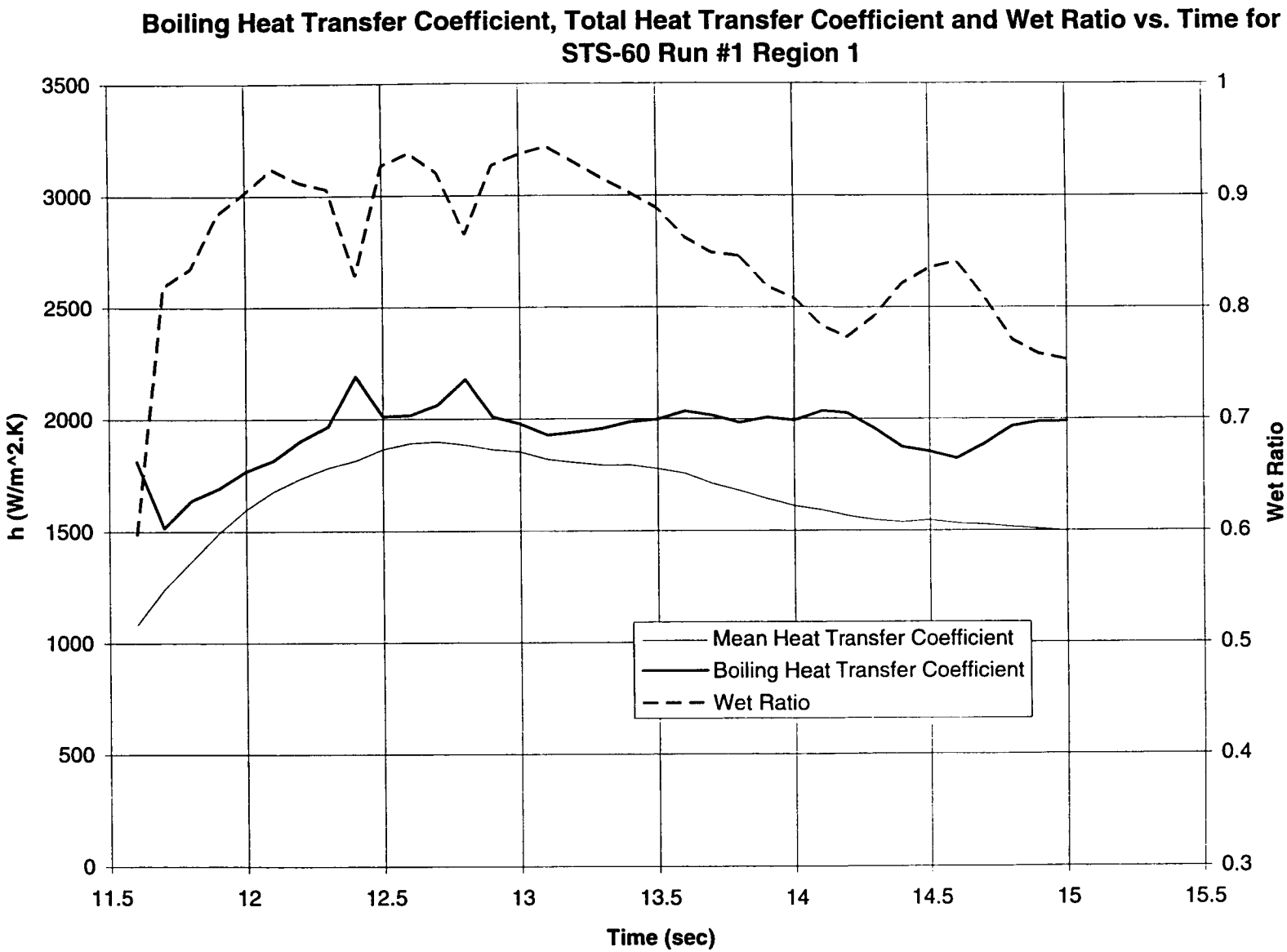

Figure C-10a-1-iii. Development of microgravity boiling heat transfer coefficient. PBE-IC (STS-60). Run No. 1. Time interval: 11.6 - 15.1 seconds.

STS-60 Run #1, Region 1

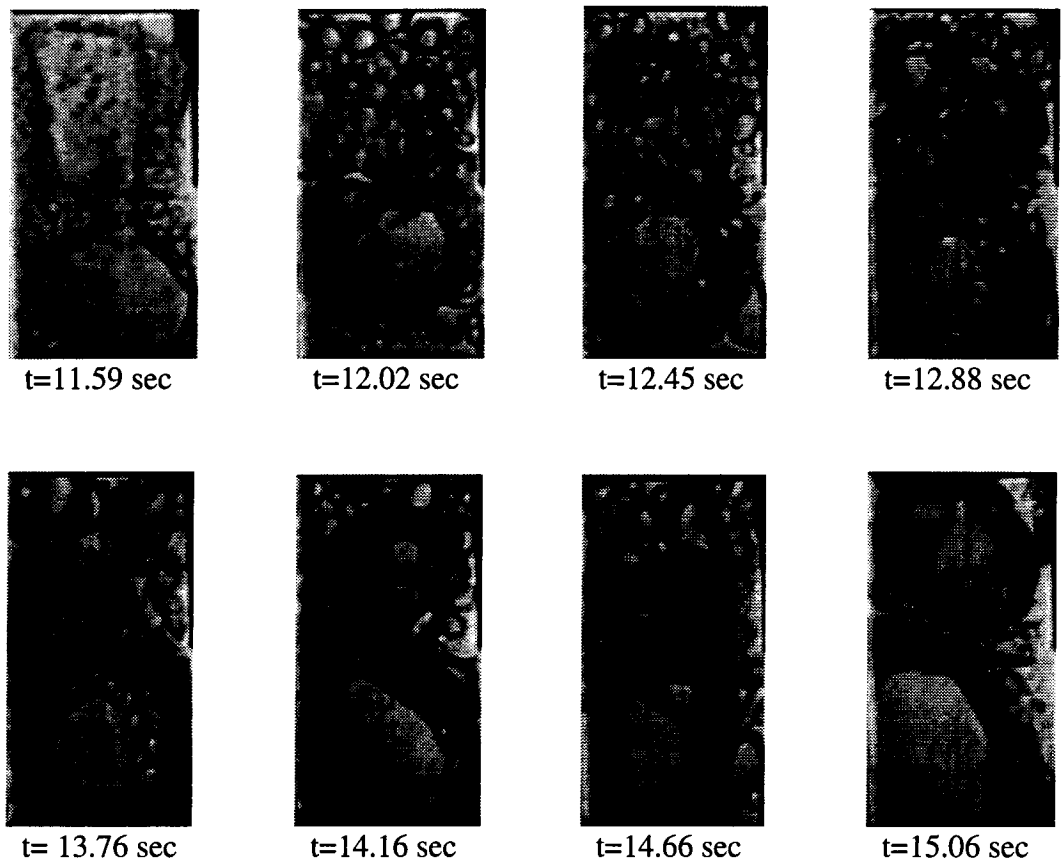

Figure C-10a-1-iv. Sample images showing dryout/rewetting. PBE-IC (STS-60). Run No. 1. Time interval: 11.6 - 15.1 seconds.

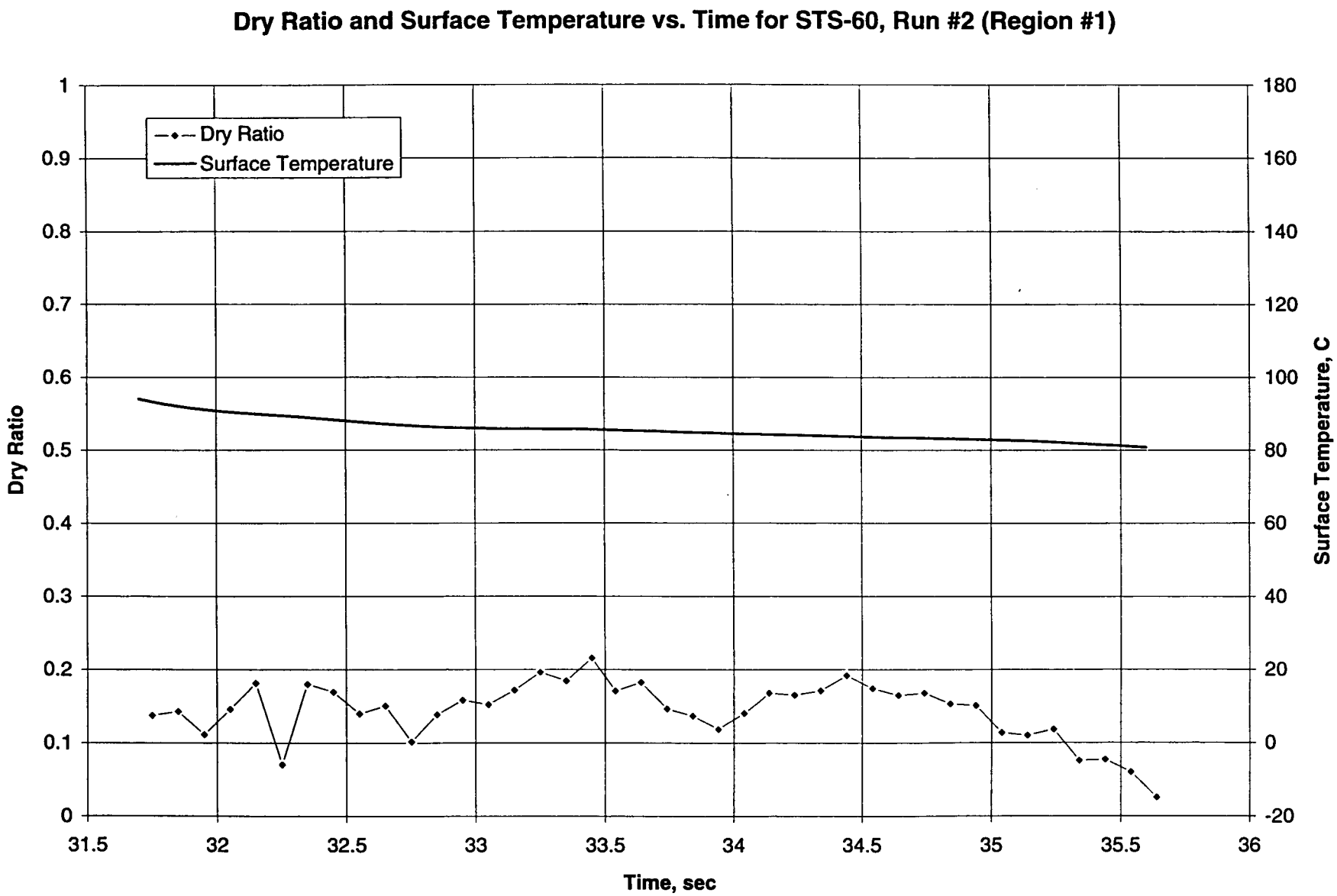

Figure C-10b-1-i. Heater surface dry fraction and mean temperature. PBE-IC (STS-60). Run No. 2. Time interval: 31.7 - 35.7 seconds.

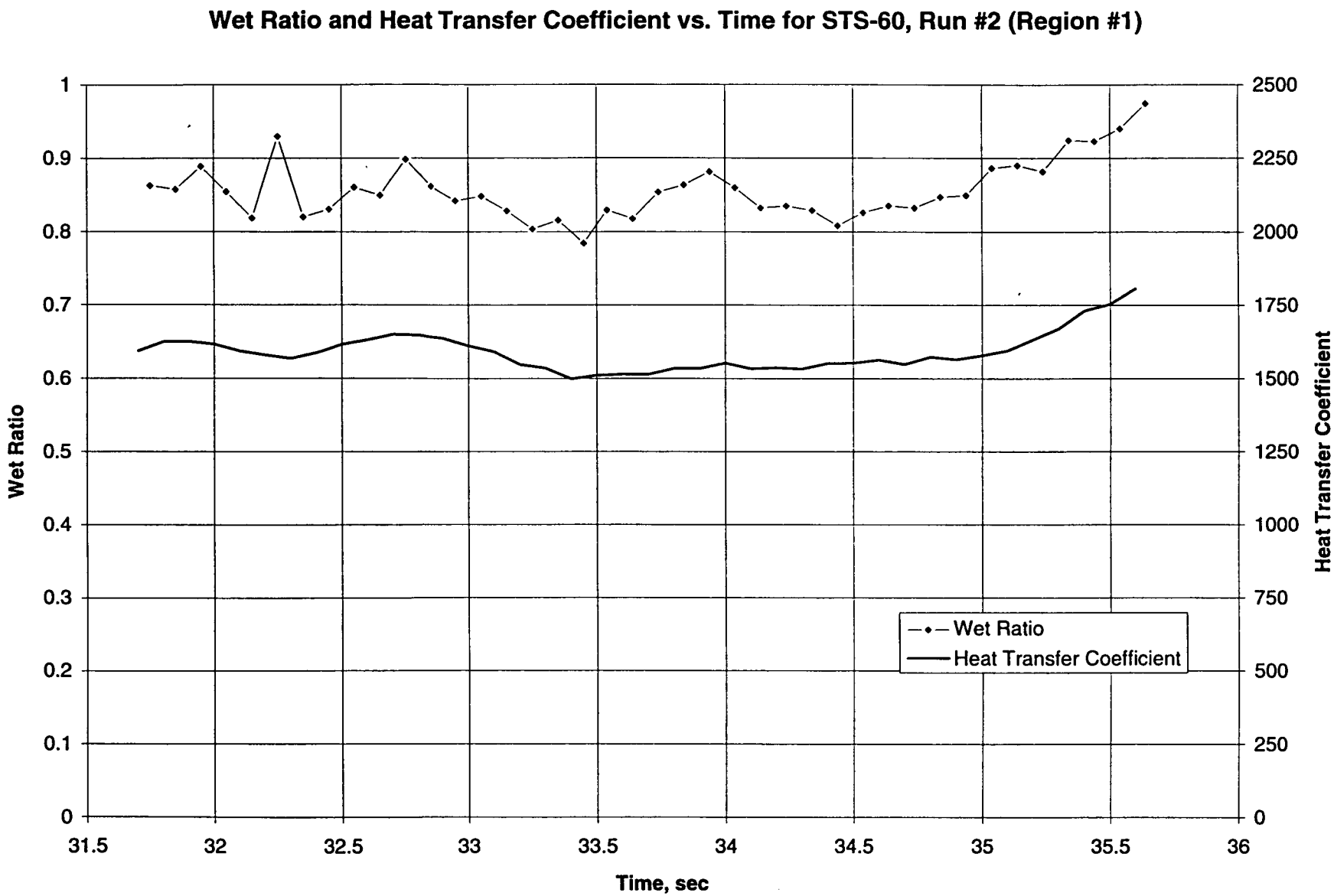

Figure C-10b-1-ii. Heater surface wet fraction and mean heat transfer coefficients. PBE-IC (STS-60). Run No. 2. Time interval: 31.7 - 35.7 seconds.

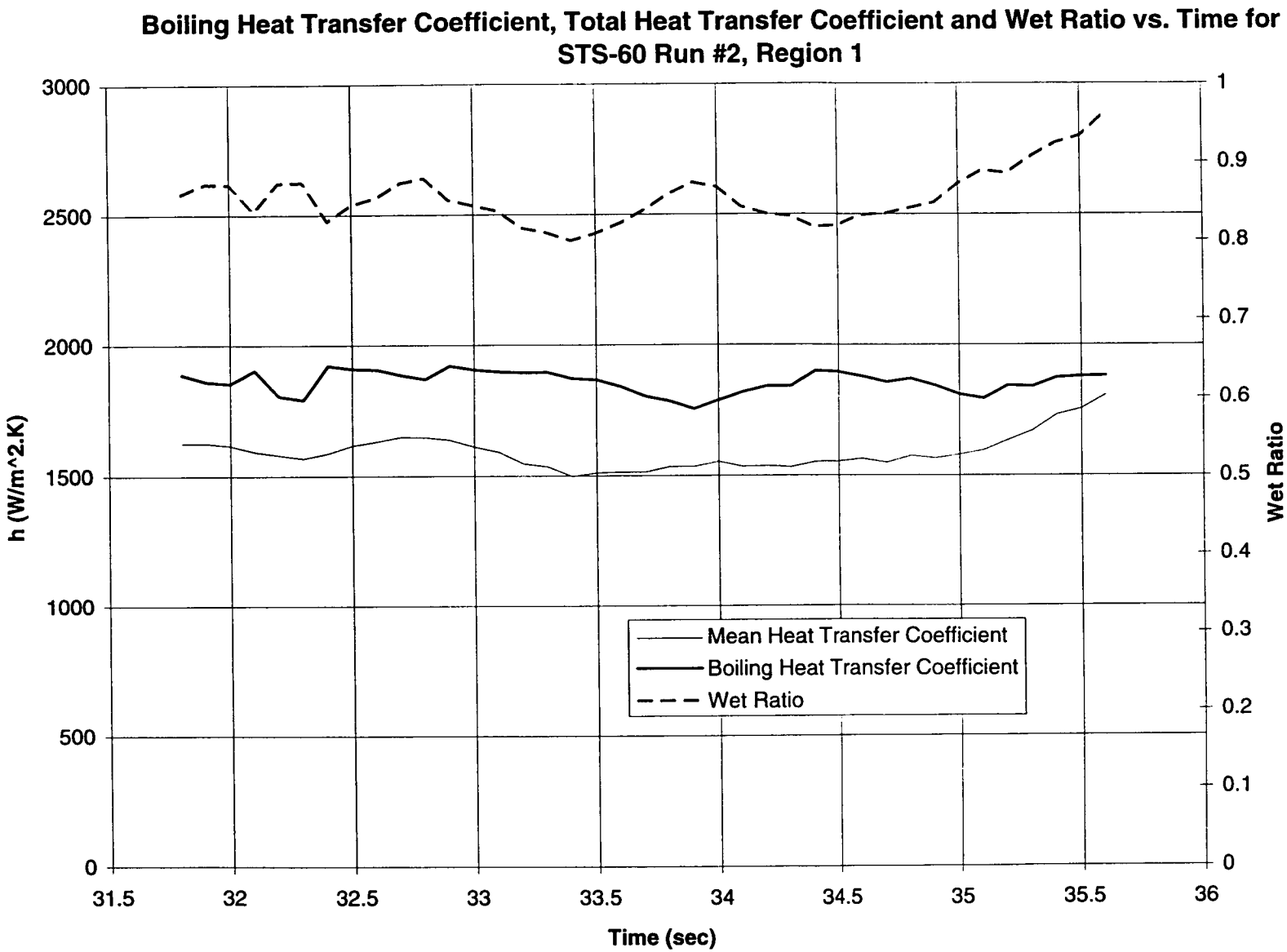

Figure C-10b-1-iii. Development of microgravity boiling heat transfer coefficient. PBE-IC (STS-60). Run No. 2. Time interval: 31.7 - 35.7 seconds.

STS-60 Run #2, Region 1

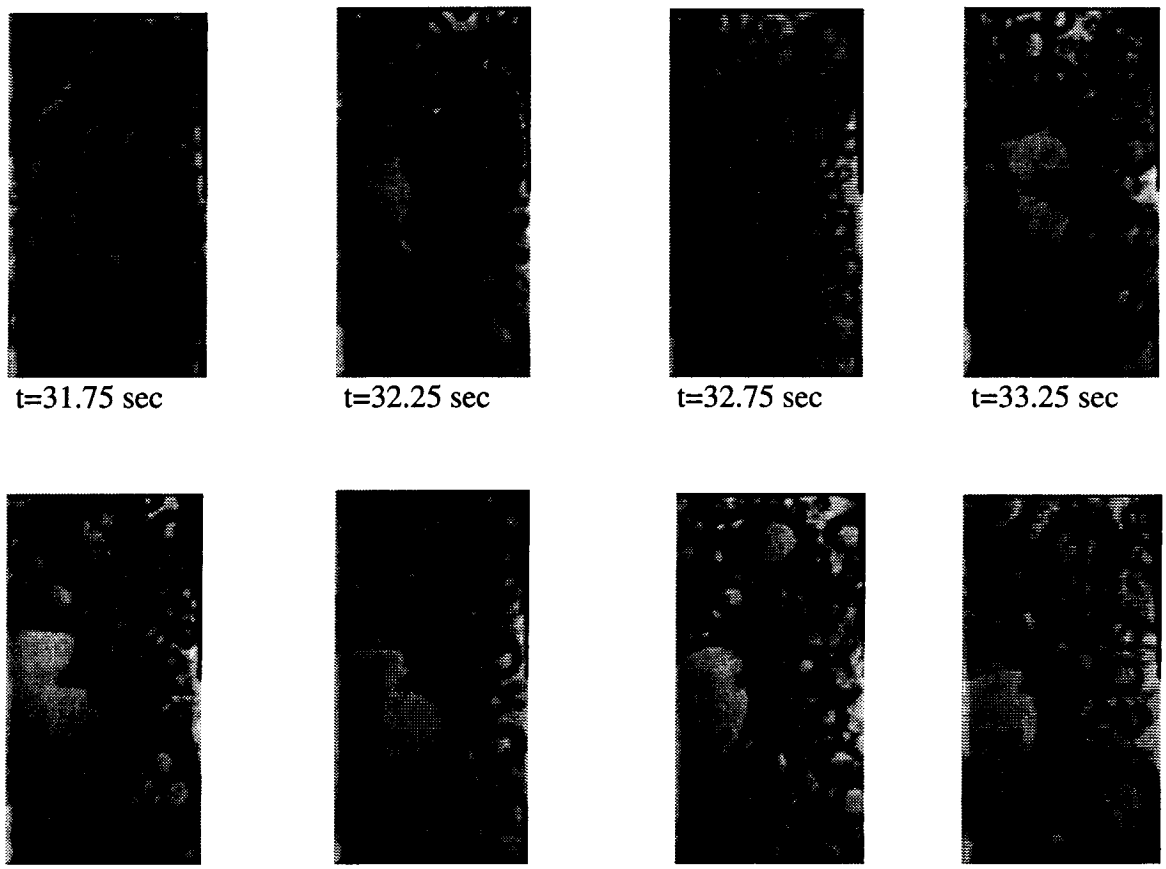

Figure C-10b-1-iv. Sample images showing dryout/rewetting. PBE-IC (STS-60). Run No. 2. Time interval: 31.7 - 35.7 seconds.

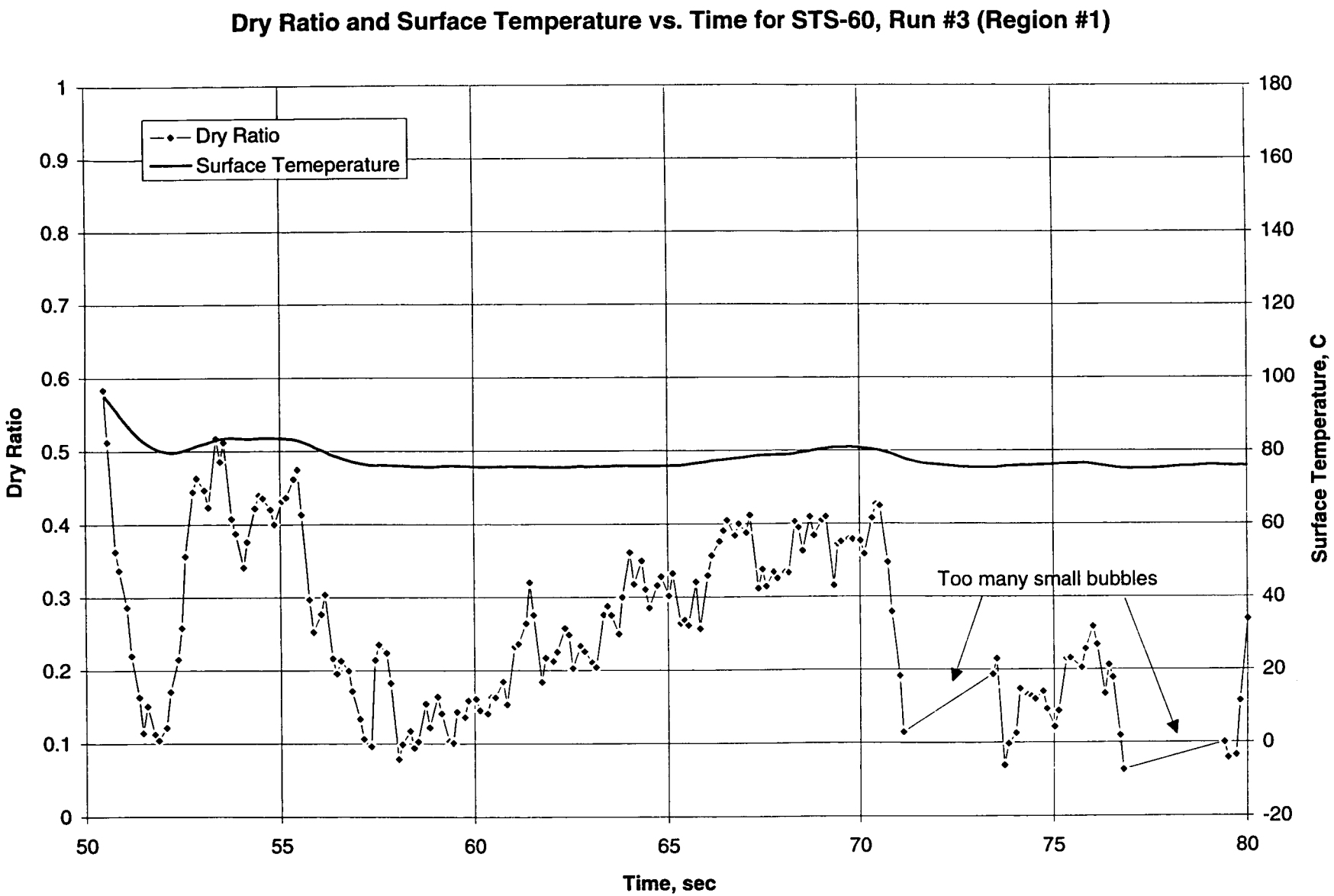

Figure C-10c-1-i. Heater surface dry fraction and mean temperature. PBE-IC (STS-60). Run No. 3. Time interval: 50.5 - 80.0 seconds.

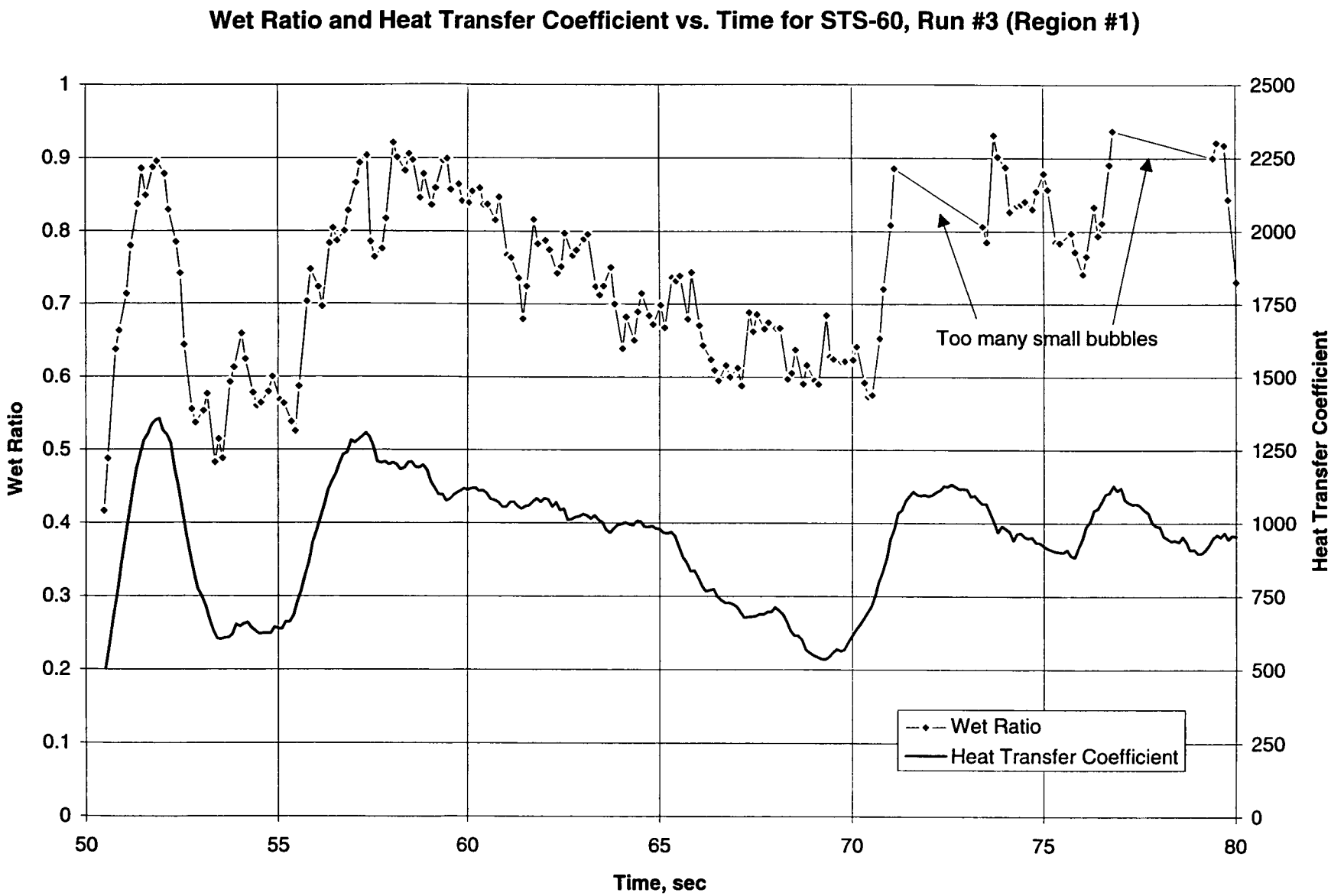

Figure C-10c-1-ii. Heater surface wet fraction and mean heat transfer coefficients. PBE-IC (STS-60). Run No. 3. Time interval: 50.5 - 80.0 seconds.

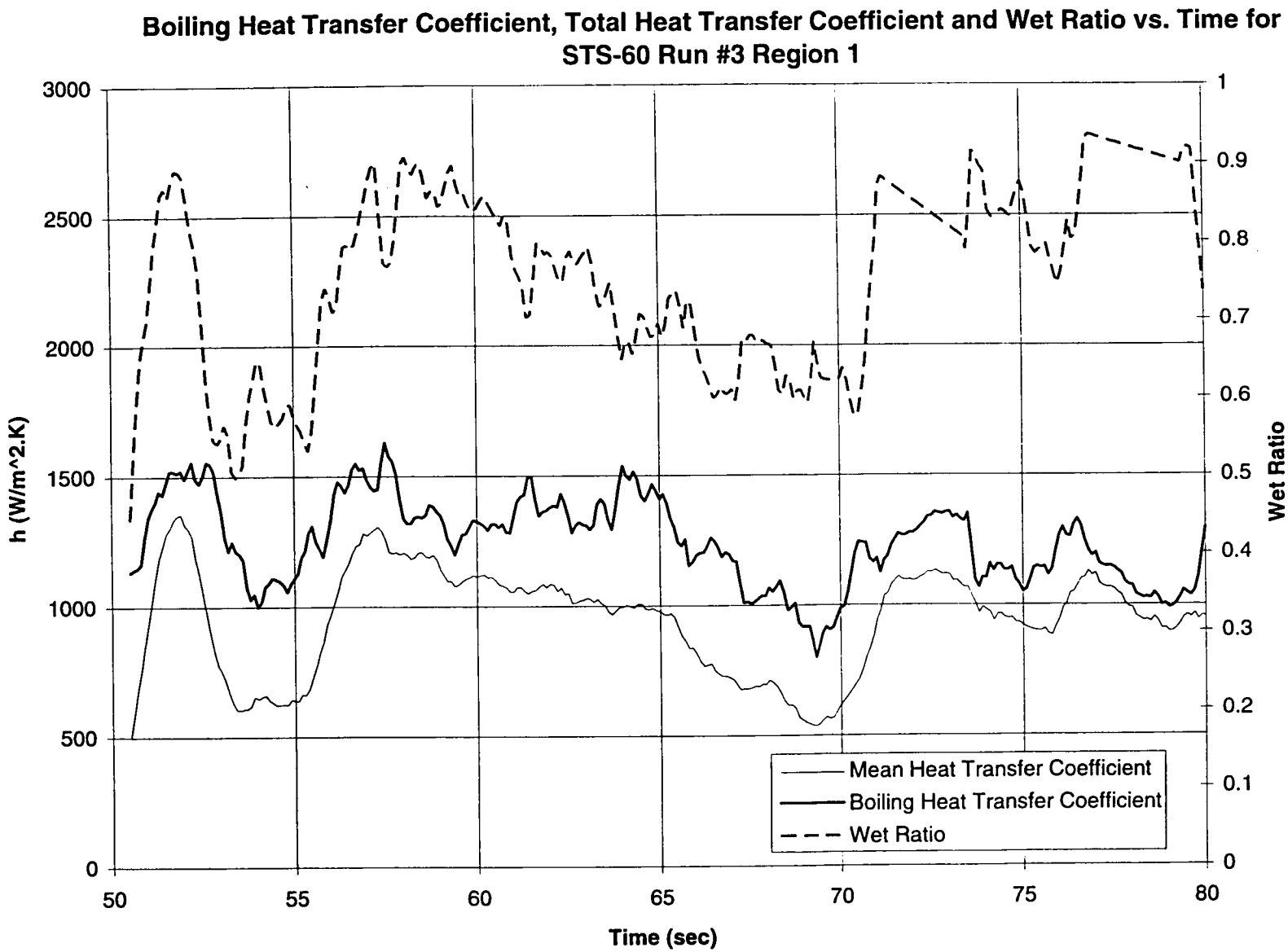

Figure C-10c-1-iii. Development of microgravity boiling heat transfer coefficient. PBE-IC (STS-60). Run No. 3. Time interval: 50.5 - 80.0 seconds).

STS-60 Run #3, Region 1

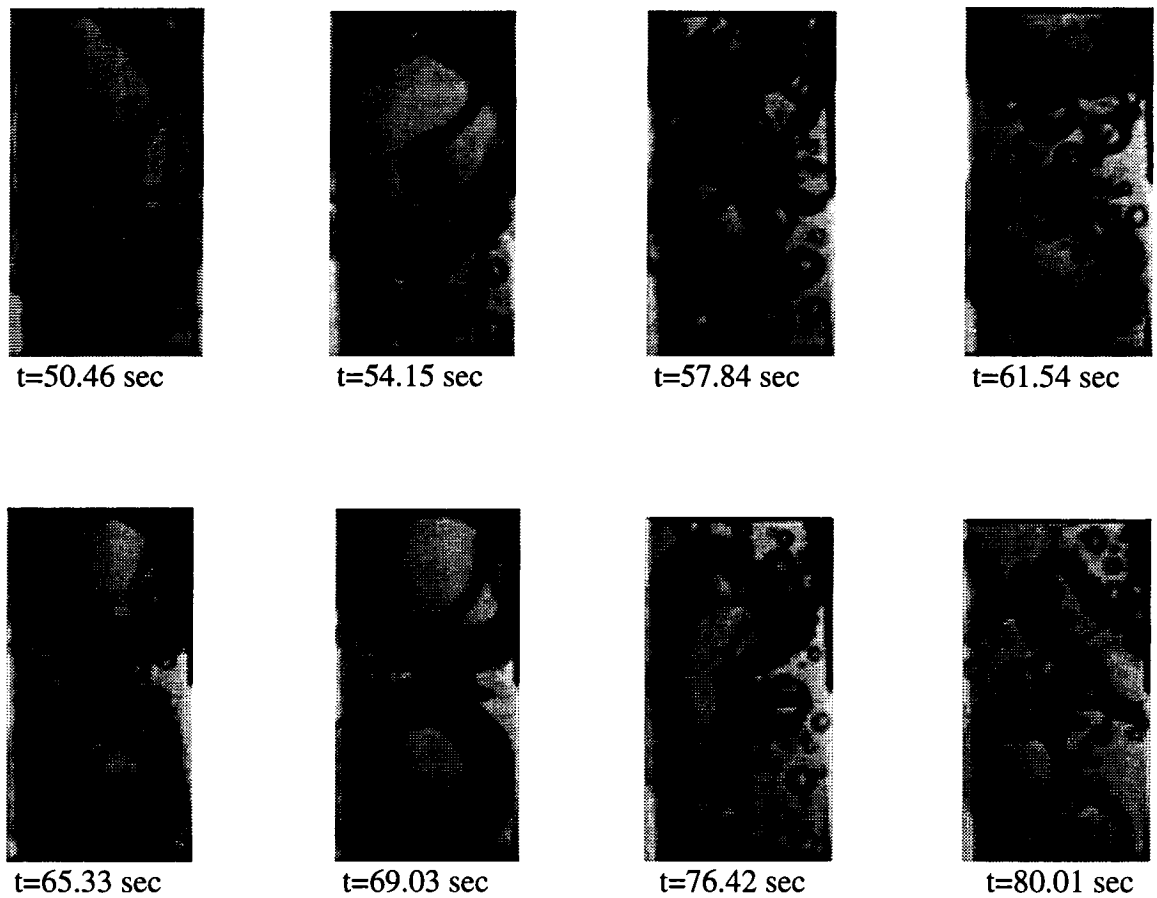

Figure C-10c-1-iv. Sample images showing dryout/rewetting. PBE-IC (STS-60). Run No. 3. Time interval: 50.5 - 80.0 seconds.

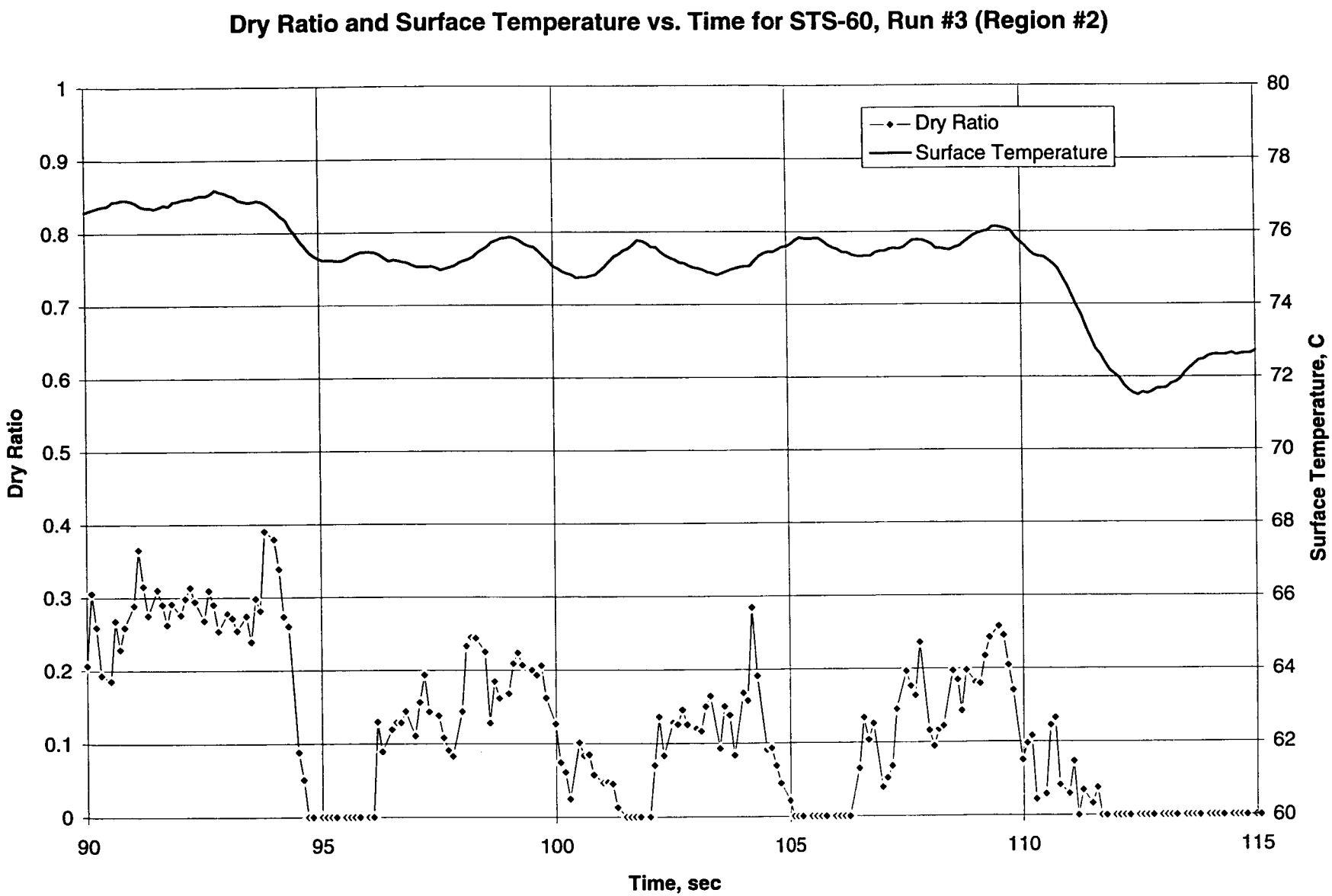

Figure C-10c-2-i. Heater surface dry fraction and mean temperature. PBE-IC (STS-60). Run No. 3. Time interval: 90 - 115 seconds.

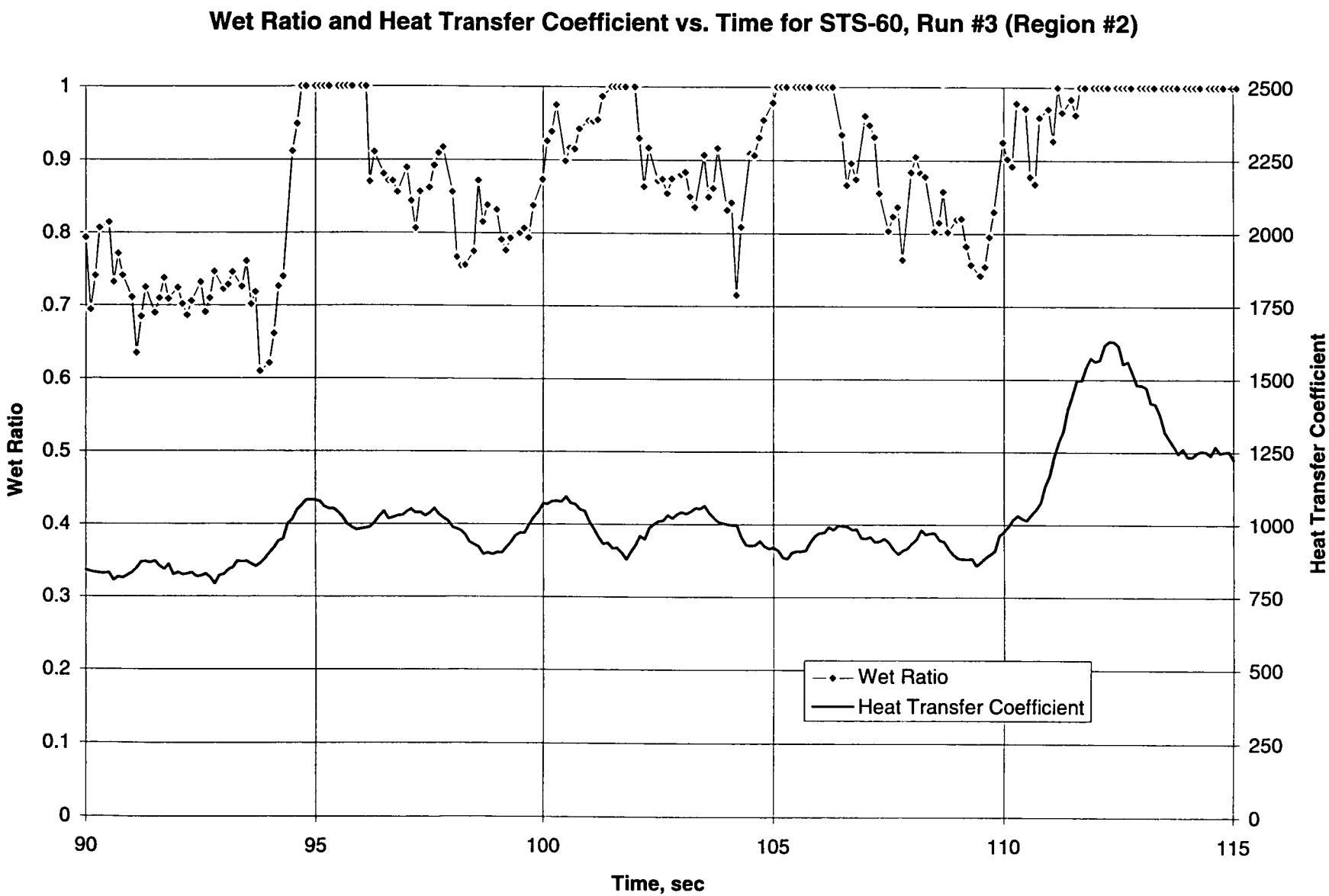

Figure C-10c-2-ii. Heater surface wet fraction and mean heat transfer coefficients. PBE-IC (STS-60). Run No. 3. Time interval: 90 - 115 seconds.

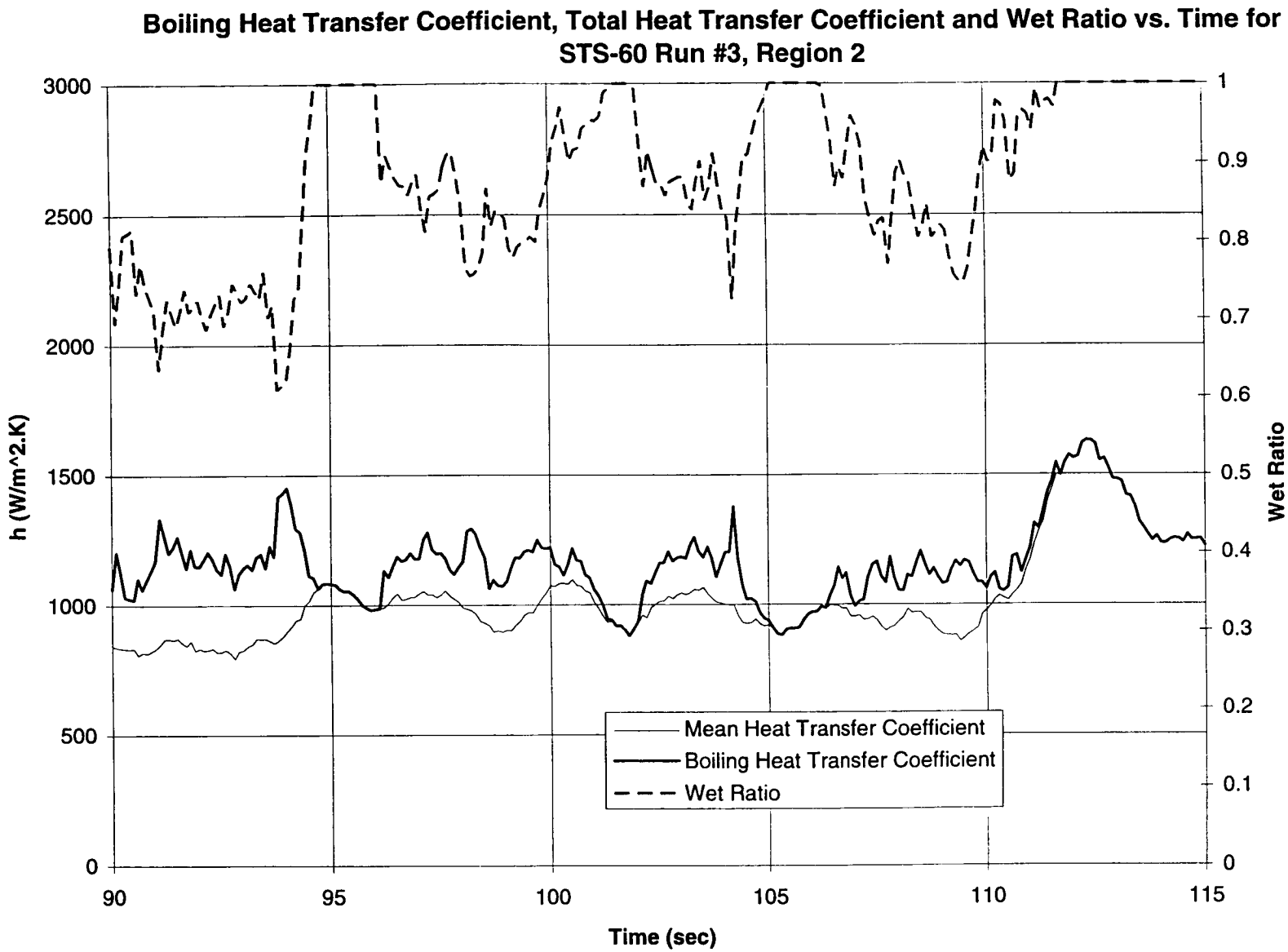

Figure C-10c-2-iii. Development of microgravity boiling heat transfer coefficient. PBE-IC (STS-60). Run No. 3. Time interval: 90 - 115 seconds.

STS-60 Run #3, Region 2

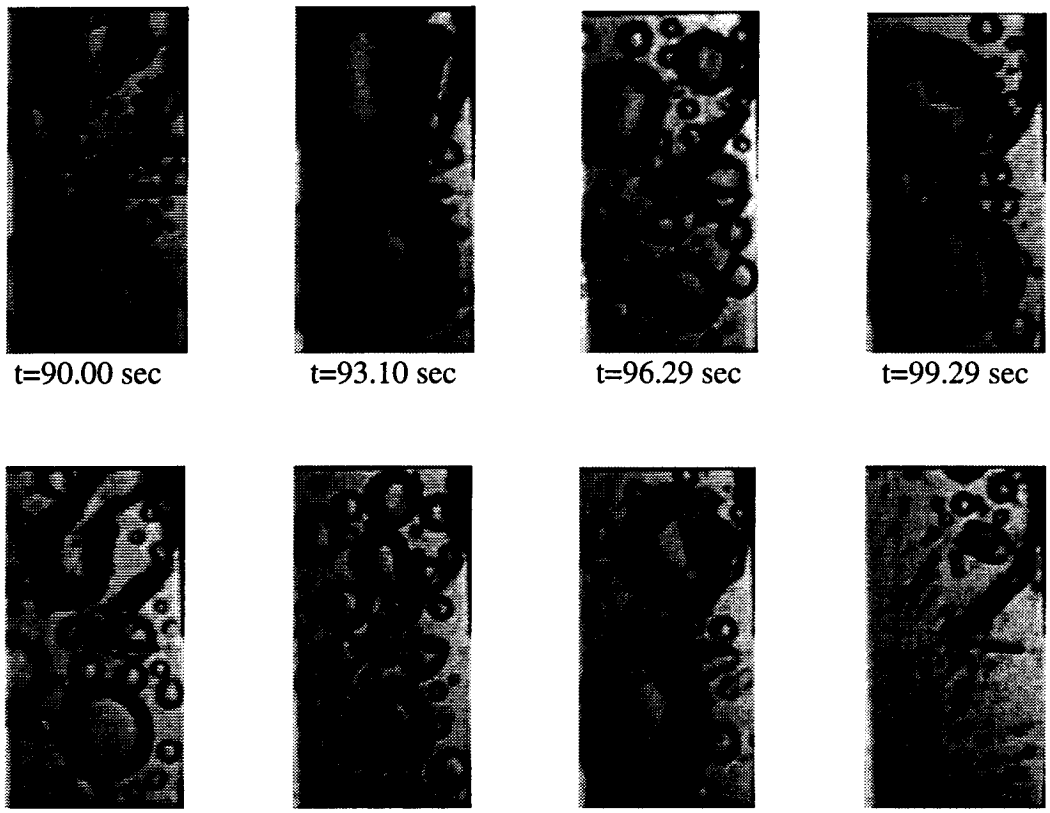

Figure C-10c-2-iv. Sample images showing dryout/rewetting. PBE-IC (STS-60). Run No. 3. Time interval: 90 - 115 seconds.

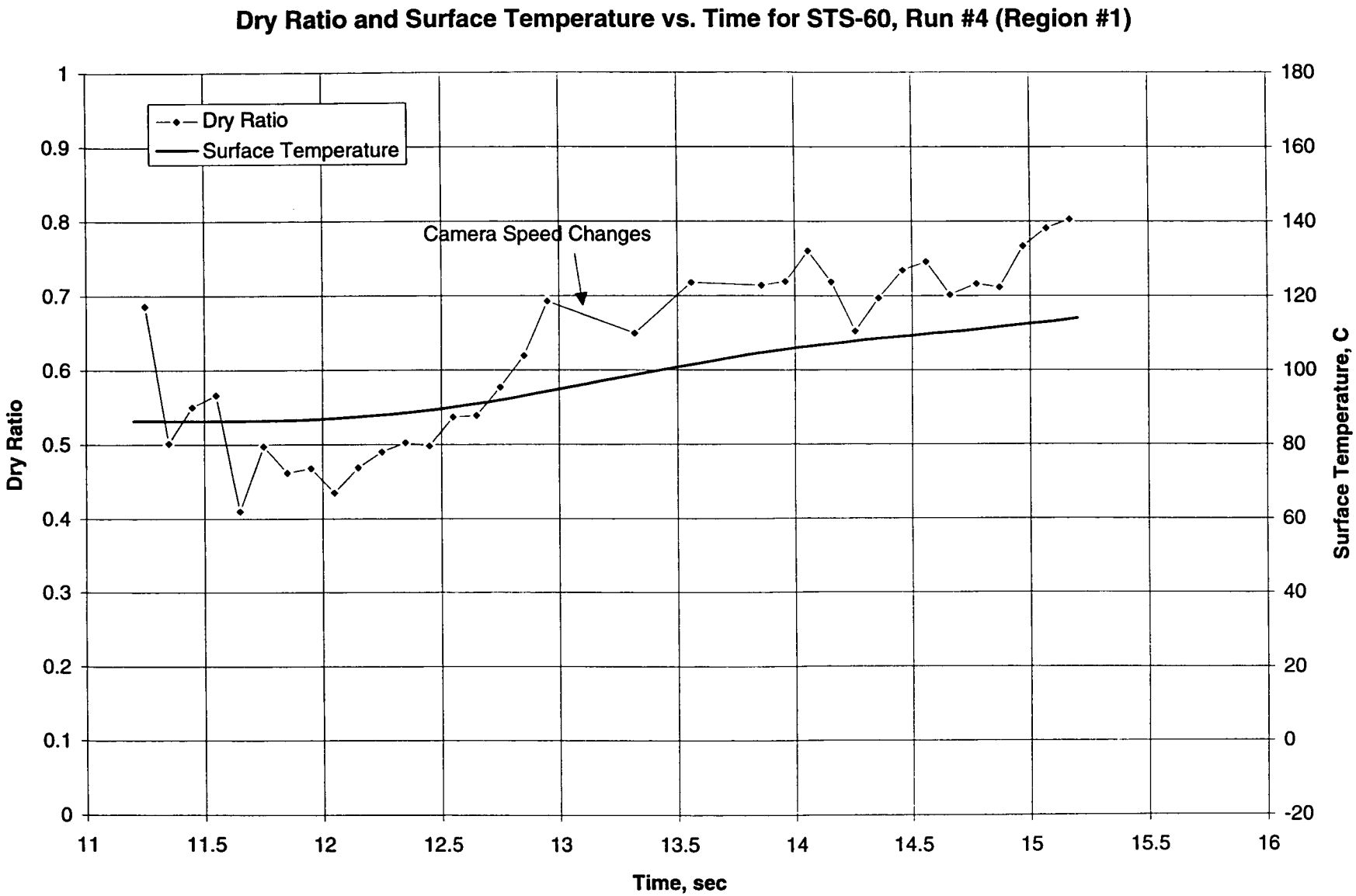

Figure C-10d-1-i. Heater surface dry fraction and mean temperature. PBE-IC (STS-60). Run No. 4. Time interval: 11.2 - 15.2 seconds.

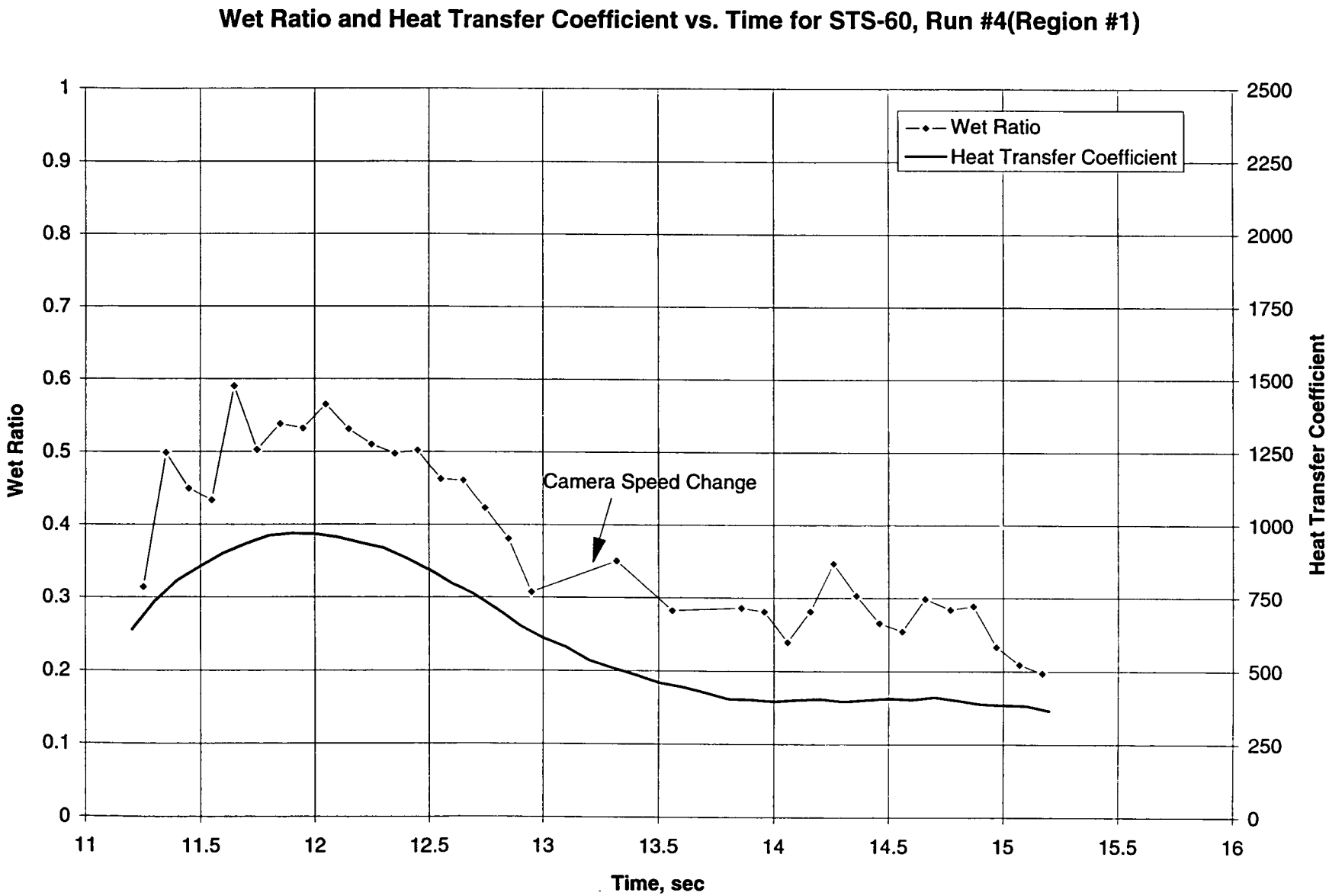

Figure C-10d-1-ii. Heater surface wet fraction and mean heat transfer coefficients. PBE-IC (STS-60). Run No. 4. Time interval: 11.2 - 15.2 seconds.

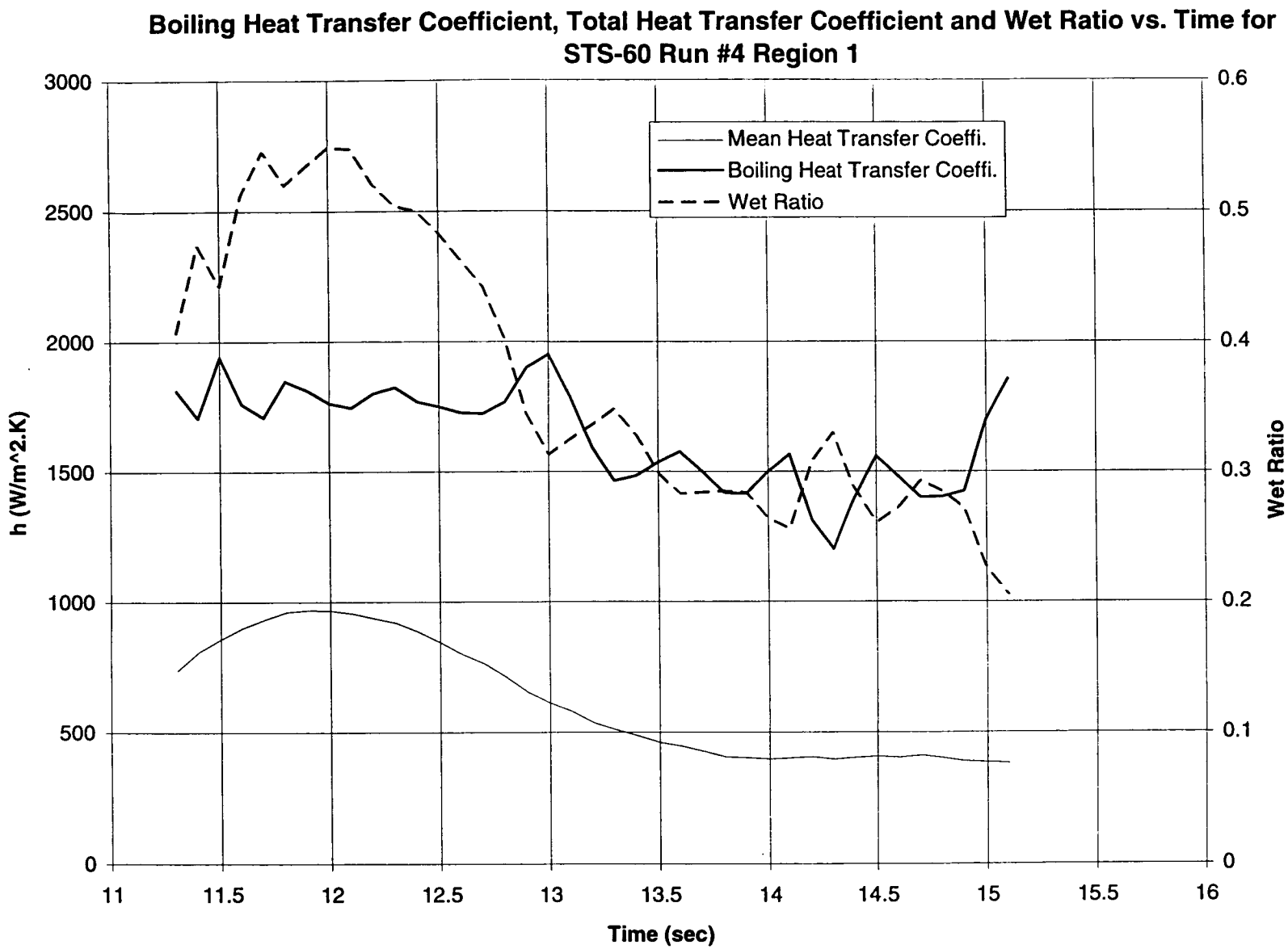

Figure C-10d-1-iii. Development of microgravity boiling heat transfer coefficient. PBE-IC (STS-60). Run No. 4. Time interval: 11.2 - 15.2 seconds.

STS-60 Run #4, Region 1

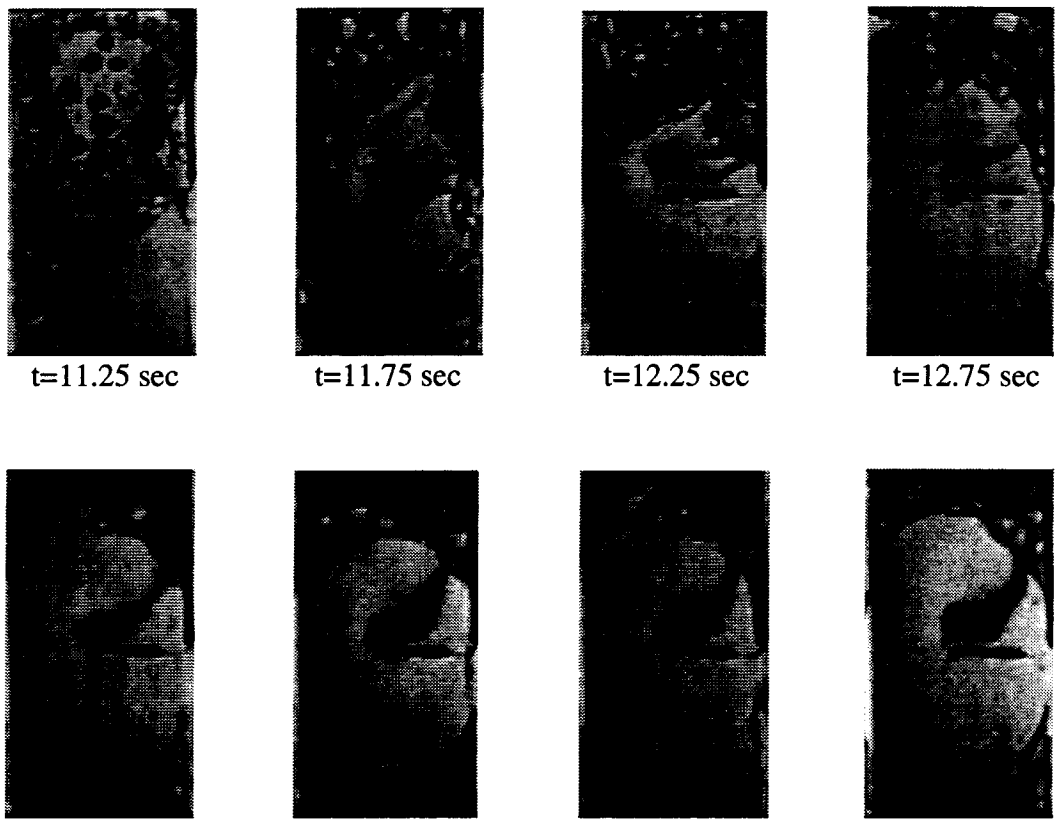

Figure C-10d-1-iv. Sample images showing dryout/rewetting. PBE-IC (STS-60). Run No. 4. Time interval: 11.2 - 15.2 seconds.

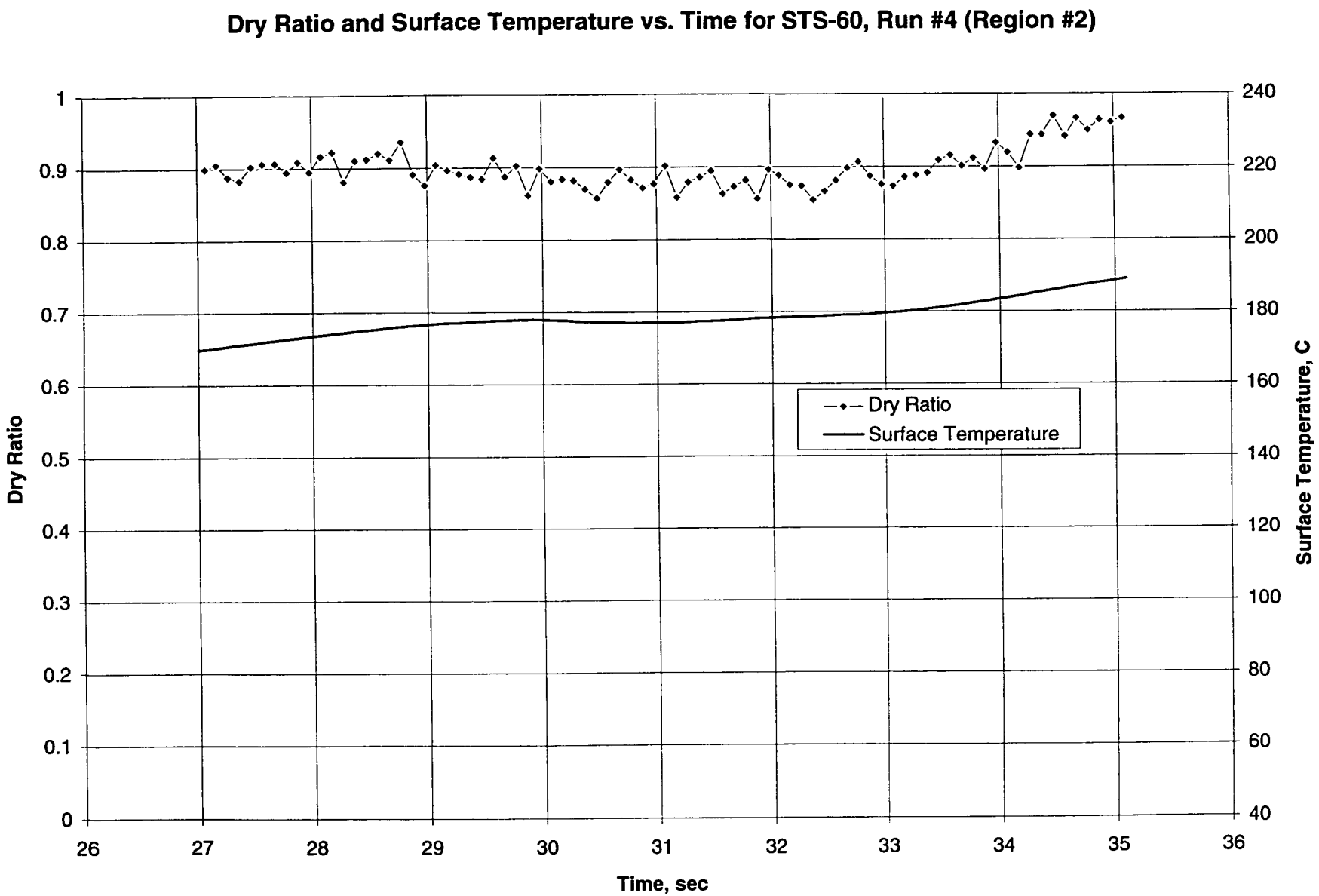

Figure C-10d-2-i. Heater surface dry fraction and mean temperature. PBE-IC (STS-60). Run No. 4. Time interval: 27 - 35 seconds.

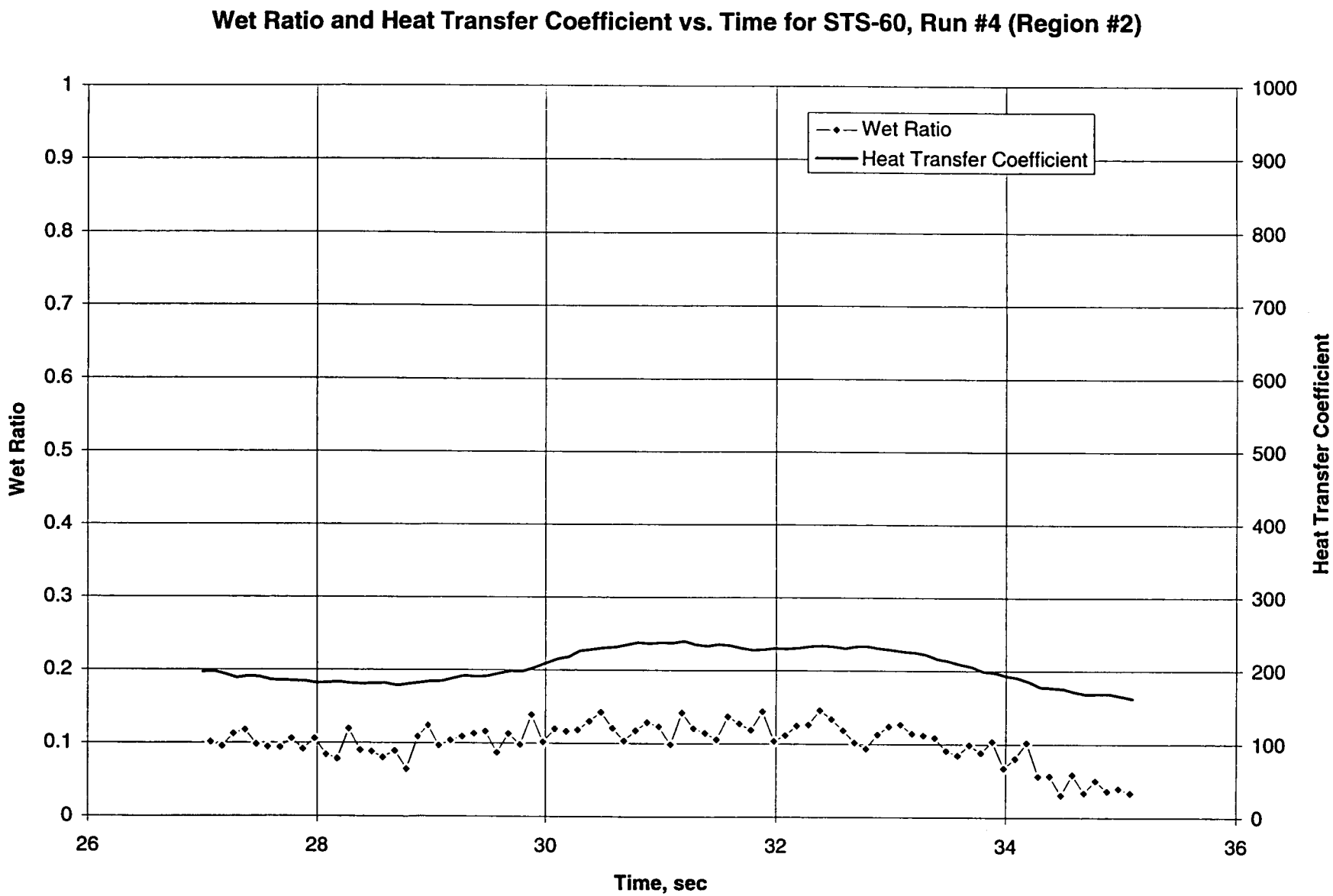

Figure C-10d-2-ii. Heater surface wet fraction and mean heat transfer coefficients. PBE-IC (STS-60). Run No. 4. Time interval: 27 - 35 seconds.

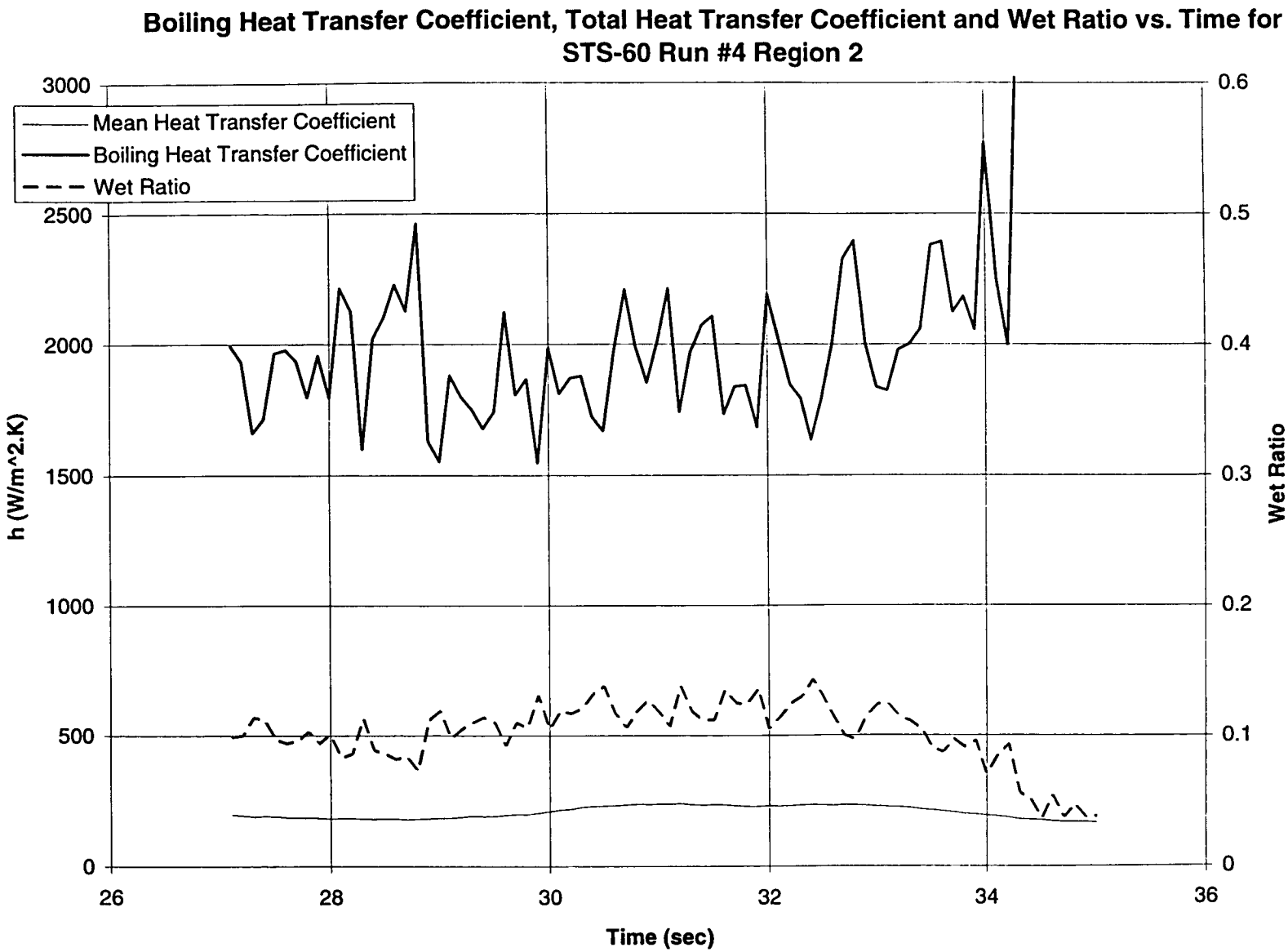

Figure C-10d-2-iii. Development of microgravity boiling heat transfer coefficient. PBE-IC (STS-60). Run No. 4. Time interval: 27 - 35 seconds.

STS 60 Run #4, Region 2

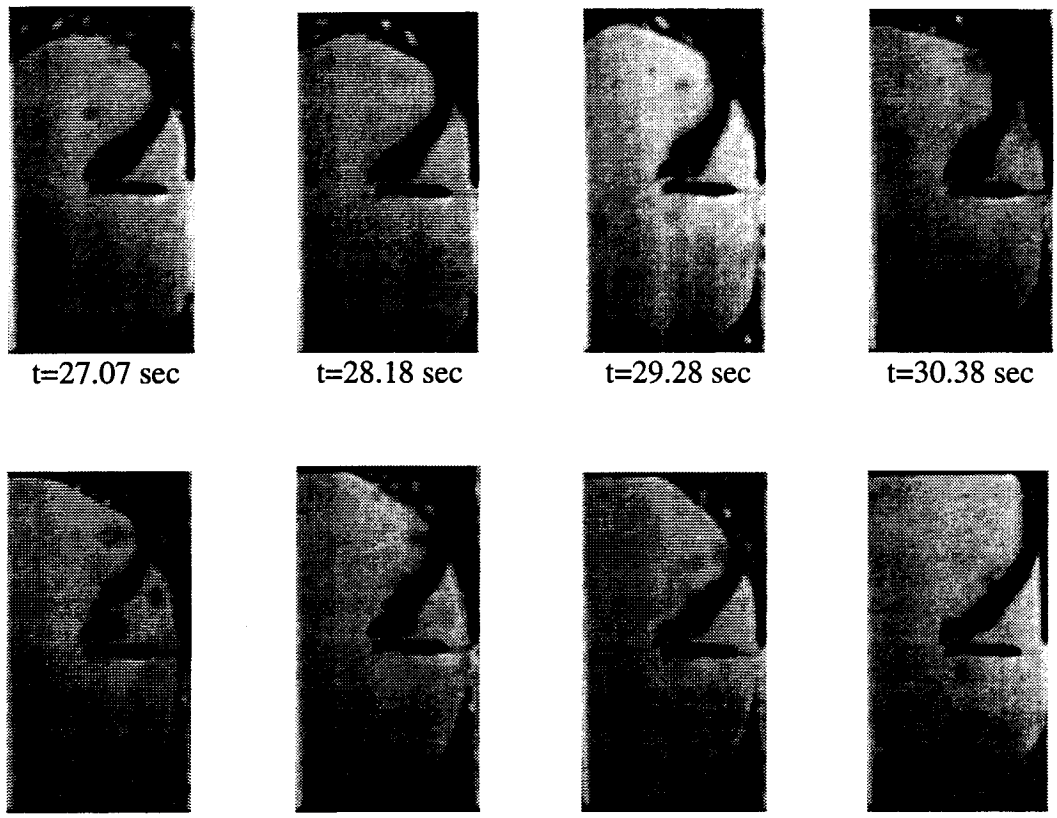

Figure C-10d-2-iv. Sample images showing dryout/rewetting. PBE-IC (STS-60). Run No. 4. Time interval: 27 - 35 seconds.

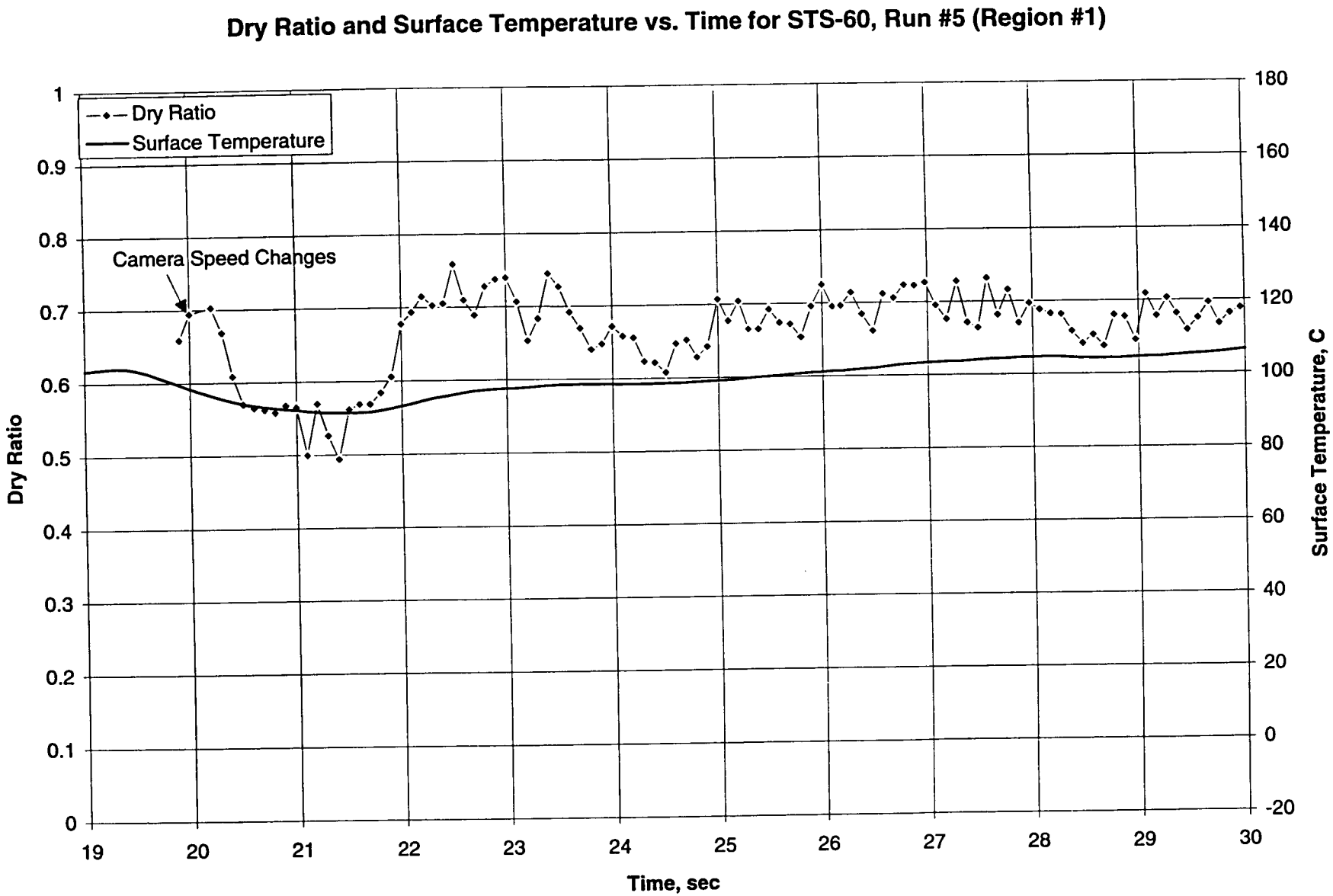

Figure C-10e-1-i. Heater surface dry fraction and mean temperature. PBE-IC (STS-60). Run No. 5. Time interval: 19.9 - 30.0 seconds.

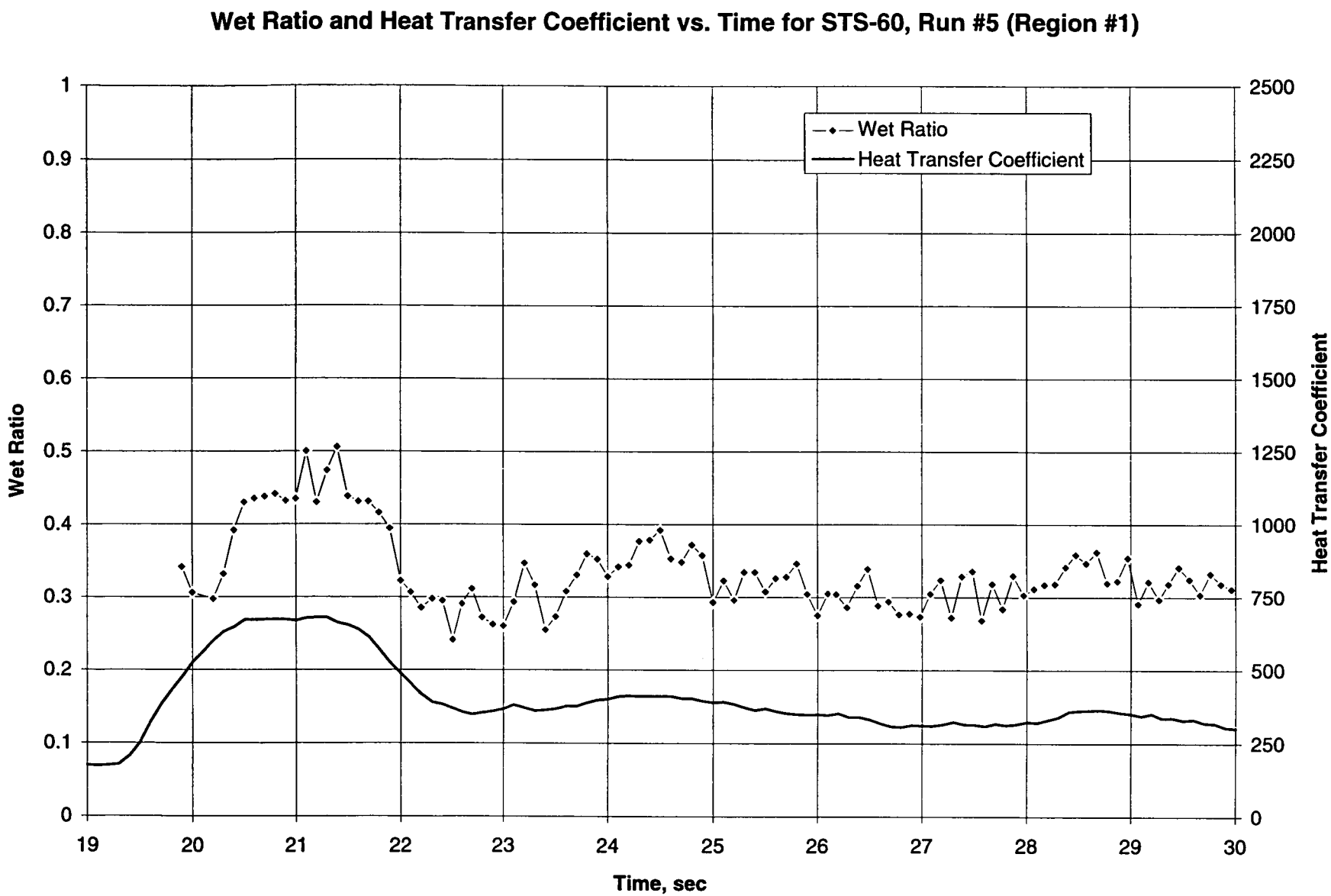

Figure C-10e-1-ii. Heater surface wet fraction and mean heat transfer coefficients. PBE-IC (STS-60). Run No. 5. Time interval: 19.9 - 30.0 seconds.

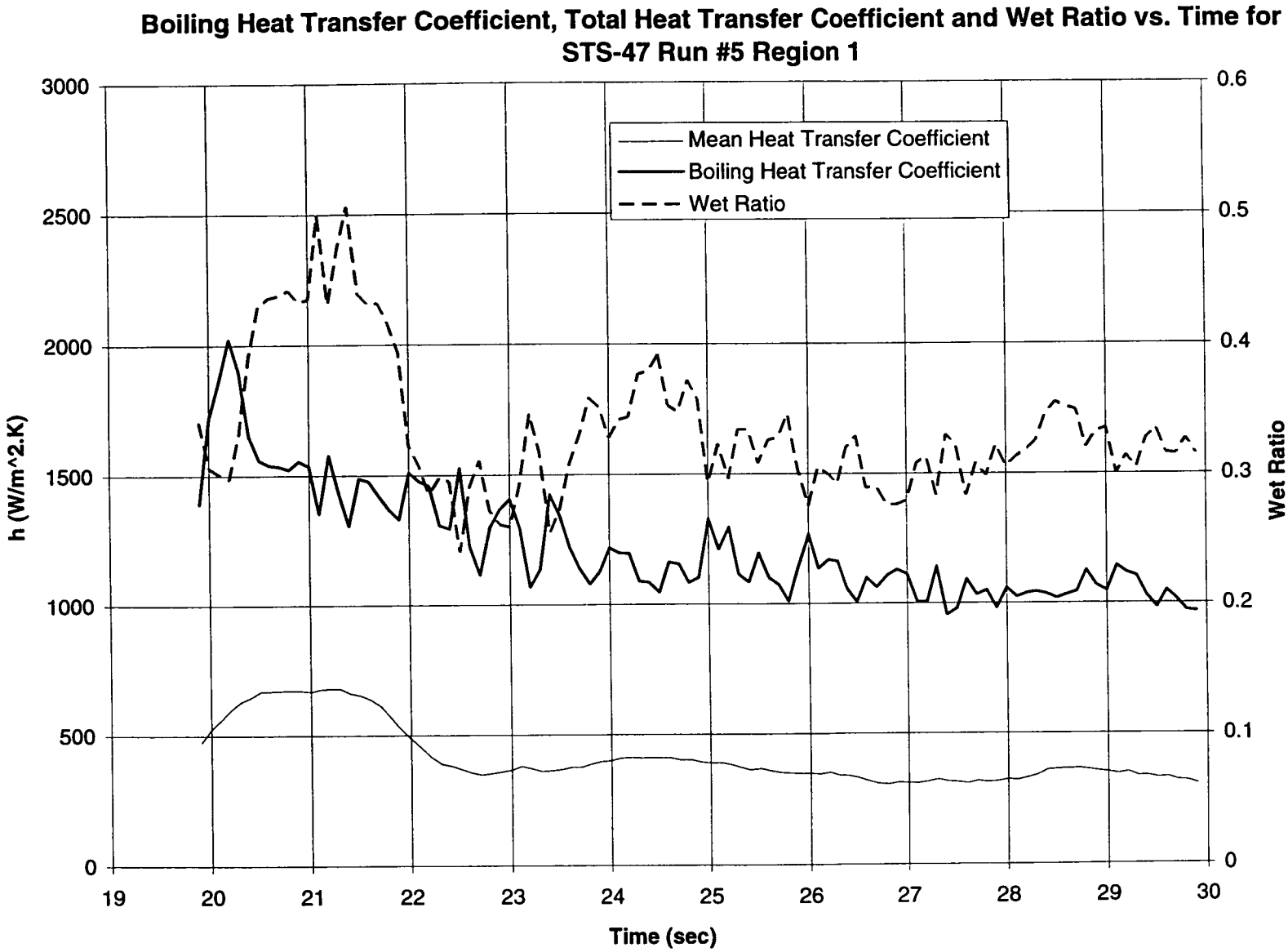

Figure C-10e-1-iii. Development of microgravity boiling heat transfer coefficient. PBE-IC (STS-60). Run No. 5. Time interval: 19.9 - 30.0 seconds.

STS 60 Run #5, Region 1

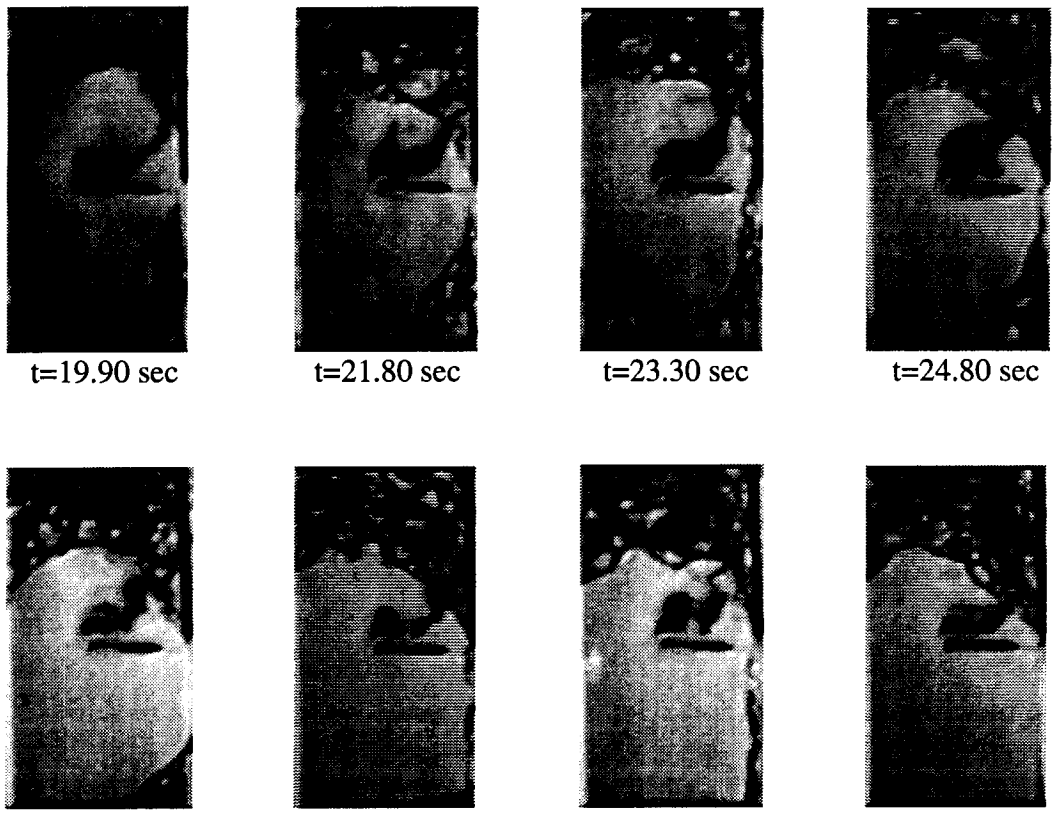

Figure C-10e-1-iv. Sample images showing dryout/rewetting. PBE-IC (STS-60). Run No. 5. Time interval: 19.9 - 30.0 seconds.

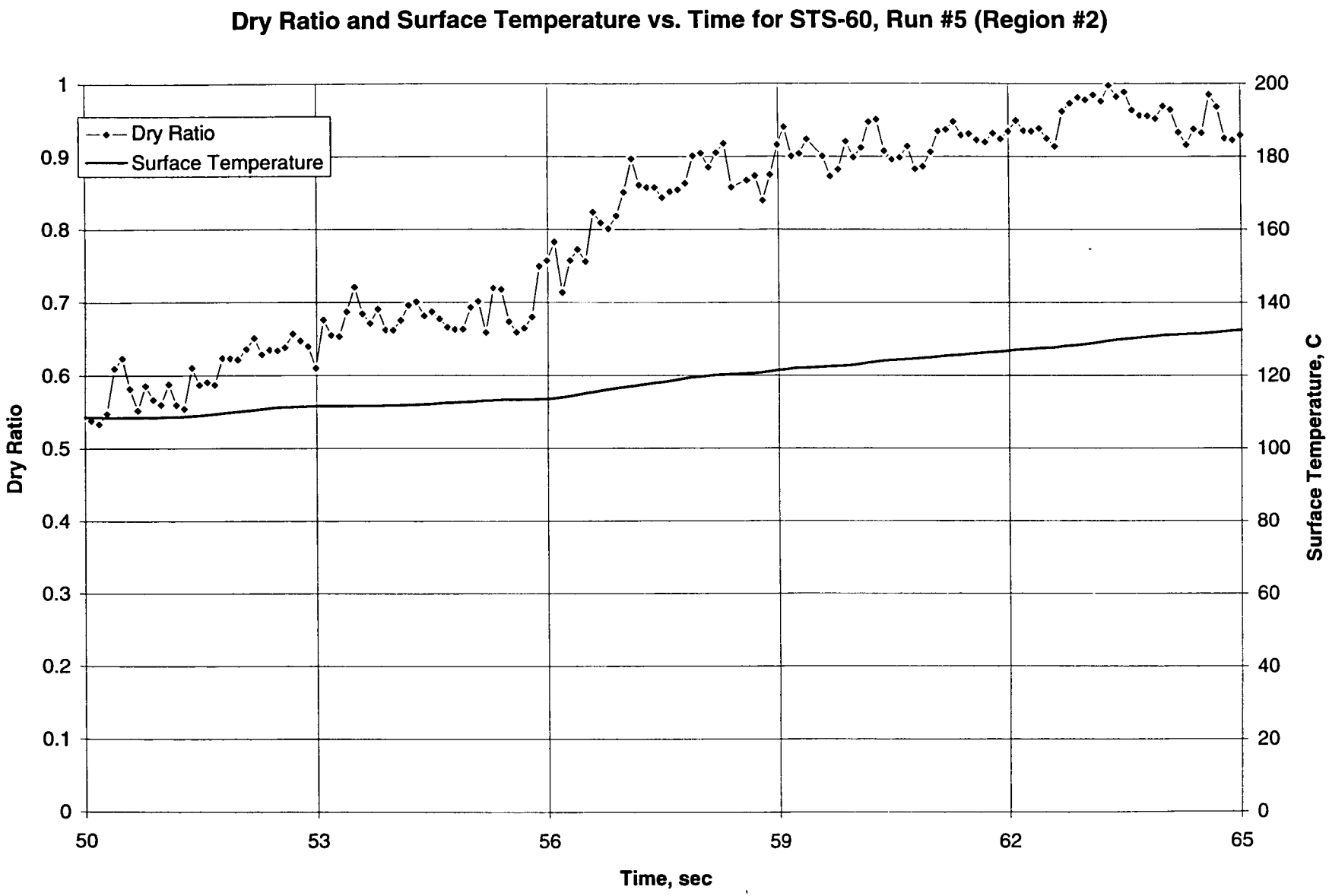

Figure C-10e-2-i. Heater surface dry fraction and mean temperature. PBE-IC (STS-60). Run No. 5. Time interval: 50-65 seconds.

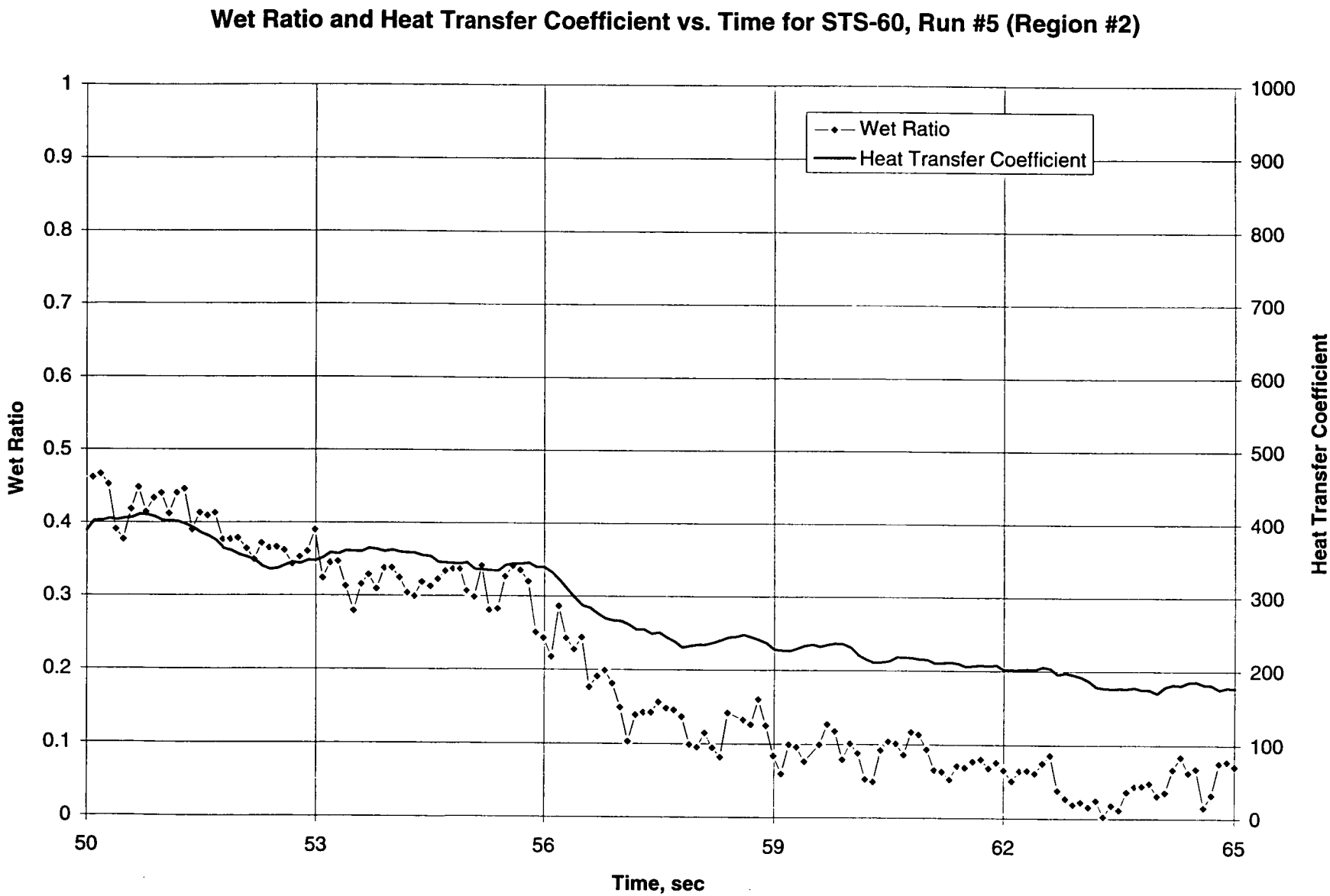

Figure C-10e-2-ii. Heater surface wet fraction and mean heat transfer coefficients. PBE-IC (STS-60). Run No. 5. Time interval: 50-65 seconds.

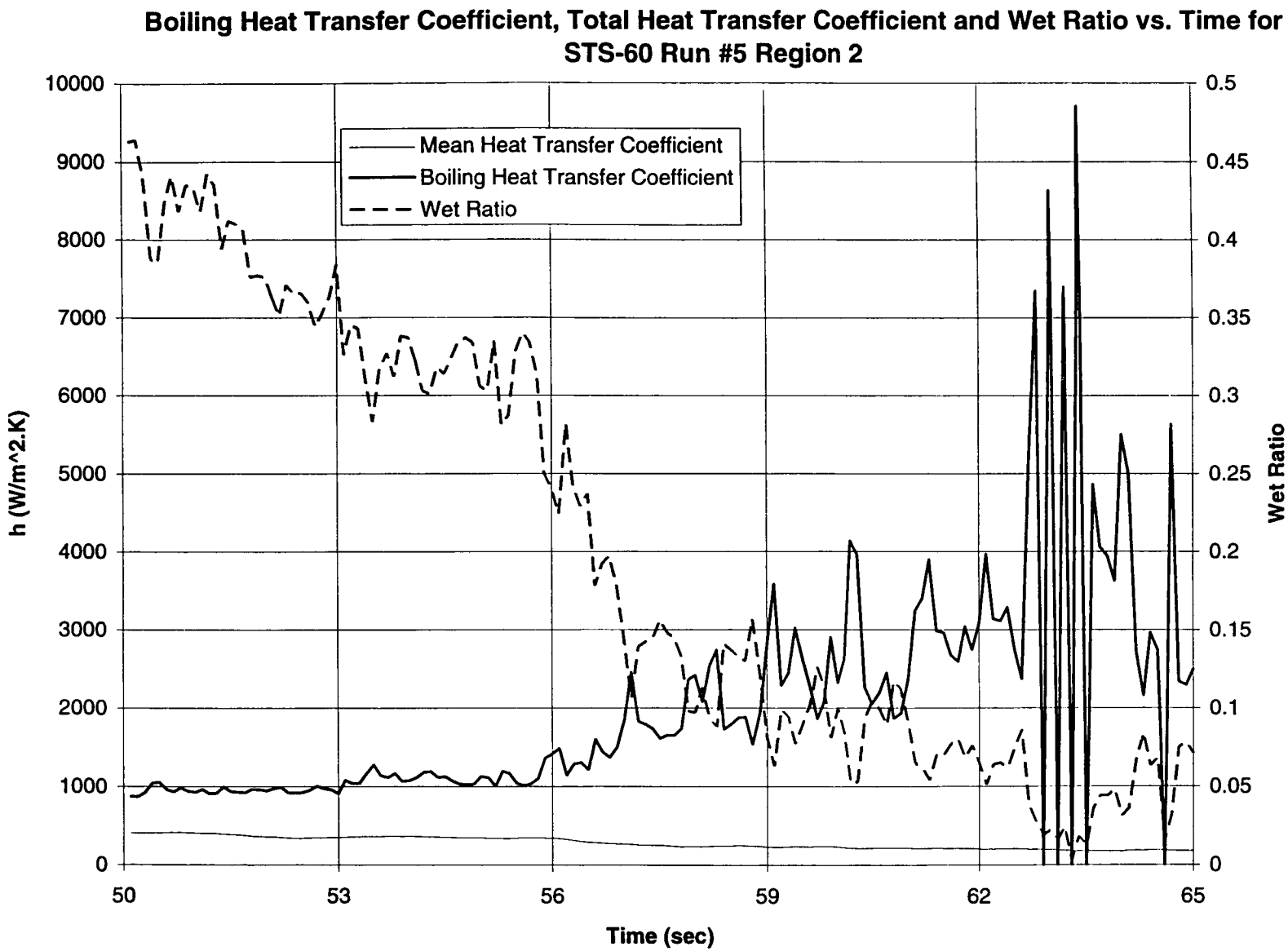

Figure C-10e-2-iii. Development of microgravity boiling heat transfer coefficient. PBE-IC (STS-60). Run No. 5. Time interval: 50-65 seconds.

STS 60 Run #5, Region 2

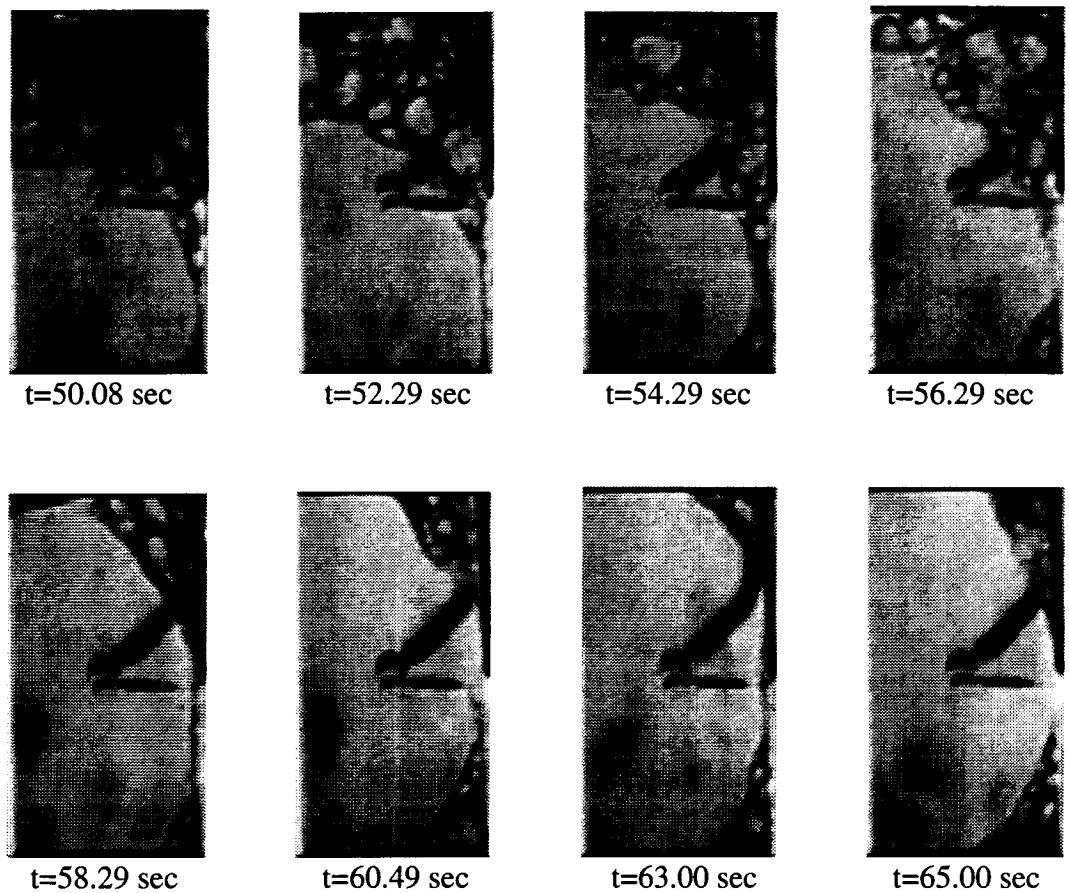

Figure C-10e-2-iv. Sample images showing dryout/rewetting. PBE-IC (STS-60). Run No. 5. Time interval: 50-65 seconds.

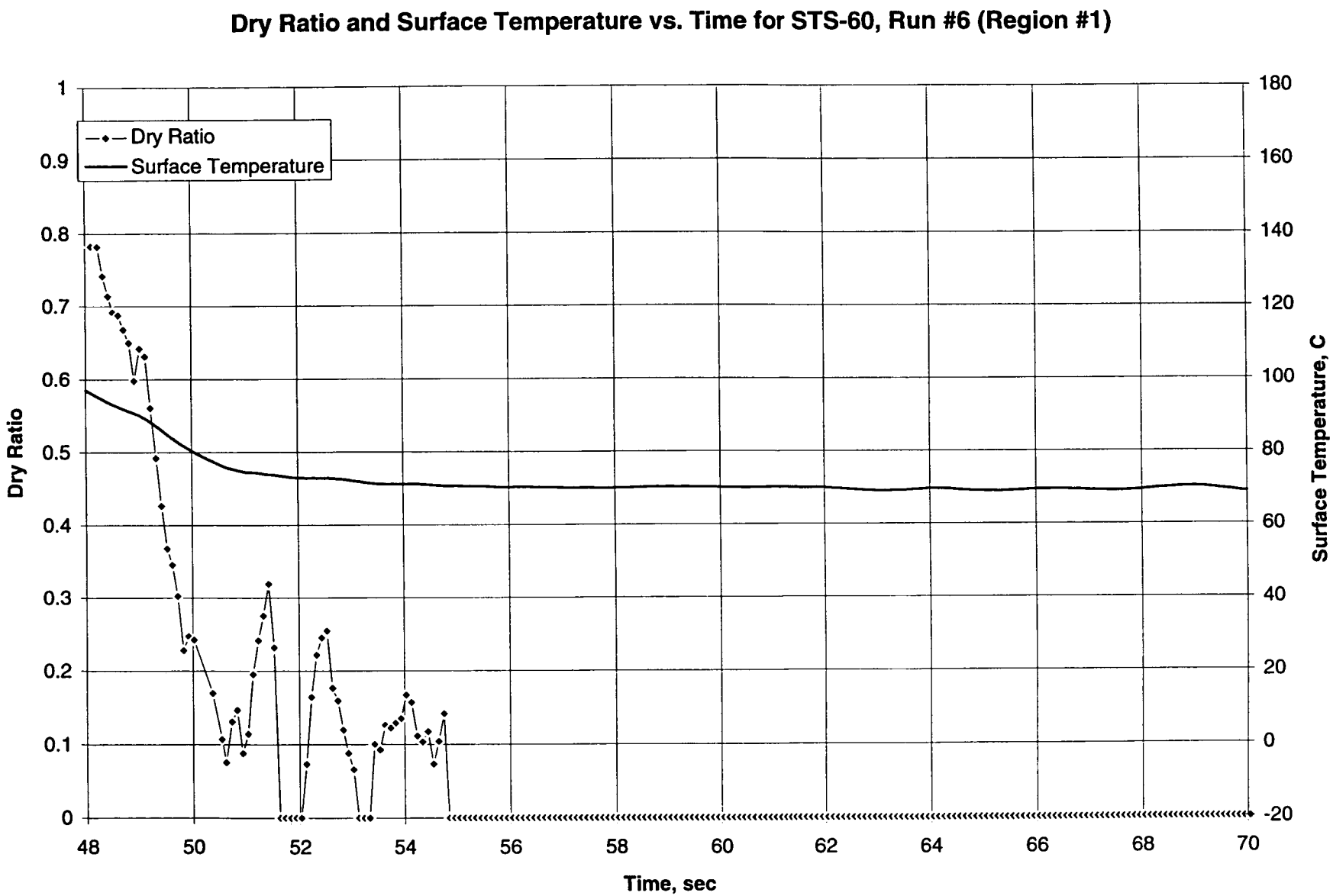

Figure C-10f-1-i. Heater surface dry fraction and mean temperature. PBE-IC (STS-60). Run No. 6. Time interval: 48 - 70 seconds.

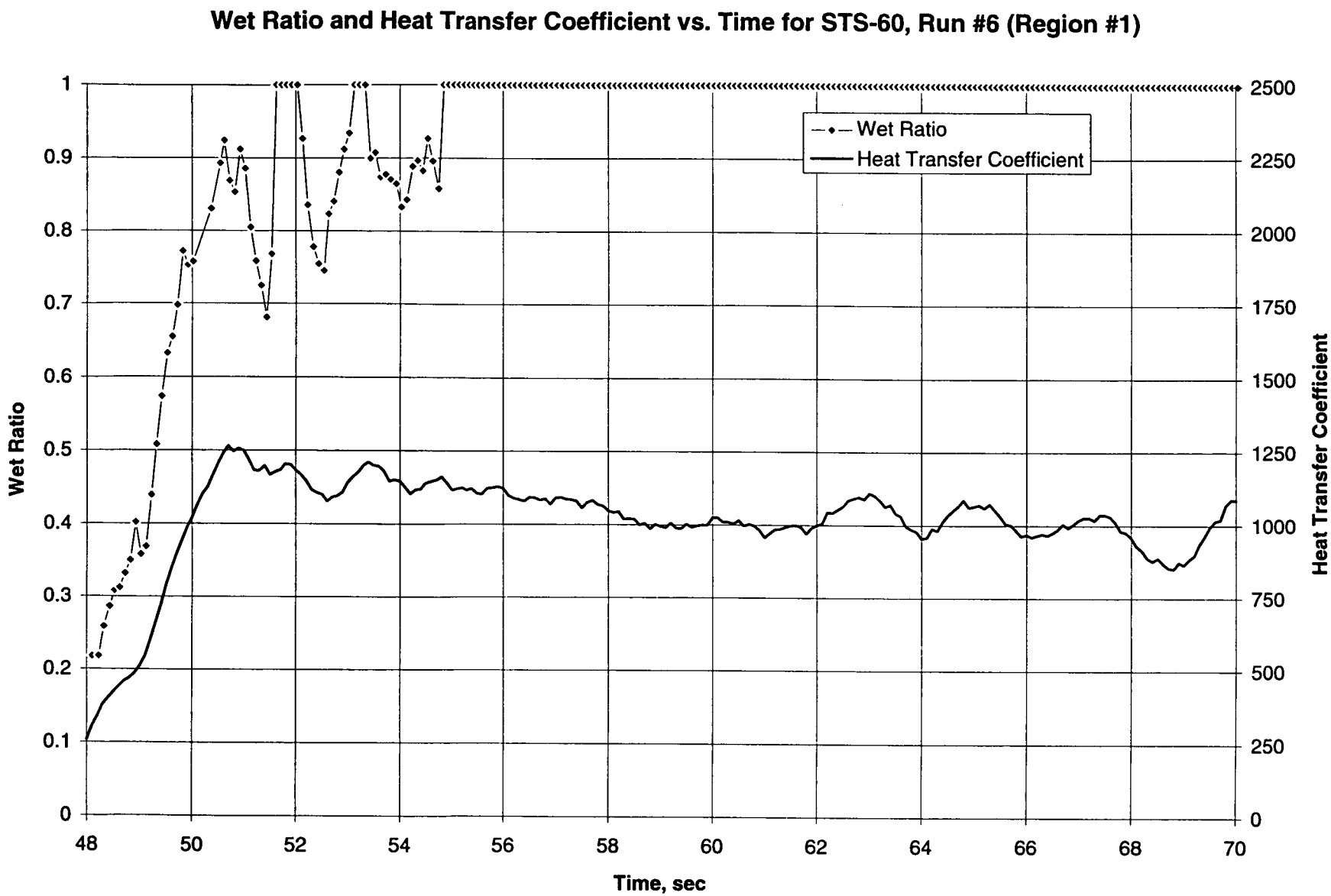

Figure C-10f-1-ii. Heater surface wet fraction and mean heat transfer coefficients. PBE-IC (STS-60). Run No. 6. Time interval: 48 - 70 seconds.

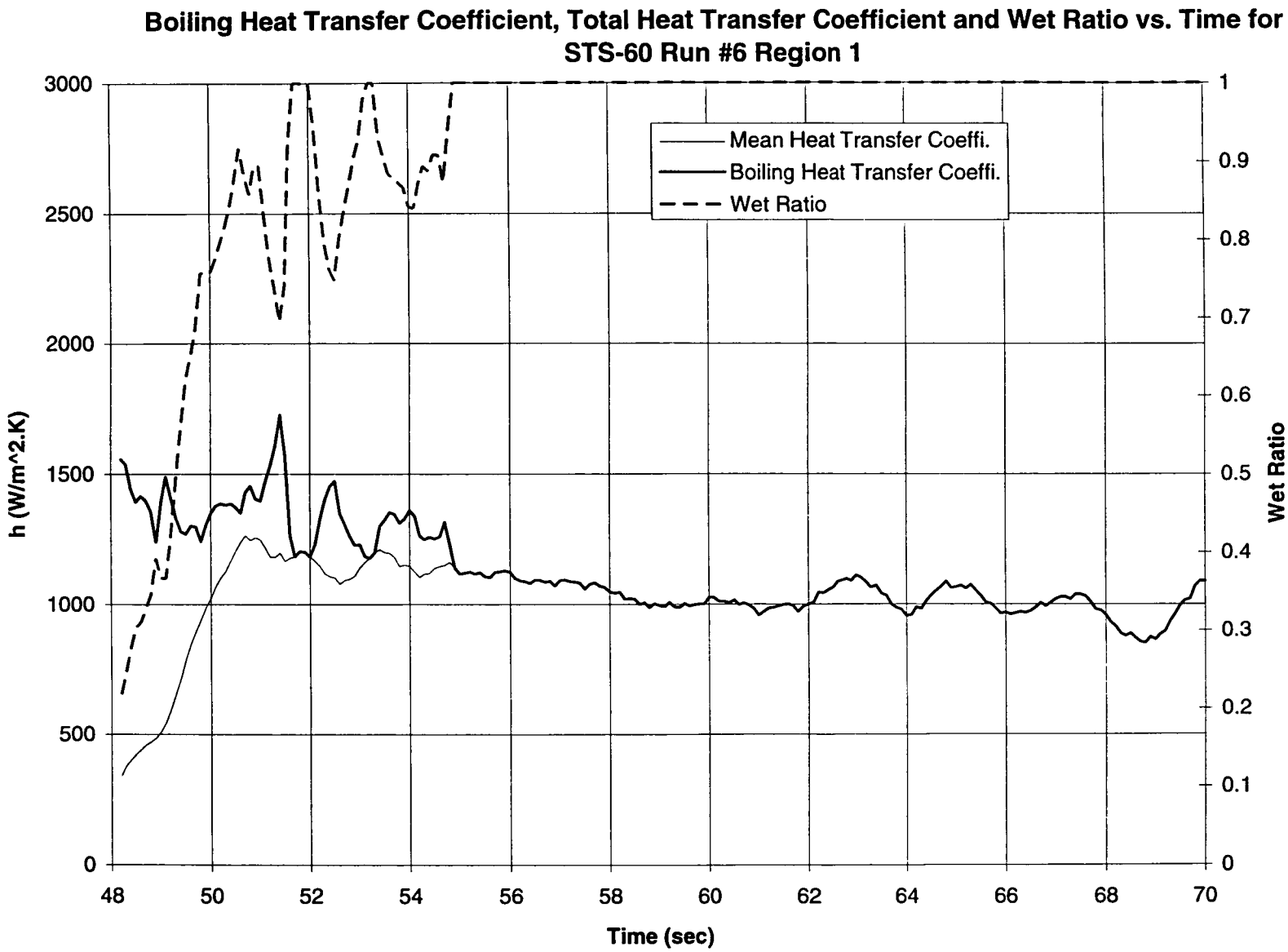

Figure C-10f-1-iii. Development of microgravity boiling heat transfer coefficient. PBE-IC (STS-60). Run No. 6. Time interval: 48 - 70 seconds.

STS 60 Run#6, Region 1

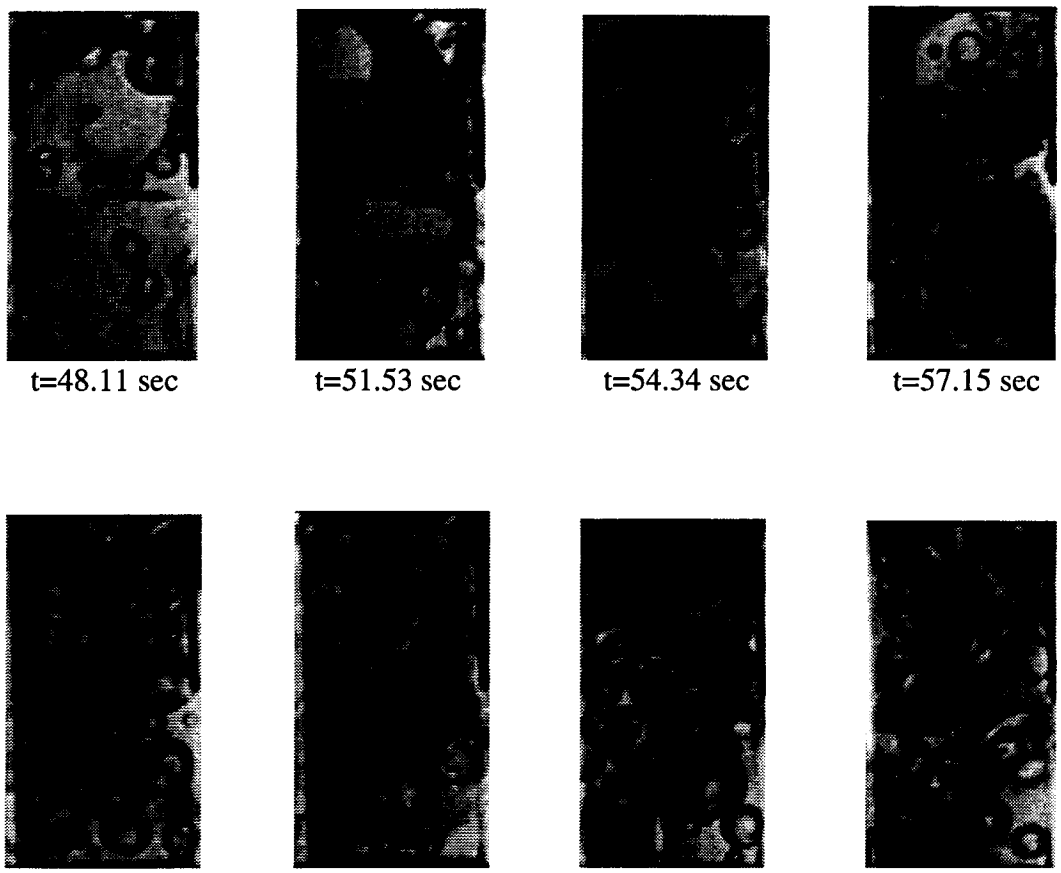

Figure C-10f-1-iv. Sample images showing dryout/rewetting. PBE-IC (STS-60). Run No. 6. Time interval: 48 - 70 seconds.

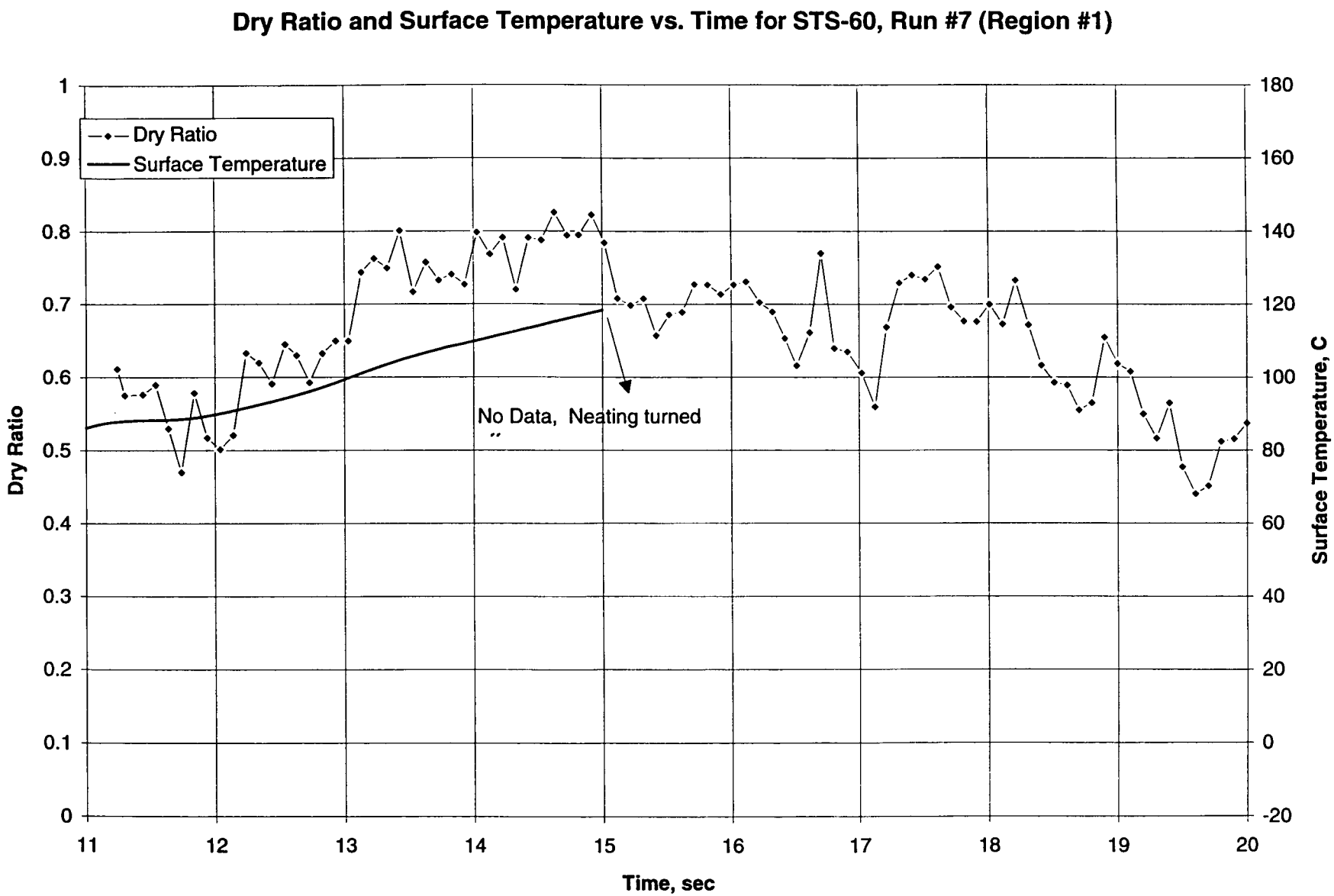

Figure C-10g-1-i. Heater surface dry fraction and mean temperature. PBE-IC (STS-60). Run No. 7. Time interval: 11.2 - 20.0 seconds.

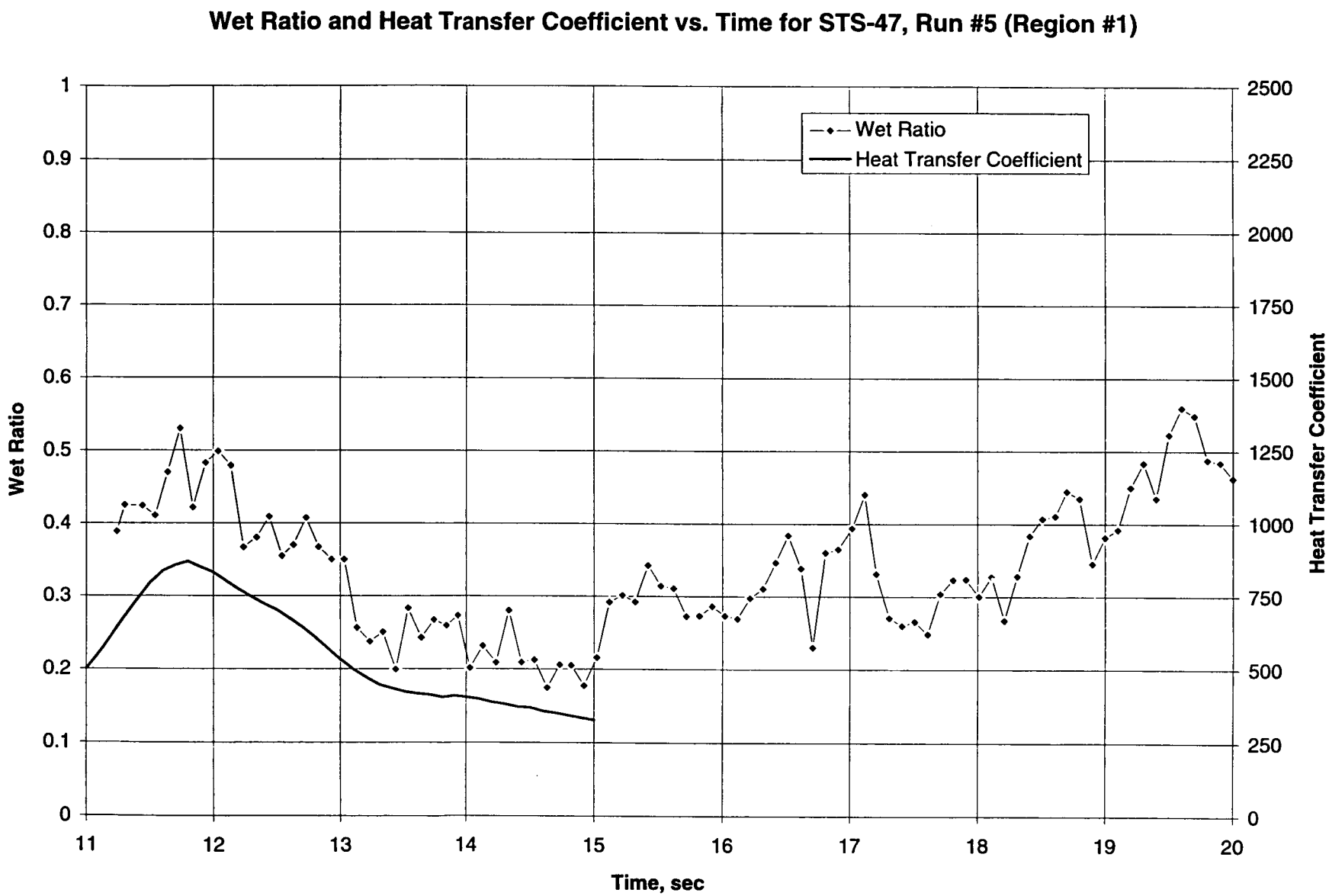

Figure C-10g-1-ii. Heater surface wet fraction and mean heat transfer coefficients. PBE-IC (STS-60). Run No. 7. Time interval: 11.2 - 20.0 seconds.

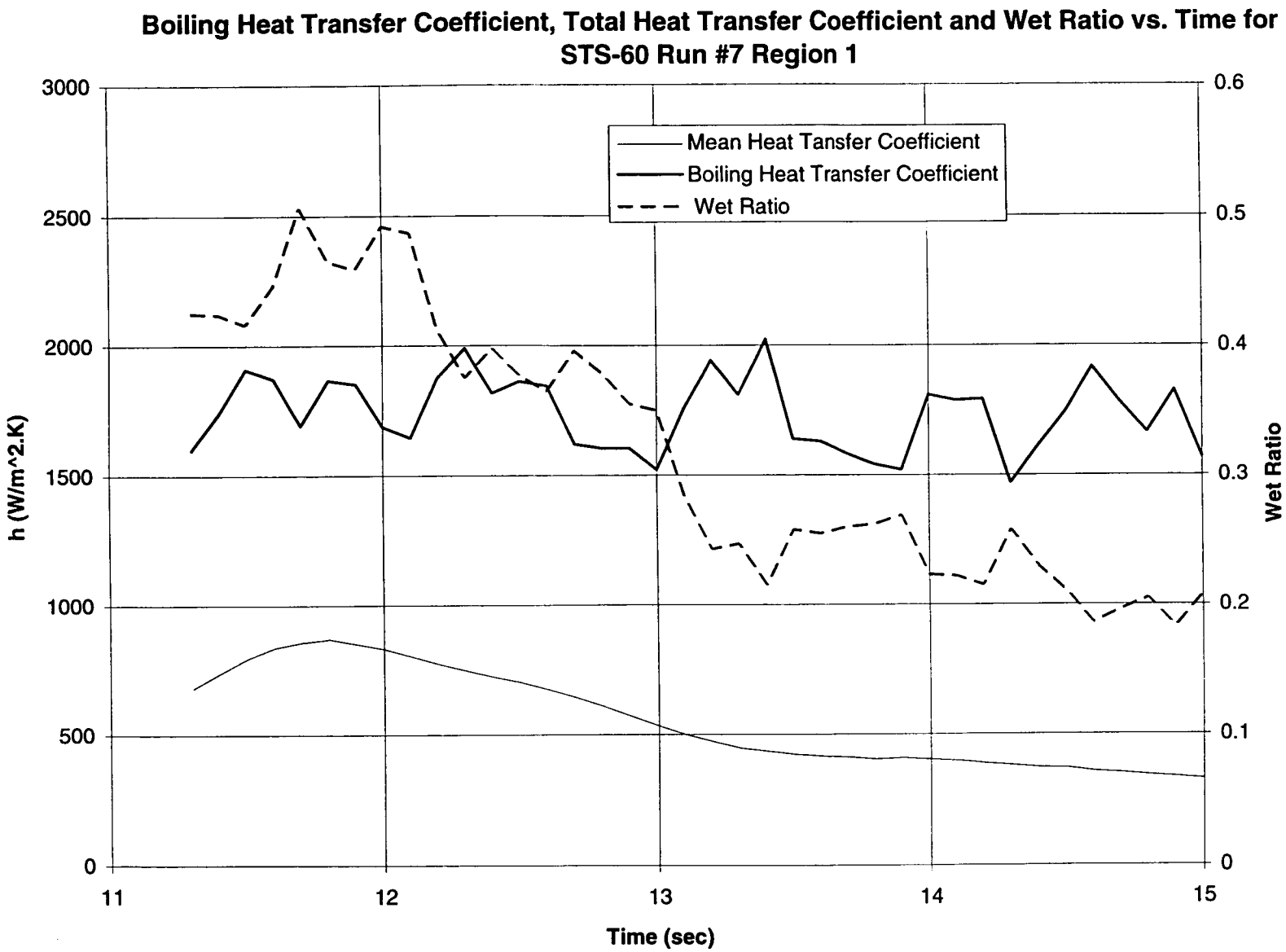

Figure C-10g-1-iii. Development of microgravity boiling heat transfer coefficient. PBE-IC (STS-60). Run No. 7. Time interval: 11.2 - 20.0 seconds.

STS 60 Run #7, Region 1

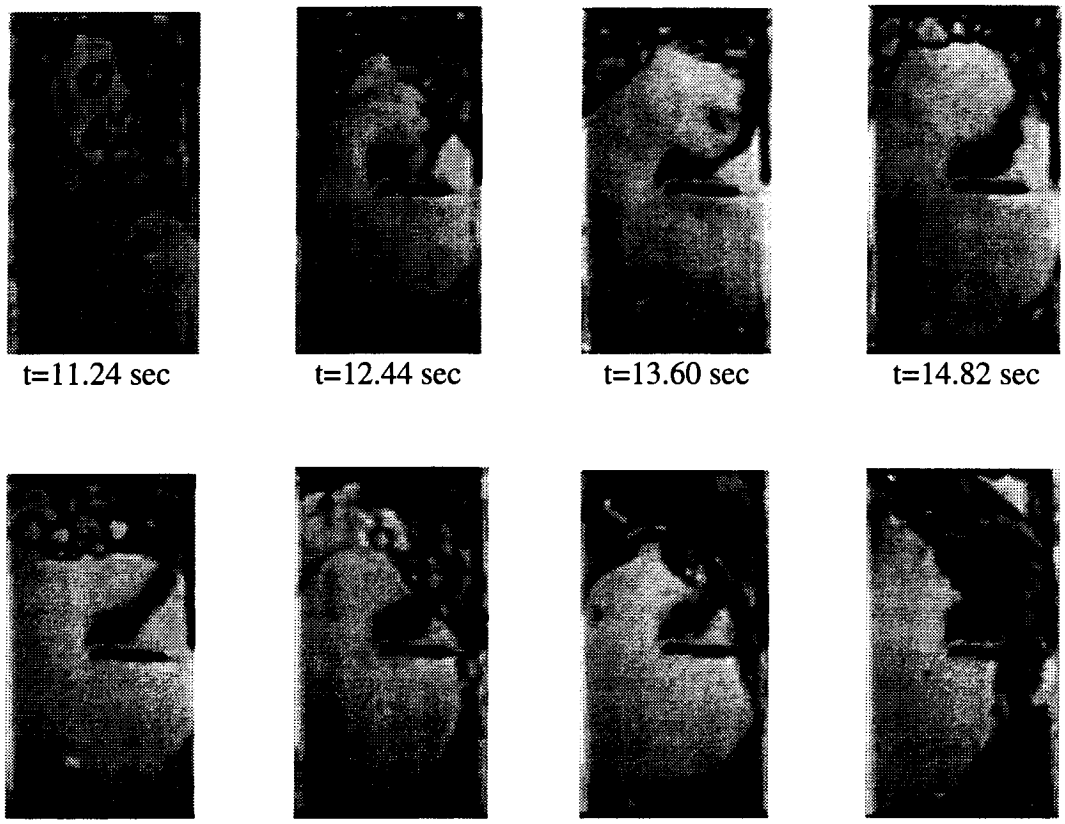

Figure C-10g-1-iv. Sample images showing dryout/rewetting. PBE-IC (STS-60). Run No. 7. Time interval: 11.2 - 20.0 seconds.

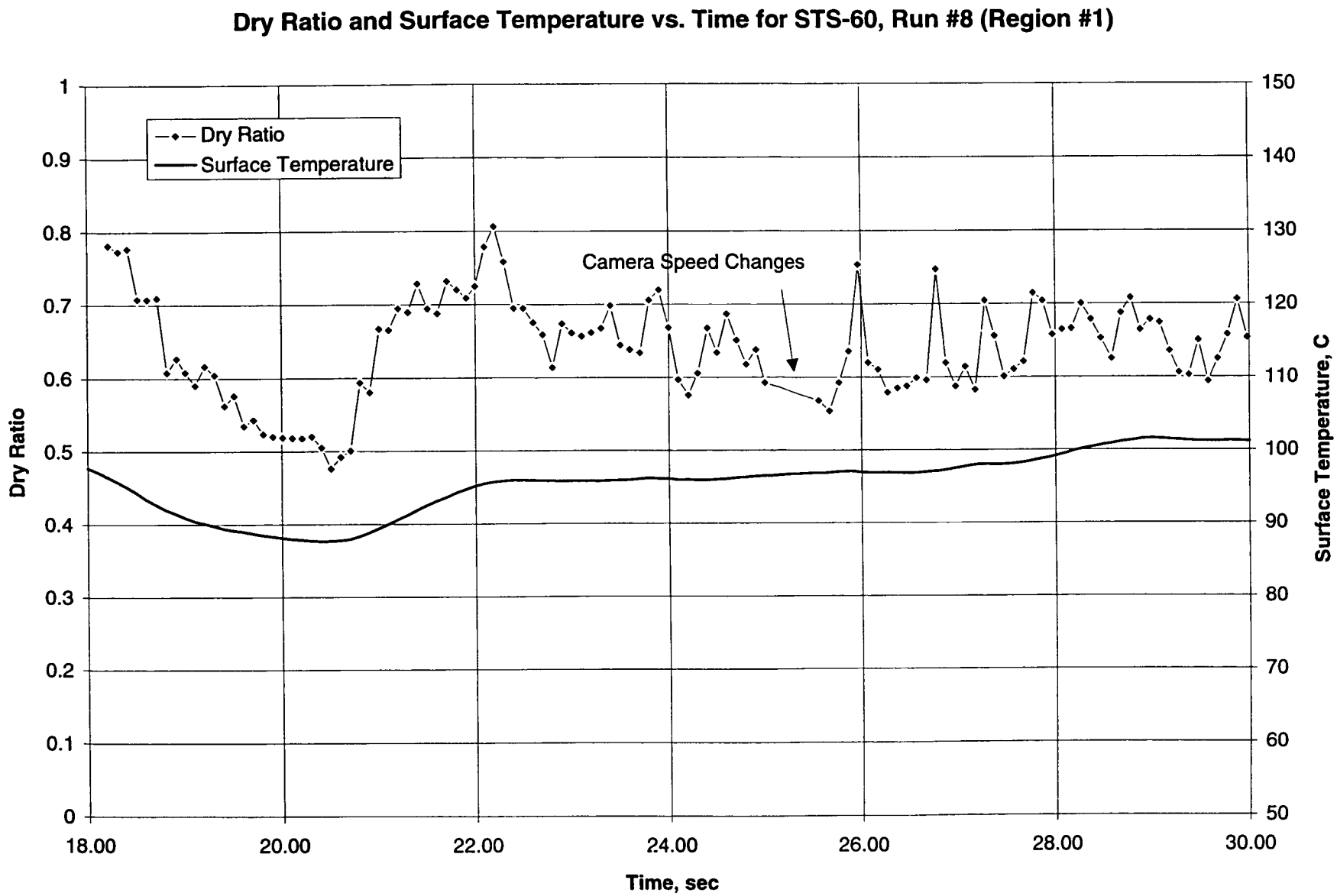

Figure C-10h-1-i. Heater surface dry fraction and mean temperature. PBE-IC (STS-60). Run No. 8. Time interval: 18.2 - 30.0 seconds.

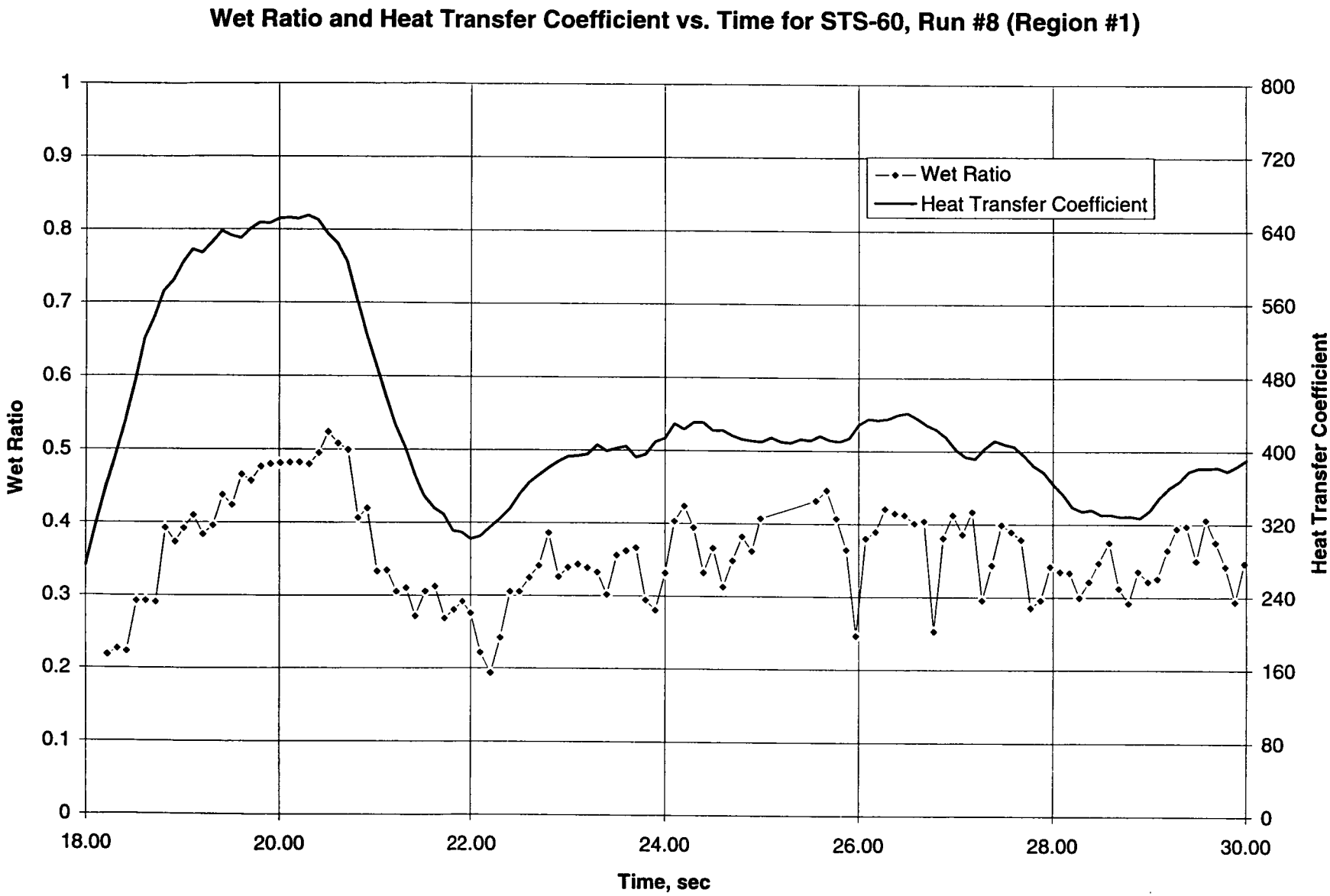

Figure C-10h-1-ii. Heater surface wet fraction and mean heat transfer coefficients. PBE-IC (STS-60). Run No. 8. Time interval: 18.2 - 30.0 seconds.

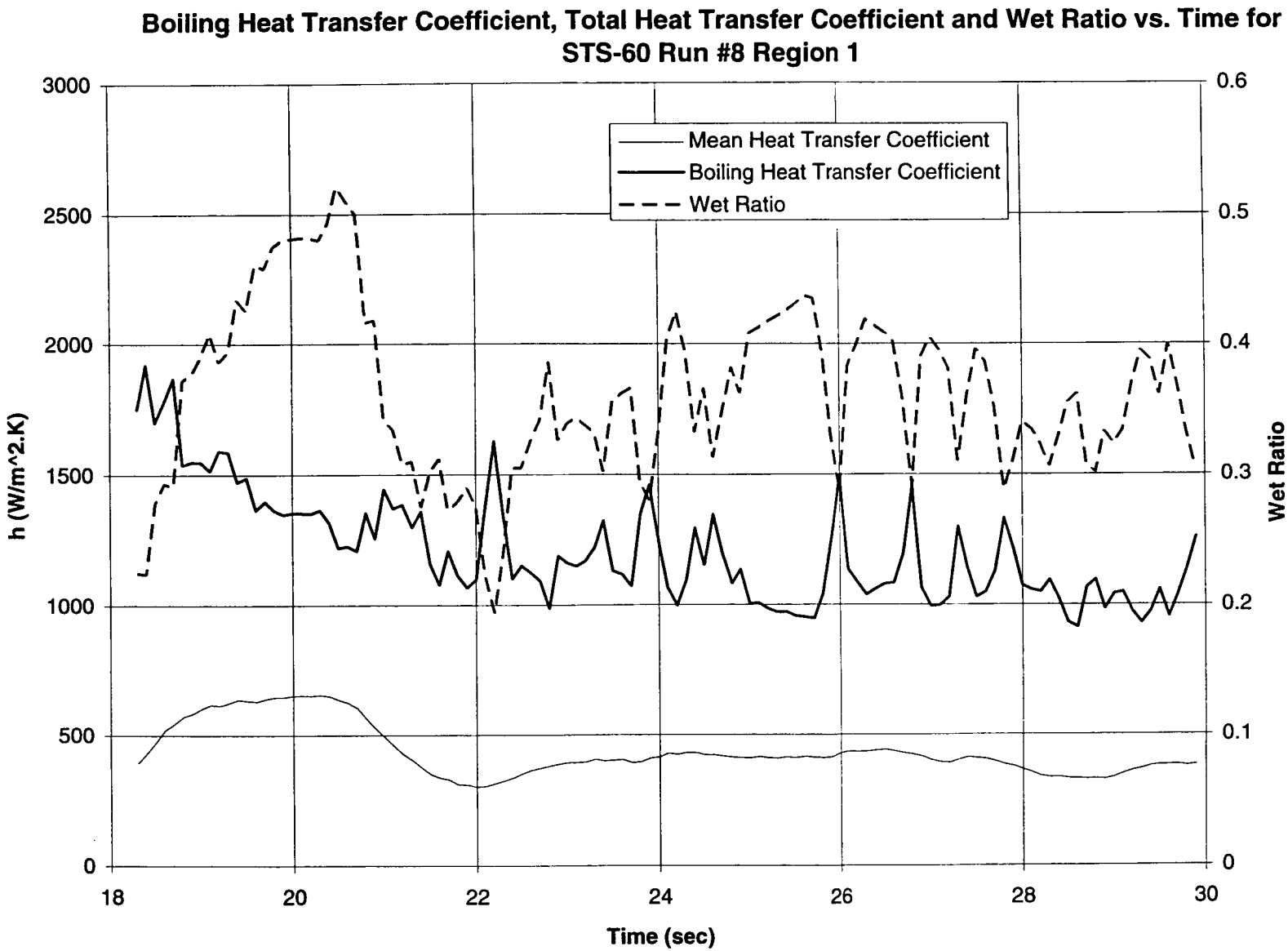

Figure C-10h-1-iii. Development of microgravity boiling heat transfer coefficient. PBE-IC (STS-60). Run No. 8. Time interval: 18.2 - 30.0 seconds.

STS 60, Run#8, Region#1

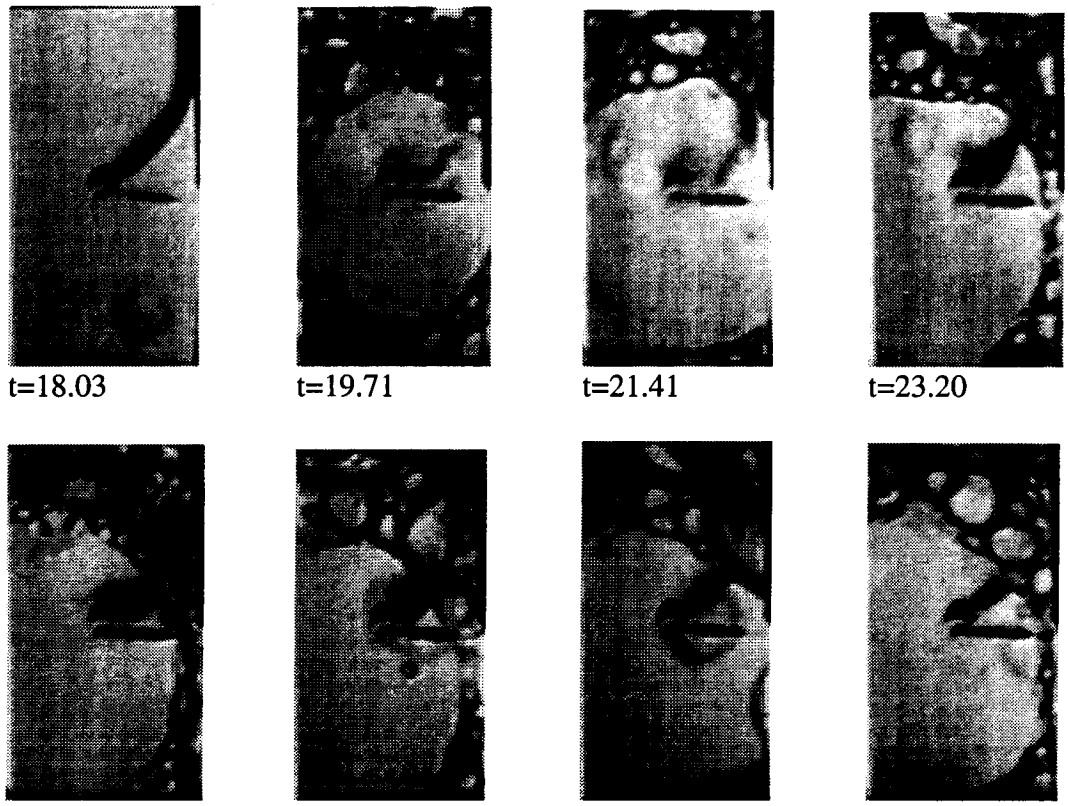

Figure C-10h-1-iv. Sample images showing dryout/rewetting. PBE-IC (STS-60). Run No. 8. Time interval: 18.2 - 30.0 seconds.

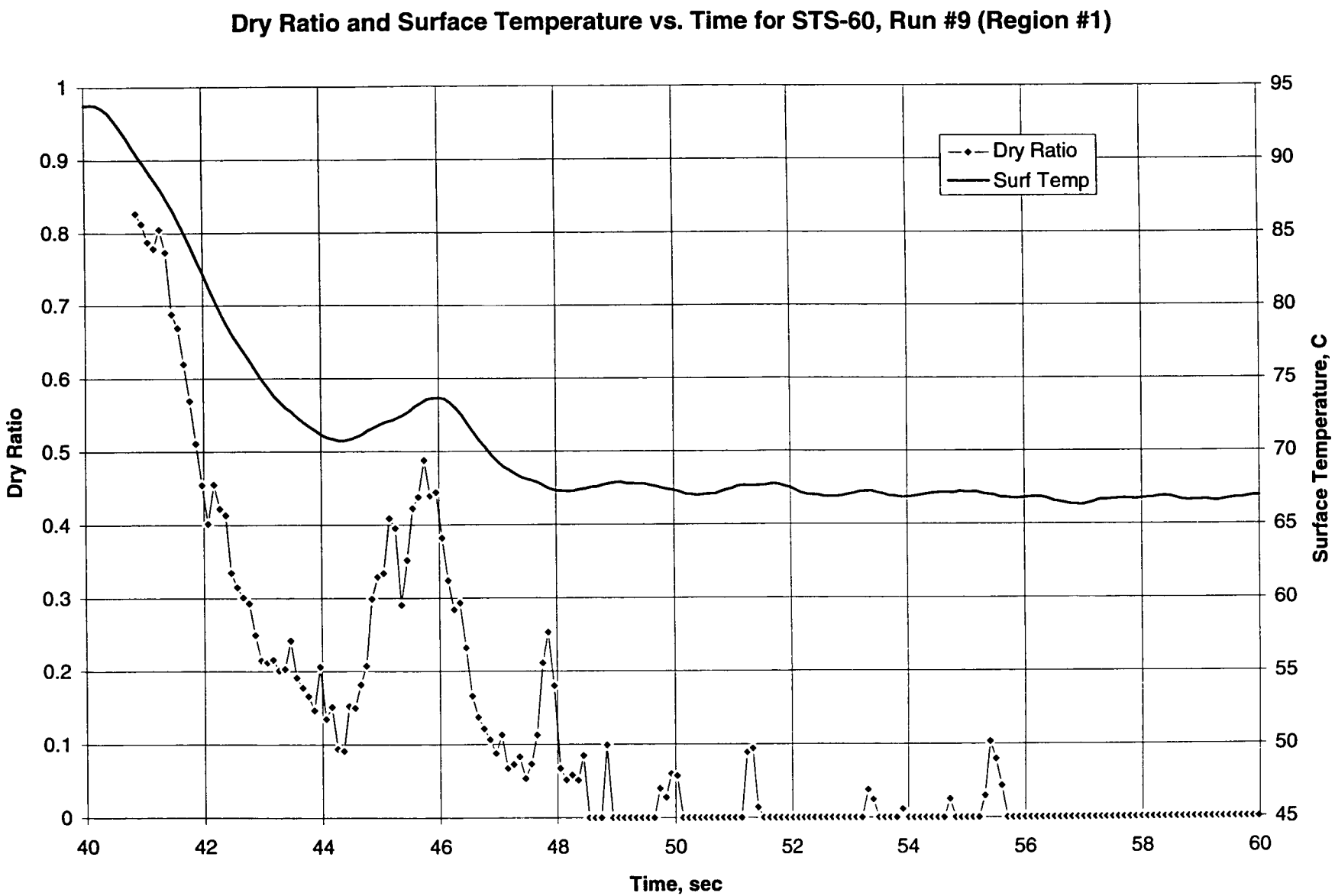

Figure C-10i-1-i. Heater surface dry fraction and mean temperature. PBE-IC (STS-60). Run No. 9. Time interval: 40.9 - 60.0 seconds.

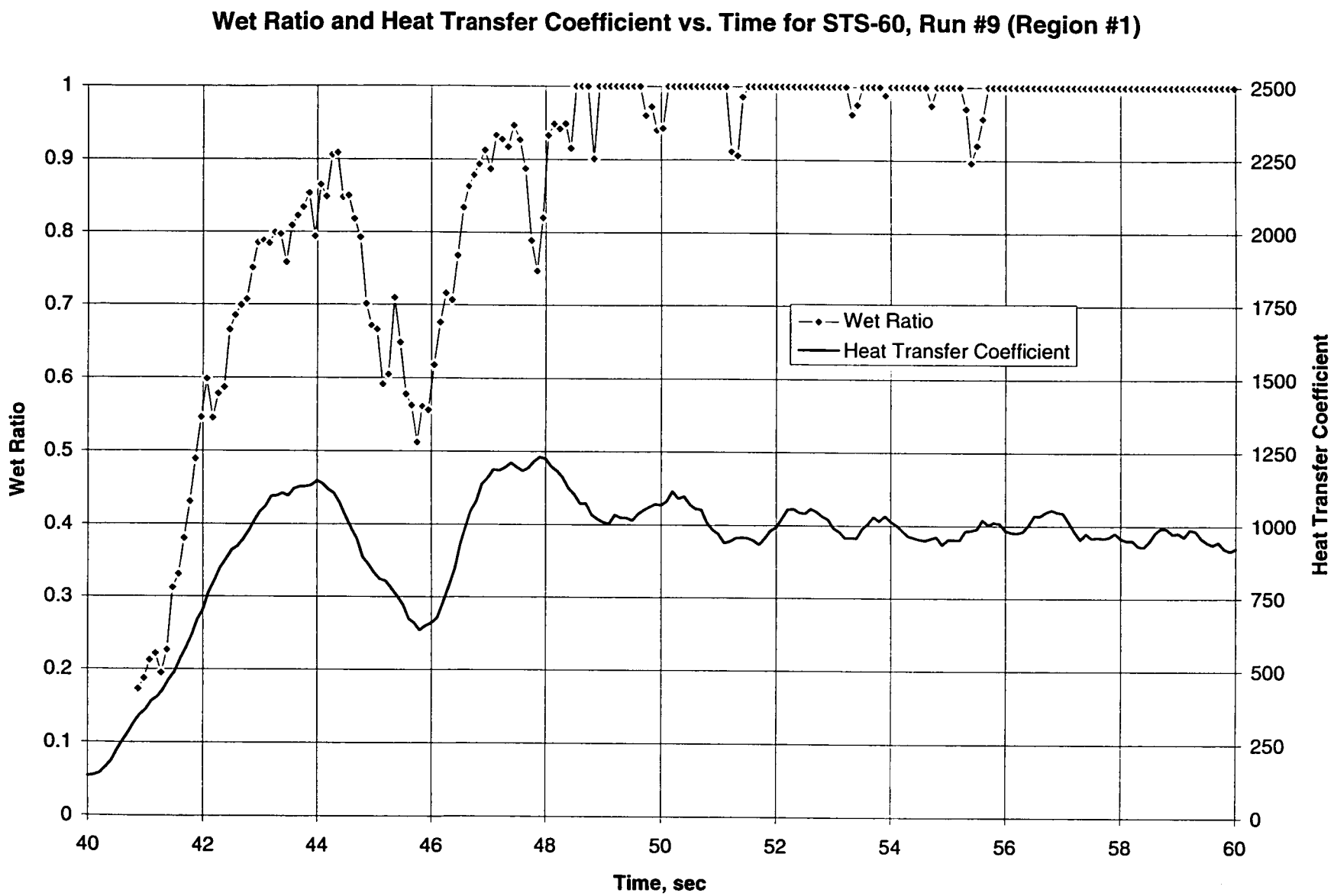

Figure C-10i-1-ii. Heater surface wet fraction and mean heat transfer coefficients. PBE-IC (STS-60). Run No. 9. Time interval: 40.9 - 60.0 seconds.

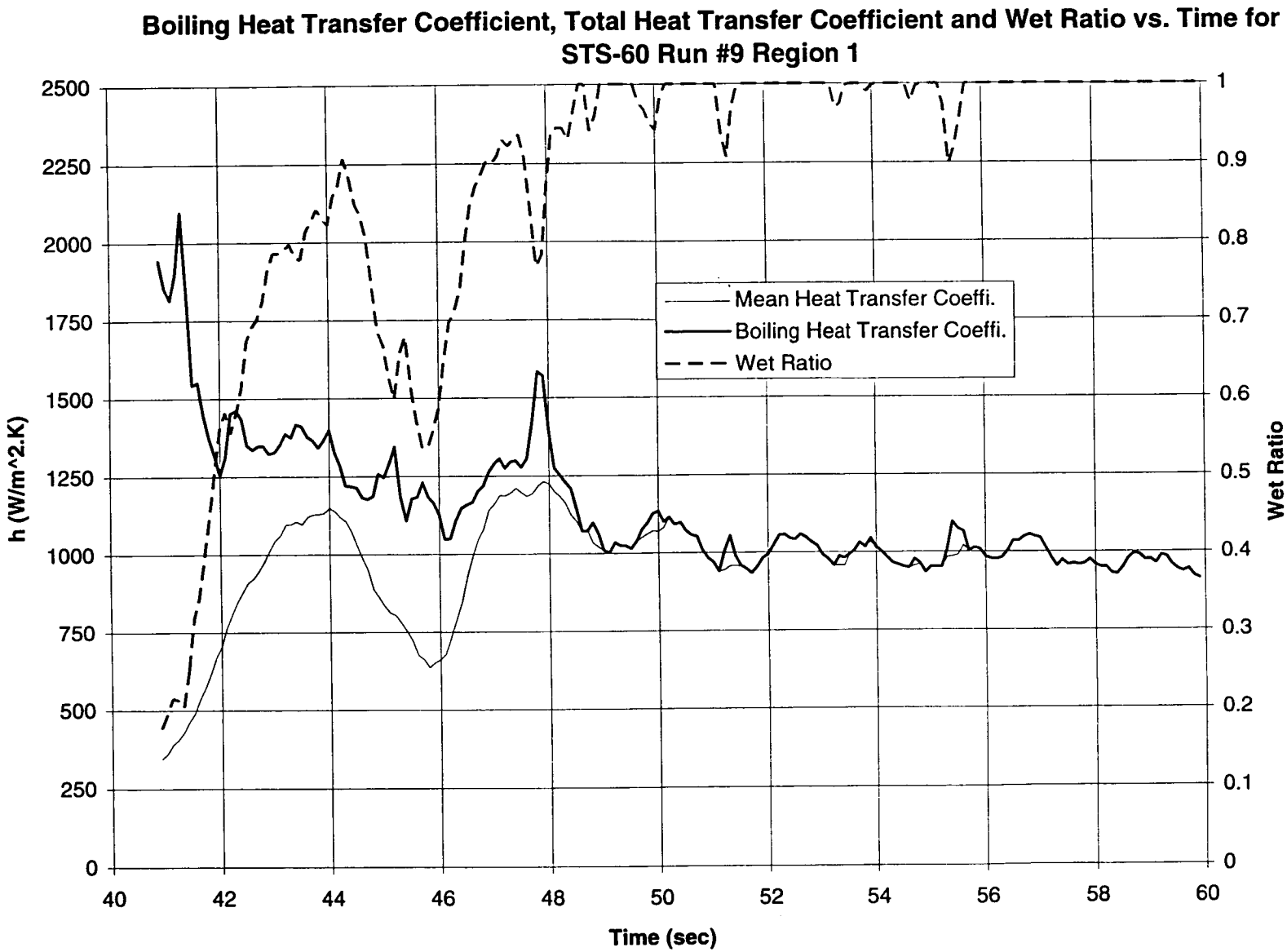

Figure C-10i-1-iii. Development of microgravity boiling heat transfer coefficient. PBE-IC (STS-60). Run No. 9. Time interval: 40.9 - 60.0 seconds.

STS 60, Run#9, Region#1

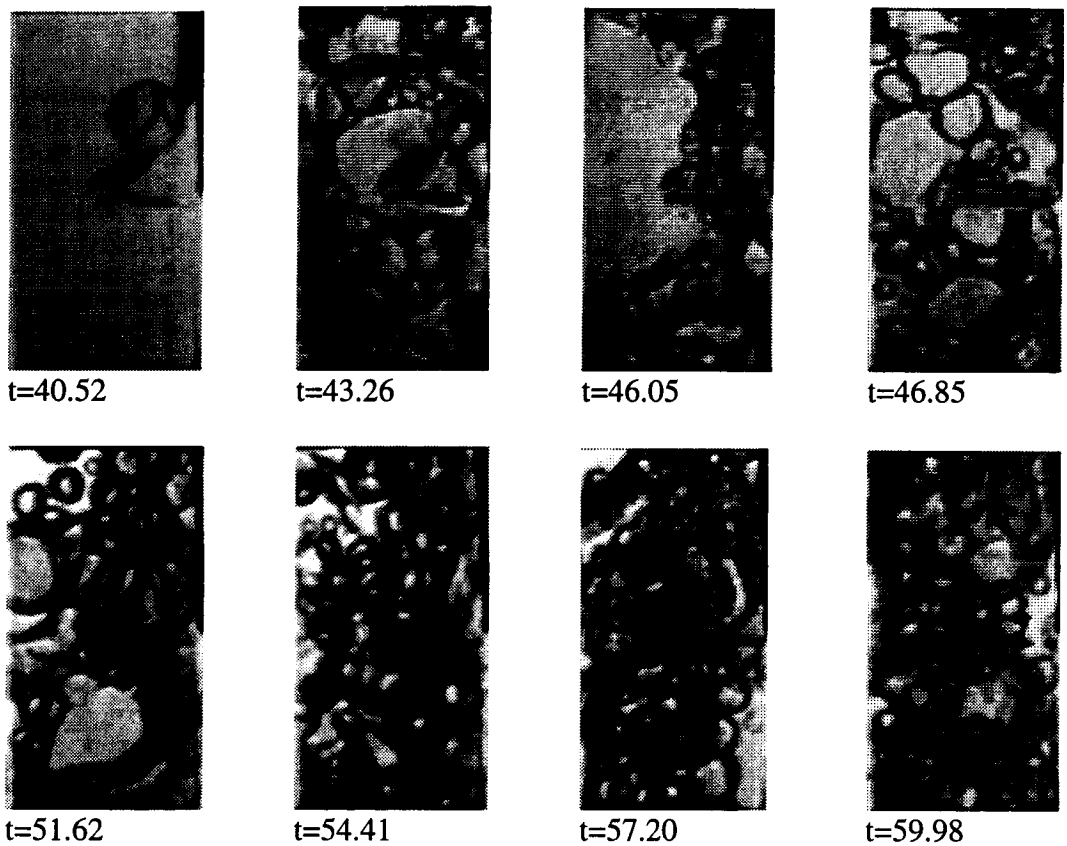

Figure C-10i-1-iv. Sample images showing dryout/rewetting. PBE-IC (STS-60). Run No. 9. Time interval: 40.9 - 60.0 seconds.

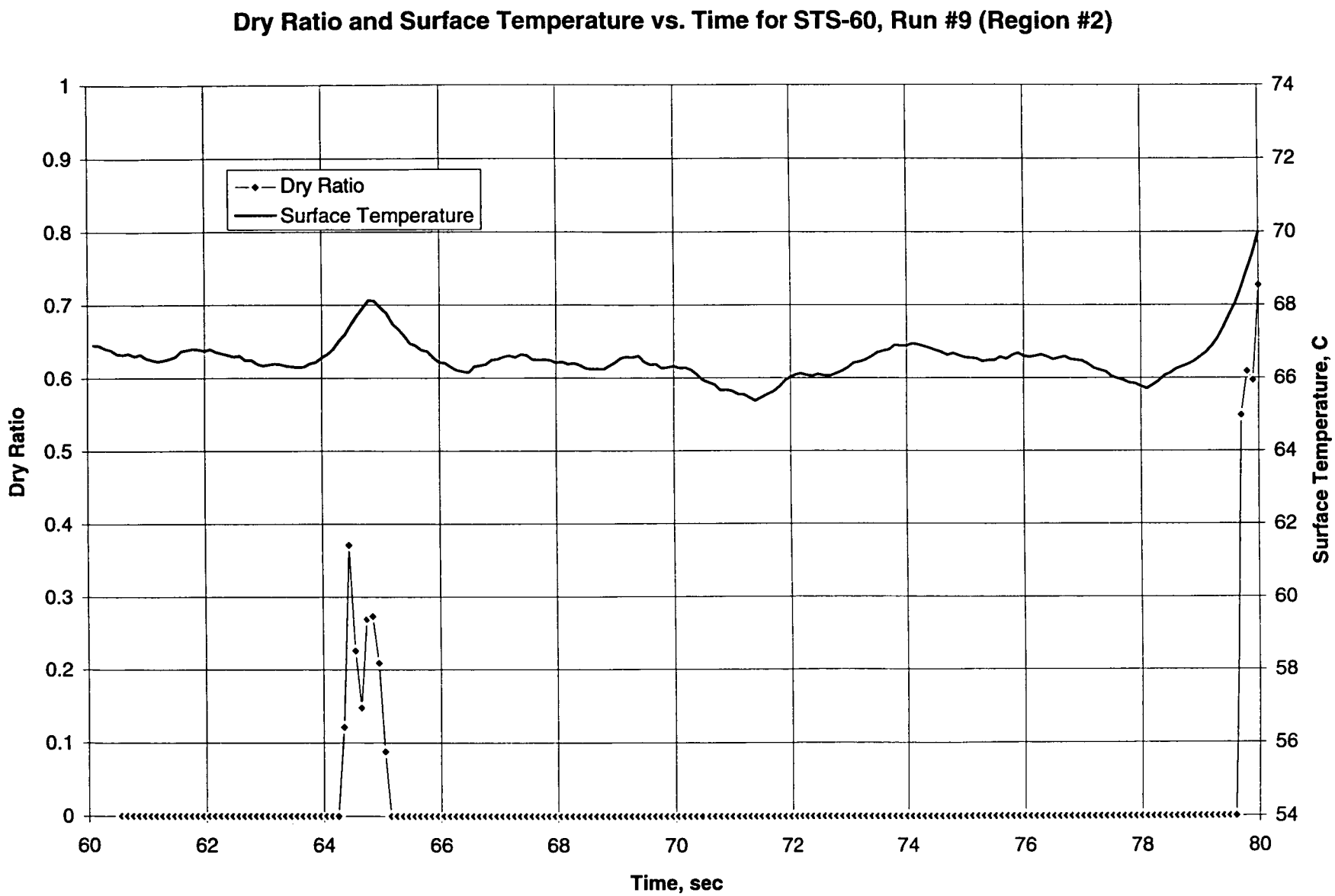

Figure C-10i-2-i. Heater surface dry fraction and mean temperature. PBE-IC (STS-60). Run No. 9. Time interval: 60 - 80 seconds.

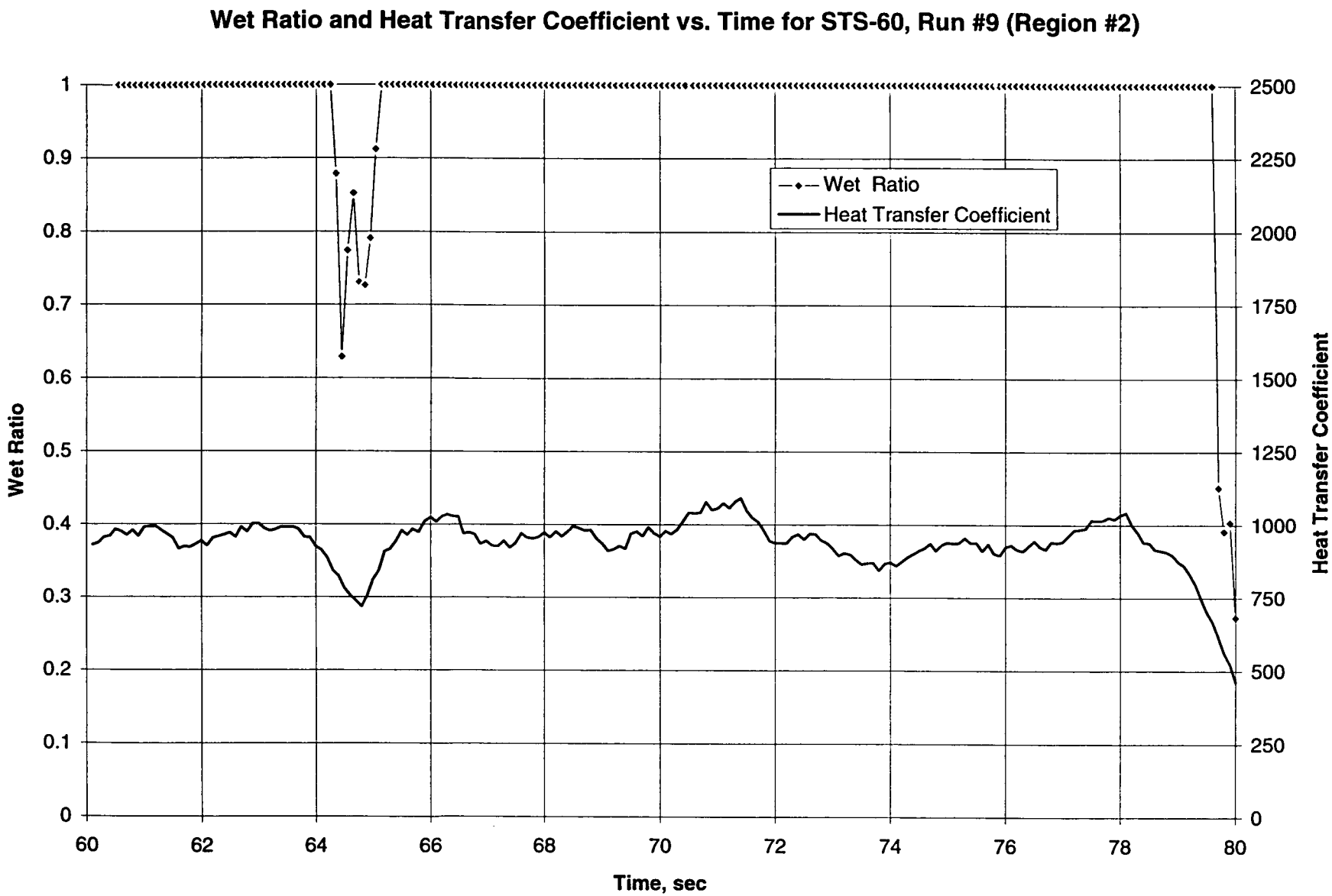

Figure C-10i-2-ii. Heater surface wet fraction and mean heat transfer coefficients. PBE-IC (STS-60). Run No. 9. Time interval: 60 - 80 seconds.

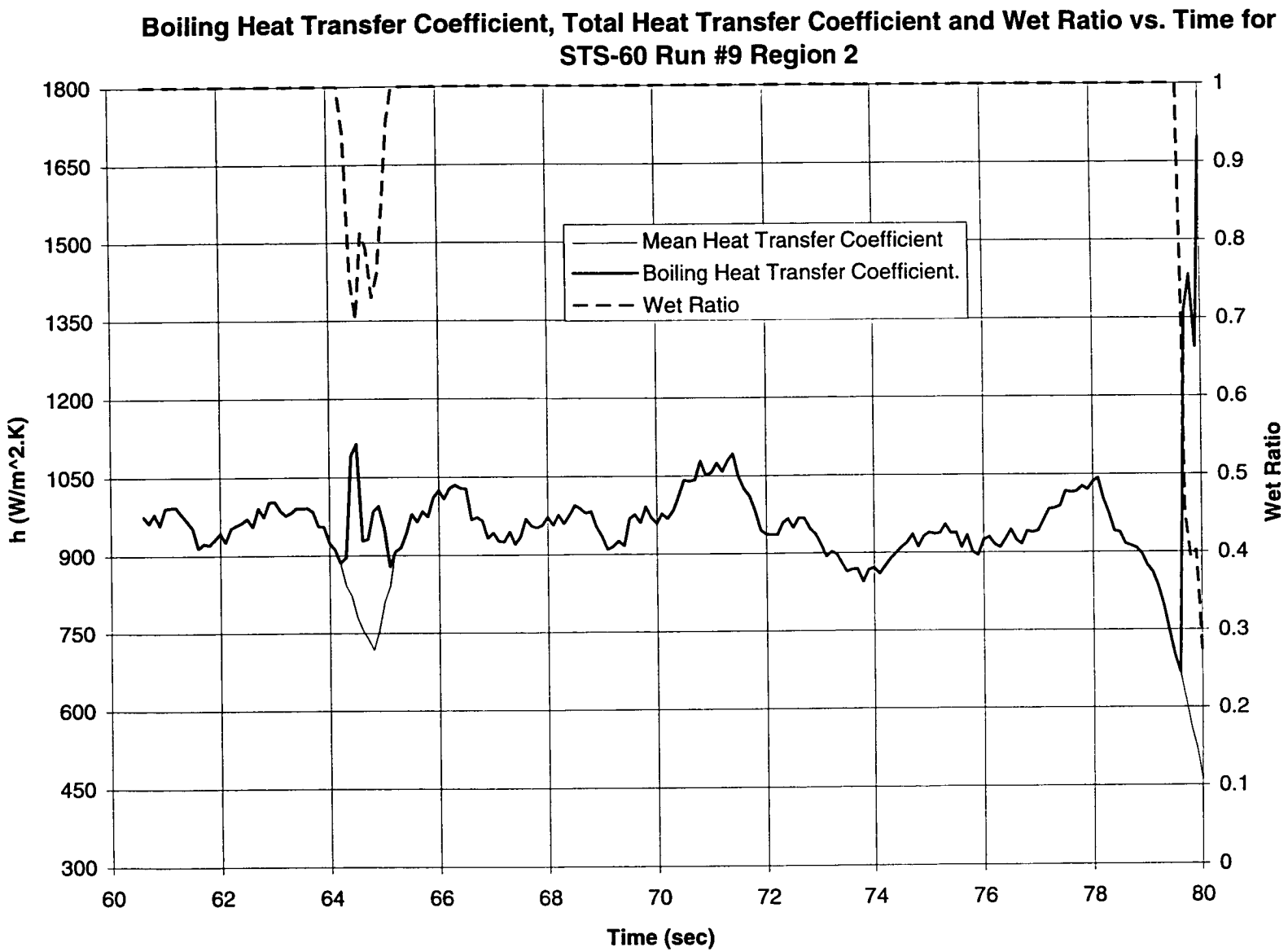

Figure C-10i-2-iii. Development of microgravity boiling heat transfer coefficient. PBE-IC (STS-60). Run No. 9. Time interval: 60 - 80 seconds.

STS 60, Run #9, Region#2

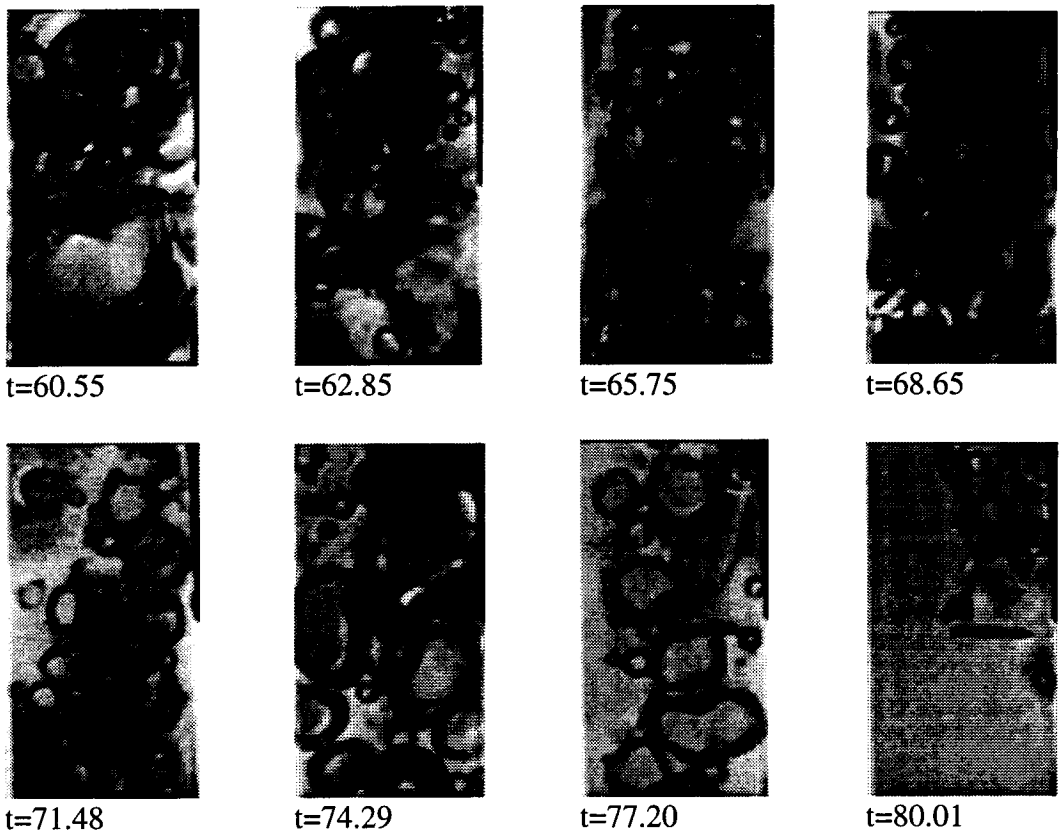

Figure C-10i-2-iv. Sample images showing dryout/rewetting. PBE-IC (STS-60). Run No. 9. Time interval: 60 - 80 seconds.

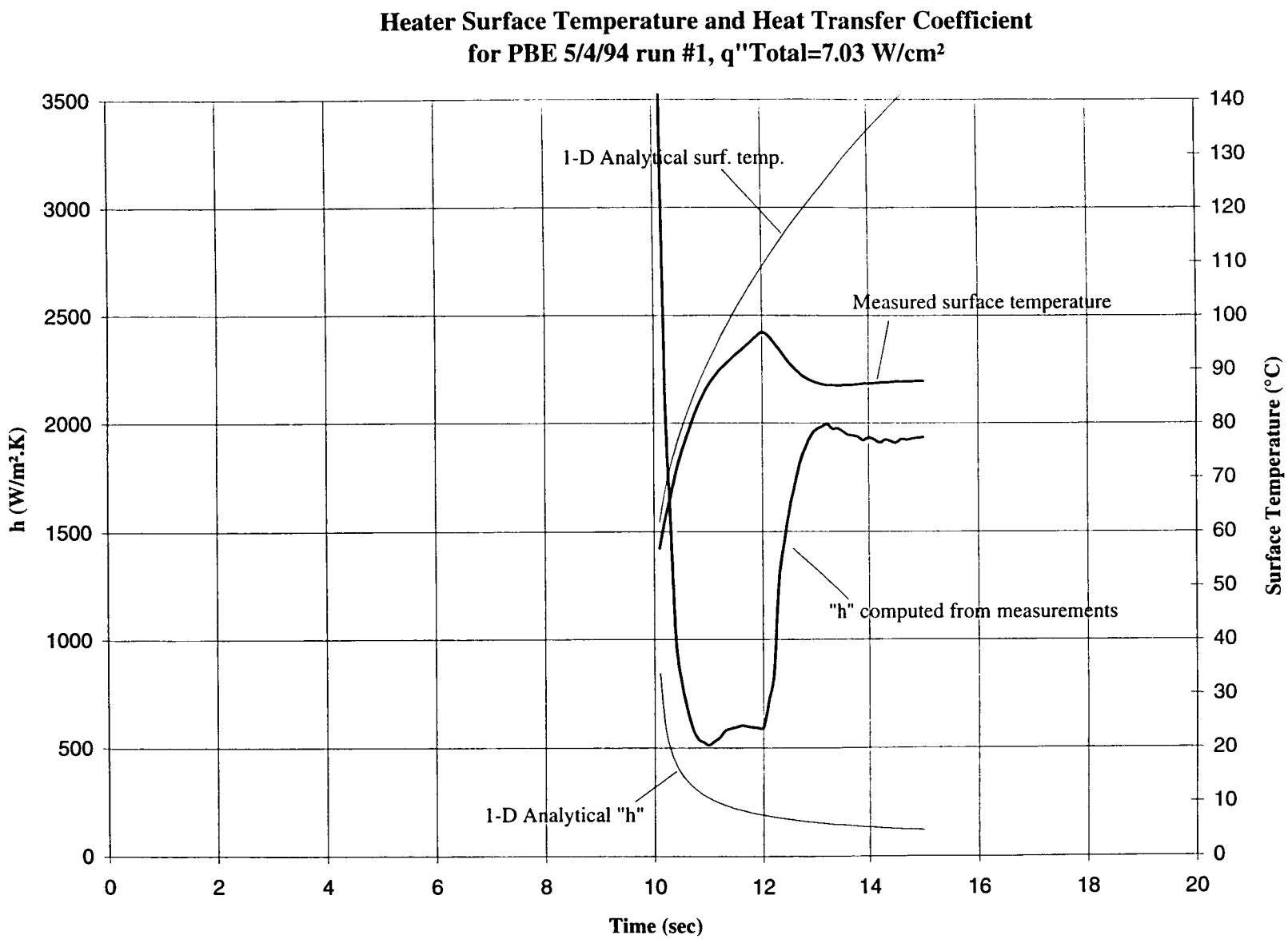

Figure C-11a. a/g = +1 Postflight test. Mean heater surface temperature and derived heat transfer coefficient. PBE-IC (STS-60). Run No. 1.

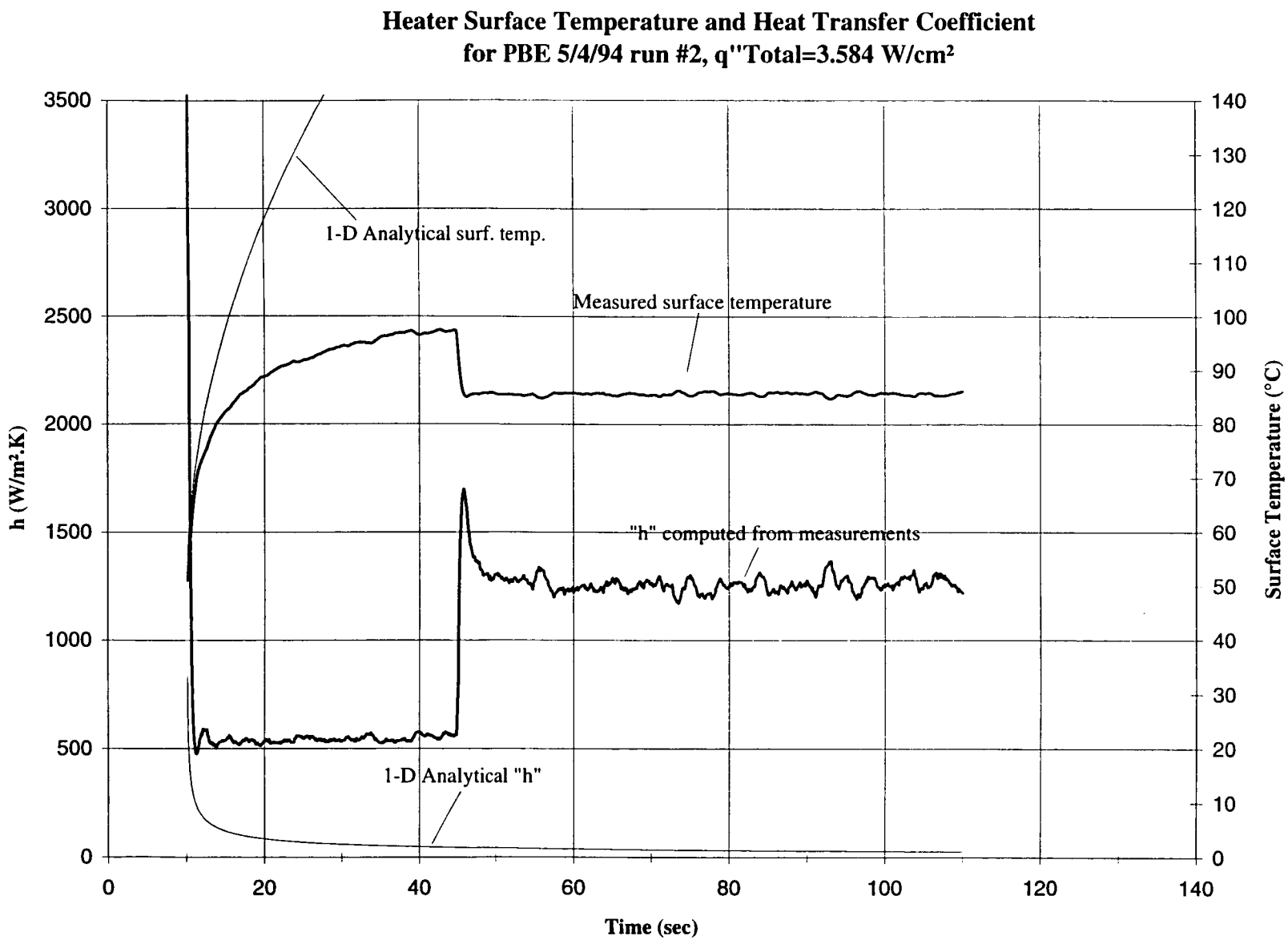

Figure C-11b. a/g = +1 Postflight test. Mean heater surface temperature and derived heat transfer coefficient. PBE-IC (STS-60). Run No. 2.

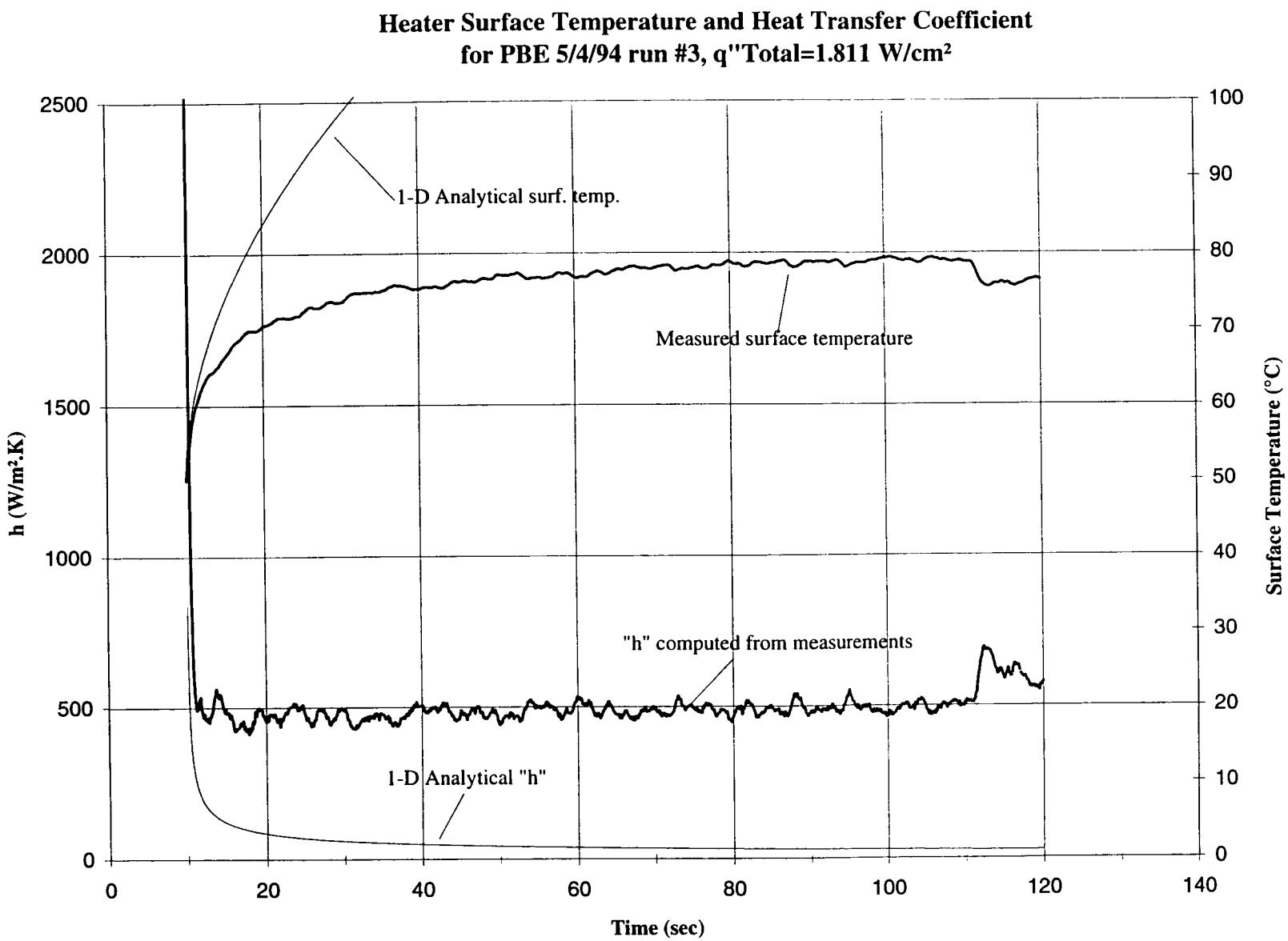

Figure C-11c. a/g = +1 Postflight test. Mean heater surface temperature and derived heat transfer coefficient. PBE-IC (STS-60). Run No. 3.

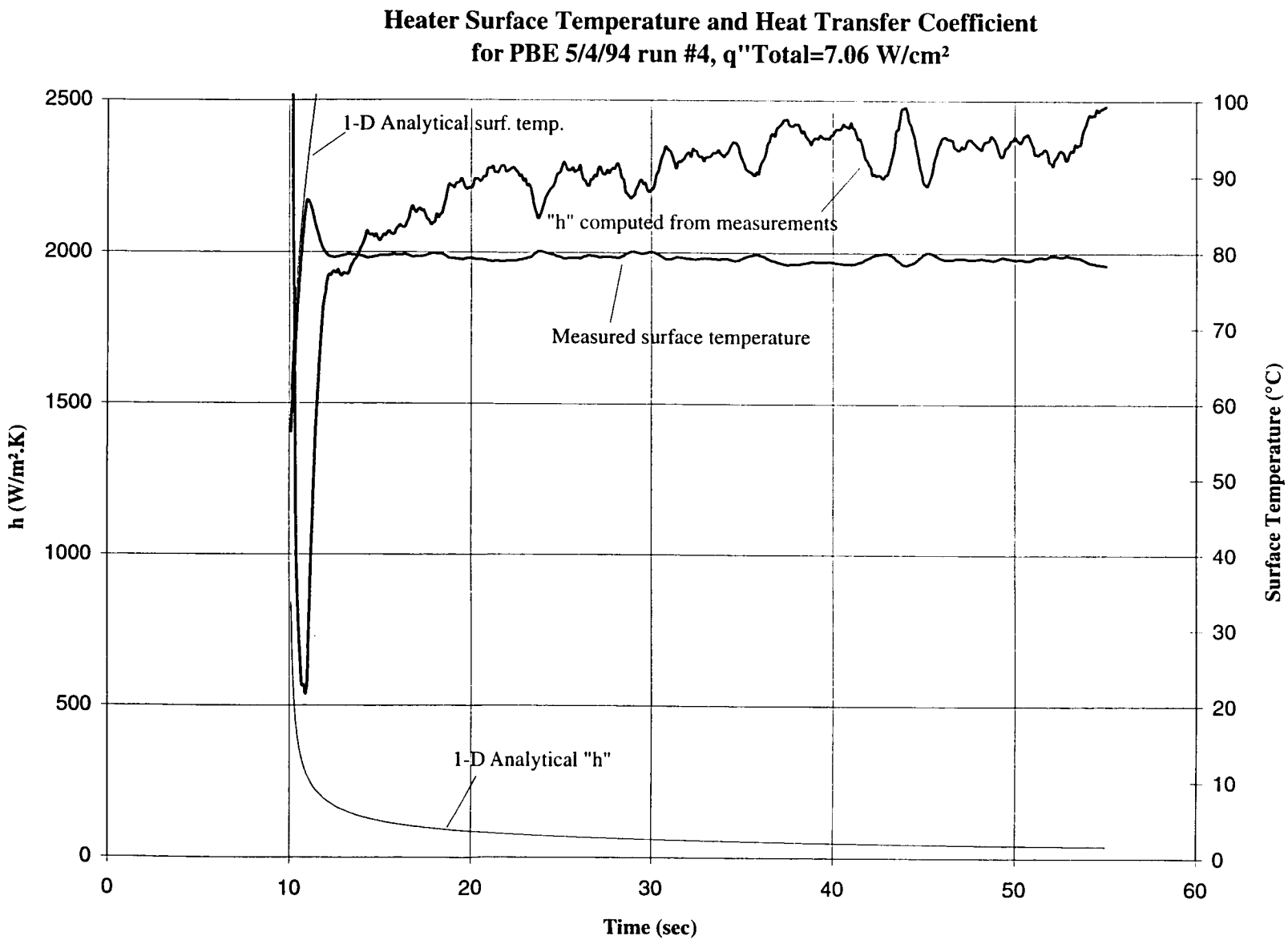

Figure C-11d. a/g = +1 Postflight test. Mean heater surface temperature and derived heat transfer coefficient. PBE-IC (STS-60). Run No. 4.

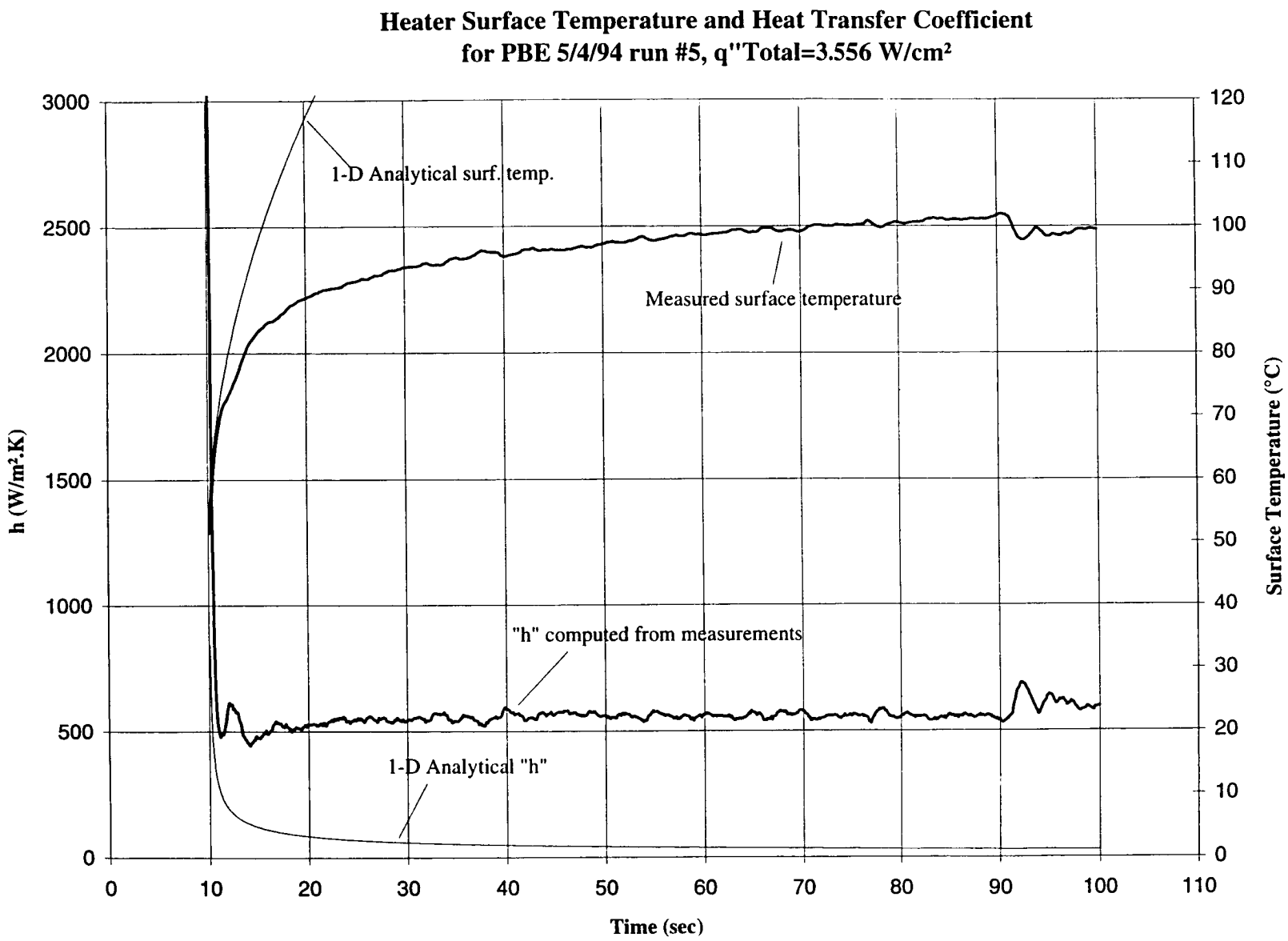

Figure C-11e. a/g = +1 Postflight test. Mean heater surface temperature and derived heat transfer coefficient. PBE-IC (STS-60). Run No. 5.

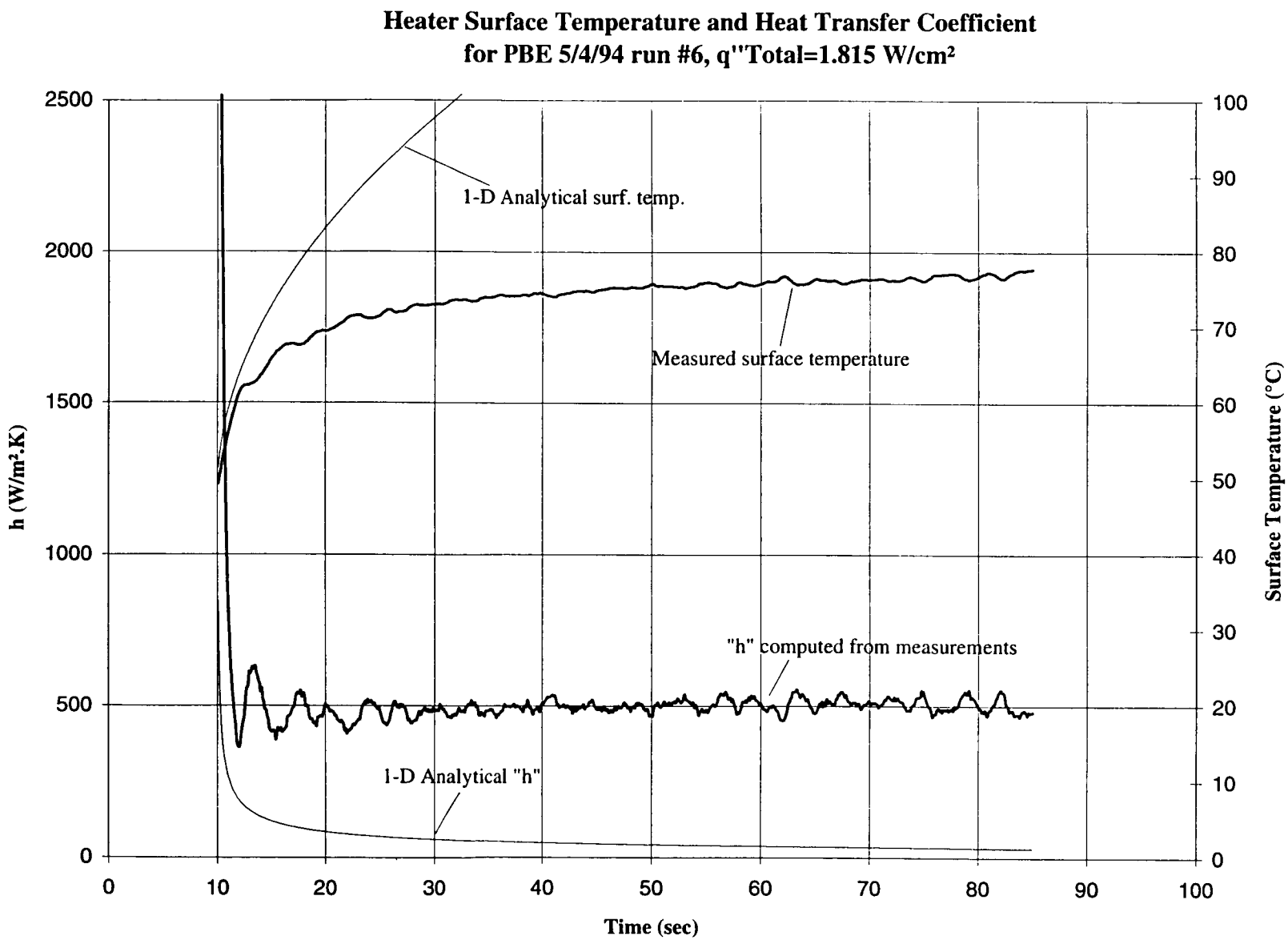

Figure C-11f. a/g = +1 Postflight test. Mean heater surface temperature and derived heat transfer coefficient. PBE-IC (STS-60). Run No. 6.

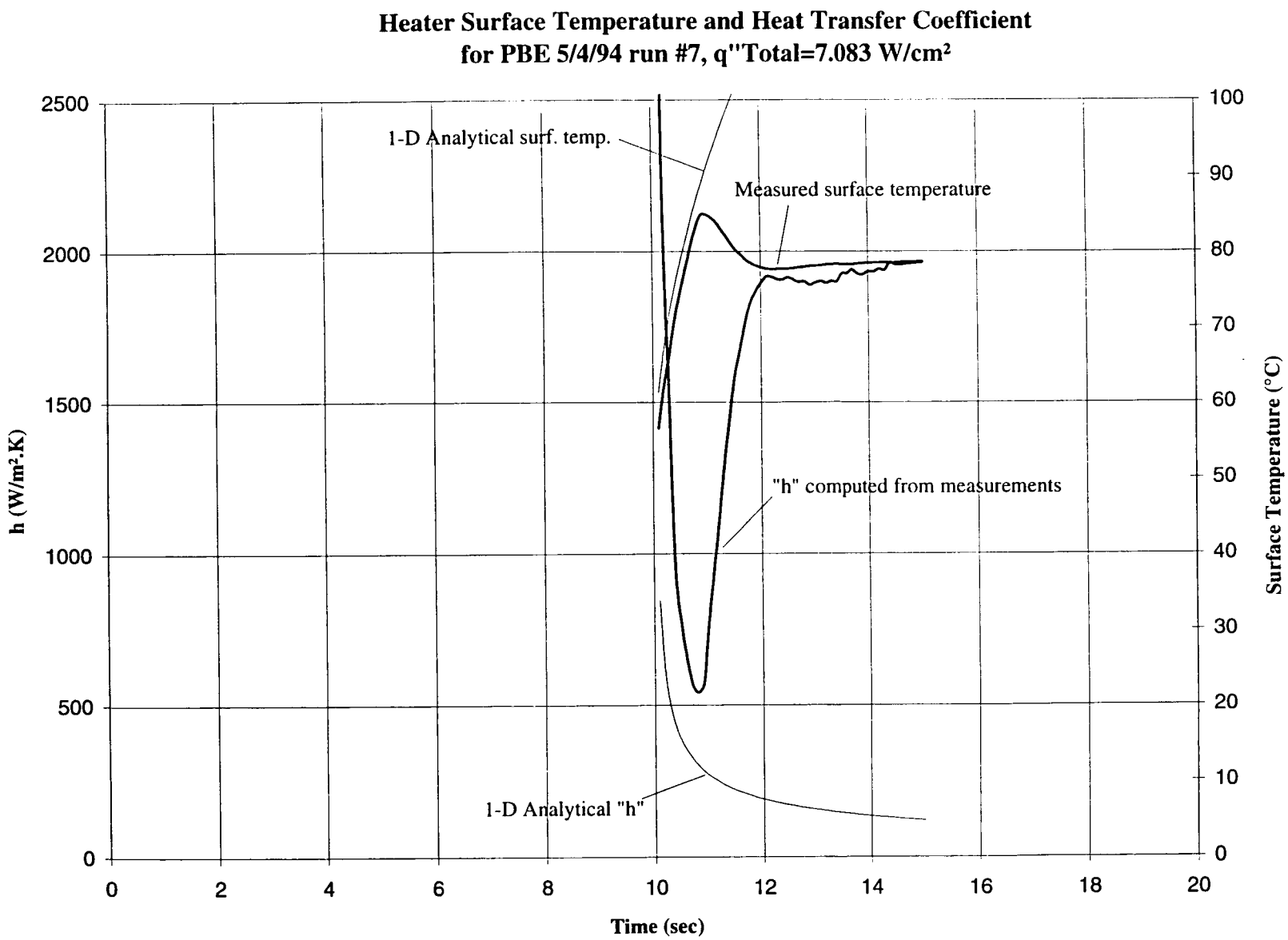

Figure C-11g. a/g = +1 Postflight test. Mean heater surface temperature and derived heat transfer coefficient. PBE-IC (STS-60). Run No. 7.

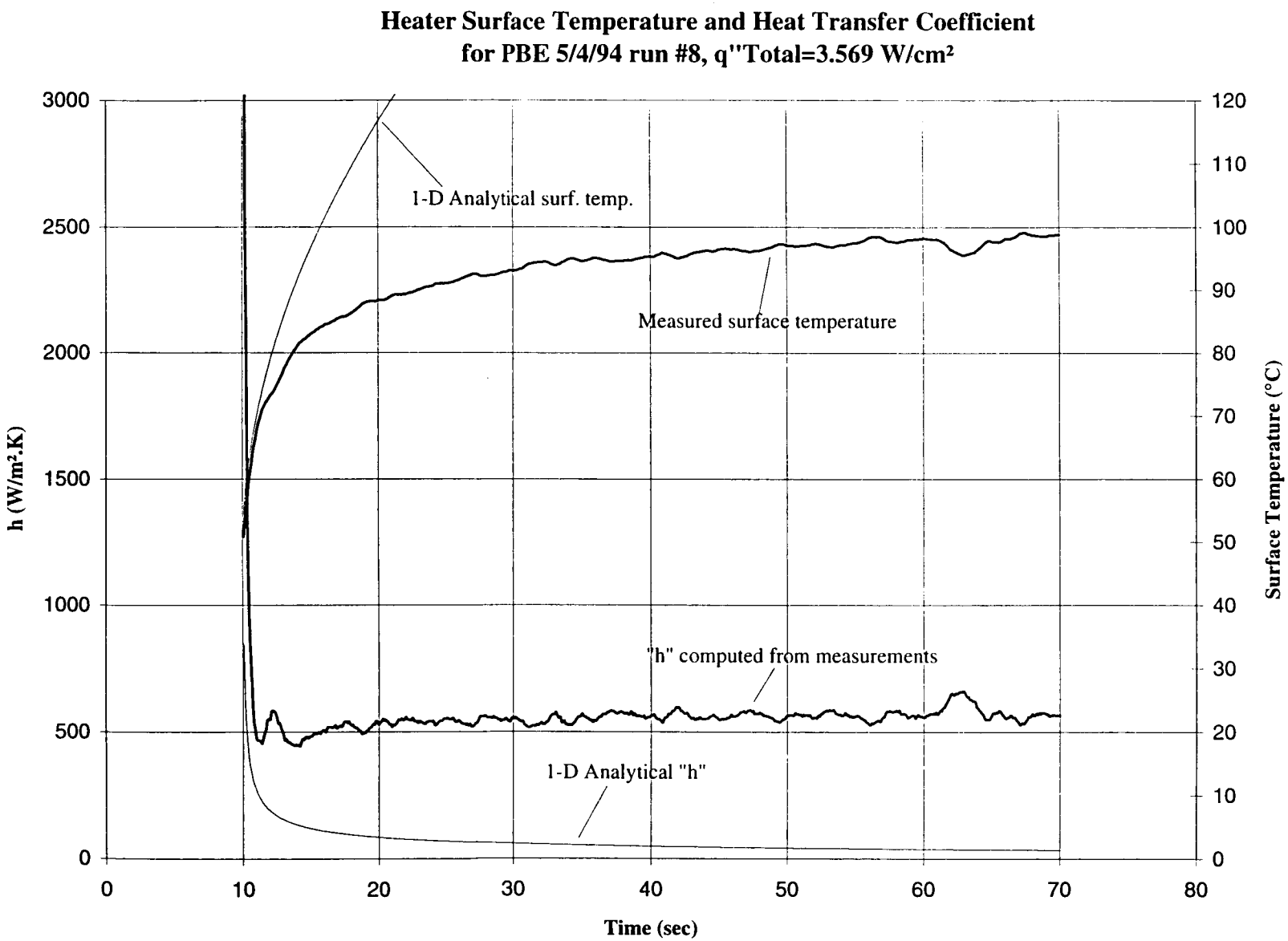

Figure C-11h. a/g = +1 Postflight test. Mean heater surface temperature and derived heat transfer coefficient. PBE-IC (STS-60). Run No. 8.

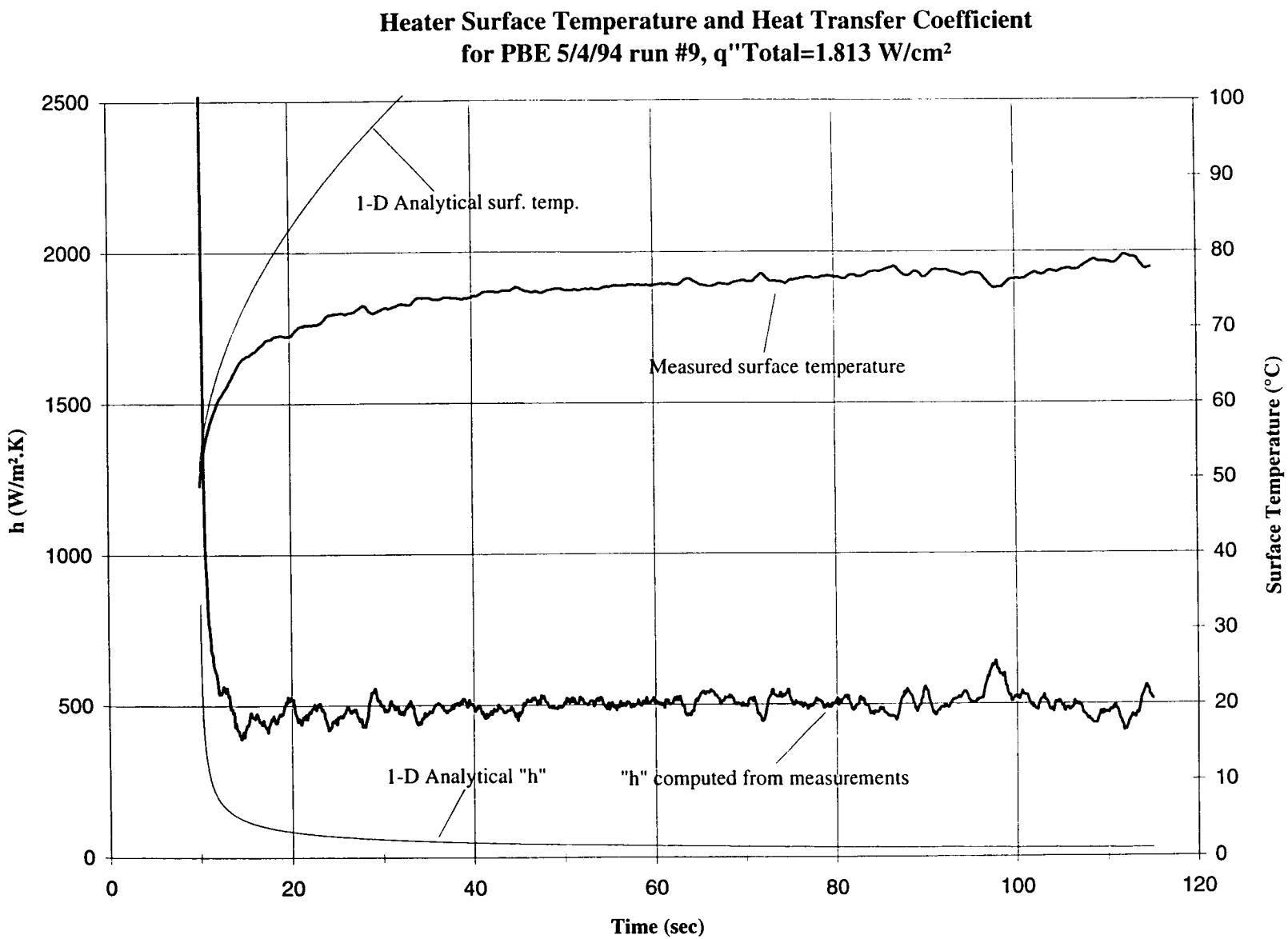

Figure C-11i. a/g = +1 Postflight test. Mean heater surface temperature and derived heat transfer coefficient. PBE-IC (STS-60). Run No. 9.

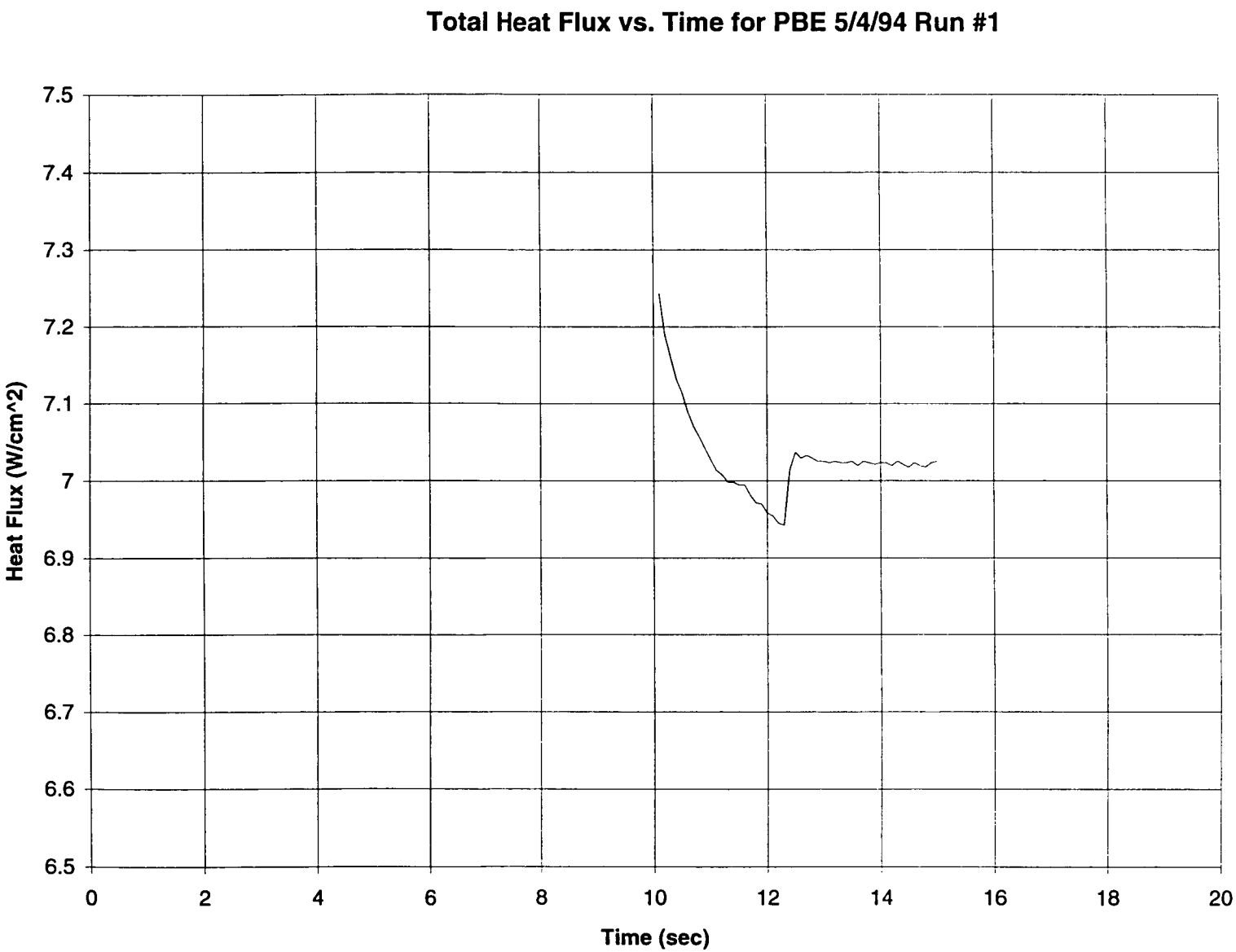

Figure C-12a. a/g = +1 Postflight test. Heat flux input. PBE-IC (STS-60). Run No. 1.

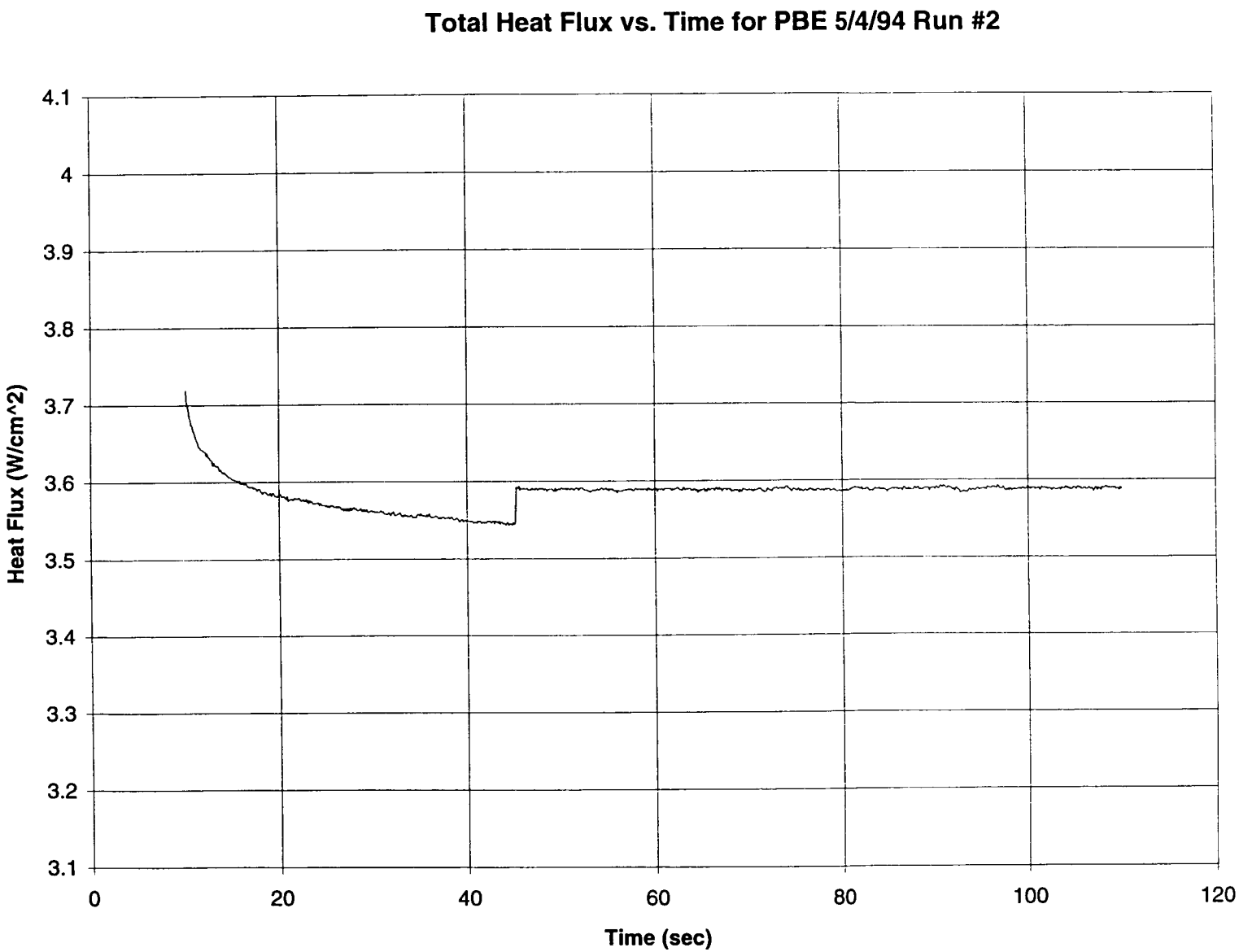

Figure C-12b. a/g = +1 Postflight test. Heat flux input. PBE-IC (STS-60). Run No. 2.

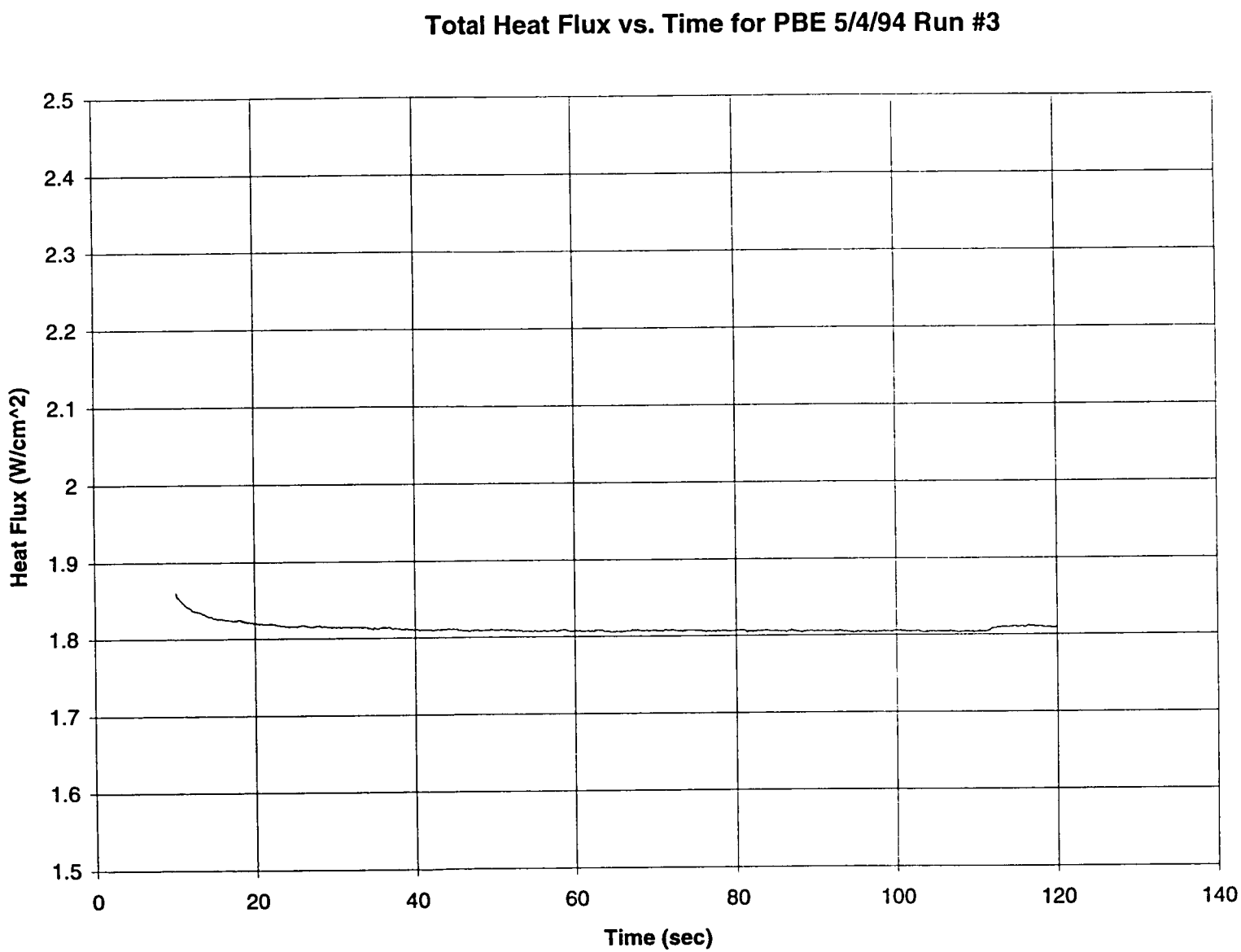

Figure C-12c. a/g = +1 Postflight test. Heat flux input. PBE-IC (STS-60). Run No. 3.

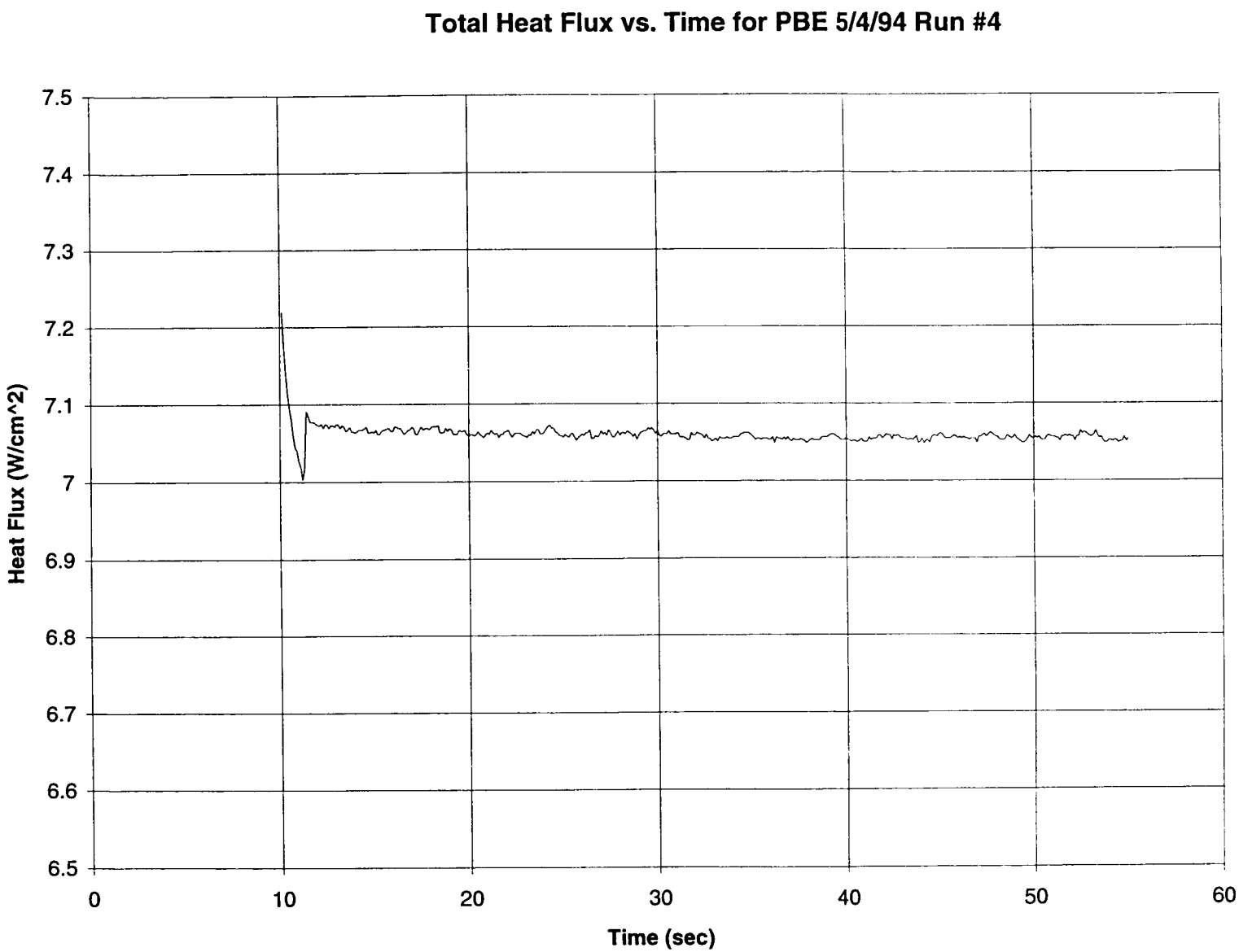

Figure C-12d. a/g = +1 Postflight test. Heat flux input. PBE-IC (STS-60). Run No. 4.

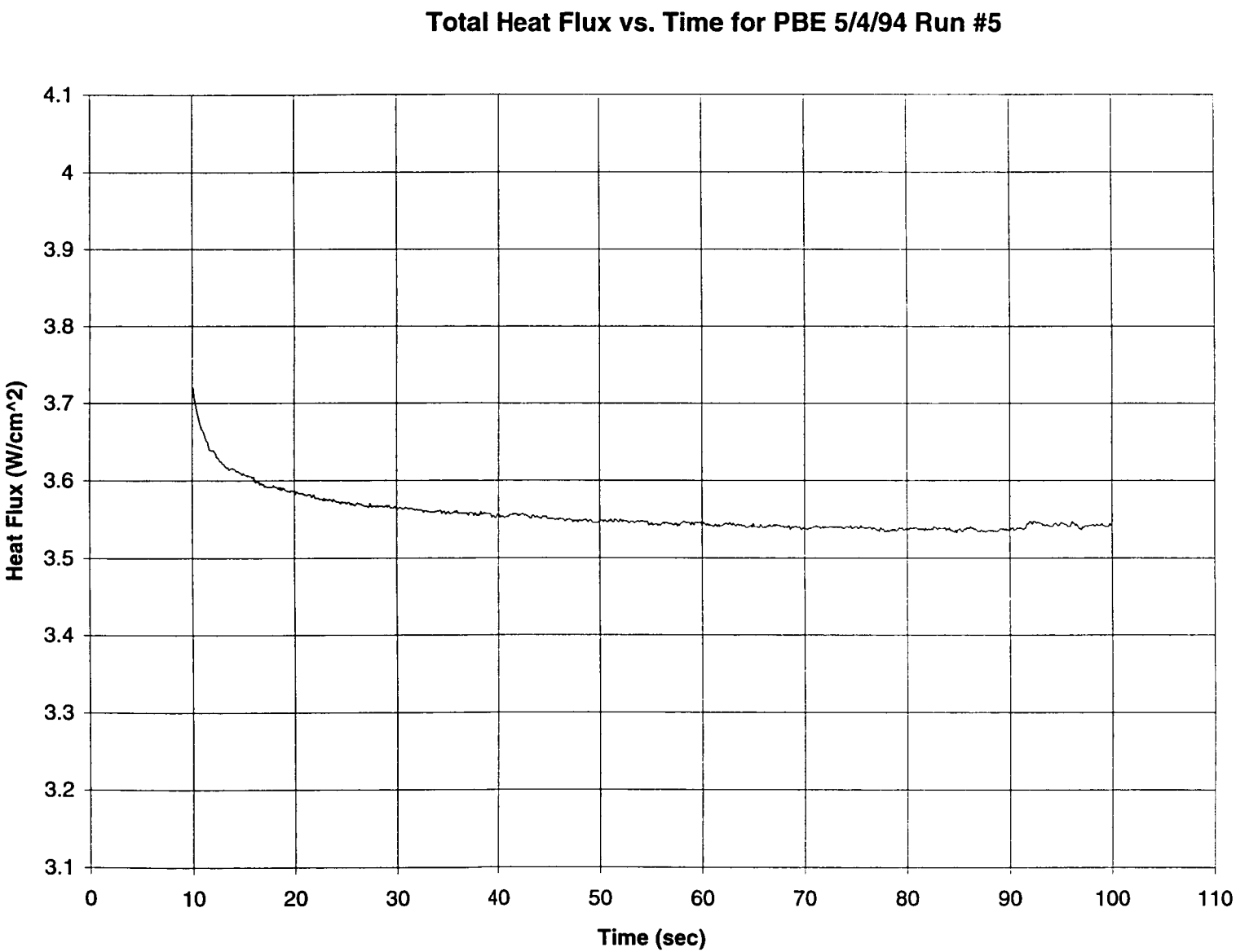

Figure C-12e. a/g = +1 Postflight test. Heat flux input. PBE-IC (STS-60). Run No. 5.

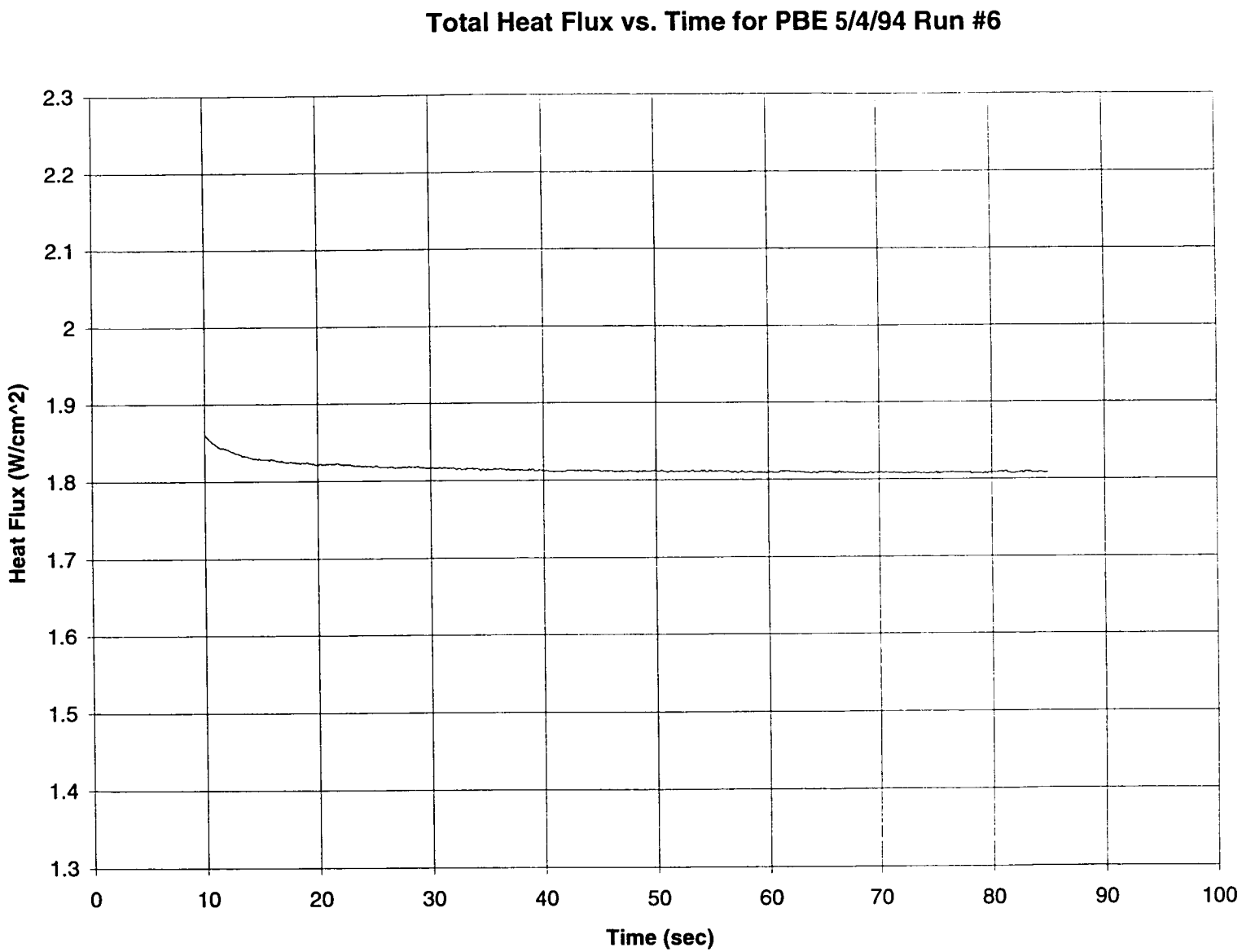

Figure C-12f. a/g = +1 Postflight test. Heat flux input. PBE-IC (STS-60). Run No. 6.

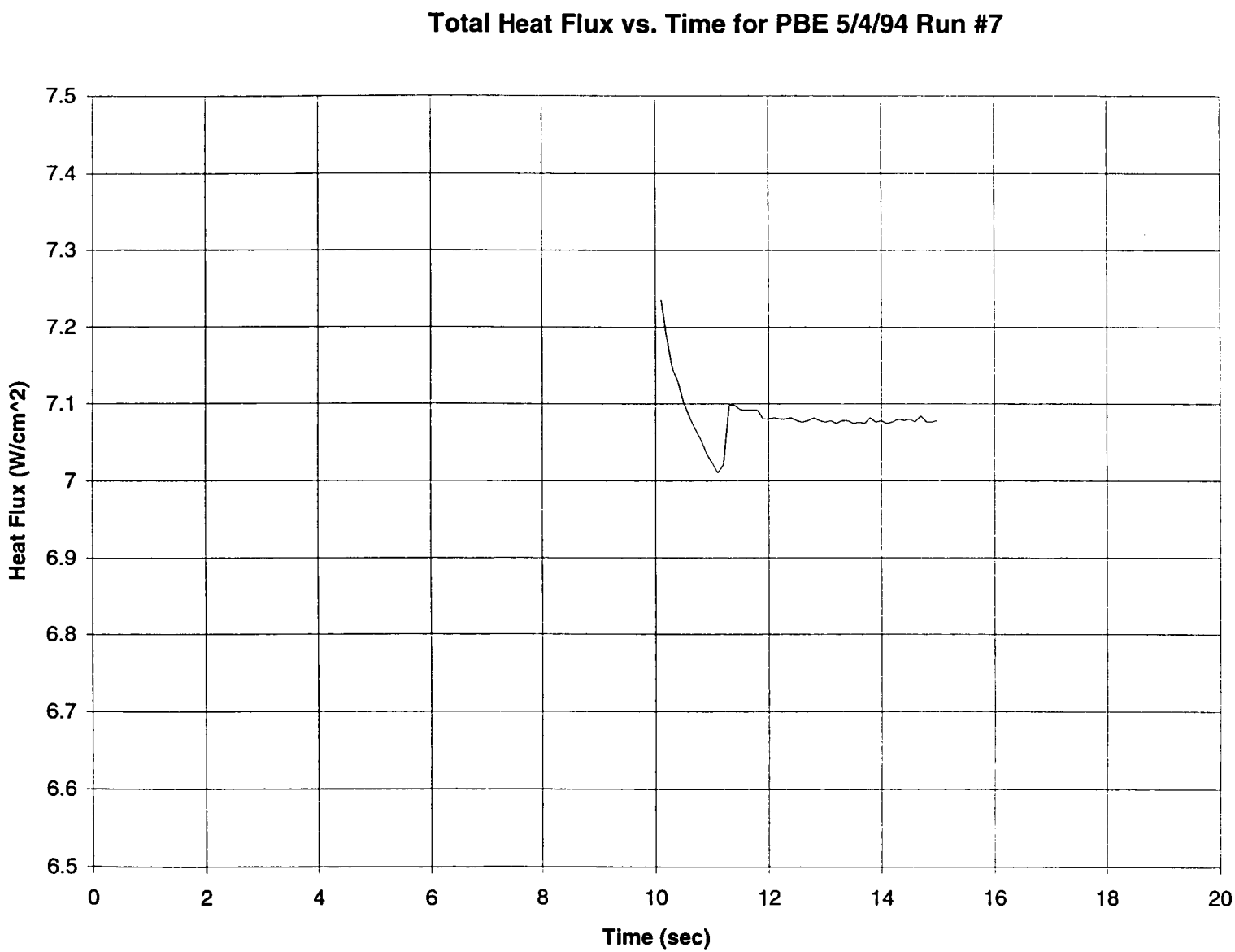

Figure C-12g. a/g = +1 Postflight test. Heat flux input. PBE-IC (STS-60). Run No. 7.

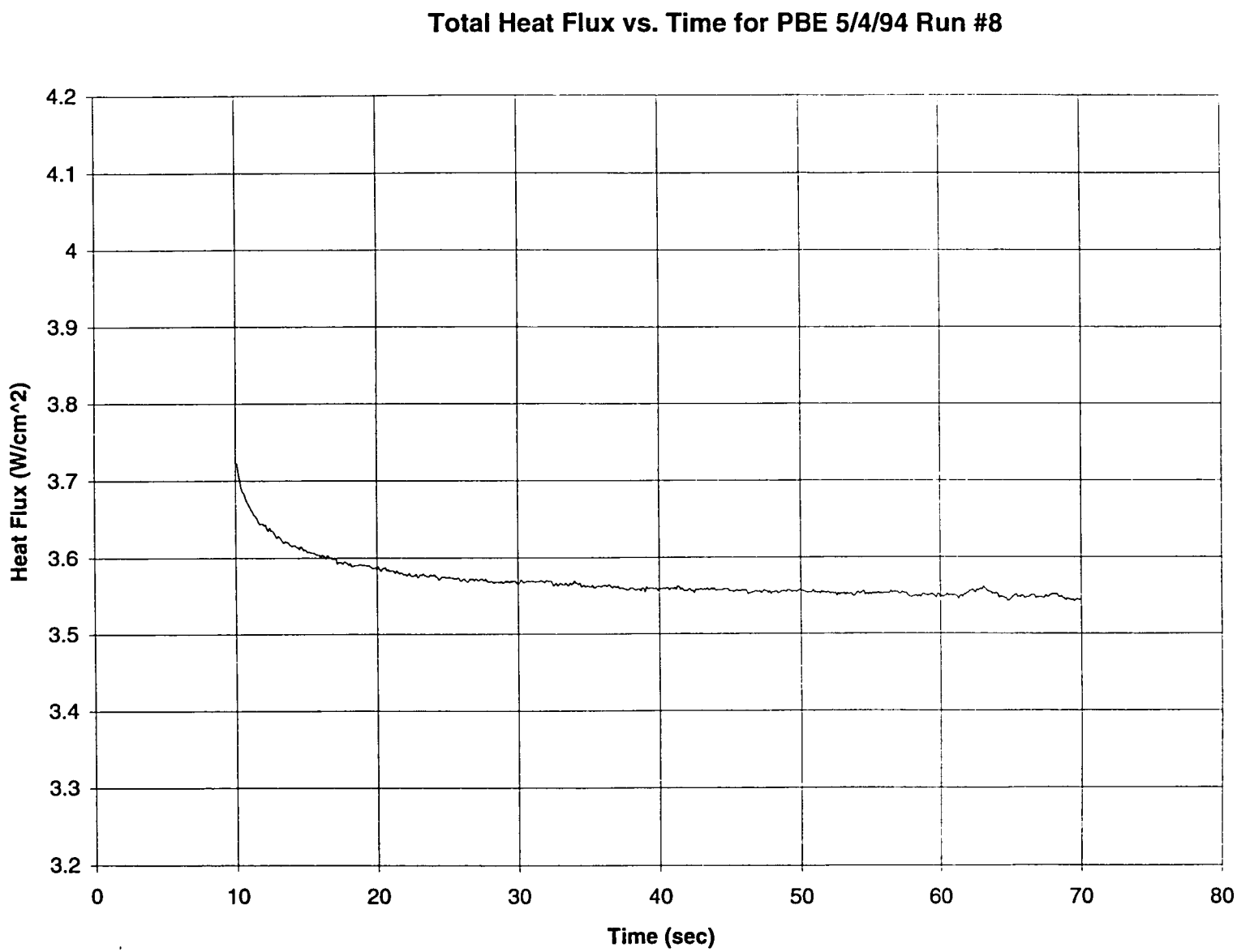

Figure C-12h. a/g = +1 Postflight test. Heat flux input. PBE-IC (STS-60). Run No. 8.

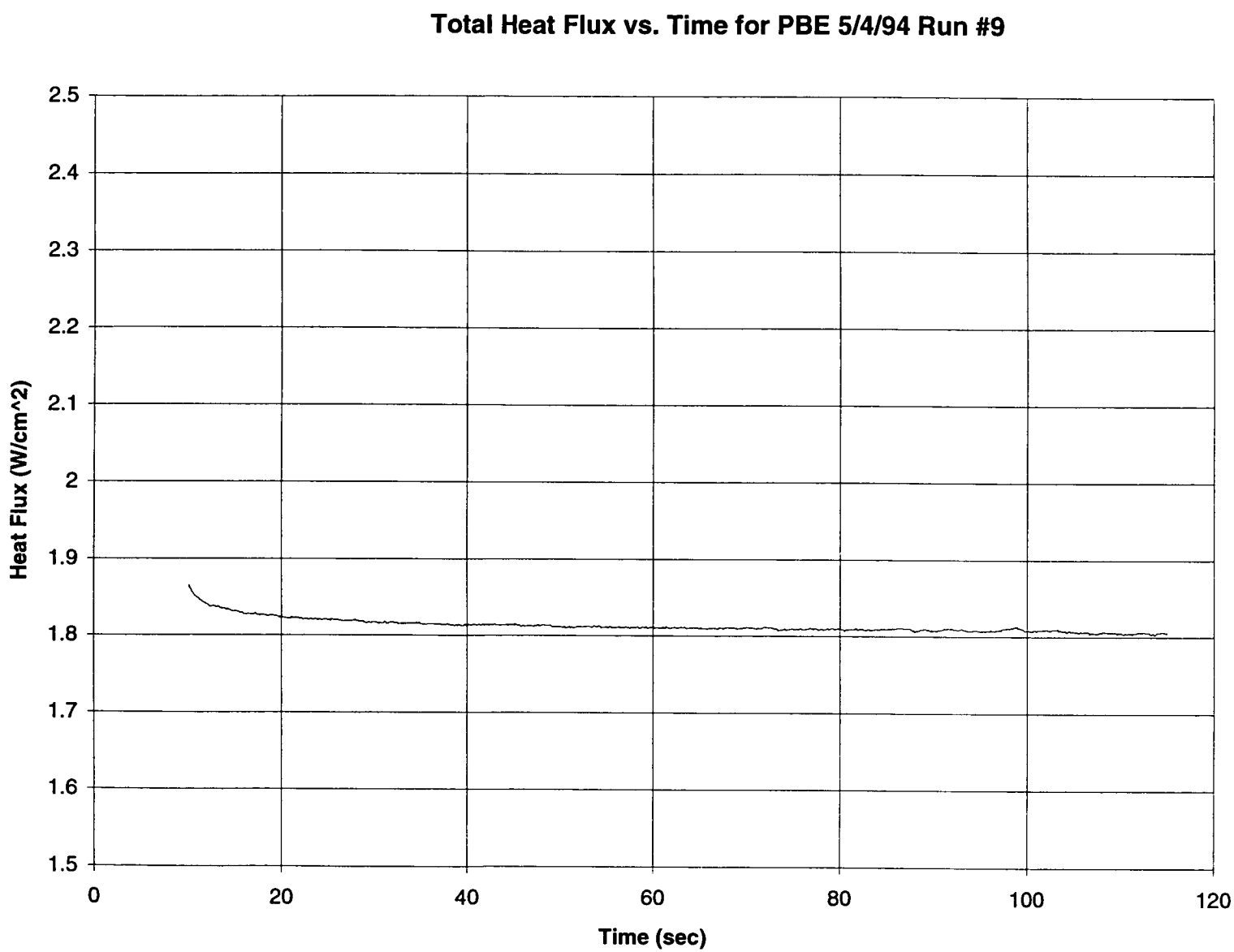

Figure C-12i. a/g = +1 Postflight test. Heat flux input. PBE-IC (STS-60). Run No. 9.

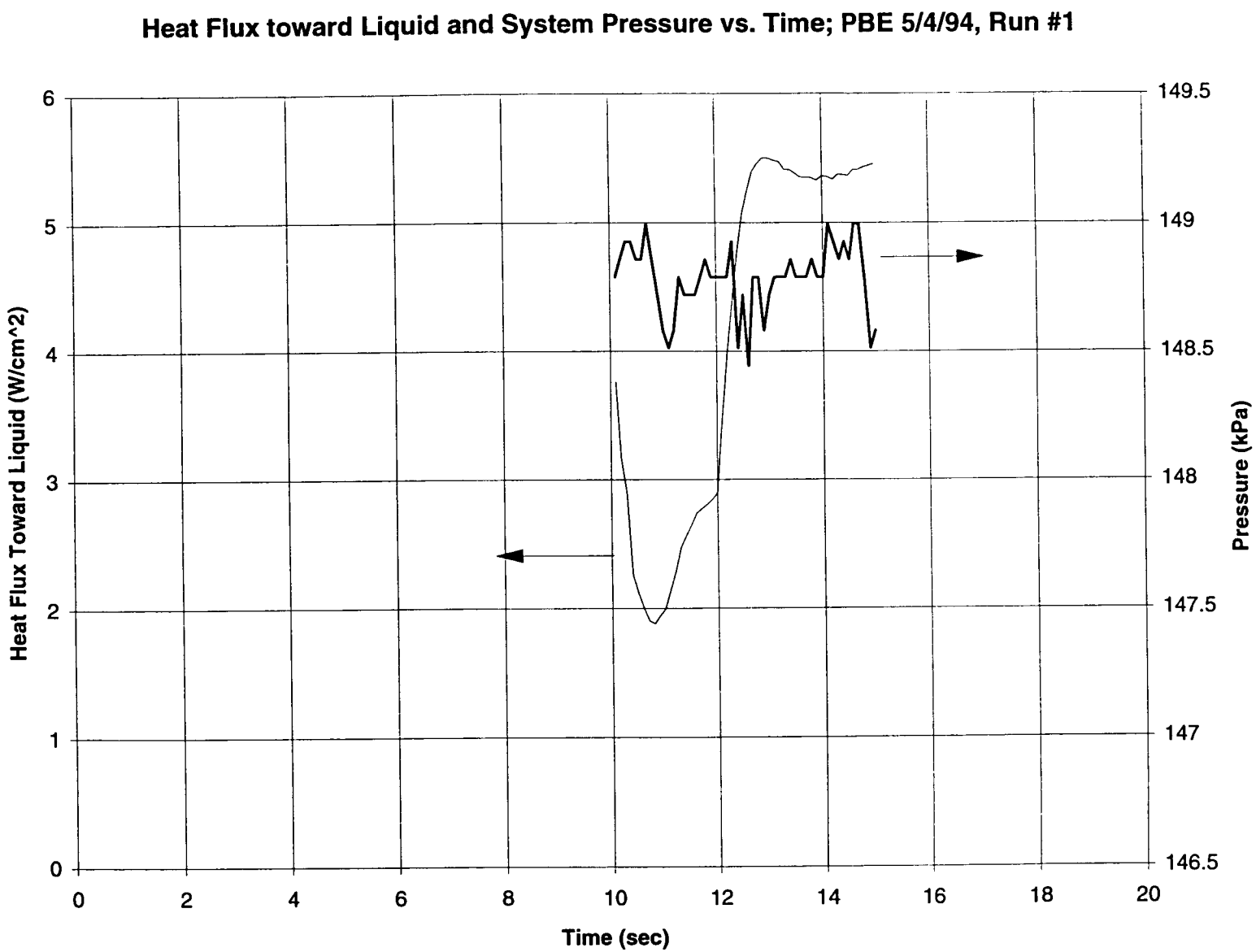

Figure C-13a. a/g = +1 Postflight test. System pressure and heat flux into fluid. PBE-IC (STS-60). Run No. 1.

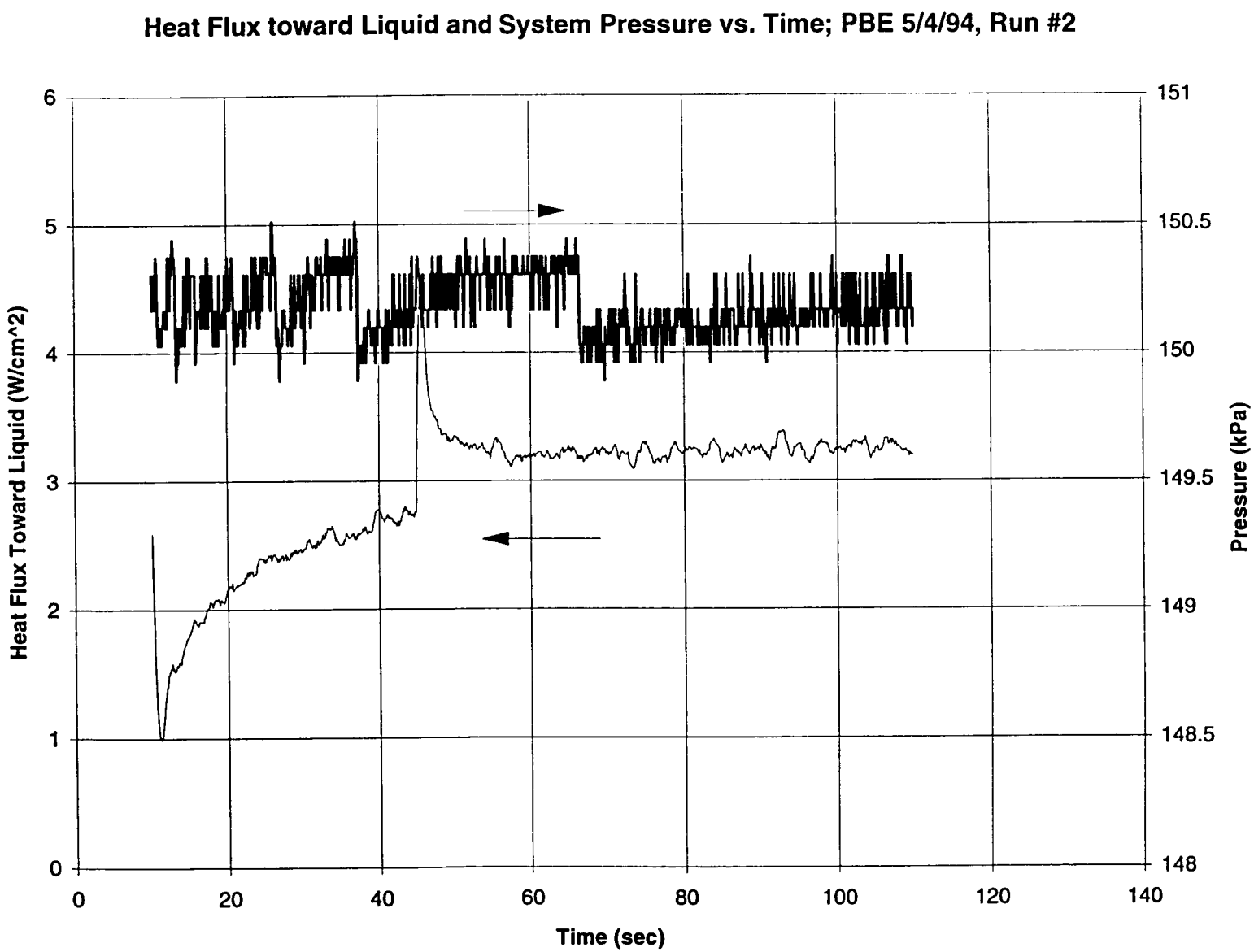

Figure C-13b. a/g = +1 Postflight test. System pressure and heat flux into fluid. PBE-IC (STS-60). Run No. 2.

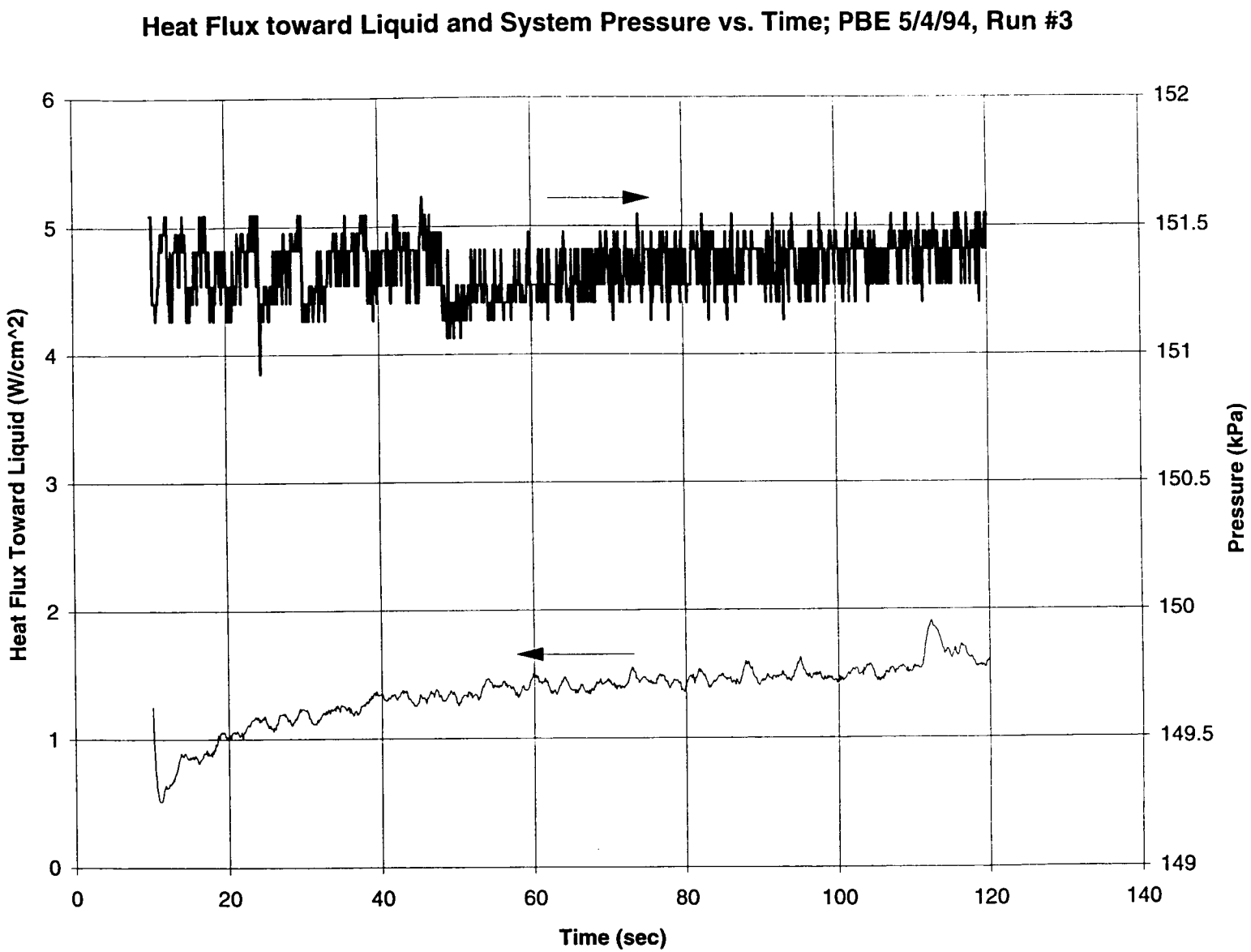

Figure C-13c. a/g = +1 Postflight test. System pressure and heat flux into fluid. PBE-IC (STS-60). Run No. 3.

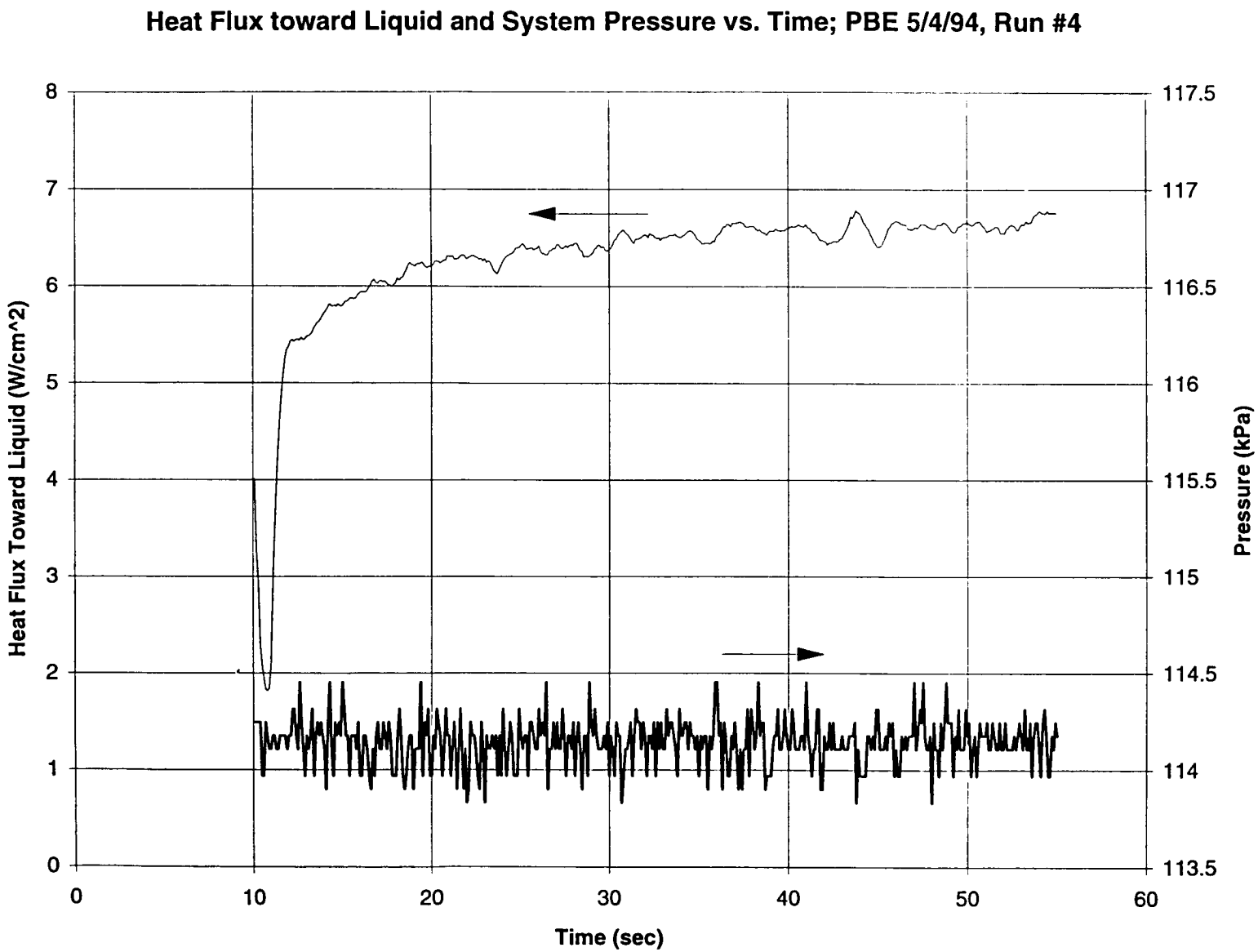

Figure C-13d. a/g = +1 Postflight test. System pressure and heat flux into fluid. PBE-IC (STS-60). Run No. 4.

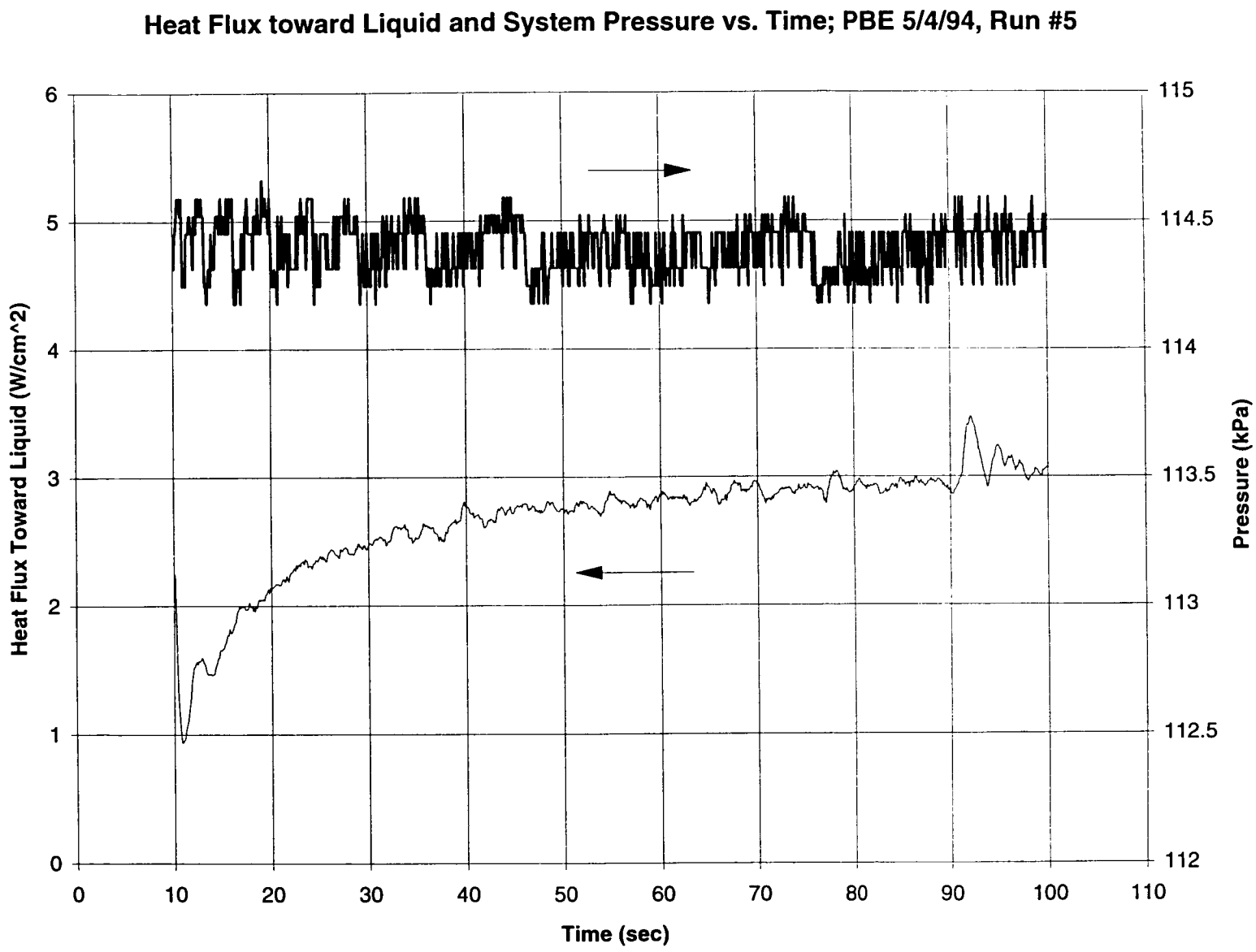

Figure C-13e. a/g = +1 Postflight test. System pressure and heat flux into fluid. PBE-IC (STS-60). Run No. 5.

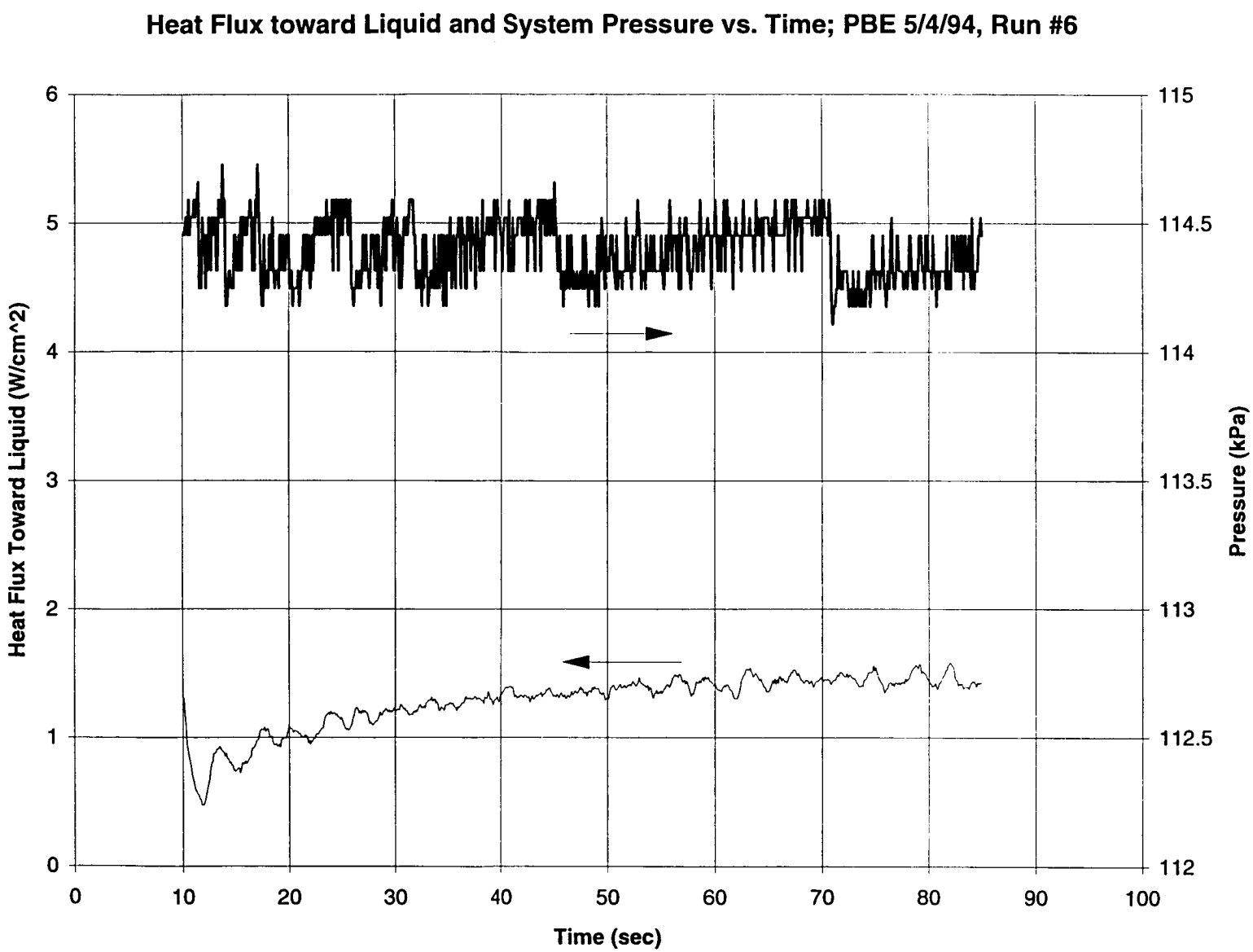

Figure C-13f. a/g = +1 Postflight test. System pressure and heat flux into fluid. PBE-IC (STS-60). Run No. 6.

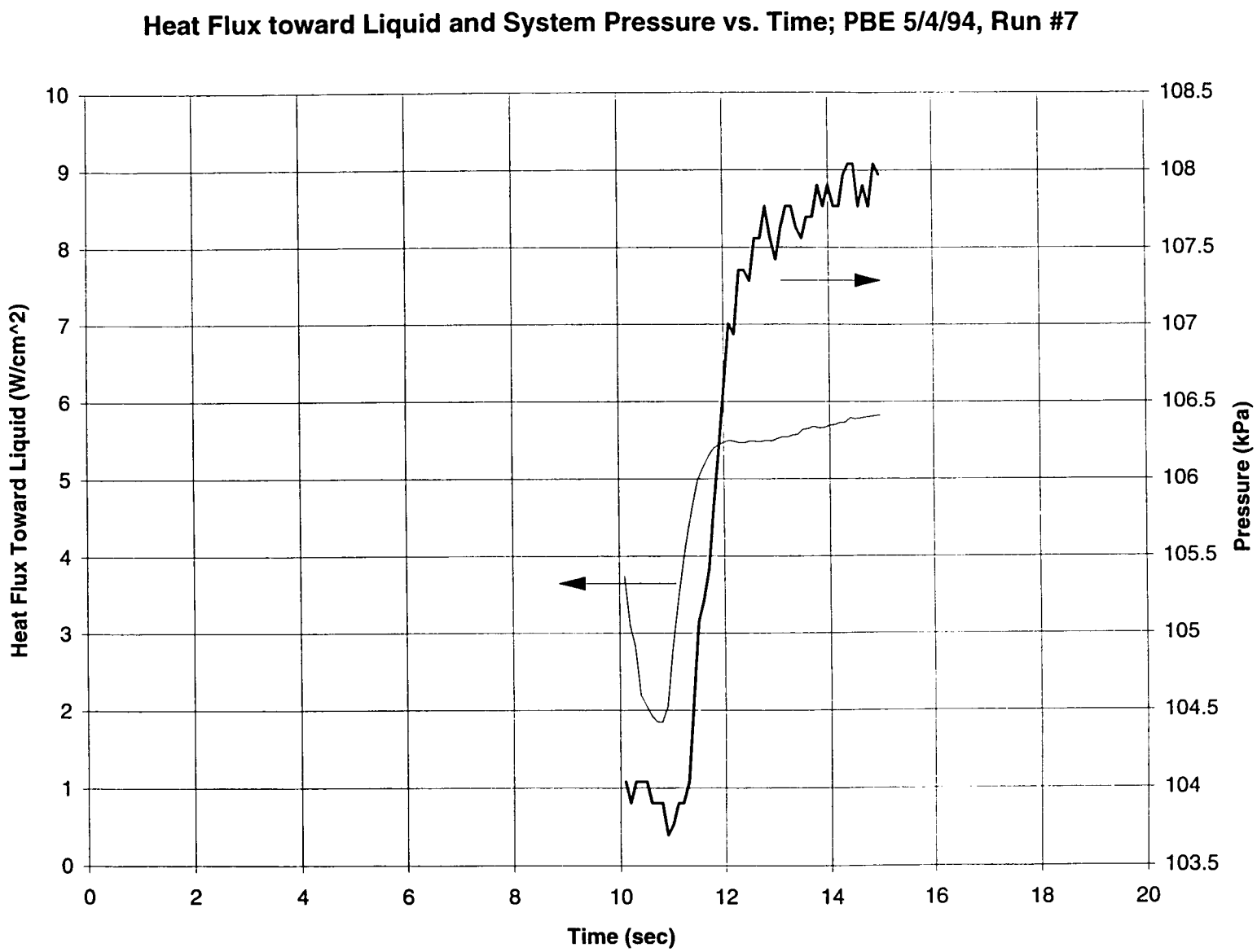

Figure C-13g. a/g = +1 Postflight test. System pressure and heat flux into fluid. PBE-IC (STS-60). Run No. 7.

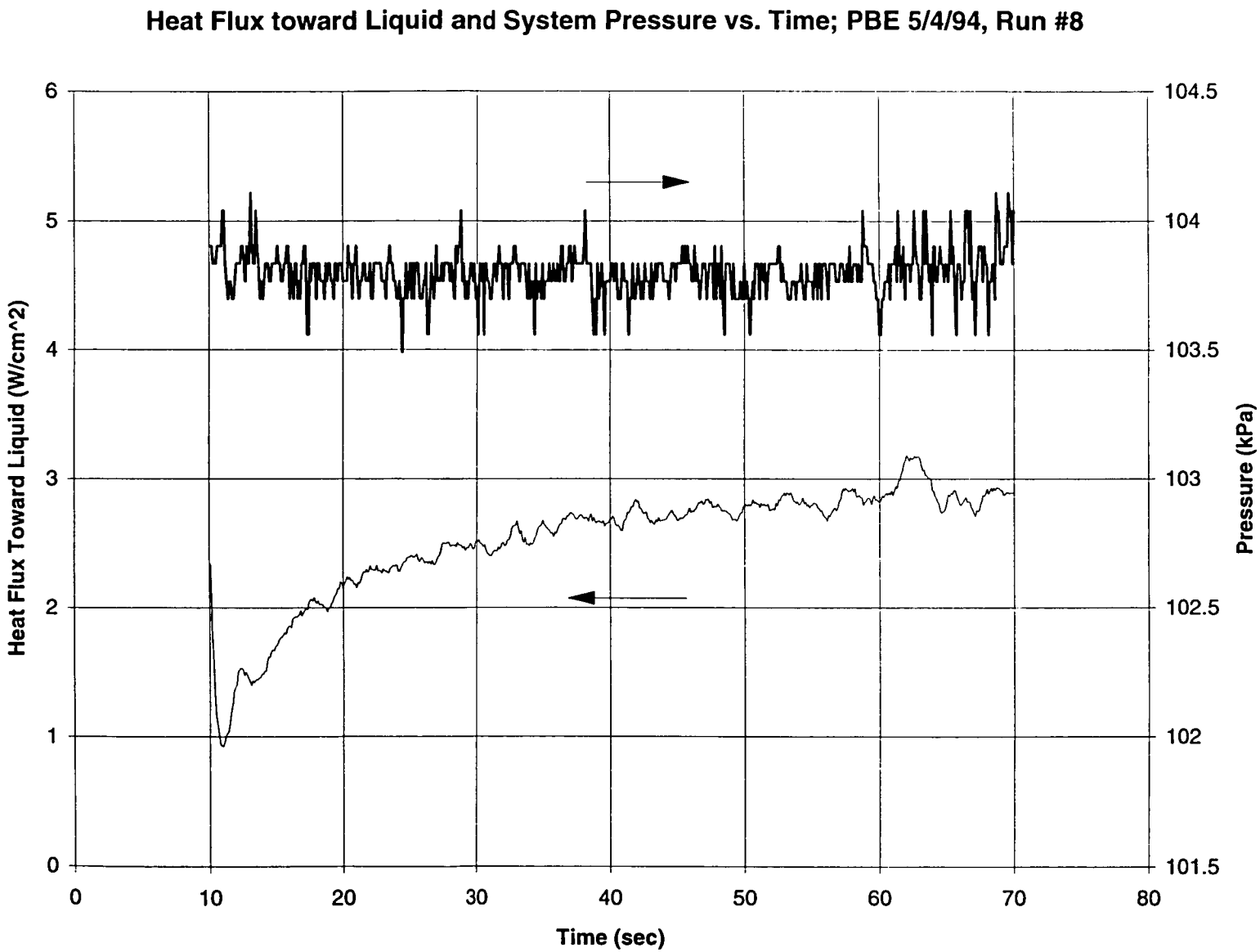

Figure C-13h. a/g = +1 Postflight test. System pressure and heat flux into fluid. PBE-IC (STS-60). Run No. 8.

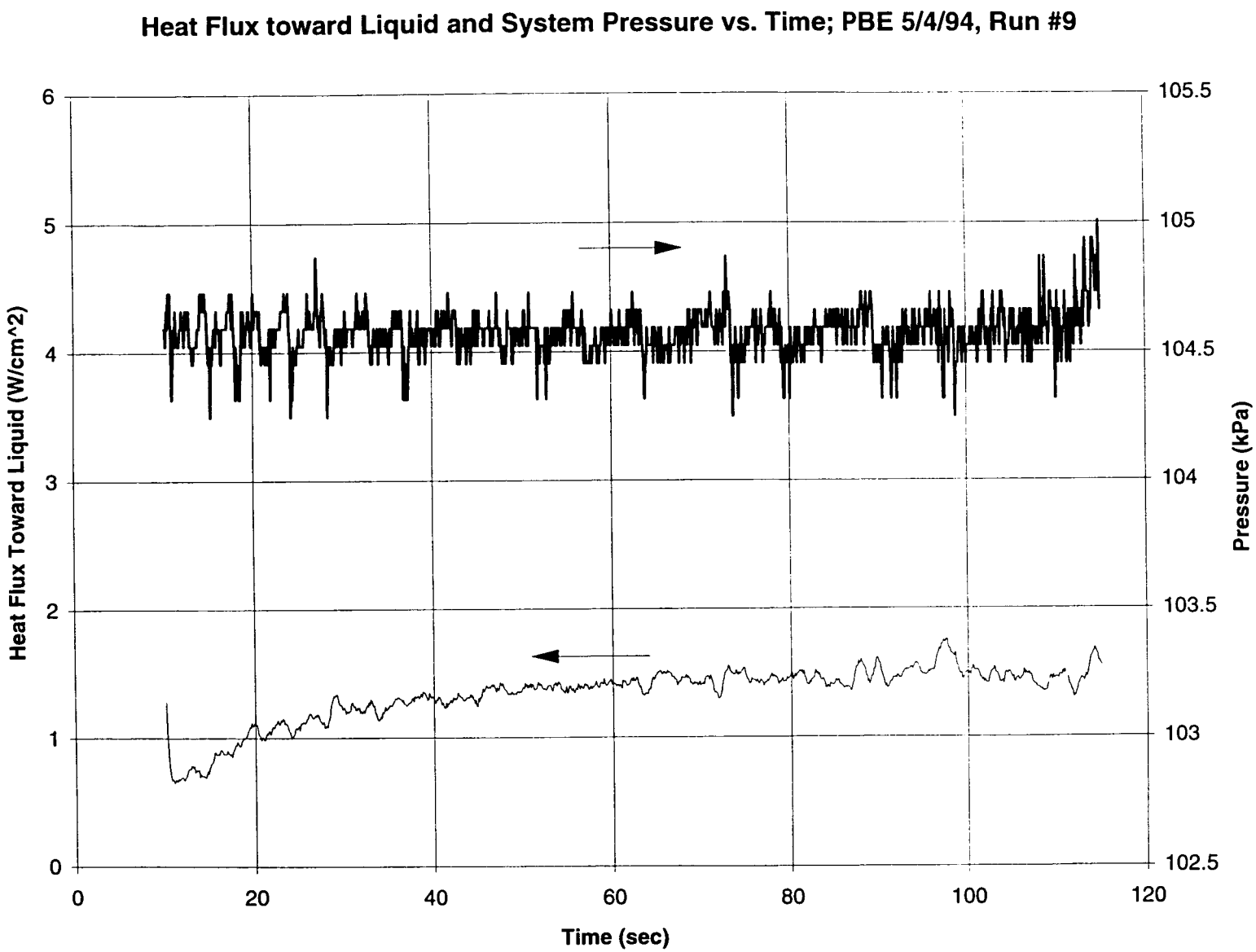

Figure C-13i. a/g = +1 Postflight test. System pressure and heat flux into fluid. PBE-IC (STS-60). Run No. 9.

Appendix D. Thin Film Heater/Resistance Thermometer: Assessment of Effect of Local Temperature Variations on Mean Temperature Measurement.

Page No. D-

1. Introduction 2

2. Analysis 2

3. One-Dimensional Solutions 4

4. Two-Dimensional Solutions 6

Figure D-1. Concept of thin film as simultaneous heater and resistance thermometer. 7

Figure D-2. Coordinate frame for finite thin film heater and resistance thermometer. 8

Figure D-3 Mean resistance temperatures of heater surface using series and parallel configurations 9

Figure D-4. Discrepancy between mean heater surface temperature and mean resistance temperature. 10

Figure D-5. Configurations used for assessment of discrepancies between the mean heater surface temperatures and the mean resistance temperatures for several Two-Dimensional configurations. $F_A = 50\%$. 11

1. Introduction

Figure D-1 presents the concept of using a thin gold film deposited on a quartz substrate as a simultaneous heater and resistance thermometer for surface temperature measurements with virtually instantaneous response characteristics. The relationship between temperature and resistance is obtained by calibration in an isothermal bath. The sketch represents a surface of infinite size, so that with no fluid motion the thermal behavior corresponds to two semi-infinite solids with a plane uniform heat source at the interface, described by One-Dimensional transient conduction. Computations of the surface temperature agree well with corresponding measurements. Once the fluid has been set in motion, whether by natural or forced convection or by boiling, the temperature at the interface can be expected to o longer be uniform. Since the resistance measured is the overall mean, the corresponding temperature of the interface computed from this resistance will be some type of a mean value.

In addition to the two-dimensional effects introduced at the interface by convection or boiling of the fluid, two-dimensional interface effects are caused by the three-dimensional conduction occurring in the substrate owing to the finite size of the heater. Such effects can be ameliorated by making the heater surface area as large as possible relative to the thickness of the transient boundary layers developing in the substrate, which will be a function of the thermal properties of the substrate and of the frequency of the thermal disturbances produced by the fluid. Sample computations of the three-dimensional substrate effects using a 3-D finite element model for the geometry here are presented in Section 6.1.1.

The relationship between the mean heater surface temperature defined on the basis of the surface area distribution and that determined from the measurement of the mean heater resistance will be examined here.

2. Analysis

Figure D-2 represents the rectangular thin film heater mounted on a large substrate, undefined for present purposes. Since the response time delay of the thin film to any temperature disturbances is negligibly small, the thin film being typically on the order of 400 Angstroms in thickness and its temperature being a function of the substrate surface temperature, a quasi-steady process will be assumed.

A heater surface temperature distribution T(x, y) is taken as a result of some heat transfer process to the fluid in contact with the heater. The mean heater surface temperature is defined as:

$$\overline{T} = \frac{1}{wL} \int_{o}^{L} \int_{o}^{w} T(x, y)\, dy\, dx \qquad (D.1)$$

The local resistance of the heater, R_N, may be expressed, in ohms/square, as:

$$R_N(T) = \left(\frac{\rho(T)}{\delta}\right) \tag{D.2}$$

ρ is the resistivity and δ is the uniform film thickness. The temperature functionality is determined by calibration, eliminating the necessity for determining δ, and thus:

$$R_N(T) = R_N(x, y) \tag{D.3}$$

The measurement of $\overline{R}$ in Figure D-2 (or its computation in the present case) involves the measurement of $\Delta E = E_1 - E_2$ and the total current I. For an arbitrary $R_N(x, y)$, the computation requires the solution of Kirchhoff's network law:

$$\frac{\partial}{\partial x}\left[\frac{1}{R_N}\left(\frac{\partial E}{\partial x}\right)\right] + \frac{\partial}{\partial y}\left[\frac{1}{R_N}\left(\frac{\partial E}{\partial y}\right)\right] = 0. \tag{D4}$$

subject to the boundary conditions:

$$\left.\begin{aligned} &E(o, y) = E_1 \\ &E(L, y) = E_2 \\ &\frac{\partial E}{\partial y}(x, o) = 0 \\ &\frac{\partial E}{\partial y}(x, w) = 0 \end{aligned}\right\} \tag{D.5}$$

The solution provides E(x, y), from which the current can be determined:

$$I_T = \int_{y=o}^{w} \frac{1}{R_N(o, y)}\left(\frac{\partial E}{\partial x}\right)(o, y)\,dy \tag{D.6}$$

The mean resistance is then given by:

$$\overline{R} = \frac{E_1 - E_2}{I_T} \tag{D.7}$$

from which a mean resistance temperature can be determined from the calibration curve determined isothermally. It can be anticipated that for a given mean temperature defined by Equation (D.1), various mean resistance temperatures can result, depending on the spatial distribution of the temperature over the surface. The solution constitutes a complex inverse problem, not amenable to a unique solution.

Lacking the possibility for a unique solution, the procedure to be followed here, to demonstrate that the mean resistance temperature is a reasonable approximation to the true mean

temperature, is an empirical one. A number of severe differences in temperature distributions, using reasonable maximum temperature differences encountered in prior measurements, will be examined for their effects on the difference between the mean temperature and the mean resistance temperature.

3. One-Dimensional Solutions

Two cases will be taken for two temperatures T_1 and T_2 on the plane heater as shown in Figure D.3. In (S), T_1 exists uniformly across the heater in the y-direction so that the resistance of T_1 and T_2 are in series (S), while on (P), T_1 exists uniformly down the heater in the x-direction so that the resistances of T_1 and T_2 are in parallel (P). The resulting analysis constitutes the One-Dimensional version of Equation (D.4).

The area fraction of the heater surface at T_1 for each of (S) and ()P) in Figure D-3 is defined as:

$$F_A = \left(\frac{x}{2w}\right)_s = \left(\frac{y}{w}\right)_p \tag{D.8}$$

For a thin film heater the resistance-temperature calibration is given as:

$$T\ (°F) = A_T + B_T \times R_T \tag{D.9}$$

From the post-flight calibration of the PBE-IB on STS-57, the constants A_T (Table III) and B_T for Run No. 2 (from the single-point calibration) are:

$$A_T = -\ 1358.5°F$$
$$BT = 427.32°F/ohm$$

For purposes of the analysis here, the resistance is expressed in terms of the temperature as:

$$R_T = A + BT\ = -\frac{A_T}{B_T} + \frac{T}{B_T} \tag{D.10}$$

The constants A and B become:

$$A = -\frac{A_T}{B_T} = 3.179116 \text{ ohm}$$

$$B = \frac{1}{B_T} = 0.00234017 \text{ ohm/°F}$$

Expressing the resistance of Equation (D.10) as ohms/square, since the current flows through two isothermal squares in series during calibrations, for the heater configuration used here:

$$R_N = A_N + B_N T \tag{D.11}$$

where now

A_N = 1.589558 ohms/square
B_N = 0.00117008 ohms/square -°F

From Equation D.1, the mean heater surface temperature is:

$$\overline{T} = F_A \times T_1 + (1 - F_A) \times T_2 \tag{D.12}$$

From measurements on the PBE-IB and -IC in STS-57 and STS-60, the maximum range of the mean heater surface temperatures were measured as 70°C - 120°C, except where significant dryout existed for a long period of time. For illustrative purposes here, this range of temperature is used as:

T_1 = 158°F $\quad$ R_{N1} = 1.774431 ohm/square
T_2 = 248°F $\quad$ R_{N2} = 1.879738 ohm/square

For configuration (S) in Figure D-3:

$$R_T = R_s = \left(\frac{x}{w}\right) \times R_{N1} + \left(2 - \frac{x}{w}\right) \times R_{N2} \tag{D.13}$$

where $\quad 0 \leq x \leq 2w$

For configuration (P) in Figure D-3

$$R_T = R_p = \frac{2 \times R_{N1} \times R_{N2}}{\left(1 - \frac{y}{w}\right) \times R_{N1} + \left(\frac{y}{w}\right) \times R_{N2}} \tag{D.14}$$

where $\quad 0 \leq y \leq 2w$

Expressing R_s and R_p, Equations (D.13) and (D.14), in terms of the area fraction F_A, Equation (D.8):

$$R_s = 2\,[R_{N2} - F_A (R_{N2} - R_{N1})] \tag{D.15}$$

$$R_p = \frac{2\, R_{N1}\, R_{N2}}{(1 - F_A)\, R_{N1} + F_A\, R_{N2}} \tag{D.16}$$

where $\quad 0 \leq F_A \leq 1$

Substituting Equation (D.15) or Equation (D.16) into Equation (D.9) then provides the respective mean resistance temperature of the heater surface, corresponding to configuration s(S) or (P). By substituting Equation (D.15) into Equation (D.9) it can be demonstrated that the functionality of the resulting mean resistance temperature of $\overline{T_s}$ on F_A is identical to that given by Equation (D.12). The discrepancy between the mean heater surface temperature defined by Equation (D.12) and the mean resistance temperature given by Equations (D.16) and (D.9) is plotted in Figure D-4 as a function of the Area Fraction F_A at temperature T_1 = 158°F, with T_2 = 248°F and using the heater surface resistance calibration given above for STS-57, Run No. 2.

It is noted that the maximum discrepancy of 1.3°F, is considerably below the absolute uncertainty of ±3°F in the heater surface temperature measurements. The instrumentation equipment sensitivities are capable of detecting changes of ± 1°F, however. The maximum discrepancy of 1.3°F takes place at $F_A = 0.5$, and this value will be used in configurations other than those of Figure D-3. It was determined that if linear variations in temperature take place within the domains in Figure D-3 such that the mean values of temperature are still T_1 and T_2, the discrepancies will be identical to those for uniform temperatures.

4. Two-Dimensional Solutions

As a final assessment of the adequacy of taking the mean resistance temperature as the mean temperature, the two-dimensional solutions of Equations (D.4) - (D.7) have been obtained by a finite difference numerical procedure for $F_A = 0.50$, which value was demonstrated above to produce the maximum discrepancy, for the four (4) cases (a) - (d), shown in Figure D-5. A grid of 48 × 96 nodes was used for each case, with approximately 30,000 iterations required to achieve satisfactory convergence. The resulting maximum discrepancies for each of the cases of Figure D-5 are included in Figure D-4, and are within the same range for the case studied in detail, so that the maximum discrepancy is within ± 1.5°F, less than the absolute uncertainty of ±3°F in the heater surface temperature measurement.

It is therefore concluded that the measured mean resistance temperature is a reasonable approximation to the area averaged mean temperature in the data analysis procedures followed for the PBE.

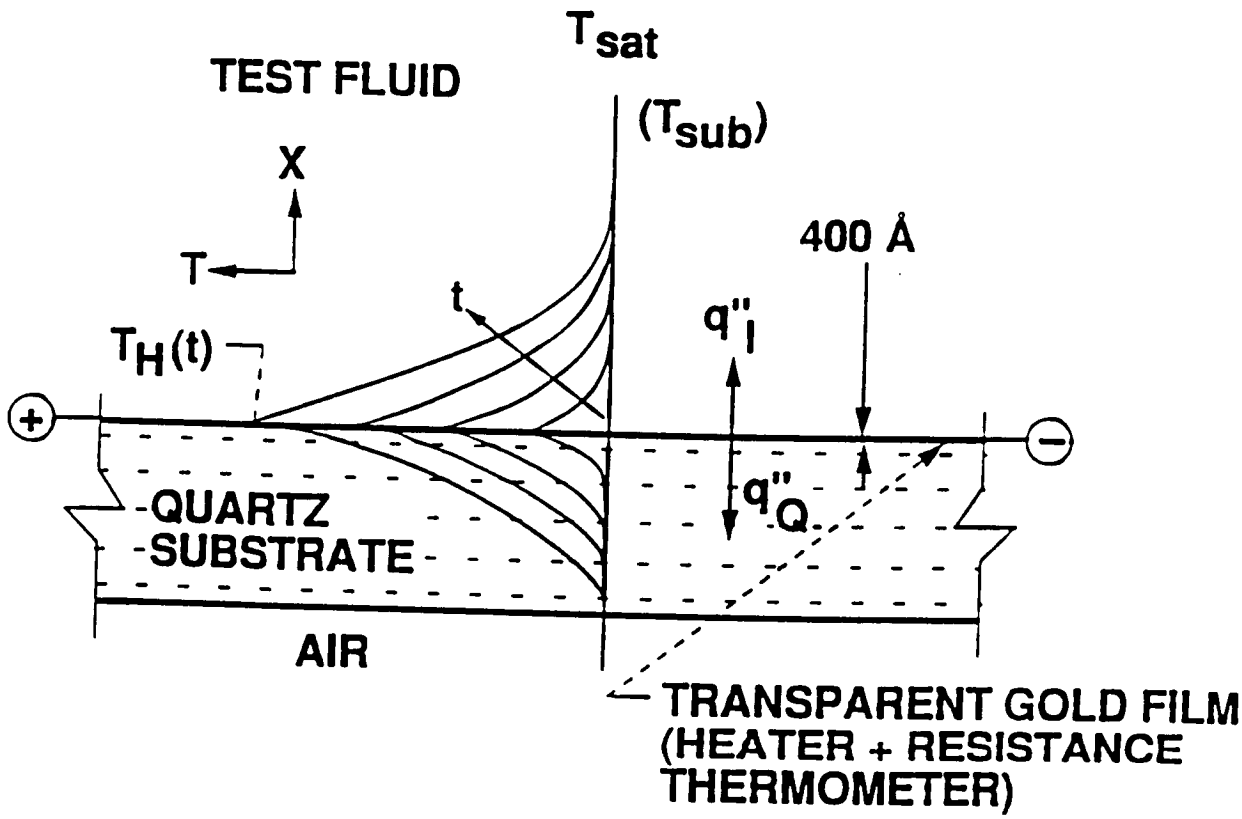

Figure D-1. Concept of thin film as simultaneous heater and resistance thermometer.

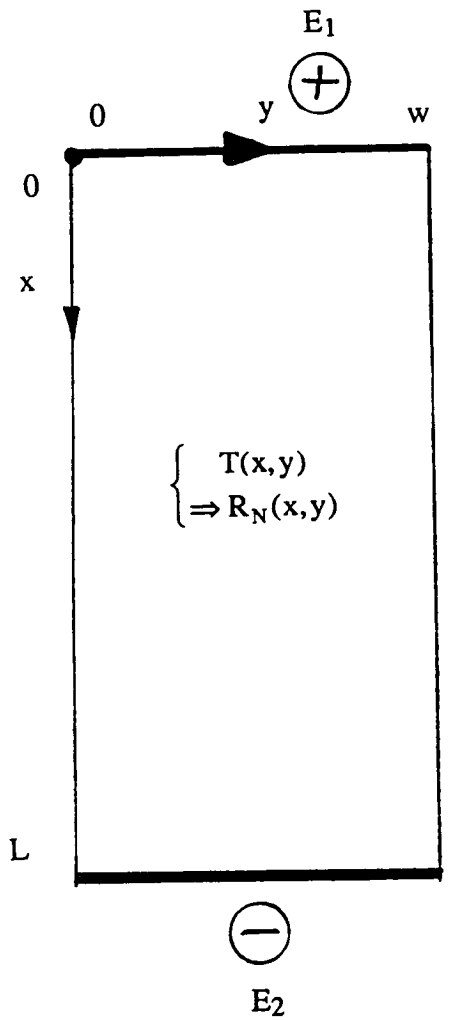

Figure D-2. Coordinate frame for finite thin film heater and resistance thermometer.

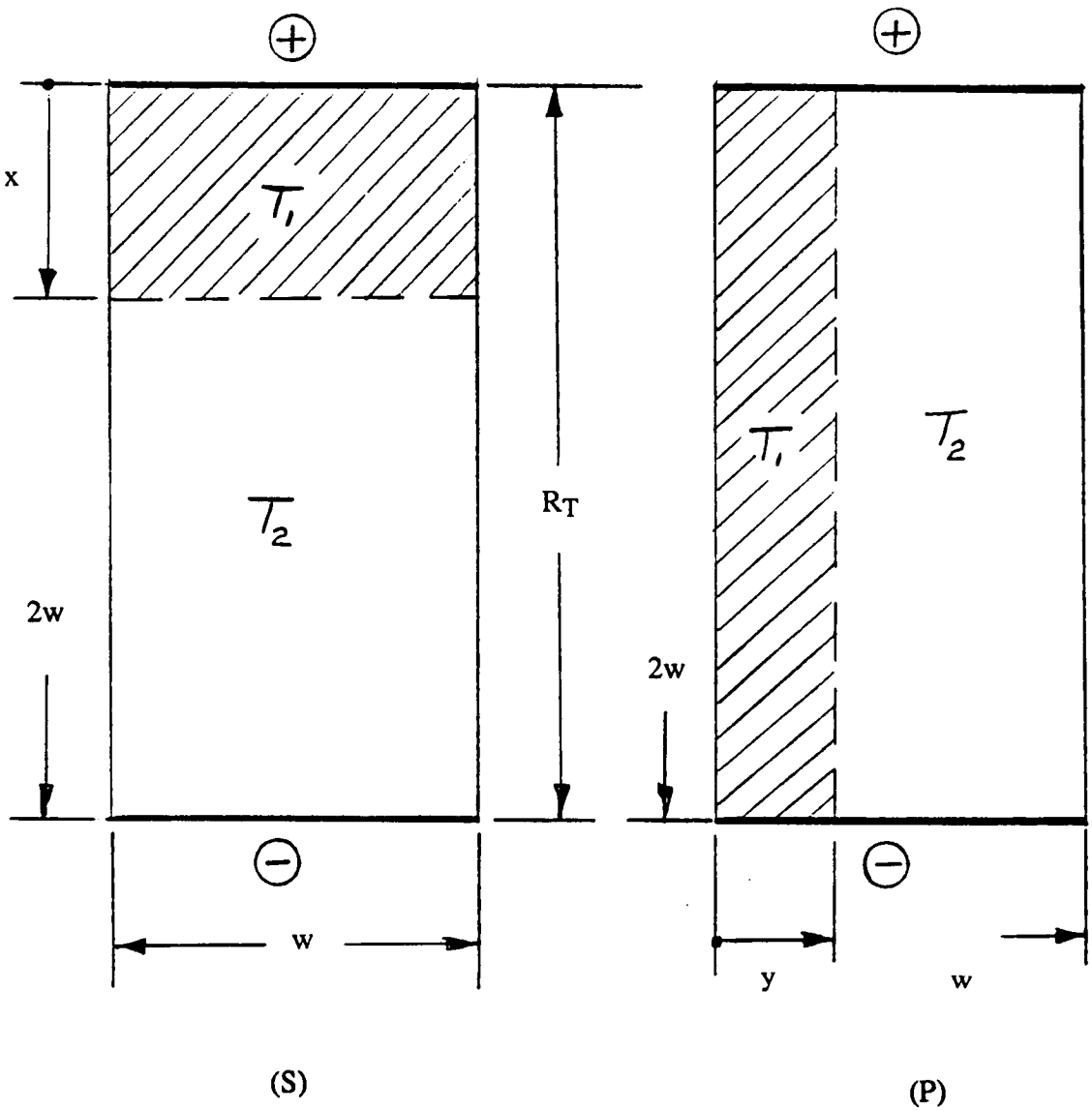

Figure D-3. Mean resistance temperatures of surface using series and parallel configurations.

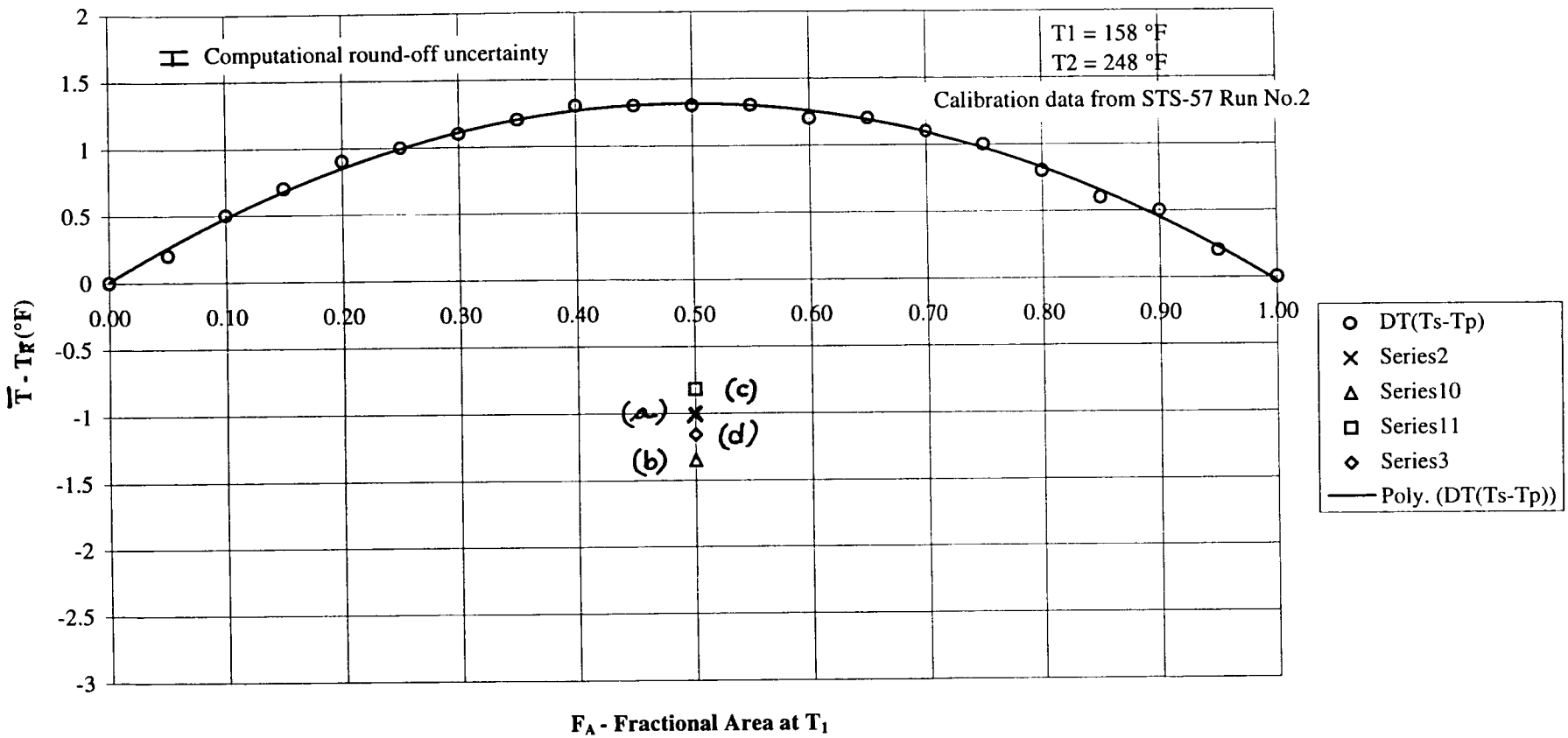

Figure D-4. Discrepancy between mean heater surface temperature and mean resistance temperature.

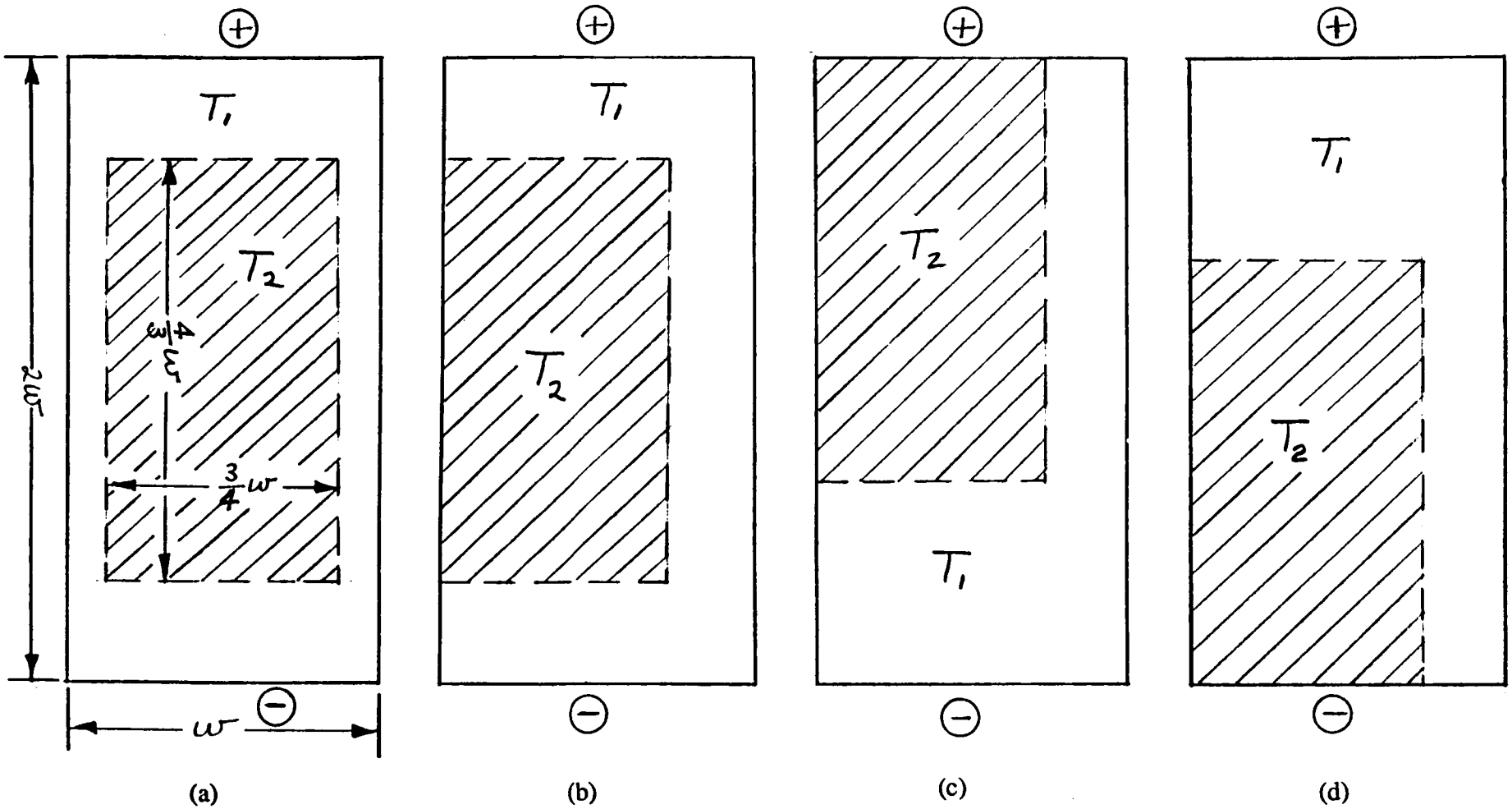

Figure D-5. Configurations used for assessment of discrepancies between the mean heater surface temperatures and the mean resistance temperatures for several Two-Dimensional configurations. $F_A = 50\%$.

Appendix E. Procedure for Computation of Mean Microgravity Nucleate Boiling Heat Transfer Coefficient

Page No. E-

1. Analysis 2

Figure E-1. Schematic representation of boiling observed on heater surface in microgravity. 5

Figure E-2. Heater surface representation from underside with defined terms 6

1. Analysis

The following will demonstrate how the measurements of the fractional dry portion of the heater area and the spatial mean heater surface temperatures $\overline{T}_w$ and heat transfer coefficients $\bar{h}_T$ may be related. Figure E-1 is a representation, from the underside, of the heater surface on which boiling is taking place in microgravity, and may be considered to be typical of, for example, Figure A-6b — Frame #0952 and Figure A-6c— Frame #2603, reproduced from digitized 16 mm frames from PBE-IA STS-47, Run Nos. 2 and 3, respectively, and are runs with the largest subcooling used. The dry portions of the heater surface are readily discernible in both cases, as is the nucleate boiling taking place over the remainder of the surface in Frame 0952 of Figure A-6b. These bubbles are then "absorbed" by the larger overlaying vapor bubble due to the action of the surface tension. In Frame 2603 of Figure A-6c, on the other hand, with the lower heat flux, part of the domain between the dry portion appears to be inactive in this frame. In reality, nucleate boiling is also occurring in these domains, but with a significantly smaller frequency and nucleation site density. It should be kept in mind that the pool boiling process in microgravity is inherently transient, because of the changing local subcooling and changing size of the overlaying vapor bubble, and consequently the nature of the local and average boiling processes will be changing as well.

Figure E-2 is a simplified representation of Figure E-1, and illustrates how the mean heater surface temperatures and heat transfer coefficients are defined for the dry and nucleate boiling areas as $\overline{T}_D$, $\bar{h}_D$ and $\overline{T}_B$, $\bar{h}_B$, respectively. The following additional definitions are made:

$$A_T = A_D + A_B \tag{E.1}$$

$$1 = \frac{A_D}{A_T} + \frac{A_B}{A_T} = F_D + F_B \tag{E.2}$$

where F_D and F_B are the fractional dry and nucleate boiling areas of the heater surface, respectively.

$$q''_T = q_T/A_T \tag{E.3}$$

$$\overline{T}_w = F_D \times \overline{T}_D + F_B \times \overline{T}_B \tag{E.4}$$

The overall mean heat transfer coefficient:

$$\bar{h}_T = q''_T/\left(\overline{T}_w - T_{sat}\right) = q''_T/\Delta\overline{T}_w \tag{E.5}$$

$$q_T = q_D + q_B \tag{E.6}$$

$$q''_T = \frac{q_T}{A_T} = \frac{q_D}{A_T} + \frac{q_B}{A_T} = \frac{A_D}{A_T} \times q''_D + \frac{A_B}{A_T} \times q''_B = F_D \times q''_D + F_B \times q''_B \tag{E.7}$$

The mean heat transfer coefficient on the dry portion of the heater surface is:

$$\bar{h}_D = q''_D/(\overline{T}_D - T_{sat}) = q''_D/\overline{\Delta T}_D \tag{E.8}$$

The mean heat transfer coefficient on the nucleate boiling portion of the heater surface is:

$$\bar{h}_B = q''_B/(\overline{T}_B - T_{sat}) = q''_B/\overline{\Delta T}_B \tag{E.9}$$

From Equations (E.5), (E.7) - (E.9):

$$q''_T = \bar{h}_T \times \overline{\Delta T}_w = F_D \times \bar{h}_D \times \overline{\Delta T}_D + F_B \times \bar{h}_B \text{ x } \overline{\Delta T}_B \tag{E.10}$$

From Equation (E.10):

$$\bar{h}_T = F_D \times \bar{h}_D \times \frac{\overline{\Delta T}_D}{\overline{\Delta T}_w} + F_B \times \bar{h}_B \times \frac{\overline{\Delta T}_B}{\overline{\Delta T}_w} \tag{E.11}$$

If, as an approximation, $\bar{h}_B$ can be considered constant for a given heat flux input and bulk liquid subcooling, and also if $\bar{h}_B >> \bar{h}_D$ and $\overline{\Delta T}_B/\overline{\Delta T}_w \approx 1$, then from Equation (E.11):

$$\bar{h}_B = \frac{\bar{h}_B}{F_B} = \frac{\bar{h}_T}{(1 - F_D)} \tag{E.12}$$

Both $\bar{h}_T$ and F_D are independently measurable quantities, and the supposition as to the constancy of $\bar{h}_B$ thus can be tested. Should this prove to be the case, then the total heat transfer rate could be approximated, from Equations (E.3), (E.5) and (E.12) as:

$$q_T = A_T \times (1 - F_D) \times \bar{h}_B \times \overline{\Delta T}_w \tag{E.13}$$

The heat transfer coefficient $\bar{h}_B$ defined by Equation (E.12) could be viewed, in these circumstances, as a microgravity nucleate pool boiling heat transfer coefficient. The assumptions made in its development are summarized:

(a) $\bar{h}_B \approx$ constant

(b) $\bar{h}_B >> \bar{h}_D$

(c) $\overline{\Delta T}_B / \overline{\Delta T}_w \approx 1$

where $\overline{\Delta T}_B$ and $\overline{\Delta T}_w$ are defined in Equations (E.9) and (E.5), respectively.

An additional assumption was implied:

(d) $F_B \neq \approx 0$

This last condition is related to the fact that F_D is measured, and in Equation (E.12) the measured $\bar{h}_T$ is divided by $F_B = 1 - F_D$. If F_D is close to unity, then F_B is close to zero, and the relative uncertainty can become quite large. The limit to which F_D can approach unity for these calculations is as yet unknown; as is shown in Figures 10 of Appendices A, B, C, measurements up to $F_D = 0.95$ have been made.

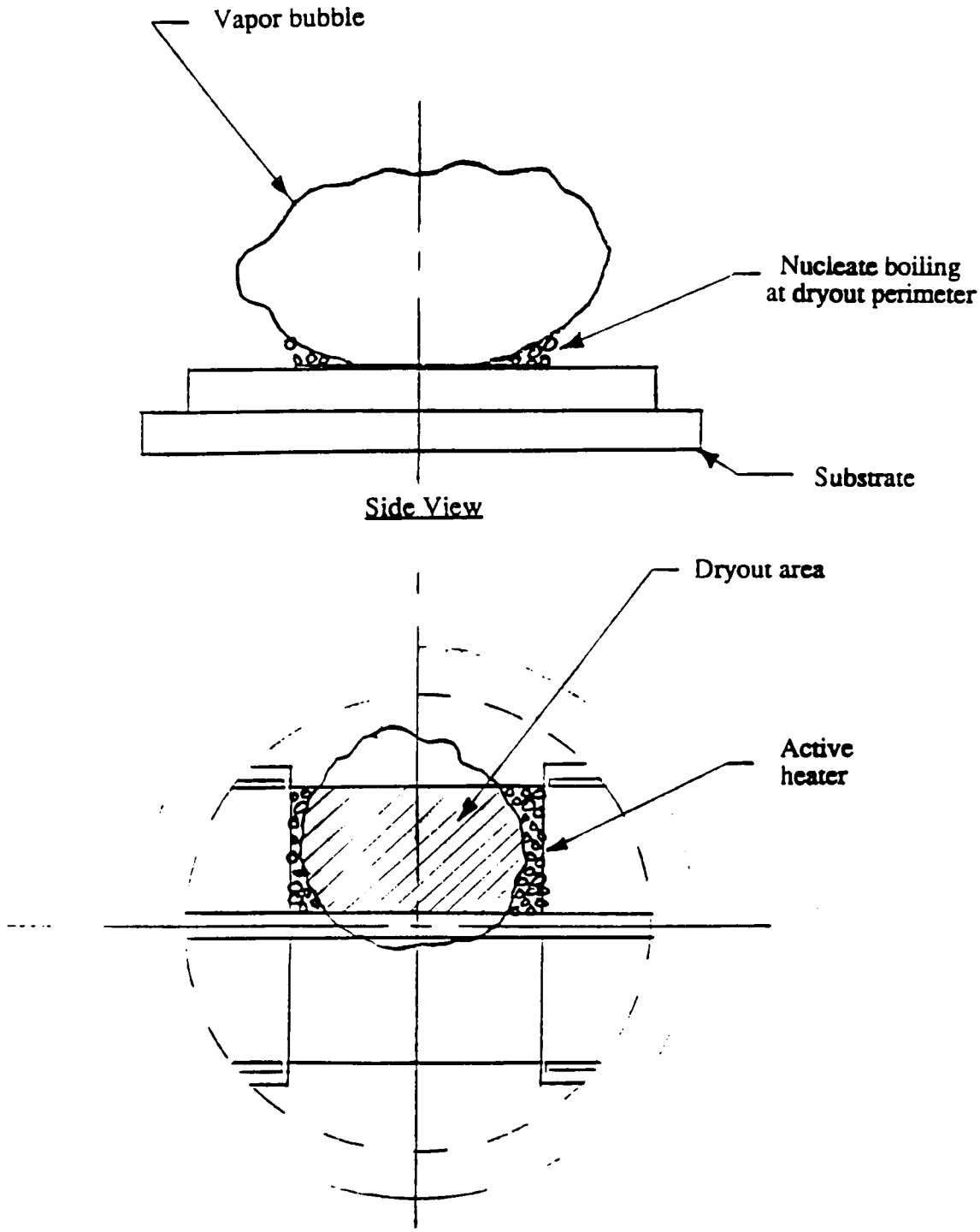

Figure E-1. Schematic representation of boiling observed on heater surface in microravity.

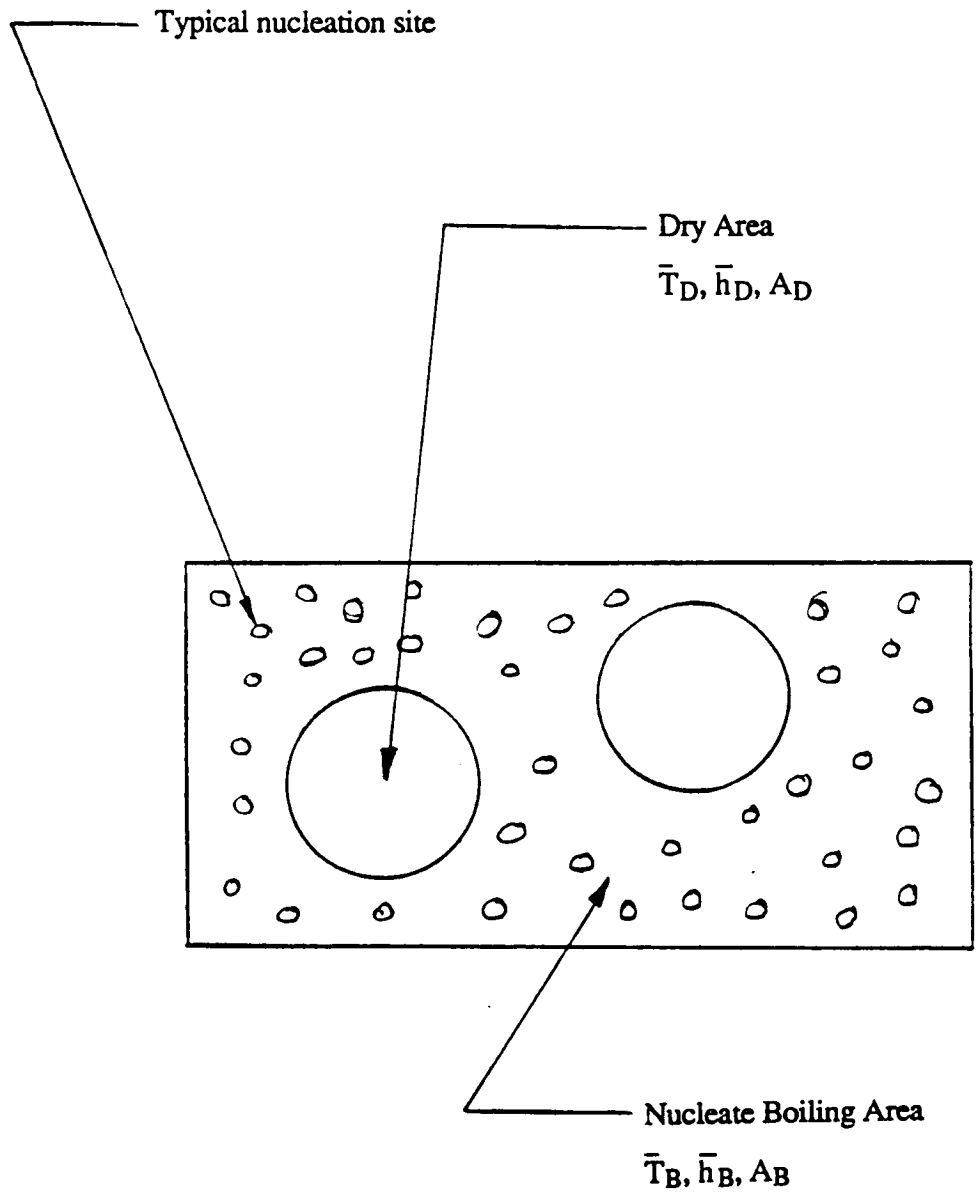

Figure E-2. Heater surface representation from underside with defined terms.

REPORT DOCUMENTATION PAGE

Form Approved
OMB No. 0704-0188

Public reporting burden for this collection of information is estimated to average 1 hour per response, including the time for reviewing instructions, searching existing data sources, gathering and maintaining the data needed, and completing and reviewing the collection of information. Send comments regarding this burden estimate or any other aspect of this collection of information, including suggestions for reducing this burden, to Washington Headquarters Services, Directorate for Information Operations and Reports, 1215 Jefferson Davis Highway, Suite 1204, Arlington, VA 22202-4302, and to the Office of Management and Budget, Paperwork Reduction Project (0704-0188), Washington, DC 20503.

1. AGENCY USE ONLY (*Leave blank*)

2. REPORT DATE
March 1996

3. REPORT TYPE AND DATES COVERED
Final Contractor Report

4. TITLE AND SUBTITLE
Report on Pool Boiling Experiment Flown on STS-47 (PBE-IA), STS-57 (PBE-IB), and STS-60 (PBE-IC)

5. FUNDING NUMBERS
WU–694–03–03
C–NAS3–25812

6. AUTHOR(S)
Herman Merte, Jr., Ho Sung Lee, and Robert B. Keller

7. PERFORMING ORGANIZATION NAME(S) AND ADDRESS(ES)
College of Engineering
The University of Michigan
Department of Mechanical Engineering and Applied Mechanics
Ann Arbor, Michigan 48109

8. PERFORMING ORGANIZATION REPORT NUMBER
E–10154

9. SPONSORING/MONITORING AGENCY NAME(S) AND ADDRESS(ES)
National Aeronautics and Space Administration
Lewis Research Center
Cleveland, Ohio 44135–3191

10. SPONSORING/MONITORING AGENCY REPORT NUMBER
NASA CR–198465
UM–MEAM–95–01

11. SUPPLEMENTARY NOTES
Project Manager, Francis P. Chiaramonte, Space Experiments Division, NASA Lewis Research Center, organization code 6712, (216) 433–8040.

12a. DISTRIBUTION/AVAILABILITY STATEMENT
Unclassified - Unlimited
Subject Category 34

This publication is available from the NASA Center for Aerospace Information, (301) 621–0390.

12b. DISTRIBUTION CODE

13. ABSTRACT (*Maximum 200 words*)

Experiments were conducted in the microgravity of space in which a pool of liquid (R-113), initially at a precisely defined pressure and temperature, is subjected to a step imposed heat flux from a semi-transparent thin-film heater forming part of one wall of the container such that boiling is initiated and maintained for a defined period of time at a constant pressure level. Transient measurements of the heater surface and fluid temperatures near the surface are made, noting in particular the conditions at the onset of boiling, along with motion photography of the boiling process in two simultaneous views, from beneath the heating surface and from the side. The conduct of the experiment and the data acquisitions are completely automated and self-contained. A total of nine tests were conducted at three levels of heat flux and three levels of subcooling under three essentially identical circumstances in three space experiments designated as PBE-IA, -IB, -IC on the STS-47, -57, -60, respectively. Minor differences in lengths of various components of the experiments were programmed in the three flights. Two of the flights (STS-47, -60) took place with the same physical hardware, while the other (STS-57) used an identically fabricated hardware. The basic mechanisms of pool boiling are reviewed, with particular emphasis on the roles of buoyancy, and the experimental concepts and parameters used are given. The hardware and operating procedures followed are described in some detail. The experimental results for each of the nine (9) Runs in each of the space flights, along with those from several post-flight ground tests, are given in sufficient detail that the derived parameters and conclusions can be independently obtained, if desired. Sample images are provided for each Run, following digitizing from the 16 mm film. The absence of buoyancy permitted the onset of boiling at low heat flux levels, with what is deemed as homogeneous nucleation taking place. The influence of these low levels of heat flux and the pressure effect used to produce the bulk liquid subcooling are accounted for by a modification of classical homogeneous nucleation theory. The high levels of liquid superheat at nucleation produced extremely energetic bubble growth rates, which resulted in unusual interfacial behaviors. In certain circumstances vapor bubbles appear to be formed both within the residual liquid microlayer remaining on the surface as the primary boiling front passes by, and in advance of this front. It appears that long term steady nucleate boiling can take place on a flat heater surface in microgravity under special conditions in which a large vapor bubble somewhat removed from the heater surface is formed, which acts as a thermal sink to remove the nucleating bubbles from the heater surface. The steady nucleate boiling heat transfer is enhanced significantly compared to that in earth gravity. Using quasi-steady data obtained from the measurements it was possible to construct two distinct composite approximate micro-gravity pool boiling curves for R-113, one for the higher level of subcooling and one for the lower level of subcooling. This is compared with a Reference Curve for pool boiling at $a/g = +1$. The microgravity pool boiling curves bear some resemblance to the Reference Curve, although the maximum heat flux is reduced considerably.

14. SUBJECT TERMS
Nucleate pool boiling; Long-term microgravity; Shuttle missions; Thin gold film heater; Fluorocarbon R113; Get Away Special canister

15. NUMBER OF PAGES
623

16. PRICE CODE
A99

17. SECURITY CLASSIFICATION OF REPORT
Unclassified

18. SECURITY CLASSIFICATION OF THIS PAGE
Unclassified

19. SECURITY CLASSIFICATION OF ABSTRACT
Unclassified

20. LIMITATION OF ABSTRACT